

به نام خدا



مرکز دانلود رایگان مهندسی متالورژی و مواد

www.Iran-mavad.com



HANDBOOK OF APPLIED SURFACE AND COLLOID CHEMISTRY

Volume 2

Edited by

Krister Holmberg

*Chalmers University of Technology,
Göteborg, Sweden*

Associate Editors

Dinesh O. Shah

*University of Florida,
USA*

Milan J. Schwuger

*Forschungszentrum Jülich GmbH,
Germany*



JOHN WILEY & SONS, LTD

Copyright © 2002 by John Wiley & Sons Ltd,
Baffins Lane, Chichester,
West Sussex PO19 1UD, England

National 01243 779777
International (+44) 1243 779777
e-mail (for orders and customer service enquiries): cs-books@wiley.co.uk
Visit our Home Page on <http://www.wiley.co.uk>
or <http://www.wiley.com>

All Rights Reserved. No part of this publication may be reproduced, stored in a retrieval system, or transmitted, in any form or by any means, electronic, mechanical, photocopying, recording, scanning or otherwise, except under the terms of the Copyright, Designs and Patents Act 1988 or under the terms of a licence issued by the Copyright Licensing Agency Ltd, 90 Tottenham Court Road, London, UK W1P 0LP, without the permission in writing of the publisher and the copyright holder.

Other Wiley Editorial Offices

John Wiley & Sons, Inc., 605 Third Avenue,
New York, NY 10158-0012, USA

Wiley-VCH GmbH, Pappelallee 3,
D-69469 Weinheim, Germany

John Wiley & Sons Australia Ltd, 33 Park Road, Milton,
Queensland 4064, Australia

John Wiley & Sons (Asia) Pte Ltd, 2 Clementi Loop #02-01,
Jin Xing Distripark, Singapore 0512

John Wiley & Sons (Canada) Ltd, 22 Worcester Road,
Rexdale, Ontario M9W 1L1, Canada

Library of Congress Cataloging-in-Publication Data

Handbook of applied surface and colloid chemistry / edited by Krister Holmberg.
p.cm.

Includes bibliographical references and index.

ISBN 0-471-49083-0 (alk. paper)

1. Chemistry, Technical. 2. Surface chemistry. 3. Colloids. I. Holmberg, Krister, 1946-

TP149 .H283 2001
660 – dc21

2001024347

British Library Cataloguing in Publication Data

A catalogue record for this book is available from the British Library

ISBN 0-471-49083-0

Typeset in 9/11pt Times Roman by Laser Words Pvt. Ltd., Chennai, India.

Printed and bound in Great Britain by Antony Rowe Ltd. Chippenham, Wiltshire.

This book is printed on acid-free paper responsibly manufactured from sustainable forestry, in which a for each one used for paper production.

Contents – Volume 2

Contributors List	ix	CHAPTER 7 Wetting, Spreading and Penetration	119
Foreword <i>Brian Vincent</i>	xiii	<i>Karina Grundke</i>	
Preface	xv	CHAPTER 8 Foam Breaking in Aqueous Systems	143
PART 3 Colloidal Systems and Layer Structures at Surfaces	1	<i>Robert J. Pugh</i>	
CHAPTER 1 Solid Dispersions	3	CHAPTER 9 Solubilization	159
<i>Staffan Wall</i>		<i>Thomas Zemb and Fabienne Testard</i>	
CHAPTER 2 Foams and Foaming	23	CHAPTER 10 Rheological Effects in Surfactant Phases	189
<i>Robert J. Pugh</i>		<i>Heinz Hoffmann and Werner Ulbricht</i>	
CHAPTER 3 Vesicles	45	PART 5 Analysis and Characterization in Surface Chemistry	215
<i>Brian H. Robinson and Madeleine Rogerson</i>		CHAPTER 11 Measuring Equilibrium Surface Tensions	217
CHAPTER 4 Microemulsions	55	<i>Michael Mulqueen and Paul D. T. Huibers</i>	
<i>Klaus Wormuth, Oliver Lade, Markus Lade and Reinhard Schomäcker</i>		CHAPTER 12 Measuring Dynamic Surface Tensions	225
CHAPTER 5 Langmuir–Blodgett Films	79	<i>Reinhard Miller, Valentin B. Fainerman, Alexander V. Makievski, Michele Ferrari and Giuseppe Loglio</i>	
<i>Hubert Motschmann and Helmuth Möhwald</i>		CHAPTER 13 Determining Critical Micelle Concentration	239
CHAPTER 6 Self-Assembling Monolayers: Alkane Thiols on Gold	99	<i>Alexander Patist</i>	
<i>Dennis S. Everhart</i>			
PART 4 Phenomena in Surface Chemistry	117		

CHAPTER 14	Measuring Contact Angle	251	CHAPTER 19	Measurement of Electrokinetic Phenomena in Surface Chemistry	371
	<i>C. N. Catherine Lam, James J. Lu and A. Wilhelm Neumann</i>			<i>Norman L. Burns</i>	
CHAPTER 15	Measuring Micelle Size and Shape	281	CHAPTER 20	Measuring Interactions between Surfaces	383
	<i>Magnus Nydén</i>			<i>Per M. Claesson and Mark W. Rutland</i>	
CHAPTER 16	Identification of Lyotropic Liquid Crystalline Mesophases	299	CHAPTER 21	Measuring the Forces and Stability of Thin-Liquid Films	415
	<i>Stephen T. Hyde</i>			<i>Vance Bergeron</i>	
CHAPTER 17	Characterization of Microemulsion Structure	333	CHAPTER 22	Measuring Adsorption	435
	<i>Ulf Olsson</i>			<i>Bengt Kronberg</i>	
CHAPTER 18	Measuring Particle Size by Light Scattering	357	Index – Volume 2		445
	<i>Michal Borkovec</i>		Index – Volume 1		455
			Cumulative Index		467

Contents – Volume 1

Contributors List	ix	CHAPTER 7 Surface Chemistry of Paper . .	123
Foreword <i>Brian Vincent</i>	xiii	<i>Fredrik Tiberg, John Daicic and Johan Fröberg</i>	
Preface	xv	CHAPTER 8 Surface Chemistry in the Polymerization of Emulsion . .	175
PART 1 Surface Chemistry in Important Technologies	1	<i>Klaus Tauer</i>	
CHAPTER 1 Surface Chemistry in Pharmacy	3	CHAPTER 9 Colloidal Processing of Ceramics	201
<i>Martin Malmsten</i>		<i>Lennart Bergström</i>	
CHAPTER 2 Surface Chemistry in Food and Feed	39	CHAPTER 10 Surface Chemistry in Dispersion, Flocculation and Flotation	219
<i>Björn Bergenståhl</i>		<i>Brij M. Moudgil, Pankaj K. Singh and Joshua J. Adler</i>	
CHAPTER 3 Surface Chemistry in Detergency	53	CHAPTER 11 Surface Chemistry in the Petroleum Industry	251
<i>Wolfgang von Rybinski</i>		<i>James R. Kanicky, Juan-Carlos Lopez-Montilla, Samir Pandey and Dinesh O. Shah</i>	
CHAPTER 4 Surface Chemistry in Agriculture	73	PART 2 Surfactants	269
<i>Tharwat F. Tadros</i>		CHAPTER 12 Anionic Surfactants	271
CHAPTER 5 Surface and Colloid Chemistry in Photographic Technology	85	<i>Antje Schmalstieg and Guenther W. Wasow</i>	
<i>John Texter</i>		CHAPTER 13 Nonionic Surfactants	293
CHAPTER 6 Surface Chemistry in Paints . .	105	<i>Michael F. Cox</i>	
<i>Krister Holmberg</i>		CHAPTER 14 Cationic Surfactants	309
		<i>Dale S. Steichen</i>	

CHAPTER 15	Zwitterionic and Amphoteric Surfactants	349	CHAPTER 20	Surfactant–Polymer Systems	445
	<i>David T. Floyd, Christoph Schunicht and Burghard Gruening</i>			<i>Björn Lindman</i>	
CHAPTER 16	Polymeric Surfactants	373	CHAPTER 21	Surfactant Liquid Crystals . . .	465
	<i>Tharwat F. Tadros</i>			<i>Syed Hassan, William Rowe and Gordon J. T. Tiddy</i>	
CHAPTER 17	Speciality Surfactants	385	CHAPTER 22	Environmental Aspects of Surfactants	509
	<i>Krister Holmberg</i>			<i>Lothar Huber and Lutz Nitschke</i>	
CHAPTER 18	Hydrotropes	407	CHAPTER 23	Molecular Dynamics Computer Simulations of Surfactants . . .	537
	<i>Anna Matero</i>			<i>Hubert Kuhn and Heinz Rehage</i>	
CHAPTER 19	Physico-Chemical Properties of Surfactants	421			
	<i>Björn Lindman</i>				

Contributors List

Joshua J. Adler

Department of Materials Science and Engineering, and Engineering Research Center for Particle Science and Technology, PO Box 116135, University of Florida, Gainesville, FL-32611, USA

Björn Bergenståhl

Department of Food Technology, Center for Chemistry and Chemical Engineering, Lund University, PO Box 124, SE-221 00 Lund, Sweden

Vance Bergeron

Ecole Normale Supérieure, Laboratoire de Physique Statistique, 24 Rue Lhomond 75231, Paris CEDEX 05, France

Lennart Bergström

Institute for Surface Chemistry, PO Box 5607, SE-114 86 Stockholm, Sweden

Michal Borkovec

Department of Inorganic, Analytical and Applied Chemistry, CABB, University of Geneva, Sciences II, 30 quai Ernest Ansermet, CH-1211 Geneva 4, Switzerland

Norman L. Burns

Amersham Pharmacia Biotech, 928 East Arques Avenue, Sunnyvale, CA 94085-4520, USA

Per M. Claesson

Department of Chemistry, Surface Chemistry, Royal Institute of Technology, SE-100 44 Stockholm, Sweden and Institute for Surface Chemistry, PO Box 5607, SE-114 86 Stockholm, Sweden

Michael F. Cox

Sasol North America, Inc., PO Box 200135, 12024 Vista Parke Drive, Austin, TX-78726, USA

John Daicic

Institute for Surface Chemistry, PO Box 5607, SE-114 86 Stockholm, Sweden

Dennis S. Everhart

Kimberly Clark Corporation, 1400, Holcombe Bridge Road, Roswell, GA-30076-2199, USA

Valentin B. Fainerman

International Medical Physicochemical Centre, Donetsk Medical University, 16 Ilych Avenue, Donetsk 340003, Ukraine

Michele Ferrari

CNR – Istituto di Chimica Fisica Applicata dei Materiali, Via De Marini 6, I-16149 Genova, Italy

David T. Floyd

Degussa-Goldschmidt Care Specialties, PO Box 1299, 914, East Randolph Road, Hopewell, VA-23860, USA

Johan Fröberg

Institute for Surface Chemistry, PO Box 5607, SE-114 86 Stockholm, Sweden

Burghard Gruening

Degussa-Goldschmidt Care Specialties, Goldschmidtstrasse 100, D-45127 Essen, Germany

Karina Grundke

Institute of Polymer Research Dresden, Hohe Strasse 6, D-01069 Dresden, Germany

Syed Hassan

Department of Chemical Engineering, UMIST, PO Box 88, Manchester, M60 1QD, UK

Heinz Hoffmann

Lehrstuhl für Physikalische Chemie I der Universität Bayreuth, Universitätsstrasse 30, D-95447 Bayreuth, Germany

Krister Holmberg

Department of Applied Surface Chemistry, Chalmers University of Technology, SE-412 96 Göteborg, Sweden

Lothar Huber

Adam Bergstrasse 1B, D-81735 München, Germany

Paul D. T. Huibers

Department of Chemical Engineering, Massachusetts Institute of Technology, Cambridge, MA 02139-4307, USA

Stephen T. Hyde

Applied Mathematics Department, Research School of Physical Sciences, Australia National University, Canberra 0200, Australia

James R. Kanicky

Center for Surface Science and Engineering, Departments of Chemical Engineering and Anesthesiology, PO Box 116005, University of Florida, Gainesville, FL-32611, USA

Bengt Kronberg

Institute for Surface Chemistry, PO Box 5607, SE-114 86 Stockholm, Sweden

Hubert Kuhn

Department of Physical Chemistry, University of Essen, Universitaetsstrasse 3-5, D-45141 Essen, Germany

Markus Lade

Institute for Technical Chemistry, Technical University of Berlin, Sekr. TC 8, Strasse der 17 Juni 124, D-10623 Berlin, Germany

Oliver Lade

Institute for Physical Chemistry, University of Cologne, Luxemburger Strasse 116, D-50939 Cologne, Germany

C. N. Catherine Lam

Department of Mechanical and Industrial Engineering, University of Toronto, 5 King's College Road, M5S 3G8 Toronto, Ontario, Canada

Björn Lindman

Department of Physical Chemistry 1, Chemical Center, Lund University, PO Box 124, SE-221 00 Lund, Sweden

Giuseppe Loglio

Department of Organic Chemistry, University of Florence, Via G. Capponi 9, 50121 Florence, Italy

James J. Lu

Department of Mechanical and Industrial Engineering, University of Toronto, 5 King's College Road, M5S 3G8 Toronto, Ontario, Canada

Alexander V. Makievski

International Medical Physicochemical Centre, Donetsk Medical University, 16 Ilych Avenue, Donetsk 340003, Ukraine

Martin Malmsten

Institute for Surface Chemistry and Royal Institute of Technology, PO Box 5607, SE-114 86 Stockholm, Sweden

Anna Matero

Institute for Surface Chemistry, PO Box 5607, SE-114 86 Stockholm, Sweden

Reinhard Miller

Max-Planck-Institute of Colloids and Interfaces, Am Mühlenberg, D-14476 Golm, Germany

Helmuth Möhwald

Max-Planck-Institute of Colloids and Interfaces, Am Mühlenberg, D-14476 Golm, Germany

Juan-Carlos Lopez-Montilla

Center for Surface Science and Engineering, Departments of Chemical Engineering and Anesthesiology, PO Box 116005, University of Florida, Gainesville, FL-32611, USA

Hubert Motschmann

Max-Planck-Institute of Colloids and Interfaces, Am Mühlenberg, D-14476 Golm, Germany

Brij M. Moudgil

Department of Materials Science and Engineering, and Engineering Research Center for Particle Science and Technology, PO Box 116135, University of Florida, Gainesville, FL-32611, USA

Michael Mulqueen

Department of Chemical Engineering, Massachusetts Institute of Technology, Cambridge, MA 02139-4307, USA

A. Wilhelm Neumann

Department of Mechanical and Industrial Engineering, University of Toronto, 5 King's College Road, M5S 3G8 Toronto, Ontario, Canada

Lutz Nitschke

Karwendelstrasse 47, D-85560 Ebersberg, Germany

Magnus Nydén

Department of Applied Surface Chemistry, Chalmers University of Technology, SE-412 96 Göteborg, Sweden

Ulf Olsson

Department of Physical Chemistry 1, Center for Chemistry and Chemical Engineering, PO Box 124, S-221 00 Lund, Sweden

Samir Pandey

Center for Surface Science and Engineering, Departments of Chemical Engineering and Anesthesiology, PO Box 116005, University of Florida, Gainesville, FL-32611, USA

Alexander Patist

Cargill Inc., Central Research, 2301 Crosby Road, Wayzata, MN-55391, USA

Robert J. Pugh

Institute for Surface Chemistry, PO Box 5607, SE-114 86 Stockholm, Sweden

Heinz Rehage

Department of Physical Chemistry, University of Essen, Universitaetsstrasse 3-5, D-45141 Essen, Germany

Brian H. Robinson

School of Chemical Sciences, University of East Anglia, Norwich, Norfolk, NR4 7TJ, UK

Madeleine Rogerson

School of Chemical Sciences, University of East Anglia, Norwich, Norfolk, NR4 7TJ, UK

William Rowe

Department of Chemical Engineering, UMIST, PO Box 88, Manchester, M60 1QD, UK

Mark W. Rutland

Department of Chemistry, Surface Chemistry, Royal Institute of Technology, SE-100 44 Stockholm, Sweden *and* Institute for Surface Chemistry, PO Box 5607, SE-114 86 Stockholm, Sweden

Wolfgang von Rybinski

Henkel KgaA, Henkelstrasse 67, D-40191 Düsseldorf, Germany

Antje Schmalstieg

Thaerstrasse 23, D-10249 Berlin, Germany

Reinhard Schomäcker

Institute for Technical Chemistry, Technical University of Berlin, Sekr. TC 8, Strasse des 17 Juni 124, D-10623 Berlin, Germany

Christoph Schunicht

Degussa-Goldschmidt Care Specialties, Goldschmidtstrasse 100, D-45127 Essen, Germany

Dinesh O. Shah

Center for Surface Science and Engineering, Departments of Chemical Engineering and Anesthesiology, PO Box 116005, University of Florida, Gainesville, FL-32611, USA

Pankaj K. Singh

Department of Materials Science and Engineering, and Engineering Research Center for Particle Science and Technology, PO Box 116135, University of Florida, Gainesville, FL-32611, USA

Dale S. Steichen

Akzo Nobel Surface Chemistry AB, SE-444 85 Stenungsund, Sweden

Tharwat F. Tadros

89, Nash Grove Lane, Wokingham, Berkshire, RG40 4HE, UK

Klaus Tauer

Max Planck Institute of Colloids and Interfaces, D-14424 Golm, Germany

Fabienne Testard

Service de Chimie Moléculaire, CE Saclay, Batelle 125, F-91191 Gif-sur-Yvette, France

John Texter

Strider Research Corporation, 265 Clover Street,
Rochester, NY 14610-2246, USA

Fredrik Tiberg

Institute for Surface Chemistry, PO Box 5607, SE-114
86 Stockholm, Sweden

Gordon J. T. Tiddy

Department of Chemical Engineering, UMIST, PO Box
88, Manchester, M60 1QD, UK

Werner Ulbricht

Lehrstuhl für Physikalische Chemie I der Universität
Bayreuth, Universitätsstrasse 30, D-95447 Bayreuth,
Germany

Staffan Wall

Department of Chemistry, Physical Chemistry, Göteborg
Universitet, SE-412 96 Göteborg, Sweden

Guenther W. Wasow

Karl-Marx-Alle 133, D-10243 Berlin, Germany

Klaus Wormuth

Institute for Technical Chemistry, Technical University
of Berlin, Sekr. TC 8, Strasse des 17 Juni 124, D-10623
Berlin, Germany

Thomas Zemb

Service de Chimie Moléculaire, CE Saclay, Batelle 125,
F-999 91 Gif-sur-Yvette, France

Foreword

I am delighted to have been given the opportunity to write a *Foreword* for this important, landmark book in Surface and Colloid Chemistry. It is the first major book of its kind to review, in such a wide-ranging and comprehensive manner, the more technical, applied aspects of the subject. Yet it does not skip the fundamentals. It would have been wrong to have done so. After all, chemical technology is the application of chemical knowledge to produce new products and processes, and to control better existing ones. One cannot achieve these objectives without a thorough understanding of the relevant fundamentals. An attractive feature of this book is that the author of each chapter has been given the freedom to present, as he/she sees fit, the spectrum of the relevant science, from pure to applied, in his/her particular topic. Of course this approach inevitably leads to some overlap and repetition in different chapters, but that does not necessarily matter. Fortunately, the editor has not taken a "hard-line" on this. This arrangement should be extremely useful to the reader (even if it makes the book look longer), since one does not have to search around in different chapters for various bits of related information. Furthermore, any author will naturally have his own views on, and approach to, a specific topic, moulded by his own experience. It is often useful for someone else, particularly a newcomer, wanting to research a particular topic, to have different approaches presented to them. (There is no absolute truth in science, only commonly accepted wisdom!). For example, someone primarily interested in learning about the roles that surfactants or polymers play in formulating a pharmaceutical product, might well gain from also reading about this in a chapter of agrochemicals, or food detergents. Alternatively, someone wishing to learn about paper making technology might also benefit from delving into the chapter on paints. It is very useful to have all this information together in one source. Of course, there are, inevitably, some gaps. The editor himself points out the absence of a comprehensive chapter on emulsions, for example, but to have covered every nook and cranny of this field would be an impossible task, and have taken

forever to achieve! A refreshing feature of this book is its timeliness.

The book will be of tremendous use, not only to those working on industrial research and development, over a whole range of different technologies which are concerned with surface and colloid chemistry, but also to academic scientists in the field, a major proportion of whom interact very strongly with their industrial colleagues. It will compliment very well, existing textbooks in surface and colloid science, which, in general, take the more traditional approach of reviewing systematically the fundamental (pure) aspects of the subject, and add in a few examples of applications, by a way of illustration.

I personally will find this book an extremely useful teaching aid, and I am certain many of my colleagues and universities (particularly at post-graduate level), but also to an activity more and more of us in the field are becoming involved in, namely presenting various aspects of surface and colloid science to industrialists, at a specialist schools, workshops, awareness forums, etc.

I believe that Krister Holmberg was the ideal choice to have edited this book. Not only does he have a wide experience of different aspects of the field, but he has successively worked in Industry, been Director of an internationally recognised research institute (The Ytkemiska Institutet – The Institute for Surface Chemistry – in Stockholm), and is now heading up the Department of Applied Surface Chemistry at Chalmers University of Technology. He has done an outstanding job in putting this book together, and has produced an extremely valuable reference source for all of us working with surfaces and colloids.

Brian Vincent

*Leverhulme Professor of Physical Chemistry and
Director of The Bristol Colloid Centre
School of Chemistry, University of Bristol
BS8 1TS, UK*

Preface

This book is intended as a comprehensive reference work on surface and colloid chemistry. Its title, "Handbook of Applied Surface and Colloid Chemistry", implies that the book is practically oriented rather than theoretical. However, most chapters treat the topic in a rather thorough manner and commercial aspects, related to specific products, etc. are normally not included. All chapters are up-to-date and all have been written for the specific purpose of being chapters in the "Handbook". As will be apparent to the user, the many topics of the book have been covered in a comprehensive way. Taken together, the chapters constitute an enormous wealth of surface and colloid chemistry knowledge and the book should be regarded as a rich source of information, arranged in a way that I hope the reader will find useful.

When it comes to the important but difficult issues of scope and limitations, there is one clear-cut borderline. The "Handbook" covers "wet" but not "dry" surface chemistry. This means that important applications of dry surface chemistry, such as heterogeneous catalysis involving gases, and important vacuum analysis techniques, such as Electron Spectroscopy for Chemical Analysis (ESCA) and Selected-Ion Mass Spectrometry (SIMS), are not included. Within the domain of wet surface chemistry, on the other hand, the aim has been to have the most important applications, phenomena and analytical techniques included.

The book contains 45 chapters. The intention has been to cover all practical aspects of surface and colloid chemistry. For convenience the content material is divided into five parts.

Part One, *Surface Chemistry in Important Technologies*, deals with a selected number of applications of surface chemistry. The 11 chapters cover a broad range of industrial and household uses, from life-science-related applications such as pharmaceuticals and food, via detergency, agriculture, photography and paints, to industrial processes such as paper-making, emulsion polymerization, ceramics processing, mineral processing, and oil production. There are several more areas in which surface chemistry plays a role and many more chapters

could have been added. The number of pages are limited, however, and the present topics were deemed to be the most important. Other editors may have made a different choice.

Part Two, *Surfactants*, contains chapters on the four major classes of surfactants, i.e. anionics, nonionics, cationics and zwitterionics, as well as chapters on polymeric surfactants, hydrotropes and novel surfactants. The physico-chemical properties of surfactants and properties of liquid crystalline phases are the topics of two comprehensive chapters. The industrially important areas of surfactant-polymer systems and environmental aspects of surfactants are treated in some detail. Finally, one chapter is devoted to computer simulations of surfactant systems.

Part Three, *Colloidal Systems and Layer Structures at Surfaces*, treats four important colloidal systems, i.e. solid dispersions (suspensions), foams, vesicles and liposomes, and microemulsions. A chapter on emulsions should also have been included here but was never written. However, Chapter 8, *Surface Chemistry in the Polymerization of Emulsion*, gives a rather thorough treatment of emulsions in general, while Chapter 24, *Solid Dispersions*, provides a good background to colloidal stability, which to a large part is also relevant to emulsions. Taken together, these two chapters can be used as a reference to the field of emulsions. Part Three also contains chapters on two important layer systems, i.e. Langmuir-Blodgett films and self-assembled monolayers.

Part Four, *Phenomena in Surface Chemistry*, consists of extensive reviews of the important phenomena of foam breaking, solubilization, rheological effects of surfactants, and wetting, spreading and penetration.

Part Five, *Analysis and Characterization in Surface Chemistry*, concerns a selected number of experimental techniques. As with the selection of topics that make up Part One, this list of 12 chapters could have been longer and another editor may have made a different choice of topics within the given number of chapters. However, the experimental methods chosen are all important and I hope that the way this part is organized will prove useful.

Most books related to analysis and characterization are divided into chapters on different techniques, such as “Fluorescence” or “Self-diffusion NMR”, i.e. the division is by method. By contrast, the division here is by problem. As an example, when the reader wants to find out how to best measure micelle size he (or she) does not need to know from the beginning which methods to consider. The reader can go directly to Chapter 38, *Measuring Micelle Shape and Size*, where the relevant information is collected.

All 45 chapters can be regarded as overview articles. They all cover the area in a broad way and in addition they often give in-depth information on specific sub-areas which the author has considered particularly important. Each chapter also gives references to literature sources for those who need deeper penetration into the area. Each of the chapters is written as a separate entity, meant to stand on its own. This means that each chapter can be read separately. However, those knowledgeable in the field know that the topics of the “Handbook” chapters are not isolated. For example, there are obviously many connections between Chapter 25, *Foams and Foaming*, and Chapter 31, *Foam Breaking in Aqueous Systems*, Chapter 27, *Microemulsions*, has much in common with both Chapter 32, *Solubilization*, and Chapter 40, *Characterization of Microemulsion Structure*, while Chapter 19, *Physicochemical Properties of Surfactants*, deals among many other things with *lyotropic liquid crystals* which is the topic of Chapter 21 and which has strong links to Chapter 39, *Identification of Lyotropic Liquid Crystalline Mesophases*. Such connections will lead to some overlap. However, this is natural and should not present any problem. First, a certain overlap is unavoidable if each chapter is to be an independent entity. Secondly, different authors will treat a particular topic differently and these different views can often complement each other. Since both of these aspects are helpful to the reader, small overlaps have not been a concern for the editor.

The “Handbook of Applied Surface and Colloid Chemistry” is unique in scope and the only work of its kind in the field of surface and colloid chemistry. There exist comprehensive and up-to-date books lean-

ing towards the fundamental side of surface chemistry, with Hans Lyklema’s “Fundamentals of Interface and Colloid Science” being one good example. There are excellent books on surfactants and there are good textbooks on surface chemistry in general, such as “The Colloidal Domain” by Fennell Evans and Håkan Wennerström and “Surfactants and Interfacial Phenomena” by Milton Rosen. However, there exists no substantial work like the “Handbook of Applied Surface and Colloid Chemistry” which covers applied surface chemistry in a broad sense. Against this background, one may say that the book fills a gap. I hope therefore that the “Handbook” will soon establish itself as an important reference work for researchers both in industry and in academia.

I am grateful to my co-editors, Milan Schwuger of Forschungszentrum Jülich and Dinesh O. Shah from the University of Florida for helping me to identify the chapter authors. We, the editors, are extremely pleased that we have managed to raise such an interest for the project within the surface chemistry community. Almost all of those that we approached expressed a willingness to contribute and the result has been that the contributors of the “Handbook” are all leading experts in their respective fields. This is the best guarantee for a balanced treatment of the topic and for an up-to-date content.

On behalf of the entire editorial team, I would like to thank all those who contributed as chapter authors. Four persons, Björn Lindman, Robert Pugh, Tharwat Tadros and Krister Holmberg, have written two chapters each. The rest of the 45 chapters have been written by different individual authors. In total 70 individuals from 10 countries contributed to the work. I hope that when they see the “Handbook” in print they will regard the result to be worth the effort. Finally, I would like to thank Dr David Hughes at Wiley (Chichester, UK) for his constant encouragement and patience.

Krister Holmberg

Chalmers University of Technology
Sweden

Göteborg, January 2001

PART 3

COLLOIDAL SYSTEMS AND LAYER STRUCTURES AT SURFACES

CHAPTER 1

Solid Dispersions

Staffan Wall

Göteborg Universitet, Göteborg, Sweden

1	Introduction	3	3	Surface Electrical Properties	9
2	Synthesis of Solid Particles	4	4	Stability of Solid Particles	13
	2.1 Hydrolysis of metal ions	6	5	Electrostatic Interactions	13
	2.2 Silica particles	7	6	Aggregation Processes	15
	2.3 Latex particles	8		6.1 Effect of polydispersity on	
	2.4 Clays	8		coagulation rate	18
	2.5 Vapour phase and aerosol methods . .	9		6.2 Orthokinetic coagulation	18
	2.6 Particles prepared by using		7	Rheology	19
	reversed-microemulsions	9	8	References	20

1 INTRODUCTION

By the concept of “solid dispersions” in this present chapter we mean a solid substance dispersed in a liquid or a gas. However, we will limit here the scope of this paper to dispersions of solid particles in liquids.

Historically, man-made solid dispersions have been utilized for several thousand years, such as clay for pottery manufacture, ink and paint. The paints for artistic purposes, as well as for the painting of houses, used since the cave paintings in Altamira (Southern France), are solid dispersions of various pigment particles. Examples of later uses of colloidal systems include the potable gold used for medical purposes and the “purple of Cassius”, gold sols made through reduction of a gold salt with tin salts, discovered by Andreas Cassius in Leiden in 1663, which soon became an important red pigment for the glass and porcelain industry. The last two examples contain colloidal gold particles which in a certain size range give beautifully red colloidal systems.

A multitude of solid dispersions occur naturally, such as the water in glacier rivers, clays and soils (1).

Although colloidal sols were used in many practical activities, systematic studies did not begin until

the middle of the 19th century. Some scattered important studies were made in the first part of this century. Francesco Selmi (1845, 1852) studied sols of AgCl and sulfur and the effect of salts on their stability. In 1827, the English botanist Robert Brown discovered the thermal motion of colloidal particles (pollen grains of *Clarkia pulchella*). This phenomenon, known as Brownian motion, is of fundamental importance for the properties of colloidal systems. F. F. Reuss (1809) studied the electrophoretic movement of clay particles and other electrokinetic phenomena. These phenomena have been of great importance in clarifying the surface electrical properties of colloidal particles. The systematic study of colloidal dispersions began in the middle of the 19th century with Thomas Graham, who coined a number of terms which are still in use today. Such terms include colloid, sol, peptization, gel and syneresis. The word “syneresis” is used to cover the phenomenon of the spontaneous shrinkage of a gel to form a more concentrated gel and a free exuded dispersion medium. Peptization refers to the spontaneous dispersion process of a precipitate to form free colloid particles.

The concept of a dispersion is very general one, and in order to focus on various aspects a number

of other terms with different meanings have therefore been coined. Thomas Graham (1861) invented the words "crystalloid" and "colloid", depending on whether they could pass through a parchment membrane or not. Roughly speaking, particles in the size regime from 10 nm to 1 μ m can be classified as colloids. The concept of colloids has since then been substantially extended to comprise all inhomogeneous systems in which there are inhomogeneities with dimensions in the colloidal size, i.e. between 10 nm and 1 μ m. In this way, fibres and thin films are also included here if there is a colloidal size in at least one dimension.

There is also the term "sol", which is often used in conjunction with the term "gel". A sol represents a general designation for particles in a liquid. The term "suspension", which appeared earlier than the word "colloid", was used, for instance, by Faraday (1857) to designate suspended particles in a liquid. Later, Wolfgang Ostwald (1911) proposed the division, suspension/emulsion, where a suspension is a finely divided solid in a liquid and an emulsion is a liquid dispersed in another liquid. The word "emulsion" was also used earlier by F. Selmi in 1845. Ostwald's meaning of the word "suspension" is also recommended by IUPAC (2). However, Zsigmondy ref. (3), p. 18 used the word suspension in a different way. The latter author makes a distinction between colloids and suspensions, where suspensions contain larger particles than do colloidal systems. This view can sometimes also be found in modern literature, although it is not recommended by IUPAC.

The upper limit for the particle size when a particle is to be considered colloidal can be discussed. One such limit is between sedimenting and non-sedimenting particles. There is, of course, a rather broad transition zone. Whether they sediment or not depends on both the particle size and the density difference between the particles and the dispersion medium. In order to explore this further, the Boltzmann distribution law can be used, as follows:

$$n = n_0 \exp\left(-\frac{\frac{4}{3}\pi r^3 \Delta\rho gh}{kT}\right) \quad (1.1)$$

which is valid for monodisperse spheres with a radius r . In the above equation, h is the height above the bottom of the container, $\Delta\rho$ the density difference, g the acceleration due to gravity, and kT the thermal energy; n and n_0 are the number densities of the particles. If a suspension is defined as a non-sedimenting dispersion, we can estimate the limitations on the size and density. An effective sedimentation height, h_0 , can be calculated by assuming that n is 1% of n_0 at h_0 . This is, of course, an equilibrium situation which can very easily

be disturbed by convection, and the calculated h_0 is a lower limit of the sedimentation height. If the density difference $\Delta\rho = 1000 \text{ kg/m}^3$, h_0 , for particle sizes of 1 μ m, 100 nm and 10 nm, is equal to 460 nm, 0.46 mm and 46.1 cm, respectively. If convection is taken into account, the particles with sizes of 10 and 100 nm form stable colloidal non-sedimenting dispersions. The 1 μ m particles will definitely sediment and can therefore not be classified as a colloidal suspension.

In the 19th century, gold dispersions were popular model systems, although other metal sols and inorganic sols of insoluble salts were also prepared, such as $\text{Fe}(\text{OH})_3$ and As_2S_3 . Many important studies were performed on these metal sols by Faraday, Zsigmondy, Svedberg, van Bemmelen, Bredig and many others. For further details of the early history of colloid chemistry, see ref. (4). Recently, colloidal gold particles have gained renewed interest. For example, they are now used as markers in immuno- and histochemistry (5). Antibodies and other molecules can be attached to the gold surface and the gold particles then stick to special sites on specific tissues.

The technological importance of various suspensions of solid particles is enormous. The literature is therefore extensive and difficult to survey. It is, in principle, possible to make a suspension of practically all solid substances, provided that they are sufficiently insoluble in the liquid. The methods used to make them take advantage of a large number of different physical principles. However, in a brief overview such as this it is not possible to give a detailed account of all available preparation methods. In the following, we will present a short outline of the most frequently used preparation methods and references to more detailed accounts. The surface electrical properties are then described and this is subsequently used to give an account of how dispersions can be stabilized and how they aggregate.

2 SYNTHESIS OF SOLID PARTICLES

Due to the the great technological importance of colloidal systems, a vast literature exists concerning the preparation of solid particles in the micrometre range and below. Colloidal dispersions can be made via a large number of methods. Such methods can roughly be divided into two groups. The first of these is where larger pieces of material are comminuted into fine particles. This group are known as *dispersion methods*. The other group of methods, termed *condensation methods*, are ones in which, starting with an initially molecularly

homogeneous solution, the molecules are then aggregated into colloidal particles.

The comminution methods include milling or exposure of the material to ultrasound. A less frequently used method utilizes the drawing of a strong electrical current through a coarsely divided dispersion, achieved, e.g. by cutting a metal wire into small pieces. When the current is applied, discharge arcs are produced between the metal pieces, thus causing them to gasify. At the recondensation stage, a colloidal system is created. This method was first reported by Bredig, and was further developed by Svedberg, who also made use of an alternating current. This technique was used extensively at the beginning of the 20th century, although interest has diminished since then. The main disadvantage of this process is that it is difficult to obtain a high purity of the colloidal particles. In more recent times, this technique has been used by Lunina and Novozhilov (6). The technology of milling is well developed and is discussed elsewhere (7). When using the latter technique, one can usually reach particle sizes or around 1 μm . Hard materials can be milled into even finer particles. For certain materials, such as metal oxides and metal carbonates, there is sufficient surface charge to electrostatically stabilize the particles. However, in most cases, a dispersion agent must be added. The latter include such materials as polyphosphates or organic polymers which stabilize the particles through either electrostatic or steric stabilization processes. Commonly used polymers include polyacrylamide or poly(acrylic acid). However, there are a number of disadvantages when using grinding methods to prepare colloidal particles. Contamination from the grinding equipment is virtually impossible to avoid, and furthermore the size distribution becomes very broad and the particle shape is generally very irregular.

Condensation methods, in which the preparation starts with a molecularly homogeneous solution, always pass through a nucleation stage. A knowledge of the latter is therefore important in order to assess whether a system is likely to form a colloidal state or macroscopic crystals. It is also important to realize that the substance must be sufficiently sparingly soluble. Otherwise, very few nuclei are formed and the excess material will at a later stage deposit on the particles, thus forming macroscopic particles rather than colloidal material. The nucleation process can be either homogeneous or heterogeneous in nature. Homogeneous nucleation requires that no fine particles, on which the nucleation can start, are present. Heterogeneous nucleation represents the case when the phase separation can start on an already existing particle. In moderately purified systems, both homogeneous and heterogenous nucleation occur

simultaneously. The latter case is usually the most common, at least in industrial situations, because it requires a very rigorous purification to remove all dust particles.

We will first consider homogeneous nucleation. It is well known, that in order to create a nucleus, the concentration of solute must exceed the saturation concentration by a certain amount.

Let us consider a simple model in order to get an idea about the pertinent features of the nucleation process. We assume that the nucleus contains n molecules and has a spherical shape. It can be shown that the Gibbs free energy for formation of such a nucleus with n molecules is given by the following:

$$\Delta G = -nkT \ln(x/x_{\text{sat}}) + \gamma b n^{2/3} \quad (1.2)$$

where x is the actual mole fraction of solute, x_{sat} is the mole fraction in a saturated solution, γ is the surface energy of the nucleus, and b is a (positive) constant. In the above equation, there are two terms, i.e. one proportional to n and the other proportional to $n^{2/3}$. When n increases, the latter term with the highest power in n will always overcome the term with a lower power in n , i.e. ΔG always has a maximum at a certain value of n , where the latter is called the "critical nucleation size", n_c . This is illustrated in Figure 1.1. It can be

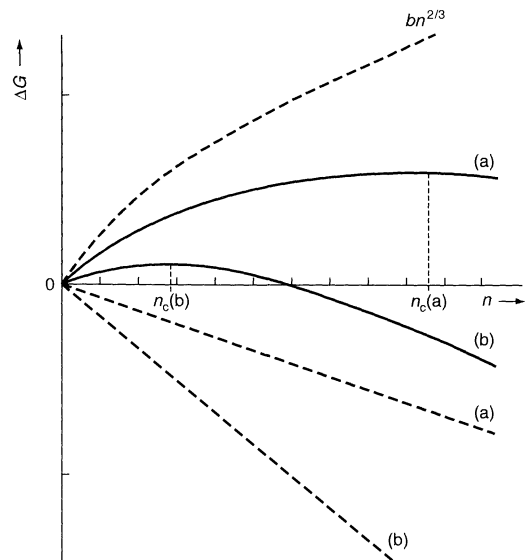


Figure 1.1. The free energy of a nucleus as a function of its size. The two terms in equation (1.2) are shown by dotted curves; plots (a) and (b) refer, respectively, to a lower and higher supersaturation. Both n_c and the height of the barrier decrease as x/x_{sat} increases. Reproduced from *Basic Principles of Colloid Science*, D. H. Everett, 1988, by permission of The Royal Society of Chemistry

seen from this figure that n_c decreases in size when the degree of supersaturation increases. Because of the rapid decrease in size of the critical nuclei with increasing supersaturation, the interval of supersaturation where nuclei begin to form is very narrow. Consequently there is a more or less sharp concentration limit at which the nucleation starts, which is known as the "critical nucleation concentration". For more details on the nucleation process, see ref. (8) (p. 203). La Mer and Dinegar (9) has used this concept in discussing the controlled formation of colloidal particles. These authors describe, in a classical piece of work (9), how a sulfur sol can be prepared from an acidified sodium thiosulfate solution. The main idea is to increase the concentration of insoluble material by a chemical reaction over a short period of time, during which a number of nuclei are formed. The excess material above the critical nucleation concentration is exhausted, although the concentration of dissolved material is kept above the saturation level by slowly producing more insoluble material. This means that the formed nuclei grow in size until the concentration of dissolved material has decreased below the saturation level. Figure 1.2 illustrates this process.

However, this concept was utilized earlier by Zsigmondy when he prepared monodisperse gold particles. This worker started with HAuCl_4 , which was rapidly reduced to free gold atoms by using a strong reducing agent such as phosphorous. The gold atoms thus produced were transferred to the nuclei present in the system and so no material was left for particle growth. In a second stage, these gold nuclei were added to a solution of HAuCl_4 containing a weak reducing agent, i.e. formaldehyde (HCHO). The concentration of gold atoms was at all times so low that no new nuclei were

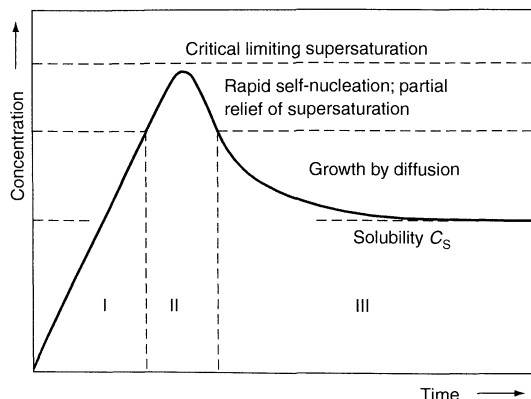
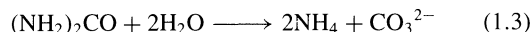


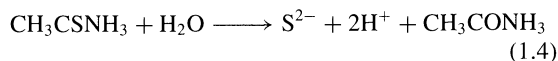
Figure 1.2. Concentration of dissolved solute before and after nucleation as a function of time. Reproduced from ref. (9) by permission of The American Chemical Society

formed and all gold atoms were deposited on the already existing particles. This way of preparation also gives a controlled particle growth and can result in the production of monodisperse particles.

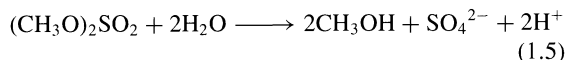
There are a number of variations of this method (10, 11). In particular, the work by E. Matijevic and co-workers (12, 13) should be mentioned. These workers have synthesized monodisperse particles of a large number of inorganic compounds. One major problem is to keep the concentration of insoluble material between the saturation and critical nucleation concentrations when monodisperse particles are desired. This can be achieved in the following way when an insoluble salt is used. In this case, an excess of one of the ion species is present, while the other ion species is produced slowly by a chemical reaction. Various ions can be produced in this way. For example, carbonate ions can be made from the hydrolysis of carbamide:



and thioacetamide gives sulfide ions:



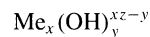
While dimethylsulfate gives sulfate ions:



In addition, the hydrolysis of diesters of oxalic acid gives oxalate ions.

2.1 Hydrolysis of metal ions

Many metal ions will coordinate water in aqueous solutions. When the pH is raised, these metal ions are hydrolyzed, forming more or less complex hydroxy complexes. The general formula of these hydroxy complexes is as follows:



They each contain a number of metal ions, and such complexes are the precursors to colloidal particles. Metal ions which can be used for this approach include Al^{3+} , Ti^{4+} , Zr^{2+} , Cr^{3+} , Zn^{2+} and Fe^{3+} .

The synthesis include the heating to 100–300°C of an aqueous solution of a metal salt at a certain pH interval. The particle morphology can be affected by various anions (10, 14), for instance Cl^- and SO_4^{2-} . Some examples of the different shapes which can be obtained are shown in Figure 1.3.

An interesting colloidal system produced by the hydrolysis of iron ions is that of the ferromagnetic

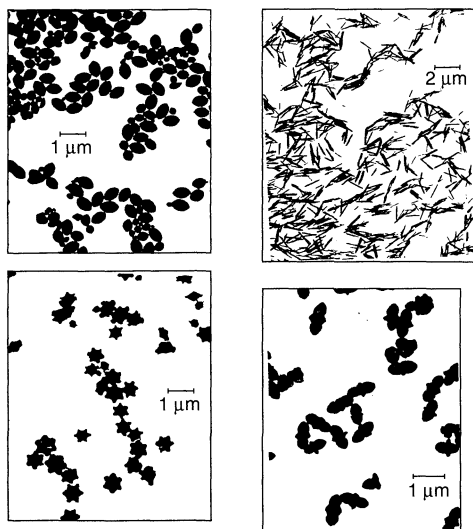


Figure 1.3. Various particle shapes created by treating ferric ions under different conditions, e.g. ageing time, temperature and chemical composition. The particles consist of either α - Fe_2O_3 or β - FeOOH from E. Matijevic and P. Scheiner, *J. Colloid Interface Sci.*, 63, 509 (1978). Reproduced by permission of Academic Press

substance haematite Fe_2O_3 . Particles of the latter behave as tiny magnets and a colloidal dispersion of such particles will form a magnetic fluid, i.e. it will respond to a magnetic field like an ordinary ferromagnet, although it retains its liquid state. Recently, a large number of commercial applications have been reported for this material, including its use in rotating shaft seals, loud speakers and hydraulic devices. A comprehensive description of the synthesis, physical properties and practical applications of magnetic fluids can be found in the text edited by Berkovski (15).

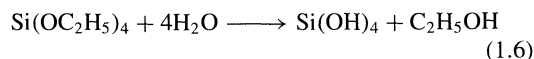
2.2 Silica particles

The term “Silica” represents all materials described by the formula SiO_2 and can appear in many different modifications (16). Crystalline forms include quartz, tridymite and cristobalite. Quartz is stable at room temperature, while the other two crystalline modifications are high-temperature forms which can exist as metastable forms at room temperature. Synthetic silica particles are usually amorphous, i.e. the silica tetrahedra are connected in a random way. Particles of silica have, in many respects, different properties when compared with colloidal particles made from other materials. In contrast to many other oxides, silica is rather soluble, at

least in its amorphous form. The surface properties are at present poorly understood (17).

The synthesis can start with monomeric silicic acid, $\text{Si}(\text{OH})_4$. Under certain conditions, the monomeric silicic acid begins to aggregate and form colloidal particles. At low salt concentrations, spherical particles are formed. When electrolyte is added to the growing particles, the primary particles begin to aggregate, thus forming more or less irregular particles (18). However, there is a preference for elongated particles. The process involved is illustrated in Figure 1.4.

Another method for preparing silica sols is the process described by Stöber, and co-workers, known as the SFB or Stöber method (see ref. 18 (p. 111)). The starting material here is a tetraalkylorthosilicate in ethanol solution; water and ammonia are also present. Tetraethylorthosilicate (TEOS) is generally used. The first step is the hydrolysis of TEOS according to the following:



The silicic acid formed in this way then aggregates into spherical particles with a size distribution which is very narrow. In this way, silica particles with a size of ca. 1 μm can be produced, as well as smaller particles in the submicron range. The resulting particle density is

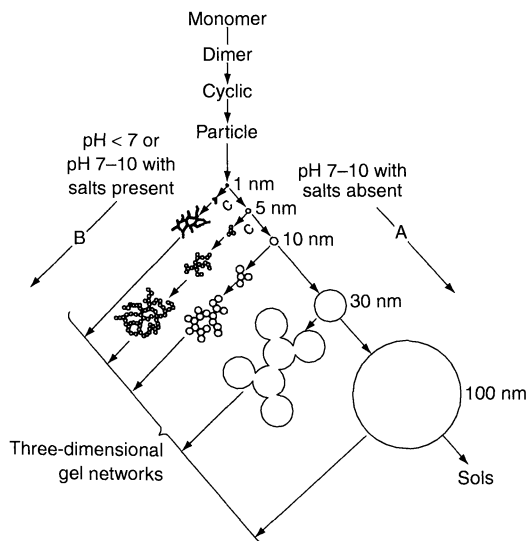


Figure 1.4. The polymerization behaviour of silicic acid to form silica. In basic solution (A), particles in the sol grow in size with a decrease in their number, while in acid solution or in the presence of flocculating salts (B), particles aggregate into three-dimensional networks and form gels. Reproduced from ref. (16) by permission of John Wiley & Sons, Inc.

2.0 g/cm³, which is less than the density of amorphous silica (2.2 g/cm³). This suggests that the particles are porous. From investigations of its optical properties, it has been found that the refractive index of silica increases from the centre out to the surface of the particles, thus implying that the density of the particle increases during growth.

2.3 Latex particles

Polymer latexes have a great technological importance, particularly in paint formulations and coatings for paper. In the chapter by K. Tauer in this Vol. 1 (chapter 8), additional material about latexes can be found. As the latter can be prepared easily as nearly perfect spheres, they are also popular model systems for fundamental studies of colloids. However, a drawback is that their surface electrical properties are poorly understood, which means that the interaction potentials are also poorly known.

There are many different methods for the syntheses of latexes (19a, b) all of which are based on free-radical polymerization. The various preparation can be broadly divided into the following methods, i.e. emulsion polymerization, dispersion polymerization and suspension polymerization. A more detailed treatment can be found in ref. 19a (p. 12).

In free-radical polymerization, the reaction is started by an initiator such as potassium persulfate, which on heating forms sulfate radicals, SO₄[•]. Other types of initiators include azocompounds, R–N=N–R, which form radicals of the type R–N[•]. The initiator can be either soluble or insoluble in water. The monomer, a compound with a double bond, is emulsified in water with or without an emulsifier (surfactant). A commonly used monomeric substance is styrene.

In emulsion polymerization, the initiator is water-soluble. The polymerization process then occurs in the water phase. The polymers are aggregated into well-shaped spherical particles, which in many cases can be almost monodisperse.

Suspension polymerization represents the case when the initiator is soluble in the monomer droplets. The polymerization process thus occurs consequently in these droplets. When the polymerization occurs in a homogeneous phase with a subsequent aggregation, the process is then designated as dispersion polymerization.

Two very important steps in these procedures are the cleaning of the latex dispersion and characterization of the dispersion medium. These procedures are in fact relevant for all kinds of colloidal systems. In the

aggregation process, much unwanted material has been incorporated into the latex particles. Such substances may, in many cases, leach out very slowly during storage and thus change the properties of the dispersion medium and the surface properties of the particles. When there are stringent requirements on the purity of the system, a lengthy cleaning procedure is necessary and the use of surfactants in the synthesis is not recommended. A systematic review of the various cleaning procedures that have been used has been carried out by Wilkinson *et al.* (20). Dialysis and ion-exchange methods, or a combination of these, seem to be the best techniques for this purpose.

2.4 Clays

Clay represent a group of very important and complicated colloidal systems (21). In soil science, the word “clay” refers to any soil material with a particle size of less than 2 µm. Here, however, we will only consider systems consisting of pure clay minerals. Such materials belong to the phyllosilicates group, where silica tetrahedra form thin layered structures. In a clay mineral, the particles are small plates, usually with negatively charged flat sides and positively charged edges. The width of the plates is up to 10 µm and the thickness is a few nanometres. There are several kinds of clay minerals. The simplest of these is kaolinite, the structure of which is illustrated in Figure 1.5. Kaolinite is the major component in kaolin, which is used in several practical applications, e.g. porcelain manufacture and paper coating. Montmorillonite is another important clay mineral and is a major component of bentonite clay which is used extensively in drilling muds and retention aids in the paper industry. Many more clay minerals exist in nature, e.g. talc and vermiculite. Because of their surface charges and asymmetric particle shapes, dispersions of clay show a very strong non-Newtonian rheological behaviour.

Natural clays are usually contaminated with other types of minerals. Therefore, it is of particular advantage to use synthetic clays. An easily obtainable synthetic clay is laponite, which is a lithium–magnesium silicate which forms extended sheaths. The laponite which is commercially available and can be obtained from Laporte Industries, is also easily synthesized in the laboratory. Due to its purity, laponite is a useful model system for studying clays. Their properties are by now fairly well known through several basic investigations (22, 23).

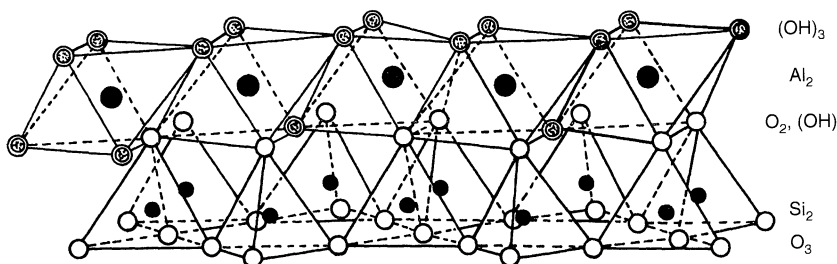


Figure 1.5. The structure of an “ideal” layer of kaolinite, $(\text{Al}(\text{OH})_2)_2 \cdot \text{O} \cdot \text{O}(\text{SiO}_2)_2$. Reproduced from ref. (28) by permission of Oxford University Press

2.5 Vapour phase and aerosol methods

Colloidal particles can also be prepared by using vapour phase methods. Here, (see ref. 18 (p. 286)) we will also include aerosol methods. In a typical method, a suitable precursor is heated in either an oxidizing, reducing or inert atmosphere. Examples of particles which have been produced in this way include oxides (SiO_2 , TiO_2 , Al_2O_3 , and ZnO), carbides (SiC and B_4C), borides (TiB_2 and ZrB_2) and nitrides (Si_3N_4 and BN). Various heating methods have been used, such as furnaces, lasers, electron beams and plasmas. One great advantage of such methods is the high purity which can be obtained. Such techniques are used in the large-scale manufacture of TiO_2 particles and fumed silica. Many of the materials referred to above are used in various ceramic processes for the manufacture of high-quality ceramic materials.

2.6 Particles prepared by using reversed-microemulsions

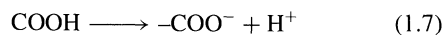
A method to prepare nanosized particles which is based on a very different concept to those mentioned above is the process based on reversed-microemulsions. A recent overview of this method has been given by Pileni (24). In such a technique, the water-soluble reactants are included in the water droplets in reversed micelles. Because the droplets exchange their contents rather frequently the two reactants will therefore mix and form an insoluble substance which then aggregates into particles. The particle size is mainly determined by the droplet size. A typical microemulsion droplet is of the order of 20–40 nm, which means that the particle size will be inside this size range. As an example of this, platinum particles can be produced by using platinum chloride and hydrazine in separate microemulsion droplets. Hydrazine reduces the platinum ions to metallic platinum and nanosized particles are

formed. In addition to Pt, several other metals, including Cu and Ag, have been used. Nanosized particles of many insoluble salts can also be prepared in this way.

3 SURFACE ELECTRICAL PROPERTIES

In order to control the colloidal stability of suspensions, it is crucial to understand the surface electrical properties, including how they arise and how they can be manipulated. The first observation that can be made is that a surface in contact with a liquid with a high dielectric constant will almost always carry a negative or positive surface charge. There is a bias towards a negative charge. However there are also a large number of positively charged systems, particularly at low pH level's. A surface will be electrically neutral only under very special conditions, a state which is called the “point of zero charge” (PZC). There are several charging mechanisms which can be described, as follows.

- (a) Protolysis of surface charge, leaving a negative charge on the surface, such as:



The surfaces of metal oxides contain OH-groups which are amphoteric and can either take up a proton at low pH or leave one proton at a high pH, i.e.



At low pH the surface is positively charged while at high pH the surface is negatively charged. This is illustrated in Figure 1.6. At a certain intermediate pH level, the oxide surface is neutral and the point of zero charge can be expressed as a pH value

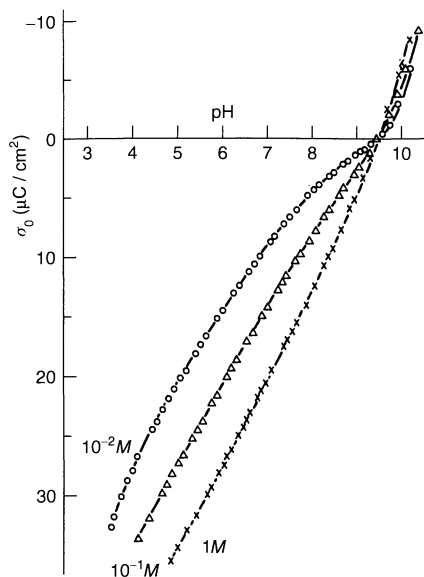


Figure 1.6. Surface charge on monodisperse haematite sols as a function of pH, shown for three different concentrations of KCl. Reproduced from *Solid/Liquid Dispersions*, M. F. Tadros (Ed.), 1987, by permission of Academic Press

Table 1.1. Pristine points of zero charge at room temperature for a number of colloidal particle materials

Particle	pH
SiO ₂ (precipitated)	2–3
SiO ₂ (quartz)	3.7
SnO ₂ (cassiterite)	5.6
TiO ₂ (anatase)	6.2
TiO ₂ (rutile)	5.7–5.8
α-Fe ₂ O ₃ (haematite)	8.5–9.5
α-FeO–OH (goethite)	8.4–9.5
ZnO	8.5–9.5
γ-Al(OH) ₃ (gibbsite)	8–9

(see Table 1.1). Extensive tables of PZC values for various oxides can be found in ref. (25).

- Adsorption of ions from solution, usually involving surfactant ions and polyelectrolytes.
- Isomorphous substitution where one ion is replaced with another ion with a lower valency. For instance, Al³⁺ can be replaced by Si⁴⁺, thus leaving a negative charge on the crystal lattice. This charging mechanism is particularly important for clay particles.
- When a crystal of a sparingly soluble salt such as AgI is brought into contact with water, Ag⁺ is dissolved to a higher degree than I[–]. If the solution does not contain an excess of Ag⁺ ions, a negative

surface is created. By the addition of Ag⁺ ions, the surface charge may switch from negative to positive. In this case, the PZC can be expressed as an Ag⁺ concentration, or pAg.

The PZC is usually measured in the presence of electrolytes. In many cases, one or both of the ions can adsorb on the surface. The PZC is then dependent on both the proper surface properties and also the content of the dispersion medium. If the medium does not contain any ions which specifically adsorb on the surface, the PZC is only dependent on the material in the colloidal particles. Such a PZC is known as a *pristine* point of zero charge (PPZC) (see Table 1.1).

An electrically charged surface in contact with water generates an electrical field which attracts oppositely charged ions. These ions are called counterions. Due to the thermal motion, these counterions form a diffuse layer of charge outside the charged surface. Co-ions with the same charge as the surface are repelled from the latter. The diffuse layer of charge and the surface charge form a so-called electrical double-layer. This concept plays a fundamental role in the discussion of electrical surface properties and the colloidal stability of dispersions. The electrical double-layer is in total electrically neutral.

Ions can be adsorbed by various mechanisms and they are then said to be *specifically* adsorbed. If counterions do not adsorb at all, they are called *indifferent* ions. For instance, small metal ions such as Na⁺ or K⁺ are usually indifferent ions.

The description of an electrical double-layer as being a charged surface and a diffuse layer with counterions and co-ions is a drastic over-simplification. In the transition zone between the charged surface and the diffuse layer, there is a complicated structure which is at present poorly understood. Both the molecules in the dispersion medium and the ions are affected by the charged wall through steric restrictions, strong electrical fields and other interactions, such as van der Waals forces. The electrical field at the surface polarizes both the molecules of the dispersion medium and also the ions which imparts other properties which they have in the bulk phase. Many models have been constructed to describe this type of interface. The first attempt was made by Stern in 1924 (26). The latter considered the ions as having a finite size, which prevents counterions and co-ions from approaching right upto the charged surface. If it is assumed that the ions are spheres with point charges at their centres, there is a narrow charge-free zone between the surface and a plane through the ion centres. This plane is called the “Stern plane” and

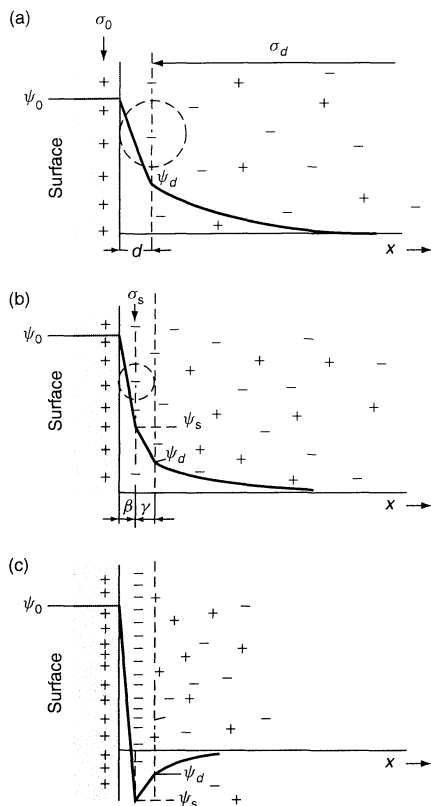


Figure 1.7. Examples of double-layer models: (a) no specific adsorption; (b) some specific adsorption of anions; (c) strong specific adsorption of anions. Reproduced from *Solid/Liquid Dispersions*, M. F. Tadros (Ed.), 1987, by permission of Academic Press

the first layer of ions close to the surface is called a “Stern layer”. The ions in the Stern layer are usually counterions but it is also known that certain co-ions, such as phosphate ions, can bind to the surface by non-electrostatic forces. The electrical potential as a function of the distance from the surface for three different cases is shown in Figure 1.7.

In 1946, D. Grahame (27) introduced a refinement of the Stern theory, in which he distinguished between hydrated ions and ions which are adsorbed by covalent bonds or van der Waals forces (or both). Grahame introduced the terms “inner-Helmholtz plane” for the locus of the electrical centres of the adsorbed ions and “outer-Helmholtz plane” for the locus of the electrical centres of the hydrated ions in contact with the charged surface. This is illustrated in Figure 1.8. A number of more sophisticated models on the same theme as Grahame’s model have been suggested (see ref. (28),

p.382). The disadvantage with these is that an increasing number of parameters which are not readily accessible are then introduced. As a consequence, the fitting of experimental data becomes increasingly arbitrary and the fitting parameters lose their physical significance.

Nevertheless, these models provide some practical tools for discussing the electrical double-layers. Until now, only a static picture of the electrical double-layer has been given. However, many dynamic phenomena, such as surface conductivity, dielectric relaxation, electrokinetic phenomena and coagulation kinetics, have shown the need to consider the dynamic properties of the double-layers. Especially during the last 10 years, the interest in the dynamic properties of the electrical double-layers of colloidal particles has increased significantly (29, 30). For instance, the application of an electrical field on a colloidal dispersion will deform the electrical double-layers surrounding the particles. When an alternating electrical field is applied, the electrical double-layers will “swing” back and forth, over a certain frequency range, causing an energy dissipation which is known as *dielectric relaxation* (29, 31).

Another effect which is important in a discussion of the conductivity of colloidal systems is the *surface conduction*, i.e. a conductivity contribution from the double-layers. This contribution is important when the electrolyte content is relatively low in the bulk phase. The surface conductance is also important when measurements of electrokinetic phenomena (electrophoresis, electro-osmosis, etc.) need to be evaluated. Recently, it

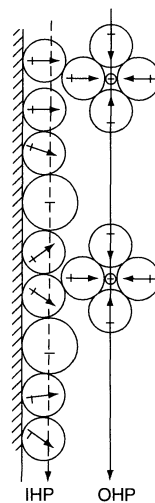


Figure 1.8. Schematic representation of the concepts of the inner-Helmholtz plane (IHP) and outer-Helmholtz plane (OHP). Reproduced from Bockris *et al.*, *Proc. Roy. Soc. Lond. A* 274, pp. 55–79 (1963) by permission of The Royal Society

has also been found that the dynamics of the electrical double-layers are important in discussions of coagulation kinetics (32).

A rigorous theoretical treatment of the electrical double-layer is very complicated. A statistical mechanics treatment of the exact problem is only possible if all interaction energies among the ions and between the molecular components in the liquid and the solid surface are known. This is not usually the case, and particularly so for the complicated liquid water which is commonly used in colloidal dispersions. By tradition, a rather crude treatment is used in colloid science. This is based on the well-known Poisson–Boltzmann equation, which is based on the physical Gouy–Chapman model. In this model, the ions are assumed to be “point-like”, and the solvent is treated as a continuous medium with a constant dielectric constant. An electrical mean potential ψ is introduced. Furthermore, the surface charge is assumed to be uniformly distributed, i.e. the discreteness of the surface charges is neglected. By using the Poisson equation and the Boltzmann distribution law, the so-called Poisson–Boltzmann equation can be formulated. In the general case, this equation has the following form:

$$\nabla^2 \psi = -\frac{1}{\varepsilon \varepsilon_0} \sum (n_i)_0 e_0 z_i \exp\left(-\frac{z_i e_0 \psi}{kT}\right) \quad (1.9)$$

where ε is the dielectric constant for the dispersion medium, ε_0 is the permittivity of a vacuum, $(n_i)_0$ is the concentration of the i th ion in the bulk phase, e_0 is the elementary charge, z_i is the valency of the i th ion, and kT is the thermal energy.

The approximations in the Gouy–Chapman model give acceptable errors only for small monovalent ions such as Na^+ , NO_3^- , etc. For larger and/or multivalent ions, large deviations may occur.

The Poisson–Boltzmann equation is a nonlinear equation in ψ and analytical solutions cannot generally be obtained. However, a number of simple cases can be treated analytically. Such a case is when the potential is sufficiently low. Then, the exponential term can be linearized. Using the electroneutrality condition:

$$\sum_i (n_i)_0 e_0 z_i = 0 \quad (1.10)$$

we obtain the following:

$$\nabla^2 \psi = \kappa^2 \psi \quad (1.11)$$

where:

$$\kappa = \left(\frac{\sum_i z_i^2 (n_i)_0 e_0^2}{\varepsilon \varepsilon_0 kT} \right)^{1/2} \quad (1.12)$$

Equation (1.11) can be solved analytically for a number of double-layer geometries including the following.

(1) Plain double-layer:

$$\psi = \psi_0 \exp(-\kappa x) \quad (1.13)$$

where x is the distance from the wall and ψ_0 is the electrical potential at the solid surface.

(2) Spherical double-layer:

$$\psi = \psi_0 \frac{a}{r} \exp[-\kappa(r-a)] \quad (1.13)$$

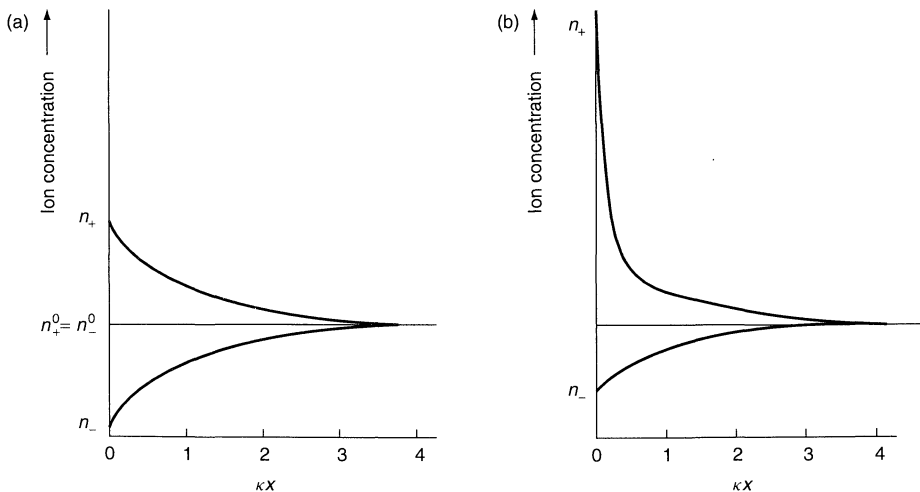


Figure 1.9. The ion concentrations for a symmetrical electrolyte outside a negatively charged plane surface shown for (a) when the surface potential is low, and (b) when the surface potential is high. Reproduced from *Zeta Potential in Colloid Science*, R. J. Hunter, 1981. Reproduced by permission of Academic Press.

where a is the radius of the sphere and r is the distance from the centre of the sphere.

(3) Cylindrical double-layer:

$$\psi = \psi_0 \frac{K_0(r\kappa)}{K_0(a\kappa)} \quad (1.14)$$

where K_0 is a modified Bessel function.

(4) Two spherical overlapping double-layers. An analytical expression is given by Ohshima (33 (p. 73)).

From equation (1.13), we can see the physical significance of κ ; the latter is the decay length for the electrical potential, while $1/\kappa$ is a measure of the thickness of the electrical double-layer and is called the *Debye length*. The nonlinear Poisson–Boltzmann equation can be solved for a plain double-layer when there is only a symmetrical electrolyte in the bulk phase, i.e. when $z_+ = -z_- = z$. The solution is then as follows:

$$\psi = \frac{2kT}{ze_0} \ln \left[\frac{1 + \gamma_0 \exp(-\kappa x)}{1 - \gamma_0 \exp(-\kappa x)} \right] \quad (1.15)$$

where:

$$\gamma_0 = \tanh \left(\frac{ze_0\psi_0}{4kT} \right) \quad (1.16)$$

Figure 1.9 illustrates the ion concentration calculated from equations (1.13) and (1.15) via the Boltzmann distribution law. Note the asymmetry between counter ions and co-ions in the high-potential case.

4 STABILITY OF SOLID PARTICLES

Colloidal particles are always subjected to Brownian motion and in many cases also to hydrodynamic forces (e.g. stirring). This movement brings them into contact and depending on whether they interact attractively or sufficiently repulsively they will stick to each other or separate again after contact. The particles interact via van der Waals forces which are always present to a varying degree. In systems where water or any other liquid with a high dielectric constant is the dispersion medium, electrostatic interactions are always present. These forces are present when the electrical double layers overlap. The assumption that only van der Waals forces and electrostatic forces are responsible for the interaction forces between colloidal particles forms the basis for the DLVO (Derjaguin, Landau, Verwey and Overbeek) theory (34).

Additional types of interaction forces are present in many cases. For instance, when polymers are present, adsorbed on the particle surfaces, and when two

polymer-covered particles approach one another the polymer coats will begin to mix. This mixing process is connected with a lowering of the entropy and thus results in a repulsive force.

The particle can also be well solvated, i.e. the solvent is more or less strongly bound to the surface. This solvent layer forms an additional energy barrier which in some cases can be rather substantial, such as in the case of silica particles. These kinds of forces are called *structural forces*. However, there are several other kinds of forces of various origins; many of these are described in ref. (35).

Here, we will limit our discussion to electrostatic double-layer forces and van der Waals forces. Thus, other interaction forces important in special cases are neglected. This means that we start with a discussion of the DLVO theory.

5 ELECTROSTATIC INTERACTIONS

When two charged particles approach, their double-layers begin to overlap. When the electrical potential deviates from the electrical potential in the bulk phase (usually set to zero), there is always an excess of ions compared to that in the bulk phase. As illustrated in Figure 1.10, an excess of ions between the two particles arises because of the electrical field. This excess of ions creates an osmotic pressure which pushes the particles apart. The excess of ions can be calculated from the Boltzmann distribution law, as follows:

$$n_i = (n_i)_0 \exp \left(-\frac{z_i e_0 \psi}{kT} \right) \quad (1.17)$$

when ψ is known between the particles. This parameter can in principle be calculated from the Poisson–Boltzmann equation more or less accurately,

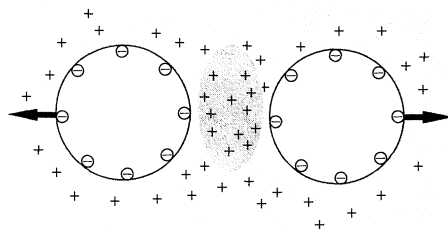


Figure 1.10. Schematic representation of the counterion concentration around two spherical electrically charged spheres; note the excess of counterions between the particles. Reproduced from ref. (33) by permission of Marcel Dekker, Inc.

although numerical methods are usually required. However, the next step to calculate the interaction energy analytically demands a rather simple (analytical) equation for the electrical potential. As already discussed, such analytical results are usually not available for non-spherical particles and approximate methods have been used unless a numerical treatment is sufficient. As the numerical methods give less of an overview, analytical equations are often preferable.

In the literature, a large number of various formulae for the electrostatic interaction energies can be found, derived under various approximations. Ohshima (33) has derived an equation for the interaction energy between two spherical particles in the low-potential case. However, the resulting equation is rather complicated. Efforts have been made to derive simple but yet accurate analytical equations for the interaction energy. In this respect, substantial progress has been made by Carnie and co-workers (36, 37). For spherical particles at an arbitrary surface potential, relatively simple equations have been derived. The approximations in the Poisson-Boltzmann equation are, of course, still included.

In order to obtain simpler equations useful for at least qualitative discussions, a number of approximations have to be made. A common strategy is first to consider the interaction between two plane double-layers, which simplifies the mathematical treatment.

By using equation (1.15), with D being the distance between the two plane surfaces, and only considering weak interactions between the double-layers, the following equation can be derived for the interaction energy per unit area, V_R :

$$V_R = \frac{64n_0kT\gamma_0^2}{\kappa} \exp(-\kappa D) \quad (1.18)$$

This equation can be transformed into a formula describing the interaction between curved surfaces, such as that between two spherical double-layers. This is carried out by using the Derjaguin equation. The latter connects the force F_s between two spherical double-layers and the interaction energy per unit area, V_R , of two plane interacting double-layers. It is assumed that both the spherical and the plane double-layers carry the same surface charge density, which leads to the following:

$$F_s = 2\pi \frac{R_1 R_2}{R_1 + R_2} V_R \quad (1.19)$$

The interaction energy, V_s , between two spheres can then easily be obtained through the following equation:

$$F_s = -\frac{dV_s}{dH} \quad (1.20)$$

where H is the shortest distance between the surfaces of the spheres. The resulting equation is given by the following:

$$V_R = \frac{64\pi\epsilon\epsilon_0 R_1 R_2 (kT)^2 \gamma_0^2}{e_0^2 z^2 (R_1 + R_2)} \exp(-\kappa H) \quad (1.21)$$

This equation is based on equation (1.17) and is therefore only valid in the presence of a symmetric electrolyte in the dispersion medium. The electrolyte concentration is contained in κ , and the latter therefore increases with increasing electrolyte concentration. This means that the interaction weakens with increasing salt content.

The other component in the DLVO theory results from the van der Waals forces. These forces are always attractive between particles of the same material. If the particles are made of different materials, the forces may in some cases be repulsive.

Between small molecules, the van der Waals interaction ϕ_A has the following form:

$$\phi_A = -\frac{\beta}{r^6} \quad (1.22)$$

where β is a positive constant and r is the distance between the molecules. This interaction energy decays too fast to be of any significance for colloidal particles. The electrostatic interactions, on the other hand, are of a much longer range. The reason why the van der Waals forces are of importance is that the total van der Waals interaction between two colloidal particles is the sum of all pair-wise interactions in the two colloidal particles containing a large number of small molecules. The total van der Waals interaction will then be much more long-ranged. In order to visualize this, consider two spherical particles. For simplicity, we will assume that they are of equal size. These spherical particles contain a large number of small molecules. The total interaction energy can then be calculated with a summation, or in practice, an integration. The result is as follows:

$$V_A = -\frac{A}{6} \left[\frac{2}{s^2 - 4} + \frac{2}{s^2} + \ln \left(\frac{s^2 - 4}{s^2} \right) \right] \quad (1.23)$$

where:

$$s = \frac{2a + H}{a} \quad (1.24)$$

In the above, A is called the *Hamaker constant*, named after H. C. Hamaker who first performed these kinds of summation for a number of different geometries. The Hamaker constant is defined by the following:

$$A = \pi^2 \rho^2 \beta \quad (1.25)$$

where ρ is the number of molecules per unit volume in the particles.

Equation (1.23) can be written in a very simple form when $H \ll a$, as follows:

$$V_A = -\frac{A}{12} \frac{a}{H} \quad (1.26)$$

Tables of Hamaker constants can be found in many books on colloid science (e.g. see ref. (38), p. 225). The Hamaker constants can also be calculated from the optical properties of the materials in the dispersion (ref. (28), p. 194).

An intervening medium always diminishes the van der Waals interaction between two particles. The degree of decrease can be estimated from following simple equation:

$$A_{123} = \left(A_{11}^{\frac{1}{2}} - A_{22}^{\frac{1}{2}} \right) \left(A_{33}^{\frac{1}{2}} - A_{22}^{\frac{1}{2}} \right) \quad (1.27)$$

where the subscripts "1" and "3" refer to the material in the particles, while subscript "2" refers to the material of the dispersion medium; A_{11} and A_{33} are the vacuum Hamaker constants for the two particles, and A_{22} is the vacuum Hamaker constant for the dispersion medium. If the particles are of the same material, i.e. $A_{11} = A_{33}$, the Hamaker constants are always positive, thus leading to an attractive interaction. If $A_{22} > A_{11}$ and $A_{22} > A_{33}$, or $A_{22} < A_{11}$ and $A_{22} < A_{33}$, the Hamaker constant is negative and the interaction is repulsive, which will happen in certain cases. The total interaction energy, V_{tot} , in the DLVO model is obtained by simply adding the electrostatic and the van der Waals components. There is a primary minimum at small values of H and a secondary minimum at fairly large distances, as illustrated in Figure 1.11. In between, an energy barrier is present if the electrolyte concentration is not too high. If the energy barrier is sufficiently low (or in some cases non-existent), the particles can pass the barrier and irreversibly end up in the primary minimum. In the latter case, the system coagulates. If the secondary minimum is sufficiently deep and the energy barrier is still reasonably high, then the system can also aggregate with the particles in this minimum. From equations (1.21) and (1.26), it is evident that V_{tot} is proportional to the particle radius. The aggregation is then loose and readily redispersable. When the radius of the particles increases it is obvious that the height of the energy maximum and the depth of the secondary minimum will both increase. An implication of this is that for small particles the secondary minimum is usually too shallow to cause an aggregation. This kind of aggregation occurs only for larger particles.

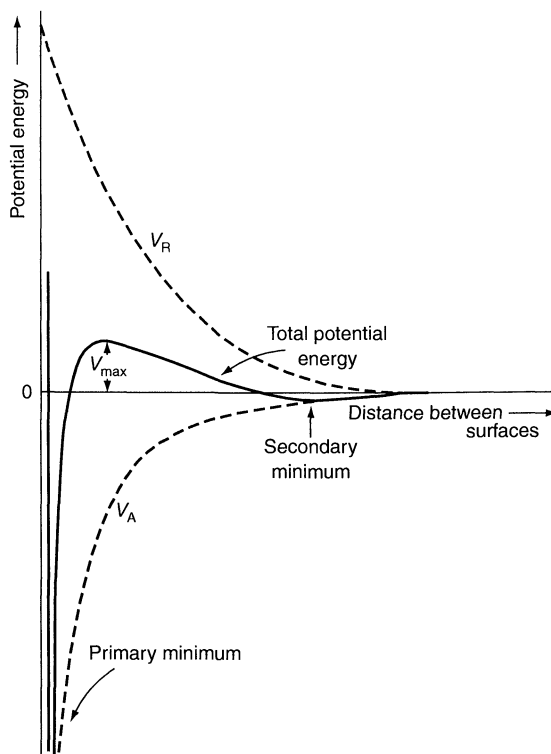


Figure 1.11. The energy as a function of the distance between two interacting charged surfaces with an intervening electrolyte solution

6 AGGREGATION PROCESSES

In many practical situations, there is a need to separate the dispersed solid, often in a colloidal state, from the fluid dispersion phase. Examples of this can be found in the paper industry and in waste-water treatment. In scientific terms, this can be expressed in the following way – “How can a dispersion be destabilized and what is the kinetics of the destabilization?” The destabilization process is always an aggregation which is called either coagulation or flocculation depending on the nature of the resulting aggregates. If the particles aggregate into a compact structure, the aggregation is called coagulation, thus leading to a macroscopic separation. The particles then interact in the primary minimum of the interaction potential. If the particles form loosely connected, voluminous aggregates, the aggregation process is called flocculation, which may or may not separate macroscopically. In a flocculation process, polymers are often involved which connect the particles in loose open networks (known as

bridging flocculation). If the secondary minimum is sufficiently deep, the particles can aggregate with a certain distance between them, thus forming loose flocs – the aggregation process in this case is also called flocculation. Such usage of the terms “flocculation” and “coagulation” is recommended by IUPAC.

Aggregation of colloidal particles has been studied since the middle of the 19th century, with important works such as those of Faraday’s studies of aggregating gold particles. The first theoretical attempts to model aggregation were made by M. von Smoluchowski; his theories treat the initial stage where only particle doublets are formed.

Aggregation starts with the formation of doublets which is a rather easily modelled process. In the subsequent aggregation, a multitude of irregular particles are formed and a conventional kinetic treatment then becomes more or less impossible. The structure of the particle aggregates is dependent on the interaction potentials. Some information can be obtained by computer simulations. We will start our consideration of the aggregation kinetics by a discussion of the Smoluchowski theory and its ramifications on more recent work.

The particles in a dispersion can be driven together either by Brownian motion or by a combination of hydrodynamic flow and Brownian motion. The first case, when only Brownian motion is present, is called *perikinetic coagulation (flocculation)*. When hydrodynamic flow is also present and dominates, the coagulation (flocculation) is called *orthokinetic*. For large particles of several nanometres in size, the collision frequency is greatly enhanced by stirring. Smoluchowski has treated simple cases of both perikinetic and orthokinetic aggregation. We will also distinguish between “fast” coagulation and “slow” coagulation. When fast coagulation is present, there is no repulsive interaction between the particles. On the other hand, when a repulsive barrier is present slow coagulation occurs.

The perikinetic aggregation is the simplest to treat. Smoluchowski considered a fixed particle and a spherically symmetric gradient of other particles diffusing towards this stationary particle. This seems to be a very artificial situation which cannot be realized in practice. However, this picture is not an actual one but a *statistical* one. The fixed particle represents an average over a large number of particles and when two particles stick together they are removed from the system. Due to the average over a large number of particles, the incoming particles are equally distributed over all angles. Therefore, we can consider the gradient outside the fixed particle as being spherically symmetric. The dispersion medium is assumed to be a continuous one without any

internal structure, i.e. the particles experience a macroscopic viscosity η and Fick’s law for diffusion can then be used, as follows:

$$J = -D \frac{dn}{dr} \quad (1.28)$$

where J is the flow of particles per unit area and unit time, D is the diffusion coefficient of the particles and n is the number density of the particles.

With these assumptions, Smoluchowski derived an expression for the collision frequency α when the particles are of the same size. The result is given by the following:

$$\alpha = \frac{8}{3} \frac{kTn^2}{\eta} \quad (1.29)$$

Here, it is assumed that the particles are spheres. This can be expressed as a rate constant k_2 defined by:

$$\frac{dn}{dt} = -k_2 n^2 \quad (1.30)$$

and:

$$k_2 = \frac{8}{3} \frac{kT}{\eta} \quad (1.31)$$

Here, we have also assumed that the particles do not interact before they are in contact and all collisions lead to doublet formation. Moreover, hydrodynamic interactions have been neglected. An experimental verification of this formula showed, not unexpectedly, deviations. The coagulation was slower than that predicted by the rate constant given in equation (1.31). Derjaguin, in 1966, proposed the reason for this was that the particles interact hydrodynamically when they were sufficiently close to each other. The dispersion medium has to be removed from the space between the particles when they approach one another and the motion of the particles is retarded. The effect is in many cases quite large, i.e. about a factor of 2. This can be expressed as a reduction in the diffusion coefficient. Honig and co-workers have derived an approximate equation for how the diffusion coefficient $D(H)$ varies with the interparticle surface-to-surface distance H . The expression is as follows:

$$\frac{D(H)}{D_{H=\infty}} = \frac{1 + (2a/3H)}{1 + (13a/6H) + (a^2/3H^2)} \quad (1.32)$$

When H approaches zero, $D(H)$ also becomes zero, which means that Brownian motion alone cannot bring the particles into contact. However, at short distances the attractive van der Waals forces can bring the particles together. Until now we have not assumed Usually, the particles interact via electrostatic and van

der Waals forces, which can substantially alter the rate constant and consequently the stability of a colloidal system.

The inclusion of this kind of interaction can be introduced in the derivation of a rate constant in the following way. Consider an interaction energy $V(r)$, including electrostatic interactions, van der Waals interaction, and possibly other non-DLVO contributions; $V(r)$ does not include the hydrodynamic forces. If the particles are spherical, $V(r)$ usually has a spherical symmetry, which is assumed here. Fick's law can then be extended to include the interaction energy $V(r)$. The equation then reads as follows:

$$J = -D \left(\frac{dn}{dr} + \frac{n}{kT} \frac{dV}{dr} \right) \quad (1.33)$$

With an analogous derivation, as for fast coagulation, the following expression for the rate constant can be derived:

$$k_2 = \frac{8\pi D}{\int_{2a}^{\infty} r^{-2} \exp\left(\frac{V(r)}{kT}\right) dr} \quad (1.34)$$

In equation (1.34), hydrodynamic interactions between the colliding particles are not included.

With an increasing electrolyte concentration, the repulsive barrier gradually decreases. When it is sufficiently small (or non-existent), the hydrodynamic forces are the dominating retarding forces and the rate constant is at a maximum. We have reached then what is called fast coagulation. The rate constant is then denoted by k_2^0 which remains constant when the electrolyte concentration increases further. Then, a stability ratio W is introduced, as follows:

$$W = \frac{k_2^0}{k_2} \quad (1.35)$$

W is evidently 1 for fast coagulation and larger than 1 for slow coagulation. This parameter is a measure of the stability of the dispersion. The stability ratio can easily be determined experimentally by, for instance, measuring the turbidity with an ordinary spectrophotometer. Of course, all kinds of interaction are then included in W , both known and unknown. Some typical experimental results are presented in Figure 1.12. The transition between slow and fast coagulation is characterized by a more or less sharp corner on plots of $\ln W$ versus $\ln c$ (where c is the electrolyte concentration). Because this transition occurs at a rather well-defined electrolyte concentration, it has been given its own name, the *critical coagulation concentration (CCC)*. This parameter has been studied for a large number of systems since the end

of the 19th century. The theoretical interpretation of this phenomenon was not made until the end of the 1940s, when the classical work by Verwey and Overbeek (34) and, independently, Derjaguin and Landau was published. This is known as the DLVO theory. Reerink and Overbeek (39) found the following linear relationship between $\ln W$ and $\ln c$:

$$\ln W = K_1 \ln c + K_2 \quad (1.36)$$

where c is the counterion concentration, and K_1 is a function of the particle radius and surface potential. The linear relationship between $\ln W$ and $\ln c$ can be found experimentally, although the dependence of K_1 on the particle radius a could not be verified. This has remained an open question for some decades. However, Overbeek pointed out in 1976 that a neglected phenomenon in the above-mentioned theory is that the redistribution of ions is neglected. These ions may be both ions in the diffuse layer and those adsorbed on the particle surface. The relaxation time for the ions in the diffuse layer is much faster than a Brownian encounter, although the relaxation times for the redistribution of ions adsorbed on the particle surfaces can be of the same order. Kijlstra and van Leeuwen (32) were able to show that an inclusion of these ion redistribution processes could under certain circumstances make the stability ratio W independent of the particle radius.

It is known that the CCC depends strongly on the valency z of the counterion. If the surface potential at low salt concentration is sufficiently high (> 50 mV) one finds experimentally the following approximate formula:

$$CCC \propto \frac{1}{z^6} \quad (1.37)$$

This relationship is known as the Schulze-Hardy rule, and was first reported in 1882. It is followed fairly well for a rather large number of counterions. When the surface potential is low, < 20 mV, the z^6 dependence

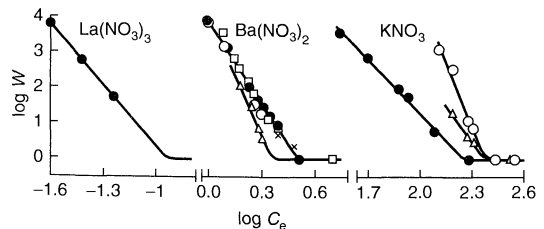


Figure 1.12. Stability curves for various silver iodide sols; electrolyte concentrations are given in mM. Five different silver iodide sols were used, designated by the use of different symbols in the plots. Reproduced from ref. (39) by permission of The Royal Society of Chemistry

is replaced by a z^2 dependence. The derivation of the Schulze–Hardy rule is usually made in the literature by using equations such as (1.21) and (1.26). These expressions are added to a total interaction potential, $V(H) = V_A + V_R$, where H is the distance of closest approach. By putting:

$$V(H) = \frac{dV(H)}{dH} = 0 \quad (1.38)$$

equation (1.37) can be obtained. In this derivation, γ_0 is set to 1, i.e. the electrical surface potential is high and independent of the electrolyte concentration. However, at the CCC the electrolyte content is usually so high that the surface charge is effectively screened and the electrical surface potential is so low that $\gamma_0 \ll 1$ and the derivation is therefore not correct. To date, a strictly correct derivation of the Schulze–Hardy rule has not been published, although notwithstanding this, it remains a well-established experimental fact.

6.1 Effect of polydispersity on coagulation rate

Up until now, we have only considered the coagulation behaviour of monodisperse systems. However, colloidal dispersions are usually polydisperse, and we will now also briefly discuss the effect of polydispersity on the coagulation behaviour. The Smoluchowski theory for monodisperse particles does not contain any dependence on radius. The reason for this is that there is an exact cancelling out of the increase in the diffusivity and the increase in the collision cross-section. However, when a dispersion contains small and large particles, there is an increase in collision frequency because of the high diffusivity of the small particles and the large collision cross-section of the big particles. There is also an increased coagulation rate if a polydisperse system is centrifuged. The large particles sediment faster than the smaller ones and therefore they collide with the latter.

6.2 Orthokinetic coagulation

It is a general observation that gentle stirring promotes coagulation. The reason for this is that velocity gradients in the flow field create relative particle movements and therefore an increased collision frequency. The simplest case to treat is that of a uniform shear field.

Smoluchowski has already treated this situation. However, this is a rather artificial one and occurs rather infrequently. We will now briefly discuss this case and

investigate some of its implications. Consider, as in the perikinetic case, that we have a stationary particle and then consider other particles moving relative to this particle due to a uniform shear field. The Brownian motion is then neglected. This means that the shear field must be sufficiently strong. Further electrostatic and van der Waals interactions are also neglected, i.e. only fast coagulation is considered initially. The complicated inter-particle hydrodynamic interactions are important, in particular the deformation of their trajectories caused by such interactions. These interactions are not included in Smoluchowski's simple theory.

Under the simplified conditions described above, the collision frequency can easily be obtained by considering the volume of liquid passing through a cylinder with a radius R , where R is the radius of the particles (see ref.(40), p.165). All particles in this liquid volume collide with the stationary particle. The collision frequency is then given by the following:

$$\frac{4}{3} R^3 G n^2 \quad (1.39)$$

where G is the shear gradient. The rate constant defined by equation 1.30 is then given by:

$$(k_2^0)^S = \frac{4}{3} R^3 G \quad (1.40)$$

This simple model suggests that $(k_2^0)^S$ depends very strongly on the radius. The ratio between the rate constants of orthokinetic and perikinetic coagulation is then given as follows:

$$\frac{(k_2^0)^S}{k_2^0} = \frac{R^3 \eta G}{2kT} \quad (1.41)$$

For a typical shear gradient (stirring at 100 s^{-1}), the ratio $(k_2^0)^S/k_2^0 = 1$ when the particle radii are around 400 nm. This suggests that shear-induced coagulation is much more effective when the particle radius is in the size range of $1 \mu\text{m}$ or larger. Generally, the perikinetic coagulation ceases when the aggregates become too big, and when the aggregated dispersion is then agitated the aggregation process is continued as an orthokinetic coagulation.

When the stirring speed increases, there is a transition from laminar to turbulent flow. Treatment of this kind of orthokinetic coagulation is much more difficult than the case of laminar flow. An approximate way to treat this situation is to use the Smoluchowski equation for orthokinetic coagulation in laminar flow and to employ an average shear gradient in the turbulent flow. Various estimates of this average have been derived. One of these

is given by the following:

$$G = \frac{2}{15} \left(\frac{\varepsilon_d}{\nu} \right)^{\frac{1}{2}} \quad (1.42)$$

where ε_d is the energy dissipation per unit mass of fluid and ν is the kinematic viscosity. A more detailed discussion of this can be found in the recent text by Friedlander (41).

From the model described above, an approximate expression for the rate constant $(k_2^0)^T$ can be derived

$$(k_2^0)^T = 1.3 \left(\frac{\varepsilon_d}{\nu} \right)^{\frac{1}{2}} R^3 \quad (1.43)$$

In this derivation, interparticle interactions, including hydrodynamic interactions, have been neglected. It should be emphasized that the effects of turbulence on coagulation are only partially understood. There are uncertainties in the fundamental theory of turbulence and in the motion of small particles in close proximity in the turbulent flow field. As a result, theoretical predictions of turbulent coagulation rates must be considered as only being approximate, perhaps to within a factor of 10, and are also likely to be on the high side.

7 RHEOLOGY

The flow properties of colloidal dispersions are of great importance in handling dispersions in various practical situations. Another important aspect is that the viscosity and other rheological parameters can be used to determine the size, shape and interaction potentials of the dispersed particles. For most simple liquids, the viscosity is independent of the shear force. In this case, the liquid is then called Newtonian. For more complicated systems, when the liquid contains colloidal particles and/or polymers, the (apparent) viscosity depends on the shear force, except at very low concentrations of dispersed material. The fluid is then designated non-Newtonian. In this section, only systems containing particles are discussed, without the complicating influence of macromolecules.

The source of the viscosity in a fluid is energy dissipation and when colloidal particles in a shear field begin to rotate, further energy dissipation occurs and the viscosity increases. From this it is also easy to realize that rod-like or plate-like particles gain more kinetic energy than a spherical particle with the same volume. Thus, the viscosity increases when the particles deviate more and more from spherical symmetry at the same volume fraction of particles. A significant viscosity

contribution can also come from deformation of the particles and the electrical double-layers around the particles when they rotate in a shear field. The viscosity contribution from the electrical double-layer is called the *primary electroviscous effect*.

In very dilute dispersions when the interactions between the particles can be neglected, the viscosity increases linearly with the volume fraction ϕ of the particles. The dispersions also show Newtonian behaviour if the shear force is sufficiently low. For this case, the following expression is valid:

$$\frac{\eta}{\eta_s} = 1 + \nu\phi \quad (1.44)$$

where η is the viscosity of the dispersion, η_s is the viscosity of the dispersion medium and ϕ is the volume fraction of particles. For spherical particles, $\nu = 5/2$. This case is described by the well-known equation derived by Einstein in 1911 (42). When the particles are asymmetric, $\nu > 5/2$. Simha (43) has derived general equations for ellipsoids, characterized by an axial ratio a/b , with a and b being the lengths of the rotational axes of the ellipsoid. Asymmetric particles can be modelled as ellipsoids and from the viscosity of a dispersion of these particles an estimate of the axial ratios can be made by using Simha's equations.

When the particle concentration increases, interparticle interactions come into play and a quadratic term in ϕ must then be included. Equation (1.44) for hard spheres then has the following form:

$$\frac{\eta}{\eta_s} = 1 + \frac{5}{2}\phi + c\phi^2 \quad (1.45)$$

where $c = 5.91$ (44).

Colloidal particles can interact in a number of ways, as described above. Information about the interaction potentials can be obtained from the Huggins coefficient, k_H , defined by the following:

$$\frac{\eta}{\eta_s} = 1 + [\eta]c + [\eta]^2 k_H c^2 \quad (1.46)$$

where $[\eta]$ is the intrinsic viscosity and c is the concentration of the particles.

The size of the shear gradient, G , is important for the internal structure of a dispersion. This gradient can be so small that the Brownian motion can "keep up" with the structural deformation due to hydrodynamic forces. On the other hand, if the shear gradient is very large, the flow affects the internal structure of the fluid. A rough estimate of the relative importance of the Brownian force and the hydrodynamic force is given by the *Peclet*

number, defined by the following:

$$Pe = \frac{6\pi\eta_s Ga^3}{kT} \quad (1.47)$$

If $Pe \ll 1$, the Brownian motion is dominating and the fluid is Newtonian, while if $Pe \gg 1$, the hydrodynamic forces dominate and induce a non-equilibrium structure. The fluid shows then a non-Newtonian behaviour. If $Pe \approx 1$, the dispersion usually shows a so-called shear thinning behaviour which means the apparent viscosity decreases with increasing shear force (45). On the other hand, if the shear is further increased, the apparent viscosity begins to increase again, and the dispersion is now *shear-thickening*. In fact, the Newtonian plateau at low shear fields is, for large colloidal particles, limited to very low shear fields. In an aggregating system, the non-Newtonian behaviour starts very early in the aggregation process and it is very important to have control of the shear field if the aggregation process is to be studied by measurements of the viscosity. Generally, the shear field must be very low in order to avoid non-Newtonian effect.

For elongated particles, rods or plates, non-Newtonian effects appears very early, at low shear fields and concentrations. Here, the rotational Brownian motion, in addition to the translational motion, must dominate if the dispersion is to behave in a Newtonian way. A group of systems of special theoretical and practical importance is clays which show very interesting rheological behaviours. These are plates, negatively charged on the flat sides, with positively charged edges. This uneven charge pattern leads to the formation of so-called "house-of-cards" structures. When such structures are sheared, they break down and the apparent viscosity decreases. Moreover, at prolonged stirring, the viscosity decreases gradually with time until there is a steady state between the breakdown process and the recovery of the "house-of-cards" structure. Such a gradual time-dependent apparent viscosity decrease is called *thixotropy*. If the apparent viscosity increases with time under steady shearing, it is designated as *rheopexy*. This behaviour can also be found in clay systems. After a powerful shearing, the apparent viscosity then starts to slowly increase with time. However, a slight shearing will speed up the increase in the apparent viscosity.

Although the rheological literature may not usually be that easily accessible for "traditional" chemist, there are a number of readable accounts, with one of these being the text by Barnes *et al.* (46). The latter is recommended as good introductory book on rheology. In addition, a good overview of the hydrodynamics of colloidal dispersions is given in ref. (47).

In conclusion, I hope that this brief account of the properties of solid particles dispersed in liquids can serve as an introduction to the literature on this subject. A comprehensive treatise on the material can be found in the recent (planned) five-volume work by Lyklema (48), of which three volumes have been published to date.

8 REFERENCES

1. Yariv, S. and Cross, H., *Geochemistry of Colloid Systems for Earth Scientists*, Springer-Verlag, Berlin, 1979.
2. Everett, D. H., IUPAC, Manual of Symbols and Terminology for Physicochemical Quantities and Units, Appendix II. Definitions, Terminology and Symbols in Colloid and Surface Chemistry, *Pure Appl. Chem.*, **31**, 578–621 (1972).
3. Zsigmondy, R., *Kolloidchemie*, Verlag Otto Spamer, Leipzig, Germany, 1912.
4. Alexander, A. E. and Johnson, P., *Colloid Science*, Oxford University Press, Oxford, UK, 1949.
5. Hayat, M. A., (Ed.), *Colloidal Gold*, Academic Press, San Diego, CA, 1989.
6. Lunina, M. A. and Novozhilov, Yu. A., *Kolloid. Zh.*, **31**, 370–373 (1969).
7. Stein, H. N. (Ed.), *The Preparation of Dispersions in Liquids*, Surfactant Science Series, Vol. 58, Marcel Dekker, New York, 1996.
8. Parfitt, G. D. (Ed.), *Dispersions of Powder in Liquids*, 3rd Edn, Applied Science Publishers, London, 1981.
9. La Mer, V. K. and Dinegar, R. H., Theory, production and mechanism of formation of monodispersed hydrosols, *J. Am. Chem. Soc.*, **72**, 4847–4854 (1950).
10. Otterstedt, J. -E. and Brandreth, D. A., *Small Particle Technology*, Plenum Press, New York, 1998.
11. Tadros, Th. F., *Solid Liquid Dispersions*, Academic Press, London, 1987.
12. Matijevic, E., Preparation and characterization of well defined powders and their applications in technology, *J. Eur. Ceram. Soc.*, **18**, 1357–1364 (1998).
13. Goia, D. V. and Matijevic, E., Preparation of monodispersed metal particles, *New J. Chem.*, 1203–1215 (1998).
14. Buining, P. A., Pathmamanoharan, C., Philippse, A. P. and Lekkerkerker, H., Preparation of (non)aqueous dispersion of colloidal boehmite needles, *Chem. Eng. Sci.*, **48**, 411–417 (1993).
15. Berkovski, B. (Ed.), *Magnetic Fluids and Applications Handbook*, Begell House Inc., New York, 1996.
16. Iler, R., *The Chemistry of Silica*, Wiley, New York, 1979.
17. Vansant, E. F., van der Voort, P. and Vrancken, K. C., *Characterization and Chemical Modification of the Silica Surface*, Studies in Surface Science and Catalysis, Vol. 95, Elsevier, Amsterdam, 1995.
18. Brinker, C. J. and Scherer, G. W., *Sol–Gel Science*, Academic Press, Boston, MA, 1990.

19. (a) Gilbert, R. G., *Emulsion Polymerization*, Academic Press, London, 1995; (b) Fitch, R. M., *Polymer Colloids*, Academic Press, San Diego, CA, 1997.
20. Wilkinson, M. C., Hearn, J. and Steward, P. A., The cleaning of polymer colloids, *Adv. Colloid Interface Sci.*, **81**, 77–165 (1999).
21. van Olphen, H., *An Introduction to Clay Colloid Chemistry*, 2nd Edn, Wiley, New York, 1963.
22. Saunders, J. M., Goodwin, J. G., Richardson, R. M. and Vincent, B., A small-angle scattering study of the structure of aqueous laponite dispersions, *J. Phys. Chem., B*, **103**, 9211–9218 (1999).
23. Porion, M., Faugere, P., Lecolier, E., Gherardi, B. and Delville, A., ^{23}Na nuclear quadrupolar relaxation as a probe of the microstructure and dynamics of aqueous clay dispersions: an application to laponite gels, *J. Phys. Chem., B*, **102**, 3477–3485 (1998).
24. Pileni, M. P., Colloidal assemblies used as microreactors, in *handbook of surface and colloid chemistry*, Birdi, K. S. (Ed.), CRC Press, Boca Raton, FL, 1997, pp. 495–532.
25. Janusz, W., Electrical double layer at the metal oxide–electrolyte interface, in *Interfacial Forces and Fields. Theory and Application*, Hsu, J.-P. (Ed.), Surfactant Science Series, Vol. 85, Marcel Dekker, New York, 1999, pp. 135–206.
26. Stern, O., Zur Theorie der elektrolytischen Doppelschicht, *Z. Electrochem.*, **30**, 508–516 (1924).
27. Grahame, D. C., The electrical double layer and the theory of electrocapillarity, *Chem. Rev.*, **41**, 441–501 (1947).
28. Hunter, R. J., *Foundations of Colloid Science*, Vol. 1, Oxford University Press, Oxford, UK, 1987.
29. Russel, W. B., Saville, D. A. and Schowalter, W. R., *Colloidal Dispersions*, Cambridge University Press, Cambridge, UK, 1989.
30. Lyklema, J., Leeuwen, H. P. and Minor, M., *Adv. Colloid Interface Sci.*, **83**, 33–69 (1999).
31. Dukin, S. S., and Shilov, V. N., *Dielectric Phenomena and the Double Layer in Disperse Systems and Polyelectrolytes*, Wiley, Jerusalem, Israel, 1974.
32. Kijlstra, J. and van Leeuwen, H. P., Surface charge relaxation during coagulation, *J. Colloid Interface Sci.*, **160**, 424–434 (1993).
33. Ohshima, H., Interaction of electrical double layers, in *Electrical Phenomena at Interfaces*, 2nd Edn, Ohshima, H. and Furusawa, K. (Eds), Surfactant Science Series, Vol. 76, Marcel Dekker, New York, 1998, pp. 57–85.
34. Verwey, E. J. W. and Overbeek, J. Th. G. *Theory of the Stability of Lyophobic Colloids*, Elsevier, New York, 1948.
35. Israelachvili, J., *Intermolecular and Surface Forces*, 2nd Edn, Academic Press, London, 1992.
36. Sader, J. E. Carnie, S. and Chan, D. Y., Accurate analytic formulas for the double-layer interaction between spheres, *J. Colloid Interface Sci.*, **171**, 46–54 (1995).
37. Stankovitch, J. and Carnie, S. L., Interactions between two spherical particles with nonuniform surface potentials, The linearized Poisson–Boltzmann theory, *J. Colloid Interface Sci.*, **216**, 329–347 (1999).
38. Ross, S. and Morrison, I. D., *Colloidal Systems and Interfaces*, Wiley, New York, 1988.
39. Reerink, H. and Overbeek, J. Th. G., *Discuss. Faraday Soc.*, **18**, 74–84 1954.
40. Elimelech, M., Gregory, J., Jia, X. and Williams, R. A., *Particle Deposition and Aggregation*, Butterworth-Heinemann, Oxford, 1995.
41. Friedlander, S. K., *Smoke, Dust and Haze*, 2nd Edn, Oxford University Press, New York, 2000.
42. Einstein, A., *Investigation on the Theory of the Brownian Movement*, Dover Publications, New York, 1956.
43. Simha, R., The influence of brownian movement on the viscosity of solutions, *J. Phys. Chem.*, **44**, 25–34 (1940).
44. Batchelor, G. K., The effect of Brownian motion on the bulk stress in a suspension of spherical particles, *J. Fluid. Mech.*, **83**, 97–117 (1977).
45. Brady, J. F. and Bossis, G., *Annu. Rev. Fluid. Mech.*, **20**, 111–157 (1988).
46. Barnes, H. A., Hutton J. F. and Walters, K., *An Introduction to Rheology*, Rheology Series, Vol. 3, Elsevier, Amsterdam, 1989.
47. Dobias, B., Qui, X. and von Rybinski, W., *Solid–Liquid Dispersions*, Surfactant Science Series, Vol. 81, Marcel Dekker, New York, 1999.
48. Lyklema, J., *Fundamentals of Interface and Colloid Science*, Volumes 1–3, Academic Press, London, 1991, 1995, 2000.

CHAPTER 2

Foams and Foaming

Robert J. Pugh

Institute for Surface Chemistry, Stockholm, Sweden

1	Introduction and Background	23	4.9	The stability of the froth can be controlled by emulsion and pseudo-emulsion films	30
2	Classification of the Stability of Foam	25	4.10	Stability enhanced by the use of phase diagrams	31
2.1	Unstable (transient) and high-stability (metastable) foams	25	5	Test Methods for Foam Stability	31
3	Rupture Mechanisms of Thin Liquid Foam Films	26	5.1	Shaking in a glass container	32
4	Theories of Foam Stability	26	5.2	Bikerman test with a cylindrical column (Sparge tube technique)	32
4.1	Stability increase caused by increase in bulk viscosity	27	5.3	Funnel-shaped test	33
4.2	Stability increase caused by increase in surface viscosity	27	5.4	Pour test method (the Ross–Miles test)	34
4.3	The adsorbed surfactant film can control the viscosity of the surface layer	27	5.5	Foaming in a rotor mixer	34
4.4	Gibbs/Maragoni effect, surface elasticity and viscosity	27	6	Research Techniques for Studying Foam Stability	34
4.5	Thin films stabilized by surface forces under static (equilibrium) conditions in dilute surfactant	28	6.1	Microscopic and photographic methods	34
4.6	Stabilization of foam films containing a high surfactant concentration (> CMC) by stratification and long-range ordered microstructures in thin films	29	6.2	Optical fibre probes	35
4.7	Stabilization of foam by liquid crystals	29	6.3	Measurement of head space in foam	35
4.8	Stabilization of foam films by a combination of surfactants (mixed films)	30	6.4	Foam pressure drop technique	35
			6.5	Drainage of foam films	36
			6.6	Electrical conductivity	36
			6.7	Back-scatter techniques	37
			6.8	Lamellae lifetime	37
			7	Industrial Material and Food Foams	37
			7.1	Polymeric foams	37
			7.2	Porous metallic foams	41
			7.3	Low-density cement foams	42
			7.4	Food foams	43
			8	References	43

1 INTRODUCTION AND BACKGROUND

Foams are used today in many different types of environments, in either the liquid or solid state. For

example, in the kitchen aqueous foams are found as whipped cream, beer, mouse, soapy dishwater, etc., whereas in the bathroom, bath foams and hair shampoos are used. In the living room, polymeric foams are used in packing (seat cushions and “Styrofoam”) and

in carpet backing, etc. In addition to household use, new types of material foams, such as concrete foams, have found special applications in the building and insulation industry (1). Metal foams have shown considerable potential in aerospace and automobiles, since these systems have unique properties due to their structure, stability and ultra-light weight (2). Recently, an interesting novel uses of polymeric foams in the area of bone replacement was reported (2). Aqueous foams have also found a unique use in the decontamination of nuclear components where complicated shaped valves, turbines and pipes occur in plants (2). Under these circumstances, spraying does not reach all internal surfaces and mechanical methods are ineffective. In this situation, foams provide a good alternative since only small amounts of liquid are required and the volume of secondary waste is small.

However, we will begin the background to this chapter by reviewing the preparation of foams. Initially, it is important to stress that a foam cannot be produced in a pure liquid, *unless* a surface-active material is present. In considering *surface-active foaming materials* in an aqueous environment, we must include particles, polymers, specific adsorbed cations or anions from inorganic salts, etc., and many of these substances can often cause foaming at extremely low concentrations (as

low as $10^{-9}M$). In fact, the cleanliness of the system and the vessel can have an important influence on foaming. Although foams can be produced by simple agitation, alternative methods for preparing foams are by nucleation of gas bubbles after supersaturating the liquid with gas or producing gas *in situ* (for example, from a chemical reaction). Gas can be released from solution by lowering the pressure and the bubble size is influenced by the dynamic surface chemical properties. These types of foams are produced in the food industry (for example, in beers and soft drinks) and since alcohol in the water causes a lowering of the surface tension, then alcoholic beverages have smaller bubbles than soft drinks.

In foam systems, two fairly easily recognizable, more or less extreme structures, can be described. Initially, *kugelschaum* or *sphere foam* is produced in freshly prepared systems and consists of small roughly, spherical bubbles separated by *thick films* of viscous liquid. The foam may be considered as a temporary dilute dispersion of bubbles in the liquid, but on ageing the structure gradually changes and the bubbles transform into polyhedral gas cells with thin flat walls. To maintain mechanical equilibrium within the structure, the film walls drain until they meet at an angle of 120° . The junction points of the interconnecting channels are known as the *plateau borders* (Figure 2.1(b)).

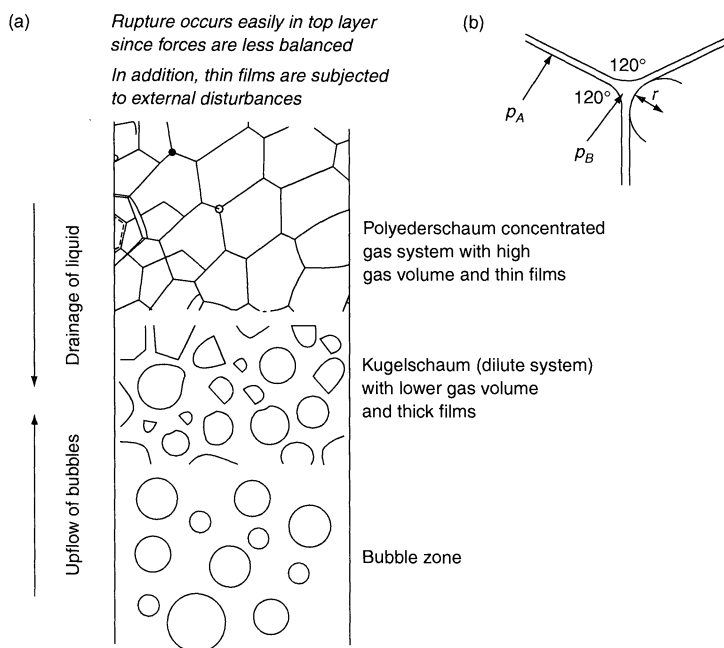


Figure 2.1. (a) Froth structure occurring during formation and drainage of foam in a column. (b) plateau borders, where the capillary pressure sucks liquid into the borders

Due to the interfacial curvature, the pressure P_B is lower and the film is thicker in the plateau border, so that a sucking effect on the liquid from the centre of the film to its periphery occurs. The pressure difference between neighbouring cells (Δp) is related to the radius of curvature (r) of the plateau border by $\Delta p = 2\gamma/r$. The resulting thin film structure, on thinning to about 1000 nm (where interference colours are observed), is referred to as a *polyederschaum*. The terms *foams* and *froths* are often used interchangeably, but it is more usual to refer to the gas–water macrocluster systems where the broken structure leaves a homogeneous aqueous phase as a foam. The froth usually contains dispersed solid particles, so that the broken structure gives a two-phase system (aqueous solution and finely divided particles).

In a foam column, several different transitional structures may occur. Near the surface, a high gas content structure is usually formed with the low gas content structure near the base of the column and a gradual transition occurring throughout the column length. Overall, the foam density decreasing with the height in the column (Figure 2.1(a)). The drainage of excess liquid from the foam column into the underlying solution is initially driven by hydrostatics, which causes the bubbles to become distorted. Foam collapse usually occurs from the *top to the bottom* of the column, since thin films in the kugelschaum foams are more susceptible to rupture by shock, temperature gradients or vibration.

As well as drainage, instability of the foam can be caused by a diffusion mechanism, in which gas is forced across the thin films from smaller bubbles into large bubbles. This is known as *disproportionation* and the driving force for this behaviour is again the Laplace pressure, over a curved surface. Since the pressure inside a small bubble is greater than in a larger sized bubble, and the gas solubility increases with pressure, then more gas dissolves near the small bubbles than the larger ones. This causes diffusion of gas to occur across the walls, with the smaller bubbles growing at the expense of the large ones.

2 CLASSIFICATION OF THE STABILITY OF FOAM

2.1 Unstable (transient) and high-stability (metastable) foams

All foams are thermodynamically unstable, due to their high interfacial free energy, which decreases on rupture. For convenience, the instability has been expressed

according to the kinetics and has been classified into two extreme types, as follows:

- (i) unstable or transient foams with lifetimes of seconds;
- (ii) metastable or so-called permanent foams with lifetimes which may be measured in hours or days.

Metastable foams are capable of withstanding ordinary disturbances (thermal or Brownian fluctuations, etc.) but collapse in an irregular manner from abnormal disturbances (evaporation, temperature gradients, etc.).

Unstable (transient) foams are frequently prepared from aqueous solutions of short-chain (low-molecular-weight) alcohols and fatty acids. The lifetimes of these foams range from several seconds to about 20 seconds. Mild surfactants, such as short-chain alcohols (ethyl, propyl, isobutyl, etc.), aniline, phenol, pine oil and short-chain undissociated fatty acids (formic, propionic, etc.) belong to this group of weak frothers. The lifetime (t) of these unstable foam appears to be sensitive to the concentration of surfactant in solution and usually shows a maximum value at a critical concentration.

Essentially, the stability of the foam depends on the stability of the individual film, with champagne foams being a classic example of an unstable foam (Figure 2.2(a)). In this case, the lifetime is controlled by the drainage (hydrodynamics), but also gas diffusion and Oswald ripening probably play a role in destabilizing the system.

High-stability (metastable) foams are prepared from detergents, proteins, long-chain fatty acids (near or above the critical micelle concentration (CMC)), particles, etc. These foams usually have a lifetime up

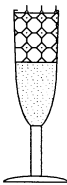

(a) 	(b) 
<u>Dynamic Foam</u>	<u>Static Foam</u>
Lifetime < 30 seconds	Lifetime > 30 minutes
Subject to:	Subject to:
drainage	disjoining pressure
diffusion	(thermodynamically stable)
disproportionation	

Figure 2.2. Examples of (a) transient and (b) metastable foams (from V. Bergeron in ref. (2)), with kind permission from Kluwer Academic Publishers

to several hours, and the surfactant concentrations are fairly high (near or above the CMC). In other cases, the systems are stabilized by polymers or water-soluble proteins, causing steric interfacial forces which prevent thin film rupture. Beer foams are essentially polypeptide foams, and a “Guinness” foam (Figure 2.2(b)) is a typical example of a thermodynamic (sterically) stabilized system.

3 RUPTURE MECHANISMS OF THIN LIQUID FOAM FILMS

Foam liquid films gradually thin and may rupture after drainage to a critical thickness (h_{cr}). Early studies attributed this rupture to the onset of a thermodynamically unstable state caused by a squeezing action during the thinning process. However, this thermodynamic approach did not take into account the kinetic mechanism of rupture. Significant advancement was made later, by assuming that thermal and mechanical disturbances (having a wave-like nature) caused thickness fluctuations in thin films, thus leading to rupture or coalescence of bubbles at a critical thickness. From an early theoretical analysis of the hydrodynamic interfacial force balance, the critical thickeners of rupture was expressed in terms of the attractive van der Waals interactions (characterized by the Hamaker constant), the surface tension and disjoining pressure. The critical wavelength, λ_{cr} , for the perturbation to grow (assuming

the disjoining pressure just exceeds the capillary pressure) was determined. Film collapse usually occurs when the amplitude of the fast-growing perturbation was equal to the thickness of the film. The critical thickness of rupture, h_{cr} , is defined by the following relationship:

$$h_{cr} = 0.267(a_f A_m^2 / 6\pi\sigma\Delta p)^{1/7} \quad (2.1)$$

where A_m is the Hamaker constant, Δp is the excess pressure in the film, σ is the surface or interfacial tension and a_f is the initial area of the film. However, more recently several discrepancies in the theory have been reported, leading to modifications of this equation (3).

4 THEORIES OF FOAM STABILITY

Not surprisingly, there is no single theory which can satisfactorily explain the mechanism of foam stability. In fact, over the years, several different types of mechanisms have been established. These include the early surface viscosity theories and the mechanical dynamic surface elasticity theories of Gibbs and Maragoni. Prior to 1950, Russian researchers invoked the “equilibrium thin lamella films, stabilized by the disjoining pressure” theories, which were subsequently developed by various Bulgarian research groups. Some of these different types of mechanisms which lead to the stability of foams are summarized in Figure 2.3.

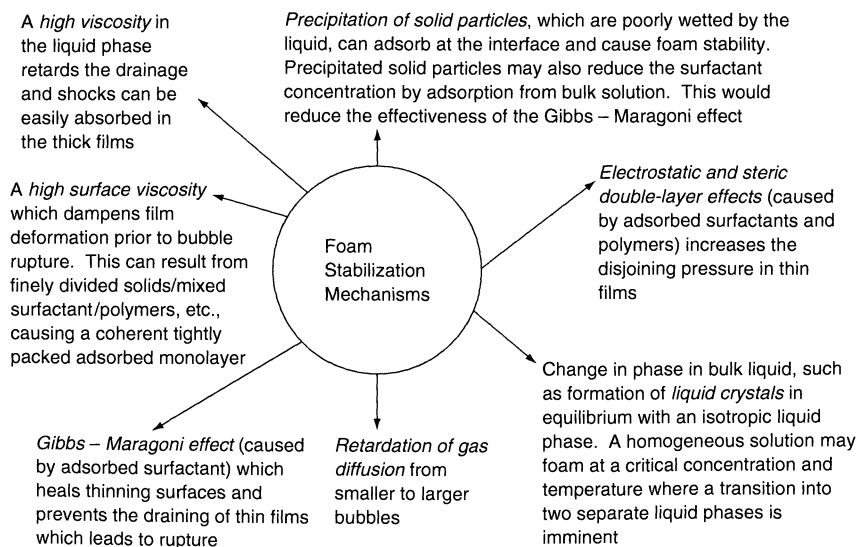


Figure 2.3. Various mechanisms of foam stability www.iran-mavad.com

4.1 Stability increase caused by increase in bulk viscosity

As a general rule, the *drainage rate of foams may be decreased by increasing the bulk viscosity of the liquid from which the foam is prepared*. This may be achieved in aqueous systems by simply adding a solute such as glycerol, liquid paraffin or polyoxyethylene (high molecular weight) to the aqueous phase. Alternatively, the phase of the aqueous surfactant solution can be changed by adding electrolyte, thus producing a gel network. For many practical systems, such as food foams, the drainage can be easily halted by hydrous gel formation and the lamella stabilized at relatively large thicknesses ($\approx 1 \mu\text{m}$). Overall, the more viscous the liquid, then the slower is the drainage between layers between the bubbles.

4.2 Stability increase caused by increase in surface viscosity

An alternative method to decrease the foam drainage kinetics is by increasing the surface viscosity. Generally, the surface viscosity can be increased by packing a high concentration of surfactant or particles in the surface, thus causing high adhesive or cohesive bonding (this type of mechanism is illustrated in Figure 2.4). For example, by adding relatively high-molar-mass polymers, proteins, polysaccharides or certain types of particle. Many food foams are stabilized by protein polymers adsorbed at the air/water interface. In addition, in many cases, high cohesion forces in the surface film can be achieved by using mixed surfactant systems. For example, many nonionic surfactants increase the persistence of foams stabilized by ionic detergents by forming highly condensed films (rigid or highly viscous). Other examples include sodium dodecyl sulfate

with dodecyl alcohol, and dodecylbenzene sulfonate with lauryl isopropanolamide. Such additives are usually classified as *foam builders*.

4.3 The adsorbed surfactant film can control the viscosity of the surface layer

Early ideas on foam stability assumed that the foam stability was determined by the adsorbed surfactant which controlled the mechanical-dynamical properties of the surface layer. The experimentally measurable parameters that characterize the mechanical-dynamical properties of monolayers are the surface elasticity and surface viscosity. Essentially, surface viscosity reflects the speed of the relaxation processes which restore the equilibrium in the system after imposing stress on it. It is also a measure of the energy dissipation in the surface layer. In contrast, the surface elasticity is a measure of the energy stored in the surface layer as a result of an external stress. Surface light scattering has proved a useful technique for determining the viscoelastic properties of monolayers. This enables the viscoelastic behaviour of equilibrium and non-equilibrium monolayers at an air–water interface to be studied without disturbing the original state of the monolayer. Although there was a certain amount of experimental evidence to support this idea, i.e. the mechanical-dynamical ideas of foam stability, there have been many exceptions to the rule.

4.4 Gibbs/Maragoni effect, surface elasticity and viscosity

The Gibbs coefficient of surface elasticity (E) was introduced as a variable resistance to surface deformation

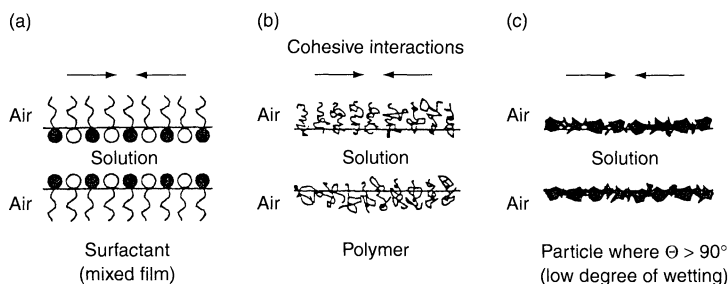


Figure 2.4. An increase in surface viscosity can be achieved by the presence of a high packing density of certain types of surfactant species which can cause strong cohesive interactions. Examples include (a) mixed surfactant systems, (b) polymers, and (c) particles with high contact angles, attached to the air/solution interface

during thinning. This parameter relates the increase in surface tension, γ , for a unit of relative increase in the surface area, A , and can be expressed by the following equation:

$$E = 2(d\gamma/d \ln A) = -2(d\gamma/d \ln l) \quad (2.2)$$

where $d \ln A$ is the relative change in the surface area A and $d \ln l$ is the relative change in the lamella thickness. Because of the two surfaces, the stress is equal to twice the increase of surface tension.

In the case where E is used to describe purely the elasticity, then E can be termed the "film elasticity of compression modulus". In the general case where the surface behaviour has both an elastic and viscous component, then E can be termed the "surface dilational modulus". Basically, E is the measure of the ability of a film to adjust its surface tension in an instant of stress and should be relatively large for the film to remain stable. By combining equation (2.2) with the Gibbs adsorption isotherm equation, it can be shown that E is proportional to $(d\gamma/dc)^2$, where c is the concentration of the surfactant in the thin film.

Two major variables which effect E are the film thickness and surface concentration. The concentration of surface-active material influences the concentration gradients. *For a freshly produced foam to survive, then surface tension gradients are necessary.* However, the main deficiency in the early studies on Gibbs elasticity was that it applies to thin films and the diffusion effects from bulk solution were neglected. In fact, the Gibbs theory only applies to a hypothetical equilibrium state (i.e. it is assumed that there is insufficient surfactant in the film to diffuse to the surface and lower the surface tension).

For thick lamellae, under dynamic conditions, the Marangoni effect becomes important and operates on both expanding or contracting films. The Marangoni effect tends to oppose any rapid displacement of the surface (the Gibbs effect) and may provide a temporary restoring or stabilizing force to "dangerous" thin films or at fairly high surfactant concentrations which can easily rupture. In fact, the Marangoni effect is superimposed on the Gibbs elasticity, so that the effective restoring force is a function of the rate of extension, as well as the thickness.

4.5 Thin films stabilized by surface forces under static (equilibrium) conditions in dilute surfactant

In addition to these early mechanical-dynamical stability theories, the equilibrium or static stability of free films in many surfactant systems, *black spots appear at a*

thin single films was later shown to be important. As described above, in the early stages of formation, foam films drain under the action of gravitational or capillary forces. Providing that they remain stable during this drainage process, they may gradually approach a thickness range of about 100 nm. At this stage, surface forces come into play and it was proposed during the 1950s that a positive disjoining pressure may slow down and prevent drainage. This results in the formation of a thin metastable (equilibrium) film.

It has been well established that four types of forces can operate in aqueous film layers at low surfactant concentrations ($< \text{CMC}$): (a) the Laplace capillary pressure, (b) the electrostatic double-layer repulsion, Π_{el} , (c) the van der Waals interactions Π_{vdw} , and (d) the short-range hydration or structural repulsive forces caused by steric hindrance in oriented and packed layers, Π_{st} . Initially, the Deryaguin disjoining pressure, Π , encompasses two of these contributions, as follows:

$$\Pi = \Pi_{el} + \Pi_{vdw} \quad (2.3)$$

In regions of low electrolyte concentration where Π_{el} dominates over Π_{vdw} (Π_{vdw} is usually relatively small), then Π_{el} can compensate for the capillary pressure, i.e. $\Pi_{el} = P_c$. This results in the formation of an *equilibrium-free* film, which is usually referred to as a thick common film (CF) (~ 50 nm thickness). This type of film has reached a state of metastable equilibrium, which persists until thermal or mechanical fluctuations cause rupture.

As discussed earlier, the critical thickness value at which the common films may rupture (due to thickness perturbations) has been designated as h_{cr} and since the process of rupture is statistical, then experimental observations of the thickness of rupture always show a distribution around h_{cr} . However, an alternative situation can occur as h_{cr} is reached, and instead of rupturing, a metastable film (high stability) may be formed with a thickness $h < h_{cr}$. The formation of this metastable film can be experimentally observed through the formation of "islands of spots" which appear black in light reflected from the surface. The spots are sometimes referred to as "holes" in order to emphasize the thinner regions in the film and the holes will spread over the complete film surface. This is often referred to as a "first black" or "common black" film. The lowest bulk concentration at which nuclei of the thinner black films are formed has been designated "c- black" (c_b), and this concentration is characteristic for every surfactant. For dilute surfactant systems, c_b values are about one to two orders of magnitude less than the CMC, and it has been reported

surfactant concentration above which the foam becomes extremely stable with a lifetime greater than 10 minutes. (Highly persistent froths are produced.)

In addition, further thinning can cause an additional transformation into a thinner stable region (stepwise transitions). This usually occurs at high electrolyte concentrations and leads to a second, very stable, thin black film, known as Newton, Perrin or secondary black films (~ 4 nm thickness). In these circumstances, short-range steric/hydration forces control the stability, and the disjoining pressure versus film thickness isotherms can be defined by the following relationship:

$$\Pi = \Pi_{el} + \Pi_{vdw} + \Pi_{st} \quad (2.4)$$

Figure 2.5 shows the Π versus h isotherm which can be conveniently used to explain equilibrium conditions and transitions from common to Newton black films. Two stable (equilibrium) thicknesses which correspond to given disjoining pressures are feasible, which thus correspond to the two types of black films. The thicknesses of the two equilibrium states can be obtained by measuring the intensity of the reflected light using photoelectric detectors. Usually in foam films, although the two types of black films may be formed, it is only possible to have one stable region since the stability of the two types of films are controlled by the different types of interfacial forces.

Later, the relevance of the van der Waals forces in foam films was realized and it was suggested that the black films correspond to a secondary minimum. However, the DLVO theory could not adequately describe

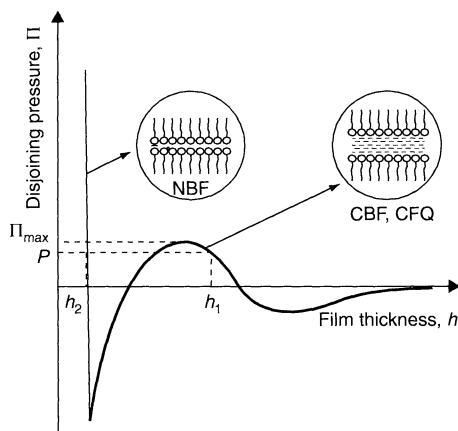


Figure 2.5. The general form of the force curves (pressure Π versus film thickness h) for a thin film containing fairly low concentrations of surfactant: NBF, Newton black film; CBF, common black film; CF, common film

the stability of Newton black films where the stability is controlled by the short-range molecular forces. In the case of sodium dodecyl sulfate (SDS), the thickness was reported to be about 33 Å and this film has a minimum dependence on salt concentration. The stability (which prevents further thinning) is determined by the short-range repulsive disjoining pressure, caused by the thin bilayer structures with a few molecules of water separating the two opposing monolayers.

4.6 Stabilization of foam films containing high surfactant concentrations ($> \text{CMC}$) by stratification and long-range ordered microstructures in thin films

At surfactant concentrations *beyond the CMC*, organized molecular structures can be formed within the thin film. This causes thinning of the film to occur, through a stepwise drainage mechanism known as *stratification* (Figure 2.6(a)). This gives an entirely different drainage pattern than that observed for films containing low levels of surfactant (Figure 2.6(b)).

The organized structures may form from micelles of ionic or nonionic surfactants in the aqueous solution which provide an additional contribution to the disjoining pressure. These micelle layers flow out of the film surface to the plateau borders, thus causing stepwise thinning, with each step corresponding to specific c_b concentrations. Further experiments by Wasan *et al.* (4) studied the ordering due to the interaction (via repulsive forces) of surfactant micelles or colloidal particles with narrow size distributions which were forced into the restricted volume of the film. These workers clearly showed that the ordered microstructure could play an important role in stabilizing foam lamellae. They suggested that the driving force for the stepwise thinning of the film was caused by the gradient of the chemical potential of the micelles at the film's periphery.

4.7 Stabilization of foam by liquid crystals

In addition to thin film models, the stabilizing action of liquid crystals in foams has been well established, especially in the case of nonionic surfactant systems. At low concentrations, no significant structure build-up has been detected. However, in the early 1960s convincing evidence of a stabilizing effect of liquid crystals at high concentrations was reported. It was suggested that the crystals had a twofold function, in that

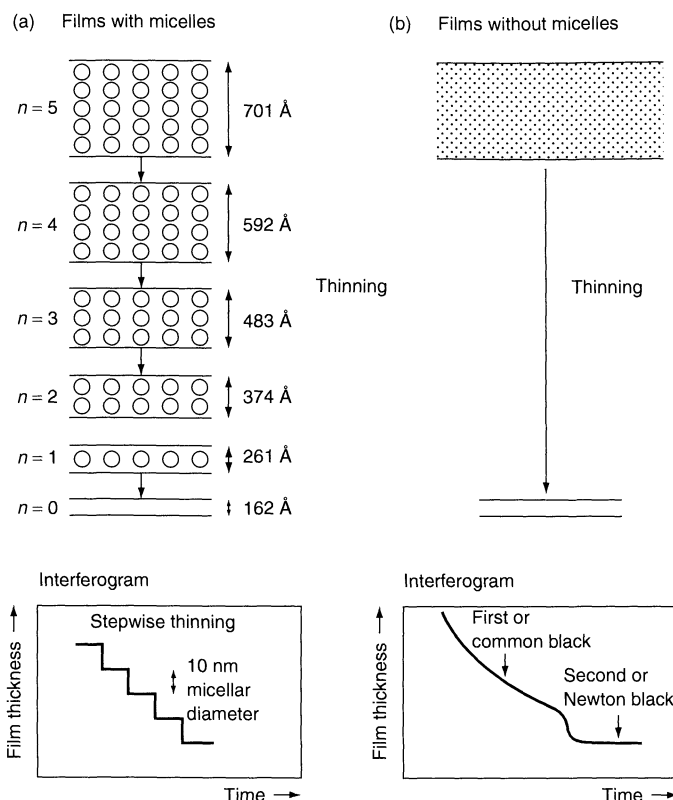


Figure 2.6. (a) Stratification thinning mechanism at high surfactant concentration ($> \text{CMC}$) and the main stages in the evolution of a thin film, and (b) thinning at low surfactant concentrations ($< \text{CMC}$) (From ref. (22))

the high viscosity reduces the liquid drainage through the lamellae because of frictional resistance, while they also serve as a reservoir of surfactant of the optimal composition to stabilize the foam (5).

4.8 Stabilization of foam films by a combination of surfactants (mixed films)

As described briefly above, in many cases it has been found that a combination of surfactants gives slower drainage and improved foam stability through interfacial cohesion. For example, the surface plasticity of a mixture of tannin and heptanoic acid in aqueous solution reaches high values, whereas there is no such effect from the two constituents separately. In addition, it has been reported that there are frequent cases where an alcohol or nonionic in the presence of another less surface-active component can lead to good interfacial cohesion. There are several possible explanations for the enhanced stability, including the following:

- (i) The nonionic causes a reduction in the CMC of the anionic solution.
- (ii) Although the anionic should not be too strongly adsorbed, a lowering of the surface tension, however, should occur for the nonionic/anionic combination.
- (iii) An increase in surface viscosity and drainage should occur for the surfactant combination. In many cases, a gelatinous surface layer is believed to be formed which gives low gas permeability and the formation of black films.

4.9 The stability of the froth can be controlled by emulsion and pseudo-emulsion films

Wasan *et al.* (4) investigated the influence of oil (in the micellar environment) on the stability of foam. Two different types of emulsified oil systems were studied, as follows:

- a microemulsion (solubilized within the micelle)
- a macroemulsion.

It was found that in each case the foam stability was effected by a completely different mechanism. In the first case, where the foam film containing oil is solubilized within the micelle to form a microemulsion, the normal micellar interactions are changed. It had been earlier demonstrated that micellar structuring causes stepwise thinning due to layer-by-layer expulsion of micelles and that this effect was found to inhibit drainage and increase the foam stability. Generally, this stratification phenomenon was found to be inhibited by the oil solubilized within the micelle which decreased the micelle volume (representing a decrease in the repulsion between the micelles).

In the case of the macroemulsified oil system, the important role of the so-called *pseudo-emulsion film* (formed between the air/water interface and an approaching oil droplet) on the stability of the aqueous foaming system was emphasized. (Figure 2.7). Clearly, the entering and spreading coefficients are thermodynamic properties which determine whether the particular configuration of the oil droplet is energetically favourable and they cannot predict the fate of the oil droplet under the dynamic conditions which exist within

the draining film. Under these circumstances, two distinct cases were considered:

- where the pseudo-emulsion film is unstable and the oil spreads;
- where the pseudo-emulsion film is stable and the oil drops do not enter the air/water interface.

4.10 Stability enhanced by the use of phase diagrams

Two-component systems (consisting of two liquids) are well known for showing a maximum in foam stability at a temperature and composition near the critical point, while three-component systems show a maximum in stability near the *plait* or *consolute point*. However, the region where enhanced foaming occurs corresponds to that where systems remain as homogeneous one-phase solutions, *but where a transition into two separate liquid phases is imminent*. However, in the case of complete separation of a liquid phase, then a conjugate solution may be produced which acts as a defoamer. Such a foaming enhancement in the one-phase system can be explained by the surface activity of one of the components which has a lower surface tension in the system and adsorbs at the surface. Surface activity and the tendency to foaming can therefore be related to solubility curves and other features of phase diagrams, as well as the relative surface tensions of the individual components. This type of foaming frequently occurs in fractionation or distillation towers processing liquids with several components, and thus foaming problems of this kind can be anticipated and avoided by studying the phase diagram of the particular system.

5 TEST METHODS FOR FOAM STABILITY

The most important factors in foaming are the “foamability” (or ease in producing a foam) and the stability of the foam. There are a range of test methods available for determining the stability of foams, although the shaking, bubbling and pouring methods are the most popular. Details of these have been reported in several publications (6–9). An overview of these test methods is illustrated in Figure 2.8 and some details are given in the following discussion. Many techniques have been developed by industry to answer specific foaming problems and frequently the results obtained fail to correlate with those from other test methods, while in other cases,

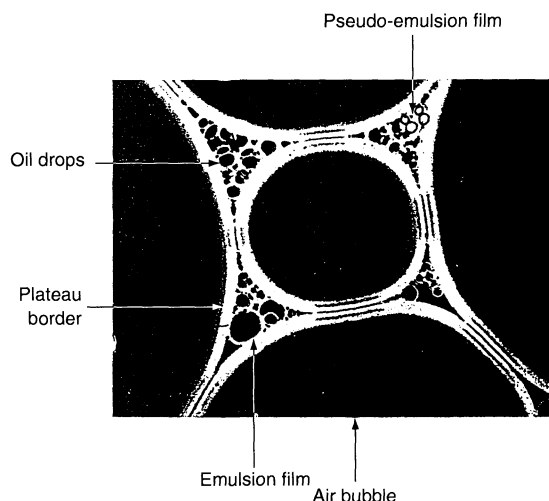


Figure 2.7. Illustration of a macroemulsified oil system. The drainage of the film may be reduced due to accumulation of emulsified oil droplets within the plateau borders. The formation of the emulsion film and pseudo-emulsion film are indicated. Factors effecting the foam stability were found to be oil volume fraction, drop size and oil phase density (from ref. (4))

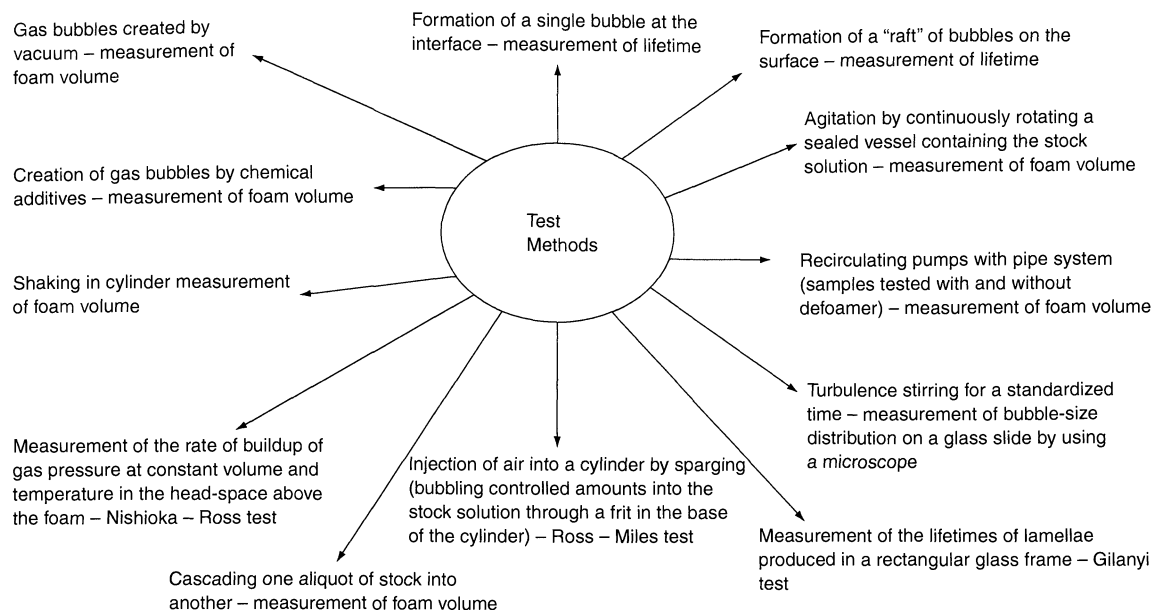


Figure 2.8. An overview of the test methods used for measuring foam stability

the methods are more general and correlation between the results from various methods can be achieved.

Overall, two groups of test methods may be identified. These may be broadly classified into the following:

- (i) dynamic foam methods, which measure the volume in a state of dynamic equilibrium between formation and decay;
- (ii) static foam methods, in which the rate of foam formation is zero and the foam is allowed to collapse with no regeneration since the gas flow into the foam is eliminated.

The dynamic foam stability is usually measured by the volume of foam at a specific equilibrium flow rate, while the static foam stability is measured by the rate of collapse. Dynamic measurements are particular relevant for transient foams, while for foams of high stability, the static or equilibrium methods are usually more useful, particular for highly stabilized foams such as protein-stabilized foam systems.

5.1 Shaking in a glass container

This is a simple method and obviously depends on the method of shaking. For example, the intensity, the solution viscosity, and the ratio between gas and liquid volumes in the vessel all play important roles in the

generation of foam. The greater the quantity of solution in the cylinder, then the higher the volume of foam produced. In addition, the narrower the cylinder, then the greater the height. The initial height of the foam and the rate of decay can be measured fairly easily.

5.2 Bikerman test with a cylindrical column (Sparge tube technique)

The Bikerman test is a relatively old method, which was first proposed in 1938. Samples of liquid are foamed in a thermally insulated glass column with a glass frit in the base to create the foam bubbles. The column is 70 cm high and 3 cm in diameter. The gas is thermally equilibrated, saturated with vapour from the liquid and bubbled through the liquid sample (which usually has a volume of about 50 ml). The equipment used is shown in Figure 2.9(a). The steady-state volume, V (cm^3), is measured at a series of gas flow rates, U (cm^3/s), and the ratio $V/U = \sum(s)$ gives a time in which should be independent of the gas flow rate. Usually, a height/flow rate profile is determined Figure 2.9(b). Transitions in the slope of the profile can indicate transitions in the foam state near critical points in two-component systems. The Bikerman test *assumes* the steady-state foam volume to be independent of the container shape. The weakness of this cylindrical test is that wall effects

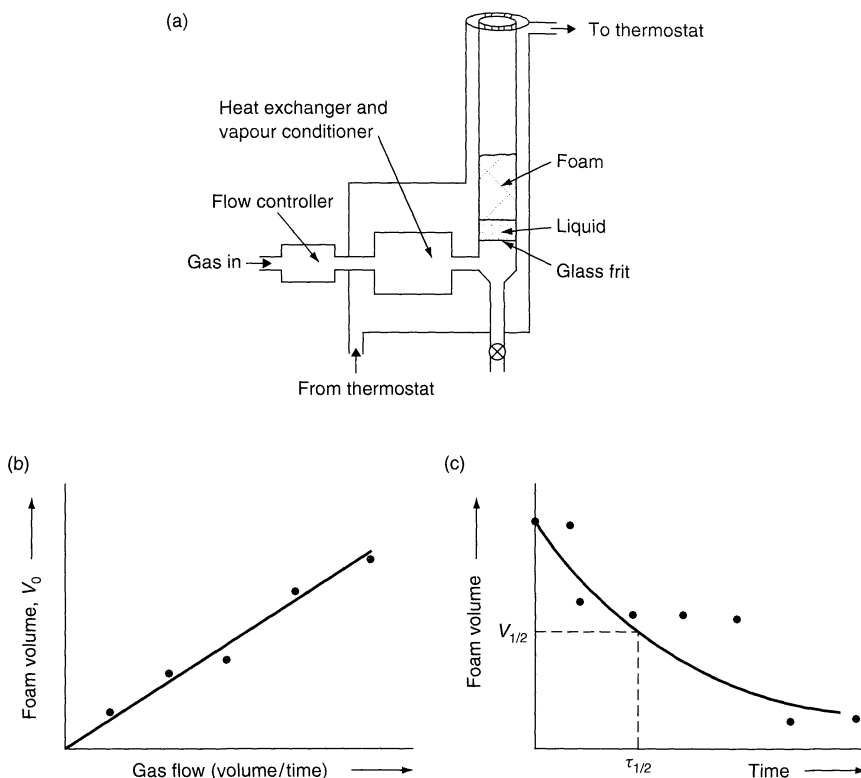


Figure 2.9. The Bikerman method for measuring both the dynamic and equilibrium foam stabilities by using a cylindrical container: (a) Schematic of the apparatus; (b) dynamic testing from foam volume as a function of gas flow; (c) equilibrium testing from foam volume as a function of decay time (note that wall effects may cause scatter in the results obtained)

occur and the height of the foam near the walls is higher than in the centre. This results in a non-distinct or diffused liquid foam boundary. *The Bikerman test also assumes that the steady-state volume is independent of the container shape, although this is invalid and is a fundamental weakness of cylindrical containers.* In addition, the surfactant is consumed during testing and in order to obtain a steady-state foam, then the duration of foaming or the volume of the foaming solution should be restricted.

It is also important to stress that the Bikermann test determines foam stability under dynamic conditions, and as the bubbles move up the column to the interface under the buoyancy force (Archimedes), they are also subjected to (Stokes) frictional forces. Therefore, the time to reach the surface can be defined by the following:

$$t = (9l\eta/2r^2)\rho g \quad (2.5)$$

where η and ρ are the viscosity and density of water, respectively r is the bubble radius and l is the column

length (to the water/air interface). In this test, the time period would normally correspond to about 10^{-2} to 10^{-1} s, and this period may be insufficient for the surfactant to diffuse and adsorb on the bubbles, so that the surface coverage may not be complete. In this case, the thin film separating two bubbles at the surface may not be in equilibrium and the stability cannot be related to the disjoining pressure where relatively large liquid film separation distances are usually involved (2000 \AA). Under these circumstances, it is more feasible that the foam stability will be related to the dynamic rheological properties of the monolayer.

The foam equilibrium decay time can also be determined by switching off the gas flow and measuring the decay of the foam as a function of time (Figure 2.9(c)).

5.3 Funnel-shaped test

This method can be used for foams whose stability is column-dependent on the container geometry. A comparison

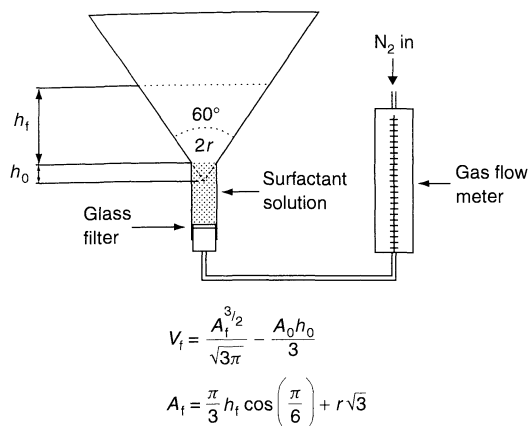


Figure 2.10. Schematic of the apparatus used in funnel-shaped testing. The foam volume, v_f , is calculated from the equations shown, where A_f and A_0 are the areas of the normal cross-sections at heights of h_f and h_0 , respectively; h_f is the foam height and r is the radius of the base of the truncated cone. The steady-state volume is determined at a set gas flow and the slope of the foam volume versus gas flow curve gives the kinetic foam stability (lifetime of gas in the foam) measurement

between the average lifetime of foam bubbles in a cylindrical and conical vessel for alkyl glycosides was reported recently by Waltermo *et al.* (10). In all cases, the results obtained corresponded to lifetimes close to 10–40 s. For a given solution and fixed gas injection rate, the foam height was constant and the stability was independent of the container geometry. The apparatus used is shown in Figure 2.10.

5.4 Pour test method (the Ross–Miles test)

This method is based on the pouring of a liquid from a certain height on to a volume of the same liquid. The apparatus used for this is shown in Figure 2.11. This test is sometimes inconclusive since the foam produced is often of non-homogeneous dispersity, i.e. it is coarser in the upper layers and less stable. However, this pour test probably gives more meaningful results than stirring, beating or whipping tests.

5.5 Foaming in a rotor mixer

In a rotor mixer, foaming is defined as the maximum amount of gas that can be dispersed into a solution as the mixer is supplied with constant gas and liquid flows. Foaming has been carried out at different rotation

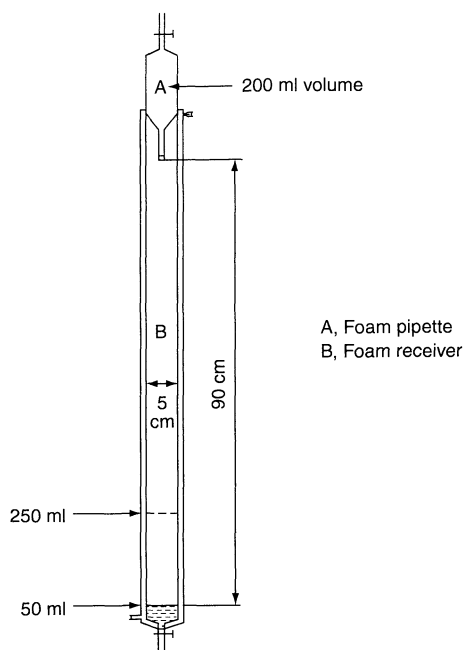


Figure 2.11. Schematic of the apparatus used in the Ross–Miles pour test. (ASTM (American Society for Testing and Materials) D1173-63 Standard test method). The foam volume is measured immediately after the generation of the foam, and again after periods of 5 and 10 min

speeds with silica suspensions and it has been found that at low liquid flow rates, the solid particles have no influence on foamability, although at high liquid flow rates the foamability decreased with increasing silica constant, with this effect becoming smaller for high rotation speeds. The foaming ability is characterized by the volume of foam generated, which depends on the method of generation, temperature and the stability with respect to internal collapse. Figure 2.12 shows a schematic of a ball mixer used to evaluate foaming in the paper industry.

6 RESEARCH TECHNIQUES FOR STUDYING FOAM STABILITY

6.1 Microscopic and photographic methods

A relatively simple method for evaluating foam stability consists of “flash-freezing” the foam in liquid nitrogen, slicing the frozen foam and then observing the cells under the microscope. Image analysis and optical probe

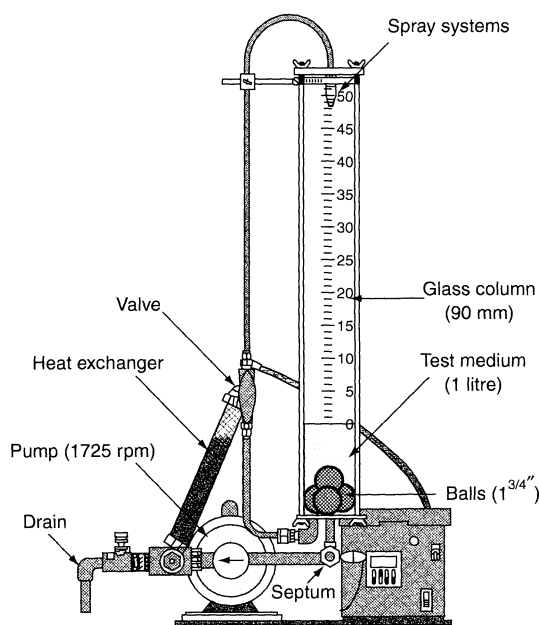


Figure 2.12. Schematic of a rotar ball mixer used to evaluate foams in the paper industry

techniques have also been used to measure the change in bubble size distribution in wet foams during ageing. Typical image analysis pictures of an ageing aqueous foam against a wetted wall are shown in Figure 2.13. Transformation of the raw data to final bubble size distribution enables this technique to be used to monitor drainage and stability (11). Such data are useful for distinguishing between coalescence (where larger bubbles appear) and disproportionation (which can result in both smaller and large bubbles appearing, sometimes giving a bimodal distribution). However, since the processes are interrelated, it is therefore usually difficult to distinguish the two processes quantitatively. Video recording is often useful for studying the kinetics of the system.

By using low-magnification microscopy (25–1000x), a general overview of the structure can be obtained, whereas medium magnification (1000–25 000x) gives specific bubble shapes and the extent of anisotropy. High magnification enables evaluation of the position and density of chemical ingredients such as surfactant, emulsifier or frother. The unaided eye is also sensitive to fine difference in structure between different foams. The thermal printer video microscope is a relatively simple and rapid method for comparing foam structures and can be used in a range of different systems. Figure 2.14 shows comparative video microscope images of a foamed chocolate and a sample of shaving foam.

6.2 Optical fibre probes

This method enables the bubble size distribution in wet foams to be measured. An optical fibre probe of about 20 μm diameter is inserted into the foam and moved through the sample at a controlled speed, with light being sent through the probe. The light reflected is measured continuously. If the probe is in air (e.g. in a gas cell), then part of the light is reflected, while if the probe is in the liquid phase then most of the light is transmitted. From an alternating analog signal, the length of the gas and liquid traversed is recorded and also the cord length of the cells (as they are pierced). Wet cord lengths corresponding to the liquid phase while dry cord lengths correspond to the gas phase. The equipment and procedure used is illustrated in Figure 2.15, and are described in detail in reference (12). This is a useful technique for determining the cell size on-line and can be used for, e.g. wet material and cement foams. However, the method has limitations in that the foam cells must be greater in size than the probe and the movement of the fibre probe may rupture the cell walls. The method can be used at high temperatures and pressures and can thus play an important role in foam studies.

6.3 Measurement of head space in foam

Measurement of the head-space pressure with time in a closed thermostated chamber enables the area decay of the foam to be calculated. The stability of static foam can also be determined from the rate at which the total area of liquid lamellae disappears. This can be measured photographically or by using digital image analysis. The interfacial area can be determined by monitoring the pressure, external to the foam in a container of constant volume and constant temperature, if the total volume of the system and the surface tension of the foamed liquid are known.

6.4 Foam pressure drop technique

A direct comparison between different methods of evaluating foaming is rarely feasible, since each method involves different parameters, and also foam stability is determined at different pressures in the foam liquid phase. These features mean that the rate of drainage and the time to reach the equilibrium state are different. However, the foam pressure drop method enables small

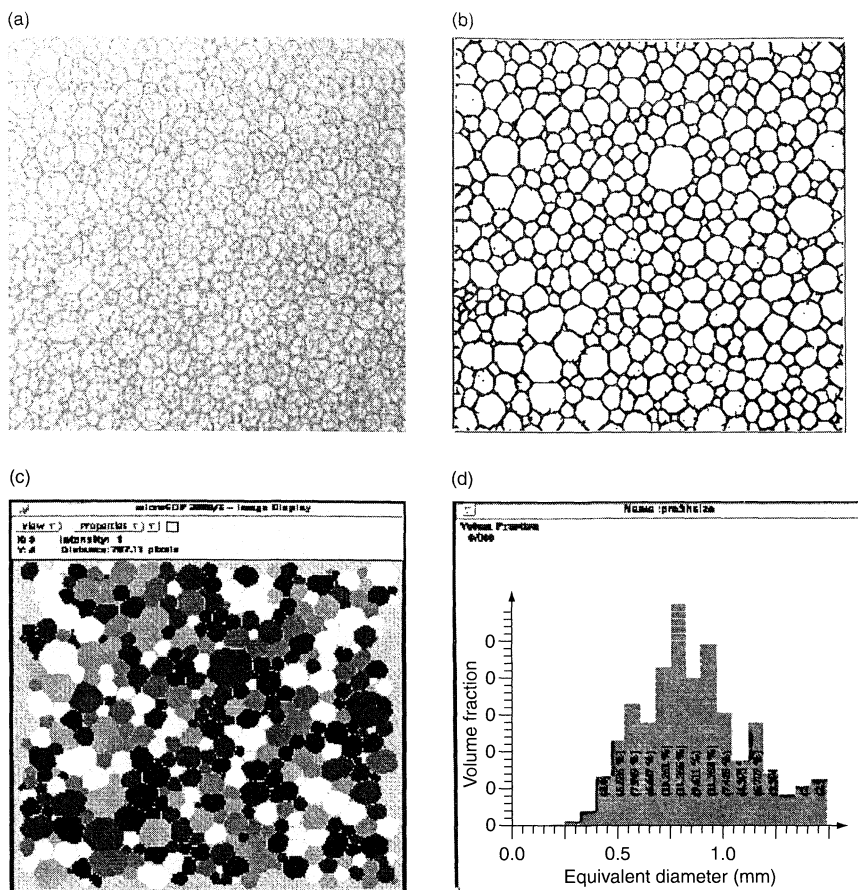


Figure 2.13. Foam stability as observed against a wetted wall, where the foam cell size is determined by image analysis by using the following. Transformation steps: (a) raw image; (b) process binary image; (c) measured grey-scale image; (d) bubble size distribution (from ref. (11)), reproduced with permission

differences in the foam stabilities of surfactants to be detected by measuring the lifetimes of the foams at constant pressures (6).

In this method the pressure in the foam plateau borders is regulated by a porous plate and the foam is generated by injecting compressed air through the plate into the foaming solution. Initially, the foam is produced and is then transferred along a glass wall to a collecting vessel. The measuring cell is then filled with the foam to a specific level, which is covered by a lid to ensure a constant vapour pressure atmosphere. The foam properties are investigated by employing platinum electrodes for measuring the conductivity and a capillary micromanometer for measuring pressure in the plateau borders. A sintered glass cell has been used and was found to be useful in the study of structured foams obtained from proteins and saponin solutions.

6.5 Drainage of foam films

By using the thin-film balance developed by Scheduluko and Exerowa (6), the drainage of foam films has been extensively studied. The apparatus employed is shown in Figure 2.16.

6.6 Electrical conductivity

This method is useful for the continuous monitoring of drainage rates and the stabilities of foams. The technique is similar to the Bikerman column test, although in this case pairs of silver-or platinum-plated electrodes are situated at different heights in the column. The electrodes are connected to an analog digital converter

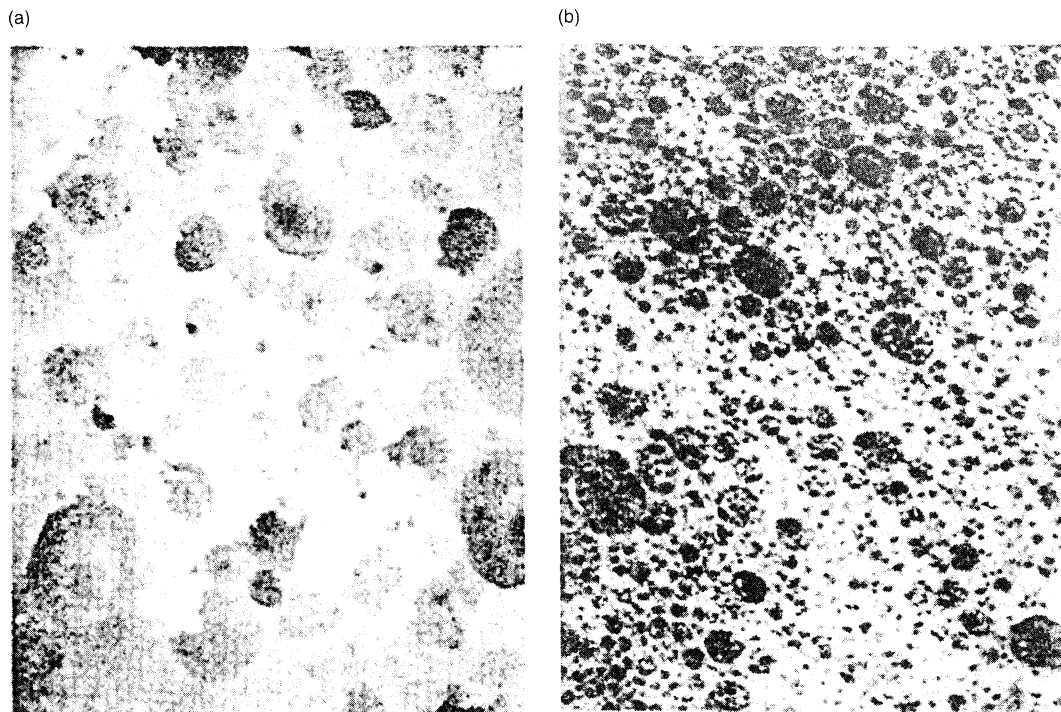


Figure 2.14. Thermal printer video microscope images of (a) foamed chocolate, and (b) shaving foam (from ref. (4)), with permission from American Chemical Society

and microcomputer, and the conductivity between the electrode pairs is followed over a period of time.

6.7 Back-scatter techniques

By using a “Turbiscan MA 10 000” instrument, a relationship between the back-scattering and bubble size of a foam system can be evaluated (13). The latter can be related to the foam stability. This way, mean bubble size determination can be made from a large population of foam bubbles. The results obtained have been reported to show a linear relationship, with a good correlation between the mean back-scatter level and bubble size, in spite of refractive index differences between the products. Figure 2.17 presents a series of results obtained for various proprietary shaving and hair foam products.

6.8 Lamellae lifetime

A simple method for measuring the effectiveness of foam stabilizers in, for example, polymer foam systems

such as polyurethane involves the use of a ring immersed in a liquid which is, pulled out vertically at a controlled rate (similar to the standard method used for surface tension measurements (the de Nouy ring technique)). The height of the liquid column pulled by the ring can be directly related to the foaming stability.

7 INDUSTRIAL MATERIAL AND FOOD FOAMS

Foams exist widely in nature, for example, as cellulositic wood, biominerals, marine organisms, etc. However, today many different types of foam materials are produced by synthetic processes and those are used for a wide range of applications.

7.1 Polymeric foams

Foamed plastics (known as cellular or polymeric foams) usually have a high strength to weight ratio and are used in a wide range of industries (building and construction, furniture, bedding, clothing, packaging, carpeting, automobiles, military applications etc.). In addition, certain

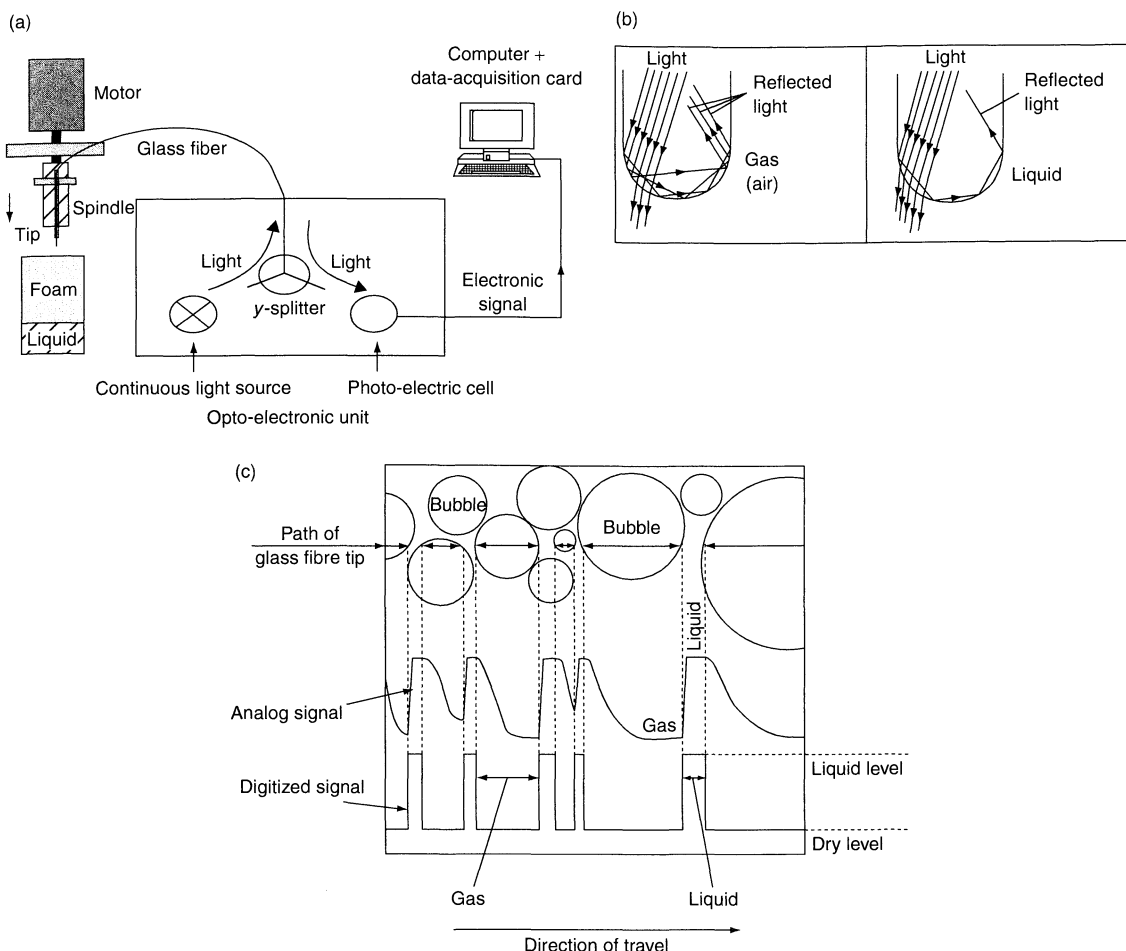


Figure 2.15. Optical fibre probe foam analysis showing schematic representations of: (a) the foam analyser; (b) the fibre tip with light reflected in the gas and liquid phases; (c) the events which take place when the probe is moved through a foam. In the latter, the path of the probe and the chord lengths are shown at the top, while in the middle and at the bottom, respectively, the analog and digitized signals are shown (from ref. (12)), with permission from Elsevier Science

polymeric foams are used for reducing the impact of explosions and for cleaning up oil spills. One of their many advantages is that they retain many of the structural properties of solid materials but with a considerably reduced density. Typical examples of well-established polymeric structured foams include polyurethane, poly (vinyl chloride), epoxy and polystyrene. These consist of a polymer (or blends) and inorganic fillers (such as glass, ceramic, fibre and gypsum) or other filler waste products. Several experimental products have been recently produced, such as polymers mixed with mineral (clay) wastes and other additives to achieve a foam with a density equivalent to that of wood.

Generally, foam plastics can be classified in several different ways, including the following:

- flexible or rigid
- by dimension or geometry, e.g. sheets or boards
- by weight, e.g. low or high density

There are also *two separate groups of gas-filled polymer foam structures*. These may be classified as the *closed-cell type* where the cells are predominately isolated from each other, and the *open-cell structures*, where the cells are connected so that the bubbles exist in a continuous phase. Only the closed-packed structures are considered

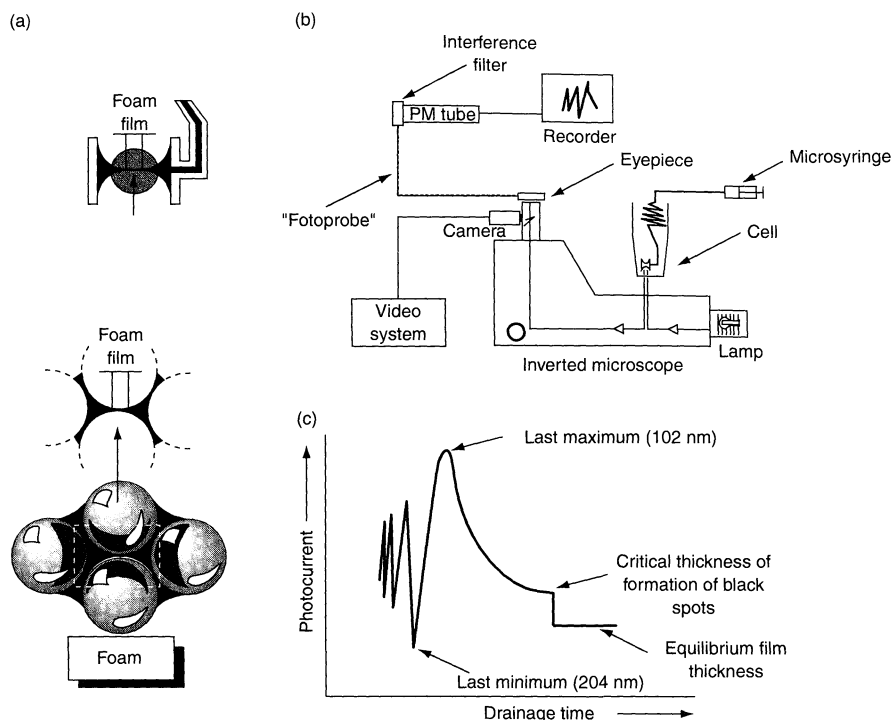


Figure 2.16. The thin-film balance method used for evaluating the stability and drainage of foam films: (a) schematic representation of the geometry of films in a foam, which occurs in the measuring cell of the Scheludko-Exerowa system; (b) schematic of the set-up used for studying microscopic thin aqueous films; (c) a typical interferogram of photocurrent versus time of drainage for the thinning process (adapted from ref. (6)), with permission from Elsevier Science

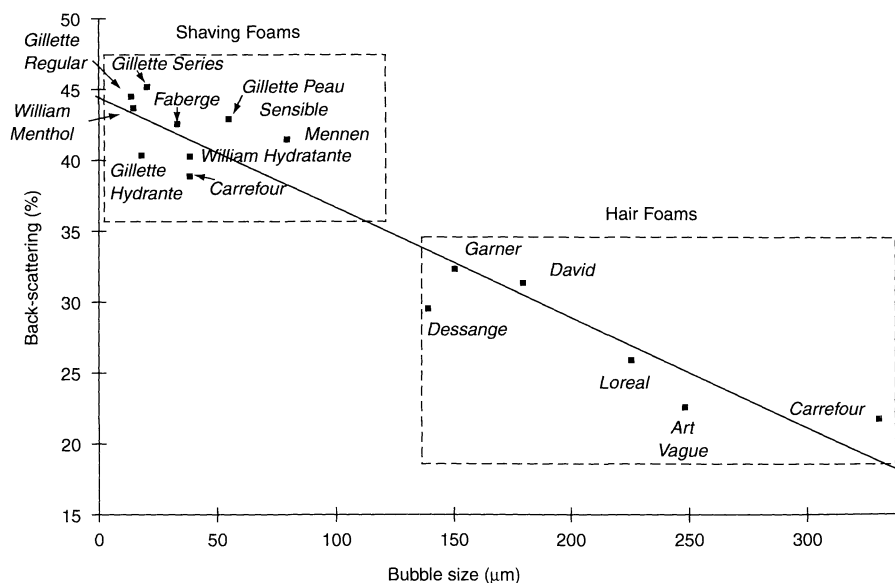


Figure 2.17. Correlation between back-scattering and bubble size, showing the results obtained from "Turbiscan MA 10000" measurements on a selection of various proprietary shaving and hair foam products (from ref. (13))

to be true polymer foams. Such forms are generally produced by two different techniques. The first involves the thermoplastic production technique, while the second uses liquid oligomers which contain active groups. The latter method is more common, since it can be carried out at lower temperatures and pressures and is also more economical.

Thermoplastic foams are produced with a range of densities (from 3 to 50% of the polymer density). Foaming involved bubble nucleation and bubble growth (where phase separation occurs) when the applied pressure in the system falls and the bubbles nucleate. Bubble formation can also occur by the action of heat, vacuum, motion, reaction and cavitation. Table 2.1 presents some of the common phase separation phenomena and the possible mechanisms involved. Microcellular plastics can be produced by nucleating a large number of bubbles using a rapid pressure drop to suppress cell coalescence. The foam polymers are characterized by a cell density greater than 10^9 cells/cm³ and a full-grown cell size of 10 μ m. A typical scanning electron micrograph for a microcellular plastic is shown in Figure 2.18.

High-density foams utilize blowing agents that decompose and release gas which dissolves in the melt.

Table 2.1. Phase separation phenomena and mechanism of foam formation (from ref. (14))

Phenomenon	Mechanism
Boiling	Heat
Plastic foaming	Heat and/or reaction or pressure reduction
Cavitation	Pressure variation
Devolatilization	Vacuum, inert gas seeding
Wave foaming	Hydrodynamic pressure

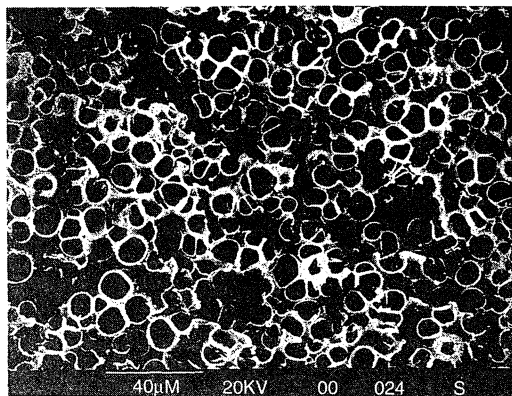


Figure 2.18. A scanning electron micrograph of a typical microcellular plastic foam (from ref. (9)), reproduced with permission

As the pressure is reduced, by passing through a die, the gas is released, thus producing the foam. Lower-density foams utilize liquid- or gas-blowing agents (physical blowing gases) injected into the plastic. The gas must be soluble at high pressures and temperatures, and must also become partially soluble as the pressure is reduced so that nucleation is initiated.

The type of polymer, the type of foaming or blowing agent, the expansion process, the post foam-curing, etc., can all influence the final product. During the foaming process, the type of gas, gas content, processing conditions and foaming dynamics all affect the final structure and morphology. Unfortunately, a full understanding of the processes involved has not yet been achieved, although there are several publications available which give a useful guide to the physics, chemistry and engineering involved in the processing (14–17).

Although foamed materials can be manufactured fairly easily at low cost, the processing steps are complex and very sensitive to external influences. Slight changes in environment (thermal, pressure, wetting, and interfacial properties) can cause changes in the process step conditions. These may cause changes in the bubble expansion rate, diffusion, drainage and coalescence. If this occurs before loss of movement and solidification (quenching), then dramatic changes in the final foam structure may result. By understanding the relationship between final structure and interfacial processing, one cannot only improve established manufacturing processes but also generate new materials. The challenge is to identify the best processing conditions and steps which will generate the desirable structures.

The formation and preservation of the cell structure is an important step in processing the polymer. If bubbles are sparsely distributed in the foam, they will occur as spherical cells since this is the shape with the lowest surface energy. If the foam is less dense then the cell will move towards a tetrahedral shape, with the wall stability being achieved by careful control of the factors that influence the membrane thinning. Capillary action and drainage cause thinning, while an increase in viscosity of the fluid reduces the drainage effects. Viscosity increases can result from chemical reactions that increase the molecular weight through polymerization or cross-linking, or by temperature reduction. Ultimate stabilization occurs as a result either of chemical reactions which continue to the point of complete gelation, or may result from the physical effect of cooling.

Foaming agents are important additives in foamed thermoplastics. Such ("physical") foaming agents are low-boiling point liquids (pentane or isopropyl alcohol)

Table 2.2. Commercially used chemical foaming agents (from ref. (14)), reproduced with permission from Academic Press

Common name	Chemical name	<i>endo-lexo-</i>	Decomposition temperature (°C)	Gas evolution (cm ³ /g)	Main foaming gas evolved
Citric acid/Sodium bicarbonate	—	<i>endo-</i>	160–210	120	CO ₂
ADCA	Azodicarbonate	<i>exo-</i>	205–212	220	N ₂
OBSH	<i>p, p'</i> -Oxybis(benzene) sulfonyl hydrazide	<i>exo-</i>	158–160	125	N ₂
TSH	<i>p</i> -Toluene sulfonyl hydrazide	<i>exo-</i>	110–120	115	N ₂
TSS	<i>p</i> -Toluene sulfonyl semicarbazide	<i>exo-</i>	228–235	140	N ₂
DNPT	Dinitrosopenta methylenetetramine	<i>exo-</i>	190	190	N ₂
SPT	5-Phenyltetrazole	<i>exo-</i>	240–250	220	N ₂
SBH	Sodium borohydride	<i>endo-</i>	— ^a	2000	H ₂

^aSBH is chemically activated by exposure to water.

which remain liquid when the melt is under pressure, but where the foaming agents change from liquid to vapour when the pressure is reduced. Other types of foaming agents include inert gases such as CO₂ or N₂. Chemical foaming agents utilize a chemical which decomposes to produce a gas or gases, which then act similarly to physical foaming agents. A selection of commercially used chemicals foaming agents are given in Table 2.2.

In typical systems, such as polyurethane foams, the foam is produced by the polymerization of polyols with isocyanates and it is necessary to provide “cell-openers” to obtain an open foam structure that does not shrink on cooling. In the manufacture of cold-hardening urea–formaldehyde foam plastics, an alkylnaphthalene acid derivative is used as a foam-forming agent, although flexible polyurethane products are also widely produced. During the processing of this foam, water reacts with the isocyanate groups and produces carbon dioxide gas, which thus causes bubbles expansion and finally occupies over 95% of the volume of the product. The four stages of the foaming process leading to cell opening are shown in Figure 2.19, while Figure 2.20 shows a scanning electron micrograph of a typical curved polyurethane foam. The formulation used for the latter is shown in Table 2.3.

Recently, a series of polydimethylsiloxane (PDMS) polymeric surfactants with poly(ethylene oxide)-*co*-(propylene oxide) pendant groups grafted to the PDMS backbone were used to stabilize the foam cells in flexible polyurethane foam (18). It was found that the surfactant influenced the bubble generation and “cell window” stabilization stage. Surfactants with higher film elasticities yielded slower drainage rates and better foam-cell stabilities. In latex foams and sponge systems, potassium soap solution is often used as a foam stabilizer.

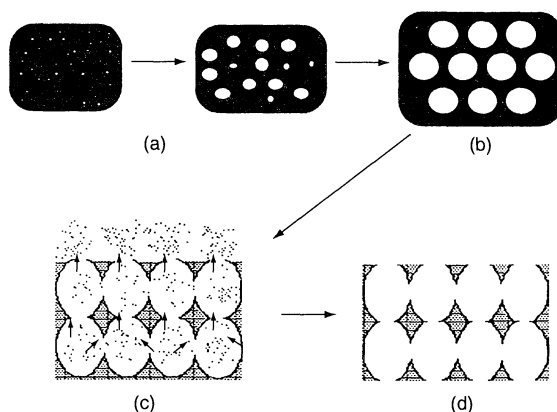


Figure 2.19. Macroscopic views of the different stages during polyurethane foaming: (a) bubble generation and growth; (b) packed bubble network (bubble expansion); (c) urea microphase separation (polymer stiffening) and cell opening; (d) final curing (from ref. (18)), reproduced with permission from Academic Press

7.2 Porous metallic foams

Metal foams such as aluminium have shown potential use in the manufacture of aircraft carrier and aircraft components (tailfins and wings). Aluminium foams have been tested in the bodies of cars and have been shown to improve safety by adsorbing the energy involved in collisions and crashes. Metal foams have found an interesting use as heat exchangers, in an analogous way to that of common “finned” structures and thermal insulation. Several companies are manufacturing metallic foams and trying to establish themselves in various emerging markets.

Many different methods are used to make metallic foams with one interesting method involving starting

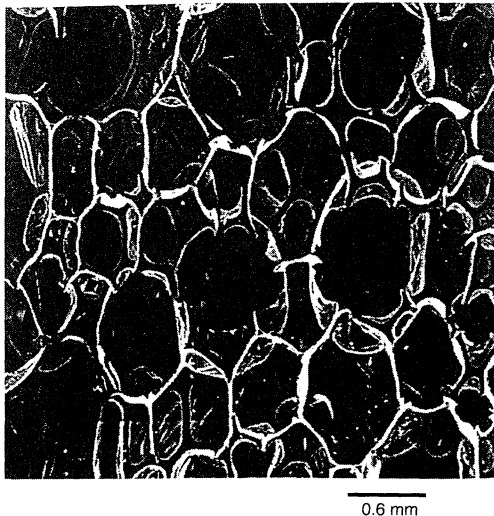


Figure 2.20. Scanning electron micrograph of a typical curved polyurethane foam (from ref. (18)), reproduced with permission from Academic Press

Table 2.3. Polyurethane foam formulation (cf. Figure 2.20) (from ref. (18))

Component	Content (pphp ^a)
Voranol TM 3137 ^b	100.0
Water	4.0
Dabco TM 33LV ^c	0.30
Dabco TM T-9 ^d	0.20
Silicone surfactant ^e	1.0
Voranate TM T-80 ^f index	110.0

^aParts per hundred parts of VoranolTM 3137 polyol (by weight).

^bA 1000 equivalent weight triol containing 13% ethylene oxide, 87% propylene oxide and all secondary hydroxyl groups (Dow Chemical).

^c33% Triethylenediamine in dipropylene glycol (Air Products and Chemicals).

^dStabilized stannous octoate (Air Products Chemicals).

^ePolysiloxane-polyoxyalkylene block copolymer (Witco Corporation).

^fAn 80:20 mixture of 2,4- and 2,6-toluene diisocyanate (Dow Chemical).

with polymeric foam and then depositing the metal from the vapour phase; Later, the polymer is burnt out from the system (19).

7.3 Low-density cement foams

In the building industry, concrete foams are mainly used as lightweight blocks, load-compensating structures

in soft soil, trench filling, roof-decks, frost and fire proofing, and in reinforced walls (1). Cement foams can be made by either chemical or mechanical processes. For the chemical processes, a finely divided powder such as aluminium is added to the slurry (consisting of cement, lime, siliceous filler, fly ash, etc.). After reaction between the lime and the aluminium, hydrogen bubbles are released and replaced by air. Mechanical foams are produced by pressuring with air or by agitating the cement after adding a solution of foaming agent. The latter include proteins, wood resins, sodium aliphatic sulfates, sodium naphthalene isopropyl sulfate, petroleum sulfate derivatives or synthetic tensides. At present, many companies are generally using well-known surfactants, ranging from commercial brands such as "Brixol" and "Nicerol" to fish protein oil, although the choice of surfactant has mainly been based on a trial-and-error basis.

The main advantages of using foam concrete is that the density of the material can be varied between 300 and 1600 kg/m³, and the foam provides good insulation properties and it is easy to handle by pumping. However, several properties still need to be modified in order to make foam concrete an even more competitive material. There is a need to decrease the shrinkage and the water uptake, and to increase the strength and the insulation ability. At present, the foam structures can be enhanced by the use of various additives, such as micro-silica or superplasticizers which reduce the cement/water ratio and improve the stability. Polyester fibre additives enhance the hardening and also improve the tensile properties.

Foamed cement systems are also used in engineered fills for geotechnical applications, for example, in the oil industry in drilling operations for well completion. The slurry foams are pumped into the wells to displace the mud after drilling. In recent years, many patents concerning the generation of foamed slurries have been issued, dealing mainly with the mechanical approach, i.e. developing processing generators for high-pressure foaming production and new types of foaming equipment. These patents emphasize the need to produce a light, stable slurry, although very few investigations have been carried out to study the influence of the foaming surfactant in these systems. In oilfield applications, the pressure and temperature may vary widely during the blending of the cement foam slurry at ground level to the curing process in the drilling holes. This demands that the foam generated must be very stable during the pumping operations.

7.4 Food foams

Solid foams are produced in the baking process (in bread and the making of sponges). In addition, extruding foaming liquids are processed in the production of chocolate bars. In food foams, the surrounding matrix frequently sets, with this being caused by coagulation of proteins and gelatinization of starch. Bread is probably one of the most ancient food foams. The latter consists of flour, water and yeast. After mixing and incubating the enzyme from the flour, amylase breaks up the long starch chains to produce the shorter sugar, maltose. This then reacts with the yeast to produce alcohol and carbon dioxide. The gas causes the dough to rise during warming in the oven, so resulting in an increase in bubble size. Food foams also exist as buttercreams, marshmallows, filling creams, sponge cakes, souffles, etc. Several books have been published which extensively cover the area of food foams (20, 21).

8 REFERENCES

1. Tonyan, T. D. and Gibson, L. J., Structure and mechanics of cement foams, *J. Mater. Sci.*, **27**, 6371–6378 (1992).
2. Sadoc, J. F. and Rivier N. (Eds), *Foams and Emulsions*, NATO ASI Series, Series E, Applied Science, Vol. 354, Kluwer Academic Publishers, Dordrecht, The Netherlands, 1999.
3. Ivanov, I. B. and Dimitrov, D. S., Thin film drainage, in *Thin Liquid Films* Ivanov, I.B. (Ed.), Surfactant Science Series, Vol. 29, Marcel Dekker, New York, 1988, pp. 379–496.
4. Wasan, D. T., Koczko, K. and Nikolov, A. D., Mechanism of aqueous foam stability and antifoaming action with and without oils; a thin film approach, in *Foams, Fundamentals and Applications in the Petroleum Industry*, Advances in Chemistry Series, No. 242, Schramm, L. L. (Ed.), American Chemical Society, Washington, DC, (1994), pp. 47–114.
5. Akers, R. J., *Foams*, Academic Press, London, 1976.
6. Exerowa, D. and Kruglyakov, P. M., *Foam and Foam Films*, *Studies in Interface Sciences Series*, Vol. 3, Möbius, D. and Miller, R. (Series Eds), Elsevier, Amsterdam, 1998.
7. Wilson, A. J., *Foams: Physical Chemistry and Structure*, Springer-Verlag, Berlin, 1989.
8. Bickerman, J. J., *Foams*, Springer-Verlag, New York, 1973.
9. Prud'homme, R. K. and Khan, S. A. (Eds.) Experimental results in foam rheology, in *Foams*, Surfactant Science Series, Vol. 57, Marcel Dekker, New York, Ch. 4, pp. 217–242.
10. Waltermo, A., Manev, E. R., Pugh, R. J. and Claesson, P., Foam studies and surface studies of aqueous solutions of octyl- β -glucoside, *J. Disp. Sci. Technol.*, **15**, 273–296 (1994).
11. Weissenborn, P. and Pugh, R. J., Measurement of bubble size distribution in froths and its application to studying froth structures and stability, in *Proceedings of the 12th Scandinavian Symposium on Surface Chemistry*, Stenius, P. and Sarvaranta, L. (Eds), Department of Forestry Production, Helsinki University of Technology, Publication C6, Helsinki, 1994, pp. 152–154.
12. Bisperink, C. G. J., Ronteltap, A. D. and Prins, A., Bubble size distribution in foams, *Adv. Colloid Interface Sci.*, **38**, 13–32 (1992).
13. Puech, K., Stability analysis methods of colloidal systems with a new instrument; the Turbiscan MA 1000, Diploma Studies, Paul-Sabatier University, Toulouse, France, 1996.
14. Lee, S. T., *Foam Extrusion, Principles and Practice*, Technomic Publishing Company, Lancaster, PA, 2000.
15. Benning, C. J., *Introduction in Polymeric Foams*, Wiley-Interscience, New York, 1969.
16. Gibson, L. J. and Ashby, M. F., *Cellular Solids: Structure and Properties*, Pergamon Press, Elmsfors, NY, 1988.
17. Klempner, D. and Frisch, K. C., *Polymeric Foams*, Hanser, New York, 1991.
18. Zhang, X. D., Macosko, C. W., Davies, H. T., Nikolov, A. D. and Wasan, D. T., Role of silicon surfactants in flexible polyurethane foam, *J. Colloid Interface Sci.*, **215**, 270–279 (1999).
19. Weaire, D. and Banhart, J., Foams and films, in *Proceeding of an International Workshop on Foam and Films*, Leuven, Belgium, March, 1999, Verlag MIT Publishing, Bremen, Germany, 1999.
20. Dickenson, E., *Introduction to Food Colloids*, Oxford University Press, Oxford, UK, 1992.
21. Dickenson, E. and Stainsby, G. (Eds), *Advances in Food Emulsions and Foams*, Elsevier Applied Science, London, 1988.
22. Lobo, L. and Wasan, D. T., Mechanism of aqueous foam stability in the presence of emulsified non-aqueous liquids, *Langmuir*, **9**, 1668–1677 (1993).

CHAPTER 3

Vesicles

Brian H. Robinson and Madeleine Rogerson

University of East Anglia, Norwich, UK

1	Introduction	45	6	Phospholipid Vesicles with Fatty Acids . . .	49
2	Properties of Vesicles	46	7	Interactions between Phospholipids and	
3	Phase Structure and Phase Transition	46		Fatty Acids: Considerations of	
4	Dynamic Processes involving Vesicles	47		Autopoiesis	50
5	Vesicle Formation	47	8	Summary	52
	5.1 Polymerization in vesicles	49	9	References	52

1 INTRODUCTION

Vesicles are microscopic spherical bilayer structures containing an aqueous compartment enclosed by a lipid or surfactant bilayer. When a phospholipid (PL) is used, the structures formed are also referred to as liposomes. Bangham and Horne first described and characterized phospholipid vesicles in the early 1960s (1). In the vesicle structure, the surfactant hydrophilic head-group is directed towards the water, while the hydrophobic tail forms the bilayer core. The vesicles are typically 50 nm in diameter, although giant vesicles with radii from 500 nm to 10 μm can also be made. The surfactants used to form vesicles are usually based on systems containing two alkyl chains. Micellar structures are not favoured because the two alkyl chains are too bulky to fit into the interior of a spherical-type micellar configuration.

Liposomes form spontaneously when phospholipids are hydrated in hot water to form extended liquid crystalline sheets. These break down to form vesicles when ultrasound is applied (see Figure 3.1). In such situations, a range of aggregate structures may be present, including rod and sheet-like structures. In the case of synthetic

surfactants, vesicles can sometimes form spontaneously when the solid is added to water at room temperature, or by perturbing another structure, e.g. micelles, by a change in ionic strength.

Vesicles are also dynamic structures in that various exchange processes can take place, although they are considerably less dynamic than micelles. Surfactant exchange between a micelle and water takes place typically over the microsecond time-scale and total micelle breakdown occurs in the millisecond to second region. In vesicles, the surfactant exchange process is very much slower and the disintegration process does not generally take place in the absence of an external perturbing force. Studies have been made of the rate of formation/breakdown of vesicles, with the transition being induced, for example, by a change of ionic strength. For sodium dialkylbenzene sulfonates, micelles and/or monomers are favoured at low salt concentrations. The rates of formation and breakdown are quite slow (seconds), but there is still uncertainty over the nature of the intermediate structures which are formed.

Various forms of vesicles have been characterized, including single-walled (or single-lamellar) vesicles (SLVs) and multi-walled vesicles (MLVs) (see

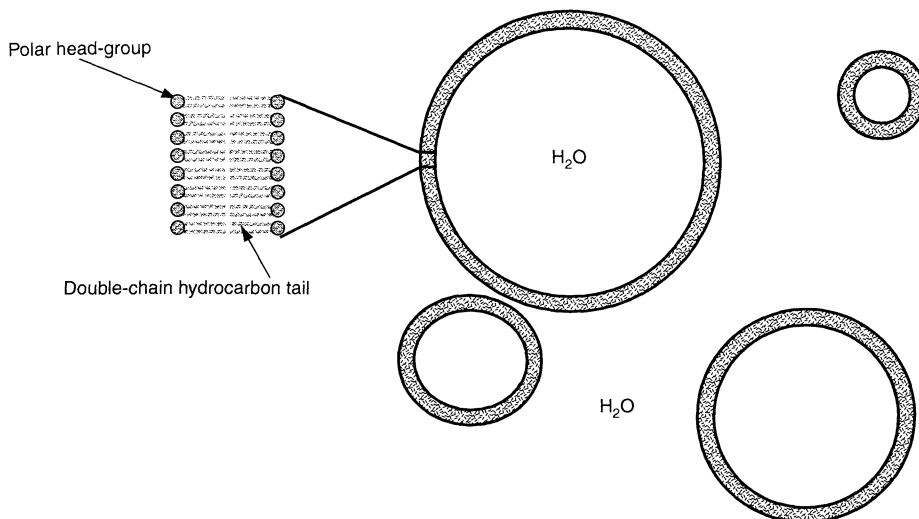


Figure 3.1. Schematic representation of a vesicle dispersion

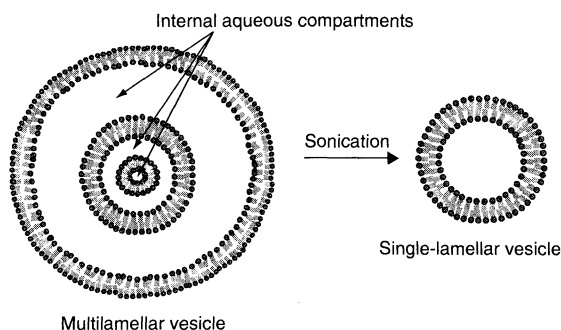


Figure 3.2. Schematic representation of the sonication of multilamellar vesicles to single-lamellar vesicles (not to scale)

Figure 3.2). SLVs can be formed from MLVs when they are sonicated above the bilayer phase transition temperature. SLVs can also be formed from MLVs by the freeze–thaw method, followed by extrusion through nanometre filters to give a more monodisperse system.

2 PROPERTIES OF VESICLES

The properties of vesicles have been extensively studied. They are model systems for cell membranes and have potential application as carriers for small molecules, particularly drugs. Additionally, vesicles can be used as templates for reactions, either by using the bilayer as a receptive surface or by utilizing the bilayer interior as a restricted aqueous reaction environment.

3 PHASE STRUCTURE AND PHASE TRANSITION

The bilayer structure of vesicles can undergo a number of phase transitions in response to changes in temperature and water content. These include transitions between different liquid crystalline phases, for example, between lamellar phases and hexagonal or cubic phases. The predominant structural arrangement is the lyotropic lamellar liquid crystalline phase, L_α , which is obtained spontaneously when phospholipids or surfactants are brought into contact with water at a temperature close to, or above, the main bilayer phase transition temperature (2). At the phase transition temperature, the lipid (surfactant) domain changes from a highly ordered phase, known as the gel phase, to a more fluid structure, i.e. the liquid crystalline phase. The phase transition temperature is dependent on the specific phospholipid or surfactant used and is closely related to the configuration of the acyl chains. The presence of *cis*-double bonds reduces the phase transition temperature. Chain branching and chain length are also important. As a result, the addition of, e.g. *cis*-fatty acids to phospholipid membranes can significantly reduce the phase transition temperature.

For most vesicles, the phase transition temperature is between 10 and 60°C, with the lower values tending to occur in natural phospholipids that have a high proportion of unsaturated acyl chains, thus preventing too much rigidity at lower temperatures (see Table 3.1).

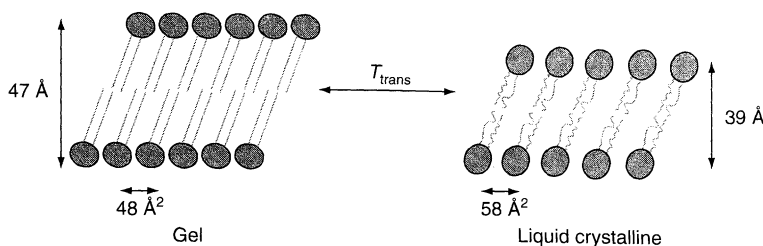


Figure 3.3. Schematic representation of the arrangement and dimensions of dipalmitoyl phosphatidylcholine (based on Papahadjopoulos and Kimelberg (3))

Table 3.1. Phase transition temperatures for different types of vesicle from Papahadjopoulos and Kimelberg (3)

Vesicle type ^a	Chain length	T_{trans} (°C)
PC vesicles	C ₂₂	75
	C ₁₈	58
	C ₁₆	41
	C ₁₂	23
PG charged vesicles	C ₁₆	38
	C ₁₂	21
Natural phospholipids		10–30

^aPC, phosphatidylcholine; PG, phosphatidyl glycerol sodium salt.

The phase transition at T_{trans} causes changes in the structure and mobility of the bilayer. For phospholipid membranes, below T_{trans} the bilayer molecules are generally arranged in an ordered manner with tightly packed straight hydrocarbon chains, and with C–C bonds in the *trans*-conformation. In this gel phase, the bilayer is solid-like and lateral mobility is very limited. Above T_{trans} , the molecules become more fluid, showing considerable movement, with an increased proportion of C–C bonds in the *gauche*-conformation (see Figure 3.3). As the bilayer becomes more mobile, the molecules are less tightly packed and occupy a larger area; typically, there is an increase of 15–30%, but with a decrease in the width of the vesicle. More recent measurements, however, have indicated that the structural changes can be more complex (4). The kinetics associated with the main phase transition of 1,2-dimyristoyl-*sn*-glycero-3-phosphatidylcholine (DMPC) unilamellar vesicles have been investigated in the time-range from microseconds to seconds. Three discrete relaxation phenomena were observed. In the fastest time-range, molecular rotation and lateral displacement are important. Over longer time-scales, domains are observed in which regions of fluid lipid co-exist with crystalline clusters.

4 DYNAMIC PROCESSES INVOLVING VESICLES

Above the phase transition temperature, there is rapid lateral diffusion of the lipid molecules in the bilayer but transverse diffusion (flip-flop), is very slow, as indicated in Figure 3.4.

The flip-flop of phospholipid molecules in spin-labelled phosphatidylcholine vesicles has been directly measured by electron spin resonance techniques, which show that a phospholipid molecule flip-flops once in several hours, whereas lateral diffusion is 10^9 times faster. The lateral exchange of bilayer molecules is dependent to some extent on the length of the hydrophobic tails, the extent of head-group hydration, and temperature.

5 VESICLE FORMATION

Vesicles form spontaneously from extended L_α sheets when phospholipids or surfactants are dissolved in water, and heated above the gel-to-liquid crystalline transition temperature. Bergstrom and Eriksson (5) suggested that the free energy required to form a spherical bilayer from sheets is made up of two contributions, i.e. an energy associated with bending the monolayers and the work required to stretch the bilayer, with the latter being determined by the planar bilayer tension. A major

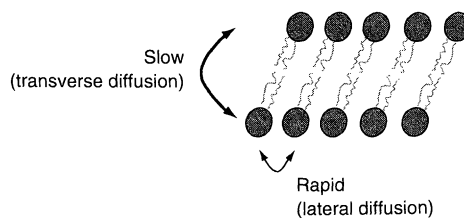


Figure 3.4. Schematic representation of the motions inside a bilayer

part of the bending free energy arises from the reduction in the overall hydrocarbon chain volume when a vesicle is formed from a flat sheet. Bergstrom and Eriksson suggested that a mixed surfactant/alcohol system lowers this bending energy, thus facilitating spontaneous curvature.

Commonly, it is considered that vesicles are not thermodynamically stable, and over time they revert to the lamellar phase. With time, they grow by cell fusion which results in larger vesicles in which the curvature is reduced, as indicated in Figure 3.5.

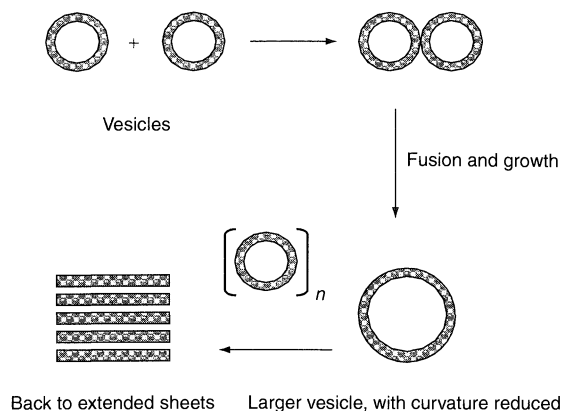
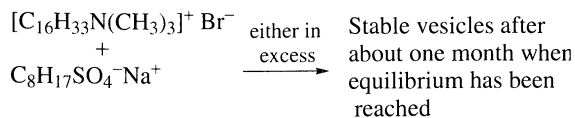


Figure 3.5. Schematic representation of the formation of large vesicles

To obtain vesicles that are thermodynamically stable, it has been suggested that a combination of a cationic and an anionic surfactant be used. Early work was carried out by Kaler and co-workers (6–9), using single chain surfactants, as shown below:



Recently, these measurements have been extended to include mixtures of hydrocarbon and fluorocarbon surfactants, e.g. cetyltrimethylammonium bromide (CTAB) and sodium perfluorohexanoate. Again, a stable region was found which included co-existing micelles and vesicles (10). One general problem with work in this field is that the composition of a vesicle phase may well be quite complex; species other than vesicles may well be present, as may distorted vesicles in the form of, for example, tubules.

Other groups have used combinations of double- and single-chain surfactants carrying the same charge. In general, these systems were found to have a large size polydispersity (11). However, use of the single surfactant $[(\text{C}_{18}\text{H}_{37})_2\text{N}(\text{CH}_3)_2]^+ \text{Br}^-$ (DODAB) will give a reasonably stable system after extrusion, which is

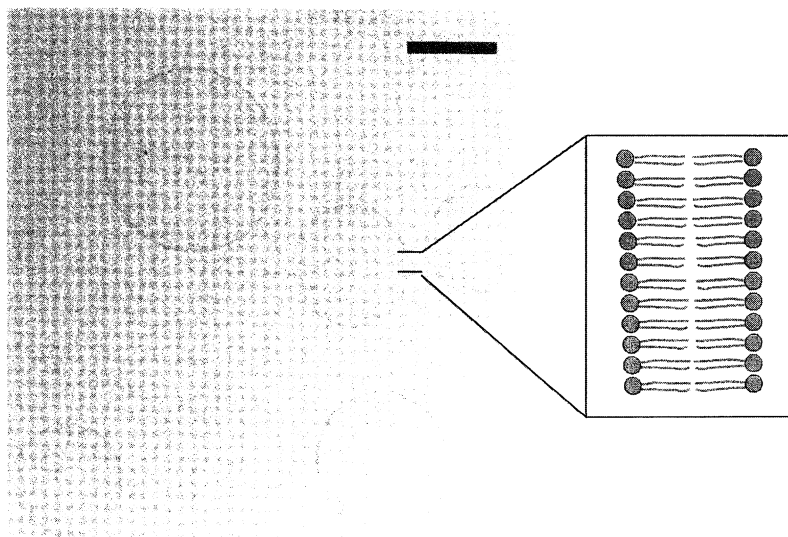


Figure 3.6. Cryo-transmission electron micrograph of a vesicle population obtained after extrusion at 60°C of 10 mM DODAB; the scale bar corresponds to 100 nm (from Martin Jung, *Ph.D. Thesis*, Technische Universiteit Eindhoven, The Netherlands, 2000)

convenient for template synthesis. This type of vesicle is shown in Figure 3.6.

5.1 Polymerization in vesicles

Vesicles have been used as templates for the synthesis of polymers (12, 13). The first reports of polymerization were to polymerize a solubilized monomer to give a rigid polymer. An early attempt, using this approach, was reported by Murtagh and Thomas (14). It was found to be difficult to get polymerization over the whole surface, so that the morphology was uncertain. There are two extreme situations which are possible, indicated schematically in Figure 3.7.

Where the polymer is essentially miscible with the bilayer lipid/surfactant, then a polymer shell is the preferred product. Where there is incompatibility between

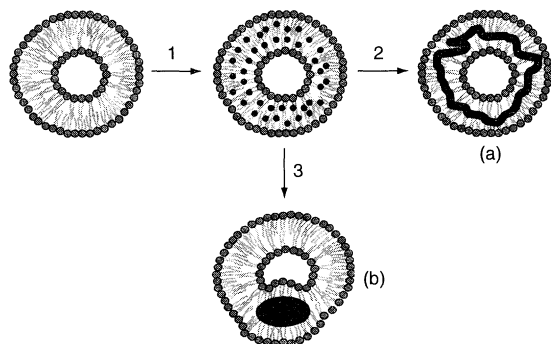


Figure 3.7. The concept of polymerization: (1) incorporation of monomer into vesicle; (2) formation of polymer shell (a); (3) formation of parachute (b)

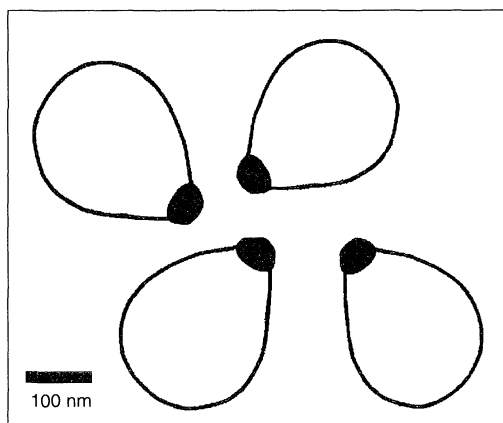


Figure 3.8. Schematic representation of the parachute morphology

the polymer-forming species and the lipid/surfactant then “parachute-type” structures might be predicted. In a recent study, styrene was solubilized in a DODAB vesicle system and polymerized *in situ* by using either photochemical or thermal initiation. Using this approach, the Eindhoven group have produced some interesting structures which they refer to as “parachute” morphologies (15, 16), as indicated in Figure 3.8.

6 PHOSPHOLIPID VESICLES WITH FATTY ACIDS

Phospholipid (PL) vesicles are generally considered to be thermodynamically unstable but as the PL surfactant is relatively immobile and fusion is difficult they are kinetically stable for months (depending somewhat on the method of preparation), and the tendency to return to the lamellar state is very slow. It would appear that monodisperse vesicles tend to be more stable than polydisperse systems.

Gebricki and Hicks systematically studied vesicular fatty carboxylic acids in 1973 (17). At pH values greater than 10, the fatty acid surfactant is fully ionized and micelles are formed. As the pH is reduced into the region 7.5 to 9, partial protonation of the anion at the surface occurs and there is a transition from micellar to vesicular structures. These vesicles are much less stable than phospholipid vesicles; for example, oleic acid vesicles are stable for only a few hours, while capric acid vesicles apparently can last for a few days. The difference is thought to be due to oleic acid being unsaturated and liable to autooxidation. Fatty acid vesicles made from micelles tend to be polydisperse and are multilamellar in structure. They are, however, easy to prepare and relatively inexpensive.

When fatty acid monomers/micelles are added to pre-existing phospholipid vesicles, the fatty acid will insert into the phospholipid bilayer. Doody *et al.* (18) have investigated the rate of migration of fatty acid monomers in and out of phospholipid bilayers and their results suggest that fatty acid exchange between the monomer state in solution and the vesicle is relatively fast. In addition, Kleinfeld *et al.* (19) have shown that the rate-limiting step for transporting a number of fatty acids through the bilayer membrane is the rate of flip-flop. Rate constants in the range 0.1 to 15 s^{-1} were measured, with the rates being dependent, to some extent, on the nature of the fatty acid and the composition of the membrane.

Langer and Sekwen (20) investigated the effect of free fatty acids on the permeability of the 1,2-dimyristoyl-*sn*-glycero-3-phosphatidylcholine (DMPC) bilayer at the main phase transition. When vesicles were formed between DMPC and oleic acid, the phase transition temperature was reduced drastically, but at the phase transition from the gel to liquid crystalline phase, membrane permeability reaches a maximum. Saturated fatty acids did not have the same effect on the bilayer as unsaturated fatty acids, in that there was a reduced effect on the phase transition temperature. They also concluded that *trans*-bilayer flip-flop is at a maximum at the phase transition temperature of DMPC being in the millisecond range for oleic acid. DMPC was found to have a flip-flop rate of 4 h at the phase transition and even longer rates at other temperatures.

7 INTERACTIONS BETWEEN PHOSPHOLIPIDS AND FATTY ACIDS: CONSIDERATIONS OF AUTOPOIESIS

Present-day life forms are cellular with phospholipid bilayer membranes forming the primary barrier that separates the interior of the cell from the external environment. It has been proposed that similar encapsulating structures, based on, for example, fatty acids, could have self assembled in the prebiological environment, thus providing an enclosed reaction system. It should be noted that in presently evolved biological systems, membranes can contain up to 15% fatty acid content, mixed with phospholipid.

In the past few years, experiments have shown that vesicular lipid bilayer structures can grow by spontaneous addition of membrane-forming materials from the surrounding medium, and these can encapsulate both ions and macromolecules.

Examples of self-bounded chemical structures which have the capacity to replicate are termed *autopoietic* self-reproducing systems. An autopoietic unit is regarded as a structure capable of self-maintenance by means of processes which all occur within its boundary, with the synthesis of copied structures also being possible.

Mavelli and Luisi (21) suggest that such autopoietic systems are a minimalist definition of a living system. They further suggest that self-reproduction is one of the possible kinetic aspects of autopoiesis and therefore autopoietic molecular aggregates can be considered as the most elementary chemical structures capable of simulating certain essential properties of the simplest living systems. In considerations of molecular evolution

to date, most emphasis has been given to the role of proteins and nucleic acids. However, there is a developing view that supramolecular aggregates such as vesicles will have played a crucial role in the prebiological phases of development of life on earth.

The first supramolecular self-reproduction experiments involved reverse micelles. Bachman *et al.* (22) have demonstrated that a reverse micellar system or water-in-oil microemulsion is endowed with the property of self-reproduction. The starting point is a microemulsion stabilized by octanol and octanoic acid. To this system, the fatty acid ester octyl octanoate was added. This is hydrolysed by LiOH to give the fatty acid and alcohol. As the reaction proceeds, more droplets of a similar structure/composition to those present initially are produced. This is because the reaction is localized within the boundary of the structure and so the reaction leads to the production of components of the boundary.

Walde *et al.* (23) have investigated a system which leads to self-reproducing vesicles using oleic acid/oleate. These vesicles form spontaneously when the pH is between 7.5 and 9.3. The vesicles were reacted with oleic anhydride, with the water-insoluble anhydride binding to the oleic acid/oleate vesicles where it is subsequently rapidly hydrolysed to the acid. This brings about an increase in the number of oleic acid/oleate vesicles. Another example reported by Walde *et al.* (24) uses an immiscible liquid fatty acid anhydride hydrolysed by an aqueous phase. Caprylic anhydride can react with aqueous sodium hydroxide, whereas oleic anhydride is hydrolysed by a pH-buffered aqueous solution. Different conditions are imposed on the two systems because caprylate and oleate anions form stable vesicles at somewhat different pH values. This experiment showed that the concentration of surfactant monomer (caprylate or oleate) builds up gradually until at a certain point the hydrolysis reaction rapidly accelerates – this point is when vesicles form. Once the vesicles are formed, they solubilize the remaining immiscible anhydride molecules into the aqueous phase, thus dramatically accelerating the rate of the reaction. The reaction therefore becomes autocatalytic since the enhanced production of surfactant monomer leads to an increased concentration of vesicles, which further accelerates the hydrolysis process.

Mavelli and Luisi (21) have described a simple kinetic model for Walde's systems and concluded that, in both of these, there exists a critical aggregation concentration for the acids at which the monomers aggregate into vesicles in appreciable quantities.

Morigaki *et al.* (25) have described the autopoietic self-reproduction of chiral fatty acids with the aim

of establishing a connection between self-reproduction and chirality. The self-reproduction of vesicles formed by (*S*) and (*R*)-2-methyldodecanoic acid vesicles was used to catalyse the hydrolysis of the water-insoluble 2-methyldodecanoic anhydride. The reaction rates for the (*S*)- and (*R*)-enantiomers were similar, hence indicating that chiral vesicles cannot induce a significant enantioselectivity. However, an interesting effect was observed at 10°C where racemic vesicles destabilized during hydrolysis, so causing phase separation, whereas homochiral vesicles remained stable and continued to self-reproduce.

Blöchliger *et al.* (26) have studied the mechanism of oleic acid/oleate vesicle formation under a variety of conditions. A matrix effect was observed on adding oleate vesicles to pre-existing phospholipid vesicles which resulted in more vesicles being produced of a similar size to the original phospholipid vesicles. Blöchliger and co-workers described the phospholipid vesicles as acting as a matrix; there appeared to be evidence that the oleate vesicles were combining with the phospholipid vesicles, and the final size when distribution was similar to that of the original phospholipid vesicles. Should addition of oleate to pre-existing PL vesicles occur with no interaction between the phospholipid and oleic acid, it would be reasonable to expect the final vesicle size distribution to be much larger.

Lonchin *et al.* (27) have also studied the matrix effect of phospholipid vesicles. These authors investigated the formation of mixed phospholipid/fatty acid vesicles by using a combination of kinetic and structural methods to study the process of spontaneous formation of vesicles on addition of oleate micelles to pre-existing vesicles of 1-palmitoyl-2-oleoyl-*syn*-glycero-3-phosphocholine (POPC).

Evidence was found for a POPC matrix effect, in that the pre-added vesicles influenced the size distribution of the newly produced vesicles. The matrix effect leads to rapid formation of vesicle aggregates and control over the final size distribution, such that the mixed systems are more monodisperse than in the absence of the matrix, where the oleic acid vesicles grow in an uncontrolled way. This effect was more obvious at lower concentrations of oleic acid/oleate than at higher concentrations.

Recent work on the DMPC (Figure 3.9) phospholipid system (28) has helped to provide further evidence in support of the template effect.

The kinetics of addition of oleic acid to DMPC vesicles has been followed at pH 8.5, and the time evolution of the system, as detected by light scattering, is typically illustrated by data as shown in Figure 3.10. In

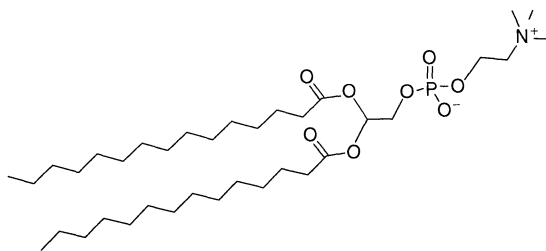


Figure 3.9. Structure of 1,2-dimyristoyl-*syn*-phosphatidylcholine (DMPC)

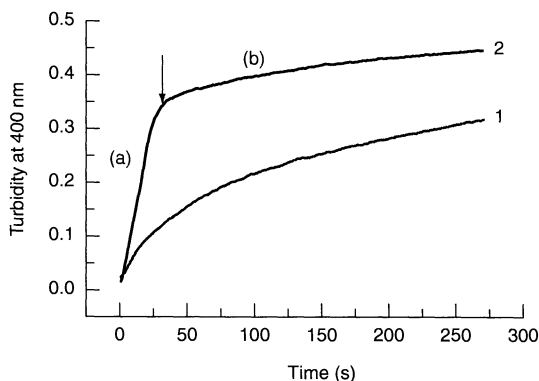


Figure 3.10. Kinetic data, obtained by light scattering, for the addition of oleic acid to DMPC vesicles at pH 8.5 and 15°C: (1) [oleate]_{final} = 10 mmol dm⁻³ + buffer; (2) [DMPC]_{final} = 0.25 mmol dm⁻³ + [oleate]_{final} = 10 mmol dm⁻³

the absence of DMPC vesicles, fatty acid vesicles grow spontaneously but slowly to give a very polydisperse system. In the presence of DMPC, the reaction is a lot faster, and proceeds under control of the pre-existing DMPC vesicles.

It is clear that the rate of growth of aggregates in the presence of DMPC is much faster than when DMPC is absent. It can also be seen from the kinetic traces that there is evidence for bi-phasic kinetics in the presence of DMPC; the arrow in this figure indicates where there is a change in the nature of the process. This can be identified with two stages in the aggregation process – an initial growth of PL vesicles (a) followed by rupture of these vesicles when the size exceeds a certain value (b). It is possible that the final structures formed are multilamellar (bilamellar) vesicles. Confirmation that this process is taking place is provided by direct measurements of the size of the aggregates using the technique of photon correlation spectroscopy, as shown in Figure 3.11.

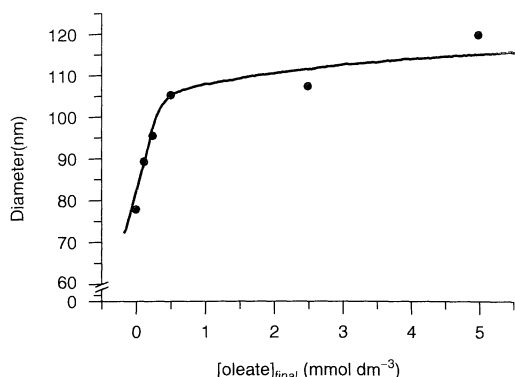


Figure 3.11. DMPC/oleate vesicle diameter data at 15 and 35°C, as determined by photon correlation spectroscopy, showing results obtained from all concentrations measured: [DMPC]_{final} = 0.25 mmol dm⁻³; pH 8.5

The template effect of DMPC to change vesicle size by addition of fatty acid is therefore thought to occur by the mechanism shown in Figure 3.12, which describes the nature of the two-step process, (a) and (b).

At low concentrations of added fatty acid, only step (a) is thought to be relevant. Step (b) therefore, provides a mechanism to ultimately limit the growth.

8 SUMMARY

For many years, vesicles and liposomes are systems that have been relatively neglected by colloid scientists. This situation has now changed and there is increasing interest in the exploration of these systems for a wide range of applications.

9 REFERENCES

1. Bangham, A. D. and Horne, R. W., Negative staining of phospholipids and their structural modification by surface active agents as observed in the electron microscope, *J. Mol. Biol.*, **8**, 660–665 (1964).
2. Jones, M. N. and Chapman, D., *Micelles, Monolayers and Biomembranes*, Wiley-Liss, New York, 1995.
3. Papahadjopoulos, D. and Kimelberg, H. K., *Phospholipid Vesicles (Liposomes) as Models for Biological Membranes: Their Properties and Interactions with Cholesterol and Proteins*, Pergamon Press, Oxford, 1973.
4. Groll, R., Böttcher, A., Jäger, J. and Holzwarth, J. F., Temperature dependent intermediate structures during the main phase transition of dimyristoyl phosphatidylcholine vesicles – a combined iodine laser-temperature jump and time resolved cryo-electron microscopy study, *Biophys. Chem.*, **58**, 53–65 (1996).
5. Bergström, M. and Eriksson, J. C., The energetics of forming equilibrated bilayer vesicles, *Langmuir*, **12**, 624–635 (1996).
6. Kaler, E. W., Murthy, A. K., Rodriguez, B. E. and Zasadzinski, J. A., Spontaneous vesicle formation in aqueous mixtures of single-tailed surfactants, *Science*, **245**, 1371–1374 (1989).
7. Kaler, E. W., Herrington, K. L., Murthy, A. K. and Zasadzinski, J. A., Phase behavior and structure of mixtures of anionic and cationic surfactants, *J. Phys. Chem.*, **96**, 6698–6709 (1992).
8. Herrington, K. L., Kaler, E. W., Miller, A. K. and Zasadzinski, J. A., Phase behavior of aqueous mixtures of dodecyltrimethylammonium bromide (DTAB) and sodium dodecyl sulfate (SDS), *J. Phys. Chem.*, **97**, 13792–13802 (1993).
9. Yacilla, M. T., Herrington, K. L., Brasher, L. L., Kaler, E. W., Chiruvolu, S. J. and Zasadzinski, J. A., Phase behavior of aqueous mixtures of cetyltrimethylammonium

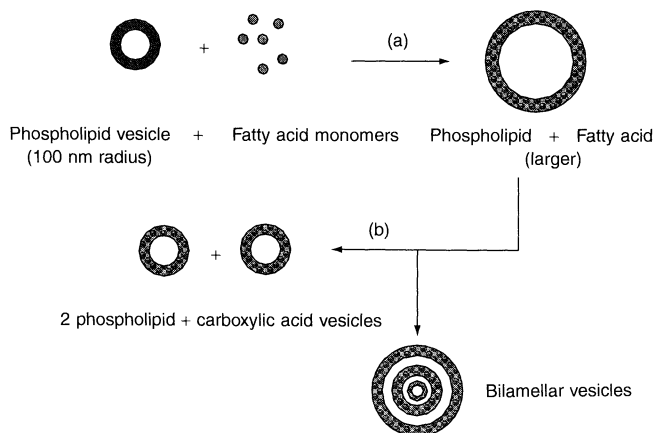


Figure 3.12. Mechanism of the reaction of DMPC with oleic or capric acid

- bromide (CTAB) and sodium octyl sulfate (SOS), *J. Phys. Chem.*, **100**, 5874–5879 (1996).
10. Iampietro, D. J. and Kaler, E. W., Phase behavior and microstructure of aqueous mixtures of cetyltrimethylammonium bromide and sodium perfluorohexanoate, *Langmuir*, **15**, 8590–8601 (1999).
 11. Viseu, M. I., Edwards, K., Campos, C. S. and Costo, S. M., Spontaneous vesicles formed in aqueous mixtures of two cationic amphiphiles, *Langmuir*, **16**, 2105–2114 (2000).
 12. Jung, M., van Casteren, I., Monteriro, M. J., van Herk, A. M. and German, A. L., Pulsed-laser polymerization in compartmentalized liquids. 1. Polymerization in vesicles, *Macromolecules*, **33**, 3620–3629 (2000).
 13. Jung, M., den Ouden, I., Montoya Goni, A., Hubert, D. H. W., van Herk, A. M. and German, A. L., Polymerization in polymerizable vesicle bilayer membranes, *Langmuir*, **16**, 4185–4195 (2000).
 14. Murtagh, J. and Thomas, J. K., *Faraday Discuss. Chem. Soc.*, **81**, 127–136 (1986).
 15. Jung, M., Hubert, D. H. W., van Herk, A. M. and German, A. L., The parachute morphology as equilibrium morphology of vesicle–polymer hybrids? *Macromol. Symp.*, **151**, 393–398 (2000).
 16. Jung, M., Hubert, D. H. W., van Veldhoven, E., Frederik, P., van Herk, A. M. and German, A. L., Vesicle–polymer hybrid architectures: a full account of the parachute architecture, *Langmuir*, **16**, 3165–3174 (2000).
 17. Gebicki, M. and Hicks, M., Ufasomes are stable particles surrounded by unsaturated fatty acid membranes, *Nature (London)*, **243**, 232–234 (1973).
 18. Doody, M. C., Pownall, H. J., Kao, Y. J. and Smith, L. C., Mechanism and kinetics of transfer of a fluorescent fatty acid between single-walled phosphatidylcholine vesicles, *Biochemistry*, **19**, 108–116 (1980).
 19. Kleinfeld, A. M., Chu, P. and Romero, C., Transport of long-chain native fatty acids across lipid bilayer membranes indicates that transbilayer flip-flop is rate limiting, *Biochemistry*, **36**, 14146–14158 (1997).
 20. Langer, M. and SekWen, H., Effect of free fatty acids on the permeability of 1,2-dimyristoyl-*syn*-glycero-3-phosphocholine bilayer at the main phase transition, *Biochim. Biophys. Acta*, **1463**, 439–447 (2000).
 21. Mavelli, F. and Luisi, P. L., Autopoietic self-reproducing vesicles: A simplified kinetic Model, *J. Phys. Chem. B.*, **100**, 16600–16607 (1996).
 22. Bachman, P. A., Walde, P. and Luisi, P. L., Self-replicating micelles and chemical autopoiesis, *J Am. Chem. Soc.*, **112**, 8200–8201 (1990).
 23. Walde, P., Goto, A., Monnard, P. A., Wessicken, M. and Luisi, P. L., Oparin's reactions revisited: enzymatic synthesis of poly(adenylic acid) in micelles and self-reproducing vesicles, *J Am. Chem. Soc.*, **116**, 7541–7547 (1994).
 24. Walde, P., Wick, R., Fresta, M., Mangove, A. and Luisi, P. L., Autopoietic self-reproduction of fatty acid vesicles, *J. Am. Chem. Soc.*, **116**, 11649–11652 (1994).
 25. Morigaki, K., Dallaralle, S., Walde, P., Colonna, S. and Luisi, P. L., Autopoietic self-reproduction of chiral fatty acid vesicles, *J. Am. Chem. Soc.*, **119**, 292–301 (1997).
 26. Blöchliger, E., Blocher, M., Walde, P. and Luisi, P. L., Matrix effect in the size distribution of fatty acid vesicles, *J. Phys. Chem., B*, **102**, 10383–10390 (1998).
 27. Lonchin, S., Luisi, P. L., Walde, P. and Robinson, B. H., A matrix effect in mixed phospholipid/fatty acid vesicle formation, *J. Phys. Chem., B*, **103**, 10910–10916 (1999).
 28. Bucak, S., Robinson, B. H. and Rogerson, M. L., To be published.

CHAPTER 4

Microemulsions

Klaus Wormuth[†], Oliver Lade[‡], Markus Lade[†] and Reinhard Schomäcker[†]

[†]Technical University of Berlin, Berlin, Germany, [‡]University of Cologne, Cologne, Germany

1	Introduction	55	2.6	Addition of polymers	67
1.1	Phenomenological description and definition	55	2.7	Microemulsions of compressible and supercritical fluids	68
2	Phase Behaviour	57	2.8	A practical guide for the formulation of microemulsions	68
2.1	Monodisperse nonionic surfactants . .	57	3	Links between the Phase Behaviour, Microstructure and Interfacial Tensions . .	70
2.2	Mixtures of nonionic surfactants (commercial surfactants)	63	3.1	Spontaneous curvature and characteristic sizes	70
2.3	Ionic surfactants: the role of salt and alcohol cosurfactants	64	3.2	Interfacial tensions	72
2.4	Nonionic plus ionic surfactants: temperature-insensitive mixtures	66	3.3	Dynamic processes	73
2.5	Other types of surfactants, oils and non-aqueous mixtures	67	4	Applications of Microemulsions	73
			5	References	74

1 INTRODUCTION

1.1 Phenomenological description and definition

Salad dressings that separate, oil slicks on water, and difficult-to-remove grease spots on dishes and clothing are everyday reminders that oil and water do not mix. Thankfully, surfactants, i.e. surface-active molecules containing water-loving (hydrophilic) and oil-loving (lipophilic) moieties, promote the mixing of liquids as incompatible as oil and water, and help to solve some of these everyday problems.

Significant mechanical agitation of oil and water along with a small amount of an appropriate surfactant often creates an emulsion, i.e. a two-phase dispersion, where surfactant-coated droplets of one phase are dispersed into a continuous phase (see Chapter 8

by Tauer for further details). Typically, the droplet diameter in emulsions ranges from 0.1 to 1 micron, and thus emulsions most often look milky and turbid. As a general rule, hydrophilic surfactants stabilize droplets of oil in a continuous water phase, while lipophilic surfactants stabilize droplets of water in a continuous oil phase (1). Emulsions may be long-lived or “kinetically stable”; however, emulsions are two-phase dispersions and given time, the microscopic emulsion droplets will merge, the dispersed phase will sediment or cream, and macroscopic oil and water layers will form.

In some cases, however, a fundamentally different type of mixture of oil and water forms. If, when compared to typical emulsion formulations, two changes are made, i.e. (i) carefully choosing a surfactant of an intermediate hydrophilic–lipophilic nature, and (ii) increasing the surfactant concentration, spontaneous

dispersion of oil and water occurs upon gentle mixing. By this process, a translucent and bluish dispersion usually results, rather than a milky emulsion.

Scientifically described for the first time in 1943 by Hoar and Schulman (2), the latter author coined the term “microemulsion” in 1959 to describe these “optically isotropic transparent oil and water dispersions” (3). Since this early work, many experimental and theoretical efforts have shown that these “dispersions” are actually solutions, namely thermodynamically stable equilibrium phases (4). Consequently, the most widely, but still not universally accepted definition of a microemulsion is that of a thermodynamically stable mixture of oil and water. Occasionally, the term microemulsion (5) or “mini-emulsion” (6) is used to describe long-lived emulsions with ultra-small droplet sizes (30–100 nm). Sometimes, stable emulsions may be created by agitation of systems while passing through regions of the phase diagram where microemulsion phases form; however, the final state is in the emulsion region (7, 8). In this present chapter, we use the most widely accepted definition of microemulsions, namely equilibrium phases of oil and water (9).

In most cases, microemulsions are easily differentiated from emulsions by their ease of formation, stability and translucent nature. Differentiation is most difficult in the case of optimized microemulsion formulations with very efficient surfactants (10, 11). Such microemulsions contain only 1 to 3 wt% surfactant, and qualitatively look like opaque emulsions due to strong light scattering. However, careful study of stability and reproducibility by using short-optical-path vials, and an understanding of the phase behaviour (see below), allows such concentrated microemulsions to be distinguished from standard emulsions.

Relatively, efficient microemulsion formulations, typically those with less than 20 wt% surfactant, differ significantly from non-ideal solutions in that they contain a distinct type of microstructure, i.e. topologically ordered oil and water domains coated by surfactant. The microstructures within microemulsions typically range from 3 to 100 nm in size, and fluctuate rapidly in time. As the oil-to-water ratio in microemulsion phases is increased, many experimental studies indicate that a *continuous* progression of microstructures is observed. At low concentrations of oil, droplets of oil, coated with surfactant, swim in a continuous water domain (an “oil-in-water” microemulsion). As the concentration of oil is increased, the spherical droplets form oblong and globular structures. At intermediate ratios of oil to water (near 50/50), a so-called “bicontinuous” structure of oil and water domains is observed (12). As a

dynamic “sponge-like” phase, bicontinuous microemulsions contain intertwined sample spanning the oil and water domains (13). In order to visualize the structure, imagine a sponge soaked in water: the solid parts of the sponge are the oil domains, the water domains intertwine with the oil domains, and the surfactant resides at the interface between the two domains. As the oil-to-water ratio is further increased, the continuous channels of water break up into oblong and globular structures, and at the highest concentrations of oil, spherical droplets of water, coated with surfactant, swim in an oil-continuous domain (a “water-in-oil” microemulsion) (see Chapter 17 by Olsson for details of the methods used to characterize microemulsion structures).

Extensive experimental results indicate that the small droplets, globules, and bicontinuous structures in microemulsions are highly dynamic rather than static in time – the structures are labile, fluctuate in shape, and globular and droplet structures exchange contents rapidly (14). The microstructures in microemulsions are substantially longer-lived than the small clusters and associations found in non-ideal solutions, although shorter-lived than typical emulsion droplets.

In microemulsions, oil and water mix over small length scales, and thus an extraordinarily large interfacial area spans the oil and water domains. In order to thermodynamically stabilize such fine structures, the surfactant must generate an ultra-low free energy per unit of interfacial area between oil and water microdomains within the microemulsion phase. Such low free energies result from a precise balancing of the hydrophilic–lipophilic nature of the surfactant. As a consequence of this precise balancing, the macroscopic interfacial tensions between microemulsion phases and excess oil phases are also ultra-low (of the order of 10^{-3} mN/m) (15, 16).

The important properties unique to microemulsions – thermodynamic stability, ultra-low interfacial tensions, translucence, small and tunable microstructures – make microemulsions interesting for a variety of applications. Microemulsions find application as a reaction medium for formation of polymeric and inorganic nanoparticles, for the dispersion of drugs, food stuffs, agrochemicals, and cosmetic ingredients, and in detergency, the enhancement of oil recovery from reservoirs, and the extraction of contaminated solids (17).

In the following sections of this chapter, the properties of microemulsions sketched out in this introduction are fleshed out in more detail, especially the

important patterns of phase behaviour. In particular, emphasis is placed on methodologies for the formulation of microemulsions. Next, the links between phase behaviour, and the important microstructure and interfacial tension properties are outlined. Finally, some reviews describing the current and potential applications of microemulsions are presented.

2 PHASE BEHAVIOUR

As defined in the introduction, microemulsions are phases in thermodynamic equilibrium with their environment. Unfortunately, microemulsion phases are not ubiquitous, but only found under certain carefully defined conditions. Formulation of microemulsion phases can be difficult since microemulsions often co-exist with other phases such as excess oil and/or water, and are often close to lyotropic liquid crystalline phases. A map of the locations of microemulsion phases in composition space is known as a “phase diagram.” Generation of complete phase diagrams for each specific mixture of interest is rather time-consuming, and thus formulators of microemulsions can benefit from an intimate knowledge of how the phase diagram depends upon the chemical structures of the oil and surfactant, temperature, pressure, and additives such as salt and polymers. The dependence of the phase diagram upon variables of interest, i.e. the “phase behaviour,” is described in detail in this present section. Luckily for the formulator of microemulsions, both measurement and understanding the patterns of phase behaviour in systems containing microemulsions have intrigued researchers for the last 40 years (15, 17–19).

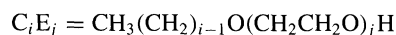
This rich base of information on phase behaviour is systematically covered here, starting with the simplest mixtures that form microemulsions, and building up to the more complex formulations of practical interest. At the end of this section, a summary of the trends in phase behaviour is given, followed by a practical guide for the formulation of microemulsions.

2.1 Monodisperse nonionic surfactants

As first noted by Shinoda (7), simple three-component mixtures of nonionic ethoxylated alcohol surfactants mixed with oil and water form microemulsions. Ethoxylated alcohols, the most widely used nonionic surfactants, are prepared by the reaction of ethylene oxide

with aliphatic or aromatic alcohols. Most commercially available ethoxylated alcohols contain a relatively broad distribution of degrees of ethoxylation (20). Such a distribution of surfactant oligomers complicates the understanding of the phase behaviour, because the oligomers exhibit a range of hydrophilic–lipophilic natures, and consequently the oligomers partition unequally between the oil, water, and microemulsion phases (21). A much clearer understanding of the patterns of phase behaviour comes from first examining the simplest mixtures that produce microemulsions, i.e. mixtures of water, non-polar oils, and monodisperse (single oligomer) nonionic surfactants. Later, we will deal with the more complicated polydisperse commercial surfactants, and find that the patterns observed when using monodisperse ethoxylated alcohols qualitatively mimic those found when using commercial polydisperse ethoxylated alcohols.

The shorthand notation used here for the ethoxylated alcohols is C_iE_j where:



Ethoxylated alcohols are “amphiphiles” containing hydrocarbon tails which prefer oil environments and ethoxylated alcohol groups which prefer water environments. However, short-chain amphiphiles such as C_4E_1 are inefficient at mixing oil and water and only form weakly structured solutions (22). Longer-chained amphiphiles such as $C_{12}E_5$ are true “surfactants” which efficiently mix oil and water, and also form distinct droplet and bicontinuous microemulsion microstructures (23).

Maps of the phase behaviour of three-component mixtures (water, oil and surfactant) are best plotted by constructing the “Gibbs triangle,” which describes ternary compositions of oil, water and surfactant in two-dimensional space (Figure 4.1). Each of the corners of the triangle represent the three pure components (100 wt%), while the three edges of the triangle map the three binary combinations. In our example, the bottom edge maps water–oil mixtures, the left edge maps water–surfactant mixtures, and the right edge maps oil–surfactant mixtures. For example, a point fixed at the water corner represents 100 wt% water, and a point fixed two thirds of the way towards the surfactant corner, on the water–amphiphile edge of the diagram, represents 66.7 wt% surfactant in water. The interior of the triangle maps the composition of mixtures of all three components, i.e. oil, water and surfactant. For example, a point exactly at the middle of the diagram describes equal amounts of water, surfactant, and oil (each 33.33 wt%). As the composition point moves closer to

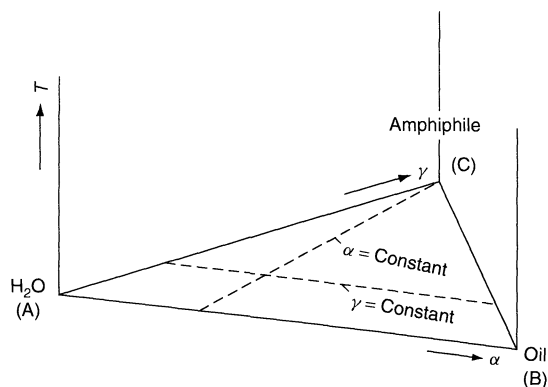


Figure 4.1. Gibbs triangle for water (A), oil (B) and amphiphile (surfactant) (C) mixtures, showing lines of constant oil/water ratio ($\alpha = \text{Constant}$) and constant surfactant concentration ($\gamma = \text{Constant}$). Reproduced by permission of the American Chemical Society (from Kahlweit *et al.* (105))

one of the corners, the composition becomes richer in that particular component. As described in detail below, paths of constant oil-to-water ratio (constant α), and paths of constant surfactant concentration (constant γ), are particularly important (see Figure 4.1).

The Gibbs triangle can be used to plot the compositions of oil, water and surfactant at which microemulsion phases occur when temperature, pressure, type of oil and type of surfactant are fixed. If any of these variables are changed, a new Gibbs triangle must be constructed. The generic pattern of phase behaviour found upon changing variables of interest is qualitatively sketched by the three Gibbs triangles shown in Figure 4.2. In these diagrams, regions of 1, 2 and 3 phase co-existence are shown. Liquid crystalline phases (usually lamellar (L_α)) typically found at higher surfactant concentrations are omitted for clarity. Since oils are usually less dense than water (due to gravity), water-rich phases will reside at the bottom of the container (e.g. test tube), while oil-rich phases will float on top.

The “1” in Figure 4.2 denotes regions where the oil and water are completely mixed into a single microemulsion phase. The ends of the “tie-lines” within the two-phase region denote the compositions of the two phases in equilibrium when a sample is mixed at the overall composition located along the line. The “2” denotes a two-phase sample where the majority of the surfactant, along with some oil, resides in the lower water-rich phase (an “oil-in-water” microemulsion phase), and excess oil floats on top. It also denotes a two-phase sample where the majority of the surfactant, along with some water, resides in the upper oil-rich

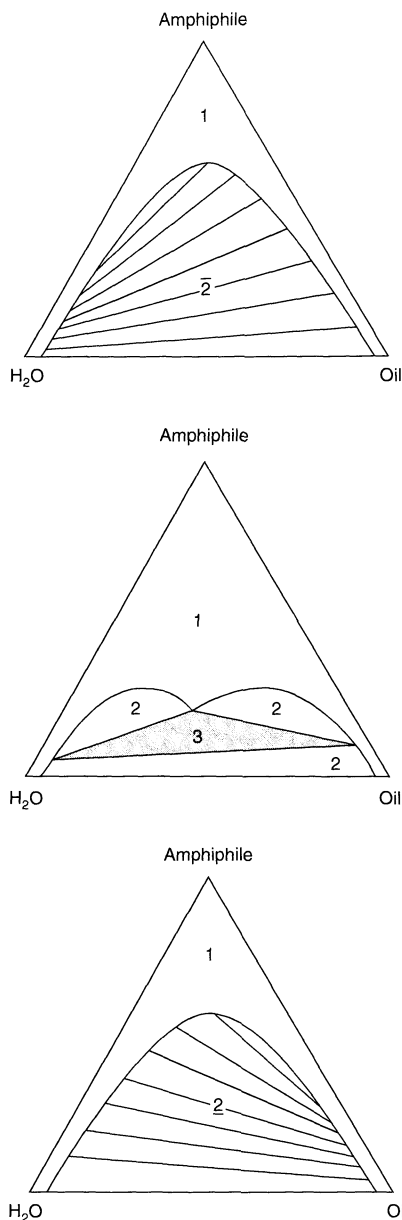


Figure 4.2. Schematic phase diagrams of water, oil and amphiphile (surfactant) mixtures, showing regions of the 1, 2 and 3 phases. The tie-lines within the 2 phase regions connect the compositions of the two phases in equilibrium. Reproduced by permission of the American Chemical Society (redrawn from Schwuger *et al.* (81))

phase (a “water-in-oil” microemulsion phase), with excess water lying underneath. Finally, “3” denotes a three-phase sample, where the middle phase, rich in

oil and water (a “bicontinuous” microemulsion phase) is in equilibrium with excess water (bottom phase) and oil (top phase). The three corners of the 3 phase triangle denote the compositions of the three phases in equilibrium. At very low surfactant concentrations (just below the phase-“3” region in the middle of Figure 4.2) are regions denoted as “2,” being a two-phase sample where the surfactant concentration is below the “critical microemulsion concentration” of the surfactant, where essentially no mixing of oil and water occurs, and all surfactant is dissolved as monomers in the water and oil phases.

Visual observations allow determination most precisely and reliably of phase boundaries. Single-phase systems are usually more transparent than mixed multiphase systems which are turbid. Liquid crystalline phases, found at higher surfactant concentrations, are birefringent and easily identified by using crossed polarizers along with a strong light source. Differentiation of 2 and 3 phase regions usually requires waiting for phase separation of the samples. However, since electrical conductivity changes by orders of magnitude as samples progress from water-continuous to oil-continuous, conductivity measurements of stirred multi-phase systems may be used to estimate the location of the 3 phase samples (region of intermediate conductivity) (24). The relative partitioning of ethoxylated alcohol surfactants between water and oil phases strongly depends upon temperature (4, 25). In order to better visualize the progressions shown schematically by the three triangular phase diagrams (Figure 4.2), imagine a test tube, filled with equal amounts of oil and water, with enough surfactant added to achieve some mixing of oil and water (above the 2 region), but not enough to completely mix oil and water into a single microemulsion phase (below the “1” region).

At low temperatures, ethoxylated alcohols prefer water-rich phases, the test tube contains a “2” phase system (a lower “oil-in-water” microemulsion phase in equilibrium with excess oil), and the entire phase diagram schematically resembles the bottom Gibbs triangle shown in Figure 4.2. At intermediate temperatures, the surfactant prefers both oil and water, the test tube contains a “3” phase system (a middle “bicontinuous” microemulsion phase, in equilibrium with excess oil and water), and the entire phase diagram schematically resembles the middle Gibbs triangle shown in Figure 4.2. At high temperatures, the surfactant prefers oil-rich phases, the test tube contains a “2” phase system (an upper “water-in-oil” microemulsion phase in equilibrium with excess water), and the entire phase diagram

Table 4.1. Qualitative effects of increasing the variables listed upon the phase behaviour of ethoxylated alcohol, non-polar oil and water mixtures

Increasing parameter	2	3	2̄
Temperature (<i>T</i>)		→	
Pressure (<i>P</i>)		←	
Salt concentration (lyotropic) (<i>ε</i>)		→	
Oil hydrophobicity (<i>k</i>)		←	
Surfactant lipophilicity (<i>i</i>)		→	
Surfactant hydrophilicity (<i>j</i>)		←	

schematically resembles the top Gibbs triangle shown in Figure 4.2.

An interesting and simple principle of the patterns of phase behaviour in microemulsion systems is that the pattern of phase behaviour described above for increasing temperature (Figure 4.2) is also found for a number of different variables of interest. In Table 4.1, the direction in which the phase behaviour of ethoxylated alcohols progresses is shown as a function of increasing temperature, salinity, pressure, oil “hydrophobicity”, and changing the “hydrophilic/lipophilic” balance of the surfactant. For example, oil “hydrophobicity” is increased by increasing the chain length (*k*) of aliphatic hydrocarbons (*B_k*) where:

$$B_k = \text{CH}_3(\text{CH}_2)_{k-2}\text{CH}_3$$

The “hydrophilicity” of ethoxylated alcohol surfactants increases upon adding mole quantities of ethylene oxide to the surfactant (increasing *j*), which is equivalent to increasing hydrophilic–lipophilic balance (HLB) number (26). The “lipophilicity” of ethoxylated alcohols increases upon increasing the length of the aliphatic chain (increasing *i*) of the *C_iE_j* amphiphile, which is equivalent to decreasing the HLB number (26). Note that the “amphiphilicity” of ethoxylated alcohols, i.e. the strength of the “chemical dipole” between hydrophilic and lipophilic groups, is increased by increasing both *i* and *j* simultaneously.

However, when addressing the role of surfactant “amphiphilicity”, which is intimately connected with the efficiency of a particular ethoxylated alcohol in mixing oil and water into a microemulsion, the schematic progression of phase diagrams (Figure 4.2) must be made more quantitative. Here, the phenomenological framework for understanding phase behaviour developed systematically by Kahlweit, Strey and co-workers (10, 25, 27) leads to a more complete understanding of the phase behaviour of mixtures of model monodisperse ethoxylated alcohol surfactants, non-polar aliphatic or aromatic oils, and water.

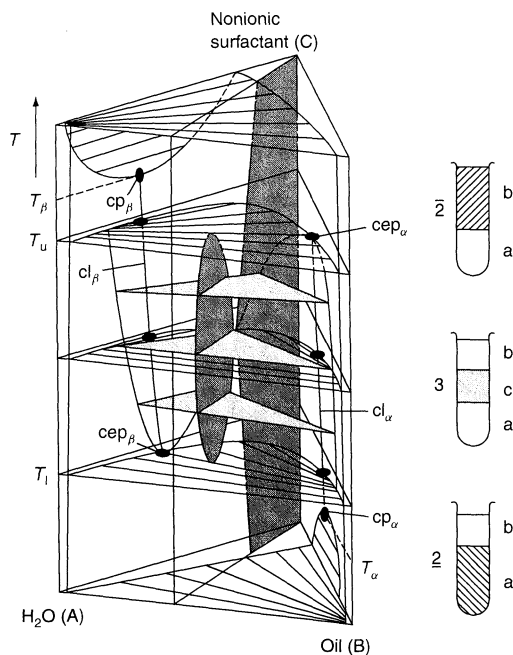


Figure 4.3. Schematic phase diagram (prism) of mixtures of water (A), oil (B) and nonionic surfactant (C) as a function of temperature; tie-lines are shown within the two-phase regions. In addition, the three phase triangles, critical points (cps), critical lines (cls), and critical end-points (ceps) are shown. Also shown is a slice through the prism at equal masses of oil and water ($\alpha = 0.5$; dark shaded region). Next to the prism are test tubes illustrating the phase behaviour ($\alpha = 0.5$) at low, intermediate and high temperatures. Reproduced by permission of Academic Press (redrawn from Kahlweit *et al.* (86))

The dependence of the ternary Gibbs phase diagram upon changing a variable such as temperature is mapped in three dimensions by vertically stacking the Gibbs triangles shown in Figure 4.2 into a “prism”, with temperature as the vertical ordinate (Figure 4.3). Based upon many measurements of the phase behaviour, Kahlweit *et al.* (27) have developed a phenomenological framework which describes the patterns of phase behaviour inside the prism, and also shows how these patterns of the ternary mixtures are intimately related to the phase behaviour of the binary mixtures (25).

Schematic phase diagrams of the three binary mixtures of oil/water, surfactant/water and surfactant/oil, which form the three sides of the phase prism, are shown in Figure 4.4. First some comments on the binary mixtures:

- (i) Oil/Water. Non-polar oils and water remain essentially immiscible over the temperature range of interest.

www.fran-mavad.com

مرجع دانشجویان و مهندسين مواد

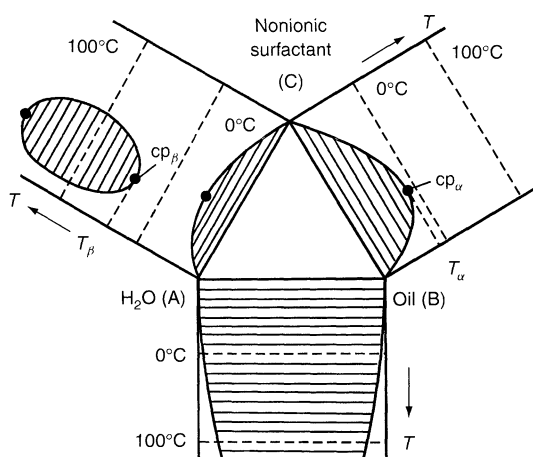


Figure 4.4. Schematic phase diagrams as a function of temperature of the three binary mixtures, oil/water, water/nonionic surfactant and oil/nonionic surfactant, showing critical points (cps) and tie-lines within the 2 phase regions. Reproduced by permission of Wiley-VCH (redrawn from Kahlweit and Strey (25))

- (ii) Surfactant/Water. As the temperature is raised, ethoxylated alcohol surfactants become less miscible with water, and phase-separate at the so-called “cloud point.” The critical point (cp_β) at temperature T_β is where the two phases first appear, i.e. a surfactant-rich phase and a surfactant-poor phase.
- (iii) Surfactant/Oil. As the temperature is raised, ethoxylated alcohols become more miscible with oil, and at the temperature T_α the miscibility gap between oil and surfactant disappears at the critical point cp_α .

The shift in miscibility of the surfactant from water to oil as the temperature is raised drives the complicated patterns of the 1, 2 and 3 phase regions observed in the middle of the phase diagram (see Figure 4.3). Rather than dwell on the complex and difficult to visualize three-dimensional phase prism which includes critical points, critical end-points and three phase triangles (Figure 4.3) (25), simplicity and greater understanding comes from going back to two-dimensional space by taking slices through the phase prism, and looking at how the variables of interest influence the patterns of phase behaviour seen in these slices. In order to do this, we define two variables, the mass fraction of oil in the two-component water/oil mixture:

$$\alpha = \frac{m_o}{m_o + m_w} \quad (4.1)$$

and the mass fraction of surfactant in the entire three-component oil, water and surfactant mixture:

$$\gamma = \frac{m_s}{m_s + m_o + m_w} \quad (4.2)$$

where m_s , m_o and m_w are the masses of surfactant, oil and water, respectively.

Figure 4.5 shows a “pseudo-binary” slice through the phase prism obtained when the weight ratio of oil to water is fixed at 50/50 ($\alpha = 0.5$). The phase diagram as a function of temperature (T) and surfactant concentration (γ) takes the shape of a fish: the three-phase region (3) is the body of the fish, the tail of the fish is the one-phase region (1), and the body of the fish lies above a $\bar{2}$ region and below a $\bar{2}$ region (see Figure 4.5).

The surfactant concentration at the head of the fish, γ_0 , is a measure of the “critical microemulsion concentration” (cmc). At this surfactant concentration, the middle microemulsion phase forms first. Below the head of the fish (below γ_0), $\bar{2}$ systems are observed where the surfactant is dissolved as monomers in the oil and water phases, and no mixing of oil and water is found. At γ_0 , the three-phase region first appears indicating the formation of a middle microemulsion phase with an internal interface of surfactant separating oil and water microdomains. At γ_0 , the concentration of surfactant in the excess water phase is identical to the critical micelle concentration ($\gamma_{\text{water}} = cmc$) (28). Thus, the amount of surfactant in the excess oil phase (γ_{oil}) is the overall surfactant concentration minus that dissolved

in excess water ($\gamma_0 - \gamma_{\text{water}}$) (28). Since ethoxylated alcohols dissolve in significant concentrations in the excess oil phase, a knowledge of γ_{oil} is important for calculation of the amount of surfactant available to coat the internal interfaces within the microemulsion phase (29).

As the overall surfactant concentration is increased beyond γ_0 at constant temperature, the amounts of oil and water that are mixed into the microemulsion phase increase, and the volume fraction of the middle microemulsion phase grows (see the test tubes in Figure 4.5). Eventually, enough surfactant is added to totally mix oil and water into one microemulsion phase. Consequently, an important feature of the “fish” phase diagram is that it describes the conditions at which a particular surfactant is most effective at completely mixing equal amounts of oil and water into a single microemulsion phase. The condition of greatest surfactant efficiency is denoted as \bar{X} , where the tail (1 phase) and the body of the fish (3 phases) join (Figure 4.5); \bar{X} has the surfactant concentration coordinate ($\bar{\gamma}$) and the temperature coordinate (\bar{T}). As can be seen from Figure 4.5, the efficiency of the ethoxylated alcohol surfactant depends strongly on temperature: the amount of surfactant required to mix equal amounts of oil and water into a one-phase system increases rapidly as the temperature is varied away from the optimal value of \bar{T} . The latter, i.e. the temperature at which the surfactant hydrophilic–lipophilic nature is optimally balanced for formation of microemulsions, has also been called the “HLB temperature” or “phase-inversion temperature” (4). The inverse of $\bar{\gamma}$ is a measure of the efficiency with which the surfactant forms microemulsions.

Kahlweit and Strey and their co-workers have systematically measured the dependence of \bar{X} , as described by $\bar{\gamma}$ and \bar{T} , upon the chemical structure of the ethoxylated alcohol surfactants (i and j) and hydrocarbon chain length (k) (27). The following presents a summary of the patterns observed:

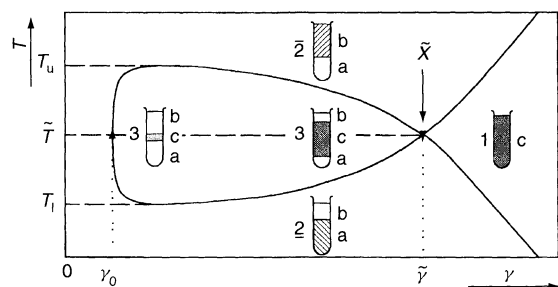


Figure 4.5. Schematic phase diagram of equal amounts of oil and water ($\alpha = 0.5$) as a function of ethoxylated alcohol surfactant concentration (γ) and temperature (T); γ_0 denotes the “critical microemulsion concentration”, i.e. the surfactant concentration where the middle microemulsion phase first appears. In addition, T_l and T_u denote the temperature range of the three-phase region, while \bar{X} , the point at which the tail and the body of the fish meet, denotes the temperature and surfactant coordinates (\bar{T} , $\bar{\gamma}$) for the most efficient formation of single microemulsion phases. The test tubes show the types of phase behaviour found in the various regions of the phase diagram. Reproduced by permission of the American Chemical Society (redrawn from Kahlweit and Strey (46))

www.iran-mavad.com

1. Upon increasing the hydrophilicity of the surfactant (increase j at fixed i and k), \bar{T} rises, the body of the fish fattens, and the surfactant becomes *less* efficient ($\bar{\gamma}$ increases).
2. Upon increasing the hydrophobicity of the surfactant (increase i at fixed j and k), \bar{T} falls, the body of the fish shrinks, and the surfactant becomes substantially *more* efficient ($\bar{\gamma}$ decreases).
3. Upon increasing the “amphiphilicity” of the surfactant (increase $i + j$ at fixed k), \bar{T} rises only slightly, the body of the fish shrinks, and the surfactant becomes dramatically *more* efficient ($\bar{\gamma}$ decreases).

- Upon increasing the chain length of the oil (increase k at fixed i and j), \tilde{T} rises, the body of the fish fattens, and the surfactant becomes significantly *less* efficient at mixing oil and water ($\tilde{\gamma}$ increases).
- Additional work carried out by Wormuth and Zushma (30) found that increasing the degree of branching of the hydrocarbon tail of monodisperse ethoxylated alcohols causes \tilde{T} to *fall* (a hydrophobic shift), and the surfactant to become *less* efficient at mixing oil and water ($\tilde{\gamma}$ increases).

For octane, the trends in \tilde{T} and $\tilde{\gamma}$ are shown as a function of surfactant structure (i, j) in Figure 4.6 (28). Note that the trends described above also hold for low-molecular-weight ethoxylated alcohols such as butoxyethanol (C_4E_1). However, the minimum concentration of C_4E_1 required to mix equal amounts of octane and water is 52 wt%, much higher than that of the substantially more “amphiphilic” and efficient $C_{12}E_6$ ($\tilde{\gamma} = 7.6$ wt% (Figure 4.6)). On the other hand, upon increasing the amphiphilicity of ethoxylated alcohols by increasing both i and j , the region of liquid crystalline phases (L_α) grows, which reduces the size of the region where single-phase microemulsions are found (31). (See

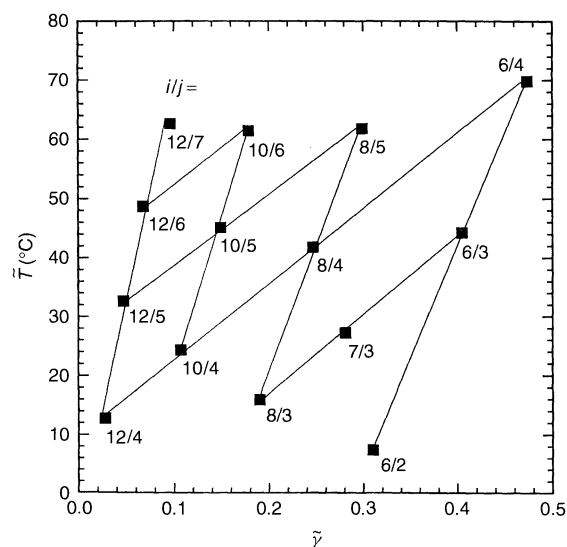


Figure 4.6. The temperature (\tilde{T}) and surfactant concentration ($\tilde{\gamma}$) coordinates at which optimal microemulsions form when equal amounts of octane and water ($\alpha = 0.5$) are mixed with a variety of ethoxylated alcohol surfactants (C_iE_j) of different lipophilic (i) and hydrophilic (j) balances. Reproduced by permission of The Royal Society of Chemistry (from Burauer *et al.* (28))

Section 2.6 below for one potential solution to this problem.)

In addition to the effects of changing the structure of the ethoxylated alcohol and the oil, two other important variables strongly affect the phase behaviour, namely pressure and addition of salts. As with temperature, pressure is also a “field” variable and uniform in all phases. An increase in pressure drives ethoxylated alcohols to partition more into water (hydrophilic shift), induces a $\bar{2}$ -to-3-to- $\bar{2}$ pattern, and thus has the opposite effect to increasing the temperature (27).

Inorganic electrolytes (salts) mimic the trends found with the field variables of temperature and pressure. Upon increasing the concentration of a “lyotropic” salt (such as NaCl), i.e. a salt which “salts out” ethoxylated alcohols from water into oil, a lipophilic shift is observed ($\bar{2}$ -to-3-to- $\bar{2}$ progression). Upon increasing the concentration of a “hydrotropic” salt (such as $NaClO_4$), i.e. a salt which “salts in” ethoxylated alcohols into water, a hydrophilic shift is observed ($\bar{2}$ -to-3-to- $\bar{2}$ progression) (27). An interesting observation is that ionic surfactants such as sodium dodecyl sulfate also act as strong “hydrotropic” salts (32).

Another useful pseudo-binary phase diagram is found upon fixing the surfactant concentration (γ constant), and varying the ratio of oil to water (vary α) as a function of temperature. For surfactant concentrations greater than $\tilde{\gamma}$, a one-phase channel is observed in the phase diagram, which spans all oil to water ratios (Figure 4.7). In the example shown in this figure, the

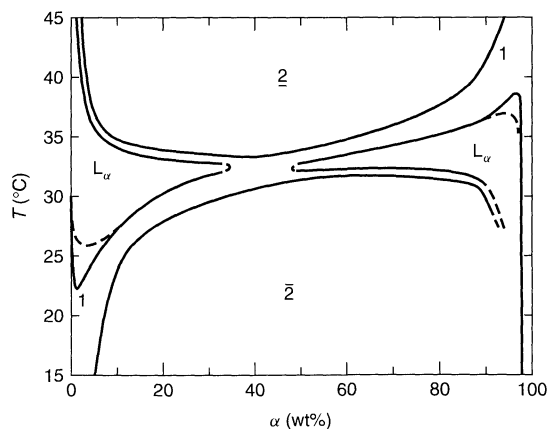


Figure 4.7. Slice through the phase prism at constant surfactant concentration ($\gamma = 0.07$) as a function of oil/water ratio (α) and temperature for the system $C_{12}E_5$ /octane/water; 1 denotes regions of one phase, while L_α denotes regions of liquid crystalline phases. Below the one-phase channel lie $\bar{2}$ systems, and above this lie $\bar{2}$ systems. Reproduced by permission of Academic Press (from Kahlweit *et al.* (86))

one-phase channel is narrow, and liquid crystalline (L_α) regions lie nearby.

The work of Kahlweit and Strey and their co-workers (27) thoroughly describes the patterns of phase behaviour of model monodisperse ethoxylated alcohols in non-polar oil and water mixtures (19, 27). Most importantly, \tilde{T} measures the optimal hydrophilic–lipophilic temperature for a particular combination of surfactant and oil, while $\tilde{\gamma}$ measures the minimum amount of surfactant required to mix the particular oil with water into a single microemulsion phase.

2.2 Mixtures of nonionic surfactants (commercial surfactants)

The phase behaviour generated upon the addition of a fourth component, for example, a second monodisperse ethoxylated alcohol of different hydrophilic–lipophilic balance, must be mapped in three-dimensional space in the form of a pyramid or phase tetrahedron (Figure 4.8). Each of the four corners of the diagram represent 100 wt% of that particular component, and the three sides of the tetrahedron represent Gibbs triangles describing the phase behaviour of the three possible ternary combinations.

Upon fixing the temperature and pressure, the phase behaviour found upon mixing a more lipophilic surfactant (the “cosurfactant” in Figure 4.8) with a more

hydrophilic surfactant (the “surfactant” in Figure 4.8) can be fully described in the phase tetrahedron. However, in order to simplify the phase behaviour, it is best to take two-dimensional slices through the phase tetrahedron. We define two new composition variables, i.e. the mass fraction of cosurfactant (m_{cs}) in the mixture of the two surfactants:

$$\delta = \frac{m_{cs}}{m_{cs} + m_s} \quad (4.3)$$

and the mass fraction of both surfactants in the total mixture:

$$\gamma = \frac{m_{cs} + m_s}{m_{cs} + m_s + m_o + m_w} \quad (4.4)$$

At constant ratio of the two surfactants (constant δ), a so-called surface of constant hydrophilic–lipophilic balance (HLB) is created (this has been well studied by Kunieda and co-workers (29, 33)). As also shown by Kahlweit *et al.*, slices of constant $\alpha = 0.5$ (equal masses of oil and water) yield pseudo-binary phase diagrams which look quite similar to those obtained by using one surfactant: a “fish” appears, where the variable δ in mixtures of two surfactants plays a similar role to temperature with one surfactant (Figure 4.8) (34). Thus, at constant temperature, the phase behaviour can be shifted from water-rich to oil-rich microemulsions by simply changing the mixing ratio of the two surfactants (δ) of different hydrophilic–lipophilic nature. Mixing rules quantify such behaviour (29). As mentioned above, commercially available ethoxylated alcohols contain a broad polydispersity in the degree of ethoxylation of the alcohol. A complete description of the phase behaviour of such polydisperse surfactant mixtures requires many dimensional spaces, i.e. one for each of the surfactant components, in addition to oil and water. However, if the commercial ethoxylated alcohol surfactant mixture is assumed to behave as a single surfactant (a pseudo-component assumption), polydisperse surfactants do generate qualitatively similar patterns of phase behaviour to those found with monodisperse surfactants. However, rather than finding a symmetric “fish”-shaped three-phase region at constant oil to water ratio (constant α), as observed with monodisperse surfactants, the “fish” becomes highly skewed as a function of surfactant concentration with polydisperse surfactants (Figure 4.9). Thus, at a constant temperature above \tilde{T} , increasing the concentration of polydisperse surfactants induces an effective “lipophilic” shift, i.e. a $\underline{2}$ -to-3-to- $\underline{2}$ phase progression (Figure 4.9).

Important to understanding the phase diagram of polydisperse surfactants is an understanding of the

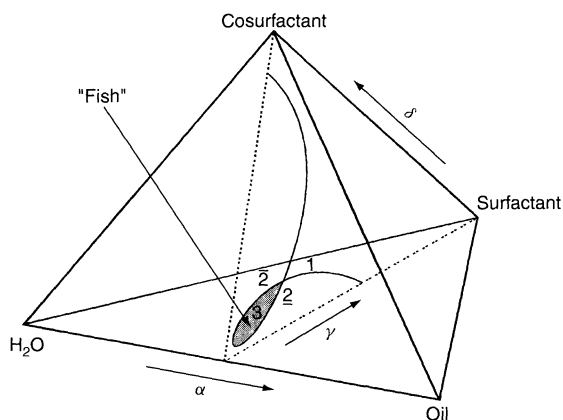


Figure 4.8. Tetrahedral representation of the phase diagram of water, oil, surfactant and cosurfactant. The slice taken at equal masses of oil and water ($\alpha = 0.5$; shaded region) schematically shows the “fish” phase diagram. Reproduced by permission of the American Chemical Society (redrawn from Strey and Jonstomer (106))

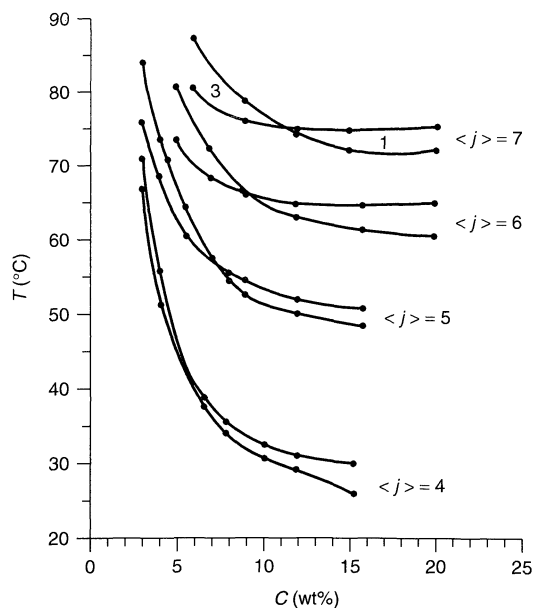


Figure 4.9. Phase diagrams of four different polydisperse ethoxylated alcohol surfactants ($C_iE_{(j)}$) where the average j , $\langle j \rangle = 4, 5, 6$ and 7) as a function of temperature (T) and surfactant concentration (c equivalent to γ) at equal ratios of octane to water ($\alpha = 0.5$). Reproduced by permission of Academic Press (from Wormuth and Geissler (21))

partitioning of the surfactant oligomers between the three “pseudo-phases” or “microdomains” within the microemulsion phase: the oil, water, and surfactant-rich interface between these two (29, 35). The solubility of the oligomers in the water microdomains and excess water phase is low (equivalent to the CMC of the mixtures); however, solubility in oil microdomains and excess oil phase (γ_{oil}) is significant and changes in this parameter strongly influence the phase behaviour. Empirical correlations have described some of the patterns of phase behaviour (29).

Due to partitioning effects, microemulsion phases occur at higher temperatures (higher \tilde{T}) with polydisperse ethoxylated alcohols than with monodisperse oligomers of an equivalent average degree of ethoxylation (21). Chromatographic studies of the partitioning of the individual surfactant components between excess oil, water and microemulsion phases show that the differences can be traced to significant amounts of unreacted alcohol (C_iE_0) and ethoxylated alcohols with low levels of ethoxylation being present in the polydisperse surfactant mixture (21). These lipophilic oligomers preferentially partition into excess oil phases, and are not

active as surfactants at the oil–water interface. Consequently, the dilution of the truly surface-active components (higher degrees of ethoxylation) with weakly surface-active alcohols (low degrees of ethoxylation) makes a polydisperse mixture less efficient at mixing equal amounts of oil and water into single microemulsion phases (higher $\tilde{\gamma}$) when compared to monodisperse ethoxylated alcohols. However, as the degree of ethoxylation is increased, the amount of unreacted alcohol and low-ethoxylation oligomers decreases as a fraction of the total oligomer distribution, with the “fish” becoming less skewed (see Figure 4.9) and the differences between polydisperse and monodisperse surfactants decreasing (21).

2.3 Ionic surfactants: the role of salt and alcohol cosurfactants

The above discussion clearly shows that optimal mixing of a particular oil and water into a microemulsion when using ethoxylated alcohol surfactants comes about by carefully choosing i and j of C_iE_j , and by carefully tuning the hydrophilic–lipophilic nature of the surfactant with temperature.

Unfortunately, ionic surfactants do not form balanced middle-phase microemulsions without the addition of at least a fourth component, namely salt, and often a fifth component, i.e. an alcohol “cosurfactant”. Since the head-groups of ionic surfactants tend to be substantially more hydrophilic than lower-molecular-weight poly(ethylene oxide) moieties ($j = 4$ to 8) (36), salts and alcohol cosurfactants must be added to move the overall hydrophilic–lipophilic balance of the mixture into the range required for formation of optimally balanced middle-phase microemulsions.

Whereas an ethoxylated alcohol with dodecyl tails (e.g. $C_{12}E_5$) forms middle-phase microemulsions, ionic surfactants with dodecyl tails, such as sodium dodecyl sulfate (SDS) or dodecyltrimethylammonium bromide (DTAB), are too hydrophilic for formation of middle-phase microemulsions. Simply increasing the length of the hydrocarbon tail to compensate for the high hydrophilicity of the ionic head-groups favours the formation of viscous liquid crystal line phases rather than fluid microemulsion phases (36, 37). However, increasing the hydrophobicity by adding double tails to the surfactant, as for example with didodecyltrimethylammonium bromide surfactant (DDAB), suppresses some of the tendency to form liquid crystals, and allows for formation of oil-rich microemulsions (38). However, this surfactant is too hydrophobic, and is far from the

balanced hydrophilic–lipophilic condition required for formation of highly efficient middle-phase microemulsions containing significant amounts of both oil and water.

However, a few double-tailed surfactants with intermediate-length tails do form balanced microemulsions with addition of salt (39, 40). One particular double-tailed surfactant, i.e. sodium bis(2-ethylhexyl) sulfosuccinate (Aerosol OT), forms optimal middle-phase microemulsions upon addition of only a small amount of salt (10). If the weight fraction of salt in water (ε) is fixed and the temperature is varied, or if the temperature is fixed and the weight fraction of salt is varied, the phase diagram at a fixed equal ratio of water to oil ($\alpha = 0.5$) also looks like a “fish” (Figure 4.10). Note that while ionic surfactants respond to salts in the same direction as nonionic surfactants do (a lipophilic shift), ionic surfactants respond to temperature in the *opposite* direction to that found with nonionic surfactants. At a fixed salt concentration, raising the temperature drives the ionic surfactant to partition more into the water-rich phases (a hydrophilic shift, see Figure 4.10). Consequently, with temperature as the ordinate, $\bar{2}$ systems (water-rich microemulsion phases) lie above the body of the fish, while $\bar{1}$ systems lie below the body of the fish. For Aerosol OT and salt mixtures, an increase in the salt concentration from 0.6 to 1.0 wt% causes a lipophilic shift, and consequently \tilde{T} rises by 20° (Figure 4.10). However, addition of salt substantially decreases the efficiency of the Aerosol OT surfactant ($\tilde{\gamma}$ increases). As expected, upon increasing the hydrophobicity of the oil (increasing k), an increase in the salinity is required to adjust the phase behaviour to remain optimal at constant temperature. Note that the phase behaviour of Aerosol OT is especially sensitive to impurities, and that Aerosol OT may degrade with time, and thus the phase behaviour may shift in the salt/temperature space.

The driving force for the inverse temperature dependence of ionic surfactants when compared to non-ionic surfactants lies in the behaviour of the binary water/surfactant mixtures. In contrast to mixtures of ethoxylated alcohols and water, which become less miscible with water and de-mix and exhibit a cloud point upon heating (see Figure 4.4), ionic surfactants become more miscible with water (10).

Without addition of salt, Aerosol OT forms a much-studied region of oil-rich microemulsions (41). However, the even more hydrophilic single-tailed surfactants such as sodium dodecyl sulfate (SDS) and dodecyltrimethylammonium bromide (DTAB) are so far from the optimal hydrophilic–lipophilic balance that addition of salt alone is not enough for the formation

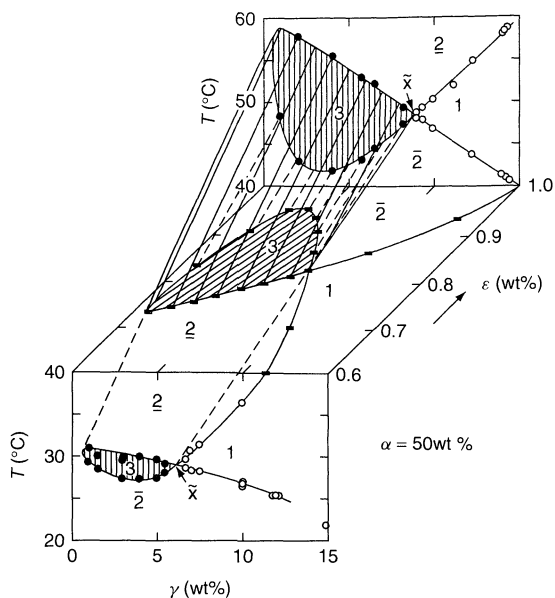


Figure 4.10. Phase diagram of the anionic surfactant Aerosol OT (AOT) as a function of temperature (T), surfactant concentration (γ) and NaCl concentration in water (ε), at a fixed equal ratio of decane to water ($\alpha = 0.5$). Reproduced by permission of the American Chemical Society (from Kahlweit *et al.* (10))

of microemulsions. One solution is to add significant amounts of low-molecular-weight alcohols as “cosurfactants”.

The term “cosurfactant” is misleading, since alcohols are amphiphilic but are not true surfactants (i.e. surface-active and microstructure-forming molecules with a strong chemical dipole). Most commonly, addition of low-molecular-weight aliphatic alcohols (eg. butanol, pentanol or hexanol) as “cosurfactants” reduces the overall hydrophilicity of ionic surfactant plus cosurfactant mixtures, and allows the formation of microemulsions (2, 42, 43). Such alcohols are not strongly surface-active, and although will partition into both excess water and oil-rich phases, they will preferentially partition into oil-rich phases, and thus are significantly lipophilic. An additional advantage of adding low-molecular-weight alcohols is the suppression of liquid crystalline phases (37). Note that other types of low-molecular-weight amphiphiles, such as amines, also facilitate microemulsion formation with ionic surfactants (44).

Substantial effort has gone into measuring the phase behaviour of quaternary mixtures of water, oil and ionic surfactant plus an alcohol cosurfactant (42, 43). However, even upon addition of significant amounts of

alcohol cosurfactant, a further addition of salt is often required to tune the system towards optimal middle-phase microemulsions (15). In these five-component mixtures, which tend to be temperature-insensitive, cosurfactant and salt concentration are the main tuning parameters (15).

A description of five-component mixtures in three-dimensional space is only possible by combining two of the components into a “pseudo-component” and plotting the four components as a tetrahedron (see Figure 4.8). One possibility is to fix the water and salt as a “brine” pseudo-component, and vary the ratio of alcohol to ionic surfactant. Indeed, this is a common way to formulate microemulsions (2, 15, 18). Titration of an emulsion of a hydrophilic surfactant, oil and brine with alcohol as cosurfactant eventually results in the initially turbid emulsion clearing into a translucent single microemulsion phase. Near optimal conditions, an increase in the ratio of alcohol cosurfactant to ionic surfactant (increasing δ) induces a lipophilic shift ($\underline{2}$ -to- $\underline{3}$ -to- $\underline{2}$ progression) (15, 42). Thus, if a slice at a fixed oil/water ratio of 50/50 ($\alpha = 0.5$) is taken, a “fish”-shaped phase diagram is found as the overall ionic surfactant plus cosurfactant concentration (γ) and the ratio of alcohol cosurfactant to ionic surfactant (δ) are varied (see Figure 4.8).

Rather than fix the water/salt ratio as a brine pseudo-component, another useful possibility is to fix the alcohol/ionic surfactant ratio as the pseudo-component (fix δ) and vary the salt concentration. An increase of the lyotropic salt concentration in ionic surfactant plus alcohol cosurfactant systems has the same effect as increasing temperature or salt in nonionic surfactant mixtures – a lipophilic shift is observed, and the phase behaviour progresses from $\underline{2}$ to $\underline{3}$ to $\underline{2}$ (15). If salt is placed in the position occupied previously by the cosurfactant in Figure 4.8, and the fixed ratio of alcohol/ionic surfactant placed as a combined pseudo-component (fixed δ) at the surfactant position, at equal amounts of oil and water ($\alpha = 0.5$) a plot of salt concentration (ε) versus overall cosurfactant/surfactant concentration (γ) also yields a “fish”-shaped phase diagram (45). Therefore, in either the case of fixed salt concentration (fixed ε) or the case of fixed alcohol/ionic surfactant ratio (fixed δ), the optimally formulated microemulsions for the chosen fixed ratio of δ or ε , are found at \bar{X} , where the tail and body of the fish meet (see Figure 4.8). Consequently, the phase behaviour of simple monodisperse ethoxylated alcohol surfactants in oil and water qualitatively mimics that of much more complicated mixtures containing ionic surfactants, cosurfactants and salt. Alcohol

cosurfactants and salt are additives required to reduce the hydrophilicity of ionic surfactants into the proper range required for the formation of optimal middle-microemulsion phases.

2.4 Nonionic plus ionic surfactants: temperature-insensitive mixtures

Rather than use a low-molecular-weight amphiphile (alcohol) as a “cosurfactant” in combination with ionic surfactants to create microemulsions, certain advantages arise when the “cosurfactant” is a true nonionic surfactant, e.g. a higher-molecular-weight ethoxylated alcohol such as $C_{12}E_5$. Mixtures of nonionic and ionic surfactants find many applications due to their synergistic effects in aqueous mixtures, such as lowering of the critical micelle concentration, or lowering of the Krafft temperature.

One particular advantage of using mixtures of non-ionic and ionic surfactants as microemulsifiers is the formation of temperature-insensitive microemulsions (17). Recall that the temperature-dependence of the phase behaviour of balanced microemulsion mixtures with ionic surfactants such as Aerosol OT (see Figure 4.10) is opposite to that found for ethoxylated alcohols (see Figure 4.5). Upon raising the temperature of Aerosol OT mixtures, a hydrophilic shift occurs ($\underline{2}$ – $\underline{3}$ – $\underline{2}$), although with ethoxylated alcohols, a lipophilic shift occurs ($\underline{2}$ – $\underline{3}$ – $\underline{2}$). Intuitively, upon mixing ionic and nonionic surfactants, the temperature dependence should cancel at a particular ratio (δ) of the two surfactants.

Since salt must be added to Aerosol OT surfactant in order to form balanced middle-phase microemulsions (ionic surfactants are salt-sensitive), and salt also induces a lipophilic shift in ethoxylated alcohol mixtures (nonionics are less salt-sensitive than ionics), the salt concentration (ε) is an important tuning parameter in addition to δ . As an example, consider the system of $C_{12}E_5$ /AOT/decano/water/NaCl, where δ is the amount of AOT in the $C_{12}E_5$ plus AOT mixture.

Measurements of the optimal temperature for microemulsion formation (\bar{T}) are plotted as a function of AOT surfactant concentration (δ) and salinity (ε) in Figure 4.11 (46). Rather than \bar{T} simply averaging upon mixing the two surfactants, due to the opposing temperature-dependence of the nonionic and ionic systems, the curves of constant salinity (ε) diverge at a value of $\delta \approx 70$ wt%. A “pole” is found in the phase behaviour (a flip in the curvature of the lines of constant ε) for ε between 0.8 and 1.0 wt%. Thus, at $\delta \approx$

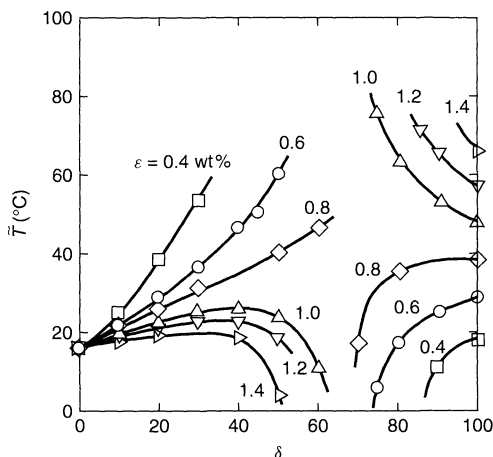


Figure 4.11. Phase behaviour of mixtures of ionic and nonionic surfactants in microemulsion systems of $C_{12}E_5$ /AOT/decane/water/NaCl. Optimal temperatures for microemulsion formation (\tilde{T}) are plotted as a function of wt% AOT in the surfactant mixture (δ), and wt% NaCl in water (ϵ). Reproduced by permission of the American Chemical Society (from Kahlweit and Strey (46))

70 wt%, and $\epsilon \approx 0.8$ wt%, the opposing temperature-dependencies of nonionics and ionics cancel out, and optimal temperature-insensitive microemulsions form.

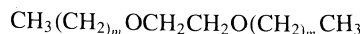
2.5 Other types of surfactants, oils and non-aqueous mixtures

Microemulsion formulations are not limited to the range of ethoxylated alcohol, ionic surfactant, non-polar oil and water mixtures discussed above. Indeed, other classes of surfactants and oils form microemulsions. Even non-aqueous microemulsions form upon the substitution of protic solvents for water.

Nonionic surfactants with sugar hydrophilic groups – alkylpolyglucoside surfactants – are highly hydrophilic, and form temperature-insensitive microemulsions upon addition of alcohol (47, 48), as do sucrose ester surfactants (49). Zwitterionic surfactants such as lecithins also form microemulsions upon the addition of cosurfactant (50–52). In addition, trisiloxane surfactants microemulsify silicon oils (53), and fluorocarbon-tailed surfactants microemulsify fluorinated oils (54, 55).

The patterns of phase behaviour discussed above focused on non-polar aliphatic and aromatic oils, which are essentially completely immiscible with water. However, many practical applications require the mixing of more polar oils, i.e. oils that are partially miscible with

water. Upon increasing the miscibility of the oil with water, the patterns of phase behaviour change qualitatively. As an example, take ether oils where the ratio of polar ether linkages to non-polar hydrocarbon moieties, and thus the overall polarity of the oil, is increased upon decreasing m :



Upon increasing the oil polarity (decreasing m), the three-phase body of the “fish” shrinks and eventually disappears altogether (56). In the absence of the three-phase body, the progression of phase behaviour found upon increasing temperature is $\underline{2}$ -to- $\underline{2}$ -to- $\underline{2}$, rather than $\underline{2}$ -to-3-to- $\underline{2}$. In addition, as the oil polarity is increased, the temperature at which optimal microemulsions form, \tilde{T} , falls, and the minimum amount of surfactant required to mix more polar oils with water ($\tilde{\gamma}$) decreases slightly (56). Note that the microstructures in such mixtures appear to “dissolve”, i.e. become smaller and less well defined, as oil polarity is increased and the oil and water phases become more miscible (56).

As noted above, a variety of surfactants and oils may be microemulsified with water. In addition, non-aqueous microemulsions form when polar protic solvents such as formamide and glycerol are substituted for water. However, ethoxylated alcohol surfactants are much less effective at mixing formamide or glycerol with non-polar oils, when compared to mixing water and non-polar oils (57, 58). Upon decreasing the ratio of propylene glycol (a good solvent for ethoxylated alcohols) to glycerol (a non-solvent for ethoxylated alcohols), the phase behaviour follows the same progression as found upon increasing temperature ($\underline{2}$ -to-3-to- $\underline{2}$), and a “fish”-shaped phase diagram results (59). A similar pattern of phase behaviour is found upon increasing the concentration of glycerol in water, with viscous microemulsions resulting (23).

2.6 Addition of polymers

Salt and cosurfactants are common additives used to “tune” microemulsion phase behaviour. Less common is the addition of polymers, i.e. additives that increase the viscosity in addition to influencing the phase behaviour. Polymers of interest may be water-soluble, oil-soluble, or contain hydrophilic and hydrophobic groups and thus be interfacially active.

Water-soluble polymers of low molecular weight (less than $M_w = 10000$), such as poly(ethylene oxide) (PEO) and ethylhydroxyethyl cellulose (EHEC) tend

to partition between microemulsion phases and excess water phases in a fixed relationship to water, and only influence the phase behaviour at relatively high concentrations (60–62). However, higher-molecular-weight polymers are often excluded from microemulsion phases, mostly likely due to osmotic effects (61, 62). The osmotic effect causes the polymer to extract water (or oil) from the microemulsion phase, and thus addition of even low concentrations of high-molecular-weight water-soluble or oil-soluble polymers substantially reduces the amount of water or oil solubilized into the middle microemulsion phases (61). Note that these effects hold for nonionic polymers in nonionic surfactant systems; ionic polyelectrolytes combined with nonionic or ionic surfactants may interact strongly, depending upon the polymer and surfactant charge, and salt concentration.

On the other hand, interfacially active polymers can dramatically *increase* the solubilization of oil and water into microemulsions. Addition of 1 wt% of a hydrophobically modified ethylhydroxyethyl cellulose causes the middle microemulsion phase to grow and take up substantially more water, and somewhat more oil (62). At higher polymer concentrations, however, this effect disappears. More dramatic effects are observed upon addition of carefully chosen block copolymers of poly(ethylenepropylene)-*co*-poly(ethylene oxide) (PEP–PEO) (11). Addition of only a small amount of these surfactant-like block copolymers substantially reduces the amount of nonionic surfactant required to form microemulsion phases. For example, addition of only 0.4 wt% of PEP–PEO (where each block is of 5000 molecular weight) reduces the amount of $C_{10}E_4$ required to mix equal amounts of decane and water ($\tilde{\gamma}$) from 13 to only 3 wt% (11). The overall molecular weight of the polymer must be relatively low to maximize the effect, and the block lengths roughly equal in order to avoid changing \tilde{T} (11). An additional benefit is that the region of liquid crystalline (L_α) phases is suppressed when using block copolymers.

2.7 Microemulsions of compressible and supercritical fluids

As noted above, raising the pressure in mixtures of ethoxylated alcohol, liquid alkane oil and water mixtures induces a 2-to-3-to-2 pattern, and thus pressure has the opposite effect of increasing temperature (27). Indeed, a “fish”-shaped phase diagram is observed at a fixed

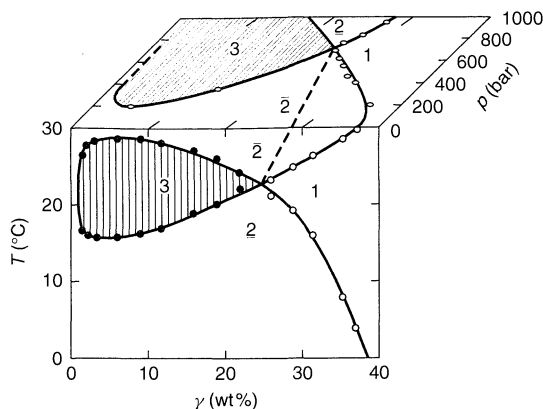


Figure 4.12. Phase diagram of C_8E_3 /decane/water mixtures as a function of surfactant concentration (γ), temperature (T), and pressure (P) at equal ratio of decane to water ($\alpha = 0.5$)

temperature as a function of pressure and surfactant concentration (Figure 4.12). As the pressure is increased, ethoxylated alcohols become less miscible with alkanes.

In addition to liquid alkanes, formation of microemulsions is possible with “oils” which are hydrophobic gases at standard conditions, but highly compressible fluids near or above the supercritical fluid state. Low amounts of water mix with ethane and propane upon adding surfactants such as anionic Aerosol OT (63) or cationic DDAB (64) and increasing the pressure. More balanced systems exhibiting a “fish”-shaped phase diagram as a function of pressure arise with ethoxylated alcohols, propane and brine (65). In this case, as pressure is increased, the surfactant undergoes a hydrophilic shift similar to that mapped in Figure 4.12. In addition, at high pressures, fluorocarbons and hydrochlorofluorocarbons form microemulsions with water when using Aerosol OT (66) and hexafluoropropylene mixes with water when using fluorinated surfactant plus fluorinated alcohol (67). In addition, application of fluorocarbon surfactants facilitates the formation of microemulsions of water in supercritical carbon dioxide (68).

2.8 A practical guide for the formulation of microemulsions

The above discussion of phase behaviour clearly shows that while a wide variety of mixtures form microemulsions, the conditions under which optimal microemulsion form are narrow and sharply defined. Above all, the proper hydrophilic–lipophilic balance must be set by an appropriate choice of surfactant and additives.

Table 4.2. Summary of the qualitative effects of variables and additives upon the phase behaviour of nonionic (N) and ionic (I) surfactants in mixtures with oil and water

Property	System type	Variable	HL shift ^a	Efficiency ^b
Temperature	N	Increase T	L	–
Temperature	I + Salt	Increase T	H	–
Pressure	N	Increase P	H	↓
Lipophilicity of C_iE_j	N	Increase i	L	↑
Hydrophilicity of C_iE_j	N	Increase j	H	↓
Polydispersity of ethoxylation	N		L	↓
Branching of tail	N or I	Single → double tail	L	↓
Hydrophobicity of oil	Alkane oils (B_k)	Increase k	H	↓
Oil Polarity	Ether oils	Decrease m	L	↑
Salt concentration, lyotropic	N	Increase ε	L	↑
Salt concentration, lyotropic	I	Increase ε	L	↓
Salt concentration, hydrotropic	N	Increase ε	H	↑
Alcohol cosurfactant concentration	I	Increase δ	L	↓
Nonionic polymer concentration	Oil or water soluble, high MW	Increase δ	–	↓
Surfactant block copolymer concentration	Balanced, moderate MW	Increase δ	–	↑↑

^aHydrophilic (H)–lipophilic (L) shift (related to \tilde{T}).

^bRepresents the inverse of the minimum amount of surfactant required to form single-phase microemulsions ($\tilde{\gamma}$).

The understanding developed over the last 50 years of research on microemulsions – the trends in phase behaviour, and the special conditions under which microemulsions form – can be exploited to speed up the process of finding microemulsion phases for a given oil and aqueous mixture. Table 4.2 summarizes the trends, and provides a qualitative guide for the formulation of microemulsions. The effect of variables upon the hydrophilic–lipophilic balance of the system (HL shift) and the minimum amount of surfactant required to form one-phase microemulsions ($\tilde{\gamma}$, efficiency) give important information on which directions to follow in the formulation process. These trends, along with partitioning information, and the “step-by-step” process described below, provide guidelines for the formulation of microemulsion phases.

As noted above, quite hydrophilic or quite lipophilic surfactants tend to form emulsions (1), whereas surfactants of intermediate hydrophilic–lipophilic balance are more likely to form microemulsions. As a rough starting point, the concepts of hydrophilic–lipophilic balance quantified by the HLB number (26), along with group contribution methods to calculate the latter (69) can give some information as to which surfactants might form microemulsions. However, the HLB number neglects the effects of the oil type, salinity, pressure, temperature and other additives, which have a dramatic influence on the microemulsion phase behaviour. More complete attempts to correlate the phase behaviour in microemulsions began with the concept of the phase-inversion temperature (PIT) (70), the temperature at which a water-in-oil (w/o) emulsion

inverts to an oil-in-water (o/w) emulsion. For monodisperse ethoxylated alcohol systems, the PIT is similar to \tilde{T} . Other methods, such as the R -ratio (71), a precursor to packing and interface bending concepts (see below), along with the equivalent alkane carbon number equation (EACN) (15, 72), also provide some guide.

Again, these HLB-related concepts do not take into account effects of the oil type and additives, and unfortunately no models currently exist for the quantitative prediction of phase behaviour. Thus, formulation of microemulsions becomes a trial-and-error process. However, knowledge of the “hydrophobicity” or “polarity” of the oil of interest relative to oils of known phase behaviour can significantly help in finding microemulsions (72). Mixtures of oils can be assigned an equivalent alkane carbon number equation (EACN) (72), and the polarity of oils may be measured by quantifying miscibility with water in the absence of surfactant (56). Upon mixing equal volumes of oil and water *without* surfactant, the relative volumes of the phases may change if the oil is miscible with water. If an emulsion forms, the oil probably contains lipophilic surface-active ingredients, which tend to form water-in-oil emulsions. Similarly, the partitioning of additives from the aqueous phase into the oil phase can also be examined.

Even without knowledge of oil polarity or hydrophobicity, a “step-by-step” approach provides the quickest results. As an illustration of this approach, consider the microemulsification of a soybean oil (triglyceride) (73). Start with the phase behaviour of a known oil and surfactant combination, in this case decane and the commercial ethoxylated alcohol surfactant “Marlowet

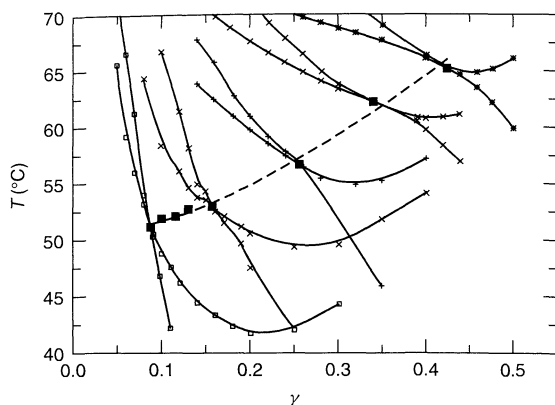


Figure 4.13. Phase diagram as a function of temperature (T) and Marlowet EM50 ethoxylated alcohol surfactant concentration (γ) in mixtures of water and decane plus soybean oil. The overall oil-to-water ratio is fixed ($\alpha = 0.5$), while the ratio of soybean oil to decane is systematically varied from $\beta = 0$ (100% decane, “fish” on left side of phase diagram) to $\beta = 1$ (100% soybean oil, “fish” on upper right side of phase diagram). The path of $\tilde{X}(\tilde{T}, \tilde{\gamma})$ is shown by squares and the dashed line (from Lade (73))

EM 50” (Condea). Gradually substitute soybean oil for decane, and follow the direction in which the phase diagram moves (Figure 4.13). The concentration of soybean oil in the overall oil mixture is defined by β where:

$$\beta = \frac{m_{so}}{m_{so} + m_{do}} \quad (4.5)$$

and m_{so} is the mass of soybean oil, and m_{do} the mass of decane oil.

As β is increased, the point \tilde{X} moves as shown by the squares and dashed line in Figure 4.13: the efficiency of the surfactant decreases ($\tilde{\gamma}$ increases), and the optimal microemulsions move to higher temperature (\tilde{T} increases). In this example, the Marlowet EM 50 surfactant is inefficient at forming microemulsions of pure soybean oil and water, and so repeating the process with another class of surfactant, for example, an ionic surfactant or adding a cosurfactant is recommended. Using the same “step-by-step” approach, the Marlowet EM 50 surfactant is found to be much more effective at microemulsifying mixtures of non-polar oils such as “Gravex 915” ($\tilde{\gamma} = 10$ wt%) which contains aromatic and aliphatic hydrocarbons, than soybean oil (73). If the “fish” phase diagram begins to move out of the temperature range of interest, a surfactant of different HLB number can be substituted, or the appropriate HLB shift induced with additives (see Table 4.2).

If the system of interest contains additives that are soluble in water, such as salt or polymer, a gradual “step-by-step” addition of these ingredients also allows one to follow the direction in which the phase diagram moves. Key to the “step-by-step” approach is starting from a known microemulsion-forming system, and looking at which direction the phase diagram moves upon substitution of oil or aqueous components.

3 LINKS BETWEEN THE PHASE BEHAVIOUR, MICROSTRUCTURE AND INTERFACIAL TENSIONS

Once formulated, exploitation of the special properties of microemulsions is facilitated by knowledge of the types of microstructure, characteristic sizes, and the dynamics of structure fluctuations. Unfortunately, determination of microemulsion microstructure and dynamics remains difficult, and thus is discussed elsewhere in this book (see Chapter 40). Here, the relationships between microstructure, interfacial tensions and phase behaviour are discussed, and a qualitative description of the dynamic processes in microemulsions is given. For simple ethoxylated alcohol–water mixtures, the correlations below allow an estimation of the sizes and interfacial tensions in microemulsions without resort to any complex measurements.

3.1 Spontaneous curvature and characteristic sizes

Key to understanding which types of microstructure form is an appreciation of the concept of “spontaneous” curvature of the interfacial film between the oil and water domains. The surfactant geometry and chemical structure, and *more importantly*, the intermolecular forces acting between surfactant molecules, set the curvature at the interface (74). Repulsive hydrophilic forces act between the surfactant head-groups, and these forces are balanced by attractive hydrophobic forces acting at the oil–water interface, steric repulsive forces between the tails of the surfactants, and forces due to penetration of oil into the tails of the surfactants (Figure 4.14). According to the concept of Israelachvili (74), the hydrophilic interactions determine the effective area per head-group (a_0) of the surfactant molecule, while steric interactions and oil penetration determine the volume of the hydrocarbon tail (V), and its extended chain length (l_c). The “packing parameter”, $V/a_0 l_c$ is less than one for oil-in-water (o/w) structures, near unity for flatter

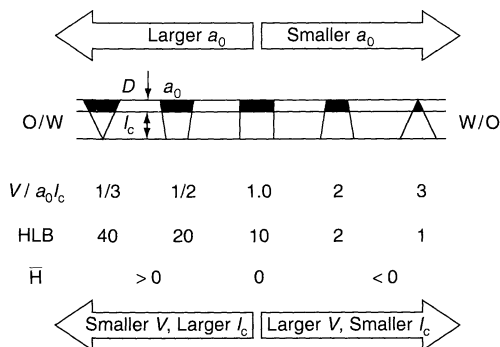


Figure 4.14. Effect of surfactant structure on the spontaneous curvature of surfactant films; V is the volume of the surfactant tail, l_c the extended length of the surfactant tail, and a_0 the effective area per head-group. Reproduced by permission of Elsevier Science (redrawn from Isrealachvili (74))

bicontinuous and lamellar structures, and greater than one for water-in-oil (w/o) structures. Conceptually, upon changing parameters such as temperature, salinity, surfactant structure (tail branching) and oil properties, the packing parameter changes in the directions shown in Figure 4.14, and thus the curvature at the oil–water interface changes.

The curvature (c) of the two-dimensional interface of the surfactant separating the oil and water microdomains within a microemulsion phase is geometrically described by two radii of curvature (r):

$$r_1 = \frac{1}{c_1} \quad (4.6)$$

and:

$$r_2 = \frac{1}{c_2} \quad (4.7)$$

while the mean curvature of the surface is given by the following:

$$H = \frac{c_1 + c_2}{2} \quad (4.8)$$

For the case of droplet microemulsions, $r_0 = r_1 = r_2$, and so the mean curvature $H = 1/r_0$. According to convention, H is positive for oil-in-water (o/w) droplets, and negative for water-in-oil (w/o) droplets. For bicontinuous microemulsions, which according to freeze-fracture electron microscopy have saddle-shaped surfaces of negative and positive curvature (13), $c_1 \approx -c_2$, and so the mean curvature $H \approx 0$. Note that lamellar liquid crystalline phases (L_α), which are planar layers of oil and water, also have zero mean curvature ($c_1 = c_2 = 0$), and are often located at higher surfactant concentrations nearby bicontinuous microemulsion phases (19).

In the case of monodisperse ethoxylated alcohol surfactants, alkane and water mixtures, the relationships between phase behaviour, the microstructure and the interfacial tension are fully measured and correlated (23). Small-angle neutron scattering (SANS) of the microemulsion phase allows measurement of the sizes and curvatures of the microstructures in the microemulsions along a path of maximum solubilization of oil and/or water as a function of temperature. Upon increasing temperature in $C_{12}E_5$ /octane/water mixtures, the mean curvature (H) decreases continuously and linearly upon increasing the temperature (see Figure 4.15(b)). In other words, there is a *continuous* progression in the structure of the microemulsions from o/w droplets to w/o droplets through a bicontinuous region. The mean curvature is found to be zero at the mid-point temperature of the three-phase region.

Along the same path, SANS measurements show that the average characteristic size in the microemulsions (ξ) goes through a sharp cusp-shaped maximum at \bar{T} (Figure 4.15(a)). In this case, the average sizes range from 3 to 50 nm (30 to 500 Å), and the droplet microstructures (high positive or negative curvature) are the smallest structures, and the bicontinuous structures (zero mean curvature) are the largest structures. Note that the same trends arise when the chemical structures of the oil and ethoxylated alcohol are varied (16).

According to various models of the microstructures in microemulsions (75, 76) near equal volumes of oil and water ($V_{oil} \sim V_{water}$), the characteristic size of the bicontinuous microstructure varies with volume fractions of oil, water and surfactant as follows:

$$\xi = a \frac{\phi(1-\phi)v_s}{a_s \phi_{si}} \quad (4.9)$$

while for droplet structures, the radius of the droplets is given by the following:

$$r_0 = 3 \frac{v_s(\phi + \frac{\phi_{si}}{2})(1+p^2)}{a_s \phi_{si}(1+3p^2)} \quad (4.10)$$

where ϕ is the volume fraction of the dispersed phase, ϕ_{si} the volume fraction of surfactant at the internal interfaces in the microemulsion, v_s the volume per surfactant molecule, a_s the area per surfactant molecule, p the droplet polydispersity index (77) and a is a constant of proportionality. As noted above, ϕ_{si} , the amount of surfactant at the internal interfaces within a microemulsion, can be calculated from the phase diagram by subtracting the solubility of the surfactant in the excess oil and water phases from the overall surfactant concentration by using γ and γ_0 , and knowing the critical micelle concentration of the surfactant (28).

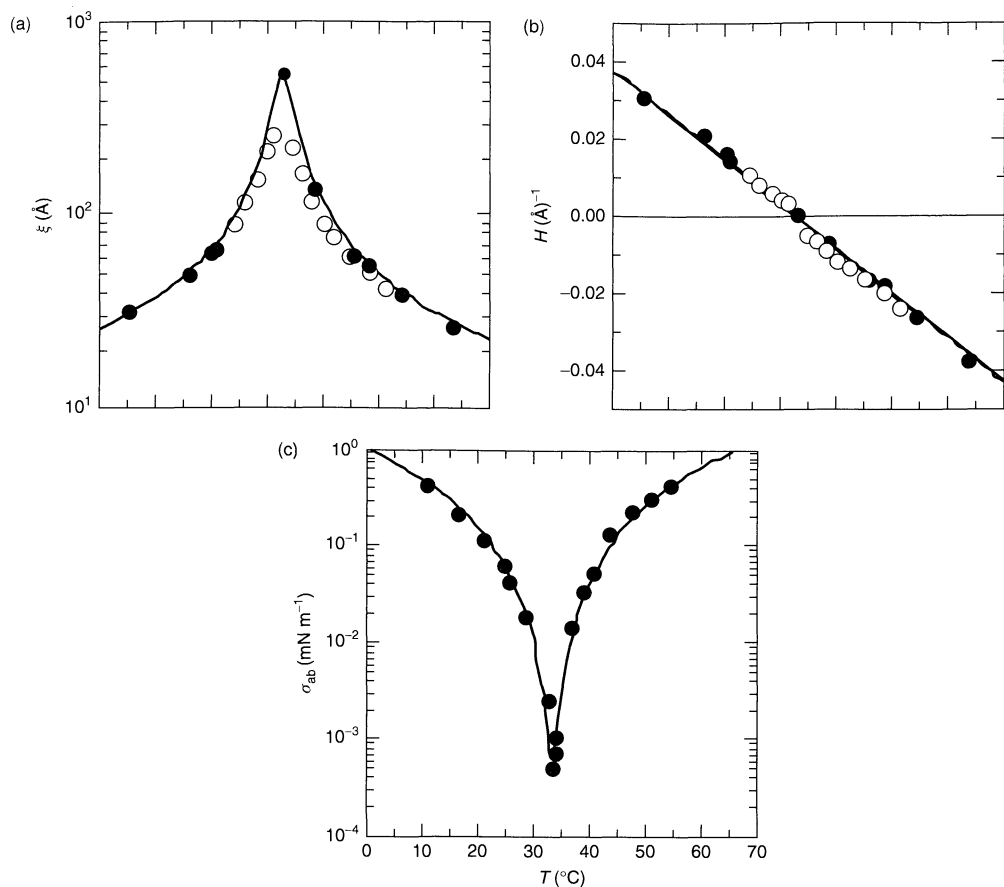


Figure 4.15. Temperature dependence of (a) the mean characteristic size of the microstructures (ξ), (b) the mean curvature of the surfactant film separating oil and water microdomains in the microemulsion (H), and (c) the interfacial tension between the microemulsion phase and excess oil and water phases (σ_{ab}), for mixtures of $C_{12}E_5$ /octane/water. Reproduced by permission of Springer Verlag (from Strey (23))

The volume per surfactant molecule is calculated from the surfactant bulk density, the area per surfactant is measured by SANS, and the constant of proportionality $a = 7.2$ comes from correlations of many measurements on various ethoxylated alcohol systems (16).

The SANS measurements (78), freeze-fracture electron microscopy (13), electrical conductivity (24), and self-diffusion measurements using NMR spectroscopy (79, 80) along paths of varying oil/water ratios (α) and temperature within the one-phase channel (constant surfactant concentration, γ) allow the generation of the schematic diagram shown in Figure 4.16 (81). Within the one-phase channel, droplet microemulsions reside at very low α values and low temperatures, or at high α values and high temperatures. Droplet microemulsions become globular and then bicontinuous as the water/oil

ratio (α) is moved closer to 50/50. Qualitatively similar trends in the mean curvature and characteristic sizes are found upon changing salinity in more complex four- or five-component microemulsion mixtures containing ionic surfactants and cosurfactants (82–84). Many of these observations of the structure in microemulsions may be thermodynamically understood in terms of changes in the spontaneous curvature and the “bending energy” of the surfactant film separating oil and water microdomains within the microemulsion phases (85).

3.2 Interfacial tensions

Besides the small microstructures in microemulsions, another unique feature of the latter are the ultra-low interfacial tensions found between microemulsion

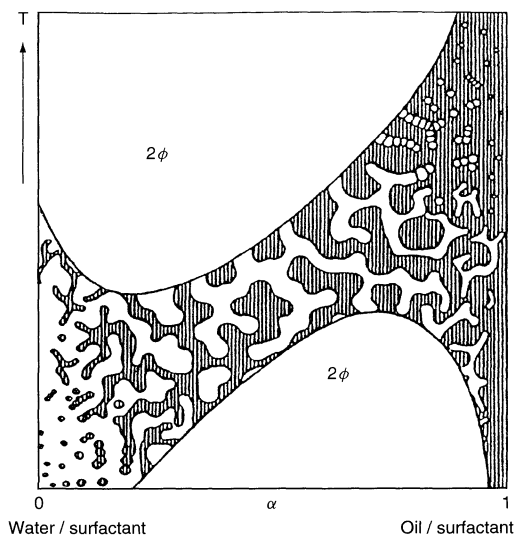


Figure 4.16. Schematic representation of the types of microstructures found within the one-phase channel of the phase diagram at constant surfactant concentration (γ) when the oil/water ratio (α) and temperature (T) are varied. Reproduced by permission of Wiley-VCH (from Schomäker (107))

phases and excess oil and water phases. Measurements on many different systems find a sharp minimum in interfacial tension where optimal middle-phase microemulsions occur, regardless of whether the system is a simple three-component mixture of ethoxylated alcohol, oil and water (vary the temperature) (86), or a five-component mixture containing ionic surfactant, cosurfactant and salt (vary the salt concentration) (15).

For example, using the same system highlighted above ($C_{12}E_5$ /octane/water), the interfacial tension between oil and water as a function of temperature exhibits a sharp inverted cusp, with the minimum and ultra-low interfacial tension ($5 \times 10^{-4} \text{ mN m}^{-1}$) found at \tilde{T} (Figure 4.15(c)). Optimally formulated microemulsions with high solubilization of oil and water exhibit the lowest interfacial tensions. Note, however, that the interfacial tension curves and the characteristic sizes exhibit exactly the opposite dependence as the mean curvature changes (see Figure 4.15).

For the ethoxylated alcohol, alkane and water systems set at \tilde{T} , combination of the interfacial tension data with the data on characteristic sizes (Figure 4.15) yields the following relationship (23, 87):

$$\sigma_{ab} \xi^2 \approx kT \quad (4.11)$$

where k is the Boltzman constant. This relationship allows approximation of the characteristic size of the

microstructure, given a knowledge of the interfacial tension, or vice versa. In addition, combination of equation (4.11) with equation (4.9) yields $\sigma_{ab} \sim \phi_{si}^{-2}$, and thus the interfacial tension decreases as the amount of surfactant at the internal interfaces within the microemulsion increases. Equation (4.11) also confirms theoretical observations that thermodynamically stable mixtures of oil and water will only occur if the interfacial energy per microemulsion droplet ($\sigma_{ab} \xi^2$) is roughly equal to the thermal energy (kT) (23, 87).

3.3 Dynamic processes

As equation (4.11) indicates, the energy of self-assembly of the surfactant at the oil–water interface is of the same order of magnitude as the thermal energy (kT). Thus, microemulsion structures are close to their limit of stability, are “soft” structures (74), and many experiments indicate that the structures fluctuate rapidly in time (14, 88). Experiments suggest that four types of dynamic processes occur in microemulsions, as follows:

1. The diffusion of individual molecules within the microstructures – most importantly, the diffusion of surfactant molecules back and forth from the internal interfaces to the oil or water domains.
2. The fluctuations in the curvature of the surfactant film separating oil and water domains, which cause fluctuations in globule shapes and inter-globule interactions.
3. The diffusion of droplets or globules through the continuous phase.
4. The kinetics of the collision, merging, and separation of droplets or globules, and the exchange of the contents between the droplets.

Some of these parameters are directly measured with self-diffusion NMR spectroscopy (79, 80, 89) or indirectly by fluorescence probes (88). In addition, the relaxation of the microstructure after a sudden jump in a field variable such as temperature or pressure yields information on the dynamics of the structures (86). Depending upon composition of the mixtures, the time-scales of the dynamic processes range from microseconds to milliseconds (14, 88).

4 APPLICATIONS OF MICRO-EMULSIONS

The unique properties of microemulsions – spontaneous formation, high solubilization of oil and water, low

interfacial tensions, fine microstructures, transparent systems – mean that microemulsions find wide application in a variety of products and processes. Here, a sampling of the potential applications along with useful review articles are highlighted. No attempt is made to critically examine the merits of using microemulsions as opposed to emulsions or solutions. The information covered in this chapter on the basics of microemulsion formulation, combined with review articles and expert articles on specific applications, should allow a formulator to apply microemulsions in an efficient manner.

One of the original driving forces for research into microemulsions was exploitation of the low interfacial tensions and wetting properties of microemulsions as a way to enhance the recovery of crude oil trapped in porous rock (72, 90, 91). In a similar way, microemulsions can be used to extract pollutants from contaminated solids (81, 92), and treat organohalide contaminants (93). The ability to solubilize water-soluble ingredients into an oil-continuous medium, and vice versa, means that microemulsions find application in drug formulations (81), food preparations and agricultural chemical formulations (17). Microemulsions also may be a stage in the detergency process whereby oily soils are wetted, dispersed and removed from surfaces (17, 81).

Similarly, the ultra-low interfacial tensions and spontaneous solubilization of *microemulsion* phases can be exploited for the creation of stable and finely dispersed *emulsions* (7). By quenching the temperature and quickly passing from 2 through 3 or 1 phase mixtures and on down to temperatures in or below the 2 region, small emulsion droplets of oil dispersed in water result without application of high shear processes (5, 8, 81, 94, 95).

In addition to exploiting their wetting and solubilization properties, microemulsions also find application as a reaction medium for the formation of nanoparticles, and for organic, inorganic, bioorganic and photochemical reactions (18). Small polymer latexes of controlled monodisperse size and monomer composition, and often of high molecular weight, result from the polymerization of hydrophobic monomers in water-rich microemulsions, and hydrophilic monomers in oil-rich microemulsions (96–99). The water droplets in water-in-oil microemulsions appear to control the nucleation and slow the growth of inorganic nanoparticles of various types (17, 81, 100, 101). Also of increasing interest is the application of microemulsions in phase-transfer catalysis. One example is the solubilization of organic catalysts in microemulsion water droplets, which

then, due to the high interfacial area between the oil and water microdomains, accelerate the catalysis of reactions with oil-soluble ingredients (102–104). The literature encompassing applications of microemulsion continues to grow, and the interested reader is therefore encouraged to search the literature for the latest ideas.

5 REFERENCES

1. Bankcroft, W. D., The theory of emulsification, V, *J. Phys. Chem.*, **17**, 501 (1913).
2. Hoar, T. P. and Schulmann, J. H., Oleophilic micelles, *Nature (London)*, **329**, 309 (1943).
3. Schulmann, J. H., Stoeckenius, W. and Prince, L. M., Mechanism of formation and structure of micro emulsions by electron microscopy, *J. Phys. Chem.*, **63**, 1677 (1959).
4. Shinoda, K. and Kunieda, H., Conditions to produce so-called microemulsions: factors to increase the mutual solubility of oil and water by solubilizer, *J. Colloid Interface Sci.*, **42**, 381 (1973).
5. Nakajima, H., Microemulsions in cosmetics, in *Industrial Applications of Microemulsions*, Solans, C. and Kunieda, H. (Eds), Marcel Dekker, New York, 1997, pp. 175.
6. Sudol, E. D. and El-Aasser, M. S., Miniemulsion polymerization, in *Emulsion Polymerization and Emulsion Polymers*, Lovell, P. A. and El-Aasser, M. S. (Eds), Wiley, New York, 1997, pp. 699.
7. Shinoda, K., The correlation between the dissolution state of nonionic surfactant and the type of dispersion stabilized with the surfactant, *J. Colloid Interface Sci.*, **24**, 4 (1967).
8. Forster, T., Von Rybinski, W. and Wadle, A., Influence of microemulsion phases on the preparation of fine-dispersion emulsions, *Adv. Colloid Interface Sci.*, **58**, 119 (1995).
9. Danielsson, I. and Lindman, B., The definition of microemulsions, *Colloid Surf.*, **3**, 391 (1981).
10. Kahlweit, M., Strey, R., Schomäcker, R. and Haase, D., General patterns of the phase behaviour of mixtures of H₂O, nonpolar solvents, amphiphiles and electrolytes. 2, *Langmuir*, **5**, 305 (1989).
11. Jakobs, B., Sottmann, T. and Strey, R., Amphiphilic block copolymers as efficiency boosters for microemulsions, *Langmuir*, **15**, 6707 (1999).
12. Scriven, L. E., Equilibrium bicontinuous structures, *Nature (London)*, **263**, 123 (1976).
13. Jahn, W. and Strey, R., Microstructure of microemulsions by freeze fracture electron microscopy, *J. Phys. Chem.*, **98**, 2294 (1988).
14. Moulik, S. P. and Paul, B. K., Structure, dynamics and transport properties of microemulsions, *Adv. Colloid Interface Sci.*, **78**, 99 (1998).

15. Bourrel, M. and Schechter, R. S., *Microemulsions and Related Systems*, Marcel Dekker, New York, 1988.
16. Sottmann, T. and Strey, R., Shape similarities of ultra-low interfacial tension curves in ternary microemulsion systems of the water-alkane- C_iE_j type, *Ber. Bunsenges. Phys. Chem.*, **100**, 237 (1996).
17. Solans, C. and Kunieda, H. (Eds), *Industrial Applications of Microemulsions*, Surfactant Science Series, Vol. 66, Marcel Dekker, New York, 1997.
18. Sjoblom, J., Lindberg, R. and Friberg, S. E., Microemulsions - phase equilibria characterization, structures, applications, and chemical reactions, *Adv. Colloid Interface Sci.*, **95**, 125 (1996).
19. Schubert, K.-V. and Kaler, E. W., Nonionic microemulsions, *Ber. Bunsenges. Phys. Chem.*, **100**, 190 (1996).
20. Schick, M. J., *Nonionic Surfactants*, Surfactant Science Series, Vol. 23, Marcel Dekker, New York, 1987.
21. Wormuth, K. R. and Geissler, P. R., Phase behaviour of monodisperse and polydisperse ethoxylated alcohols, *J. Colloid Interface Sci.*, **146**, 320 (1991).
22. Kilpatrick, P. K., Davis, H. T., Scriven, L. E. and Miller, W. G., Microstructure in n -alkane-water-electrolyte mixtures with small ethoxylated alcohols, *J. Colloid Interface Sci.*, **118**, 270 (1987).
23. Strey, R., Microemulsion microstructure and interfacial curvature, *Colloid Polym. Sci.*, **272**, 1005 (1994).
24. Kahlweit, M., Busse, G. and Winkler, J., Electrical conductivity in microemulsions, *J. Chem. Phys.*, **99**, 5605 (1993).
25. Kahlweit, M. and Strey, R., Phase behaviour of ternary systems of the type H_2O -oil-nonionic amphiphile (microemulsions), *Angew. Chem. Int. Ed. Engl.*, **24**, 654 (1985).
26. Griffin, W. C., Classification of surface-active agents by "HLB", *J. Soc. Cos. Chem.*, **1**, 311 (1949).
27. Kahlweit, M., Strey, R., Firman, P., Haase, D., Jen, J. and Schomäcker, R., General patterns of the phase behaviour of mixtures of H_2O , nonpolar solvents, amphiphiles, and electrolytes 1, *Langmuir*, **4**, 499 (1988).
28. Burauer, S., Sachert, T., Sottmann, T. and Strey, R., On microemulsion phase behaviour and the monomeric solubility of surfactant, *Phys. Chem. Chem. Phys.*, **1**, 4299 (1999).
29. Kunieda, H., Nakano, A. and Pes, M. A., Effect of oil on the solubilization in microemulsion systems including nonionic surfactant mixtures, *Langmuir*, **11**, 3302 (1995).
30. Wormuth, K. R. and Zushma, S., Phase behaviour of branched surfactants in oil and water, *Langmuir*, **7**, 2048 (1991).
31. Kahlweit, M., Strey, R. and Firman, P., Search for tricritical points in ternary systems: water-oil-nonionic amphiphile, *J. Phys. Chem.*, **90**, 671 (1986).
32. Firman, P., Haase, D., Jen, J., Kahlweit, M. and Strey, R., On the effect of electrolytes on the mutual solubility between H_2O and nonionic amphiphiles, *Langmuir*, **1**, 718 (1985).
33. Kunieda, H. and Ishikawa, N., Evaluation of the hydrophilic-lipophilic balance (HLB) of nonionic surfactants II. Commercial surfactant systems, *J. Colloid Interface Sci.*, **107**, 122 (1985).
34. Kahlweit, M., Strey, R. and Busse, G., Effect of alcohols on the phase behaviour of microemulsions, *J. Phys. Chem.*, **95**, 5344 (1991).
35. Graciaa, A., Lachaise, J., Sayous, G., Grenier, P., Yiv, S., Schechter, R. S. and Wade, W. H., Partitioning of complex surfactant mixtures between oil/water/microemulsion phases at high surfactant concentrations, *J. Colloid Interface Sci.*, **93**, 474 (1983).
36. Laughlin, R. G., *The Aqueous Phase Behaviour of Surfactants*, Academic Press, London, 1994.
37. Ekwall, P., Composition, properties, and structures of liquid crystalline phases in systems of amphiphilic compounds, in *Advances in Liquid Crystals*, Vol. 1, Brown, G. H. (Ed.), Academic Press, London, 1975, pp. 1.
38. Evans, D. F., Mitchell, D. J. and Ninham, B. W., Oil, water, and surfactant: properties and conjectured structure of simple microemulsions, *J. Phys. Chem.*, **90**, 2817 (1986).
39. Abe, M., Schechter, R. S., Wade, W. H., Weerasooriya, U. and Yiv, S., Microemulsion formation with branched tail polyoxyethylene sulfonate surfactants, *J. Colloid Interface Sci.*, **114**, 342 (1986).
40. Kunieda, H. and Shinoda, K., Solution behaviour and hydrophilic-lipophilic balance temperature in the aerosol OT-isooctane-brine system: correlation between microstructure and ultralow interfacial tensions, *J. Colloid Interface Sci.*, **75**, 601 (1980).
41. Meier, W. and Eicke, H. F., Electric, dielectric and Kerr effect investigations in water-in-oil microemulsions, *Curr. Opinion Colloid Interface Sci.*, **1**, 279 (1996).
42. Bellocq, A. M., Biais, J., Bothorel, P., Clin, B., Fourche, G., Lalanne, P., Lemaire, B., Lemanceau, B. and Roux, D., Microemulsions, *Adv. Colloid Interface Sci.*, **20**, 167 (1984).
43. Clause, M., Perelyasse, J., Boned, C., Nicolas-Margantini, L. and Zradba, A., Influence of the cosurfactant chemical structure upon the phase diagram features and electrical conductive behaviour of Winsor-IV type media (so-called microemulsions), in *Surfactants in Solution*, Vol. 3, Mittal, K. and Lindman, B. (Eds), Plenum, New York, 1984, pp. 1583.
44. Wormuth, K. R. and Kaler, E. W., Amines as microemulsion cosurfactants, *J. Phys. Chem.*, **91**, 611 (1987).
45. Kahlweit, M., Strey, R. and Haase, D., Phase behaviour of multicomponent systems of water-oil-amphiphile-electrolyte. 3, *J. Phys. Chem.*, **89**, 163 (1985).
46. Kahlweit, M. and Strey, R., Phase behaviour of quinary mixtures of the type H_2O -oil-nonionic amphiphile-ionic amphiphile-salt, *J. Phys. Chem.*, **92**, 1557 (1988).
47. Kahlweit, M., Busse, G. and Faulhaber, B., Preparing nontoxic microemulsions with alkyl monoglucosides and

- the role of alkanediols as cosurfactants, *Langmuir*, **12**, 861 (1996).
48. von Rybinski, W., Guckenbiehl, B. and Tesmann, H., Influence of co-surfactants on microemulsions with alkyl polyglycosides, *Colloid Surf., A*, **142**, 333 (1998).
 49. Bolzinger-Thevenin, M. A., Grossiord, J. L. and Poelman, M. C., Characterization of a sucrose ester microemulsion by freeze fracture electron micrograph and small angle neutron scattering experiments, *Langmuir*, **15**, 2307 (1999).
 50. Kahlweit, M., Busse, G. and Faulhaber, B., Preparing microemulsions with lecithins, *Langmuir*, **11**, 1576 (1995).
 51. Kahlweit, M., Busse, G., Faulhaber, B. and Eibl, H., Preparing nontoxic microemulsions, *Langmuir*, **11**, 4185 (1995).
 52. von Corswant, C., Olsson, C. and Soderman, O., Solubilization of sparingly soluble active compounds in lecithin-based microemulsions: influence on phase behaviour and microstructure, *Langmuir*, **14**, 6864 (1999).
 53. Li, X., Washenberger, R. M., Scriven, L. E., Davis, H. T. and Hill, R. M., Phase behaviour and microstructure of water/trisiloxane E6 and E10 polyoxyethylene surfactant/silicone oil systems, *Langmuir*, **15**, 2287 (1999).
 54. Schubert, K.-V. and Kaler, E. W., Microemulsifying fluorinated oils, *Colloid Surf., A*, **84**, 97 (1994).
 55. Monduzzi, M., Self-assembly in fluorocarbon surfactant systems, *Curr. Opinion Colloid Interface Sci.*, **3**, 467 (1998).
 56. Wormuth, K. R. and Kaler, E. W., Microemulsifying polar oils, *J. Phys. Chem.*, **93**, 4855 (1989).
 57. Schubert, K.-V., Strey, R. and Kahlweit, M., Similarities in phase behaviour and microstructure of nonaqueous microemulsions, *Prog. Coll. Polym. Sci.*, **89**, 263 (1992).
 58. Martino, A. and Kaler, E. W., Phase behaviour and microstructure of nonaqueous microemulsions, *Langmuir*, **11**, 779 (1995).
 59. Martino, A. and Kaler, E. W., Phase behaviour and structure of nonaqueous microemulsions, *J. Phys. Chem.*, **94**, 1627 (1990).
 60. Bellocq, A. M., Phase equilibria of polymer-containing microemulsions, *Langmuir*, **14**, 3730 (1998).
 61. Kabalnov, A., Olsson, U. and Wennerstrom, H., Polymer effects on the phase behaviour of a balanced microemulsion, *Langmuir*, **10**, 2159 (1994).
 62. Kabalnov, A., Olsson, U., Thuresson, K. and Wennerstrom, H., Polymer effects on the phase behaviour of a balanced microemulsion: adsorbing versus nonadsorbing polymers, *Langmuir*, **10**, 4509 (1994).
 63. Fulton, J. L. and Smith, R. D., Reverse micelle and microemulsion phases in supercritical fluids, *J. Phys. Chem.*, **92**, 2903 (1988).
 64. Tingey, J. M., Fulton, J. L., Matson, D. W. and Smith, R. D., Micellar and bicontinuous microemulsions formed in both near-critical and supercritical propane with didodecyltrimethylammonium bromide and water, *J. Phys. Chem.*, **95**, 1445 (1991).
 65. McFann, G. J. and Johnston, K. P., Phase behaviour of nonionic surfactant/oil/water systems containing light alkanes, *Langmuir*, **9**, 2942 (1993).
 66. Jackson, K. and Fulton, J. L., Microemulsions in supercritical hydrochlorofluorocarbons, *Langmuir*, **12**, 5289 (1996).
 67. Dobрева-Veleva, A. N., Kaler, E. W., Schubert, K.-V., Feiring, A. E. and Farnham, W. B., Phase behaviour and microemulsion formation in compressible perfluorinated monomer oil and water mixtures, *Langmuir*, **15**, 4480 (1999).
 68. Johnston, K., Harrison, K. L., Clarke, M. J., Howdle, S. M., Heitz, M. P., Bright, F. V., Carlier, C. and Randolph, T. W., Water-in-carbon dioxide microemulsions: an environment for hydrophiles including proteins, *Science*, **271**, 624 (1996).
 69. Davies, J. T., in *Proceedings of the 2nd International Congress on Surface Activity*, Vol. 1, Butterworths, London, 1957, pp. 220.
 70. Shinoda, K. and Ogawa, T., Solubilization of water in nonaqueous solutions of nonionic surfactants, *J. Colloid Interface Sci.*, **24**, 56 (1967).
 71. Winsor, P. A., Binary and multicomponent solutions of amphiphilic compounds. Solubilization and the formation, structure and theoretical significance of liquid crystalline solutions, *Chem. Rev.*, **68**, 1 (1968).
 72. Bourrel, M., Salager, J. L., Schechter, R. S. and Wade, W. H., A correlation for the phase behaviour of nonionic surfactants, *J. Colloid Interface Sci.*, **75**, 451 (1980).
 73. Lade, M., *Characterization of Microemulsions from Technical Nonionic Surfactants*, Technische Universitt Berlin, Berlin, 2000.
 74. Israelachvili, J., The science and application of emulsions – an overview, *Colloid Surf., A*, **91**, 1 (1994).
 75. Talmon, Y. and Prager, S., Statistical thermodynamics of phase equilibria in microemulsions, *J. Chem. Phys.*, **69**, 2984 (1978).
 76. De Gennes, P. G. and Taupin, C., Microemulsions and the flexibility of the oil/water interface, *J. Phys. Chem.*, **86**, 2294 (1982).
 77. Gradzielski, M., Langevin, D. and Farago, B., Experimental investigation of the structure of nonionic microemulsions and their relation to the bending elasticity of the amphiphilic film, *Phys. Rev., E*, **53**, 3900 (1996).
 78. Lichterfeld, F., Schmeling, T. and Strey, R., Microstructure of microemulsions of the system H₂O–n–tetradecane–C₁₂E₅, *J. Phys. Chem.*, **90**, 5762 (1986).
 79. Lindman, B., Shinoda, K., Olsson, U., Anderson, D., Karlstrom, G. and Wennerstrom, H., On the demonstration of bicontinuous structures in microemulsions *Colloid Surf.*, **38**, 205 (1989).
 80. Olsson, U., Shinoda, K. and Lindman, B., Change in the hydrophilic–lipophilic balance of nonionic surfactant as revealed by

- NMR self-diffusion studies, *J. Phys. Chem.*, **90**, 4083 (1986).
81. Schwuger, M.-J., Stickdorn, K. and Schomäcker, R., Microemulsions in technical processes, *Chem. Rev.*, **95**, 849 (1995).
 82. Auvray, L., Cotton, J.-P. and Ober, R., Evidence for the zero mean curvature of microemulsions, *J. Phys. Chem.*, **88**, 4586 (1984).
 83. De Geyer, A. and Tabony, J., Evidence for Intercontiguous structures in concentrated microemulsions. Neutron small-angle scattering results, *J. Chem. Phys. Lett.*, **113**, 83 (1985).
 84. Billman, J. F. and Kaler, E. W., Structure and phase behaviour in five-component microemulsions, *Langmuir*, **6**, 611 (1990).
 85. Safran, S. A., Curvature elasticity of thin films, *Adv. Phys.*, **48**, 395 (1999).
 86. Kahlweit, M., Strey, R., Haase, D., Kunieda, H., Schmelting, T., Faulhaber, B., Borkovec, M., Eicke, H. F., Busse, G., Eggers, F., Funck, T., Richmann, H., Magid, L., Soderman, O., Stilbs, P., Winkler, J., Dittich, A. and Jahn, W., How to study microemulsions, *J. Colloid Interface Sci.*, **118**, 436 (1987).
 87. Strey, R., Phase behaviour and interfacial curvature in water-oil-surfactant systems, *Curr. Opinion Colloid Interface Sci.*, **1**, 402 (1996).
 88. Zana, R. and Lang, J., *Microemulsions: Structure and Dynamics*, CRC Press, Boca Raton, FL, 1988.
 89. Guering, P. and Lindman, B., Droplet and bicontinuous structures in microemulsions from multicomponent self-diffusion measurements, *Langmuir*, **1**, 464 (1985).
 90. Reed, R. L. and Healy, R. N., in *AICHE Symposium: Improved Oil Recovery by Surfactant and Polymer Flooding*, Shah, D. O. and Schechter, R. (Eds), Academic Press, New York, 1977, pp. 383.
 91. Baviere, M. and Canselier, J. P., Microemulsions in the chemical EOR process, in *Industrial Applications of Microemulsions*, Solans, C. and Kunieda, H. (Eds), Marcel Dekker, New York, 1997, pp. 331.
 92. Bonkhoff, K., Schwuger, M. J. and Subklew, G., Use of microemulsions for the extraction of contaminated solids, in *Industrial Applications of Microemulsions*, Solans, C. and Kunieda, H. (Eds), Marcel Dekker, New York, 1997, pp. 355.
 93. Rusling, J. F., Schweizer, S., Zhang, S. and Kamau, G. N., Microemulsions as media for the destruction of organohalide pollutants by electrolysis, *Colloid Surf., A*, **88**, 41 (1994).
 94. Minana-Perez, M., Gutron, C., Zundel, C., Anderez, J. M. and Salager, J. L., Miniemulsion formation by transitional inversion, *J. Disp. Sci. Tech.*, **20**, 893 (1999).
 95. Ruckenstein, E., Thermodynamic insights on macroemulsion stability, *Adv. Colloid Interface Sci.*, **79**, 59 (1999).
 96. Candau, F., Polymerization in microemulsions, in *Handbook of Microemulsion Science and Technology*, Kumar, P., Mittal, K. L. (Eds), Marcel Dekker, New York, 1999.
 97. Antonietti, M., Basten, R. and Lohnmann, S., Polymerization in microemulsions – a new approach to ultrafine, highly functionalized polymer dispersions, *Macromol. Chem. Phys.*, **196**, 441 (1995).
 98. Ralani Raj, W. R. and Cheung, H. M., Porous polymeric membranes synthesized from microemulsions, in *The Polymeric Materials Encyclopedia*, Vol. 6, Salamone, J. C. (Ed.), CRC Press, Boca Raton, FL, 1996, pp. 4082–4088.
 99. Desai, S. D., Polymerized Microemulsions, *Curr. Opinion Colloid Interface Sci.*, **1**, 519 (1996).
 100. Eastoe, J. and Warne, B., Nanoparticle and polymer synthesis in microemulsions, *Curr. Opinion Colloid Interface Sci.*, **1**, 800 (1996).
 101. Pileni, M., Water in oil colloidal droplets used as microreactors, *Adv. Colloid Interface Sci.*, **46**, 139 (1993).
 102. Stamatis, H., Bioorganic reactions in microemulsions: the case of lipases, *Biotech. Adv.*, **17**, 293 (1999).
 103. Holmberg, K., Organic and bioorganic reactions in microemulsions, *Adv. Colloid Interface Sci.*, **51**, 137 (1994).
 104. Oldfield, C., Enzymes in water-in-oil microemulsions (reversed micelles): principles and applications, *Biotech. Genetic Eng. Rev.*, **12**, 255 (1994).
 105. Kahlweit, M., Strey, R. and Busse, G., Microemulsions: a qualitative thermodynamic approach, *J. Phys. Chem.*, **94**, 3881 (1990).
 106. Strey, R. and Jonstromer, M., Role of medium-chained alcohols in interfacial films of nonionic microemulsions, *J. Phys. Chem.*, **96**, 4537 (1992).
 107. Schomäcker, R., Microemulsions as media for chemical reactions, *Nachr. Chem. Tech. Lab.*, **40**, 1344 (1992).

CHAPTER 5

Langmuir–Blodgett Films

Hubert Motschmann and Helmuth Möhwald

Max-Planck-Institute of Colloids and Interfaces, Golm, Germany

1	Langmuir–Blodgett Films	79	2.1.4	Frequency doubler for low-power laser diodes	88
1.1	What makes LB films appealing? . . .	80	2.1.5	Electro-optics	89
1.2	Details of the deposition process . . .	80	2.1.6	Promising future directions	90
1.3	New types of LB films based on nanoparticles	83	2.2	Sensors	90
1.4	Summary	84	2.3	Command surfaces	91
2	Molecular Assemblies with Functions . . .	85	2.4	Molecular electronics	92
2.1	Nonlinear optical devices based on second-order effects	86	2.4.1	Molecular rectifier	93
2.1.1	Background	86	2.4.2	Challenges and hurdles	93
2.1.2	Model systems	86	3	Final Remarks	95
2.1.3	Hyperpolarizability and adsorption trade-off	87	4	References	95

1 LANGMUIR–BLODGETT FILMS

In the 1980s, there was great enthusiasm about molecular assemblies based on Langmuir–Blodgett (LB) films. Visions were proposed for the next millennium such as “Molecular electronics in which organic molecules perform an active function in the processing of information and in transmission and storage” (1–3). These proposals raised many expectations. Being now at the beginning of a new millennium, this review will aim to critically assess the accomplishments and perspectives. This present chapter will cover applications, as well as some fundamental experiments in which LB films have served as model surfaces to study interactions. The selection is somewhat personal since it is not possible to give this whole field full coverage on account of space restrictions. This chapter covers conventional LB films, as well as novel new types obtained by the organization of nanoparticles at the air–water interface. The LB technique extended to this class of materials allows the

fabrication of ordered arrays of quantum dots of semiconductor, metal or insulator particles, and provides a convenient handle on decisive parameters such as the inter-particle spacing. LB films possess a high orientational order, and for this reason, an inherent potential for nonlinear optical devices such as frequency doublers or modulators. We will discuss in detail selected nonlinear optical devices where the control of the internal layer structure on a molecular level was utilized for maximization of the efficiency. These assemblies operate close to a practical level of performance, but face a strong competition with alternative approaches and technologies. Another promising application is the field of sensing and we will report on recent advances in the design of gas sensors. We will report also on some exciting new achievements which are far away from practical utilization, such as the molecular rectifier or the design of command surfaces where a single photoactive moiety may be sufficient to determine the orientation of a bulk liquid crystal.

1.1 What makes LB films appealing?

The appealing features of Langmuir–Blodgett films is the intrinsic control of the internal layer structure down to a molecular level and the precise control of the resulting film thickness. Sophisticated LB troughs allow us to process several materials with different functionalities and offer the possibility to tune the layer architecture according to the demands of the desired molecularly engineered organic thin-film devices. It is worthwhile to start this review with a brief consideration of the fabrication process. Further details can be found in the books by Gaines (4) or Ulman (5); the latter also presents a good introduction to the surface analytical tools which are commonly used for the investigation of the structure of monolayers and various physical properties.

The first step of the LB deposition process is the formation of a well defined monolayer at the air–water interface. These so-called Langmuir monolayers are a precursor film within the LB fabrication. The preparation process is illustrated schematically in Figure 5.1. The amphiphile is dissolved in an organic solvent and subsequently spread at the air–water interface. The solvent evaporates and a monolayer of the amphiphile at the air–water interface is then produced. These Langmuir monolayers can be further manipulated by means of a moveable barrier which allows us to control the area per molecule. Monolayers at the air–water interface have been extensively studied and possess a richness of phases and structures. They serve as quasi-two-dimensional model systems and have thus attracted a significant amount of research effort. The advent of sophisticated surface analytical tools such as X-ray reflection and scattering techniques, together with novel optical techniques such as the Fluorescence and Brewster Angle Microscopy (BAM), have provided a detailed picture of the general phase diagrams, structure and morphology. Grazing-Incidence X-ray diffraction has revealed the existence of several phases in which the aliphatic chain is tilted with respect to the surface normal and in which the tilt azimuth adopts a well-defined arrangement with respect to the underlying bond orientational order (6). The organization of the tilt azimuth can extend to macroscopic dimensions and thus shows up in BAM images in various facets such as the formation of domains with an internal structure. The review articles of Möhwald (7), McConnel (8), Knobler and Desai (9), Riviere *et al.* (10) and Knobler and Schwartz (11) are excellent guides through the vast amount of publications covering the field of Langmuir monolayers.

The Langmuir–Blodgett technique utilizes these monolayers as building blocks for the fabrication of thin layers by transferring the Langmuir monolayer on to a solid support. The deposition process is controlled by the hydrophilicity or hydrophobicity of the solid support. A monolayer at the air–water interface can be transferred by an up-stroke on to a hydrophilic surface (see Figure 5.1(c)) and via a down-stroke on to a hydrophobic surface. Several trough designs have been proposed and there are also commercially available multi-compartment troughs which allow the simultaneous processing of different materials (as shown in Figure 5.1(d)). In this figure, compartment A contains a different material to compartment B. Both monolayers can be independently compressed to their target pressure and the dipping robotic control is programmed for the desired dipping sequence which determines the layer architecture on the molecular level, as well as the upside-down orientation of the molecule (Figure 5.1(e)). Many applications, such as nonlinear optical devices, require a stacking of the molecules in a predefined arrangement with a high orientational order. LB films possess an inherent potential for such applications. However, unfortunately molecules quite frequently do not behave in the way that they are depicted in simple schematics and the deposition process actually turns out to be a fairly complex process governed by many parameters such as surface viscosity, surface energies, hydrodynamic flow and water drainage. It is therefore worthwhile to consider the deposition process in a bit closer detail.

1.2 Details of the deposition process

The deposition is usually monitored by the corresponding transfer ratio. During monolayer transfer, a further compression is required in order to maintain a constant surface pressure. The transfer ratio is defined as the ratio of the decrease in Langmuir monolayer surface area divided by the area of the solid support which has been coated. The user tries to adjust the experimental conditions such as the transfer speed, temperature and sub-phase composition (e.g. indifferent electrolytes) such that a transfer ratio close to one is achieved. The underlying assumption is that the Langmuir monolayer then serves as a simple building block which resembles the features of the pre-formed monolayer at the air–water interface. Repeated dipping cycles simply provide replicas of the monolayer and such monolayers thus allow the formation of stratified layer structures in the same manner as bricks are used to set up a wall in the

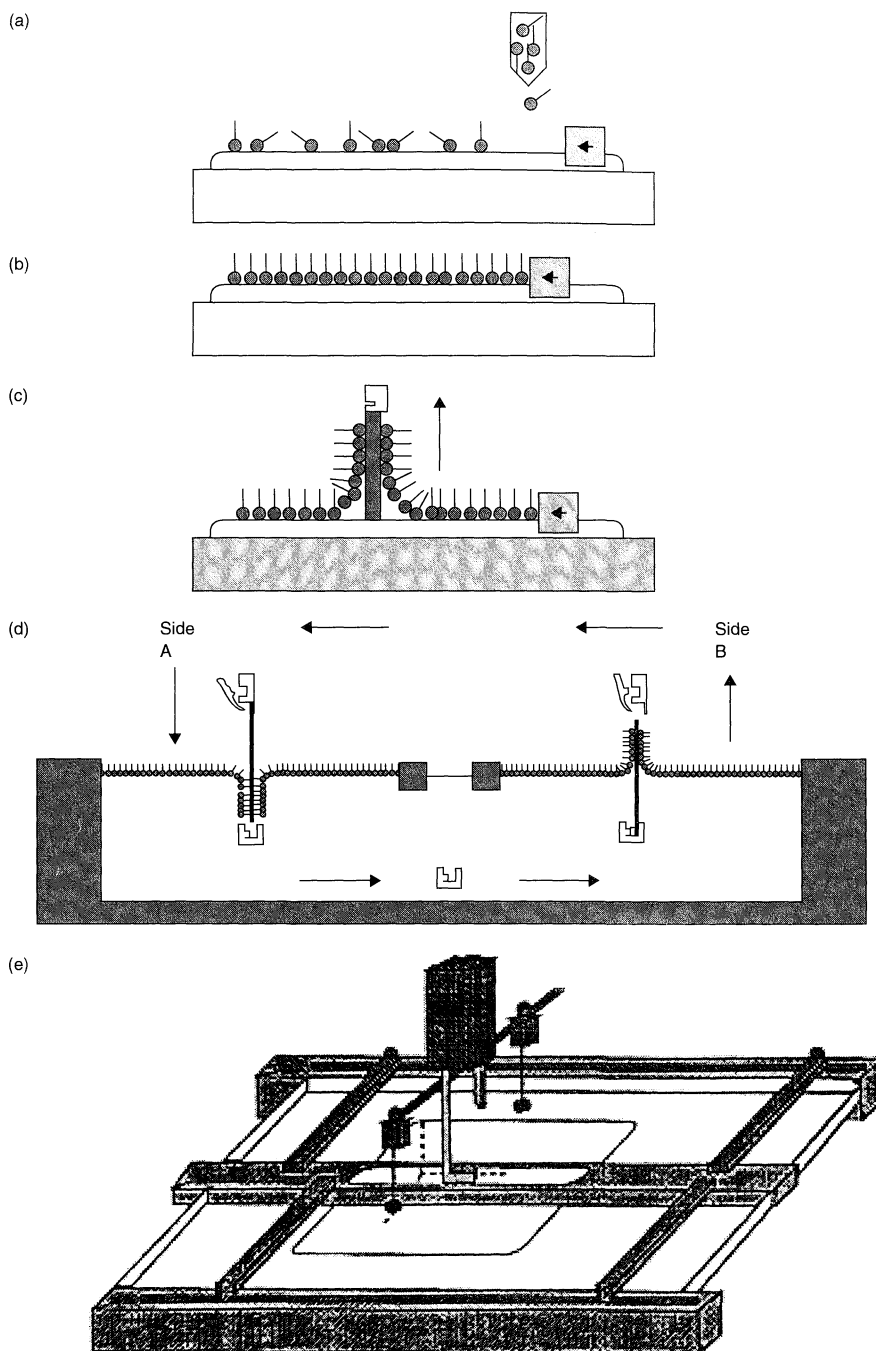


Figure 5.1. Schematic of the Langmuir–Blodgett deposition process. The amphiphile is dissolved in an organic solvent and subsequently spread at the air–water interface. The solvent evaporates and a monolayer of the amphiphile at the air–water interface remains (a). The monolayer at the air–water interface can be further manipulated by means of a movable barrier allowing control of the area per molecule (b). The Langmuir monolayer can be transferred by an up-stroke on to a hydrophilic surface (c) and via a down-stroke on to a hydrophobic surface. A dual compartment trough enables the simultaneous processing of two different materials (d), while a programmed dipping sequence allows the determination of layer architecture at a molecular level.

macroscopic world. However, the difference in the local environment on a solid support and at the air–water interface may give rise to certain structural changes. The transfer requires a drainage of the film and the monolayer properties will also be partly governed by the hydrodynamic flow during the transfer. The film may reorganize and there is a high chance that the deposited film may not reach its local thermodynamic minimum and remains instead in a non-equilibrium state. The transfer is the crucial step within the LB technique and many experimental groups have addressed the relationship between the monolayer structure of the precursor film at the air–water interface and the one observed on a solid support. This is not a unique picture and there are examples where no changes are observed, as well as examples with strikingly different structures and features between the monolayers at the air–water interface and on the solid support.

Tippmann-Krayer *et al.* (12) have investigated the monolayer structure of cadmium arachidate at the air–water interface and on a hydrophilic support by using grazing incidence X-ray diffraction. In both cases, they observed a very similar hexagonal structure with the aliphatic chains oriented normal to the surface. Shih *et al.* (13) investigated the structure of fatty acid monolayers (heneicosanoic acid) transferred to glass substrates from three different phases of the monolayer at the air–water interface by also using grazing incidence X-ray diffraction. In all cases, the transferred films adopt the very same structure with an upright orientation and hexagonal packing, irrespective of the structure of the monolayer phase, even if the Langmuir monolayer adopts a distorted hexagonal packing in which the molecules are tilted towards their neighbours. Apparently, the upright hexagonal packing represents a local energy minimum of the hydrocarbon chains. Durbin *et al.* (14) have performed detailed *in situ* X-ray diffraction studies of the deposition process. The experimental set-up allowed an investigation of the Langmuir monolayer as well as the freshly prepared LB film in the same closed temperature-controlled environment. Monolayers of fatty acids have been deposited from three different phases. In all cases, the very same structure was also observed on the solid support immediately after the deposition. The monolayer survived the transfer; however, these authors report on some structural changes occurring long after deposition as a result of the drying process. The data suggest the possibility of preserving the structure of the Langmuir layer provided that the heating and drying condition are carefully adjusted. Gehlert *et al.* (15) demonstrated that domains of condensed monolayer phases can be transferred on to a

solid support without any changes in morphology. The domains of a condensed phase of certain glycerol esters possess a “star texture” which is the result of a tilt organization on a macroscopic scale. The same tilt organization was found on a solid support. In a beautiful experiment, these layers have been used as command layers which determine the anchoring and orientation of the bulk phase of nematic liquid crystals (16). A conventional microscope is then sufficient to visualize the texture, as shown in Figure 5.2.

During LB deposition, remarkable phenomenon such as wetting instabilities may occur which show up in the formation of regular stripes on the support (17). The underlying mechanism is likely to be caused by a feedback between the meniscus height, as determined by the contact angle, and changes in the work of adhesion at the substrate, caused by changes in the packing density within the monolayer (18). The static meniscus height is governed by the surface tension and is higher than the planar water surface. The transfer on to the solid support is determined by the prevailing interaction of amphiphile and solid surface. A strong interaction leads

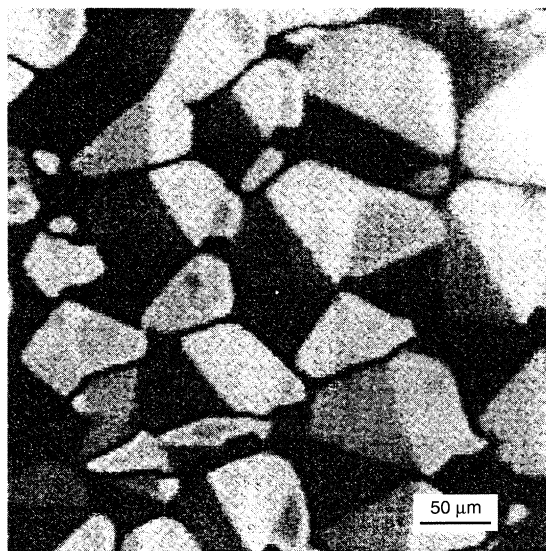


Figure 5.2. Monolayers of the amphiphile 1-monopalmitoyl-(±)-glycerol at the air–water interface assemble in domains in which the molecular tilt azimuth is organized in “star-shaped” patterns. It is possible to preserve this order during the transfer on to a solid support. LB monolayers of this material have been utilized for the anchoring of nematic liquid crystals. The order within the monolayer determines the order within the bulk phase of the nematic liquid crystal (LC). The image here shows the LC cell between crossed polarizers. (From J. Fang, U. Gehlert, R. Shashidar and C. Knobler, *Langmuir* (1999), 15, 297)

to a rapid adherence of the molecules, which in turn reduces the surface energy and leads to an increase in the contact angle, as described by Young's equation (19). As a consequence, the meniscus height decreases. On the other hand, the meniscus height will tend to exceed its equilibrium height during the continuous up-stroke movement of the solid support, hence leading to an accelerated adsorption. Thus, the dynamic behaviour of the meniscus is governed by two counteracting processes which show up in an oscillation of the meniscus. Gleiche and Chi. (20) demonstrated recently that it is possible to obtain quite regularly spaced stripes with channels of a size of 200–300 nm, as shown in Figure 5.3.

1.3 New types of LB films based on nanoparticles

The fabrication of size-quantized semiconductor and metal nanoparticles has attracted a lot of attention (21–23) because of their novel optical and electrical properties and their appealing features as models for basic science. The LB deposition process originally developed for amphiphiles can also be extended

to nanoparticles. It has been demonstrated that properly coated nanoparticles can be organized at the air–water interface by using a similar procedure to that illustrated in Figure 5.1. The corresponding films possess striking similarities to those observed for classical Langmuir monolayers. The coating of the nanoparticle is a decisive factor in the ability of such particles to form monolayers with well-defined π , A -isotherms. Once the hydrophobicity is too low the particles sink, whereas the particles tend to stick to unwanted aggregates if the coating is too hydrophobic. Fendler and co-workers have demonstrated that a variety of different metal or metal oxide particles can be properly coated and processed at the air–water interface, e.g. cadmium sulfide (24), titanium dioxide (25, 26), magnetic iron oxide (27), and several noble metal particles (28, 29). It was further demonstrated that the films of nanosized particles at the air–water interface can also be transferred on to a solid support by using the established standard LB dipping technique or the horizontal lifting techniques originally developed by Langmuir and Schäfer (30). In many cases, a transfer ratio close to one could be achieved. In addition, experimental evidence has been provided that the layer thickness of properly designed systems changes in a linear fashion with the number of deposited layer, thus allowing the fabrication of rather complex superlattices of different particles.

Heath *et al.* have (31) investigated in great detail the pressure/temperature phase diagrams of organically passivated Ag and Au nanocrystals with diameters of 20–75 Å. The particles were self-assembled at the air–water interface and the structures of the observed phases were investigated by transmission electron microscopy of the corresponding Langmuir–Blodgett films. The roles of particle size, size distribution and the size of the passivating organic ligand were addressed. The features could be categorized according to the excess volume available to the ligand as it extends from the surface of the particle. At large excess volumes, low-density structures with chain and ring morphologies are observed, while at higher surface pressures foam-like phases which can be further compressed into a two-dimensional closed packing are seen, before a transition to irreversible non-equilibrium structure is observed. The crystalline order within the close-packed phase is limited by the width of the particle distribution.

The appealing feature offered by the LB deposition of nanoparticles is the possibility to generate ordered arrays of metal quantum dots with new features due to the prevailing confinement. The band gap of a semiconductor nanoparticle is strongly size-dependent, while the optical absorption of metal nanoparticles depends on

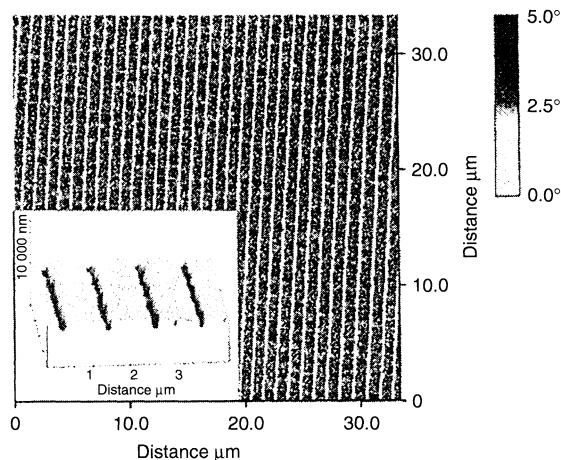


Figure 5.3. Dipalmitoyl phosphatidylcholine (DPPC) transferred on to a solid support at a rather high transfer speed of 1000 $\mu\text{m/s}$ at a lateral surface pressure of 3.0 mN/m^{-1} . Dynamic scanning force microscopy (SFM) images provide evidence for the formation of a regularly structured surface, revealing channels with a width of about 200 nm separated by 800 nm wide stripes of the monomolecular film. The main figure represents phase and the inset ($4 \times 4 \mu\text{m}^2$) topography imaging. The monolayer was prepared on pure water at room temperature; A change in the temperature influences the periodicity. (From M. Gleiche and L. F. Chi), *Nature*, **403**, 2000, 173)

size and inter-particulate spacing. The LB technique and the choice of the passivating organic layer provides a handle on the latter and allows tuning of the electronic properties. Heath and co-workers have measured the linear and nonlinear responses of several monodisperse Ag particles with a diameter of 2–7 nm, capped by alkanethiols of different chain lengths (32). The metal dots were organized at the air–water interface and the optical properties were monitored as a function of the inter-particle distance. At a latter distance of less than 5 Å, the second-harmonic generation (SHG) response exhibits a sharp discontinuity and the linear reflectance and adsorbance resembles the features of thin metal films, thus indicating an insulator-to-metal transition (32). The linear response is dominated by the surface plasmon resonance, ω_{sp} , which resembles the physical dimensions of the particle (33). At lower inter-particle distances, the dielectric medium in between the particles is modified by the presence of the conducting spheres and a quantum mechanical coupling occurs which allows a delocalization of charge carriers over several particles. As a result, the plasmon resonance shifts to lower values which resemble the features of thin metal films in the case of a complete delocalization. Direct evidence for a reversible metal–insulator transition was provided by impedance spectroscopy measurements on the same system (34). With compression of the nanocrystal monolayer, the complex impedance of the films undergoes a transition from a parallel resistance-capacitance (RC) equivalent circuit to an inductive circuit. At large particle distances the particles maintain their individual electronic identity and the film is insulating, while it resembles the features of a thin metal at higher coverage. Meanwhile, four different electronic signatures have been identified within thin assemblies of metallic nanocrystals, which depend on the inter-particle distance and the order within the film (35). The investigation of these systems also provides an insight into the impact of disorder in superlattices of nanocrystals on the corresponding electronic properties. An understanding of the underlying relations thus allows us to deliberately tune the electronic properties.

Similar studies have been carried out for monodisperse magnetic particles deposited on water surfaces (36). The resulting structures are the result of a balance between van der Waals and magnetic dipole–dipole interactions.

The detailed knowledge gained in the last few decades about the organization of amphiphiles at the air–water interface can also be utilized for the design of proper templates for the organization of nanoparticles. A nice example was recently given by Torimoto *et al.* (37).

A Langmuir monolayer of a mixture of the cationic amphiphile alkyltrimethylammoniumpropane (DOTAP) and a phospholipid (OPPC) was prepared and compressed to a defined state. The Langmuir monolayer possesses a positive net charge, and DNA double strands injected in the sub-phase readily adsorb at the interface due to the electrostatic attraction between the phosphate groups of the DNA and the quaternary ammonium groups of DOTAP (see Figure 5.4(a)). This performed assembly was then exposed to a very dilute solution of positively charged CdS particles. These particles adsorb and are immobilized along the DNA strands due to the prevailing electrostatic interaction (Figure 5.4(b)). The assembly was transferred on to an electron microscope grid and characterized by using transmission electron microscopy. The images reveals a dense packing of the nanoparticles along the DNA strand, with a line width equal to the diameter of a particle. Figures 5.4(c–e) shows the corresponding images.

1.4 Summary

At this stage, the reader should be aware that the transfer process is governed by many parameters and the adopted structure is the result of a subtle interplay of various interactions. A transfer ratio of one does not mean that Langmuir layer and deposited layer will adopt an identical structure. This may hold, although the corresponding structures can also be completely different. The probability for structural changes during the deposition is linked to the rigidity of the system. Structural changes are more likely to occur in less rigid structures which are fairly sensitive to details of the local environment. Rigid structures lack this sensitivity, and hence structural changes with deposition are less likely to occur. However, it is extremely difficult to work out proper deposition conditions for stiff systems and LB films of such materials commonly exhibit a fairly high number of defects such as domains or grain boundaries. The way out of this apparent dilemma is opened up by using polymeric LB layers which form fairly smooth and defect-free films. Usually, LB layers of polymeric materials are fairly insensitive to the local environment and can be transferred on to a solid support with little or no changes when compared to the precursor film at the air–water interface. The structure adopted at the solid support may also be frozen in a non-equilibrium state and not in its local energetic minimum. This may also be the reason for some contradictions between findings within different laboratories. Further details can be found in the article by Schwartz (38). The utilization

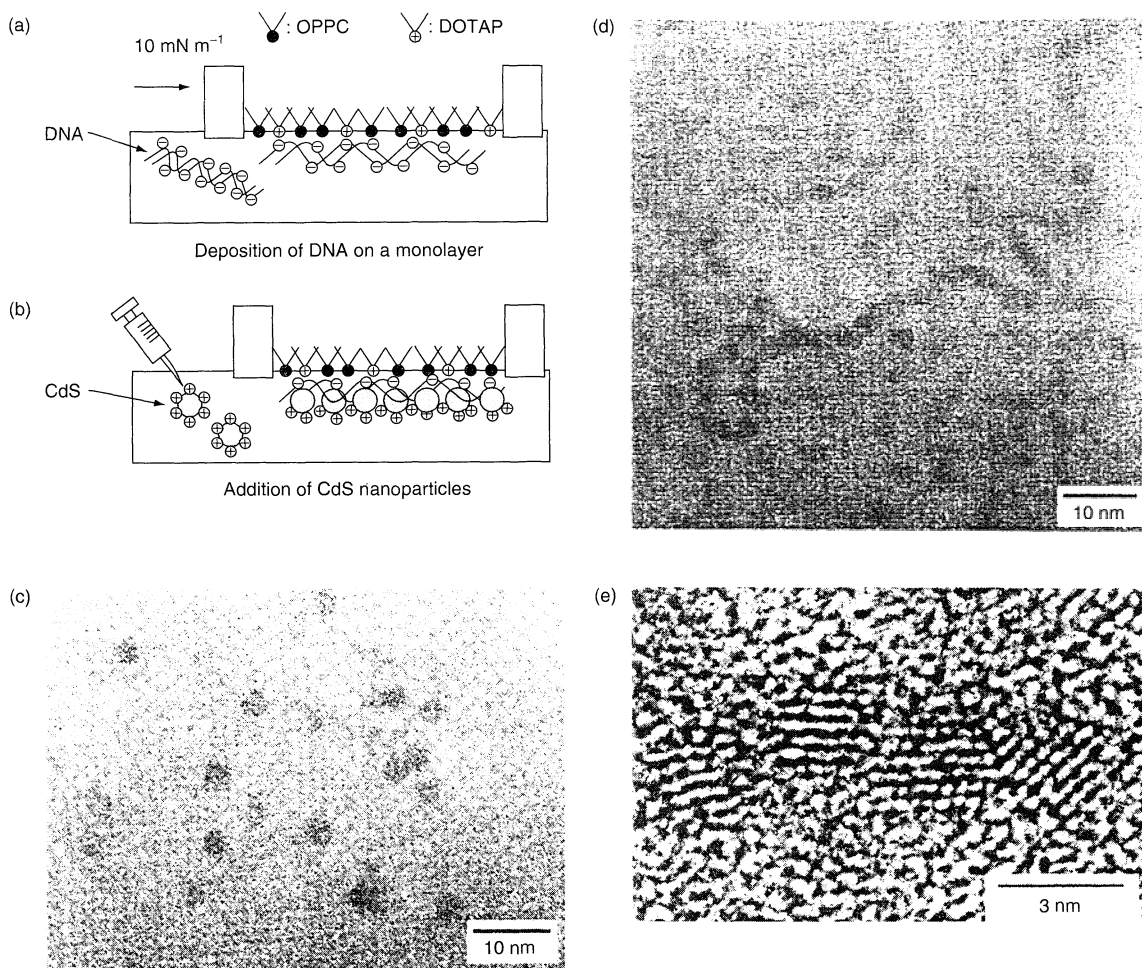


Figure 5.4. A mixed monolayer of a cationic amphiphile DOTAP and a phospholipid (OPPC) was prepared at the air–water interface. DNA readily adsorbs at the monolayer due to the electrostatic interaction (a). CdS nanoparticles can then organize as a chain along the DNA strands (b), as revealed in the TEM images (c–e). (From T. Torimoto, M. Yamashita, S. Kuwabata, T. Sakata, H. Mori and H. Yoneyama, *The Journal of Physical Chemistry B*; (1999) **103**(42); 8799)

of the LB technique requires a careful choice of *all* parameters which can unfortunately be rather a tedious enterprise.

Several attempts were undertaken to modify the trough instrumentation in order to upgrade the LB deposition from laboratory scale to one of an industrial pilot project, which required a complete automatization of all of the underlying procedures. The troughs in this case are completely different to conventional troughs with moving barriers, and utilize instead the stress generated by a flowing sub-phase for the compression of the monolayer (39). The results reported by O. Albrecht *et al.* at Canon (40) are encouraging, showing that it is

indeed possible to bring LB technology to a state that is compatible with the necessary reliability, throughput and quality for mass production provided that all parameters are well adjusted.

2 MOLECULAR ASSEMBLIES WITH FUNCTIONS

Two applications have been earlier identified where LB films might have great potential, namely nonlinear optical devices based on a second-order effect, and sensors. The research on these topics is quite advanced

and at the present time there are thin-film assemblies available which are already close to a practical level of performance. One of the long-term goals is application as molecular electronic devices, which is discussed in the Section 2.4 below.

2.1 Nonlinear optical devices based on second-order effects

2.1.1 Background

Nonlinear optical (NLO) effects are the result of the interaction of intense laser light with matter. The electric field strength generated by an intense laser pulse is comparable to the inner atomic electric fields. As a result, the electric field induces a nonlinear polarization. The nonlinear interaction gives rise to two fascinating effects not known in linear optics, namely photons can be split into two parts or can be merged together. A sound introduction to this field can be found in the texts by Boyd (41) or Shen (42). Facets of the prevailing nonlinearity are the generation of new frequencies such as in frequency-doubling or sum-frequency generation, the modulation of light by an external electric or magnetic field via the Pockels or Faraday effects, or the possibility to influence "light with light", which is the major hurdle towards all-optical signal processing. Several photonic devices have been proposed which exploit and utilize these effects. For the scope of this present review, a brief phenomenological treatment is sufficient in order to introduce some basic terms and equations and familiarize the reader with some device concepts. The interaction between the external electric field \mathbf{E} and the resulting polarization \mathbf{P} is nonlinear and can be represented as a power series, as follows:

$$\mathbf{P} = \varepsilon_0(\chi^{(1)}\mathbf{E} + \chi^{(2)}\mathbf{E}\mathbf{E} + \chi^{(3)}\mathbf{E}\mathbf{E}\mathbf{E} + \dots) \quad (5.1)$$

A propagating electromagnetic wave is accompanied by a nonlinear polarization wave which in turn may act as a source term for radiation at new frequencies. This is used for an extension of the frequency range of laser light sources (43). All effects of the second-order are governed by the quadratic term in \mathbf{E} and the utilization requires a maximization of the magnitude of the macroscopic susceptibility tensor of the second-order, $\chi^{(2)}$. The relation of $\chi^{(2)}$ with the corresponding molecular quantities is provided by the oriented gas model, which successfully describes, despite certain simplifying assumptions, thin film assemblies of organic

molecules as follows:

$$\chi^{(2)} \propto \sum_{\text{molecules}} \beta \propto N \langle \beta \rangle \quad (5.2)$$

Equation (5.2) states that the macroscopic susceptibility $\chi^{(2)}$ is proportional to the sum of all hyperpolarizabilities β of all molecules, where β is the molecular pendent to $\chi^{(2)}$ and relates the induced dipole moment with the quadratic term of the local field acting on the molecule. This can alternatively be expressed by the number density N of the active unit and the orientational average of β (as denoted by the angular brackets). Obviously, $\chi^{(2)}$ vanishes if the molecules adopt a centrosymmetric arrangement, even if the molecules possess a high β . Equation (5.2) outlines the requirements for structures with a high $\chi^{(2)}$. Molecules with a high hyperpolarizability β should be arranged in a non-centrosymmetric fashion with a high and uniform orientation. Furthermore, the number density of the active unit should be maximized.

Molecules with a high β have some structural elements in common. They all possess an extended π -system, further modified with groups "pushing" and "pulling" the electron density of the molecules (44–46). The π electrons provide the required high polarizability and the push pull system provides the noncentrosymmetry on a molecular scale which is required for a non vanishing hyperpolarizability β . Extremely high values of the effective hyperpolarizabilities have been reported for organic molecules (44, 47, 48) and these findings motivate further applied research. At present, the major obstacle towards efficient devices is not the availability of suitable chromophores, but the fabrication of a proper macroscopic structure which has to simultaneously meet many requirements, such as a high $\chi^{(2)}$, sufficient thermal and mechanical stabilities, and the possibility to enable phase-matching. Many of these issues will be discussed in the following. LB films have an inherent potential for these applications due to the intrinsic orientation order and the possibility to precisely tune the thickness and the internal layer structure.

2.1.2 Model systems

Organic molecules can be tailored according to specific demands and different desired functionalities can be incorporated within a single molecule (5, 44). In order to be able to process the material via the LB technique, the NLO chromophore has to be incorporated within an amphiphile. An unwanted side effect is the dilution of the active unit within the assembly. A

non-centrosymmetric arrangement further requires that the NLO active material is interleaved with compatible spacer materials. The fabrication requires a dual-compartment trough. The active unit is still assembled in an non-centrosymmetric fashion with a high orientation, while the deposition is still governed by the thermodynamically stable head–head and tail–tail arrangements between active and inactive material (see Figure 5.1).

A lot of research is still devoted to the identification and design of suitable model systems which meet the requirements imposed by both the LB technique and nonlinear optics. The focus of this work is the achievement of a uniform film with a high nonlinear susceptibility. Furthermore, the film quality should not degrade with the number of deposition cycles. An established and quite sensitive test relies on an investigation of the relation between the second-harmonic generation (SHG) intensity measured in reflection or transmission and the layer number. A quadratic dependence provides experimental evidence that the properties of the bilayer do not change with the deposition. Hence, a bilayer of NLO active material and spacer can be regarded as a simple building block for the design of complex molecular assemblies.

There are numerous investigations which address these issues, and many systems have been identified which fulfil these properties. Ashwell and co-workers have investigated two different systems which all exhibit the quadratic dependence and which do not show any signs of degradation during the deposition of many layers (49–52). The results obtained with a coumarine dye interleaved with an inert spacer dye are remarkable (53). These authors report an extremely high susceptibility of $\chi_{\text{eff}}^{(2)} = 190 \pm 30 \text{ pm/C}$. This is the highest susceptibility reported to date. However, this value was measured under resonance enhancement and should be regarded with some scepticism. Non-centrosymmetry requires the processing of two materials and in most studies an active and an inactive material is used which leads to a unwanted dilution of the active unit. This problem was tackled in and reported in refs (54) and (55). Instead of using active and inactive materials, two different NLO chromophores were processed. The chromophore orientation in one amphiphile is upside-down with respect to that of the second amphiphile. Thus, the stable head-to-head and tail-to-tail configurations are still maintained while the chromophore adopts a uniform non-centrosymmetric arrangement. Both experiments used a polymeric material with the active unit in the side-chain. The model systems obeyed the oriented gas model and lead to a significant enhancement in the SHG efficiency as a result of the higher number density.

A new approach to second-order nonlinear materials was reported by Verbiest *et al.* (56) in which chirality plays the key role. These authors investigated Langmuir–Blodgett films of chiral helicenes which lack features commonly associated with a high SHG response. The molecules adopt a helical structure on a solid support and this chiral supramolecular arrangement enhances the second-order NLO susceptibility by a factor of 30 when compared to the corresponding racemic mixture. An adequate description of the SHG response in a chiral system requires additional tensor elements. Experimental evidence was provided that those tensor elements which are only allowed in a chiral environment dominate the SHG response of the helicene system.

To summarize these achievements – several model systems have been designed which allow the formation of fairly thick layers with a sufficiently high susceptibility to meet the requirement imposed by application. However, while there are still efforts aiming for the design of new model systems, the challenging task is now the integration of structures with a high $\chi^{(2)}$ in photonic devices.

2.1.3 Hyperpolarizability and adsorption trade-off

A discussion of many photonic devices can be found in the book by Prasad and Williams (44). Promising application are modulators which exploit the electro-optic effect or frequency doubler properties for an extension of the frequency range of laser light sources. In particular, high-efficiency converters capable of doubling the continuous-wave (CW) light of near-infrared laser diodes have a tremendous potential market. The advent of blue laser diodes is desirable in order to increase the storage density of optical storage devices. The storage density is linked to the wavelength of light used for “reading” and “writing” devices. A doubling of the frequency increases the storage capacity by a factor of four. This has motivated intense research in this field involving different strategies. One is the frequency doubling of cw-low-power laser diodes by using supramolecular organic structures and this also provides a nice example as to how a molecular assembly can perform new desired functions.

The figure of merit for all devices based on a second-order effect is given by the ratio of the susceptibility $\chi^{(2)}$ and refractive index n as $\chi^{(2)2}/n^3$. Organic materials possess a lower refractive index ($n \approx 1.4$ – 1.6) than inorganic materials ($n \approx 2.2$ – 3.5), and this also gives them, in this respect, an edge over their inorganic counterparts.

All practical applications require the use of a waveguide format. An optical waveguide is a region with an elevated refractive index, and where the light is confined in one or two dimensions. The propagation of light can be described in the ray picture by total reflection. The light is propagating in well-defined modes characterized by a specific field distribution with several nodal planes. The waveguide format overcomes diffraction and allows the maintenance of high power over a long interaction length. The waveguide format is also compatible with other concepts of integrated optics (58) and several papers have successfully demonstrated the integration of organic films with semiconductor devices (59, 60). However, several complications are imposed from the need for a waveguide format. The thickness of a waveguide is comparable to the wavelength of light and hence the deposition of several hundreds of bilayers is required. Furthermore, the waveguide has to be transparent at all propagating wavelengths in order to prevent a rapid photodegradation due to the prevailing high power densities.

The requirement of transparency is accompanied by a significant loss in the value of the hyperpolarizability β of the molecule. Rikken and co-workers (61, 62) have investigated the conjugation dependences of molecular optical hyperpolarizabilities and found a connection between the maximum of the linear adsorption spectrum and the corresponding hyperpolarizability β . A wide range of different components was investigated, including benzene, stilbene, diphenylacetylene, various phenylvinyl heterocycles, oligomeric polyphenyl, α -phenylpolyene, and α, ω -diphenylpolyene, as well as other extended phenylvinyl derivatives. DC electric-field-induced second-harmonic generation (EFISH) and third-harmonic generation (THG) measurements were used for the determination of the hyperpolarizabilities. The experimental finding within a class of related derivatives could be described by power laws, i.e. $\beta \propto \lambda^4 - \lambda^9$. Hence, the requirement of blue transparency for the design of a frequency doubler of low-power diodes is accompanied by a significant loss in the hyperpolarizability. This loss in efficiency can only be counterbalanced by a long interaction length in which the fundamental and second-harmonic waves propagate with the same velocity.

2.1.4 Frequency doubler for low-power laser diodes

The design of a real device is by no means trivial since a number of performance criteria have to be fulfilled simultaneously, i.e. a high nonlinearity, transparency,

wave guide with low loss and the establishment of phase-matching conditions. Numerous materials match and optimize one property; however, the simultaneous fulfilment of all requirements still remains a challenge. Penner *et al.* (57) have reported on the fabrication of a low-loss optical waveguide fabricated by the LB technique in which precise control of the film thickness, together with inversion of the nonlinear susceptibility across the film, are used to simultaneously achieve phase-matching and improve the optical-field overlap between the propagating (fundamental and second-harmonic) waveguide modes. The resulting structure converts low-power near-infrared laser light efficiently to blue light. The performance in this case reached a practical level of performance. The assembly used is depicted in Figure 5.5. The precise control of the film thickness to a value determined by the linear optical constants enables phase-matching between the zero-order mode of the fundamental and the first-order mode of the second-harmonic wave. The modal dispersion of a waveguide allows us only to achieve phase-matching between modes of different order and not between modes of equal order. Modes of different order possess a strikingly different field distribution and this leads to a low overall efficiency due to a nearly vanishing value of the overlap integral. The latter is a peculiarity of the waveguide format and is given by the product of the field distribution of the interacting modes multiplied by the susceptibility and integrated across the cross-sectional area of the guide. Since phase matching can only be achieved between modes of different order, the resulting overlap integrals would be fairly low. However, if the sign in χ^2 is reversed at the nodal plane of the first-order mode, the overlap integral would be maximized as well. The reverse can be achieved by an upside-down orientation of the NLO active unit. Such a device has the potential to reach a practical level of performance and was able to convert low-power CW light to blue light.

In short, these papers demonstrate significant accomplishment and the viability of organic thin-film devices for nonlinear optics. They also demonstrate the possibility to tune the features of an organic molecule and establish new functions within a molecular assembly. Such devices exploit the control of the internal layer architecture on a molecularly defined level. However, despite these remarkable accomplishments the strong competition of other approaches has to be considered as well, and these alternative approaches may eventually be commercially successful. Discussions and a realistic judgement of the potential of the LB technique in this context cannot ignore the tremendous progress

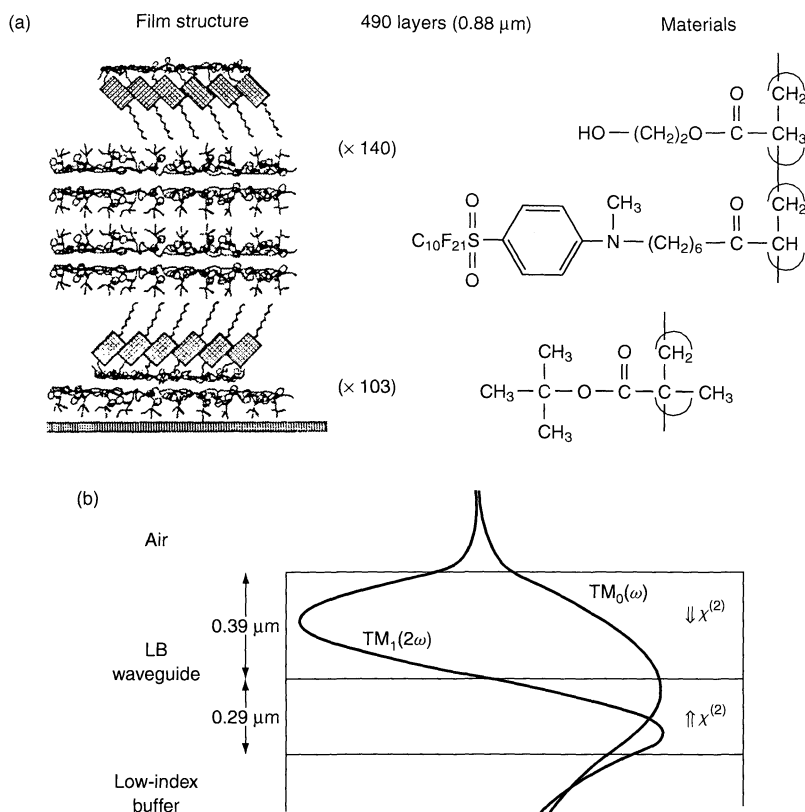


Figure 5.5. (a) Optical layer structure of the waveguide prepared by LB deposition. The thickness was adjusted to achieve phase-matching between the zero-order mode of the fundamental and the first-order mode of the generated second-harmonic by using the modal dispersion of the guide. The exact thickness is given by the linear optical constants, with only low tolerances within the nm region being acceptable. Part (b) shows the electric field distribution for the zero-order mode of the fundamental at 900 nm and the first-order mode of the second-harmonic light. The power confinement was greater than 80%. Phase-matching can only be achieved between modes of different order which limits the value of the overlap integral, where the latter is given by the product of the field distribution of the interacting modes multiplied by and the nonlinear susceptibility. A reversal of the sign of the nonlinear susceptibility at the nodal plane maximizes the value of the overlap integral. The sign reversal was achieved by a macroscopic inverted structure. The layer architecture is schematically represented in (a), where the NLO-active unit in the upper part is inverted with respect to the lower part. The performance of the system scaled up to a channel waveguide confinement is close to a practical level of performance. (From T. L. Penner, H. R. Motschmann, N. J. Armstrong, M. C. Enzenyilimba and D. J. Williams, *Nature*, **367**, 49 (1994))

of other technologies such as recent advances towards direct blue-emitting laser diodes.

2.1.5 Electro-optics

Electro-optic devices do not have the same tight tolerances as frequency doublers since they do not require phase-matching. The latter requires a careful control of the film thickness of the guide with tolerances in the nm region. All this is not required for an electro-optic modulator and opens the way to be exploited. Even though LB waveguides meet

for far simpler preparation techniques, such as the use of poled polymers (44). Most commonly, electro-optic modulators are based on a Mach–Zehnder interferometer in the waveguide format. The refractive index in one arm of this system is controlled by the applied electric field which slows down the propagation of light and induces a phase shift with respect to the light propagating in the other arm of the interferometer. Since modulators are operating at the frequencies used for telecommunications (1.33 or 1.5 μm), the higher values of the susceptibilities of extended π -systems

these requirements, the lower tolerances will make this field the domain of simpler preparation techniques. The review of Ren and Dalton (64) gives a good overview on recent accomplishments. However, one should at least mention some progress with the use of LB films, such as the hybrid four-layer guide (FLG) which includes a glass guide and a 2-docosylamino-5-nitropyridine Langmuir–Blodgett film, as reported by Palchetti *et al.* (63). This device did not require a Mach–Zehnder interferometer and relied instead on guided mode interference.

2.1.6 Promising future directions

In the future, it will be necessary to process a steadily increasing flow of information. The processing speed of the currently used silicon technology has nearly reached the physical limit, and hence the future will demand faster alternatives such as all-optical data processing (65). The major hurdle for a realization of this vision is the design of an opto–opto switch, with the proposed device concepts exploiting third-order, $\chi^{(3)}$, nonlinear optical effects (66). The refractive index of organic materials with extended π -systems can be instantaneously changed by the exposure to light of a sufficiently high power level. The power dependence of the nonlinear refractive index can be used to control the phase of a propagating wave and is utilized in the nonlinear Mach–Zehnder interferometer as an optical switch. Suitable $\chi^{(3)}$ materials for the design of an opto–opto switch in a waveguide format have to fulfill a variety of criteria and two merit factors have been introduced, thus allowing us to judge the quality of a material and the magnitude of the achievable nonlinear phase shift (66). There have been tremendous efforts to design suitable materials and a survey and assessment can be found in the review of Luthor-Davies and Samoc (67). So far, only a few materials partially meet the requirements and none have the potential to reach a practical level of performance, which has caused some resignation within the $\chi^{(3)}$ community. In the last decade, a much more efficient way to introduce a nonlinear optical phase shift has been identified which utilizes a cascading of second-order nonlinearities (68, 69). The combination of two second-order nonlinear processes can induce a third-order nonlinearity. For instance, the combination of frequency-doubling and difference frequency mixing yields a nonlinear phase shift which is proportional to the square of the effective nonlinear susceptibility of the second order, $\chi^{(2)}$, and the same holds for a cascade of optical rectification

and the linear electro-optical effect. A good overview on the cascaded second-order nonlinear interactions can be found in the review by Bosshard (70). The concept of cascading is based on second-order effects and allows utilization of the highly developed knowledge in designing efficient $\chi^{(2)}$ materials and their structures in a new promising area. It is our belief that there is also some potential left for LB devices in such applications and that this would be a promising field for thin-film assemblies.

2.2 Sensors

Another promising application for LB films is in the field of sensors. The basic idea is simple and appealing – the Langmuir–Blodgett films are deliberately functionalized by selected moieties which specifically react to the target species, while the thin-film assemblies ensure fast response times. This specific interaction or binding change properties of the LB films are then subsequently detected and further quantified. The most simple way to monitor the binding relies on a measurement of the mass coverage at the surface via use of the quartz microbalance; however, a better sensitivity can be achieved by using optical reflection techniques, such as ellipsometry or surface plasmon spectroscopy (SPS). In the last few years, several novel detection schemes have been developed which are capable of recording a sub-monolayer coverage, as in, for instance, the heterodyne concept for the phase detection in SPS, as introduced by Nelson *et al.* (71). A discussion of various detection schemes and assessments of their sensitivities, as well as various concepts for miniaturization, is presented in the review article by Kambhampati and Knoll (72).

The design of gas sensors is meanwhile quite advanced, being driven by a growing awareness of the hazards caused by toxic or flammable gases. Safety regulations in the workplace demands an easy means to reliably detect even trace amounts of such gases. A recent review on this topic can be found in ref. (73). Many gas sensors utilize the properties of metallophthalocyanine macrocycles (74). The electronic states of such macrocycles change significantly with oxidation, with partial oxidation transforming an insulator into a conductive material. The resistance is therefore a function of the concentration of the oxidizing species, and this can be utilized for the detection of oxidizing species such as nitrogen dioxide or reducing species such as amines. The sensitivity is high and values of about 100 ppm for NO_2 or 30 ppm for NH_3 have been reported (75).

The response time and the sensitivity is linked to the order within the LB film and the use of mixtures of different materials can significantly improve the device characteristics. Emelianov and Khatko (76) have reported on an improved kinetic response and sensitivity of NO sensors based on copper tetra-*t*-butyl phthalocyanine (CuTTBPc) Langmuir–Blodgett films. The performance was greatly improved if a mixture of CuTTBPc with arachidic acid (AA) was used instead of the phthalocyanine derivative alone. De Saja *et al.* (77) have fabricated electronic sensors based on LB films of phthalocyanine derivatives which monitor volatile amines produced by the decomposition of fish and seafood. The sensor consists of an array of differently functionalized units. Each individual sensing unit undergoes changes in its electrical resistivity that are proportional to the concentration of volatile amines. The combined responses of such an array allowed an assessment of the freshness of samples of seafood.

The critical point for all of these sensors is the specificity for the target species, with different oxidizing agents, e.g. ozone, O₃, leading to similar changes. The specificity is also a critical issue for biosensors but here the “lock and key” principle of certain receptors, such as the biotin streptavidin system, can be exploited (78).

2.3 Command surfaces

Photochromic molecules have attracted a lot of research in the last few decades due to the possibility of reversibly changing their properties by the action of light (79). *Photochromism* describes the phenomenon whereby the absorption spectra of certain molecules change upon photoirradiation. Here, the exposure to light of a certain wavelength induces a new conformation or shape of the molecule, plus new physical properties. Thin-film assemblies of photochromic systems can be utilized for the design of a *command surface*, where a single monolayer of these “Smart” molecules can be sufficient to control the properties and the order in the adjacent bulk phase.

The most widely investigated photochromic system is the azobenzene chromophore (see Figure 5.6). The azobenzene possesses two distinct conformations, i.e. the (*E*)- and (*Z*)-states. Illumination of light in the near-ultraviolet region (at around 350 nm) induces an (*E*)-(*Z*) photoisomerization, while exposure to blue light reverses this isomerization. Such a reversible photoisomerization can take place with little degradation after thousands of switching cycles. The azobenzene chromophore can be incorporated in an amphiphile and

processed according to the LB technique. The switching properties are maintained in the thin-film assembly provided that there is sufficient free volume. Seki and Ichimura have investigated in detail monolayer formation and LB deposition of poly(vinyl alcohol) (PVA) with an azobenzene side-chain (80). The switching efficiency in the LB films was significantly increased if the LB layer was deposited from the *cis*-state, which was explained in terms of the free volume within this layer.

These Smart surfaces can be used for controlling order in liquid crystals (LCs). Ichimura has demonstrated several light-driven liquid crystal systems, and an overview and detailed discussion is presented in a recent review article (81). The basic principle is outlined in Figure 1.6. The nematic liquid crystal is confined in a cell whose surfaces have been modified by LB films containing azobenzene units. The orientation of the nematic liquid crystal is controlled by the *cis*-/*trans*-state at the surface. The *trans*-state induces a homeotropic alignment, whereas the corresponding *cis*-state leads to a parallel alignment of the liquid crystal. It is quite remarkable that, on average, one photochromic molecule in the top-most layer is sufficient to rearrange the orientation of 10⁴ LC molecules, and for this reason the terms “commander” and “soldier” molecules can properly describe such systems. The switching process is reversible and the tilt angle adopted by the LC molecules can be deliberately controlled by the (*E*)/(*Z*) ratio of the azobenzene at the surface, as monitored by waveguide spectroscopy (82). A systematic variation of the chemical structure of the command molecules and their number densities at the surface was performed by Aoki *et al.* (83) and new insights on the relevant prerequisites for an efficient photoregulation of LC orientation have been gained. The nature and the position of the substituent is decisive, with the best efficiencies being observed for *n*-alkyl chains in the *p*-position. Furthermore, it is advantageous to decouple the azobenzene from the substrate by a long spacer and adjust the number density of the azobenzene unit within certain limits. An area per azobenzene unit of 0.5–1.3 nm² works best.

Möller *et al.* have used this command effect to design surfaces with a photocontrollable wetting behaviour (84). The surface of a quartz slide was modified by an azobenzene species containing fluorinated alkyl chains in the *p*-position. *Cis* and *trans* surfaces possess different wetting behaviours, which was attributed to a combination of changes in polarity and orientation order of the fluorinated substituent. It was possible to write rather fine *cis*-*trans* patterns in the surface in a reversible way and to control the formation of water droplets by light.

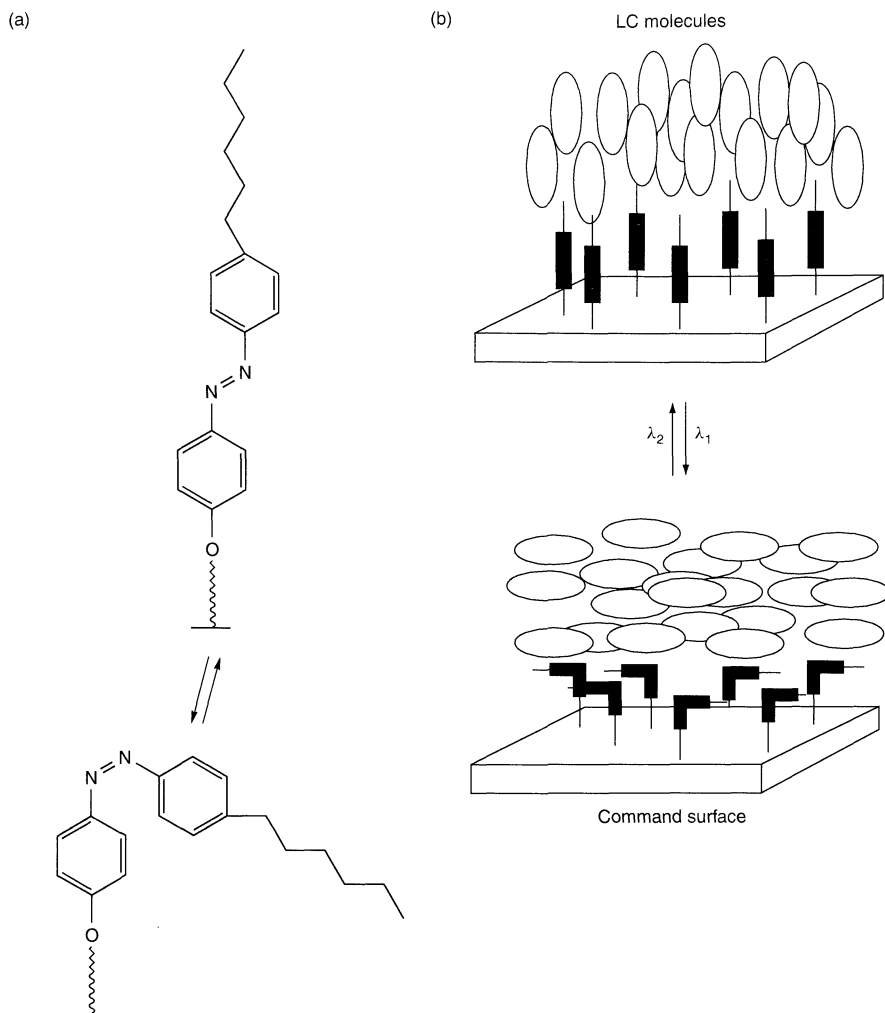


Figure 5.6. Illustration of the command effect. (a) The azobenzene possesses two distinct conformations, i.e. (*E*) and (*Z*). Illumination with UV light leads to the (*Z*)-state, whereas blue light switches to the (*E*)-state. This photochromic transition is reversible. (b) The different shapes of both states are sufficient to change the orientation of a nematic liquid crystal from an out-of-plane to an in-plane alignment. On average, one photochromic molecule at the top-most layer is sufficient to rearrange the orientation of 10^4 LC molecules. (From K. Ichimura, *Supramolecular Science*, 3 (1996))

Figure 1.7 shows a microscopic image of such a pattern, created by UV light and a mask. The dark areas are covered with droplets which provide the contrast in the image.

The wetting properties of structured surfaces have attracted a lot of research, both from the theoretical, as well as from the experimental point of view (85), and several wetting phases with a variety of various morphologies, such as droplets, channels or films, have been predicted. LB layers containing photochromic moieties are suitable and simple model systems for

studying the scale-dependence of the predicted wetting morphologies.

2.4 Molecular electronics

One of the long-term goal of LB research defined by some groups is the field of molecular electronics with the prospect that assemblies of molecules or even individual molecules can improve certain functions required within a computer. Recent overviews on this topic can be

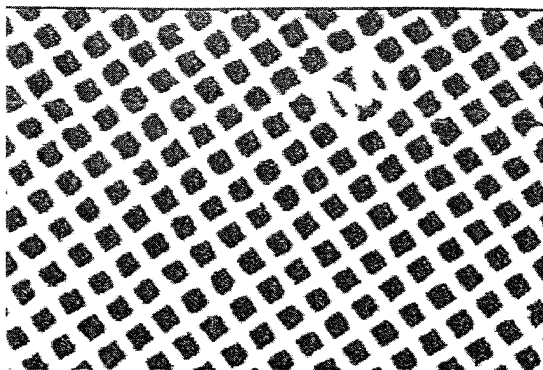


Figure 5.7. A *cis*–*trans* pattern was written in an LB monolayer containing azobenzene units with fluorinated alkyl chains in the *p*-position. Both corresponding surfaces (*cis* and *trans*) differ in their wetting behaviours. Water microdroplets are formed on the illuminated regions (*cis*-state) during cooling of the sample in a humid atmosphere. The optical microscope image shows the formation of water droplet at two different stages and magnifications. The width of the bars is 2 μm and the mesh size is 10 μm . The wetting behavior can be controlled by light, and droplet formation is reversible. (From G. Möller, M. Harke, D. Prescher, H. Motschmann, *Langmuir*, 14, 4955, (1998))

found in the reviews by Martin and Sambles (86) and Metzger (87).

2.4.1 Molecular rectifier

Aviram and Ratner (88) proposed in the mid-1970s that a single organic molecule of the type $D-\sigma-A$, with an electron donor D and an acceptor A , separated by a σ -bond, can perform as a rectifier of electric current once properly assembled between two metal electrodes. The electronic asymmetry between the highest occupied molecular orbital (HOMO) and the lowest unoccupied molecular orbital (LUMO) of A and D should ease electron transfer from A to D and act as a high-electron-tunneling barrier in the opposite direction. Hence, an organic molecule can perform as a molecular rectifier. The proposal was made as a “Gedanken experiment” and leads to vivid research aiming for the design of suitable molecules and an experimental verification of the rectifying properties. It is worthwhile to mention in this context the ongoing activities in China with the foundation of the Laboratory of Molecular and Biomolecular Electronics dedicated to these topics (89) and an overview about these activities in China presented in the review by Wei (90). Meanwhile, experimental evidence has been provided that LB multilayer and monolayer can possess rectifying properties (91–93). Metzger *et al.* (94)

have observed asymmetries in current–voltage measurements within LB monolayers in benzochalcogenazolium derivatives which possess a donor– σ –acceptor architecture. The measurements were carried out on macroscopic Al|LB|Al sandwiches, as well as via a scanning tunnelling microscopy (STM) tip. The maximum rectification ratio was 26:1, although a rapid degradation in performance with time was also observed. The current–voltage measurements are obtained are shown in Figure 5.8, together with a schematic of the experimental set-up. Brady *et al.* (95) have also reported on the rectification behaviour in ($D-\sigma-A$) molecules. In this work, the molecules were assembled in non-centrosymmetric LB multilayer structures and sandwiched between two metal electrodes. The electronic structure was modelled by a density-functional approach and the results were used to discuss the underlying conduction mechanisms. Thus, about 25 years after it was first proposed, the Aviram–Ratner mechanism has been finally verified experimentally.

2.4.2 Challenges and hurdles

Can the knowledge gained in this area be further exploited for the fabrication of real devices? These present authors do not share the visions proposed for molecular electronics in the sense that individual molecules can “overtake” logic functions. The uncertainty principle is a good argument against overenthusiastic proposals which may even jeopardize the credibility of this area. However, small assemblies of molecules or nanoparticles have the potential to overtake the functions required within a computer. In the following, we will outline our personal views regarding which niches, perspectives and problems we foresee in this context, plus some issues and remarks which also hold for the currently so-fashionable field of Nanoscience.

There are essentially two approaches to enter the “microworld”, namely the top-down approach used by engineers and the bottom-up approach borrowed from nature. The top-down approach is based on lithography and related patterning techniques. Microstructures with function are fabricated by lithography, with a rapid trend towards smaller and smaller structures. The closest distance between adjacent electronic components within an integrated circuit (IC) defines the clock cycles and determines the speed of a processor. The current generation of chips is based on 180 nm structures which are produced by photolithography. There is a trend known as Moore’s law which states that the scale of an IC halves every 18 month (96). Meanwhile, structures

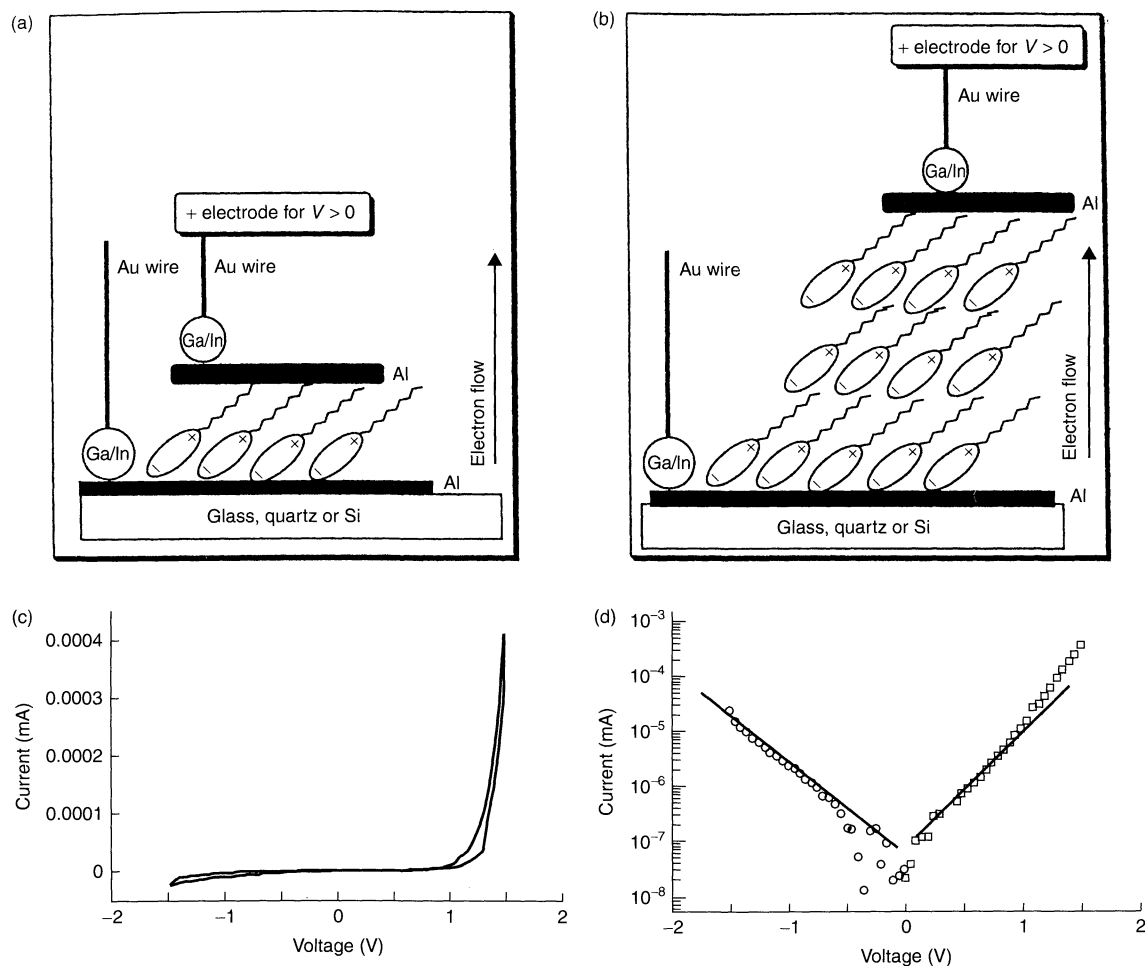


Figure 5.8. Schematic representation (a) of the experimental set-up used to verify molecular rectification in a donor- σ -acceptor molecule; the electrode (+) for the positive bias and the direction of an easy electron flow for $V > 0$ are marked. (b) Demonstration of rectification through a single monolayer sandwiched between Al electrodes. The DC voltage is swept at a rate of 10 mV/s and the DC current versus applied DC voltage is shown on a linear (c) and logarithmic scale (d). (From R. Metzger, B. Chen, U. Hopfner; M. Lakshmikantham, D. Vuillaume; T. Kawai, XL Wu, H. Tachibana, T. Hughes, H. Sakurai, J. W. Baldwin, C. Hosch, M. Cava, L. Brehmer, *Journal of the American Chemical Society*, 119(43):10455 (1997))

of about 50 nm have been successfully produced by X-ray or by electron-beam lithography, although the cost and failure rate increased tremendously, along with severe engineering problems such as capacitive coupling between components or heat dissipation (96). The top-down approach reaches physical and economic limits, and this is where the bottom-up approach may contribute as a cheap alternative.

The bottom-up approach is copied from nature and utilizes the profound knowledge gained in the self-organization of molecular assemblies and nanocrystals. Molecules and nanocrystals with different functionalities

can be designed and stacked in the desired fashion to give superlattices with novel functions. Experimental evidence has been provided that assemblies of molecules can overtake functions of the classical domain of semiconductors. However, the major challenge and hurdle for a further utilization is a combination of the macroscopic world with these nanoassemblies. A molecular assembly which overtakes the function of a transistor cannot find its place in the next generation of chips as it is not compatible with the top-down approach. This linkage between the two worlds is the major challenge. Eventually, the

bottom-up approach may provide cheap alternatives for the currently manufactured devices. However, the utilization requires a different computer architecture which takes the inherent imperfection of self-assembled structures into account. There is also research in this direction and an interesting study with an experimental computer has been performed in the laboratories of Hewlett Packard. This computer has a massively parallel architecture and was built to investigate a wide range of computational architectures and in particular address the influence of hardware defects on the overall performance (97). The machine contains over 200 000 hardware defects, and although any of these could be lethal to a conventional computer, yet it performed much faster than “high-end” single-processor workstations. The defect-tolerant architecture is due to a high communication bandwidth which enables a route around the defects. The underlying philosophy differs significantly from the usual ideas for building complex computer systems. The insight gained by these experiments may have some important implications for future computers based on any nanoassembly since the building concept of the machine takes defects into account as an inherent part of its construction (98).

3 FINAL REMARKS

LB films have been proposed for many practical applications covering a wide range of different areas from bio-sensing, to anti-reflection coatings, to all-optical processing units. Significant accomplishments in designing molecules and LB structures with functions have been made and the relationship between the macroscopic and molecular structures was in great detail addressed. Meanwhile a sound understanding of the underlying principles governing the packing and the structure of an LB film has been established. However, despite this remarkable progress, LB films have not yet found their way into the market-place and competitive approaches have been commercially more successful. Nevertheless, the LB techniques remains potentially useful due to its simplicity and the ability to build molecular assemblies defined on the molecular scale. In this respect, LB films will continue to serve as valuable model systems for addressing basic scientific problems such as wettability, friction and molecular recognition.

4 REFERENCES

1. Roberts, G., *Langmuir–Blodgett Films*, Plenum Press, New York, 1990.
2. Roberts, G. G., An applied science perspective of Langmuir–Blodgett Films, *Adv. Phys.*, **34**, 475–512 (1985).
3. Peterson, I. R., Langmuir–Blodgett techniques, in *The Molecular Electronic Handbook*, Mahler, G., May, V. and Schreiber, M. (Eds), Marcel Dekker, New York, 1994, pp. 47–77.
4. Gaines, G. L., *Insoluble Monolayers at Liquid–Gas Interfaces*, Wiley-Interscience, New York, 1966.
5. Ulmann, A., *Introduction to Ultrathin Organic Films: From Langmuir–Blodgett to Self-Assembly*, Academic Press, San Diego, CA, 1991.
6. Kaganer, M., Peterson, I. R., Kenn, R., Shih, M., Durbin, M. and Dutta, P., Tilted phases of fatty acid monolayers, *J. Chem. Phys.*, **102**, 9412–9422 (1995).
7. Möhwald, H., Phospholipid and phospholipid–protein monolayers at the air/water interface, *Annu. Rev. Phys. Chem.*, **41**, 441 (1990).
8. McConnel, H. M., Structures and transitions in lipid monolayers at the air–water interface, *Annu. Rev. Phys. Chem.*, **42**, 171–205 (1991).
9. Knobler, C. M. and Desai, R. C., Phase transition in monolayers, *Annu. Rev. Phys. Chem.*, **43**, 207–236 (1991).
10. Riviere, S., Henon, S., Meunier, J., Schwartz, D. K., Tsao, M. W. and Knobler, C. M., Texture and phase transitions in Langmuir monolayers of fatty acids – a comparative Brewster angle microscope and polarized fluorescence study, *J. Chem. Phys.*, **101**, 10045–10051 (1994).
11. Knobler, C. and Schwartz D., Langmuir and self-assembled monolayers, *Curr. Opinion Colloid Interface Sci.*, **4**, 46–51 (1999).
12. Tippmann-Krayer, P., Kenn, R. M. and Möhwald, H., Thickness and temperature dependent structure of Cd-arachidate Langmuir–Blodgett films, *Thin Solid Films*, **210/211**, 577–582 (1992).
13. Shih, M. C., Peng, J. B., Huang, K. G. and Dutta, P., Structure of fatty-acid monolayers transferred to glass substrates from various Langmuir monolayer phases, *Langmuir*, **9**, 776–778 (1993).
14. Durbin, M. K., Malik, A., Richter, A. G., Huang, K. G. and Dutta, P., *In situ* X-ray diffraction study of Langmuir–Blodgett deposition, *Langmuir*, **13**, 6547–6549 (1997).
15. Gehlert, U., Fang, J. and Knobler C., Relating the organization of the molecular tilt azimuth to lateral-force images in monolayers transferred to solid substrates, *J. Phys. Chem., B*, **102**, 2614–2617 (1998).
16. Fang, J., Gehlert, U., Shashidar, R. and Knobler, C., Imaging the azimuthal tilt order in monolayers by liquid crystal optical amplification, *Langmuir*, **15**, 297–299 (1999).
17. Spratte, K., Chi, L. and Riegler, H., Physisorption instabilities during dynamic Langmuir wetting, *Europhys. Lett.*, **25**, 211–217 (1994).
18. Spratte, K. and Riegler, H., Steady-state morphology and composition of mixed monomolecular films at the air–water interface in the vicinity of the three-phase line: Model calculations and experiments, *Langmuir*, **10**, 3161–3173 (1994).

19. Adamson, A. W., *Physical Chemistry of Surfaces*, Wiley, New York, 1993.
20. Gleiche, M. and Chi, L. F., Nanoscopic channel lattices with controlled anisotropic wetting, *Nature (London)*, **403**, 173–175 (2000).
21. Klimov, V. I., Mikhailovsky, A. A., McBranch, D. W., Leatherdale, C. A. and Bawendi, M. G., Quantization of multiparticle Auger rates in semiconductor quantum dots, *Science*, **287**, 1011–1013 (2000).
22. Murray, C. B., Kagan, C. R. and Bawendi, M. G., Self-organization of CdSe nanocrystallites into three-dimensional quantum dot superlattices, *Science*, **270**, 1335–1338 (1995).
23. Collier, B. P., Vossmeier, T. and Heath, J. R., Nanocrystal superlattices, *Annu. Rev. Phys. Chem.*, **49**, 371–404 (1998).
24. Kotow, N., Meldrum, F., Wu, C. and Fendler, J., Monoparticulate layer and Langmuir–Blodgett type multiparticulate layers of size-quantized cadmium sulfide clusters, *J. Phys. Chem.*, **98**, 2735–2738 (1994).
25. Kotow, N., Meldrum, F., Wu, C. and Fendler, J., Monoparticulate layers of titanium dioxide nanocrystallites with controllable interparticle distances, *J. Phys. Chem.*, **98**, 8827–8830 (1994).
26. Cassagneau, T., Fendler, J. H. and Mallouk, T. E., Optical and electrical characterizations of ultrathin films self-assembled from 11-aminoundecanoic acid capped TiO₂ nanoparticles and polyallylamine hydrochloride, *Langmuir*, **16**, 241–246 (2000).
27. Meldrum, F., Kotow, N. and Fendler, J., Preparation of particulate monolayers and multilayers from surfactant stabilized nanosized magnetic crystallites, *J. Phys. Chem.*, **98**, 4506–4510 (1994).
28. Meldrum, F., Kotow, N. and Fendler, J., Utilization of surfactant stabilized colloidal silver nanocrystallites in the construction of monoparticulate and multiparticulate Langmuir–Blodgett films, *Langmuir*, **10**, 2035–2040 (1994).
29. Guerin, F., Tian, Y. C. and Fendler, J. H., Dihexadecyl phosphate monolayer supported [Ru(bpy)₃]⁽²⁺⁾ crystallites investigated by near-field scanning optical microscopy, *J. Phys. Chem., B*, **103**, 7882–7888 (1999).
30. Langmuir, I. and Schäfer, V., *J. Am. Chem. Soc.*, **57**, 1007 (1938).
31. Heath, J. R., Knobler, C. M. and Leff, D. V., Pressure/temperature phase diagrams and superlattices of organically functionalized metal nanocrystal monolayers – the influence of particle size, size distribution, and surface passivant, *J. Phys. Chem., B*, **101**, 189–197 (1997).
32. Collier, P., Saykally, R., Shiang, J. J., Henrichs, S. E. and Heath, J. R., Reversible tuning of a silver quantum dot monolayer through the metal–insulator transition, *Science*, **277**, 1978–1979 (1997).
33. Bohren, C. F. and Huffman, D. R., *Absorption and Scattering of Light by Small Particles*, Wiley, New York, 1983.
34. Markovich, G., Collier, C. P. and Heath, J. R., Reversible metal–insulator transition in ordered metal nanocrystal monolayers observed by impedance spectroscopy, *Phys. Rev. Lett.*, **80**, 3807–3810 (1998).
35. Kim, S. H., Medeiros-Ribeiro, G., Ohlberg, D. A. A., Williams, R. S. and Heath, J. R., Individual and collective electronic properties of Ag nanocrystals, *J. Phys. Chem., B*, **103**, 10341–10347 (1999).
36. Lefebvre, S., Ménager, C., Cabuil, V., Assenheimer, M., Gallet, F. and Flament, C., Langmuir monolayers of monodispersed magnetic nanoparticles coated with a surfactant, *J. Phys. Chem., B*, **102**, 2733–2738 (1998).
37. Torimoto, T., Yamashita, M., Kuwabata, S., Sakata, T., Mori, H. and Yoneyama, H., Fabrication of CdS nanoparticle chains along DNA double strands, *J. Phys. Chem., B*, **103**, 8799–8803 (1999).
38. Schwartz, D. K., Langmuir–Blodgett film structure, *Surf. Sci. Rep.*, **27**, 241–334 (1997).
39. Kurthen, C. and Nitsch, W., Langmuir–Blodgett film of a water-soluble amphiphilic by convective monolayer compression, *Thin Solid Films*, **188**, 5–8 (1990).
40. Albrecht, O., Matsuda, H., Eguchi, K. and Nakagiri, T., Construction and use of LB deposition machines for pilot production, *Thin Solid Films*, **285**, 152–156 (1996).
41. Boyd, R. W., *Nonlinear Optics*, Academic Press, Boston, MA, 1992.
42. Shen, R., *Principles of Nonlinear Optics*, Wiley, New York, 1984.
43. Koechner, W., *Solid State Laser Engineering*, Springer-Verlag, 1992.
44. Prasad, P. and Williams, D. J., *Introduction to Nonlinear Optical Effects in Molecules and Polymers*, Wiley, New York, 1991.
45. Cai, C. Z., Liakatas, I., Wong, M. S., Bosch, M., Bosshard, C., Gunter, P., Concilio, S., Tirelli, N. and Suter, U. W., Donor-acceptor-substituted phenylethenyl bithiophenes: Highly efficient and stable nonlinear optical chromophores, *Org. Lett.*, **1**, 1847–1849 (1999).
46. Marder, S. R., Kippelen, B., Jen, A. K. -Y. and Peyghambarian, N., Design and synthesis of chromophores and polymers for electrooptic and photorefractive applications, *Nature (London)*, **388**, 845–851 (1997).
47. Williams, D. J., Organic polymeric and non-polymeric materials with large optical nonlinearities, *Angew. Chem. Int. Ed. Engl.*, **23**, 690–697 (1984).
48. Schrader, S., Zauls, V., Dietzel, B., Fluerau, C., Prescher, D., Reiche, J., Motschmann, H. and Brehmer, L., Linear and nonlinear optical properties of Langmuir–Blodgett multilayers from chromophore-containing maleic acid anhydride polymers, *Mater. Sci. Eng. C*, **8–9**, 527–537 (1999).
49. Ashwell, G. J., Zhou, D. J. and Skjonnemund, K., Z-type films of a two-legged optically nonlinear dye, *Mol. Cryst. Liq. Cryst., Sect. A*, **337**, 413–416 (1999).
50. Ashwell, G. J., Zhou, D. J. and Huang, C. H., Z-type Langmuir–Blodgett films of a three-component optically nonlinear dye, *Colloids Surf., A*, **155**, 47–50 (1999).
51. Ashwell, G. J., Handa, T. and Ranjan, R., Improved second-harmonic generation from homomolecular Langmuir–Blodgett films of a transparent dye, *J. Opt. Soc. Am., B*, **15**, 466–470 (1998).

52. Zhou, D. J., Ashwell, G. J. and Huang, C. H., Improved second-harmonic generation from Langmuir–Blodgett monolayers of an ionically combined bis-chromophore zinc complex, *Chem. Lett.*, 7–8 (1997).
53. Ashwell, G. J., Walker, T. W., Leeson, P., Grummt, U. W. and Lehmann, F., Improved second-harmonic generation from Langmuir–Blodgett films, *Langmuir*, **14**, 1525–1527 (1998).
54. Motschmann, H., Penner, T., Armstrong, N. and Enzenyilimba, M., Additive second-order nonlinear susceptibilities in Langmuir–Blodgett multibilayers: testing the oriented gas model, *J. Phys. Chem.*, **97**, 3933–3936 (1993).
55. Wijekoon, W. M. K. P., Wijaya, S. K., Bhawalkar, J. D., Prasad, P. N., Penner, T. L., Armstrong, N. J., Enzenyilimba, M. C. and Williams, D. J., Second harmonic generation in multilayer Langmuir–Blodgett films of blue transparent organic polymers, *J. Am. Chem. Soc.*, **118**, 4480–4483 (1996).
56. Verbiest, T., Elshocht, S. V., Kauranen, M., Hellemans, L., Snauwaert, J., Nuckolls, C., Katz, T. and Persoons, A., Strong enhancement of nonlinear optical properties through supramolecular chirality, *Science*, **282**, 913–915 (1998).
57. Penner, T. L., Motschmann, H. R., Armstrong, N. J., Enzenyilimba, M. C. and Williams, D. J., Efficient phase-matched second-harmonic generation of blue light in an organic waveguide, *Nature (London)*, **367**, 49–51 (1994).
58. Dalton, L. R., Polymeric electro-optic modulators. from chromophore design to integration with semiconductor and silica fiber optics, *Ind. Eng. Chem. Res.*, **38**, 8–33 (1999).
59. Kalluri, S., Ziari, M., Chen, A., Chuyanov, V., Steier, W. H., Chen, D., Jatali, D., Fettermann, H. R. and Dalton, L. R., Monolithic integration of waveguide polymer electrooptic modulators on VLSI circuits, *IEEE Photon. Tech. Lett.*, **8**, 644–646 (1996).
60. Cheng, D., Fettermann, H. R., Steier, W. H., Dalton, L. R., Weng, W. and Shi, Y., Demonstration of a 110 GHz electrooptic polymer modulator, *Appl. Phys. Lett.*, **70**, 2082–2084 (1997).
61. Cheng, L. -T., Tam, W., Marder, S. R., Stiegman, A. E., Rikken, G. and Spangler, C. W., Experimental investigations of organic molecular nonlinear optical polarizabilities. II. A study of conjugation dependences, *J. Phys. Chem.*, **95**, 10643–10652 (1991).
62. Cheng, L. -T., Tam, W., Stevenson, S. H., Meredith, G. R., Rikken, G. and Marder, S. R., Experimental investigations of organic molecular nonlinear optical polarizabilities. I. Methods and results on benzene and stilbene derivatives, *J. Phys. Chem.*, **95**, 10631–10643 (1991).
63. Palchetti, L., Sottini, S., Grando, D., Giorgetti, E., Ricceri, R. and Gabrielli, G. I., Electrooptic modulation of laser diode light by mode interference in a multilayer waveguide including a 2-docosylamino-5-nitropyridine Langmuir–Blodgett film, *Appl. Phys. Lett.*, **72**, 873–875 (1998).
64. Ren, A. and Dalton, L. R., Electroactive polymers, including nonlinear optical polymers, *Curr. Opinion. Colloid Interface Sci.*, **4**, 165–171 (1999).
65. Halvorson, C. and Heeger, A. J., Two photon absorption and ultrafast optical computing, *Synth. Met.*, **71**, 1649–1652 (1995).
66. Stegeman, G. and Torruellas, W., Nonlinear materials for information processing and communications, *Philos. Trans. R. Soc. Lond., Phys. Sci. Eng.*, **354**, 754–756 (1996).
67. Luther-Davies, B. and Samoc, M., Third-order nonlinear optical organic materials for photonic switching, *Curr. Opinion Solid State Mater. Sci.*, **2**, 213–219 (1997).
68. Wang, Z., Hagan, D., VanStryland, E., Zyss, J., Vidakovik, P. and Torruellas, W., Cascaded second-order effects in *N*-4-nitrophenyl-L-prolinol in a molecular single crystal, *J. Opt. Soc. Am., B*, **14**, 76–86 (1997).
69. Baek, Y., Schiek, R., Stegeman, G., Krijnen, G., Baumann, I. and Sohler, W., All-optical integrated Mach-Zehnder switching due to cascaded nonlinearities, *Appl. Phys. Lett.*, **68**, 2055–2057 (1996).
70. Bosshard, C., Cascading of second-order nonlinearities in polar materials, *Adv. Mater.*, **8**, 385–392 (1996).
71. Nelson, S. G., Johnston, K. S. and Yee, S. S., High sensitivity surface plasmon resonance sensor based on phase detection, *Sensors Actuators, B*, **35/36**, 187–199 (1996).
72. Kambhampati, D. and Knoll, W., Surface plasmon optics, *Curr. Opinion Colloid Interface Sci.*, **4**, 273–280 (1999).
73. Guillaud, G., Simon, J. and Germain, J. P., Metallophthalocyanines – gas sensors, resistors and field effect transistors, *Coord. Chem. Rev.*, **180**(2), 1433–1484 (1998).
74. Leznoff, C. C. and Lever, A. B., *Phthalocyanines, Properties and Applications*, Vols 1–4, VCH, New York, 1989–1996.
75. Arnold, D. P., Manno, D., Micocci, G., Serra, A., Tepore, A. and Valli, L., Porphyrin dimers linked by a conjugated alkyne bridge – novel moieties for the growth of Langmuir–Blodgett films and their applications in gas sensors, *Langmuir*, **13**, 5951–5956 (1997).
76. Emelianov, I. L. and Khatko, V. V., Gas sensing properties of the composite Langmuir–Blodgett films: effects of the film thickness and the Cd²⁺ addition into the subphase, *Sensors Actuators, B*, **60**, 221–227 (1999).
77. de Saja, R., Souto, J., Rodriguez-Mendez, M. L. and de Saja, J. A., Array of lutetium bis-phthalocyanine sensors for the detection of trimethylamine, *Mater. Sci. Eng., C*, **8–9**, 565–568 (1999).
78. Zislperger, M. and Knoll, M., Multispot parallel online monitoring of interfacial binding reactions by surface plasmon microscopy, *Prog. Colloid Polym. Sci.*, **109**, 244–253 (1998).
79. Dürr, H. and Laurent, B., *Photochromism: Molecules and Systems*, Elsevier, Amsterdam, 1991.
80. Seki, T. and Ichimura, K., Formation and Langmuir–Blodgett deposition of monolayers of poly(vinyl alcohol) having azobenzene side-chains, *Polym. Commun.*, **30**, 108–110 (1989).
81. Ichimura, K., Surface-assisted photoregulation of molecular assemblages as commander/soldier molecular systems, *Supramol. Sci.*, **3**, 67–73 (1996).
82. Knobloch, H., Orendi, H., Büchel, M., Seki, T., Ito, S. and Knoll, W., Photochromic command surface induced

- switching of liquid crystal optical waveguide structures, *J. Appl. Phys.*, **77**, 481–487 (1995).
83. Aoki, K., Seki, T., Suzuki, Y., Tamaki, T., Hosoki, A. and Ichimura, K., Factors affecting photoinduced alignment regulation of nematic liquid crystals by azobenzene molecular films, *Langmuir* **8**, 1007–1013 (1992).
 84. Möller, G., Harke, M., Prescher, D. and Motschmann, H., Controlling microdroplet formation by light, *Langmuir*, **14**, 4955–4958 (1998).
 85. Lipowsky, R., Lenz, P. and Swain, P. S., Wetting and dewetting of structured and imprinted surfaces, *Colloids Surfaces, A*, **161**, 3–22 (2000).
 86. Martin, A. S. and Sambles, J. R., Molecular rectification, photodiodes and symmetry, *Nanotechnology*, **7**, 401–405 (1996).
 87. Metzger, R. M., Electrical rectification by a molecule: The advent of unimolecular electronic devices, *Acc. Chem. Res.*, **32**, 950–957 (1999).
 88. Aviram, A. and Ratner, M., *Chem. Phys. Lett.*, **29**, 277–283 (1974).
 89. Wei, Y., Lu, Z., Yuan, C. and Gan, Q., Molecular electronics: strategies and progress in China, *IEEE Eng. Med. Biol.*, **16**, 53–61 (1997).
 90. Wei, Y., Molecular electronics – the future of bioelectronics, *Supramol. Sci.*, **5**, 723–731 (1998).
 91. Polymeropolos, E., Möbius, D. and Kuhn, H., Molecular assemblies with functional units of sensitizing and conducting molecular components: photovoltage, dark conduction and photoconduction, *Thin Solid Films*, **68**, 173–179 (1980).
 92. Geddes, N. J., Sambles, J. R., Jarvis, D., Parker, W. and Sandman, D. J., Fabrication and investigation of asymmetric current voltage characteristics of a metal/Langmuir–Blodgett/metal structure, *Appl. Phys. Lett.*, **56**, 1916–1919 (1990).
 93. Ashwell, G. J., Sambles, J. R., Martin, A. S., Parker, W. G. and Slablewski, M., Rectifying characteristics of $\text{Mg/C}_{16}\text{H}_{33}\text{-Q}_3\text{C}$ LB films/Pt structures, *J. Chem. Soc., Chem. Comm.*, 1374–1376 (1990).
 94. Metzger, R. M., Chen, B., Hopfner, U., Lakshmikantham, M., Vuillaume, D., Kawai, T., Wu, X. L., Tachibana, H., Hughes, T., Sakurai, H., Baldwin, J. W., Hosch, C., Cava, M. and Brehmer, L., Unimolecular electrical rectification in hexadecylquinolinium tricyanoquinodimethanide, *J. Am. Chem. Soc.*, **119**, 10455–10466 (1997).
 95. Brady, A. C., Hodder, B., Martin, A. S., Sambles, J. R., Ewels, C. P., Jones, R., Briddon, P. R., Musa, A. M., Panetta, C. A. F. and Mattern, D. L., Molecular rectification with M vertical bar(D -sigma- A LB film) vertical bar M junctions, *J. Mater. Chem.*, **9**, 2271–2275 (1999).
 96. Schaller, R. R., Moore's law: past, present and future, *IEEE Spectrum*, **34**(6) 52–56 (1997).
 97. Clark, D., TERAMAC – pointing the way to real-world nanotechnology, *IEEE Comput. Sci. Eng.*, **5**, 88–90 (1998).
 98. Heath, J., Kuekes, P., Snider, G. and Williams, R., A defect tolerant computer architecture: opportunities for nanotechnology, *Science*, **280**, 1716–1721 (1998).

CHAPTER 6

Self-Assembling Monolayers: Alkane Thiols on Gold

Dennis S. Everhart

Kimberly Clark Corporation, Roswell, USA

1	Introduction	99	5	Self-Assembled-Monolayer-Protected Metal Clusters	113
2	Properties and Characterization	100	6	Conclusions	114
3	Self-Assembled Monolayers to Control Interfacial Chemistry	103	7	References	114
4	Patterned Self-Assembled Monolayers	109			

1 INTRODUCTION

A wide variety of technologies associated with adhesion, corrosion, sensing, lithography and biocompatible materials are affected by the chemistry and materials science of organized thin films. Until the advent of self-assembled monolayers (SAMs), the most popular approach to develop well-defined organic monolayers was via Langmuir–Blodgett (LB) films assembled at an interface for subsequent transfer to a solid surface by its immersion and controlled retraction. The use of LB techniques for generating organized organic monolayers dates back to the early years of the 20th century where systematic studies on the organization of amphiphilic organic molecules at the air/water interface first appeared. Building off the work of Pockels, who was one of the first to report the design of a trough for the transfer of monolayers from water (1), Langmuir and Blodgett pioneered the formation of monolayers and multilayers of *n*-alkyl chain carboxylate terminated surfactants as antireflective coatings on glass. Many years elapsed during which a large number of chemistries and technologies were developed for the

systematic modification of surfaces with organic monolayers. During the 1970s, scientists interested in electron transport across organic monolayers reported the use of fatty acids and reactive siloxanes for the surface modification of platinum, carbon and modified tin oxide electrodes. Some of the pioneering electrochemistry reported by Murray and co-workers (2, 3), Buttry and Anson (4), and Rubinstein and Bard (5) involved the as yet undiscovered SAMs on Pt, Au and glassy carbon. In 1983, Nuzzo and Allara published their seminal paper demonstrating that oriented monolayers of bifunctional organic disulfides spontaneously adsorb and assemble onto gold from solution (6). Organized monolayers with site densities of 4×10^{14} molecules/cm were verified with infrared, ellipsometry, radioactive labeling and contact-angle measurements. US Patent 4690715, issued to AT&T in September of 1987, was based on the work of Nuzzo and Allara. By the early 1990s, self-assembled monolayers were well recognized as a novel and powerful approach for surface modification involving organic chemistries.

A large number of SAM-forming molecules have been reported during the last five years. For example,

octadecyl phosphate esters have been found to produce oriented, well-ordered monolayers on tantalum oxide, analogous to alkane thiol SAMs on gold (7). Thiol phosphonates have been used to construct multi-layered thin films with SAMs of controlled thicknesses, a contemporary demonstration of SAM methodology which parallels the work reported using LB methods at the turn of the 19th century (8). Alkane thiols on gold and trialkoxy alkyl silanes on refractory materials containing surface hydroxide have received considerable attention because of their relative ease of formation, stability and versatility. This review will concentrate principally on alkane thiol SAMs on gold, their characterization and some of their technology applications.

2 PROPERTIES AND CHARACTERIZATION

The formation of a SAM is facilitated by chemisorption of a pendant functionality on to a substrate. At 300 K,

the thermal energy is 0.6 kcal/mol, requiring interaction energies indicative of those for strong hydrogen bonds or higher (> 5 kcal/mol) for molecular adsorption. Covalent (100–300 kT), coordination (100 kT) and isolated charged-pair ionic (200 kT) interactions are sufficient to promote head-group interactions with the substrate which minimizes thermal desorption of the SAM-forming molecule. Without strong chemisorption, thermal energies would randomize surface orientation and conformational ordering, thus restricting or more likely preventing SAM formation.

Figure 6.1 illustrates the importance of interactions between the SAM end-group and the surface to promote chemisorption. Solutions of a variety of end-functionalized hydrocarbons were contacted with Au, and the resulting Au surfaces were evaluated by water and hexadecane (HD) contact angles (9). Ellipsometry measured thicknesses were compared against those calculated from molecular dimensions, assuming an extended chain conformation. End-group functionalities having low interaction energies with Au produced contact angles and measured thicknesses typical of

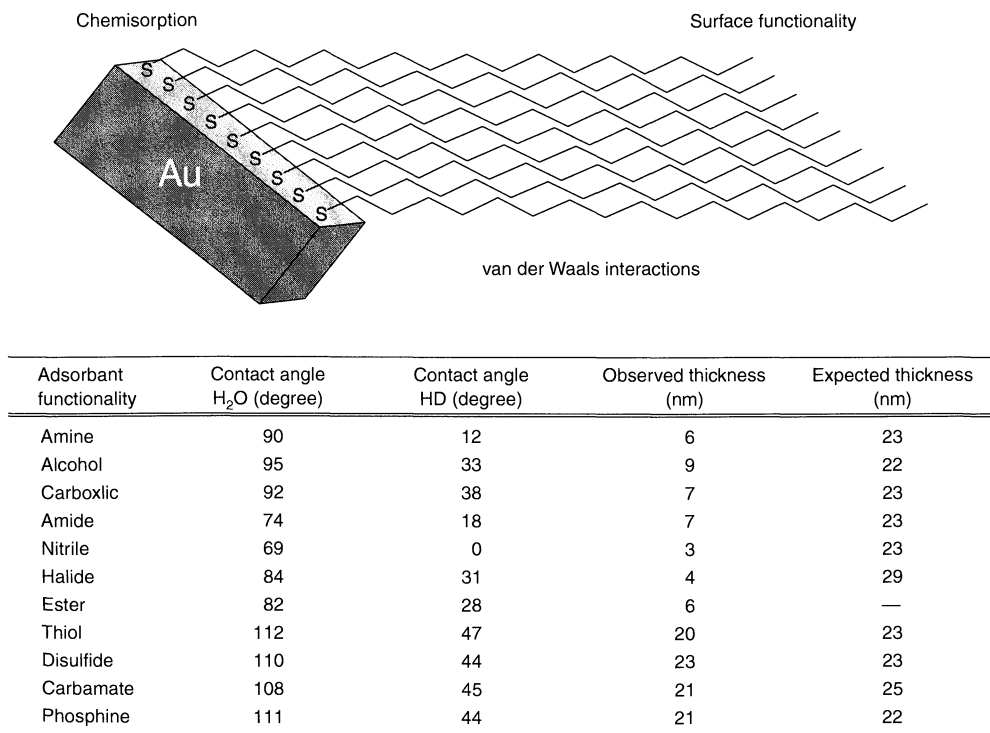


Figure 6.1. Chemisorption and alkane ordering for a thiol monolayer on gold. The table summarizes water and hexadecane (HD) contact angles, measured as a function of observed and expected thicknesses of various C₁₈ adsorbents on gold (adapted from ref. (9))

sub-monolayer quantities of poorly organized, predominately hydrocarbon organics. For groups such as thiol, disulfide, carbamate and phosphine that are known to chemisorb on Au with dissociation energies of about 30–40 kcal/mol, a distinct change in surface order is indicated. Water and HD contact angles are typical for organized hydrocarbon lamellae such as those measured on crystalline polyolefins. Measured monolayer thicknesses are within 0.3 nm of the calculated values, consistent with alkyl chain orientations which are normal to the surface. These results are consistent with the simple model portrayed in Figure 6.1 and demonstrate the importance of chemisorption for SAM formation.

Chemisorption alone is not sufficient, however, to generate an organized SAM. Interactions between an additional functionality of adjacent chains are required to stabilize the structure. For linear hydrocarbons with segment lengths greater than C₁₀, lateral interactions between adjacent methylene groups via van der Waals association is a facile process that orders the SAM. The optimum chain lengths for these interactions are C₁₆–C₂₄. A *trans*-methylene conformation stabilizes the packing. For hydrocarbon SAMs, their formation and stabilities parallel the initial stages of lamellae formation in micelle-forming hydrocarbon surfactants, with chemisorption of the SAM reducing or eliminating the more rapid dynamics of micellar processes which are known to occur in solution (10). Alkane branching reduces the ability to pack, thus increasing the void volume, while other functionalities can be introduced within the SAM at the expense of reducing order and structure. Internal groups can also promote additional interactions such as donor-acceptor or ion-pair complexes that stabilize the structure. Examples of this approach are those reported by Ullman (11) who incorporated a sulfone functionality within the methylene backbone of the SAM, and Xia and Whitesides (12) who incorporated an amide functionality β to the chemisorbed thiol. The more stable SAMs reported to date rely on inter-chain associations of extended linear hydrocarbons with segment lengths between C₁₆ and C₂₀ (13).

A number of spectroscopic and imaging techniques have been adapted for SAM characterization (14). One of the more widely used spectroscopies is polarized attenuated total reflection (ATR) infrared, with an example of the capabilities of this method being illustrated in Figure 6.2. It is well established that the symmetric and asymmetric methylene stretching vibrations can be used to determine the relative amounts of *trans*- and *gauche*-conformers (14). As indicated in Table 6.1, the higher energy *gauche*-conformation, associated with packing disorder, is shifted about 6 cm⁻¹ higher in absorbance than the more stable *trans*-configuration. This shift is easily resolved with modern IR spectrophotometers, and is apparent as the shoulder on the large CH₂ asymmetric absorbance at 2919 cm⁻¹ in Figure 6.2(a). Using curve-fitting algorithms, the relative absorbances of these two peaks can be resolved. The ratio of these two signals is proportional to the % *gauche*-conformation (Figure 6.2(b)). The effect of temperature, time, chain length and solvent disordering on the SAM structure can be determined from this ratio. As shown in Figure 6.2(b), thermal disordering of a hexadecyl thiol SAM begins at about 250 K. The introduction of *gauche* content correlates with changes in physico-chemical properties such as decreased sessile drop contact angles and the extent of etching of the underlying gold with an oxygenated cyanide solution. A well-ordered SAM protects gold from cyanide etching, while fluidity and defects of alkane chains allows for chemical etching of the underlying substrate. In addition to CH stretching, methylene scissoring motion vibrations (1460 cm⁻¹) and chain-end *gauche* waggings associated with defect structures (1345 cm⁻¹) provide information on alkane packing. IR sum-frequency generation has provided additional insights into the kinetics of conformational ordering of alkane thiol SAMs on Au or Ag for samples not possessing inversion symmetry (15). Typically, the outermost two or three methylene units of a SAM contain the highest *gauche*-isomer content. Another popular method for characterizing SAMs

Table 6.1. Infrared absorbances useful for determining the alkyl chain order in SAMs

Alkyl group	C–H stretching	Peak absorbance (cm ⁻¹)	
		Ordered	Disordered
CH ₂	Asymmetric	2918	2924
	Symmetric	2850	2855
CH ₃	Symmetric	2873	2870
	Asymmetric-(in plane)	2965	2957
	Asymmetric-(out of plane)	2956	2957

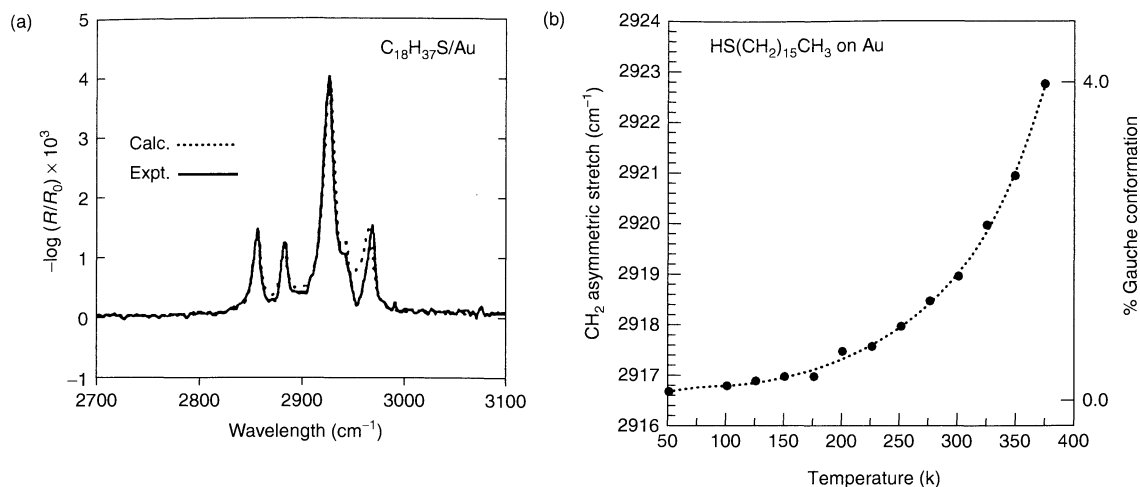


Figure 6.2. Polarized reflection infrared spectroscopy to determine structure and order in alkane thiol SAMs; (a) comparison of theoretical and experimental C–H stretching IR spectra for octadecyl thiol adsorbed on to gold; (b) effect of temperature on increasing the disorder in the alkane chain

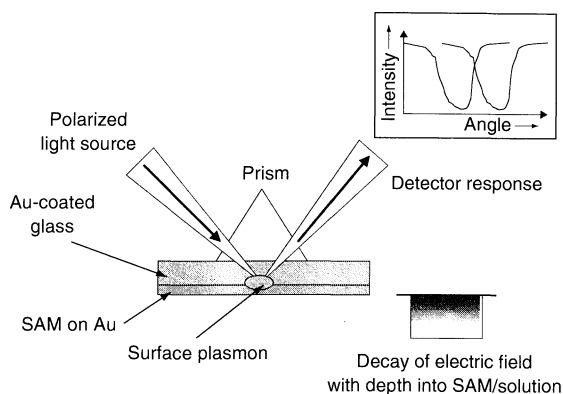


Figure 6.3. Schematic of the surface plasmon resonance (SPR) technique for the study of SAM structures; changes in the inter-phase dielectric constant produce shifts in the angle of minimum reflectivity

(and the reactions of SAMs) is surface plasmon resonance (SPR), an optical technique that is sensitive to the refractive index of the medium near a metal surface (Figure 6.3). Monochromatic, plane-polarized radiation is directed through a metal-coated, optically transparent substrate in contact with a solution (16). An alkane thiol SAM coated on Au-modified glass is an excellent substrate for SPR. Upon reflection from the Au/glass interface, surface plasmons, i.e. non-radiative oscillations of conduction-band electrons, in the metal are excited as a result of resonant coupling. Excitation of plasmons

is detected as a minimum in the intensity of reflected radiation at a well-defined resonance angle which is determined by the dielectric constants of the interfacial regions of the metal surface/SAM/solution. An evanescent wave propagates through the SAM into the solution. A plot of reflected intensity versus the angle of incidence exhibits a minimum at maximum plasmon excitation. With visible irradiance and for organic films less than about 100 nm thick, the angle of incidence for minimum reflection is proportional to the thickness of the film. Reactions and chemical adsorption occurring within the SAM change the dielectric constant of the interfacial region to produce a shift in minimum reflection angle. An example of the use of SPR for probing the SAM structure is shown in Figure 6.4. Multilayers of alkyl diphosphonate (DBP) are sequentially deposited on an alkane thiol template terminated with phosphonate (8). Coupling of the latter is achieved by ionic crosslinking with Zr^{4+} . Azobenzene chromophores are alternatively included in the multilayer assembly. Each consecutive layer produces an increase in the minimum angle of reflectivity that is readily detected with SPR. Equilibrium and kinetic constants can also be determined by using this technique.

Based on a large number of reported studies, an accepted model has been developed for the structure of alkane thiols on the Au(111) surface (see Figure 6.5). The various spectroscopies and diffraction methods used to help establish these structures are shown on the figure. Alkylthiols are chemisorbed in a next-nearest-neighbor three-fold hollow site within a trimetallic Au cluster. The

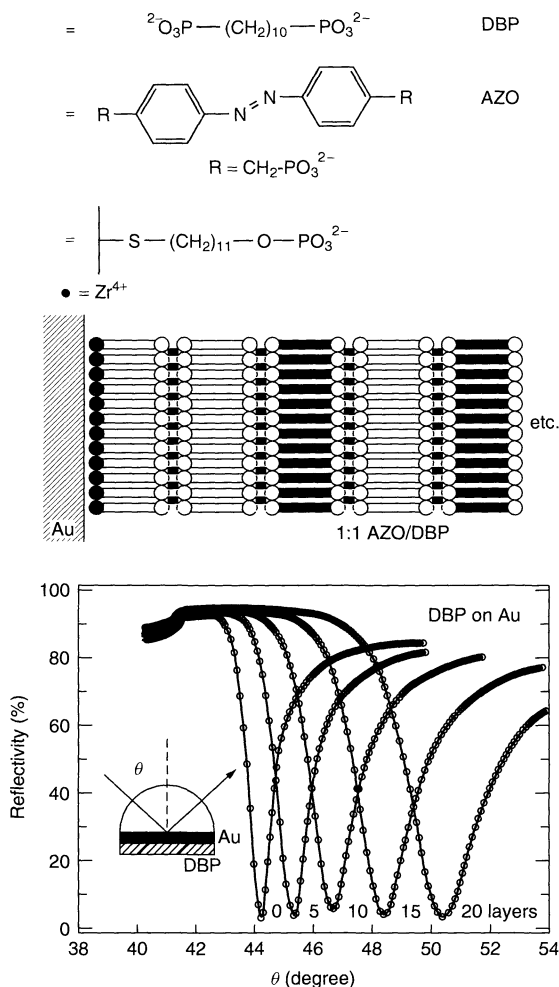


Figure 6.4. The use of SPR to measure the sequential deposition of a difunctional phosphonate SAM ionically cross-linked with Zr^{4+} . Note the shift in angle of minimum reflectivity with increasing SAM deposition (adapted from ref. (8))

overlayer structure on this gold terrace is described by crystallographic nomenclature as $\sqrt{3} \times \sqrt{3}R30$; the average distance between sulfur atoms is about 0.50 nm. XPS Au(4f) and S(2p) binding energies are consistent with Au (0) and RS^- (16). The alkyl chain orientation to the surface normal requires specifying a tilt and rotation angle, and assumes an all-*trans* conformation of methylene units. The van der Waals interaction diameter for alkane chains with this configuration is about 0.46 nm, a distance compatible with the chemisorbed sulfur. The values of tilt and rotation angles for a defect-free structure on an atomically smooth Au(111) surface are shown

in Figure 6.5 for a variety of omega-functionalized hexadecane thiols. Values such as these were used in the calculation of the theoretical IR spectrum shown against the measured spectrum in Figure 6.1. Real systems deviate from this idealized model due to lattice edges and defects, grain boundaries and surface roughness, and adsorption on to additional Au crystal faces, as well as from variables associated with the purity and stability of the chosen thiol. Chemical reactions of functionality in the SAM also affect this idealized structure, with the photo-oxidation of thiol to sulfate being a well-documented example (17).

The growth kinetics of alkane thiol SAMs on Au can be described by a modified Langmuir model involving two principal processes, i.e. attachment and nucleation (18). Monolayer formation begins at low surface coverage with a lateral, rapidly diffusing alkane chain, surface confined by the chemisorbed thiol. Orientation of the alkane chain is predominantly parallel to the surface. At a critical sub-monolayer coverage, islands of adsorbed thiol begin to nucleate and associate, thus reorienting alkyl chains more normal to the surface. Interchain interactions become prevalent. The size and population of these clusters continue to grow as more monomer is incorporated into the SAM. As monolayer saturation occurs, condensation of low-density islands begins, with an increase in density as the structure depicted above in Figure 6.1 develops. Increasing *trans*-conformer content is concomitant with increased density. It is important to appreciate that island formation and nucleation reflect the kinetic rather than the thermodynamic aspects of assembly. The effects of solvent, temperature and chain length on the kinetic behaviour of SAM formation have received considerable attention. The final SAM structures are typically developed within hours of initial chemisorption.

3 SELF-ASSEMBLED MONOLAYERS TO CONTROL INTERFACIAL CHEMISTRY

The ability to control the end-group functionality on a stable, well-oriented SAM has led to a number of fundamental surface chemistry studies and emerging technology developments. As suggested in Figure 6.6, concentration gradients of the end-group functionality can be incorporated into alkane thiol SAMs. One caveat of this model that has not yet been reconciled is whether nucleation of specific functional groups into islands occurs as opposed to the random spatial distributions of functionality as predicted from the overall bulk

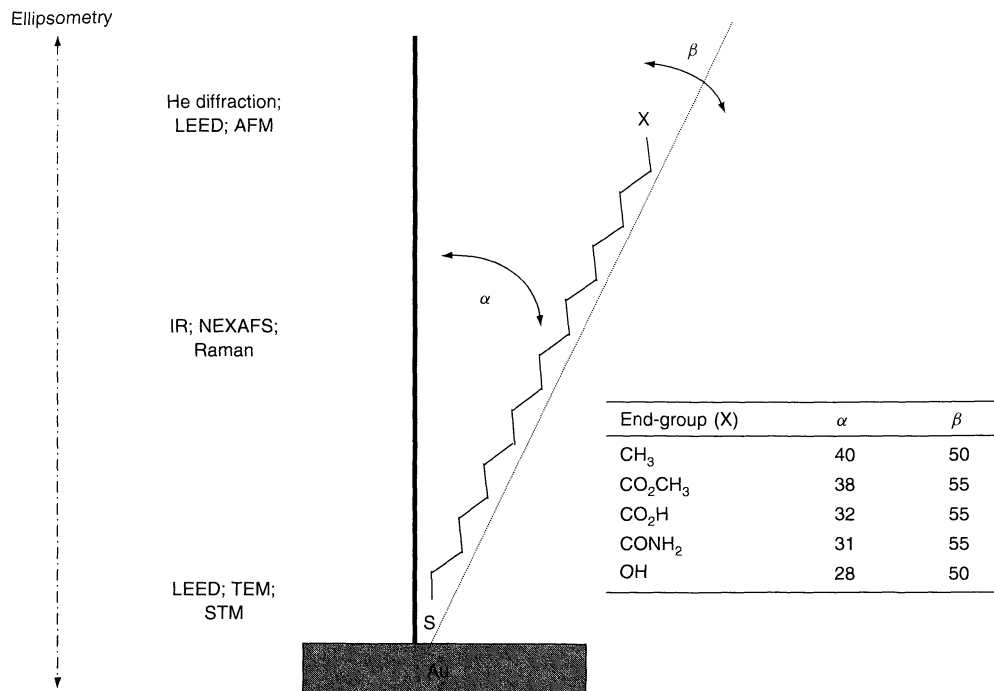


Figure 6.5. Accepted model for equilibrium adsorption of an alkane thiol SAM on gold. The indicated spectroscopies have provided site-specific information consistent with this structure

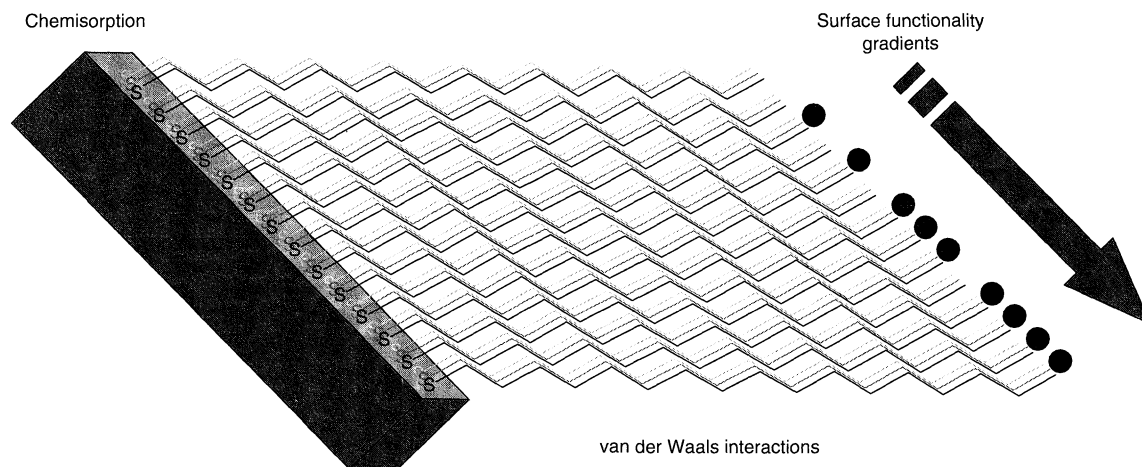


Figure 6.6. Concentration gradients of end-group functionality in an alkane thiol SAM

concentrations. The scale-length of the gradient is poorly defined.

By utilizing cross-diffusion from reservoirs containing different thiols, Liedberg and Tengvall (19) have demonstrated a method capable of generating chemical

composition gradients on gold. One end of the gradient contains hexadecyl thiol, while the other end is an omega-functionalized thiol selected from either an alcohol, carboxylic acid, nitrile or methyl carboxylate ester. Across 40 mm, a gradient starting with

a 100% methyl-terminated SAM and ending with a 100% carboxylic-acid-terminated SAM was generated and characterized with contact angle, infrared (IR), X-ray photoelectron spectroscopy (XPS) and ellipsometry. Spectroscopic characterization was facilitated by incorporating perdeuterated methylene within the SAM, which shows unique IR absorbencies between 2075, and 2220 cm^{-1} ; CH_2 and CD_2 are well resolved by IR spectroscopy. Highly organized gradients of densely packed *trans* assemblies over macroscopic distances of several mm were established, with molecular gradients on the *nM* scale being suggested. The clustering of functionality into islands of homogeneous SAMs could not be excluded from an interpretation of the results

reported. Nevertheless, gradients such as those suggested in Figure 6.6 would provide a valuable substrate for fundamental studies of wettability, cellular adhesion, chemical sensor selectivity and microbiological chemotaxis.

The ability to end-functionalize a SAM has led to a number of schemes to produce reactive surfaces for further derivatization. Starting with a carboxylic-acid-terminated alkane thiol SAM of 16-mercaptohexadecanoic acid, condensation to the interchain anhydride was demonstrated by reaction with trifluoroacetic anhydride, producing the mixed anhydride as an intermediate (Figure 6.7) (20). XPS confirmed that the level of mixed anhydride containing

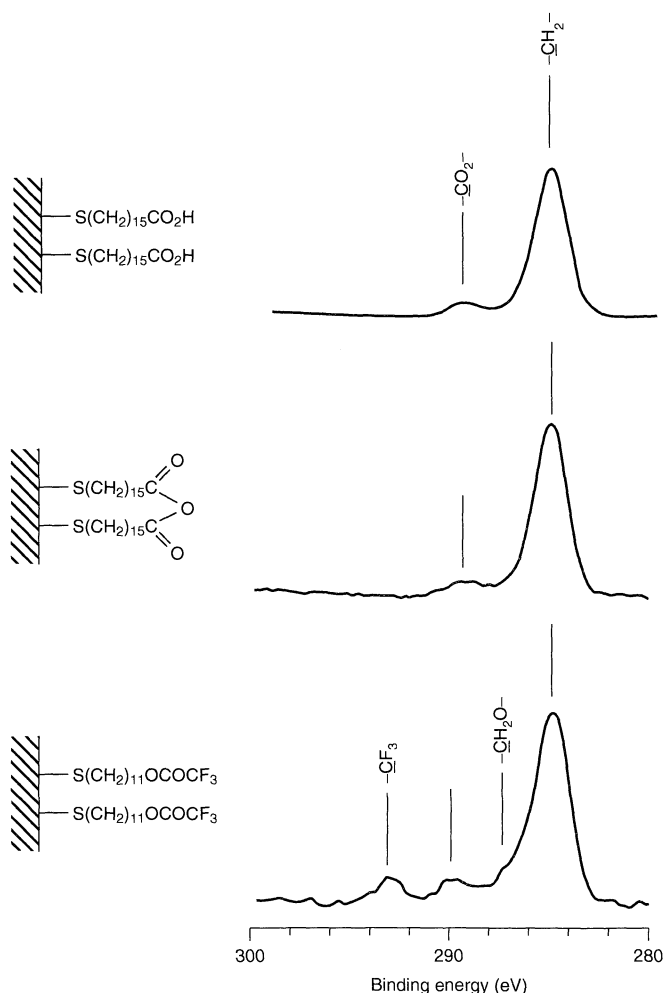


Figure 6.7. Formation of the reactive SAM anhydride via condensation of the adjacent carboxylic-acid-terminated SAM; C(1s) XPS spectra for the corresponding products are shown to the right of each structure (taken from ref. (20))

the trifluoroacetyl group is less than 0.1 atom% of the surface. IR spectroscopy provides conclusive evidence for the near-quantitative conversion of carboxylate to the anhydride, with the carbonyl absorbencies for these respective functionalities being distinct and well-resolved. The inter-chain, terminal anhydride of the resulting SAM provides a reactive intermediate for subsequent surface modifications that could be expected based on the known chemistries of anhydride, i.e. formation of ester, amide, carbamate, urethane, etc.

Reactions of anhydride-terminated SAMs with alkyl amines to produce mixtures of SAMs terminated with carboxylic acids and *N*-alkyl amides in yields greater than 90% has been demonstrated (21). Varying the chain length of the alkyl amine produced a surface with a controlled amount of hydrocarbon separating the resulting polar acid and *N*-alkyl amide functionality from the air interface. A correlation with the water contact angles was found (see Table 6.2). For alkyl amine chain lengths greater than C₈, the water contact angles were independent of pH and typical of hydrocarbon surfaces, thus reflecting either a difficulty in ionizing the carboxylate in a low dielectric strength environment or a restriction in the access of hydroxide. Organization of the *N*-alkyl amide into a second SAM overlay is suggested by the contact-angle data. Below alkyl amine chain lengths of C₆, contact angles vary with solution pH, thus suggesting acid neutralization of the underlying carboxylic acid. For short-chain-length alkyl amines, contact angles are consistent with a more hydrophilic surface. Short-chain-length hydrocarbon overlays cannot organize laterally to restrict access of hydroxide to the acidic carboxylate. These schemes demonstrate the control of structure and molecular composition of organic monolayers and interfaces that can be achieved via the use of SAMs.

Reactive functionality has been exploited to covalently attach proteins and other biologically active molecules onto a SAM. Much of the activity in this

Table 6.2. Effect of *N*-alkyl amide chain length on water contact angles. Amides were produced from the reaction of anhydride-terminated SAMs with an alkylamine (adapted from ref. (21))

Alkyl Amine Chain Length	Water contact angle	
	pH = 4	pH = 11
C ₁	58	35
C ₄	80	69
C ₆	88	85
C ₁₁	97	97
C ₁₈	105	105

Table 6.3. Some examples of functional SAMs used for surface coupling

End-group functionality	Coupled molecule
–CO ₂ H	Cytochrome C
–CO ₂ H	Catalase
Quinone	Diels–Alder adduct
Biotin	Streptavidin
RGD ^a peptides	Integrin receptors

^aRGD, tripeptide containing–glycine–aspartate sequences

area is directed at developing biological and chemical sensors, as well as fundamental studies to better understand specific ligand/receptor interactions of biologically important molecules and particles. Protein deposition, cell adhesion and motility, and intercellular communication are receiving considerable attention with SAM-directed templates. Some examples of these are shown in Table 6.3. A SAM, end-functionalized with carboxylic acid, can be readily coupled to the *N* termini of proteins, as well as to specific amino-acid-containing pendant amines. A terminally attached hydroquinone on an alkane thiol SAM can be electrochemically oxidized to quinone (22). The latter serves as a reagent for the effective coupling of 1,3-diolefins via the classic Diels–Alder reaction, as outlined in Figure 6.8, as a method to attach biotin to a SAM containing poly(ethylene glycol) (PEG) (23). The strong association of biotin with avidin ($K_d \sim 10^{-14}M$) allows for essentially irreversible coupling of this protein to a surface. The streptavidin\biotin couple continues to receive widespread recognition due to its versatility, although non-specific protein adsorption using this method restricts certain applications. PEG modifications, such as the one depicted in Figure 6.8, are reported to attenuate non-specific protein binding, while the biotin promotes site-directed streptavidin association with the monolayer.

By controlling functional groups that are displayed at a SAM surface, the degree of protein adsorption on to that surface can be controlled. Alkane thiols containing PEG or tripropylene sulfoxide as a means of reducing non-specific protein adsorption has been reported by several investigators (23–25). By using a hexamer PEG sequence, the adsorption of fibrinogen, a protein particularly prone to interfacial adsorption and denaturation, was suppressed to less than 0.5% of its saturated monolayer value of 250 nG/cm² (26). The mechanism through which PEG suppresses non-specific protein adsorption is believed to involve both the reduction of Coulombic forces between ionized surface functional groups and charged amino acids of the peptide and a reduction of hydrophobic interactions via the hydrated

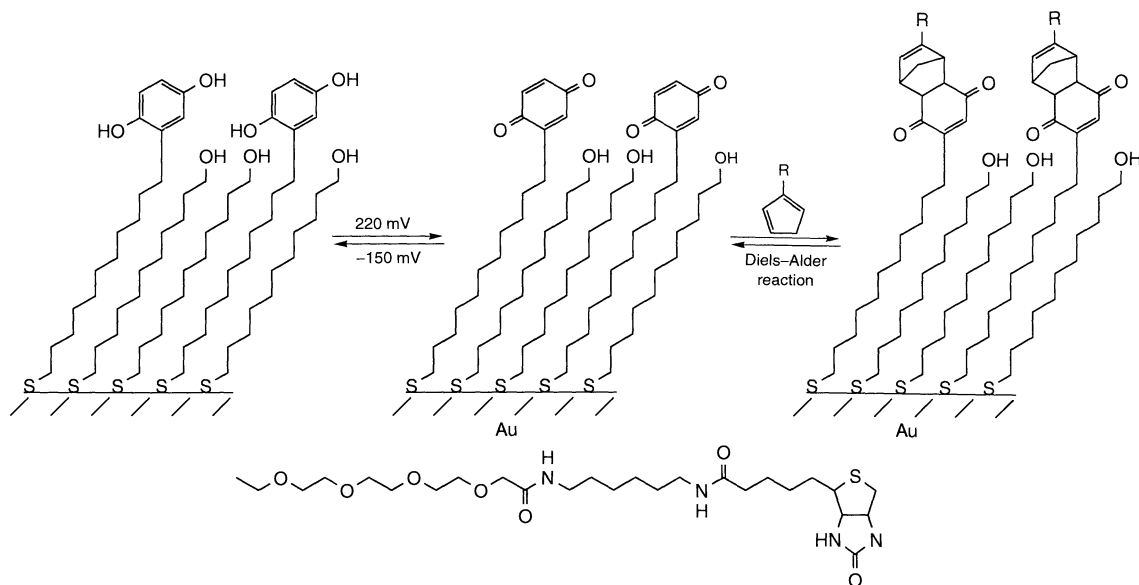


Figure 6.8. An SAM end-functionalized with an electrochemically active quinone as a Diels–Alder reagent for coupling activated dienes. Biotin can be incorporated via this method by the use of a PEG-modified diene (adapted from ref. (22))

ethylene glycol helix. For studies on cell attachment, motility and viability, the suppression of non-specific protein adsorption is essential since the medium used to propagate the cell culture contains a number of poorly classified peptides which would complicate data interpretation. Cell attachment to a surface also results in the secretion of additional adhesion molecules from the cell that “remodel” the surface and complicate the identification of specific cell surface/receptor interactions important to the initial attachment. Reducing the adsorption of these surface-remodelling proteins has been demonstrated with PEG-containing SAMs (23).

Mixed SAMs are now becoming available to provide synergistic properties which cannot be achieved by homogeneous monolayers. For example, mixtures of PEG-terminated SAMs with Self-assembling monolayers that contain controlled densities of specific ligand receptors allow for the study of cell attachment or receptor–protein interactions, while preventing non-specific protein adsorption. Mixed monolayers of thiol analogues of cholesterol and fatty acids have been reported, and provide insight into the role of cholesterol on biological membrane stability and permeability (27). As with fatty acid/cholesterol bilayers, SAMs containing these two classes of molecules show a packing density that is dependent on composition. Multi-component SAMs with increasingly sophisticated end-groups are under development in attempts to systematically introduce an

array of functionalities that model intact cell membranes.

The use of SAMs containing both PEG and arginine–glycine–aspartate (RGD) sequences to promote eucaryote cell attachment has been recently reported (28). The tripeptide RGD is known to promote cell adhesion via its binding to specific cellular transmembrane receptors known as integrins, while the PEG suppresses adsorption of media and cell adhesion proteins. RGD is a common peptide sequence found in many extracellular matrix proteins of tissue. Compositions containing as much as 5 mol% RGD, based on total PEG and RGD content, adsorbed undetectable amounts of fibrinogen, hence indicating the efficiency of PEG to suppress non-specific protein adsorption. In addition, 0.001 mol% RGD allowed for the attachment and spreading of viable bovine capillary endothelial cells to the SAM. Addition of competitive RGD sequences in solution eliminated endothelial cell attachment, consistent with specific site-directed attachment to RGD incorporated in the modified SAM. Similar results were reported with attachment of fibroblasts. These results demonstrate the value of functionalized alkane thiol SAMs for the study of cell adhesion, migration and differentiation.

SAMs functionalized with carbohydrate have also been reported (29, 30). These monolayers serve as model systems for the study of cell-surface interactions, as well as for the interactions of plasma proteins with specific

receptors on the cell surface. Expression of cell-surface carbohydrates is believed to be important in a number of biological processes, including cell differentiation, cell-to-cell signaling, cell pathogenesis and cell apoptosis.

The Gangliosides GM1 and GM2 have been incorporated into alkane SAMs via interdigitation of pendant hydrocarbon chains, thus allowing the presentation of sialic acid (*N*-acetylneuraminic acid) to the aqueous interface (Figure 6.9) (31). This lipocarbohydrate is implicated in many cell surface-signaling pathways and is prevalent in many glycoproteins, including proteoglycans. The association and binding constants of strep enterotoxins with a SAM containing sialic acid has been measured by using surface plasmon resonance.

The reactions of glucose containing a SAM with the lectin, concanavalin A, has been reported (29). This large protein complex interacts specifically with terminal *D*-glucose and *D*-mannose sugars that are frequently incorporated on complex glycoproteins which function as cell surface receptors and in transmembrane

signalling mechanisms. Glucose containing a SAM was used to construct a biosensor for yeast. By using a SAM derivatized with a disaccharide known to interact with the lectin from *Bauhinia purpurea* (BP), Whitesides and co-workers (30) have demonstrated that secondary interactions, which develop at high surface densities of the sugar, alter carbohydrate-lectin binding selectivity. At low site densities, BP shows selectivity for one carbohydrate ligand, while a shift in selectivity for a different carbohydrate ligand occurs as the site density of the sugar within the SAM increases. The principal differences between the two ligands evaluated are the conformation of the glycosidic bond joining the two cyclic sugars and the alkyl substituent on the glucoamine. This switch in selectivity suggests a mechanism by which cells can use carbohydrate site densities to control interactions with extracellular proteins. In a related study, a SAM was used to evaluate the role of carbohydrate ligand density on enzymatic glycosylation (32). The addition of galactose to *N*-acetylglucosamine via the

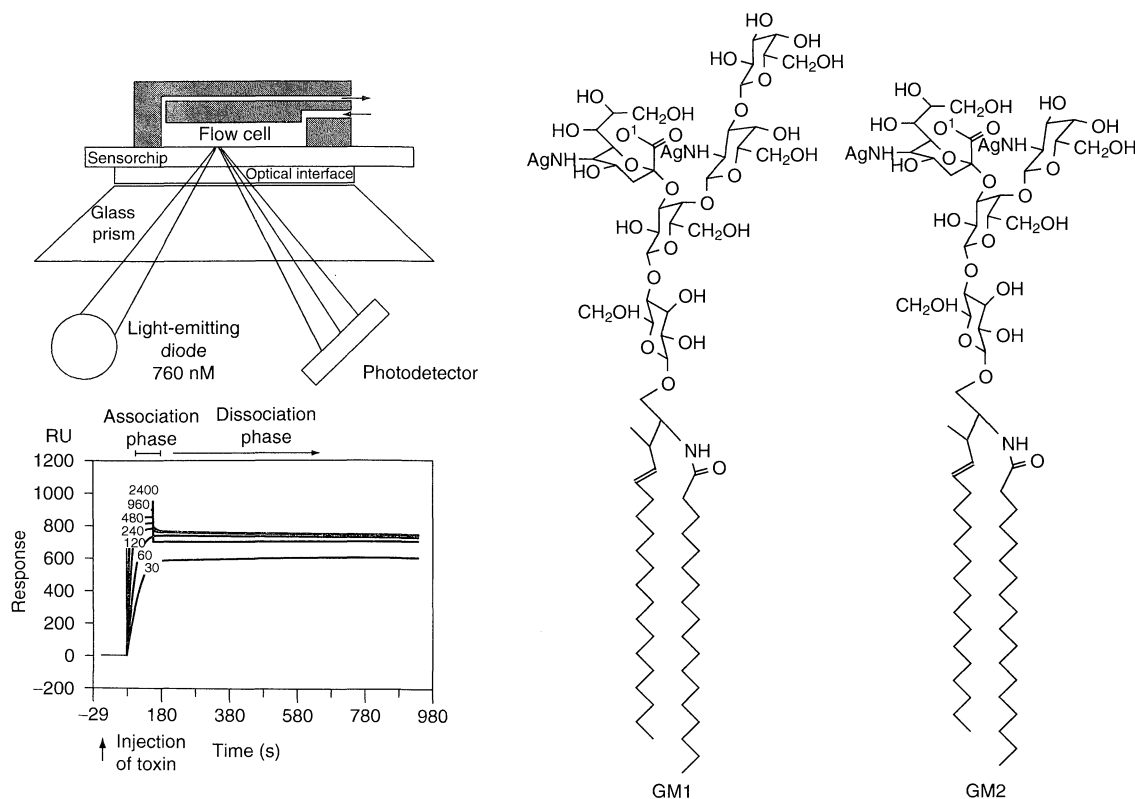


Figure 6.9. The use of surface plasmon resonance to measure interactions of strep enterotoxin with a SAM containing a ganglioside. The alkane chains of the gangliosides GM1 and GM2 interdigitated into the alkane thiol SAM (adapted from ref. (31))

enzyme, galactosyltransferase, was shown to be dependent on the density of immobilized carbohydrate. These studies demonstrated the value of a SAM to construct models for the study of complex biological interfaces. Control of site densities and selective incorporation of defined peptide and carbohydrate sequences have been demonstrated at the initial research level. This field of modifying a SAM with biologically active molecules is in its infancy, although is expected to grow, as it undoubtedly will contribute to the science and applied technology of molecular cell biology. SAM-protected colloidal particles of gold clusters or polystyrene latexes provide additional opportunities to mimic complex surface chemistries of dispersed biological systems. The field of biomimetic colloids is just beginning to develop.

4 PATTERNED SELF-ASSEMBLED MONOLAYERS

The mass transfer of a pattern of SAM-forming organic compounds to a surface via micro-contact printing (μ CP) has been pioneered by the Whitesides' group (33). The steps encompassing this process are summarized in Figure 6.10. A predetermined pattern is encoded in a master via conventional approaches such as photolithography. An electronic-grade silicon wafer is an ideal substrate for preparing the master, which is spin-coated with a photocurable polymer to produce a positive resist. Chrome metal or high-definition transparencies produced from a microfiche can be used as a photomask in

the lithography to encode the latent image of the pattern in the photopolymer (34, 35). From the processed master containing the desired pattern in a three-dimensional relief structure, a polydimethylsiloxane (PDMS) stamp is made by a metal-catalysed polymerization of liquid elastomer pre-polymer poured over the master. The room temperature viscosity of the elastomer before polymerization is sufficiently low as to allow its intimate wetting of micron-sized relief features in the master. After curing, PDMS is removed and contains a negative image of the pattern on the master. Feature sizes for patterning a SAM via this direct contact printing approach one micron, with ten microns being readily obtainable. The stamp is exposed to dilute solutions of thiol that remain on the PDMS after solvent evaporation. Alternative methods of transferring thiol to the stamp include contacting it with a thiol-containing "inking" pad or direct inclusion of the thiol into the stamp via solvent-assisted permeation (36). A comparison of these methods has been reported. Contacting a gold-coated substrate with the stamp transfers thiol from the elevated features of the stamp, thus forming a pattern of the SAM on gold that reflects the original pattern in the master. Typically, an additional thiol, end-terminated with a functionality different from that of the thiol delivered with the stamp is used to passivate the remaining areas of gold not contacted in the stamping process.

Figure 6.10 shows an electron micrograph of a PDMS stamp produced from a photolithographic master of 10 μ m diameter circles spaced 5 μ m apart (37). Note the excellent reproduction of features in the stamp that

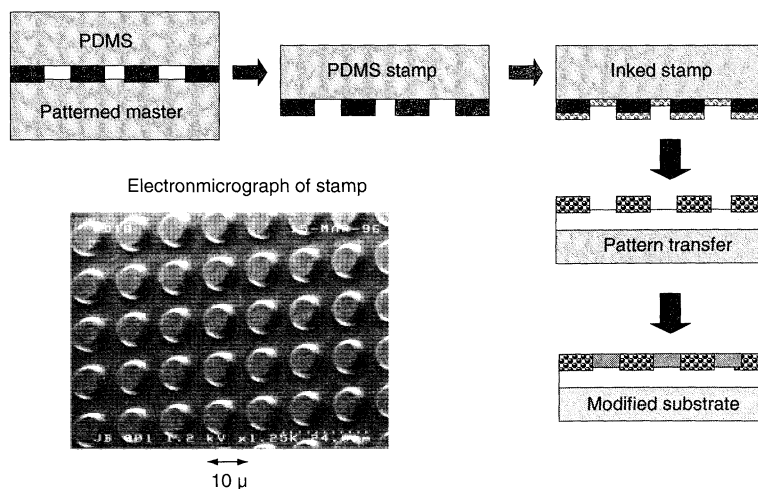


Figure 6.10. Illustration of the process of contact printing a patterned SAM on a gold-coated substrate. The electron micrograph is of a polysiloxane stamp, where the circles are 10 μ m in diameter, 2 μ m high and spaced 5 μ m apart

is the negative image of the pattern encoded in the master. More complex arrays of similar sized features with a variety of geometries and spacings are easily produced via conventional lithography.

The stamp represented in Figure 6.10 can pattern a SAM of alkane thiol on a gold-coated substrate such as borosilicate glass, tin oxide or silicon oxide. Gold-coated glass that has been primed with a sub-monolayer of Ti is the most commonly used substrate. Stamp/substrate contact times as short as 300 ms are sufficient for pattern transfer. The organization, stability and extent of coverage by the SAM transferred via rapid contact printing has been shown by scanning tunnelling microscopy, infrared spectroscopy and contact-angle measurements to be indistinguishable from a SAM prepared by equilibration adsorption from ethanol solution (38). In addition, contact printing with PDMS was shown not to disrupt the basic epitaxial organization of the gold surface (39). The ability to rapidly transfer a patterned SAM via a contact printing process offers abundant opportunities for technology development and micro-device fabrication.

The selection of omega functionality on the SAM forming compound has a tremendous effect on the surface properties of the resulting patterned organic monolayer. Figure 6.11 shows water assembled on a patterned surface energy discontinuity produced by stamping circles of 16-carboxyhexadecane thiol (CDT) on gold, followed by passivating the bare areas of gold not exposed to the elevated features in the stamp with hexadecane thiol (HDT) (40). A carboxyl-terminated, hydrophilic SAM is patterned as discontinuous 10 μm

diameter circles into a hydrophobic SAM which is methyl-terminated. This surface has well-organized surface energy discontinuities with steep wettability gradients of sub-micron dimensions existing at the circle circumference. The contact angle of water on these respective SAMs is 110° for HDT and 55° for CDT. Based on these wettability differences, the spontaneous dewetting of high-surface-tension fluids such as water from the methyl-terminated SAM to the carboxyl-terminated SAM circle is readily accomplished by controlled immersion/retraction. Water spontaneously assembles on the CDT-containing circles. These patterned surface energies have been shown to be useful for controlling a variety of optical (41), crystallization (42) and biological attachment properties (43). Condensation drops of moisture on carboxyl-terminated circles produce white light diffraction, and other high-surface-tension fluids can be assembled on to the CDT circles (44).

Field emission secondary electron microscopy (FESEM) and atomic force microscopy (AFM) studies of the patterned SAM are consistent with the expected morphology (Figures 6.12 and 6.13). Contrast between the methyl- and carboxyl-terminated SAMs is detected with both imaging microscopies. Contrast is also detected in the lateral force image in Figure 6.13 and results from differences in adhesion of terminal carboxyl versus the terminal methyl of the respective SAM with the AFM tip. These micrographs were produced from a SAM on a gold-coated substrate via contact printing with the stamps shown in Figure 6.10 (40).

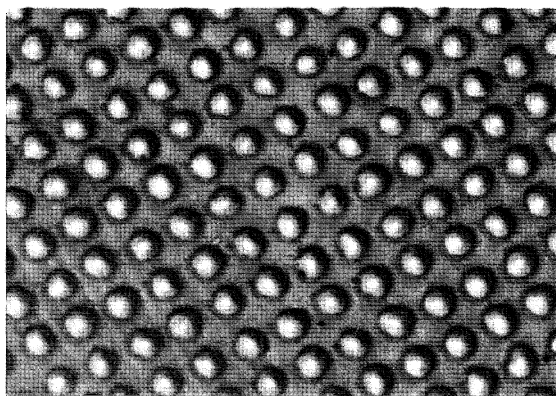


Figure 6.11. Illustration of assembly of high-surface-tension fluids on a carboxylic-acid-terminated SAM. The stamp shown in Figure 6.10 was used to produce 10 μm diameter circles of a hydrophilic SAM on to which a UV-curable polymer was assembled

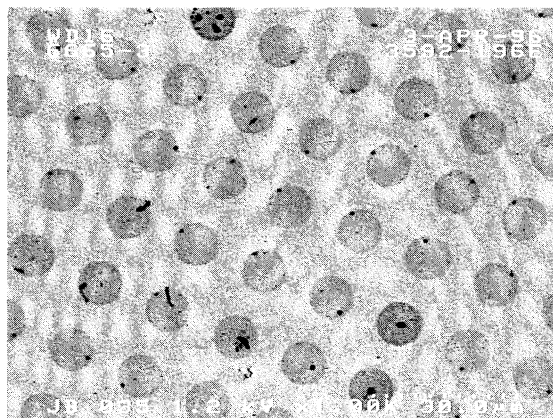


Figure 6.12. Field emission secondary electron micrograph of a 10 μm diameter carboxyl-terminated SAM on a gold-coated substrate

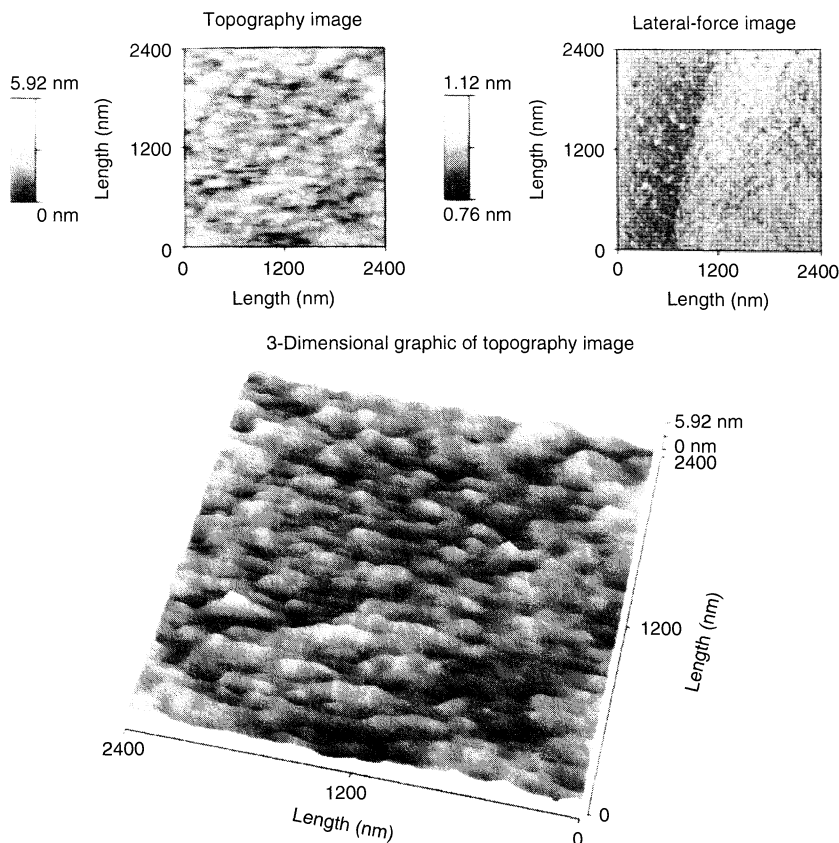


Figure 6.13. Topography and lateral-force images of a 10 μm diameter carboxyl-terminated SAM on a gold-coated substrate

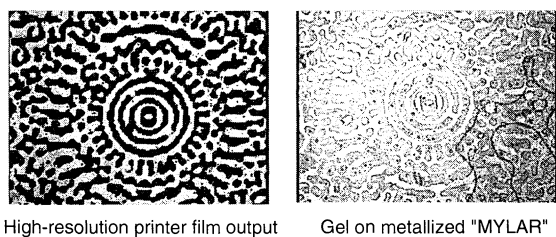


Figure 6.14. Assembly of a polymer on a complex SAM pattern. The centre of the holographic diffraction element represents an example of pattern transfer from the film to the responsive gel (intermediate steps are not shown) (adapted from ref. (40))

The ability to assemble polymers in complex patterns on SAMs is illustrated in Figure 6.14 (40). The smallest feature size obtained via this process is about 5 μm . Cellulose acetate was used as a lithographic photomask to produce a silicon stamp for μCP of a patterned SAM

on to gold-coated substrate. A photocurable mixture of acrylate copolymer was subsequently assembled to produce a gel of the original pattern. The polymer wets the hydrophilic, carboxyl-terminated SAM and de-wets from regions of methyl-terminated SAM. UV light was used to cure the assembled polymer. Accurate image definition was preserved between the photomask and the patterned polymer. These results demonstrate the ability to assemble complex patterns of a hydrophilic polymer on to a contact-printed SAM.

A patterned SAM, end-terminated with a binder to promote specific ligand attachment, can be used to localize cells, bacteria, yeast and polystyrene microspheres to a surface (29). A variety of binders are available to facilitate selective particle attachment, e.g. simple sugars, sialic acid containing gangliosides, lectins, RGD peptides and immunoglobulins have been reported. SAMs containing these receptors were discussed in the previous section. An alkane thiol derivative of a polysaccharide of glucose was prepared (29) and stamped in a

pattern of 10 μm diameter circles such as those illustrated in Figure 6.10. After washing and passivation of gold with HDT, this sample was then exposed to concanavalin A (Con A) containing a 10 nm gold colloid (useful as a Scanning electron microscopy (SEM) marker). Non-specific protein adsorption was maintained by blocking with serum albumin. Labelled Con A allows the patterned saccharide to be imaged by the back-scattering SEM contrast of the gold colloid. Figure 6.15 shows the degree of saccharide patterning that was achieved. The low-magnification image shows nice contrast definition of the circles containing the sugar/lectin complex. No significant background adsorption of lectin on HDT is detected, while no lectin adsorbed on to a CDT containing a SAM control which was void of glucose. At higher magnifications, the individual gold colloids of the labelled lectin can be resolved, a sub-micron interface exists. These results demonstrate the ability to pattern carbohydrate receptors via μCP of functionalized SAMs.

The use of a patterned-glucose SAM to study the adsorption of yeast is illustrated in Figure 6.16. Circles of sugar thiol were exposed to an aqueous solution of baker's yeast, *Saccharomyces cerevisiae* (29). After 40 min exposure, the sample becomes modified with spatially organized, assembled yeast on the areas containing glucose. Bridging of the yeast colonies is detected, thus suggesting that the adsorbed organism is viable and able to "sense" the presence of yeast colonies in close proximity. No adsorption of yeast to the hydrophobic hexadecane thiol (HDT) is detected.

Reducing the length of the carbohydrate receptor results in slower adsorption of yeast. Lower-molecular-weight sugars are more strongly affected by the steric and reduced hydration constraints of the surface, project less into solution and produce higher activation energies for attachment. Co-operative binding of cell surface

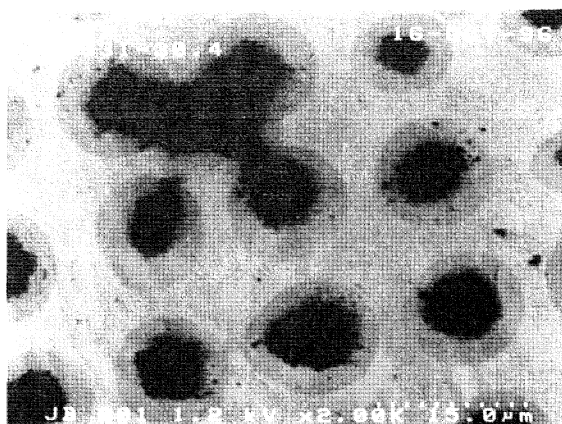


Figure 6.16. Attachment of *Saccharomyces cerevisiae* on to a patterned SAM containing glucose

receptors to carbohydrate oligomers can also facilitate more rapid adsorption and change the selectivity of specific sugar–lectin interactions (30). For a fructose receptor, the yeast has not completely covered the 10 μm diameter circles of the patterned sugar after 8 days exposure and bridging is minor. After 2 days exposure, individual yeast cells are attached as viable organisms, as determined by detected mitosis. The fraction of yeast colonies originating from multiple attachment of many organisms versus those colonies that result from the attachment of a single organism followed by its division was not determined. Control samples not containing either glucose or fructose do not adsorb the yeast, thus indicating that specific interactions of the organism with the sugar promote attachment. These results demonstrate the use of patterned SAMs to study the attachment and spatial communication of organisms on to modified surfaces.

Methodologies to produce reactive SAMs, such as inter-chain anhydrides, have been adapted to forming patterns of SAMs with μCP (45–47). Monolithic films of SAMs containing reactive pentafluorobenzyl esters were converted into patterned amides by using a stamp containing a primary amine. In the areas of contact, the amine reacts with the activated surface to form a patterned amide. Printing of benzenesulfonamide was detected by binding carbonic anhydrase (CA) to the sulfonamide-derivatized SAM. Benzenesulfonamide binds to CA with a dissociation constant of less than $10^{-7}M$. Similarly, the stamp can be treated with poly(ethylene imine) (PEI) to transfer a pattern of amide-coupled PEI, where the pendant, unreacted amine groups of PEI can be used for subsequent nucleophilic reactions. This procedure can introduce patterned biotin



10 μm diameter circle of glucose

10 nm Au colloid

Figure 6.15. Gold-labelled lectin binding to a SAM which is ω -functionalized with glucose. The gold-labelled "Concanavalin A" adsorbed on to the 10 μm diameter circles on glucose containing the SAM (adapted from ref. (40))

on a surface. Images of fluorescently labelled anti-biotin antibodies confirmed patterned association of the antigen–antibody complex. The patterning of reactive SAMs for the study of cell and biomolecule attachment to surfaces should continue to provide insight into many fundamental aspects of surface and colloid science of biological systems.

5 SELF-ASSEMBLED-MONOLAYER-PROTECTED METAL CLUSTERS

As summarized in the earlier sections of this review, a considerable amount of research has been reported during the last ten years on alkane thiols adsorbed on to gold. These materials are best described as pseudo-two-dimensional (2D) organic monolayers whose chemical and material properties often differ from those of homogeneous solution analogues. A well-documented example is the differences in S_N2 nucleophilic displacement reactions that readily occur in solution but are severely restricted on 2D surfaces due to the constraints on transition state inversion.

An emerging field of interest is three-dimensional SAMs produced by adsorbing alkane thiols on to multimetal clusters, where these materials are referred to as monolayer-protected clusters (MPCs). Due to their size, these clusters resist flocculation, are stable in solution and have organized organic monolayers at the cluster/solution interface. Reduction of tetrachloroaurate in the presence of alkane thiols was first used by Schiffrin and co-workers to prepare MPCs (48). The diameter of these SAM-stabilized nanoparticles is smaller than 5 nm and is determined by the ratio of chloroaurate to thiol, the rate of reductant addition and the reaction temperature. Clusters between 1.2 and 1.4 nm are readily synthesized and isolated, containing a cuboctahedron structure of 310–550 gold atoms and 95–175 thiolate ligands; a typical molecular formula is $Au_{145}[S(CH_2)_5CH_3]_{50}$. The number of gold atoms per cluster favour closed-shell structures having an octahedral shape.

In addition to the tremendous change in the surface/volume ratio relative to 2D-SAMs, MPCs offer a number of property improvements. Depending on the choice of end-groups on the SAM, MCPs show adequate solubilities in a number of organic solvents and are stable in oxygen atmospheres. Due to the high surface content, the concentration of exchanged thiols is amenable to quantitative solution analysis. Thiol-exchange reactions on the MPC allow formation of polyfunctionalized clusters with a controlled density of several different functional groups. Clusters are easy to isolate and

can be characterized by methods which are not readily useful for 2D-SAMs e.g. high-resolution NMR spectroscopy, UV–Visible spectroscopy, acid/base titrations, and laser desorption mass spectrometry (49–51). Flocculation of ω -functionalized MPCs containing ionizable end-groups shows a pH-dependence consistent with expected acid–base chemistry and DLVO theory (52). Electrochemistry of MPCs also allows for a detailed understanding of electron transport across the SAM and into the metal core. Multi-step insertion of electrons into the metal cluster is providing fundamental information for redox processes. Mixed metal clusters, such as those with Au:Cu, Au:Ag or Au:Cu:Ag, can be prepared since the thiolate prevents metal-core aggregation that would otherwise occur with alloyed metal colloids.

Several structural differences between 2D- and 3D-SAMs have been reported. The number of defect sites available for thiol binding is considerably higher on MPCs, with edge defects, corner sites and Au (100) terraces predominating. Defect sites account for about 43% of all gold sites for a 561-atom cluster. Unlike 2D-SAMs on gold where the thiol/Au ratio is about 0.33, up to 65% of surface sites can be occupied on MPCs. The large numbers of defect sites allow for ligand exchange reactions that are restricted for a Au (111) terrace. In addition, curvature introduced by the geometry of the cluster affects the packing and reactivity of alkanes relative to that observed for 2D-SAMs. The end-groups of MPCs are more solvated. An example of these differences is the ability of MPCs to interact via inter-cluster digitation of alkane groups.

A thorough IR characterization of MPCs has been reported (50). Using absorbance assignments from 2D systems, the degree of order and chain packing can be determined. No internal *gauche* defects are detected for chain lengths greater than about C_8 , with an increase in chain packing with longer alkane lengths. End-group defects become predominating with chain lengths greater than C_{10} , and when dispersed in solvent, the alkane structure of the MPC resembles the disordered state of liquid alkanes. The most notable differences from 2D-SAMs are associated with the chain-end disorder in MPCs.

Differences in structure have provided some important distinctions in the reactivity of 2D- and 3D-SAMs. As previously noted, ligand exchange reactions are kinetically more favourable for MPCs. In addition, S_N2 reactions known to be essentially absent in 2D-SAMs proceed with rate constants similar to those for homogeneous solution reactions for 3D-SAMs. The site inversion required for an S_N2 mechanism is severely restricted with a well-organized 2D-SAMs, whereas the

Table 6.4. Emerging applications of SAM-stabilized dispersions

Diagnostic sol particle immunoassay
microscopy labelling reagents
Chemical and biosensing
Nanoscale electronics
Homogeneous catalysis
High-order nonlinear optical
susceptibility
Biological particle surrogates

end-group mobilities of alkanes in 3D-SAMs allow facile nucleophilic displacement. The reaction of ω -bromo-functionalized MPCs with substituted amines proceeds at rates and yields typical for homogeneous reactions in solution. The decomposition of a gold MPC by cyanide follows a first-order decay and is most rapid for short-chain-length alkanes. Increasing the chain length up to C₁₀ retards the CN-induced decomposition after which the decay rate becomes independent of the chain length. A complete resistance to the cyanide etching of MPCs has not yet been achieved (52). These results are consistent with a gradient of chain-packing density from the core to the outer surface of the cluster/solution interphase. Although still in its infancy, MPCs show promise for technology development in a number of fields, some of which are highlighted in Table 6.4. The understanding and evolution of these materials should help bridge gaps between the material science of condensed states and the chemistry of homogeneous solutions.

6 CONCLUSIONS

It is apparent from this review that self-assembling monolayers (SAMs) offer the capability to develop well-ordered organic coatings with defined surface functionalities. SAMs allow for the control of structure and chemistry of organic surfaces that was not possible prior to their discovery in the 1980s.

One of the most useful SAM platforms is alkane thiols adsorbed on to gold. Stable and chemically defined organic surfaces are readily produced via techniques that are common to the modern laboratory. Multi-layer, lateral gradients and SAMs with combinations of surface chemistries can be easily synthesized. A plethora of surface characterization techniques have been adapted to elucidate the molecular reactivity and structure of such surfaces.

Surfaces modified with functionalized SAMs are finding use in the study of cell and molecular biology, materials science, chemical and biosensing, heterogeneous catalysis and nonlinear optical phenomena. The science and technology of SAMs will undoubtedly continue to develop in parallel with the trends and needs for miniaturized devices displaying control of surface and interface structure at the molecular level.

7 REFERENCES

1. Pockels, A. Surface tension, *Nature (London)*, **43**, 437–439 (1891).
2. Moses, P. R. and Murray, R., Chemically modified electrodes. 3. Tin dioxide and titanium dioxide electrodes bearing an electroactive reagent, *J. Am. Chem. Soc.*, **98**, 7435–7436 (1976).
3. Untereker, D. F., Lennox, J. C., Wier, L. M. and Murray, R., Chemically modified electrodes. Part IV. Evidence for formation of monolayers of bonded organosilane reagents, *J. Electroanal. Chem., Interfacial Electrochem.*, **81**, 309–318 (1977).
4. Buttry, D. A. and Anson, F. C. J., Electrochemically active polymer films, *Electroanal. Chem. Interfacial Electrochem.*, **130**, 333–338 (1981).
5. Rubinstein, I. and Bard, A. J., Polymer-films on electrodes. 5. Electrochemistry and chemiluminescence at Nafion-coated electrodes, *J. Am. Chem. Soc.*, **103**, 5007–5012 (1981).
6. Nuzzo, R. G. and Allara, D. L., Adsorption of bifunctional organic disulfides on gold surfaces, *J. Am. Chem. Soc.*, **105**, 4481–4483 (1983).
7. Brovelli, D., Hahner, G., Ruiz, L., Hofer, R., Kraus, G., Waldner, A., Schlosser, J., Oroszlan, P., Ehrat, M. and Spencer, N., Highly oriented self-assembled alkanephosphate monolayers on tantalum (V) oxide surfaces, *Langmuir*, **15**, 4324–4327 (1999).
8. Hanken, D. and Corn, R., Variable index of refraction ultrathin films formed from self-assembled zirconium phosphonate multilayers: characterization by SPR measurements and polarization/modulation FT-IR spectroscopy, *Anal. Chem.*, **67**, 3767–3774 (1995).
9. Bain, C. D., Evall, J. and Whitesides, G. M., Formation of monolayers by the coadsorption of thiols on gold: variation in the head group, tail group, and solvent, *J. Am. Chem. Soc.*, **111**, 7155–7164 (1989).
10. Leung, R. and Shah, D. O, Dynamic properties of micellar solutions, *J. Colloid Interface Sci.*, **113**, 484–490 (1986).
11. Ulman, A., Monolayers having large in-plane dipole moments: characterization of sulfone-containing self-assembling monolayers of alkanethiols on gold by Fourier transform infrared spectroscopy, X-ray photoelectron spectroscopy and wetting, *Langmuir*, **7**, 2700–2706 (1991).
12. Xiaom, and Whitesides, G. M., Soft lithography, *Angew. Chem. Int. Ed. Engl.*, **37**, 550–575 (1998).

13. Atre, S., Liedberg, B. and Allara, D., Chain length dependence of the structure and wetting properties of binary composition monolayers of OH- and CH₃-terminated alkanethiolates on Gold, *Langmuir*, **11**, 3882–3893 (1995).
14. Benziger, J., Infrared spectroscopy of surfaces, in *The Handbook of Surface Imaging and Visualization*, Hubbard, A. (Ed.), CRC Press, Boca Raton, FL, 1995, Ch. 21, pp. 265–288.
15. Dannenberger, O., Buck, M. and Grunze, M., Self-assembly of *n*-alkanethiols: a kinetic study by second harmonic generation, *J. Phys. Chem.*, **103**, 2202–2208 (1999).
16. Ulman, A., *An Introduction to Ultrathin Organic Films from Langmuir–Blodgett to Self-Assembly*, Academic Press, San Diego, CA, 1991.
17. Huang, J. and Hemminger, J. C., Photooxidation of thiols in self-assembled monolayers on gold, *J. Am. Chem. Soc.*, **115**, 3342–3343 (1993).
18. Peterlinz, K. and Georgiadis, R., *In situ* kinetics of self-assembly by surface plasmon resonance spectroscopy, *Langmuir*, **12**, 4731–4740 (1999).
19. Liedberg, B. and Tengvall, P., Molecular gradients of ω -substituted alkanethiols on gold: preparation and characterization, *Langmuir*, **11**, 3821–3827 (1995).
20. Yan, L., Marzolin, C., Terfort, A. and Whitesides, G. M., Formation and reaction of interchain carboxylic anhydride groups on self-assembled monolayers on gold, *Langmuir*, **13**, 6704–6712 (1997).
21. Yan, L., Zhao, X. and Whitesides, G. M., Patterning a preformed, reactive SAM using microcontact printing, *J. Am. Chem. Soc.*, **120**, 6179–6180 (1998).
22. Yousaf, M. and Mrksich, M., Diels–Alder reaction for the selective immobilization of protein to electroactive self-assembled monolayers, *J. Am. Chem. Soc.*, **121**, 4286–4287 (1999).
23. Houseman, B. and Mrksich, M., Efficient solid-phase synthesis of peptide-substituted alkanethiols; the preparation of substrates that support the adhesion of cells, *J. Org. Chem.*, **63**, 7552–7555.
24. Prime, K. L. and Whitesides, G. M., Self-assembled organic monolayers: model systems for studying adsorption of proteins at sur., *Science*, **252**, 1164–1167 (1991).
25. Li, D., Mrksich, M. and Whitesides, G. M., Self-assembled monolayers of alkanethiolates presenting tris(propylene sulfoxide) groups resist the adsorption of protein, *J. Am. Chem. Soc.*, **118**, 5136–5137 (1996).
26. Mrksich, M., Signal, G. and Whitesides, G. M., Surface plasmon resonance permits *in situ* measurements of protein adsorption on self-assembled monolayers of alkanethiolates on gold, *Langmuir*, **11**, 4383–4385 (1995).
27. Yang, Z., Engquist, I., Wirde, M., Kauffmann, J., Ulrik, G. and Liedberg, B., Preparation and characterization of mixed monolayer assemblies of thiol analogs of cholesterol and fatty acids, *Langmuir*, **13**, 3210–3218 (1997).
28. Roberts, C., Chen, C., Mrksich, M., Martichonok, V., Ingber, D. and Whitesides, G. M., Using mixed self-assembled monolayers presenting RGD and (EG)_nOH groups to characterize long-term attachment of bovine capillary endothelial cells to surfaces, *J. Am. Chem. Soc.*, **120**, 6548–6555 (1998).
29. Everhart, D., Grunze, M., Kaylor, R. and Morhard, F., Biosensing Devices which produce Diffraction images, *US Patent 5 922 550* (1999).
30. Horan, N., Yan, L., Isobe, H., Whitesides, G. and Kahne, D., Nonstatistical binding of a protein to clustered carbohydrates, *Proc. Natl. Acad. Sci. USA*, **96**, 11782–11786 (1999).
31. Stevens, R., Cholera toxin binding affinity and specificity for gangliosides determined by surface plasmon resonance, *Biochemistry*, **35**, 6375–6380 (1996).
32. Houseman, B. and Mrksich, M., The role of ligand density in the enzymic glycosylation of carbohydrates presented on self-assembled monolayers of alkanethiolates on gold, *Angew. Chem. Int. Ed. Engl.*, **38**, 782–850 (1999).
33. Kumar, A. and Whitesides, G., Features of gold having micrometer to centimeter dimensions can be formed through a combination of stamping with an elastomeric stamp and an alkanethiol “ink” followed by chemical etching, *Appl. Phys. Lett.*, **63**, 2002–2004 (1993).
34. Qin, D., Xia, Y., Black, A. and Whitesides, G., Photolithography with transparent reflective photomasks, *J. Vac. Sci. Technol. B*, **16**, 98–103 (1998).
35. Deng, T., Tien, J., Xu, B. and Whitesides, G., Using patterns in microfiche as photomasks in 10 μ m-scale micro-fabrication, *Langmuir*, **19**, 6575–6581 (1999).
36. Libiouille, L., Bietsch, A., Schmid, H., Michel, B. and Delamarche, E., Contact-inking stamps for microcontact printing of alkanethiols on gold, *Langmuir*, **15**, 300–304 (1999).
37. Everhart, D., Methods of contact printing on gold coated films, *US Patent 6 048 623* (2000).
38. Larsen, N., Biebuyck, H., Delamarche, E. and Michel, B., Order in microcontact printed self-assembled monolayers, *J. Am. Chem. Soc.*, **119**, 3017–3026 (1997).
39. Poirier, G. and Pylant, E., The self-assembly mechanism of alkanethiols on Au(111), *Science*, **272**, 1145–1148 (1996).
40. Everhart, D., Using self-assembling monolayers for sensors, *Chemtech*, 30–37 (April 1999).
41. Chen, C., Mrksich, M., Sui, H., Whitesides, G. and Ingber, D., Geometric control of cell life and death, *Science*, **276**, 1425–1428 (1997).
42. Aizenberg, J., Black, A. and Whitesides, G., Engineering the microenvironment of crystals nucleation and growth using micropatterned polymers, *Polym. Mater. Sci. Eng.*, **81**, 2–3 (1999).
43. Mrksich, M., Dike, L., Tien, J., Ingber, D. and Whitesides, G., Using microcontact printing to pattern the attachment of mammalian cells to self-assembled monolayers of alkanethiolates on transparent films of gold and silver, *Exp. Cell. Res.*, **235**, 305–313 (1997).
44. Kumar, A. and Whitesides, G., Patterned condensation polymerization as optical diffraction gratings, *Science*, **263**, 60–62 (1994).

45. Yan, L., Zhao, X. and Whitesides, G., Patterning a pre-formed, reactive SAM using microcontact printing, *J. Am. Chem. Soc.*, **120**, 6179–6180 (1998).
46. Lahiri, J., Ostuni, E. and Whitesides, G., Patterning ligands on reactive SAMs by microcontact printing, *Langmuir*, **15**, 2055–2060 (1999).
47. Yan, L., Huck, W., Zhao, X. and Whitesides, G., Patterning thin films of poly(ethylene imine) on a reactive SAM using microcontact printing, *Langmuir* **15**, 1208–1214 (1999).
48. Brust, M., Walker, M., Bethell, D., Schiffrin, D. and Whyman, R., Synthesis of thiol-derivatised gold nanoparticles in a two-phase liquid–liquid system, *J. Chem. Soc. Chem. Commun.*, 801–807 (1994).
49. Hostetler, M., Stokes, J. and Murray, R., Infrared spectroscopy of three-dimensional self-assembled monolayers: *N*-alkanethiolate monolayers on gold cluster compounds, *Langmuir*, **12**, 3604–3612 (1996).
50. Templeton, A., Hostetler, M., Kraft, C. and Murray, R., Reactivity of monolayer-protected gold cluster molecules: steric effects, *J. Am. Chem. Soc.*, **120**, 1906–1911 (1998).
51. Hostetler, M., Zhong, C., Yen, B. and Murray, R., Stable, monolayer-protected metal alloy clusters, *J. Am. Chem. Soc.*, **120**, 9396–9397 (1998).
52. Weisbecker, C., Merritt, M. and Whitesides, G., Molecular self-assembly of aliphatic thiols on gold colloids, *Langmuir*, **12**, 3763–3772 (1996).

PART 4

PHENOMENA IN SURFACE

CHEMISTRY

CHAPTER 7

Wetting, Spreading and Penetration

Karina Grundke

Institute of Polymer Research, Dresden, Germany

1	Introduction	119			
2	Thermodynamics of Wetting	121			
2.1	Contact angle, Laplace and Young's equations	121			
2.2	Modification of Young's equation	122			
2.2.1	Film pressure concept	122			
2.2.2	Line tension approach	123			
2.3	Spreading parameter, work of cohesion and adhesion	124			
2.4	Wettability of solid surfaces	126			
2.4.1	Critical surface tension	126			
2.4.2	Geometric mean combining rule	127			
2.4.3	Equation-of-state approach for solid-liquid interfacial tensions	127			
2.4.4	Surface tension component approaches	128			
2.5	Contact angles on imperfect solid surfaces	129			
2.5.1	Equilibrium contact angles on a rough surface	129			
2.5.2	Equilibrium contact angles on a chemically heterogeneous surface	130			
2.5.3	Causes of contact angle hysteresis	130			
2.5.4	Definitions of contact angles	133			
3	Dynamics of Spreading	134			
3.1	Tanner's law	134			
3.2	Precursor film	134			
3.3	Spreading on inhomogeneous surfaces	135			
3.4	Spreading of solutions	136			
4	Wetting Caused by Capillary Penetration	136			
4.1	Driving force for capillary penetration	136			
4.2	Kinetics of penetration	138			
4.3	Wettability of porous solids	138			
5	References	140			

1 INTRODUCTION

Wetting involves the interaction of a liquid with a solid, including the formation of a contact angle at the solid/liquid/fluid interface, the spreading of a liquid over a surface (displacing the fluid initially in contact with that surface), or the penetration of a liquid into a porous solid medium. Wetting and non-wetting phenomena are ubiquitous in the natural and technological worlds. Examples include droplet spreading on leaves

during insecticide spraying or the self-cleaning of plant surfaces through rain, fog or dew due to the interdependence between water repellency, surface roughness and reduced particle adhesion. The flow of oil and water through the porous rock of an oil reservoir and the rise of nutrient-bearing fluids in the stem of a plant are examples of situations strongly influenced by capillary forces. Such forces are, at least in part, determined by the wetting of a solid surface by the two fluid phases involved. Wetting phenomena are also of considerable technical interest. Many technological processes

include the wetting of solids by liquids, such as painting, printing, coating and textile finishing, polymer blending or reinforcement of polymers with fibres, and mineral flotation. The importance of wettability in adhesion is also well-known: the quality of adhesive bondings and coatings depends strongly on the spreading of these materials on the adherend or solid substrate. The reason is that for good adhesion to take place, the adhesive and the adherend must come into intimate contact. Most liquids in these technical solid/fluid systems are solutions, melts or even multi-component systems, such as paints or lubricants. The solid may have a simple surface or a porous structure (membranes), or be finely divided (powders, fibres, etc.).

Despite their importance, wetting, spreading and capillary penetration mechanisms and the related controlling factors are still poorly understood. This present chapter is concerned with basic principles and relationships, including recent developments in this area which are important for different fields of applied surface and colloid chemistry. It is not a comprehensive review of the literature. In the past two decades, many theoretical and experimental studies have demonstrated that both the static and dynamic properties of wetting exhibit a great variety of behaviours depending on the liquid and on the substrate. Because of the immense quantity of theoretical and experimental knowledge that is now available, one has to focus on some selected subjects.

At first, *the thermodynamics of wetting* are reviewed. A large number of wetting phenomena can be explained by using the classical thermodynamic and mechanical description of capillarity which has been put forward by Gibbs, Laplace and Young in the 19th century. This deals with the macroscopic behaviour of interfaces rather than with the details of their molecular structure, and is reviewed in the texts by Adamson (1), Rowlinson and Widom (2), and Neumann and Spelt (3). In the centre of the classical theory of capillarity is the notion of interfacial tension, γ_{ij} , which is the free energy necessary to increase the contact area between two different phases i and j . Gaydos, Neumann and co-workers (4) developed a generalized theory of capillarity that is based on the Gibbs' concept of the dividing surface; their treatment differs from the classical theory in that it is not restricted to moderately curved liquid–fluid interfaces, and also explicitly considers the role of contact lines in addition to surface phases.

Special emphasis is given on the *contact angle concept*. Contact angles are often used simply as empirical parameters to quantify the wettability in technical solid–liquid systems. However, it is of great

fundamental, but also practical interest, to know *how the contact angle depends on the chemical composition of both the solid and the liquid*. The pioneering work on this goes back to Zisman (5). Today, it is generally agreed that the measurement of contact angles of pure liquids with known surface tensions on a given solid surface is the most practical way to obtain the solid–vapour surface tension. Unfortunately, the interpretation of contact angles in terms of solid surface tensions has been very controversial between the two major schools, i.e. the equation-of-state approach (6) and the surface tension component approach (7). At the centre of contact angle research is Young's equation, which is valid for an ideal solid surface, namely a perfectly smooth, chemically homogeneous, rigid, insoluble and non-reactive surface. However, most real solid surfaces are rough and chemically heterogeneous to some extent. In addition, swelling and reorientation of functional surface groups may occur on solid surfaces. As a result, apparent contact angles on real surfaces exhibit hysteresis. At present, many questions relating to the contact angle hysteresis and interpretation of contact angles still remain unanswered (8, 9).

In the second part of this chapter, the *spreading of a liquid on a solid surface* is considered as a *dynamic process*. This is a very complicated process because it is related to fluid dynamics, surface physics and to physical chemistry (wettability). There are features of spreading that cannot be described sufficiently by classical capillarity. Decisive progress could be achieved in the understanding of spreading and wetting phenomena by considering the effects of long-range forces and adding these to the classical capillarity descriptions. New theoretical approaches have led to a general framework in which many experimental observations on spreading can be explained. It has been shown that universal laws, experimentally found at the macroscopic level, result from processes occurring on a microscopic scale, typically between 1 and 100 nm (10–15).

In the last part of this review, *wetting* is considered as a *capillary penetration* phenomenon. The subject of porous media wettability is very important in pharmaceutical practice for preparing compacted powder tablets, or in the paint industry for dispersing pigments in organic solvents for paints or in printing inks on papers and fabrics. The term “wicking” has often been used in a broader practical sense to describe the spontaneous flow of a liquid in a porous substrate as driven by capillary forces. The processes of fluid movement inside porous media are extremely complex due to the irregular morphology of the pore space and solid surface (16).

Several key review articles and textbooks on wetting, spreading and penetration phenomena have been consulted in order to prepare this chapter.

2 THERMODYNAMICS OF WETTING

2.1 Contact angle, Laplace and Young equations

From the point of view of thermodynamic equilibrium, complete and partial wetting are two distinct equilibrium regimes. Complete wetting means that the contact angle between a liquid and a flat solid surface is zero ($\theta_e = 0$, see Figure 7.1(c)). In this case, the liquid forms a very thin film on the solid surface and the long-range character of the molecular interactions must be taken into account (10, 12, 13, 17, 18).

Partial wetting occurs if the contact angle is finite ($\theta_e > 0$, see Figures 7.1(a) and 7.1(b)). The liquid does not spread down to a mesoscopic or a microscopic thickness. Thus, it can be described in terms of macroscopic quantities, as will be discussed in this section. Partial wetting, with contact angles greater than 90° (Figure 7.1(a)), are often called “non-wetting” situations when the liquid tends to “ball-up” and run off the surface easily.

In the case of partial wetting, the liquid drop deposited on a solid surface will form an equilibrium shape. Classical capillarity predicts this equilibrium shape, which obeys the Laplace law, as follows:

$$\Delta P = \gamma \left(\frac{1}{R_1} + \frac{1}{R_2} \right) \quad (7.1)$$

According to this well-known equation, the pressure difference ΔP across a liquid–fluid interface is related to its interfacial tension γ and curvature, where R_1 and R_2 are the principal radii of curvature. Derivations of this equation which describes the mechanical equilibrium condition for the liquid–fluid interface can be found in several textbooks (see, for instance, refs (1) and (3)).

The equilibrium in the boundary region between two bulk phases can be treated mathematically, by

using either the concept of “surface tension” or the (mathematically) equivalent concept of “surface free energy”. Because of this mathematical equivalence, both terms can generally be used interchangeably. Frequently, the terms “surface tension” or “surface free energy” are used if one of the phases is a gas or a vapour. The term “interfacial tension” is often used to describe the tension between two immiscible liquids, i.e., water and oil. The terms “interfacial tension” or “interfacial free energy” are also used in a more general sense to describe the free energy of solid–liquid, solid–vapour, liquid–vapour and liquid–liquid interfaces.

The surface tension can be defined as a force per unit length (1). If the value of this force per unit length is denoted by γ , then the work done in extending a movable side by a distance dx is given by the following:

$$\text{work} = \gamma l dx \quad (7.2)$$

Since $l dx = dA$, this gives the change in area and equation (7.2) can be equally written as follows:

$$\text{work} = \gamma dA \quad (7.3)$$

Now, γ represents the work required by any reversible process to form a unit area of new surface. This parameter is generally reported in dyn/cm or mN/m, but also in erg/cm² or mJ/m², which have the same numerical values. In the case of normal pure liquids, only plastic deformation is possible and the total work in deforming the surface is just γ . In the case of solids, both plastic and elastic deformations are possible. A new surface area can also be created elastically by stretching a pre-existing surface. These elastic deformations are described by the surface stress, f . The relationship between the surface stress f and the surface tension γ is given by the following equation (19):

$$f_{ij} = \gamma \delta_{ij} + \left(\frac{\delta \gamma}{\delta \varepsilon_{ij}} \right) \quad (7.4)$$

where ε_{ij} is the surface strain tensor and δ_{ij} is the Kronecker delta (parameter). It can be seen from equation (7.4) that surface stress and surface tension

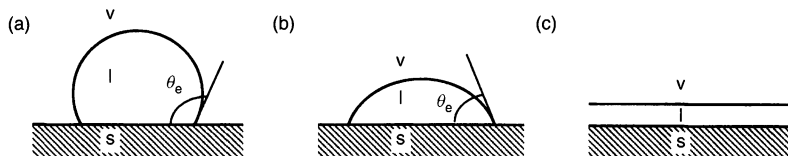


Figure 7.1. Different wetting situations of a small droplet in contact with a solid surface, where (a) and (b) correspond to partial wetting ($\theta_e > 0$), and (c) corresponds to complete wetting ($\theta_e = 0$)

www.irani-mavad.com

will be numerically equal only if γ is unaffected by deformation. Since the surface stress for liquids is isotropic with zero shear components, it can be characterized by a single quantity, f , where $f = \gamma$. Because of the low mobility of molecules in solids, it is not possible to keep constant the local configuration around any particular molecule in the surface region where the deformation of the surface area is performed. Therefore, for solids γ will be altered, i.e. $(\delta\gamma/\delta\varepsilon_{ij}) \neq 0$. Even at elevated temperatures, where the mobility of the molecules in the solid is higher, it is expected that $(\delta\gamma/\delta\varepsilon_{ij}) \neq 0$ so that the surface tension and surface stresses, generally, not be numerically equal in solids (19).

According to the thermodynamics of interfaces, γ_{ij} can be described as the area derivative of the surface free energy per unit area of an interface, either a solid–vapour, solid–liquid, liquid–liquid or liquid–vapour interface, respectively:

$$\gamma_{ij} = \left(\frac{\partial G}{\partial A_{ij}} \right)_{T,p,n} \quad (7.5)$$

or:

$$\gamma_{ij} = \left(\frac{\partial F}{\partial A_{ij}} \right)_{T,V,n} \quad (7.6)$$

where G is the Gibbs free energy of the system and F the Helmholtz free energy, and A_{ij} the area of the interface between phases i and j . The subscript “ n ” denotes the assumption of adsorption equilibrium, in the case of multi-component systems. In the thermodynamics of interface-containing systems, both quantities, i.e. the Gibbs and the Helmholtz free energies, are defined as excess quantities, thus drawing an imaginary and arbitrary dividing mathematical surface (Gibbs surface) between the two phases separated by the interface.

Three interfaces come into play if a liquid drop is deposited on a solid surface, and three interfacial tensions are involved: γ_{sv} , γ_{sl} and γ_{lv} , respectively the solid–vapour, solid–liquid and liquid–vapour interfacial tensions. The mechanical equilibrium of the triple line fixes the value of the contact angle θ_e at which the liquid–vapour interface meets the solid plane defined by Young’s relationship (Figure 7.2):

$$\cos \theta_e = \frac{\gamma_{sv} - \gamma_{sl}}{\gamma_{lv}} \quad (7.7)$$

It should be noticed that Young’s law is valid even in the presence of gravity because it stems from a mechanical equilibrium condition on the contact line where the effect of the body forces are vanishingly small. Gravity affects the shapes of sessile liquid drops in their central

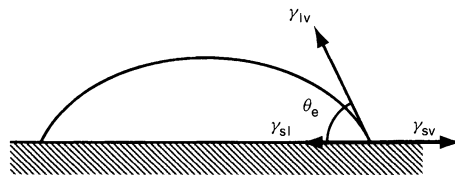


Figure 7.2. Young’s force balance giving the equilibrium contact angle

region where they are flattened, but not in a small region close to the contact line where the angle is given by Young’s law. Nevertheless, there are several problems and limitations of Young’s equation, mainly due to the structure and constitution of the solid surface and the mutual interactions of the three phases in the close vicinity of the contact line.

2.2 Modification of Young’s equation

Modification of the Young equation is required if the interfacial tension of the solid–vapour interface is changed due to adsorption of species from the vapour. In order to solve this problem, the film pressure concept was introduced (1). In addition, molecular interactions between the three phases that meet at the contact line may affect the interfacial tensions between each pair of phases. This problem is still an open one. An attempt to solve it was the introduction of the line tension concept (20). In the very vicinity of the contact line, the so-called “core region” (10), the situation is more complex and the validity of the macroscopic approach must be questioned. However, if partial wetting occurs in macroscopic experiments (radii of curvature are much larger than the radius of the core region which is often $r_c < 10$ nm), it is proposed that the equilibrium contact angle, θ_e , is related to the interfacial tensions between the three phases without any knowledge of the core region (10).

2.2.1 Film pressure concept

The solid surface in a solid–liquid–vapour system may be modified by adsorption from the vapour phase. Depending on the nature of the liquid, i.e. non-volatile liquids or volatile liquids, one has to distinguish between “dry” wetting and “moist” wetting, corresponding to two extreme situations. In the case of dry wetting, the vapour pressure of the liquid is negligible and it is assumed that the liquid molecules, adsorbed on the solid surface, do not significantly change the surface

properties during wetting. If moist wetting occurs, the drop is in equilibrium with the vapour of the liquid (1) and usually a film of liquid is adsorbed on the solid surface. The film may become thick and even macroscopic in the case of complete wetting. Since wetting processes usually take place under a more or less controlled atmosphere, the gas phase does not only contain the vapour of the liquid, but also other gases. This effect of adsorption can be expressed by the following equation for the interfacial tension γ_{sv} of the modified solid surface:

$$\gamma_{sv} = \gamma_{sv}^0 - \pi_{e(sv)} \quad (7.8)$$

where γ_{sv}^0 is the surface tension of the bare solid and $\pi_{e(sv)}$ is the so-called “film pressure”. Since adsorption is a spontaneous process, the interfacial tension, γ_{sv} , after adsorption is lower than that of the bare solid. The parameter $\pi_{e(sv)}$ can be determined according to the following equation by measuring the adsorption of the vapour of the liquid:

$$\pi_{e(sv)} = RT \int_0^{P_{sat}} \Gamma(P) d \ln P \quad (7.9)$$

where $\Gamma(P)$ is the adsorbed amount of the vapour on the solid surface. This amount can be measured by ellipsometry (1). The film pressure can also be obtained from Derjaguin’s disjoining pressure isotherm (21). The disjoining pressure, $\pi(h)$, is a function of the film thickness. It is expressed in terms of the Gibbs free energy per unit area of the film. According to Frumkin and Derjaguin, the equilibrium macroscopic contact angle is a function of the disjoining pressure, as follows:

$$\gamma_{lv} \cos \theta_e = \gamma_{lv} + \int_0^\infty \pi(h) dh = \gamma_f(h) - \gamma_{sl} \quad (7.10)$$

where $\gamma_f(h)$ is the film tension. For an infinite film thickness, $h = \infty$, $\cos \theta_e = 1$, $\pi(h) = 0$, and $\gamma_f(h) = \gamma_{lv} + \gamma_{sv}$.

It is assumed that the term $\pi_{e(sv)}$ is usually unimportant for non-wetting liquids (1), but it is quite possible that vapour adsorption can be important for more hydrophilic surfaces, particularly if $\gamma_{lv} \sim \gamma_{sv}$ or $\gamma_{lv} < \gamma_{sv}$. Unfortunately, one cannot distinguish the effect of vapour adsorption on the contact angle from other effects.

2.2.2 Line tension approach

Another problem which is still an open one is the fact that the interfacial tensions that appear in Young’s equation (equation (7.7)) are those evaluated far from

the contact line. Young’s equation ignores the three-phase molecular interactions at the line between the solid, liquid and fluid phases. The interfacial tensions at the contact line may have different values. The introduction of the line tension as a correction term that accounts for the three-phase molecular interactions was an attempt to solve this problem. It is assumed that line tension effects have important implications in a number of areas, as, for example, in heterogeneous nucleation or composite energetics of thin soap films. Depending upon the magnitude of the line tension and the characteristic length-scale of the system, it may also have an impact on the wetting/spreading of liquids, spontaneous emulsification and cell adhesion.

In complete analogy to the accepted thermodynamic definitions for pressure and surface tension, line tension is the one-dimensional analogue of surface tension, just as surface tension is the two-dimensional analogue of bulk pressure. Although the line tension is a well-defined thermodynamic quantity, there is still a large number of problems associated with determining both the magnitude and sign of this parameter (20).

On smooth, homogeneous, and horizontal solid surfaces, a liquid drop would form a circle of contact with radius R , and the corresponding corrected Young’s equation can be expressed as follows:

$$\frac{\sigma}{R} + \gamma^{(lv)} \cos \theta_l = \gamma^{(sv)} - \gamma^{(sl)} \quad (7.11)$$

where R is the radius of the solid–liquid contact circle in the tangent plane of the solid and σ is the line tension (20). If the drop is extremely large ($R \rightarrow \infty$), the corrected Young’s equation may be replaced by the classical Young’s equation, as follows:

$$\gamma^{(lv)} \cos \theta_\infty = \gamma^{(sv)} - \gamma^{(sl)} \quad (7.12)$$

where θ_∞ is the contact angle for a large (infinite) drop. Rearranging equations (7.11) and (7.12) yields the following:

$$\cos \theta_l = \cos \theta_\infty - \frac{\sigma}{\gamma^{(lv)} R} \quad (7.13)$$

If θ_l is measured as a function of R , a plot of $\cos \theta_l$ versus $1/R$ permits one to determine both the contact angle θ_∞ at infinite radius, from the intercept, and the line tension, σ , from the slope. From equation (7.13), it can be concluded, that $\cos \theta_l$ should be a linear function of $1/R$, provided that both the line tension and the liquid surface tension are constant. Figure 7.3 shows the hypothetical behaviour of both the contact angle θ and the cosine of the contact angle as a function of the drop size when the line tension is a contributing factor to the

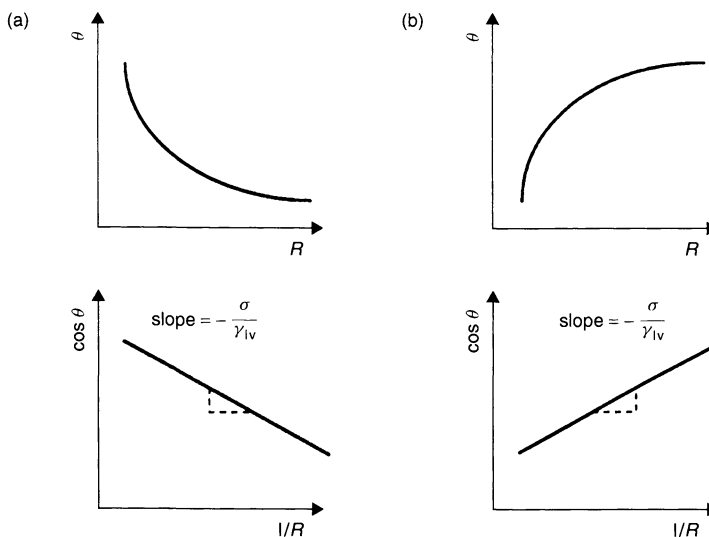


Figure 7.3. Schematic representations of the contact angle, θ , and cosine of the contact angle, $\cos \theta$, versus the drop contact radius, R , and the reciprocal of the drop contact radius, $1/R$, respectively, when the line tension, σ , is a contributing factor to the mechanical equilibrium of the contact line: (a) case of positive line tension; (b) hypothetical negative line tension (from ref. (20)), reproduced by permission of Marcel Dekker Inc

mechanical equilibrium of the contact line, i.e. the line tension term is present in Young's equation, either as a positive (Figure 7.3(a)) or a negative (Figure 7.3(b)) factor.

From experimental results of a study of contact angle drop size dependence for several alkanes on "Teflon" (FEP(fluorinated ethylene propylene)) surfaces, the line tension was estimated as approximately 10^{-6} J/m in all cases (20). If the contact radius changed from about 1 to 5 mm, the contact angle decreased by approximately $2-5^\circ$. The contact angles were measured by using a very accurate technique (axisymmetric drop shape analysis) which eliminates the subjective error present in goniometer measurements (cf. Chapter 37 in this volume). Line tension values, several orders of magnitude lower than the above cited value, have also been determined and there is no consensus in the literature on either the magnitude or even the sign of the line tension. Only a few investigators have examined line tension effects for liquids in contact with solids, mainly because it is very difficult to prepare suitable solid surfaces without any imperfections. Equation (7.13) is only applicable if the three-phase contact line is indeed a circle. For a corrugated three-phase contact circle due to substantial contact angle hysteresis (see Section 2.5 below), where the radius of curvature varies from point to point, one cannot expect to obtain a meaningful value for the line tension by interpreting the observed dependence of the

contact angle on the apparent three-phase contact radius in terms of equation (7.13).

2.3 Spreading parameter, work of cohesion and adhesion

Complete and partial wetting are controlled by the spreading parameter S . This important quantity is defined as the free energy difference between a solid, directly in contact with the vapour, and a solid covered by a flat, thick liquid layer, as follows:

$$S = \gamma_{sv} - (\gamma_{sl} + \gamma_{lv}) \quad (7.14)$$

If S is negative ($S < 0$), the solid-vapour interface has the lower free energy, i.e. the liquid does not spread and partial wetting occurs. In this case, the liquid drop deposited on a solid surface will form an equilibrium shape. In the case of a positive S ($S \geq 0$), *spontaneous spreading* occurs, and the equilibrium state corresponds to a complete coverage of the solid by a liquid film. Therefore, if S is known, the wetting behaviour of a liquid on a solid surface can be predicted. If complete spreading is desired, γ_{sl} and γ_{lv} should be made as small as possible. Unfortunately, γ_{sv} and γ_{sl} cannot be measured directly. However, there are strategies, empirically modified and theoretically sound

approximations, to determine these important quantities indirectly from wetting measurements (see Sections 2.4 and 4.2 below).

The parameter S can also be defined as the “work of spreading”, W_s , required to expose a unit area of solid-vapour interface while destroying a corresponding amount of the solid-liquid and liquid-vapour interfaces (22). Therefore, W_s refers to the retraction of a thin film of liquid from a solid surface and is the negative free energy associated with the process of the spreading of a liquid over a solid surface (see Figure 7.4).

In addition, Figures 7.4(b) and 7.5 schematically illustrate further thermodynamic expressions for solid-liquid interactions, i.e. the “work of wetting” or “work of immersion” and the “work of cohesion” and the “work of adhesion”, respectively. As can be easily seen, each of these parameters represents the work associated with a de-wetting process.

Thermodynamically, a relationship of the free energy of adhesion per unit area of a solid-liquid pair is that it is equal to the work required to separate a unit area of the solid-liquid interface, thus creating a unit area of a liquid and solid interface (Figure 7.5(b)). This relationship is the well-known Dupré equation, as follows:

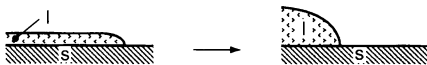
$$W_{sl}^a = \gamma_{sv} + \gamma_{lv} - \gamma_{sl} \quad (7.15)$$

The Dupré equation plays a central role in the study of adhesion. Combining Young’s equation (equation (7.7)) with the Dupré equation (equation (7.15)) provides the Young–Dupré relationship, as follows:

$$W_{sl}^a = \gamma_{lv}(1 + \cos \theta) \quad (7.16)$$

This equation relates a thermodynamic parameter to two easily measurable quantities, namely the contact

(a) Work of spreading: $W_s = \gamma_{sv} - \gamma_{lv} - \gamma_{sl}$



(b) Work of wetting: $W_w = \gamma_{sv} - \gamma_{sl}$

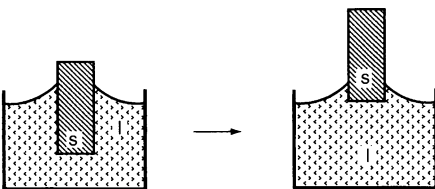
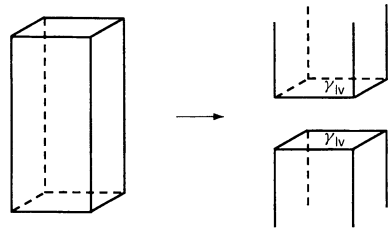


Figure 7.4. Definitions of thermodynamic parameters for (a) work of spreading, and (b) work of wetting

(a) Work of cohesion: $W_c = 2\gamma_{lv}$



(b) Work of adhesion: $W_a = \gamma_{sv} + \gamma_{lv} - \gamma_{sl}$

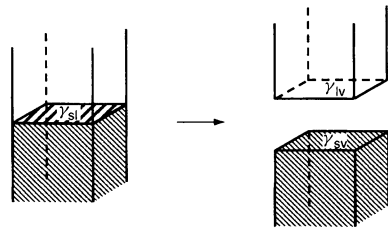


Figure 7.5. Definitions of (a) the thermodynamic work of cohesion, and (b) thermodynamic work of adhesion

angle θ and the liquid surface tension γ_{lv} . One can easily estimate the thermodynamic work of adhesion, W_{sl}^a , between a liquid and a solid if the liquid, completely wets the solid surface. This parameter is of the order of 100 mJ/m² which is an exceedingly small quantity compared to the actual amount of energy necessary to break an adhesive bond. From this comparison, one would assume that the work of adhesion plays an insignificant role in the practical work of adhesion. However, it has been found that the practical adhesion is, in fact, related to the thermodynamic work of adhesion (23).

Similarly, as can be seen from Figure 7.5(a), the work of cohesion of a liquid is defined as follows:

$$W_{ll}^c = 2\gamma_{lv} \quad (7.17)$$

The work of adhesion and cohesion, W_{sl}^a and W_{ll}^c , respectively, can be used to explain the spreading of a liquid on a solid surface. Combining equation 7.14 with Young’s equation (equation (7.7)), yields the following:

$$S = \gamma_{lv} \cos \theta - \gamma_{lv} = \gamma_{lv}(\cos \theta - 1) \quad (7.18)$$

Furthermore, by combining equation (7.18) with equations (7.16) and (7.17), we obtain:

$$S = W_{sl}^a - 2\gamma_{lv} = W_{sl}^a - W_{ll}^c \quad (7.19)$$

From equation (7.19), it can be concluded that when the free energy of adhesion per unit area between a liquid

and a solid is larger than the free energy of cohesion of the liquid, the initial spreading parameter is larger than 1 and the liquid spreads over the solid surface.

Girifalco and Good (24) proposed that the free energy of adhesion, W_{sl}^a , can be approximated in terms of the free energy of cohesion of the solid, W_{ss}^c , and the free energy of cohesion of the liquid, W_{ll}^c , as follows:

$$W_{sl}^a = \sqrt{W_{ll}^c W_{ss}^c} \quad (7.20)$$

From the definitions, $W_{ll}^c = 2\gamma_{lv}$ and $W_{ss}^c = 2\gamma_{sv}$, equation (7.20) then becomes:

$$W_{sl}^a = 2\sqrt{\gamma_{lv}\gamma_{sv}} \quad (7.21)$$

In combination with the Dupré equation (equation (7.15)) and Young's equation (equation (7.7)), this geometric mean combining rule is the basis for different approaches to calculate the solid surface tension from contact angle data (see Section 2.4 below).

As can be seen from Figure 7.4(b), there is a third wetting parameter, called the "work of wetting", W_w (or more commonly, the "wetting tension" or "adhesion tension"). This parameter is defined as the work expended in eliminating a unit area of the solid-liquid interface while exposing a unit area of the solid-vapour interface, as follows:

$$W_{sl}^w = \gamma_{sv} - \gamma_{sl} = \gamma_{lv} \cos \theta \quad (7.22)$$

This process corresponds to withdrawing a solid material from a pool of liquid. The parameter W_{sl}^w is the negative free energy associated with the process of engulfment of a solid surface by a liquid. The energy change associated with completely immersing a solid into a liquid is also related to this parameter. By using this concept of immersional wetting, the wetting of powders in liquids can be described (1).

2.4 Wettability of solid surfaces

It is of great fundamental, but also practical interest, to know how the contact angle depends on the chemical composition of both the solid and the liquid. Solids can be divided into two main types depending on the strength of bonding within the bulk, i.e. hard solids (covalent, ionic or metallic bonds), and weak molecular solids (bound by van der Waals forces and hydrogen bonds) (10). Due to the very different binding forces of these materials, the surface free energy at the solid-vacuum interface is also very different and is a fundamental parameter of a solid. Metals and inorganic materials have "high-energy" surfaces ($\gamma_s < 100 \text{ mJ/m}^2$), while polymers (and also molecular

liquids) have "low-energy" surfaces ($\gamma_s < 100 \text{ mJ/m}^2$). This difference in surface free energy causes solid surfaces to show different kinds of wetting behaviour when brought into contact with a liquid. Although the wetting behaviour is determined by Young's equation (equation 7.7), and hence by the relationship between the three interfacial tensions, a simplistic argument using γ_{sv} and γ_{lv} can roughly predict the wetting behaviour. For a liquid with $\gamma_{lv} < \gamma_{sv}$, the total free energy would in general be minimized by maximizing the area of the liquid-vapour interface, and the liquid would wet the solid. However, if a liquid has $\gamma_{lv} > \gamma_{sv}$, the total free energy would in general be minimized by minimizing the area of the liquid-vapour interface and the liquid would partially wet the solid. Therefore, a knowledge of γ_{sv} for a particular solid surface provides a means of gaining insight into the wetting behaviour of liquids on that surface.

2.4.1 Critical surface tension

The pioneering work goes back to Zisman (5). The key observation made by Zisman and his co-workers was that for a given solid, the measured contact angles did not vary randomly as the liquid was varied. They found that for a homologous series of liquids (alkanes) and a given solid, $\cos \theta$ changed smoothly with γ_{lv} , and they suggested a straight-line relationship (Figure 7.6). The extrapolation of this straight line to the point where $\cos \theta = 1$ yielded "the critical surface

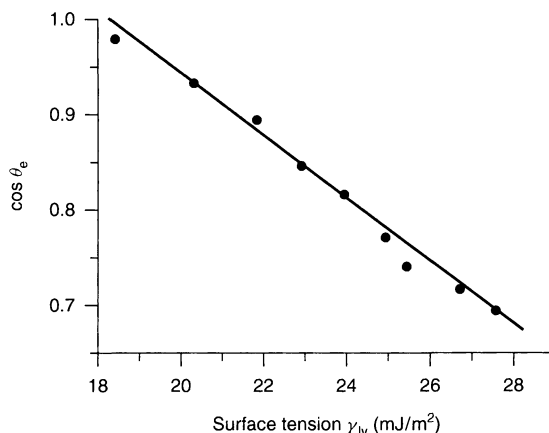


Figure 7.6. A typical Zisman plot (cosine of θ vs. liquid surface tension) for a polytetrafluoroethylene ("Teflon") surface in contact with liquid *n*-alkanes. The critical surface tension γ_c for this system is $\sim 18 \text{ mJ/m}^2$ (from ref. (5)), reproduced with permission from American Chemistry Society

tension", γ_c , i.e. the surface tension of a liquid which would just wet the solid completely. Using different types of liquids, such as homologous series of alkanes and alcohols, the contact angles changed with the liquid surface tension in a similar manner although the different series did not superimpose completely. However, in the case of simple liquids, such as alkanes, where van der Waals forces are dominant, Zisman observed that γ_c is essentially independent of the nature of the liquid, and is a characteristic of the solid alone. Therefore, this empirical quantity was taken to be a measure for the experimentally inaccessible γ_{sv} . The variation in values of γ_c for different solid surfaces shows the same qualitative behaviour as one would expect of γ_{sv} and thus γ_c is a useful quantity for roughly characterizing the wetting behaviour of a solid surface (5, 10).

2.4.2 Geometric mean combining rule

Based on Young's equation (equation (7.7)), different approaches were developed to determine the solid surface tension. The main difficulty is that Young's equation contains two non-measurable quantities, i.e. γ_{sv} and γ_{sl} , that cannot be measured independently. The strategy pursued by all approaches is, therefore, to express γ_{sl} in terms of the other two interfacial tensions, $\gamma_{sl} = f(\gamma_{sv}, \gamma_{lv})$, thus reducing the number of unknowns in Young's equation. Hence, the interfacial tension which is caused by the interaction between solid and liquid molecules has to be calculated from the knowledge of the surface properties of the solid and of the liquid phase. Strictly speaking, this is impossible. The available models are, therefore, either empirically

modified or they should be theoretically sound approximations.

One such approximation that has proved to be very stimulating to research on contact angle phenomena was proposed by Girifalco and Good, by assuming that mainly van der Waals forces act between all molecules (24). This approach is based on Berthelot's (geometric mean) combining rule. According to this rule, the free energy of adhesion, W_{sl}^a , can be approximated in terms of the free energy of cohesion of the solid, W_{ss}^c , and the free energy of cohesion of the liquid, W_{ll}^c (see equation (7.20)). Girifalco and Good modified the geometric mean combining rule by introducing an empirical correction factor, called the interaction parameter, Φ , as follows:

$$\gamma_{sl} = \gamma_{sv} + \gamma_{lv} - 2\Phi\sqrt{\gamma_{sv}\gamma_{lv}} \quad (7.23)$$

This interaction parameter Φ is a characteristic of a given system which can be evaluated from the molecular properties of the solid and the liquid phase. It was found to be very close to unity when dominant cohesive and adhesive forces were of the same kind.

2.4.3 Equation-of-state approach for solid-liquid interfacial tensions

Based on experimental contact angle data, Neumann and co-workers have shown that the values of $\gamma_{lv} \cos \theta$ change systematically with γ_{lv} in a very regular fashion, from hydrophobic surfaces, such as polytetrafluoroethylene, to hydrophilic surfaces, such as poly(propene-*alt*-*N*-methylmaleimide), and that the patterns are independent of the experimental technique used (25) (cf. Figure 7.7).

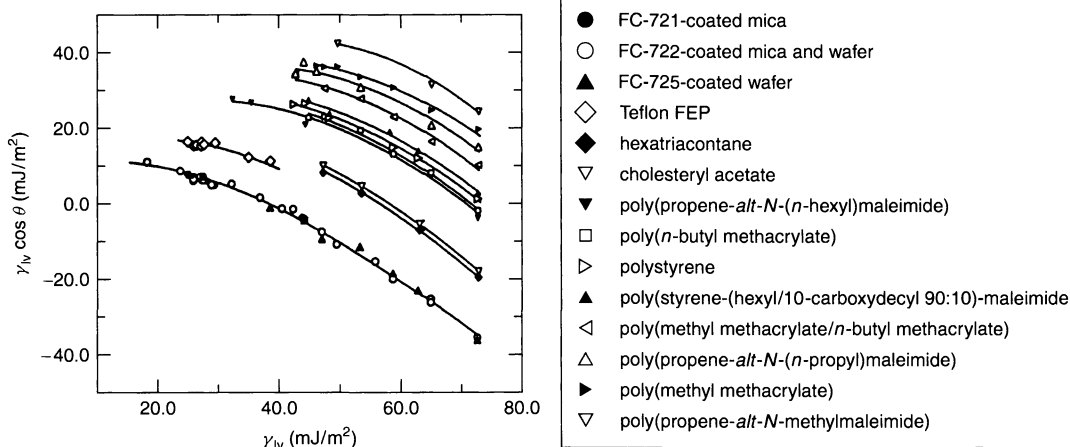


Figure 7.7. Plots of $\gamma_{lv} \cos \theta$ vs. γ_{lv} for various solid surfaces (from ref. (25)), with permission from Elsevier Science

Thus, one can conclude that the values of $\gamma_{lv} \cos \theta$ depend only on γ_{lv} and γ_{sv} , i.e. $\gamma_{lv} \cos \theta$ is a function of γ_{lv} and γ_{sv} :

$$\gamma_{lv} \cos \theta = F(\gamma_{lv}, \gamma_{sv}) \quad (7.24)$$

Because of Young's equation (equation (7.7)), the experimental contact angles imply that γ_{sl} can be expressed as a function of only γ_{lv} and γ_{sv} , as follows:

$$\gamma_{sl} = F(\gamma_{lv}, \gamma_{sv}) \quad (7.25)$$

These experimental results are consistent with the equation-of-state approach for interfacial tensions (6): A recent formulation of this can be written as follows:

$$\gamma_{sl} = \gamma_{sv} + \gamma_{lv} - 2\sqrt{\gamma_{sv}\gamma_{lv}} e^{-\beta(\gamma_{lv}-\gamma_{sv})^2} \quad (7.26)$$

By combining equation (7.26) with Young's equation (equation (7.7)), one obtains the following:

$$\cos \theta = -1 + 2\sqrt{\frac{\gamma_{sv}}{\gamma_{lv}}} e^{-\beta(\gamma_{lv}-\gamma_{sv})^2} \quad (7.27)$$

Thus, the solid surface tension can be determined from experimental contact angles and liquid surface tensions when β is known. The latter was determined experimentally for a given set of γ_{lv} and θ data measured on one and the same type of solid surface by a least-squares analysis technique. A weighted mean β was calculated as $0.0001247 \text{ (m}^2/\text{mJ)}^2$ (6). It was found that calculations of γ_{sv} values with slightly different β values have very little effect on the outcome (25). However, it is still an open question as to whether or not β in equation (7.27) is a "universal" constant, i.e. independent of the solid surface. Such a question can be addressed only after an even larger body of accurate contact angle data on various solids has been generated.

It could be shown that the equation-of-state approach can be used to good advantage in numerous applications, including the interfacial phenomena of powders (26) (see also Section 4 below). It has often been argued in the literature that this approach is only applicable to apolar systems. However, as can be seen from Figure 7.7, the experimental contact angle patterns were obtained for a large number of polar and non-polar liquids on different solid surfaces containing also polar groups in their surface regions (25). Such patterns imply that the contact angle of a liquid drop on a certain solid surface appears to depend almost entirely on the liquid-vapour surface tension and very little on the other properties of the liquid. However, in the literature, curves far less smooth, or even no unique curves at all, are frequently reported. Since the contact angle and the surface tension are macroscopic quantities, which have their origin in

molecular interactions, these effects were explained by specific intermolecular forces. Recently, it was shown that a scatter in experimental curves of $\gamma_{lv} \cos \theta$ vs. γ_{lv} can also be caused by very complex contact angle responses of certain solid-liquid systems resulting in non-constant γ_{lv} , γ_{sv} and γ_{sl} values during the experiment (27). Scatter due to these causes prohibits the application of all contact angle approaches. These complicated phenomena cannot be revealed by a simple conventional goniometer sessile drop technique which is frequently used to measure contact angles. It was found that low-rate dynamic contact angle measurements using axisymmetric drop shape analysis (ADSA) allow one to distinguish the thermodynamically meaningful from the meaningless contact angles (see Section 2.5 below).

Recently, van Giessen *et al.* have used a generalized van der Waals theory to model a diverse series of liquids on a low-energy substrate and to calculate the corresponding surface tensions and contact angles. The aim of this study was to investigate how the behaviour of $\cos \theta$ with γ_{lv} is related to molecular interactions (28). Their results showed that it was indeed possible to reproduce a behaviour similar to that seen in experiments (cf. Figures 7.6 and 7.7), with the data for $\cos \theta$ plotted versus γ_{lv} falling in a narrow band which could almost be interpreted as a smooth curve. In their calculation, the width of the band depended on the ranges of the model parameters and on the details of the molecular structure. The main limitations of their model were its simplicity and the fact that they had to use a combining rule to estimate the interaction between the solid and the fluid.

2.4.4 Surface tension component approaches

Several other approaches have been developed to calculate the solid-vapour surface tension from contact angle measurements (22). The surface tension component approach was pioneered by Fowkes. He postulated that the total surface tension can be expressed as a sum of different surface tension components, each of which arises due to a specific type of intermolecular forces. Fowkes (e.g. see ref. (22)) argued that in van der Waals systems, only dispersion forces could effectively operate across the interface. Therefore, he obtained the following expression:

$$\gamma_{sl} = \gamma_{sv} + \gamma_{lv} - 2\sqrt{\gamma_{sv}^d \gamma_{lv}^d} \quad (7.28)$$

where γ_{sv}^d and γ_{lv}^d are the dispersion force components of the solid and liquid surface tensions, respectively.

By combining equation (7.28) with Young's equation (equation (7.7)), one thus obtains the following:

$$\cos \theta = -1 + \frac{2(\gamma_{sv}^d \gamma_{lv}^d)^{1/2}}{\gamma_{lv}} \quad (7.29)$$

Equation (7.29) is known as the Girifalco–Good–Fowkes–Young equation. By using this relationship, the dispersion components of the solid or liquid surface tension could be evaluated.

Owens, Wendt, Kaelble and others (see ref. (22)) argued that the “polar” interaction could be computed by using the same geometric mean mixing rule as for the dispersion force interaction. One then obtains the following equation:

$$\gamma_{sl} = \gamma_{sv} + \gamma_{lv} - 2\sqrt{\gamma_{sv}^d \gamma_{lv}^d} - 2\sqrt{\gamma_{sv}^p \gamma_{lv}^p} \quad (7.30)$$

where γ_{sv}^p and γ_{lv}^p are the polar force components of the solid and liquid surface tensions. If the contact angles of at least two liquids, usually a polar and a non-polar liquid, with known γ_{lv}^d and γ_{lv}^p parameters are measured on a solid surface, the γ_{sv}^d and γ_{sv}^p parameters of that solid can be calculated by combining equation (7.30) with Young's equation. One then obtains two equations with two unknowns. This concept of the “polar fraction” for the surface tension and the principle of “polarity matching” to optimize adhesion became widespread in many fields of applied surface science. However, the theoretical background of this approach is poor, especially concerning the assumption that the polar component of the surface tension can be calculated by a geometric mean combining rule from the internal polar cohesive forces. It can easily be proved that different sets of probe liquids lead to different polarity splits for a given solid.

Another approach using the concept of surface tension components was developed by Good and van Oss (7). According to this model, characteristic acid and base parameters of the surface tension can be determined from contact angle measurements. Three parameters can be calculated characterizing the solid surface tension, namely the Lifshitz–van der Waals component, γ_1^{LW} , which contains the dispersion component, the electron donor component, γ_1^- , and the electron acceptor component, γ_1^+ . One has to use three liquids with known surface tension components, i.e. γ_{lv}^{LW} , γ_{lv}^- and γ_{lv}^+ , to measure the contact angles of these three liquids on the solid surface. It was found that most solids appear to be almost totally basic, including materials with known acidic character, such as poly(vinyl chloride), and this therefore suggested that the consistency of the method should be checked (22).

At present, no general consensus exists on the interpretation of contact angles in terms of solid

surface tensions. The incompatibility of the two major schools, i.e. the equation-of-state approach (6) and the surface tension component approach (7) is rooted in the theory. Recent progress in the correlation of contact angles with solid surface tensions has been summarized in a review by Kwok and Neumann (25).

2.5 Contact angles on imperfect solid surfaces

The derivation of equations (7.1) and (7.7) assumes that the solid surface in contact with the liquid is smooth, homogeneous, isotropic, insoluble, non-reactive and non-deformable. Since the Laplace equation describes the equilibrium shape of a liquid–vapour or liquid–liquid interface, away from the solid–vapour and solid–liquid interfaces, this assumption is of little or no consequence for its range of validity. However, Young's equation involves properties which are a function of the solid surface, i.e. γ_{sv} and γ_{sl} . Since real surfaces are often rough or heterogeneous, many questions regarding the validity and applicability of Young's equation remain still open today. Young's equation predicts a single value for the contact angle because the equilibrium contact angle, θ_e , in Young's equation is a unique function of the interfacial tensions γ_{sv} , γ_{sl} and γ_{lv} . However, a range of contact angles on a solid surface normally exists, and each contact angle gives rise to a mechanically stable liquid meniscus. In particular, when a liquid is added to a drop on a solid or is withdrawn from it, the contact angle is observed to increase or decrease, respectively. The maximum contact angle is called the *advancing* angle, while the minimum is known as the *receding* angle. This behaviour is shown schematically in Figure 7.8. The difference between the maximum (advancing) and the minimum (receding) contact angles is known as the *contact angle hysteresis*. In pioneering publications (reviewed in refs (3) and (29)), simple models were developed showing that multiple thermodynamic equilibrium states exist on rough and/or heterogeneous solid surfaces. The equilibrium state which corresponds to the absolute minimum in energy is the stable state; the others are metastable, with energy barriers between them.

2.5.1 Equilibrium contact angles on a rough surface

Wenzel (see, for example, ref. (9)) was the first to discuss the *influence of surface roughness* on the apparent or macroscopic contact angle. He introduced a roughness

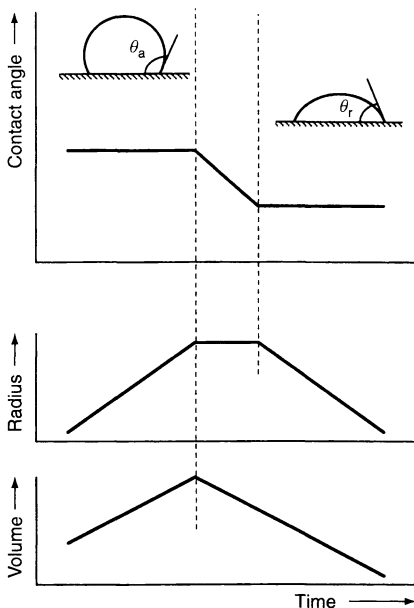


Figure 7.8. Representations of advancing (θ_a) and receding (θ_r) contact angles. The maximum contact angle upon addition of liquid into a sessile drop is called the *advancing* angle. The apparent contact angle decreases upon withdrawal of the liquid, thus resulting in a minimum contact angle, which is known as the *receding* contact angle

factor, r_w , into Young's equation because he argued that, in the case of a rough solid surface, the interfacial tensions γ_{sv} and γ_{sl} should not be referred to the geometric area, but to the actual surface area. Thus, if:

$$r_w = \frac{\text{true surface area}}{\text{geometric surface area}} \quad (7.31)$$

one obtains the so-called Wenzel equation, as follows:

$$r_w(\gamma_{sv} - \gamma_{sl}) = \gamma_{lv} \cos \theta_w \quad (7.32)$$

and the following equation for the contact angle on a rough surface:

$$\cos \theta_w = r_w \cos \theta \quad (7.33)$$

The Wenzel contact angle θ_w is the equilibrium contact angle, on a rough solid surface corresponding to the absolute minimum in the free energy of the system. Based on this equation, it can be predicted that roughness should have a major effect on the contact angle and, hence, on the wettability of surfaces. Since the roughness factor is always greater than unity, equation (7.33) predicts that the Wenzel contact angle will increase with roughness if the contact angle on a smooth surface is greater than 90° and will decrease if it is less

than 90° . It is important to note that this conclusion seemingly conflicts with experimental observations: one finds that with increasing roughness, the advancing contact angle always increases and the receding contact angle decreases. When regarding these discrepancies, one has to take into account that the Wenzel equation does not describe contact angle hysteresis and hence the relationship between roughness and the phenomenon of hysteresis. In addition, since the physical feature affecting the Wenzel angle is the increased surface area of rough surfaces, no simple correlation is expected with surface roughness alone, as measured, for instance, by a profilometer.

2.5.2 Equilibrium contact angles on a chemically heterogeneous surface

Real surfaces are not only more or less rough. They can also be heterogeneous and, therefore, can be composed of domains of different compositions with different wetting properties. Causes of domain structures are surface contaminations or phase separation. However, whereas the effect of roughness on the contact angle is well known from many observations, the effect of chemical heterogeneity is more difficult to visualize. Cassie and Baxter, at first, calculated an apparent contact angle that represented the absolute minimum in the free energy of a system consisting of a composite surface made up of two types of patches. These authors obtained the following equation for the apparent contact angle on such a composite surface, as reviewed in many textbooks (see, for example, ref. (9)):

$$\cos \theta_c = a_1 \cos \theta_1 + a_2 \cos \theta_2 \quad (7.34)$$

where a_1 and a_2 are the fractional surface areas occupied by the two types of patches such that $a_1 + a_2 = 1$, and θ_1 and θ_2 are the corresponding intrinsic contact angles. θ_c is the *Cassie contact angle* or, like θ_w for a rough surface, the equilibrium contact angle for a heterogeneous solid surface. It should be pointed out that θ_w and θ_c will normally not be amenable to experimental determination (9). The Cassie contact angle for a heterogeneous surface is only a conceptual measure of wettability and cannot be identified in practice.

2.5.3 Causes of contact angle hysteresis

As has been already pointed out, in addition to the stable equilibrium state, there exist many apparent metastable

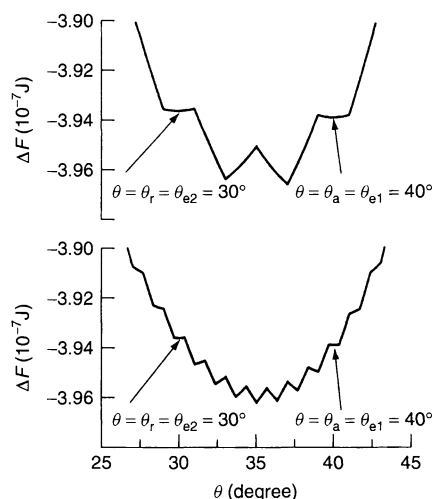


Figure 7.9. Free energy changes as a function of instantaneous contact angle, θ , on two surfaces consisting of two types of horizontal strips of equal width according to Li and Neumann. The equilibrium contact angles of type-1 and type-2 strips are $\theta_{e1} = 40^\circ$ and $\theta_{e2} = 30^\circ$, respectively, for respective strip width of 2° and $(2/3)^\circ$ (from ref. (9)), reproduced by permission of Marcel Dekker Inc

contact angles with energy barriers between them. These were initially discussed by using simple models for roughness and heterogeneity (3, 29). These models show that heterogeneity and roughness can produce contact angle hysteresis. Li and Neumann (9) calculated the free energy changes as a function of instantaneous contact angle, θ , on two heterogeneous surfaces consisting of two types of horizontal strips of equal width. Figure 7.9 shows the results when the equilibrium contact angles of “type-1” and “type-2” strips are $\theta_{e1} = 40^\circ$ and $\theta_{e2} = 30^\circ$, respectively, with a strip width of 2° and $(2/3)^\circ$, respectively. The free energy curves have a “sawtooth” structure between 30° and 40° , which corresponds to a number of metastable equilibrium configurations. It should be noted that outside the contact angle range from 30° to 40° , the sawtooth structure is still present but there are no more local minima and therefore, no more metastable equilibrium configurations. The first local minimum on the lower-angle side corresponds to the intrinsic contact angle, θ_{e2} , of the higher-energy strips, while the first local minimum on the higher-angle side corresponds to the intrinsic contact angle, θ_{e1} , of the lower-energy strips. Therefore, the experimental advancing contact angle θ_a is equal to θ_{e1} , and the experimental receding contact angle θ_r is equal to θ_{e2} . Although neither θ_a nor θ_r are equal to the equilibrium contact angle of this system, corresponding to the

absolute minimum of the free energy, they are intrinsic equilibrium contact angles of the two types of strips and may be used in Young’s equation.

The thermodynamic model described above has also been applied to idealized rough surfaces. It was found that the model rough surface produces metastable states such as the horizontal strips. However, in this case, the advancing and receding contact angles are meaningless in terms of Young’s equation (9).

Figure 7.10 shows the experimental results obtained by Dettre and Johnson (30) which are fairly typical for the influence of surface roughness if the contact angle on the smooth surface is greater than 90° . As can be seen from this figure, hysteresis increases as roughness increases due to increasing advancing and decreasing receding angles.

The sharp upturn in the receding angle occurred at a certain point where the surface became composite in nature due to trapped air, which means that the liquid drop is in contact with a surface composed in part by the solid and in part by air. Such a composite system is a

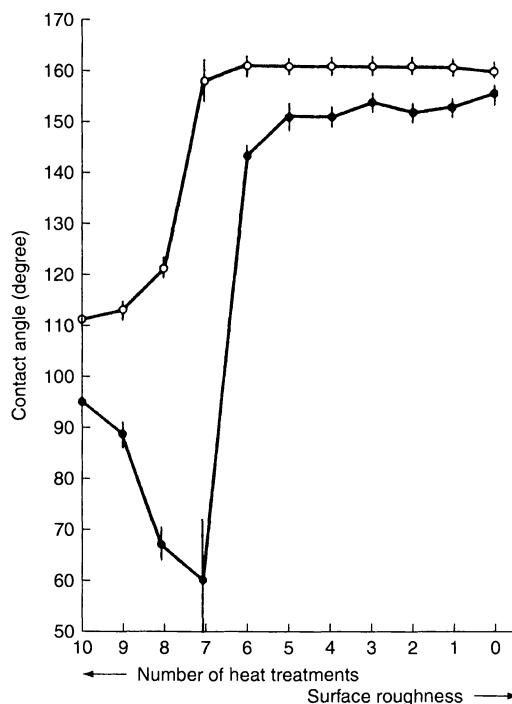


Figure 7.10. Water contact angles on a tetrafluoroethylene (TFE)–methanol telomer wax surface as a function of roughness: \circ , advancing contact angles; \bullet , receding contact angles (from ref. (30)), reproduced with permission from American Chemical Society

special case of a heterogeneous surface. The equilibrium contact angle can be expressed as follows by using equation (7.34) and assuming that the contact angle of the liquid with air is 180° :

$$\cos \theta_{cb} = a_1 \cos \theta_1 - a_2 \quad (7.35)$$

Equation (7.35) is known as the equation of Cassie and Baxter. It could be shown theoretically that the free energy barrier between metastable states is greatly reduced on composite surfaces. This may explain the large reduction in hysteresis which has been observed experimentally.

Figure 7.11 shows schematically the expected behaviour of the advancing and receding contact angles as a function of roughness for surfaces whose contact angle on the corresponding smooth surface is lower or greater than 90° (31). For both cases, the advancing contact angle increases and the receding angle decreases as the roughness increases. Above a certain degree of roughness, depending on the roughness dimensions and geometry, wettability becomes a capillary phenomenon.

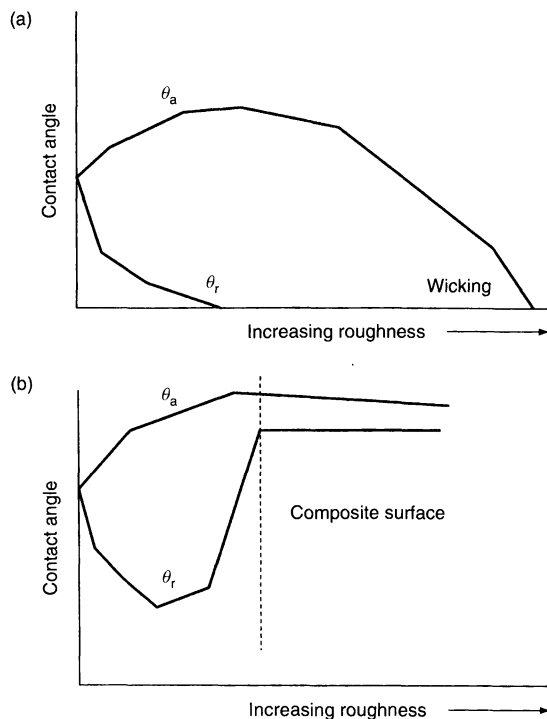


Figure 7.11. Behaviours of advancing and receding angles as a function of roughness when the equilibrium contact angle on the corresponding smooth surface is (a) $< 90^\circ$, and (b) $> 90^\circ$ (from ref. (31)), reproduced with permission of John Wiley & sons Limited

If the contact angle on the corresponding smooth surface is lower than 90° (Figure 7.11(a)), liquid penetration promoted by capillary forces occurs, thus causing the advancing contact angle to decrease, so resulting in total wetting. On the other hand, on hydrophobic surfaces characterized by an intrinsic contact angle greater than 90° (Figure 7.11(b)), the liquid cannot penetrate into the cracks and crevices of the surface and is in contact with a composite surface. Various concepts used to explain hysteresis by microporosity of the solid were supported by the experimental observations that hysteresis was strongly linked to the liquid molar volume and, hence, to the size of the liquid molecules. However, quantification of the above-mentioned effects is still difficult. There are as yet no general criteria to quantify roughness and the level of smoothness where surface topography has no longer an effect on the contact angle. It is proposed that the answers to such questions have to involve considerations of line tension (20) and the contortions of the three phase line.

Several approaches to contact angle hysteresis and to the study of the effect of heterogeneities on the contact line have been developed. Li and Neumann (9) were able to explain from an analysis of a heterogeneous surface model with two different types of horizontal strips with different widths why the advancing contact angles are more reproducible than the receding angles. These authors considered the case of a low-energy (high-contact-angle) solid surface with impurities of higher energy. The advancing contact angle is expected to represent the property of the predominant material of the surface in this case, while the receding contact angle is only a manifestation of the impurities of that solid surface.

Joanny and de Gennes have analysed the origin of hysteresis in terms of pinning of the contact line on a defect on the surface (see, for example, refs (10) and (12)). According to their analysis, there is an analogy between physically rough and chemically heterogeneous surfaces so that their conclusions can be applied to both types of surfaces. These authors concluded that the hysteresis created by a dilute assembly grows like the number of defects (or heterogeneous regions). Schwartz and Garoff (32) concluded from an analysis using various shapes and arrangements of patches that hysteresis is found to be a strong function of the details of the arrangements of such patches, in addition to the dependence on the coverage fraction.

In addition to roughness and heterogeneity, there are other causes of contact angle hysteresis. It is well known that hysteresis can be observed which results from time-dependent liquid–solid interactions.

For example, the solid can swell in contact with a certain liquid or even interact by chemical interfacial reactions; it can also be partially dissolved. In the case of polymer surfaces, the molecular reorientation in the surface region under the influence of the liquid phase is assumed to be a major cause of hysteresis. This reorientation or restructuring is thermodynamically favoured: at the polymer–air interface, the polar groups are buried away from the air phase, thus causing a lower solid–vapour interfacial tension. In contact with a sessile water drop, the polar groups turn over to achieve a lower solid–liquid interfacial tension. Time-dependent changes in contact angles can also be observed (33).

Since contact angle hysteresis is a very complex phenomena, a complete theory for such a process is not yet available because the existing models give only a partial explanation of the hysteresis. It should be stated that the precise scale and degree of non-uniformity in the case of rough and/or heterogeneous surfaces necessary to cause detectable effects in hysteresis are not yet clear. There still remain difficulties in relating the observed hysteresis to practical measures of surface roughness and inhomogeneities.

2.5.4 Definitions of contact angles

Various definitions of contact angles can be found in the literature (cf. refs (1, 3, 8, 10)). Generally, the contact angle is the angle between the tangent to the liquid–fluid interface and the tangent to the solid–fluid interface. However, as can be seen from Figure 7.12 this definition is ambiguous because the scale at which the interfaces are looked at is not clear. According to Marmur (8), one can distinguish between intrinsic, actual and apparent contact angles. The contact angle on an ideal solid surface is called the “intrinsic contact angle”, and applies at the smallest distance from the solid surface for which the concept of contact angle may hold. Since most practical solid surfaces are not ideally smooth, the “intrinsic contact angle” cannot usually be measured. Due to mutual interactions at the contact line and their effect on the intrinsic contact angle, it may be different from the Young contact angle, θ_Y , which is calculated from equation (7.7).

Due to roughness and heterogeneity, the contact angle may change from one point to another along the contact line. Usually, the “apparent contact angles” are obtained by optical methods, e.g. using a microscope of low power. It is only on perfectly smooth solid surfaces that the apparent contact angle is identical with the “actual contact angle” (see Figure 7.12). On rough surfaces, they may be very different. In addition, the

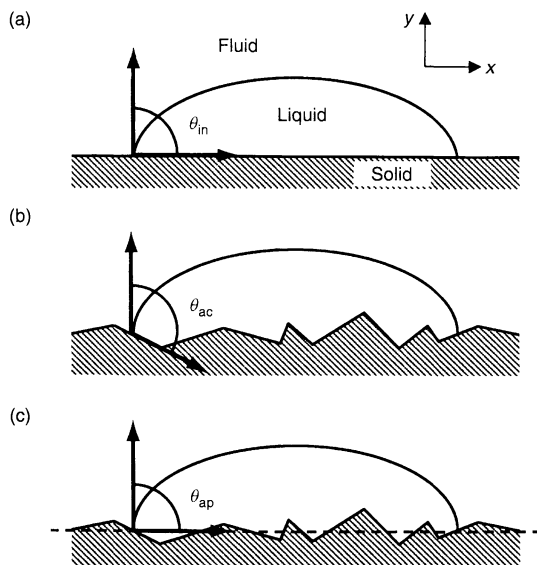


Figure 7.12. Definitions of different types of contact angles: (a) intrinsic contact angle, θ_{in} ; (b) actual contact angle, θ_{ac} ; (c) apparent contact angle, θ_{ap} (from ref. (8)), with permission from Elsevier Science

three-phase line may be contorted on a microscopic scale, due to heterogeneities, thus causing the contact angle to vary along this line. In this case, the observable, macroscopic contact angle may well be constant (9).

The contact angles which can be measured at a macroscopic level by optical means, or from the rise of a liquid in a fine capillary, are also called “phenomenological contact angles”. This type of contact angle governs phenomena in which the Laplace pressure plays a role, such as the penetration of a liquid into a capillary (3).

For the determination of the solid surface tension from contact angle data, it is important to use experimentally accessible contact angles which are *Young contact angles*. On ideal solid surfaces, there is no contact-angle hysteresis and the experimentally observed contact angle is equal to θ_Y , which is just the equilibrium contact angle θ_e . Since on real solid surfaces, contact angle phenomena are very complicated (see Section 2.5.3 above), the thermodynamic status of contact angles is often not clear and experimentally observed apparent contact angles, θ_{ap} , may or may not be equal to the Young contact angle θ_Y . These problems were treated by Neumann and co-workers (9, 25). They considered the circumstances under which experimental contact angles may be used in conjunction with Young’s equation, even if the contact angle hysteresis is not negligible. They concluded that the experimental

advancing contact angle, θ_a , on a smooth, but chemically heterogeneous solid surface can be expected to be a good approximation of θ_Y (see Figure 7.9). While the receding angle on a heterogeneous and smooth surface can also be a Young contact angle, it is frequently found to be non-reproducible. Unlike the situation of the heterogeneous surface, contact angle hysteresis due to roughness precludes an interpretation in terms of solid surface tension. On a rough surface, no equality between θ_a and θ_Y exists.

The contact angles associated with moving solid–liquid–vapour three-phase contact lines are called “dynamic contact angles”, in contrast to static contact angles. It was found experimentally that static and dynamic advancing contact angles tend to be identical on well-prepared solid surfaces if the rate of motion of the three-phase line is relatively low (up to 0.5 mm/min) (34). However, they can be quite different at higher velocities of the moving meniscus. In situations where the contact angle depends on the velocity of a moving contact line, one can distinguish between forced flow and spontaneous spreading or penetration (10, 12, 14, 16). The phenomena of spontaneous spreading and penetration will be considered in the following sections.

3 DYNAMICS OF SPREADING

3.1 Tanner’s law

The dynamic wetting of solid surfaces can be characterized, on the macroscopic scale, by the relationship between the static and dynamic values of the contact angle and the velocity of the three-phase contact line. Complete wetting corresponds to a dynamic situation where the macroscopic contact angle θ goes to zero when the time t goes to infinity. In this case, where S is positive, spontaneous spreading of a drop on a horizontal solid surface occurs and one follows the dynamics of spreading by measuring the radius $R(t)$ and the contact angle $\theta(t)$ as a function of time (Figure 7.13).

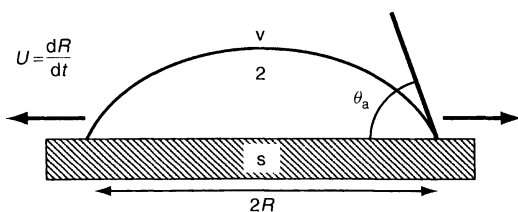


Figure 7.13. Apparent behaviour of a drop during spreading (on the macroscopic scale)

It was found experimentally that $R(t)$ increases rapidly at the early stages of spreading, and then very slowly. Generally, there are two forces that drive spreading, namely capillarity (Laplace pressure) and gravity (drop weight). Both forces decrease considerably as a drop flattens out, whereas the opposing viscous force increases.

The measured experimental data for a large variety of liquids and substrates can often be represented by power-law variations for both the size and the apparent contact angle. Depending on the dominating driving force for spreading in the different regimes, the power law gets a different exponent (10). If the drop is smaller than the capillary length, $\kappa^{-1} = (\gamma/\rho g)^{1/2}$, gravity effects can be neglected, and the whole shape of the drop is that of a spherical cap. The radius R of the wetted spot grows according to the following:

$$R \sim \Omega^{3/10} (\gamma t / \eta)^{1/10} \quad (7.36)$$

for small drops of volume Ω , viscosity η , density ρ , and surface tension γ . For large drops, where gravity is the main driving force, the expression changes to:

$$R \sim \Omega^{3/8} (\rho g t / \eta)^{1/8} \quad (7.37)$$

For non-polymeric or low-molecular-weight molten polymers, the dynamic contact angle is related to the spreading velocity by Tanner’s law, given by:

$$\frac{\eta U}{\gamma} \equiv Ca \propto \theta_a^3 \quad (7.38)$$

where U is the spreading velocity, Ca is the capillary number (defined as the viscosity η multiplied by the spreading velocity U , divided by the surface tension γ), and θ_a is the dynamic contact angle of the spreading wedge. From these results, it was concluded that the spreading parameter S and, hence, the exact nature of the solid surface appears to play no role in the spreading dynamics, i.e. there seems to be no dependence on the chemical nature of the surface, provided that it is smooth and completely wetted ($S > 0$).

It should be noted that the spreading of entangled polymer melts is quite different from that of low-molecular-weight liquids. The macroscopic shape of the drops is not a spherical cap, as it is with non-polymeric, pure liquids – there is a macroscopic protruding “foot”. The basic idea was that entangled polymers, flowing near a smooth, passive surface, should show a highly and molten slippage (10).

3.2 Precursor film

An important key to the spreading analysis was the experimental observation of a microscopically thin film which always precedes a spreading droplet, as can be seen schematically from Figure 7.14. This film, called “precursor film”, whose thickness is normally below the micron range (typical thickness 100 Å), is also present in the dry case.

Based on these experimental findings, a refined theory of spreading has been developed (10). The fundamental result of this theory is that the energy associated with the spreading parameter S is presumably nearly entirely spent through viscous dissipation in this film. Therefore, the macroscopic dynamics of the drop is independent of the microscopic behaviour of the precursor film. This explains why the macroscopic dynamics of these systems do not contain the parameter S .

The basic idea in the thorough description of the spreading kinetics, developed by Joanny and de Gennes, is to assume that the dissipation can be decomposed into three parts, as follows:

$$T \sum^0 = T \left(\sum_{\text{macro}}^0 + \sum_{\text{precursor}}^0 + \sum_{\text{line}}^0 \right) \quad (7.39)$$

Each contribution in equation (7.39) comes from the corresponding part of the drop schematically presented in Figure 7.14. Since the total dissipation can be related to the product of the unbalanced Young force F by the line velocity, i.e.

$$T \sum^0 = F U = [S + \gamma(1 - \cos \theta_a)] U \approx S U + \frac{1}{2} \gamma \theta_a^2 U \quad (7.40)$$

it follows from equation (7.40) and, assuming a negligible contribution of the line:

$$T \sum_{\text{macro}}^0 + T \sum_{\text{precursor}}^0 = \frac{1}{2} \gamma \theta_a^2 U + S U \quad (7.41)$$

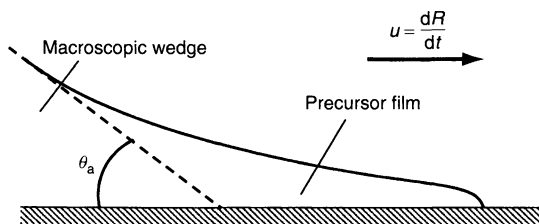


Figure 7.14. Droplet spreading on a solid (microscopic scale); the precursor film precedes the macroscopic wedge of the drop, which advances with the velocity $U = dR/dt$

The basic hypothesis of the de Gennes and Joanny's approach is to identify each term of the sum as follows:

$$T \sum_{\text{macro}}^0 = \frac{1}{2} \gamma \theta_a^2 U \quad (7.42)$$

and:

$$T \sum_{\text{precursor}}^0 = S U \quad (7.43)$$

Then, by computing the dissipation directly in each region and assuming a Poiseuille-type flow, one can deduce the evolution law of $\theta_a(t)$ and the shape of the precursor film. It could be shown that the free energy S is entirely used up in the film region. The thickness of the precursor film is controlled by the spreading parameter S and by the effective Hamaker constant of the system, while the macroscopic part of the spreading drop follows Tanner's law independently of S (10). Within this theory, it was predicted that the film is thicker for smaller and more developed for a larger S or smaller θ_a . These predictions could be established experimentally by using direct visualization of the precursor film through a microscope in polarized light and by ellipsometric measurements (11).

Recently, it has been shown that the molecular dynamics technique allows for a very detailed study of the dynamics of spreading on the microscopic scale for both complete and partial wetting regimes (15). It could be confirmed that at the molecular level, the mechanism of spreading can be viewed as a competition between a surface driving force and friction between the liquid and solid atoms. This result supports the molecular kinetics theory of wetting (14), not reviewed here, as well as the de Gennes–Cazabat model of spreading (10).

3.3 Spreading on inhomogeneous surfaces

It is well known that *surface heterogeneities* change the static wetting properties by causing, for example, contact angle hysteresis (see Section 2.5 above). Although it is also well known that inhomogeneities cause problems in many technological processes where wetting dynamics are involved, such as printing and coating, only a few studies can be found about the effect of surface inhomogeneities on the dynamics of wetting (13). On chemically inhomogeneous, but smooth surfaces, it is expected that the macroscopic dynamics of spreading do not change as long as S remains positive. If S is locally negative, a non-wetted spot develops.

Due to *surface roughness*, the relationship between the spreading velocity and the dynamic contact angle changes (equation (7.38)). In the case of parallel V-shaped surface channels, measurements of the spreading of polydimethylsiloxane parallel to the surface channels showed that Tanner's law is still approximately valid at short times, shifted by a constant, k_2 , to higher spreading velocities. The data followed a modified Tanner law, as follows:

$$U^{1/3} = k_1\theta_a + k_2 \quad (7.44)$$

where k_1 is roughly constant and of the same magnitude as that predicted by hydrodynamic theories, while k_2 increases with the fraction of the surface covered by channels (35). For roughness in the micron range, a macroscopic foot (with thickness of the order of the roughness amplitude) starts "diffusing" from the edge of the drop, which spreads with unchanged velocity (36).

The spreading of liquid in the channels ahead of the macroscopic drop front on both parallel and grid-like channels follows the well-known scaling with the square root of time that was initially proposed by Washburn (cf. see equation (7.54) below) (35). One consequence of this behaviour is that non-wetting liquids may spread on a rough surface (13).

3.4 Spreading of solutions

The spreading behaviour of solutions is important in many technical processes, such as coating and printing. In such cases, the liquid is a multi-component system. If we consider the simple case of a binary solution containing a solvent and a surfactant, the latter has a tendency to adsorb at the liquid-vapour and solid-liquid interfaces where it lowers the interfacial tensions γ_{lv} and γ_{sl} . If this adsorption is not uniform, the interfacial tensions are not constant, Marangoni stresses are generated, which are caused by surface tension gradients. It is proposed that the physics of droplet spreading is then dominated by the competition between the hydrodynamic motion of the liquid and the adsorption kinetics of the surfactant. Leger and Joanny (12) studied the spreading of a liquid with an insoluble surfactant on to a solid surface. If the affinity of the solid for the surfactant molecules is low, the contact angle is still qualitatively given by Tanner's law (equation (7.38)), but the pre-factor is larger than for a simple liquid with the same surface tension. When the affinity of the surfactant for the solid is larger, the Marangoni force drives the spreading. Tanner's law is no longer applicable and the contact angle can depend explicitly on the spreading power. Wetting by solutions has been reviewed by Bose (37).

4 WETTING CAUSED BY CAPILLARY PENETRATION

Wettability and pore structure determine the fluid distribution and fluid flow in porous media (38). In many practical situations, the liquid is required to penetrate into porous materials. Therefore, it is of great importance to understand the relationships between pore structure, wettability and capillarity in order to predict and to control the penetration of liquids into porous solid systems, such as fibre bundles, membranes or powder packings. Conversely, the dispersion of a powder in a liquid is also important, for example, when stable suspensions of particles have to be prepared (e.g. colour pigments in paints) or when inorganic particles have to be filled into polymer melts. With regard to these technologically important processes, the surface energetics and wettability of porous solid systems is of great interest.

4.1 Driving force for capillary penetration

The phenomena of capillary penetration of liquids into pore spaces filled with a fluid are related to the rise of liquids in capillary tubes where the flow is driven by interfacial pressure differences, as described by the Laplace equation of capillarity (equation (7.1)). The magnitude of the pressure difference across each liquid-fluid interface (meniscus) depends on the local curvature which is determined by the local wetting properties and pore geometry. In a cylindrical capillary, where the capillary wall is completely wettable by the liquid, the liquid-vapour interface can be assumed to be a hemisphere and $R_1 = R_2 = r$ ($r \ll a$, cf. equation (7.48) below), where r is the capillary radius. Then, equation (7.1) becomes particularly simple and reduces to the following:

$$\Delta P = \frac{2\gamma_{lv}}{r} \quad (7.45)$$

If the liquid meets the circular cylindrical capillary at a certain apparent contact angle θ (see Figure 7.15), then $R_1 = R_2 = r/\cos\theta$ and one obtains the following expression:

$$\Delta P = \frac{2\gamma_{lv} \cos\theta}{r} \quad (7.46)$$

It should be noted that the apparent contact angle is the one that determines the curvature of the meniscus and, consequently, the pressure difference that drives capillary penetration.

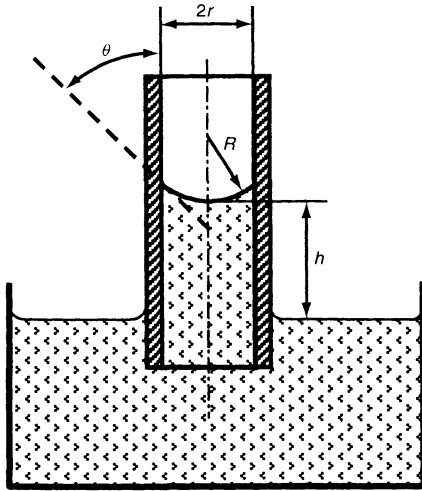


Figure 7.15. Schematic representation of the capillary rise of a liquid in a thin capillary

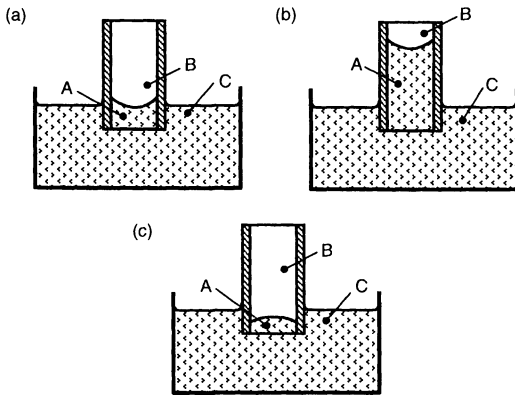


Figure 7.16. Schematic representations of the capillary rise for $\theta_a < 90^\circ$, for (a) formation of a meniscus, and (b) rise to the equilibrium height. (c) Schematic representation of the capillary depression for $\theta_a > 90^\circ$

For infinite reservoirs of penetrating liquids, capillary penetration is possible only for $\theta < 90^\circ$ (Figures 7.16(a) and 7.16(b)). In this case, the meniscus is convex on the penetrating liquid side (point A) and the pressure there is lower than the pressure at the concave side of the interface (point B), and also lower than the pressure which is located outside of the capillary (point C). The unbalanced pressure difference within the bulk resulting from the interfacial pressure difference causes penetration of the liquid into the capillary. Figure 7.16(c) shows the situation in the case of capillary depression ($\theta > 90^\circ$).

Marmur (16) has considered small liquid drops that penetrate into capillaries. In this situation, the reservoir of the displaced fluid is infinite, but the penetrating liquid comes from a limited reservoir with a finite radius of curvature. If the radius of the penetrating drop is sufficiently small (effect of gravity on the drop shape can be neglected), penetration should be possible for $\theta > 90^\circ$ due to the increased pressure inside the penetrating drop. It was assumed that this pressure may overcome the adverse effect of a concave meniscus. Marmur observed practically complete penetration for apparent contact angles as high as about 115° for sufficiently small drops.

The most common case is penetration under the action of gravity which affects the shape of the meniscus and the height of rise in the capillary. In a capillary-rise situation, ΔP is equal to the hydrostatic pressure drop in the liquid column in the capillary, as follows:

$$\Delta P = \Delta \rho g h = \frac{2\gamma_{lv}}{r} \quad (7.47)$$

where $\Delta \rho$ is the difference in density between the liquid and vapour phases and g is the acceleration due to gravity. By rearranging equation (7.47), we obtain:

$$a^2 = rh = \frac{2\gamma_{lv}}{\Delta \rho g} \quad (7.48)$$

where a is defined as the capillary constant. Neglecting the effect on the shape of the meniscus ($r \ll a$), the height of rise, h_c , in a capillary connected to two infinite reservoirs, is easily calculated when the hydrostatic and the interfacial pressure differences are equated:

$$h_c = \frac{2\gamma_{lv} \cos \theta}{\Delta \rho g r} \quad (7.49)$$

Figure 7.16(b) shows schematically the rise to the equilibrium height. The flow stops when the bulk pressure difference between points A and C is balanced by the hydrostatic pressure (point B).

For the height of rise in a porous medium, the following equation was developed (16):

$$h_0 = \frac{(1 - \varepsilon_0) S_0 \gamma_{lv} \cos \theta}{\Delta \rho g \varepsilon_0} \quad (7.50)$$

This porous medium is only characterized by its overall porosity ε_0 and the overall specific area of the solid S_0 . Since this neglects local structural details it is termed as being *microscopically uniform*. Such a model is useful for estimating the expected height of rise and for comparison with the cylindrical capillary model. By comparing equations (7.49) and (7.50), an effective capillary radius for the porous medium can be defined,

as follows:

$$(r_0)_{\text{eff}} = \frac{2\varepsilon_0}{(1 - \varepsilon_0)S_0} \quad (7.51)$$

However, this model can only predict a single equilibrium height, since it ignores local details. The above equations were derived for simple capillary systems. The situation in porous media is immensely more complex due to variations in the local structure and in the direction of penetration. This leads to a multiplicity of equilibrium positions and to hysteresis. The thermodynamics of interfaces in porous media has been reviewed by Marmur (16).

4.2 Kinetics of penetration

For practical applications, the kinetics of penetration of liquids into porous media is of major interest, in particular the interrelationship between the kinetics of penetration and the structure of a porous medium, as well as its surface energetic properties.

In order to interpret the results of capillary penetration experiments, theoretical models are required. The simplest theoretical model is the well-known Washburn equation (1). Washburn considered the flow of a Newtonian liquid of viscosity η displacing air in a cylindrical capillary tube of radius r , under a pressure gradient $(\Delta P/h)$. He has shown that the velocity v ($= dh/dt$) of the liquid–air meniscus along the tube drops very quickly to such a value that the conditions of laminar flow assumed in the Hagen–Poiseuille equation are established:

$$v = \frac{dh}{dt} = \frac{r^2 \Delta P}{8\eta h} \quad (7.52)$$

where h is the height of the liquid front, i.e. the distance travelled along the tube by the meniscus in time t , and η is the viscosity of the liquid. By assuming that the driving pressure is solely the capillary pressure, equation (7.52) can be combined with the Laplace equation of capillarity for a vertical capillary of circular cross-section (equation (7.46)). Thus, the Washburn equation for the flow in a single capillary results, provided the effects of slip, gravity and inertial effects can be neglected, and there are no external pressure gradients:

$$\frac{dh}{dt} = \frac{r\gamma_{lv} \cos \theta}{4\eta h} \quad (7.53)$$

After integration, one obtains the following:

$$h^2 = \frac{rt}{2\eta} \gamma_{lv} \cos \theta \quad (7.54)$$

In many cases, it has been found experimentally that for liquids penetrating a porous medium, the Washburn law is dimensionally applicable ($h \sim t^{1/2}$). Therefore, the simplest approach toward modelling and understanding the kinetics of penetration into a porous medium is to treat it as a capillary with an “effective radius”. However, the model of an “effective radius” may be insufficient, especially when a significant distribution of pore sizes exists. It was concluded that the effective pore radius of a network of interconnected capillaries of varying radius, calculated by using the Washburn equation, may be very different from the radius calculated by other measurements, such as mercury porosimetry (39). A more sophisticated approach is based on the idea to model a porous medium as a group of capillaries of various sizes (16).

4.3 Wettability of porous solids

It is well known that serious problems arise when contact angles of sessile liquid drops are measured directly on the surfaces of porous materials, such as membranes or powders. Surface roughness, heterogeneity and the penetration of the liquid drop into the porous material may affect the measured contact angles, thus causing meaningless angles in terms of Young’s equation and hence in terms of a surface-energetic interpretation of the contact angle data (9). At present, many authors follow another concept to determine contact angles on porous materials. They use an indirect method based on the capillary penetration of liquids.

The use of equation (7.54) has been extended from cylindrical capillaries to powders in order to determine dynamic liquid contact angles by measuring the penetration rates of liquids into powder packings (40). In this case, the powder (uniformly packed into a tube) is modelled as a bundle of capillary tubes so that the plot of h^2 as a function of t should be linear. Other models propose that the powder can be represented by a bundle of capillaries with an added tortuosity factor. If it is assumed that a liquid completely wets the powder packing, $\cos \theta = 1$, the value of \bar{r} (the average equivalent radius) can be obtained. Then, for the same packing, measurements with other liquids give values of $\cos \theta$. In this way, an “effective” wettability is found – “effective” because it is derived from the capillary tube model of porous media and not by direct measurements. This procedure reveals a main deficiency of this approach. Only the product $r \cos \theta$ can be elucidated and not r or $\cos \theta$ separately (cf. equation (7.54)). Nevertheless, these contact angles have

been often used to determine the solid surface tension of porous materials (41–43). This procedure is dubious because, as was mentioned above, it can be expected that these contact angles are apparent contact angles which are affected by the geometry (roughness and porosity) of the porous medium, as for example, the local inclination angles of the capillary walls. It is only in a cylindrical capillary of smooth and homogeneous walls that the calculated θ coincides with the intrinsic contact angle. In general, it has been found that capillary penetration experiments tend to overestimate the contact angles compared to directly measured contact angles on smooth surfaces of the same material (44–46). For example, the contact angle of hexadecane was calculated to be $\theta = 88^\circ$ for a polytetrafluoroethylene (PTFE) powder by using the Washburn equation (44). On a flat and smooth PTFE surface, this contact angle is well known to be 46° . Obviously, the former value only reflects the contact angle/wettability of hexadecane on “rough” PTFE powder, which is meaningless for energetics calculations in conjunction with Young’s equation. A second example – for an organic liquid on cellulose fibres, the intrinsic contact angle may very well be close to zero. However, from capillary penetration experiments using filter papers of cellulose fibres, $\cos \theta$ comes out to be far from unity (45). Thus, it can be concluded that experimentally determined contact angles of porous materials do not reflect the material properties of the surface; rather, they reflect the morphological ones. In addition, if the rate of motion of the three-phase line is relatively high, it cannot be excluded that the “dynamic” contact angles calculated from capillary penetration experiments differ from static advancing contact angles. It is well known that they can be quite different at higher velocities of the moving meniscus (14).

For this reason, another strategy was pursued to characterize the wettability of porous media (44). This strategy is also based on a modified Washburn equation. By plotting $K\gamma_{lv}\cos\theta$ versus the liquid surface tension γ_{lv} , the solid surface tension, γ_{sv} , can be directly derived from these curves. The term $K\gamma_{lv}\cos\theta$ is obtained indirectly from capillary penetration experiments, when the liquid properties and the penetration velocities are known (K is an unknown parameter that depends on the geometry of the porous medium). This approach is based on the following considerations.

If the Washburn equation (equation (7.54)) is used, which describes the flow in a single capillary, one can replace h by the weight M of the liquid which penetrates into the capillary, as follows:

$$M = \rho V = \rho h A$$

where A is the cross-sectional area of the capillary and ρ is the density of the liquid. It follows that:

$$\frac{M^2}{\rho^2 A^2} = \frac{rt}{2\eta} \gamma_{lv} \cos \theta \quad (7.56)$$

and by rearranging:

$$\gamma_{lv} \cos \theta = \left(\frac{2}{A^2 r} \right) \left(\frac{\eta}{\rho^2} \right) \left(\frac{M^2}{t} \right) \quad (7.57)$$

where $(2/A^2 r)$ is a factor representing the geometry of the capillary, (η/ρ^2) reflects the properties of the test liquid and (M^2/t) is determined in the experiment.

In powder packings or other porous solids, such as membranes, the geometry of the capillary system is not known. The value of $(2/A^2 r)$ in equation (7.57) is therefore replaced by an unknown factor, $1/K$, i.e.

$$\gamma_{lv} \cos \theta = \frac{1}{K} \left(\frac{\eta}{\rho^2} \right) \left(\frac{M^2}{t} \right) \quad (7.58)$$

or:

$$K \gamma_{lv} \cos \theta = \left(\frac{\eta}{\rho^2} \right) \left(\frac{M^2}{t} \right) \quad (7.59)$$

This modified Washburn equation is valid when using the following assumptions: (i) laminar flow predominates in the pore spaces, (ii) gravity can be neglected, and (iii) the geometry of the porous solid is constant.

The quantity (M^2/t) is determined by measuring the weight M of a penetrating liquid into a porous solid as a function of the time t by using a tensiometer. If M is plotted versus \sqrt{t} , the experimental quantity (M^2/t) can be obtained by determining the slope of the linear part of these plots. There are two basic requirements that the test liquids must satisfy in order to be used for capillary penetration experiments, namely (i) they should be chemically inert with respect to the porous material of interest, and (ii) the range of the surface tension γ_{lv} of the test liquids should cover the anticipated surface tension of the powder. Experimental results obtained for powders and membranes consisting of hydrophobic and hydrophilic polymer materials show that an extremum (maximum) exists when the values $K\gamma_{lv}\cos\theta$ are plotted against the surface tension of the liquids γ_{lv} , at a value of $\gamma_{lv} = \gamma_{lv}^*$ (44, 47, 48). It is argued that the surface tension can then be determined as $\gamma_{sv} = \gamma_{lv}^*$. As an example, Figure 7.17 shows the results obtained for a PTFE (“Teflon 807-N”) powder; the maximum occurs at $\gamma_{lv}^* = 20.4 \text{ mJ/m}^2$. Thus, the γ_{sv} value of the PTFE particles would be 20.4 mJ/m^2 . When this γ_{sv} value and $\gamma_{lv} = 72.5 \text{ mJ/m}^2$ for water are used in conjunction with the equation-of-state approach for solid–liquid interfacial tensions (6), a water contact angle of 104° can be predicted. Remarkably, this is exactly what one would observe on a smooth “Teflon” surface. Other polymer

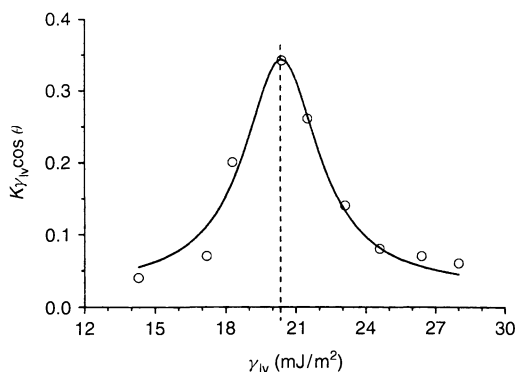


Figure 7.17. A plot of $K\gamma_{lv} \cos \theta$ versus γ_{lv} for nine liquids obtained from capillary penetration experiments using PTFE ("Teflon 807-N") powder (from ref. (44)), reproduced with permission from Springer-Verlag

powders, as for example, polypropylene, polyethylene, and polystyrene, were investigated and it was found that the derived γ_{sv} values are in good agreement with the γ_{sv} values obtained from contact angle measurements on flat and smooth solid surfaces of the same materials (48).

Although the packed powder bed certainly does not represent a flat and smooth solid surface, the derived value for γ_{sv} is that obtained by contact angle measurements on a flat and smooth surface. It is well known that even a highly compacted hydrophobic powder, presenting a seemingly flat and smooth solid surface, does not yield the same contact angle as truly smooth and coherent solid surfaces. It appears that an indirect method, such as capillary penetration, may provide much more relevant information concerning the solid surface energetics than direct contact angle measurements on imperfect solid surfaces.

Since only the product $K \cos \theta$ can be elucidated, and not K or $\cos \theta$ separately, in capillary penetration experiments, K , which reflects the geometry of the porous medium, may change in a non-predictable way during the penetration of different liquids and, hence, the shape of the curve of $K\gamma_{lv} \cos \theta$ versus γ_{lv} . From experiments carried out with microporous expanded PTFE membranes of different pore geometries, it could be concluded that information about the geometric constant K is not needed. The position of the maximum, which is expected to reflect the solid surface tension, γ_{sv} , of the porous material was not affected by the different geometries of the membranes (47).

Figure 7.18 shows that the above described approach is not only applicable to hydrophobic surfaces but also to very hydrophilic surfaces, such as cellulose

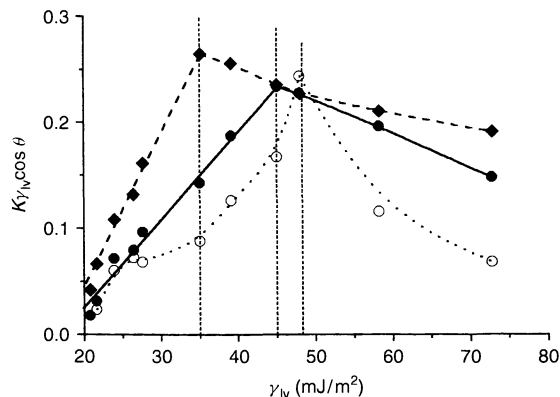


Figure 7.18. A plot of $K\gamma_{lv} \cos \theta$ versus γ_{lv} obtained for eleven liquids by using three differently modified cellulose hollow fibres: O, unmodified cellulose (CUPROPHAN); ●, chemically modified cellulose (M1); ◆, chemically modified cellulose (M2) (from ref. (44)), reproduced with permission from Springer-Verlag

membranes (44). As in the case of the PTFE powder (see Figure 7.17), we obtain curves with a maximum if $K\gamma_{lv} \cos \theta$ versus the surface tension γ_{lv} of the test liquids is plotted. It can be seen that the unmodified cellulose fibre indicates the highest γ_{sv} value, whereas the modified types have a lower γ_{sv} , i.e. a less hydrophilic surface. We can predict a water contact angle of 59° for an ideally smooth unmodified cellulose hollow fibre (CUPROPHAN), if we input $\gamma_{sv} = 48 \text{ mJ/m}^2$ and $\gamma_{lv} = 72.5 \text{ mJ/m}^2$ for water in equation (7.27). It has to be considered that processing agents are applied during the manufacture of the CUPROPHAN fibres, which can be expected to influence even the surface properties of the unmodified cellulose material. By chemical modification of the cellulose, γ_{sv} could be decreased to 35 mJ/m^2 , as can be seen from Figure 7.18; a water contact angle of 80° is predicted for this modified cellulose material by using equation (7.27).

5 REFERENCES

1. Adamson, A. W., *Physical Chemistry of Surfaces*, 5th Edn, Wiley, New York, 1990.
2. Rowlinson, J. and Widom, B., *Molecular Theory of Capillarity*, Oxford University Press, Oxford, UK, 1982.
3. Neumann, A. W. and Spelt, J. K. (Eds), *Applied Surface Thermodynamics*, Surfactant Science Series, vol. 63, Marcel Dekker, New York, 1996.
4. Gaydos, J., Rotenberg, Y., Boruvka, L., Chen, P. and Neumann, A. W., The generalized theory of capillarity, in

- Applied Surface Thermodynamics*, Neumann, A. W. and Spelt, J. K. (Eds), Surfactant Science Series, vol. 63, Marcel Dekker, New York, 1996, pp. 1–51.
5. Zisman, W., Relation of the equilibrium contact angle to liquid and solid constitution, in *Contact Angle, Wettability and Adhesion*, Fowkes, F. M. (Ed.), Advances in Chemistry Series, vol. 43, American Chemical Society, Washington, DC, 1964, pp. 1–51.
 6. Spelt, J. K. and Li, D., The equation of state approach to interfacial tensions, in *Applied Surface Thermodynamics*, Neumann, A. W. and Spelt, J. K. (Eds), Surfactant Science Series, vol. 63, Marcel Dekker, New York, 1996, pp. 239–292.
 7. Good, R. J. and van Oss, C. J., The modern theory of contact angles and the hydrogen bond components of surface energies, in *Modern Approaches to Wettability – Theory and Applications*, Schrader, M. E. and Loeb, G. I. (Eds), Plenum Press, New York, 1992, pp. 1–27.
 8. Marmur, A., Equilibrium contact angles: theory and measurement, *Colloids Surf., A*, **116**, 55–61 (1996).
 9. Li, D. and Neumann, A. W., Thermodynamic status of contact angles, in *Applied Surface Thermodynamics*, Neumann, A. W. and Spelt, J. K. (Eds), Surfactant Science Series, vol. 63, Marcel Dekker, New York, 1996, pp. 109–168.
 10. de Gennes, P. G., Wetting: statics and dynamics, *Rev. Mod. Phys.*, **57**, 827–863 (1985).
 11. Leger, L., Spreading of liquids on solid surfaces, in *Physicochemical Hydrodynamics: Interfacial Phenomena*, Velarde, M. G. (Ed.), Plenum Press, New York, 1988, pp. 721–740.
 12. Leger, L. and Joanny, J.-F., Liquid spreading, *Rep. Prog. Phys.*, **55**, 431–486 (1992).
 13. Cazabat, A.-M., How does a droplet spread?, *Contemp. Phys.*, **28**, 347–367 (1987).
 14. Blake, T. D., Dynamic contact angles and wetting kinetics, in *Wettability*, Berg, J. C. (Ed.), Surfactant Science Series, vol. 49, Marcel Dekker, New York, 1993, pp. 251–309.
 15. Blake, T. D., Clarke, A., De Conink, J., de Ruijter, M. and Voue, M., Droplet spreading: a microscopic approach, *Colloids Surf., A*, **149**, 123–130 (1999).
 16. Marmur, A., Penetration and displacement in capillary systems, in *Modern Approaches to Wettability – Theory and Applications*, Schrader, M. E. and Loeb, G. I. (Eds), Plenum Press, New York, 1992, pp. 327–358.
 17. Derjaguin, B. V. and Churaev, N. V., *Wetting Films*, Nauka, Moscow, 1984.
 18. Valignat, M. P., Voue, M., Oshanin, G. and Cazabat, A. M., Structure and dynamics of thin liquid films on solid substrates, *Colloids Surf., A*, **154**, 25–31 (1999).
 19. Blakely, J. M., *Introduction to the Properties of Crystal Surfaces*, Pergamon Press, Oxford, UK, 1973.
 20. Gaydos, J. and Neumann, A. W., Line tension in multiphase equilibrium systems, in *Applied Surface Thermodynamics*, Neumann, A. W. and Spelt, J. K. (Eds), Surfactant Science Series, vol. 63, Marcel Dekker, New York, 1996, pp. 169–238.
 21. Derjaguin, B. V., Churaev, N. V. and Muller, V. M., *Surface Forces*, Consultants Bureau, New York, 1987.
 22. Berg, J. C., Role of acid–base interactions in wetting and related phenomena, in *Wettability*, Berg, J. C. (Ed.), Surfactant Science Series, vol. 49, Marcel Dekker, New York, 1993.
 23. Pocius, A., *Adhesion and Adhesive Technology, an Introduction*, Carl Hanser, New York, 1997.
 24. Girifalco, L. A. and Good, R. J., A theory for the estimation of surface and interfacial energies. 1. Derivation and application to interfacial tension, *J. Phys. Chem.*, **61**, 904–909 (1957).
 25. Kwok, D. Y. and Neumann, A. W., Contact angle measurement and contact angle interpretation, *Adv. Colloid Interface Sci.*, **81**, 167–249 (1999).
 26. Li, D. and Neumann, A. W., Wettability and surface tension of particles, in *Applied Surface Thermodynamics*, Neumann, A. W. and Spelt, J. K. (Eds), Surfactant Science Series, vol. 63, Marcel Dekker, New York, 1996, pp. 509–556.
 27. Kwok, D. Y., Gietzelt, T., Grundke, K., Jacobasch, H.-J. and Neumann, A. W., Contact angle measurements and contact angle interpretation: I. Contact angle measurements by axisymmetric drop shape analysis and a goniometer sessile drop technique, *Langmuir*, **13**, 2880–2894 (1997).
 28. van Giessen, A. E., Bukman, D. J. and Widom, B., Contact angles of liquid drops on low-energy solid surfaces, *J. Colloid Interface Sci.*, **192**, 257–265 (1997).
 29. Johnson, Jr, R. E. and Dettre, R. H., Wetting of low-energy surfaces, in *Wettability*, Berg, C. (Ed.), Surfactant Science Series, vol. 49, Marcel Dekker, New York, 1993, pp. 1–73.
 30. Dettre, R. H. and Johnson, Jr, R. E., Contact angle hysteresis. II. Contact angle measurements on rough surfaces, in *Contact Angle, Wettability and Adhesion*, Fowkes, F. M. (Ed.), Advances in Chemistry Series, vol. 43, American Chemical Society, Washington, DC, 1964, pp. 136–144.
 31. Garbassi, F., Morra, M. and Occhiello, E., *Polymer Surfaces, from Physics to Technology*, Wiley, New York, 1994.
 32. Schwartz, L. W. and Garoff, S., Contact angle hysteresis on heterogeneous surfaces, *Langmuir*, **1**, 219–230 (1985).
 33. Andrade, J. D., Smith, L. M. and Gregonis, D. E., The contact angle and interface energetics, in *Surface and Interfacial Aspects of Biomedical Polymers*, vol. 1, Andrade, J. D. (Ed.), Plenum, New York, 1985, Ch. 7, pp. 249–292.
 34. Kwok, D. Y., Neumann, A. W. and Li, D., Capillary rise at a vertical plate as a contact angle technique, in *Applied Surface Thermodynamics*, Neumann, A. W. and Spelt, J. K. (Ed.), Surfactant Science Series, vol. 63, Marcel Dekker, New York, 1996, pp. 413–440.
 35. Gerdes, S., Cazabat, A.-M., Ström, G. and Tiber, F., Effect of surface structure on the spreading of a PDMS droplet, *Langmuir*, **14**, 7052–7057 (1998).

36. Cazabat, A. M. and Cohen Stuart, M. A., Dynamics of wetting: effects of surface roughness, *J. Phys. Chem.*, **90**, 5845–5849 (1986).
37. Bose, A., Wetting by solutions, in *Wettability*, Berg, J. C. (Ed.), Surfactant Science Series, vol. 49, Marcel Dekker, New York, 1993, pp. 149–181.
38. Morrow, N. R. and McCaffery, F. G., Fluid displacement studies in uniformly wetted porous media, in *Wetting, Spreading and Adhesion*, Padday, J. F. (Ed.), Academic Press, New York, 1978, pp. 289–319.
39. Mosquera, M. J., Rivas, T., Prieto, B. and Silva, B., Capillary rise in granit rocks: interpretation of kinetics on the basis of pore structure, *J. Colloid Interface Sci.*, **222**, 41–45 (2000).
40. Van Brakel, J. and Heertjes, P. M., Capillary rise in porous media, Part I, A problem; Part II, Secondary phenomena; Part III, Role of contact angle, *Powder Technol.*, **16**, 75–96 (1977).
41. Costanzo, P. M., Giese, R. F. and van Oss, C. J., Determination of the acid–base characteristics of clay mineral surfaces by contact angle measurements – implications for the adsorption of organic solutes from aqueous media, *J. Adhes. Sci. Technol.*, **4**, 267–275 (1990).
42. van Oss, C. J., Giese, R. F., Li, Z., Murphy, K., Norris, J., Chaudhry, M. K. and Good, R. J., Determination of contact angles and pore sizes of porous media by column and thin layer wicking, *J. Adhes. Sci Technol.*, **6**, 413–428 (1992).
43. Chibowski, E. and Holysz, L., Use of the Washburn equation for surface free energy determination, *Langmuir*, **8**, 710–716 (1992).
44. Grundke, K., Bogumil, T., Gietzelt, T., Jacobasch, H. - J., Kwok, D. Y. and Neumann, A. W., Wetting measurements on smooth, rough and porous solid surfaces, *Progr. Colloid Polym. Sci.*, **101**, 58–68 (1996).
45. Marmur, A. and Cohen, R. D., Characterization of porous media by the kinetics of liquid penetration: the vertical capillaries model, *J. Colloid Interface Sci.*, **189**, 299–304 (1997).
46. Parsons, G. E., Buckton, G. and Chatham, S. M., Comparison of measured wetting behaviour of materials with identical surface energies, presented as particles and plates *J. Adhes. Sci. Technol.*, **7**, 95–104 (1993).
47. Tröger, J., Lunkwitz, K., Grundke, K. and Bürger, W., Determination of the surface tension of microporous membranes using wetting kinetics measurements, *Colloids Surf., A*, **134**, 299–304 (1998).
48. Grundke, K. and Augsburg, A., On the determination of the surface energetics of porous polymer materials, *J. Adhes. Sci. Technol.*, **14**, 765–775 (2000).

CHAPTER 8

Foam Breaking in Aqueous Systems

Robert J. Pugh

Institute for Surface Chemistry, Stockholm, Sweden

1	Introduction	143	2.6	Droplets and oil lenses	148
1.1	Background	143	2.7	Superspreaders	149
1.2	Commercial chemical antifoamers	145	2.8	Elimination of the surface tension gradients	150
2	Types of Antifoamers and Mechanisms	147	2.9	Particles	150
2.1	Liquids (inhibitors) which may lower the viscosity and increase drainage	147	2.10	Mixtures of particles and oils	151
2.2	Surfactant-precipitation antifoamers	147	2.11	Emulsion and pseudo-emulsion films	152
2.3	Solubilized chemicals	147	2.12	Electrolytes	154
2.4	Defoaming caused by changes in stability of the micellar aggregates	148	3	Ageing Effects with Chemical Defoamers	154
2.5	Cloud-point defoamers	148	4	Physical Methods of Defoaming	155
			4.1	Ultrasonics	155
			5	References	156

1 INTRODUCTION

1.1 Background

Antifoamers or defoamers are a group of important specialized chemicals which are used throughout a range of industrial processes where foaming causes problems, e.g. in the production of paper, pharmaceuticals, materials and coatings, etc., and in oil recovery. In many industrial plants and sites (distillation columns, pipes, boilers, water discharges, etc.) foams can reduce the process efficiency and cause environmental problems in waste discharge. Antifoamers are also used as formulation additives in the preparation of commercial products such as detergents, paints, foodstuffs, beer, tomato juice, etc. Early definitions of antifoamers referred to the chemicals which were added to the aqueous phase, *prior to foam formation*, which act to prevent foam formation (foam inhibitors), while defoamers were referred to chemicals

added to eliminate an *existing foam*. However, today this distinction is confusing since many chemical additives appear to cover both roles.

There are at least sixty defoamer suppliers listed and many of these companies provide both technical and sales services. The market is over 150 000 metric tons per year in North America for the paper industry alone, which is about the same as for the rest of the world. Defoamer economics are usually measured as the cost per unit of product manufactured, e.g., the cost per litre of paint, the cost per ton of paper or the cost per batch of chemical produced. In many cases, this results in the use of relatively small amounts of expensive defoamer, which thus gives a lower cost per unit product. However, although expensive antifoamers may be more efficient, the wastage may be high, so that it is often cheaper to use an inexpensive defoamer. In many industries, special equipment has been developed to control the minimum defoamer consumption.

At present, the most effective and versatile chemical antifoamers are mixtures. In fact, modern commercial formulations often contain mixtures of silicone oils, silicone surfactants or silica gels, with possibly two or more types of dispersed hydrophobic aggregates (with sizes around 1 micron, specific gravity 1.0–1.3, with rough fractal shapes). These mixed-type antifoamers are very effective at low concentrations (10–1000 ppm) and are widely used. The (hydrophobic) particles may be hydrophobized silica or glass and are often referred to as the *activator*, with the hydrocarbon or polydimethylsiloxane (PDMS) liquid or oil being referred to as the *carrier*. However, less expensive single-system antifoamers are commonly used, and these exist in many different forms such as soluble liquids, insoluble

liquids, oils, gels, hydrophobic particles, emulsions and microemulsions. A typical list of single-system chemical antifoamers might include tributyl phosphate (TBP), polydimethylsiloxane (PDMS), alkyl amines, amides, thioethers, mineral and vegetable oils, waxes, silicone fluids, fatty acid esters ("Span 20"), alcohols (octanol), fatty acids and their derivatives (tall oil, aluminium stearate, and the calcium, aluminium and zinc salts of fatty acids) and many other different types of particles. The different types of chemicals and the physical methods used in defoaming are summarized in Figure 8.1.

It is important to note that antifoaming occurs by a range of both physical and chemical mechanisms. Many of these will be discussed in detail in

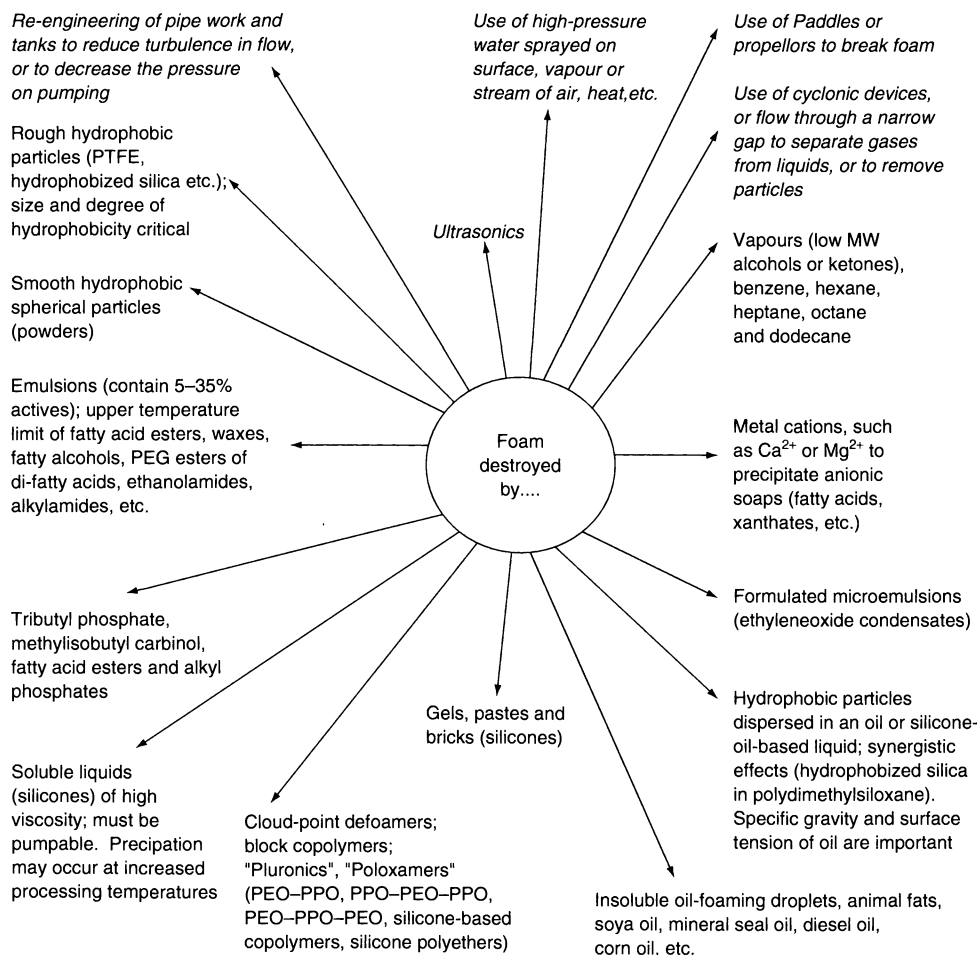


Figure 8.1. Chemical and physical methods of foam breaking; the latter, which are usually of low efficiency, are indicated in italic script

www.iran-mavad.com

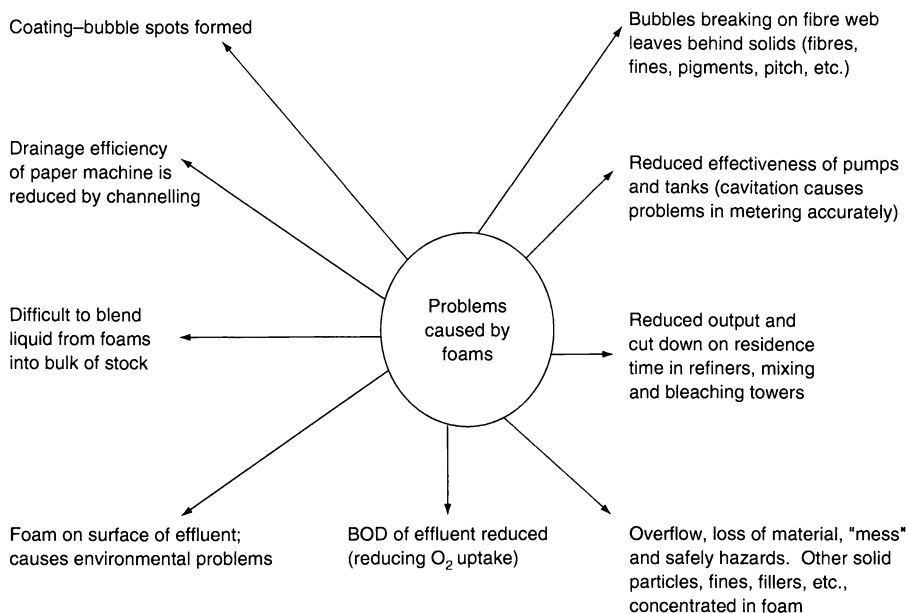


Figure 8.2. Problems caused by foams in the pulp and paper industry

the following sections. In addition, the most important use of antifoamers is in the pulp and paper industry, where foams are produced at various stages in the processing. Foaming causes many different types of problems, which must be eliminated by the use of effective antifoaming agents. Some of these problems are outlined in Figure 8.2. Modern paper mills need easy-to-pump, easy-to-mix, stable-on-storage, cost-effective antifoamers.

1.2 Commercial chemical antifoamers

The patent literature contains a large range of chemicals which have been recommended as antifoamers, ranging from simple compounds, such as octyl alcohol, to more sophisticated mixtures of antifoamers, which are sometimes required in special applications. From a universal viewpoint, polydimethylsiloxanes are probably the most expensive, yet the most effective materials for inhibiting foam. Such compounds are involatile and have extremely low surface tensions and low interfacial tensions against water. The surface tensions of liquid hydrocarbons are usually between 25 and 30 mN/m and since the silicones have lower surface tensions, they then can easily enter the hydrocarbon substrate. In addition, they are chemically inert, insoluble in water,

and with a lower density than water and lubricating oils. Other special polymers such as perfluorinated hydrocarbons are also involatile and have low surface tensions.

However, in cases where the surface tension of the substrate is no more than about 20 mN/m less than that of water, it is then not necessary to use silicone or perfluorinated hydrocarbon foam inhibitors (with such extreme surface tensions) and cheaper chemicals can be employed, such as glyceryl esters in the form of "pork", fat or butter. If fats prove ineffective, then synthetic esters of polyhydric alcohols can be used.

Since such a wide range of antifoaming chemicals are employed, it is therefore not altogether surprising that so many alternative mechanisms have been proposed to explain their action. Recently, many extensive experimental studies dealing with the basic mechanisms of antifoam action have been reported. It also appears that there may be several different mechanisms occurring concurrently in some systems. Over the years, this has caused many different theories to be put forward, depending on the type of antifoaming agent being used. However, overall it has been generally concluded that the mode of action of oil droplets, hydrophobic particles and mixtures of hydrophobic particles/oils *must first involve the emergence of this phase from bulk solution into the air/water interface*. This first stage of the process

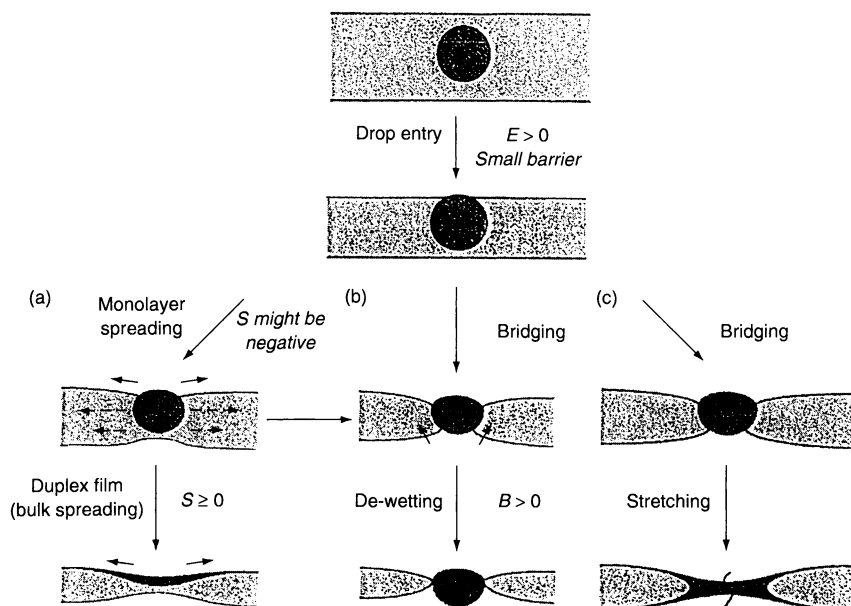


Figure 8.3. Mechanisms for foam film rupture by antifoam particle (a) spreading–fluid entrapment; (b) bridging de-wetting; (c) stretching bridging. In all of the mechanisms, the first step is the particle entry, which requires a positive entry coefficient and a small force barrier, thus enabling thinning of the thin film to occur. The spreading (a) leads to a Marangoni–driven flow of water, so causing local thinning. Alternatively, de-wetting (b) or stretching (c) could also lead to a rupture of the foam lamella (adapted from ref. (2)), reprinted with permission from American Chemical Society

is characterized by an entry coefficient (E) which must have a value > 0 . This aspect will be discussed later in this review.

The entry step is followed by a *fluid entrainment or bridging process*, which involves the antifoam oil spreading rapidly over the lamella surfaces, which may cause a Marangoni (1) driven flow of liquid in the foam film (fluid entrainment). The enhanced drainage is due to capillary effects and this can lead to film rupture, by bridging the aqueous films by a de-wetting mechanism. A bridging/stretching mechanisms have also been recently suggested (2). These different types of mechanisms are outlined in Figure 8.3. For mixtures of hydrophobic particles and oils, the particles must rupture the oil/water *pseudo-emulsion film* to facilitate the process of the emergence of the oil droplets into the air/water interface. This is a necessary *precursor step* in the formation of an unstable bridging-oil-drop configuration.

The above description presents a broad generalization of the theoretical mechanisms that have been proposed, although and there are many important problems which still require more intensive studies, in order to improve the efficiency of antifoamers. These are based on the following questions:

- (i) Why do antifoamers become less efficient with time?
- (ii) What is the effect of the particle size, shape, interfacial properties, specific gravity and concentration on the performance?
- (iii) What is the influence of the antifoamer viscosity?
- (iv) What is the influence of surface tension and specific gravity of the oil?
- (v) What is the effect of the adsorption of surfactant on the antifoamer additive?
- (vi) To what extent is there a synergistic effect between the particle and liquid, and can this be enhanced?
- (vii) What is the influence of the size, fractal characteristics and hydrophobicity of the particles in the mixed antifoamer?
- (viii) What is the concentration of hydrophobic particles in the oil which gives the most effective performance?

In the following sections, some of these problems are discussed, together with a more detailed review of the theoretical mechanisms that are involved.

2 TYPES OF ANTIFOAMERS AND MECHANISMS

2.1 Liquids (inhibitors) which may lower the viscosity and increase drainage

Chemicals, which are dispersed in the liquid, will emerge at the thin film interface as a lens and can cause a lowering of the viscosity and an increase in the drainage, which generally leads to a decrease in stability. In this group, we include chemicals which may (a) reduce the bulk viscosity and increase the drainage, or (b) reduce the surface viscosity and elasticity. For the latter case, the surface elasticity is eliminated by a swamping of the surface layer with an excess of a compound with a lower viscosity. If the compound is soluble, then a sufficient amount must be added to exceed the solubility limit. The insoluble monolayer cannot provide any elasticity, while the soluble monolayer in equilibrium with the dissolved form can do this. One of the more general theories suggests that the spreading film of antifoam may simply displace the stabilizing surfactant monolayers. As the oil lens spreads and expands on the surface, the tension will gradually reach a reduced uniform value. *This may cause elimination of both the stabilizing surface tension gradient and the surface elasticity.*

There are several other different mechanisms for reducing the surface viscosity, depending on the conditions in the surface layers. For example, many low-molecular-weight bulky surfactants, such as tributyl phosphate, can be used to reduce the coherence of the layer. Alternatively, small amounts of nonionic surfactants can be effective in disrupting the coherent layer, with such effects depending on the molecular structure of the additive. Other materials may not be surface-active, but may act as a cosolvent and thus reduce the concentration of surfactant in the surface layer. Unfortunately, fairly large quantities (e.g. 10% ethanol or methanol) would be needed in many cases. This may be reduced for low-molecular-weight (short-lasting) antifoamers by spraying the solution, which is a more economical approach. In addition, although small amounts of solubilized dodecanol may increase the foam stability of an anionic surfactant in water, a like quantity of solubilized octanol will have a contrary effect. The octanol rapidly diffuses to the surface, and will reduce the dynamic surface tension more rapidly, and thus allows less time for a Marangoni effect (1) to function. This will be discussed further below.

2.2 Surfactant-precipitation antifoamers

Foam films stabilized by anionic surfactants can be destroyed by the addition of an *oppositely charged inorganic species or near-stoichiometric concentrations of metallic ions to form insoluble salts*. For example, fatty acids and their derivatives (tall oil, stearate, etc.) can be precipitated by the addition of calcium, aluminium and zinc salts (forming insoluble salts of the acids). There have been several attempts to relate the defoaming action to the *solubility product* of the particles. A typical series of results for metal oleates are shown in Figure 8.4. The influence of hydrophobic calcium fatty acid soaps on foaming, and quantification of the data in terms of the solubility product of the calcium and sodium fatty acids have also been reported. Cationic surfactants added to foam stabilized by anionic surfactants could also destroy the foam. Unfortunately, due to the formation of solid contaminants and the adverse consumption of chemicals, precipitation antifoamers are used infrequently in industry.

2.3 Solubilized chemicals

As discussed earlier, many of the basic theories assumed that for effective antifoam action to occur, the antifoaming agent must be in the form of insoluble or undissolved particles or droplets, which transfer to the interface. However, this is not necessarily the case since there is some evidence that some solubilized antifoamers, such as tributyl phosphate and methylisobutyl carbinol (MIBC), can reduce the stability of sodium dodecyl sulfate (SDS) and sodium oleate foam systems. However, in some cases, the oils may exceed the solubility limit,

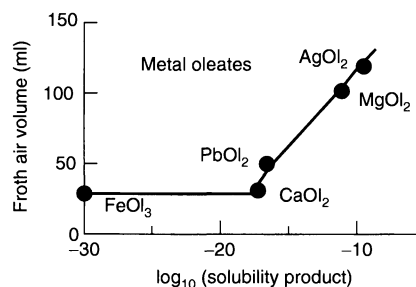


Figure 8.4. The importance of the solubility product of the particles in defoaming, as shown by a plot of the froth air volume versus the solubility product of various metal oleates ($2 \times 10^{-5} M$ in a 10 mg dm^{-3} commercial frother solution. (from ref. (3))

and the emulsifier droplets of oil may then have an influence on the antifoam action. In addition, it has been claimed that oil solubilized in the surfactant micelle can also cause a weak defoaming action. Mixed micelle formation with extremely low concentrations of surfactant may explain the actions of insoluble fatty acid esters, alkyl phosphates (esters) and alkyl amines. At present, there appears to be no complete explanation. While there are many cases which demonstrate that solubilized antifoams may reduce the foam stability in micellar solutions, there are also examples where dissolved antifoams can give enhanced foaming.

2.4 Defoaming caused by changes in stability of the micellar aggregates

It is well known that certain antifoams, such as methyl or ethyl alcohol, when added to the foaming solution may change the CMC or solubility of the surfactant and thus indirectly affect the adsorbed layer. In fact, detailed studies by Jha and co-workers (4) clearly emphasized the relationship between the stability of a surfactant micelle and the stability of the foams. From experiments carried out with foam stabilized by SDS, it was shown that several chemicals, such as 2-ethylhexanol (EH), tributyl phosphate (TBP) and tetrabutylammonium chloride (TBAC), can change the stability of the micellar aggregates, thus leading to changes in the stability of the foam systems. In these studies, the stability of micelles was determined from the micellar relaxation times, as measured by pressure jumps. As the antifoam concentration increases, the micellar relaxation time also increases (indicating increasing micellar stability), until a critical concentration was reached. Further increases in antifoamer lead to a decrease in the micellar relaxation time (indicating a decrease in micellar stability). The initial increase was attributed to a stabilization of the micelle by the added chemicals, which minimized the repulsion between the head-groups of the SDS molecules at the micellar surface or at the interface. Two opposing effects were therefore reported to be occurring, depending on the concentrations of antifoamer. The antifoaming agents can stabilize the SDS micelle at lower concentrations and in turn act as a foam inhibitor. However, beyond a critical concentration, the antifoaming agents destabilize the micelle, which then begins to improve the formability of the SDS. The microstructure changes for SDS micelles on the addition of an antifoaming agent is shown in Figure 8.5.

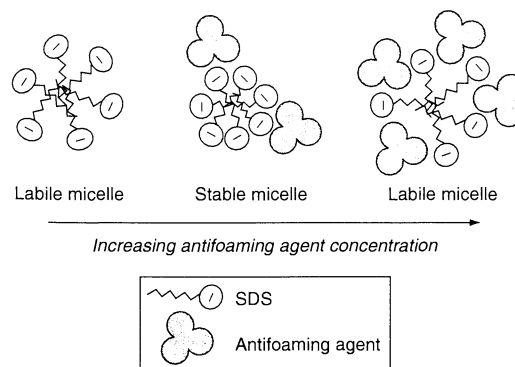


Figure 8.5. Schematic of the microstructure changes for SDS micelles on the addition of an antifoaming agent (from ref. (4), reprinted with permission from American Chemical Society)

2.5 Cloud-point defoamers

Block polymers of poly(ethylene oxide) (PEO) and poly(propylene oxide) (PPO) adsorb at interfaces in aqueous solution and can form organized micellar structures. The polarity of these copolymers depends on the ratio of the PEO (hydrophilic) and PPO (hydrophobic) components. Aqueous solutions of these polymers show a *cloud point* (CP) at increasing temperatures due to dehydration of the hydrophilic (PEO) units, and the general view is that they act as antifoamers in the region of the cloud point (due to the formation of this heterogeneous phase). Triblock copolymers (PEO–PPO–PEO or PPO–PEO–PPO types, “Pluronics” and poloxamers) are interesting systems since the CP varies with the PEO/PPO ratio. Such polymers have a wide range of applications (in textiles, dishwashing, etc.) since they show effective spreading, adsorption and foaming behaviour at lower temperatures. They display defoaming characteristics at elevated temperatures (above the CP), while at lower temperatures they remain soluble in the aqueous phase. Siloxane-based copolymers (silicone polyethers) are PEO–PPO-modified antifoamers, and again the CP changes by changing the PEO/PPO ratio. With these surfactant solutions, mixed micelles are formed and the foam breaks up a few degrees below the CP (5). Other commercial surfactants, such as Triton X100, OP-10 and DC-10, behave in a similar manner, with liquid drops being observed in solutions above the CP.

2.6 Droplets and oil lenses

Many antifoamers *cause undissolved oil droplets to be formed on the surface* of the film and this can

successfully leads to film rupture. Chemicals such as alkyl phosphates, alcohol, fatty acid esters and polydimethylsiloxanes are included in this group. Several possible mechanisms for foam film rupture by antifoaming droplets or oil lenses have been suggested.

As briefly discussed earlier, a widely accepted mechanism for antifoaming action is that first the oil drop enters the air/water interface, and in a secondary step, begins to spread over the foam film, so causing rupture. An entering coefficient (E) and a spreading coefficient (S) have been defined in terms of the change in free energy when the oil droplet enters the interface or spreads at the surface. These are defined as follows:

$$E = \gamma_{W/A} + \gamma_{W/O} - \gamma_{O/A} \quad (8.1)$$

$$S = \gamma_{W/A} - \gamma_{W/O} - \gamma_{O/A} \quad (8.2)$$

where $\gamma_{W/A}$, $\gamma_{O/A}$ and $\gamma_{W/O}$ are the macroscopic interfacial tensions of the aqueous phase and oil phase, and the interfacial tension of the oil/water interface, respectively.

It was originally suggested that for efficient defoaming, the oil drop after entering the air/water interface must spread as a duplex film on each side of the original film. This acts to drive out the original liquid film and leaves an oil film, which is unstable and easily breaks up. Clearly, two important steps need to be considered, since the mechanism is only feasible under certain critical conditions. These can be defined by $E > 0$, where the oil enters the air/water interface, and $S > 0$, where the oil spreads on the duplex film on each side of the original film. This situation is illustrated in Figure 8.6, where the balance between the relevant surface tension and spreading coefficient is shown.

It was assumed that it was the purely mechanical action of the spreading liquid which ruptures the aqueous foam film. As the lens slips over the underlying liquid, the lateral stress to the liquid below communicates a shearing stress to a depth of several microns. This causes the adjacent liquid to move in the same

direction, and such liquid movement induces a thinning which increases the probability of rupture. The possible mechanisms involved are illustrated above in Figure 8.3. Although equations (8.1) and (8.2) are useful in that they give a rough guide to antifoaming action, they are often inadequate since they do not consider the geometry of the system or the interactions of thin film forces, and hence their application is severely limited.

Another possible explanation for the unreliability of these spreading equations ((8.1) and (8.2)) is that there is a difference in magnitude between the initial entry coefficient (where the components are pure) and the equilibrium values (where contamination often occurs). In some cases, it may be that the operative entry coefficient lies between an initial (E) and final (E_e) value. In addition, it may be useful to define both an initial and a final spreading coefficient (i.e. S and S_e). Garrett (3) has stressed the importance of the formation of the oil lens (but not necessarily the spreading) in the mechanism of antifoaming. It was suggested that the oil lens could break the foam by a bridging mechanism. The oil drop first enters one surface and forms a lens, followed by thinning, until it enters the other surface to form an oil bridge. The stability of oil bridges in the bridging – de-wetting mechanism was quantified in terms of the oil/water contact angle and the bridging coefficient B , as defined by the following:

$$B = \gamma_{W/A}^2 + \gamma_{W/O}^2 - \gamma_{O/A}^2 \quad (8.3)$$

From a theoretical analysis, it was shown that positive values of B correspond to bridge de-wetting. However, although values of E, S and B can be determined from measurements of the interfacial tension, these models do not account for the rupture barrier of asymmetrical oil–water–air films which appear when the oil approaches the foam film surface.

2.7 Superspreaders

Several studies suggest that effective defoaming is related to polymolecular spreading or other types of spreading which involve the acceleration or transformation of non-stable polymolecular films into lenses. The spreading of defoamers is rather complex and non-ionic trisiloxane surfactants have been reported to show superior wetting properties, particularly on hydrophobic surfaces. This is the so-called *superspreading* concept. These surfactants not only have low surface tensions but also a tendency to form bilayers, which aggregate (into vesicles, lamellar phases, etc.), in aqueous solution (6). Based on molecular packing, there

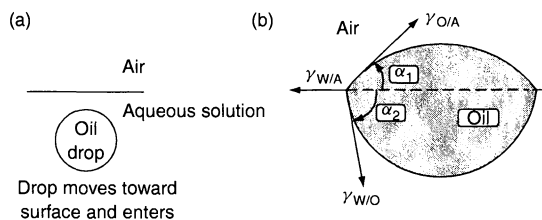


Figure 8.6. (a) Entry of oil droplet into air/solution interface; $E = \gamma_{W/A} + \gamma_{W/O} - \gamma_{O/A} > 0$. (b) Spreading of oil droplet: $S = \gamma_{W/A} - \gamma_{W/O} - \gamma_{O/A} > 0$

www.iran-mavad.com

is a fundamental difference in behaviour at the interface of a micelle-forming surfactant and of a vesicle-forming surfactant. Models for spreading have been suggested from experiments of the spreading kinetics of ethoxylated and propoxylated trisiloxane surfactants on a polypropylene substrate.

2.8 Elimination of the surface tension gradients

It has also been reported that antifoaming action may lead to the elimination of the surface tension gradient in foam films by reducing the Marangoni effect (1). Since the spreading is driven by a surface tension gradient between the spreading front and the leading edge, then *thinning and foam rupture can occur by this gradient acting as a shear force, thus dragging the underlying liquid away from the source*. It has been suggested that three different types of antifoam materials may function by this mechanism, i.e. (a) solids or liquids containing surfactants other than those stabilizing the foam, (b) liquids which contain foam stabilizers at higher concentrations than that which is present in the foam, and (c) the vapours of surface-active liquids.

2.9 Particles

Solid particles, which have some degree of hydrophobicity (e.g. coal dust, sulfur, non-wetting quartz, etc.) usually exhibit a finite contact angle when adhering to an aqueous interface, and may cause destabilization of froths. Many practical examples of such behaviour can be found in mineralised foams. In addition, the mechanism may not necessary involve wetting, since hydrophobic silica can deplete the stabilizing surfactant (through rapid adsorption) and can result in weak spots in the film.

In earlier studies, there was a tendency to try and emphasize the importance of wetting by showing that an increase in contact angle can cause an increase in defoaming action. However, much experimental data are erroneous due to the difficulties of measuring contact angles and the influence of the shape and roughness of the particles in the foaming action. Other studies have been reported in which foaming was related to the degree of wetting of the inert particles and this leads to the idea of a particle bridging mechanism (a similar mechanism as for the oil droplets), leading to rupturing of the thin film. Garrett (3) carried out a series of shake-test experiments with finely divided ($\sim 5 \mu\text{m}$)

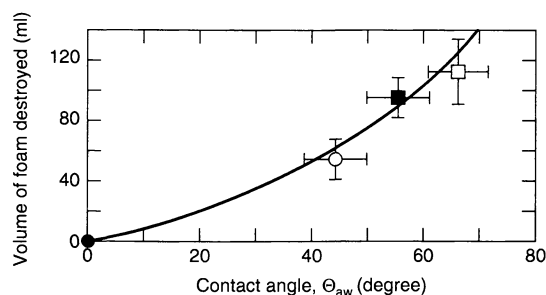


Figure 8.7. Antifoam effect of polytetrafluorethylene particles ($\sim 5 \mu\text{m}$) as a function of the receding contact angle (from ref. (3))

PTFE particles as the antifoam material. A correlation between the foam volume destroyed and the receding contact angle was found from this study (Figure 8.7). The antifoam action for these spherical particles was related to the wettability, contact angle and the bridging characteristics for this particular system.

However, for particles with rough edges, the situation then becomes somewhat more complex. Johansson and Pugh (7) have studied the stability of foams in the presence of finely ground quartz particles of different size fractions. In this work, the surfaces of the different particles were methylated to produce a range of hydrophobicities. Both the dynamic and static froth stabilities were then determined in a froth column. From this, the concept of “maximum enhanced foam stability”, which corresponded to a critical surface hydrophobicity shape and size, was developed.

The mechanism of film collapse by single spherical particles has been studied in cinematographic experiments carried out by Dippennar (8, 9), and the results obtained generally confirmed Garrett’s de-wetting mechanism. In fact, Dippennar (9) emphasized the *dynamic contact angle*, rather than the *equilibrium situation*. This is particularly relevant since foam generation is a non-equilibrium process in which the air–water interface is expanding rapidly. This study appeared to indicate that with large particles and high contact angles, the film easily becomes destabilized. Further experiments carried out with galena (cubic shaped particles) also showed that with contact angles $< 90^\circ$, the froth was destabilized and this was explained by the ease of movement of the three phase boundaries across the smooth regular surface. (Figure 8.8). All of these studies more or less confirm the importance of the size, the shape, and the hydrophobicity of the particle on the foam stability. In fact, the particles characteristics can govern the degree of penetration into the individual foam films and also

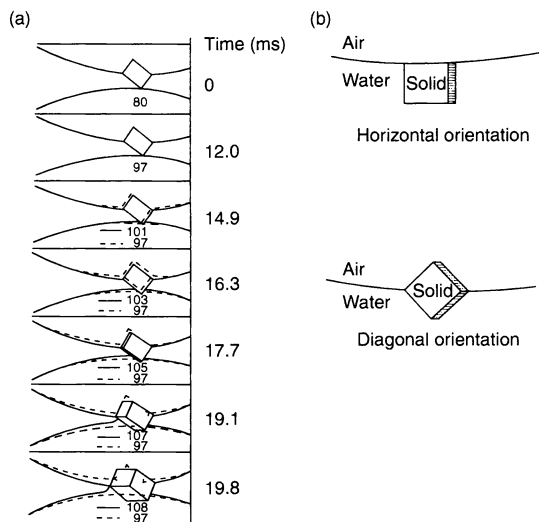


Figure 8.8. (a) Sequence taken from high-speed photography experiments showing the interaction of cubic galena particles with a thinning film, thus demonstrating the importance of the contact angle on the film rupture. The latter can occur as the bubble can bridge both surfaces of the film, whatever the contact angle. With cleaved surfaces, the contact angle gives only a rough guide to stability. (b) Orientation of the cleavage plane can occur in, or diagonally to, the surface. Stable films will interface and thus allow easy movement of the three-phase contact (from ref. (8)), with permission from Elsevier Science

the movement of the three-phase boundary along the surface. In addition, Dippennar (9) demonstrated that in addition to size, the number of particles in the froth could also be related to the stability (thus proving the particles were of uniform hydrophobicity and shape). A simple relationship for the rate of thinning was derived as followed:

$$a^2x = \text{stability constant} \quad (8.4)$$

where x is the number of particles and a is the particle radius.

In an attempt to study the difference between the solid and the emulsified liquid states in defoaming, several thermal (melting) investigations have been carried out by using hydrocarbon particles. Triglycerides and long-chain fatty acids with melting points $< 100^\circ\text{C}$ have been frequently used. Dispersions of the hydrocarbon particles were prepared by first emulsifying the molten material and then cooling below the melting point. Several experiments have shown a *sharp deterioration in the antifoaming effect in the region of the melting points for paraffin waxes in sodium alkylbenzene sulfonate solution* (i.e. where a sharp melting point transition occurs). At higher temperatures, where all of the solid is converted

to liquid, the antifoaming effect has been reported to be much less effective. This behaviour has been explained by the solid particles having a more irregular shape, with sharp and rough edges and apexes, thus producing finite contact angles under dynamic conditions. As the wax melts, the edges are removed and the particles become more symmetrical. Under such circumstances, it would appear that a bridging mechanism comes into play.

Frye and Berg (10) carried out a hydrodynamic analysis of the mode of action of smooth-shaped, inert, solid hydrophobic particles (spheres, discs, rods and ellipsoids) on thin films. It was concluded that for de-wetting and rupture to occur, the receding contact angle must be $> 90^\circ$, while to achieve rapid film rupture and high breakdown rates, then an extra 5° or 10° over this critical angle was required. However, in "foamy" solutions, these values were difficult to achieve and it was suggested that it was then preferential to use rough-shaped particles, which gave sharp angles.

2.10 Mixtures of particles and oils

The synergistic antifoaming effect of mixtures of insoluble hydrophobic particles and hydrophobic oils (filled antifoams) when dispersed in aqueous media has been well established in the patent literature since the early 1950s. Some examples taken from various industrial patents, which indicate the complex nature of the chemistry involved, are shown in Table 8.1. The effect appears to be quite general and even precipitates of polyvalent metal ions with long-chain alkyl phosphates and carboxylates may be combined with mineral oil or PDMS to produce a synergistic antifoaming effect. The sizes of the particles are within the range $0.001\text{--}1\text{ }\mu\text{m}$, with the solid content of the mixture being $1\text{--}20\text{ wt}\%$.

One possible idea for the role of the hydrophobic particles in the synergistic effect is that the *spreading coefficient of the (PDMS) oil is modified by the addition of the hydrophobic particle*. In late studies, Garrett (3) suggested that oil-particle mixtures form composite entities where the particles can adhere to the oil-water surface. The particles alone only show a weak antifoaming action (probably involving de-wetting and bridging in foam films to form holes in a manner similar to that caused by the PTFE particles). However, the behaviour of the particles in adhering to the oil-water interface may facilitate the emergence of oil droplets into the air-water interface to form lenses, thus causing rupturing of the oil-water-air films. This mechanism is similar to that of oil droplets forming mechanically unstable bridging lenses in foam films, where the configuration

Table 8.1. Some examples, taken from the patent literature, of the synergistic antifoaming effect of various mixtures of hydrophobic mineral particles and silicone oils (from ref. (3))

Oils claimed to be effective	Particles claimed to be effective	Actual examples given	Preferred concentration of particles (wt%)
Partially oxidized methylsiloxane polymer. May be diluted with dimethyl siloxane polymer and dispersed in benzene	Silica aerogel, presumably rendered hydrophobic by reaction <i>in situ</i> with the siloxane	As claimed	7.5
Methyl polysiloxane	Finely divided silica, presumably rendered hydrophobic by reaction <i>in situ</i> with the siloxane	Silica + methyl polysiloxane + emulsifiers	2–10
Silicone oils (product may be diluted by hydrocarbons, ethers, ketones or chlorohydrocarbons, although this does not, however, appear as a specific claim)	Aluminium oxides, titanium dioxides, plus various silicas. These react with silicone oil <i>in situ</i> , with the reaction being catalyzed by an acid-condensation reagent	(1) Dimethyl polysiloxane + silica + aerogel + AlCl_3 diluted by toluene. (2) Dimethyl polysiloxane + alumina + SnCl_4 diluted by toluene. (3) Dimethyl polysiloxane + precipitated silica + phosphorous nitrile chloride + poly(ethylene glycol) stearate	1–30
Silicone oils	Pyrogenic or precipitated silicas, hydrophobized with “chemically bound methyl groups” ^a . Special reference is made to the relative ineffectiveness of the oil alone	As claimed	2–8 (preferably 5)

^aprobably silanized.

requires the rupture of oil–water–air films by particles, although the contact angle for rupture is less severe than that required for symmetrical air–water–oil films.

2.11 Emulsion and pseudo-emulsion films

Lobo and co-workers (11) investigated the influence of oil (in the micellar environment) on the stability of foam. Two different types of emulsified oil systems were studied, i.e. (a) a microemulsion (solubilized within the micelle), and (b) a macroemulsion system. It was found that in each case, the foam stability was affected by a completely different mechanism. In the case of (a), where the foam films containing oil is solubilized within the micelle to form a microemulsion, the normal micellar interactions are changed. It had been earlier demonstrated that micellar structuring causes a step-wise thinning due to layer-by-layer expulsion of the micelles and such as effect was found to inhibit drainage and thus increase the foam stability.

In the case of the macroemulsified oil system, the important role of the so-called “pseudo-emulsion” film (formed between the air/water interface, and an

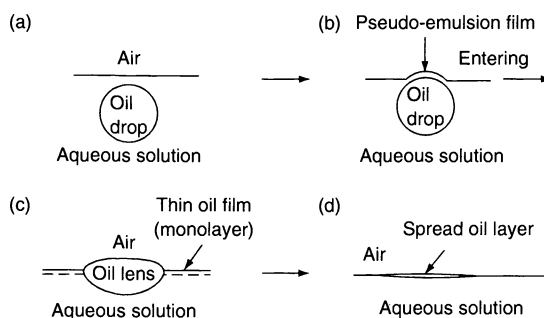


Figure 8.9. A macroemulsified oil system, showing the configurations of the oil at the gas/aqueous interface: (a) oil drop inside the solution; (b) oil drop at the surface separated from the gas phase by a pseudo-emulsion film; (c) oil lens; (d) spread oil layer at the solution surface. The pseudo-emulsion film is unstable, thus enabling the oil to spread on the surface (from ref. (12)), reproduced by permission of Academic Press

approaching oil droplet) on the stability of the aqueous foaming system was emphasized (Figure 8.9). Clearly, the entering and spreading coefficients are

thermodynamic properties, which determine whether the particular configuration of the oil droplet is energetically favourable, although they cannot predict the fate of the oil droplet under dynamic conditions, which exist within the draining film.

Under these circumstances, two distinct cases were considered, i.e. (a) where the pseudo-emulsion film is unstable and the oil spreads, and (b) where the pseudo-emulsion film is stable and the oil drops do not enter the air/water interface. These workers again found that the classical entering and spreading coefficients cannot predict the configuration of oil at the air–water surface, and thus cannot predict the effect of the oil on the foam stability (i.e. even in the case of $E > 0$, the oil droplet will not necessary enter the air/water interface if this film is stable and its stability is controlled by drainage). In fact, the classical theories generally do not consider the excess pseudo-emulsion film energy. In addition, the drainage of the pseudo-emulsion film is extremely complex and may be controlled by several parameters, either singly or in combination. These factors include surface gradients at the interface and the surface viscosity of the film, as well as thermodynamic quantities such as the disjoining pressure and film stratification. In addition, the emulsified oil droplets may also accumulate within the plateau borders of the draining foam films, thus inhibiting the drainage (Figure 8.10).

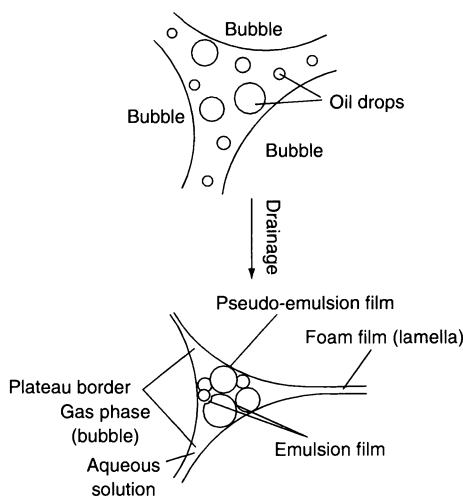


Figure 8.10. Schematic of a macroemulsified oil system. The drainage of the film may be reduced due to accumulation of emulsified oil droplets within the plateau borders. The formation of both the emulsion and pseudo-emulsion films is indicated. The factors effecting the foam stability were found to be the oil volume fraction, drop size and oil phase density (from ref. (12))

Koczko and co-workers (12) also considered the role of the pseudo-emulsion film in the breaking of foam by using both hydrophobic particles and heterogeneous antifoamers (hydrophobic particles and oil). The rupture of the pseudo-emulsion film was again considered to be the primary step for heterogeneous (particle/oil) antifoaming, which eventually leads to a bridging mechanism and finally rupture of the foam film (Figure 8.11). Models for the role of the pseudo-emulsion film in mixed-type antifoamers (containing oil droplets and particles) were also developed.

Wasan and coworkers (13) have discussed an antifoaming mechanism for hydrophobic particles in insoluble liquids which involves the oil droplet containing the particle moving to the plateau border of the draining foam and becoming trapped during the thinning process. The droplets enter the air/solution interface, so forming a lens because the particles destabilize the pseudo-emulsion film, and on further drainage the trapped lens enters another surface of the plateau border, thus forming a bridge and hence leading to rupture.

More recent studies, based on fluorescence labelling and microscopy, by Wang *et al.* (14), were carried out with hydrophobic particles in mineral-based defoamers. In this work, it was clearly shown that the hydrophobic silica particles concentrate in the oil/water interface near the three-phase contact angle line. The sequence of

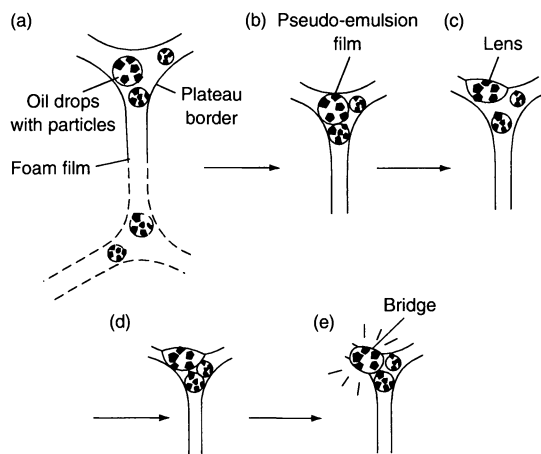


Figure 8.11. The suggested antifoaming mechanism for a mixed-type antifoamer: (a) oil drops (containing solid particles) collect in the Plateau border; (b) the drops become trapped in the thinning border; (c) the pseudo-emulsion film breaks and a drop enters and forms a solid plus oil lens; (d) the lens becomes trapped during thinning; (e) the lens bridges the film at the plateau border and the bridge (from ref. (12)), reproduced by permission of Academic Press

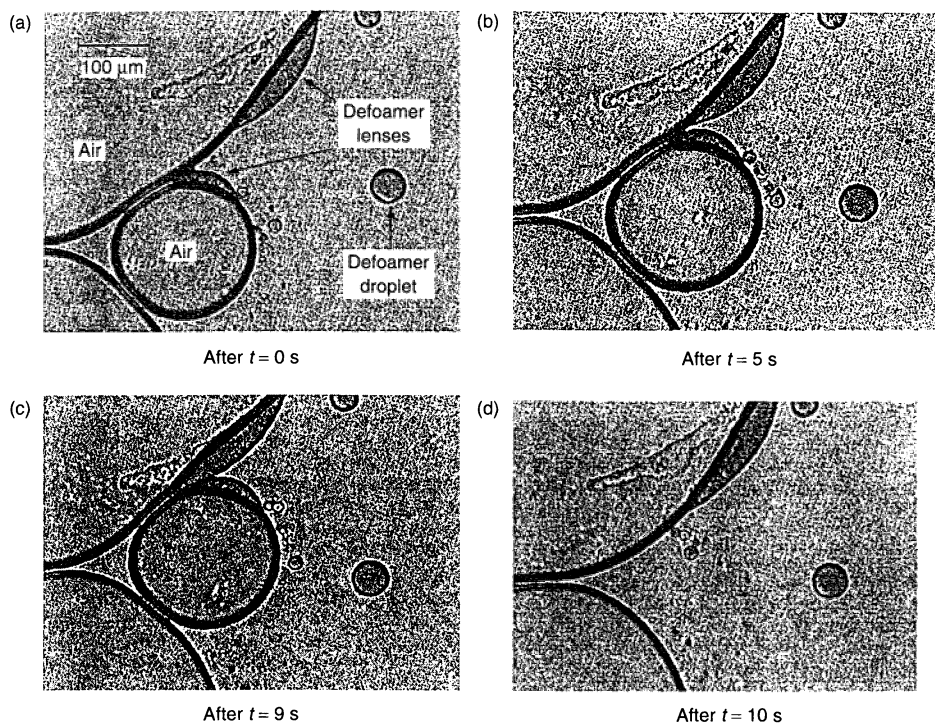


Figure 8.12. A sequence of captured video frames showing the migration progress of the defoamer lens into the film between two air bubbles, thus causing coalescence (from (ref. 14)), reprinted with permission from American Chemical Society

events shown in Figure 8.12 illustrates the migration process of the defoamer lens between two air bubbles which leads to coalescence.

2.12 Electrolytes

Schick and Schmolka (15) have summarized the influence of electrolytes on the foam film thickness and stability for nonionic surfactant systems. Specific effects of such anions on the film “blackening” times have been reported. The order of the magnitude of the effect follows the lyotropic series, where SCN^- and Cl^- act as inhibitors while PO_4^{2-} , SO_4^{2-} , CO_3^{2-} , F^- and OH^- act as promoters of the black film formation, thus promoting foam stability. It has been suggested that the effect is related to the dehydration of the nonionic surfactant molecules.

3 AGEING EFFECTS WITH CHEMICAL DEFOAMERS

There are many explanations available for the decrease in antifoamer performance with time. Some of these

are outlined in Figure 8.13. For example, decomposition due to chemical oxidation of a fatty acid containing unsaturated groups, or the hydrolysis of certain silicones under acidic or basic conditions, may occur with time. This could lead to changes in the surface tension of the materials, thus causing differences in the entering, spreading and bridging characteristics of the antifoamer. In addition, the size of the antifoaming droplet may change. Droplets may become emulsified under shear, and when the size falls below $5\ \mu\text{m}$ thermal energy will dominate over gravity. There is also the possibility that the globules will remain in solution and will no longer be buoyant and capable of entering the air/water interface. By predicting the balance between the buoyancy forces and the thermal forces, Bergeron (16) derived an equation for the critical radius, which corresponded to the optimum antifoamer performance. Drop size reduction may be achieved by increasing the drop viscosity and the interfacial tension. A patent from Diamond Shamrock describes a microemulsion defoamer, composed of an oil in water colloidal dispersion, which is prepared by mixing an ethylene oxide condensate, a coupling agent, water and an anti-gelling agent (17).

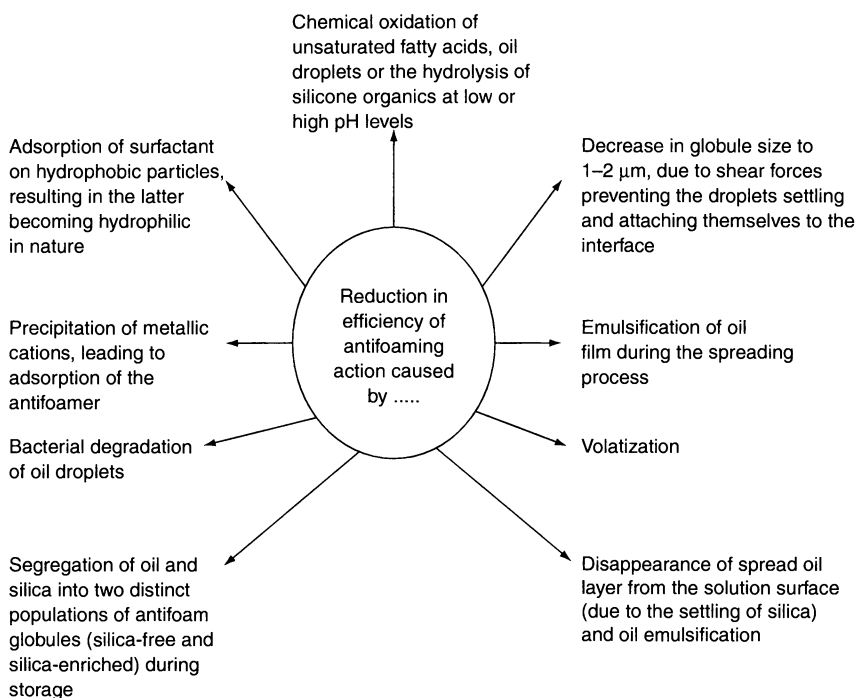


Figure 8.13. Some of the ageing effects of antifoamers

This composition is claimed to be more stable than conventional defoamer systems and also has a lower viscosity.

4 PHYSICAL METHODS OF DEFOAMING

4.1 Ultrasonics

The use of “breaking chemicals” or inhibitors may contaminate the required product and cause additional pollution. A possible solution to this problem is to use weak shock waves to destroy the foam. The idea of utilizing such shock waves to simulate thickness fluctuations in foam films, so leading to accelerated drainage and film rupture, is not altogether novel. In fact, there are several industrial patents describing the application of low frequency vibrations (20–20 000 Hz) to destroy certain types of detergent foams. In addition, a considerable amount of success has been achieved in breaking low viscosity foams produced in the textile and dairy industries. For medium-viscosity foams, which are produced from poly(vinyl chloride)-based adhesives,

the technique has been reported to be only partially successful.

Several attempts have also been made to destroy high-viscosity foams in the food industry (e.g. sugar and molasses), but unfortunately with these highly stabilized systems, the success rate is much lower. However, for the case of particle-stabilized foams (i.e. in the mineral industry, e.g. clays and carbonates) some degree of success has been achieved. Preliminary studies carried out by Sandor and Stein (18) clearly indicate that ultrasonic vibrations can both prevent the formation of foams and destroy foams stabilized with SDS surfactant and that those vibrators, which give the higher power consumption are more effective. It was also shown that the power consumption could be greatly enhanced when a broader tip was used.

In the brewing industry, there is no ideal foam-control method currently in use, although ultrasonics have been tested to suppress foaming in fermenting vessels. The ultrasound generated by ceramic piezoelectric transducers has the unusual property that when an electric voltage is applied across their crystalline ceramic structure, deformation occurs, so that an alternating current thus produces a sinusoidal vibration. The resonance frequency depends on the physical dimensions of the

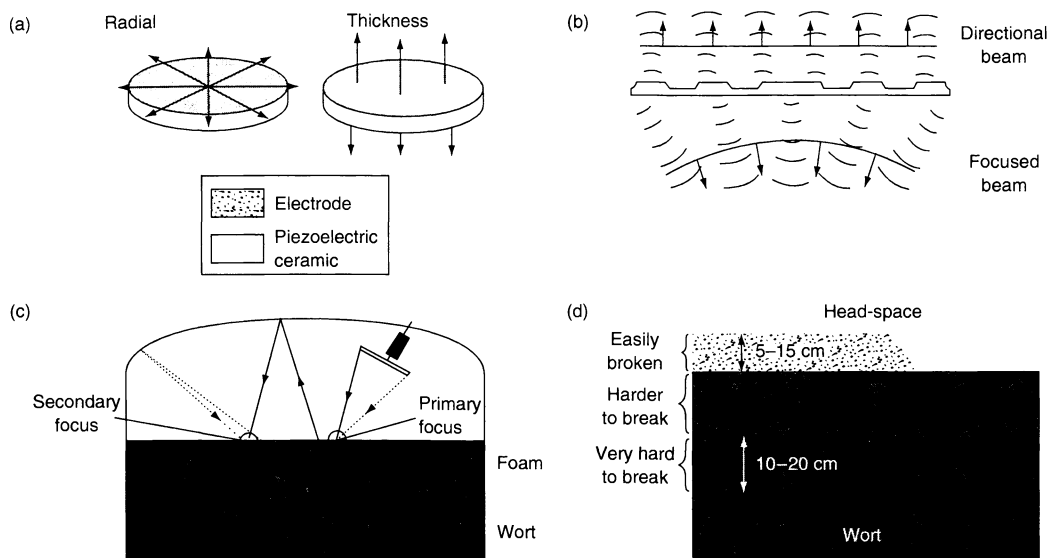


Figure 8.14. Ultrasonic foam breaking: (a) equipment; (b) ultrasonic fields from the radiation plate; (c) effect of reflection around the vessel head-space; (d) the effect of foam position on ultrasonic foam breakage (from ref. (19))

transducer and its surroundings. By using such a system, it is possible to focus the ultrasonic power on to a small volume of the surface foam.

Furtherwork on the use of ultrasound was carried out at the Guinness Brewing Worldwide Pilot Brewery in London (19). It was found that the older foams at the top of the foam layer are more susceptible to breakage with ultrafoam and there was an effect over the entire foam surface. This was explained by reflection around the head-space of the vessel, where the ultrasound can be reflected off the vessel walls and the liquid surfaces. The equipment, plus schematics of the ultrasonic fields from the radiation plate and the influence of the position of the foam on the effectiveness of the breakage, are shown in Figure 8.14. It was also shown that a wide beam of ultrasonic radiation was less effective than a focused beam. From these pilot-scale studies, it was shown that a fermented foam could prove useful in controlling a high-foaming wort.

Other non-chemical methods for foam breaking include projecting air-streams, horizontal rotating discs, paddle wheels, forcing foam through a wire stream, heat (hot wires above the rising foam), sparks, etc.

5 REFERENCES

- Marangoni, C., Difesa della teoria dell'elasticita' superficiale dei liquidi: Plasticita superficiale, *Nuovo Cimento*, **3**, 50–58, 97–123, 193–211 (1878).
- Denkov, N. D., Cooper, P. and Martin, J.-Y., Mechanism of action of mixed solid/liquid antifoamers 1. Dynamics of foam film rupture, *Langmuir*, **15**, 8514–8529 (1999).
- Garrett, P. R., The mode of action of antifoams, in *Defoaming*, Garrett, P. R. (Ed.), Surfactant Science Series, Vol. 45, Marcel Dekker, New York, 1993, pp. 1–118.
- Jha, B. K., Patist, A. and Shah, D. O., Effect of antifoamer on the micellar stability and foamability of SDS solution, *Langmuir*, **15**, 3042–3044 (1999).
- Zemeth, Z., Racz, G. and Koezo, K., Foam control by silicone polyethers – mechanism of cloud point antifoamers, *J. Colloid Interface Sci.*, **207**, 386–394 (1998).
- Venzer, J. and Wilkowski, S. P., Trisiloxane surfactants – mechanism of spreading and wetting, in *Pesticide Formulations and Applications Systems*, Vol. 18, ASTM Special Technical Publication, STP 1347, American Society for Testing and Materials, West Conshohocken, PA, 1998, pp. 140–151.
- Johansson, G. and Pugh, R. J., The influence of particle size and hydrophobicity on the stability of mineralized froths, *Int. J. Min. Process*, **34**, 1–22 (1992).
- Dippennar, A., The destruction of froths by solids, 1. Mechanism of film rupture, *Int. J. Min. Process*, **9**, 1–14, (1982).
- Dippennar, A., The destruction of froths by solids, 2. The rate determining step, *Int. J. Min. Process*, **9**, 15–22 (1982).
- Frye, G. C. and Berg, J. C., Mechanism of the synergistic antifoam action of hydrophobic solid particles in insoluble liquids, *J. Colloid Interface Sci.*, **130**, 54 (1989).

11. Lobo, I., Nikolov, A. D. and Wasan, D. T., Foam stability in the presence of oil, *J. Disp. Sci. Technol.*, **10**, 143–159 (1989).
12. Koczko, K., Kozono, J. K. and Wasan, D. T., Mechanism of antifoaming action in aqueous solutions by hydrophobic particles and insoluble liquids, *J. Colloid Interface Sci.* **166**, 225–238 (1994).
13. Wasan, D. T., Koczko, K. and Nikolov, A. D., Mechanism of aqueous foam stability and antifoaming action with and without oils; a thin film approach, in *Foams, Fundamentals and Applications in the Petroleum Industry*, Advances in Chemistry Series, No. 242, Schramm, L. L. (Ed.), American Chemical Society, Washington, DC, (1994), pp. 47–114.
14. Wang, G., Pelton, R., Hrymak, A., Shawafaty, N. and Heng, Y. M., On the role of hydrophobic particles and surfactants in defoaming, *Langmuir*, **15**, 2202–2208, 1999.
15. Schick, M. and Schmolka, I. R., Foaming, in *Nonionic Surfactants, Physical Chemistry*, Schick, M. (Ed.), Surfactant Science Series, Vol. 23, Marcel Dekker, New York, 1987, pp. 835–879.
16. Bergeron, V., PDMS based antifoams, in *Foams and Films*, Weaire, D. and Banhart, J. (Eds), MIT Verlag, Bremen, Germany, 1999, pp. 41–47.
17. Microemulsion Defoamer, *US Patent* 4 208 301, to Diamond Shamrock (1980).
18. Sandor, N. and Stein, H. N., Foam destruction by ultrasonics, *J. Colloid Interface Sci.*, **161**, 265–267 (1993).
19. Freeman, G. J., Reid, A. I., Valdecantos Martinez, C., Lynch, F. J. and Gallego Juarez, J. A., The use of ultrasonics to suppress foaming in fermenters, in *Proceedings of 26th European Brewery Convention (EBC) in Maastricht, Netherlands*; 24–29 May 1997, Amsterdam, Elsevier, pp. 405–412.

CHAPTER 9

Solubilization

Thomas Zemb and Fabienne Testard

Service de Chimie Moléculaire, Saclay, Gif-sur-Yvette, France

1	Introduction	159	3.1	Definition of solubilization in this case	173
2	Solubilization in Binary Solutions	162	3.2	Soft systems: low bending rigidity, with fluctuations dominating	174
2.1	Small micelles in water	162	3.2.1	Curvature towards water	174
2.2	Solubilization results	163	3.2.2	Curvature towards oil and bicontinuous phase	177
2.3	Jönsson model: solutes in ionic surfactant aggregates and associated phase boundaries	165	3.3	Stiff surfactant system, with rigid interface	181
2.4	When sterical effects dominate: nonionic surfactant and nonionic solute	166	3.3.1	Curvature towards water	181
2.5	Maximum of water solubilization in water-in-oil microemulsions	169	3.3.2	Other cases with a stiff interface: curvature directed towards oil-forming oil-in-water droplets with a stiff interface and lamellar phase	184
2.6	Case of flat interfaces: solubilization of a solute in bilayers dispersed in water	171	4	Conclusion: Open Problems	185
3	Solubilization in Initially Ternary Systems	173	5	References	186

1 INTRODUCTION

McBain and Hutchinson (1) were the first to give a definition of solubilization, i.e. *the increase in the solubility of an insoluble or slightly soluble substance in a given medium*. This phenomenon involves the presence of surfactant molecules or colloidal particles in a single phase which will totally incorporate the insoluble substance.

The expression "single phase" means that all observable properties are independent from the macroscopic locus of the sampling point. By using this definition, micellar solutions, microemulsions, lyotropic liquid crystals or colloids covered by surfactants are single-phase fluids, while emulsions, i.e. microphase

fluid-fluid dispersions, are not single-phase fluids. Some cases are ambiguous, such as the co-existence of small micelles and vesicles, attested by a combination of scattering and microscopy. The swollen lamellar or cubic phase, when the repetition period becomes of the order of the wavelength of light, could also be considered as heterogeneous solutions. By the usual IUPAC definition, dispersions containing observable grains of a different nature are heterogeneous, while a colloidal dispersion contains heterogeneities of the order of one nanometre to one micron.

In the initial state, the solute can be in the form of a pure solid, a liquid or a solution. When the solute is added to a single phase containing surfactant in the form of droplets or solid grains, a kinetic process occurs

which leads to the final thermodynamic equilibrium state. "Complete solubilization" refers to the case where the total amount of initial solute is incorporated in the final single phase. In solubilization, with saturation of the solute, the final state is in equilibrium with excess solute. Experimental investigations often make use of the fixed chemical potential due to the presence of excess solute. For example, the osmotic pressure of a solution is the derivative of the free energy versus the concentration of one component in water, with the chemical potentials of all of the others being constant. This implies the presence of the excess solute to maintain its constant chemical potential.

In this review, we will consider the initial and final states, without considering the general rules of solubilization kinetics (2). These are of crucial importance in detergency formulation, but up to now have been mainly determined via an heuristic approach without any direct relationship with the thermodynamic equilibrium properties. The solubilization of membrane proteins or other intrinsically insoluble proteins by bilayers is a large sub-case of the general case for which detailed reviews (3) are available, and will not be described here. However, in the general approach, no distinction will be made between single-chain surfactants, detergents, synthetic double-chain surfactants and double-chain surfactants of biochemical origin, usually called lipids.

Solubilization of an insoluble solute molecule in a surfactant solution is primarily governed by fundamental properties linked to thermodynamics and structure. These quantities, also at the origin of the general layout of ternary or quaternary phase diagrams, are spontaneous curvature and surfactant layer bending constants. These notions will be briefly introduced and will allow us to distinguish between the different types of solubilization which are observed experimentally.

We will consider the initial surfactant solution containing C surfactant molecules per cm^3 . For typical 30 g/l formulations (3 wt%), C is of the order of 10^{20} molecules/ cm^3 . If the surfactant molecules are randomly distributed, the individual molecules are on average about 20 Å apart. However, the self-assembly, which occurs for certain surfactants produces a water-oil interface with a specific area, Σ , in cm^2/cm^3 of solution, given by the following:

$$\Sigma = C\sigma \quad (9.1)$$

where σ is the interfacial area per molecule, a fundamental quantity which is usually of the order of 50 to 100 Å²/molecule. The area σ is either the inner area of micelles in the case of binary surfactant solutions, or the total oil/water interface in ternary systems, which

may adopt droplet or bicontinuous microstructures. The specific area Σ can be experimentally determined by small-angle-scattering (SAXS or SANS) experiments in the Porod region. A basic problem for a given solute is to determine if the presence of the solute will have an effect on the value of σ .

About 25 years ago, Ninham and co-workers (4) introduced a scalar quantity, P , which reflects the possibility of packing surfactant molecules laterally. This parameter is given by the following:

$$P = V/\sigma\ell \quad (9.2)$$

where V is the effective volume associated with each hydrocarbon chain, including the penetration of oil in the case of ternary system. Since the film thickness, ℓ , corresponds to the radius in the case of spherical or cylindrical micelles, it cannot be directly accessed in the case of a ternary solution. The interfacial area σ corresponds to the area of the surfactant at the polar/apolar interface, as defined above.

A common problem in the evaluation of binary and ternary systems to which a solute has been added is the basic distinction between the mean area per molecule and the partial molecular surface. When areas per molecules are measured, the link between total area and molar fraction may be highly nonlinear, in particular for the case of solutes denominated as cosurfactants which are solubilized in the palisade layer. The partial molar area is the increase of surface per surfactant due to the addition of a solute at a constant density of surfactant, while the area is the observed average. This problem has been discussed in detail by Boden *et al.* (5).

The physical meaning of the surfactant parameter P is the steric possibility of packing laterally, preferring direct, i.e. oil-in-water (o/w) or reverse, water-in-oil (w/o) structures and is related to the chemical potential. Phase diagrams and micellar preferred shapes can be calculated as a function of P , which usually depends only on temperature and oil/chain wetting in the case of nonionic surfactants. In the case of ionic surfactants, the "dressed" model has to be considered since the area per head-group is strongly linked to the ionic strength of the solution (6). Again, a basic question for solubilization is to determine whether the surfactant parameter varies when the solute is added to the initial surfactant solution.

In the case of binary systems, the values of V and ℓ are linked to micellar size. In water-oil-surfactant ternary solutions, more degrees of freedom for the shape come into play. Thus, two more quantities are usually considered, i.e. the average and Gaussian curvatures of the interface, averaged over the whole sample, $\langle H \rangle$ (Å⁻¹) and $\langle K \rangle$ (Å⁻²), respectively. The condition

for the complete coverage (7) of a surface by a surfactant film of packing parameter P is as follows:

$$P = 1 - \langle H \rangle \ell + 1/3 \langle K \rangle \ell^2 \quad (9.3)$$

if $\langle H \rangle$ is positive when the film is curved towards the oil.

If we consider now the energy of the surfactant film, a classical relationship for the bending energy per unit area, E_b , is given by the following:

$$E_b = 2k_c(\langle H \rangle - H_0)^2 + \bar{k}_c(K - K_0) \quad (9.4)$$

where H_0 and K_0 are the spontaneous values of the membrane curvature. This expression leads to inconsistencies (8) in the case of non-zero spontaneous values of H_0 and K_0 . It is therefore difficult to determine k_c and \bar{k}_c independently. A more usable form of the bending energy can be obtained from the variation of the packing parameter, as given by the following:

$$E_b = 1/2k^*(\langle P \rangle - P_0)^2 \quad (9.5)$$

where k^* is an elastic constant and P_0 is the spontaneous value of the surfactant parameter, linked to the spontaneous value of the membrane curvature by the following relationship:

$$P_0 = 1 - \langle H_0 \rangle \ell + 1/3 \langle K_0 \rangle \ell^2 \quad (9.6)$$

Surfactant solutions can be separated into two different categories, namely soft interfaces, where $k^* < k_B T$ and stiff interfaces, where $k^* > k_B T$. The first category includes the case of short single-chain ionic surfactants, together with a cosurfactant which may be a nonionic surfactant, while the second class typically contains surfactants with charged head-groups and long hydrophobic tails, double-chain surfactants, and lipids. We will consider these two cases separately in the following discussions.

A central issue in understanding and approaching predictive theories for solubilization is the ability to predict how the spontaneous packing parameter P_0 will increase or decrease due to the presence of the solute.

A concept equivalent to spontaneous curvature is used in the petroleum industry, i.e. the R -ratio quantifying the hydrophilic-lipophilic balance (HLB), as introduced by Winsor (9). The R -ratio is arbitrarily set to 1 when the spontaneous curvature is zero. Then, by using differential values, the R -ratio for a given water-oil-surfactant combination is given by the following:

$$R = \frac{A_{co} - A_{oo} - A_{ll}}{A_{cw} - A_{ww} - A_{hh}} \quad (9.7)$$

where A_{co} , A_{oo} and A_{ll} represent interaction energies between chains and oil, oil and oil and chain-chain, respectively, while A_{cw} , A_{ww} and A_{hh} represent interaction energies between chains and water, water-water and the repulsion between head-groups, respectively. These R values can also be used to investigate the effect of salts or cosurfactants on solubilization, by the introduction of an equivalent ethoxy number (EON), experimentally determined by some change in the physico-chemical behaviour. This general numerical approach is successful in deriving, by analogy, the different solubilization properties from one nonionic surfactant mixture to another.

Winsor also introduced the convenient and popular classification of "Winsor I", "Winsor II" and "Winsor III" phase equilibria which are widely found in the literature. "Winsor III" means that three fluids are in thermodynamic equilibrium, while the other two denominations represent the symmetric cases of emulsification failure: "Winsor I" refers to the case where the excess phase is mainly oil, while "Winsor II" is that where mainly water is rejected. If the microstructure is made up of isolated droplets, a general assumption – necessary for "Bancroft's rule" to hold – is made such that the fluid inside the droplets is of similar composition to that of the excess bulk. However, bicontinuous microstructures have been demonstrated to exist whether in Winsor I, Winsor II or Winsor III regimes (10).

However, there is a hidden complication common to the generalized approach of using one parameter to represent spontaneous curvature in the form of the surfactant parameter P or the HLB-related R value. In the case of charged surfactants, the water/oil interface curvature is strongly influenced by the effective charge per unit area. This effective charge has a maximum value, i.e. the structural charge per unit area. Some counterions are located in the polar region of the interface due to strong specific chemical binding or to general physical condensation. This partial "binding" of counterions may reduce the charge per unit area by a factor of typically one third in the case of ions such as sodium, and up to one tenth in the case of strongly binding ions such as bromide or cesium. Therefore, the binding of counterions can vary by a factor of up to 2, due to the presence of a solute in the palisade or polar layers. Hence, the generalized approach of solubilization using an intrinsic value or the surfactant parameter P , self-consistent for uncharged surfactants, is limited by this "bootstrap" effect in the case of charged interfaces, particularly in the absence of "background salt".

2 SOLUBILIZATION IN BINARY SOLUTIONS

2.1 Small micelles in water

In water, above the critical micelle concentration (CMC), surfactant molecules self-assemble into micelles. Figure 9.1 illustrates the microenvironment of a micelle. The core of the micelle is comparable to a pure alkane, but with a significantly higher viscosity. The area of contact per molecule is in the range 0.5 to 1.5 nm^2 , larger than the geometrical area of the polar head-group. The effective area is determined by the balance between repulsive and attractive surface forces (6). This means that a significant part of the hydrocarbon interior is exposed to water. The volume where only hydrocarbon is found is significantly smaller than the total micellar volume, which includes all water molecules “bound” to the head-groups (10). This experimental observation implies the existence of a transition region, which is neither a pure “interior”, nor a pure polar region. The latter contains head-groups as well as “bound” water, and is included in the effective excluded volume of the micelle (10). The transition region between the polar region and the interior is traditionally referred to as the “palisade layer”. Figure 9.1 shows a scaled view of a typical ionic micellar microstructure. The transition from the core of the micelle to bulk water through the palisade layer also corresponds to the region where permittivity and other local properties change from those of an oil to that of water. This permittivity change induces a lowering of the free energy for the insertion, of partly polar molecules or aromatic groups, as well as strong dispersion forces (11, 12). The permittivity change associated with the transition from core to bulk is schematized in Figure 9.1. The core permittivity is close to 1, while the water bulk one is around 80. The palisade and head-group regions correspond to steeply varying values of permittivity (as well as a local variation of water volume fraction). Hence, for all partially polar solutes, there is a definite average distance from the centre of the droplet where dispersion interactions can be enhanced. This variation of permittivity is also the origin of mirror charges which are taken into account in predictive theories able to evaluate the distribution of counterions and charged molecules in reverse micelles (12).

Whatever the detailed free energy balance involved in transferring a solute from outside to a micellar solution, four microenvironments have to be considered, i.e. bulk solvent, polar region, palisade layer and core of the micelles. The two intermediate regions shown

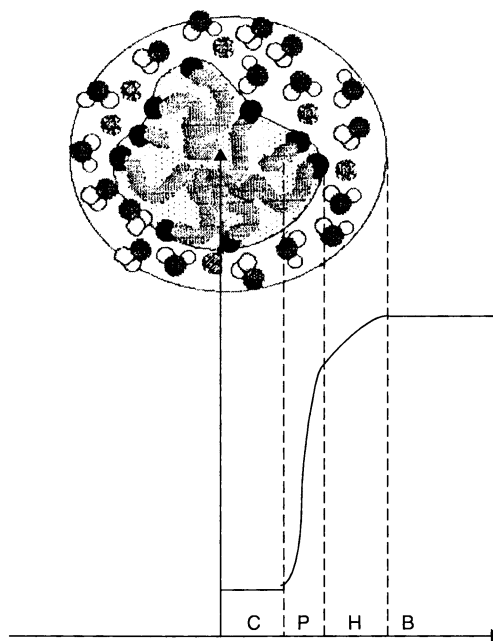


Figure 9.1. Schematic representation of the interior of an oil-in-water direct micelle, with the corresponding radial distributions of polar heads, local permittivity and water penetration. The region with partial water penetration is known as the palisade layer. The polar layer contains the head-groups, the non-dissociated counterions and the water bound to head-groups included in the excluded volume of the micelles. The core of the micelle is pure liquid hydrocarbon. Four environments are hence available for solubilization, namely hydrophobic core (C), palisade layer (P), polar layer (H) and bulk solvent (B)

in Figure 9.1 are involved in most of the cases. The core is pure hydrocarbon, while the palisade layer is the region where some penetration of solvent can be found. The radial distribution of head-groups extends over the whole polar region. High-resolution neutron scattering results for the well-studied sodium dodecyl sulfate (SDS) give the radius of the core as 1.5 nm , and the thickness of the palisade layer as 0.3 nm , with a polar layer volume equivalent to the core volume (13). These orders of magnitude are important when maximum volume concentrations of solutes are compared to the volumes of the different solubilization sites.

Water-insoluble molecules may be incorporated either in the core or in the palisade layer of the micelles. However, solubilization could induce a shape transition of the micelles and even a global phase transition in the thermodynamic sense.

2.2 Solubilization results

Our aim here is not to present all of the experimental methods which allow quantitative determination of solubilization. In all cases, either composition determination of surfactant and solute have to be carried out separately, or the use of a spectroscopic method is reliable enough to give an unambiguous measure of the surfactant and solute content of a sample (14, 15).

By analogy with solid particle dispersions, adsorption isotherms can be determined as a function of the chemical potential of the solute. An indirect, but rapid and powerful, example is given by surface tension measurements, which can detect very low amounts of surface-active solute in the form of contaminant. This property is used to determine purity in easily hydrolysable surfactants such as SDS or sodium bis(2-ethylhexyl)sulfosuccinate (AOT). A minimum in the surface tension near the CMC directly detects the presence of a surface-active contaminant such as dodecanol or octanol, which will desorb from the interface at high surfactant concentrations. This desorption is the origin of the a priori counter-intuitive increase of surface tension with surfactant content (16).

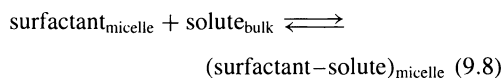
In solubilization studies (15), different definitions and concentration units are used. As several quantities could change through a solubilization experiment, the initial, final and reference states have to be defined precisely. Usually, mainly one point of the solubilization isotherm is studied, i.e. the maximum additive concentration (MAC). This concentration is obtained when the solution is in equilibrium with the pure solute. Another easily accessible region is the diluted region of the isotherm where the number of moles of solute per mole of surfactant is low (of the order of 1% maximum).

The saturated solution is sometimes difficult to determine, especially when a pure liquid solute is in equilibrium with a surfactant phase. In collections of thermodynamic equilibrium surfactant phase diagrams (17), solubilization is represented by tie-lines between an isotropic or liquid crystal phase and a nearly pure solute. Experimental determinations of these tie-lines require two separate experiments: the first of these is the analysis of the total solute content in a well-separated surfactant solution, while the second one is to control that any initial point taken on a given tie-line produces identical compositions of the phase containing the solute. When micro-phase separation occurs in one part of the phase diagram, the surfactant solution appears to be isotropic, although two phases are co-existing. In such a case, the two experiments are the only way to determine this microphase separation concentration.

For different initial compositions of the sample along a tie-line determined from one phase-separation experiment, the composition of the two macroscopically separated phases will change. In this case, it is very difficult to obtain the amount of solute solubilized in one surfactant phase.

Different definitions of solubilization and related constants are used in the literature, as described in the following.

1. One general concept is the pseudo-phase model where the micelles are considered as a separate macroscopic phase. One considers all micelles as a separate "bulk" of mole fraction determined by the overall content. Within the framework of the pseudo-phase model, solubilization is considered as an equilibrium of the solute between the micellar phase and the bulk, i.e. $\mu_{\text{solute}}^{\text{bulk}} = \mu_{\text{solute}}^{\text{micelle}}$, where μ_{solute}^i is the chemical potential of the solute in the aqueous bulk phase or in the micellar phase. The equilibrium between the two phases is described by the partition coefficient, P_{coef} , which is given by $X_{\text{micelle}}/X_{\text{bulk}}$, where X_{micelle} represents the molar fraction of solubilize in the micelle and X_{bulk} the molar fraction of the solubilize in the water bulk (18). Concentration units can be used instead of the molar ratio, but this requires a knowledge of the volume of surfactant and solute in the micellar phase. These are generally unknown and have to be determined via precision densitometry (10). The partial volumes reflect the interactions between solvent and surfactant film. It has been proved recently (19) that the volume variation of water in AOT surfactant films of oil reversed-micelles could be very important ($\sim 30\%$), thus inducing large errors in equilibrium constants if volumes are simply supposed to be additive from infinitely diluted states.
2. An alternative general approach (20) is the mass action model where the transfer of the solute in the micelle is treated as a binding phenomenon through the equilibrium process:



The binding constant is given by the following:

$$K = \frac{[(\text{surfactant-solute})_{\text{micelle}}]}{[\text{surfactant}_{\text{micelle}}][\text{solute}_{\text{bulk}}]} \quad (9.9)$$

The concentrations are defined with respect to the entire volume of the solution. In this case, the concentration of the micellized surfactant is the excess

over the CMC. A dangerous implicit hypothesis is that the concentration of monomers in equilibrium with the micelles is equal to the CMC and independent of the presence of the solute. This is a poor approximation near the CMC, since the presence of apolar solutes is known to decrease the concentration of monomers in equilibrium with micelles by nucleation of the micelles around the insoluble material (18). However, far from the CMC, it is possible to relate the binding constant with the partition coefficient through the following equation:

$$K = \frac{X_{\text{micelle}}}{(1 - X_{\text{micelle}})[\text{solute}_{\text{bulk}}]} \quad (9.10)$$

where $[\text{solute}_{\text{bulk}}]$ is related to X_{bulk} , where the latter is given by $[\text{solute}_{\text{bulk}}]/(55.5 + [\text{solute}_{\text{bulk}}])$

3. In recent studies of solubilization (14), another equilibrium constant has been defined, i.e. $K' = X_{\text{micelle}}/[\text{solute}_{\text{bulk}}]$, with the M^{-1} units of the binding constant K , but more closely related to the partition coefficient, P_{coef} .

In order to obtain thermodynamic data, all of these constants have to be transformed into thermodynamic constants, K_{γ} . Because of co-operative effects in the micelles, the solution is not ideal and the activity of the solute has to be used instead of the molar fraction or concentration. This approach requires the precise definition of standard states. In the articles of Ben-Naim (21) or of Tanford (22), some different standard states are proposed for the solute, i.e. a pure solute or an infinitely dilute state.

By using vapour pressure measurements (14), the activity of the solute, $a = \gamma X_{\text{micelle}}$, can be determined as the ratio between the partial pressure above the micellar solution and the partial pressure above the pure solute. In this case, the standard state refers to the pure liquid solute or to solute in a supercooled liquid state. The activity coefficient which gives the deviations from ideality is a way of measuring the interaction between solute and surfactant in the aggregates. Once the activity is determined, the standard Gibb's energy of solubilization could be obtained, as follows:

$$\Delta G_t^0 = -RT \ln K_{\gamma} \quad (9.11)$$

This Gibb's energy, which is associated with transfer in micelles, is tabulated in the literature (18, 23) and is often compared to the Gibb's energy of transfer between octanol and water. The octanol/water scale has been used to correlate the solubility data in micellar systems for compounds belonging to the same series (18). As illustrated in Figure 9.2 (24) for some solutes solubilized

in an SDS micellar solution, the average solubilization site has macroscopic properties similar to that of octanol–water mixtures.

The limitations of the mass action model are due to the fact that this model introduces constants which ignore the effect of solute on the microstructure of the micelle. On the other hand, the limitations of the pseudo-phase model are also severe, but appear in different cases. Take, for example, the study of the solubilization in mixed micelles. Treiner and co-workers (25) have studied the solubilization of pentan-1-ol and benzyl alcohol in binary mixture of two cationic surfactants in water, i.e. benzyldimethyltetradecylammonium chloride ($C_{14}\text{BzCl}$) and trimethyltetradecylammonium chloride ($C_{14}\text{Cl}$). From calorimetric experiments, they observed a maximum and a minimum in the curve describing the partition coefficient versus the micellar composition. Because of the chemical similarity between the two surfactants being used, the overall shape of the micelle is not expected to change with micellar composition. Therefore, determination of the macroscopic partition coefficient, P_{coef} , is not sufficient to describe precisely the mechanism of solubilization in such a system. It is too simple to consider the micelle as a homogeneous pseudo-phase. The solute is not uniformly dispersed in the micelle: several solubilization sites exist, with different associated solubilization free energies. This situation can also be detected by nonlinearity in the adsorption isotherm. For example, Ekwall *et al.* have summarized all cases where a well-defined threshold for solubilization exists (26). This threshold appears at a lower concentration than the CMC, and is the first

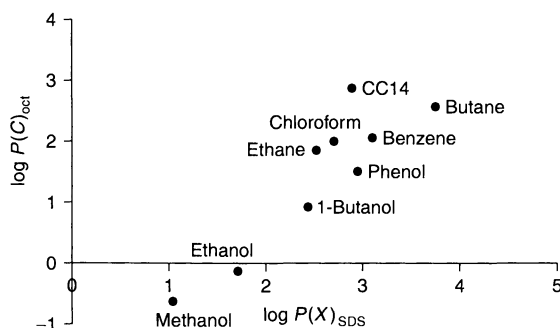


Figure 9.2. Correlation between the logarithm of the octanol–water concentration partition coefficient and the logarithm of the molar partition coefficient between SDS micelles and water for a series of simple solutes in SDS micelles. The average solubilization site has macroscopic properties which are similar to those of octanol–water mixtures. (Reprinted with permission from ref. (24), copyright 1994, The Journal of Colloid and Interface Science)

concentration where solubilization occurs via nucleation of a mixed micelle: this specific concentration is designated as the limiting association concentration (LAC). From molar compositions near the LAC, a typical aggregate contains one solute molecule and forms at CMC/LAC ratios of 5. The origin of a maximum of the solubility constants close to the LAC is counter-intuitive, and inconsistent within the frame work of the mass-action model, as well as the microphase separation models, and can only be explained by the general electrostatic model developed by Jönsson and co-workers (27), as will be explained below.

Mukerjee *et al.* (28) proposed a two-site model, i.e. core and palisade layer, associated with the partition of the solute in the micelle. However, the physical origin of the solubilization effect is not explained. Some general results are also not explained within the frame work of this two-site model, as, for example, why the solubility of an alkane is lower in the core of the micelle than in the same volume of pure oil.

Various standard experimental techniques employed in physical chemistry, such as NMR spectroscopy, titration, fluorescence spectroscopy, etc., are used routinely to determine the partition coefficients in solubilization studies, and a large number of publications tabulate the experimental results obtained in terms of equilibrium constants (14, 16).

However, to our knowledge, only three published models are able to predict the localization of the solute in the aggregate and/or the phase transitions induced by the presence of a solute. In the following, we will summarize the main inherent underlying assumptions. Jönsson and co-workers have developed a predictive model concerning the solubilization and phase transitions in ionic micellar solutions (27, 29). This model correctly predicts the localization of solute and presents the phase diagram as a function of the polarity of the solute. Kunieda *et al.* (30, 31) developed a model of solute localization in hexagonal and lamellar phases of nonionic surfactants. Finally, Leung and Shah (32) have shown the generality of the observed maximum of water solubilization in the reversed-micellar phase via a qualitative model of the interfacial film.

2.3 Jönsson model: solutes in ionic surfactant aggregates and associated phase boundaries

Jönsson and co-workers (27, 29) introduced a general explicit model which uses a numerical evaluation of the free energy variation associated with solubilization in

order to predict the behaviour of uncharged molecules in ionic surfactant aggregates. This model evaluates the thermodynamic properties of the solution from the knowledge of the molecular properties of both surfactant and solute. In such a model, the micelle is divided into two regions, i.e. the core and the palisade layer. The tendency of the solute to be localized in one of these two regions is given by its polarity, which is assessed by the difference in the standard chemical potentials of the solubilize between the two regions, $\Delta\mu_{p-c}^0$. This difference is not a free parameter, but is calculated from γ_{mac} , the macroscopic value of the surface tension between pure solute and water. Assuming no difference in standard potential between a solubilize in the core of the micelle and one in the pure bulk solubilize phase, we have the following relationship:

$$\Delta\mu_{p-c}^0 = (\gamma_{mac} - \gamma)A_s + \mu_{mix} \quad (9.12)$$

where A_s is the minimum interfacial area for a solubilize molecule and μ_{mix} is a correction term for the deviation from the standard state of the pure solubilize due to the presence of water. The interfacial energy resulting from the contact between hydrocarbon and water is given by $G = \gamma n_{mic}A$, where n_{mic} is the number of micelles, A the interfacial area per micelle and γ a proportionality constant. As the experimental value of γ for many different lamellar phases is 18 mJ/m², γ was fixed at this value for all types of systems.

Then, consistent with the dressed model of ionic micelles (6) dominated by charge regulation and surface tension associated with partial water/oil contact at the surface of the micelle, the thermodynamic model takes into account the electrostatic free energy, the entropy of mixing, the interfacial energy and some geometrical constraints. Therefore, this model could predict not only the localization of the solute in the micelle (core or palisade layer), but also the extension of the different phases in the three-component phase diagram, i.e. ionic surfactant–water–solute. By using this general model and examining the extension of the mixed micellar phase, as well as the lamellar and hexagonal phases, Jönsson and co-workers deduced the balance of a solute in a given micellar system between the core and palisade layer. In the reverse sense, once the localization is known by analogy, the extension of the different phases in the three-component phase diagram (ionic surfactant–water–solute) could be obtained.

For micelles, the localization of the solute depends on both the charge density of the micelle and the polarity of the solute. The localization of the solute is given by the main effect of the competition between the gain in surface charge density and the reduction in interfacial

energy. By using a large set of solutes and surfactants, the following general conclusions were made:

- (i) Apolar solutes such as hydrocarbons are solubilized in the interior of the micelles with a low charge density (< 0.2 charge/nm²), because geometrical packing produces a large reduction in the interfacial energy in this case. The same apolar solutes are preferentially dissolved near the palisade layer for micelles with high charge density (> 0.4 charge/nm²), because of the favourable mixing with amphiphiles and the reduction of the surface charge density.
- (ii) Polar molecules such as long-chain alcohols are solubilized in the palisade layer in micelles with a high charge density. However, due to a high reduction of the micellar interfacial area per amphiphile, the first solute molecule is always solubilized in the interior of the micelle. In the case of micelles with low charge density, most polar solutes are located in the interior of the micelles.

Jönsson's model has been extended by considering the phases which could be in equilibrium with the micellar phase (29). Taking into account an approximate expression for the van der Waals energy and the hydration energy, as well as mixing between water and solubilize, lamellar and reversed-micellar phases are found in true equilibrium with direct micelles. Complete theoretical ternary phase diagrams can be constructed and compared to experimental ones when the polarity of the solute is varying.

By using potassium decanoate as an example of a highly charged micelle of well-defined volume, the phase nature and extension for competing phases co-existing with micelles at the maximum admissible concentration (MAC) can be explicitly predicted. The polarity of the solute is modified through the value of the standard chemical potential, $\Delta\mu_{p-c}^0$. For a non-polar molecule ($\Delta\mu_{p-c}^0 = 2K_B T$) the location is favoured in the core and excess pure solubilize is in equilibrium with the micellar solution. A reversed-micellar domain appears for intermediate polarities, which then disappears for higher polarities of solute ($\Delta\mu_{p-c}^0 = 0.7K_B T$). All of these three situations are observed experimentally for different solutes.

The solubilization associated with the LAC, below the CMC of the surfactant results from an interaction between the surfactant and the solute. This phenomenon has been known since 1927 for the cases of alcohols and fatty acids with a large variety of surfactants (26). The general model developed by Jönsson and co-workers predicts this increase of solubility before the CMC of the

surfactant is reached but it also predicts the shape of the curve of "solute solubility versus surfactant concentration" for polar solutes. The experimental and theoretical behaviours are illustrated in Figures 9.3(a,b) (27). The local maximum in the solubility occurs when the aqueous solution of surfactant changes from being in equilibrium with a reversed-micellar phase to being in equilibrium with a lamellar phase. The calculated phase diagram below the CMC of the surfactant is represented in Figure 9.3(c) (29). The initial increased solubility of alcohol is attributed to an attractive interaction between alcohol and surfactant. At a certain surfactant concentration, it is more favourable for the alcohol to be solubilized in the lamellar aggregates than in the alcohol-water mixture, and therefore the pre-micellar solution is in equilibrium with a highly swollen lamellar phase. This results from the influence of the van der Waals attractive forces which determine how the bilayers swell with a given decay in the net repulsion between such bilayers. The great success of this general approach (including the electrostatic terms) is the rationalization of the nonlinearity of solubilization near the LAC, due to the change in microstructure of the solute-rich phase in equilibrium with the mixed aggregates.

2.4 When sterical effects dominate: nonionic surfactant and nonionic solute

Kunieda and co-workers (30, 31) considered the general case of the effect of added oil or perfume molecules on the structure of liquid crystals in poly(ethylene glycol) monododecyl ether (C₁₂E_n)-water systems by the means of phase diagrams and small-angle X-ray scattering (SAXS) measurements. When decane is added to the C₁₂E₇-water system, a transition from a normal hexagonal liquid crystal to a water-continuous cubic phase is observed, whereas a transition from a lamellar to a reversed-hexagonal phase takes place when decane is added to the C₁₂E₃-water system. Adding oil has the opposite effects on the curvature of the surfactant layer, depending on the hydrophilic or lipophilic nature of the surfactant. This is the cause of the drastic effect on the curvature induced by oil in a binary surfactant-water system.

These effects were explained by a simple model of localization of the oil in the aggregates. The oil can penetrate into the chain layer and therefore tends to increase the effective area per surfactant molecule, σ , without increasing the volume of the aggregate. This is known as the "penetration" effect. On the other hand,

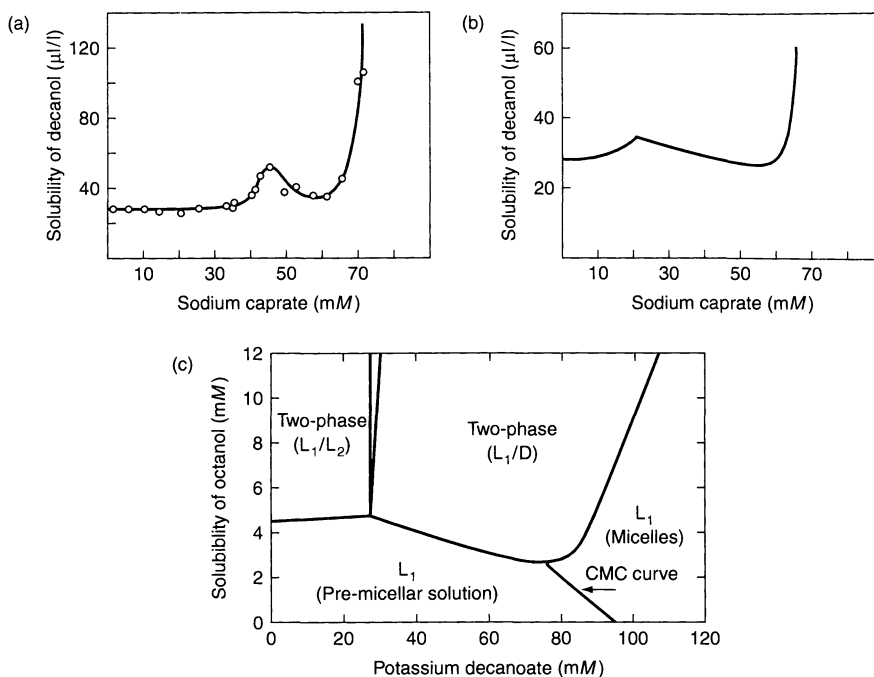


Figure 9.3. (a) Experimental solubility curve of decanol in sodium decanoate–water solution at 40°C (27). (b) Calculated solubility curve of decanol in sodium decanoate–water solution at 40°C, obtained with the model developed by Jönsson and co-workers (27). (c) Predicted octanol solubility in potassium decanoate–water solution (28). (Reprinted with permission from the American Chemical Society, copyright 1992)

the “swelling” effect means that the oil increases the volume of the lipophilic part without expanding σ . This is illustrated in Figure 9.4 (31). Hence, depending on the relative value of the variation of the area per surfactant and the hydrophobic volume, V , per surfactant, different variations in the surfactant parameter, $P = V/\sigma\ell$, are expected. The cases considered by Kunieda and co-workers were restricted to those where ℓ is fixed by the maximum extension of the chain length, i.e. cases when the solute molecule is smaller than the surfactant. The spontaneous curvature – related to the packing parameter – is the microscopic driving mechanism linked to the hydrophobic–lipophilic balance (HLB), and the observed phase sequence can follow sequences either towards normal or reversed-curvatures, depending on the solute being considered. All of these effects will remain qualitative with defined concepts if they cannot be accessed directly as in liquid crystalline phases.

Indeed, in the hexagonal phase, for example, the infinitely long cylinders are packed in an hexagonal array. The radius, r_h , of the lipophilic core and the area per surfactant molecule, σ , are calculated from geometric considerations as a function of the

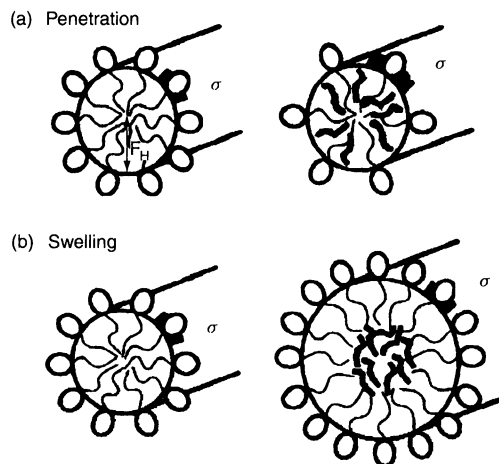


Figure 9.4. Schematic representations of (a) solute penetration and (b) swelling in the hexagonal phase. (Reprinted with permission from ref. (31), copyright 1999, The Journal of Colloid and Interface Science)

interlayer spacing, d . Assuming that for “penetration”, oil molecules are completely interdigitated in the chain

layer and never solubilized in the core region, r_h can be assumed constant, and thus the variation of d with r_h will be given by the following:

$$d = \left(\frac{\sqrt{3}\pi}{2} \frac{1}{\phi_L + \phi_O} \right)^{1/2} r_h \quad (9.13)$$

On the contrary, for a pure surface “swelling” mechanism, it is assumed that all of the oil molecules are in the core of the aggregates and will never be found in the chain layer. In this case, σ is assumed to be constant, and the following equation gives the variation of d as a function of σ :

$$d = (2\sqrt{3}\pi)^{1/2} \frac{V_L}{\sigma} \frac{(\phi_L + \phi_O)^{1/2}}{\phi_L} \quad (9.14)$$

where V_L is the volume of the chain of the pure surfactant.

In this evaluation, the values of r_h and V_L/σ for a given surfactant are obtained from the measurement of the periodic spacing d in the absence of oil by SAXS experiments. In practical cases, the change in d of the hexagonal phase in the presence of a solute should be observed between these two extreme situations because the oil molecules are distributed between the core and the chain layer of the surfactant. By employing series of insoluble molecules (including additives) which are often used in perfume formulations, Kunieda and co-workers (31) demonstrated that precise measurements of periodicities in the presence of solutes allow an identification, for a given solute, of the predominance of increase of area or increase of volume. Thus, all solutes in nonionic aggregates can be classified into two classes for a given nonionic “host system”, i.e. those that induce a curvature towards water and those that induce a curvature towards oil.

Figure 9.5 (30) illustrates the results obtained for different oils added to the $C_{12}E_7$ –water system. It is clear that decane molecules are mainly located in the core of the surfactant aggregate, whereas m -xylene molecules are distributed between the core and the chain layer of the surfactant. The first molecules of dodecanol are located in the chain layer, but solubilization in the core occurs on further addition.

Qualitatively, when the oil penetrates the chain layer, the area tends to expand, while the surface energy tends to increase; in order to minimize this increase, the contraction forces would act to shrink the surface area. In this case, the volume of the surfactant chain, V_L , in the packing parameter P will also increase. To minimize the increase in σ , a change of shape with a larger packing parameter is energetically favoured. Therefore, with the convention of a positive curvature

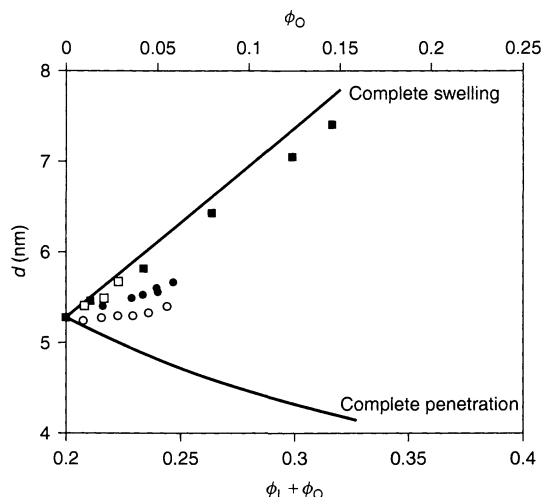


Figure 9.5. Interlayer spacing shifts as a function of the volume fraction of added solute and surfactant chain. Comparison is shown with the predicted theories of “penetration”, with r_h constant, and “swelling”, with the area per molecule, σ , constant. (Reprinted with permission from ref. (30), copyright 1998, the American Chemical Society.) (■) decane, (○) dodecanol, (●) m -xylene, (□) SH244

towards oil, the curvature becomes negative (or less positive), and a transition towards a more lipophilic system takes place. When the oil is solubilized in the core of the aggregate, the area tends to be constant and the curvature becomes positive in order to maintain the total surface area of the aggregates. Therefore, in hydrophobic systems the lamellar to reversed-hexagonal transition takes place because of the penetration effect, whereas in hydrophilic systems, the hexagonal to cubic transition takes place because of the “swelling” effect.

The solubilization of m -xylene induces a transition from the hexagonal to the lamellar phase (increase of packing parameter) because of the “penetration” effect. In the $C_{12}E_7$ –water system, the solubilization of decane induces a transition from a hexagonal to a cubic liquid crystal (decrease of packing parameter) because of “swelling”.

The localization of the oil, which is followed by a variation in the liquid crystal symmetry and periodicity, is directly related to the influence of the oil on the temperature of the zero spontaneous curvature of the water–oil– C_iE_j system. If the oil tends to penetrate into the chain surfactant layer and make the curvature negative, the surfactant has to be more hydrophilic (large polar head) to maintain the zero spontaneous curvature. This explains why in this case the temperature of the zero spontaneous curvature is low.

If liquid crystalline phases can be obtained with a large variation in molar composition, the peak position shifts as a function of composition. The magnitude and the sign of this shift of periodicity allows us in all cases to determine whether the addition of solute induces an area increase at a low V increase, or a pure apolar volume V swelling. Most cases are intermediate in behaviour and correspond to an incorporation of solutes with a constant overall curvature.

2.5 Maximum of water solubilization in water-in-oil microemulsions

Leung and Shah (32) have proposed a theory based on a phenomenological and qualitative approach to predict the maximum of water solubilization in water-in-oil (w/o) microemulsions. The solubilization in w/o microemulsions is considered to depend on two parameters, i.e. the spontaneous curvature and the elasticity constant, k , of the interfacial film. The spontaneous curvature, H_0 , is related to the packing parameter of the surfactant via the coverage relationship, whereas the elasticity of the film is related to the energy required to bend the film. Leung and Shah considered the case of water solubilized in the form of perfectly monodisperse spherical droplets in w/o aggregates where the curvature radius is much larger than the chain length. As a convention, a positive curvature towards water was chosen.

In this simplifying case, where shape variations or connections between micelles are ignored, a simple consideration of the conservation of volumes and surfaces upon the addition of a solute imposes the radius R of the reversed-micelle. The polar volume fraction is given by $\phi = n \times (4/3)\pi R^3$, whereas the specific surface is related to R by the expression $\Sigma = n \times 4\pi R^2$, if n is the density of droplets in the microemulsion. The polar volume fraction includes the polar head of the surfactant and the water. The radius can then be directly deduced, i.e. $R = 3\phi/\Sigma$.

The amount of water at a given concentration of surfactant is directly linked to the water-pool radius. The ionic strength in the core of the reversed-micelles is set by counterions of the surfactants, as well as the electric charge of the solute. In typical cases, the ionic strength is of the order of one molar unit. However, as a first approximation, variations due to this large ionic strength can be ignored.

The solubilization capacity depends on both the size and the stability of the droplets. Therefore, calculations based on the free energy of the interfacial film and the free energy of inter-droplet interactions give

the maximum of water solubilization in water-in-oil microemulsions. One assumes a saturated incompressible interfacial film (the area per molecule will not change significantly with curvature and the interfacial tension γ is set to 0). The first term, the free energy of the interfacial film (F_1), is given by the interfacial bending stress term (for oil-external microemulsions, the electrostatic energy term can be neglected), as follows:

$$F_1 = 16\pi nk(1 - R/R_0)^2 \quad (9.15)$$

where n is the density number of droplets, $R_0 (= 1/H_0)$ the radius corresponding to the spontaneous curvature or natural radius of the interfacial film, R the equilibrium radius of the droplet imposed by composition and k the curvature elasticity of the interface which describes the interfacial compressibility and flexibility.

The second term, the free energy of inter-droplet interaction (F_2), is approximated as the sum of a hard-sphere repulsive interaction (entropic) term and an attractive perturbation term.

The minimization of the total free energy ($F_1 + F_2$) with the radius gives the equilibrium droplet radius R , which depends on the natural radius R_0 , the interfacial elasticity k and the energy of inter-droplet interactions F_2 , as follows:

$$R = R_0[1 + 3F_2/(32\pi nk)] \quad (9.16)$$

This equation demonstrates that for rigid interfaces (large $k \gg k_B T$) phase separation occurs at $R = R_0$ and the solubilization capacity is determined by the spontaneous curvature. In contrast, for fluid interfaces (small k value) and $F_2 < 0$, the phase separation will occur for a radius R smaller than R_0 .

The minimization of the total free energy with the volume fraction of the dispersed phase gives information on the stability of the microemulsions droplets. For small attractive interactions, the microemulsion will demix with an excess of water because of the curvature effect, with this mechanism being called the "emulsification failure". On the other hand, for a sufficiently strong attractive droplet interaction, the droplets are destabilized, thus leading to a phase separation of a microemulsion with a smaller droplet volume fraction.

Therefore, maximum solubilization is obtained with the optimal value of the interfacial curvature and of the elasticity where the bending stress and the attractive forces between droplets are minimized. This is illustrated in Figure 9.6 (32). The left side of the figure (a) represents a region where microemulsions with highly curved and rigid interfaces are in equilibrium with water in excess at the solubilization limit. The de-mixing is

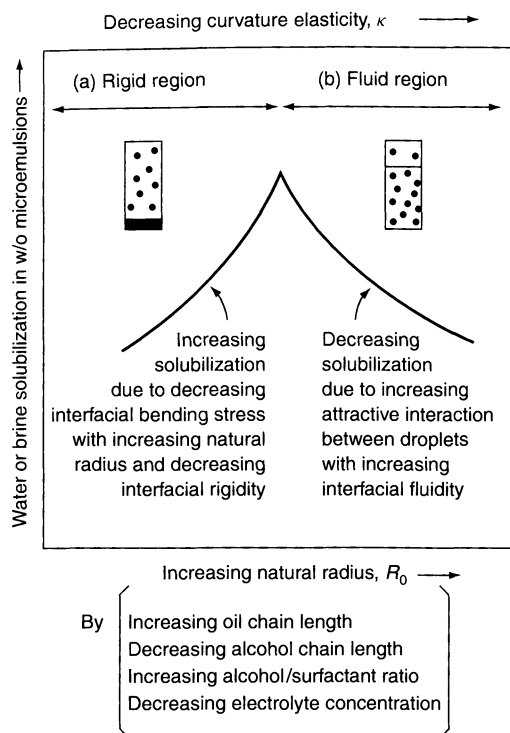


Figure 9.6. Schematic representation of the maximum of water solubilization in water-in-oil microemulsions limited by curvature or by attraction between the droplets. For a sufficiently strong attractive droplet interaction, a liquid–gas phase separation between a micellar-rich and a micellar-poor phase occurs (b). For small attractive interactions, the microemulsion will de-mix with an excess of water because of the curvature effect – this mechanism is called the emulsification failure (a). (Reprinted with permission from ref. (32), copyright 1987, the Journal of Colloid and Interface Science)

dominated by the interfacial bending energy and the solubilization is limited by the radius of spontaneous curvature. In this case, the maximum solubilization (MAC) can be improved by any changes leading to an increase of the natural radius (equivalent to a decrease in curvature) and an increase in the fluidity of the interface. Typical MAC values obtained are of the order of 50 to 100 mol/l of water in reversed microemulsions, and thus reversed micelle radii are of the order of 7 to 12 nm for a molecule showing a large area of reversed-micelles in the ternary phase diagram; this is typically ten times lower for unoptimized double-chain surfactants.

The right side of the figure (b) represents a region of fluid interface dominated by the attractive interactions between droplets. At the phase separation, the w/o microemulsions co-exist with an excess oil phase

containing a low density of water droplets. The maximum of water solubilization is determined by the stability of the droplets. In this case, the solubilization can be increased by an increase of the interfacial rigidity and a decrease of the radius of spontaneous curvature (any changes leading to a decreasing of the attractive interactions). The phase transition limiting the amount of water solubilized is a liquid–gas transition: a diluted phase or w/o micelles are in equilibrium with a concentrated phase. Experimental proof of this behaviour is obtained when microstructural determination by scattering experiments show that the size of the aggregates is identical in the two co-existing oil phases. However, these phase separations can be more complex if the packing parameter of the surfactant is close to 1, where a birefringent phase may appear on either side of the maximum of solubilization.

Finally, the increase in MAC and the associated growth of water droplets in water in oil microemulsions is limited by the radius of spontaneous curvature of the interface (R_0), because of the curvature effect, or by the critical radius of the droplet (R_c), due to the attractive interactions between the droplets. Therefore, the maximum solubilization is observed as a result of a compromise between these two opposite effects. In the case of a rigid interface, the solubilization capacity may be increased as the chain length of the oil increases, the chain length of the alcohol added as a cosurfactant decreases, or as the size of the polar head increases. On the other hand, for a microemulsion with a fluid interface, the maximum solubilization efficiency can be increased by decreasing the chain length of the oil, increasing the length of the alcohol (cosurfactant) or by decreasing the polar head.

Figure 9.7 (33) illustrates this phenomenological theory by presenting the effect of the molecular volume of oil on the solubilization capacity of a water–oil–AOT microemulsion. Oils with small molecular volumes or strong polarities interact strongly with the surfactant chain, thus leading to a high interfacial rigidity and a high spontaneous curvature (small natural radius). The solubilization capacity is dominated by the curvature effect, and at the phase separation microemulsions are in equilibrium with water in excess. From benzene to heptane, increasing the volume of oil induces an increase of the maximum of water solubilization observed for a given surfactant in oil. However, as the molecular volume increases further, the attractive interactions among droplets begin to play a major role. With larger oil molecules, the solubilization capacity is decreasing from heptane to hexadecane as the attractive interaction is increasing.

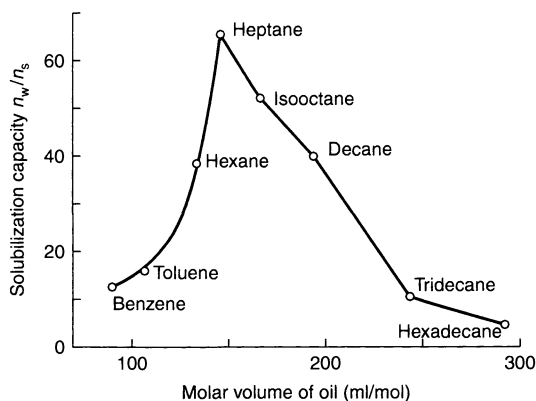


Figure 9.7. Effect of the molecular volume of oil on the capacity of a w/o microemulsion obtained with AOT at room temperature (Reprinted with permission from ref. (33), copyright 1987, the American Chemical Society)

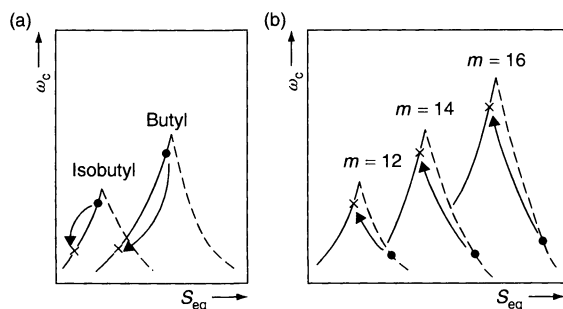


Figure 9.8. Solubility of water is plotted as a function of the equivalent salinity in arbitrary units. (a) With dodecyl(butyl or isobutyl)dimethylammonium halide. (b) With ethyl(m) (phenylethyl)dimethylammonium halide. (●) Br data, (x) Cl data (Reprinted with permission from ref. (35a) copyright 1990, the American Chemical Society)

The MAC of water in reversed-micelles is therefore either limited by attractive interactions between large droplets, or by the emulsification failure. The possible radii are contained in a large “window”, typically 0.5 to 20 nm for flexible interfaces ($k < k_B T$), while complications appear via the formation of connected networks upon the addition of water for rigid interfaces (34), where the water solubilization limit is imposed by the average curvature constraint. Zana and co-workers have tested (35) the validity of the theory of Shah by using homologous pairs of surfactants, i.e. single-chain quaternary ammoniums with bromide and chloride counterions. The lower binding of chloride

versus bromide induces a difference in P_0 for this homologous pair. The counter-intuitive maximum swelling by water observed for reversed-micelles of this type of surfactant is rationalized by using the phenomenological theory of Shah and co-workers (see Figure 9.8) (35). Zana and co-workers varied the surfactant chain length and solvent in order to demonstrate the ubiquity of the two mechanisms which limit the growth of the reversed-micelles.

2.6 Case of flat interfaces: solubilization of a solute in bilayers dispersed in water

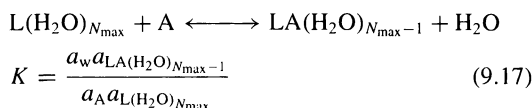
A number of studies have focused on the solubilization in bilayers (36, 37). These can be considered either as being the archetypes of membranes of biophysical interest, or as the diluted part of the region of existence of a lamellar phase, or being present as “a micelle without edges” (38), i.e. bilayers with no long-range order. The best known case of aqueous bilayer dispersions without any long-range order is that of closed unilamellar vesicles, although there are other cases, such as connected bilayers – the so-called “sponge phase” – or even multilamellar vesicles, known as “liposomes”. However, at the scale which has to be considered in order to understand and quantify solubilization, all of these cases are similar, since locally the microstructure is a bilayer, which has a net average curvature close to zero. Each monolayer can be in a situation where the spontaneous curvature is bent towards water or oil. According to the present state of knowledge, the spontaneous curvature of each monolayer forming the bilayer has surprisingly no known influence on the observed maximum solubilization equilibria. We will consider only the case of bilayers with chains in the fluid state, since solubilization can hardly be detected for chains in the frozen state.

Two types of solutes have to be considered in binary dispersions of bilayers in water. First, the water-soluble host molecules which are expected to be located in the water layers between bilayers. Secondly, insoluble apolar molecules which may be simply adsorbed on bilayers or incorporated in such layers, either in the head-group, palisade or core regions, which are defined by analogy with globular micelles.

In the case of water-soluble solutes, such as simple sugar molecules, the first question is whether an exclusion mechanism, similar to the Donnan equilibrium known for charged membranes in the presence

of salt, exists? Consider a two-phase sample containing a concentration C^* of water-soluble compound. After equilibration, the bilayer dispersion also contains some sugar, with a concentration C_b calculated as a function of the amount of water in the bilayer phase. What is the relationship between C^* and C_b ? Recently, Demé and Zemb (39) have demonstrated a depletion effect for sugar in an uncharged lamellar phase by using SANS contrast variation techniques. Neutron-scattering contrast variation allows the direct determination of the partition coefficient of sugar in microphase-separated samples. In this case, the two phases in co-existence cannot be macroscopically separated: vesicles are in equilibrium with an excess solvent. It is observed that the small sugar molecules are excluded from the crystalline domains of the sample and that to a good approximation, $C_b = C^*(1 - h[L]V_w)$, where $[L]$ is the lipid concentration in the lamellar phase, h the hydration number per lipid and V_w the volume of one water molecule. This means that, once $h = 6$ bound water molecules per lipid are considered not to be available as solvent for the water-soluble solute, the concentration of sugar in the available water is equal to the sugar concentration in the microphase in equilibrium. Therefore, the concentration of sugar is constant in the sample and depletion of sugar is a consequence of the water being thermodynamically inactive due to binding to the surfactants.

In the case of water-insoluble solutes which do not modify bilayers, such as single-chain alcohol molecules, the solubilization process can be treated within the frame work of a "solvent exchange model" (40). A liposome molecule (L) has N_{\max} potential sites for alcohol binding. These sites are occupied by water in a buffer solution, and therefore this model is based on the one-to-one exchange of water and solute in the membrane, as follows:



where a_i represents the activity of each component ("w" for H_2O).

The equilibrium constant K associated with this exchange has been used for the last 30 years even if the different solubilization sites are not explicitly taken into account. Such an equilibrium would have to be written for each solubilization site, inducing N_{\max} different possible values for the constant equilibria K_i . If this equilibrium equation is followed, the mean occupancy of a site for a host molecule can be obtained by a Langmuir-maleto model

isotherm expression as follows:

$$\theta_i = \frac{K_i a_A}{a_w + K_i a_A} \quad (9.18)$$

With the assumption that all the binding sites are similar, all of the K_i constants are equal to a unique value K .

Analysis of titration calorimetric data shows the typical values of the equilibrium constant K to be equal to 5 for ethanol and equal to 0.8 for butanol. The affinity of the bilayer for the alcohol decreases as the chain length of the alcohol increases. By using solution theory, it has been proved (41) that the effects are opposite between the solubilization of short-chain and long-chain alcohols in bilayers. Higher alcohols (known as cosurfactants) cannot be treated by considering only simple adsorption of exchange sites at the interface.

When more complex solutes, such as families of substituted phenols, are considered in the presence of dimyristoylphosphatidylcholine (DMPC) uncharged vesicles, surprisingly, more solute (as volume/volume) is taken up by the vesicles than by an equivalent volume of cyclohexane. An examination of tables of partition coefficients demonstrates the primary importance of the interface or palisade regions of the bilayer cross-section (42). In this region, the relative permittivity varies from 80 to 2 within a fraction of a nanometre, thus enhancing attractive interactions due to polarizability. In the case of highly polarizable apolar and lipophilic Xe gas, which is easily soluble in bilayers (with powerful anaesthetic properties), the location can be directly deduced from NMR spectroscopy. The presence of Xe atoms near the head-groups or in the palisade layer is evidenced by relaxation effects, together with a "quasi-absence" from the core of the hydrophobic bilayers (43).

Using a large body of solute molecules, Katz, Diamond and Wright (36) and Leodidis and co-workers (37) have established some general qualitative rules for the solubilization in membranes. The magnitude of the partition coefficient depends upon the following:

- on the ability of the solute to break the water structure
- on the membrane fluidity and all factors that influence it

Furthermore:

- good correlation is found between the partition coefficient and the octanol/water scale
- substituents on the solute or membranes that are hydrogen-bond acceptors give a reduction of the partition coefficient

A mechanism of solubilization specific to bilayers has also to be considered (44): this is the case when the

presence of the solute changes the microstructure of the bilayer. Three states have been evidenced by video-enhanced contrast microscopy in the solubilization of toluene in neutral membranes (DMPC and dipalmitoylphosphatidylcholine (DPPC)). At low toluene content, spherical aggregates are formed up to a volume fraction of 0.05. At higher toluene concentrations, a regime of easily deformable vesicles (implying low k^*) is obtained. When saturation is reached at a volume ratio of the order of 0.2, there is a true co-existence of toluene-swollen bilayers and small droplets of toluene covered by a lipid monolayer, analogous to a ternary microemulsion droplet.

3 SOLUBILIZATION IN INITIALLY TERNARY SYSTEMS

3.1 Definition of solubilization in this case

In this section, we will focus on the solubilization of a substance in water–oil–surfactant samples containing initially three components. These ternary systems include microemulsions (w/o, o/w and bicontinuous), lamellar phases and other liquid crystal mesophases. On a microscopic scale, oil microdomains are separated from water microdomains by a surfactant interface. A microdomain is here understood to be an aggregate of at least the order of a hundred self-assembled molecules, although being too small to be considered as a microphase-separated sample. A sample contains separated microphases when domains of micron size of two thermodynamically stable different phases co-exist and do not de-mix even after centrifugation, due to kinetic stability. The solute can then be located at the interface or in the oil or water microdomain (cf. Figure 9.9). Since three “environments” are available in ternary systems, “the interface” can be considered as a pseudo-phase or as a surfactant monolayer (37).

At the level of approximation of the pseudo-phase model, the surfactant tails are viewed as an independent pseudo-phase in which an uniform effective concentration of solute is assumed. In the surfactant monolayer model, the water/oil interface is supposed to be covered by a monolayer of surfactant molecules into which the solute can be adsorbed. In this latter case, the mole fraction of solute at the interface is defined by the interfacial composition λ (37), with the assumption that no water and no oil is adsorbed in the surfactant film, given as follows:

$$\lambda = \frac{N_{\text{solute}}^{\text{int}}}{N_{\text{surfactant}}^{\text{int}}} \quad (9.19)$$

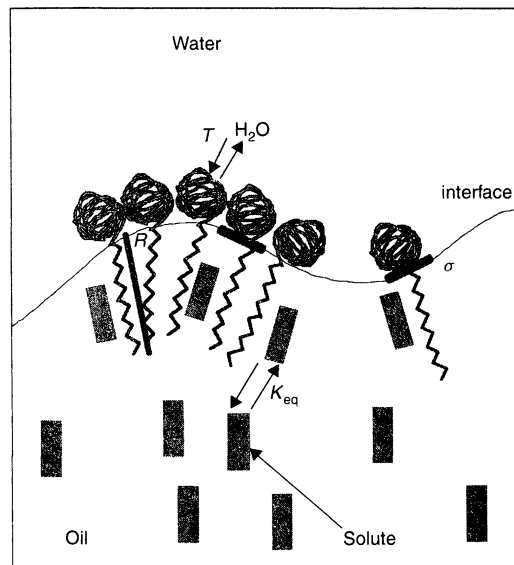


Figure 9.9. Schematic representation of the different localization states of a hydrophobic solute in a microemulsion. The solute could be solubilized in the oil microdomain or at the interface. The interfacial surfactant area is noted as σ and the curvature radius as R . This schematic represents the case of a nonionic surfactant where the hydration of the polar head is temperature (T)-dependant. With the pseudo-phase model, the solute concentration is considered over the volume occupied by the tails of the surfactant, whereas in the surfactant monolayer model, the binding of the solute into the surfactant monolayer is considered

where N_i^{int} denotes, respectively, the number of moles of solute or surfactant at the interface. When the interfacial composition λ is not zero, there is an *excess of solubilization* in the medium which solubilizes the solute, with some solute molecules being located at the interface. The macroscopic observation corresponding to this *excess of solubilization* is as follows. If we consider the amount of water-insoluble solute molecules present in a ternary solution, the amount of dispersed solute, measured by analysis composition, can be larger than the maximum value of solubility of solute in the same volume of pure bulk oil. In this case, the amount of dispersed solute is usually lower than the sum of the maximum solubilities in pure oil and in pure surfactant, taken separately as bulk phases.

This molar ratio, λ_{max} , can be easily experimentally accessed at the maximum of solubilization, where the solution is in equilibrium with pure solute.

Solubilization consequences on the intrinsic properties of the mixed film obtained in the final state depend on the nature of the surfactant. The initial surfactant

film could be dominated by fluctuations when the bending rigidity is low, or the surfactant film could be rigid when the bending energy is high. We will discuss below some solubilization studies for these two separate cases.

3.2 Soft systems: low bending rigidity, with fluctuations dominating

3.2.1 Curvature towards water

Geometrical model, with localization

A well-studied model system for the case of soft charged interfaces is that of the AOT surfactant, having two branched short chains, in the presence of oil and water. Solubilization in water-in-oil microemulsions has been studied by Zemb and co-workers (45) in the case of the water-oil-AOT system. The topology of these microemulsions is dominated by geometrical constraints as the interfacial area, $\sigma = 0.6 \text{ nm}^2/\text{molecule}$, of the surfactant is invariant with composition within experimental uncertainty. If partial molar volume of water variations are neglected, the radius of the droplets is imposed by the composition of the microemulsions.

The only possible radius of monodisperse water in oil droplets compatible with the interfacial area Σ and the polar volume ϕ , the sum of the water volume fraction and the volume occupied by the surfactant heads is given by the following:

$$R = 3\phi/\Sigma, \text{ or } \langle H \rangle = \Sigma/3\phi \quad (9.20)$$

This available Σ is the product of the concentration of the surfactant at the interface and σ , the interfacial area

of the surfactant. Therefore, the radius of the droplets observed in the domain labelled as reversed-micelles (L_2) is proportional to the ratio of the polar volume in the microemulsion (given by the water concentration) to the interfacial area (given by the surfactant concentration). This ratio, W , is defined as $W = [\text{water}]/[\text{surfactant}]$. Inserting the partial molar volumes for water, V_w , and the volume occupied by the polar head, V_h , the droplet size is practically linear with water content, as follows:

$$R = \frac{3(V_h + W V_w)}{\sigma} \quad (9.21)$$

These microscopic quantities can be accessed directly by using scattering experiments (for R and σ) and precision densitometry to determine the volumes (10). The droplet density per unit volume is given by the following:

$$n = \frac{\Sigma^3}{4\pi(3\phi)^2} \quad (9.22)$$

Since in the general case the radius of water droplets is different from the spontaneous one, the cost in bending energy has to be compensated for by fluctuations. Those fluctuations are dominant when k^* is of the order of $k_B T$.

In the general case, any added solute could a priori induce either a modification of the interfacial area or of the polar volume of the droplets. In addition to these primary effects, the rigidity of the interface, as well as the spontaneous curvature variation, are modified by the presence of the solute. Experimental determination of droplet size and density allows as a first step the determination of the site of solubilization of the solute in a given microemulsion. Figure 9.10

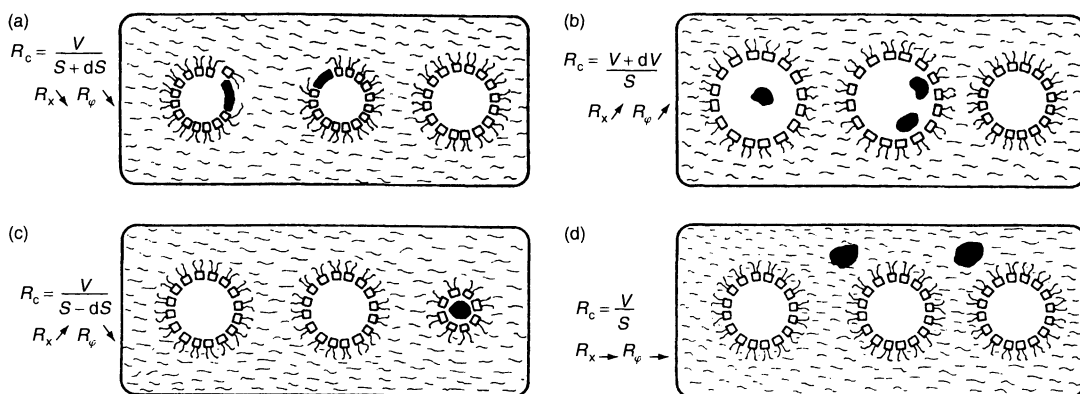


Figure 9.10. Schematic representations of the possible effects of the presence of a solute on the observed radius of water in oil microemulsions (reversed-micelles). Since the radius is imposed by the surface-to-volume ratio, localization in surfactant layers shrinks the radius, while localization in the core increases the radius. Separate micellization may induce polydispersity, while localization in the bulk oil has no effect on the reversed-micelle

illustrates the principle of solute localization from the perturbations induced by different localizations in a given w/o microemulsion. Four ideal cases are possible (shown in the figure) as follows:

- For a given water volume, the solute may increase the total interfacial area (behaves as a surfactant). In this case, the radii of the droplets will decrease, while the density of the droplets increases.
- The solute may also be localized in the core of the droplet, i.e. behave as added water. In this case, the solute increases the polar volume at a constant specific area – the radii of the droplets increases, and the number of droplets decreases.
- The solute, especially if it is a large insoluble molecule, may nucleate the formation of a second type of aggregate, with one of these being a surfactant-covered solute. It is not possible to derive directly any information, as the solution becomes polydisperse in nature. In this case, determination of the adsorption isotherm of the surfactant by the solute in the absence of water is needed before further processing can be carried out.
- If the solute is apolar and solubilized in the continuous phase, no variation will be observed for the radii or number densities of the droplets.

The variation of the average water droplet size can be deduced from small-angle X-ray or neutron scattering, as well as by classical light scattering measurements. The maximum water content can be obtained by titration and gives the evolution of W_{\max} at a given temperature. Hence, the effect of the solute on the spontaneous curvature of the surfactant film in the presence of solute can also be deduced in the quaternary final state (32, 33).

These elementary geometrical considerations always provide a first approximation about the localization of a solute in a reversed-microemulsion. In intermediate cases, when the solute increases both the interfacial area and the interior volume of the droplets, it is also important to quantify the amount of the solute at the interface or in the core of the droplets.

Solubilization of amino acids in reverse water-in-oil microemulsions

Fletcher (46) and also Leodidis and co-workers (37) have indicated a general method to determine the amount of the solute solubilized in microemulsions, its localization and the radius variation of the droplets induced by this solute.

The starting point for this is given by a complete solubilization study of amino acids in water-in-oil microemulsions, obtained with AOT as the surfactant, with the approach of a “surface monolayer” model. In a first step, the phase-transfer method is used to determine the affinity of the solute towards the interfacial film. A reversed-micellar phase is equilibrated in the presence of a solution of amino acids in water. In the final state, reversed-micelles containing some amino acids are in equilibrium with the remaining amino acids in water. After macroscopic phase separation, analysis of the composition of the amino acids in the two phases and of the surfactant content in the oil phase give the partition coefficient K_X . The underlying approximation lies in assuming that the water in excess is identical to the water in the droplets. This assumption can be used only for large droplets ($W > 10$). For small droplets, interaction of the solute with the interface may produce a non-uniform solute distribution and differences in the water activity may lead to two separate activity coefficients for water in the core and in the bulk.

With the surface monolayer model and the parameter λ as defined above (see equation (9.19)), the constant which describes the equilibrium is a mole-fraction-based partition coefficient, given as follows:

$$K_X = \frac{X_a^{\text{int}}}{X_a^{\text{mwp}}} \quad (9.23)$$

where X_a^i is the molar fraction of amino acid at the interface (int) or in the water droplet of the microemulsion (mwp). If a small part of the amino acid is anchored at the interface, the expression for the constant can be simplified as follows:

$$K_X^\infty = \frac{55.5\lambda}{C_a^{\text{aq.f}}} \quad (9.24)$$

This constant, which is related to infinite dilution is a thermodynamic one and is also related to the free energy of transfer of one solute from the bulk water to the w/o interface.

In order to determine if a solute is preferentially adsorbed at the interface or solubilized in the water core, the amino acid transfer versus the water transfer is measured. The fractional transfer of water or solute to the microemulsion phase are defined by the following ratios:

$$t_w = \frac{N_w^{\text{me}}}{N_w^{\text{aq.in}}} \cong 1 - \frac{V^{\text{aq.f}}}{V^{\text{aq.in}}}, \text{ and } t_a = \frac{N_a^{\text{me}}}{N_a^{\text{aq.in}}} \cong 1 - \frac{C_a^{\text{aq.f}} V^{\text{aq.f}}}{C_a^{\text{aq.in}} V^{\text{aq.in}}} \quad (9.25)$$

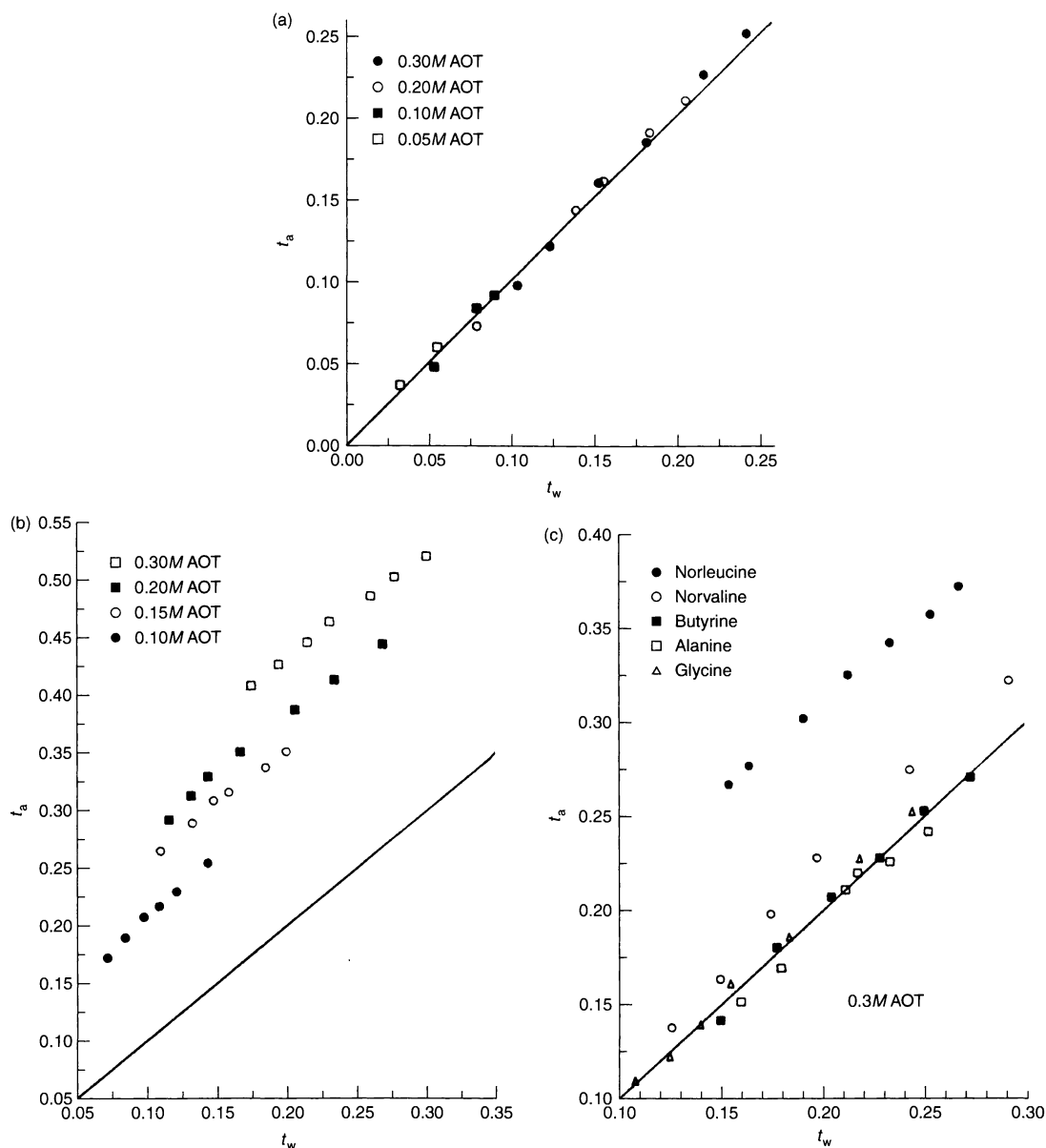


Figure 9.11. Fractional amino acid transfer (t_a) versus water transfer (t_w) to the organic phase, as a function of [AOT] for (a) glycine and (b) phenylalanine, while (c) shows similar data for different amino acids at $[\text{AOT}] = 0.3\text{M}$. (Reprinted with permission from ref. (37a), copyright 1990, the American Chemical Society)

where the exponent denotes the phase (me, microemulsion; aq.in, initial water phase; aq.f, final water phase) and the subscript denotes the water (w) or the amino acid (a); N is the absolute number of moles.

When K_X^∞ is zero, the transfer of solute, t_a , is equal to the transfer of water, t_w , and is independent of the

surfactant concentration. In contrast, when K_X is finite, t_a is different from t_w and depends on the surfactant concentration. Therefore, a plot of transfer of solute versus transfer of water gives evidence for the surface affinity of a given solute (illustrated in Figure 9.11) (37a). From the curves shown in this figure, it appears that glycine

and phenylalanine have an opposite surface affinity. The curve shown in Figure 9.11(b) indicates that phenylalanine is dispersed in the bulk water, while in the interfacial film, there is an excess of solubilization.

The excess of solubilization can be measured as a function of the nature of the oil, the salinity and the surfactant concentration. All of these factors affect the bending ability of the interface. The partition coefficient can therefore be related to the variation of the curvature of the interface.

Fletcher (46) showed experimentally that the interfacial partition coefficients of different solutes depend on both the external salinity and on the interfacial curvature. Leodidis and Hatton (37b) extended this work by illustrating a curvature dependence of the interfacial partition coefficient K_X . Figures 9.12 (37a) and 9.13 (37b) demonstrate this curvature effect. The term $1/W_0$ is directly related to the curvature $1/R_w$, if R_w is the radius of the droplet. When the curvature is increasing, the partition coefficient is decreasing. This is attributed to an increase of the rigidity of the interface, which induces a squeezing-out effect, as in the lamellar phase. Thus, a local equilibrium of solute adsorption at the interface can be directly linked to the mean curvature of the surfactant film.

In order to explain this experimental feature, Leodidis and co-workers developed a thermodynamic model where the chemical potential depends on the curvature of the film and on the bending moment or interfacial elastic constant C . The variation of K_X with curvature can be derived from the equality between the chemical potential of an amino acid in excess water and in the interface, as follows:

$$\ln K_X = \ln K_X^0 - \frac{2}{k_B T} \langle \bar{f}_a C \xi \rangle \frac{1}{R_w} \quad (9.26)$$

where K_X^0 represents the transfer coefficient from water to an interfacial film with zero curvature, i.e. for micelles of infinitely large radius; \bar{f}_i represents the partial molar area of the amino acid (a) or of the surfactant (s), while ξ is given by the following:

$$\xi = 1 + \frac{\bar{f}_s \partial \ln C}{\bar{f}_a \partial \lambda} \quad (9.27)$$

where λ is the interfacial composition ratio as defined above (equation (9.19)). The dimensionless quantity ξ is directly related to the variation of the bending moment with the amount of solute located at the interface.

The relationship describing the variation of the adsorption equilibrium as a function of the mean curvature of the surfactant film predicts the decrease of the constant K_X when the curvature increases. This describes

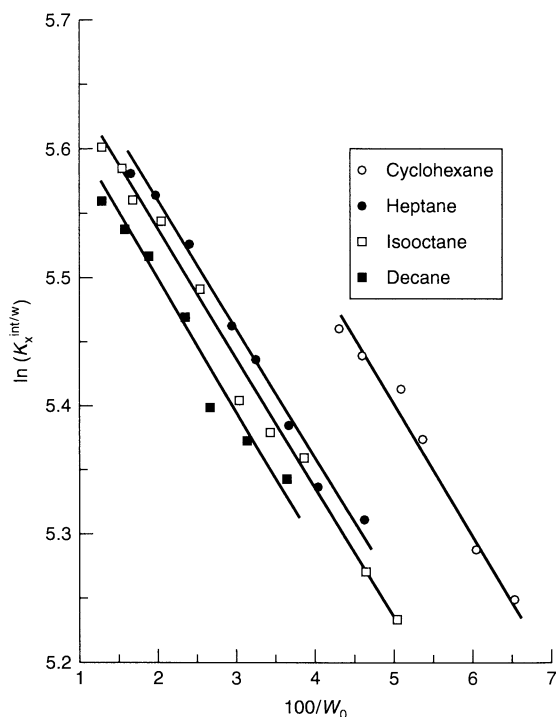


Figure 9.12. Solvent effect on the partition coefficient of tryptophan, represented by $\ln(K_X)$ versus the inverse molar ratio of water to surfactant. Plots of $100/W_0$ for $0.2M$ AOT are shown for the following solvents: \circ , cyclohexane; \bullet , heptane; \square , isooctane; \blacksquare , decane. (Reprinted with permission from ref. (37a) copyright 1990, the American Chemical Society)

the “squeezing-out” phenomenon which has been experimentally observed: curving the film squeezes out a part of the adsorbed solute. This thermodynamic model gives an explanation for the linear dependence of K_X on the mean curvature even if the slope is not exactly representative of the experimental values. With some typical values ($\bar{f}_a = 40 \text{ \AA}^2$, $\xi = 1$, $C = 10^{-12} \text{ N}$), the slope lies between 1 and 1.5, while the experimental values range between 3 and 12.

3.2.2 Curvature towards oil and bicontinuous phase

On the same basis, these present authors (47, 48) have investigated the case of solubilization of a hydrophobic solute in o/w microemulsions. By measuring separately the amount of solute adsorbed in the interfacial film and the average curvature of the relevant sample, one can experimentally establish a relationship between these two quantities. The starting point for this

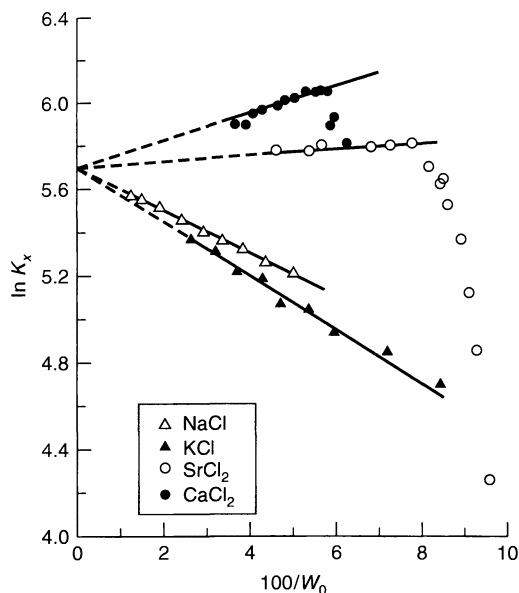


Figure 9.13. Effect of electrolytes on the partition coefficient of tryptophan, represented by plots of $\ln K_x$ versus $100/W_0$ for $0.1M$ AOT and for the following electrolytes: ●, calcium; ○, strontium; △, sodium; ▲, potassium chlorides. (Reprinted with permission from ref. (37b), copyright 1990, the American Chemical Society)

approach is to study the influence of a solute on the phase behaviour and on the microstructure of a given microemulsion.

To investigate solubilization in oil-in-water or bicontinuous microemulsions, we consider the example of a nonionic surfactant of the polyoxyethylene family (denoted as C_iE_j), i.e. $C_iH_{2i+1}(OCH_2CH_2)_jOH$.

With this type of nonionic surfactant, the presence of a cosurfactant is not needed to obtain a large microemulsion single-phase domain at a fixed temperature. Moreover, by varying the relative volumes of the polar and apolar parts of the surfactant, it is easy to modify the hydrophilic/hydrophobic balance (expressed as the spontaneous curvature H_0 , surfactant packing parameter P_0 , or HLB balance R). These quantities can be modified by temperature variations only because the hydration of the polar head is temperature-dependant. Therefore, the spontaneous curvature turns from oil to water as the temperature is increased. Shinoda, Kunieda and co-workers, as well as Kahlweit's group, have given a general description of the phase behaviour obtained with C_iE_j species (49).

Determination from phase diagrams of the solute effect on spontaneous curvature

A pseudo-binary phase diagram can be obtained by a cut at equal water-to-oil ratios in the "temperature–water–oil– C_iE_j " phase diagram. This pseudo-binary phase diagram allows the determination of the composition and temperature of the microemulsion domain. Moreover, the lowest surfactant concentration, $\tilde{\gamma}$, necessary to give a microemulsion and the temperature, \tilde{T} , of the zero spontaneous curvature is given by the so-called "fish-tail" as illustrated in Figure 9.14. This figure shows the Winsor III domain where a microemulsion is in equilibrium with both water and oil. At high temperatures, a microemulsion is in equilibrium with excess water, while at low temperatures a microemulsion is in equilibrium with excess oil.

The curvature is temperature-dependant. For \tilde{T} , the curvature is zero, and for a lower temperature, T_1 , the curvature is towards oil (and thus positive). Strey and co-workers have demonstrated a linear variation of the mean curvature with the temperature.

The influence of a solute on the curvature of the surfactant film can be determined by studying the modification of the pseudo-binary phase diagram when pure oil is replaced by an "oil + solute" pseudo-component. Figure 9.15 gives the results obtained for the solubilization of lindane (γ -hexachlorocyclohexane) in a water–oil– C_6E_5 microemulsion. As the concentration of lindane in the pseudo-component is increasing, the temperature of the zero spontaneous curvature is decreasing. It is known that the latter occurs when the surfactant is replaced by a less hydrophilic surfactant (smaller head-group volume) or when the oil is replaced by a less hydrophobic oil (more penetrating). Therefore, with this knowledge we can conclude that lindane turns the curvature towards water at constant temperature.

Evidence of excess solubilization and the associated curvature variation

Precise determination of phase boundaries allows us to demonstrate an excess of solubilization in a nonionic microemulsion and to quantify the curvature variation with the amount of lindane adsorbed in the surfactant film. We find that stable microemulsions exist with a larger amount of lindane relative to the oil than the saturation value in the same oil alone at the same temperature. This excess is quantified by titration in the Winsor III domain with the assumption of Leodidis and Hatton i.e. *the composition of excess oil (water) is equal to the*

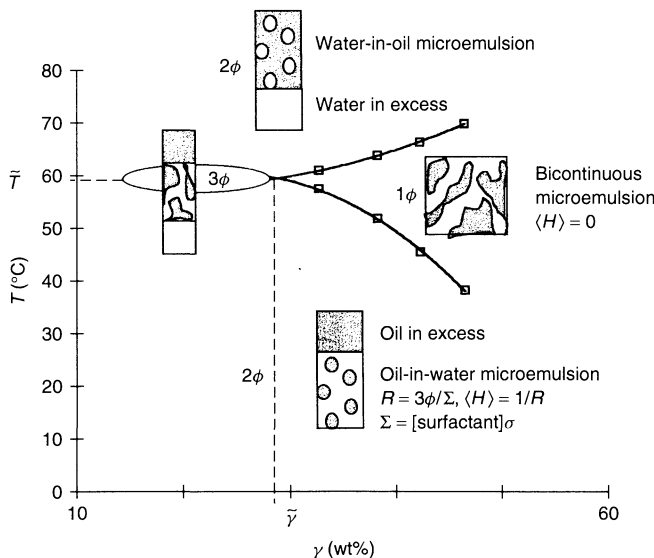


Figure 9.14. Pseudo-binary phase diagram of the water–oil– C_7E_j system at equal water-to-oil volume ratios, representing the so-called “fish-tail”. This temperature–surfactant content (T – γ) representation is used to determine the temperature of the zero spontaneous curvature and the minimum amount of surfactant needed to include equal volumes of oil and water in a single-phase microemulsion

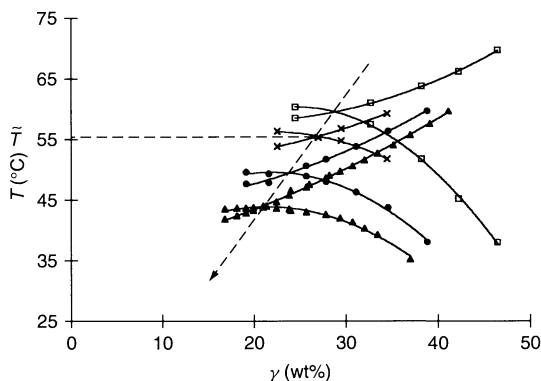


Figure 9.15. Pseudo-binary phase diagram of the water–oil(cyclohexane + lindane)– C_6E_5 system for different initial weight compositions β , of lindane in the oil: \square , 0; \times , 4; \bullet , 10; \triangle , 15%. The arrow indicates the variation of the “fish-tail” with the increasing content of lindane in the oil, while the temperature \hat{T} of the zero spontaneous curvature is given by the ordinate of the fish-tail

composition of bulk oil (water) of the microemulsion. We determine the interfacial composition ratio λ (lindane over surfactant at the interface) versus the weight ratio of lindane in the oil. Those experiments allow us to determine the curve of the adsorption of lindane at the interface of the water–cyclohexane– C_6E_5 microemulsion

with a constant mean curvature (equal to zero). Figure 9.16 gives the λ versus β plot, where β is the weight percentage of lindane in the pseudo-component “oil + lindane”. This linear relationship links the amount of lindane located at the interface for a zero curvature as a function of temperature, e.g. for C_6E_5 , $\lambda = 0.0143\beta$.

Returning to Figure 9.15, we can see that adding lindane to oil at constant temperature modifies the

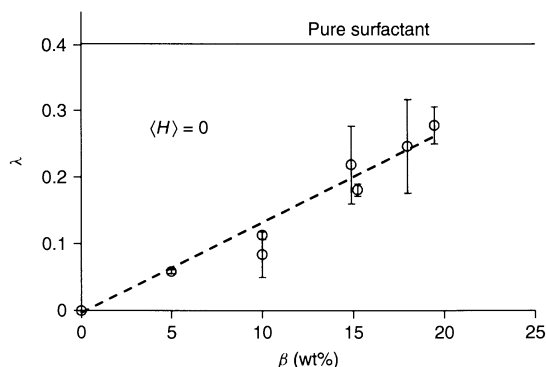


Figure 9.16. Interfacial molar composition, λ , versus β , the initial weight percentage of lindane in the oil for a water–(cyclohexane + lindane)– C_6E_5 microemulsion with a zero average curvature. This curve represents the adsorption of lindane at the interface in microemulsions with a constant zero average curvature

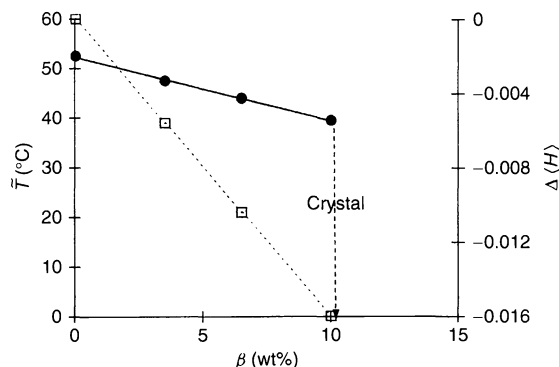


Figure 9.17. Relationship between curvature and temperature, showing β , the initial weight percentage of lindane in the oil, as a function of: ●, the temperature \bar{T} of the zero spontaneous curvature of the water-(cyclohexane + lindane)- C_8E_6 system; □, the linear variation of the average curvature, $\Delta\langle H \rangle$

curvature of the film in the same way as increasing temperature in the case of a pure oil. A linear relationship between curvature and temperature has been determined for nonionic surfactant (49). Figure 9.17 shows the linear dependence of \bar{T} with the lindane composition β . It is therefore possible to determine a relationship between the curvature variation and the lindane composition β of the oil. In the case of the water-cyclohexane- C_8E_6 system, with lindane as solute, the relationship is as follows:

$$\langle H(0) \rangle - \langle H(\beta) \rangle = -\Delta\langle H \rangle = 1.6 \times 10^{-3}\beta \quad (9.28)$$

This is illustrated in Figure 9.17.

Finally, a linear relationship links the spontaneous curvature and the solute molar ratio in the interface: in the case of the water-cyclohexane- C_8E_6 system, with lindane as solute, we find the following:

$$\Delta\langle H \rangle \ell = -0.7\lambda \quad (9.29)$$

Wedge model

To interpret the experimental results, one can rely on a geometric interpretation of the observed curvature variations. Consider first the general coverage relationship described in the introductory part of this review. Assuming that the term due to Gaussian curvature can be neglected, we have the following:

$$P = 1 - \langle H \rangle \ell \quad (9.30)$$

If an external constraint modifies the packing parameter P , the system reacts via a variation of the microstructure

to still satisfy the above relationship. By considering the volume of the surfactant and solute at the interface, we can explain at the first order of ℓ (the surfactant film thickness), the experimental results of the variation of curvature induced by the adsorption of lindane at the interface in different situations.

Finally, we consider lindane as being a wedge embedded in the surfactant film. Therefore, the volume brought at the interface by the solute is calculated with λV_L , where λ is the interfacial composition and V_L the volume of lindane.

SANS experiments carried out at the zero spontaneous curvature show that the interfacial area σ of the surfactant in the microemulsion is independent of the composition of lindane in the oil. Therefore, by considering that ℓ is constant one obtains a relationship between the induced curvature and the amount of lindane at the interface, given by the following:

$$\Delta\langle H \rangle \ell = -0.4\lambda \quad (9.31)$$

As illustrated in Figure 9.18, we see that the trend of the experimental observations is reproduced by this geometrical model, by simply assuming that the solute acts as a wedge in the surfactant film. The main term not taken into account by the wedge model comes from neglecting oil adsorption/desorption in the film induced by the presence of the solute.

The simple wedge model also explains the observed effect of oil on the solubilization of testosterone propionate (50). In this case, the excess solubilization

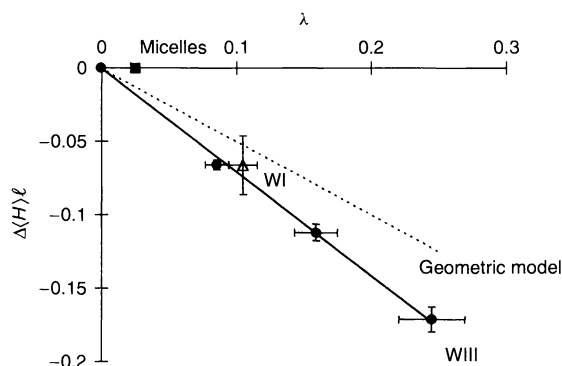


Figure 9.18. Variation of the reduced average curvature $\langle H \rangle \ell$ versus the interfacial molar composition λ , with ℓ representing the chain length of the surfactant: $\Delta\langle H \rangle \ell = \langle H(\lambda \neq 0) \rangle - \langle H(\lambda = 0) \rangle$. The dashed line is calculated with the wedge model; ●, experimental points obtained by phase diagram determination and titration in the Winsor III domain; ■, maximum of solubilization obtained in micellar system; Δ, obtained in a Winsor I microemulsion

Table 9.1. The interfacial molar composition at the saturation limit (λ_{\max}) when the microemulsion is in equilibrium with lindane as a function of the reduced curvature (ℓ/R)

ℓ/R	0	0.2	1
λ_{\max}	0.28	0.17	0.025

observed is not related to the solubility of the drug in the oil, but mainly to the volumes of the solutes which have to be interdigitated in the surfactant film. This experimental study exhibits the relationship between the solubilization and the influence of the oil on the microstructure of the microemulsion. The aim of this particular study is drug delivery (51).

Now we will consider the solubilization power at the MAC of these microemulsions, i.e. when the microemulsion is in equilibrium with excess pure solute. In this saturation case, the interfacial composition ratio at the saturation limit depends on the curvature. The maximum solubilization, λ_{\max} , is a strongly decreasing function of the mean surfactant curvature, as illustrated in Table 9.1, where ℓ/R is the reduced curvature if ℓ is the C_8 hydrophobic chain length (Tanford's formula) and R the curvature radius.

By using a similar approach, Von Corswant and Thoren (23) have shown the influence of the solubilization of an active drug in lecithin-based microemulsions. By combining phase diagram determinations, NMR spectroscopic measurements and solubility determinations of the solute in aqueous and oil phases, they have determined the effect of the solute on the phase behaviour and microstructure of the microemulsion. Depending on the nature of the solute, the influence on the curvature varies. The first solute studied (felodipine) is water-insoluble and slightly soluble in the oil. The presence of this solute increases the polarity of the oil phase and turns the film towards the water, even if this solute has no affinity for the surfactant film.

The second solute studied ("BIBP3226") is a charged molecule, insoluble in the oil and slightly soluble in water. This molecule has an affinity for the interface and partitions between the interface and the bulk water. The partitioning was determined to be 60% at the saturation limit from the position of the phase boundaries.

3.3 Stiff surfactant system, with rigid interface

3.3.1 Curvature towards water

These present authors (52) have considered the effect of a solute in a ternary microemulsion with a stiff

interface. Molecules forming stiff interfaces contain charged head-groups and/or two long chains (≥ 12 linearly arranged CH_2 groups). The curvature variation of the surfactant film induced by the solute can be determined by using conductivity and SAXS techniques. The location of the solute can be inferred by using the "Disorder-Open-Connected-Cylinder" (DOC) model of microemulsions, combining the interfacial area of the surfactant, the volume fraction and a strong spontaneous curvature constraint.

We have focused on the solubilization of lindane in a reversed-water-dodecane-DDAB microemulsion as an example. The surfactant (DDAB) is a cationic double-chain synthetic lipid, didodecyltrimethylammonium bromide. Since the bending constants are larger than $k_B T$, solubilizing a solute in such a microemulsion induces sterical constraints which modify the microstructure with easily measurable effects. The most spectacular effect of the presence of a solute is the variation of the antipercolation threshold. Electric antipercolation is the observation of a *decreasing* conductivity by orders of magnitude upon the *addition* of water for a given composition. The occurrence of antipercolation boundaries is general in microemulsions with stiff interfaces, being first discovered by Kaler and co-workers (53). This decrease of conductivity of the microemulsion with increasing water content is due to a microstructural change in the microemulsion. An abrupt change from interconnected cylinders towards water-in-oil separated spherical droplets, quantitatively described by the DOC model, is induced by the coverage relationship without excess bending energy. Conductivity measurements detect this antipercolation threshold, as the microemulsion will be conducting at low water content levels and not conducting at high water content levels. The addition of lindane solute to the water-dodecane-DDAB microemulsion induces a variation of the conductivity of the solution. These perturbations can be related to a variation of the surfactant curvature and hence to a variation of the packing parameter P .

Figure 9.19 shows the variation of the antipercolation threshold obtained when lindane is added to the water-dodecane-DDAB microemulsion. The conductivity is measured along a water dilution line at a constant surfactant-to-oil weight ratio. For a given water composition (20 wt%) the conducting microemulsion becomes non-conducting when the pure dodecane is replaced by a mixture of dodecane plus lindane, containing 1 wt% of lindane. The curvature turns towards water due to addition of the lindane. This is quantified by the measurement of the packing parameter, which can be deduced from the position of the linear phase

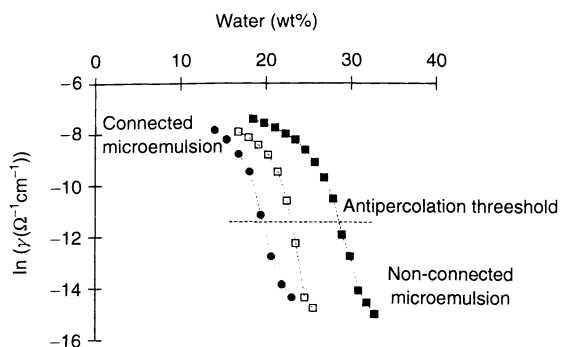


Figure 9.19. Variation of the conductivity γ as a function of the water content in a water-(dodecane + lindane)-DDAB w/o microemulsion along the water dilution line for different weight percentages β of lindane in the oil (lindane/dodecane + lindane): ■, $\beta = 0$; □, $\beta = 1$; ●, $\beta = 2$

limit where emulsification failure occurs (54). At this boundary, it has been proved that the microstructure is consistent with a random distribution of monodispersed w/o hard spheres of known radii. The determination of the maximum amount of water which can be solubilized in the microemulsion will give the radius R of the droplet, and hence the spontaneous curvature, since with stiff interfaces the curvature constraint cannot be violated, i.e. $R = 3\phi/\Sigma$, where ϕ is the hydrophilic volume ratio (polar head of surfactant and water) and Σ is the total surface area per unit volume (specific surface area). Assuming a surfactant tail, ℓ , of 13 Å (80% of the extended alkane chain (22)), the coverage relationship will give the value of the packing parameter, as follows:

$$P = 1 + \frac{\ell}{R_{\max}} + \frac{1}{3} \times \frac{\ell^2}{R_{\max}^2} \quad (9.32)$$

A relationship between this packing parameter and the composition of the oil is illustrated in Figure 9.20. As the amount of solute is increasing, the packing parameter is also increasing. This variation means that the spontaneous curvature, which is experimentally close to the average curvature in the case of stiff interfaces, turns towards water when the solute is added to the microemulsion.

These experimental results can be rationalized by the DOC-cylinders model, which is the only one consistent with the presence of antipercolation thresholds in the phase diagrams, and also with the position of the maximum peak in the scattering diagram as a function of the angle obtained from SAXS experiments. This maximum is directly linked to a preferred distance

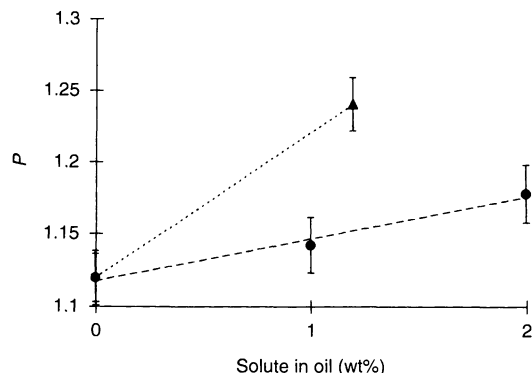


Figure 9.20. Variation of the packing parameter $P(= V/\sigma)$ as a function of the weight percentage of solute in the oil: ●, lindane; ▲, phenol. P has been determined from the position of the observed emulsification failure in the phase diagram along a water dilution line

between the centres of connected or unconnected water domains in the microemulsion.

Before explaining how to use the DOC-model in our solubilization experiment, we will summarize the physical basis of this model which allows for an analytic treatment of the microstructure. The DOC-model was introduced by Ninham *et al.* (55) in 1987. It is based on a generalized connected structure which locally satisfies three constraints, i.e. the volume fraction ϕ , the specific surface Σ and the curvature or its microscopic translation surfactant parameter P . This microstructure is assimilated to a purely geometric question which neglects entropy and curvature fluctuation effects. The structure is built from a Voronoi cell tessellation. Each centre of a cell is surrounded by a spherical droplet of radius R . When the spheres are connected, such connections are approximated by a network of cylinders linking each sphere to an average of Z neighbouring spheres. The constraint of constant curvature imposes a well-defined relationship between the radii of the co-existing spheres and cylinders. The number of intersections for one sphere represents the connectivity Z and is related to the conductivity. When Z is smaller than 1.2, the system is unconnected over macroscopic distances, while it is connected for higher values of Z . The antipercolation threshold corresponds to this value of 1.2.

The input information needed for a given sample is the polar volume fraction ϕ , and the specific surface Σ . Knowing the surfactant packing parameter and the scattering peak position, converted into real space as distance D^* , the conductivity can be deduced or, by using the analytic model in the reverse way, knowing

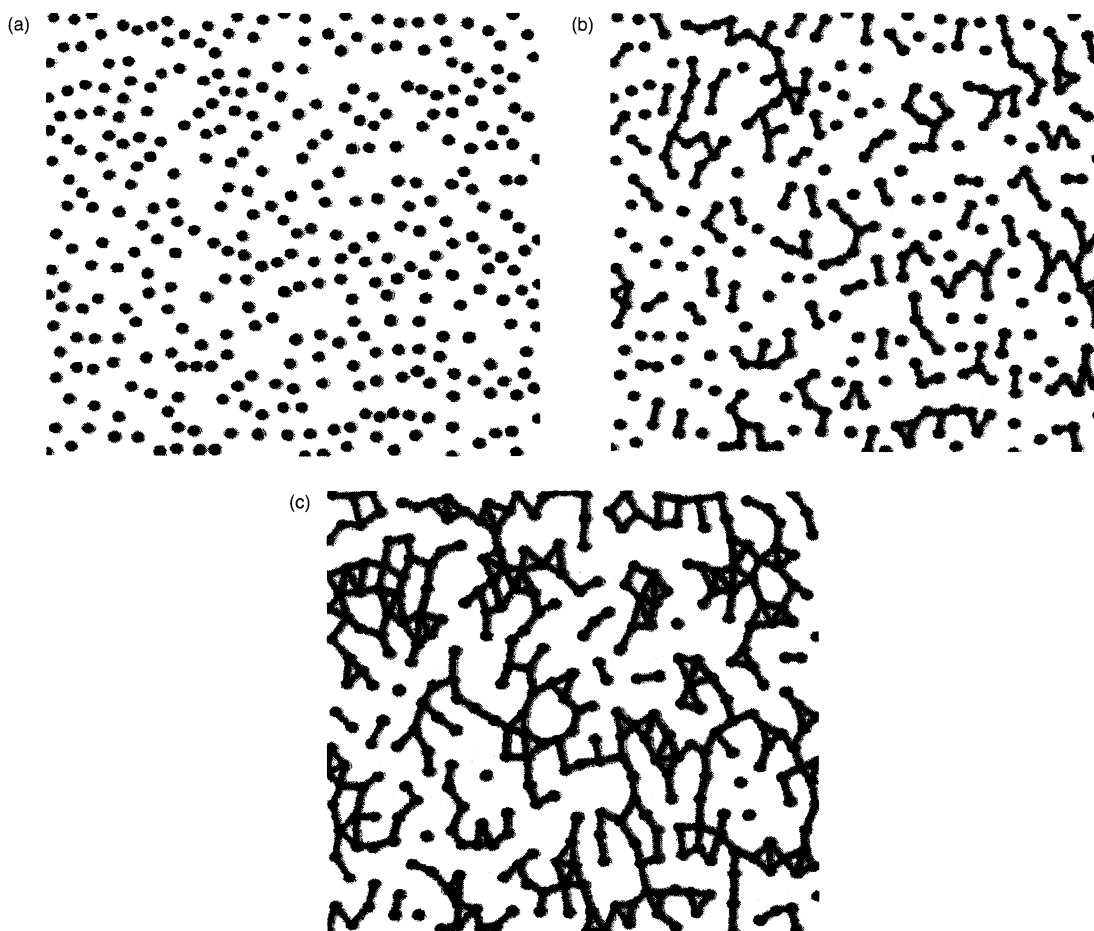


Figure 9.21. Schematic showing the evolution of the connectivity of a water-in-oil microemulsion obtained with the two-dimension DOC cylinder model: (a) non-conducting; (b) non-conducting but with clusters forming for a low value of the connectivity Z ; (c) conducting. The scale is 200 nm with a film thickness (in grey) of 1.2 nm and an unconnected droplet radius of 3.6 nm

Z and D^* , the value of the packing parameter P can be deduced. Figure 9.21 shows schematically the transition from a connected to an unconnected medium induced by a variation of P .

The method of deducing solute location from the scattering peak shift in the case of spherical reversed-micelles can be generalized to the case of connected structures (56). For instance, consider the model case of a bicontinuous structure, close to the electrical antipercolation threshold. Take the polar volume fraction to be in the range 0.3 to 0.4 and the specific area to be $\Sigma = 0.02 \text{ \AA}^2/\text{\AA}^3$, which corresponds to a 0.5M solution of a classical surfactant. In addition, consider a chain length of 15 Å and an initial surfactant packing parameter of $P_0 = 1.25$.

Minimizing elastic energy in the frame work of the DOC-cylinder model produces connected structures of typical sizes of the order of 100 Å. In the absence of solute, electrical percolation is predicted to occur at a volume fraction ϕ of 0.35 ($Z = 1.2$). The microstructure is predicted to be unstable due to emulsification failure for volume fractions lower than 0.33 and higher than 0.48 because it is impossible to minimize the elastic energy under curvature constraints at that point.

Suppose now that we add a solute, for example, a chemically reactive molecule, that induces an increase of the area per head-group by 10%; thus, the packing parameter $P_0 = V/\sigma\ell$ decreases by 10%, i.e. $P_0 = 1.13$. The consequence is a shift of the peak towards larger Bragg distances, another domain of stability and a

structure which is always bicontinuous with a high conductivity of the sample at any volume fraction.

Quite different results are expected if the effect of the solute is to induce a 10% increase of the surfactant parameter ($P_0 = 1.37$), due to an increase of the apolar volume V of the surfactant film, which includes the solute as a penetrating wedge but does not change the area σ per surfactant. The peak shift associated with the presence of the surfactant is now different, and the sample always has a low conductivity.

Thus, in the case of DOC-cylinder structures, simultaneous observations of scattering peak shifts and conductivities allow the determination of solute localization in microemulsions. Measurable and distinguishable effects occur in the scattering peak position and the conductivity when the solute is located in the polar volume, in the surfactant film or in the apolar solvent.

In order to demonstrate the suitability of the DOC-model to infer solute localization from scattering and conductivity measurements, we have summarized in Table 9.2 the action of solutes which induce different effects on the three basic constraints. The values are calculated by solving simultaneously the volume, surface and curvature constraints, illustrating this on a sample with a chain length $\ell = 12 \text{ \AA}$, a polar volume fraction ϕ of 0.25 and a specific area Σ of $0.02 \text{ \AA}^2/\text{\AA}^3$.

As can be seen from this table, the effects induced by the presence of the solute on the scattering and conductivity depend primarily on the microscopic consequences induced by the presence of the solute molecules in the surfactant film. For example, a peak shift towards smaller q -values (increase in D^*) is the signature of an increase in polar volume fraction at constant area and surfactant parameter if the sample is not conducting. If the conductivity decreases only slightly, the same peak shift is the signature of a decreased area per surfactant (independently measurable) at a constant polar volume and packing parameter. Thus, the DOC model now allows an interpretation of the effect of a solute on the

scattering spectra to be directly linked to the solute location. This observation may be used in the study of solubilization, especially since Jönsson and co-workers (27) have shown that the location of solute molecules is of primary importance for the free energy variation induced by polar/apolar solutes in ionic surfactant systems, and hence for phase diagram predictions. A practical example of how to localize a solute is detailed in the case of lindane in a water–dodecane–DDAB microemulsion (52). The experimental method compares a sample with a constant polar volume fraction when dodecane is replaced by a mixture of dodecane + lindane. The experiment consist of determining the mean variation in the microstructure induced by the solute. Figure 9.19 above shows that at the antipercolation threshold ($Z = 1.2$), the polar volume fraction is decreasing as dodecane is replaced by a mixture of dodecane + lindane. SAXS experiments performed on samples corresponding to $Z = 1.2$ give the evolution of the distance associated with the scattering peak position of those solutions. Knowing ϕ and Σ from the composition of the sample, and by inserting values of D^* and P in the DOC-model, we obtain a strict correlation between the experimental and theoretical values of the conductivity and $D^*\Sigma$.

The DOC-model allows to localize the solute, as the theory and experiments are in agreement for a decrease of the interfacial area σ of the surfactant and an increase of the film thickness induced by the presence of lindane.

3.3.2 Other cases with a stiff interface: curvature directed towards oil-forming oil-in-water droplets with a stiff interface and lamellar phase

The influence of the presence of an apolar solute on the emulsification failure has been simulated by Nelson *et al.* (57). The main effect of the presence of an apolar solute is to increase the degrees of freedom in the shape of the aggregates. For example, adding an apolar

Table 9.2. Expected effects of a solute on the position of the scattering peak and conductivity of a microemulsion showing an initial peak position $D^* = 100 \text{ \AA}$, with initial $P_0 = 1.28$ and conductivity near the percolation threshold ($Z \sim 1.2$), i.e. a high sensitivity of the conductivity towards geometrical constraints

Effect of solute			Expected effect	
Volume fraction, ϕ	Area, Σ	Packing parameter, P	Peak shift (\AA)	Conductivity
Increase to 0.3	Constant	Constant	+8	Decreases to $Z = 0$
Decrease to 0.2	Constant	Constant	−3	Increases
Constant	+10%	Constant	−7	Increase
Constant	−10%	Constant	+5	Decrease
+10%	+10%	Constant	0	Decreases to $Z = 0$
Constant	Constant	+10%	Phase separation	−
+10%	Constant	−5% www.iran-mavad.com	+10	Increase

molecule to o/w small micelles produces worm-like aggregates. A direct consequence of the presence of these worm-like aggregates is the lowering of the cloud-point temperature, due to enhanced attractions between parallel cylinders. Another effect of apolar solutes in micellar solutions is to reduce the concentration of free monomers well below the CMC, which is the value of free monomers in water in the absence of solute. However, with the exception of the general trend that apolar solutes lower the spontaneous radius of curvature of the mixed aggregate, hence favouring the presence of connected cylinders, and despite its considerable practical importance in detergency, little is known about the following:

- the induced microstructure variations
- the general underlying driving principles associated with microstructure transformation
- the maximum admissible concentrations in the presence of an added solute in o/w dispersions

A special case is that of rigid interfaces with a spontaneous curvature close to zero, such as the case of oil-swollen lamellar phases, when long-chain double-tailed surfactants form oil-swollen layers separated by water layers. These phases present strong geometrical constraints and the thickness of layers are easily measurable with precision by means of scattering experiments. The variation of composition associated with the addition of a solute can be detected by visual inspection between crossed polarizers and by chemical analysis. However, to our knowledge, no experimental results on curvature variation, area per molecule variation and maximum admissible concentration of a solute in these systems is yet available.

4 CONCLUSION: OPEN PROBLEMS

To summarize, it is up to the choice of the experimentalist to decide at which scale of organized molecular systems is selected to describe a solubilization problem.

Experimental results always rely on titration or characterization of the concentration of solutes in co-existing phases. When one of the co-existing phases is pure solute, one obtains the MAC.

The simplest level is only to consider the w/o interface as the available area for an adsorption process. At a more refined level, the surfactant solution may be conceptually divided, as follows:

- (i) into two compartments, i.e. a polar one and an apolar one of given volume fraction. In this case,

the volume fraction corresponding to the surfactant has to be split into a polar and an apolar type, given approximately by the volume ratio of the two corresponding parts of the surfactant, with the core and palisade layer usually being taken as the polar part of the surfactant.

- (ii) into three co-existing volumes, i.e. water, oil and mixed surfactant layer. This level is suitable when the determination of the solubilization excess is the objective.

Refinements in considering separately the sub-volumes as the palisade layer and the core have allowed a unique example of predicting solubilization in the case of charged w/o systems when electrostatic effects are explicitly taken into account as the dressed model of micelles (27). This example is the only work to our knowledge for which the whole phase diagram has been explicitly calculated from osmotic pressure and free energy equilibria in co-existing phases.

At a fundamental level, the effect of the presence of a solute can be evaluated by the "wedge model", since volume variation induced by the presence of the solute is known and experimental values for partial molar surfaces can be obtained from scattering experiments. All general intrinsic variables associated with a surfactant layer are profoundly influenced by the presence of solutes, namely bending constants and spontaneous radii of curvature, and hence the corresponding phase limits.

Since maximum solubilization is always the result of a competition between co-existing phases, including the bending energy, no general theory is able to predict the well-established similarity between curvature variation and cubic phase formation (such as the case of vitamin E in simple surfactants (58)).

The problem of solubilization in complex mixed fluids still remains open. Model mixed systems include surfactant solutions in the presence of inorganic two-dimensional objects such as clay, surfactants in the presence of linear polymers, and surfactants in the presence of globular nanoparticles, either inorganic or globular proteins. All of these model systems may be used to mimic solubilization in the environment. A general approach to this open problem is dealt with by Klumpp and Schwuger (59), who demonstrated that surfactants and multivalent ions are competitors for exchange at the surface of clays (as they should also be on humic acids). Once the mixed system is formed, the solubilization power (MAC) of the mixed surfactant system may be widely enhanced by reference to the separated surfactant and colloid. A spectacular example has been described

by Boyd *et al.*, who demonstrated a large enhancement of the solubilization of nonionic contaminants (NOCs) by clay particles, once cationic surfactants have ion-exchanged part of the clay counterions (60). Generalizing this type of synergetic behaviour to other cases and developing predictive models for mixed surfactant systems is very important for environment control, but is nevertheless still an open issue.

5 REFERENCES

- McBain, M. E. L. and Hutchinson, E., *Solubilization and Related Phenomena*, Academic Press, New York, 1955.
- Ward, A. J., Kinetics of solubilization in surfactant based systems, in *Solubilization in Surfactant Aggregates*, Christian, S. D. and Scamehorn, J. F. (Eds), Surfactant Sciences Series, Vol. 55, Marcel Dekker, New York, 1995, pp. 237–273.
- Zulauf, M., Detergent phenomena in membrane protein crystallization, in *Crystallization of Membrane Proteins*, Michel, H. (Ed.), CRC Press, Boca Raton, FL, 1988.
- Israelachvili, J. N., Mitchell, D. J. and Ninham, B. W., Theory of self-assembly of hydrocarbon amphiphiles into micelles and bilayers, *J. Chem. Soc., Faraday Trans. 2*, **72**, 1525–1568 (1976).
- Boden, N., Jones, S. A. and Sixl, F., Solubilization in lyotropic liquid crystals: the concept of partial molecular surface area, *J. Phys. Chem.*, **91**, 137–145 (1987).
- Evans, D. F. and Wennerström, H., *The Colloidal Domain: Where Physics, Chemistry, Biology and Technology Meet*, VCH, Weinheim, New York, 1994.
- Hyde, S., Andersson, S., Larsson, K., Blum, Z., Landh, T., Lidin, S. and Ninham, B. W., *The Language of Shape*, Elsevier, Amsterdam, 1997.
- Fogden, A., Hyde, S. T. and Lundberg, G., Bending energy of surfactant film, *J. Chem. Soc., Faraday Trans.*, **87**, 949–955 (1991).
- Bourrel, M. and Schechter, R. S. (Eds), *Microemulsions and Related Systems*, Surfactant Science Series, Vol. 30, Marcel Dekker, New York, 1988.
- Chevalier, Y. and Zemb, Th., The structure of micelles and microemulsions, *Rep. Prog. Phys.* **53**, 279–371 (1990).
- Ninham, B. W. and Yaminsky, V., Ion binding and ion specificity: the Hofmeister effect, Onsager and Lifshitz theories, *Langmuir*, **13**, 2097–2108 (1997).
- Leodidis, E. B. and Hatton, T. A., Specific ion effect in electrical double layers: selective solubilization of cations in Aerosol-OT reversed micelles, *Langmuir*, **5**, 741–753 (1989).
- Cabane, B., Duplessix, R. and Zemb, Th., High resolution neutron scattering on ionic surfactant micelles: SDS in water, *J. Phys.*, **46**, 2161–2178 (1985).
- Christian, S. D. and Scamehorn, J. F. (Eds), *Solubilization in Surfactant Aggregates*, Surfactant Science Series Vol. 55, Marcel Dekker, New York, 1995.
- Hoiland, H. and Blokus, A. M., Solubilization in aqueous systems, in *Handbook of Surface and Colloid Chemistry*, Birdi, K. S. (Ed.), CRC press, Boca Raton, FL, 1997, pp. 239–264.
- Lindman, B., Structural aspects of surfactant micellar systems, in *Surfactants*, Tadros, Th. (Ed.), Academic Press, London, 1984, pp. 239–264.
- Fontell, K. and Janssen, M., The relation between the cubic phase and the neighbouring solution phase in systems of di(alkyl)dimethylammonium bromide–hydrocarbon–water, *Progr. Colloid Polym. Sci.*, **76**, 169–175 (1988).
- Treiner, C., The partitioning of neutral solutes between micelles and water as deduced from cmc determinations, in *Solubilization in Surfactant Aggregates*, Christian, S. D. and Scamehorn, J. F. (Eds), Surfactant Science Series, Vol. 55, Marcel Dekker, New York, 1995, pp. 383–428.
- Amararene, A., Gindre, M., Le Huérou, J.-Y., Urbach, W., Valdez, D. and Waks, M., Adiabatic compressibility of AOT reverse micelles. Analysis of a simple model based on micellar size and volumetric measurements, *Phys. Rev., E*, **61**, 682–689 (2000).
- Dunaway, C. S., Christian, S. D. and Scamehorn, J. F., Overview and history of the study of solubilization, in *Solubilization in Surfactant Aggregates*, Christian, S. D. and Scamehorn, J. F. (Eds.), Surfactant Science Series, Vol. 55, Marcel Dekker, New York, 1995, pp. 3–31.
- Ben Naim, A., Standard thermodynamics of transfer. Uses and misuses, *J. Phys. Chem.*, **82**, 792–803 (1978).
- Tanford, C., *The Hydrophobic Effect: The Formation of Micelles and Biological Membranes*, 2nd Edn, Wiley, New York, 1980.
- Von Corswant, Ch. and Thoren, P. E. G., Solubilization of sparingly soluble active compounds in lecithin based microemulsions: influence on the phase behavior and microstructure, *Langmuir*, **15**, 3710–3717 (1999).
- Treiner, C. and Mannebach, M. H., Correlation analysis of solubilization data in aqueous cationic and anionic micellar solutions: case of the halocarbons, *J. Colloid Interface Sci.*, **118**, 243–251 (1987).
- Makayssi, A., Bury, R. and Treiner, C., Thermodynamics of micellar solubilization for 1-pentanol in weakly interacting binary cationic surfactant mixtures at 25°C, *Langmuir*, **10**, 1359–1365 (1994).
- Ekwall, P., Mandell, L. and Fontell, K., Solubilization in micelles and mesophases and the transition from normal to reversed structures, *Mol. Cryst. Liq. Cryst.*, **8**, 157–213 (1969).
- Aamodt, M., Landgren, M. and Jönsson, B., Solubilization of uncharged molecules in ionic surfactant aggregates. 1. The micellar phase, *J. Phys. Chem.*, **96**, 945–950 (1992).
- Mukerjee, P., Cardinal, J. R. and Desai, N. R., The nature of the local microenvironments in aqueous micellar

- systems, in *Micellization, solubilization and microemulsions*, Mittal, K. L. (Ed.), Plenum Press, New York, 1997, pp. 241–261.
29. Landgren, M., Aamodt, M. and Jönsson, B., Solubilization of uncharged molecules in ionic surfactant aggregates. 2. Phase equilibria, *J. Phys. Chem.*, **96**, 950–961 (1992).
 30. Kunieda, H., Shigeta, K., Ozawa, K. and Suzuki, M., Self-organizing structures in the poly(oxyethylene)oleyl ether–water system, *J. Phys. Chem., B*, **101**, 7952–7957 (1997); (b) Kunieda, H., Ozawa, K. and Huang, K. L., Effect of oil on the surfactant molecular curvatures in liquid crystals, *J. Phys. Chem., B*, **102**, 831–838 (1998).
 31. Kanei, N., Tamura, Y. and Kunieda, H., Effect of types of perfume compounds on the hydrophile–lipophile balance temperature, *J. Colloid Interface Sci.*, **218**, 13–22 (1999).
 32. Leung, R. and Shah, D. O., Solubilization and phase equilibria of water in oil microemulsions I., *J. Colloid Interface Sci.*, **120**, 320–329 (1987); (b) Leung, R. and Shah, D. O., Solubilization and phase equilibria of water in oil microemulsions II., *J. Colloid Interface Sci.*, **120**, 330–344 (1987).
 33. Hou, M.-J. and Shah, D. O., Effects of the molecular structure of the interface and continuous phase on solubilization of water in water/oil microemulsions, *Langmuir*, **3**, 1086–1096 (1987).
 34. Zemb, Th., The DOC model of microemulsions: microstructure, scattering, conductivity and phase limits imposed by sterical constraints, *Colloids Surf., A*, **129/130**, 435–454 (1997).
 35. (a) Jada, A., Lang, J. and Zana, R., Ternary water in oil microemulsions made of cationic surfactants, water, and aromatic solvents 1. Water solubility studies, *J. Phys. Chem.*, **94**, 381–387 (1990); (b) Jada, A., Lang, J. and Zana, R., Ternary water in oil microemulsions made of cationic surfactants, water and aromatic solvent. 2. Droplet sizes and interactions and exchange of material between droplets, *J. Phys. Chem.*, **94**, 387–395 (1990).
 36. (a) Diamond, J. M. and Wright, E. M., Biological membranes: the physical basis of ion and non electrolyte selectivity, *Ann. Rev. Physiol.*, **31**, 581–646 (1969); (b) Katz, Y. and Diamond, J. M., a method for measuring non electrolyte partition coefficients between liposomes and water, *J. Membrane Biol.*, **17**, 69–86 (1974); (c) Katz, Y. and Diamond, J. M., Non solvent water in liposomes, *J. Membrane Biol.*, **17**, 87–100 (1974); (d) Katz, Y. and Diamond, J. M., Thermodynamic constants for nonelectrolyte partition between dimyristoyl lecithin and water, *J. Membrane Biol.*, **17**, 101–120 (1974); (e) Diamond, J. M. and Katz, Y., Interpretation of nonelectrolyte partition coefficients between dimyristoyl lecithin and water, *J. Membrane Biol.*, **17**, 121–154 (1974).
 37. Leodidis, E. B. and Hatton, A., Amino acids in AOT reversed micelles. 1. Determination of interfacial partition coefficients using the phase-transfer method, *J. Phys. Chem.*, **94**, 6400–6411 (1990); (b) Leodidis, E. B. and Hatton, A., Amino acids in AOT reversed micelles. 2. The hydrophobic effect and hydrogen bonding as driving forces for interfacial solubilization, *J. Phys. Chem.*, **94**, 6411–6420 (1990); (c) Leodidis, E. B., Bommarius, A. S. and Hatton, T. A., Amino acids in reversed micelles, 3. Dependence of the interfacial partition coefficient on excess phase salinity and interfacial curvature, *J. Phys. Chem.*, **95**, 5943–5956 (1991); (d) Leodidis, E. B. and Hatton, T. A., Amino acids in reversed micelles. 4. Amino acids as cosurfactants, *J. Phys. Chem.*, **95**, 5957–5965 (1991).
 38. Fromherz, P., Röcker, C. and Ruppel, D., From discoid micelles to spherical vesicles, The concept of edge activity, *Faraday Discuss. Chem. Soc.*, **81**, 39–48 (1986).
 39. Demé, B. and Zemb, Th., Measurement of sugar depletion from uncharged lamellar phases by SANS contrast variation, *J. Appl. Crystallogr.*, **33**, 569–573 (2000).
 40. Westh, P. and Trandum, C., Thermodynamics of alcohol–lipid bilayer interactions: application of a binding model, *Biochim. Biophys. Acta*, **1421**, 261–272 (1999).
 41. Rowe, E. S., Zhang, F., Leung, T. W., Par, J. S. and Guy, P. T., Thermodynamics of membrane partitioning for a series of *n*-alcohols determined by titration calorimetry: role of hydrophobic effects, *Biochemistry*, **37**, 2430–2440 (1998).
 42. Davis, S. S., James, M. J. and Andeerson, N. H., The distribution of substituted phenols into lipid vesicles, *Faraday Discuss. Chem. Soc.*, **81**, 313–327 (1986).
 43. Xu, Y. and Tang, P., Amphiphilic sites for general anesthetic action? Evidence from $^{129}\text{Xe}\{-^1\text{H}\}$ intermolecular Overhauser effects, *Biochim. Biophys. Acta*, **1323**, 154–162 (1997).
 44. Brückner, E. and Rehage, H., Solubilization of toluene in phospholipid vesicles studied by video-enhanced contrast microscopy, *Progr. Colloid Polym. Sci.*, **109**, 21–28 (1998).
 45. Pileni, M. P., Zemb, Th. and Petit, C., Solubilization by reverse micelles: solute localization and structure perturbations, *Chem. Phys. Lett.*, **118**, 414–420 (1985).
 46. Fletcher, P. D. I., The partitioning of solutes between water in oil microemulsions and conjugate aqueous phases, *J. Chem. Soc., Faraday Trans. 1*, **82**, 2651–2664 (1986).
 47. Testard, F., Zemb, Th. and Strey, R., Excess solubilization of lindane in bicontinuous microemulsions, *Progr. Colloid Polym. Sci.*, **105**, 332–339 (1997).
 48. Testard, F. and Zemb, Th., Excess of solubilization of lindane in nonionic surfactant micelles and microemulsions, *Langmuir*, **14**, 3175–3181 (1998).
 49. Strey, R., Microemulsion microstructure and interfacial curvature, *Colloid Polym. Sci.*, **272**, 1005–1019 (1994).
 50. Malcolmson, C., Satra, C., Kantaria, S., Sidhu, A. and Lawrence, M. J., Effect of oil on the level of solubilization of testosterone propionate into nonionic oil in water microemulsions, *J. Pharm. Sci.*, **87**, 109–116 (1998).

51. Lawrence, M. J., Microemulsions as drug delivery vehicles, *Curr. Opinion Colloid Interface Sci.*, **1**, 826–832 (1996).
52. Testard, F. and Zemb, Th., Solute effect on connectivity of w/o microemulsions, *Langmuir*, **16**, 332–339 (2000).
53. Rushforth, D. S., Sanchez-Rubio, M., Santos-Vidal, L. M., Wormuth, K. R., Kaler, E. W., Cuevas, R. and Puig, J. E., Structural study of one-phase microemulsions, *J. Phys. Chem.*, **90**, 6668–6673 (1986).
54. Hyde, S. T., Ninham, B. W. and Zemb, Th., Phase boundaries for ternary microemulsions: predictions of a geometric model, *J. Phys. Chem.*, **93**, 1464–1471 (1989).
55. Ninham, B. W., Barnes, I. S., Hyde, S. T., Derian, P. J. and Zemb, Th., Random connected cylinders: a new structure in three-component microemulsions, *Europhys. Lett.*, **4**, 561–568 (1987).
56. Zemb, Th., The DOC model of microemulsions: microstructure, scattering, conductivity and phase limits imposed by sterical constraints, *Colloid Surf., A*, **129–130**, 435–454 (1997).
57. Nelson, P. H., Hatton, T. A. and Rutledge, G. C., Asymmetric growth in micelles containing oil, *J. Chem. Phys.*, **110**, 9673–9680 (1999).
58. Caboi, F., Nylander, T., Razumas, V., Talaikyte, Z., Monduzzi, M. and Larsson, K., Structural effects mobility and redox behavior of vitamin K₁ hosted in the monolein/water liquid crystalline phases, *Langmuir*, **13**, 5476–5483 (1997).
59. Klumpp, E. and Schwuger, M. J., Physicochemical interactions of surfactants and contaminants in soil, in *Detergents and the Environment*, Schwuger, M. J. (Ed.), Surfactant Science Series Vol. 65, Marcel Dekker, New York, 1997.
60. Boyd, S. A., Lee, J. F. and Mortland, M. M., Attenuation organic contaminant mobility by soil modification, *Nature (London)*, **333**, 345–347 (1988).

CHAPTER 10

Rheological Effects in Surfactant Phases

Heinz Hoffmann and Werner Ulbricht

Universität Bayreuth, Bayreuth, Germany

1	Introduction	189	3	The Rheology of Bilayer Phases	199
1.1	The rheological properties of condensed matter	189	3.1	The rheological behaviour of various bilayer phases	199
1.2	The behaviour of surfactants in aqueous solutions	190	3.2	Models for the shear moduli of lamellar phases	202
2	The Rheological Behaviour of Aqueous Surfactant Solutions	191	4	The Rheology of Cubic Phases	204
2.1	Non-interacting micelles	192	5	Shear-Induced Phenomena in Surfactant Solutions	205
2.2	Viscoelastic surfactant solutions with entangled rod-like micelles	193	5.1	Surfactant solutions with rod-like micelles under shear	206
2.3	The rheology of various surfactant solutions with rod-like micelles	195	5.2	Shear-induced phenomena in lamellar phases	211
2.4	Mechanisms for the rheological behaviour of rod-like micelles	198	6	References	214

1 INTRODUCTION

In the first part of this review, the general rheological behaviour of condensed matter will be introduced. In the second part, the aggregation and phase behaviour of surfactants in solution will be described briefly, because the rheological properties of such systems are determined by the surfactant aggregates and the interactions which exist in the solutions. Then, in the main part of this chapter, the rheology of various surfactant phases will be discussed in detail.

1.1 The rheological properties of condensed matter

In this introduction, models for the rheological behaviour of matter will be briefly discussed (1). Molecules of condensed matter show strong interactions with their

neighbouring molecules. These interactions are responsible for the fact that a condensed phase is restricted to a fixed volume, whereas gas molecules can distribute homogeneously in each given volume. The interactions between the molecules also determine the rheological properties of the condensed phases. In liquids, the interactions are strong enough to keep the molecules within a fixed volume, but too weak to restrict the molecules to a fixed position; thus, the liquid can change its form, and then flow under the influence of stress. In solids, on the other hand, the attractive forces between the molecules (or atoms) are so strong that each molecule is restricted to a fixed position in space; the solid is therefore elastic and responds with a restoring force to the application of stress.

Gases, and even ideal gases, show also a weak resistance against flow which is due to the transport of molecules with different impulses between layers with different flow velocities. This effect does not play

any role in the rheological behaviour of condensed matter because the influence of cohesive forces between these molecules is stronger by orders of magnitude. Consequently the rheology of condensed matter is determined by the intermolecular forces and can be described by the following models:

- (A) Pascalian liquid. This type of liquid does not show any resistance to flow and thus has a viscosity of zero. Such a liquid does not occur under normal conditions in laboratories, with only *suprafluid liquids* being examples of a Pascalian liquid.
- (B) Newtonian liquid. This type of liquid flows under the influence of stress, and the flow gradient is proportional to the applied stress. The viscosity η of such a liquid, which is defined as the ratio of the stress and the shear gradient, is thus constant and independent of the stress. Many solvents with low molecular weight, among these is water, are Newtonian liquids.
- (C) Dilatant liquid (shear thickening). This type of liquid also flows under the influence of stress, but the viscosity increases with increasing stress or shear gradient. For example, several polymer solutions show dilatant properties.
- (D) Structural viscous liquid (shear thinning). In this case, the viscosity decreases with increasing stress or shear gradient. Polymer solutions can also show structural viscosity, depending on the dissolved macromolecule.
- (E) Thixotropic liquid. The viscosity of these liquids depends on the time of flow and decreases with increasing time at a constant flow gradient. This effect can be both reversible or irreversible, and is also shown by many polymer solutions.
- (F) Rheoplectic liquid. The viscosity of these liquids increases with increasing time at a constant flow gradient, and in addition, this effect, which is shown again by certain polymer solutions, can be either reversible or irreversible.
- (G) Viscoelastic liquid or elastoviscous solid. These phases have both the properties of liquids and of solids; they can flow under the influence of stress, but show, in addition, restoring forces. Many polymer solutions, and also surfactant solutions, show viscoelastic properties.
- (H) Bingham solid. This type of system responds to stress with a restoring force and cannot flow as long as the stress remains below a critical value, known as the *yield stress value*; beyond this value, the sample flows like a liquid. This behaviour is shown by various polymer and surfactant solutions;

in addition, dispersions or liquid crystalline phases can behave like Bingham solids.

- (I) Hookean solid. This is a type of solid which cannot flow under the influence of stress. It responds to stress with a deformation which is proportional to the stress, i.e. its elasticity is constant and independent of the stress. Many solids, especially metals, behave as Hookean solids if the stress remains below a critical value; beyond this value, the solid is destroyed irreversibly.
- (J) Euclidean solid. This type of solid cannot be deformed by stress, i.e. its elasticity coefficient is infinite. A Euclidean solid does not exist in reality, although its properties are approached by hard materials such as diamond.

It is necessary here to point out that the rheology of all materials, especially the rheology of surfactant solutions, can depend strongly on the time-scale on which the material is studied. This can be demonstrated quite easily. For example, Newtonian liquid water behaves as an elastic solid if the stress is applied for nanoseconds or picoseconds; on the other hand, granite, which can be regarded as an Euclidean solid to a first approximation, can flow like a liquid if a strong stress acts over a period of 10^8 – 10^9 years. Therefore, it must be stated at this point that the description of the rheological effects of surfactant solutions is valid for observation times which are necessary for the measurements, i.e. several seconds up to several days, or weeks in some cases.

1.2 The behaviour of surfactants in aqueous solutions

Surfactants with low molecular weight – amphiphilic polymers which can be regarded as polymeric surfactants will not be discussed in this chapter – are characterized by their amphiphilic properties, i.e. their molecules consist of a polar (or hydrophilic) and a non-polar (or hydrophobic) group. Due to this constitution, the surfactants dissolve in water and other strongly polar liquids as monomers, which start to form aggregates beyond a characteristic concentration, which is called the *critical micelle concentration* (CMC) (2, 3). As pointed out in other chapters of this volume, the CMC is strongly dependent on the constitution of both the hydrophilic and the hydrophobic group; it can vary by several orders of magnitude over the range of μM to M .

The dimensions of the surfactant aggregates or micelles can vary over the range of several nanometres (nm) to several hundred nm, which are the typical sizes of colloids, i.e. much larger than monomeric atoms

or molecules but still below the range of microscopically visible particles. The micelles are thermodynamically stable aggregates which are in equilibrium with the monomers. Below the CMC, the monomer concentration is equal to the total surfactant concentration, while above the CMC the monomer concentration remains constant and equal to the CMC to a first approximation. With increasing surfactant concentration, the size or/and the concentration of the micelles increases. The aggregation process is reversible; there is a steady exchange of monomeric and aggregated surfactant molecules, and the aggregates disappear again on dilution below the CMC.

According to the theory of amphiphilic aggregation, the size and shape of micelles is determined by the packing parameter, $P = a_s l_s / v_s$ where a_s is the head-group area at the micellar surface, l_s the length and v_s the volume of the hydrophobic chain. For $P > 3$, spherical micelles are formed, for $3 > P > 2$ rod-like micelles, and for $2 > P > 1$ disc-like micelles or lamellar bilayers are present, while for $P < 1$, reverse aggregates exist in the solutions. The parameters l_s and v_s are determined by the constitution of the hydrophobic group, while a_s can depend not only on the constitution of the hydrophilic head-group, but also on parameters such as the dissociation degree of an ionic head-group, the ionic strength, the surfactant concentration and the temperature of the solution; a_s can be much larger than the cross-sectional area, a_0 , of the head-group. With increasing surfactant concentration, the sequence of the aggregates is therefore spherical micelles–rod-like micelles–disc-like micelles or lamellar bilayers–reverse micelles. These transitions take place at characteristic concentrations which can be called “higher CMCs”. However, not all aggregates must be formed in a surfactant solution; in many cases, rod-like micelles or bilayers have been found as the first aggregate species above the CMC.

The diameter of rod-like or spherical micelles, the short axis of ellipsoids and the thickness of bilayers are determined by the length of a surfactant molecule, and is hence independent of the concentration. Therefore, the size of the spheres is constant and their concentration increases with increasing concentration, while the long axis of rods and of bilayers usually increases with the surfactant concentration. Rods, for example, can therefore become very long and also flexible (thread-like micelles). It has also been observed that at the concentration c^* where the rotational volumes of the rods are overlapping, the rods do not grow any more, although their concentration increases again.

At higher surfactant concentrations (usually beyond 40–50 wt%), the micellar aggregates must be packed

due to hard sphere repulsions. This leads to the formation of lyotropic liquid crystalline phases with a corresponding order of the mass centres of the aggregates and/or of the orientation of anisometric aggregates.

Spherical micelles therefore form cubic phases, rod-like micelles form hexagonal phases, and bilayers form lamellar phases; reverse phases can also exist at sufficiently high surfactant concentrations. The phase sequence with increasing concentration is therefore cubic phases–hexagonal phases–lamellar phases–reverse hexagonal phases–reverse cubic phases; between the hexagonal phases and the lamellar phases, bicontinuous phases with cubic symmetry may also be present, and at lower concentrations before the hexagonal and the lamellar phases are observed, nematic calamitic or discotic phases, in which only the orientation of the anisometric aggregates is uniform, can be found in many systems.

In addition, not each phase here must be present in a given surfactant solution; systems with a hexagonal phase or also a lamellar phase as the first lyotropic mesophase are known. Of special interest are systems where, according to a packing parameter of around 1, lamellar aggregates are already formed at low surfactant concentrations. Such systems are surfactants with voluminous hydrophobic groups and/or small head-groups or ternary systems consisting of water, surfactant and cosurfactant (amphiphiles such as aliphatic alcohols or amines which do not form micelles alone in aqueous solutions). These can develop lamellar phases at low concentrations, of around 1 wt%. These lamellar phases can have various structures. They can form classical lamellar phases with flat bilayers, uni- or multilamellar spherical vesicles consisting of closed bilayers, and also bicontinuous L_3 -phases or sponge phases in which the bilayers form continuous branched tubes in the continuous water phase.

The packing parameter is therefore not suitable to explain the phase behaviour of the bilayer systems. However, a theory has been established which can explain the stability of the various lamellar structures on the basis of the bending constants and the spontaneous curvature of the bilayers; these parameters are also determined by the constitution of the surfactant molecules.

2 THE RHEOLOGICAL BEHAVIOUR OF AQUEOUS SURFACTANT SOLUTIONS

The rheological behaviour of aqueous surfactant solutions is directly related to the aggregation and phase

behaviour of these systems. Solutions below the CMC contain only monomeric surfactant molecules that have dimensions in the range of several angstroms, and to a first approximation do not influence the rheological behaviour. Consequently their rheological properties are the same as those of the pure solvent water, i.e. the solutions are Newtonian liquids with the low viscosity of water of around 1 mPa s at room temperature.

On the other hand, the micellar aggregates have similar shapes and sizes to dissolved polymer molecules; thus, they should also show a similar rheological behaviour which can deviate from that of Newtonian liquids to a large extent. Depending on the size and shape of the micelles, and on their interactions, the viscosity of micellar solutions can depend on the shear rate and also on the time during which a shear gradient is applied to the solutions. Furthermore, viscoelastic solutions, either without and also with a yield stress value, can occur in micellar solutions as has been observed in solutions of macromolecules. In comparison to polymer solutions, the rheology of surfactant solutions can be even more complex. This comes from the dynamic behaviour of micelles; in contrast to macromolecules, their size and also their concentration is steadily fluctuating due to the exchange of monomers between the aggregates and the solution.

2.1 Non-interacting micelles

The rheological behaviour of surfactant solutions with non-interacting micelles (4) is not particularly complex. Such micelles are, in most cases, spherical aggregates at concentrations not too far beyond the CMC, although small rod-like micelles at low concentrations may also fulfil the condition of negligible interaction. Preferentially, those aggregates are formed by surfactants with the corresponding packing parameter, i.e. surfactants with large head-groups. Such solutions are Newtonian liquids like the pure solvent, although the viscosity is higher than the solvent viscosity and increases linearly with increasing surfactant concentration. For non-interacting spheres, the Einstein equation has been derived, as follows:

$$\eta/\eta_s = 1 + 2.5\Phi \quad (10.1)$$

where η and η_s are the viscosities of the solution and the solvent, respectively, and Φ is the volume fraction of the micelles. For the calculation of Φ , it must be taken into account that the micelles are strongly solvated and therefore their effective volume is larger than the

product of the volume of a surfactant monomer and the aggregation number n . Qualitatively, the increase of the viscosity can be understood by regarding the micelles as hard spheres which are one to two orders of magnitude larger than the solvent molecules; these particles "feel" different flow velocities in a shear gradient which leads to additional friction in the solution.

At higher aggregate concentrations, hydrodynamic interactions between the spherical micelles must also be taken into account, which leads to an additive term of $k\Phi^2$ in equation (10.1). For ionic surfactants, electroviscous effects can also play a role, which can be corrected by further terms in the equation; this will not be discussed here in any detail.

The situation for non-interacting anisometric aggregates is more complicated, because such particles can rotate in a shear gradient and their effective volume fraction is therefore much larger than the volume of the micelles, even if their hydration shell is taken into account. Such solutions are also Newtonian liquids, although their viscosities are higher than the viscosities of spheres with the same concentrations. For such systems, the Simha equation has been derived, as follows:

$$\{\eta\} = (0.933/d) + (p^2/5d)[(1/(3 \ln(2p) - \lambda))] + [1/(\ln(2p) - \lambda + 1)] \quad (10.2)$$

where $\{\eta\} = \lim_{c \rightarrow 0}(\eta - \eta_s)/(\eta_s c)$ is called the *intrinsic viscosity*, d is the density of the solution in g/ml, λ is a constant (equal to 1.8 for rods) and p is the anisotropy ratio, i.e. the ratio of the long axis and the short axis of the aggregates.

Equation (10.1) shows that the viscosity of surfactant solutions starts to increase linearly with the concentration above the CMC. This allows in principle for a determination of the CMC by means of viscosity measurements, provided that a sufficiently precise determination of the viscosity is being carried out (since the increase of viscosity is modest even for rather high volume fractions of 0.1).

Equation (10.2) shows that the slope of the plot of the viscosity as a function of the concentration becomes larger at the transition concentration above which rods are formed. Furthermore, there is no longer a linear relationship between the viscosity and the surfactant concentration. Hence, the transition concentration can also be determined with exact viscosity measurements. From the intrinsic viscosity, the anisotropy ratio of the aggregates can be determined, and as the short axis of anisometric aggregates is given by twice the length of a monomeric surfactant molecule, from this

value the length of the rods can also be calculated. However, it must be pointed out that it is necessary to prove *unambiguously* the Newtonian behaviour of the solutions, i.e. the independence of the viscosity on the shear rate, for the validity of equations (10.1) or (10.2), respectively.

2.2 Viscoelastic surfactant solutions with entangled rod-like micelles

Many surfactant solutions are known which contain spherical micelles up to high surfactant concentrations and behave as Newtonian liquids with a low viscosity. This is especially the case for ternary systems of surfactant, hydrocarbon and water where the spheres are stabilized by the solubilization of the non-polar hydrocarbon.

On the other hand, there are also numerous surfactant solutions with rod-like micelles, the viscosity of which starts to grow rapidly at low concentrations in the range of 1 wt% and reaches values up to six orders of magnitude higher than the water viscosity. This can be explained by the presence of entangled rod-like micelles which arrange themselves in a supermolecular network (5–8). Such solutions have frequently elastic properties, but they do not show a yield stress. It is also important to point out that these systems show the typical features of entropy elasticity, i.e. their elasticity modulus is independent of the strain up to 100% and breaks down at higher strain values.

The entanglements behave therefore like a transient network with a zero shear viscosity η_0 which is given by the product of a shear modulus G_0 and a structural relaxation time τ according to the following:

$$\eta_0 = G_0 \tau \quad (10.3)$$

The shear modulus is determined by the number density ν of the entanglements:

$$G_0 = \nu kT \quad (10.4)$$

while the structural relaxation time can depend on many parameters, such as the surfactant concentration, temperature, ionic strength, concentration of counterions or of other additives. If shear stress is applied to such a solution, it can relax not only by breaking the temporary network points, but also by the dynamic behaviour of the rod-like micelles which is characterized by a steady decomposition and re-formation of the rods. According to equation (10.3), a complex behaviour of the zero shear viscosity for such solutions can be observed: G_0

is expected to increase as a power law of the surfactant concentration and to be independent of other parameters which do not affect the number density of the micelles, while τ depends in a complicated manner on various parameters which are listed below.

An example is shown in Figure 10.1 where η_0 for the cationic surfactant cetylpyridinium chloride (CPyCl) is plotted against the concentration of added sodium salicylate (NaSal). This figure shows that the viscosity of this system can vary by four orders of magnitude and shows two maxima separated by a minimum with growing NaSal concentration. This behaviour can be ascribed unambiguously to τ which shows the same dependence on the NaSal concentration, while G_0 depends only on the CPyCl and is constant with changing NaSal concentration. Similar results have been observed for many systems by various research groups.

Talmon and co-workers have succeeded in directly visualizing the networks of entangled thread-like micelles by cryo-transmission electron microscopy (TEM). These pictures clearly show the shape and the persistence length of the rods, but cannot reveal their dynamic properties. In this connection, it is noteworthy that entanglements are not the only cross-links of a network that cause viscoelastic properties. In addition, adhesive contacts between micelles or transient branching points such as many-armed disc-like micelles can act as cross-links, as has recently been shown by experimental evidence. The entangled thread-like micelles have typical persistence lengths in the range between several hundred to several thousand angstroms, and they may or may not be fused together at the entanglement points.

Cylindrical micelles steadily undergo translational and rotational diffusion processes, and furthermore they

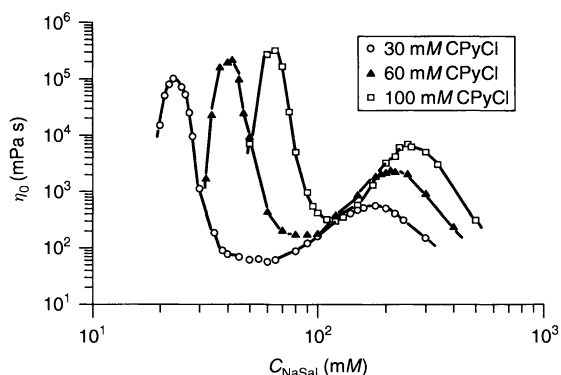


Figure 10.1. Double logarithmic plots of the zero shear viscosity η_0 for three different CPyCl concentrations against the concentration of added NaSal at 25°C

break and re-form due to their dynamics. An applied stress can therefore relax by both processes, but this relaxation needs some time. This allows for a qualitative understanding of the rheological behaviour of such systems. The possibility of stress relaxation also explains why highly viscous solutions with entangled rods do not show a yield stress. A strain with a duration shorter than the relaxation time in such solutions leads therefore to an elastic response according to a Hookean solid, as follows:

$$p_{21} = G_0 \gamma \quad (10.5)$$

where p_{21} is the stress, G_0 the spring constant and γ the strain. On the other hand, if the duration of the stress is larger than the relaxation time, the system can flow like a Newtonian liquid, giving the following:

$$p_{21} = \eta_0 \dot{\gamma} \quad (10.6)$$

with the zero shear viscosity η_0 and the shear rate $\dot{\gamma}$. Such a viscoelastic liquid can often be described by the so-called Maxwell model, consisting of a spring with the constant G_0 in series with a dashpot with the viscosity η_0 ; the viscosity is given by the product of G_0 and τ according to the equation (10.3).

These quantities can be determined by dynamic rheological measurements which yield the complex viscosity $|\eta^*|$, the storage modulus G' and the loss modulus G'' for the studied solution as a function of the oscillation frequency f . Many surfactant solutions have turned out to behave like a Maxwell element with one single shear modulus G_0 and one single structural relaxation time τ . An example of this is shown in Figure 10.2. The typical features of such solutions can be seen in this figure which presents a double

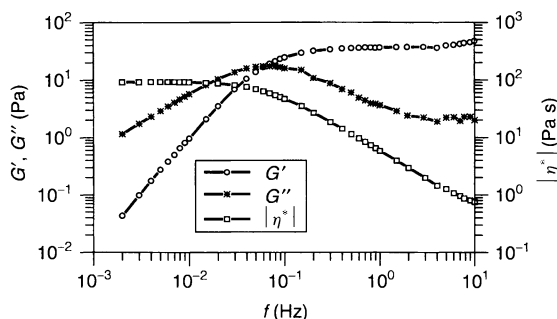


Figure 10.2. Double logarithmic plots of the storage modulus G' , loss modulus G'' and complex viscosity $|\eta^*|$ against the frequency f for a solution with 100 mM CPyCl and 60 mM NaSal at 25°C. The solution behaves like a Maxwell fluid with a single shear modulus G_0 and a single structural relaxation time τ

logarithmic plot of $|\eta^*|$, G' and G'' versus f . It can be seen that G' increases linearly with a slope of 2 and reaches a constant value G_0 at a certain frequency; G'' first increases linearly with a slope of 1, reaches a maximum, decreases to a minimum and then increases again. The frequency at the intersection point of G' and G'' is equal to the reciprocal structural relaxation time τ . The complex viscosity $|\eta^*|$ is independent of f at low frequencies and equal to η_0 , and it decreases linearly at higher frequencies with a slope of -1 . The figure shows clearly the described properties of viscoelastic surfactant solutions: there is no yield stress value, but $|\eta^*|$ approaches η_0^* at low frequencies. At the latter frequencies (which correspond to a long duration of stress – the duration time is equal to the reciprocal frequency), we find that $G'' > G'$. Here the solution behaves like a viscous liquid, while at higher frequencies and a corresponding short duration of stress, $G' > G''$ and the system behaves like an elastic solid.

However, not all viscoelastic surfactant solutions can be described by the simple Maxwell model, but may show a completely different behaviour, as shown as an example in Figure 10.3. This system also does not have a yield stress value, but no frequency-independent plateau value of G' is reached at higher frequencies. Thus, η_0 cannot be expressed as the product of one G_0 and one τ value. In such a situation, an applied stress relaxes after a rapid deformation, according to a stretched exponential function with time t , as follows:

$$p_{21} = (p_{21})_0 \exp(-t/\tau)^\alpha \quad (10.7)$$

It can be seen from Figure 10.3 that G'' increases again with f after a minimum is reached. This increase can be related to the *Rouse modes* of the cylindrical micelles, analogous to a polymer chain. The minimum value of G'' can be expressed as the product of G' and the ratio of the entanglement length l_e and the contour length l_c of the cylindrical micelles, according to the following:

$$G''_{\min} = G'(l_e/l_c) \quad (10.8)$$

From Figure 10.2, it can be seen that G' increases again at the highest available frequencies (around 10 Hz). It could be concluded that there is a rise of G' at higher frequencies which could lead to a second plateau value of G' . However, this observation is not necessarily realistic, because the oscillatory measurements can be strongly affected by the inertial forces of the used cone-plate measuring system at the high frequencies. However, studies with a high-frequency rheometer, which allows oscillatory measurements up to the kHz range, showed for a solution of tetraethylammoniumperfluorooctane sulfonate (TAFOS) that both G' and G''

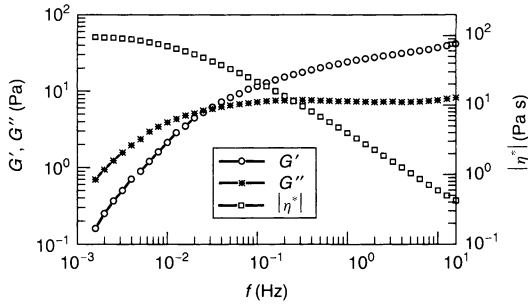


Figure 10.3. The same plots as those shown in Figure 10.2 for a solution with 80 mM tetradecyldimethylaminoxide (C_{14} DMAO), 20 mM sodium dodecyl sulfate (SDS) and 55 mM hexanol (C_6OH). In this case, the solution does not behave like a Maxwell fluid. Note the following differences to Figure 10.2: G'' does not pass over a maximum, while G' does not show a plateau value, but increases with f after the intersection with G'' , with a constant slope of 0.25

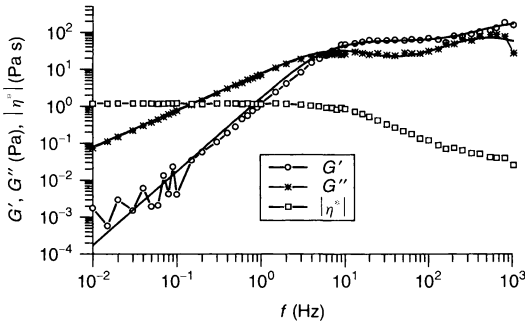


Figure 10.4. Dynamic rheograms of a 90 mM solution of $C_8F_{17}SO_3N(C_2H_5)_4$ at $T = 20^\circ C$. Below 10 Hz, the measurements were performed with a Bohlin CS 10 rheometer, while above 10 Hz an HF rheometer (with 1% deformation) was used

increase again at frequencies beyond 10 Hz, as shown in Figure 10.4.

This figure shows that at low frequencies the system can be described by the normal Maxwell model with a rise in G' with a slope 2 and in G'' with a slope 1. However, the second increases of G' and G'' do not fit into the Maxwell model. Although the second plateau value of G' is not reached at the available frequencies, it was possible to fit the data with a Burger model, which consists of two Maxwell elements with different shear moduli and structural relaxation times, as follows:

$$G'(\omega) = G_1 \omega^2 \tau_1^2 / (1 + \omega^2 \tau_1^2) + G_2 \omega^2 \tau_2^2 / (1 + \omega^2 \tau_2^2) \quad (10.9)$$

$$G''(\omega) = G_1 \omega \tau_1 / (1 + \omega^2 \tau_1^2) + G_2 \omega \tau_2 / (1 + \omega^2 \tau_2^2) \quad (10.10)$$

It is noteworthy here that the two relaxation times τ_1 and τ_2 correspond well with the two longest time constants, which can be measured by dynamic electric birefringence measurements. From Figure 10.4 it can be seen that the minimum of G'' is about a factor of 2.5 lower than the plateau value of G' ; this means, according to the theory of Granek and Cates (equation (10.8)) that the ratio of l_c and l_e is also 2.5. This value is found for each concentration, and thus it can be concluded that the mean length of the micelles decreases with increasing surfactant concentration.

This increase of G' and G'' at high frequencies can be understood on the basis of two interpretations. First, the cylindrical micelles have a broad equilibrium distribution of their lengths; hence, besides the long thread-like micelles which form the entangled network, shorter rods are also present which are not entangled. The rheological behaviour of the solution is not influenced at low frequencies by these short rods, but at higher frequencies they can contribute significantly to the moduli. Secondly, if the frequency is higher than the reciprocal Rouse time of a chain segment of the entanglement length, these segments can no longer relax by Rouse diffusion and a glass process starts under such conditions, which causes the increase of the moduli.

2.3 The rheology of various surfactant solutions with rod-like micelles

According to the theory of amphiphilic aggregation, rod-like micelles are normally formed in solutions of ionic surfactants at high ionic strength, with strongly binding or hydrophobic counterions or with large hydrophobic groups like double-chain or perfluoro surfactants. These rod-like micelles and their interactions determine the rheology of the samples. As already pointed out, solutions at low concentrations containing non-interacting rods are Newtonian liquids with low viscosities. At a characteristic concentration, c^* , at which the rotational volumes of the rods start to overlap, the viscosity starts to increase drastically with further increasing concentration. This is shown in Figure 10.5 for different surfactant solutions as double logarithmic plots of the zero shear viscosity η_0 against the concentration c .

From this figure it can be seen that in spite of the very different surfactants and the different overlap concentrations, the slope of the curves above c^* and below the first maximum of η_0 is almost the same, and equal to 8.5 ± 0.5 . Thus, in this region the increase of the viscosity with the concentration can be expressed by

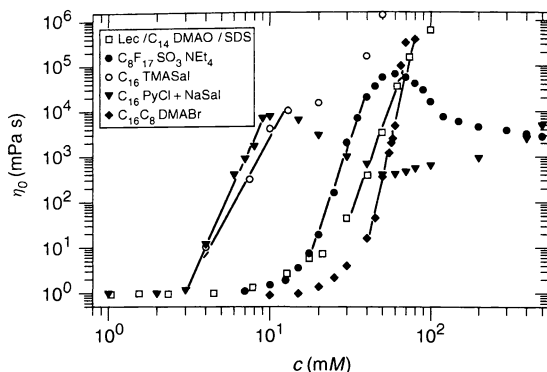


Figure 10.5. Double logarithmic plots of the zero shear viscosity η_0 against the concentration c for several solutions of different ionic surfactants. Note that all the systems show the same power law exponent within a certain concentration range above c^*

the following scaling law:

$$\eta_0 \sim (c/c^*)^x \quad (10.11)$$

with an exponent $x = 8.5 \pm 0.5$. This exponent must therefore be controlled by the electrostatic interactions in the solutions. This value is much larger than the exponent of 4.5 ± 0.5 which has been found for solutions of large polymer molecules. As macromolecules do not change their size with increasing concentration, it can be concluded that the large exponent for the surfactant solutions is due to a further growth of the length of the rods with concentration above c^* .

The exponent x was found to depend strongly on the charge of the rod-like micelles. This is demonstrated in Figure 10.6 for the system CPyCl + NaSal with different ratios of CPyCl to NaSal. The viscosity behaviour of this system at a constant CPyCl concentration as a function of the NaSal concentration has already been shown above in Figure 10.1. It has been mentioned already that the rheological behaviour of these samples can be described by a Maxwell element and that the complex behaviour is due to the structural relaxation time which is determined by the dynamics of the rod-like micelles, while G_0 increases steadily with concentration. Furthermore, it has been shown by cryo-TEM that in all concentration regions of the system entangled thread-like micelles with the same structures are present. In spite of this, Figure 10.6 shows clearly the different exponents x in the different concentration regions. At the first maximum, where the micelles are highly and positively charged, an exponent of 8, as for the other charged systems shown in Figure 10.5 is found. At the

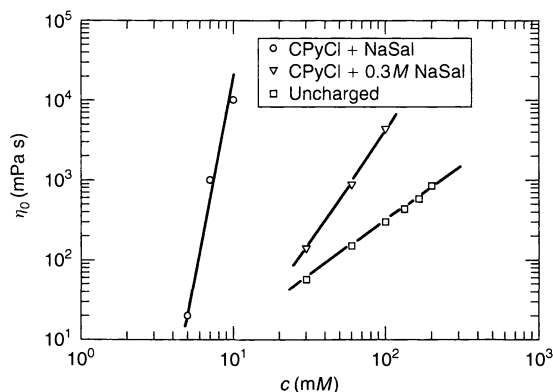


Figure 10.6. Double logarithmic plots of the zero shear viscosity η_0 against the concentration c of the CPyCl + NaSal system for solutions at the first maximum (o), the second maximum (V) and the minimum (□) viscosities, measured at 25°C (see Figure 10.1)

first viscosity minimum, the rod-like micelles are completely uncharged and the exponent is 1.3, while at the second viscosity maximum the micelles carry a negative charge and the exponent has a value of 2.5.

In addition, the zwitterionic alkyldimethylaminoxide surfactants (C_x DMAO) that are known to form rod-like micelles already at low concentrations, show a linear behaviour of $\log \eta_0 \sim \log c$ in an extended concentration region, as can be seen in Figure 10.7. Some curves show a break, which indicates that at different concentrations a different relaxation mechanism for an applied stress operates. At the lowest concentrations above c^* , the slope is the highest, being close to 4.5, as observed for polymers. This result is somewhat surprising because

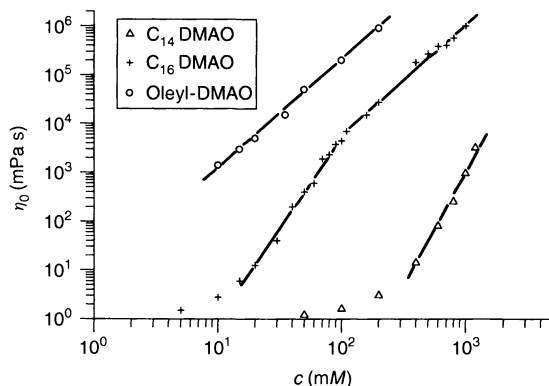


Figure 10.7. Double logarithmic plots of the zero shear viscosity η_0 against the concentration c for solutions of alkyldimethylaminoxide surfactants with various chain lengths at 25°C

it could be expected that the rod-like micelles of the zwitterionic surfactants also increase in length, which should lead to a higher exponent, as has been found for the systems shown in Figure 10.5. Thus, it can be concluded that the rheology of zwitterionic surfactant solutions is also influenced by the dynamics of the rod-like aggregates, as in the case of CPyCl + NaSal.

For higher C_{14} DMAO concentrations, a lower exponent is observed. This can be understood by the assumption that under these conditions the structural relaxation time τ is determined by the lifetime of the rod-like micelles which becomes shorter than the rotational diffusion coefficient. The shear moduli G_0 , on the other hand, always increase with the same exponent in the different concentration regions. Figure 10.7 shows furthermore that the absolute values of η_0 for oleyl-DMAO are one order of magnitude higher than for C_{16} DMAO with the same concentrations, although the slope of the curves is the same. This can also be explained by the dynamics of the rod-like aggregates which depends strongly on the length of the hydrophobic chain and becomes slower with increasing chain length.

According to the theory of amphiphilic aggregation, the addition of cosurfactants with extremely small head-groups to micellar solutions leads to a transition of the spherical micelles to rods and/or to a growth of rod-like micelles. Hence, the viscosity of such systems also has to grow; this is shown in Figure 10.8 for the example of a solution of 100 mM C_{14} DMAO with various cosurfactants. The viscosity as a function of the concentration of the cosurfactant shows similar features to that illustrated in Figure 10.1; the viscosity increases with increasing cosurfactant concentration, passes over

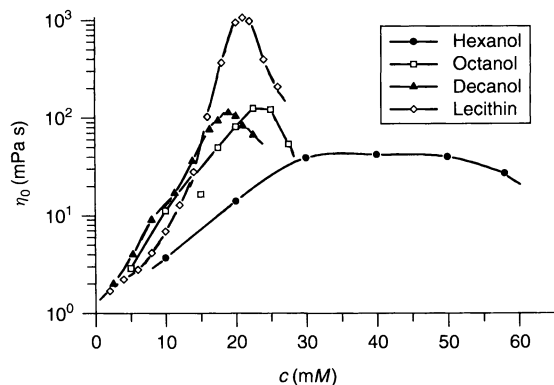


Figure 10.8. Semi-logarithmic plots of the zero shear viscosity η_0 of a 100 mM solution of C_{14} DMAO against the concentration c of added cosurfactants at 25°C. Note that all the curves pass over a maximum

a maximum and then decreases again. It is very likely that the length of the micelles increases steadily with the cosurfactant concentration; the curves can therefore be again understood by the assumption of a kinetically controlled structural relaxation time on the right-hand side of the maximum. This situation becomes obvious in Figure 10.9, which shows a double logarithmic plot of η_0 against the surfactant concentration for C_{14} DMAO with different amounts of decanol which are completely solubilized in the micelles due to its poor water solubility. The slope of the different mixtures on the left-hand side of the viscosity maximum is the same, except for the mixture with the highest content of decanol, which has the low slope of 1.3. Systems with such a low slope, which is also found for CPySal + NaSal at the viscosity minimum (Figure 10.6), are shown in Figure 10.10; this

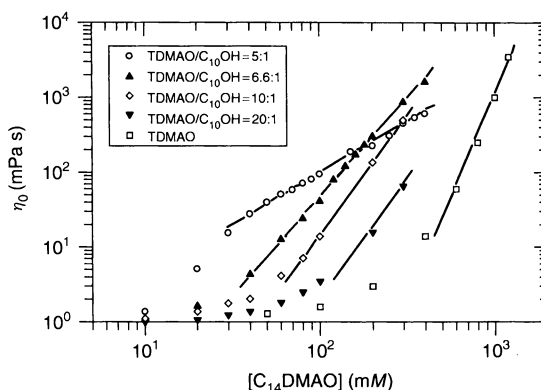


Figure 10.9. Double logarithmic plots of the zero shear viscosity η_0 of a mixture of C_{14} DMAO and C_{10} OH, with different molar ratios of cosurfactant/surfactant, against the concentration of C_{14} DMAO at 25°C

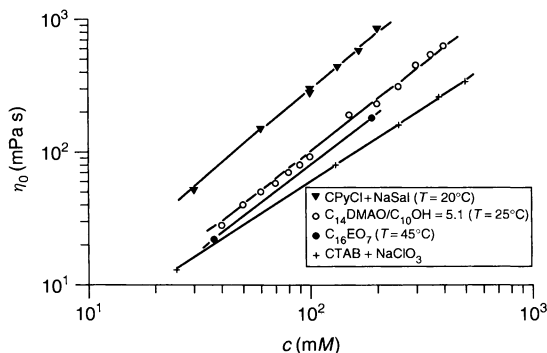


Figure 10.10. Double logarithmic plots of the zero shear viscosity η_0 against the total surfactant concentration for several surfactants systems with the same power law exponent

figure shows that the constitution and also the viscosity of the different surfactants are completely different, although the slope has still the same low value of 1.3. The shear moduli for all these different systems are very similar for the same surfactant concentration, and they also scale, with the same exponent, with the concentration. Thus, the low exponent of 1.3 comes about by the structural relaxation time which scales with an exponent of -1 according to the following:

$$\tau \sim (c/c^*)^{-1} \quad (10.12)$$

2.4 Mechanisms for the rheological behaviour of rod-like micelles

All surfactant systems containing interacting rod-like micelles show qualitatively a similar rheological behaviour (9). The viscosity increases sharply at the concentration c^* at which the rotational volumes of the rods start to overlap and a transient network is formed. This network can be an entanglement network, the micelles can also be fused together or they can hold together by adhesive contacts. It is conceivable that all of these types of networks can exist in surfactant solutions, and theoretical models have been derived for all of these situations.

In these theories the rod-like micelles are regarded as being thread-like and flexible. This is certainly the case for several systems, but not for all. For example, the solutions of C_{16} DMAO and oleyl-DMAO have very low c^* values, and if the rods are to be flexible, they would have to be coiled below c^* . However, both electric birefringence and dynamic light scattering measurements show that at around c^* the lengths of the rods are comparable with their mean distances. Thus, the rods must be stiff with persistence lengths of several thousand angstroms; this has also been confirmed by cryo-TEM studies. The abrupt increase of η_0 at c^* is therefore difficult to understand for stiff rods, even with the assumption of a further growth of the rods with increasing concentration beyond c^* . Furthermore, for many systems with rod-like micelles the rotational time constant for the rods is very little affected around c^* and the solutions do not become viscoelastic above c^* . Therefore, we have to assume that interactions other than hard-core repulsion between the overlapping rods must exist, which are responsible for the formation of the network at c^* . This could come about by adhesive bonds between the rods or by the formation of a connected network of fused rods, as has been proposed by Cates (9). In such situations, two different types of

networks have to be distinguished, namely saturated and interpenetrating networks. In the first case, the mean distance between the knots or entanglement points is equal to the mesh size, while in the second case this distance can be much larger than the mesh size between neighbouring rods.

The viscosities above c^* increase abruptly according to the power law of equation (10.11) with an exponent of $x > 3.5$, while the exponent of the power law for the shear modulus G_0 is always about 2.3. For the explanation of this behaviour it was assumed that the structural relaxation times are affected both by reptation of the rods and by bond-breaking processes. Cates distinguished three different kinetic mechanisms (9). The first mechanism assumes the breaking of a rod with the formation of two new end-caps and the recombination of two rods by collision at the ends and fusion into a new rod. In the second mechanism, the end-cap of one rod collides with a second rod and via a three-armed transition state a new rod and a new end-cap is formed. In the third mechanism, two rods collide and form two new rods through a four-armed transition state. Of course, an applied stress can relax by all three mechanisms. These mechanisms lead to somewhat different power laws for the kinetic time constant τ according to the following:

$$\tau \sim (c/c^*)^x \quad (10.13)$$

However, in all cases x comes out to be between 1 and 2. The third mechanism is probably less likely in systems with low c^* values and stiff rods. From this argument, it is likely that the second or the third mechanism is effective in the more concentrated region of the pure C_x DMAO solutions.

From Figure 10.7 it can be seen that for solutions of C_{16} DMAO the slope of the $\log(\eta_0) - \log(c)$ plots suddenly changes at a characteristic concentration c^{**} . In addition, in this case the same scaling law for G_0 with an exponent of ca. 2.3 is found over the whole concentration region, while the power exponent for the relaxation times changes from 1 to zero at c^{**} . From the constant exponent for G_0 it can be concluded that the micellar structures do not change at c^{**} . The change of the slope must therefore be due to a new mechanism which becomes effective above c^{**} . The independence of τ on the concentration makes it likely that in this region the dynamics is governed by a purely kinetically controlled mechanism and a reptation process is no longer effective. This situation has not yet been treated theoretically. Cates mentioned, however, that there might be situations where the reptation loses its importance (9). The more effective

mechanism in this range could be the bond-interchange mechanism.

For the C_{14} DMAO solutions with C_{10} OH and for the CPyCl + NaSal system at the viscosity minimum, the extremely low power law exponent of 1.3 for the viscosity and the exponent of -1 for the structural relaxation times are found. A detailed theoretical explanation for this behaviour, which has also been observed by other authors, has not been given yet. It could be due to a very high flexibility of the cylindrical micelles in systems with such low exponents. In this case, the persistence length would be much shorter than the contour length between two neighbouring entanglement points and be independent of the concentration. The diffusion of the rods can therefore take place with a constant diffusion coefficient D . For the collision of two arms of the network they have to diffuse a distance x which is equal to the mesh size. Two neighbouring rods, which undergo a bond exchange process, have to diffuse at least over the average distance x between two arms. The time constant τ_D for this diffusion should be proportional to x^2/D , and, since the mesh size x decreases with the square root of the concentration, one obtains for the structural relaxation time τ the observed law $\tau \sim 1/Dc$, which is identical with equation (10.12).

Therefore, it can be concluded that for systems with the low exponent of 1.3 the viscosity is controlled by a diffusion-controlled bond-interchange mechanism. The absolute values of η_0 and τ can still vary for different surfactants because the persistence length l_p of the rods should depend on the particular conditions of the systems. With increasing chain length of the hydrophobic group, l_p should increase and D should decrease. For such situations, the highest activation energies for the viscosity are expected.

A similar mechanism can be concluded for the assumption of a network of connected or fused thread-like micelles. The cross-links between these micelles can be regarded as disc-like micelles from which the rods extend. In this case, the transient intermediate species in the various bond interchange mechanisms are assumed to be stable. In this situation, all the end-caps could be connected and the resulting network could be in the saturated or unsaturated state. The cross-link points could then slide along the thread-like micelles, and this process represents a one-dimensional diffusion with a concentration-independent diffusion coefficient. A knot can disappear, if two network points meet on their random diffusion paths. If the structural relaxation time is determined by this random movement, a similar equation, i.e. $\tau \sim 1/c$, can be derived.

Both models can thus explain the low exponent of 1.3 for the scaling law for η_0 , and for both cases reptation is no longer necessary for the relaxation of stress. The mechanisms could probably be distinguished by the concentration dependence on the self-diffusion coefficients D_s of the surfactant molecules. In a solution with a connected network, a surfactant molecule should be in the same situation as in a bicontinuous L_3 phase, where D_s is independent of the surfactant concentration. However, Kato and co-workers have shown that the D_s values increase with concentration for a solution with rod-like micelles; thus, a diffusion-limited bond-interchange mechanism is more likely for the explanation of the scaling law of the structural relaxation time than the assumption of connected networks consisting of thread-like micelles.

3 THE RHEOLOGY OF BILAYER PHASES

As has been pointed out already, surfactant systems with a packing parameter between 2 and 1 can form lamellar phases already at low surfactant concentrations of around 1 wt%. These lamellar phases can consist of flat surfactant bilayers, of uni- or multilamellar vesicles or of flexible bicontinuous bilayers with the structures of branched tubes (L_3 or sponge phases). The formation of the various lamellar structures is determined by the natural curvature and the flexibility of the bilayers which can be expressed quantitatively by the bending modulus and the Gaussian modulus (5, 10). The different phases are thermodynamically stable and they are also separated from each other by corresponding two-phase regions. They can occur in various surfactant systems depending on their composition; for example, in ternary systems of zwitterionic or nonionic surfactants, cosurfactants and water the phase sequence is, vesicle phase–lamellar phase with flat bilayers– L_3 phase, with increasing cosurfactant concentration. With ionic surfactants, the phase behaviour is usually simpler. In particular, the L_3 phases disappear already if the bilayers are weakly charged by the addition of ionic surfactants, and often only vesicles are found in such systems. Increasing ionic strength, on the other hand, stabilizes L_3 phases and classical lamellar phases.

3.1 The rheological behaviour of various bilayer phases

The rheological behaviour of the lamellar phases is again determined by the structure and the dynamic properties

of the lamellar bilayers in the corresponding phase. L_3 phases, for example, are always Newtonian liquids with low viscosity values; this is due to the high flexibility and the rapid dynamics of the bilayers in these phases which do not develop large resistance against the flow of the systems. The same is true for lamellar phases with flat bilayers which are formed at low surfactant concentrations, because the bilayers can slide parallel to each other without much hindrance. It must be mentioned, however, that lamellar phases which are formed at high surfactant concentrations beyond 50 wt% can have a more complicated rheological behaviour which is due to the close packing of the bilayers and the resulting stronger interactions between them. In addition, vesicle phases can be Newtonian liquids with low viscosities as long as they are dilute and the vesicles do not touch each other. Such systems have been described for cationic double-chain surfactants, cationic surfactants with aromatic counterions or nonionic surfactants with cosurfactants.

On the other hand, it has been shown by electron microscopy that many vesicle phases, especially in systems with higher concentrations, contain large polydisperse multilamellar vesicles which are densely packed. In addition, the wedges that result from the dense packing are completely filled with smaller vesicles. It can be expected from this structure that the phase cannot flow without a large resistance, because each vesicle is sitting in a fixed position and the vesicles cannot pass each other without deformation of the vesicle shells. Thus, such systems must have viscoelastic properties.

Visual observation of the samples already confirms the viscoelastic properties of such vesicle phases which look like the viscoelastic solutions of rod-like micelles on the first look. However, upon a longer observation for several days, a fundamental difference between the two types of viscoelastic solutions can be recognized. On shaking of the samples, air bubbles are entrapped in the solutions and do not rise within short times. However, in the solutions containing rod-like micelles the bubbles rise slowly even if the viscosity is five to six orders of magnitude higher than the water viscosity, while in the solutions with multilamellar vesicles, which can often flow under the influence of the gravitation field, the bubbles do not rise, even after many months. From this behaviour, it can be concluded that the vesicle phases behave like Bingham solids, i.e. they possess a yield stress contrary to the viscoelastic solutions with rod-like micelles.

Dynamic rheological measurements confirm this behaviour, as can be seen from the example presented in Figure 10.11. In these systems, G' and G'' are

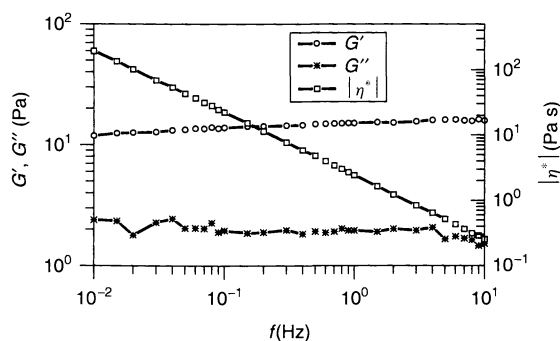


Figure 10.11. Double logarithmic plots of the storage modulus G' , the loss modulus G'' and the complex viscosity $|\eta^*|$ against the frequency f for a vesicle phase of 90 mM C_{14} DMAO, 10 mM C_{14} TMABr, 220 mM C_6 OH and water at 25°C

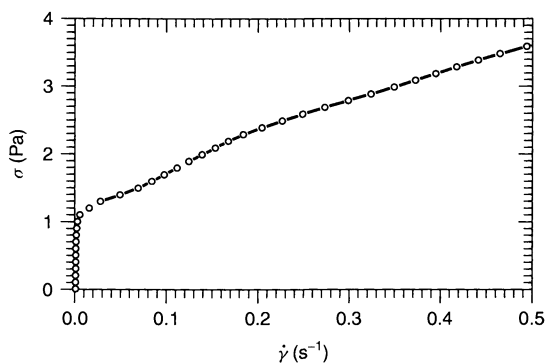


Figure 10.12. Plot of the applied shear stress σ against the shear rate $\dot{\gamma}$ for the same vesicle phase as that shown in Figure 10.11

independent of the frequency and G' is one to two orders of magnitude higher than G'' ; furthermore, $|\eta^*|$ does not reach a constant value at low frequencies, but approaches infinity with decreasing frequency. The yield stress value of the systems can be determined directly by measuring the shear rate $\dot{\gamma}$ as a function of the applied stress. As shown in Figure 10.12, the system behaves like a solid as far as the stress does not exceed the yield stress value of the sample, while for higher stresses it flows like a liquid. From these experiments, a further difference to viscoelastic samples with thread-like micelles can be derived. The vesicle phases show the typical features of energy elasticity, i.e. the storage modulus remains constant only up to deformations of 10% and then break down with higher strain, while the systems with rod-like micelles can bear deformations up to 100% before G' breaks down.

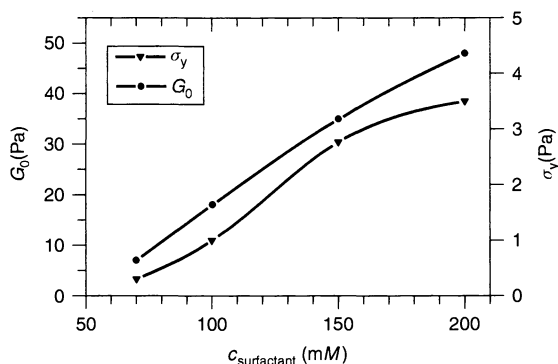


Figure 10.13. Plots of the shear modulus G_0 and yield stress σ_y against the total surfactant concentration for a vesicle phase of C_{14} DMAO and C_{14} TMABr (with a molar ratio of 9:1) and C_6 OH at 25°C

Figures 10.13–10.18 present the rheological behaviour of viscoelastic vesicle phases. Both the shear moduli G_0 and the yield stress values σ_y increase with increasing total surfactant concentration that is seen in Figure 10.13. Below concentration of 1 wt%, both quantities drop to zero, what means that the vesicles are no longer densely packed under these conditions and thus are not restricted to a fixed position. Above 1 wt%, both quantities increase almost linearly with the concentration and G_0 is about one order of magnitude higher than σ_y . This confirms that the vesicles must be deformed by about 10% until they can pass each other and the solutions start to flow like liquids.

Figure 10.14 demonstrates the influence of the charge density of the bilayers on G_0 . The modulus increases

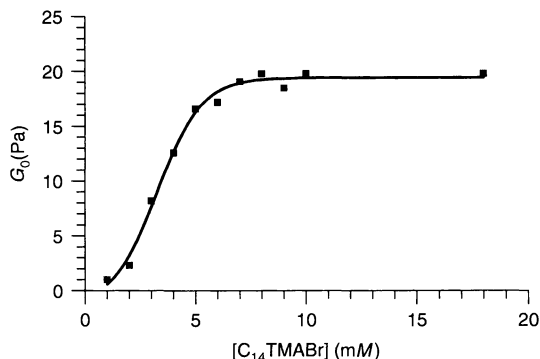


Figure 10.14. Plot of the shear modulus G_0 against the concentration of the ionic surfactant C_{14} TMABr for a vesicle phase with a total concentration of 100 mM (C_{14} DMAO + C_{14} TMABr) and 220 mM C_6 OH at 25°C

with increasing charge density, which was achieved by the addition of an ionic surfactant to the sample, and saturates at about 10% of the ionic surfactant. On the other hand, G_0 decreases linearly with the square root of the ionic strength, as can be seen from Figure 10.15.

Figure 10.16 shows the influence of the chain length of the surfactant; G_0 increases steadily with increasing length of the hydrophobic chain from C_{10} to C_{16} , and for C_{18} the modulus seems to decrease again. From this behaviour, it can be concluded that the moduli are not only determined by the electrostatic interactions between the bilayers, but they depend also on their thickness.

The hydrophilic head-group, however, has only a modest influence on the rheological properties of vesicle phases. For example, a vesicle phase of 90 mM of the nonionic surfactant C_{12} E₆, 10 mM sodium dodecyl

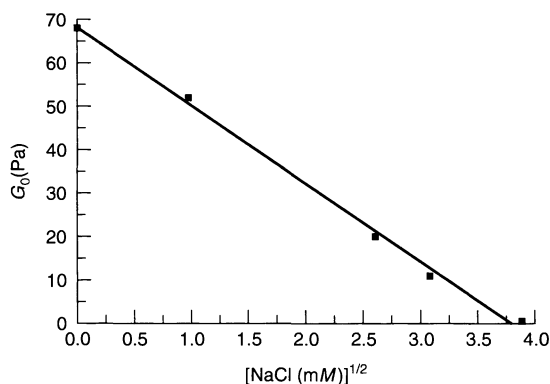


Figure 10.15. Plot of the shear modulus G_0 at 0.1 H_2 against the square root of the concentration of added NaCl for a vesicle phase with 85 mM C_{14} DMAO, 15 mM C_{14} TMABr and 300 mM C_6 OH at 25°C

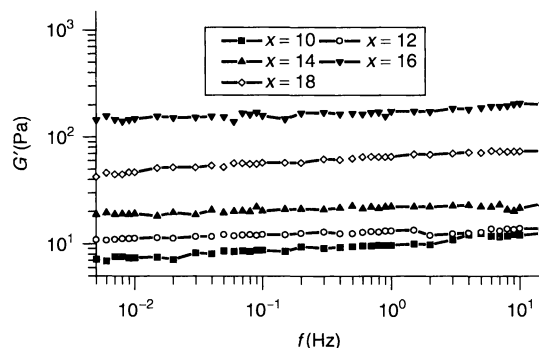


Figure 10.16. Double logarithmic plots of the storage modulus G' against the frequency f for vesicle phases of 90 mM C_{14} DMAO, 10 mM C_{14} TMABr and 220 mM C_6 OH at 25°C for various chain lengths x of the zwitterionic surfactant

sulfate (SDS) and 250 mM hexanol (C_6OH) shows a similar concentration dependence as the vesicle phase of 90 mM $C_{14}DMAO$, 10 mM tetradecyltrimethylammonium bromide ($C_{14}TMABr$) and 220 mM C_6OH ; furthermore, the absolute values of G' , G'' and $|\eta^*|$ are also very similar for both samples. In addition, the concentration and the chain length of the cosurfactant have only a modest influence on the rheological behaviour of the vesicle phases. Figure 10.17 shows, as an example, that G' and σ_y increase slightly with the cosurfactant concentration, while G'' is independent of this parameter, while Figure 10.18 shows the modest increase of G' with the chain length of the cosurfactant; in both cases, the increase is very small in comparison to the strong increase of these quantities with increasing concentration and chain length of the hydrophobic group of the surfactant. In addition, the temperature has only a very small effect on both G_0 and σ_y between 10 and 60°C.

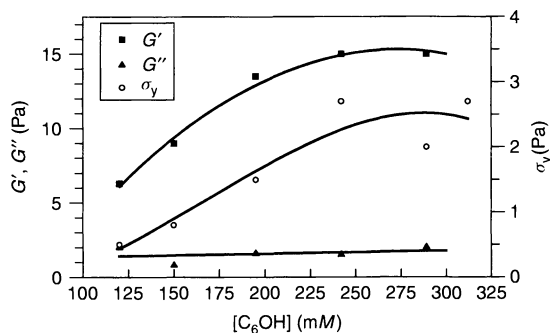


Figure 10.17. Plots of the storage modulus G' , loss modulus G'' and yield stress σ_y against the cosurfactant concentration for a vesicle phase of 90 mM $C_{14}DMAO$, 10 mM SDS and varying amounts of C_6OH at 25°C

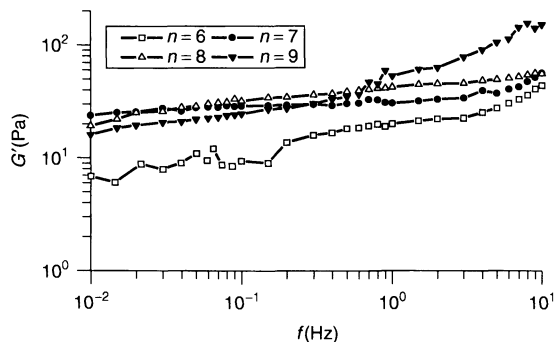


Figure 10.18. Double logarithmic plots of the storage modulus G' against the frequency f for a vesicle phase of 90 mM $C_{14}DMAO$, 10 mM $C_{14}TMABr$ and 160 mM C_nOH for cosurfactants with various chain lengths at 25°C

3.2 Models for the shear moduli of lamellar phases

Based on these experimental results, attempts were made to develop a model which could explain quantitatively all such results and give a good fit of the experimental data for the rheology of vesicle phases. This did not succeed fully until very recently due to the complexity of the problem, because any change of the parameters such as concentration, ionic strength, charge density, chain length, etc. does not only lead to a change of the rheological properties, but also to a change of the sizes and the polydispersity of the vesicles. Until now, three models have been checked for their validity for the interpretation of the rheological results (11, 12).

One model assumes that the shear modulus G_0 of the vesicle phases is determined by the osmotic compression modulus, which is simply given by the osmotic pressure of the sample. This quantity can be calculated from the concentration of ions in the mid-plane of the bilayers, which is obtained by solving the Poisson–Boltzmann equation for these conditions. This model can explain the influence of the charge density at the bilayers and of the ionic strength in the vesicle phase, but the obtained shear moduli are several orders of magnitude higher than the experimental G_0 values. Furthermore, the model cannot explain the influence of the chain length of the hydrophobic groups on G_0 .

The second model regards the vesicles as being hard spheres that are dispersed in the continuous water phase; this is comparable to the situation in microemulsions or cubic phases. As will be pointed out later, the compression modulus of the samples can therefore be calculated from the number density of the vesicles and the structure factor $S(0)$. This model allowed the explanation by Mellema and co-workers (12) of the rheological data of unilamellar and rather monodisperse phospholipid vesicles, but these systems were uncharged and in a dilute state; thus, they did not show any yield stress. It failed for the description of polydisperse and densely packed multilamellar vesicles, and furthermore it could not explain the influence of the charge density and the ionic strength on G_0 . Besides these facts, the hard sphere model also had problems in explaining the increase of G_0 with increasing chain length of the surfactant. One can argue that the moduli increase with an increasing number density of vesicles, and as this quantity is not exactly known for the different vesicle phases, it could be possible, in principal, that the number density of vesicles increases with the chain length. However, this argument cannot be proven experimentally.

Both the similar electric conductivity and the similar

birefringence of various vesicle phases with different chain lengths of the surfactants indicate that the number density does not change significantly with the chain length.

At present, a model of Van der Linden and Dröge (11) for the treatment of multilamellar vesicle phases and L_α phases gives the best agreement with the experimental data. To our knowledge, this model has not yet been applied to any experimental results. It assumes that multilamellar vesicles are deformed in shear flow from a spherical to an elliptical shape. In this deformed state, the energy of the closed shells increases because both their curvature and the interlamellar distance D is changed. Due to the interaction of the bilayers, expressed by the bulk compression modulus B , the inner shells are deformed in such a way that the total deformation energy E of the lamellar droplet is minimized. Assuming that the volume of a droplet is not changed by the deformation, its surface A must consequently increase. It is therefore possible to define an effective surface tension, $\sigma_{\text{eff}} = E/\Delta A$, which can be expressed by the following equation:

$$\sigma_{\text{eff}} = (1/2)(KB)^{1/2} \quad (10.14)$$

where K is the bulk rigidity, which is correlated to the bending constant κ of the bilayers by $K = \kappa/D$. This effective surface tension can be related to the shear modulus G of a vesicle with radius R by using the identity $G = 2\sigma_{\text{eff}}/R$, as follows:

$$G = (KB)^{1/2}/R = [(\kappa/D)B]^{1/2}/R \quad (10.15)$$

Both B and κ depend on the charge density of the bilayers and the ionic strength due to the shielding of the electric charges.

Strictly speaking, the theory results in a calculation of the geometrical average of the compression energy (E_B) and the bending energy (E_κ) per unit volume.

According to equation (10.15), the square of G is given by the following:

$$G^2 = [(\kappa/D)B]/R^2 \quad (10.16)$$

With the number, $n(= R/D)$, of bilayers in a vesicle one obtains the following:

$$G^2 = n\kappa B/R^3 = E_\kappa E_B \quad (10.17)$$

Now it is necessary to find adequate expressions and values for the quantities B and K by employing other theories.

For the electrostatic contribution to the bending constant as a function of the charge density, the following

expression, given by Lekkerkerker, can be used:

$$\kappa = [k_B T(q-1)(q+2)]/[2\pi Qk(q+1)q] \quad (10.18)$$

Here, $q = (p^2 + 1)^{1/2}$, $p = 2\pi Q|\sigma|/ke$, k_B is the Boltzmann constant, T the absolute temperature, Q the Bjerrum length, k the reciprocal Debye length, $|\sigma|$ the surface charge density and e the elementary charge.

For the bulk compression modulus, an expression can be taken that is often used to describe the interaction between two charged particles, as follows:

$$B = f_a f_s n_p k^2 d^2 V(d) \quad (10.19)$$

where $V(d)$ is the energy of interaction between a pair of spherical particles, given as follows:

$$V(d) = (z^2 e^2 / 4\pi \epsilon) [\exp(ka)/(1+ka)]^2 [\exp(-kd)]/d \quad (10.20)$$

Here, d denotes the distance of separation between the particles and a their radii, while f_a and f_s are numerical factors.

There is a further possibility for obtaining an expression for the compression modulus B . This quantity may be simply given by the osmotic pressure between the bilayers. According to a theory of Dubois, one can calculate the osmotic pressure Π from the following equation:

$$\Pi = c_m k_B T \quad (10.21)$$

where c_m is the number concentration of ions at the mid-plane between the bilayers, which can be calculated by resolving the Poisson-Boltzmann equation for the current conditions. In an earlier paper by Dubois, the possibility of identifying the shear modulus directly with the osmotic pressure was discussed. This seemed to be obvious because the osmotic pressure qualitatively increases in the same way with the charge density of the bilayers as the shear modulus, and also decreases on the addition of salt. Nevertheless, this attempt failed since the calculated values (of the order of several thousand pascals) were much too high. In the current context, it looks reasonable, however, to identify the osmotic pressure with the compression modulus B as given in equations (10.14) and (10.15).

Now there is a concept available which is appropriate for reproducing the characteristic features of the experimental results concerning the influence of the charge density and the ionic strength on the shear modulus. The growth of the shear modulus with the charge density can mainly be attributed to the increase of the osmotic pressure with the charge density, while the decrease with the ionic strength seems to come from the pair potential $V(d)$ for small ionic strengths and the linear decrease

at higher ionic strengths from the bending constants. However, we should keep in mind that for both changes the vesicular structures do not remain constant but also change. At present, it is therefore not possible to give a complete quantitative interpretation of the experimental results and fit the data precisely to an exact theoretical model.

In spite of this, attempts should be made to check whether equation (10.15) for the shear modulus gives reasonable results in comparison to the experimental data. For such a calculation, the interlamellar distance of 80 nm, the radius of a vesicle of 0.5 μm , addition of 10% of an ionic surfactant leading to a surface charge density of $e/500 \text{ \AA}^2$, the bending constant $\kappa = 0.56 k_B T$, according to equation (10.18) and the compression modulus $B = \Pi = 3000 \text{ Pa}$, according to equation (10.21), will be used. With these data, equation (10.15) yields $G_0 \approx 18 \text{ Pa}$, and this value is very close to the measured value, which indicates that a correct approach for a theoretical description of the rheological properties of the vesicle phases seems to have been found.

4 THE RHEOLOGY OF CUBIC PHASES

As already mentioned, the radius and the aggregation number of spherical micelles are practically independent of the surfactant concentration, while their number increases linearly with the concentration. At a characteristic concentration above about 40 wt%, the spheres have to be packed regularly with cubic symmetry as a consequence of their mutual hard-sphere repulsion. This leads to a transition into a lyotropic cubic phase (13–15). According to the theory of amphiphilic aggregation, cubic phases are rather rare in binary surfactant/water systems, because in most cases the transition of spheres into rod-like micelles takes place at considerably lower concentrations than the formation of the cubic phase. However, spherical micelles can generally be stabilized by the solubilization of non-polar substrates such as hydrocarbons. Thus, cubic phases are common in ternary surfactant/hydrocarbon/water systems at high surfactant concentrations. In addition, amphiphiles with large hydrophilic groups, such as (polyoxyethylene)–(polyoxypropylene)–(polyoxyethylene) block copolymers $(\text{POE})_x(\text{POP})_y(\text{POE})_x$ with large hydrophilic POE groups are known to form cubic phases in binary systems due to the formation of spherical micelles up to high concentrations.

The cubic phases are generally thermodynamically stable, optically transparent and isotropic, highly viscous

and elastic stiff gels. Many samples respond with a sound up on mechanical excitation which has led to the expression “ringing gels”. They can be easily distinguished from vesicle phases by visual observation, because they do not flow under the influence of gravitation, and the entrapped air bubbles have a non-spherical shape and do not rise, even after a period of several years. From this behaviour, it can be concluded that the cubic phases behave as Bingham solids with a yield stress. This behaviour is also observed for the bicontinuous cubic phases which can occur in the phase diagram between the lamellar and the hexagonal or the reverse hexagonal phase, and also for the reverse cubic phases.

Dynamic rheological measurements show that the cubic phases behave like the viscoelastic vesicle phases, as can be seen from the two examples shown in Figure 10.19. As can be seen, G' is independent of the frequency and at least one order of magnitude higher than G'' , and $|\eta^*|$ increases to infinity when the frequency approaches zero. However, as can be expected from the stiffness of the samples, both G_0 and σ_y are several orders of magnitude higher than for the vesicle phases. As has been found for the latter, the cubic phases have energy elasticity, i.e. the moduli break down at deformations beyond about 10%.

In this connection, it is interesting that vesicles can also form a cubic phase at high concentrations, if they are very monodisperse. This condition has been found to be fulfilled in a system of sodium oleate/octanol/water at a cosurfactant:surfactant ratio of around 3:1 in the water-rich corner; however, such cubic phases of vesicles are very rare, because the vesicles are not sufficiently monodisperse in most of the systems. These cubic phases of vesicles have similar rheological properties to the other cubic phases, and the values for G_0 and σ_y are also considerably higher than for the normal vesicle phases.

Most of the lyotropic cubic phases show a thermotropic behaviour, i.e. they “melt” at a characteristic temperature to an isotropic micellar phase without any elasticity and yield stress values. This melting process is connected with a heat of “melting”, and is reversible; below the “melting” temperature, the system returns back to the cubic gel phase. An interesting behaviour is shown by the cubic phases in the $(\text{POE})_x(\text{POP})_y(\text{POE})_x$ /water systems; these phases show a reverse thermotropic behaviour, i.e. they “melt” below a characteristic temperature and return to the stiff gel state above this temperature. This is due to the hydration of the hydrophobic POP blocks; below the characteristic temperature, the POP units are hydrated and

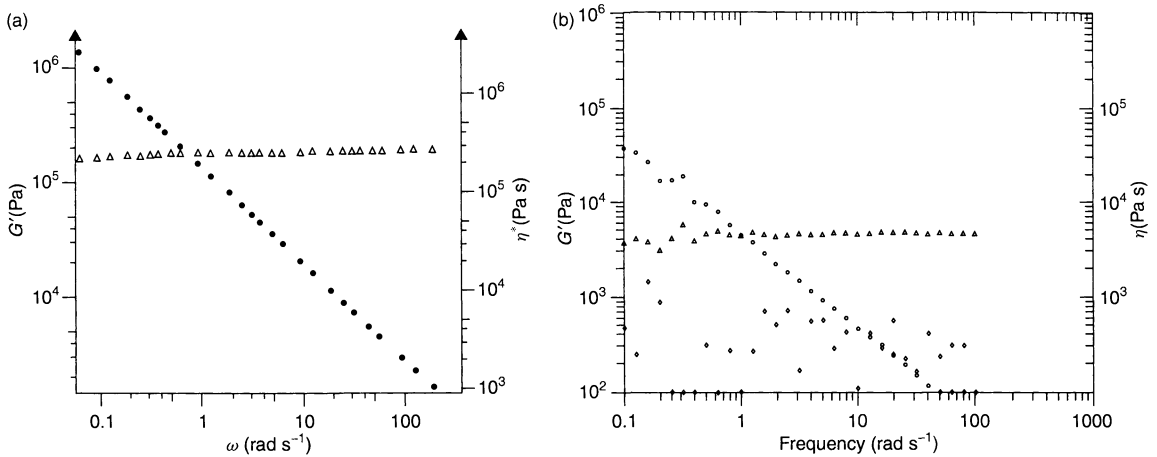


Figure 10.19. (a) Double logarithmic plots of the storage modulus G' (Δ) and the complex viscosity $|\eta^*|$ (\bullet) against the radial frequency ω for a cubic phase of 32.5 wt% C₁₄DMAO, 7.5 wt% decane and 60 wt% water at 25°C. (b) Double logarithmic plots of the storage modulus G' (Δ), loss modulus G'' (\diamond) and the complex viscosity $|\eta^*|$ (\circ) against the frequency ω for a cubic phase of 25 wt% (POE)₁₀₆(POP)₆₉(POE)₁₀₆ in water at 30°C

less hydrophobic, and hence they do not aggregate in the aqueous solution, while above this temperature the POP units are dehydrated and become more hydrophobic, which leads to the aggregation to micelles and the formation of the cubic phase at sufficiently high concentrations.

Attempts have been made to establish a relationship between the structures of cubic phases and their rheological properties. For this purpose, one assumes that the cubic phase is formed by highly concentrated and monodisperse spheres which show only hard-sphere interactions under such conditions. This assumption also seems to be justified for ionic surfactants due to the high concentration and ionic strength in the cubic phases. Thus, the structure factor $S(q \rightarrow 0)$ for a scattering vector q approaching a scattering angle of zero can be calculated, according to the Percus–Yevick approximation, as follows:

$$S(0) = (1 - \Phi)^4 / (1 + 2\Phi)^2 \quad (10.22)$$

where Φ is the volume fraction of the spherical aggregates. It must be pointed out that it is necessary to take an effective volume fraction in equation (10.22) which is larger than the value calculated from the concentration of the amphiphile and the additive due to the hydration of the spherical aggregates. With the value of $S(0)$, an osmotic compressibility modulus K can be calculated as follows:

$$K = \nu k_B T (S(0))^{-1} \quad (10.23)$$

where ν is the number density of the aggregates. This parameter can be calculated from the mean distance between two aggregates, which can be obtained from small-angle neutron scattering (SANS) measurements. The shear modulus G_0 can then be calculated by using the following equation:

$$G_0 = K 3(1 - 2\mu) / 2(1 + \mu) \quad (10.24)$$

with the Poisson number μ which can have values between 0 and 0.5, and is in this case close to 0.5, i.e. the limiting value for an incompressible sample (it should be noted here that the obtained value for G_0 depends sensitively on the choice of μ).

It has been found for many cubic phases consisting of spherical particles that the moduli calculated with the hard-sphere model are often in good agreement with the ones determined experimentally. However, it must be stated here that also for the cubic phases a generally valid model for a theoretical description of their rheological behaviour is not available at present (mainly due to the uncertainties in the choice of μ).

5 SHEAR-INDUCED PHENOMENA IN SURFACTANT SOLUTIONS

In an early part of this chapter, the responses of surfactant solutions to the mechanical stress or strain was described. The influence of the various structures in these systems on their rheological behaviour was

demonstrated and models for theoretical description of these effects have been introduced. For these studies, it was important that the structures were not changed during the measurements, i.e. the applied stress or strain, respectively, had to be below a characteristic limit so that the structures were not affected.

On the other hand, application of a shear gradient to a liquid is always connected with the input of energy into the system. Thus, shear can be a parameter such as the temperature, concentration or ionic strength that can lead to structural changes in the sheared system. This can be expected particularly for surfactant solutions, because in their case there is principally a steady exchange of monomers between the solution and the aggregates. This exchange is usually rapid for most of the systems; however, it can also be very slow in some cases. Thus, shear-induced structural changes can be either reversible or irreversible, depending on the specific properties of the surfactant solution.

5.1 Surfactant solutions with rod-like micelles under shear

A remarkable and puzzling phenomenon has been observed in some surfactant solutions containing rod-like micelles in the dilute state (5, 16–18). The concentrations of these systems were not too far above the transition concentration (usually in the range of 0.1–0.2 wt%, or a few mM), the rod-like micelles had typical dimensions of a few hundred angstroms and the mean distance between the rods was somewhat larger than their length. Furthermore, the rods had to be slightly charged, which can be achieved, for example, by using mixtures of zwitterionic and ionic surfactants in a mixing ratio of 1–3 ionic surfactant molecules per 10 uncharged surfactant molecules at low ionic strengths. In addition, ionic surfactants with strongly binding counterions can fulfil this condition. The interaction between these rod-like micelles is repulsive, which leads to a nearest-neighbour order between them. This results in a correlation peak in SANS experiments from which the mean distance between the rods can be calculated. As the rotational volumes of the rods do not overlap, they can rotate more or less freely, with times constants in the range of a few μs .

Such solutions are expected to be Newtonian liquids with low viscosities. This has also been found in rheological measurements, if the shear rate or the time, during which the shear was applied, remained below a characteristic value. With a shear rate above this critical value, the solutions show a *dilatant* and *rheopectic* flow

behaviour. The viscosity increases steeply with increasing shear rates or shear times, respectively, and reaches a plateau value. Furthermore, the solutions become birefringent and elastic, and also the birefringence and the first normal stress difference increase with the shear rate up to plateau values. The extinction angle in flow birefringence measurements drops abruptly from 45 to 0° at the critical shear rate. These effects are demonstrated in the example shown in Figure 10.20. The critical shear rate depends on various parameters of the system, such as surfactant concentration, ionic strength, temperature or charge density on the rods; the concentration dependence is demonstrated in Figure 10.21 for one such system. This shear-induced effect is reversible – the increased viscosity, the elasticity and the birefringence at a constant shear rate above the critical value increase steeply at a characteristic time and then reach a constant plateau value. They relax with a characteristic time constant back to the original values of the unsheared systems when the shear is removed, as can be seen from Figure 10.22. SANS measurements on samples which show the shear-induced effect show a symmetric correlation peak for the solutions at rest, which becomes significantly lower and anisotropic peaks develop at shear rates above the critical value; this is shown in Figure 10.23.

From these results, it follows that the rods must become oriented in the shear field; the SANS measurements show that part of the rods are aligned, while another part remains randomly distributed. The extinction angle of 0° indicates that the oriented micelles are completely oriented in the direction of flow. However, the relatively small rods have orientation time constants τ_{rot} in the μs range of according to their lengths, and this can also be proven by electric birefringence measurements. For a complete orientation of such rods, the condition ($\dot{\gamma} \tau_{\text{rot}} > 1$) must be fulfilled, and this means that complete orientation can only take place at shear rates $> 10^5 \text{s}^{-1}$. However, Figures 10.20–10.23 show that the shear-induced effects already take place at shear rates which are three to four orders of magnitude lower than this value. Thus, for the explanation of these effects a simple orientation of rod-like aggregates under the influence of the shear field cannot be taken into account.

Three different models have been proposed for the explanation of these shear-induced phenomena. The first assumes that such phenomena are due to the formation of a nematic phase under the influence of shear. According to this theory, the systems are in the isotropic micellar phase, but close to the boundary of the nematic phase, and the application of shear leads to the transition into this phase. Nematic phases can

www.iran-mavad.com

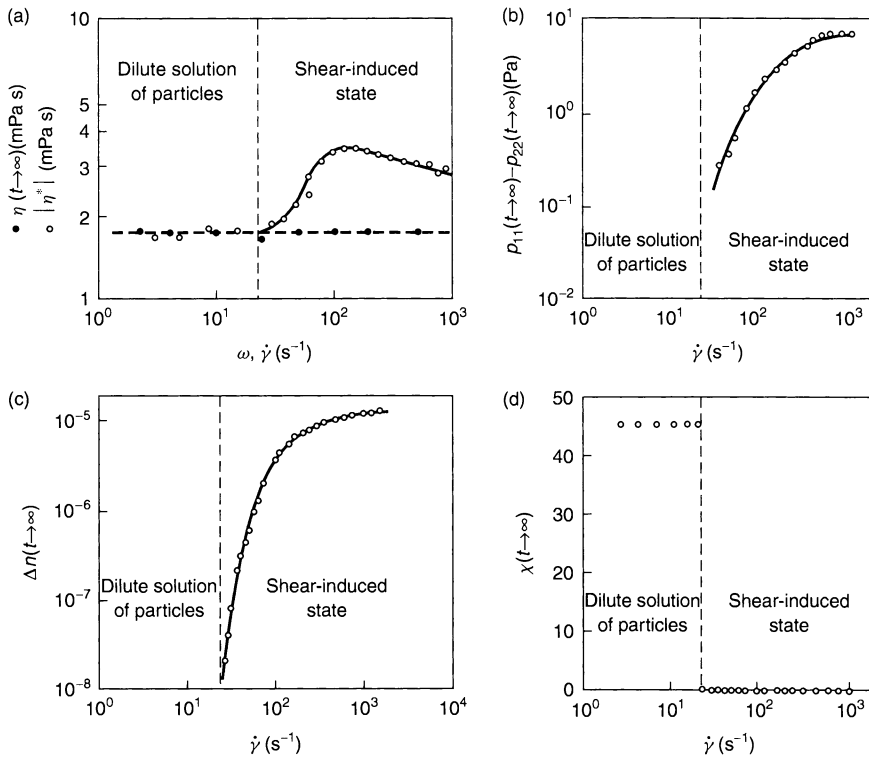


Figure 10.20. The zero shear viscosity, $\eta_{t \rightarrow \infty}$, and the complex viscosity $|\eta^*|$ (a), the first normal stress difference, $p_{11} - p_{22}$ (b), the flow birefringence Δn (c), and the extinction angle χ (d), as a function of the shear rate $\dot{\gamma}$ or the oscillation frequency ω , respectively, for a solution of 5 mM $C_{14}TMA$ at 20°C

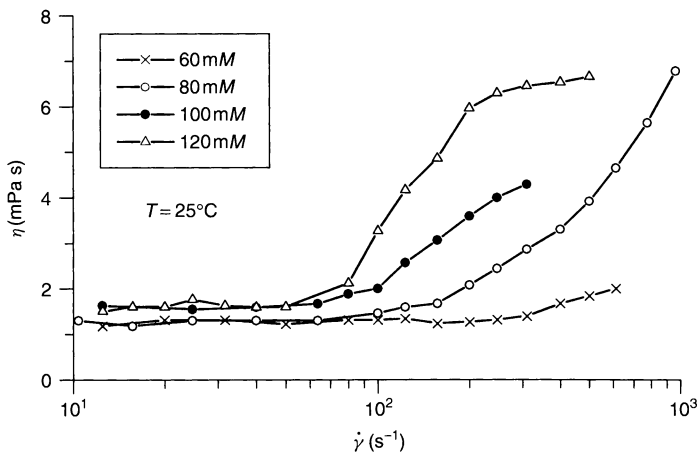


Figure 10.21. The shear viscosity η against the shear rate $\dot{\gamma}$ for mixtures of $C_{14}DMAO:SDS = 6:4$ with various total concentrations, as measured in a capillary viscometer at 25°C

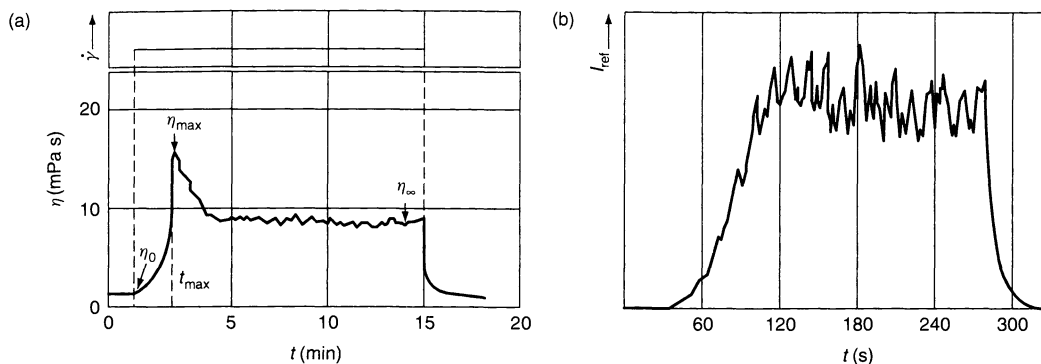


Figure 10.22. (a) The shear viscosity η at a shear rate $\dot{\gamma}$ of 50 s^{-1} for a solution of 0.9 mM CPySal at 20°C , and (b) the flow birefringence Δn at a shear rate of 10 s^{-1} for a solution of 20 mM $\text{C}_{10}\text{F}_{21}\text{CO}_2\text{N}(\text{CH}_3)_4$ at 30°C , as a function of the time t ($\dot{\gamma}$ jumped from 0 s^{-1} to the corresponding value and then dropped back to zero after a certain time interval)

be already completely aligned at shear gradients below 1 s^{-1} . Without shear, the nematic phase is not stable and the system relaxes to the isotropic solution when the shear is removed.

The second model postulates a length distribution of the rod-like micelles. Under the influence of the shear gradient, the longer rods start to incorporate monomers from the solution, and hence the shorter rods dissolve in order to keep the equilibrium concentration of monomeric surfactant molecules constant. By this process the longer rods can grow to very long aggregates which can be completely oriented by the low shear gradients, while the shorter rods disappear. The long rods are stable only under the action of the shear, and decreased again under relaxation to the original length when the solution comes to rest.

In the third model, collisions between the rod-like micelles in the flowing solution are responsible for the shear-induced structures. These collisions occur preferentially at the end-caps of the rods, because they are slightly oriented by the shear gradient. By the collisions, the short rods aggregate together, thereby forming long rod-like micelles. This aggregation process can come about either by "sticky" contacts between the micelles, thus forming necklace-type structures or by direct unification of many short rods to give one long aggregate. Again, these long rods can be completely oriented by the applied low shear rates, and they are stable only under the influence of shear and are decomposed to the originally present aggregates after the cessation of the shear. For the aggregation of the short rods, a large end-cap energy of these micelles is postulated, which can be set free by the association.

Up until here, all three models could in principle explain the shear-induced phenomena. Therefore,

detailed studies have been carried out on a system which shows the shear-induced phenomena in order to find out the mechanism for the shear-induced structural transitions. As a model system, mixtures of the zwitterionic surfactant C_{14}DMAO and the anionic surfactant SDS were selected which show the shear-induced effects at mixing ratios of C_{14}DMAO to SDS from 8:2 to 5:5. The studies were performed by electric and flow birefringence measurements for the detection of the shear-induced structures which are always accompanied by a strong anomaly of the electric birefringence signals, which indicates the strong interaction between the rod-like micelles.

In these experiments, the shear-induced effects were first studied for a selected mixing ratio of the two surfactants, and then the measurements were repeated with samples in which increasing parts of C_{14}DMAO were replaced by the nonionic surfactant C_{12}E_6 , or by the shorter zwitterionic surfactant C_{12}DMAO , respectively. In a further series, increasing parts of SDS were replaced by sodium dodecylglycoether sulfate, $\text{C}_{12}\text{E}_{2.5}\text{SO}_4\text{Na}$. This experiment showed that substitution of C_{14}DMAO by C_{12}E_6 leads to a continuous reduction of the shear-induced phenomena which then disappeared completely after the replacement of 30% of the C_{14}DMAO molecules. The micellar shape did not change significantly by this replacement, although the anomaly of the electric birefringence signal disappeared, indicating that the interaction between the micelles changes by introducing the C_{12}E_6 molecules. It was possible to restore the anomaly to its original state by increasing the concentration of the samples with C_{12}E_6 , but also in this case no trace of the shear-induced phenomena could be detected. A similar result was obtained for the replacement of SDS by $\text{C}_{12}\text{E}_{2.5}\text{SO}_4\text{Na}$.

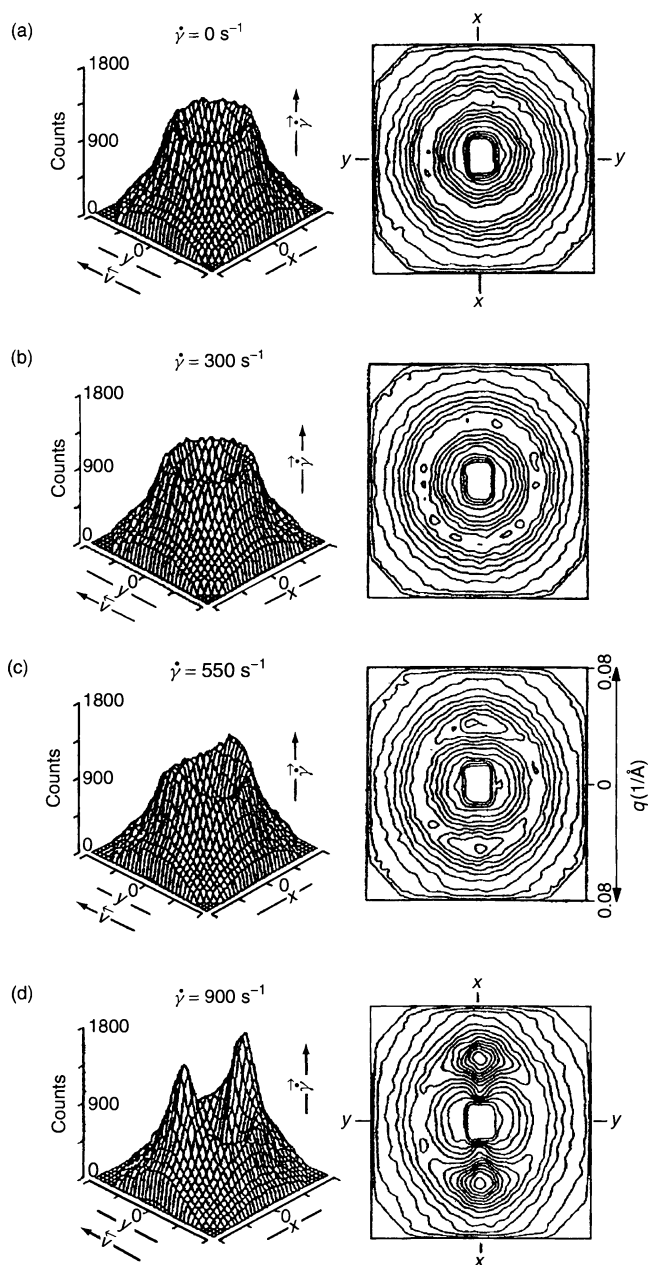


Figure 10.23. Three-dimensional and contour plots of the intensity of a scattered neutron beam as a function of the scattering vector q for a solution of 60 mM $C_{14}DMAO:SDS = 6:4$ at different shear rates, measured at $35^\circ C$

Here, the shear-induced phenomena became smaller with increasing amounts of $C_{12}E_{2.5}SO_4Na$. They disappeared for complete replacement of SDS and could not be restored by increasing the concentration or ionic strength.

Replacement of $C_{14}DMAO$ by the shorter-chain homologous $C_{12}DMAO$ leads also to a decrease of the shear-induced phenomena, which disappeared again at a certain amount of $C_{12}DMAO$. This is due to a decrease of the size of the rods and of the interaction between

them. However, by increasing the concentration both the interaction and the shear-induced phenomena could be completely restored. This shows clearly that the disappearance of the shear-induced structures does not come about by the faster dynamics of the shorter-chain surfactants.

These results prove clearly that the shear-induced phenomena are better represented by the third model, i.e. the association of short rods to long necklace-type aggregates, because it would be difficult to understand why replacement of C_{14} DMAO or SDS by $C_{12}E_6$ or $C_{12}E_{2.5}SO_4Na$, respectively, should prevent a transition into a nematic phase or a growth of small rods by incorporation of monomers, if the dimensions of the aggregates and also the interactions between them are not changed. On the other hand, protrusion of the long hydrophilic groups of $C_{12}E_{2.5}SO_4Na$ or $C_{12}E_6$ from the micellar surface can effectively hinder the aggregation of small rods by “sticky” contacts and hence suppress the shear-induced structures.

It has been argued that the aggregation of the rods is enhanced by a large end-cap energy of the rods, and one could imagine that such an assumption is likely to be due to the argument that the ionic surfactants are enriched at the end-caps of the rods by reason of the electrostatic repulsion between the charged head-groups. However, detailed SANS measurements with contrast variation on a mixed system of C_{14} DMAO and SDS indicate that the molecules of both surfactants are homogeneously mixed in the rod-like aggregates. The measurements showed furthermore that the rods in the studied systems were distorted, i.e. they are anisometric

aggregates with two different short axes. It is not clear at present whether such a distorted rod-like shape plays a role in the formation of shear-induced structures. In addition, the nature of the “sticky” contacts between the rods is still unclear. It can be stated, therefore, that until now, in spite of the increased knowledge now available, not all details of the shear-induced phenomena are completely understood.

Finally, it should be pointed out that systems which show the described shear-induced phenomena have a considerable potential for technical applications where large amounts of water have to be circulated for cooling or heating purposes. In such processes, the energy expense for the pumping purpose is a major economic factor. Usually, one is interested in pumping as fast as feasible, and hence the flow in the water pipes is generally in the turbulent flow region. Under these conditions, it is possible to reduce the friction coefficient by the addition of surfactant systems which show shear-induced phenomena, as can be seen from Figure 10.24. This effect is called “drag reduction” and is already known from studying solutions of long-chain polymers. Such polymers, however, have the big disadvantage that they deteriorate under shear because the covalent bonds of the molecules break under shear forces, while the surfactant aggregates which produce this effect do not have this disadvantage, since they are “self-healing” due to their fast dynamics and the absence of covalent bonds. Pilot operations have been running for periods of several months without loss of efficiency and the energy costs could be cut to less than half.

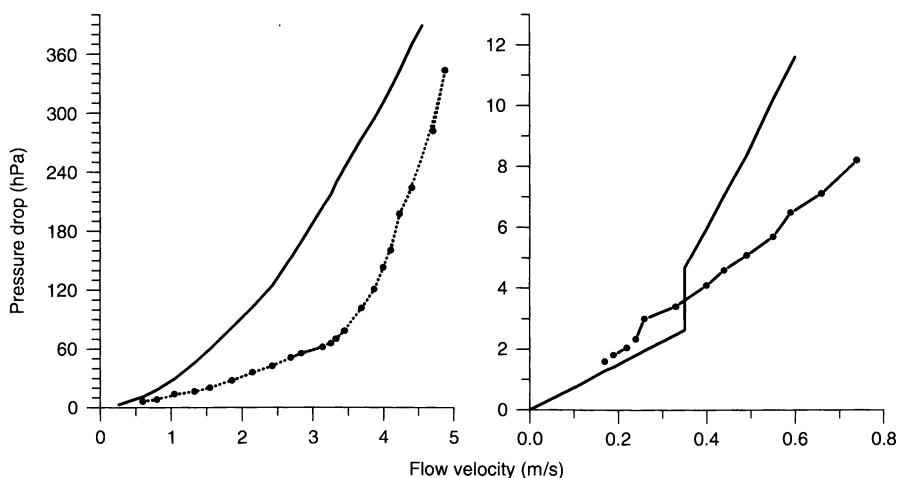


Figure 10.24. Plots of the pressure drop against the flow velocity in a capillary in the laminar and turbulent flow regions for water (continuous lines) and for a drag-reducing surfactant solution (750 ppm (C_{14} TABr + NaSal) at 27.5°C) (dashed lines)

5.2 Shear-induced phenomena in lamellar phases

Rheological measurements on various vesicle phases have shown that the Cox–Merz rule – the complex viscosity of a sample at any frequency is equal to its apparent viscosity at the frequency-equivalent shear rate – is not fulfilled for these systems (10, 19–23); two examples of this are shown in Figure 10.25. At low frequencies or shear rates, respectively, both viscosities are equal, but beyond a certain shear rate the apparent viscosity is above the complex viscosity, and this difference increases with the shear rate. This behaviour can be qualitatively understood by a structural transition under the influence of shear. The oscillatory measurements do not lead to structural changes because in these experiments the deformation is normally kept below the limiting value for such a change.

Many authors have described structural transitions in dilute lamellar phases under the influence of shear. For example, Roux and co-workers (19) studied different dilute lamellar phases which were stabilized by undulation forces and contained flat bilayers with defects, at rest. With increasing shear rates, these bilayers undergo a transition into relatively monodisperse multilamellar vesicles above a characteristic shear rate. The size of the formed vesicles is indirectly proportional to the shear rate. Beyond a second characteristic shear rate, the vesicles are again transformed into flat oriented bilayers. These results were explained in terms of a balance between shear stress and elastic forces which come from the bending and the Gaussian moduli of the bilayers. The same authors observed a similar sequence with increasing shear rate for other lamellar phases. It was found

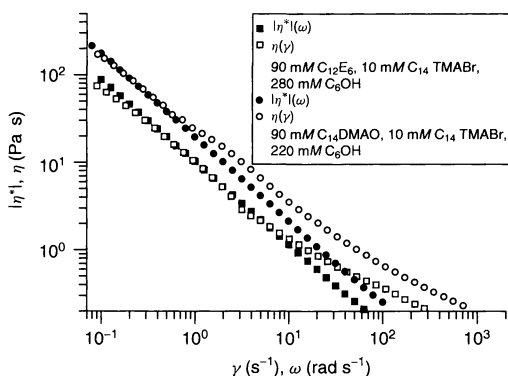


Figure 10.25. Double logarithmic plots of the shear viscosity η against the shear rate $\dot{\gamma}$ and of the magnitude of the complex viscosity $|\eta^*|$ against the angular frequency ω for two different vesicle phases at 25°C

furthermore that the monodisperse multilamellar vesicles fill the volume of the whole phase completely with a similar structure to that of a polyhedral foam. This structure does not change or relax to the original structure after cessation of the shear; on dilution, the packing density of the vesicles decreases without any change in the sizes of the vesicles.

Similar results were obtained by Wagner and co-workers (20) on a lamellar phase consisting of the double-chain surfactant Aerosol OT and water plus NaCl. At rest, flat bilayers with defects are present in the system, while with increasing shear rates a transition into turbid dispersions with multilamellar vesicles takes place, followed by monodisperse multilamellar vesicles with a long-range order, the size of which decreases with increasing shear, and finally flat oriented bilayers are formed again. These authors concluded that these transitions are correlated with the applied stress. The viscosity of the samples first increases and then reaches a maximum in the range of the dispersed multilamellar vesicles. It decreases again when the transition into multilamellar vesicles takes place with decreasing sizes and flat bilayers. A similar behaviour has also been described by several other authors on various dilute lamellar phases with flat bilayers. It has also been observed that the transition into vesicles is irreversible; no relaxation to the originally present flat bilayers takes place when the shear is stopped and the samples are left at rest for a long period of time.

Van der Linden and co-workers have developed a theory for the rheological behaviour of multilamellar vesicles on the basis of their bending and dynamic properties, which could be suitable for an understanding of the phase transitions of lamellar phases under shear. These authors calculated the energy required for the deformation of the vesicles, which is determined both by the bending energy of the bilayer and by the interactions between such layers. With this model, they could obtain relaxation times and elastic frequencies for the different modes of deformation of the multilamellar vesicles that were of the same order of magnitude, like the shear rates at which the transformation of the lamellar phases into monodisperse multilamellar vesicles takes place.

Similar phase transitions in lamellar phases have been observed by Hoffmann and Ulbricht (21) who studied the influence of shear on lamellar phases of C₁₄DMAO, C₆OH and water where the charge density of the bilayers was changed by adding C₁₄TMABr. These systems were studied by means of electron microscopy, small-angle neutron scattering (SANS), small-angle X-ray scattering (SAXS), rheology, and anisotropy of the electric conductivity under the influence of shear.

The systems form flat stacked bilayers at rest when the systems have a small charge density, while at higher charge densities multilamellar vesicles are present. Increase of the ionic strength also again leads to the formation of flat bilayers with high amounts of the cationic surfactant.

The experiments carried out with increasing shear rates first show for the flat bilayers at low charge densities an orientation parallel to the wall and then a switch to an orientation perpendicular to the wall. At higher shear rates, a transformation into multilamellar vesicles takes place where the vesicles can also be deformed in the shear field. With a further increase of the shear rate, the outer shells of the vesicles are continuously stripped off until unilamellar vesicles remain at the

highest available shear rates of 6000 s^{-1} . The samples at higher charge densities where multilamellar vesicles are already present at rest show an analogous behaviour; with increasing shear rates, the outer vesicle shells are stripped off until unilamellar vesicles remain. The transition back into flat bilayers cannot be observed for these systems, even at the highest shear rates.

The vesicle transitions are irreversible, i.e. some relaxation processes can, however, be observed after stopping the shear, but a return to the originally present structures has not been detected even when the samples were left standing for periods of weeks. This situation is demonstrated by the example shown in Figure 10.26 for SANS measurements under shear. Figure 10.27(a) shows the influence of the structural transitions on

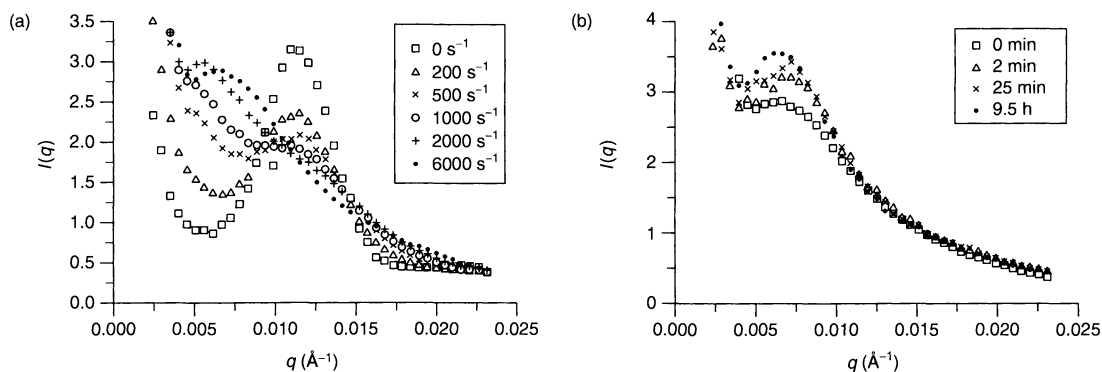


Figure 10.26. (a) The radially averaged intensity $I(q)$ (in arbitrary units) of the neutron beam as a function of the scattering vector q for the system of 90 mM C_{14}DMAO , 10 mM $\text{C}_{14}\text{TMABr}$, 220 mM C_6OH and D_2O , sheared for at least 1 h under various shear rates at 25°C . (b) The radially averaged intensity $I(q)$ (in arbitrary units) of the neutron beam as a function of the scattering vector q for the same system at different times after switching off a shear gradient of 6000 s^{-1} and 2 h duration at 25°C

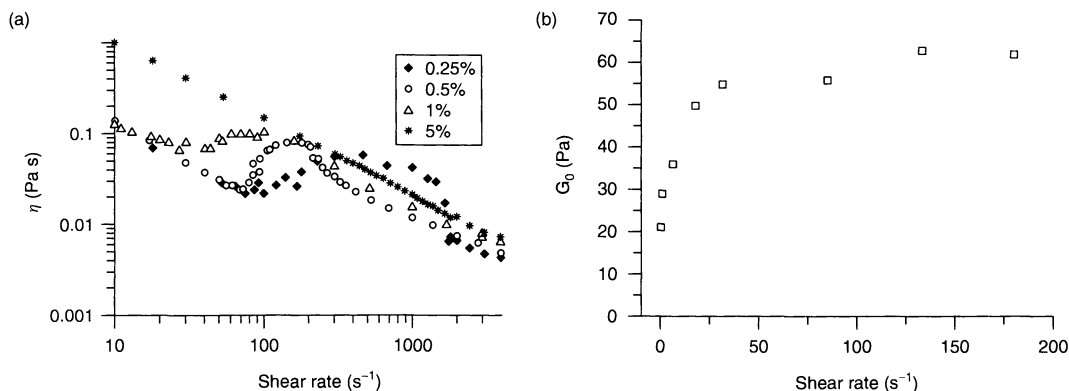


Figure 10.27. (a) Double logarithmic plots of the apparent shear viscosity η for systems of 100 mM ($\text{C}_{14}\text{DMAO} + \text{C}_{14}\text{TMABr}$)/220 mM $\text{C}_6\text{OH}/\text{H}_2\text{O}$ with different molar ratios of $\text{C}_{14}\text{TMABr}$ as a function of the shear rate $\dot{\gamma}$ at 25°C . (b) The shear modulus G_0 for a system of 90 mM C_{14}DMAO , 10 mM $\text{C}_{14}\text{TMABr}$, 220 mM C_6OH and H_2O as a function of the shear rate at 25°C after the application of a shear gradient until the apparent shear viscosity was constant

the rheological behaviour of the samples. At high charge densities, a continuous decrease of the apparent viscosity, i.e. shear thinning or structural viscosity, can be observed due to the peeling off of the outer vesicle shells, while at low charge densities the transition into vesicles leads to an increase of the viscosity at intermediate shear rates, followed by a decrease which is again caused by the peeling of the vesicle shells. The shear modulus G_0 for the systems increases with increasing shear rate, as shown by the example given in Figure 10.27(b), this can be understood easily because G_0 is mainly determined by the number density of the vesicles which has to increase automatically with the peeling of vesicle shells with increasing shear rates. In addition, the other experiments confirm the described structural changes in the lamellar phases under the influence of shear. It is thus possible to adjust the sizes of the vesicles and the number of vesicle shells in a reproducible manner by shearing the systems with corresponding shear rates.

Very striking and unexpected structural transitions in lamellar phases under shear have been described by Candau and co-workers. By optical microscopy, NMR spectroscopy, fluorescence anisotropy, light scattering, rheology and SANS measurements, they found that a vesicle phase in the binary system of cetyltrimethylammonium hydroxynaphthalenecarboxylate (CTAHNC) and water under shear undergoes a transition into a micellar phase with entangled worm-like micelles. This transition is accompanied by a strong increase of the viscoelastic properties of the system and by a pronounced correlation peak in the SANS experiments. The mechanism of this vesicle-to-micelle transition, which has not previously been observed for other systems, is not known yet.

Based on the result that the structures, and hence also the properties of lamellar phases can depend strongly on the history of the preparation, Hoffmann and Ulbricht (21) studied the influence of defined shear gradients on lamellar phases which have been produced without shear. These authors started from thermodynamically stable phases which are in an equilibrium state, for instance micellar L_1 or L_3 phases. To such phases, a further component was added which can bring the system into the region of a lamellar or a vesicle phase. The addition of this component was achieved without shear by producing this component via a chemical reaction. This is possible, for example, with a L_3 phase consisting of a zwitterionic surfactant such as C_x DMAO, a cosurfactant C_7 OH, and water. This phase can be transformed into a vesicle phase by adding an acid which protonates the zwitterionic aminoxide group and thus charges

the bilayers so that the L_3 phase is no longer stable. The addition of the acid is possible without shear if the acid is produced by a slow chemical reaction, i.e. the hydrolysis of an added ester such as methylformate or methyloxalate. Another example is a micellar L_1 phase consisting of a surfactant and water. Addition of a cosurfactant can bring this phase into the range of vesicle existence, and this cosurfactant can be produced without shear by the alkaline hydrolysis of an added ester such as hexylformate.

Electron micrographs for such systems that have been produced without shear show that the first phase after the hydrolysis of the ester is a lamellar phase with flat stacked bilayers. This phase is transformed into a phase of polydisperse multilamellar vesicles after shearing the sample by shaking it for a short time. These vesicles lose their outer shells more and more with increasing shear rate, until above a critical shear rate rather monodisperse unilamellar vesicles are present in the solutions. In addition, in this case no transition back to flat bilayers can be observed, even at the highest available shear rates.

The phase transitions turn again out to be irreversible; the different lamellar phases after the application of shear do not relax back to the originally present structures. In addition, no spontaneous transition from one phase into another takes place without shear, and thus it cannot be decided at present which of these phases is the thermodynamically stable one.

An example of such an experiment is shown in Figure 10.28, where the shear-induced transformation of the originally present phase of planar lamellae to vesicles has been followed by conductivity measurements

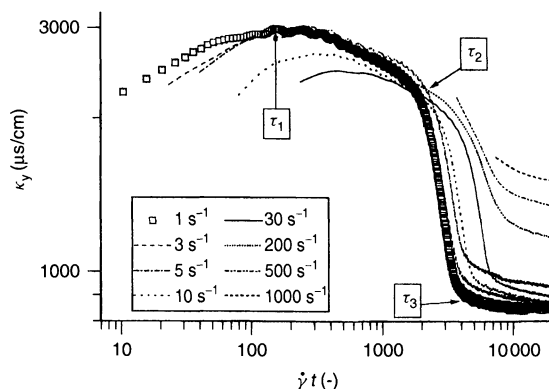


Figure 10.28. Electrical conductivity κ_y in the flow direction as a function of the time at which various constant shear rates are applied to a system of 100 mM C_{14} DMAO/10 mM diethyloxalate/250 mM C_6 OH/water

in the flow direction in a Couette cell for various shear rates. This figure shows that this transformation at constant shear rates is characterized by three different time-constants. The shortest time can be ascribed to the orientation of the stacked bilayers parallel to the wall. The second time is due to the onset of the transformation of the stacked bilayers into vesicles, while the third time characterizes the end of the transformation process. These time-constants are indirectly proportional to the applied shear rates. They increase with the chain length of both the surfactant and the cosurfactant, what could be due to the increasing thickness of the bilayers. Furthermore, the time increases with the total concentration of the components, what may be explained by the fact that the required energy for the transformations increases with the area of the bilayers which, of course, also increases with the concentration.

These experiments have thus shown that it is possible to produce in a reproducible manner vesicles with defined sizes and shell numbers with the corresponding rheological properties by accordingly adjusting the composition of the starting systems and choosing the required shear conditions. Such a controlled formation of defined vesicle systems can be of importance for various applications in cosmetics, pharmacy, food processing, etc., where such vesicles with well-defined properties are often required.

6 REFERENCES

1. Darby, R., Viscoelastic fluids, in *Chemical Processing and Engineering*, Vol. 9, Albright, L. F., Maddox, R. N. and Mc Ketta, J. J. (Eds), Marcel Dekker, New York, 1976, pp. 51–70.
2. Israelachvili, J. N., Mitchell, D. J. and Ninham, B. W., Theory of self-assembly of hydrocarbon amphiphiles into micelles and bilayers, *J. Chem. Soc., Faraday Trans. 2*, **72**, 1525–1573 (1976).
3. Tiddy, G. J. T., Surfactant liquid crystal phases, *Phys. Rep.*, **57**, 1–46 (1980).
4. Hoffmann, H. and Ulbricht, W., Physikalische Chemie der Tenside, in *Die Tenside*, Kosswig, K. and Stache, H. (Eds), Carl Hanser, München, 1993, pp. 1–114.
5. Hoffmann, H. and Ulbricht, W., Viscoelastic surfactant solutions, in *Structure–Performance Relationships in Surfactants*, Esumi, K. and Ueno, R. (Eds), Marcel Dekker, New York, 1997, pp. 285–324.
6. Schmiedel, P., Weiterentwicklung eines dynamischen Rheometers für Frequenzen bis 1 kHz und rheologisches Verhalten viskoelastischer Tensidlösungen im Frequenzbereich bis 1 kHz, *Ph. D. Dissertation*, Universität Bayreuth, 1995.
7. Cates, M. E. and Candau, S. J., Statics and dynamics of wormlike surfactant micelles, *J. Phys., Condensed Matter*, **2**, 6869–6880 (1990).
8. Granek, R. and Cates, M. E., Stress relaxation in living polymers: Results from a Poisson renewal model, *J. Chem. Phys.*, **96**, 4758–4769 (1992).
9. Cates, M. E., Flow behaviour of entangled surfactant micelles, *J. Phys. Condensed Matter*, **8**, 9167–9176 (1996).
10. Hoffmann, H. and Ulbricht, W., Vesicle phases and their macroscopic properties, *Recent Res. Devel. Phys. Chem.*, **2**, 113–158 (1998).
11. van der Linden, E. and Dröge, J. H. M., Deformability of lamellar droplets, *Physica A*, **193**, 439–447 (1993).
12. de Haas, K. H., Blom, C., van den Ende, D., Duits, M. H. G., Haveman, B. and Mellema, J., *Langmuir*, **13**, 6658–6668 (1997).
13. Radiman, S., Toprakcioglu, C. and McLeish, T., Rheological study of ternary cubic phases, *Langmuir*, **10**, 61–67 (1994).
14. Wanka, G., Hoffmann, H. and Ulbricht, W., The aggregation behaviour of poly(oxyethylene)–poly(oxypropylene)–poly(oxyethylene) block copolymers in aqueous solution, *Colloid Polym. Sci.*, **268**, 101–117 (1990).
15. Gradzielski, M., Kubische Phasen und ihnen benachbarte Phasengebiete – Struktur und Eigenschaften, *Ph. D. Dissertation*, Universität Bayreuth, 1992.
16. Pils, H., Hoffmann, H., Hofmann, S., Kalus, J., Kencono, A. W., Lindner, P. and Ulbricht, W., Shape investigation of mixed micelles by small angle neutron scattering, *J. Phys. Chem.*, **97**, 2745–2754 (1993).
17. Hoffmann, S. and Hoffmann, H., Shear-induced micellar structures in ternary surfactant mixtures: The influence of the structure of the micellar interface, *J. Phys. Chem., B*, **102**, 5614–5624 (1998).
18. Wang, S. Q., Transient network theory for shear-thickening fluids and physically cross-linked systems, *Macromolecules*, **25**, 7003–7010 (1992).
19. Panizza, P., Roux, D., Vuillaume, V., Lu, C.-Y. D. and Cates, M. E., Viscoelasticity of the onion phase, *Langmuir*, **12**, 248–252 (1996).
20. Bergenholtz, J. and Wagner, N. J., Formation of AOT/brine multilamellar vesicles, *Langmuir*, **12**, 3122–3126 (1996).
21. Hoffmann, H. and Ulbricht, W., Vesicle phases of surfactants and their behaviour in shear flow, *Tenside Surf. Det.*, **35**, 421–438 (1998).
22. Läger, J., Weigel, R., Berger, K., Hiltrop, K. and Richter, W., Rheo-small-angle-light-scattering investigation of shear-induced structural changes in a lyotropic lamellar phase, *J. Colloid Interface Sci.*, **181**, 521–529 (1996).
23. Hassan, P. A., Valaulikar, B. S., Manohar, C., Kern, F., Bourdieu, L. and Candau, S. J., Vesicle to micelle transition: rheological investigations, *Langmuir*, **12**, 4350–4357 (1996).

PART 5

ANALYSIS AND CHARACTERIZATION IN SURFACE CHEMISTRY

CHAPTER 11

Measuring Equilibrium Surface Tensions

Michael Mulqueen and Paul D. T. Huibers

Massachusetts Institute of Technology, Cambridge, MA, USA

1	Introduction	217	6	Pendant/Sessile Drop and Bubble Methods	221
	1.1 Limitations	217	7	The Spinning Drop Method	222
2	Capillary Rise	218	8	The Maximum Bubble Pressure Method	223
3	The Wilhelmy Plate Method	219	9	Conclusions	223
4	The Du Noüy Ring Method	220	10	References	223
5	The Drop Weight Method	220			

1 INTRODUCTION

The measurement of equilibrium surface tension is one of the oldest experimental techniques in the study of surfaces. Many of the techniques that are still in use today were originally developed in the 19th century. Significant improvements in accuracy and precision have been made over time, most recently as a result of the use of modern electronics and computers. This chapter briefly summarizes and discusses the advantages and disadvantages of the many experimental techniques that are in use today.

There is significant overlap in describing techniques for the measurement of equilibrium surface tension with those for dynamic surface tension, as discussed in the following chapter. Many of those dynamic surface tension methods can be used to measure equilibrium tension simply by performing the experiment over sufficiently long times. The time required for equilibration can range widely, from the practically instantaneous equilibration for pure liquids, to many hours or even days for dilute surfactant or polymer solutions. Thus, some of the dynamic techniques, particularly those that can only be used to study short times, such as the oscillating jet method, are not well suited for equilibrium measurements.

The surface tension measurement techniques can be divided into the following three categories: (i) Force Methods, which include the truly static methods of the capillary rise and Wilhelmy plate methods, as well as the dynamic detachment methods of the Du Noüy ring and drop weight, (ii) Shape Methods, which include the pendant or sessile drop or bubble, as well as the spinning drop methods, and (iii) Pressure Methods, which are represented by the maximum bubble pressure method. These techniques are summarized in the following sections of this chapter.

1.1 Limitations

One key difference among the techniques covered in this review is that some involve processes that are not truly static, i.e. the interfacial area is changing as the critical measurement is made. For example, in the drop weight or the maximum bubble pressure method, the size of the drop or bubble, and therefore the interfacial area, is continuously increasing. If the rate of change is sufficiently small, the measurement will approach that of the equilibrium condition. This is often difficult to achieve and verify, particularly for dilute solutions of highly surface-active materials, which may take a long time (hours or even days) to reach

equilibrium. With a truly static method, such as the capillary rise or Wilhelmy plate methods, one could allow the experiment to run for an indefinite amount of time in order to assure that equilibrium has been reached. For such cases, caution must be taken to ensure that evaporation of the liquid is not significant. For solutions that take a very long time to equilibrate, or for measurements at elevated temperatures near the boiling point of the liquid, the pendant or sessile bubble methods are preferred as the vapour phase is small and inherently contained. This distinction does not necessarily segregate techniques into those suited only for equilibrium surface tension measurements and those suited only for dynamic measurements, since just as dynamic methods can be used to measure the equilibrium surface tension, static methods can be used to measure the dynamic surface tension.

One should also note that techniques which require a relatively small amount of the solution of interest, which is listed as an advantage in the descriptions that follow, may pose a problem for dilute solutions of highly surface-active materials. In these cases, the adsorption of the solute at the interface may significantly lower its concentration in the bulk solution. Theoretically, one could account for this by applying the following correction:

$$C' = C - \frac{\Gamma A}{V} \quad (11.1)$$

where C' and C are the corrected and uncorrected concentrations, respectively, A is the area of the interface, V is the volume of the solution, and Γ is the amount of solute adsorbed at the interface per unit area, which can be obtained from surface tension measurements through the use of the Gibbs adsorption equation. However, there may also be a loss of material due to adsorption on to the solid walls of the vessel containing the solution which is difficult to quantify. Therefore it is typically desirable to keep $\Gamma A/CV \ll 1$ and thus avoid the need for such corrections.

The precision for all of the techniques discussed below can be very good; typically, uncertainties between 0.1 and 0.01 dyn/cm are reported, provided the appropriate correction factors are used. However, one should note that for surface or interfacial tension measurements of dilute solutions of highly surface-active materials, such as surfactants, surface-active polymers or surface-active biological materials, the presence of unknown and undesirable surface-active impurities can have a significant impact on the measured surface tension. The error introduced by these impurities is often much larger than the precision of the experimental technique.

2 CAPILLARY RISE

One of the oldest and simplest methods of measuring surface tensions is the capillary rise technique. This method utilizes the fact that when a tube is dipped into a liquid, surface tension (γ) forces cause the liquid to rise into the tube, as shown in Figure 11.1. In the less common case where the liquid does not wet the walls of the tubes, that is, the contact angle is greater than 90° , the liquid level will fall in the tube but the subsequent analysis remains the same. The liquid rises in the tube, pulled by a force in the vertical direction, given by $(2\pi r)\gamma \cos \theta$, where r is the radius of the tube and θ is the contact angle. At equilibrium, this force will be balanced by the weight of the liquid in the tube, which to a first approximation is given by $(\pi r^2)h\Delta\rho g$, where h is the height of capillary rise (measured from the minimum of the meniscus – see the following paragraph), $\Delta\rho (= \rho_1 - \rho_2)$ is the difference in density of the bottom fluid (liquid 1) and the top fluid (liquid 2 or vapour), and g is the gravitational constant. Note that in the liquid–vapour case, $\rho_1 \gg \rho_2$ and thus $\Delta\rho \approx \rho_1$. This yields the following expression for the surface tension:

$$\gamma = \frac{r\Delta\rho gh}{2\cos\theta} \quad (11.2)$$

It is important to note that with all else being equal, a smaller tube radius (r) will give a larger and more accurately measurable capillary rise (h). In addition, as will be discussed below, the ideal limit given by equation (11.2) is approached only when $r/h \ll 1$, so again a thin capillary tube is needed. Furthermore, the contact angle is usually difficult to measure; however, glass, provided it is thoroughly cleaned, is fully wetted ($\theta = 0$) by most aqueous solutions. Glass also has the advantage of being transparent so that h is easily measured. To accurately measure the capillary rise, one

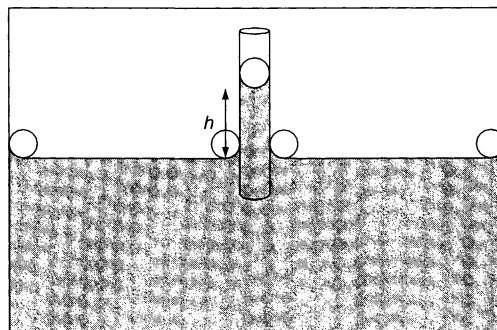


Figure 11.1. Schematic of the capillary rise method

needs a relatively large vessel holding the liquid into which the capillary tube is placed so that the meniscus formed in the vessel does not interfere with the height measurement (see Figure 11.1). Therefore, a relatively large amount of liquid is required by this method.

Since this is a very old and well-understood technique, a number of corrections to the ideal limit given in equation (11.2) have been proposed. These arise from the fact that this equation is derived by only accounting for the weight of the fluid below the apex of the meniscus. However, in theory the weight of the fluid in the meniscus (the shaded region in Figure 11.1) should also be included. The first and possibly easiest correction to implement is the polynomial expansion proposed by Lord Rayleigh (1) in 1915, given as follows:

$$\gamma = \frac{r\Delta\rho g}{2} \left(h + \frac{r}{3} + \frac{0.1288r^2}{h} + \frac{0.1312r^3}{h^2} + \dots \right) \quad (11.3)$$

By measuring h when r and $\Delta\rho$ are known, one can solve equation (11.3) by using numerical techniques to arrive at a more accurate value of γ . Note that equation (11.2) is recovered as r/h becomes vanishingly small, and all but the first terms in the left-hand side are negligible. The second term of the series in equation (11.3) provides a correction for the weight of the fluid in the meniscus, assuming it is spherical, and the subsequent terms provide corrections (obtained by solving the Young–Laplace equation in differential form) to the spherical geometry assumption. Even more accurate corrections can be obtained by a more exact solution to the Young–Laplace equation. For example, Lane (2) provides an iterative method for obtaining a corrected surface tension. A more exact numerical solution of the Young–Laplace equation can now be obtained by advanced computational techniques to determine the meniscus profile (see Section 6 below for more details), leading to an even more precise correction to the measured surface tension.

In summary, the advantages of this technique are that (i) it is relatively quick, easy, and inexpensive to set up, (ii) it is a static method (the interfacial area is not changing as the measurement occurs (see Section 1)), and (iii) although most commonly used for liquid/vapour surface tension measurements, it can also be used to measure liquid/liquid interfacial tensions. The disadvantages are that (i) a relatively large amount of the solution of interest is required, (ii) the results depend on a contact angle that is usually difficult to measure (and thus one usually must trust that it is equal to zero), and (iii) for improved accuracy, theoretical corrections to the ideal case are needed.

3 THE WILHELMY PLATE METHOD

Another classic and popular technique for the measurement of equilibrium surface tensions is the Wilhelmy plate method. This technique involves dipping a thin plate into a liquid and directly measuring the force on the plate normal to the interface. Two different approaches can be used, i.e. the plate can be left suspended, bridging the two phases, or the plate can be pulled through the interface. The former case is often used in monolayer studies with a Langmuir trough, where surface tension changes can be monitored over time, due to changes in the surface coverage and packing of surface-active molecules. Such experiments can often run for hours. In the latter case, the plate is put in contact with the interface, and is then pulled out again, which is a common technique to measure the static surface tension of liquids (for air–liquid interfaces), or for the measurement of interfacial tension (for liquid–liquid interfaces). In practice, a wire attached to a scale or balance usually suspends the plate. The solution of interest is raised so that its surface just touches the bottom of the plate (see Figure 11.2). The increase in force measured by the balance, F , can be related to the surface tension as follows:

$$\gamma = \frac{F}{P \cos \theta} \quad (11.4)$$

where P is the perimeter of the plate (approximately twice its length for a thin plate). As with the capillary rise method, the contact angle is usually difficult to measure. Often the plate is made of glass or platinum, which will be fully wetted ($\theta = 0$) if thoroughly cleaned. In this case equation (11.4) reduces to simply $\gamma = F/P$. Surface roughness is often “added” to the plate to

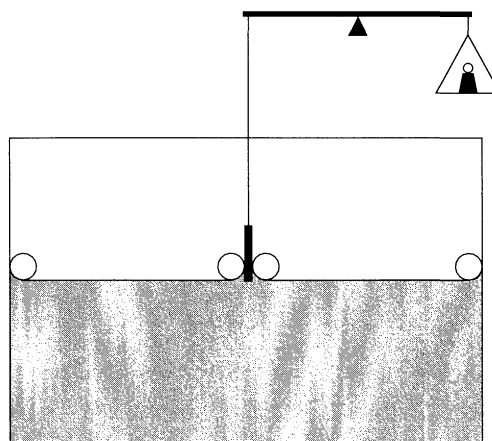


Figure 11.2. Schematic of the Wilhelmy plate method

Table 11.1. Companies manufacturing instrumentation for surface tension measurement^a

Company	Website
Cahn Instruments	www.cahn.com
Camtel Ltd	www.camtel.co.uk
DataPhysics Instruments GmbH	www.dataphysics.de
FIBRO System AB	www.fibro.se
Future Digital Scientific	www.FDSC.com
First Ten Ångströms	www.firsttenangstroms.com
Kibron Inc.	www.kibron.com
KRÜSS GmbH	www.kruss.de
KSV Instruments Ltd	www.ksvltltd.fi
Nima Technology Ltd	www.nima.co.uk
SensaDyne Instrument Division	www.sensadyne.com
SITA Messtechnik GmbH	www.sita-messtechnik.de
Surface Tensimetry, Inc.	www.tensimetry.com
Tantec Inc.	www.tantecusa.com

^aSource – *The Surfactants Virtual Library*, www.surfactants.net

ensure complete wetting. Practically, though, the contact angle is never measured, but the surface tension–force relationship is calibrated by the prior measurement of known pure liquids (water).

With the use of a modern electro-balance, very precise surface tension measurements can be obtained without the use of any theoretical corrections. This fact, along with the fact that this is a static measurement technique, makes the plate method a popular choice for precise equilibrium surface tension measurements. Note also that instrumentation which makes use of this method is readily available commercially (see Table 11.1). The disadvantages of this method are that a relatively large amount of liquid is needed.

4 THE DU NOÛY RING METHOD

In this method, a thin wire ring is inserted below the interface (which can be either a liquid–vapour or liquid–liquid interface) and held horizontal. It is then pulled up through the interface and the force required to detach it from the interface, F , is measured by a balance. The surface tension is then given by the following:

$$\gamma = \frac{F}{4\pi R} \quad (11.5)$$

where R is the radius of the ring. Note that for equation (11.5) to hold, the radius of the wire must be much smaller than the radius of the ring and that the solution must wet the wire (thus, a clean platinum wire is usually used).

This method is similar to the plate method described above, with a notable difference being the fact that it is

not truly a static method. That is, the force measurement occurs while the wire ring is moving, and thus the interfacial area is increasing throughout the process. By performing the process in a slow enough fashion, a good approximation to the equilibrium surface tension can be obtained. However, this is often difficult to achieve, particularly for dilute solutions of highly surface-active materials that may require a relatively large amount of time to reach equilibrium. In addition, for precise measurements, the use of a correction factor, f , to the ideal case is required, i.e. the surface tension can be written as $\gamma = f\gamma_{\text{obs}}$, where γ_{obs} is the observed surface tension obtained from equation (11.5). The correction factor is often given by the manufacturer of the tensiometer or can be found by using the tables given by Harkins and Jordan (3), who have tabulated this parameter as a function of R/r and R^3/V , where r is the radius of the wire and $V(= F/(g\Delta\rho))$ is the volume of the liquid raised above the free surface. The practical measurements are similar to those of the Wilhelmy plate technique, where the surface tension–force relationship is calibrated by prior measurements with known pure liquids.

In summary, the advantages of this technique are that (i) it is a classic technique for which systems are commercially available, and (ii) it can be used for liquid/vapour and liquid/liquid interfaces. The disadvantages are that (i) it is not a static technique, (ii) correction factors are usually required, (iii) a near-zero contact angle (which is difficult to observe) is essential, and (iv) a relatively large amount of the solution of interest is required.

5 THE DROP WEIGHT METHOD

Another classical method of surface tension measurement is the drop weight method, where a drop is formed and then expelled from the tip of a vertical tube by slowly pumping the liquid through the tube, as shown in Figure 11.3. Initially, when the drop is relatively small, surface tension forces hold it to the tube. As more liquid is added, the drop grows. Eventually, the weight of the drop surpasses the surface tension forces and the drop falls. By measuring the weight of the drop, one can obtain this detachment force. In the ideal limit (discussed below), the surface tension can then be calculated from the following expression:

$$\gamma = \frac{W}{2\pi r} \quad (11.6)$$

where W is the weight of the drop and r is the outer radius of the tube (if the liquid wets the tube material)

www.iran-mavad.com

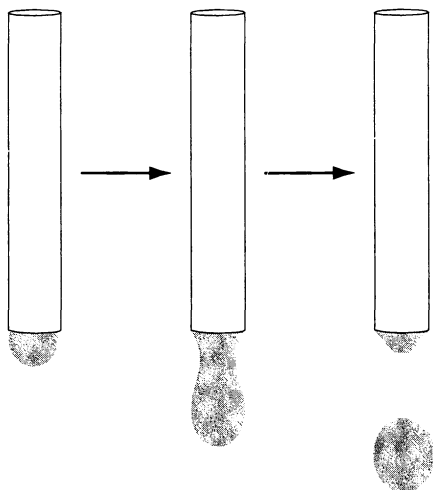


Figure 11.3. Schematic of the drop-weight method

or the inner radius (if the liquid does not wet the tube). In practice, to improve the accuracy, one usually measures the combined weight of several drops and then W is given by the total weight divided by the number of drops. This method can also be used to measure interfacial tensions by immersing the tip in another liquid. In this case, the volume of the drop, V , is usually measured, with the weight being given by $\Delta\rho gV$. Note that as with the ring method described above, this technique is not a static measurement, as the interfacial area is increasing as the drop is formed. An approximation to the true equilibrium is obtained only if the drop is formed at a sufficiently slow rate.

For precise measurements, the use of a correction factor is extremely important when using this method. That is, the surface tension can be written as $\gamma = \gamma_{\text{obs}}/f$ where γ_{obs} is the observed surface tension obtained from equation 11.6 and f is a correction factor (defined in this manner so that $f < 1$). The need for this correction factor arises from the fact that a portion of the liquid contained in the drop remains attached to the tube when the drop detaches itself (as shown schematically in Figure 11.3), and thus the measured drop weight is less than the actual drop weight. Values of this correction factor have been empirically tabulated as a function of $r/V^{1/3}$ by Harkins and Brown (4), as well as Lando and Oakley (5).

In summary, the advantages of this technique are that (i) it is relatively quick, easy, and inexpensive to set up, (ii) a relatively small amount of material is needed, (iii) the results do not depend on a difficult-to-measure contact angle, and (iv) it can be used to measure both

liquid/vapour and liquid/liquid interfacial tensions. The disadvantages are that (i) an important correction factor is needed for accurate results, and (ii) the method is not a static one.

6 PENDANT/SESSILE DROP AND BUBBLE METHODS

A number of surface or interfacial tension measurement techniques rely on the geometric analysis of the interface formed by a drop or bubble. This analysis can be performed on a drop of liquid surrounded by a vapour (or less dense liquid), or a bubble of vapour (or less dense liquid) surrounded by a more dense liquid. The drop or bubble can take either a pendant (hanging) or sessile geometry form (see Figure 11.4). To simplify the analysis, axial symmetry is highly desired. This is easily accomplished in the pendant geometry case by the use of a circular, horizontal tip. It is more difficult to obtain in the sessile geometry situation, but can be accomplished primarily by using a smooth, flat and thoroughly cleaned solid surface. The drop or bubble is then photographed and digitized to obtain the profile of the interface. Note that only a two-dimensional image is required since the drop or bubble is cylindrically symmetric.

The key to all shape techniques is that a balance between the counteracting forces dictates the

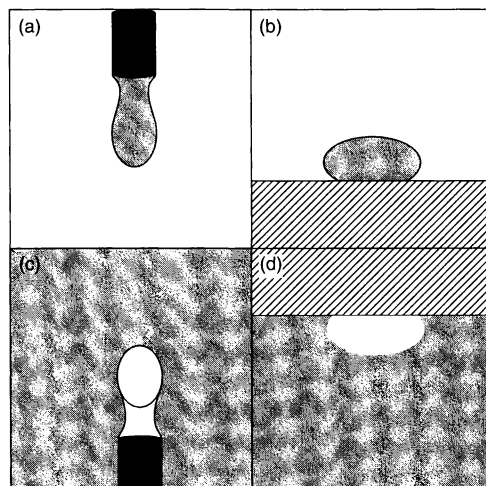


Figure 11.4. Schematics of the various shape methods: (a) the pendant drop method; (b) the sessile drop method; (c) the pendant bubble method; (d) the sessile bubble method. In all cases, the shaded areas represent the denser fluids, while the white areas represent air (in the case of liquid–air interfaces) or the less dense fluid (in the case of liquid–liquid interfaces)

shape or profile of the interface, i.e. (i) surface forces, which drive towards a perfectly spherical shape, and (ii) gravity, which drives towards a more (in the pendant geometry) or less (in the sessile geometry) elongated shape. An important parameter in these techniques is the Bond number, B , which represents the ratio of body forces (in this case gravitational) to surface forces, defined by the following:

$$B = \frac{\Delta\rho g r^2}{\gamma} \quad (11.7)$$

where r is the length scale of the drop or bubble (often taken to be the radius of curvature at the drop or bubble apex). Typically, a bond number near unity is desired since these techniques rely on competition between body and surface forces.

For a given value of B , one can predict the shape of the interface by solving the Young–Laplace equation in differential form (where the boundary conditions are specific to each geometry). One can then determine the surface or interfacial tension, γ , by finding the value of B which best matches the measured profile and by directly measuring r . A number of simplified, approximate technique were developed that do not require the entire profile to be matched. However, these approximations are less practical now that high-speed computers can be used to efficiently solve for the profile (see for example, Rotenberg *et al.* (6) and Cheng and Neuman (7)). This technique has become quite popular in recent years with the advent of inexpensive digital cameras for the acquisition of the interfacial profile, thus providing the data needed for the numerical analysis of the Young–Laplace equation. Several commercially produced tensiometers are available which use this technique (see Table 11.1).

There are various significant advantages for using this techniques. It is truly a static technique in that once equilibrium is reached, the interfacial area *does not change*. In particular, it is easy to control evaporation with these methods, so that one can study solutions which take a very long time to reach equilibrium, or volatile solutions (for example, aqueous solutions at a temperature near 100°C). For the drop methods, only a very small amount of liquid is needed, i.e. just enough to form one drop. However, as discussed above, for dilute solutions of highly surface-active materials, the depletion of the bulk solution concentration due to interfacial adsorption may be a problem and therefore, in such cases, the bubble methods, with a relatively large reservoir of liquid, are preferred. For pendant drops or bubbles, the results do not necessarily depend on a contact angle. For sessile drops or bubbles, a

contact angle can be used as a boundary condition to the Young–Laplace equation, but this can easily be obtained from the imaged profile. Alternatively, one can analyse only the profile above (for the sessile drop) or below (for the sessile bubble) the equatorial plane and thus avoid the region of contact between the interface and the solid. Finally, these techniques can be used for both liquid/vapour and liquid/liquid interfacial tensions. The primary disadvantage to these techniques is that they are more difficult to set up compared to the other methods. However, this disadvantage is somewhat diminished now that commercial instruments are readily available.

7 THE SPINNING DROP METHOD

A different shape method to the ones described above is the spinning drop method, used for the measurement of ultra-low interfacial tensions. Here, two immiscible liquids are placed in a vessel, which is rotated, as shown in Figure 11.5. The centrifugal force resulting from the rotation causes the less dense liquid to collect at the centre and form the “drop”. As in the previous shape methods, there is a balance of forces, but here the interfacial forces balance the centrifugal force. As with the other shape methods described in Section 6, an image of the interface is taken and the Young–Laplace equation is used to determine the interfacial tension, which provides the best match between the theoretical and measured profile. For nearly cylindrical drops, the following approximate expression is often used:

$$\gamma = \frac{\omega^2 r^3 \Delta\rho}{4} \quad (11.8)$$

where r is the radius of the drop and ω is the rotation rate. Practically, the ratio of the elongated length to the width of the drop as a function of rotation speed is correlated to the surface tension.

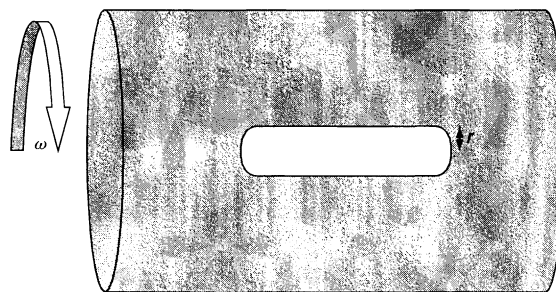


Figure 11.5. Schematic of the spinning drop method; note that the white region in the centre represents the less dense fluid, which is surrounded by the more dense fluid (shaded region)

The primary advantage of this method over the other shape techniques given in Section 6 is that for pendant or sessile drops or bubbles of a given size, the gravitational force cannot be adjusted, where as for a spinning drop the centrifugal force can be adjusted by varying the rotational frequency. As a result, this technique can be used to measure extremely low interfacial tensions (as low as 0.001 dyn/cm). In order to measure these extremely low interfacial tensions with the techniques described in Section 6, one would have to use an extremely small bubble or drop size to maintain a balance between body and surface forces. However, there is a practical limit to the size of a bubble that can be photographed and thus there is a practical limit to the values of the interfacial tensions that can be measured in this way. For the spinning drop method, the ability to vary the body force overcomes this limitation.

In theory, liquid/vapour measurements can be made by using this approach, where a vapour bubble replaces the less dense liquid drop. However, this would be rarely done for such measurements due to the difficulty of implementation, as discussed below. As with the other shape techniques described above, this is a static measurement and only small amounts of the liquids of interest are required. The primary disadvantage to this technique is that it is very difficult to set up and perform. Thus, this approach is usually only used to make measurements of extremely low interfacial tensions, where it would be the only reliable method available.

8 THE MAXIMUM BUBBLE PRESSURE METHOD

Although more often used to measure dynamic surface tensions (and thus is discussed in more detail in the following chapter), the maximum bubble pressure method can also be used to measure equilibrium surface tensions. With this technique, a tube or needle is immersed in the liquid and bubbles of vapour are continuously blown through it. If a needle with a small enough radius is used, such that the Bond number is much less than unity, the bubble will be approximately spherical and the radius of curvature will be at a minimum exactly when the bubble is a hemisphere of radius r (where r is the inner radius of the needle if the solution wets the needle, or the outer radius if it does not). By using the Young-Laplace equation, one can then determine that the pressure will be at a maximum at this point, and the surface tension is thus given by the following

expression:

$$\gamma = \frac{r \Delta P_{\max}}{2} \quad (11.9)$$

where $\Delta P = P_{\text{bubble}} - (P_{\text{air}} + \Delta \rho gh)$ (h is the depth to which the needle is submerged). Correction factors have been introduced, particularly to account from the deviations from spherical geometry caused by gravity/buoyancy (see the following chapter). As with some of the detachment force methods, this is not truly a static measurement and thus equilibrium is only approximated by blowing the bubbles through at a slow enough rate. Again, as a practical matter, the ratio between the surface tension and the voltage given by the bubble pressure transducer is calibrated for a pure liquid (which will have no dynamic aspect to its surface tension). A two-point calibration with two known liquids is often sufficient for accurate measurements of surfactant-containing solutions.

The advantages of this method include the following: (i) it is relatively easy and inexpensive to set up (and commercial systems are available), thanks to the advent of inexpensive electronic pressure transducers; (ii) it can be used in extreme environments, such as to measure the surface tension of molten metals, where it would be difficult to image the bubble interface, needed for use in the shape methods and where it would also be difficult to obtain a plate, ring or capillary tube made of suitable materials; (iii) the results do not depend on a difficult-to-measure contact angle; (iv) a relatively small amount of material is needed; (v) in theory, this technique can be applied to liquid/liquid interfaces. The main disadvantage to this technique is that it is not truly a static measurement, as discussed above in Section 1.

9 CONCLUSIONS

As can be seen from this brief review, the measurement of static surface tension is a well-established area, and there are many techniques available for this purpose. As a practical matter, many commercial instruments are now available for carrying out such measurements. In addition, several of the techniques can also be performed in the laboratory without resort to the use of any specialized instrumentation.

10 REFERENCES

1. Lord Rayleigh, O. M., On the theory of the capillary tube, *Proc. R. Soc. London, A*, **92**, 184-195 (1915).

2. Lane, J. E., Correction terms for calculating surface tension from capillary rise, *J. Colloid Interface Sci.*, **42**, 145–149 (1973).
3. Harkins, W. D. and Jordan, H. F., A method for the determination of surface and interfacial tension from the maximum pull on a ring, *J. Am. Chem. Soc.*, **52**, 1751–1772 (1930).
4. Harkins, W. D. and Brown, F. E., The determination of surface tension (free surface energy), and the weight of falling drops: the surface tension of water and benzene by the capillary height method, *J. Am. Chem. Soc.*, **41**, 499–524 (1919).
5. Lando, J. L. and Oakley, H. T., Tabulated correction factors for the drop-weight–volume determination of surface and interfacial tensions, *J. Colloid Interface Sci.*, **25**, 526–530 (1967).
6. Rottenberg, Y., Boruvka, L. and Neuman, W., Determination of surface tension and contact angle from the shapes of axisymmetric fluid interfaces, *J. Colloid Interface Sci.*, **93**, 169–183 (1983).
7. Cheng, P. and Neuman, A. W., Computational evaluation of axisymmetric drop shape analysis–profile (ADSA-P), *Colloids Surf.*, **62**, 297–305 (1992).

CHAPTER 12

Measuring Dynamic Surface Tensions

Reinhard Miller[†], Valentin B. Fainerman[‡], Alexander V. Makievski[‡], Michele Ferrari[§], and Giuseppe Loglio[¶]

[†]Max-Planck-Institute of Colloids and Interfaces, Golm, Germany [‡]Donetsk Medical University, Donetsk, Ukraine [§]CNR–Istituto di Chimica Fisica Applicata dei Materiali, Genova, Italy [¶]University of Florence, Florence, Italy

1	Introduction	225	5	Drop Volume Technique	230
2	Dynamic Surface and Interfacial Tension Methods	226	6	Drop and Bubble Shape Tensiometry	232
3	Maximum Bubble Pressure Tensiometry	227	7	Drop and Bubble Pressure Techniques	234
4	Oscillating Jet Method	229	8	Ring and Plate Tensiometry	236
			9	Acknowledgements	237
			10	References	237

1 INTRODUCTION

Surfactants and other surface-active molecules, such as polymers, and in particular proteins, change and sometimes even provide completely new properties to interfaces. This is caused by the capability of such molecules to adsorb at interfaces. The process of adsorption has been described in general elsewhere in this present text. Several of the chapters deal with the characteristic properties of surface-active molecules, both in the bulk and at interfaces, so such aspects will not be touched upon here.

While in the previous chapter, methods have been described for the measurement of equilibrium surface tensions, in the present one methods have been discussed which are particularly suited for the study of interfaces under dynamic conditions. As we have seen from the interfacial thermodynamics, the amount of a surfactant adsorbed at an interface is in correlation with the interfacial tension. This relationship holds also usually under non-equilibrium conditions, starting with the creation of a freshly formed surface (bare of any adsorbed molecules) until the establishment of the equilibrium

state of the interfacial layer. If this is true, the adsorbed amount $\Gamma(t)$ at an interface can unambiguously be determined from the measured interfacial tension γ with time, as follows:

$$\Gamma(t) = -\frac{1}{RT} \frac{d\gamma(t)}{d \ln c(0, t)} \quad (12.1)$$

where R and T are the molar gas constant and temperature, respectively, and $c(0, t)$ is the concentration of the surfactant in the so-called sub-surface, i.e. the bulk phase localized immediately adjacent to the interface.

This form of the Gibbs fundamental equation demonstrates the importance of surface and interfacial tension measurements of interfacial layers out of the adsorption equilibrium. These methods are the most frequently used techniques to follow the time-dependence of the adsorption process. However, for very slow processes, which occurs in systems with extremely small amounts of surfactants, other methods such as the radio-tracer technique and ellipsometry, or the very recently developed technique of neutron reflectivity, can be used to directly follow the change of surface concentration with time.

This present chapter will present a subjectively selected number of methods designed to measure the surface and interfacial tension as a function of time. Each of the methods has its own particular "time window", which partly overlaps with the others. One has to mention here that none of the methods can cover the entire time interval of interest. Moreover, only a few of the methods are applicable to both liquid/gas and liquid/liquid interfaces.

2 DYNAMIC SURFACE AND INTERFACIAL TENSION METHODS

The surface activity of surfactants varies over a broad concentration range and hence a broad time interval has to be studied in order to obtain the complete dependence $\gamma(t)$. Therefore, complementary experiments are necessary to cover the extensive time range from less than one millisecond up to minutes, hours and sometime even days. While it seems possible to easily expand the range of application to longer times, it is extremely difficult to improve the existing measurement techniques such that times actually shorter than 100 microseconds can be reached reliably.

Table 12.1 demonstrates that a set of methods is needed in laboratories where the study of dynamic tensions is the main research topic. The given values represent the interval available by standard instruments, while particular modifications certainly allow us to go beyond these limits. Some of these methods belong to the group of "classical techniques", and have already been used for a long time, while others have been developed only recently. It is most important to note that several of

the methods are available in the form of commercial instrumentation, so that such methods can be easily used for standard investigations. For some of the methods, international norms (standards) exist and thus the results obtained can be compared directly. The comparison of dynamic surface tension methods is rather complex due to the following fact. All dynamic methods working at short adsorption times require a particular measurement procedure, which is typically of a very dynamic character. In the maximum bubble pressure method, for example, bubbles are formed with as high a frequency as possible. The important point of the measurement here is when the bubble exceeds the size of a hemisphere, as at this particular moment the capillary pressure is at a maximum. In the drop volume method, however, the volume is measured for the drops detaching themselves from a capillary of a given diameter. Here, the moment of drop detachment gives the measurement information. For each dynamic method, such peculiarities exist and for direct comparison of different methods the concept of the so-called effective time t_{eff} was developed by Joos (1). On this scale, all methods can be directly compared with each other by simply recalculating the experimental time "into" t_{eff} .

There are surface or interfacial tension methods for liquid systems, which cover quite a wide range of time. In many cases, however, several methods are required in order to produce the complete time-dependence of surface tension of a surfactant system. The following sections will briefly present the most frequently used methods for measuring dynamic surface and interfacial tensions, while the physical principles and a typical experimental set-up, as well as some experimental examples, will also be given.

Table 12.1. Overview of the methods available for measuring dynamic surface and interfacial tensions

Method	Suitable for l/l interface	Suitable for l/g interface	Time range	Temperature range (°C)
Capillary rise	Possible	Good	10 s–24 h	20–25
Drop volume ^a	Good	Good	1 s–1000 s	10–90
Growing drop/bubble	Good	Good	0.01 s–600 s	10–90
Inclined plate	Problematic	Good	0.1 s–10 s	20–25
Maximum bubble pressure ^a	Possible	Good	0.1 ms–10 s	10–90
Oscillating jet	Problematic	Good	0.001 s–0.02 s	20–25
Oscillating bubble	–	Good	0.01 Hz–500 Hz	20–90
Oscillating drop	Good	–	0.01 Hz–10 Hz	20–90
Pendent drop/bubble ^a	Good	Good	10 s–24 h	20–90
Plate tensiometer ^a	Possible	Good	10 s–24 h	20–45
Ring tensiometer ^a	Problematic	Good	30 s–24 h	20–45
Sessile drop ^a	Possible	Possible	10 s–24 h	10–90
Spinning drop ^a	Good	Possible	–	10–90
Static drop volume ^a	Good	Good	10 s–1000 s	10–90

^aMethods where commercial instruments are available. [iran-mavad.com](http://www.iran-mavad.com)

3 MAXIMUM BUBBLE PRESSURE TENSIOLOGY

In 1851, Simon proposed the maximum bubble pressure method for surface tension measurements of liquids. At this time, due to technical difficulties, this method was believed to be unreliable. During the last 20 years, however, many publications on theoretical and experimental aspects have made bubble pressure tensiometry the most frequently used method for very short adsorptions, i.e. times from a few milliseconds to several seconds. One of the advantages of this technique is the small amount of liquid required for the measurements, which is particularly important in studies of biological liquids (2).

Since precise electrical pressure transducers have been introduced, the progress in designing commercial instruments has been tremendous, with instrumentation available now from several producers. In a recent book, the principles of bubble pressure tensiometry and the theoretical background to this technique have been summarized by Fainerman and Miller (3). As an example, the maximum bubble pressure tensiometer MPT2 from Lauda is shown schematically in Figure 12.1. This device has some peculiarities, which are of great advantage for measurements in the short-time range. As it was possible to demonstrate recently, a special design of the capillary allows this instrument to reach effective adsorption times of the order of 100 microseconds, and

maybe even shorter. The functioning of this instrument is different from most of the common bubble pressure instruments. Due to the rather large internal gas volume (about 35cm³), an easy procedure for determining the effective adsorption time at the moment of maximum pressure could be derived. The surface tension γ can be calculated from the measured maximum capillary pressure P and the known radius r_{cap} of the capillary by using the Laplace equation in its simplified form for spherical bubbles, as follows:

$$\gamma = \frac{r_{\text{cap}} P}{2} \quad (12.2)$$

If the bubble dimension is larger and deviates from a spherical shape, a correction factor has to be added to the equation. This correction factor f , available either as a table or as a polynomial equation, is needed only when the capillary radius $r_{\text{cap}} > 0.2$ mm.

The measured capillary pressure, P , can be expressed via the excess maximum pressure in the measuring system, P_s , the hydrostatic liquid pressure, $P_H (= \Delta \rho g H)$, and an excess pressure, P_d . The excess pressure P_d results between the measuring system and the bubble due to dynamic effects, such as the aerodynamic resistance of the capillary, viscous and inertia effects in the liquid, etc; $\Delta \rho$ is the difference between the densities of the liquid and the gas, g is the gravitational constant and H is the immersion depth of the capillary into the liquid. Therefore, we have the following:

$$\gamma = \frac{r_{\text{cap}}}{2} (P_s - P_H - P_d) \quad (12.3)$$

In order to reach extremely short adsorption times in the millisecond and sub-millisecond ranges, we have to use short and wide capillaries so that the ratio $P_d/P \leq 0.02$.

In order to calculate the effective adsorption time t_{eff} , an exact determination of the so-called "deadtime" t_d is required (the time between the moment of maximum pressure and the detachment of the bubble). The Poiseuille approximation yields the following (3):

$$t_d = t_b \frac{L}{k_p P} \left(1 + \frac{3}{2} \frac{r_{\text{cap}}}{r_b} \right) \quad (12.4)$$

where k_p is the Poiseuille equation constant for a capillary not immersed in the liquid ($L = k_p P$), L is the gas flow rate, $P = P_s - P_H$, and t_b is the time interval between two successive bubbles of radius r_b . From the lifetime, which is the time period between the moment of bubble detachment and the formation of a new bubble, and the moment of maximum pressure, $t = t_b - t_d$, the effective surface age t_{eff} can be calculated

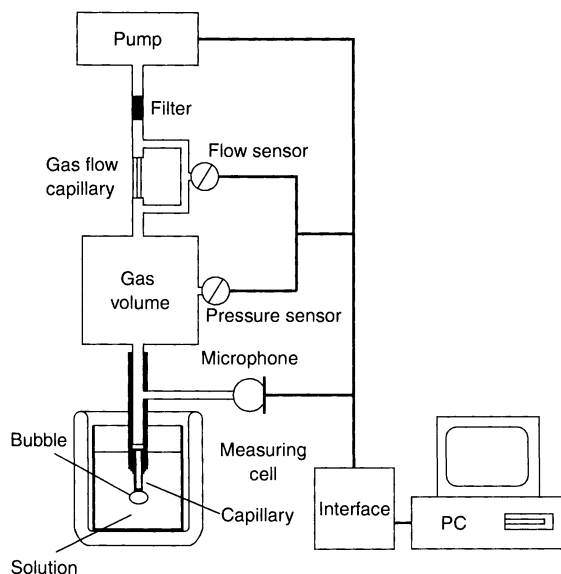


Figure 12.1. Schematic of a maximum bubble pressure tensiometer (MPT2, LAUDA, Germany)

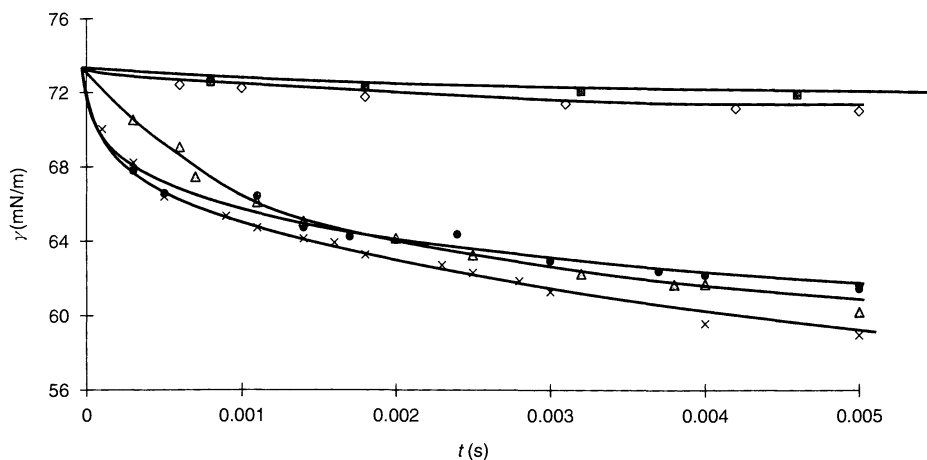


Figure 12.2. Dynamic surface tensions of different aqueous “Triton X-*n*” solutions as measured by the maximum bubble pressure method (MPT2, Lauda, Germany): ■, X-100, $c_0 = 1.55 \times 10^{-7}$ mol/cm³; ♦, X-114, $c_0 = 4.23 \times 10^{-7}$ mol/cm³; ●, X-165, $c_0 = 1.07 \times 10^{-6}$ mol/cm³; ▲, X-305, $c_0 = 4.52 \times 10^{-7}$ mol/cm³; ×, X-405, $c_0 = 5.08 \times 10^{-7}$ mol/cm³

via the following relationship:

$$t_{\text{eff}} = \frac{t}{2\alpha + 1} \quad (12.5)$$

This equation is only an approximate description, since a rigorous treatment of the problem shows that α is not a constant (with the value 2/3) but a function of a number of parameters (3).

As mentioned above, the maximum bubble pressure method provides dynamic surface tension data at the shortest adsorption times. By choosing optimum conditions, values for the adsorption times as short as a few hundred microseconds can be obtained. On the other hand, this method yields results only for adsorption times not longer than about 10 seconds. In Figure 12.2, an example is given for solutions of members of the nonionic surfactant series “Triton X-*n*,” where *n* represents different numbers of oxyethylene groups. The concentrations have been chosen such that data in the time interval from 100 μs to few milliseconds can be shown. Typically, with this range of short adsorption times, the MPT2 tensiometer covers almost six orders of magnitude of time, and is hence suitable for measuring the entire process of adsorption, starting from a bare surface with the surface tension of pure water and levelling off at the equilibrium surface tension value. As an example of such long time dependencies, the dynamic surface tensions of three sodium dodecyl sulfate (SDS) samples in the presence of 0.5 mol NaCl are shown in Figure 12.3. One can see that for these concentrations, neither do the surface tension curves, $\gamma(t_{\text{eff}})$, at short times start at the value of water, nor

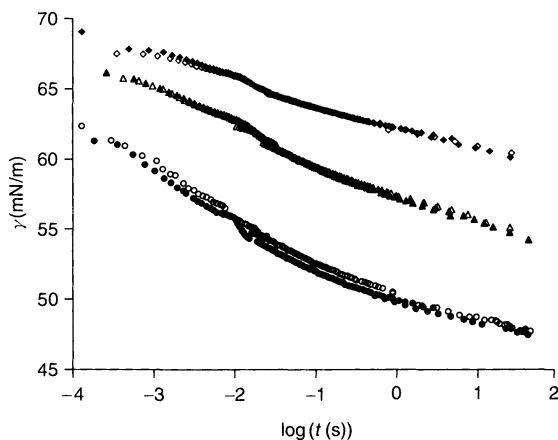


Figure 12.3. Dynamic surface tensions of three aqueous solutions of SDS, as measured by the maximum bubble pressure method (MPT2, Lauda, Germany): ■, $c_0 = 2 \times 10^{-6}$ mol/cm³; ♦, $c_0 = 3 \times 10^{-6}$ mol/cm³; ▲, $c_0 = 5 \times 10^{-6}$ mol/cm³; the open and filled symbols refer to different experimental runs

are the equilibrium values reached after long adsorption times, $t_{\text{eff}} > 50$ s. This example demonstrates, impressively, that one experimental method, although covering six orders of magnitude of time, is insufficient to study the entire adsorption dynamics of these surfactants solutions. Recalculation of the dynamic surface tension curves, $\gamma(t)$, into the adsorption as a function of time, $\Gamma(t)$, via equation (12.1) allows us to compare the experimental data with theoretical models. We cannot go here into details of adsorption kinetics models

and refer only to the book by Dukhin *et al.*, where a comprehensive discussion is given (4). Just as a very brief explanation of the idea, the adsorption process is controlled by molecular diffusion in the bulk. The classical model describing this process is the Ward and Tordai equation (5), which is the fundamental relationship for all diffusion-controlled adsorption models, and is given as follows:

$$\Gamma(t) = 2\sqrt{\frac{D}{\pi}} \left[c_0\sqrt{t} - \int_0^{\sqrt{t}} c(0, t - \tau) d\sqrt{\tau} \right] \quad (12.6)$$

where D is the diffusion coefficient, c_0 is the surfactant bulk concentration and $c(0, t)$ is the so-called sub-surface concentration. Procedures to solve this equations have been also shown in ref. (4); however, most of these are very cumbersome. For low concentrations, i.e. when a linear adsorption isotherm can be used to describe the relationship between adsorption and bulk concentration, $\Gamma = K \times c$, a simple analytical solution was derived by Sutherland (6), as follows:

$$\Gamma(t) = \Gamma_0[1 - \exp(Dt/K^2)\text{erfc}(\sqrt{Dt}/K)] \quad (12.7)$$

Via the Gibbs equation (equation (12.1)), we obtain a relationship which can be used to directly compare the theory with experimental results, as follows:

$$\gamma(t) = \gamma_0 - RT\Gamma_0[1 - \exp(Dt/K^2)\text{erfc}(\sqrt{Dt}/K)] \quad (12.8)$$

The parameters with the subscript "0" are the surface tension of the bare surface (γ_0) and the equilibrium adsorption (Γ_0).

The maximum bubble pressure technique has been developed in various directions over recent years. One of the most promising of these is the use of this measurement technique in medicine. In a recent book, the capacity of dynamic surface tension measurements is shown as a new diagnostic tool, as well as for monitoring therapies in medicine (2). Quite a number of statistically significant relationships between selected surface tension values and biochemical data have been proven to exist.

An example is shown in Figure 12.4, where the dynamic surface tension data of four different human liquids from patients suffering from various diseases are displayed. The curves start at about 10 ms, because for the study of highly concentrated solutions (such as blood) capillaries of larger diameter are used to avoid experimental problems (blocking of the capillary by clots, etc.). This, however, simultaneously means that measurements in the time range of milliseconds and below are impossible. The results show that the curves

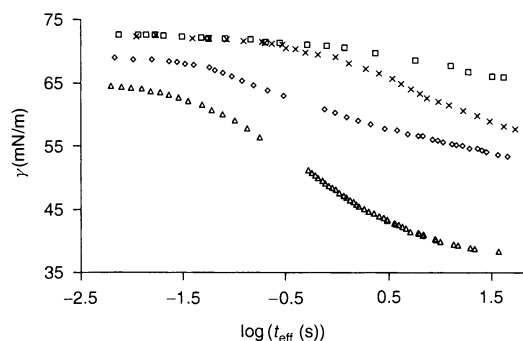


Figure 12.4. Dynamic surface tensions as a function of $\log t$ for various biological liquids: \times , serum of a 49 years old patient suffering from acute kidney insufficiency; Δ , gastric juice of an 18 years old patient suffering from gastric ulcer; brain \square , liquor of a 13 year old patient suffering from cerebrospinal encephalitis; \diamond , urine of a 49 years old patient suffering from chronic nephritis

start at different values, which is certainly caused by the electrolyte content. The time at which $\gamma(t)$ starts to decrease strongly is a measure of the total contents of surface-active compounds, such as proteins and low-molecular-weight surface-active molecules. The higher this concentration, then the earlier the strong decrease of $\gamma(t)$ will set in. Finally, the value at which the curves level off is a measure of the composition of the surface-active compounds. The larger the protein content, then the higher is this value. A comprehensive and more detailed discussion is given in ref. (2).

4 OSCILLATING JET METHOD

The method of the oscillating jet is one of the oldest experiments for determining the surface tension of liquids. In this technique, a horizontal liquid jet is issued from the orifice of an elliptic capillary with a small eccentricity. The schematic design is shown in Figure 12.5. The container is designed such that the liquid level is constant over the whole experiment. The velocity of the liquid flow is then only controlled by the height difference between the liquid level and the capillary. One of the parameters to be measured is shown in the magnified part on the right-hand side of the figure, i.e. the wavelength of the oscillating jet, λ , and the amplitude, which is given by the difference between the two radii, $b = r_{\max} - r_{\min}$. The operation of the experiment is extremely easy; however, the accurate determination of the important parameters is very difficult.

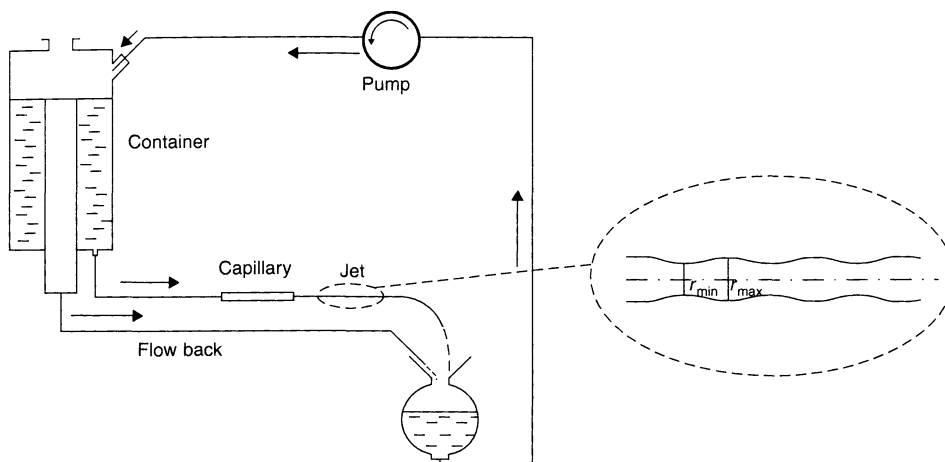


Figure 12.5. Schematic of the set-up used for the oscillating jet method; further details are given in the text (according to Joos (1))

The theory for this hydrodynamic problem was given first by Bohr (7), leading finally to the following complex relationship:

$$\gamma = \frac{4\rho F^2}{6a\lambda^2} \frac{1 + \left(\frac{37b^2}{24a^2}\right)}{1 + \frac{5}{3}\left(\frac{\pi^2 a^2}{\lambda^2}\right)} \left[1 + 2\left(\frac{\eta\lambda}{\rho F}\right)^{3/2} + 3\left(\frac{\eta\lambda}{\rho F}\right)^2 \right] \quad (12.9)$$

where a is the average radius of the jet, ρ and η are the density and viscosity, respectively, of the liquid, and F is the flow rate. The terms in brackets correct for the viscosity effect and are usually small, and hence negligible (1).

The length λ and the amplitude b of the wave depend on the surface tension γ . As the age of the jet is a function of the distance from the orifice, this method should be suitable for measuring the dynamic surface tension of solutions in the range of short adsorption times.

For pure liquids with a constant surface tension, the measured tension depends on the distance from the orifice, and is higher than the static value. Since a dynamic surface tension for pure liquids does not really make sense(!), this is certainly an artifact. It is only at longer distances from the orifice that the surface tension becomes equal to the static value, and therefore the shorter adsorption times must be discarded and cannot be used for adsorption dynamics studies of solutions containing surfactants.

In order to determine dynamic surface tensions with the oscillating jet method we can consider that at the orifice of the jet a new surface is created. By travelling along the jet, the surfactant is adsorbed, thus giving rise to a decrease in surface tension. The age of the surface, t , corresponding to the surface tension at a distance z from the orifice is $t = z/v_z$, where $v_z = F/\pi a^2$ is the mean jet velocity. Hence, to obtain the dynamic surface tension with time one has to measure the flow rate F , the distance from the orifice z , the mean radius of the capillary, and the length λ and amplitude b of the wave. Problems of convection inside the jet, which causes changes in the surfactant transport and Marangoni flow on the jet surface, thus affecting the effective surface age, are discussed in ref (1). A comparison of the jet method with the maximum bubble and inclined plate methods is given in ref. (4) and shows that the method does provide dynamic surface tension data over an interesting and useful time interval. As this interval is very narrow and commercial instrumentation for this method is not available, it is less popular these days. Note that the technique of maximum bubble pressure tensiometry covers the time window of this method completely.

5 DROP VOLUME TECHNIQUE

Drop volume tensiometry is one of the oldest available methods for measuring surface and interfacial tensions between two fluids. The first rather primitive design for this method is the so-called "stalagmometer", consisting

of simply counting the number of drops formed from a definite liquid volume which detach themselves from a capillary of given diameter. This drop number is then compared with the numbers obtained for liquids of known interfacial tension. The stalagmometer method is still used in many laboratories for a first quick estimation of the interfacial tension of liquids. Apparatus required can be easily built from standard equipment available in the laboratory.

Lohnstein had already established the theoretical basis of the drop volume method at the beginning of this century (cf. ref. (3)). This method is now one of the most frequently used techniques. Modern commercial devices, based on the drop volume principle, have many advantages when compared with other commercial surface tension instruments, namely easy handling, easy temperature control over a wide range, application to all liquid/fluid interfaces without any modifications, and no disturbing wetting effects. It is essentially comparable with the drop shape methods with respect to advantages, but has the important disadvantage of a comparatively short surface age available by such experiments. Due to easy handling, it is, however, the most frequently used method for dynamic interfacial tension measurements.

In the drop volume technique, the size of a drop formed at the tip of a capillary with a diameter of $2r_{\text{cap}}$ has to be determined accurately, which is typically realized by means of a precise dosing system. In Figure 12.6, the principle of the drop volume technique is shown. The motor controller–encoder system linked to the syringe provides a constant and accurate dosing

rate, while the light barrier is used to detect the detaching drops. In this way, the time between two detaching drops is measured. This time, multiplied by the dosing rate, then gives the volume of a detaching drop.

In such an instrument, the dosing system and the light barrier are linked via an interface to the serial port of a standard computer, which controls the complete measurement sequence and then calculates the interfacial tension values according to the theory. Due to the force balance between the acceleration due to gravity and the interfacial tension, the volume of a detaching drop correlates directly with the interfacial tension γ and the density difference $\Delta\rho$ of the two adjacent phases, and is given by the following:

$$2\pi r_{\text{cap}}\gamma \sim V\Delta\rho g \quad (12.10)$$

The interfacial tension γ acts along the circumference of the drop $2\pi r_{\text{cap}}$ and counter-balances the force $V\Delta\rho g$, where V is the volume of the drop and g is the acceleration due to gravity. As the drop does not detach directly at the tip of the capillary, but at its neck, equation (12.10) needs to be corrected by a factor f , available as a polynomial equation (3), giving the following:

$$\gamma = \frac{\Delta\rho g V}{2\pi r_{\text{cap}} f} \quad (12.11)$$

When the drops are formed very fast, i.e. less than 10 s per drop, additional hydrodynamic effects appear which simulate slightly higher interfacial tension values. This so-called “hydrodynamic effect” can be corrected by multiplying the apparent value of γ with the factor $[1 - (\alpha + \beta r_{\text{cap}}/t)]$ to obtain the correct surface tension value; α and β are constants valid for liquids of low viscosity – $\alpha = 0.008$ s and $\beta = 0.041$ s/mm (8).

For extremely short drop times and comparatively large capillary diameters, some unexpected irregularities have been observed. The measured drop volumes are then no longer proportional to the surface tensions but show various oscillatory behaviours. Thus, measurements in this short drop time range should be avoided.

The effective surface age has been determined on the basis of a diffusion-controlled adsorption model. Similar to the maximum bubble pressure technique, where the bubble time t is about 3/2 times longer than t_{eff} , the drop formation time t is also significantly longer than the effective surface age t_{eff} and can be obtained as $t_{\text{eff}} = 3t/7$ (see, for example, ref. (3)). This estimation assumes a radial flow both inside and outside the growing drop and a homogeneous expansion of the drop surface.

The drop volume technique, as is implemented in the TVT2 instrument from LAUDA, also allows

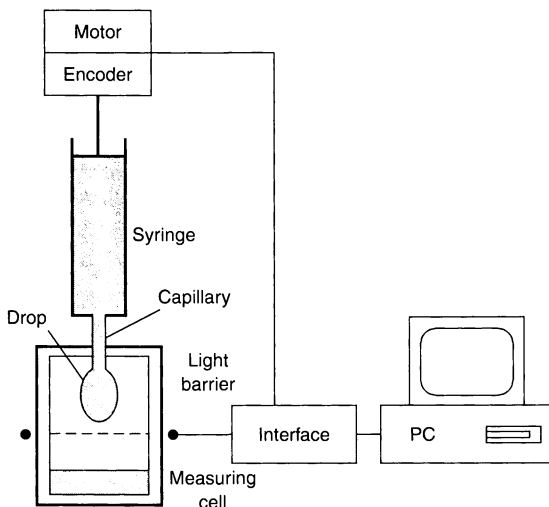


Figure 12.6. Schematic of an automated drop volume instrument (TVT2, LAUDA, Germany)

measurements in the so-called “quasi-static mode”. In the latter, each drop is formed quickly and is then kept constant and the time measured until it falls off of the capillary, due to the decrease in surface tension, i.e. reaching the critical weight. This measurement mode, first used by Addison, directly yields surface tension values, $\gamma(t)$, as a function of time $t = t_{\text{eff}}$. Compared to data obtained in the so-called dynamic mode, i.e. with continuously growing drops, the rate of decrease in surface tension should be 7/3 times faster.

An example of typical data obtained from a drop volume experiment is given in Figure 12.7, where the surface tension is plotted as a function of $1/\sqrt{t_{\text{eff}}}$. It is evident that the higher concentration of the surfactant diethyl decyl phosphine oxide leads to a faster decrease in $\gamma(t)$. In addition, the equilibrium values to which the curves are extrapolated at infinite time are lower with increasing concentration. Thus, the particular plot of γ against $(1/\sqrt{t_{\text{eff}}})$ provides a possibility for estimating the equilibrium surface tensions via extrapolation to $t \rightarrow \infty$. As mentioned above, the two modes of the drop volume technique, i.e. the dynamic and the quasi-static modes, yield results on different time scales. In Figure 12.8, results obtained in experiments for the two measurement modes are plotted. As can be seen, there is a difference between the two sets of measurement points. When we recalculate the effective surface age from the dynamic measurements via the relationship $t_{\text{eff}} = 3t/7$ (where t is the drop formation time) we obtain data which are moved closer to those obtained by the quasi-static measurement mode. The remaining difference to

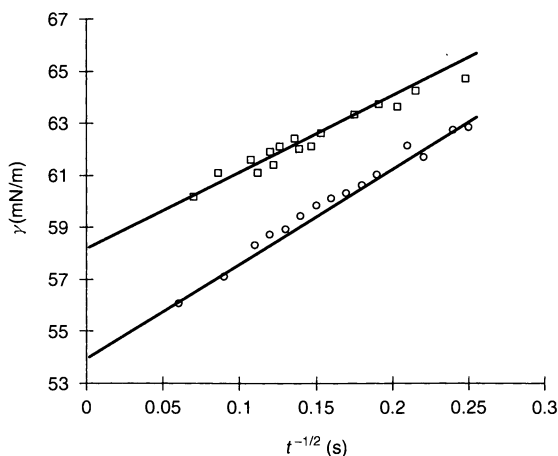


Figure 12.7. Dynamic surface tension data of two diethyldodecylphosphine oxide solutions, as measured by the drop volume method (TVT2, LAUDA, Germany) in the dynamic mode; \square , $c_0 = 10^{-8} \text{ mol/cm}^3$; \circ , $c_0 = 10^{-7} \text{ mol/cm}^3$

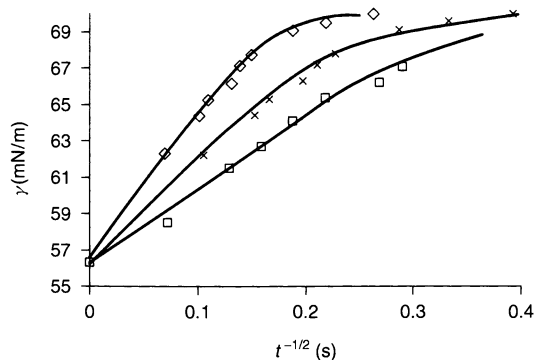


Figure 12.8. Dynamic surface tension data of a dimethyldodecylphosphine oxide solution, as measured by the drop volume method (TVT2, LAUDA, Germany): \diamond , dynamic mode; \square , quasistatic mode; \times , recalculated to the effective surface age

the quasi-static data may be explained by the rough approximation made in the simple theoretical model. The two modes of drop volume tensiometry extend the time window of this measuring technique significantly.

6 DROP AND BUBBLE SHAPE TENSOMETRY

An alternative approach to obtaining the liquid–vapour or liquid–liquid interfacial tension is based on the shape of a pendant drop or buoyant bubble. In essence, the shape of a drop or bubble is determined by a combination of surface tension and gravity effects. Surface forces tend to make drops and bubbles spherical whereas gravity tends to elongate them. The principle of this method has been described in the previous section. As an example of a commercial instrument (PAT1), Figure 12.9 shows a schematic of the pendent drop set-up and the corresponding image obtained by the camera–digitizer system. The advantages of this method are numerous. Only very small amounts of the liquid are required, just enough to form one drop. It is suitable for both liquid–vapour and liquid–liquid interfaces, and applicable to materials ranging from organic liquids to molten metals, and from pure solvents to concentrated solutions. There is also no limitation to the magnitude of surface or interfacial tensions, accessible over a broad range of temperatures and pressures. The time window ranges from parts of a second up to hours and even days, so that even extremely slow processes can be easily followed.

Today, a number of commercial set-ups and respective software packages exist. Most of the instruments

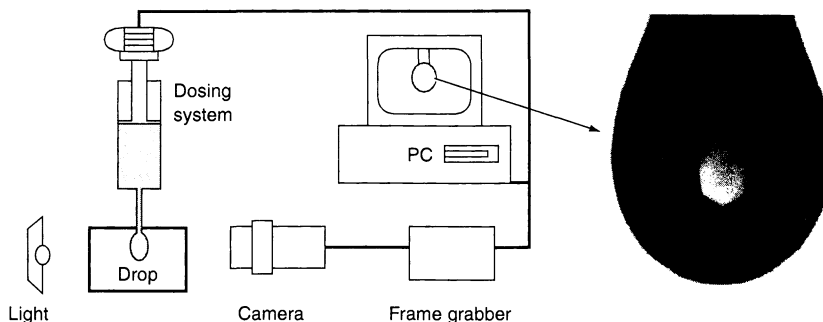


Figure 12.9. Schematic of a pendent drop set-up (PAT1, SINTECH-Berlin, Germany)

yield the same quality of results. In addition, due to the improved quality of video techniques, the corrections of various distortions introduced into the most famous ADSA package (9) have become less important so that nowadays simple calibration procedures can be applied, rather than use a calibration with a grid covering homogeneously the whole field of the screen. It has been demonstrated that a determination of the magnification by using a single sphere is largely sufficient to reach a high accuracy of measurements, which is typically better than 0.1 mN/m.

The experimental results shown in Figure 12.10 demonstrate the capacity of the drop and bubble shape technique. After the adsorption process has reached an equilibrium state, over a period of time of about 6 h, some square pulses of the drop area are subsequently, produced. Such area perturbations are suitable for determining the surface dilational elasticity of the interfacial layer. Efficient dosing systems even allow a sinusoidal area change, again providing information

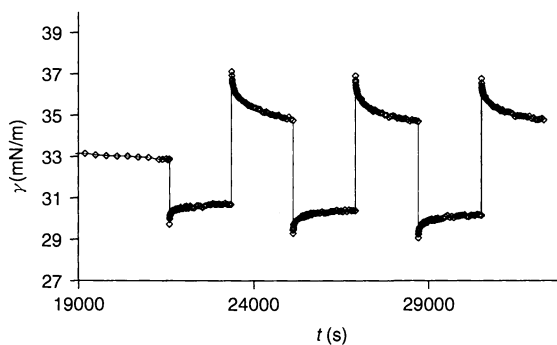


Figure 12.10. Dynamic surface tensions obtained during three subsequent square pulse perturbations of a 5×10^{-10} mol/cm³ human serum albumin (HSA) solutions, as measured by the drop shape method (PAT1, SINTECH-Berlin, Germany)

for the dilational rheology of the adsorption layers (see ref. (3) for various examples). The option to use a bubble instead of a drop does not appear to be important. However, in particular for extremely low bulk concentrations of highly surface-active compounds, studies with bubbles produce results superior to those which use drops. The reason for this is the difference in the available reservoir (10). While the adsorption at the surface of a drop can lead to a significant decrease in the bulk concentration, the reservoir around a bubble supplies enough molecules so that a depletion of surfactant is negligible for concentrations up to at least two orders of magnitude lower than for drops. Note that experiments with bubbles require a real-time control of the bubble volume due to the enormous effect of small temperature changes on the bubble size. Only very few instruments provide this possibility (including the PAT1 machine from SINTECH-Berlin, Germany).

Another experimental example of the use of the drop and bubble shape technique is given in Figure 12.11. The latter shows the dynamic surface tensions of blood serum as measured by the maximum bubble pressure (filled symbols) and drop shape techniques (open symbols). It becomes evident that both methods complement each other perfectly when the data from the MPT2 studies are plotted as a function of t_{eff} . The results impressively demonstrate that during the radiotherapy process the dynamic surface tension parameters return to the normal values (2), i.e. approach those characteristic of healthy females from the respective control group.

Another field of application of the drop and bubble shape techniques is in studying the penetration of soluble surface-active molecules into spread insoluble monolayers. In general, the obtaining of quantitative information on penetrated layers under dynamic and equilibrium conditions requires much attention

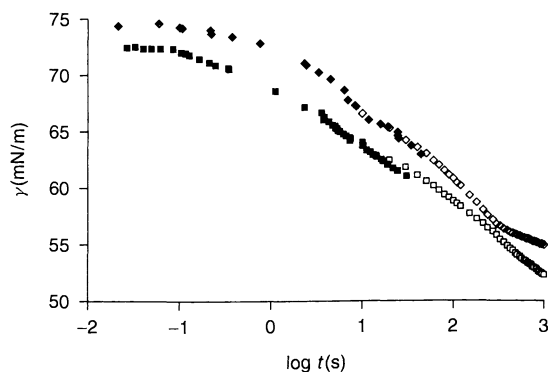


Figure 12.11. Dynamic surface tensions of blood serum samples as measured by the drop shape technique (PAT1, SINTECH-Berlin, Germany, (\diamond , \square)) and maximum bubble pressure method (MPT2, LAUDA, Germany, (\blacklozenge , \blacksquare)), samples taken from a 43 years old woman suffering from cervical carcinoma: \square , \blacksquare , before radiotherapy; \diamond , \blacklozenge , at the end of treatment

with respect to the experimental technique. There are a number of possible penetration experiments with different advantages and drawbacks. The classical experiment is the injection technique, where a soluble component is injected into the sub-phase below a spread monolayer. Experiments can then be performed at constant monolayer coverage or by using compression and expansion cycles. Another possibility is to exchange the sub-phase below a spread monolayer by using a laminar pumping system. Other experiments were carried out by using the so-called sweeping technique.

Drop shape experiments are a very new experimental technique for studying penetration systems. The insoluble monolayer is spread carefully on to the drop surface by using a micro-syringe. The exchange of the bulk drop can be easily performed by using a coaxial double-capillary, as first described by Wege *et al.* (11), and shown in Figure 12.12.

While the new liquid is pumped into the drop through the inner tube, its bulk is pumped out via the outer tube. Due to the liquid flow, the drop volume is permanently mixed. In this way, the drop volume is completely exchanged when an amount of more than 250% of the drop volume has been pumped through. This experimental procedure has the only drawback that it is difficult to control the spread amount very accurately. On the other hand, it has quite a number of advantages when compared to other penetration techniques, in particular, the easy temperature control and the easy applicability to liquid/liquid interfaces.

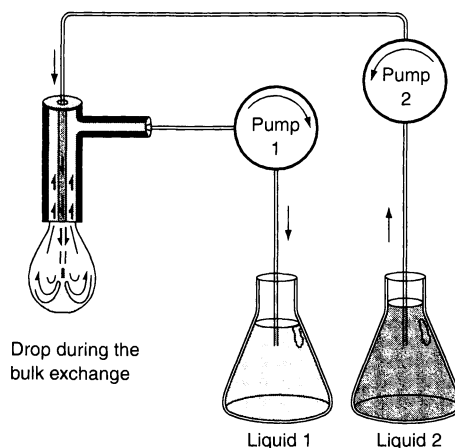


Figure 12.12. Exchange of the bulk drop by using a double-syringe system and a coaxial double-capillary (according to Wege *et al.* (11))

7 DROP AND BUBBLE PRESSURE TECHNIQUES

In addition to the maximum bubble pressure technique discussed above, a group of methods based on static or growing drops and bubbles exists which give access to interfacial tensions at short adsorption times, i.e. parts of a second, up to several minutes and even hours (3). These methods are based on the measurement of the capillary pressure; however, in this case, the entire process of the drop or bubble formation is used to study the adsorption processes at the respective interfaces.

All drop and bubble methods are based on the Laplace equation of capillarity. In order to study dynamic aspects of adsorption, the growing drop or bubble and the expanded drop methods are suitable (3). In Figure 12.13, the schematic of a static or growing drop instrument is shown. In applications of capillary pressure tensiometry, an equation which is equivalent

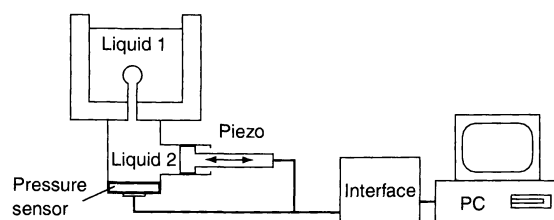


Figure 12.13. Schematic set-up for the growing drop method (according to Liggieri and Ravera (3))

to equation (12.2) is used in the two particular cases in which either the surface tension (pressure derivative method) or the drop curvature (expanded drop method) is constant. In other applications, such as the expanding or growing drop methods, the capillary pressure is monitored while the surface area is continuously increased. In these methods, the changes of the capillary pressure ΔP due to the variation of the drop radius and interfacial tension caused by the dilation of the surface are registered. The problem here is that area change, flow in the bulk phases, and the adsorption kinetics of surface-active compounds have to be simultaneously considered in the theoretical modelling.

The experimental set-ups, as well as the corresponding theories for these and other capillary pressure methods, have been described in detail in a chapter by Liggieri and Ravera in ref. (3). These authors also discuss in much detail the problems connected with the various experimental procedures used in investigations involving drop pressure methods. Most of the theoretical basis for this group of experiments is well described and offers a good chance to quantitatively understand surfactant systems.

An example of the results obtained from drop pressure experiments is given in Figure 12.14, where the dynamic interfacial tension is displayed as a function of time. For the lowest concentration of 2×10^{-9} mol/cm³, the time interval from 0.1 to 10 s is far from sufficient to obtain the equilibrium interfacial tension, while at the highest concentration of 4×10^{-8} mol/cm³ the equilibrium is almost reached after a period of 10 s. Plots of γ against $(1/\sqrt{t})$ allow a good extrapolation of equilibrium tension values. As the pressure sensor can be read with

a high precision and frequency, very accurate data can be obtained. This method is a *direct* one and does not require a large amount of technical equipment, such as video apparatus, etc. However, most of the instruments which are exclusively built in scientific laboratories are usually equipped with video controls, etc.

In recent years, several theoretical and experimental attempts have been made to develop methods based on oscillations of supported drops or bubbles. For example, quadrupole shape oscillations provide information on the equilibrium surface tension, Gibbs elasticity, and surface dilational viscosity. The oscillating bubble system uses oscillations of a bubble formed at the tip of a capillary. The amplitudes of the bubble area and pressure oscillations are measured in order to determine the dilational elasticity, while the frequency dependence of the phase shift yields the exchange mechanism of the material at the bubble surface (3). A comprehensive analysis of oscillating drops and bubbles has been performed recently (12). The apparatus shown schematically in Figure 12.15 is designed according to the conditions analysed in this study. It has been shown that these type of geometries and measuring cells best fulfil the requirements for stable radial drop and bubble oscillations.

In this set-up, a temperature-controlled closed measuring cell is filled with a liquid or a surfactant solution as a first liquid. After a small drop of a second liquid is formed at the tip of a narrow capillary immersed in the cell, the drop volume, and consequently the drop area and radius, are subjected to sinusoidal oscillations via a piezoelectric transducer connected to the measuring cell. Through changes in the drop radius, a sinusoidal

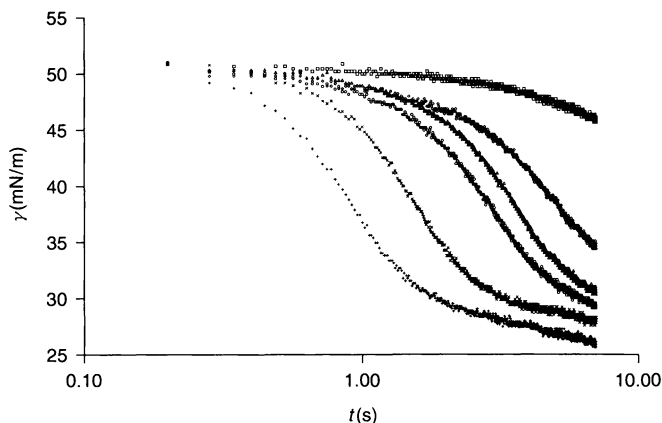


Figure 12.14. Dynamic interfacial tensions of C₁₀EO₈ solutions at the water/hexane interface for six concentrations (C_0) at 25°C, measured by the drop pressure method: □, 2; ◇, 4; △, 8; ○, 10; ×, 20; +, 40 10^{-9} mol/cm³

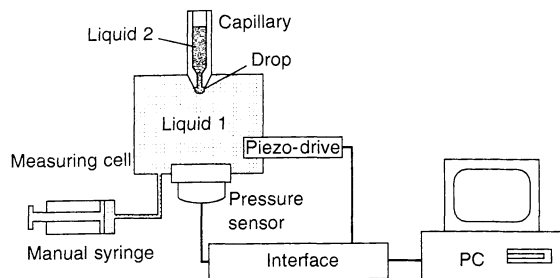


Figure 12.15. Schematic of an oscillating drop or bubble instrument

change of the interfacial area can be generated which in turn induces harmonic changes in the pressure in the closed cell. These changes are monitored by a sensitive pressure sensor which is mounted at the bottom of the measuring cell. The resulting electrical signals are measured so as to obtain the pressure amplitude and the phase difference between the motion of the piezoelectric transducer and the sinusoidal changes of the pressure in the measuring cell. In order to observe the geometry of approximately hemispherical drops or bubbles, the cell contains two optical glass windows, through which the drop can be observed by a video camera.

The measured pressure amplitude can be written as the sum of a geometric (radius) component, a contribution caused by changes in the interfacial tension, $\Delta\gamma$, and a hydrodynamic contribution. The dynamic pressure can be described by the following equation

$$\Delta p = \frac{2\gamma\Delta r}{(r_0)^2} - \frac{2\Delta\gamma}{r_0} + \Delta\tilde{p}_{\text{hydrod}} \quad (12.12)$$

where r_0 is the radius of curvature at the apex of the drop. The first term is a geometric component which

is only controlled by the capillary size and the interfacial tension of the system in equilibrium. The second term is used to calculate the dilational properties, while $\Delta\gamma$ as the change in interfacial tension also incorporates the elastic and viscous contributions. The third term in this equation is controlled by hydrodynamic effects. For example, at higher frequencies inertia effects must be considered.

As an example, we will consider the experimental data obtained in an oscillating bubble study performed under “micro-gravity” conditions on board the space shuttle “Discovery” in 1998 (13). The pressure change Δp (given in bits of the analogue-digital (AD) converter) due to harmonic oscillations of the bubble volume is shown in Figure 12.16. As can be seen, after a short time of about 3 oscillation periods a steady state of the oscillation is reached.

It can be seen that there is an ideal harmonic response, even at frequencies as high as 450 Hz. From experiments carried out on the ground, i.e. “on earth”, it is known that “wobbling” modes set in at much lower frequencies. The reason for this could be the very small deviation from the spherical shape on the ground, even for bubbles of 0.5 mm diameter. The inertia may then induce a flow that deviates from a radial field, which in turn yields oscillations with overtones. A more quantitative analysis is currently under way, which takes into account all possible factors which influence bubble oscillations. This theory will also allow us to describe the transition region at the beginning of the experiment.

8 RING AND PLATE TENSOMETRY

These two techniques belong to the class of “standard methods” in a surface science laboratory. The principle

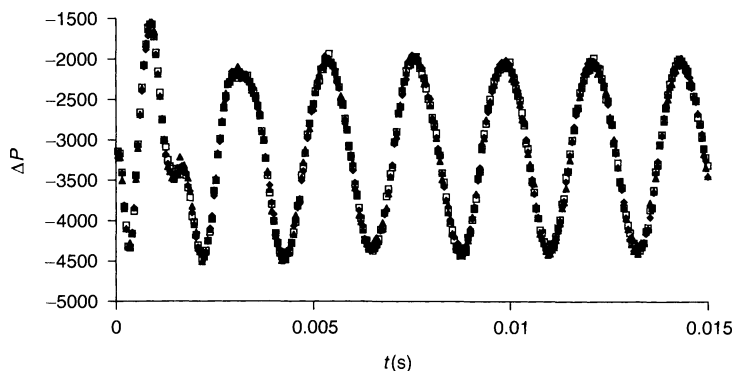


Figure 12.16. Experimental data obtained from oscillating bubble studies performed under micro-gravity at 450 Hz with water at 15°C, where the different symbols correspond to three runs of the experiment
www.iran-mavad.com

has already been explained in the preceding chapter of this volume. Both methods are called static methods (14), although the standard principle of the ring method includes a repeated expansion and compression of the surface layer (15). The expansion occurs along with a decrease in the adsorbed amount, and hence with higher surface tension values.

Experiments involving ring and plate tensiometry are suitable for measurements of the dynamic surface tensions of solutions of slowly adsorbing molecules, which can take place over periods of several hours. The plate method works in a completely static fashion, if one does not consider the slight compression of the adsorption layer due to the decrease in surface tension as adsorption proceeds, and hence a decrease of the liquid meniscus. This effect is, however, negligible in comparison to the rather large surface expansion during ring tensiometry experiments. Thus, the time-dependences of the surface tension data obtained from plate experiments should be slightly lower than those measured with the ring method.

Typically, ring and plate tensiometers are controlled by user-friendly software that allows us to perform and monitor surface tension measurements over long periods of time, by using various time schedules of measurements, for example, measurements based on a linear or logarithmic processes (as provided by the TE2 machine (LAUDA, Germany)).

As is the case for the drop and bubble profile method, the ring method can also be used to induce transient relaxations. In such experiments, the movement of the ring is programmed such that during a first step the surface tension value is measured by determining the maximum weight of the meniscus. After the ring is moved back into the solution and a defined period of time has passed, the ring is then pulled a certain distance out of the solution (less than in the previous measurement) and the ring is left in this position. As the surface layer is expanded during this process, a relaxation sets in and the surface tension decreases until equilibrium is re-established. The change in the measured weight at constant meniscus height can be recalculated to give a surface tension change with time. For this method, the standard software does not provide support and therefore, data interpretation has to be performed off-line by the user. In an analogous way, harmonic changes of the surface area can be investigated by moving the ring accordingly up and down around a well-defined position. Such experiments are also not yet "standard" for ring tensiometers; however, they should be easy to perform by available techniques and could give additional information on the surface dilational

rheology without the use of too complicated, and in general, not commercially available equipment.

9 ACKNOWLEDGEMENTS

This work was supported financially by projects of the Max Planck Society (VBF, AVM), and by projects of the ESA and DLR (FASES and FAST).

10 REFERENCES

1. Joos, P., *Dynamic Surface Phenomena*, Fainerman, V. B., Loglio, G., Lucassen-Reynders, E. H., Miller, R. and Petrov, P. (Eds), VSP, Utrecht, The Netherlands, 1999.
2. Kazakov, V. N., Sinyachenko, O. V., Fainerman, V. B., Pison, U. and Miller, R., *Dynamic surface tension of biological liquids in medicine, Studies in Interface Science*, Möbius, D. and Miller, R. (Series Eds), Vol. 8, Elsevier, Amsterdam, 2000, pp.
3. Möbius, D. and Miller, R., *Drops and Bubbles in Interfacial Research*, Studies in Interface Science, Möbius, D. and Miller, R. (Series Eds), Vol. 6, Elsevier, Amsterdam, 1998, pp.
4. Dukhin, S. S., Kretzschmar, G. and Miller, R., *Dynamics of Adsorption at Liquid Interfaces*, Studies in Interface Science, Möbius, D. and Miller, R., (Series Eds), Vol. 1, Elsevier, Amsterdam, 1995.
5. Ward, A. F. H. and Tordai, L., Time-dependence of boundary tensions of solutions, *J. Phys. Chem.*, **14**, 453–461 (1946).
6. Sutherland, K. L., The kinetics of adsorption at liquid surfaces, *Aust. J. Sci. Res.*, **A5**, 683–696 (1952).
7. Bohr, N., Determination of the surface-tension of water by the method of jet vibration, *Phil. Trans. R. Soc. London, A*, **209**, 281–317 (1909).
8. Miller, R., Bree, M. and Fainerman, V. B., Hydrodynamic effects in measurements with the drop volume technique at small drop times. 3. Peculiarities for high-viscous liquids, *Colloids Surf., A*, **142**, 237–242 (1998).
9. Neumann, A. W. and Spelt, J. K., *Applied Surface Thermodynamics*, Marcel Dekker, New York, 1996.
10. Makievski, A. V., Loglio, G., Krägel, J., Miller, R., Fainerman, V. B. and Neumann, A. W., Adsorption of protein layers at the water/air interface as studied by axisymmetric drop and bubble shape analysis, *J. Phys. Chem.*, **103**, 9557–9561 (1999).
11. Wege, H. A., Holgado-Terriza, J. A., Neumann, A. W. and Cabrerizo-Vilchez, M. A., Axisymmetric drop shape as penetration film balance applied at liquid–liquid interfaces, *Colloids Surf. A*, **156**, 509–517 (1999).
12. Kovalchuk, V. I., Zholkovskij, E. K., Krägel, J., Miller, R., Fainerman, V. B., Wüstneck, R., Loglio, G. and Dukhin, S. S., Bubble oscillations in a closed cell, *J. Colloid Interface Sci.*, **224**, 245–254 (2000).

13. Liggieri, L., Ravera, F., Ferrari, M., Passerone, A., Miller, R., Krägel, J., Makievski, A. V., Loglio, G. and Pandolfini, P., The FAST Project: surface tension and adsorption studies in microgravity – first pre-evaluation of STS-95 Flight Mission, in *The Proceedings of the 2nd European Symposium on the Utilisation of the International Space Station*, ESTEC, The Netherlands, November 1998, pp. 219–224.
14. Rusanov, A. I. and Prokhorov, V. A., *Interfacial Tensiometry*, Studies in Interface Science, Möbius, D. and Miller, R. (Series Eds) Vol. 3, Elsevier, Amsterdam, 1996.
15. Lunkenheimer, K. and Wantke, K. D., On the applicability of the du Nouy (ring) tensiometer method for the determination of surface tensions of surfactant solutions, *J. Colloid Interface Sci.*, **66**, 579–581 (1978).

CHAPTER 13

Determining Critical Micelle Concentration

Alexander Patist

Cargill Inc., Wayzata, Minnesota, USA

1	Introduction	239	3.13	Vapour pressure osmometry	244
2	Importance of CMC	240	4	Methodical Differences in Determining CMC	244
3	Methods to Determine CMC	241	5	Factors Influencing CMC	245
3.1	Surface tension	241	5.1	Surfactant structure	245
3.2	Electrical conductivity	242	5.2	Electrolyte and counterions	246
3.3	Static light scattering	242	5.3	Organic compounds	246
3.4	Dynamic light scattering	242	5.4	Temperature	246
3.5	Refractive index	242	5.5	Pressure	246
3.6	Dye solubilization	242	6	Micellization in Non-Aqueous Media	246
3.7	Dye micellization	243	7	Determining CMC in Non-Aqueous Media	247
3.8	Molecular absorption	243	8	Factors Influencing CMC in Non-Aqueous Media	248
3.9	Diffusion coefficient	244	9	References	248
3.10	Viscosity	244			
3.11	Partial molal volume	244			
3.12	Sound velocity	244			

1 INTRODUCTION

Since the beginning of the study of surfactant solutions, it was recognized that the physical properties of these solutions, such as surface tension, electrical conductivity and detergency, show an abrupt change in the neighbourhood of a critical concentration. These unusual properties indicated the formation of molecular aggregates. The formation of colloidal-sized clusters of individual surfactant molecules in solution is now better known as *micellization*. Although first suggested by McBain in 1913, the earliest concrete model for spherical micelles is attributed to Hartley (1). Figure 13.1 shows schematically the three environments in which surfactant molecules reside in a typical (aqueous) surfactant solution. Surfactant

molecules disperse as monomers in the aqueous phase, form aggregates (micelles), or adsorb as a film at the air/water interface. The surfactant is in dynamic equilibrium between these states. Thus, at a given temperature, pressure and concentration, the number of monomers, micelles and monomers adsorbed at the air/water interface is fixed under equilibrium conditions.

The process of surfactant clustering or micellization is primarily an entropy-driven process. When surfactants are dissolved in water, the hydrophobic group disrupts the structure of water and therefore increases the free energy of the system. Surfactant molecules therefore concentrate at interfaces, so that their hydrophobic groups are directed away from the water and the free energy of the solution is minimized. The distortion of

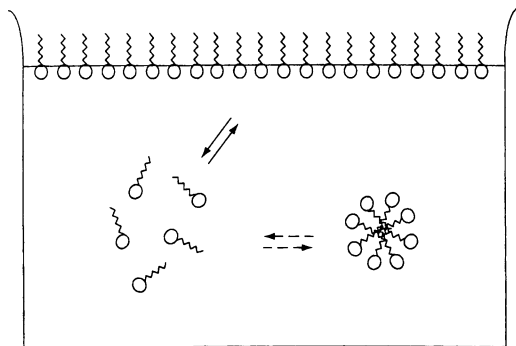


Figure 13.1. Schematic representation of the three states in which surfactant molecules reside in water, i.e. monomers adsorbed at the air/water interface, monomers in the bulk solution and micelles

the water structure can also be decreased (and the free energy of the solution reduced) by the aggregation of surface-active molecules into clusters (micelles) with their hydrophobic groups directed toward the interior of the cluster and their hydrophilic groups directed toward the water. However, the surfactant molecules transferred from the solution to the micelle may experience some loss of freedom from being confined to the micelle. In addition, they may experience an electrostatic repulsion from other similarly charged surfactant molecules in the case of ionic surfactants. These forces increase the free energy of the system and oppose micellization. Hence, micelle formation depends on the force balance between the factors favouring micellization (van der Waals and hydrophobic forces) and those opposing it (kinetic energy of the molecules and electrostatic repulsion). The explanation for the entropy-dominated association of surfactant molecules is called the “hydrophobic effect” or “hydrophobic bonding” (2).

The concentration of surfactant at which micelles first appear in solution is called the critical micelle concentration or CMC. Representing the surfactant by S , the micellization process can be described by the following reaction:



in which S_n is the micelle with a degree of aggregation n . The formation of micelles from the constituent monomers involves a rapid, dynamic, association–dissociation equilibrium. Micelles are undetectable in dilute solutions of monomers, but become detectable over a narrow range of concentrations as the total concentration of surfactant is increased, above which nearly all additional surfactant species form micelles. The concentration of free surfactant, counterions and micelles

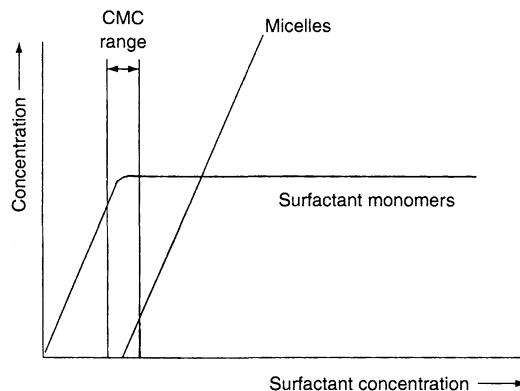


Figure 13.2. Concentration of individual species in a surfactant solution

as a function of the overall surfactant concentration is shown in Figure 13.2. Above the CMC, the concentration of free surfactant is essentially constant, while the counterion concentration increases and the micellar concentration increases approximately linearly.

The concentration at which micelles first become detectable depends on the sensitivity of the experiment used to determine the CMC. The purpose of this chapter is to discuss the experimental methods that have been used to determine the critical micelle concentration for aqueous systems, as well as to give an overview of CMC determination techniques for surfactants in non-aqueous media.

2 IMPORTANCE OF CMC

The value of the critical micelle concentration (CMC) is an important parameter in a wide variety of industrial applications involving adsorption of surfactant molecules at interfaces, such as foams, froths, emulsions, suspensions, and surface coatings. It is probably the simplest means of characterizing the colloid and surface behaviour of a surfactant solute, which in turn determines its industrial usefulness. Many industrial processes are also dynamic processes in that they involve a rapid increase in interfacial area, such as foaming, wetting, emulsification and solubilization. First, the available monomers adsorb on to the freshly created interface. Then, additional monomers must be provided by the breakup of micelles. Especially when the free monomer concentration (i.e. CMC) is low, the micellar breakup time or diffusion of monomers to the newly created interface can be rate-limiting steps in the supply of monomers, which is the case for many nonionic surfactant solutions (3).

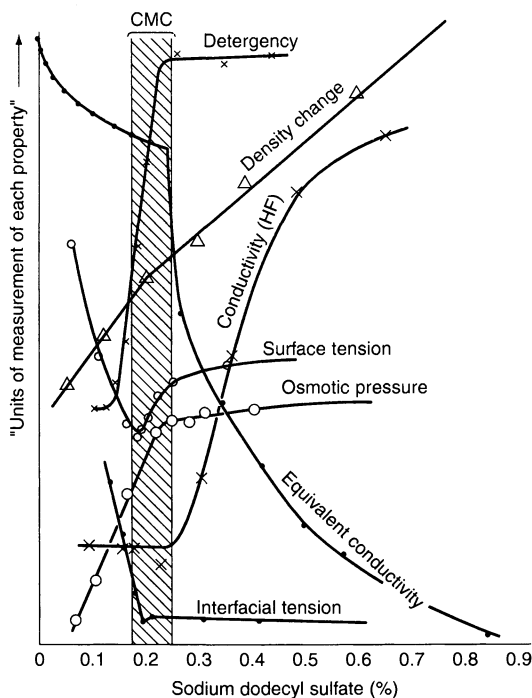


Figure 13.3. Changes in some physical properties for an aqueous solution of sodium dodecyl sulfate (SDS) in the neighborhood of the CMC (from ref. (4)), reprinted with permission from American Chemical Society

Experimentally, the CMC is determined from the discontinuity or inflection point in the plot of a physical property of the solution as a function of surfactant concentration. This is demonstrated in Figure 13.3 (4). Clear breaks of almost every measurable physical property that depends on size and number of particles in solution are shown by all types of surfactants, i.e. nonionic, anionic, cationic and zwitterionic, in aqueous media. A wide variety of techniques involving the measurement of physical properties have been used to determine CMC values. The experimental methods by which the CMC of surface-active agents in aqueous solution may be determined are discussed in the next section.

3 METHODS TO DETERMINE CMC

A large number of methods have been applied to the determination of the critical micelle concentration of surface-active agents. Most of the physico-chemical property changes can be used to determine the CMC,

provided that the measurement can be carried out accurately. For an extensive compilation of the CMCs of surfactants in aqueous and non-aqueous media, the reader is referred to books by Mukerjee and Mysels (5), Rosen (6), and more recently by van Os *et al.* (7), and references therein.

3.1 Surface tension

The surface tension of aqueous solutions of surface-active agents decreases very rapidly until the CMC is reached and then stays constant above the CMC. Above this concentration, the surface tension of the solution remains constant since only the monomeric form contributes to the reduction of the surface or interfacial tension. For concentrations below, but near the CMC, the slope of the curve is essentially constant, indicating that the surface concentration has reached a constant maximum value. In this range the interface is considered to be saturated with surfactant molecules and the continued reduction in the surface tension is mainly due to the increased activity of the surfactant in the bulk, rather than at the interface.

The equilibrium surface tension can be measured by a variety of methods, such as the Wilhelmy plate, du Nouy ring, drop weight or by volume and shape of the drop (see Chapter 11 earlier). The data are generally plotted against the logarithm of concentration as the abscissa and the transition between a descending line (often assumed to be straight) and another one close to the horizontal is taken as the CMC. In the case where the concentration of surfactant is plotted linear against the surface tension, the curvature of the descending portion is much less sharp. If the sample contains highly surface-active impurities, however, the inflections in the surface tension versus log concentration plot become more ambiguous and show a minimum (see the surface tension curve in Figure 13.3). The presence of a minimum is often observed for technical-grade nonionic surfactants, due to the broad molecular weight distribution owing to the degree of ethoxylation, and ionic surfactants that are partially hydrolysed (e.g. long-chain alcohols). This minimum disappears as the impurity dissolves in the micelles above the CMC. The surface tension method is very sensitive to impurities, since it only measures the surface concentration of all surface-active species present in solution and does not detect the presence of micelles in the bulk. Therefore, it is recommended that other techniques being applied as well to confirm the CMC values obtained by the surface tension method.

From the surface tension versus log concentration curves thus obtained, a very useful parameter can be derived, namely the area per molecule of the surfactant. As early as 1878, Gibbs derived a differential equation relating the surface tension, the number of moles and the chemical potentials of the components at the interface, as follows:

$$d\gamma = - \sum_i \Gamma_i d\mu_i \quad (13.2)$$

where $d\gamma$ is the change in interfacial tension of the solvent, Γ_i is the surface excess concentration, which can be approximated by the number of moles per unit area, and $d\mu_i$ is the change in chemical potential of the components in the system. The Gibbs equation can be used to calculate the surfactant concentration at the interface, and hence the area per molecule from the simple measurement of surface tension. For dilute solutions of a nonionic surfactant or a 1:1 ionic surfactant in the presence of electrolyte, equation (13.2) can be written as follows:

$$\Gamma = - \frac{1}{RT} \left(\frac{d\gamma}{d \ln C} \right)_T \quad (13.3)$$

where R is the gas constant, T the absolute temperature and C the concentration of surfactant (8). The surface excess concentration, Γ , can be obtained from the slope of a plot of the surface tension γ versus $\ln C$ at constant temperature, which then can be used to calculate the area per molecule a (in squared angstroms) from the following relationship:

$$a = \frac{10^{20}}{N_{\text{Avog}} \Gamma} \quad (13.4)$$

where N_{avog} is the Avogadro constant and Γ is the surface excess concentration. An extensive list of areas per molecule for a variety of surfactants and counterions is given by Rosen (6).

3.2 Electrical conductivity

Electrical conductivity is based on the measurement of the electric resistance of the (ionic) surfactant solution. This method does not involve any special problems, except the application of external electrical forces. Since the mobility of the ions when present as single species resembles that of dissociated salts and differs significantly from that of aggregated ions, there is an abrupt change in specific conductivity at the CMC. The data can also be converted to equivalent conductivity plotted against the square root of concentration.

www.iran-mavad.com

3.3 Static light scattering

The aggregation of surface-active agents is reflected in the increase of scattered light. Most of the CMC measurements are carried out at a scattering angle of 90° . In applying this technique to the study of micellar solutions, the intensity versus concentration plot is usually extrapolated to obtain the CMC. The results can also be evaluated by application of the classical Debye equation or Zimm plot (9, 10), leading to the aggregation number of the micelles via molecular weight. Although this technique is certainly surpassed by the dynamic light scattering technique (discussed next), it can still serve as a convenient method to study the absolute scattered intensity of small colloidal particles. Very careful elimination of dust particles from solution is necessary though, since the presence of only very small amounts of impurities will result in significant errors.

3.4 Dynamic light scattering

This technique is related to the classical light scattering method as discussed above. The dynamic light scattering technique measures time correlations in scattered intensity to determine the relaxation of density fluctuations (due to Brownian motion) (11). As surfactant monomers are below the detection limit of the technique, no autocorrelation function will show. However, above the CMC, aggregates will scatter light, thus giving rise to the autocorrelation function. By applying the Stokes–Einstein relationship, one can obtain information about the particle size (hydrodynamic radius).

3.5 Refractive index

Since this method does not involve the addition or the application of a strong external field of force, no change in the CMC can occur throughout the experiments. The method is applicable to any kind of surfactant and solvent. Very careful temperature control and determination of the concentration of surfactant are indispensable for this method.

3.6 Dye solubilization

The fact that many oil-soluble dyes dissolve in water in the presence of micelles, i.e., are solubilized, has been used in the determination of the CMC. After sedimentation of the dye, transmission measurements either by

UV-Vis spectroscopy or colorimetry give the amount of solubilization. The solubility of the dye remains almost constant until the concentration of surface-active agent attains the CMC, and then increases rapidly and almost linearly. The CMC value thus determined by solubilization is lower than those obtained from other measurements for the reasons discussed in the next section. This method is applicable to both aqueous and non-aqueous solutions. The latter requires the use of a water-soluble dye. Common oil-soluble dyes for this measurement are Orange OT, Sudan III and IV, Yellow OB and Aniline Blue, while common water-soluble dyes include Eosin, Merocyanin 540 and Methylene Blue.

3.7 Dye micellization

Another common approach involving the use of dyes is the dye micellization method. This technique is based on the fact that the spectra of many dyes added in very small amounts to a surfactant solution are different in the region below and above the CMC. The dye-micelle interaction causes this shift in the absorbance spectrum. Solutions having concentrations "bracketing" the CMC should contain the same concentration of dye and their spectrum or absorbance can be determined at a specific wavelength by using UV-Vis spectroscopy (see Figure 13.4). The CMC is determined from a plot of the absorbance at a fixed wavelength versus the surfactant concentration. Common dyes used for this method are Fluorescein, Erythrosin, Pinacyanol Chloride, Eosin Y, Merocyanin 540, Trypan Blue, Crystal Violet, Methyl Orange and Rhodamine 6G. These dyes have large extinction coefficients and are very sensitive to the particular micro-environment. An example of the

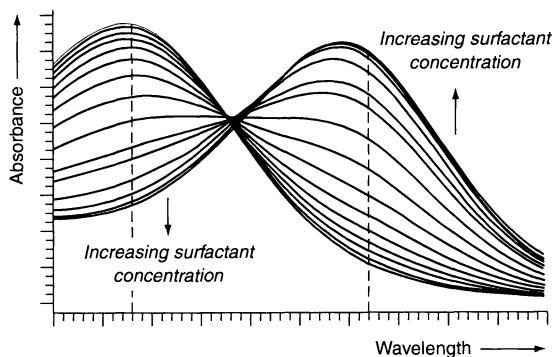


Figure 13.4. UV-Vis absorbance spectrum of Eosin Y in aqueous surfactant solution; the maximum absorbance shifts as the surfactant concentration increases (from ref. (12)), reprinted with permission from AOCS

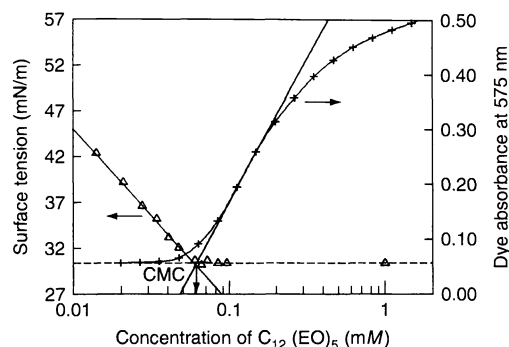


Figure 13.5. CMC determination of pure $C_{12}(EO)_5$ by surface tension and dye micellization methods. The horizontal dashed line represents dye absorbance in water as well as the equilibrium surface tension (from ref. (12)), reprinted with permission from AOCS

determination of CMC for a pure nonionic surfactant ($C_{12}(EO)_5$) by using surface tension and dye micellization methods is shown in Figure 13.5 (12).

One important point has to be made concerning the use of dyes. It is well known that micelles form at a lower concentration of monomers in the presence of the dye. Therefore, the presence of a dye always lowers the CMC. This effect reaches a maximum if the micelle is saturated with the indicator during the determination. Another important complication occurs when the indicator is a high-molecular-weight organic ion, such as most of the dyes mentioned here. If the charge of the dye is the opposite of that of the surfactant, an insoluble salt may form. This precipitate often remains finely dispersed by an excess of the surfactant and escapes detection. It is this precipitate which becomes solubilized by micelles when the concentration of surfactant is further increased, thus causing a second colour change which is generally reported as the CMC. Dye indicators are mostly used in small concentrations ($10^{-4} - 10^{-5} M$), which is limited by the sensitivity of the spectrophotometer. Hence, the amount of surfactant consumed by precipitation is often negligible compared to the CMC, but becomes significant for very low CMCs. In the case of ionic surfactants it is better to use similarly charged dyes. The formation of a water-insoluble, micelle-soluble salt is then avoided. The dye remains in the aqueous "undersaturated" solution and its mole fraction in the micelle is then only a corresponding fraction of the saturation value.

3.8 Molecular absorption

The absorption spectrum of some surfactants is different when they are in micellar and in free form.

Hence, plotting the absorbance (as measured by UV–Vis spectroscopy) at a particular wavelength against the surfactant concentration can give a change of slope corresponding to the CMC. This micellar spectral change should be distinguished from the other spectral change methods involving dyes (as discussed earlier) in that it does not require any additive.

3.9 Diffusion coefficient

The different mobilities of monomers versus micelles can be used as a means to determine the value of CMC. The self-diffusion coefficients of the water and surfactant can be measured by pulsed-gradient spin Fourier-transform nuclear magnetic resonance echo (FT-NMR) spectroscopy, following the ^1H NMR spectra (13). Hence, a plot of the diffusion coefficient D versus the surfactant concentration shows a change in slope corresponding to the CMC.

3.10 Viscosity

The viscosity of a surfactant solution plotted as the specific viscosity $[\eta - \eta_0/\eta_0]$ or as the intrinsic viscosity, being the limiting value of η_{sp}/C at infinite dilution, shows a change of slope at the CMC. This way of determining the CMC requires a very sensitive viscosity measurement. Good results have been obtained by using the Ostwald viscometer. In addition, this method is more reliable for nonionic surfactants where no electroviscous effects arise.

3.11 Partial molal volume

This method involves the accurate measurement of the density of the solution and the determination of the surfactant concentration. Any change in the partial molal volume of surfactant will be reflected in the density of the solution. As with all of the other methods, very careful measurement procedures and precise temperature control are required in order to obtain reliable data. This method can be used for any type of surfactant in aqueous, as well as non-aqueous, systems.

3.12 Sound velocity

The velocity of sound in a liquid medium can be related theoretically to the molecular weight by an equation

which involves the density and refractive index of the medium and two empirically derived constants (14). This relationship can be modified to apply to binary solutions of liquids. The CMC can be determined from the break point of the velocity versus concentration graph.

3.13 Vapour pressure osmometry

The change in the vapour pressure of a solvent as a result of the presence of a surface-active agent is a measure for determining the CMC. This method is direct and very useful in measuring the change of activity of the solvent by using a vapour pressure osmometer. The technique is based on the temperature comparison between two droplets, i.e. one of the solution, and the other of the solvent. Even though this method does not give accurate measurements of the change in activity, it is sufficient to give the CMC from graphs of vapour pressure depression versus concentration.

Other techniques that have been applied for the determination of CMC are X-ray diffraction and NMR spectroscopy. A change in the X-ray pattern may indicate the CMC, while shifts in the NMR peaks are indicative of the CMC. However, both of these methods are time-consuming and have relatively low sensitivities. Moreover, careful data interpretation is crucial.

4 METHODOLOGICAL DIFFERENCES IN DETERMINING CMC

As shown by the above review of the common methods used for the determination of the CMC, a series of measurements of some property of the surfactant solution as a function of surfactant concentration is usually involved. This is followed by the detection of some characteristic point – which is called the CMC. Methodological differences may originate from the choice of the characteristic point, the kind of plot on which this point is chosen, the kind of data which are plotted and the effect of the dye. The CMC is not a very sharply defined point above which properties are qualitatively different from those below. In fact, all properties of a solution in the CMC region vary in a continuous manner and so do all of their derivatives. A micelle is by definition *a reversible aggregate of a large but not infinite number of monomers*. The micelle formation reaction must obey the laws of chemical equilibrium and, as such, the concentration dependence of the degree of micellization has to change gradually. Consequently, all properties of the

solution must show similarly rapid but gradual changes. In addition, it is well understood that there is not a unique number of monomers which can form a micelle but a range with relatively wide limits. Hence, micelles are polydisperse (15). This is in agreement with the fact that the average micellar size continuously varies with conditions, such as temperature, counterion concentration or other additives, nature of the counterion, chain length and structure. In conclusion, the CMC region contains many micelles of different aggregation number, each with a different concentration dependence, which further spreads and complicates the changes of bulk properties occurring in this region.

5 FACTORS INFLUENCING CMC

In this section, the most important factors which influence the value of the CMC are discussed. Among these are the structure of the surfactant molecule, the presence of electrolyte or organic compounds, temperature and pressure. For a much more comprehensive discussion on the factors influencing the CMC, the reader is referred to Rosen (6) and Shinoda (16).

5.1 Surfactant structure

In general, the CMC decreases as the hydrophobic character of the surfactant increases, i.e. as the number of carbon atoms in the hydrophobic tail increases. A common rule is that for ionic surfactants the CMC is halved by the addition of one methylene group to a straight-chain hydrophobic group attached to a single terminal hydrophilic group. A clear example of this rule is shown in Table 13.1 for alkyltrimethylammonium bromide, a cationic surfactant. As the hydrophobic tail is increased by two methylene groups, the CMC approximately decreases by a factor of four.

This effect is larger for nonionics and zwitterionics: an increase by two methylene groups reduces the CMC

by one tenth of its previous value. When the number of carbon atoms in a straight chain exceeds 16, however, the CMC does not decrease so rapidly anymore with increasing chain length. In fact, the CMC may remain basically unchanged, due to coiling of these chains in water or on account of solubility limits. If the CMC exceeds the solubility of the surfactant at a particular temperature, the minimum surface tension will be achieved at the point of maximum solubility, rather than the CMC. The temperature at which the solubility of an ionic surfactant becomes equal to the CMC is known as the Krafft temperature (T_k). For long-chain ionic surfactants, the Krafft point is higher and hence the CMC is never reached unless the temperature is increased. The effect of carbon branches on the straight chain is about one half of the effect of carbon atoms on the straight chain. The presence of double bonds in the hydrocarbon chain decreases the hydrophobic character somewhat, thus resulting in generally higher CMC values than those of the corresponding saturated compounds. Furthermore, the *cis*-isomer has a higher CMC than the *trans*-isomer. In general, surfactants with either bulky hydrophobic or bulky hydrophilic groups have larger CMCs than those with less bulky groups. This can be attributed to steric hindrance affecting the micellar packing and thereby inhibiting micelle formation. The presence of polar groups in the hydrophobic tail causes a significant increase in the CMC. The replacement of a hydrogen group by an ionic group also significantly increases the CMC.

In aqueous media, the CMC of ionic surfactants is much higher than nonionic surfactants containing a similar hydrophobic tail. This difference can be up to a factor of one hundred. Zwitterionics have slightly lower CMCs than ionics with the same number of carbon atoms in the hydrophobic group. When the hydrophilic group is moved from a terminal position to a more central position, the CMC increases. The hydrophobic group seems to act as if it had become branched at the position of the hydrophilic group.

For nonionics surfactants of the polyoxyethylene type, the CMC increases as the PEO length increases. This effect, however, is much smaller than that per methylene group in the hydrophobic tail. As discussed earlier, commercial nonionic surfactants tend to have slightly lower CMC values than the pure nonionics due to the distribution in their degree of ethoxylation. The components with low PEO content are more surface-active than those with a high PEO content, thus causing a reduction in the CMC.

Table 13.1. The CMC values of alkyltrimethylammonium bromides with increasing chain length at 25°C (6)

Chain length	CMC (mM)
8	140
10	68
12	16
14	3.6
16	0.92

5.2 Electrolyte and counterions

The effect of electrolyte on the CMC in aqueous media is very pronounced for ionic surfactants, and less so for zwitterionics and nonionics. The reduction in CMC is due mainly to the decrease in electrical repulsion between the ionic head-groups. A second effect is the so-called "salting-out" effect, which is the major reason for CMC lowering for zwitterionics and nonionic surfactants. The work needed to create the volume in water required to accommodate a non-polar compound is changed in an electrolyte solution because of the water-ion interactions. If the required work is increased by the presence of electrolyte, the surfactant monomers are salted-out and micellization is favoured. The effect of the electrolyte present in solution depends on the radius of the hydrated ion. The smaller the radius, then the greater the salting-out effect.

The CMC is also reflected by the degree of binding of the counterion to the micelle. In general, an increased binding of the counterion results in a decrease of the CMC. The extent of binding of the counterion increases with increases in its polarity and valence, and decreases with an increase in hydrated radius. It is important to mention that the value of the CMC is *not* a measure for the binding of the counterion, when comparing different surfactants. Other factors, such as the surface charge density and area per molecule, will also play an important role (6, 16).

5.3 Organic compounds

Hydrocarbons, such as benzene or heptane, are solubilized in the interior of the micelle. They increase the micelle size and change the curvature of the micelle surface. This change in curvature may slightly decrease the electrical potential, and therefore the work for micellization. The surface free energy decrease in the hydrocarbon chain of the surfactant upon micellization may also slightly increase due to the presence of solubilized hydrocarbon in the interior. These two factors tend to decrease the CMC. The effect is smaller compared to that of electrolyte or alcohols. The latter penetrate the oriented structure of the micelle, thus forming a mixed micelle. The presence of long-chain alcohols decreases the charge density on the micelle surface, as well as causing an increase in the entropy of mixing due to the penetration of the alcohol molecule, hence resulting in a lower CMC. Short-chain alcohols, such as glycols, methanol and ethanol, are too soluble in water and only a few molecules may penetrate into the micelle due to partition equilibrium. The effect of the addition of

these alcohols is accordingly very small, and only large amounts can change the properties associated with the environment of a micelle. For example, the free energy required to bring the hydrocarbon chain of the surfactant into solution may decrease and the CMC tends to increase. In addition, the dielectric constant of the medium may decrease slightly, which tends to decrease the CMC. However, both of these effects may be very small when compared with the effects of long-chain alcohols or electrolyte, which decrease the charge density or electrical potential of the micelle surface.

5.4 Temperature

The effect of temperature on the CMC of surfactants in aqueous media is rather complicated. First, the CMC tends to decrease with temperature to a minimum value and then increases with further increases in the temperature. Two opposing effects occur. The temperature increase causes a decreased hydration of the hydrophilic group, which favours micellization. However, a temperature increase also causes disruption of the structured water surrounding the hydrophilic group – an effect opposing micellization. The relative magnitude of these two effects determines whether the CMC increases or decreases over a particular temperature range.

5.5 Pressure

The primary effect of pressure on a micellar system is a change in the CMC, which is closely related to changes in the partial molar volume of micelle formation, aggregation number, and water penetration into the micelles. In general, the CMC increases with pressure, undergoes a maximum and then tends to decrease again.

6 MICELLIZATION IN NON-AQUEOUS MEDIA

The link between non-aqueous colloid science and commercial technologies is often overlooked. However, a continuously increasing interest can be observed with regard to surfactants in non-polar media, due to a number of industrial applications, including magnetic colloids in particulate magnetic recording, high-technology ceramics for integrated circuits, liquid-ink development in reprographic technologies, display devices, paints, lubricants, oils, cosmetics, and many others. Since the physico-chemical properties of micelles in non-aqueous

media are significantly different from those in aqueous systems, it is justified to present here some of the reversed micellar features, and in particular, the methods used to determine the critical micelle concentration in non-aqueous media. For comprehensive studies and reviews, the reader is referred to Eicke (17), Kitahara and Kon-No (18) and Mittal (19).

The most obvious difference between micelles in polar and non-polar surfactant solutions is their mutual structural reversion. The orientation of the surfactant molecule is just reversed from that in water. The head-groups are oriented toward each other in the interior of the micelle, while the hydrophobic groups (hydrocarbon tails) are oriented toward the non-aqueous solvent. The driving force for the formation of an aggregate comes from the strong attraction of the polar groups, either as a generalized dipole attraction, by hydrogen bonds, or by the formation of specific coordination bonding, together with some segregation of the hydrophilic portion of the molecule with the solvent. In general, the aggregation number of inverted micelles is much smaller (10 to 25) than the large micellar aggregates in aqueous systems (25 to 500, and even higher). On the solvent side, two classes of solvents can be classified. The first is the type of solvent in which inverted micelles are formed, while the second is the type in which micelles do not exist neither at low nor at medium surfactant concentrations. In general, the more non-polar the solvent, then the more pronounced the aggregation tendency of the surfactant, due to a decreasing amount of non-associated surfactant molecules. On the other hand, solvents which are hydrogen-bond donors or acceptors, even if they appear to belong to the class of non-polar solvents, seem to prevent aggregation. In addition, due to the low solubility of many surfactants in non-polar media, the CMC is often higher than the maximum solubility. Thus, raising the temperature increases the solubility of the monomers up to the Krafft point, above which the total solubility is determined by the aggregates. All of the factors discussed above, together with the often insignificant changes of the physical properties used to follow the aggregation process, makes it difficult to define a critical concentration. Nevertheless, some of the most common methods used to determine the CMC of surfactants in non-aqueous media will be discussed below.

7 DETERMINING CMC IN NON-AQUEOUS MEDIA

The main procedures and essential ideas, both theoretically and experimentally on which the determination of

micelles in non-polar media are based, originate from comparable investigations in aqueous systems. However, in contrast with aqueous micellar solutions, the choice of parameters indicating micellization is limited for several reasons. First, in general the aggregates are very small. This implies that the onset of micellization is in many instances less pronounced and causes some uncertainty regarding the determination of a CMC. Secondly, the CMC values are very low, which requires high-sensitivity detection techniques. Thirdly, a number of techniques are mainly applicable to aqueous systems, for example, electrical conductivity or standard relaxation techniques, such as pressure-jump and temperature-jump methods. Vapour pressure osmometry (VPO) and depression of the freezing point are the techniques which are often used to determine the apparent number-average molecular weight of the aggregates and the CMC. Vapour pressure osmometry can also be performed at different temperatures, thus allowing the investigation of the temperature-dependence of the CMC and aggregation number. An important factor in VPO measurements is the equilibration time. Long equilibration times are required for the solvent to penetrate the surfactant layer covering the solution droplet in the osmometer. Classical light scattering (LS) or dynamic light scattering (DLS) are only occasionally and approximately applicable with respect to the determination of the CMC in non-aqueous media. Both methods suffer from insensitivity at very low surfactant concentrations.

As discussed earlier, the use of an indicator to determine the CMC can be applied to aqueous as well as non-aqueous systems. Rhodamine B, for example, can be added to detect reversed micelles at very low surfactant concentrations. The transition from monomers to micelles can then be followed by the depolarization of the fluorescence. Another method involving the use of a dye is dye solubilization. For non-aqueous systems, a water-soluble dye should be used, for example, Eosin Y or Merocyanin 540. As soon as the first aggregates form, the solubilized dye can be measured by its UV-Vis absorbance. This method yields satisfactory results for some surfactants. However, sometimes the solubilization of such a dye is so high that the micellar structure is affected by the dye. If the solubilization is weaker, the dye taken up by the micelles is often insufficient to produce a reasonable signal. Especially when the CMC is very low, the pseudo-phase volume fraction of the micellar phase at concentrations just above the CMC is far too low to solubilize a significant amount of dye. This makes it difficult to define a clear CMC and requires the evaluation of different water-soluble

Table 13.2. The CMC values and aggregation numbers of AOT in non-aqueous media (6, 16)

Solvent	T (°C)	CMC (mM)	N	Technique
Cyclohexane	37	0.39	17	VPO
CCl ₄	25	0.16	17	VPO
CCl ₄	37	0.40	17	VPO
Pentane	25	0.49	15	LS
Benzene	37	0.35	13	VPO

systems, the addition of dye also causes a shift of the CMC to lower concentrations for non-aqueous solutions. Surface tension has also been successfully applied to the determination of CMC in non-aqueous systems, yielding similar results as dye solubilization and light scattering techniques (20).

Other techniques discussed earlier, which are also applicable to non-aqueous systems, include refractometry, viscometry and diffusivity. Electrical conductivity has been used for ionic surfactants in (slightly polar) non-aqueous systems too, for example, alcohol-benzene mixtures. The CMC decreases as the solvent becomes more non-polar (i.e. increasing benzene content). Some investigators have determined the CMC by dipole moment calculations using the Guggenheim relationship (21). Many surfactants, especially ionics, frequently possess rather large dipole moments. In the course of the aggregation process, the overall dipole moment of the molecular cluster changes due to mutual compensation of the dipole moments of the individual surfactant molecules. By plotting the dipole moment versus surfactant concentration, two straight lines are obtained, intersecting at the CMC. The dielectric increment $\Delta\epsilon$ can also be plotted versus surfactant concentration, showing a sudden drop at the CMC. Since the dielectric measurements only yield indirect information on the formation of aggregates, it is necessary to consult other methods in order to identify the above-mentioned breaks with a CMC.

Some CMC values and aggregation numbers found for one of the most extensively studied ionic surfactants in non-aqueous medium, sodium bis(2-ethylhexyl) sulfosuccinate (AOT), are listed in Table 13.2. It is clear that the CMC values, as well as the micellar aggregation numbers, are very small when compared to aqueous systems.

8 FACTORS INFLUENCING CMC IN NON-AQUEOUS MEDIA

The forces governing the formation of micelles are quite different in non-aqueous solution from those in aqueous

solution. In aqueous systems, the added hydrocarbon exerts only a small effect on the CMC since hydrocarbons solubilized in the interior of the micelle do not change the heat of micellization appreciably. However, the strong interaction between the ion pairs seems to be the driving force for aggregation of surfactant molecules in non-aqueous solvents and the water solubilized in the core of the micelle will change the dielectric constant in the core and thus affect the CMC and size of the micelle (17). The length of the hydrocarbon chain does not affect the CMC significantly. Although the purity of the sample is always important, small amounts of higher homologues may not affect the results as much as in the case of aqueous solutions because impurities which are highly surface-active in aqueous solution are no longer highly surface-active in non-aqueous solution. Small amounts of water or free fatty acids seem to significantly affect the CMC, size and shape of the surfactants in non-aqueous media (17).

At constant temperature, the CMC increases and the solubilizing power decreases with an increase in chain length. As discussed earlier for aqueous systems, the CMC decreases approximately one third per additional methylene group in aqueous solutions of nonionic surfactants, but the change is small in non-aqueous solutions, since the intermolecular forces between the solvent and hydrocarbon chain are similar.

9 REFERENCES

1. Hartley, G. S., *Aqueous Solutions of Paraffin Chain Salts*, Hermann, Paris, 1936.
2. Tanford, C., *The Hydrophobic Effect. The Formation of Micelles and Biological Membranes*, 2nd Edn, Wiley, New York, 1980.
3. Patist, A., Oh, S. G., Leung, R. and Shah, D. O., Kinetics of micellization: its significance to technological processes, *Colloid Surf., A*, **176**, 3–16 (2001).
4. Preston, W. C., Some correlating principles of detergent action, *J. Phys. Colloid Chem.*, **52**, 84–96 (1948).
5. Mukerjee, P. and Mysels, K. J., *Critical Micelle Concentrations of Aqueous Surfactant Systems*, NSRDS-NBS 36, US Department of Commerce, Washington, DC, 1971.
6. Rosen, M. J., *Surfactants and Interfacial Phenomena*, 2nd Edn, Wiley, New York, 1989.
7. van Os, N. M., Haak, J. R. and Rupert, L. A. M., *Physico-Chemical Properties of Selected Anionic, Cationic and Nonionic Surfactants*, Elsevier, Amsterdam, 1993.
8. Hiemenz, P. C. and Rajagopalan, R., *Principles of Colloid and Surface Chemistry*, 3rd Edn, Marcel Dekker, New York, 1997, pp. 297–354.
9. Debije, P., Light scattering in soap solutions, *Ann. N.Y. Acad. Sci.*, **51**, 575–592 (1949).

10. Anacker, E. W., Micelle formation of cationic surfactants in aqueous media, in *Cationic Surfactants*, Jungermann, E. (Ed.), Marcel Dekker, New York, 1970, pp. 203–309.
11. Berne, B. J. and Pecora, R. (Eds), *Dynamic Light Scattering*, Wiley, New York, 1976.
12. Patist, A., Bhagwat, S. S., Penfield, K. W., Aikens, P. and Shah, D. O., On the measurement of critical micelle concentrations of pure and technical-grade nonionic surfactants, *J. Surf. Det.*, **3**, 53–58 (2000).
13. Stilbs, P., Fourier transform pulsed-gradient spin echo studies of molecular diffusion, *Progr. NMR Spectrosc.*, **19**, 1–45 (1987).
14. Weissler, A., Fitzgerald, J. W. and Resnick, I., A sound velocity method for determination of molecular weight of liquid polymers, *J. Appl. Phys.*, **18**, 434–438 (1947).
15. Lang, J. and Zana, R., Chemical relaxation methods, in *Chemical Relaxation Methods in Surfactant Solutions – New Methods of Investigation*, Zana, R. (Ed.), Marcel Dekker, New York, 1987, pp. 405–452.
16. Shinoda, K., *Colloidal Surfactants: Some Physicochemical Properties*, Academic Press, New York, 1963, 1–96.
17. Eicke, H. F., *Surfactants in Nonpolar Solvents – Aggregation and Micellization*, in *Topics in Current Chemistry*, Vol. 87, Springer-Verlag, Berlin, 1980, pp. 85–145.
18. Kitahara, A. and Kon-No, K., Micelle formation in non-aqueous media, in *Colloidal Dispersions and Micellar Behavior*, Mittal, K. L. (Ed.), ACS Symposium Series, Vol. 9, American Chemical Society, Washington, DC, 1975, 225–232.
19. Mittal, K. L., *Solution Chemistry of Surfactants*, Plenum Press, New York, 1987.
20. Brown, C. W., Cooper, D. and Moore, J. C. S., Micelle formation in *o*-xylene solutions of sorbitan monostearate, *J. Colloid Interface Sci.*, **32**, 584–591 (1970).
21. Saad, A. L. G., Mead, A. I., El-Kholy, S. A. and Barakat, Y., Dielectric properties of some primary amines in nonaqueous medium. Effect of added alcohol on dipole moment and cmc values, *Z. Phys. Chem.*, **211**, 199–221 (1999).

CHAPTER 14

Measuring Contact Angle

C. N. Catherine Lam, James J. Lu and A. Wilhelm Neumann

University of Toronto, Toronto, Ontario, Canada

1	Introduction	251	3.1.2	Solid of cylindrical geometry	268
2	Background Theory	252	3.2	Indirect approaches	269
	2.1 The Laplace equation of capillarity and the Young equation	252	3.2.1	Powders, granules and porous solids	269
	2.2 The equation of state	252	4	Acknowledgements	277
3	Contact Angle Measurement	253	5	References	277
	3.1 Direct approaches	253			
	3.1.1 Flat surfaces	253			

1 INTRODUCTION

Contact angle is an important parameter in surface science. It is defined as the angle θ formed between the liquid–vapour and the liquid–solid interfaces, at the solid–liquid–vapour three-phase contact line. Several drop and bubble configurations are shown in Figure 14.1. Contact angle is also a common measure of the hydrophobicity of a surface. It can provide information about surface energies, surface heterogeneity and surface roughness. Surface energies (i.e. surface tensions), especially of solid–vapour and solid–liquid interfaces, are important parameters in many areas of applied science and technology. These interfacial tensions are responsible for the behaviour and properties of many materials such as paints, adhesives, detergents and lubricants. However, due to the lack of mobility of the molecules in a solid surface, solid surface tensions cannot be measured directly. Several independent approaches have been used to estimate solid surface tensions, including contact angle measurements (1–6), direct force measurements (7–14), gradient theory (15–18), the Lifshitz theory of van der Waals forces (18–20), and the theory of molecular interactions (21–23), to name just a few. Among these

methods, contact angle measurements are believed to be the simplest and the most straightforward approach, and certainly have attracted many researchers. In spite of the conceptual simplicity, experience has shown that the acquisition of thermodynamically significant contact angles requires painstaking effort. The accuracy of the results in contact angle measurements can be affected by the quality of solid surfaces, the purity of the measuring liquids, and the skill of the experimenter, but also by methodology and procedure.

There are different methods for measuring contact angles. The choice of a particular method depends on the geometry of the system and the size, as well as the shape, of samples. An accurate measurement of contact angle is obviously essential for the interpretation in terms of surface energetics (i.e. determination of solid surface tensions). This present chapter provides a review of the background theory used in the determination of contact angles, and then presents different methods of measuring contact angles. For the convenience of the reader, these methods are categorized according to the solid geometries involved.

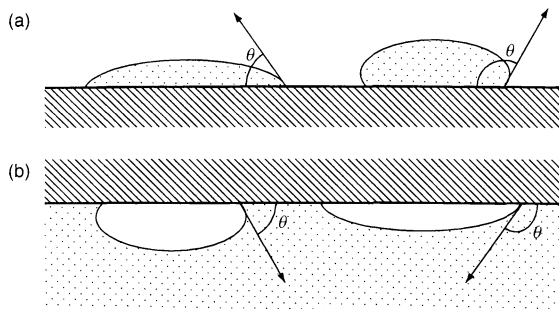


Figure 14.1. Some examples of three-phase systems: (a) sessile drops; (b) adhering bubbles

2 BACKGROUND THEORY

2.1 The Laplace equation of capillarity and the Young equation

The Laplace equation of capillarity and the Young equation are two principal equations in contact angle measurements. In essence, the shape of a liquid drop is determined by a combination of surface tension and gravity effects. Surface forces tend to make drops spherical, whereas gravity tends to elongate a pendant drop or flatten a sessile drop. The shape of the drop is governed by the Laplace equation of capillarity, as follows:

$$\Delta P = \gamma_{lv} \left(\frac{1}{R_1} + \frac{1}{R_2} \right) \quad (14.1)$$

where ΔP is the pressure difference across the curved air–water interface, and R_1 and R_2 are the principal radii of curvature of the drop at the point of interest. This equation is important in this chapter because one of the most powerful methods (i.e. Axisymmetric Drop Shape Analysis), which will be discussed in detail later, relies on this equation.

The Young equation governs the equilibrium or Young contact angle θ_Y of a liquid drop on a solid (see Figure 14.2). This was first derived in 1805 by Thomas Young, and is given as follows:

$$\gamma_{lv} \cos \theta_Y = \gamma_{sv} - \gamma_{sl} \quad (14.2)$$

where γ_{lv} is the liquid–vapour surface tension, γ_{sv} the solid–vapour surface tension, γ_{sl} the solid–liquid surface tension, and θ_Y is the Young contact angle. The derivation of the Young equation assumes that the solid surface is smooth, homogeneous and rigid; it should also be chemically and physically inert with respect to the liquids to be employed. Ideally, a unique contact

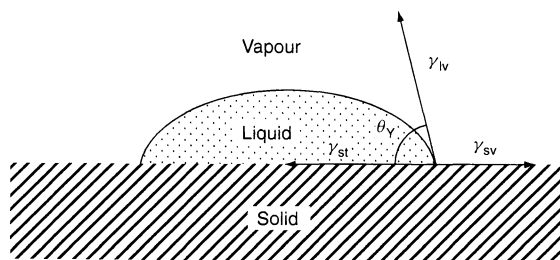


Figure 14.2. Schematic of a sessile drop contact angle system

angle is expected for a given system (e.g. a liquid drop on a solid surface), according to Young's equation. In a real system, however, a range of contact angles is usually obtained instead. The upper limit of the range is the advancing contact angle, θ_a , which is the contact angle found at the advancing edge of a liquid drop. The lower limit is the receding contact angle, θ_r , which is the contact angle found at the receding edge.

The above classical Young equation does not take into account possible effects of the three-phase line. In a more complete thermodynamic analysis, the line tension appears explicitly in the Young equation. The modified Young's equation is then written as follows:

$$\frac{\sigma}{R} + \gamma_{lv} \cos \theta = \gamma_{sv} - \gamma_{sl} \quad (14.3)$$

where σ is the line tension, R is the radius of the solid–liquid contact circle in the plane of the solid, and θ is the contact angle at that radius. If the drop is sufficiently large (i.e. as $R \rightarrow \infty$), the modified Young equation reduces to the classical Young equation. Despite being a well-defined thermodynamic quantity, there is controversy in determining both the magnitude and the sign of the line tension. As proposed by Gaydos and Neumann (24), line tensions are positive with magnitudes of the order of 10^{-6} J/m for many solid–liquid–vapour systems. This implies that the effect of line tension is negligible in contact angle measurements for drops with a radius larger than a few millimeters. The methods for measuring contact angle, which will be discussed below, do not depend on line tension considerations (24).

2.2 The equation of state

It is very difficult to measure surface tensions of a solid phase directly. Therefore, several approaches have been used to determine these values indirectly. Due to the relative ease of measuring contact angles on suitable

solid surfaces, numerous researchers use contact angles to estimate γ_{sv} and γ_{sl} . All these approaches rely on the Young equation (equation (14.2)). Among the parameters in Young's equation, only the liquid–vapour interfacial tension, γ_{lv} , and contact angle, θ , can be measured directly, and hence there remain two unknown quantities, i.e. γ_{sv} and γ_{sl} . Therefore, in order to calculate γ_{sv} and γ_{sl} from the Young equation, additional information is required.

Zisman (1) was the first to discover that for a given solid, the measured contact angles do not vary randomly from liquid to liquid, but rather changed more or less smoothly with liquid surface tension. More recent work by Li and Neumann (25, 26) and Kwok and Neumann (27) verify that values of $\gamma_{lv} \cos \theta$ depend only on γ_{lv} and γ_{sv} :

$$\gamma_{lv} \cos \theta = f(\gamma_{lv}, \gamma_{sv}) \quad (14.4)$$

where f is an, as yet, unknown function. By applying the Young equation, the relationship given in equation (14.4) can be rewritten as follows:

$$\gamma_{sv} - \gamma_{sl} = f(\gamma_{lv}, \gamma_{sv}) \quad (14.5)$$

and therefore:

$$\gamma_{sl} = \gamma_{sv} - f(\gamma_{lv}, \gamma_{sv}) = F(\gamma_{lv}, \gamma_{sv}) \quad (14.6)$$

where F is also an undetermined function. Equation (14.6) is called *the equation of state* for interfacial tensions. Its existence has been proven by the interfacial Gibbs–Duhem equations and the phase rule for interfacial systems (5, 28). By combining the Young equation and the equation of state, the interfacial tensions of solids, γ_{sl} and γ_{sv} , can be determined by using a liquid of known surface tension, γ_{lv} , and measuring the contact angle, θ , on the solid of interest, once the function F has been determined.

An explicit formulation for the equation of state of interfacial tensions has been given empirically (29), as follows:

$$\gamma_{sl} = \gamma_{lv} + \gamma_{sv} - 2\sqrt{\gamma_{lv}\gamma_{sv}} e^{-\beta(\gamma_{lv}-\gamma_{sv})^2} \quad (14.7)$$

Combining equation (14.7) with the Young equation, yields the following:

$$\cos \theta = -1 + 2\sqrt{\frac{\gamma_{sv}}{\gamma_{lv}}} e^{-\beta(\gamma_{lv}-\gamma_{sv})^2} \quad (14.8)$$

where β is an empirical constant. From the experimental contact angles, an average value of $\beta = 0.0001247 \text{ (m}^2/\text{mJ)}^2$ was obtained (25), by a scheme of multi-variable optimization. Details on the formulation of

the equation of state to determine interface tensions, i.e. equation (14.7), and the experimental evidence supporting the validity of both the equation-of-state concept and the accuracy of the equation formulation are discussed elsewhere (27).

Contact angles can only be measured accurately on a well-prepared solid surface (i.e. smooth, rigid, and chemically and physically inert). If the solid of interest is in the form of, say, a powder, and cannot be converted into a flat and smooth solid surface without drastic changes in its surface structure, the contact angle can still be obtained by using equation (14.8), by indirect means, as will be discussed later. In such cases, the solid–vapour surface tension, γ_{sv} , is obtained indirectly through the use of equation (14.8), and the contact angle, θ , is subsequently calculated. The reason for discussing the background theory of the equation of state in this section is to emphasize its importance in the determination of contact angles on powder particles and on porous solids. The indirect approaches for determining contact angles will be discussed later.

3 CONTACT ANGLE MEASUREMENT

3.1 Direct approaches

3.1.1 Flat surfaces

Sessile drop or adhering gas bubble

There are several methods for measuring contact angles. The choice of a particular method has to take into consideration the geometry of the surface. For flat surfaces, the most commonly used technique is the sessile drop method or, alternately, the adhering gas bubble method (see Figure 14.1). The contact angle of a sessile drop or an adhering gas bubble can be measured from the drop profile. A comparison between the sessile drop and the adhering bubble can be found in ref. (30).

Direct contact angle measurement from a drop profile can be conducted by either the conventional goniometer–telescope or the more advanced Axisymmetric Drop Shape Analysis (ADSA). In the former, the contact angle can be read off directly from the scale of a goniometer–telescope device, by placing a movable cross hair tangent to the drop. In the ADSA methodology, images of a drop or a bubble are acquired, and the contact angle is determined by a computer program, which is based on the rigorous integration of the Laplace equation of capillarity, and a fitting strategy to experimental drop/bubble profiles. It is usually claimed that the accuracy of the former method is $\pm 2^\circ$, whereas a standard deviation

of $\pm 0.2^\circ$ can be achieved by using ADSA. Despite the limited accuracy in the goniometric method, it is frequently used to characterize the wettability of solid surfaces, due to the relative ease of operation and immediate availability of results.

Goniometer–telescope Although many contact angle measurement techniques have been described in the literature, only a few have been widely used. Among these techniques, the most frequently used is the direct contact angle measurement of a sessile drop, which can be simply carried out by aligning a tangent to the sessile-drop profile at the point where the three interfaces (i.e. solid–vapour, liquid–vapour, and solid–liquid) meet. The contact angle of a liquid drop on a solid can be measured, either directly by using a telescope equipped with a goniometer eyepiece or from a photograph of a drop profile. Although the accuracy in the latter case may be higher, the results in either case are somewhat subjective and depend on the experience of the operator. Although certain training procedures can be used to improve the reproducibility, the accuracy of this method is usually $\pm 2^\circ$ at the best.

The primary components of a goniometer–telescope are a high-magnification (up to $50\times$) telescope and a goniometer eyepiece. The telescope permits a detailed examination of the intersection line between a drop profile and the solid surface. The goniometer eyepiece allows the alignment of a cross hair tangent to the bottom edge of the drop, and the contact angle can then be read off. The telescope may be tilted down slightly (approximately $1\text{--}2^\circ$) away from the horizontal position, in order to obtain the view of a portion of the profile reflected by the surface. By tilting the telescope, a tip (when $\theta < 90^\circ$) or a cusp (when $\theta > 90^\circ$) can be created, using a smooth reflective surface (see Figure 14.3). The

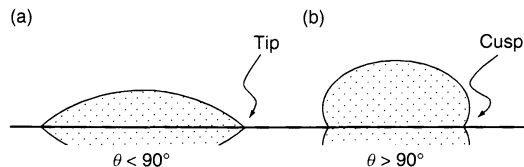


Figure 14.3. Schematics of sessile drops on reflective surfaces: (a) $\theta < 90^\circ$; (b) $\theta > 90^\circ$

tip or the cusp is used to locate the point where the drop profile contacts the solid. The experimenter can thereafter align the tangent to the profile at this point (the tip or the cusp). Ideally, the contact angle measured at the left side of the drop should be equal to the one measured at the right side, providing that the drop is perfectly symmetric. However, discrepancy of the measurements at the two sides may arise, due to the lack of axisymmetry of the drop. Therefore, contact angles at both sides of the drop should be measured and averaged in order to achieve higher accuracy.

In order to establish advancing contact angles and receding contact angles of a sessile drop, liquid is injected into or withdrawn from a drop slowly, by means of a syringe assembly. There are two ways of increasing or decreasing the volume of a sessile drop: liquid can be added into or withdrawn from a drop, using a syringe assembly with its needle passing through the upper surface of the drop, as shown in Figure 14.4(a); on the other hand, liquid can be added into or withdrawn from the drop, using a syringe assembly with its needle passing through the solid surface from the bottom of the drop, as shown in Figure 14.4(b). The former one is more convenient since the experimenter does not need to drill a hole through the solid surface to insert the needle. However, more attention is needed in the former

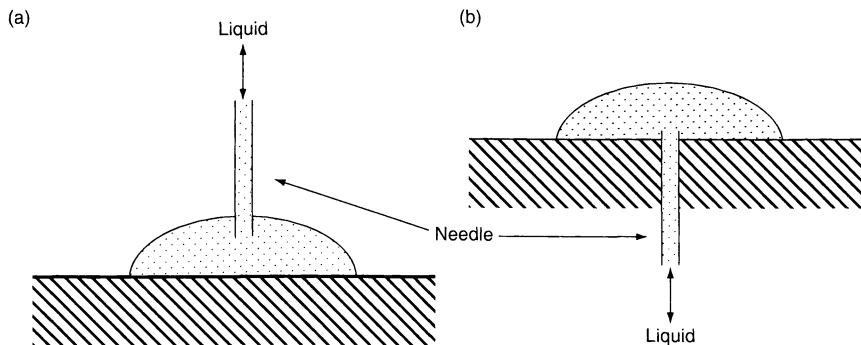


Figure 14.4. Two ways of supplying liquid to the sessile drop by a syringe assembly: (a) passing through the upper surface of the drop; (b) passing through the solid surface from the bottom of the drop

www.iran-mavad.com

method, because the position of the needle tip inside the drop, as well as the size of the needle, may have an effect on the contact angle measurements. For example, if the needle enters the drop at a point too close to the solid, it may distort the drop profile. If the drop is not symmetrical with respect to the needle position, particularly if the distance from the needle to the surface is close to the diameter of the needle, it is likely to have unequal angles at the left and right side, during advancing and receding contact angle measurements. This inequality is more pronounced in small drops. If this effect is present, either the measurements should be disregarded or the measurements at locations farther from the needle should be considered as being more representative of the system. Furthermore, although the needle will distort the drop profile when it passes through the upper surface of the drop, this does not perturb the liquid in the region of the contact line if the diameter of the drop is larger than the diameter of the needle.

It is advantageous to have liquid added into or withdrawn from the drop from below the solid surface, since the needle will not distort the drop surface in this case. However, no matter which configuration is used, the distortion of the profile due to the needle will not affect the measured contact angles, provided that the needle diameter is not larger than approximately one-fifth of the drop diameter. Moreover, contact angles should be measured on both sides of a drop profile, whenever feasible. By repeatedly adding small amounts of liquid to the drop and measuring the contact angle each time, more accurate results can be achieved by means of averaging.

Axisymmetric Drop Shape Analysis-Profile The technique of Axisymmetric Drop Shape Analysis-Profile (ADSA-P), as practiced by the present authors, is a powerful method for determining contact angles and liquid–fluid interfacial tensions from the profile of liquid drops. Besides these two parameters, the drop volume and the drop surface area, as well as the drop radius, all with their corresponding 95% confidence limits, or other statistical information are also output.

The earliest efforts in the analysis of axisymmetric drops were made by Bashforth and Adams (31) in 1883. The strategy was to generate sessile-drop profiles for different values of surface tension and radius of curvature at the apex of the drop, and then to determine the interfacial tension and contact angle of an actual drop by interpolating the tabulated theoretical profiles. Hartland and Hartley (32) improved this method by using a computer program to perform the above comparisons. The

use of these tables is limited to drops of a certain size and shape range, and the procedures are somewhat cumbersome and hence not amenable to automation. Maze and Burnet (33, 34) have developed a more satisfactory scheme for the determination of interfacial tensions from the shape of sessile drops. These authors used a numerical nonlinear regression procedure to generate a theoretical drop shape, which is used to fit a number of points selected from an experimental drop profile. In order to generate a theoretical drop shape, initial estimates of the drop shape and size are required. These initial estimates have to be reasonable, or otherwise the theoretical drop profile will not converge to the experimental drop profile. To this end, values of initial estimates are usually obtained from the tables of Bashforth and Adams (31). Despite the progress in strategy, there are several limitations in this approach. One of them is the computation of the error function, i.e. the difference between the theoretical drop profile and the experimental drop profile. This is computed by summing the squares of the horizontal distances between the theoretical drop profile and the experimental profile. This computation is not adequate for some drop shapes, particularly for those sessile drops with low liquid–vapour surface tensions. More details can be found in refs (35, 36).

ADSA-P, initially developed by Rotenberg *et al.* (35), has removed the above limitations. This utilizes a combination of a nonlinear least-squares fit approach and the Newton–Raphson method, in conjunction with the incremental loading method to fit experimental drop profiles to Laplacian curves. From the best-fitted theoretical profile, we are able to find the liquid–vapour surface tension, as well as the contact angle of sessile drops. The best-fit curve is identified by finding the minimum deviation of the experimental drop profiles from the theoretical profiles. Therefore, an objective function is utilized to measure the deviation between the experimental drop profile and the theoretical profile (i.e. Laplacian curve). This function is computed by summing the squares of the normal distances between the calculated curve and the experimental points. Figure 14.5 illustrates the comparison between experimental profile points, U_i , $i = 1, 2, \dots, N$, which are obtained from image analysis, and the Laplacian curve, $u = u(s)$. Therefore, for an experimental drop profile, the theoretical Laplacian curve which minimizes the objective function is used to calculate the surface tension and contact angle.

Initially, drop coordinate points had to be obtained by some manual procedure. In the early 1990s, Cheng *et al.* (37) developed an enhanced digital image acquisition technique for extracting the drop profile coordinate points from the images of experimental drop

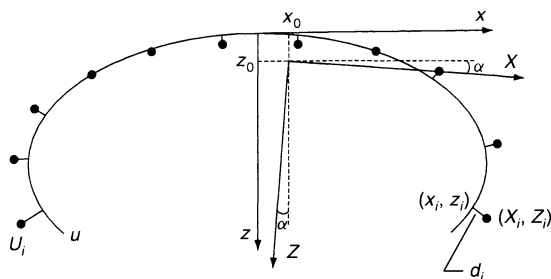


Figure 14.5. Comparison between experimental points and a Laplacian curve. The curve $u = u(s)$ is a theoretical profile based on the Laplace equation of capillarity, while points U_i , $i = 1, 2, \dots, N$, are points selected from the meridian of an experimental drop profile. The deviation of the i th point from the Laplacian curve, d_i , can be calculated. The purpose of the objective function of ADSA is to minimize the sum of the square of the minimum distance, d_i . Since the coordinate systems of the experimental profile and the predicted Laplacian curve do not necessarily coincide, their offset (x_0, z_0) and rotation angle (α) must be considered. Both of the latter are optimization parameters. Since the program does not require the coordinates of the drop apex as input, the drop can be measured from any convenient reference frame, and all measured points on a drop profile are equally important (from ref. (36))

automatically. Later on, del Río and Neumann (38) modified and re-wrote ADSA-P by using the “C language” and more sophisticated numerical methods with higher accuracy and efficiency. ADSA-P can achieve an accuracy of $\pm 0.05 \text{ mJ/m}^2$ or better for surface tensions and $\pm 0.2^\circ$ or better for contact angles. Details of ADSA-P, including background mathematical analysis, fundamental equations and optimizations, are provided in refs (36, 38).

ADSA-P has several advantages over traditional methods, as follows:

1. Since the coordinates of the drop apex are optimization parameters, the drop can be measured from any convenient reference frame, and all measured points on a drop profile are equally important.
2. Only the conceptual minimum of input is required, namely the density difference across the interface, the magnitude of the local gravity acceleration, and several arbitrary coordinate points selected along the drop profile.
3. There is no restriction on the drop-size, the surface tension and the contact angle, as long as the latter is not close to zero.
4. Besides interfacial tensions and contact angles, volume, surface area and radius of curvature are also output of ADSA-P.

When using ADSA, it is important to acquire good quality images so that the accuracy of selecting coordinate points along the experimental drop profile can be guaranteed. Figures 14.6(a) and 14.6(c) (36) illustrate the side views of actual drops taken by ADSA-P. A schematic of the ADSA-P set-up is shown in Figure 14.7. In this technique, a high-resolution camera is mounted on a microscope. The drops are illuminated from behind, by using a white-light source. The illuminating light travels through a heavily frosted diffuser in order to minimize the heat adsorption into the drop, and also to provide a uniformly lightened background, which produces high contrast in the acquired images. The video signal of the sessile drop is transmitted to a digital video processor or an image processor (such as a Parallax XVideo board or ITI image processor), which performs the task of frame grabbing and image digitization. The digitized image contains data in the form of pixels. Usually, there are 640×480 pixels in an image with each pixel having a value from 0 (i.e. black) to 255 (i.e. white), which represents the intensity or grey level at the corresponding position. In other words, a digitized image is mathematically represented by an array of integer numbers from 0 to 255. In this fashion, a computer (such as a Sun SPARCstation or a personal computer) can acquire images of a drop through the digital camera, and perform the image analysis and computation on the acquired images. It is important to note that the experiment is performed on a vibration-free table, in order to isolate the system from any possible external vibration.

Experimental procedure As mentioned above, dynamic contact angle measurements (i.e. advancing and receding contact angles) can be performed by adjusting the volume of the drop from above or below the solid surface. However, if it is adjusted from the top, its profile will be disturbed as the needle pierces the drop. Since ADSA requires a complete drop profile for determining contact angles, liquid has to be supplied from the bottom of the drop. Therefore, liquid is pumped into or withdrawn from the drop by a motorized syringe through a small hole in the solid surface. This strategy of pumping liquid from below the surface was pioneered by Oliver *et al.* (39). The procedure allows measurement of the true advancing contact angles without any disturbing influences, such as the vibration of the drops. It has been shown that contact angles on well-prepared solid surfaces are independent of the rate of the advancing at moderate rates up to at least 1 mm/min . In other words, low-rate dynamic contact angles are identical to the static contact angles. However, there are advantages to measuring dynamic contact angles rather than static

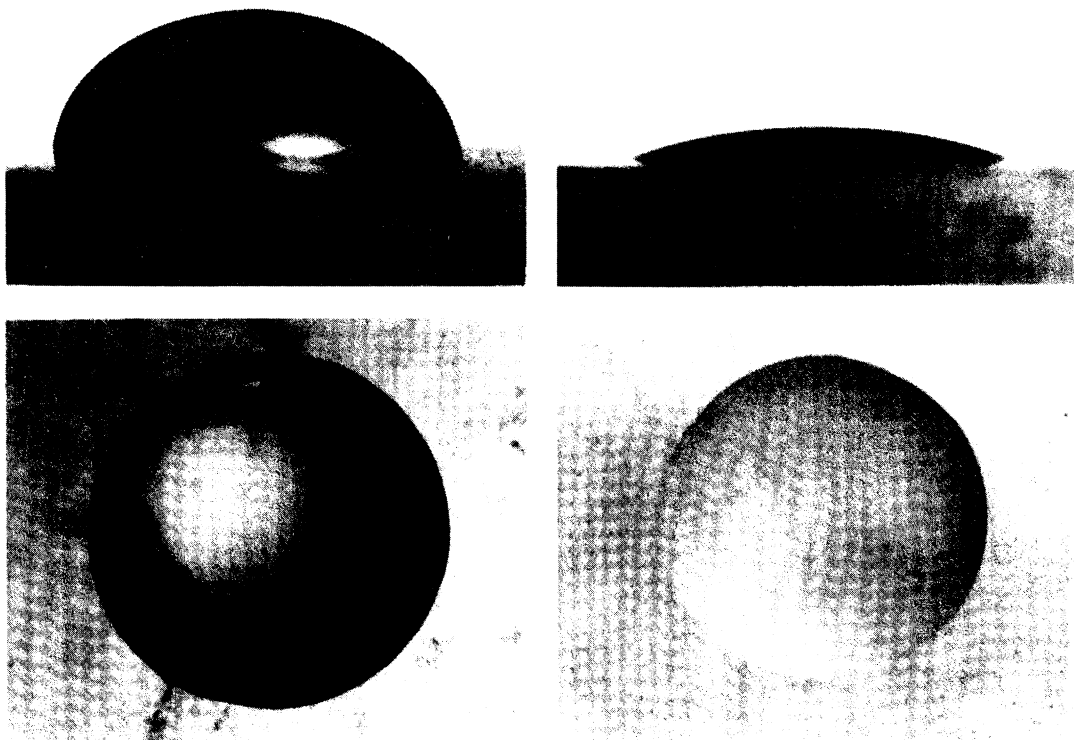


Figure 14.6. Side (a) and top (b) views of a sessile drop with a large contact angle, and side (c) and top (d) views of a sessile drop with a small contact angle (from ref. (36))

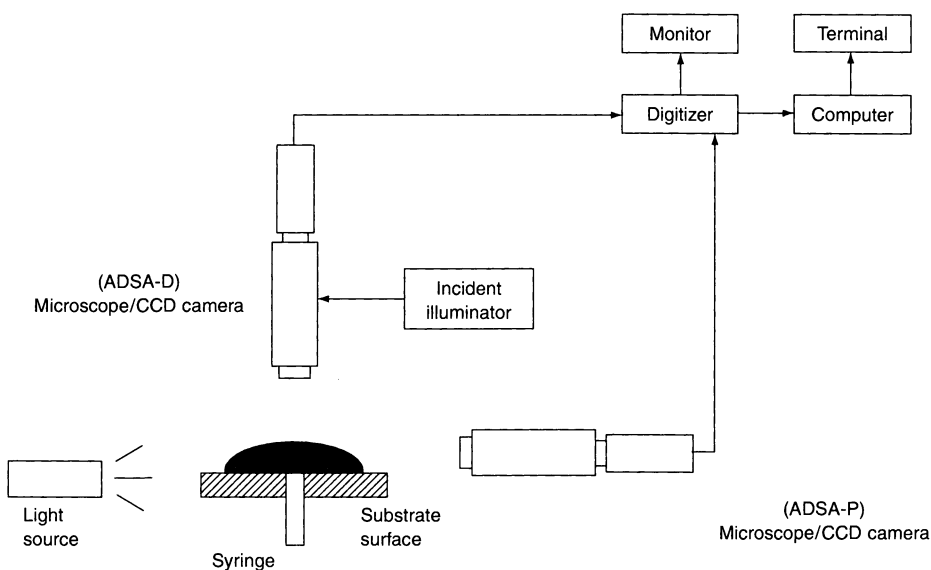


Figure 14.7. Schematic of the experimental set-up for analysis of a sessile-drop system by ADSA-P and ADSA-D (from ref. (36))

ones: the initial drop placed on the surface may not reach the proper advancing contact angle but rather an angle between advancing and receding, due to initial manipulation or evaporation. Therefore, with an increasing volume of the drop and hence contact radius, one can ensure that the contact angle of the drop reaches the proper advancing contact angle, i.e. that the three-phase line moves. Furthermore, the moving three-phase contact line may alleviate the effect of equilibrium spreading pressure, local irregularities, and defects on the surface. Therefore, it is a good strategy to conduct contact angle measurements dynamically, by using a motor-driven syringe to pump liquid steadily into the sessile drop from below the surface. In order to facilitate such an experimental procedure, a hole with the diameter of about 1 mm on the solid surface is required. A schematic of this set-up is shown in Figure 14.8.

In the sessile drop experiments, a bubble level is first used to level the surface stage. A sample surface is then carefully placed on the surface stage in such a way that the stainless steel needle (Chromatographic Specialities, Brockville, Ontario; N723 needles pt.#3, 2" long, 23 GA, cat# H91023) will pass through the hole in the centre of the surface. In order to avoid leakage between the needle and the hole, Teflon[®] tape (Labcor, Anjou, Quebec, cat# H-088782-27) is wrapped around the end of the needle, before being inserted through the

hole. The needle is positioned in a way that its tip is just above the sample surface. In order to ensure that the advancing drop increases axisymmetrically in the centre of the image field and does not hinge on the lip of the hole, an initial liquid drop of about 0.3 cm radius is carefully deposited from *above* to cover the hole on the surface.

The motorized syringe is then operated at a constant speed, which can be controlled by adjusting the voltage from a voltage controller. The motorized syringe mechanism pushes the syringe plunger (Chromatographic Specialities, Brockville, Ontario; gas-tight Hamilton syringe: 81201, 1750LT, cat# 063283) during advancing and pulls it back during receding, thus leading to an increase and decrease, respectively, in drop volume and hence the three-phase contact radius. The growing and shrinking drop is then recorded in a sequence of images by a computer, using an image acquisition speed of approximately one image every two seconds. It has proven convenient to follow the change of contact radius from approximately 3 mm to 5 mm. If receding angles are desired, the drop volume can be reduced by switching the motor to reverse mode. Since the contact angle and the drop radius can be determined simultaneously by ADSA, the advancing or receding dynamic contact angles are obtained in each image as a function of the drop radius. By plotting the drop radius over time, the actual speed of advancing and receding can be determined as the slope of the radius versus time trace. By adjusting the speed of the pumping mechanism, different rates of advancing and receding can be studied.

It has been found that the liquid surface tension values measured from sessile drops are less accurate than those obtained from pendent drops. This is a consequence of the assumption that the drop shape is axisymmetric. While the shape of sessile drops is very sensitive to even a very small surface imperfection, such as roughness and heterogeneity, axisymmetry is enforced in the case of a pendent drop through the circularity of the capillary orifice supporting the drop, thus resulting in more reliable surface tension results. The contact angle measurement, on the other hand, is less sensitive to geometrical imperfections than the surface tension measurement.

A typical result obtained from the dynamic contact angle experiment of *n*-dodecane on a silicon wafer coated with FC-732 (3M Inc. FluoradTM brand anti-migration coating) is illustrated in Figure 14.9. As mentioned earlier, ADSA not only determines (a) contact angles, θ , but also (b) the radius, R , (c) the volume, V , and (d) the liquid-vapour interfacial tension, γ_{lv} , of

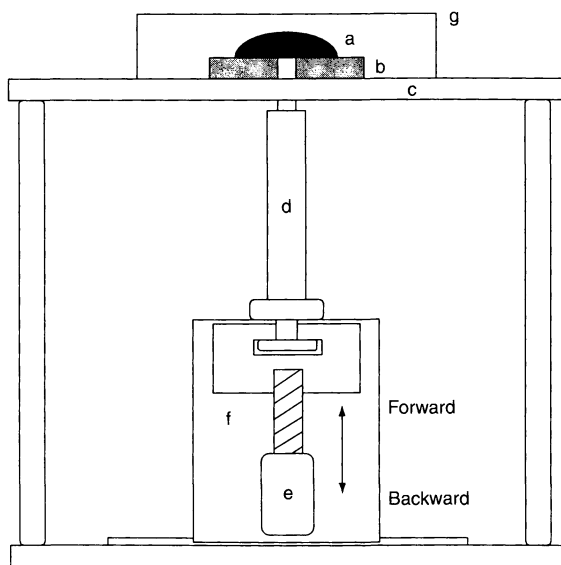


Figure 14.8. Schematic of a motorized syringe mechanism for dynamic contact angle measurements: a, liquid; b, solid; c, stage; d, syringe; e, motor; f, driving mechanism; g, quartz curvette

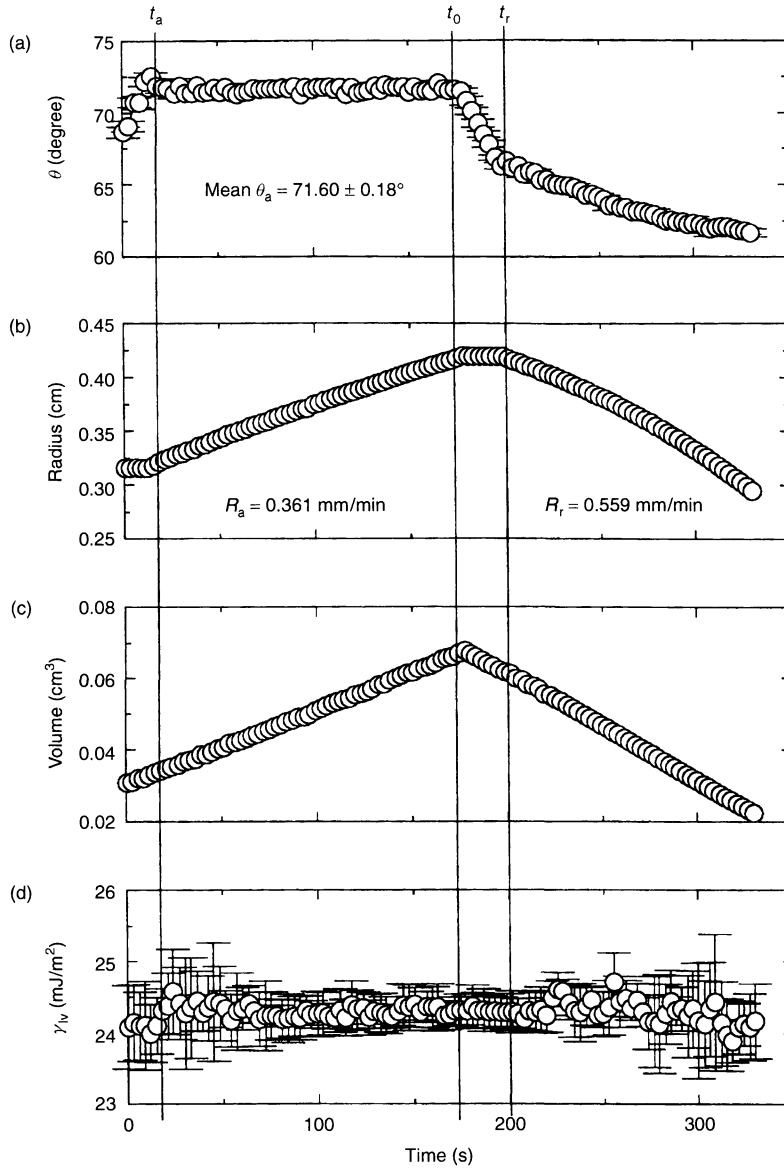


Figure 14.9. Typical experimental results obtained for dynamic contact angle measurements of *n*-dodecane on a silicon wafer: (a) contact angle; (b) contact radius; (c) volume; (d) liquid–vapour interfacial tension of the drop. R_a is the rate of advancing of the drop front, while R_r is the rate of receding of drop front (from ref. (40))

the liquid drop, as shown in Figure 14.9. For convenience, these graphs are divided into four domains by three vertical lines. In the example given in Figure 14.9, the first domain ranges from the beginning of the experiment when the motor is switched on to time t_a when the three-phase contact line starts to advance. It can be observed in this domain that as the drop

volume (Figure 14.9(c)) increases, the apparent contact angle (Figure 14.9(a)) increases at essentially constant radius (Figure 14.9(b)). This happens before the contact angle reaches the proper advancing contact angle, and it occurs because the initial contact angle lies somewhere in between the advancing and receding contact angles even if the drop is carefully placed on the solid

surface. This effect is pronounced for liquids with high evaporation rates. Therefore, the advancing procedure is necessary to ensure that the measured contact angle is the advancing contact angle. From a certain point (i.e. at time t_a in this case) on, the drop radius starts to increase with constant contact angle until time t_0 . At this time, the motor is switched to the reverse mode and the liquid starts to flow back into the syringe. The mean advancing contact angle is found by averaging the constant contact angles, in this case $\theta_a = 71.60 \pm 0.18^\circ$. From time t_0 to time t_r , the three-phase contact line of the drop is immobile. This is characterized by constant radius, and a rapid decrease in contact angle. This domain represents the transition from advancing to receding contact angles, i.e. the period during which the three-phase line is stationary. This pattern continues until a point (t_r) is reached at which the periphery starts to recede. This domain is characterized by decreasing radius, and, in this case, a decrease of the receding contact angle. Unlike the advancing contact angle, the receding contact angle very often changes with time, presumably due to liquid retention by the solid surface (40). The liquid–vapour surface tension, γ_{lv} , is fairly constant throughout the experiment, as shown in Figure 14.9(d). This suggests that there was no significant dissolution of the solid coating within the time-frame of the experiment. As discussed earlier, the rates of advancing and receding can be determined as the slope of the drop radius versus time. As given in Figure 14.9(b), the actual speeds of advancing and receding are found to be 0.361 mm/min and 0.559 mm/min, respectively, by linear least-squares fitting.

Goniometer versus ADSA-P Despite the high precision and accuracy of the contact angle measurements by ADSA-P, the conventional goniometric method is still a popular technique for measuring contact angles, because of its relative ease of use. Figure 14.10 (41) shows a typical $\gamma_{lv} \cos \theta$ versus γ_{lv} plot of contact angle data from the goniometer study for two copolymers. It can be seen from this figure that, due to the scatter, no functional dependence seems to exist. However, it was found (41) that such measurements can be misleading, in that certain complex contact angle patterns which preclude the use of Young's equation are not recognized. An example of such a case is illustrated in Figure 14.11 (41) where ADSA-P is used for measuring diiodomethane contact angles on poly(propene-*alt*-*N*-(*n*-propyl)maleimide) copolymer, showing a “slip–stick” pattern. From this figure, it can be seen that initially, as the drop volume increases

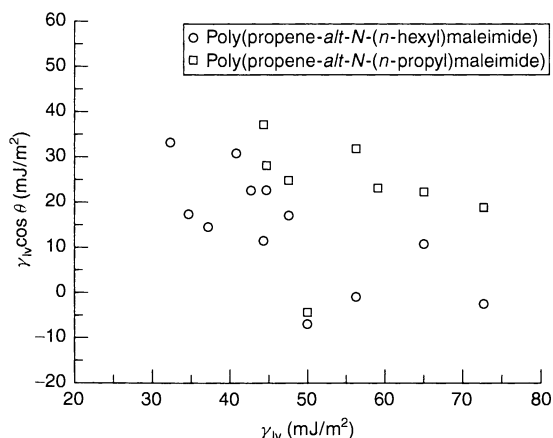


Figure 14.10. Plots of $\gamma_{lv} \cos \theta$ versus γ_{lv} , obtained from goniometer studies, for the poly(propene-*alt*-*N*-(*n*-propyl)-maleimide) and poly(propene-*alt*-*N*-(*n*-hexyl)maleimide) copolymers (from ref. (41))

linearly, the contact angle increases from 45° to 65° at an essentially constant drop radius (i.e. the drop front “sticks” on the surface). Suddenly, the drop front “slips” as liquid is continuously supplied into the sessile drop. The resulting contact angle decreases sharply from 65° to 40° . As more liquid is supplied into the drop, the drop front sticks again to the surface and the contact angle increases again.

Other complex contact angle patterns, such as a decrease of contact angle with decreasing liquid–vapour surface tension and an increase of contact angle with decreasing liquid–vapour surface tension, are also obtained in dynamic ADSA-P measurements, in certain cases. These patterns are presumably due to dissolution of polymer by liquid and physico-chemical reactions between the solid and the liquid. Further details of these can be found elsewhere (41).

Obviously, in these complex cases, the measured contact angles cannot be used to calculate the solid surface tension: according to Young's equation, since γ_{sv} and γ_{lv} (and γ_{sl}) are constants, θ should be a constant. Since these contact angles cannot be used in conjunction with Young's equation and/or the assumption of constant γ_{sv} , they have to be excluded in the characterization of surface properties. If only the “meaningful” contact angle data (from both ADSA-P and goniometer experiments) are used and those contact angle data which show complex patterns in the ADSA-P study are eliminated, smooth curves (i.e. $\gamma_{lv} \cos \theta$ changes smoothly with γ_{lv}) are obtained instead of the scatter in Figure 14.10, as shown in Figure 14.12. It is apparent that, in this figure,

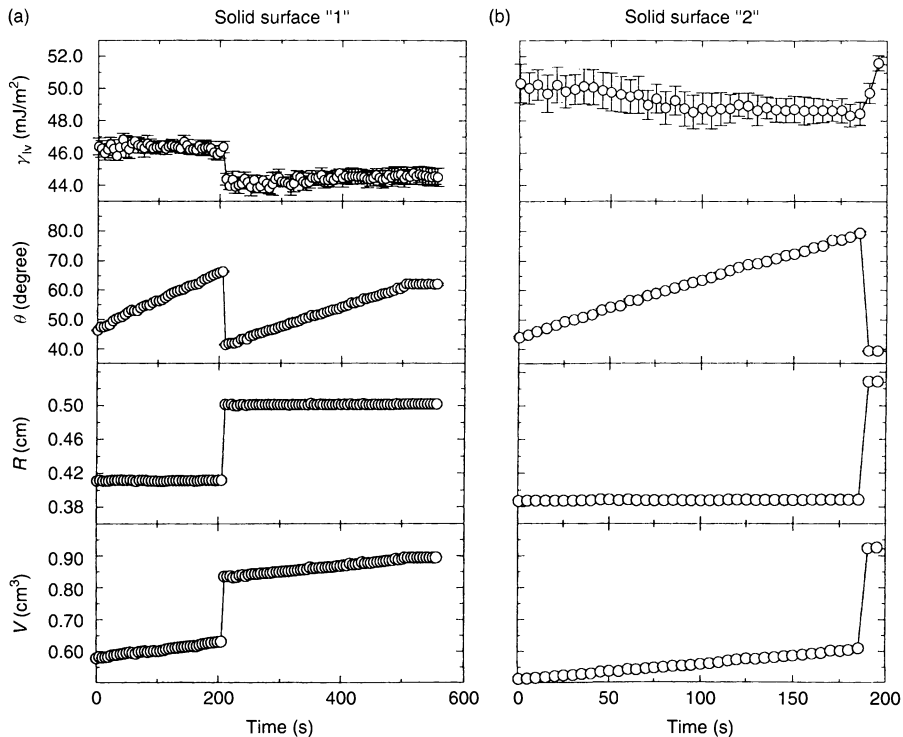


Figure 14.11. Low-rate dynamic contact angle data obtained for diiodomethane on two poly(propene-*alt*-*N*-(*n*-propyl)maleimide) copolymer surfaces, as measured by ADSA-P, showing “slip–stick” patterns (from ref. (41))

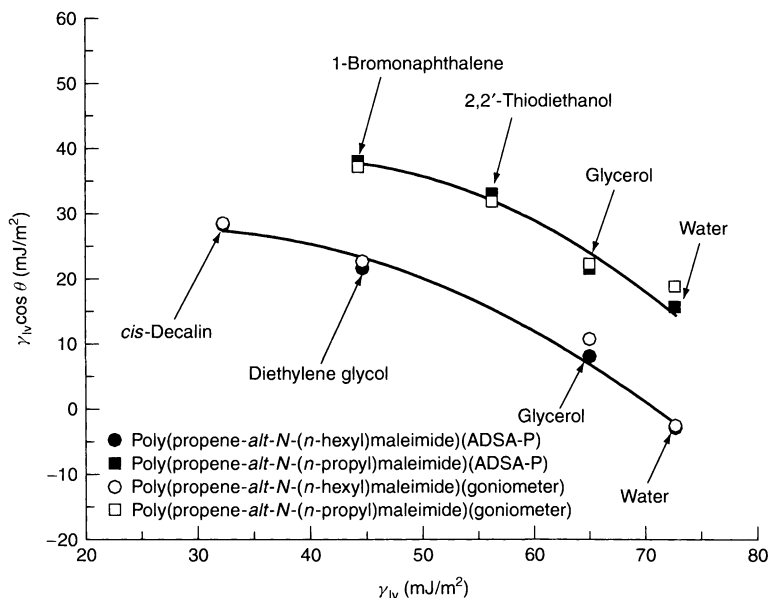


Figure 14.12. Values of $\gamma_{lv} \cos \theta$ versus γ_{lv} obtained from ADSA-P and goniometer studies, for the poly(propene-*alt*-*N*-(*n*-propyl)maleimide) and poly(propene-*alt*-*N*-(*n*-hexyl)maleimide) copolymers, after deletion of inconclusive data (from ref. (41))

the goniometer results agree quite well with the ADSA results. The problem with the goniometer is thus not so much a limited accuracy, but its inability to distinguish clearly between the regular pattern as shown in Figure 14.9, from an inconclusive pattern, such as that illustrated in Figure 14.11.

It was verified by del Rio *et al.* (42) that the difference found between the contact angle results obtained with the two methods is not a consequence of the measurement principle *per se*, but largely due to the difference between the static (goniometer) and dynamic (ADSA) procedures. In their study (42), an automated polynomial fit (APF) program was written for putting tangents to the same drop images on which ADSA-P operates. The results show that the contact angles computed by APF are in good agreement with the ones computed by ADSA-P. In other words, the result implies that the different outcome in ADSA-P (see Figure 14.12) and the goniometric method (Figure 14.10) is due to the degree of automation utilized in the two types of experiments (i.e. *dynamic* contact angles are studied by ADSA-P, while the conventional goniometer method measures essentially *static* contact angles) (42). Since dynamic measurements allow one to detect the complex patterns and to distinguish the meaningful contact angles from the meaningless ones, automated methods, such as ADSA-P, are preferable if not outright necessary. Static contact angles, such as those measured by a goniometer, are liable to produce a mixture of meaningful and meaningless contact angles.

It should also be noted that APF gives a strictly two-dimensional account of the meridian section, fitting the profile points near the contact line. Thus, its measuring scheme is the same as that of the goniometer method. It is interesting to note that the error limits are significantly larger for APF than for the ADSA-P. Presumably ADSA, by considering the whole drop profile, will average out small irregularities near the three-phase line, which can be expected to have a pronounced effect in APF.

Axissymmetric Drop Shape Analysis-Diameter As discussed earlier, a drop shape method, such as ADSA-P, utilizes the meridian profile of a sessile drop to calculate the contact angle and the interfacial tension. Despite its versatility, this technique does suffer from some limitations. In cases of very low contact angles (less than 20°), it may be difficult to measure contact angles accurately by using profile techniques, e.g. ADSA-P. In order to avoid this difficulty, an alternate method called ADSA-(C)D (contact diameter) has been developed by utilizing the drop contact diameter (see Figure 14.6(b)

and (d)) (43). In order to obtain this parameter, i.e. the contact diameter, the sessile drop is viewed from above instead of from the side, as in ADSA-P. Besides the contact diameter, ADSA-D requires the volume of the sessile drop and the surface tension of the liquid, in addition to the density difference across the liquid-fluid interface, and the gravitational constant, as inputs. The contact angle is computed by numerically minimizing the difference between the volume of the drop that is given from experiment and the one predicted by the Laplace equation of capillarity.

The experimental set-up for analysis of a sessile-drop system by ADSA-D is similar to that for ADSA-P (see Figure 14.7), except that the imaging system is aligned vertically rather than horizontally. As with ADSA-P, digital image acquisition and analysis is used. The procedures for determining the desired diameter can be performed either manually or automatically (44).

In the manual scheme, a number of coordinate points, approximately 8 to 10, on the periphery of the drop are extracted by a cursor on a video screen (45). An average drop diameter is then calculated by finding a circle which best fits the selected points, via a least-squares curve fitting method. The ADSA-D program calculates the contact angle, based on the drop diameter and the other required input parameters.

An automated module was also developed (44). This uses a region-growing algorithm to calculate the drop area as it is viewed from above. The equivalent drop diameter is calculated from the known drop area. Contact angles measured by ADSA-D through the automated scheme are more accurate and reproducible than those obtained through the manual digitization scheme. Details of the automated technique can be found in ref. (44).

Due to the feature that ADSA-D utilizes an average contact diameter to evaluate the contact angle, it has proved to be very useful for the measurement of drops on non-ideal, i.e. rough and heterogeneous, surfaces, such as biological surfaces. In these cases, an average contact diameter leads to an average contact angle. Since it is not possible to form an axial-symmetric drop on such a surface, ADSA-P cannot be employed. As an example, Figure 14.13 (45) illustrates typical shapes of double-distilled water drops formed on a layer of *Thiobacillus ferrooxidans* cells. Several points on the perimeter of the drop have to be selected in order to estimate the average drop diameter. Figure 14.14 illustrates the manner in which points are selected from a hypothetical sessile drop perimeter. Details of the numerical procedure for ADSA-D are given in ref. (36).

The ability of ADSA-D to produce average contact angles on imperfect solids, even when the drops deviate

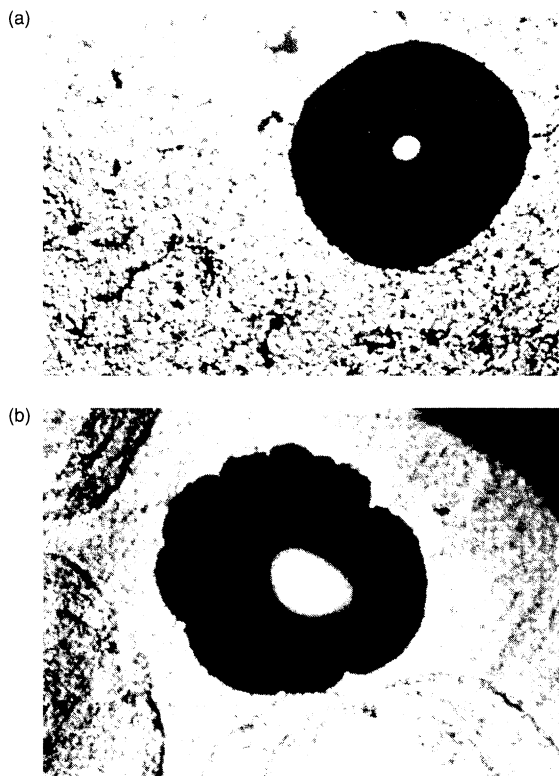


Figure 14.13. Images of sessile drops of water on a layer of *Thiobacillus ferrooxidans* cells. The contact angles calculated by using ADSA-D are (a) 12.7° and (b) 11.3° (from ref. (36))

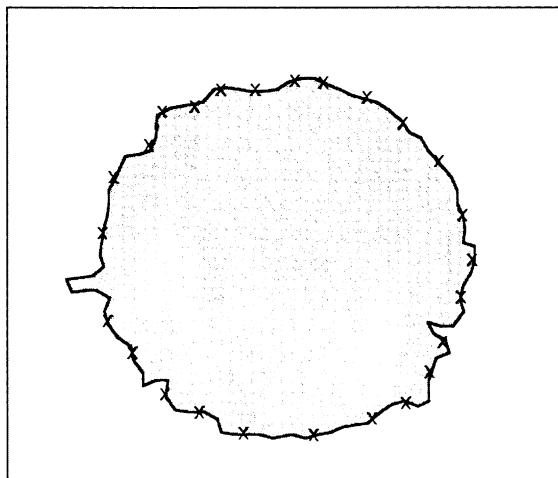


Figure 14.14. Schematic of the determination of the perimeter of a hypothetical sessile drop on a video screen using a cursor navigated and controlled by a mouse to select perimeter points (from ref. (36))

significantly from axial symmetry, makes it a suitable method for such surfaces, even when the contact angles are not particularly small. For contact angles above 90° , since the three-phase line is not visible from above, another version of ADSA-D was developed (46). This modification is similar to the standard ADSA-D, except that it relies on the observable maximum equatorial diameter instead of the contact diameter, which cannot be readily observed. The ADSA-D software package unifies the versions for the different situations (36). The numerical analysis is simpler than ADSA-P, since the liquid surface tension and the drop volume are used as input in ADSA-D.

The accuracy of this technique for contact angle measurements on smooth and homogeneous surfaces is found to be better than $\pm 0.3^\circ$ (45, 47). It should be noted that there is practically no limitation for measuring contact angles by ADSA-D. For example, a contact angle of as low as $4.50 \pm 0.36^\circ$ (*n*-heptane on a carboxylic-acid-terminated self-assembled monolayer surface) was obtained by using ADSA-D. Table 14.1 (36) presents some contact angle data measured by ADSA-P, ADSA-D and the direct goniometric method. It can be seen that the two ADSA techniques provide greater accuracy and reproducibility than the direct method (36). However, low contact angles will result in low drop profiles and hence somewhat larger errors in ADSA-P. In ADSA-D, on the other hand, the contact diameter increases as the contact angles decrease at constant drop volume, thus increasing the accuracy. Therefore, ADSA-D produces a higher degree of precision than ADSA-P for low contact angles, as can be seen in Table 14.1.

Interference microscopy

Interference microscopy provides another way of measuring contact angles under certain circumstances (48).

Table 14.1. Comparison of contact angles (degree), obtained with ADSA-D and ADSA-P on siliconized glass with ethylene glycol (EG) and undecane (UN). The error limits are 95% confidence limits for ADSA-P and ADSA-D, while for the direct method, the errors are a subjective estimate (from ref. (36))

Sample No./liquid	ADSA-D	ADSA-P	Direct (goniometer)
1/EG	84.1 ± 0.4	83.2 ± 0.6	84 ± 3
2/EG	84.9 ± 0.2	84.7 ± 0.5	83 ± 3
3/EG	85.2 ± 0.3	85.2 ± 0.5	84 ± 3
4/UN	22.7 ± 0.2	21.8 ± 0.7	19 ± 3
5/UN	21.2 ± 0.2	22.2 ± 0.6	20 ± 3
6/UN	21.5 ± 0.2	22.2 ± 0.5	20 ± 3

Depending on the relative reflectivities of the solid and the liquid surface, there are several constellations possible. For example, in a solid–liquid–vapour system, if the reflectivities at the solid–liquid and the liquid–vapour interfaces are comparable, fringes generated by interfering beams reflected from the two interfaces may be detected easily. When the optical path difference between adjacent interfering beams satisfies the following relationship:

$$t = \frac{\lambda}{2\mu} \quad (14.9)$$

dark fringes can be observed. Here, t is the optical path difference between adjacent interfering beams, μ is the refractive index of the liquid and λ the wavelength. Figure 14.15 (30) illustrates a schematic of the set-up used in the above case.

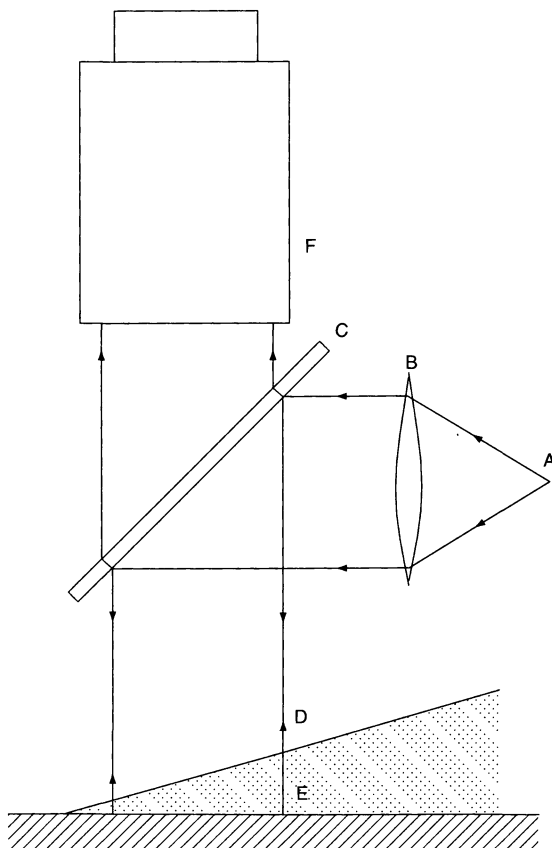


Figure 14.15. Optical arrangement employed for measuring contact angles by interference microscopy: A, light source; B, lens; C, half-silvered glass mirror; D, liquid–vapour interface; E, substrate–liquid interface; F, microscope (from ref. (30)).

The contact angle can be written as follows:

$$\theta = \tan^{-1} \frac{t}{x} \quad (14.10)$$

where x is the separation between dark fringes. Therefore, the contact angle can be determined by combining equations (14.9) and (14.10), to give the following:

$$\theta = \tan^{-1} \frac{\lambda}{2\mu x} \quad (14.11)$$

In a solid–liquid–vapour system where the solid substrate is opaque and less reflective than the liquid surface, Michelson optics (i.e. those based on the Michelson interferometer) can be employed. In this case, the light reflected from a flat optical mirror is superimposed on to the light reflected from the liquid drop surface. If the underlying solid phase is transparent, other constellations of interferometry can be applied (49).

For very tiny drops of liquids that form low contact angles, interference microscopy offers many advantages over other methods, and can be used to investigate the drop-size dependence of contact angles (50, 51). However, due to the limitations imposed by the lateral magnification for resolving fringes, large contact angles cannot be measured conveniently by interference microscopy.

Capillary rise at a vertical plate

The drop shape techniques (e.g. ADSA) of measuring contact angles have certain limitations. For example, the largest meridian section used to calculate contact angles only reflects the contact angles at a point at which the meridian plane intersects the three-phase contact line. Surface heterogeneity and/or roughness of the surface may cause a change in the shape of the drop, and hence affect the accuracy of the measured contact angle.

The measurement of contact angles from the capillary rise at a vertical plate produces an accuracy comparable to ADSA. Assuming a vertical plate of infinite width, the Laplace equation can be integrated to give the following (52):

$$\sin \theta = 1 - \frac{\Delta \rho g h^2}{2\gamma_v} \quad (14.12)$$

In practice, plates that are about 2 cm wide will satisfy the theoretical requirement of “infinite” width. A schematic of capillary rise at a vertical plate is shown in Figure 14.16 (53). If the solid surface is smooth and homogeneous, the three-phase contact line in the central part of the plate will be straight and independent of

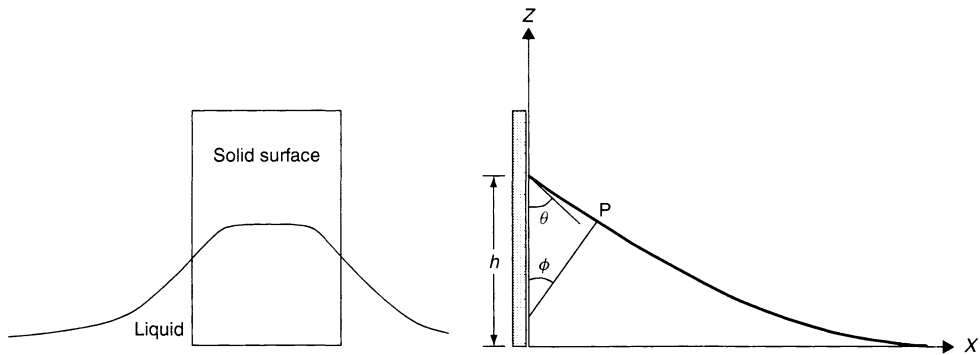


Figure 14.16. Schematic of capillary rise at a vertical plate, where ϕ is the angle between the vertical axis and the normal at a point P on the liquid–vapour surface, θ is the contact angle, and h is the capillary rise at a vertical plate (from ref. (53))

edge effects. If the gravitational acceleration, g , the density difference between liquid and vapour phases, $\Delta\rho$, and the liquid–vapour surface tension, γ_{lv} , are known, then the contact angle, θ , can be determined by measuring the height of the capillary rise, h . This task can be accomplished optically with a very high degree of accuracy by means of a cathetometer. Readings can conveniently be made with commercial optical measuring equipment to a precision of approximately 2×10^{-4} cm. While the three-phase line is easily visible with appropriate lighting, it may be difficult to make the level of the liquid surface visible. The problem may be overcome by mounting a needle or fibre besides the plate and slightly above the liquid level (see Figure 14.17). The location of the liquid level is then half-way between the point of the needle and its mirror image. By using a second fibre on the other side of the plate, the levelling of the optics can be checked.

Since irregularities in the measured contact angle data due to defects on the solid surface can be eliminated through averaging, the capillary rise technique offers a number of advantages. By immersing the vertical plate into or withdrawing it from the liquid at constant speed, the three-phase contact line remains essentially stationary. By changing the rate of immersion and emersion, rate-dependent dynamic advancing and receding contact angles can be measured. It is possible to select a rate in such a range that the capillary rise, and hence the contact angle, is essentially independent of rate, just as with ADSA-P.

Table 14.2 shows a comparison of measured contact angles using ADSA and capillary rise. It can be seen that the capillary rise technique is also able to produce contact angle data with high accuracy, and there is excellent agreement between the two techniques.

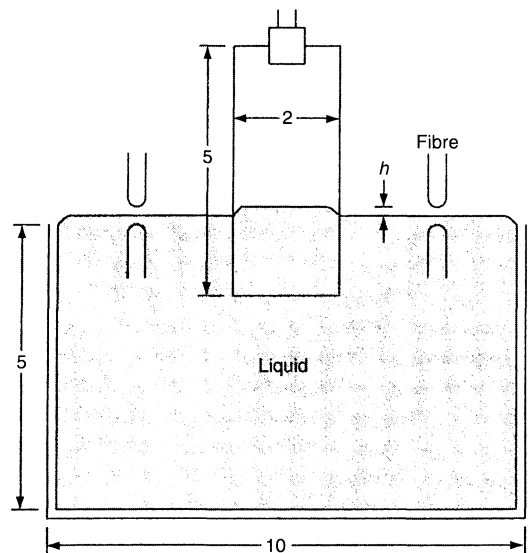
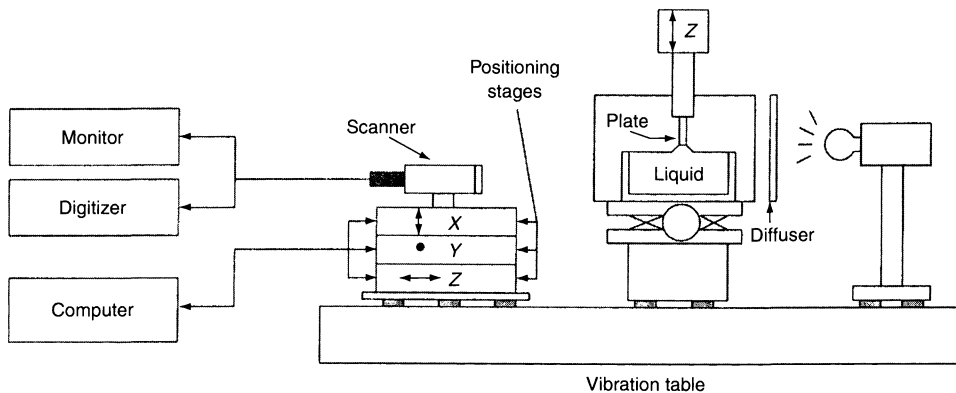


Figure 14.17. Schematic of capillary rise at a vertical plate dipping into a pool of liquid for contact angles less than 90° ; dimensions in cm (from ref. (53))

The contact angle measurements with the capillary rise technique can be time-consuming, and hence automation of the measurements is desirable. Figure 14.18 shows a schematic of an automated capillary rise apparatus. In the automated capillary rise measurements, the cathetometer, which is used to measure the capillary rise, is replaced by a computer and a microscope on motorized positioning stages. Three computer-controlled motorized translational stages (Micro-control) are used to move a horizontally mounted microscope fitted with a video scanner (Cohu CCD) in three directions, i.e. x , y and z . The x -, y - and z -axis stages

Table 14.2. Comparison of measured contact angles, θ (degree), using the capillary rise technique and ADSA-P for two solid surfaces, FC-721 and FEP. The error limits are 95% confidence limits

Liquid	FC-721		FEP	
	ADSA-P	Capillary rise	ADSA-P	Capillary rise
Tetradecane	73.31 \pm 0.14 72.96 \pm 0.21	73.5 \pm 0.1 —	52.51 \pm 0.23 —	52.5 \pm 0.1 —
Hexadecane	75.32 \pm 0.27	75.6 \pm 0.1	53.75 \pm 0.22	53.9 \pm 0.1
Dodecane	69.82 \pm 0.25	70.4 \pm 0.1	47.96 \pm 0.21	47.8 \pm 0.1
Dimethylformamide			68.52 \pm 0.21	68.6 \pm 0.2

**Figure 14.18.** Schematic of an automated capillary rise apparatus (from ref. (53))

have a travelling displacement of 5, 150 and 50 mm, respectively, and a resolution of 0.1 μm per step for the x - and z -axis and 10 μm per step for the y -axis (53). Since it is difficult to find the location of the liquid surface, it is convenient to have fibre references at both side of the vertical plate to identify the true horizontal of the surface and fix any optical distortions in the system (47). Therefore, three types of image frames are required for each capillary rise measurement, namely the real images of the reference fibres, the images of their reflections in the liquid, and the contact line between the solid and the liquid. These images are acquired through the digital camera and digitized by using a digital video processor. Subsequently, the array of intensity levels is stored in the memory of a computer. A Sobel 3×3 edge detection operator is employed to locate the edge of these images. The location of the liquid surface is found by determining the location of the tip of the reference fibres and their reflective images below the liquid surface. Using the Sobel edge operator, the computer locates the edge coordinates of the reference fibres in the image frame.

Since the image of the three-phase contact line has a very simple geometry, the linearity of the contact line can be easily tested and any defects or distortions in the

line can be easily detected and handled. If the three-phase contact line is linear and horizontal, its relative position in the image frame is calculated as an average over the entire horizontal length, i.e. approximately 512 pixel points. Similar to the manual procedure, a high magnification of, for example, $160\times$ with a focal distance of approximately 90 mm, is required in order to maintain or improve the precision of the capillary rise measurements. As a result, the field of vision is small, and it is necessary to move the microscope using the computer controlled translational stages between the three-phase contact line and the meniscus of the undisturbed liquid. The height of the capillary rise, h , is then calculated directly from the precise displacement of the z -axis stage, and the output from the digital analysis of the image frames.

The automated capillary rise technique has been employed to carry out various dynamic advancing and receding contact angle measurements (54) at different immersion speeds ranging from 0.008 to 0.9 mm/min. This technique has also been utilized to study both dynamic advancing and receding contact angles on dry, pre-wetted, and soaked fluorocarbon FC-722 (3M Inc.) surfaces (55). Such measurements reveal that the

behaviour of a polymer surface can be affected by prolonged contact with liquids as inert as alkanes. The above technique has also been used to study the temperature dependence of contact angles (53).

Wilhelmy method

The Wilhelmy balance is an excellent technique for indirectly measuring contact angles on a flat plate of known perimeter of the plate cross-section. The technique is based on the following relationship:

$$f = p\gamma_{lv} \cos \theta - V\Delta\rho g \quad (14.13)$$

where p is the perimeter of the Wilhelmy plate in contact with the liquid, γ_{lv} is the liquid–vapour surface tension, θ is the contact angle of liquid lens on the plate, V is the volume of the liquid displaced on the plate, $\Delta\rho$ is the density difference between the liquid and air phases, g is the (local) gravitational acceleration, and f is the measured force of the liquid on the plate.

In equation (14.13), the diameter of the plate can be determined by using a liquid of known surface tension for which the contact angle is zero. Therefore, if the parameters γ_{lv} , V , $\Delta\rho$ and g are known, equation (14.13) can be used to calculate the perimeter p . The contact angle of the liquid on the solid surface can then be determined by measuring the force of the liquid on the plate.

Figure 14.19 shows a schematic of an experimental set-up for the Wilhelmy plate technique (30). The plate (1), with a constant perimeter, is suspended by a thin rod (2) from the electrobalance (3). The pulling force on the plate from the liquid is recorded and displayed on a computer (4). A beaker (5) is used to hold the liquid of interest, and is partially covered by a lid (11) to minimize evaporation. The beaker is put on a supporting table (7), which can be moved up or down by means of a screw (8) driven by the electric motor (9). The motion of the motor can be used to generate advancing and receding contact angles. A clamp (10) is used to tighten the moving table (7) to a heavy vertical rod, after a preliminary positioning of the table. It should be noted that the motor and the table must not be sources of appreciable vibration, which might interfere with the measurement.

After suspending the plate from the electrobalance, the table, together with the motor, is lifted and fixed by the clamp at such a position that the surface of the liquid is about 1 mm below the lower edge of the plate. Subsequently, the table is raised slowly by lifting the screw using the electric motor. The motor is stopped

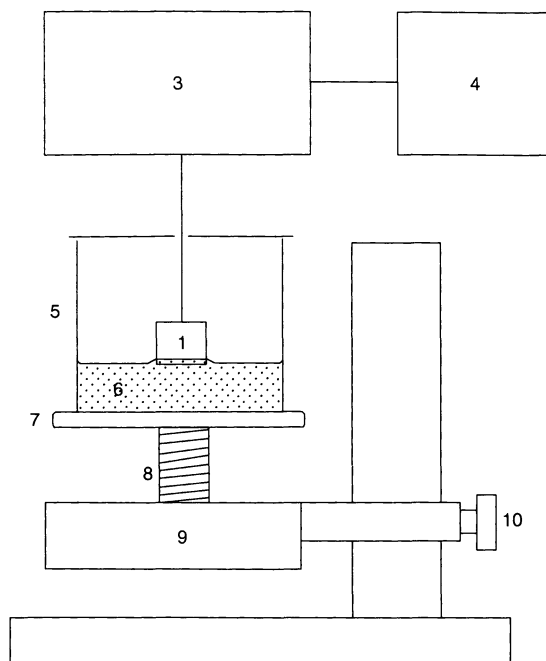


Figure 14.19. Schematic of the apparatus used in the Wilhelmy plate technique: 1, measuring plate; 2, glass fibre or rod; 3, electrobalance; 4, computer; 5, measuring cell; 6, liquid; 7, movable platform; 8, screw or gear mechanism to raise or lower the platform; 9, motor; 10, clamp and support; 11, lid (from ref. (30))

immediately after a contact between the liquid and the solid plate has been established. The measured contact angle in this configuration is an advancing contact angle. Since the depth of the immersion is zero, the displacement volume of the liquid in equation (14.13) is zero, and the following reduced equation can be used:

$$f = p\gamma_{lv} \cos \theta \quad (14.14)$$

Receding contact angles might be established by immersing the solid plate to some depth into the liquid, and subsequently withdrawing the plate through exactly the same distance. This may be performed by using a cathetometer to measure the immersion and the withdrawal distance.

The advantages of the Wilhelmy method are obvious. The measurement of contact angles is replaced by the measurement of an applied force on a plate, which can be performed with much higher accuracy and objectivity than directly reading the contact angle from a goniometer. The reproducibility of the results is only limited by two factors, i.e. (i) the constancy of the perimeter p of the cross-section of the plate, and (ii) the

reproducibility of the plate surfaces. Another advantage of the Wilhelmy method is the ease of automation. Since an entire Wilhelmy experiment can be recorded continuously by using a computer, this method is suitable for studying of dynamic behaviour of advancing and receding contact angles, and hence contact angle hysteresis.

However, there are also several disadvantages in the Wilhelmy method. First, in order to deliver high-precision results, the value of the perimeter of the solid plate has to be assumed constant along the plate, which may be difficult to achieve. Secondly, the plate should have the same composition and morphology at all surfaces, i.e. the front, back and both edges. Yet, this ideal condition is difficult to satisfy, especially in anisotropic systems or with polished surfaces. Thirdly, swelling or dissolution of the solid plate may occur, which causes complications in the measurement. Swelling or dissolution of the solid may change the displacement volume, V , and the mass of the displaced liquid in an unpredictable manner, and hence introduce errors in the measurements. In addition, adsorption of the vapour of the liquid at various parts of the gravimetric system other than the plate may change the output readings. The effect is pronounced for measurements of the temperature-dependence of contact angles. Finally, if the surface of the plate is not uniform in terms of surface composition and morphology, the interface will not intersect the solid in a perfectly smooth curve of constant shape. Such effects may not be noticed in the Wilhelmy method because it does not provide for a direct, optical observation of the surface.

3.1.2 Solid of cylindrical geometry

Capillary rise

When a capillary tube is vertically immersed into a liquid phase, if the diameter of the tube is sufficiently small, the meniscus may be considered to be spherical. Therefore, the following equation applies:

$$\Delta P = \Delta \rho g h = \frac{2\gamma_v \cos \theta}{r} \quad (14.15)$$

where r is the capillary radius and h is the height of the capillary rise. Both r and h can be determined by using optical measuring devices. It should be noted that since the validity of equation (14.15) is based on the assumption that the meniscus is spherical, the diameter of the tube should be sufficiently small. In this method, advancing and receding contact angles may be obtained by raising or lowering the capillary tube at a slow rate.

In addition to the capillary tube, the capillary rise technique can also be used with certain other geometries. For example, in the work of Gu *et al.* (56), a novel technique called the Analysis of Capillary Rise Profile Around a Cylinder (ACRPAC) can be used to determine contact angles of capillary rise profiles around a carefully coated conic glass cylinder. The accuracy of contact angle measurements using this technique is claimed to be approximately $\pm 0.1^\circ$. Using this technique, line tension effects were investigated by studying the contact angle dependence of n -alkane liquids at different locations of a conical glass cylinder coated with FC-725 (56). In another approach (57), the line tension was studied by measuring the capillary rise in a conical capillary tube. By determining the slope of the linear relationship between $\cos \theta$ (θ is the local contact angle) and $\cos \beta/R$ (β is the cone angle, and R is the radius of the three-phase contact line), according to a modified Young equation, the line tension can be studied (57). It should be noted that when the cone angle β reaches a limiting value of 90° , the above technique can be used to study the capillary rise on a straight cylinder/fibre.

Wilhelmy method

Since the equations for the Wilhelmy technique, i.e. equations (14.13) and (14.14), do not depend on the geometry of the solid surface, as long as the walls or outer surfaces of the solid are parallel and normal to the liquid surface, the method is applicable not only to plates, but also to rods, wires, capillary tubes and fibres. In the case of a very thin fibre, the perimeter p can be determined by the Wilhelmy technique by using a liquid with known surface tension γ_v which produces a zero contact angle when contacting the fibre. The absence of contact angle hysteresis is a convenient test for a zero contact angle. By using $\cos \theta = 1$, the perimeter p of the fibre can be calculated. Therefore, with a known perimeter, the fibre can be immersed or withdrawn from the liquid, just as with plates, and dynamic contact angle measurements can be performed. The detailed procedures of measuring contact angles on a thin fibre by using the Wilhelmy method are identical to the ones using a solid plate, as described in the previous section. Some sample results are given in Table 14.3.

It should be noted that the Wilhelmy technique can be readily used to measure liquid surface tensions, e.g. with a straight piece of platinum wire of a diameter of 1–2 mm, which can be cleaned readily by heating it in a methanol flame. The contact angle is then zero for many liquids, as required.

Table 14.3. Summary of contact angle, θ , and surface tension, γ_{pv} , data obtained by the Wilhelmy balance technique and the solidification front technique for carbon and Kevlar fibres, respectively (from ref. (75))

Fibre	Wilhelmy balance technique			Prediction of solidification front technique		
	θ (degree)		γ_{pv} (mJ/m ²)	θ (degree)		γ_{pv} (mJ/m ²)
	With water	With glycerol		With water	With glycerol	
Carbon	68.4	50.8	42.4	68.9	51.2	41.8
Kevlar	66.2	49.0	43.7	61.2	45.1	46.4

3.2 Indirect approaches

3.2.1 Powders, granules and porous solids

A general review of contact angles and techniques of measuring contact angles has been given in the above section. The choice of methods for measuring such angles depends directly on the geometry of the system (i.e. the geometry of the solid). Among these methods, measuring contact angles on a flat surface is believed to be the simplest and produces the most reliable results. When it comes to small particles, one might be tempted to compress the particles into a flat surface. However, contact angle measurements on compressed powders are usually unsatisfactory because of the low quality of the surface (i.e. cracks and pores on the surface, and the roughness of the surface). Therefore, indirect methods have to be used for determining surface tensions and contact angles of solids of various geometry, such as powders, irregular fibres and microscopic particles.

Heat of immersion, one of these indirect approaches, is a measure of the wettability of the powder immersed into a liquid (58). It is defined as the heat evolved per square centimetre of powder immersed in a liquid. The heat of immersion is a measurable quantity and can be related, in principle, to contact angles. However, it is not only related to the contact angle, but also to the temperature-dependence of the contact angle. In view of this complication, this method is not generally effective because the temperature-dependence of contact angles will not normally be known unless the contact angle itself is already known. Therefore, only relative and semi-quantitative information is provided from this method.

In film floatation, which was developed by Fuerstenaу and co-workers (59, 60), particles of similar size are sprinkled on the surface of a liquid with a known surface tension and the fraction of particles that sink into the liquid is measured. From this, the critical wetting surface tension, γ_c (of Zisman), of solid particles (i.e. the liquid surface tension at which the solid surface is completely wetted by the test liquid) can be determined.

By tentatively equating γ_c and γ_{sv} , contact angles can be evaluated by the equation-of-state approach. Other indirect methods for determining contact angles will be described below.

Sedimentation volume

The sedimentation volume method is a well-established technique for studying the suspension stability of powders in liquids. The behaviour of such systems is governed mainly by van der Waals and electrostatic interactions. It is important to note that the former interactions can be related to the interfacial tensions of the solid particles suspended in a liquid (61), whereas the effect of the latter interactions can be considered negligible, e.g. for polymer particles, particularly in non-aqueous media (62). When two solid particles are brought into contact and if only van der Waals forces are considered, the free energy of adhesion of two solid phases in a liquid can be determined as follows:

$$\Delta F^{\text{adh}} = \gamma_{ps} - \gamma_{pl} - \gamma_{sl} \quad (14.16)$$

where γ_{ps} , γ_{pl} and γ_{sl} are the interfacial tensions between the particle and the solid phase, the particle and the liquid phase, and the solid and the liquid phase, respectively. In equation (14.16) if $\Delta F^{\text{adh}} > 0$, the two solids will repel each other, and if $\Delta F^{\text{adh}} < 0$, they will be attracted.

While the free energy of adhesion (and van der Waals interactions) between unlike materials in a liquid may be positive (attractive) or negative (repulsive), it can be shown from the underlying thermodynamics (4, 63) that like solids can only attract each other, with zero interaction as the limiting case. The interaction, which is between particles of the same kind embedded in a liquid, is governed by the free energy of cohesion, as follows:

$$\Delta F^{\text{coh}} = -2\gamma_{pl} \quad (14.17)$$

Since the solid-liquid interfacial tension is always greater than (or equal to, as a limiting case) zero, i.e. $\gamma_{pl} \geq 0$, there will always be an attraction between

like particles suspended in a liquid. For systems of solid particles immersed in a single-component liquid, the particle–liquid interfacial tension, γ_{pl} , only depends on the liquid–vapour surface tension, γ_{lv} , and the solid–vapour surface tension, γ_{pv} , i.e. $\gamma_{pl} = f(\gamma_{lv}, \gamma_{pv})$. There is a constraint in the above function, i.e. $\gamma_{pl} = 0$ when $\gamma_{lv} = \gamma_{pv}$. When the ΔF^{coh} of a system reaches the maximum, i.e. $\Delta F^{\text{coh}} = 0$, this implies that $\gamma_{lv} = \gamma_{pv}$. In order to illustrate this point, a plot of the free energy of cohesion, ΔF^{coh} , against the liquid surface tension, γ_{lv} , for hypothetical particles with a surface tension $\gamma_{pv} = 20 \text{ mJ/m}^2$, is shown in Figure 14.20. It is apparent that $\Delta F^{\text{coh}} = 0$ occurs at $\gamma_{lv} = \gamma_{pv} = 20 \text{ mJ/m}^2$. In view of this, it can be expected that the sedimentation volume of particles will show an extremum when $\Delta F^{\text{coh}} = 0$. Such an extremum may provide a means to determine the solid–vapour surface tension of the particles.

Experimental procedure In order to perform an appropriate experiment, one needs to prepare a series of liquids or binary liquid mixtures with a range of surface tensions that covers the surface tensions of the particles of interest. For this purpose, it is preferable to have relatively tall cylinders with a small diameter and increments (e.g. 0.01 ml), in order to maximize the accuracy of the final sedimentation volume, V_{sed} , readings. It should be noted that the liquids used must satisfy the following criteria, i.e. (i) liquids should be chemically inert with respect to the sample particles, (ii) liquids

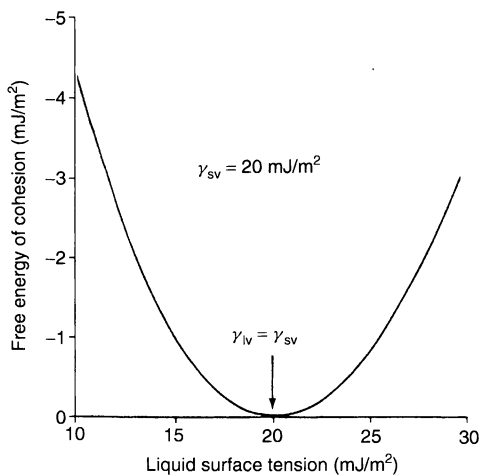


Figure 14.20. The free energy of cohesion, ΔF^{coh} , between solid particles of surface tension $\gamma_{pv} = 20 \text{ mJ/m}^2$, as a function of the surface tension of the suspending liquid, γ_{lv} (from ref. (64))

should have relatively high boiling temperatures in order to minimize evaporation and also be completely miscible with each other, and (iii) liquids should have densities that are less than the particles.

Equal amounts of particles, say 1 g, should be filled into each cylinder. Then, each cylinder should be filled to a given volume with the appropriate liquid. The suspension should be vigorously shaken in order to disperse the particles completely and to remove any entrapped air bubbles. The cylinders are then sealed to prevent evaporation of the liquid, and the particles are allowed to settle. The reading of the sedimentation volume, V_{sed} , of the particles is taken until no further change in V_{sed} occurs. The time span for this experiment depends on the sample used. This often takes three days to one week to complete. The final V_{sed} values are plotted over the surface tension of the suspending liquids. The value of γ_{lv} at which the extremum in the sedimentation volume occurs, is the value of the surface tension of the solid particles. As illustrations, Figures 14.21 and 14.22 show the patterns of V_{sed} of Teflon® (PTFE) particles in binary mixtures of *n*-hexane/*n*-hexadecane and of diethyl ether/*n*-hexanol, respectively. It is noted that a minimum occurs in the *n*-hexane/*n*-hexadecane solution and a maximum in the diethyl ether/*n*-hexanol solution. The difference between these patterns may be caused by two possible sedimentation mechanisms, which depend on the occurrence of particle agglomeration (64). The extrema in these experiments with Teflon® powder (Figure 14.23) occur at approximately $\gamma_{lv} = 20 \text{ mJ/m}^2$, i.e. the known value of the surface tension of Teflon®. Once the solid surface tension is obtained, the contact angle can be evaluated via the equation-of-state approach.

Table 14.4 summarizes extrema of sedimentation volumes for polymers in different liquid combinations (65, 66). It is interesting to note that the extrema are minima for non-polar or slightly polar solids/liquids, and maxima for more polar systems.

In practice, sedimentation volume experiments are performed frequently by using binary liquid mixtures as the suspending media, because they allow a close control of the surface tension of the suspending liquid, γ_{lv} . By varying the volume/volume concentrations of the two liquids, experimenters are able to utilize a sufficiently large range of surface tensions. However, the equation of state equation (14.6), i.e. $\gamma_{pl} = 0$ when $\gamma_{lv} = \gamma_{pv}$, is applicable only to single-component liquid systems. Therefore, there might be some doubt about the validity of this approach. However, a detailed study (62) has shown that the positions at which the extrema occur in the sedimentation volume for Teflon® powders are very

Table 14.4. Liquid surface tension, γ_v , at which maximum (Max) or minimum (Min) in sedimentation volume occurs, for several polymers: PTFE, polytetrafluoroethylene; PVDF, poly(vinylidene fluoride); PVF, poly(vinyl fluoride); HDPE; high-density polyethylene; PA 66, poly(hexamethylene adipamide) (nylon 6, 6); PSF, polysulfonate. Experiments were performed at room temperature, and the extrema are to be understood as being the surface tensions of the polymers (from refs (65, 66))

Liquid combination	Surface tension range, γ_v mJ/m ²	Dipole moments $\mu \times 10^{-30}$ (cm)	γ_v mJ/m ²							
			Polymer							
			PTFE		PVDF	PVF	HDPE	PA 66	PSF	
			Grade 1	No. 6						
<i>n</i> -Hexane	18.3	0	20.0	20.0	–	–	–	–	–	–
<i>n</i> -hexadecane	27.0	0	Min	Min	–	–	–	–	–	–
<i>n</i> -Octane	21.8	0	–	–	27.1	29.0	29.2	–	–	–
tetralin	36.5	1.63	–	–	Min	Min	Min	–	–	–
Diethyl ether	17.4	3.84	20.2	19.6	–	–	28.4	–	–	–
tetralin	36.5	1.63	Min	Min	–	–	Min	–	–	–
Diethyl ether	17.4	3.84	20.2	19.4	–	–	–	–	–	–
<i>n</i> -hexanol	25.2	5.17	Max	Max	–	–	–	–	–	–
<i>n</i> -Propanol	23.8	5.60	–	–	27.8	28.6	–	38.5	–	–
ethylene glycol	48.9	7.61	–	–	Max	Max	–	Max	–	–
<i>n</i> -Propanol	23.8	5.60	–	–	–	–	30.5	–	–	–
cyclohexanone	34.3	9.01	–	–	–	–	Max	–	–	–
<i>n</i> -Propanol	23.8	5.60	–	–	–	–	–	39.6	–	–
thiodiethanol	52.5	– ^a	–	–	–	–	–	Max	–	–

^a Unknown.

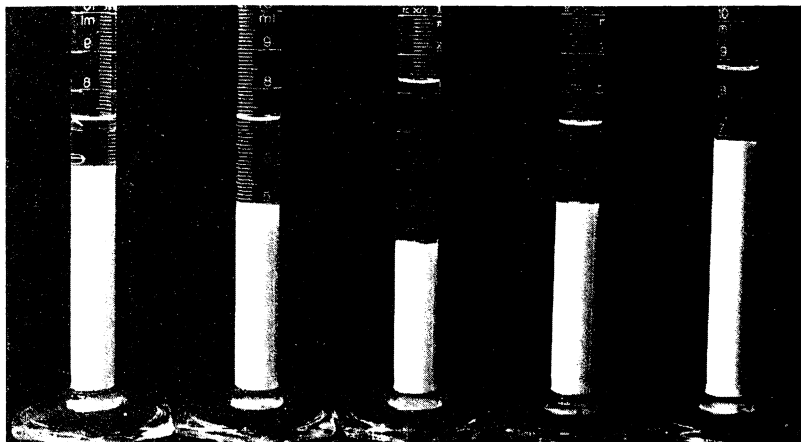


Figure 14.21. Illustration of sedimentation volumes of powdered PTFE in mixtures of *n*-hexane and *n*-hexadecane (from ref. (5))

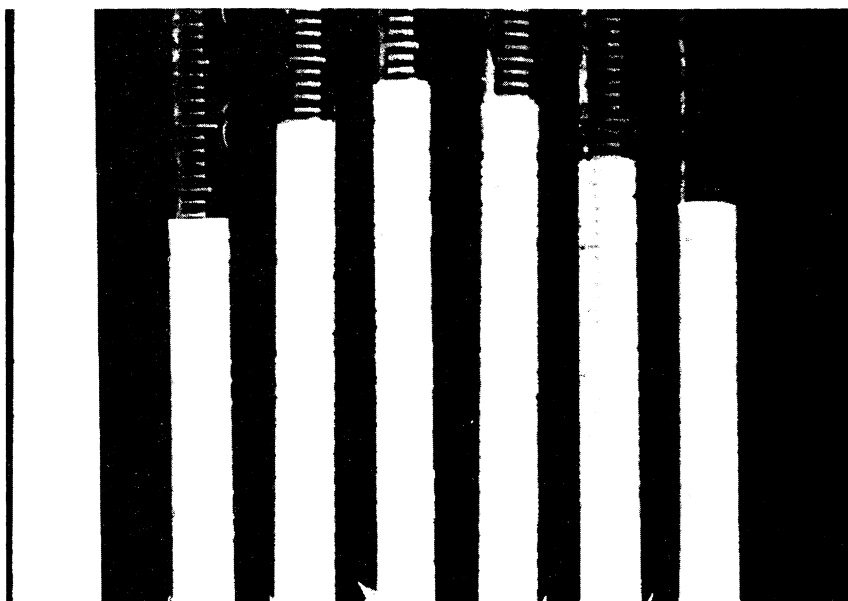


Figure 14.22. Illustration of sedimentation volumes of powdered PTFE in mixtures of diethyl ether and *n*-hexanol (from ref. (5))

similar for both the single-component liquids and binary liquid mixtures. The γ_{sv} values of Teflon® powders obtained from these experiments are in good agreement with the corresponding γ_{sv} values obtained from direct contact angle measurements, which were performed on smooth Teflon® films.

Studies on the sedimentation behavior of Teflon® (62, 66) and other polymers (62, 66), coal particles (62, 64), steroidal and other drugs in powder form (67, 68), and liposomes (67–69) have been carried out by Vargha-Butler, Neumann and co-workers, in both

single-component liquids and binary liquid mixtures. It can be concluded from the sedimentation experiments that the surface tension of solid particles can be estimated from the location of the extremum of the V_{sed} versus γ_{lv} plot.

Particle suspension layer stability/droplet sedimentation

Droplet sedimentation is another technique for estimating the contact angles of small particles by determining

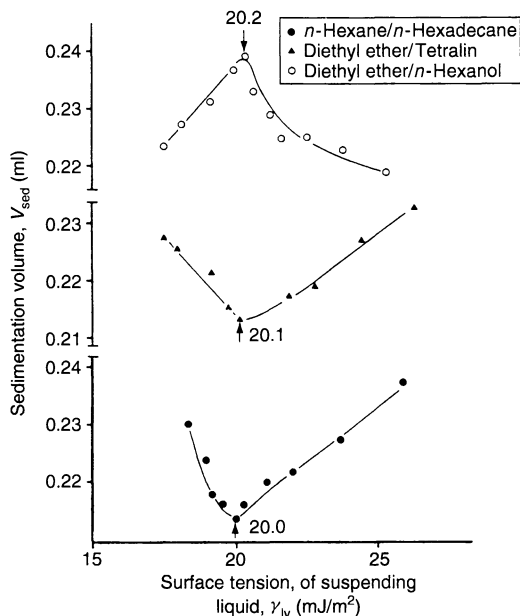


Figure 14.23. Sedimentation volume, V_{sed} , as a function of the surface tension, γ_{lv} , of the suspending liquid for a PTFE powder; the extrema indicate the particle surface tension (from ref. (5))

particle solid surface tensions. When a dilute suspension of small particles is carefully layered on to a dense liquid, a well-formed interfacial region can be observed between the suspension and the supporting liquid. However, when the suspension layer becomes unstable, droplets of suspension form in the interface and then fall into the supporting liquid cushion. Since the total energy of interaction between like particles can be modelled as the sum of repulsive components due to electrostatic charge and attractive components due to van der Waals forces, it was found that when the particle surface tension is equal to the surface tension of the suspending liquid, the attractive van der Waals force, which is responsible for particle agglomeration and droplet sedimentation, is zero (63). Therefore, the solid surface tension of particles can be determined by searching for a suspension liquid with a known surface tension that produces the maximum suspension stability. Once the particle surface tension is known, contact angles can be estimated by applying the equation-of-state approach.

The method has been applied to determine the surface tension of biological cells (70). Results for fixed erythrocytes of several species are given in Table 14.5 (70), together with solidification front results (see below).

Capillary penetration

This method allows evaluation of the solid surface tension by measuring the velocity of the penetration of a liquid into a powder bed or other porous material. Contact angles can again be determined indirectly from the solid surface tension data, by using the equation of state. Figure 14.24 shows an experimental set-up for the capillary penetration experiment. Details of the experimental procedures are discussed elsewhere in this volume. The starting point of this method is the Washburn equation for liquid penetration into a single capillary, given as follows:

$$h^2 = \frac{rt}{2\eta} \gamma_{lv} \cos \theta \quad (14.18)$$

where h is the capillary height of the liquid front, r is the radius of the capillary, t is the time, η is the viscosity of the liquid, γ_{lv} is the liquid–vapour surface tension, and θ is the contact angle. This equation is a combination of the Laplace equation of capillarity for a vertical capillary with a circular cross-section and the Hagen–Poiseuille equation for steady flow. Grundke *et al.* (71) modified the Washburn equation by relating the contact angle to a readily measurable rate parameter, to give the following:

$$K \gamma_{lv} \cos \theta = \left(\frac{\eta}{\rho^2} \right) \left(\frac{M^2}{t} \right) \quad (14.19)$$

where K is a constant reflecting the effective capillary radius of the capillary and M is the weight of the liquid penetrating into the capillary. The term (M^2/t) can be determined from capillary penetration experiments by using an electrobalance, and hence the value of $K \gamma_{lv} \cos \theta$ can be obtained. From the plot of $K \gamma_{lv} \cos \theta$ versus γ_{lv} (Figure 14.25), the surface tension of the testing solid can be determined by locating the maximum of the curve. The contact angle can then be calculated by using the equation of state (equation (14.8)). Although the packed powder bed does not represent a flat and smooth solid surface, the contact angle values obtained from this indirect method are close to the value of contact angles measured directly from a flat and smooth solid surface.

Capillary penetration is also applicable to other geometries, i.e. solids which have pathways for liquid penetration, such as bundles of fibres, mats of fibres and woven or non-woven fabrics, as well as porous materials. Studies of surface free energy by this method have been carried out with some microporous membranes (polytetrafluorethylene, polyethylene and polypropylene) (72), a polymer powder (polytetrafluorethylene) (71), and cellulose

Table 14.5. Comparison of the surface tensions of fixed erythrocytes obtained by the droplet sedimentation and solidification front techniques, using water/ice (from ref. (70))

Erythrocyte species	Technique	
	Droplet sedimentation (mJ/m ²)	Freezing front (mJ/m ²)
Turkey	65.7	65.4
Chicken	65.2	65.1
Canine	64.4	64.2
Horse	65.4	64.5
Human	64.3	64.1

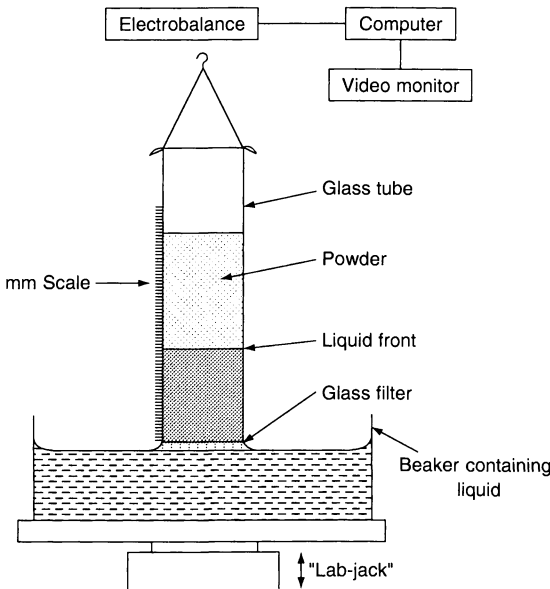


Figure 14.24. Schematic of the set-up used for the capillary penetration experiment (from ref. (70))

hollow fibres (CUPROPHAN) (71). The surface tension value of polytetrafluorethylene obtained from this method is in good agreement with that obtained from ADSA experiments (72), or the sedimentation volume.

Solidification fronts

The contact angles of solid particles can also be determined indirectly by the advancing-solidification-front technique. This indirect approach of measuring contact angles is based on the behaviour of microscopic solid particles at advancing solidification fronts and depends on interfacial free energy changes (61). This approach is very powerful, although quite involved;

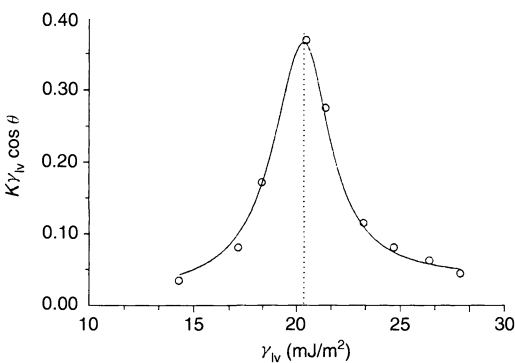


Figure 14.25. A plot of $K\gamma_{lv} \cos \theta$ versus γ_{lv} for nine liquids and PTFE (Teflon® 807-N) powder; the maximum indicates the particle surface tension. (from ref. (70))

in-depth comprehension may require consultation of the literature, e.g. ref. (62).

The scheme of this technique is to first determine the so-called critical velocity, V_c , of a solidification front. A particle which is “pushed” by a solidification front through the liquid matrix may be engulfed by the solid phase when the repulsion (i.e. a positive value of ΔF^{adh}) is just balanced by the viscous drag. As this drag will increase with an increasing rate of solidification, engulfing will occur at a specific velocity V_c , where viscous forces balance the rate-independent ΔF^{adh} . By using measured V_c values, the free energy of adhesion, ΔF^{adh} , can be determined through a scheme of dimensional analysis (73). Having obtained a value of ΔF^{adh} , one can then determine various relevant interfacial tensions through the equation-of-state approach. Knowing the surface tensions, γ_{lv} and γ_{sv} , of the matrix material, the surface tension of the particle, γ_{pv} , can be determined. Once γ_{pv} is known, the contact angle can be calculated from the Young equation. Therefore, the sequence of steps required to obtain contact angles may be summarized as follows:

$$\begin{aligned} V_c &\longrightarrow \text{Dimensional analysis} \longrightarrow \Delta F^{adh} \\ &\longrightarrow \text{Equation-of-state approach} \longrightarrow \gamma_{pv}, \gamma_{pl} \\ &\longrightarrow \text{Young's equation} \longrightarrow \theta \end{aligned} \quad (14.20)$$

Experimental procedure The aim of the advancing-solidification-front experiment is to determine the value of the critical velocity, V_c , i.e. the velocity of the solidification front that separates the pushing and engulfing of

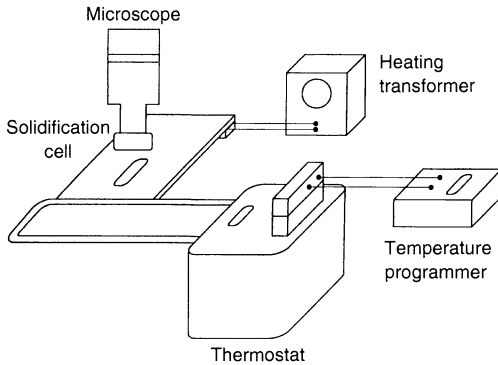


Figure 14.26. Schematic of an experimental set-up used to study the behaviour of small particles at solidification fronts (from ref. (64))

particles. As an experimental fact, particle engulfment depends on both the rate of the advancing solidification front and the size of the particle. Therefore, in order to obtain V_c , it is necessary to study both rate- and size-dependent phenomena. The schematic of an apparatus used to study the behaviour of small particles at the solidification front is shown in Figure 14.26. The particles and matrix material are contained in a small horizontal copper cell with a machined groove, and the latter is covered with a glass microscope slide. In order to establish a temperature gradient along the copper cell, it is heated at one end while the other end is cooled by water flowing through a copper cooling coil. The heating and cooling operations are controlled by thermoelectric devices (Cambion 801-3958-01), which are mounted at each end of the copper cell. The temperature at each end is measured by a thermistor and is independently controlled by a feedback controller (at each end). The measured value of temperature at each end of the channel is then compared with a pre-determined value; the difference between these values determines the amount of energy required to be put into the thermoelectric device in order to control the rate of heat transfer to or from the copper cell. The input energy is generated by a bipolar controller (Cambion 801-3958-01). The velocity of the advancing solidification front can then be adjusted over a wide range from approximately 1 to 100 $\mu\text{m/s}$. This apparatus is designed to operate in a temperature range from 0 to 100°C. Furthermore, it is desirable to use matrix materials with a melting point between 20 and 80°C.

The solidification cell is mounted on a movable stage of a Leitz Orthomat-Orthoplan photomicroscope, so that particle interactions with the interface can be observed. The microscope, as shown in Figure 14.26, can be used through

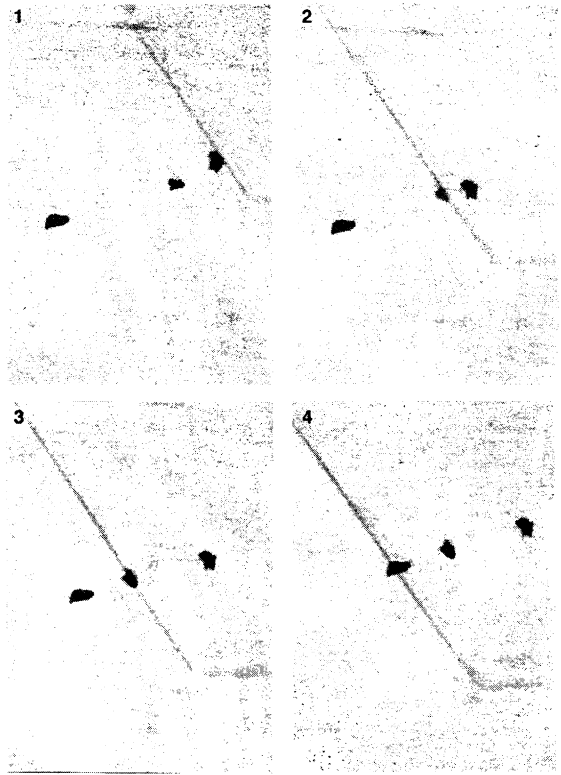


Figure 14.27. Photomicrographs illustrating various episodes of engulfing and rejection (pushing) of coal particles by an advancing solidification front of thymol. from ref. (64)

with a video camera, so that the entire experiment can be recorded on a videotape or a computer disk for further analysis. Figure 14.27 illustrates some typical photomicrographs obtained for coal particles at the solidification front of thymol.

In order to obtain the critical velocity, V_c , a series of advancing-solidification-front experiments are performed, using different velocities of the solidification. It should be noted that the rates of solidification can be measured by timing the progress of the solidification front over some distance, measured by using a micrometer eyepiece graticule. In the actual experiments, a sharp transition from particle rejection to particle engulfment cannot be observed. Therefore, three types of particle behaviour, "rejection", "transition" and "engulfment", have been defined. If the particle is pushed continuously by the advancing solidification front for more than approximately 20 μm , this movement is classified as *rejection*. This event usually occurs at relatively low velocities of solidification. If the particle is pushed through various distances (i.e. less than 20 μm) before

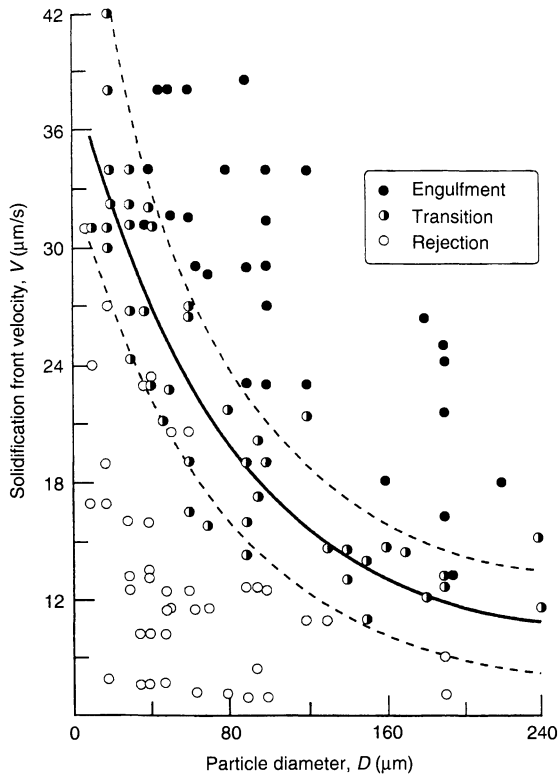


Figure 14.28. Pushing and engulfing velocities as a function of the particle diameter for the naphthalene (matrix)–nylon (particle) system (from ref. (61))

being engulfed, this is recorded as *transition*. If the particle is engulfed instantly or without significant pushing (i.e. less than 2 μm) by the solidification front, this is classified as *engulfment*. As a typical example, these three types of movements of various particle diameters are presented in Figure 14.28. As can be seen from this figure, the three types of patterns are delineated by two dashed lines. The critical velocity, V_c , is defined as the central line of the area representing the transition mode, i.e. the solid line in between the dashed lines. It is apparent that the critical velocity depends on the particle size (61, 63, 70, 74). It should be noted that the final results are not very sensitive to errors in V_c , as determined in Figure 14.28. A scheme of dimensional analysis (73) was developed to relate the free energy of adhesion ΔF^{adh} to V_c . This relationship for particles less than 300 μm in diameter is given by the following:

$$\Delta F^{\text{adh}} = 6.07 \times 10^3 \frac{\rho_L^{0.685} T^{0.400} k_P^{0.601}}{\mu^{0.085} (\rho_P \times C_P)^{0.201}} D^{0.484} V_c^{0.685} \quad (14.21)$$

www.iran-mavad.com

where ρ_P is the particle density, ρ_L is the liquid matrix density, C_P is the specific heat of the particle, k_P is the thermal conductivity of the particle, μ is the viscosity of the liquid matrix, T is the melting temperature of the matrix material, D is the particle diameter, and V_c is the critical velocity. The quantities of these properties are measurable (and are in SI units).

In order to obtain the surface tension of a particle, γ_{ps} , the solid–vapour and liquid–vapour interfacial tensions of the matrix material must also be determined. The liquid–vapour surface tension of the matrix material, γ_{lv} , at its melting/freezing point can be determined from temperature-dependent surface tension measurements, using, e.g. the Wilhelmy plate method. Figure 14.29 shows typical results obtained for the temperature-dependence of the liquid–vapour surface tensions of thymol at and above its melting point (i.e. 51.5°C). The surface tension at the melting point of the matrix material can be obtained from the temperature-dependent liquid surface tension curve, by using a linear regression curve fitting. Similarly, the solid–vapour surface tension of the matrix material, γ_{sv} , at the melting point is obtained from the extrapolation of the temperature-dependent contact angles measured with a suitable liquid on the matrix material in the solid state. An example of temperature-dependent contact angle measurements of thymol–glycerol, using the capillary rise method, together with the resulting γ_{sv} values, is shown in Figure 14.30.

Using the values of ΔF^{adh} , γ_{lv} , and γ_{sv} obtained above, γ_{pv} and γ_{pl} can be calculated via the equation of state for interfacial tensions. Once γ_{pv} and γ_{pl} are known, the contact angle θ can be determined from the Young equation. Table 14.6 shows values of ΔF^{adh} , γ_{pv} , and θ of water for poly(methyl methacrylate) (PMMA)

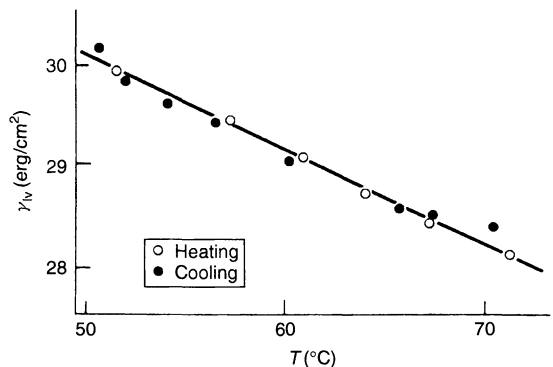


Figure 14.29. Temperature-dependence of the liquid–vapour surface tension for thymol at and above its melting point (51.5°C)

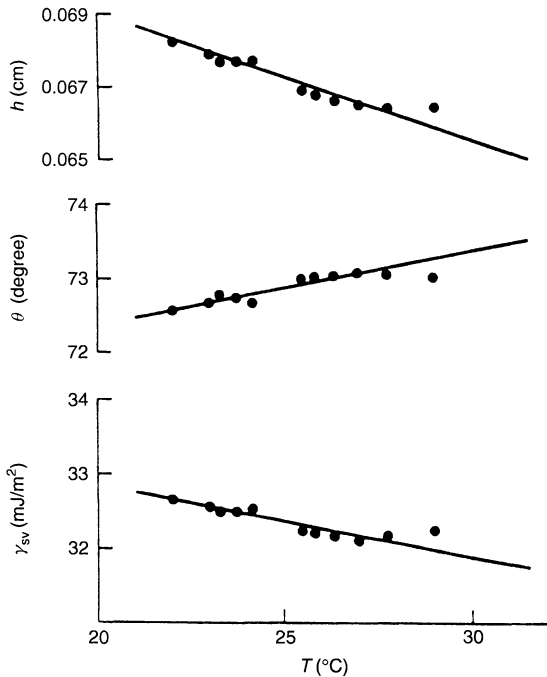


Figure 14.30. Temperature-dependence of the contact angle, θ , of glycerol on solid thymol, determined from the capillary rise, h , on a flat vertical surface, and the temperature-dependence of the resulting surface tension, γ_{sv} , of thymol in the solid state (from ref. (52))

particles, as determined from the critical velocities in naphthalene, biphenyl and salol. It should be noted that the values of γ_{pv} calculated from the ΔF^{adh} values refer to the respective melting points of the three matrix materials. Therefore, the γ_{pv} values for 20°C were calculated by assuming a temperature coefficient $(d\gamma_{pv})/(dT) = -0.075 \text{ mJ}/(\text{m}^2 \cdot ^\circ\text{C})$. With these γ_{pv} values at 20°C, contact angles are determined from Young's equation. The average value for the contact angle with water, in this case $\theta = 74.6 \pm 1.0^\circ$, compares favorably

with the result of the direct contact angle measurement performed on a solvent-cast film of PMMA, i.e. $\theta = 73.0 \pm 2.0^\circ$.

Table 14.3 above (75) shows a comparison of the contact angle (θ) and surface tension (γ_{pv}) results for carbon and Kevlar fibres obtained by using the solidification front technique and the Wilhelmy balance technique. It is apparent that the γ_{pv} values obtained from the two techniques are in good agreement. Furthermore, the contact angles determined for carbon fibres are essentially the same, and independent of the technique being used. Table 14.5 (70) shows a comparison of the surface tension of fixed erythrocytes obtained by the droplet sedimentation technique and the solidification front technique. In addition to fibres and biological cells, solidification front experiments with various polymer particles (62), glass spheres (70) and coal particles (62, 64) have been performed. It is concluded that the contact angle results obtained from the solidification front technique compare favourably with the results obtained from other direct as well as indirect methods.

4 ACKNOWLEDGEMENTS

This work was supported by the Natural Science and Engineering Research Council (NSERC) of Canada under Grant no. A8278. Financial support through an NSERC Postgraduate Scholarship (CNCL) and a University of Toronto Open Fellowship (JL) is gratefully acknowledged. The authors express their appreciation to R.H.Y. Ko for her technical assistance with this work.

5 REFERENCES

1. Zisman, W. A., Relation of the equilibrium contact angle to liquid and solid constitution, in *Contact Angle, Wettability and Adhesion*, Advances in Chemistry Series, Vol. 43, Gould, R. F. (Eds), American Chemical Society, Washington, DC, 1964, 1–51.

Table 14.6. Free energy of adhesion, ΔF^{adh} , surface tension, γ_{pv} , and contact angle, θ , with water for PMMA, determined from the critical velocities, V_c , in naphthalene, biphenyl, and salol (from ref. (74))

Parameter	Naphthalene T_m at 80°C	Biphenyl T_m at 70°C	Salol T_m at 43°C	Average
$\Delta F^{adh}(\text{mJ}/\text{m}^2)$	0.330	0.324	0.040	–
γ_{pv} at T_m (mJ/m^2)	34.0	34.2	37.7	–
γ_{pv} at 20°C (mJ/m^2)	38.5	37.9	39.4	38.6 ± 0.6
θ at 20°C (degree)	74.8	75.8	73.3	74.6 ± 1.0
θ at 20°C (degree)	– ^a	– ^a	– ^a	73.0 ± 2.0

^a From direct goniometer measurement.

2. Fowkes, F. M., Attractive forces at interfaces, in *Chemistry and Physics of Interfaces*, Gushee, D. E. (Ed.), American Chemical Society, Washington, DC, 1965, pp. 1–12.
3. Driedger, O., Neumann, A. W. and Sell, P. J., An equation of state approach for surface free energies, *Kolloid-Z. Z. Polym.*, **201**, 52–57 (1965).
4. Neumann, A. W., Good, R. J., Hope, C. J. and Sejjal, M., An equation-of-state approach to determine surface tensions of low-energy solids from contact angles, *J. Colloid Interface Sci.*, **49**, 291–304 (1974).
5. Spelt, J. K. and Li, D., The equation of state approach to interfacial tensions, in *Applied Surface Thermodynamics*, Neumann, A. W. and Spelt, J. K. (Eds), Marcel Dekker, New York, 1996, pp. 239–292.
6. van Oss, C. J., Chaudhury, M. K. and Good, R. J., Interfacial Lifshitz–van der Waals and polar interactions in macroscopic systems, *Chem. Rev.*, **88**, 927–941 (1988).
7. Derjaguin, B. V., Muller, V. M. and Toporov, Y. P., On different approaches to the contact mechanics, *J. Colloid Interface Sci.*, **73**, 293–294 (1980).
8. Johnson, K. L., Kendall, K. and Roberts, A. D., Surface energy and the contact of elastic solids, *Proc. Soc. R. London, A*, **324**, 301–313 (1971).
9. Muller, V. M., Yushchenko, V. S. and Derjaguin, B. V., General theoretical consideration of the influence of surface forces on contact deformations and the reciprocal adhesion of elastic spherical particles, *J. Colloid Interface Sci.*, **92**, 92–101 (1983).
10. Fogden, A. and White, L. R., Contact elasticity in the presence of capillary condensation, *J. Colloid Interface Sci.*, **138**, 414–430 (1990).
11. Pashley, R. M., McGuiggan, P. M., Horn, R. G. and Ninham, B. W., Forces between bilayers of cetyltrimethylammonium bromide in micellar solutions, *J. Colloid Interface Sci.*, **126**, 569–578 (1988).
12. Christenson, H. K., Interactions between hydrocarbon surfaces in a nonpolar liquid: effect of surface properties on solvation forces, *J. Phys. Chem.*, **90**, 4–6 (1986).
13. Claesson, P. M., Blom, C. E., Horn, P. C. and Ninham, B. W., Interactions between water-stable hydrophobic langmuir–blodgett monolayers on mica, *J. Colloid Interface Sci.*, **114**, 234–242 (1986).
14. Pashley, R. M., McGuiggan, P. M., Ninham, B. W. and Evans, D. F., Attractive force between uncharged hydrophobic surfaces: direct measurements in aqueous solution, *Science*, **229**, 1088–1089 (1985).
15. Hemingway, S. J., Henderson, J. R. and Rowlinson, J. R., The density profile and surface tension of a drop, *Faraday Symp. Chem. Soc.*, **16**, 33–43 (1981).
16. Guermeur, R., Biquard, F. and Jacolin, C., Density profiles and surface tension of spherical interfaces. Numerical results for nitrogen drops and bubbles, *J. Chem. Phys.*, **82**, 2040–2051 (1985).
17. Carey, B. S., Scriven, L. E. and Davis, H. T., Semi-empirical theory of surface tension of binary systems, *AIChE J.*, **26**, 705–711 (1980).
18. Moy, E. and Neumann, A. W., Theoretical approaches for estimating solid–liquid interfacial tensions, in *Applied Surface Thermodynamics*, Neumann, A. W. and Spelt, J. K. (Eds), Marcel Dekker, New York, 1996, pp. 333–378.
19. Israelachvili, J. N., The calculation of van der Waals dispersion forces between macroscopic bodies, *Proc. Roy. Soc. London, A*, **331**, 39–55 (1972).
20. van Giessen, A. E., Bukman, D. J. and Widom, B., Contact angles of liquid drops on low-energy solid surfaces, *J. Colloid Interface Sci.*, **192**, 257–265 (1997).
21. Fender, B. E. F. and Halsey, Jr, G. D., Second virial coefficients of argon, krypton, and argon–krypton mixtures at low temperatures, *J. Chem. Phys.*, **36**, 1881–1888 (1962).
22. Sullivan, D. E., Surface tension and contact angle of a liquid–solid interface, *J. Chem. Phys.*, **74**, 2604–2615 (1981).
23. Matyushov, D. V. and Schmid, R., Calculation of Lennard-Jones energies of molecular fluids, *J. Chem. Phys.*, **104**, 8627–8638 (1996).
24. Gaydos, J. and Neumann, A. W., Line tension in multi-phase equilibrium systems, in *Applied Surface Thermodynamics*, Neumann, A. W. and Spelt, J. K., (Eds), Marcel Dekker, New York, 1996, pp. 169–238.
25. Li, D. and Neumann, A. W., Contact angles on hydrophobic solid surfaces and their interpretation, *J. Colloid Interface Sci.*, **148**, 190–200 (1992).
26. Li, D. and Neumann, A. W., Equation of state for interfacial tensions of solid–liquid systems, *Adv. Colloid Interface Sci.*, **39**, 299–345 (1992).
27. Kwok, D. Y. and Neumann, A. W., Contact angle measurement and contact angle interpretation, *Adv. Colloid Interface Sci.*, **81**, 167–249 (1999).
28. Li, D., Gaydos, J. and Neumann, A. W., The phase rule for systems containing surfaces and lines. I. Moderate curvature, *Langmuir*, **5**, 1133–1140 (1989).
29. Li, D. and Neumann, A. W., A reformulation of the equation of state for interfacial tensions, *J. Colloid Interface Sci.*, **137**, 304–307 (1990).
30. Neumann, A. W. and Good, R. J., Techniques of measuring contact angles, in *Experimental Methods in Surface and Colloid Science*, Vol. 11, Good, R. J. and Stromberg, R. R., (Eds), Plenum Press, New York, 1979, pp. 31–91.
31. Bashforth, F. and Adams, J. C., *An Attempt to Test the Theory of Capillary Action*, Cambridge University Press, Cambridge, UK, 1883.
32. Hartland, S. and Hartley, R. W., *Axisymmetric Fluid–Liquid Interfaces*, Elsevier, Amsterdam, 1976.
33. Maze, C. and Burnet, G., A non-linear regression method for calculating surface tension and contact angle from the shape of a sessile drop, *Surface Sci.*, **13**, 451–470 (1969).
34. Maze, C. and Burnet, G., Modification of a non-linear regression technique used to calculate surface tension from sessile drops, *Surface Sci.*, **24**, 335–342 (1971).
35. Rotenberg, Y., Boruvka, L. and Neumann, A. W., Determination of surface tension and contact angle from the shapes of axisymmetric fluid interfaces, *J. Colloid Interface Sci.*, **93**, 169–183 (1983).

36. Lahooti, S., del Río, O. I., Cheng, P. and Neumann, A. W., Axisymmetric drop shape analysis (ADSA), in *Applied Surface Thermodynamics*, Neumann, A. W. and Spelt, J. K. (Eds), Marcel Dekker, New York, 1996, pp. 441–507.
37. Cheng, P., Li, D., Boruvka, L., Rotenberg, Y. and Neumann, A. W., Automation of axisymmetric drop shape of a liquid meniscus near a stripwise heterogeneous wall, *Colloid Surf.*, **43**, 151–167 (1990).
38. del Río, O. I. and Neumann, A. W., Axisymmetric drop shape analysis: Computational methods for the measurement of interfacial properties from the shape and dimensions of pendant and sessile drops, *J. Colloid Interface Sci.*, **196**, 136–147 (1997).
39. Oliver, J. F., Huh, C. and Mason, S. G., An experimental study of some effects of solid surface roughness on wetting, *Colloids Surf.*, **1**, 79–104 (1980).
40. Lam, C. N. C., Kim, N., Hui, D., Kwok, D. Y., Hair, M. L. and Neumann, A. W., The effect of liquid properties to contact angle hysteresis, *Colloid Surf., A*, **189**, 265–278 (2001).
41. Kwok, D. Y., Gietzelt, T., Grundke, K., Jacobasch, H.-J. and Neumann, A. W., Contact angle measurements and contact angle interpretation: I. Contact angle measurements by axisymmetric drop shape analysis and a goniometer – sessile drop technique, *Langmuir*, **13**, 2880–2894 (1997).
42. del Río, O. I., Kwok, D. Y., Wu, R., Alvarez, J. M. and Neumann, A. W., Contact angle measurements by axisymmetric drop shape analysis and an automated polynomial fit program, *Colloid Surf. A*, **143**, 197–210 (1998).
43. Skinner, F. K., Rotenberg, Y. and Neumann, A. W., Contact angle measurements from the contact diameter of sessile drops by means of a modified axisymmetric drop shape analysis, *J. Colloid Interface Sci.*, **130**, 25–34 (1989).
44. Alvarez, J. M., Amirfazli, A. and Neumann, A. W., Automation of the axisymmetric drop shape analysis – Diameter (ADSA-D) for contact angle measurements, *Colloid Surf., A*, **156**, 163–176 (1999).
45. Duncan-Hewitt, W. C., Policova, Z., Cheng, P., Vargha-Butler, E. I. and Neumann, A. W., Semi-automatic measurement of contact angles on cell layers by a modified axisymmetric drop shape analysis, *Colloid Surf.*, **42**, 391–403 (1989).
46. Moy, E., Cheng, P., Policova, Z., Treppo, S., Kwok, D., Mack, D. R., Sherman, P. M. and Neumann, A. W., Measurement of contact angles from the maximum diameter of non-wetting drops by means of a modified axisymmetric drop shape analysis, *Colloid Surf.*, **58**, 215–227 (1991).
47. Budziak, C. and Neumann, A. W., Automation of the capillary rise technique for measuring contact angles, *Colloid Surf.*, **43**, 279–293 (1990).
48. Longman, G. W. and Palmer, R. P., Two microscopical methods of determining the contact angles of small drops, *J. Colloid Interface Sci.*, **24**, 185–188 (1967).
49. Jameson, G. J. and Del Cerro, M. C. G., Theory for the equilibrium contact angle between a gas, a liquid and a solid, *J. Chem. Soc., Faraday Trans.*, **1**, **72**, 883–895 (1976).
50. Aveyard, R., Clint, J. H., Nees, D. and Paunov, V., Size-dependent lens angles for small oil lenses on water, *Colloid Surf., A*, **146**, 95–111 (1999).
51. Aveyard, R., Clint, J. H. and Nees, D., Small solid particles and liquid lenses at fluid/fluid interfaces, *Colloid Polym. Sci.*, **278**, 155–163 (2000).
52. Neumann, A. W., Methods for measuring surface energetics. part I: Contact angles, *Z. Physik. Chem. (Frankfurt)*, **41**, 339–352 (1964).
53. Kwok, D. Y. and Neumann, A. W., Capillary rise at a vertical plate as a contact angle technique, in *Applied Surface Thermodynamics*, Neumann, A. W. and Spelt, J. K. (Eds), Marcel Dekker, New York, 1996, pp. 413–440.
54. Kwok, D. Y., Budziak, C. J. and Neumann, A. W., Measurements of static and low rate dynamic contact angles by means of an automated capillary rise technique, *J. Colloid Interface Sci.*, **173**, 143–150 (1995).
55. Sedev, R. V., Budziak, C. J., Petrov, J. G. and Neumann, A. W., Dynamic contact angles at low velocities, *J. Colloid Interface Sci.*, **159**, 392–399 (1993).
56. Gu, Y., Li, D. and Cheng, P., A novel contact angle measurement technique by analysis of capillary rise profile around a cylinder (ACRPAC), *Colloid Surf., A*, **122**, 135–149 (1997).
57. Jensen, W. C. and Li, D., Determination of line tensions from the capillary rise in a conical tube, *Colloid Surf., A*, **156**, 519–524 (1999).
58. Harkins, W. D. and Jura, G., Surfaces of solids. XII. An absolute method for the determination of the area of a finely divided crystalline solid, *J. Am. Chem. Soc.*, **66**, 1362–1366 (1944).
59. Fuerstenau, D. W. and Williams, M. C., Characterization of the lyophobicity of particles by film flotation, *Colloid Surf.*, **22**, 87–91 (1987).
60. Fuerstenau, D. W., Diao, J. and Hanson, J., Estimation of the distribution of surface sites and contact angles on coal particles from film flotation data, *Energy Fuels*, **4**, 34–37 (1990).
61. Omenyi, S. N., Neumann, A. W. and van Oss, O. J., Attraction and repulsion of solid particles by solidification fronts. I. Thermodynamic effects, *J. Appl. Phys.*, **52**, 789–795 (1981).
62. Li, D. and Neumann, A. W., Wettability and surface tension of particles, in *Applied Surface Thermodynamics*, Neumann, A. W. and Spelt, J. K. (Eds), Marcel Dekker, New York, 1996, pp. 239–292.
63. Neumann, A. W., Omenyi, S. N. and van Oss, C. J., Negative Hamaker coefficients. I. Particle engulfment or rejection at solidification fronts, *Colloid Polym. Sci.*, **257**, 413–419 (1979).
64. Vargha-Butler, E. I., Absolom, D. R., Neumann, A. W. and Hamza, H. A., Characterizations of coal by contact-angle and surface-tension measurements, in *Interfacial Phenomena in Coal Technology*, Botsaris, G. D. and Glazman, Y. M. (Eds), Marcel Dekker, New York, 1989, pp. 33–84.
65. Vargha-Butler, E. I., Moy, E. and Neumann, A. W., Sedimentation behaviour of low surface energy powders in different non-polar liquid systems, *Colloid Surf.*, **24**, 315–324 (1987).

66. Vargha-Butler, E. I., Zubovits, T. K., Hamza, H. A. and Neumann, A. W., Surface tension effects in the sedimentation of polymer particles in various liquid mixtures, *J. Disp. Sci. Technol.*, **6**, 357–379 (1985).
67. Vargha-Butler, E. I., Foldvari, M. and Mezei, M., Study of the sedimentation behaviour of liposomal drug delivery system, *Colloid Surf.*, **42**, 375–389 (1989).
68. Vargha-Butler, E. I., Sveinsson, S. J. and Policova, Z., Wettability studies on drugs and drug delivery vesicles, *Colloid Surf.*, **58**, 271–286 (1990).
69. Vargha-Butler, E. I. and Hurst, E. L., Study of liposomal drug delivery systems. I. Surface characterization of steroid loaded MLV liposomes, *Colloid Surf., B*, **3**, 287–295 (1995).
70. Omenyi, S. N., Snyder, R. S., Absolom, D. R., van Oss, C. J. and Neumann, A. W., Enhanced erythrocyte suspension layer stability achieved by surface tension lowering additives, *J. Disp. Sci. Technol.*, **3**, 307–333 (1982).
71. Grundke, K., Bogumil, T., Gietzelt, T., Jacobasch, H.-J., Kwok, D. Y. and Neumann, A. W., Wetting measurements on smooth, rough and porous solid surfaces, *Progr. Colloid Polym. Sci.*, **101**, 58–68 (1996).
72. Tröger, J., Lunkwitz, K., Grundke, K. and Bürger, W., Determination of the surface tension of microporous membranes using wetting kinetics measurements, *Colloid Surf., A*, **134**, 299–304 (1998).
73. Omenyi, S. N., Neumann, A. W., Martin, W. W., Lespinaud, G. M., and Smith, R. P., Attraction and repulsion of solid particles by solidification fronts. II. Dimensional analysis, *J. Appl. Phys.*, **52**, 796–802 (1981).
74. Omenyi, S. N., Smith, R. P. and Neumann, A. W., Determination of solid/melt interfacial tensions and of contact angles of small particles from the critical velocity of engulfing, *J. Colloid Interface Sci.*, **75**, 117–125 (1980).
75. Li, S. K., Smith, R. P. and Neumann, A. W., Wilhelmy technique and solidification front technique to study the wettability of fibres, *J. Adhes.*, **17**, 105–122 (1984).

CHAPTER 15

Measuring Micelle Size and Shape

Magnus Nydén

Chalmers University of Technology, Göteborg, Sweden

1	Introduction	281	2.2.5	Concentration dependence . . .	287
2	NMR Relaxation and Self-Diffusion	281	2.2.6	Solvent diffusion	288
2.1	NMR self-diffusion	282	2.2.7	The time-scale in PGSE NMR	288
2.1.1	Pulse sequences	282	2.3	NMR relaxation	289
2.2	Experimental considerations	282	3	Fluorescence Techniques	290
2.2.1	Calibration of the gradient strength	283	4	Small-Angle Scattering Techniques	292
2.2.2	Temperature gradients	284	5	Static and Dynamic Light Scattering	294
2.2.3	Eddy currents	284	6	References	296
2.2.4	Self-diffusion measurements in dilute micellar solutions	285			

1 INTRODUCTION

One of the most important and interesting properties of surfactants in solution is that they form micelles. The size and shape of these aggregates can be studied by a number of experimental techniques, such as fluorescence, scattering and nuclear magnetic resonance (NMR) techniques, just to mention a few. Each method gives its own unique contribution when elucidating both static and dynamic aspects of micellar solutions. The first method described is NMR. In particular, NMR self-diffusion and relaxation are considered. Due to the difficulties in performing accurate NMR self-diffusion measurements (which is a prerequisite for measuring the micellar size and shape), this method is discussed in detail with regards to experimental difficulties. The method is quite sensitive to small errors in the performance of hardware – a situation that is sometimes neglected when experiments are carried out on spectrometers not properly equipped for these types of measurements. The Steady-State Fluorescence Quenching (SSFQ) and the Time-Resolved Fluorescence Quenching

(TRFQ) methods will also be described. Traditional and very powerful tools for the detailed study of micellar size and shape in the case of micelles are small-angle scattering techniques. Small-Angle Neutron Scattering (SANS) and also Small-Angle X-ray Scattering (SAXS) will be discussed in this respect. Light Scattering will also be described with the application to small micelles in solution.

2 NMR RELAXATION AND SELF-DIFFUSION

To start with, NMR is a very powerful tool for the study of surface and colloid chemistry in general and several good reviews on this subject have been produced (1–5). As far as micelle size and shape are concerned, two main experiments prevail in the literature, namely NMR relaxation and self-diffusion measurements. The technique of NMR self-diffusion is a “relative” tool for the study of micellar size and shape since it uses the Stokes–Einstein relationship (or modifications to it) to

relate the measured diffusion coefficient to the hydrodynamic radius. When using the NMR relaxation technique, one is more model-dependent by the fact that in order to interpret the data some motional model must be introduced.

2.1 NMR self-diffusion

The NMR self-diffusion experiment is performed with the aid of a spin-echo in combination with pulsed field gradients, with the common nomenclature being Pulsed Gradient Spin-Echo NMR (PGSE NMR) (6, 7). This is a technique that enables the measurements of the true molecular *self*-diffusion coefficients. In the case of micelles diffusing in a dilute solution, the size and shape is what determines (except for the viscosity of the solvent) the self-diffusion coefficient D , which is then used to calculate the hydrodynamic radius. In contrast to small-angle scattering techniques, both light scattering and the NMR self-diffusion experiments give a measure of the hydrodynamic radius R_H , a value that depends on the number of water molecules that the aggregate “binds”.

With the PGSE technique, it is relatively easy to measure the size of small spherical micelles, either by measuring the micellar self-diffusion coefficient in dilute solution or by investigating the concentration dependence of the micellar diffusion and extrapolating to zero concentration. In fact, this way is often suggested for determining accurate values of the hydrodynamic radius. However, for large micelles or large microemulsion drops, for example, the experiment can be much more difficult to perform, mostly due to a combination of fast signal relaxation and slow diffusion. In the following, some focus on how to experimentally perform accurate PGSE NMR measurements in micellar solutions will be discussed. For a very comprehensive and useful text on the subject of PGSE NMR for the study of translational diffusion, the reader is referred to ref. (7).

2.1.1 Pulse sequences

The two most commonly used pulse sequences for PGSE NMR are shown in Figure 15.1. Starting with the pulse sequence shown in Figure 15.1(a), we note that the pulsed field gradients are placed shortly after (typically a few microseconds) the 90–180° radiofrequency pulse. The theoretical expressions for the signal decay when using the basic version (PGSE, Figure 15.1(a)) and the stimulated version (PGSTE, Figure 15.1(b)) of the spin-echo method are shown in equations (15.1)

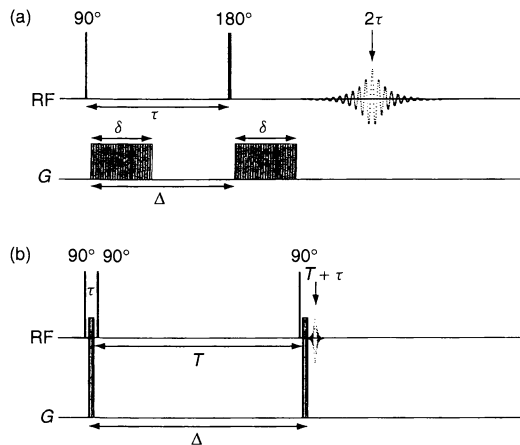


Figure 15.1. Pulse sequences for the “standard” pulsed field gradient spin-echo (a) and pulsed field gradient stimulated spin-echo (b) techniques. Note that in the latter case, the length (δ) and strength (G) of the gradient pulse is omitted for clarity but have the same meaning as in part (a)

and (15.2), respectively, as follows:

$$A(2\tau) = A(0) \exp(-2\tau/T_2) \exp[-(\gamma G \delta)^2 D(\Delta - \delta/3)] \quad (15.1)$$

$$A(T + \tau) = A(0) 0.5 \exp(-2\tau/T_2) \exp(-T/T_1) \exp[-(\gamma G \delta)^2 D(\Delta - \delta/3)] \quad (15.2)$$

where $A(0)$ is the signal amplitude after the first 90-degree pulse, T_2 and T_1 are the transverse and longitudinal relaxation times, respectively, γ is the magnetogyric ratio for protons, G is the gradient strength, δ the length of the gradient pulse, D the diffusion coefficient and Δ the time-separation between the gradient pulses.

Using either of these pulse sequences and increasing the gradient strength, G , or the length of the gradient, δ , will result in a linear decrease of the signal when $\log(A)$ is plotted versus $(\gamma G \delta)^2 D(\Delta - \delta/3)$, thus giving a straight line with slope D (note that the relaxation terms simply contribute to a signal offset and not to the measured diffusion coefficient since τ and T is kept constant throughout the experiment). However, it should be mentioned that when using the PGSTE sequence, extensive phase cycling should be employed in order to obtain the wanted echo shown in Figure 15.1(b).

2.2 Experimental considerations

When performing the PGSE or PGSTE experiment, it is very important to first check whether the hardware is

performing properly. In particular, there are a few critical aspects that must be carefully examined before any measurements can be used for accurate determination of the self-diffusion coefficient. The most important of these features for the pulsed field gradient set-up are described below, as well as a discussion on how to deal practically with these in order to maximize the accuracy of the experiment.

2.2.1 Calibration of the gradient strength

For any NMR spectrometer equipped with pulsed field gradients facilities, it is necessary to first measure the field gradient strength of the gradient coil. With regards to diffusion measurements, the field gradient strength (G) appears as a squared term in equations (15.1) and (15.2). Thus, small errors in G will cause severe errors in D and therefore a careful calibration is necessary. It is relatively easy to perform a gradient calibration at low-field gradient strengths since one can simply choose H_2O , D_2O or any other solvent with a known self-diffusion coefficient. However, it is also very important to control the amplifier so that it works in a linear manner up to the highest accessible gradient strength, i.e. up to the highest current that the amplifier can produce. This means that a slowly diffusing molecule/compound should be chosen, since for a small molecule with fast diffusion the signal will be quickly submerged by the noise, according to equations (15.1) and (15.2).

Another important point concerning the choice of system for calibration of the field gradient strength is that if a highly volatile compound (CDCl_3 , toluene, benzene, cyclohexane, etc.) is chosen, care must be taken to seal the NMR tubes properly. If possible, flame sealing is strongly recommended. Otherwise, solvent will easily evaporate through the plastic NMR cap and creates heat of evaporation at the interface between solvent and air in the tube. This, in turn, creates a temperature gradient in the sample with a subsequent flow. Of course, any flow of solvent will make self-diffusion measurement impossible with the standard choice of pulse sequences as shown above. So what should one then choose as a model system when calibrating the pulsed field gradient set-up? For calibration at low currents/field gradient values, a simple solvent is a good choice. The self-diffusion coefficients of many solvents are well known and solvents are, of course, often easily accessible in the laboratory. For a list of self-diffusion constants for some simple solvents at different temperatures the reader is referred to refs (7–9). For higher currents, a well-characterized

polymer standard is recommended. One such standard is the poly(ethylene oxide) (PEO) standard, where molecular weights between 100 and 1 000 000 can be obtained with a very low polydispersity index. Accurate values for these have recently been published (10). In the literature, glycerol is sometimes used for gradient calibration at high field gradient strengths. However, this is not recommended since the self-diffusion of glycerol is strongly dependent on temperature and contamination by small amounts of water.

At this stage, it is also important to emphasize the effect of a non-constant magnetic field gradient, i.e. a field gradient which is not constant over the sample volume which is measured by the NMR probe. This effect has been examined by Håkansson *et al.* (11) by careful calculations of the signal decay in a PGSE experiment in the presence of an inhomogeneous field gradient. If the nonlinearity is a big problem, it may affect the calibration of G . One way to check for this is to perform the PGSE experiment on a sample with say 1% of PEO in water with a well-determined low molecular weight. Since this polymer has an exceptionally long T_2 , it is very good to use for calibration purposes as long as monodisperse polymers can be obtained. However, a deuterated solvent may also be used¹. In Figure 15.2, the signal decay in a PGSE experiment for toluene in deuterated toluene is shown.

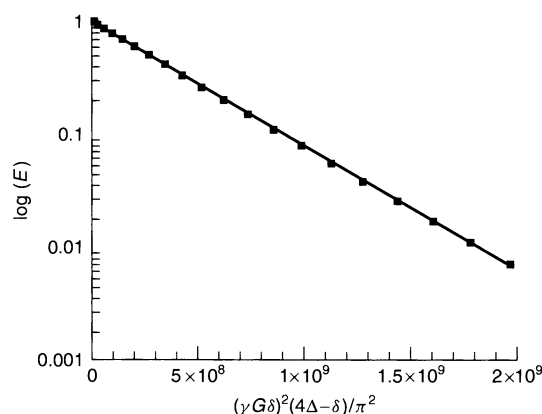


Figure 15.2. The echo-decay for (trace amounts of) toluene in deuterated toluene, plotted on a log scale, versus $(\gamma G \delta)^2 (4\Delta - \delta) / \pi^2$ (see Section 2.2.3 below). In this representation, the result should be a straight line giving the correct diffusion coefficient if the gradient strength is properly calibrated

¹ Fully protonated solvents may give rise to radiation damping due to the very strong signals and this may also result in a nonlinear decrease of the signal.

The signal decays linearly down to an attenuation of $0.01 \times A(2\tau)$. At even higher signal attenuations, deviations from linearity can be observed. However, this deviation is so small that the calibration of G is almost insensitive to the extent of signal attenuation.

2.2.2 Temperature gradients

In the previous section, the effect of solvent evaporation was discussed and the reason for flame sealing the NMR tube was discussed in terms of temperature gradients. Even though the NMR sample is flame sealed, temperature gradients are sometimes present and can be a disaster to the experiment. It turns out that in a poorly designed diffusion probe, temperature gradients can be a large problem, even at 25°C. At this stage, it is important to mention that only temperature gradients obtained at temperatures higher than room temperature cause problems in the self-diffusion experiment. The physical reason for this is that then the density differences work *with* the gravitational field, thus leading to a flow of the solution. Although large temperature gradients are also formed at low temperatures, this is not such a big problem since the density difference works *against* gravity.

The effect of temperature gradients can be made much smaller by using small amounts of sample in the tube. For example, when measuring water diffusion at 25°C in a 5 mm NMR tube which is filled with 1 ml D_2O , with a properly calibrated pulsed field gradient set-up, the obtained self-diffusion coefficient can be 50% larger than the literature value. When decreasing the sample amount to 0.3 ml, the result may lie within the error of the literature value. If experiments are to be performed at higher temperatures, a careful investigation of these effects is necessary and the experimentalist should then choose small sample amounts. However, with small sample amounts it is more difficult to obtain a homogeneous magnetic field (i.e. good “shimming” of the magnetic field) which may complicate the interpretation of the diffusion experiment if narrow lines in the NMR spectrum are needed for spectral resolution reasons. Another possibility is to use smaller NMR tubes. The effect of temperature gradients on the self-diffusion experiment is greatly reduced when choosing, for example, a 3 mm instead of a 5 mm NMR tube. In addition, the tempered air flow through the sample must be kept as high as possible without lifting the sample. One way to check for temperature gradients is to measure diffusion for a pure solvent (e.g. D_2O). If G is properly calibrated, the literature value for diffusion of the solvent should be obtained. Another result of a problem

temperature gradients is that the measured diffusion becomes dependent on Δ (12). Thus, by measuring diffusion in a non-complex system (such as water or other solvents), the obtained diffusion coefficient should be independent of Δ .

If problems from temperature gradients still remain, another possibility is to use a specific pulse sequence that is insensitive to flow but measures only diffusion (6). It is important to mention at this stage that flow affects the signal intensity in that a phase shift is introduced. In contrast to diffusion, which is monitored as a damped exponential term according to equations (15.1) or (15.2), flow causes an oscillatory behaviour that can sometimes be clearly observed at high signal attenuation (12, 13). In a recent paper (12), the effect of temperature gradients when determining the micellar shape in a nonionic micellar system was investigated. These authors concluded that measurements were best performed when choosing optimal sample tubes and pulse sequences that suppress the effect of convection arising from temperature gradients.

2.2.3 Eddy currents

Eddy currents arise from the steep rise and fall times of the pulsed-field gradients. These pulses induce currents in the probe body surrounding the sample and probably also in the superconducting parts of the magnet system outside of the NMR probe. These oscillating currents produce an oscillating magnetic field at the position of the sample. In addition to the static magnetic field and the pulsed-field gradients, there is then an extra random field that may completely destroy the NMR signal. An even worse scenario is a small random field that only to a small extent affects the signal. This may result in a measured diffusion coefficient which is orders of magnitude larger than the true value. Many self-diffusion probes are equipped with active shielding, i.e. an extra coil is placed outside the primary coil. The current in this coil is opposite to that of the primary coil and the position is such that the field produced at the position of the sample is effectively the same, while the field outside the two coils is essentially zero. In a perfect world, this would remove any eddy currents but, of course, this is never the case. However, in a pulsed-field gradient set-up, equipped for state-of-the-art self-diffusion experiments, eddy currents may be as short as a few 100 microseconds. Of course, the eddy currents depend strongly on the strength of the applied pulsed-field gradient and at low currents (1–5 A) the

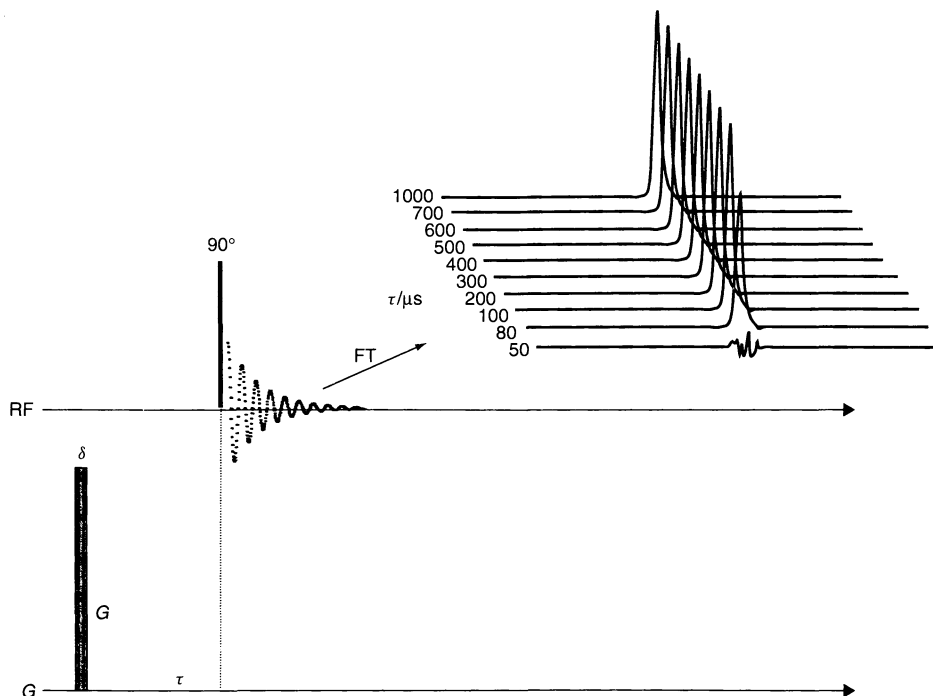


Figure 15.3. The pulse sequence used to check for eddy current. By varying τ from long to short values, the effect of eddy currents will be noticed as a distortion of the signal in terms of phase and signal height. The effect should be investigated with respect to all possible settings of G and δ . The right inset shows how a typical eddy current test might turn out. Note that as τ decreases to 80 μ s the signal is artificially attenuated due to eddy currents and not due to diffusion

the coil has to be increased (5–40 A)¹ due to slow diffusion and/or a fast T_2 , relaxation eddy currents become an increasing problem. As was also the case for temperature gradients, the effect of the problem is slowly incorporated into the results and it may be difficult to separate these from the actual diffusion (13). Having mentioned this, one can note that on a standard narrow-bore spectrometer this is seldom the case and (much) longer eddy currents can sometimes be obtained. The way to check for eddy currents is to perform the pulse sequence shown in Figure 15.3. By varying τ , the time needed in order for the eddy currents to be negligible is obtained and subsequently incorporated after the pulsed-field gradients in the pulse sequences shown in Figure 15.3.

One very efficient way of decreasing eddy currents is not to produce rectangular pulses but shaped pulses (14). By doing this, the rise time is made smaller, thus

decreasing the induction of current in the surroundings of the coil. On modern spectrometers, this can easily be incorporated in a number of different shapes. For theoretical reasons, the use of linearly ramped or sine pulses are favoured. In this way, the time needed for eddy currents to die out can be decreased by orders of magnitudes. In the case of sine pulses, the corresponding expression for the signal decay when using the PGSE pulse sequence is given by the following equation (13):

$$A(2\tau) = A(0) \exp(-2\tau/T_2) \exp[-(\gamma G \delta)^2 D(4\Delta - \delta)/\pi^2] \quad (15.3)$$

The theoretical expression when using the PGSTE sequence is modified accordingly.

2.2.4 Self-diffusion measurements in dilute micellar solutions

After the necessary steps have been taken in order to ensure the performance of the pulsed-field-gradient

¹ This is what a current state-of-the-art gradient amplifier can produce in terms of current. In a typical self-diffusion probe produced by leading manufacturers, this would then give 10–20 T/m as a field gradient strength.

hardware, as mentioned above, one can start the diffusion measurements. In the following, a working example of measuring the size of cetyltrimethylammonium bromide (CTAB) micelles in water is described. After this, the self-diffusion experiment performed in a CTAB solution will be described. Before going into some results, some aspects on the accuracy of the PGSE or PGSTE experiments will be discussed.

In order to perform accurate measurements, it is necessary that the temperature in the probe is very stable (preferably an accuracy better than $<0.05^\circ$) and accurately determined. For a thorough discussion on these matters the reader is referred to ref. 15. Secondly, a careful calibration of the field gradient strength is very important. In addition, the effect of temperature gradients has to be very accurately determined, since such a problem can be substantial, even at temperatures close to room temperatures. With these careful efforts in maximizing the accuracy of the self-diffusion experiments, errors smaller than 1% may be obtained, a prerequisite for separating spherical from prolate or oblate structures (as will be discussed further below).

In Figure 15.4 the results from a PGSE experiment performed on a 1% CTAB solution is shown. The experiment was carried out on a 500 MHz spectrometer equipped with a broad-band probe and pulsed-field gradients with a maximum of 0.6 T/m at 10 A

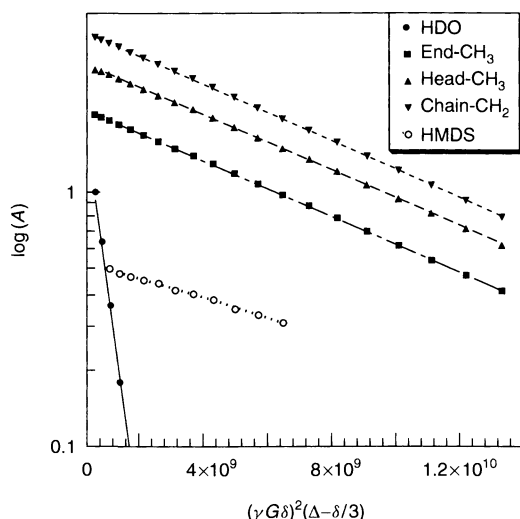


Figure 15.4. The echo-decay for a 1 wt% CTAB solution containing trace amounts of hexamethyldisiloxane (HMDS): ●, the HDO signal; ▼, the signal from the CH₂ group of the surfactant tail; ▲, the signal from the CH₃ group at the surfactant head; ■, the signal from the end-methyl group of the surfactant chain; ○, the signal from HMDS (Nydén, unpublished data)

current. This particular probe is not designed for self-diffusion measurements, but for much less demanding tasks with respect to the need for high field gradient strengths. Nevertheless, the experiment works fine since the slope is perfectly linear (in the representation chosen) and the measured micellar diffusion coefficient ($8.7 \times 10^{-11} \text{ m}^2 \text{ s}^{-1}$) is what is expected from a CTAB micelle. In this particular experiment, a hydrophobic probe, i.e. hexamethyldisiloxane (HMDS), was added to the solution. The amount was chosen to be approximately 0.1 “probe”/micelle in order not to influence the micellar structure. By doing so, the micellar self-diffusion coefficient could be measured without the influence of free surfactant. Since there is an exchange between free and micellized surfactant, the measured/observed diffusion coefficient is the weighted average of the two sites, as follows:

$$D_{\text{obs}} = p_{\text{free}} D_{\text{free}} + p_{\text{mic}} D_{\text{mic}} \quad (15.4)$$

where p_{free} is the fraction of surfactant in the free unmicellized state with diffusion coefficient D_{free} , p_{mic} is the fraction of surfactant in the micellized state, and D_{mic} is the micellar diffusion coefficient (note that $p_{\text{free}} = 1 - p_{\text{mic}}$). In Figure 15.4, the surfactant diffusion coefficient is $1.21 \times 10^{-10} \text{ m}^2 \text{ s}^{-1}$ and the HMDS diffusion coefficient is $8.7 \times 10^{-11} \text{ m}^2 \text{ s}^{-1}$. This also allows us to calculate the critical micelle concentration (CMC) if the diffusion for the free surfactant can be measured ($p_{\text{free}} = \text{CMC}/c_{\text{tot}}$). One complication in this respect is that the free surfactant concentration is not always constant above the CMC. This has to be carefully considered since the measured diffusion is heavily weighted by this free surfactant, according to equation (15.4).

For prolate or oblate forms, the measured diffusion coefficients at infinite dilution is given by the following expressions:

$$D_{\text{prol}}^0 = \frac{k_B T}{6\pi\eta b} \frac{\ln[r + (r^2 - 1)^{1/2}]}{(r^2 - 1)^{1/2}} \quad (15.5)$$

$$D_{\text{obl}}^0 = \frac{k_B T}{6\pi\eta b} \frac{\arctan[(r^2 - 1)^{1/2}]}{(r^2 - 1)^{1/2}} \quad (15.6)$$

where b is the length of the minor semi-axis and $r = a/b$ is the axial ratio, where a is the length of the major semi-axis. It turns out from equations (15.5) and (15.6) that the self-diffusion experiment is relatively non-sensitive to small deviations from spherical shape. For example, with $r = 2$, a 2–3% difference between prolates and oblates is obtained. However, as aggregates grow larger, a significant decrease in micelle self-diffusion is observed, as can be seen in Figure 15.5 where the diffusion coefficients of prolates and oblates

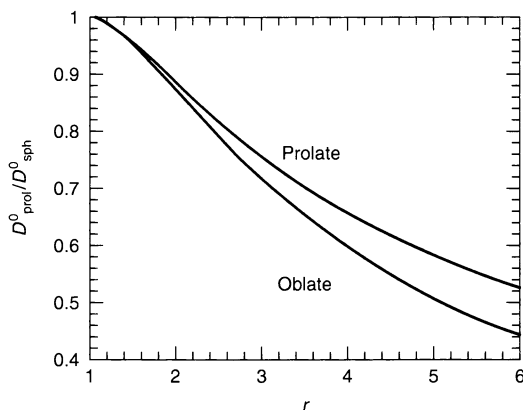


Figure 15.5. Normalized (with respect to the self-diffusion of spherical micelles) self-diffusion coefficients of prolate- and oblate-shaped micelles as a function of the axial ratio r (keeping the short axis constant and equal to the radius of the sphere). Plots obtained according to equations (15.5) and (15.6) and by using the constant-area-to-enclosed-volume constraint

are normalized with the diffusion coefficient for a sphere and plotted as a function of r . Due to the relatively strong dependence on r at small values of this parameter, it is of vital importance to perform very accurate self-diffusion measurements and any experimental difficulties as described above have to be carefully considered.

2.2.5 Concentration dependence

In the case of CTAB micelles, it is known that upon increasing the concentration they form non-spherical aggregates. As was shown in the above section, self-diffusion of non-spherical aggregates depends on the axial ratios of the aggregate and it was argued that the self-diffusion experiment could be used for detailed structural information if very accurate self-diffusion experiments were performed. Another important feature of aggregate shape in terms of self-diffusion coefficient is the dependence on aggregate concentration. As the ratio of micelles/aggregates is increased, the surrounding matrix obstructs the diffusion path and the functional form of the decrease in diffusion coefficient can be used to obtain further details about micellar size and shape. In the case of spherical aggregates, a functional form according to the following equation is often used:

$$D_{\text{obs}} = D_0(1 - k\phi) \quad (15.7)$$

where D_{obs} is the measured diffusion coefficient, D_0 is the micelle diffusion coefficient at infinite dilution, k is

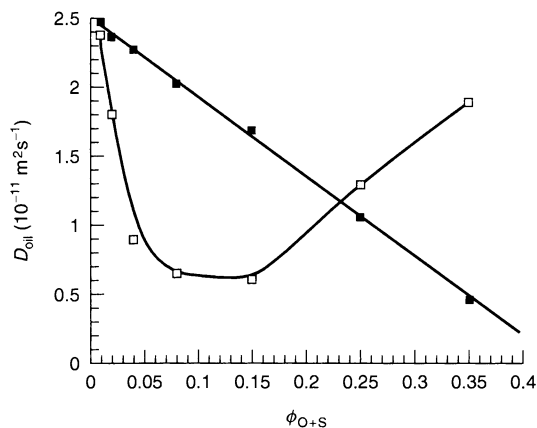


Figure 15.6. Self-diffusion measurements of the oil component in a microemulsion containing didodecyldimethylammonium sulfate (DDAS)/dodecane/water (D_2O) at different ratios of surfactant to oil. The X-axis represents the total volume of oil plus surfactant, i.e. the volume fraction of aggregates/micelles according to equation (15.7); ■ represents oil diffusion when the system solubilizes a maximum amount of oil (the emulsification failure line), with the continuous line being a fit of equation (15.7) to the data; □ represents the oil diffusion at lower oil-to-surfactant ratios when the system forms prolate structures; the corresponding line is simply a guide for the eye (Nydén, unpublished data)

a constant and ϕ is the volume fraction of micelles. In the case of spherical aggregates, $k \approx 2-2.5$, depending on the surfactant. Thus, from a concentration-dependent investigation any deviation from spherical symmetry may be determined. In Figure 15.6, the results obtained from a self-diffusion experiment for an oil-in-water microemulsion are shown. The two sets of data originate from different oil-to-surfactant ratios. In this figure, the solid symbols represent maxima in the oil-to-surfactant ratios (often referred to emulsification failure) at which the system forms spherical aggregates, while open symbols represent lower oil-to-surfactant ratios where the system adapts a different structure. In the case of maximum oil/surfactant ratios, the diffusion coefficients perfectly follow the theoretical expression for spherical aggregate diffusion as a function of concentration, thus yielding $D_0 = 2.5 \times 10^{-11} \text{ m}^2 \text{ s}^{-1}$ and $k = 2.1$. Through D_0 , the hydrodynamic radius, R_H , is obtained according to the following equation:

$$D = \frac{k_B T}{6\pi\eta R_H} \quad (15.8)$$

When the oil/surfactant ratio is decreased (by ca. 35%), the diffusion coefficient as a function of concentration is much different. At low concentrations of aggregates,

the rapid decrease in self-diffusion most likely depends on aggregate growth in one dimension since at even higher volume fractions of aggregates a hexagonal phase is formed.

Figure 15.6 illustrates a problem in the determination of micellar shape as a function of concentration if significant deviation from spherical symmetry is expected. When aggregates grow rapidly as temperature, salt or aggregate concentration is changed, at some stage the measured self-diffusion coefficient (of oil in this case) is affected not only by diffusion of the aggregate as such but also by an additional diffusion mechanism. For very large aggregates, one such mechanism is the diffusion of a surfactant from one prolate/oblate to the next since the aggregates are close together "in space". In effect, this severely complicates the interpretation of self-diffusion data. However, for moderate growth it may still be possible to obtain a quantitative measure of the axial ratio, according to equations (15.5) or (15.6), depending on the choice of model.

One way to treat the obstruction effect for spherical particles has been considered by Jonströmer *et al.* (16). These authors express the reduction in self-diffusion at low concentrations according to a cell-diffusion model, as shown in the following equation:

$$D = D_0[1 - k(r_H/R)^3] \quad (15.9)$$

where r_H is the hydrodynamic radius of the micelle and R is the radius of the cell. By measuring the concentration dependence of the micelle diffusion, it is then possible to separate prolates from oblates by the use of equations (15.5) and (15.6) (for a detailed description of a working protocol, the reader is referred to ref. (17)).

2.2.6 Solvent diffusion

Not only the aggregate self-diffusion, but also the self-diffusion of solvent molecules depends on the shape of aggregates. Intuitively, one realizes that the obstruction of solvent diffusion is larger for an oblate form than for a prolate, which in turn obstructs solvent diffusion more than a spherical aggregate. The method as such is very easy to use since solvent diffusion (most often water) is simple to measure and accurate values may be obtained. This allows the determination of micellar shape through the measurement of solvent diffusion. In particular, the method is very powerful when combined with calculations of the obstruction factor for differently shaped aggregates, as reported by Jönsson *et al.* (18). This method has been combined with PGSE NMR and NMR relaxation to determine the structure of nonionic

micelles, where obstruction of water diffusion became decisive for the shape determination (19).

2.2.7 The time-scale in PGSE NMR

Some words on the time-scale in the PGSE NMR experiment might be useful at this stage since in some complex systems there might exist a time-dependency of the measured diffusion coefficient.

Equation (15.4) holds for a situation with fast exchange between the two sites and in PGSE NMR the time-scale is controlled by Δ , which is the effective time-scale in the PGSE or PGSTE experiments. If the lifetime for the surfactant in a micelle is much smaller than Δ , the exchange is fast while if the lifetime of the surfactant is much longer than Δ the exchange is slow. Although a situation of slow exchange is fairly uncommon for simple surfactant systems, it can often be found in associating polymer systems. In particular, this is often seen in block copolymers. In this case, slow exchange between monomers and micelles can be observed as a large curvature of the PGSE data (when the axes are represented as in Figure 15.4) which indicates slow exchange between monomer and micelle and also between micelles of different sizes.

In PGSE NMR, Δ can be varied within a certain range which is determined by the hardware performance of the pulsed field gradient equipment, and also by the T_1 and T_2 relaxation times. For example, when small micelles are considered T_2 might be around 20–100 ms and T_1 slightly higher, usually 200–500 ms. In a situation where a slow or intermediate exchange is observed (as revealed by the fact that the signal decay in the PGSE or PGSTE experiment is non-exponential), the surfactant dynamics can be further investigated by varying Δ . Since T_1 is longer than T_2 , the stimulated echo approach (PGSTE) is preferably used. However, in order to carefully examine the effect of exchange, experiments should be performed so that the signal in the PGSE experiment decays by at least a factor of 10 or maybe even a factor of 100 (i.e. $0.01 \times A(2\tau)$). For small values of Δ , the limiting factor for reaching this large signal attenuation is the available field gradient "area", $G\delta$. Since δ has to be short (due to a short T_2 and hence the use of the PGSTE pulse sequence), G has to be large. This is a situation when the standard equipment is normally not powerful enough to perform accurate measurements. In particular, an error in the measured diffusion coefficient is likely to appear as the limit of the hardware performance is reached. In Figure 15.4 above,

$\Delta = 70$ ms, $\delta = 10$ ms and $G = 0.17$ T/m. With $\Delta = 35$ ms, $\delta = 10$ ms and $G = 0.24$ T/m, the diffusion constant turned out to be twice as large, indicating that this experiment had failed to give the correct diffusion constant as the hardware did not perform properly¹. In this case, the limiting factor was the short time available for the pulsed-field-gradient amplifier to recharge after the first gradient pulse – a situation not uncommon for spectrometers equipped only with standard pulsed-field-gradient equipment. It is, however, non-trivial to separate the effect of eddy currents from the effect mentioned in this last section. For a detailed discussion on this subject, the reader is referred to ref. (13).

2.3 NMR relaxation

The rate of NMR relaxation of molecules or aggregates depends on the molecular/aggregate motion. In micellar systems, these motions can be modelled as two independent motions occurring on different time-scales. This model is often referred to as the two-step model (as suggested in ref. (20)). The fast motions correspond to the fast local dynamics which the surfactant undergoes within the micelle. Slow motions represent the diffusion of surfactant along the micellar aggregate and the aggregate tumbling as such. One often used nuclei for NMR relaxation studies is the ^2H nucleus. The reason for this choice is that the quadrupolar relaxation mechanism is the dominant mechanism for relaxation, which greatly simplifies the analysis. In particular, the two relaxation times, T_1 and T_2 , can be correlated to fast local motions and to rotational and diffusive correlation times² of the aggregate. Thus, by ^2H labelling of the surfactant, further information concerning both the size and shape of micelles may be obtained.

In terms of the reduced spectral densities the motions in the model mentioned above can be described by the following expression:

$$\tilde{J}(\omega) = (1 - S^2)\tilde{J}_f(\omega) + S^2\tilde{J}_s(\omega) \quad (15.10)$$

where the first term describes the fast motions and the second the slow motions; S is the so-called order parameter, which is a measure of the local order of the surfactant. In the case of ^2H NMR, the NMR relaxation rates, R_1 and R_2 ($R_i = 1/T_i$), depend on the spectral

densities, according to the following:

$$R_1 = \left(\frac{3\pi^2}{40}\right) \chi^2 (2\tilde{J}(\omega) + 8\tilde{J}(2\omega)) \quad (15.11)$$

$$R_2 = \left(\frac{3\pi^2}{40}\right) \chi^2 (3\tilde{J}(0) + 5\tilde{J}(\omega) + 2\tilde{J}(2\omega)) \quad (15.12)$$

where χ is the quadrupolar coupling constant³. Thus, by measuring the frequency dependence of both R_1 and R_2 , detailed information about the micellar size and shape may be obtained. In a paper by Söderman *et al.* (17), this was nicely demonstrated by measuring the NMR relaxation rates at three different spectrometer frequencies. By assuming prolate-shaped or hemisphere-capped rods, these authors showed that the micelles had an axial ratio of approximately 6. In addition, it was shown that PGSE NMR, NMR relaxation and time-resolved fluorescence quenching gave almost perfect agreement with respect to micellar size and shape.

When spherical aggregates are considered, it is enough to perform NMR relaxation experiments on a single spectrometer since the difference between R_2 and R_1 , ΔR , depends only on slow motions (see equations (15.11) and (15.12)). A combination of equations (15.10)–(15.12) then gives the following:

$$\Delta R = \frac{9\pi^2}{20} (\chi^2 S^2) \tau_s \quad (15.13)$$

where τ_s is the correlation time for slow motions as mentioned above, i.e. the rotational diffusion of the surfactant along the surface of the micelle and the rotation of the whole aggregate. These motions are uncorrelated which effectively means that the total inverse correlation time can be expressed as follows:

$$\frac{1}{\tau_s} = \frac{1}{\tau_r} + \frac{1}{\tau_d} \quad (15.14)$$

where τ_r is the micellar rotational correlation time and τ_d is the correlation time for the surfactant diffusion along the curved aggregate. These particular motions of a surfactant residing in a spherical micellar aggregate with radius R can be quantified according to the following equations:

$$\tau_r = \frac{4\pi\eta R^3}{3k_B T} \quad (15.15)$$

$$\tau_d = \frac{R^2}{D_s^{\text{lat}}} \quad (15.16)$$

¹ From equations (15.1) and (15.2), it is clear that if Δ is decreased by a factor of 2, G must increase by a factor of $\sqrt{2}$ in order to keep the same signal attenuation.

² Refers to the diffusion of a surfactant around the micelle.

³ This can be calculated from the splitting of the ^2H NMR spectra of the same deuterated surfactant in a lamellar or hexagonal phase.

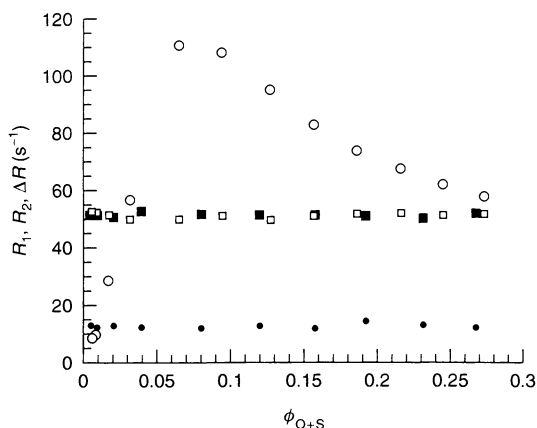


Figure 15.7. Results obtained from relaxation experiments carried out on the same system as in Figure 15.6: ○ represents ΔR for a deuterated DDAS at the methyl position ($2 \times \text{CD}_3$) at the quaternary nitrogen, for the lower ratio of oil-to-surfactant, while □ represents the corresponding R_1 relaxation rate; ● represents ΔR for the maximum amount of oil-to-surfactant, i.e. when the system is most likely to form spherical aggregates, while ■ represents the corresponding R_1 relaxation rate (Nydén, unpublished data)

Where D_s^{lat} is the lateral diffusion of surfactant along the micelle surface. In Figure 15.7, the results obtained from relaxation experiments performed on the same system as that in Figure 15.6 are shown. In these experiments, H_2O was used (or actually deuterium-depleted water) and the DDAS is now consequently deuterated. In this case, the surfactant (DDAS) was deuterated at the two methyl groups at the position close to the quaternary ammonium. When the microemulsion consists of a maximum amount of oil that can be solubilized (emulsification failure situation, as discussed above) and is then diluted with water, both R_1 and R_2 (data not shown for clarity) are independent of the volume fraction of aggregates. However, some deviation at very high volume fractions of aggregates can be noted. As a consequence, ΔR also shows some deviation, indicating that the size and shape of aggregates remain unchanged since any change in the correlation time describing the slow motions would be picked up as a change in ΔR (through R_2 , not R_1) according to equation (15.13). When the ratio of oil/surfactant is decreased, R_1 is still unchanged as the volume fraction of micelles is changed, although large changes in ΔR are seen in Figure 15.7 with a maximum at approximately 0.08 wt%, thus indicating a rapid micellar growth up to this point. It is worth noting that the maximum in ΔR is in good agreement with the minimum in

oil self-diffusion shown in Figure 15.6. Thus, from measuring R_1 and R_2 it is possible to calculate the radius of a spherical aggregate if the lateral self-diffusion coefficient of the surfactant along the surface of the micelle is known (or vice versa).

From equation (15.11), it can be seen that the R_1 relaxation is induced by motions occurring on fast time-scales (typically 10–100 MHz) and can thus be used as a probe for the fast motions of the surfactant. These motions depend on the local environment in terms of, for example, available head-group area, a value that may change as the micellar size and shape is altered. However, in this case this is apparently not so.

3 FLUORESCENCE TECHNIQUES

There are different types of fluorescence experiments that can be performed in micellar systems in order to obtain both static and dynamic properties. Which method one chooses depends on the type of information being searched for (and of course on the availability of a particular instrument). For example, the fluorescence technique is very useful for the study of the CMC of surfactants in solution. The experimentalist then uses a fluorescence probe and simply measures the emitted light from a continuously illuminated sample containing very small amounts of the probe. Since the emission spectrum has the feature of being sensitive to the polarity of its surroundings, one can follow a situation when hydrophobic aggregates are formed in a surfactant solution.

By using the information obtained when the emission of the probe molecule is quenched, i.e. either by excimer formation of the probe itself or by addition of a molecule that quenches the excited state of the probe, it is possible to further characterize the system in terms of micellar shape. This is a technique frequently used in a wide variety of systems, including binary water–surfactant or polymer–surfactant systems, or microemulsions. Two methods are worth extra attention, namely the steady-state fluorescence quenching (SSFQ) and the time-resolved fluorescence quenching (TRFQ) methods. For more comprehensive texts describing these techniques, the reader is referred to refs (21) and (22).

The SSFQ experiment can be performed in many laboratories today since the equipment needed is commonly available. In SSFQ, the response is the emitted light from a probe when being continuously illuminated with light with a constant low intensity. By choosing very low concentrations of probe, one ensures that the number of probes inside a micelles is never larger than 1 (which is

more a theoretical problem than a practical one). As the quencher concentration is increased, the amount of emitted fluorescent light decreases due to the non-radiative relaxation of the excited state.

Starting with small fractions of quencher inside the micelles, the intensity of the emitted light increases with increasing concentration of quencher, according to the following equation:

$$I_q = I_0 \exp\left(-\frac{c_q}{c_M}\right) \quad (15.17)$$

where c_q and c_M are the concentrations of quencher and micelles, respectively, and I_q and I_0 are respectively the light intensities with and without quencher. The aggregation number, N_{SS} , can then be obtained from the following:

$$N_{SS} = \frac{c_{tot} - CMC}{c_M} \quad (15.18)$$

where c_{tot} is the total concentration of surfactant. Thus, the method is quite simple to perform and little theory is needed in order to interpret the results. However, some care has to be taken in order to ensure the correctness of the method. First, this way of measuring the aggregation number of a micellar-like aggregate supposes a Poisson-distributed quencher in the micelles, which is most often the case for simple binary mixtures of surfactant and water. However, when dealing with mixtures of surfactants one must ensure that the quencher does not have a preferential distribution in micelles that are rich in one type of surfactant (23). Secondly, the size of the aggregates must be quite small. In a recent paper (24), this point was demonstrated by a correlation plot between N_{SS} from SSFQ and the aggregation number (N_D) as measured by the TRFQ method (small aggregates is not a prerequisite for TRFQ measurements), which is presented in Figure 15.8.

It is evident that the SSFQ method underestimated the aggregation number when the latter is larger than 70–80. The physical reason for this state of affairs is that equations (15.17) and (15.18) are correct only if $k_q \gg k$, i.e. when the rate at which quenching of the probe by the quencher is much faster than the rate at which the probe emits light by spontaneous emission. In a situation when aggregates are large (or grow large as the concentration is increased or if other external parameters are changed), this assumption is not necessary fulfilled since the quenching rate depends (among other things) on the rate at which the probe and quencher collide in an aggregate.

Turning now to the TRFQ method, we first note that the experimental set-up is much more demanding

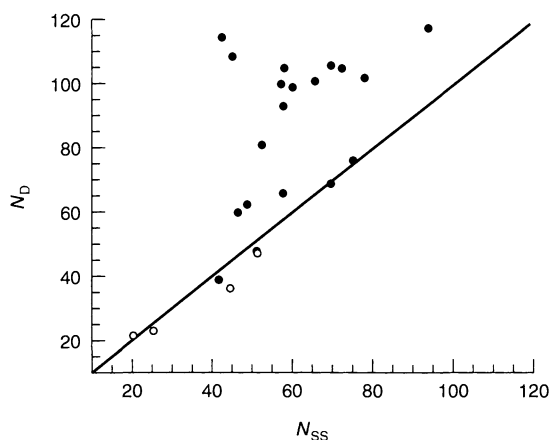


Figure 15.8. Aggregation numbers, N_{SS} and N_D (see ref. (24) for details), obtained from different sized micellar and polymer systems with the SSFQ and TRFQ methods, respectively. Note that as the micelle size is increased, the SSFQ method yields values of the aggregation numbers that are smaller than those obtained by the TRFQ measurements

than that used in SSFQ measurements. The experiment is carried out by exciting the probe with a very short pulse of light and then the fluorescence decay of the probe is monitored as function of time with the aid of, e.g. a single-photon-counting apparatus. The experiment requires control measurements with the unquenched probe, i.e. samples must be prepared both with and without quencher. From experiments without quencher, the lifetime of the probe in the excited state is measured and a single exponential decay is most often obtained from which the deactivation rate constant for the probe without quencher is calculated. In this context, it is important to mention that for practical reasons the solutions are often de-gassed, since one mechanism for probe quenching is the presence of oxygen gas in the sample. When quencher is added to the system, the lifetime of the probe in the excited state decreases and a functional form of the decay curve is well described by the equation proposed by Infelta *et al.* (25), as follows:

$$I(t) = I_0 \exp\left\{\frac{t}{\tau_0} - R[1 - \exp(-k_q t)]\right\} \quad (15.19)$$

where I_0 is the light intensity of $t = 0$, $R = c_q/c_M$, i.e. the average number of quenchers per micelle, τ_0 is the unquenched lifetime of the excited state and k_q is the first-order rate constant for quenching in a micelle with only one quencher present. In Figure 15.9, the decay curves for a micelle system with and without quencher is presented. As can be seen from this figure, the curve without quencher displays a single exponential

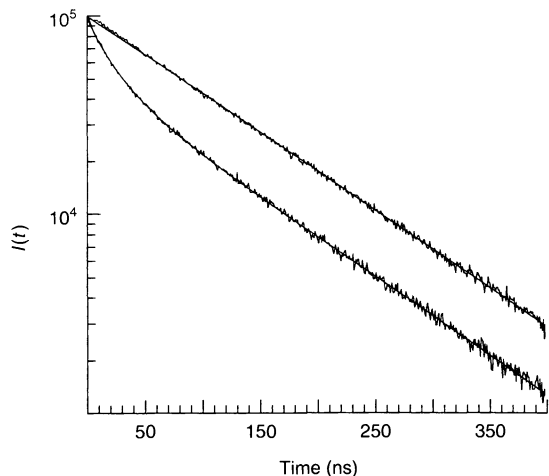


Figure 15.9. TRFQ results obtained from a 0.044 molal dodecyltrimethylammonium bromide solution. The probe used is pyrene and the quencher is dodecylpyridinium bromide at 25°C. The fit of equation (15.19) to the data yields the following for the unquenched curve, $I_0 = 1.01 \times 10^5$ (normalized to the same value as for the quenched curve), and $\tau_0 = 117$ ns, while for the quenched curve, we obtain $I_0 = 1.01 \times 10^5$, $\tau_0 = 116$ ns, $R = 0.70$, and $k_q = 0.029 \text{ ns}^{-1}$. (By courtesy of Per Hansson, Uppsala University, Sweden)

behaviour from which the lifetime of the probe is calculated. When the quencher is present, the curve displays a more complex behaviour which fits very nicely to equation (15.18). In the example shown, the aggregates are small enough so that at long periods of time the slope of the quenched curve is the same as that of the unquenched curve. This is a necessity since the intercept ($-R$ in equation (15.19)) must be correctly evaluated in order to calculate the number of micelles, M , according to $M = c_q/R$. The aggregation number is then obtained by dividing the concentration of surfactants in the micelles by the concentration of the latter.

The intra-micellar collision rate between probe and quencher depends not only on the size but also on the shape of the micelles, an effect that can also be investigated since k_q depends on N as $1/N^a$, where $a = 1$ for spherical micelles and larger for other geometries. However, a complication of interpreting k_q in terms of micellar shape is that it depends not only on the aggregate size and shape but also on the micro-viscosity of the environment for probe and quencher.

When investigating the emission spectrum from a probe in the presence of quencher and when using the steady-state fluorescence technique (SSFQ), it was argued that the method works fine for small aggregates.

www.iran-mavad.com

In particular, the quenching rate must be much faster than the lifetime of the probe without quencher. One of the main advantages of this technique is the availability of the necessary instrument, since it is standard equipment in many laboratories.

The TRFQ method is a very powerful technique for the study of closed micellar aggregates and the method has been used extensively for the study of micelles and of polymer aggregates, both with and without micelles being present. In contrast to the SSFQ method, the calculated aggregation number does not depend on the ratio between the quenching rate of the probe in the presence of quencher and the rate without any quencher present (i.e. k_q/k). However, the method suffers somewhat from being model-dependent in that the distribution between the quencher in the water and in the micelles must be known. It should be emphasized, however, that these effects are generally quite small.

Both the SSFQ and TRFQ methods are sensitive to small amounts of contaminants and every experiment performed must be carried out after first checking that traces of other fluorescing molecules are not present.

4 SMALL-ANGLE SCATTERING TECHNIQUES (SANS AND SAXS)

Small-angle neutron scattering (SANS) and small-angle X-ray scattering (SAXS) are extensively used in order to measure the size and shape of micelles in solution. The physical reason for the use of these two methods is that the scattering pattern from aggregates in solution contains information about the aggregate *form factor*, $P(q)$, and the *structure factor*, $S(q)$. In the case of monodispersed spherical aggregates, the scattering cross-section (which is what is measured in a small-angle experiment) depends on $P(q)$ and $S(q)$ according to the following relationship:

$$\frac{d\sigma(q)}{d\Omega} = n\Delta\rho^2 P(q)S(q) \quad (15.20)$$

where n is the number density of colloidal material and $\Delta\rho$ is the difference in scattering length density between the solvent and the colloid. The functional form for $P(q)$ is related to the shape of the micelles – for some common shapes often found in surfactant micelles and polymer systems, the reader is referred to ref. (26). The parameter $S(q)$ describes the interactions between aggregates in solution and is generally more difficult both to predict and to model, with the models available today often assuming a spherical shape for the aggregates.

Scattering methods, in general, use the fact that an ensemble of particles/aggregates scatter light (or neutrons, X-rays, etc.) at different angles. The angle-dependence on the scattered intensity contains information about all average correlations in the sample, i.e. concerning aggregate size and shape but also about the aggregate–aggregate interactions. As a consequence, as far as the size and shape of micelles are concerned, the interpretation of scattering data is greatly simplified if measurements can be performed in the very dilute region where the particle–particle interactions are negligible (then $S(q) = 1$). For practical reasons, this might be difficult in some situations, for example, if the *CMC* is high and/or the aggregates are charged, in which case the particle–particle interactions are acting over much longer distances than for nonionic aggregates. If the measurements can be performed in the very dilute region, equation (15.20) only depends on the form factor $P(q)$. If it is not possible to perform the experiments in the dilute region, a hard-sphere model for the particle–particle interactions is often used. In practice, both SANS and SAXS are very powerful tools for the detailed study of micellar size (distributions) and shape, and even though the structure factor can represent a problem, very detailed studies of the size and shape of colloidal aggregates are possible.

At this stage, a few words about the physical basis for scattering in SANS and SAXS might be appropriate. In SANS, neutrons are scattered by the nuclei and the amount of scattering contrast depends first on the spin quantum number, where a higher spin number gives a stronger scattering. Thus, the experimentalist can create contrast by using deuterated solvent or by deuterating the surfactant and/or the oil in a microemulsion in combination with either H_2O or D_2O . In SAXS, contrast is created by differences in electron density across the sample volume, with the larger the difference in electron density across an aggregate, then more the scattering obtained. For the study of micelle size and shape, SANS is generally more applicable and powerful than SAXS since it is possible to create contrast without changing the chemistry of the system to any great extent. For example, when dealing with small water-in-oil microemulsion drops, it is possible to study not only the size and shape of aggregates but also more detailed structural features such as the degree of oil penetration into the surfactant tail. In a recent paper (27), this was elegantly shown for a series of microemulsion drops which consisted of twin-tailed cationic surfactants, water and oil. These authors used deuterated water, oil (*n*-heptane and cyclohexane) and surfactant (deuterated in the tail), with the basic idea

www.iran-mavad.com

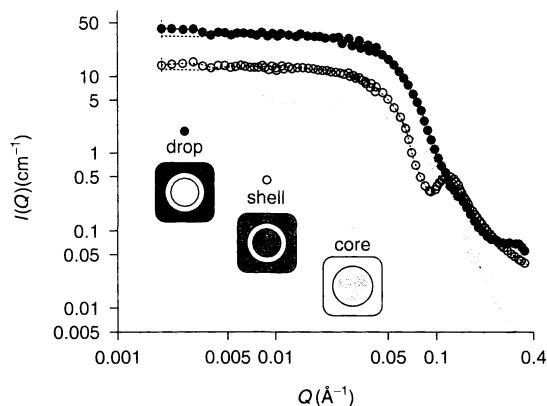


Figure 15.10. An example of the use of contrast matching in SANS experiments in order to obtain detailed information about size and shape in micelles or microemulsions. This figure is re-plotted from ref. (27) and represent the SANS results from a water-in-oil microemulsion containing C_{12} – C_{18} -dimethylammonium bromide (C_{12} – C_{18} DAB)/heptane and water. In the “drop” case, the heptane was deuterated creating contrast against the whole drop, while in the “shell” case both water and heptane were deuterated, and finally in the “core” case only the water was deuterated. By this way of contrast matching systematically, very detailed structural information may be obtained (for further details the reader is referred to ref. (27)), reproduced by permission of The Royal Society of Chemistry

of this experiment being shown in Figure 15.10. In this case, the model that best described the experimental data was that of spherical aggregates. By this way of contrast matching, very detailed information about the aggregate radius and surfactant film structure can be obtained. In addition, it is possible to obtain detailed information about polydispersity.

When analysing SANS and SAXS data there are two dominating ways which one can choose in order to obtain aggregate shape and size information, namely *model-free* and *model-fitting*. When using the model-dependent path, assumptions about the aggregate shape are made (for example, spherical, prolate, oblate, etc.) and some parameters are adjusted in the fit so as to minimize the least-square sum of the fit. With the model-free approach, no a priori assumption is made about the shape of aggregates. In the method of Glatter (28), the raw data are transformed (Indirect Fourier Transformation (IFT)) so that the pair-distance-distribution function is obtained. If the experiments are performed in the very dilute region, the size and shape of the aggregates is then given by a numerical deconvolution of the pair-distance-correlation function. The method was recently improved to include size polydispersity (29). In a recent

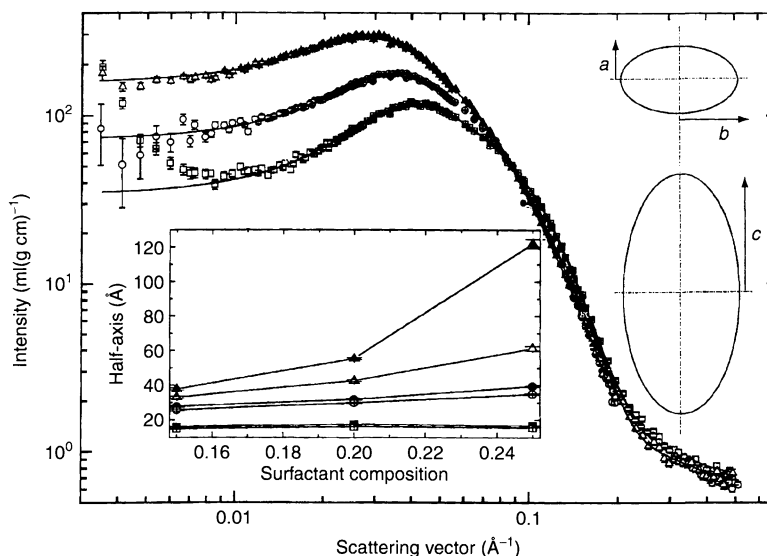


Figure 15.11. SANS data from a mixture of sodium dodecylsulfate and dodecyltrimethylammonium bromide at different mixing compositions in water, where the plots represent the fits using a model for monodisperse triaxial ellipsoids (see the right inset). The left inset shows the half-axes related to the thickness a (squares), the width b (circles) and the length c (triangles) plotted against the surfactant composition ($1 - X$) for SDS-rich micelles (open symbols) and X for DTAB-rich micelles (solid symbols) at 1.0 wt% in water (see ref. (32) for further details)

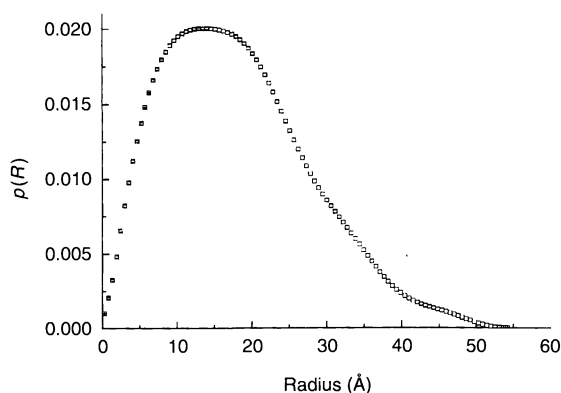


Figure 15.12. The obtained cross-section pair distribution function $p(R)$ as obtained by the indirect Fourier transformation method, where the composition of SDS/DTAB was 80:20. The results almost perfectly correlate with the results obtained by the model-dependent method illustrated in Figure 15.11. (see ref. (32) for further details)

paper by Hansen and Pedersen (30), the different methods were tested against each other. As pointed out by Pedersen in an excellent review on the analysis of small-angle scattering data (31), for a quantitative analysis the model approach should be chosen whereas the model-free method provides a qualitative approach to evaluate

the data in terms of aggregate size and shape. Pedersen also points out that the two methods complement each other very well for complex systems, as was also shown in a recent paper by Bergström and Pedersen (32) (see Figures 15.11 and 15.12). In this paper, the authors combine model-dependent and model-independent forms of evaluation when interpreting the scattering data from small aggregates with the shape of tri-axial micelles.

5 STATIC AND DYNAMIC LIGHT SCATTERING

Light Scattering (LS) performed in surfactant solutions is a very important experimental technique for the study of the size of micelles, polymers and particles. Light scattering in colloidal/micro-heterogeneous systems occurs due to differences in refractive index across the sample. The scattered intensity depends on four factors, as follows:

$$I_s(\text{sample}) - I_s(\text{solvent}) = A_{\text{instr}} \times B_{\text{angle}} \times C_{\text{opt}} \times D_{\text{conc-fluct}} \quad (15.21)$$

where A_{instr} is an instrumental constant, B_{angle} describes the angular dependence of the scattered light, and C_{opt} depends on the wavelength of the light, the refractive

index of the solution and its variation with concentration; $D_{\text{conc-fluct}}$ describes the scattering of light that originates from concentration fluctuations in the sample. When using light scattering data in the static manner, i.e. by simply measuring the excess scattering from a micellar solution as compared to the pure solvent, it is possible to calculate the aggregation number from the concentration-dependence in the excess scattered light. From the knowledge of how $D_{\text{conc-fluct}}$ depends on the variation in concentration, it is possible to show that the excess scattering, ΔR_θ , from a micellar solution depends on the micellar molar mass, M , according to the following:

$$\Delta R_\theta = \frac{C_{\text{opt}}(c - \text{CMC})}{1/M + 2B_2(c - \text{CMC})} \quad (15.22)$$

where B_2 is the second virial coefficient. Thus, when plotting $C_{\text{opt}}(c - \text{CMC})/\Delta R_\theta$ versus $(c - \text{CMC})$ a straight line is obtained with intercept $1/M$ for the micelles, from which the aggregation number is easily calculated. In addition, information about the interactions occurring is also contained in the plot since the slope gives the second virial coefficient, which is a measure of particle–particle interactions. However, for a very dilute system this term can be neglected. It should be emphasized that in the above discussion it is assumed that the micelles are small when compared to the wavelength of the light (often around 500 nm). If this is not the case, the scattering data become more difficult to interpret due to the fact that the particle form factor $P(q)$ becomes important. Then, an angular dependence of the scattered data is introduced. Independent of the shape of an aggregate, the *radius of gyration*, R_G , can be evaluated in a so-called Zimm plot by using the fact that at small angles the scattered light depends only on R_G . The radius of gyration may then be used to calculate the radius for aggregates of simple geometries (see Figure 15.13). The light scattering experiment described above for extracting information about aggregation numbers is performed in the static light scattering (SLS) mode. Light scattering can also be performed in the dynamic light scattering (DLS) mode. The main reason for carrying out this type of data collection is the fact that the scattered light contains information about the motion that aggregates undergo due to their kinetic energies. These motions cause the scattered light to depend not only on angle but also on time. Since motions introduced by the kinetic energy are random, a random variation of the scattered light with time is also obtained. Since this time-scale (or time-scales) is related to the motional processes of aggregates, information about aggregate size and shape is also contained in this time dependency of scattered light. The measured intensity as a

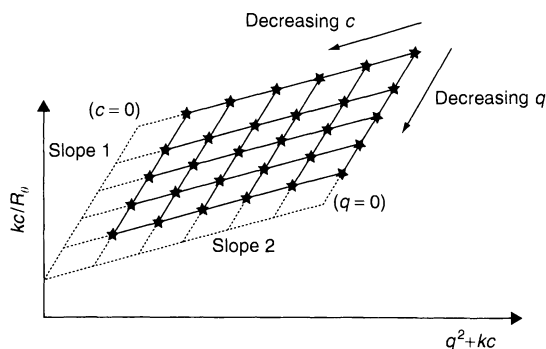


Figure 15.13. Zimm plot used to measure the radius of gyration

function of the angle (here represented by the wave vector, $s = (4\pi/\lambda) \sin(\theta/2)$) and time, i.e. $I(s, t)$, can be used to calculate (carried out in the DLS computer by a so-called correlator) the *autocorrelation* function, $C(s, t)$. This function is sometimes referred to as a *memory function* because it describes the time needed for a particle to lose track of its previous position/motion. In particular, it contains information about the rotational and/or translational diffusion constants. By normalizing the autocorrelation function with its asymptotic value, $[\bar{i}(s)]^2$, the *Siebert* relation is written as follows:

$$\frac{C(s, t)}{[\bar{i}(s)]^2} = 1 + \xi |g_1(s, t)|^2 \quad (15.23)$$

where ξ is an instrumental parameter and $g_1(s, t)$ is a function that now can be related to the diffusion constant D of a spherical aggregate by the following:

$$g_1(s, t) = \exp(-s^2 Dt) \quad (15.24)$$

The Stokes–Einstein relationship then relates the diffusion constant to the hydrodynamic radius of the spherical aggregate, according to equation (15.8).

Thus, by measuring the dynamics of the scattered light it is possible to measure the size of spherical particles in dilute solution. It is also important to mention that the effect of polydispersity can be accounted for by introducing a distribution in the diffusion constants. In this way, $g_1(s, t)$ then becomes a sum over different sizes and the way to deal with this problem is to either assume a functional form, i.e. model-dependent, cf. the discussion above on the interpretation of SANS data (one often used distribution of aggregate sizes is the log-normal distribution function), or by performing a numerical inverse Laplace transform of $g_1(s, t)$ to obtain the distribution in diffusion coefficients (33).

In briefly mentioning some of the limitations concerning direct light scattering, one can note that since micelles are small when compared to the wavelength of the light being used, dirt or other large particles will complicate the interpretation of the data obtained. In order to obtain accurate results, careful cleaning of all glassware is essential and very pure chemicals must be used. Small amounts of large particles is often revealed as a strong background scattering in the steady-state mode and a very long relaxation time in the DLS measurements.

6 REFERENCES

1. Lindmsan, B., Söderman, O. and Wennerström, H., NMR studies of surfactant systems, in *Surfactant Solutions. New Methods of Investigations*, Zana, R. (Ed.), Marcel Dekker, New York, 1987, pp. 295–358.
2. Söderman, O. and Stilbs, P., NMR studies of complex surfactant systems, *Progr. NMR Spectrosc.*, **26**, 445–482 (1994).
3. Söderman, O. and Olsson, U., Dynamics of amphiphilic systems studied using NMR relaxation and pulsed field gradient experiments, *Curr. Opinion Colloid Interface Sci.*, **2**, 131–136 (1997).
4. Halle, B., Amphiphilic liquid crystalline samples: Nuclear spin relaxation, in *Encyclopedia of Nuclear Magnetic Resonance*, Grant, D. M. and Harris, R. K. (Eds), Wiley, Chichester, 1995, pp. 790–797.
5. Halle, B. and Furó, I., NMR studies of lyotropic liquid crystals, in *Phase Transitions in Complex Fluids*, Tolédano, P. and Figueiredo Neto, A. M. (Eds), World Scientific, Singapore, 1998, pp. 81–109.
6. Callaghan, P. T., *Principles of Nuclear Magnetic Resonance Microscopy*, Oxford University Press, Oxford, UK, 1991.
7. Price, W. S., Pulsed-field gradient nuclear magnetic resonance as a tool for studying translational diffusion: Part 1. Basic theory; Part 2. Experimental aspects, *Concepts Magn. Reson.*, **9**, 299–336 (1997); **10**, 197–237 (1998).
8. Ertl, H. and Dullien, F. A. L., Self-diffusion and viscosity of some liquids as a function of temperature, *AIChE J.*, **19**, 1215–1223 (1973).
9. Mills, R., Self-diffusion in normal and heavy water in the range 1–45 degrees, *J. Phys. Chem.*, **77**, 685–690 (1973).
10. Håkansson, B., Nydén, M. and Söderman, O., The influence of polymer molecular-weight distributions on pulsed field gradient nuclear magnetic resonance self-diffusion experiments, *Colloid Polym. Sci.*, **278**, 399–405 (2000).
11. Håkansson, B., Jönsson, B., Linse, P. and Söderman, O., The influence of a nonconstant magnetic-field gradient on PFG NMR experiments. A Brownian-dynamics computer simulation study, *J. Magn. Reson.*, **124**, 343–351 (1997).
12. Hedin, N., Yu, T. Y. and Furó, I., Growth of $C_{12}E_8$ micelles with increasing temperature. A convection-compensated PGSE NMR study, *Langmuir*, **16**, 7548–7550 (2000).
13. Price, W. S., Hayamizu, K., Ide, H. and Arata, Y., Strategies for diagnosing and alleviating artifactual attenuation associated with large gradient pulses in PGSE NMR diffusion measurements, *J. Magn. Reson.*, **139**, 205–212 (1999).
14. Price, W. S. and Kuchel, P. W., Effect of nonrectangular field gradient pulses in the Stejskal and Tanner (diffusion) pulse sequence, *J. Magn. Reson.*, **94**, 133–139 (1991).
15. Furó, I. and Jóhannesson, H., Accurate anisotropic water-diffusion measurements in liquid crystals, *J. Magn. Reson.*, **A**, **199**, 15–21 (1996).
16. Jonströmer, M., Jönsson, B. and Lindman, B., Self-diffusion in nonionic surfactant–water systems, *J. Phys. Chem.*, **95**, 3293–3300 (1991).
17. Söderman, O., Jonströmer, M. and van Stam, J., Non-spherical micelles in the sodium dodecylsulphate–brine system, *J. Chem. Soc. Faraday Trans.*, **89**, 1759–1764 (1993).
18. Jönsson, B., Wennerström, H., Nilsson, P. G. and Linse, P., Self-diffusion of small molecules in colloidal systems, *Colloid Polym. Sci.*, **246**, 77–88 (1986).
19. Leaver, M., Furó, I. and Olsson, U., Micellar growth and shape change in an oil-in-water microemulsion, *Langmuir*, **11**, 1524–1529 (1995).
20. Halle, B. and Wennerström, H., Interpretation of magnetic resonance data from water nuclei in heterogeneous systems, *J. Chem. Phys.*, **75**, 1928–1943 (1981).
21. Almgren, M., Diffusion-influenced deactivation processes in the study of surfactant aggregates, *Adv. Colloid Interface Sci.*, **41**, 9–22 (1992).
22. Behera, G. B., Mishra, B. K., Behera, P. K. and Panda, M., Fluorescent probes for structural and distance effects in micelles, reversed micelles and microemulsions, *Adv. Colloid Interface Sci.*, **82**, 1–42 (1999).
23. Almgren, M., Hansson, P. and Wang, K., Distribution of surfactants in a non-ideal mixed micellar system. Effect of a surfactant quencher on the fluorescence decay of solubilized pyrene, *Langmuir*, **12**, 3855–3858 (1996).
24. Alargova, R. G., Kochijashky, I. I., Sierra, M. L. and Zana, R., Micelle aggregation numbers of surfactants in aqueous solutions: A comparison between the results from steady-state and time-resolved fluorescence quenching, *Langmuir*, **14**, 5412–5418 (1998).
25. Infelta, P. P., Grätzel, M. and Thomas, J. K., Luminescence decay of hydrophobic molecules solubilized in aqueous micellar systems. A kinetic model, *J. Phys. Chem.*, **78**, 190–195 (1974).
26. Pedersen, J. S., Analysis of small-angle scattering data from colloids and polymer solutions: modelling and least-squares fitting, *Adv. Colloid Interface. Sci.*, **70**, 171–210 (1997).
27. Bumajdad, A., Eastoe, J., Heenan, R. K., Lu, J. R., Steytler, D. C. and Egelhaaf, S., Mixing in cationic surfactant

- films studied by small-angle neutron scattering, *J. Chem. Soc. Faraday Trans.*, **94**, 2143–2150 (1998).
28. Glatter, O., The interpretation of real-space information from small-angle scattering experiments, *J. Appl. Crystallogr.*, **12**, 166–175 (1979).
29. Mittelbach, R. and Glatter, O., Direct structure analysis of small-angle scattering from polydisperse colloidal particles, *J. Appl. Crystallogr.*, **31**, 600–608 (1998).
30. Hansen, S. and Pedersen, J. S., A comparison of three different methods for analysing small-angle scattering data, *J. Appl. Crystallogr.*, **24**, 541–548 (1991).
31. Pedersen, J. S., Analysis of small-angle scattering data from micelles and microemulsions: free-form approaches and model fitting, *Curr. Opinion Colloid Interface. Sci.*, **4**, 190–196 (1999).
32. Berström, M. and Pedersen, J. S., A small-angle neutron scattering (SANS) study of tablet-shaped and ribbon-like micelles formed from mixtures of an anionic and a cationic surfactant, *J. Phys. Chem. B*, **103**, 8502–8513 (1999).
33. Horn, D., Klingler, J., Schorf, W. and Graf, K., Experimental progress in the characterization of colloidal systems, *Progr. Colloid Polym. Sci.*, **111**, 27–33 (1998).

CHAPTER 16

Identification of Lyotropic Liquid Crystalline Mesophases

Stephen T. Hyde

Australian National University, Canberra, Australia

1	Introduction: Liquid Crystals versus Crystals and Melts	299	2.1.8	Intermediate mesophases: (novel bi- and polycontinuous space partitioners)	316
2	Lyotropic Mesophases: Curvature and Types 1 and 2	301	2.2	Between order and disorder: topological defects	317
	2.1 Ordered phases	307	2.2.1	Molten mesophases: microemulsion (L_1 , L_2) and sponge (L_3) phases	318
	2.1.1 Smectics: lamellar ("neat") mesophases	307	2.3	Probing topology: swelling laws	319
	2.1.2 Gel mesophases (L_β)	307	3	A Note on Inhomogeneous Lyotropes	321
	2.1.3 Lamellar mesophases (L_α)	308	4	Molecular Dimensions Within Liquid Crystalline Mesophases	323
	2.1.4 Columnar mesophases	308	5	Acknowledgements	326
	2.1.5 Globular mesophases: discrete micellar (I_1 , I_2)	310	6	References	327
	2.1.6 Bicontinuous mesophases	310			
	2.1.7 Mesh mesophases	315			

1 INTRODUCTION: LIQUID CRYSTALS VERSUS CRYSTALS AND MELTS

Liquid crystals are a distinct phase of condensed materials, which typically form under physical conditions that lie between those giving rise to solids and melts.

In the (crystalline) solid phase, the relative locations of all atoms in the material are fixed, defining the crystal structure that can adopt a variety of symmetries commensurate with our three-dimensional (3D) Euclidean space. The crystal is *optically isotropic* if it crystallizes in a cubic space group, and anisotropic otherwise, with distinct physical features along different directions in the crystal. There is some uncertainty in atomic

positions, due to thermal motion of the atoms. However, this motion is small, and typically far less the average spacing between the atoms. (In some solids, the material forms a glass rather than a crystal, in which case the solid consists of a spatially disordered and non-crystalline arrangement of atoms, although it does exhibit short-range order, and is locally similar to a crystal.) The melt is typically freely flowing, and characterized by large fluctuations in the atomic positions, both in time and space, so that it is invariably optically isotropic. Those fluctuations imply that it is difficult to associate the atomic arrangement with a geometric structure, in contrast to crystals.

Liquid crystals share features of both a crystal and a melt, i.e. with partial order/disorder of atomic species. The ordering may be purely orientational, with no spatial

order (nematics and cholesterics), or spatial. Spatial order in liquid crystals can occur on the atomic scale (with melting of some atoms in the molecule, while the others remains frozen) or on longer length scales, such as the mesoscale ordering found in many solvent-induced liquid crystals. In the latter case, the material may exhibit no atomic ordering, so that the material is a pure melt on the atomic scale. Collective order of molecular aggregates leads to a well-defined structure on a larger length scale, typically beyond 20 Å. Like crystals, liquid crystals are sometimes optically isotropic (cubic phases), or otherwise optically anisotropic (lamellar “smectics”, hexagonal and intermediate phases). Liquid crystalline phases are called, to quote a pioneer of the field, Jacques Friedel, *mesophases*, from the Greek prefix denoting an intermediate. In addition to the clear biological and materials importance of liquid crystals, they are of fundamental importance to the issue of *disorder*. Despite its frequent use in the scientific literature, the term is a difficult one to define precisely. (For example, all melts are conventionally “disordered”, but how can one compare disordered materials at a structural level?) It is becoming clear that the notion of disorder is a “prickly” one, with the possibility of many distinct types of disorder disguised within that classification.

Many pure molecular substance form liquid crystals during the melting process. Where the chemically pure material is found to melt over a temperature range, rather than the abrupt first-order transition expected for the solid–melt phase transformation, the formation of liquid crystals within that range is certain. Such substances exhibit *thermotropic* liquid crystals, whose stability is a function of temperature. (The term is used loosely to denote the temperature-dependent phase behaviour of any liquid crystal condensate, including chemical mixtures.) A good overview of thermotropic phases is that of Seddon (1). Materials (possibly mixed) that form liquid crystals by the addition of solvents are *lyotropic* liquid crystals. Many materials exhibit both thermotropic and lyotropic liquid crystalline transitions, i.e. *mesomorphism*. Liquid crystals are typically organic molecules, ranging from polyelectrolytes (e.g. DNA, vegetable gums, etc.) to small molecules (membrane lipids, detergents, etc.), in the presence of (sometimes aromatic) hydrocarbon “oils” and water. Other solvents, including glycerol, formamide, etc., result in lyotropic mesophases in the absence of water. The hydrophobic chemical moieties are not limited to hydrocarbons: perfluorinated species – both as amphiphiles and solvents – also exhibit lyotropic liquid crystalline mesophases.

Lyotropic mesophases contain at least two chemical components: the organic molecule and its solvent. The organic moiety must exhibit some chemical complexity, or otherwise the solvent will simply dissolve the molecule, forming a structureless – and certainly not liquid crystalline – molecular solution of dispersed and disordered molecules. The simplest examples are *amphiphilic* molecules. The addition of a solvent such as water will selectively hydrate the hydrophilic moiety of each molecule, avoiding the hydrophobic regions. This “schizophrenic” relationship between the solvent and solute drives the molecules to self-assemble, thereby minimizing the exposure of hydrophobic moieties to the water. (Clearly, the argument holds in reverse if a lipophilic solvent, such as an alkane, is used. Indeed, a combination of hydrophobic and hydrophilic solvents can also lead to the formation of liquid crystalline mesophases.)

The essential phenomenon common to all liquid crystalline states is the presence of (at the bare minimum) *orientational order*. In order to characterize the generic phase behaviour of liquid crystalline systems, it is essential to acknowledge the existence of other mesophases, which are not (*stricto sensu*) liquid crystals. These include the isotropic microemulsion and sponge mesophases (and, if one ignores the somewhat academic constraint of thermodynamic equilibrium, emulsions). We include some discussion of their role in the scheme, as their physical properties also lie between those of crystals and molecular melts. They retain a central feature of lyotropes: self-assembly of the chemical moieties into multi-molecular domains, thus reducing the miscibility of one species in the other from the monomolecular miscibility characteristic of a pure melt phase. This self-assembled mesostructure is often idealized in terms of the geometry and topology of the interface(s) separating immiscible domains. From such a perspective, microemulsions and sponge mesophases are closely related to lyotropic liquid crystals, although the interfaces may themselves be devoid of any translational and/or orientational order. They are partial melts of the liquid crystalline mesophases, although not dispersed at the molecular scale.

We have introduced two distinct perspectives of the liquid crystalline state. The first views them as partially defective crystals. The second as partially self-organized melts. Such alternative understandings lead to subtly different approaches to measuring and understanding lyotropic mesophase behaviour.

The former has led to a crystallographic analysis of lyotropes. This view has been championed particularly by one of the pioneers of the field, Vittorio Luzzati.

There is a strong emphasis on the (typically small-angle X-ray or neutron) diffraction features of the mesophases, and most mesophases are conventionally distinguished on that basis. Diffraction, a Fourier-transform technique, probes the *geometric correlations* within the material. Detailed models of the idealized mesostructure can therefore be constructed. For this reason, mesophase structure is dominated by such an approach.

The latter is less developed, but, in this author's opinion, equally important, certainly in an applied or industrial context. It implies the investigation of X-ray or neutron *scattering*, rather than *diffraction* (if the reader will allow some momentary pedantry). Furthermore, an explicit focus on the "molten" allows for the possibility of mesostructural determination in terms of, most importantly, the *topology* of the mesophase, e.g. the domain connectivity and possible "knottedness" of discrete domains. The practical surface scientist may or may not need to know whether the chemical mixture under investigation is liquid crystalline, with translational ordering (i.e. crystallinity) on the mesostructural scale. However, more importantly, a scientist needs to know the topology of the micro-domains within that mixture, as domain topology determines the macroscopic material behaviour of the mixture (such as fluidity, turbidity, etc.) as much as the presence or absence of translational ordering. Thus, for example, bicontinuous cubic mesophases share a sponge-like topology with the sponge mesophases. They also share similar viscosity and diffusion characteristics; the former are liquid crystals, while the latter are not.

Here I will describe first lyotropic liquid crystallinity from the more conventional crystallographic approach, with some discussion of other techniques, including calorimetry, NMR spectroscopy and optical microscopy. Following that, an analysis of topological probes of mesostructure will be given.

Features of liquid crystallinity (both lyo- and thermotropic) are also to be found in exclusively inorganic systems. For example, metal carbonates can be crystallized in gels to form dense μm -sized aggregates of many crystallites that are themselves orientationally ordered, and devoid of any translational ordering. So, while the material is (micro)crystalline, its mesostructure on the μm scale deserves to be recognized as liquid crystalline.

The possibility of liquid crystallinity in hybrid organic–inorganic systems is a fascinating area that still awaits study. Investigations in this area are of interest to both the fundamental scientist and to those concerned with synthesis of novel materials. The remarkable diversity of biominerals being revealed currently makes it

likely that such hybrid inorganic/organic liquid crystals are already synthesised *in vivo*.

2 LYOTROPIC MESOPHASES: CURVATURE AND TYPES 1 AND 2

A brief catalogue of currently known and labelled lyotropic mesophases follows. For the reasons outlined above, we will focus first on those mesophases that are spatially ordered and lead to Bragg diffraction (sometimes in an approximate sense, with rather diffuse diffraction "spots").

The coarsest topological feature of any molecular assembly consisting of (at least) two immiscible domains – A and B, say¹ – is that of the domain curvatures. For A–B assemblies, two gross morphologies are possible: A-in-B or B-in-A. (For example, hydrophobic micelles dispersed in water, or water droplets dispersed in a hydrocarbon continuum.) A more precise description of the domain morphology comes from the *curvatures* of the interface(s) separating immiscible domain(s), and lying at the boundaries of A and B. Curvature of the interface towards the A domain implies an A-in-B morphology, and vice versa (Figure 16.1).

However, a two-dimensional (2D) interface separating three-dimensional (3D) domains has *two* independent curvatures, which can be either concave or convex. The product of those curvatures determines the intrinsic geometry: both convex (or concave) leads to an elliptic "cap", one vanishing curvature gives a planar, cylindrical or conical parabolic sheet, and opposite curvatures to a saddle-shaped hyperbolic surface (Figure 16.2).

The average value of the surface curvatures is one useful measure of the morphology (the "mean curvature", H). If the mean curvature of the interface is convex when viewed from A, the structure is of type

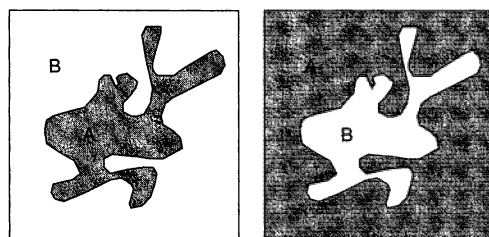


Figure 16.1. Two-dimensional 'A-in-B' (left) and 'B-in-A' (right) morphologies

¹ A = water plus polar fractions of a surfactant and B = hydrocarbon fractions.

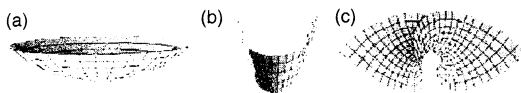


Figure 16.2. Different types of interfacial curvatures (surface patches): (a) elliptic; (b) parabolic; (c) hyperbolic

A-in-B. This concept is consistent with the following convention in the surfactant literature, due to Per Ekwall: a “Type 1” mesostructure is oil-in-water, while “Type 2” refers to the water-in-oil morphology.

Other more complex morphologies also arise for A–B mixtures. In particular, domains A and B may “enclose” each other, forming entangled networks, separated by a hyperbolic interface. Those cases include “mesh”, bicontinuous microemulsions, bicontinuous cubic phases and their disordered counterparts, “sponge” phases, which are discussed below. In these cases too, the sign (convex/concave) of the interfacial mean curvature sets the “Type”. A representation of the disordered mesostructure in a Type 2 bicontinuous microemulsion is shown in Figure 16.3. A hyperbolic interface may be equally concave and convex (a *minimal surface*, e.g. see Figure 16.2(c)) so that the mesophase is neither Type 1 nor Type 2. Lamellar mesophases (“smectics” or “neat” phases) are the simplest examples. Bicontinuous “balanced” microemulsions, with equal polar and apolar volume fractions are further examples.

To infer whether a model structure is Type 1 or 2, one can determine the variation in cross-sectional area

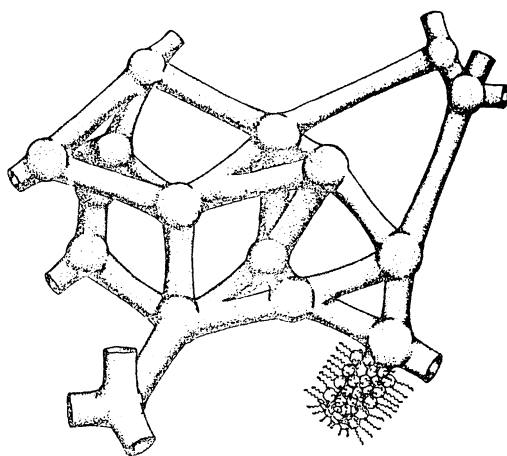


Figure 16.3. Representation of a bicontinuous microemulsion, containing interwoven oil and water networks, separated by a hyperbolic amphiphilic monolayer. In this case, the structure is Type 2, and (slightly) more curved towards the interior polar region than the apolar chain region

on moving from hydrophobic to aqueous domains: if this area increases/decreases, the mesostructure is of Type 1/2. Experimental determination is more uncertain, and dependent on the likely interfacial membrane topology. For example, electrical conductivity measurements, or NMR self-diffusion data (polar or apolar) will distinguish discrete micelles in a water continuum (Type 1) from water droplets in an “oil” continuum (Type 2).

How does one decide whether a mesophase formed in the test-tube is Type 1 or 2? First, it is useful to determine the optical isotropy of the mesophase. This can be done by observing whether the sample rotates the plane of polarization of polarized light. If crossed polars – which do not normally transmit light – do allow some transmission when the sample is placed between the polarizers, the sample is anisotropic. This implies (i) it is liquid crystalline and (ii) the mesostructural symmetry belongs to a non-cubic space group. Further investigation of “optical textures” in a polarizing optical microscope is useful, as, for example, lamellar mesophases can often be distinguished from hexagonal ones in this manner (both are anisotropic). A host of information on mesomorphism in lyotropic systems has been collected by Gordon Tiddy using only optical textures, following the “flooding” technique developed by Lawrence: the lyotropic phase diagram is laid out by introducing a drop of solvent to one end, and then observing the sequence of textures formed as the solvent “wicks” thorough the sample. Optical textures do vary between different lyotropes, even if they are in the same mesophase, so that data may be uninformative (2). However, some familiarity with possible textures is very useful as a preliminary identifier of mesophase behaviour. A collection of textures are gathered together at the end of this review (see Figure 16.35).

In the simplest cases, electrical conductivity, or NMR diffusion measurements, may allow determination of the continuity of polar or apolar domains. If the polar domain is continuous, and the sample is electrically conducting, it is either a Type 1 mesophase (of any description), or a bicontinuous cubic, or microemulsion Type 2 mesophase. If the membrane is made up of amphiphiles whose molecular architecture is straightforward (e.g. straight-chain surfactants), the shape of the amphiphilic molecule itself can be estimated, thus giving the variation in cross-sectional area along the molecule. If the hydrophobic oily chains of the amphiphile are bulky, and the polar head-group smaller, the aggregate is likely to be of Type 2 and vice versa. Thus, single-chained ionic surfactants form Type 1 mesophases in general, while double-chained surfactants form Type 2 mesophases.

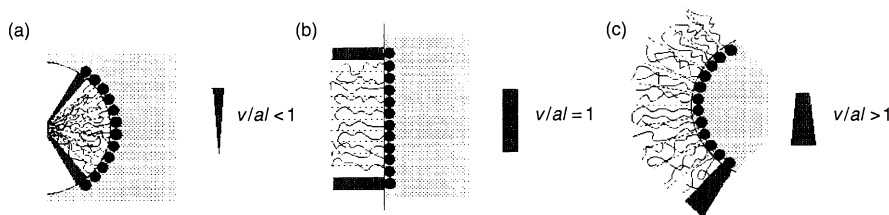


Figure 16.4. Molecular shape and aggregate morphology: (a) Type 1, (b) lamellar and (c) Type 2 mesophases (small circles denote head-groups, and shaded domains polar solvent)

Such an intuition has been developed in some detail, and has led to a useful understanding of the generic sequence of mesophases expected on water dilution for Types 1 and 2 systems. A single dimensionless “shape parameter” turns out to be an extremely useful measure of aggregation morphology (Type 1 or 2) and topology. This parameter can often be crudely estimated from the molecular dimensions. It is defined in terms of the area per surfactant molecule at the head-group/chain interface, a , the chain length of the molecule in its molten state, l , and the chain volume, v , as follows:

$$s \equiv \frac{v}{al} \quad (16.1)$$

The magnitude of this parameter can be estimated for simple hydrocarbon amphiphiles from molecular dimensions, by using Tanford’s formulae (3). For each (linear) chain, volume and lengths are given by the following approximate relationships:

$$v = (27.4 + 26.9n) \text{ \AA}^3 \quad (16.2)$$

$$l_{\text{crystal}} = (1.5 + 1.26) \text{ \AA} \quad (16.3)$$

and the length of the molten hydrocarbon chain is approximately 80% of the fully extended (l_{crystal}) value (3). The magnitude of the head-group area depends on the amphiphile, as well as the degree of hydration and temperature. As a general rule, it increases with hydration (4), and (less so) with temperature. Note that we locate the interface at the location in the amphiphile separating polar from apolar (paraffin) domains, rather than at the water–head-group interface. As a crude estimate, the area per linear hydrocarbon chain in liquid crystalline systems is between 30–35 \AA^2 . The area per head-group in charged amphiphiles may be delicately tuned by the counterion, and the electrolyte concentration of the polar solvent. Specific-ion effects can dramatically affect counterion binding to head-groups. Strong binding neutralizes the electrostatic repulsion between adjacent head-groups, thereby reducing the head-group

area. Similarly, increased salt in the solvent screens interactions, also reducing the area.

If s exceeds 1, the mesophase is likely to be Type 2, and Type 1 otherwise. (Bicontinuous microemulsions are the single exception to that otherwise robust rule.) (see Figure 16.4).

The shape parameter defines the volume scaling for a fixed area as a function of the chain length, and characterizes an average “block shape” for the amphiphiles in the aggregate. For example, this shape is a cone in a Type 1 spherical micelle (Figure 16.5), whose volume (v) scales as 1/3 the area of the base (a) multiplied by its height (l).

The connection between molecular shape and interfacial curvature evident from Figure 16.4 is expressed by the following equation that relates the shape parameter to the membrane curvatures (Gaussian curvature, K , and mean curvature, H) and monolayer thickness, l :

$$s = 1 + Hl + \frac{Kl^2}{3} \quad (16.4)$$

This equation provides a useful link between the chemical reality of amphiphilic aggregates and the mathematically convenient fiction of an smooth, infinitely thin partitioning surface that separates polar from apolar

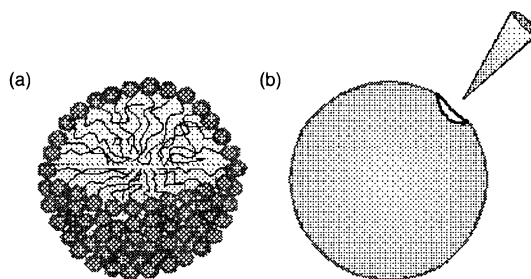


Figure 16.5. (a) Representation of a spherical micelle; the micelle can be built up of identical conical blocks (b), which define the shape of the constituent amphiphiles making up the aggregate

domains. The exploration of possible mesophases can be mapped then to investigations of surface geometry and topology in 3D space. For example, straightforward geometry tell us that the smallest possible value of s – averaged over a super-molecular aggregate – is $1/3$, which is realized for Type 1 spherical micelles, while $s = 1/2$ defines Type 1 cylinders (e.g. hexagonal phase, H_1). In other words, the aspect ratio (and length) of discrete micelles increases continuously as s varies between $1/3$ and $1/2$ (ellipsoidal micelles are discussed in more detail at the end of this article). The link between surfaces and amphiphilic aggregates allows an idealized catalogue of simple aggregate shapes to be drawn up, based on the variety of 2D surface forms (realized as the curvatures, H and K , vary). Consider a small patch of a surface: this can have positive, zero or negative K , cf. Figure 16.2.

Identification of a particular mesostructure requires knowledge of the global structure of the membrane, as well as the local curvatures of a typical membrane element. The patch can be extended to remove all edges to give an infinite variety of shapes. A coarse measure of the shape can be provided by surface topology. From the topological perspective, (edge-free) shapes are distinguished from each other not by their local curvatures, but by their connectivity, i.e. the number of channels or handles in the surface, known as the surface *genus* (Figure 16.6).

Most shapes (of any genus) have dramatically varying curvatures from point to point. Those forms are, for now, excluded, partly for convenience, but also on good chemical grounds. We will mention them later. Given the coupling between molecular shape and

curvatures (equation (16.4)), an *inhomogeneous* membrane with large curvature variations is less likely to form under usual conditions than a more *homogeneous* candidate, unless the membrane itself is chemically very polydisperse. Thus, the self-assemblies of simple amphiphile–solvent systems are likely to be reasonably homogeneous space partitions, and this expectation is confirmed by studies of lyotropic liquid crystalline systems.

Assume, for now, that the surface curvatures are close to constant. We describe the surface curvatures by their averages, determined over the surface area (area element da), as follows:

$$\langle H \rangle \equiv \frac{\iint_{\text{surface}} H da}{\iint_{\text{surface}} da} = \frac{\iint_{\text{surface}} H da}{A}$$

$$\text{and } \langle K \rangle \equiv \frac{\iint_{\text{surface}} K da}{\iint_{\text{surface}} da} = \frac{\iint_{\text{surface}} K da}{A} \quad (16.5)$$

where A denotes the surface area.

This simplification allows one to draw up a useful catalogue, involving both local shape (curvatures) and global topology. There is an intimate connection between local and global form under these conditions, provided by the Gauss–Bonnet theorem of surface geometry, which relates the surface genus, g , to its integral (Gaussian) curvature, as follows:

$$\iint_{\text{surface}} K da = 4\pi(1 - g)$$

or, from equation (16.5)

$$\langle K \rangle = \frac{4\pi(1 - g)}{A} \quad (16.6)$$

Thus, surfaces of genus zero have (on average) a positive Gaussian curvature, K . The single homogeneous genus zero case is the sphere. Ellipsoids – also genus zero – are less homogeneous. We call zero genus structures “globules”. Similarly, the sole unit genus homogeneous (and edge-free) shape is the cylinder. Less homogeneous examples – with, for example, radius variations along their length – are also “rods”. Higher genus structures (pretzels, etc.) are inevitably inhomogeneous. They can be spatially ordered, as in lyotropic liquid crystalline mesophases, or disordered, relevant to the

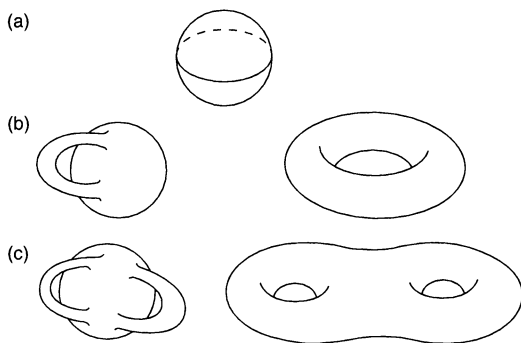


Figure 16.6. A short catalogue of edge-free surface shapes, classified by their genus: (a) genus zero, (b) two examples of genus one surfaces, and (c) two examples of genus two surfaces. Adding extra handles (or donut channels) increases the genus, and arbitrarily high genus surfaces are realizable

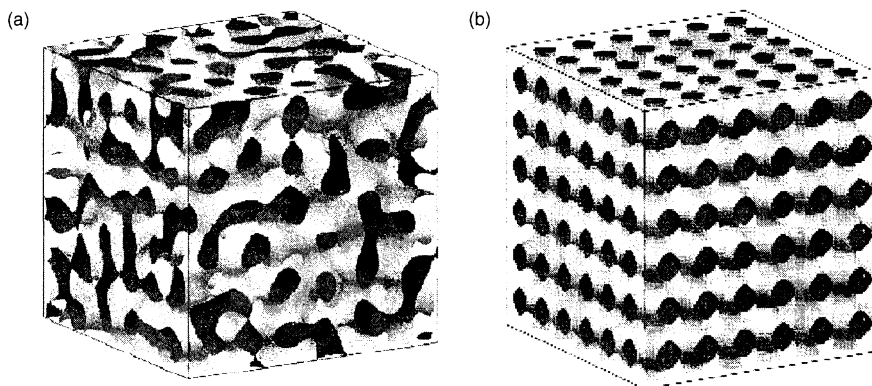


Figure 16.7. (a) Fragment of a disordered sponge, and (b) an ordered sponge with the “P” surface morphology

noncrystalline “sponge” phase (Figure 16.7). Both structures – if extended endlessly in all directions – have infinite genus.

The most homogeneous high genus cases, in fact, have infinite genus, and form crystalline surfaces, with 2D or 3D unit cells. In these cases, it is convenient to classify them according to their surface genus per unit cell. This calculation gives the genus of an imaginary surface formed by “gluing” bounding faces of the unit cell separated by a lattice vector. So, for example, a unit cell of the infinite, three-periodic minimal surface ($H = 0$) P-surface structure has genus equal to three. In practice, the genus of these structures increases as the channels within a unit cell becomes more numerous.

Among infinite-genus surfaces, two distinct morphologies are known, i.e. “meshes” and “sponges”, with 2D and 3D lattices, respectively. The genus of a mesh (per unit cell) is at least two, while that of a sponge at least three. There is a subtle distinction between the genus of sponges defined in terms of its surface geometry, and that measured experimentally, the *crystallographic genus*, γ . Unfortunately, we need to retain both notions of genus, as the surface genus, g , is a useful indicator of the surface homogeneity, while the crystallographic genus, γ , is the parameter that can be determined in the laboratory. This difference is due to the mathematical requirement that the surface be “oriented”, so that the top and bottom faces are distinct. Membranes composed of amphiphiles may, in fact, have identical top and bottom faces – as in a symmetric bilayer. In this case, γ may differ from g , and is dependent on the choice of unit cell.

A preliminary catalogue of aggregate shape can be drawn upon this basis: we include all “quasi-homogeneous” forms of genus zero, one, two, three, etc., corresponding to globules, rods, meshes, sponges

and sheets. We can go a little further already, since the local shape (which is set by the architecture of the amphiphilic molecules, s) – under the assumption of homogeneity – sets also the surface-to-volume ratio of the global structure. Given a fixed head-group area of the amphiphile, and fixed molecular volumes, the surface-to-volume ratio can be recast in terms of the polar/apolar volume fraction of the lyotrope, i.e. its concentration. A detailed discussion of this approach can be found elsewhere (5). These calculations allow a simple “phase diagram” to be drawn, which relates molecular shape to composition, assuming homogeneity. Such a diagram is reproduced in Figure 16.8, using formulae listed in Table 16.2 at the end of this article.

The calculations plotted in Figure 16.8 assume homogeneity, with constant curvatures and polar/apolar layer thicknesses throughout the structure. The exact equations are listed in Table 16.2, at the end of the text. Such an assumption is a mathematically convenient one, but it turns out to also be a useful one for the simplest lyotropic amphiphile–solvent(s) mixtures. Their simplicity is explicitly chemical: for example, a binary amphiphile–water system with a monodisperse molecular distribution of amphiphiles will self-organize into a quasi-homogeneous (constant s) amphiphilic bilayer arrangement, so that the constituent molecules can attain (as far as the global extension of the membrane is geometrically possible) their single-valued preferred molecular shape, s .

A profound feature of 3D Euclidean space – the space of chemistry in the real world – is that homogeneity can rarely be achieved, due to the shape of our space itself. In most cases, it is impossible to extend a homogeneous local form globally without the introduction of some inhomogeneities – this is an example of “frustration”, a concept useful to many branches of condensed

www.iran-mavad.com

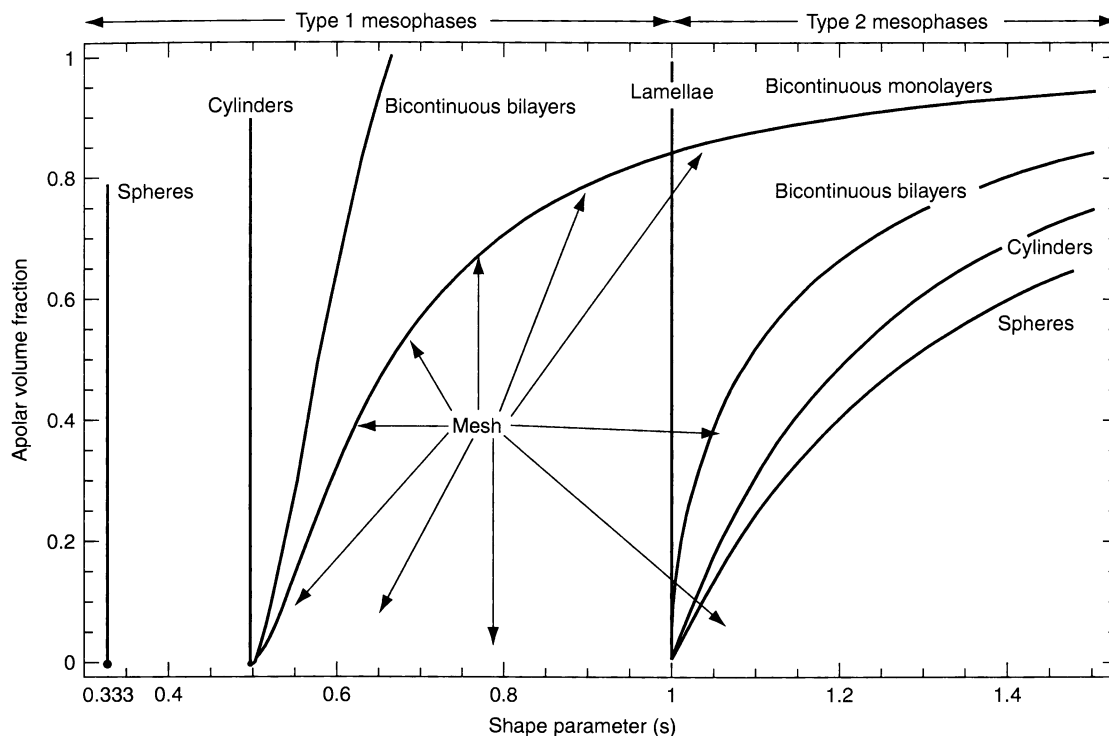


Figure 16.8. Generic “phase diagram” of lyotropic systems. This diagram relates the molecular shape to the apolar volume fraction. For Type 1 phases, the inner volume is composed of hydrophobic material, while for Type 2 phases it contains the polar solvent plus head-groups. The diagram includes all (idealized) homogeneous realizations of aggregate topologies: Types 1 and 2 globules (spherical micelles, e.g. discrete cubic phases), rods (cylindrical micelles, e.g. hexagonal phases), meshes (tetragonal and rhombohedral) whose upper bound on volume fraction is defined by the bicontinuous monolayer curve (relevant to bicontinuous microemulsions), sponges (bicontinuous bilayers, e.g. bicontinuous cubic phases), and lamellae. There are some deviations from the curves due to the quasi-homogeneous nature of many phases (cf. Figures 16.15 and 16.19)

matter physics. *With the exception of planar, smectic lamellar phases, all well-characterized liquid crystalline mesophases are quasi-homogeneous realizations of homogeneous morphologies, i.e. sponges, meshes, rods and globules.*

In many cases of simple lyotropic systems – typically two-component amphiphile–solvent systems with a monodisperse distribution of amphiphiles (and therefore a single preferred shape parameter) – the symmetry and topology of the observed liquid crystalline mesophase is that which is least frustrated, i.e. the most nearly homogeneous. Indeed, the origin of ordered symmetric mesophases – lyotropic liquid crystals no less – can be ascribed to this frustration. The least frustrated packings of spheres, rods, meshes and sponges correspond to cubic and hexagonal discrete micellar, hexagonal, rhombohedral and tetragonal and bicontinuous cubic mesophases, respectively. Those cases the the most frequently encountered mesophases (along with lamellar

phases), and they are relevant to the simpler lyotropic systems.

In many real cases, the lyotropic system is more complex, and may include more than one type of amphiphile, cosurfactants, polar and apolar solvents, etc. By selective partitioning of molecular species within the structure, less homogeneous forms can result; these systems are more able to relieve spatial frustration. In many cases, entropically favoured mesostructures without long-range order may form. However, more exotic liquid crystalline phases may also result. These include intermediate phases. Their structures remain largely speculative. We will canvass some possibilities later in this chapter. First, we will deal with simpler, “classical” cases, that are, we repeat, relevant above all to simpler lyotropic systems. We will then discuss disordered mesophases, to bring out their common features to ordered systems. Finally, we will discuss possible, as yet unknown, mesostructures, and offer

some suggestions how to decipher membrane topology and geometry, with simple “swelling analyses” and X-ray (or neutron) scattering data.

2.1 Ordered phases

The clearest evidence of polymorphism in lyotropic liquid crystals lies in X-ray or neutron diffraction data. One of the most spectacular findings in the early days of lipid polymorphism was the realization (by Luzzati) that hydrocarbons chains in liquid crystal mesophases are *almost* always molten, and conformationally similar to liquid hydrocarbons. A clear X-ray signature is the presence of a diffuse scattering peak around 4.5\AA^{-1} , characteristic of the in-plane spacing between adjacent molten chains. That means that a simple rule of thumb can be used to estimate the (straight) chain length, l , in an amphiphilic mesophase: about 80% of the fully extended all-*trans* conformation (cf. equation (16.3)). As the temperature is increased, the chain length, l , *decreases* due to enhanced thermal access to *cis* configurations, in common with longer polymer molecules. (This decrease implies an *increase* in the shape parameter, s , with temperature, driving thermotropic phase changes (mesomorphism) in amphiphilic liquid crystals.)

In general, conventional wide angle ($2\theta > 5^\circ$) X-ray data contains little information, with the exception of the diffuse chain packing band mentioned in the previous paragraph. Thus, most experimental scattering data are collected in the small-angle regime, characteristic of longer meso-scale spacings in the structure. Occasionally, however, some discrete Bragg peaks are also seen in mesophases. These are sometimes due to remnant crystallinity, either within the chains, or confined to the packing of the head-groups. These cases are exclusively lamellar mesophases, and are described next.

2.1.1 Smectics: lamellar (“neat”) mesophases

Lamellar mesophases are the most commonly encountered mesophases, ubiquitous in double- and higher-chained amphiphiles (including virtually all concentrated lipid–water systems). Their *ideal* mesostructure consists of planar, parallel stacks of amphiphilic bilayers, forming a 1D “smectic” lattice (Figure 16.9).

Lamellar phases are identified by the typical signature of a smectic lattice: equally spaced peaks, corresponding to α , 2α , 3α , etc., where α is the spacing between adjacent bilayers.

Evidently, such an idealization need not be found in practice. Entropically driven fluctuations of the bilayers can bend them beyond planarity, and punctures and channels between bilayers may occur. Conventionally, one calls a mesophase “lamellar” when it is (i) optically anisotropic, and (ii) exhibits a smectic diffraction pattern. In some systems, more than one distinct lamellar mesophase is found.

2.1.2 Gel mesophases (L_β)

Gel mesophases are occasionally found under condition intermediate to those resulting in the crystalline state and the more fluid mesophases, particularly where the crystal structure itself consists of parallel stacks of bilayers. They are characterized by a crystalline packing of the chains of the amphiphile, evidenced by sharp Bragg diffraction peaks in the wide-angle X-ray scattering regime (typically $4.1\text{--}4.2\text{\AA}^{-1}$), in place of the usual diffuse 4.5\AA^{-1} band. This partial crystallinity induces long-range ordering between lamellae, thus resulting in many small-angle diffraction peaks in the ratio 1:2:3:4, etc. A range of gel mesophases are found in dry “lyotropes” (formally thermotropes), as shown in Figure 16.10. A fuller account of possible gel

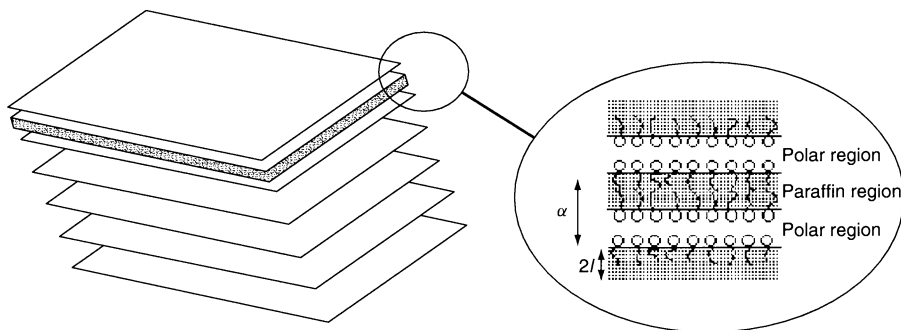


Figure 16.9. Idealized structure of a lamellar mesophase

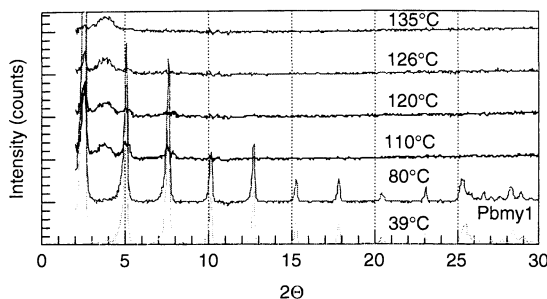


Figure 16.10. Typical scattering spectrum of a lamellar “gel” L_β mesophase as a function of temperature, showing gradual melting, with the formation of an intermediate (hexagonal) phase at ca. 110°C (courtesy of R. Corkery)

smectics can be found in the literature on thermotropic systems (1).

A noteworthy feature of gel phases is the occasional expression of the molecular chirality, typically about an atom that bridges the chains and head-group, particularly common to lipids. “Twisted ribbons”, with remarkably regular corkscrew-like structures, have been seen in electron microscopic images (5).

2.1.3 Lamellar mesophases (L_α)

The α subscript used here refers to the molten chains in this mesophase. Thus, L_α X-ray (or neutron) spectra are characterized by scattering peaks in the ratio 1:2:3, etc., characteristic of the inter bilayer spacing (broader, and fewer than seen in typical L_β mesophases), and a diffuse 4.5 \AA^{-1} scattering band. They are of intermediate, though very variable, viscosity to the more freely flowing micellar mesophases and stiffer bicontinuous mesophases (and often comparable to hexagonal mesophases in their viscosity). Like all anisotropic phases, lamellar mesophases exhibit distinct optical textures, when confined in thin slabs between crossed polarizers and viewed through an optical microscope (sometimes enhanced by the insertion of a quarter-wave plate). Typically, the texture is “streaky” or mosaic-like and (to quote the late Krister Fontell) resembles the marbling in freshly cut steak. Alternatively, lamellae can eradicate all edges by folding into vesicles – essentially spherical globules. These are typically multiwalled (liposomes), exhibiting characteristic “Maltese cross” textures in the optical microscope. (Single-walled (sometimes giant) vesicles are also found; these are not lamellar mesostructures.) Freeze-fracture microscopy will often allow identification of these forms. Unusual spiral textures have also been

found in L_α mesophases of lyotropes that also exhibit L_β phases (6).

The formation of lamellar mesophases is almost unavoidable in the majority of amphiphile–water systems. Double-chain surfactants typically form lamellar phases on water dilution, and single-chain detergents form a lamellar mesostructure under more concentrated conditions. However, the distinction between smectic ordering (a 1D lattice) and a lamellar membrane topology must be acknowledged. As will be explored in more detail later, the formation of disconnected, puncture-free sheets is *not* the inevitable consequence of a smectic mesophase with a 1:2:3, etc. scattering pattern. Any topology that is geometrically ordered along a single axis, with smectic ordering, will produce a 1:2:3, etc. pattern (superimposed on more or less significant amounts of diffuse “background” scattering). It follows then that if one is after a convenient classification of a mesophase, “lamellar phases” are well characterized. On the other hand, if the true mesostructure – the membrane connectivity as well as stacking – is of interest, such a convenience disguises a potential multitude of distinct structures.

2.1.4 Columnar mesophases

Hexagonal (“middle”) mesophases (H_1, H_2)

This anisotropic phase is of intermediate viscosity to discrete micellar and bicontinuous cubic phases. The standard picture of a hexagonal mesophase consists of a dense packing of cylindrical micelles, arranged on a 2D hexagonal lattice. It is often identified by a characteristic “fan” texture in the optical microscope, due to focal conic domains of columns. This mesophase is the archetypal “columnar” (rod) lyotropic mesophase.

In contrast to lamellar phases, which are equally curved towards both sides, hexagonal phases come in two “flavours”, i.e. Types 1 ($H_1, s = 1/2$) and 2 ($H_2, s > 1$), cf. Figures 16.8 and 16.11. In all cases, X-ray scattering has revealed that the chains are molten, and the small-angle spectrum contains an number of Bragg peaks in the ratio $1:\sqrt{3}:\sqrt{4}$, etc. (Figure 16.12) corresponding to allowed reflections from the 2D $p6mm$ hexagonal symmetry group (cf. Table 16.1, at the end of this article).

It is useful to consider this mesostructure as a packing of monolayer surfaces, or as bilayers. The monolayer picture has it that the aggregates consist of cylindrical, infinitely long micelles. The bilayer picture is less familiar, consisting of a hexagonal honeycomb, with a 2D hexagonal lattice of line singularities, the junctions

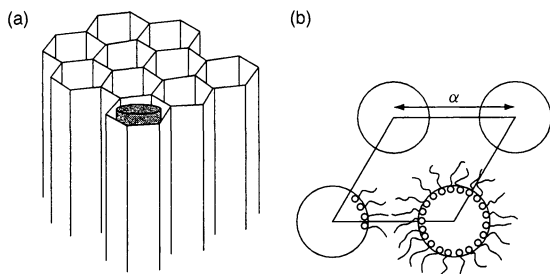


Figure 16.11. Idealized mesostructure of a (p6mm) hexagonal phase: (a) a hexagonal packing of infinite cylindrical micelles, with line singularities in the bilayer running along the prism edges; (b) top view of a Type 2 hexagonal mesophase (H_2), showing a single 2D unit cell (lattice parameter, α)

of three bilayers (so that the monolayers display a hexagonal cross-section).

Ribbon mesophases

From the earliest days of X-ray scattering studies (e.g. Luzzati and co-workers), there have been reports of variations on the hexagonal mesostructure. Many modifications are not seen regularly, although some distinct packings of parallel deformed rods are. The (anisotropic) optical textures of ribbon mesophases vary, sometimes resembling the fan texture of hexagonal mesophases, and sometimes not.

Other parallel elliptical cylinder packings have been proposed repeatedly, with 2D rectangular symmetries, cmm., pmm, p2 and pgg. The most recent detailed study has supported most strongly the centred (cmm) mesophase, although others may also exist (7). The polar-apolar (monolayer) structures are illustrated in Figure 16.13.

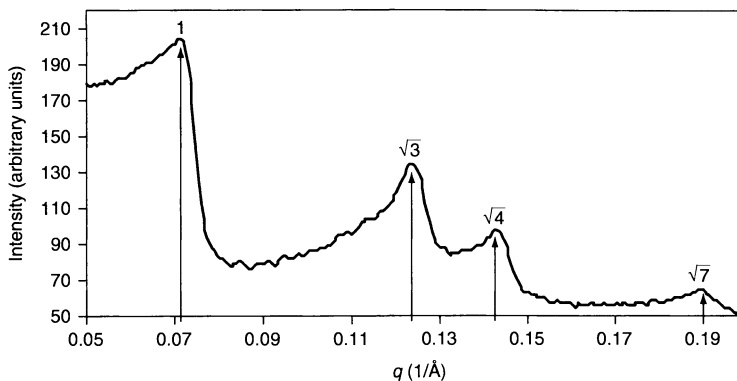


Figure 16.12. Small-angle X-ray scattering pattern from a hexagonal phase, with four diffuse peaks (wide-angle diffuse band not shown)

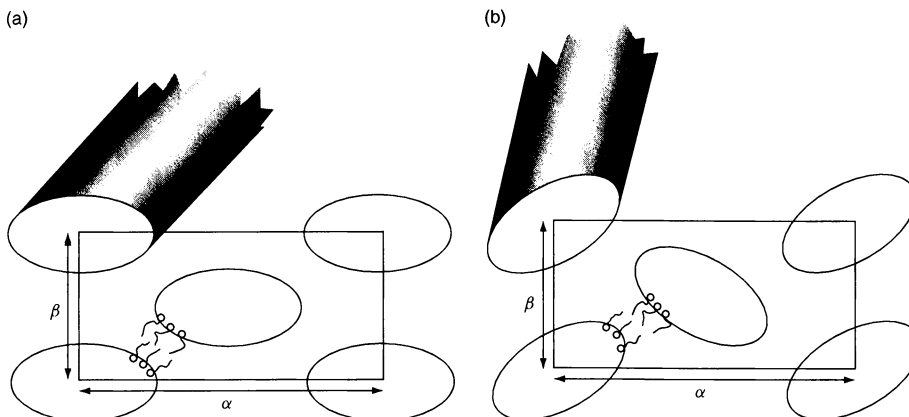


Figure 16.13. Idealized mesostructures of (Type 2) ribbon mesophases: (a) centred (cmm) phase; (b) primitive (pgg) phase

www.iran-mavad.com

Note that these phases are more frustrated, and less homogeneous, than the standard hexagonal columnar mesophase, and so we expect them to be found predominantly in multi-component systems. Much work remains to be done to positively identify these mesostructures, which to date have been proposed largely on the basis of their scattering patterns.

2.1.5 Globular mesophases: discrete micellar (I_1 , I_2)

Since the pioneering work of the New Zealander G. W. Hartley in the 1930s, globular micelles have been the archetypal amphiphilic aggregate. It is now clear that these micelles sometimes arrange themselves on 3D lattices. These mesophases are more less freely flowing, and less viscous than lamellar or columnar mesophases, due to their discrete globular micellar structure. Evidently, all discrete cubic mesophases are optically isotropic, and no texture is visible. Such “discrete micellar” mesophases are frequently seen in aggregates containing single- and double-chained amphiphiles (Types 1 and 2, with apolar and polar domains within the micelles, respectively).

The most usual form is the body-centred cubic (bcc) array of identical micelles, with the 3D space group $\text{Im}\bar{3}\text{m}$. Recently, other cubic sphere packings have been seen, including the face-centred cubic (fcc, $\text{Fm}\bar{3}\text{m}$), clathrate (Type I, $\text{Pm}\bar{3}\text{n}$) and the Type 2 clathrate packing (identical to the melanophlogite silicate network) ($\text{Fd}\bar{3}\text{m}$) (8). Two examples of these mesostructures

are illustrated in Figure 16.14. Note that the bilayers form closed-cell foam-like structures, with singular lines (along which three bilayers meet, as in hexagonal phases) and singular points (where the singular lines intersect).

The presence of a hexagonally close-packed (hcp) micellar mesophase (space group $\text{P6}/\text{mmc}$) has also been conclusively established recently in a non-ionic polyoxyethylene surfactant–water system (9). This possibility is not unexpected, given the homogeneity of the hcp arrangement.

All discrete micellar mesophases of the same Type have very similar shape parameters: s is equal to $1/3$ for Type 1, and exceeds unity for Type 2 examples. The local/global relation for Type 2 mesophases depends on the packing. The “phase diagram” (Figure 16.8) is derived for assumed ideally homogeneous global forms. Deviations from this form result from the quasi-homogeneous 3D Euclidean crystalline packings in I_2 mesophases. The detailed differences are plotted in Figure 16.15 (using formulae displayed in Tables 16.2 and 16.3 (see later), where the chain volume fraction refers to the total apolar fraction (including apolar solvent). These suggest the following sequence of discrete micellar mesophases on dehydration for Type 2 systems: $\text{Fm}\bar{3}\text{m}$ or $\text{P6}_3/\text{mmc}$, $\text{Fd}\bar{3}\text{m}$, $\text{Im}\bar{3}\text{m}$, $\text{Pm}\bar{3}\text{n}$.

2.1.6 Bicontinuous mesophases

These mesophases exhibit the most complex spatial organization of all known lyotropic liquid crystals.

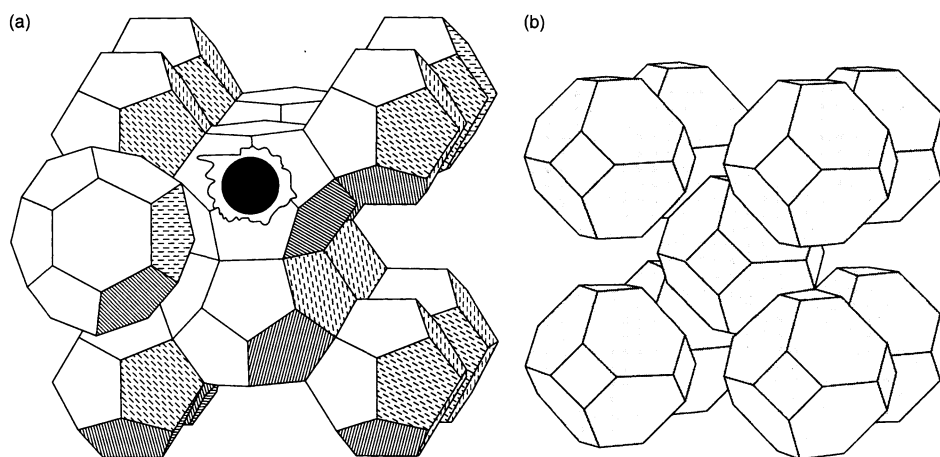


Figure 16.14. (a) Idealized mesostructure of one known discrete cubic (“I”) mesophase (space group symmetry $\text{Pm}\bar{3}\text{n}$, with a single water/chain filled micelle shown, corresponding to (I_2/I_1) mesophases). (b) Exploded view of foam cells (bilayer walls) in the $\text{Im}\bar{3}\text{m}$ mesophase. (Each cell contains a single reversed micelle, and adjacent cells share common hexagonal or quadrilateral faces)

www.iran-mavad.com

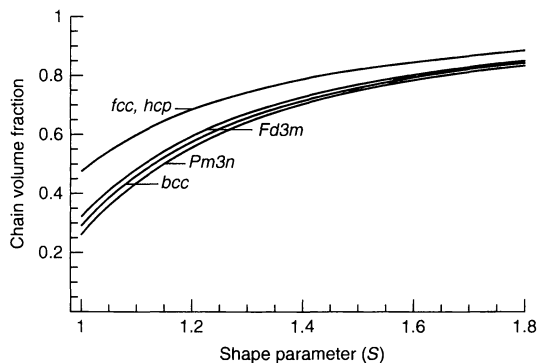


Figure 16.15. Local/global “phase diagram” for a range of discrete micellar I_2 mesophases (cf. Figure 16.8): fcc ($Fm\bar{3}m$) (or hcp ($P6_3/mmc$), bcc ($Im\bar{3}m$), and clathrate ($Pm\bar{3}n$, $Fd\bar{3}m$) packings. The ordinate is the apolar volume fraction

They are very viscous, and nearly solid in some cases (occasionally termed “ringing gels” in the older literature). All examples firmly established to date

exhibit cubic symmetries, so they do not display optical textures. They were first detected in lipid–water systems and dry metallic soaps by Luzzati and colleagues in the 1960s. Since then, they have been seen in all types of amphiphiles, i.e. ionic, nonionic, zwitterionic, copolymeric, etc. It is worth noting that swollen versions are also seen in optical micrographs of sections of cell organelle membranes, presumably reflecting the organelle membrane structure *in vivo* (5).

These mesophases are structurally “warped lamellar phases”, with the important difference that ideal crystals of bicontinuous mesophases contain a single bilayer membrane, of hyperbolic (saddle-shaped) geometry. (Recall that ideal lamellar mesophases consist of a stack of disjointed parallel bilayer membranes.) A number of studies have confirmed the membrane topology in bicontinuous mesophases: the bilayer is folded on to a triply periodic hyperbolic surface, resembling one of the three most homogeneous sponges with zero mean curvature (“minimal surfaces”): the so-called P-surface, D-surface or gyroid (Figure 16.16). To date,

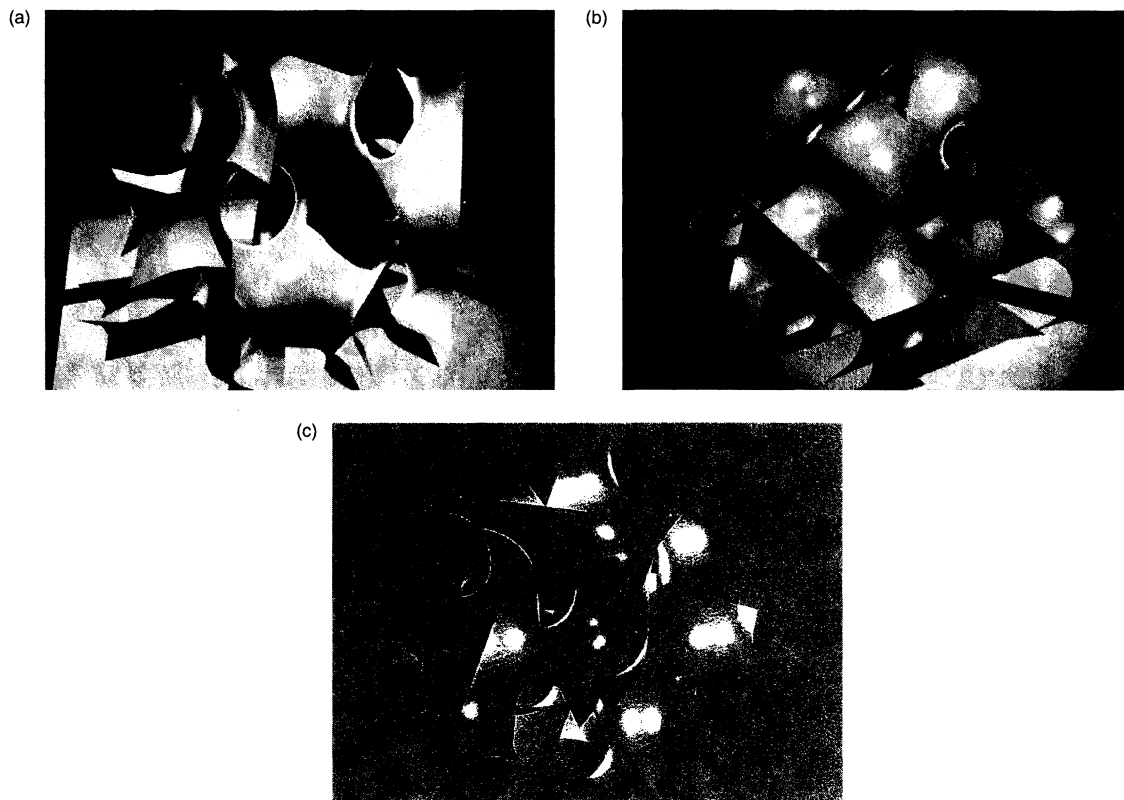


Figure 16.16. The sponge-like bilayer geometry of the known (cubic) bicontinuous mesophases: (a) the P phase; (b) the D phase; (c) the G (gyroid) phase

www.iran-mavad.com

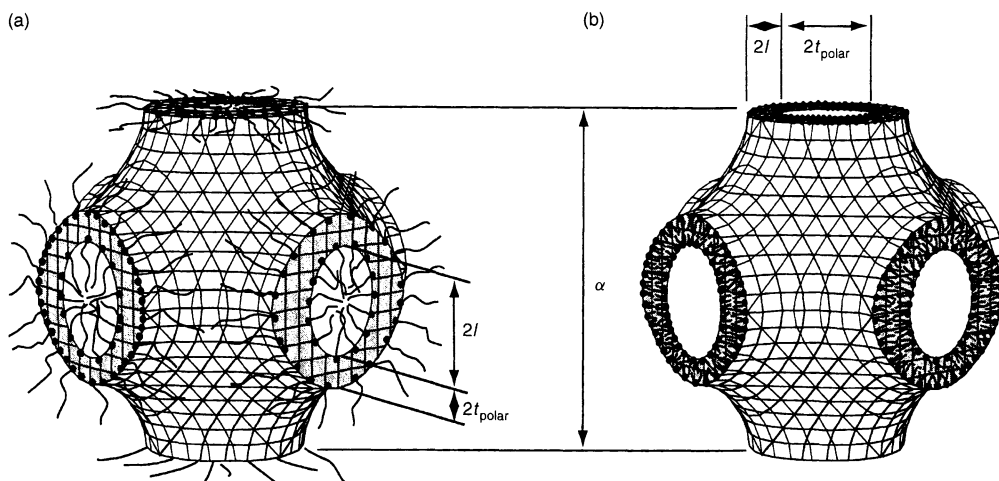


Figure 16.17. Bilayer morphologies of a bicontinuous mesophase (P) of Types 1 and 2. (a) Type 1 bicontinuous mesophases consist of a reversed, polar (e.g. water-filled) film (thickness $2t_{\text{polar}}$) folded on to the P surface, immersed in two disconnected but interwoven apolar (paraffin) continua, with one on either side of the surface. (b) Type 2 phases contain a paraffin film of thickness twice the chain length, $2l$, separating polar domains

three cubic bicontinuous (“V1” and “V2” in the notation of Tiddy) mesophases have been accepted, based on these three surfaces: the P ($\text{Im}\bar{3}\text{m}$, denoted Q^{229} by Luzzati), D ($\text{Pn}\bar{3}\text{m}$, Q^{229}), and, most frequently, the G(yroid) bicontinuous mesophase ($\text{Ia}\bar{3}\text{d}$, Q^{230}).

Such surfaces describe the mid-surface of the amphiphilic bilayer. If the bilayer is Type 2, the surface cleaves opposing hydrocarbon chain-ends, and the remaining volume (defining a pair of interwoven 3D cubic labyrinths) are water-filled. Type 1 bicontinuous cubic mesophases consist of a reversed bilayer wrapped on the surfaces, with chains filling the labyrinths (Figure 16.17). As with the other mesophases discussed above, these Types have shape parameters on either side of 1 (roughly equal to $2/3$ for Types 1; >1 for Types 2, see Figure 16.8). A brief literature overview of these mesophases can be consulted for further references (10).

An alternative structural description is that of the *monolayers*. These form a pair of inter-woven 3D

networks, whose connectivity is dependent on the mesophase. The G mesophase contains a pair of 3-connected (“Y*”) networks, related to each other by inversion symmetry, i.e. one right-handed and the other left-handed, where the D contains a pair of identical 4-connected “diamond” networks and the P a pair of identical 6-connected simple cubic networks (Figure 16.18).

Given the geometric wealth of competing bicontinuous structures, with varying symmetries *and* topologies, some analysis is needed to determine the mesostructure. Care must also be exercised in these cases, as transitions between bicontinuous mesophases are common, often requiring only small changes in composition (or temperature). The mesophase progression can be rationalized on the basis of the changing surface-to-volume parameters of bicontinuous forms with different symmetries and topologies. The progression is mapped into the shape parameters (s) – the concentration domain

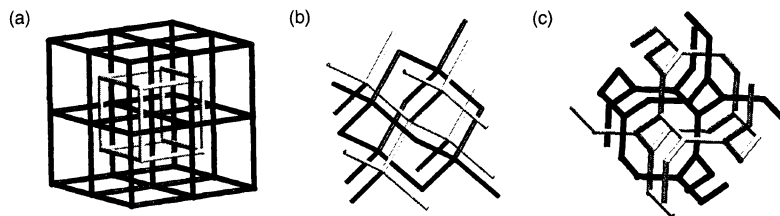


Figure 16.18. Labyrinth networks in the (a) P, (b) D and (c) G mesophases. For Type 1 mesophases these are water-filled, while for Type 2 they are chain-filled (cf. Figure 16.17) www.iran-mavad.com

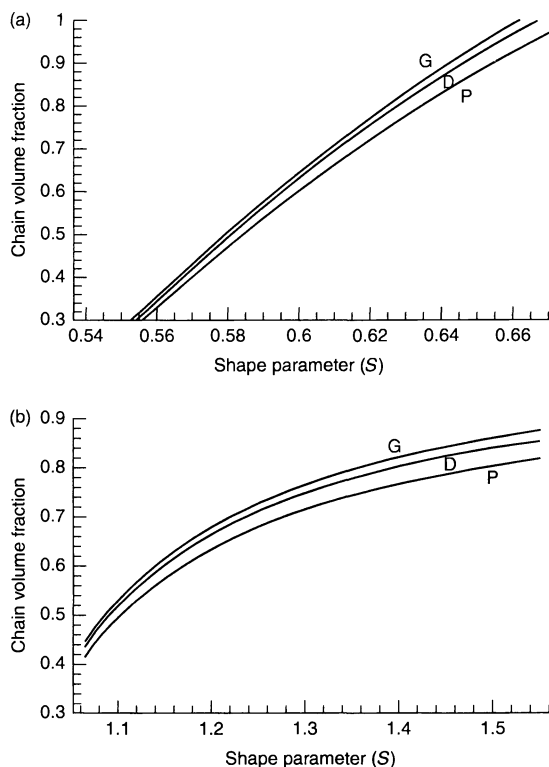


Figure 16.19. Local/global “phase diagrams” for a range of observed bicontinuous cubic mesophases, the P, D and G (gyroid) phases (cf. Figure 16.8): (a) Type V1; (b) Type V2 (cf. Figures 16.7, 16.15, 16.17)

in Figure 16.19, which represents the modification of the ideal homogeneous (frustration-free) case plotted in Figure 16.8 to real hyperbolic surfaces (analogous to the plot of Figure 16.14 above). (Exact formulae can be found in Tables 16.2 and 16.3 below).

The observed progression on water dilution of the Types 1 or 2 bicontinuous mesophases is G–D–P, in accord with the plot in Figure 16.19. Sample small-angle X-ray scattering patterns for the D and P structures are shown in Figure 16.20.

Individual samples may contain two or more bicontinuous mesophases: these exhibit a distinct, sharp interface separating isotropic, viscous mixtures visible in a transparent ampoule. Transitions between bicontinuous mesophases can also occur with small temperature changes. The transitions are first-order, and exhibit a small latent heat of transition: typically less than 0.01 kJ/mol, compared with ca. 1 kJ/mol for (Type 2) bicontinuous–(reversed) hexagonal transitions and slightly less for lamellar–bicontinuous cubic transitions.

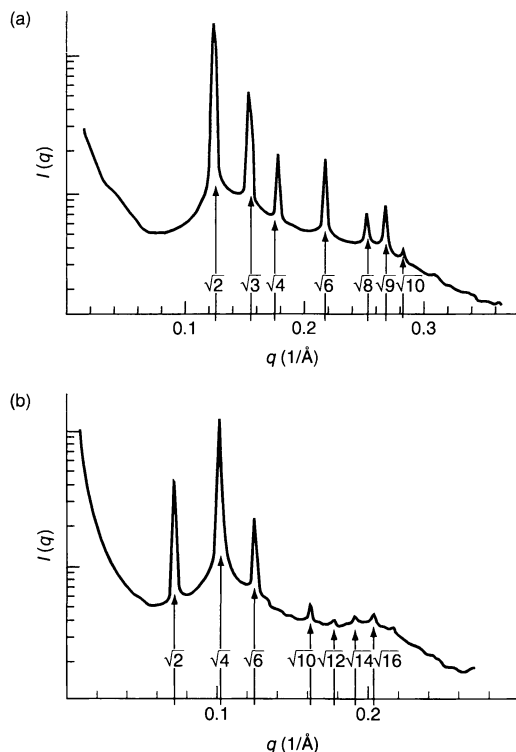


Figure 16.20. Typical (powder) small-angle scattering spectra from (well ordered!) bicontinuous (a) D and (b) P cubic mesophases. More often, fewer peaks are evident

Identification of the mesophase can be most readily done by using good small-angle diffraction data (see Table 16.1 below). Typically, a minimum of four peaks are needed to state with any confidence the symmetry *aspect* of the mesophase (which sets the range of possible space group symmetries). Since the pioneering (and to this day benchmark) X-ray studies of bicontinuous lipid–water mesophases by Luzzati and colleagues, it has been assumed that the symmetry of the mesophase is the maximally symmetric space group within that aspect. That is borne out by geometric analysis of X-ray data. First, the lattice parameter of the mesophase is measured. (This can only be determined if sufficiently numerous peaks are evident in the small-angle X-ray scattering pattern). The lattice parameter – scaled by the surfactant chain length, l (or, in the presence of extra hydrophobic additives, the monolayer thickness) – is a reasonably sensitive function of the crystallographic genus, γ , introduced above and the bilayer volume fraction (Figure 16.21). Some data collected from a range of sources (see references given in (11)) are compared via the curves shown in Figure 16.22. These curves

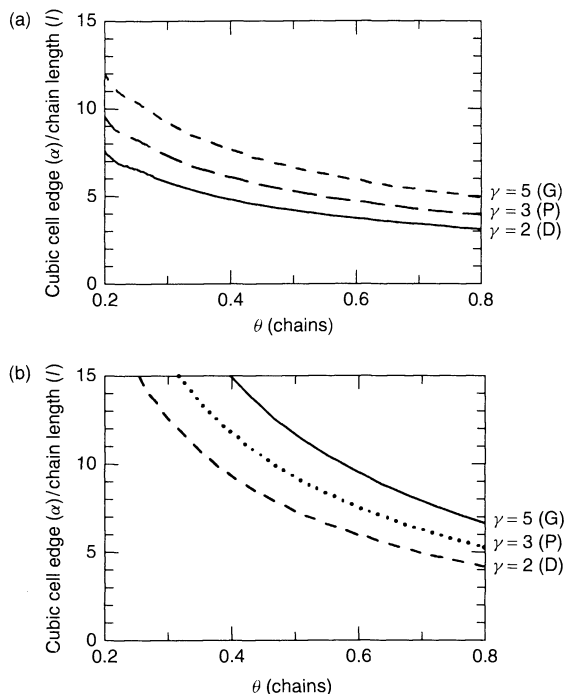


Figure 16.21. Theoretical variations of lattice parameter (α) scaled by chain length (l) as a function of bilayer volume fraction (θ) for (a) Type 1 and (b) Type 2 bicontinuous mesophases. The curves are calculated for distinct mesophase topologies per unit cell, indexed by the crystallographic genus, γ

are dependent on the surface-to-volume ratio of the underlying surface. A number of parameters have been proposed to measure this global surface-to-volume ratio. The simplest index that is independent of the choice of unit cell is the “homogeneity index”, which involves the crystallographic genus (γ), the surface area of the hyperbolic bilayer surface within the unit cell (A) and the cell volume (V), as follows:

$$h \equiv \frac{A^{3/2}}{(4\pi(\gamma - 1))^{1/2}V} \quad (16.7)$$

The values of h for the P, D and G structures are close to the ideal homogeneous (and frustration-free) value of exactly $3/4$ (see Table 16.1 below). The lattice parameter (α) scales with the crystallographic genus (γ) and the homogeneity index (h) as follows:

$$\frac{\alpha}{l} \propto \left(\frac{\gamma - 1}{h} \right)^{1/3} \quad (16.8)$$

so that the ratios of (conventional cubic unit cell) lattice parameters for G:D:P mesophases containing identical bilayer curvatures (identical s) are equal to 1.576:1:1.279, respectively. Thus, sudden jumps in lattice parameters according to these ratios with temperature or compositional variations are a signature of a transformation between the P–D–G trio of bicontinuous cubic (V_1 or V_2) mesophases. (The ideal swelling behaviour of a bicontinuous mesophase that remains within a single-phase region over a range of concentrations is discussed below.)

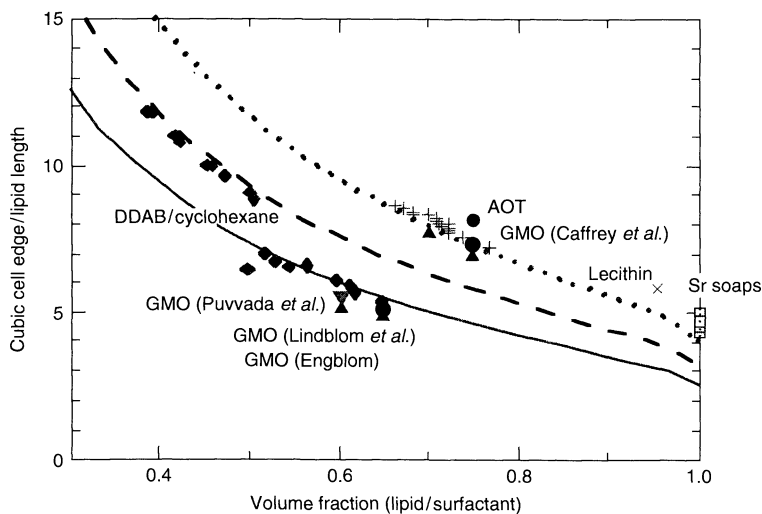


Figure 16.22. Comparison of theory with lattice data of a range of Type 2 bicontinuous mesophases: , G; - - - - , D; ————, P: AOT, Aerosol OT–water; GMO, glycerol monoolein–water; DDAB, didodecyldimethylammonium bromide–water–cyclohexane; Sr soap, strontium carboxylate–water

Other mesostructural probes are less developed for bicontinuous mesophases. Some calculations of the theoretical differences in diffusion characteristics of various surfaces have been applied to NMR diffusion data (12, 13), although the discrimination of such measurements remains uncertain. Calculated NMR bands for frozen single crystals of the P, D and G mesophases are expected to be identical (14), although they may yet prove useful to detect possible “intermediate” anisotropic bicontinuous mesophases, (as discussed below).

2.1.7 Mesh mesophases

These mesophases are intermediate to lamellar and bicontinuous mesophases. Like the bicontinuous cubic mesophases, these were first described by Luzzati and co-workers in the 1960s (in divalent metal soaps) (15). They have since been seen in, for example, perfluorinated metal salts in water and nonionic surfactant–water systems. These are characterized by a smectic stack of “punctured” bilayers, together with an ordered arrangement of punctures within each bilayer, giving, like discrete micellar and bicontinuous mesophases, 3D lattices. Two polymorphs are known, i.e. the “R” (rhombohedral) mesh mesophase (space group R3m), containing a hexagonally close-packed array of punctures, and the (body-centred) “T” (tetragonal) phase, space group I422, with a square array of punctures (Figure 16.23). Both mesophases are optically anisotropic, with two

cell parameters (the in-plane “ α ” spacing between punctures, and the smectic “ c ” spacing between bilayers (see Figure 16.23 and Table 16.1 (below))).

It is reasonable to postulate “turbostratic” derivatives of these mesophases, free of the relative register between layers, so that there is no correlations across adjacent bilayers, except smectic ordering. These derivatives should therefore lead to a “lamellar” small-angle scattering pattern (see Table 16.1 below).

It is impossible to offer estimates for relative locations of mesh mesophases within a phase diagram, due to the extreme variability of shape parameters (s) with the composition of meshes. Note that Type 1 meshes (stacked layers of 2D apolar labyrinths) can result provided that $1/2 < s < 2/3$, and Type 2 meshes (with water labyrinths) can form if $s > 2/3$, over a range of compositions (Figure 16.8). That means that Type 2 mesh mesophases can be formed in lyotropes containing single-chain amphiphiles in contrast to the other Type 2 mesophases, which form only if $s > 1$.

Armed with the current list of confirmed lyotropic mesophases, Figure 16.8 can now be crudely characterized as follows. The variety of membrane morphologies confirmed to date can be ordered according to the average shape parameter, s , of the constituent membrane amphiphiles (a horizontal cut through Figure 16.8). As s increases from its smallest value of $1/3$ (corresponding to a large head-group relative to the usually single-chain volume in the amphiphile) to greater than 1 (bulky chains – such as double-chained amphiphiles), the spectrum and relative positions of mesophases

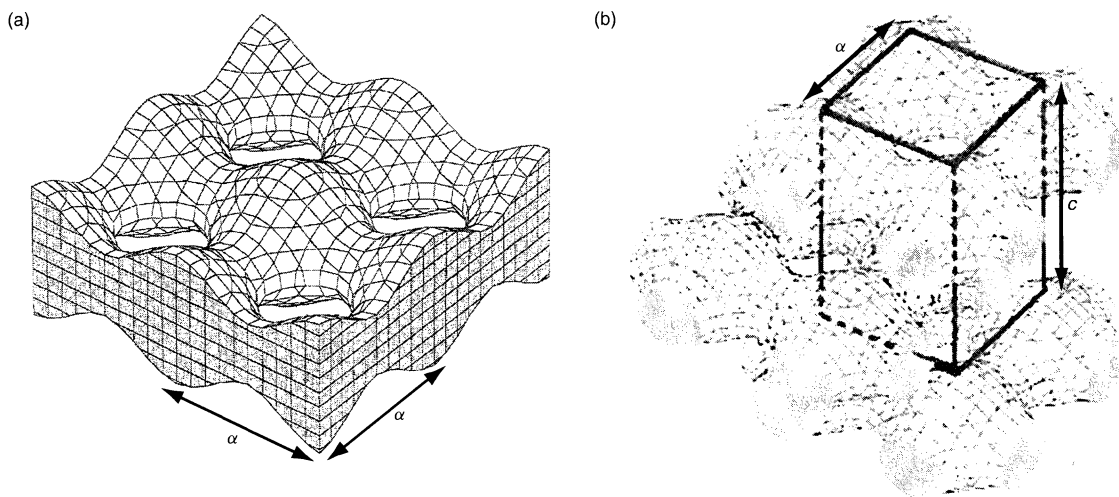
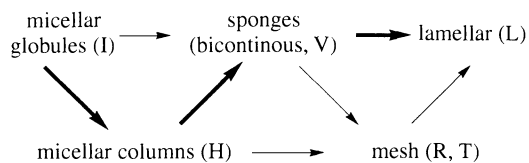


Figure 16.23. (a) View of a single monolayer in a (T)etragonal mesh mesophase. (b) The bilayers are stacked in a staggered arrangement, giving a body-centred tetragonal symmetry (I422), with lattice parameters α and c

www.iran-mavad.com

ordered according to their curvature and topology is revealed:



In the above, thicker arrows indicate the relative locations assuming homogeneity. If the essential inhomogeneities accompanying packings of sponges, globules, etc., in space are included, there is some overlap between globular and columnar phases, and between sponges, meshes and lamellar mesophases. This progression is the one found. As a very general rule, typical single-chain detergents exhibit some sub-set of the following sequence of Type 1 mesophases as the detergent fraction increases (on dehydration), I_1 , H_1 , V_1 /mesh. Likewise, double-chained surfactants form mesophases within the sequence on hydration: I_2 , H_2 , V_2 /mesh, L_α .

2.1.8 Intermediate mesophases: (novel bi- and polycontinuous space partitioners)

In this section, we will undertake the more speculative task of introducing novel interfaces, in the belief that they too may be found among lyotropic liquid crystals. A variety of other mesophases have been proposed in the scientific literature over the years. Here, we will focus on the more topologically complex examples, including novel arrays of meshes, sponges and hybrids.

It is very likely that a considerably richer repertoire of mesostructures can form in addition to those recognized and discussed above. Much evidence has been accumulated for "intermediate" mesophases, whose fingerprints from small-angle X-ray scattering, and/or a combination of NMR data, optical textures and calorimetry do not match those of known mesophases (16).

First, simple less homogeneous – and therefore likely to be more prevalent among chemically disperse membranes – lower symmetry variations on the known mesostructures deserve consideration. Consistent reports of other mesophases by experienced researchers of the calibre of Luzzati and Fontell in Sweden cannot be discounted (17). Most of the proposed mesostructures involve simple symmetry-breaking deformations of the more common phases, including hexagonal columnar and discrete micellar mesophases.

The most intriguing cases of lower symmetry relatives to known mesophases are anisotropic bicontinuous mesophases. These are sponges whose homogeneity lies one rank below the cubic genus-three P, D and gyroid surfaces. The most likely candidates are tetragonal and rhombohedral variants. These include the rPD, tP, tD, tG and rG triply periodic minimal surfaces (18). These surface are deformations of their cubic parent structures, and can be modelled as perturbations of the known bicontinuous cubic mesophases.

Secondly, the possibility of topological variants of the sponges, meshes, etc. must be faced. Prime candidates for novel bicontinuous mesophases are some homogeneous triply periodic minimal surfaces whose genus, exceeds three: the cubic ($Im\bar{3}m$) I-WP surface, cubic ($Im\bar{3}m$) Neovius (or C(P)) surface, cubic ($Fm\bar{3}m$) F-RD surface, etc. The expected lattice sizes of these structures are larger than those of the simpler P, D and G phases. They can be calculated from equation (16.7). (The geometric and topological characteristics of these structures are listed in Table 1 below.)

Thirdly, one can consider novel space partitions as models for membrane bilayers, which combine elements of sponges, honeycombs (hexagonal columnar) and closed-cell foams (discrete micellar). A number of intriguing *polycontinuous* interfaces have recently been constructed, whose labyrinths are generalizations of the bicontinuous examples. Just as bicontinuous morphologies carve space into a pair of interwoven 3D labyrinths, n -continuous cases divide a volume into n interwoven 3D labyrinths. To date, only the most homogeneous three-connected labyrinths have been analysed in any detail. These include a number of *chiral mesophases*, whose synthesis would offer exciting possibilities as novel nonlinear materials. These examples contain interwoven Y^* chiral labyrinths (2, 4 or 8) of the same hand (all $+Y^*$, or all $-Y^*$), in contrast to the gyroid (Q^{230}), that contains one right-handed ($+Y^*$) and one left-handed ($-Y^*$) labyrinth. Some examples are shown in Figure 16.24.

Novel chiral "honeycombs" (containing infinite, non-intersecting columnar channels or "rod packings" (19)) have also been constructed theoretically. Like the polycontinuous forms (and hexagonal and discrete micellar mesophases), these structures (which define bilayers) contain both line and point singularities, where the surface *branches*, spanning hyperbolic surface elements. They are therefore hybrids of the foam and sponge morphologies. Their labyrinths (the monolayer geometry) are particularly simple: they are 3D cylinder packings (including chiral examples). They are related to the hexagonal mesophase by a lattice of 3D twists. So far,

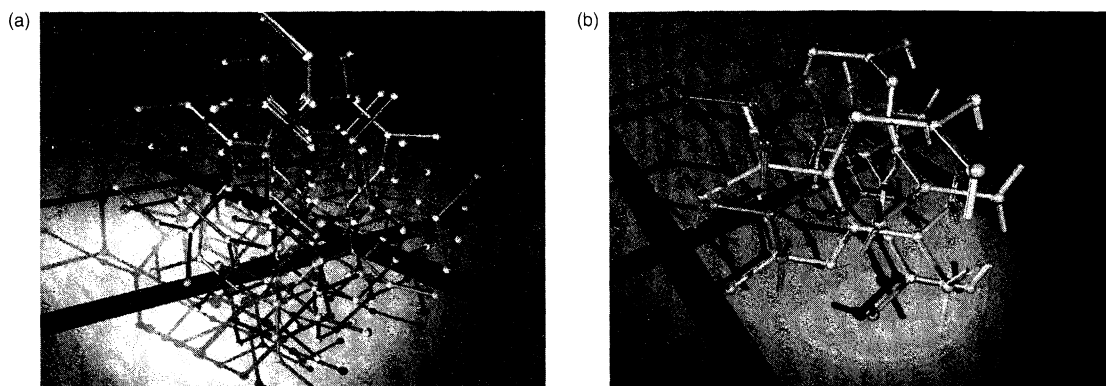


Figure 16.24. Some possible generalizations of the bicontinuous phases: (a) a tetracontinuous morphology (space group $P4_232$); (b) a tricontinuous hexagonal structure (space group $P6_3/mmc$)

only cubic examples have been modelled (space groups $I4_132$, $P4_232$), although many others remain to be constructed (Figure 16.25).

These mesostructures can result from growth of discrete micellar mesophases, giving columnar micellar packings. For example, micelles within the $Pm\bar{3}n$ phase (Figure 16.14) can fuse through hexagonal faces, giving the well-known “ β -W” rod packing ($Pm\bar{3}n$). The geometry of the bilayer membrane is warped, and consists of hyperbolic elements, fused along branch line and points.

In addition to 3D columnar packings, these branched polycontinuous forms include novel mesh structures, with 3D arrangements of meshes, rather than the smectic array common to the R and T mesh mesophases. One example, a rhombohedral arrangement of the hexagonal mesh (found also in the R phase), is shown in Figure 16.26.

It is certain that our understanding of the array of mesophases realized in lyotropic systems is incomplete. The novel hybrid structures introduced here are expected to form under conditions similar to those leading to hexagonal and bicontinuous mesophases. This domain remains poorly understood experimentally. At this stage, all that can be concluded confidently is that more work needs to be done in order to sort out the mesostructures of the many intermediate phases that have been reported.

2.2 Between order and disorder: topological defects

Lamellar and hexagonal polymorphs are the most commonly reported mesophases in lyotropic liquid crystals, usually identified from their scattering spectra.

www.iran-mavad.com

Following the previous sections, it should be noted that many other more complex mesophases may be present in a lyotrope, including (poly)continuous sponges, meshes (both smectic and 3D crystals) and novel 3D columnar packings. In addition, beyond lyotropic liquid crystals there are a number of closely related disordered mesophases, i.e. “sponge” (L_3) mesophases and microemulsions. The former phase is closely related to bicontinuous mesophases, and can be considered to be a melt of those mesostructures. The jargon “microemulsion” disguises a multitude of spatially disordered mesostructures, from globular to bicontinuous monolayers (the latter with single interwoven polar and apolar labyrinths, cf. Figure 16.3), in contrast to the multiple interwoven polar/apolar networks found in V_2/V_1 and sponge (L_3) phases, cf. Figure 16.17).

The analysis so far has focussed on the crystallographic aspects of these mesostructures. In practice, the topology of the membrane(s) in the lyotrope is of equal importance. Indeed, given the fluctuating interfaces characteristic of these soft materials, the focus on crystallographic reconstruction of the structure is perhaps overly optimistic: no self-respecting crystallographer would dare attempt to solve a solid-state crystal structure given only a handful of diffraction peaks!

Momentarily retaining the crystallographic perspective, we must recognize the likely presence of “defects” in the membrane, which may drastically affect the bulk membrane topology. Two defects are possible: bilayer punctures and channels (Figure 16.27).

Thus, a sponge may be identified as a lamellar phase with an ordered array of channels lining the leaflets, resulting in the single-sheeted structure characteristic of bicontinuous mesophases, or as a channel-ridden defective hexagonal mesophase (Figure 16.28).

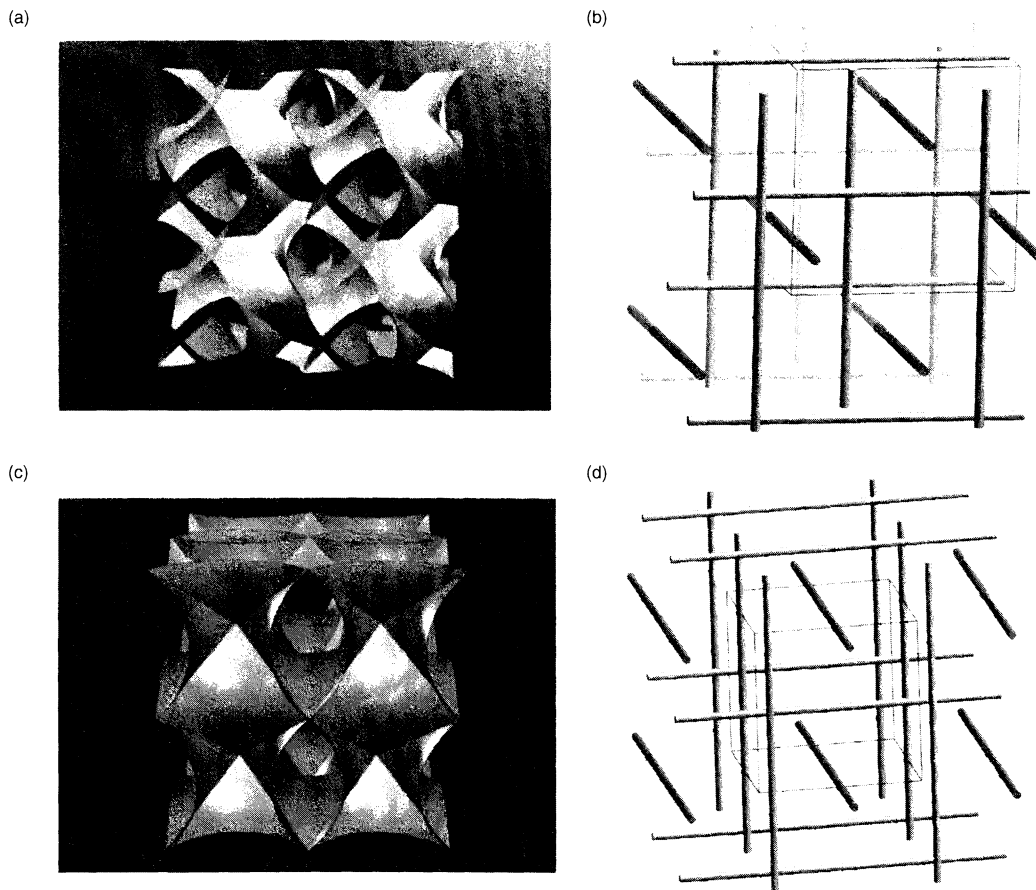


Figure 16.25. Two possible 3D columnar mesophases. (a) A hyperbolic branched surface (bilayer geometry) with line and point singularities. The surface partitions into (b) a 3D cubic rod packing (symmetry $I4_132$, the β -Mn rod packing). (c) A unit cell of the branched surface that carves space into (d) the β -W (A15) $Pm\bar{3}n$ rod packing. This surface results by puncturing all hexagonal faces in the $Pm\bar{3}n$ discrete micellar mesophase (Figure 16.14)

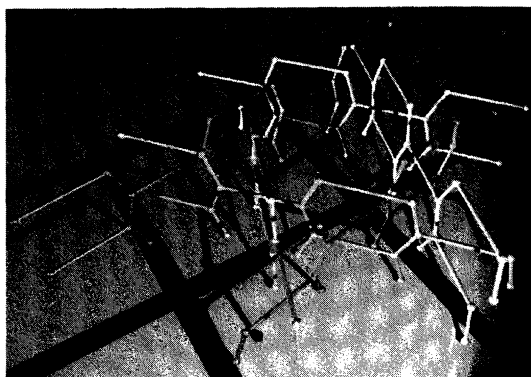


Figure 16.26. A theoretical 3D mesh mesophase, consisting of three interwoven "graphite" nets (the R mesh mesophase consists of smectic stacks of these nets)

www.iran-mavad.com

Similarly, meshes can be viewed as punctured bilayers, where ordered square and hexagonally patterned arrays of punctures result in the T and R mesophases, respectively. Inverting that argument leads to the conclusion that taking account of the diffraction peaks in the scattering pattern only allows one to reconstruct those spatially correlated domains in the mesostructure; a bicontinuous membrane could diffract as a smectic or hexagonal lattice, and yet its mesostructure is far from that of the classical lamellar or hexagonal mesophases.

2.2.1 Molten mesophases: microemulsion (L_1 , L_2) and sponge (L_3) phases

The problem of identification is most evident in the "molten" lyotropic mesophases. These mesophases are

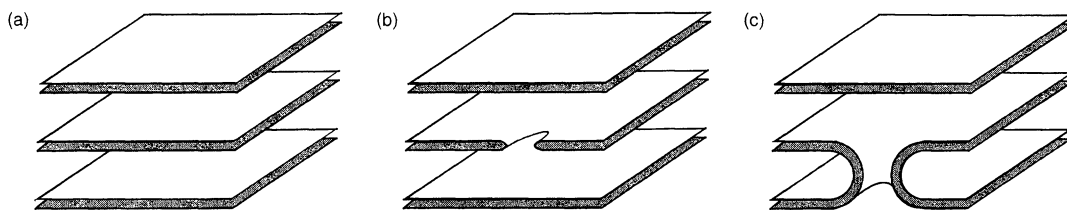


Figure 16.27. A classical lamellar arrangement of bilayers (a) containing (b) a puncture defect and (c) a channel defect

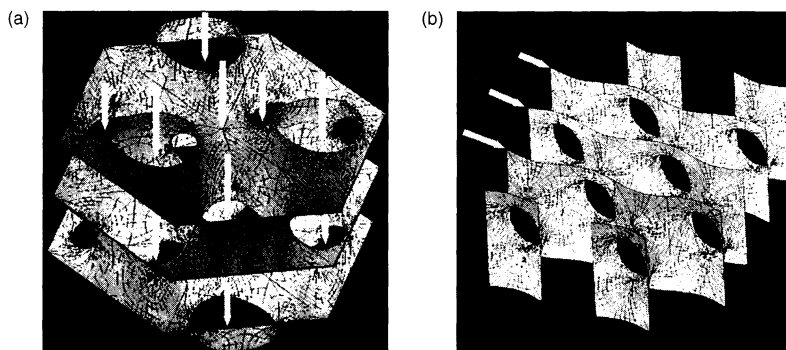


Figure 16.28. The topology of a bilayer within a mesophase is not a priori deductible from its apparent lattice. (a) For example, a sponge bilayer may exhibit no correlations along a vertical axis, but strong in-plane correlations (arrowed), leading to a “hexagonal” mesophase, whose membrane topology is very different from a classical columnar hexagonal phase. (b) Similarly, a sponge can exhibit smectic ordering only (arrowed), and can therefore be confused with a classical lamellar mesophase

characterized by poor spatial correlations. Small-angle scattering spectra typically exhibit a single broad scattering peak at small angles (in addition to the usual 4.5 \AA^{-1} wide-angle chain peak), although some microemulsions fail to lead to any peak at small angles. These phases are the analogues of liquids: they have local (meso)structure, but the very short-range ordering is insufficient to define a lattice. The aggregates in these mesophases are thus disordered. Nevertheless, they do exhibit many hallmarks of characteristic structures. They are most readily modelled as melts of some of the liquid crystalline mesophases listed above.

Sponge mesophases are characterized by flow birefringence (giving anisotropic optical textures), yet they are isotropic at rest. They are typically viscous, though less so than bicontinuous cubic mesophases. Their mesostructures are closely related to the bicontinuous cubics. They often form at high (water) dilution, usually in regions of the phase diagram intermediate to lamellar and bicontinuous cubic mesophases.

Microemulsions are defined to be freely flowing isotropic lyotropes. There are many possible mesostructures in microemulsions, ranging from Types 1 and 2 micelles (spherical, ellipsoidal, columnar, etc.) arranged in a random fashion, to bicontinuous microemulsions.

that are well modelled as bicontinuous monolayers (cf. Figure 16.8). Fuller descriptions of their mesostructures can be found elsewhere in this volume.

2.3 Probing topology: swelling laws

To probe the *topology* of the membrane may be a more useful endeavour than uncovering its *crystallography*, particularly in the case of the microemulsions and sponge mesophases. Clearly, a complete description of the mesostructure of the lyotropic system must encompass both aspects. The topology can be best measured by swelling experiments, assuming that a mesophase can form over a sufficiently large composition range to allow data to be collected on the lyotrope as a function of solvent fraction and the presence of at least one scattering peak. Meaningful conclusions can be drawn from swelling data, provided one is aware of the essential approximations involved in the analysis. Much has been written on the technique, and it has been used widely, chiefly as support for identification of lamellar and hexagonal mesophases. The standard argument has it that the variation of a scattering peak

(D^*) with amphiphile volume fraction (φ) follows the formulae:

$$D^* \propto \varphi^{-1}; D^* \propto \varphi^{-1/2} \quad (16.9)$$

These simple forms, in fact, involve some assumptions. Foremost is the requirement that the thickness of the bilayer remains fixed during the change in concentration, φ . This requirement may not hold, thus making the analysis fragile. For example, the swelling form $D^* \propto \varphi^{-1}$, commonly employed as a signature of lamellar mesophases, has also been proposed for sponge (including bicontinuous cubic) mesophases.

The simple “lamellar” scaling law, $D^* \propto \varphi^{-1}$, *cannot* in general be construed as a signature of a classical lamellar mesophase (parallel, disconnected bilayer sheets). For example, *any* Type 2 mesostructure that swells without any change in cross-sectional area per amphiphile at the bilayer centre (at the chain ends) follows this swelling law.

The plot shown in Figure 16.29 suggests that the shape parameter, s , defined above, affords a very useful generic swelling law, valid under the assumption of membrane curvature homogeneity (constant s throughout the membrane), as follows:

$$\frac{l}{D^*} \propto \varphi_{\text{apolar}}^s, \text{ i.e. } \log\left(\frac{D^*}{l}\right) \propto -s \log(\varphi_{\text{apolar}}) \quad (\text{Type 1 mesophases}) \quad (16.10a)$$

$$\frac{D^* - l}{D^*} \propto \varphi_{\text{polar}}^{s'}, \text{ i.e. } \log\left(\frac{D^*}{l} - 1\right) \propto -s' \log(\varphi_{\text{polar}}) \quad (\text{Type 2 mesophases}) \quad (16.10b)$$

Two distinct swelling exponents, i.e. s for Type 1 systems and s' for Type 2 systems, are needed. The

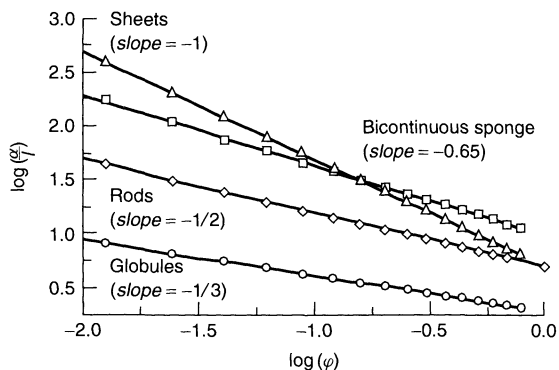


Figure 16.29. Log-log variation of lattice spacings (α) scaled by chain length (l) as a function of the amphiphile volume fraction (φ) for a range of Type 1 mesophases

former, s , is precisely the molecular shape parameter of the amphiphile (v/al). The exponent derived from Type 2 mesophases, s' , is the shape parameter of the *polar* domains of the mesostructure, rather than the (apolar) amphiphile shape parameter. (In other words, the parameter s' probes the geometry and topology of the polar domains in Type 2 systems, whereas the Type 1 swelling exponent, s , is a function of the shape of apolar domains.) The mesostructural topology assigned to swelling exponents for Types 1 and 2 mesophases are listed in Table 2 below (extracted from Figure 16.8).

These laws are remarkably simple, yet informative. For example, measurement of the lattice parameter, α , of a Type 1 lyotropic liquid crystal as a function of the apolar volume fraction (which can be calculated from the w/w composition of the lyotrope and densities) allows estimation of s , by determining the slope of a $\log(\alpha)$ versus $\log(\varphi_{\text{apolar}})$ plot. Here, we have taken the repeat spacing of equations (16.10) D^* , to be the lattice parameter, α , and assume that the bilayer thickness, l remains constant during the swelling process. In principle, provided that the mesophase swells isotropically, any (hkl) diffraction peak of the liquid crystal can be assigned to D^* . Indeed, we can choose D^* to be equal to the position of the single broad scattering peak in microemulsion and sponge phases.

Recall that the generalized local/global (s, φ) coordinates of the mesophase determine the membrane *topology* (e.g. sponge, mesh, columnar, globular, etc.), from the master plot shown in Figure 16.8. So, assuming homogeneity (an assumption that we have pointed out accords with the observed liquid crystalline mesophases in chemically homogeneous systems), swelling allows rigorous determination of the true mesostructure – including the membrane topology (and accompanying “defects”¹) – rather than the symmetries of the mesophase that can be deduced from a single small-angle scattering pattern.

Strictly speaking, equations (16.10) indicate that one must be able to estimate both the repeat spacing, D^* , of the lyotrope *and* the chain length of the amphiphile, l . It is usually assumed that l does not vary (at least compared with D^*) within a mesophase. In the absence of any direct probe of that parameter, we are forced to accept this, perhaps incorrect, assumption. It should be borne in mind, however, that variations of l do affect the experimental estimate of s .

Independent determination of l is difficult, despite claims to the contrary in the literature. These values are

¹ The term is misused here: these defects may well improve the stability of the mesophase, and are defective only with respect to our idealized mesostructures.

routinely inferred from the repeat spacing (α) in lamellar phases, derived from the swelling law for defect-free lamellae: $l = \alpha \varphi_{\text{apolar}}$. This inference is *a priori* invalid, since it involves the assumption that the “lamellar” phase indeed consists of parallel, disjoint, planar membranes, and is devoid of topological defects. Indeed, all current techniques to determine bilayer thickness require some *ad hoc* assumptions about the mesostructure. The development of a technique offering an independent estimation of l is an urgent priority. This would allow specification of the membrane mesostructure, including topological defect densities, and aggregate shapes, without any fitting parameters. As it stands, the structure can only be inferred by first fitting l , a process that is described in detail elsewhere (20). Nevertheless, the technique does provide useful structural data. For example, data from the V_1 (bicontinuous cubic, Ia $\bar{3}d$) mesophase in the glycerol monolein–water system has been analysed in this fashion (with the chain length fitted from a more complex swelling law), and its shape parameter (s) has been estimated to be equal to 0.60, in reasonable agreement with the expected value of s for ideal V_1 mesophases over the volume fractions. More careful analysis can also allow estimation of the homogeneity index of the bilayer, giving a value of 0.77 for this index, in agreement with that of the gyroid (cf. Table 16.1 below). Similarly, explicit mesostructural models can be obtained for molten L_1 , L_2 and L_3 mesophases by the same technique.

3 A NOTE ON INHOMOGENEOUS LYOTROPES

It should be noted that the catalogue of known and likely mesophases in this chapter rests on the simplifying assumption of homogeneity. This assumption, invoked repeatedly, allows for a simple characterization of the mesostructure in terms of the local molecular shape. In other words, we have assumed here that there is a single preferred molecular shape (s), and the mesostructure is the result of the global problem of embedding this shape in space with minimal shape variations and with the required volume and surface parameters, set by the composition of the lytrope. The assumption is theoretically convenient, and not unreasonable experimentally. The very formation of liquid crystals in lyotropic systems is dependent on quasi-homogeneity in chemical terms also (few components in the lytrope, and monodisperse chemical components). If the system is very polydisperse, the formation of non-crystalline mesostructures is

likely, as disordered (entropically favoured) mesostructures can form without any frustration of the array of molecular shapes.

However, there is an intermediate regime that remains largely unexplored. This is one where the lytrope remains sufficiently homogeneous in a chemical sense to form crystalline mesostructures. In such cases, the requirement of least frustrated geometries is relaxed, and the interfaces can allow variations in curvatures, and shape parameters. For example, there is ample evidence (principally reported by Gordon Tiddy and colleagues) that transitions from well-characterized bicontinuous cubic mesophases to poorly understood, optically anisotropic “Intermediate” phases result if the chain length of an amphiphile is lengthened. (A possible explanation is that longer chains imply more conformational freedom, thus leading to variations in the shape parameter.) Alternatively, addition of small amounts of cosurfactants (which can partition in both polar and apolar regions), or additional solvents, may relax the homogeneity, but not so much as to cause melting of the bilayer mesostructure. To recapitulate, these phases include (i) the less symmetric variations of the homogeneous mesophases (ribbon, deformed (possibly anisotropic) discrete micellar and anisotropic bicontinuous mesophases), and (ii) novel polycontinuous structures. We emphasize that there is good evidence for some of these phases (e.g. ribbon mesophases), while others remain speculative, although likely to appear in lyotropic systems.

To our knowledge, there are few studies – theoretical or experimental – of likely optical textures of inhomogeneous mesophases. However, *changes* of optical texture within a supposedly single mesophase domain of the phase diagram are a good indication that the mesostructure has changed (and therefore, a novel mesophase is present). For example, the classic fan texture common to hexagonal (cylindrical) mesophases changes subtly, but distinctly, with composition and temperature in two systems known to this writer, i.e. a nonionic polyoxyethylene surfactant–water system and a monoolein–water system. “Mosaic” and other textures are evident (Figure 16.30). Unusual optical textures have also been reported for intermediate mesophases (2).

Detection of novel inhomogeneous mesophases with NMR techniques also remains speculative, with very few results. One exception is the data of David Anderson (14) for anisotropic bicontinuous mesostructures, relevant to single crystals only.

Swelling data can be collected on anisotropic and other mesophases. The interpretation of these data is less straightforward than in the homogeneous cases. Again,

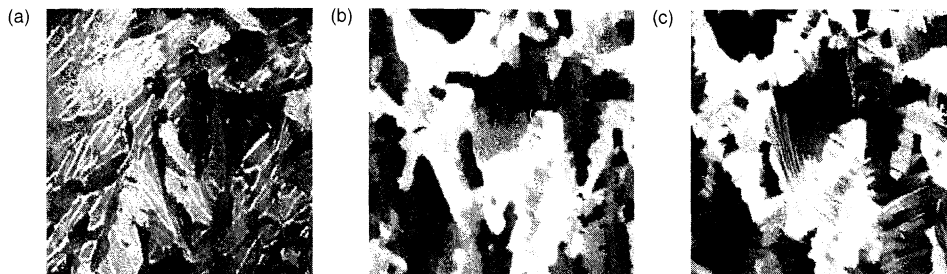


Figure 16.30. A succession of optical textures obtained on heating a “hexagonal” mesophase in an “aged” monoolein–water lyotrope. (a) The texture of the hexagonal phase (25°C), and two novel textures (b) 32.5°C and (c) 55°C, signalling likely novel mesostructures at higher temperatures with hexagonal symmetry (samples courtesy of M. Monduzzi, Cagliari, Italy)

a swelling exponent can be extracted from the data, but given the larger structural freedom associated with inhomogeneous mesophases, this exponent is no longer a unique fingerprint of the underlying mesostructure.

Consider, for example, the swelling of a hypothetical and likely anisotropic discrete micellar mesophase, containing (inhomogeneous) ellipsoidal micelles, rather than (homogeneous) spherical ones. Assume, for reckoning convenience, that the ellipsoids are surfaces of revolution, either oblate or prolate, depending on their aspect ratio, a/b (not to be confused with lattice parameters), where a refers to the semi-major axis of the ellipse along the axis of revolution of the ellipsoid, and b is the orthogonal semi-major axis (Figure 16.31). Choose a parametrization of the ellipsoid in terms of the surface coordinates (u, v) , as follows:

$$\begin{pmatrix} x_{u,v} \\ y_{u,v} \\ z_{u,v} \end{pmatrix} = \begin{pmatrix} a \cos(u) \cos(v) \\ a \sin(u) \cos(v) \\ c \sin(v) \end{pmatrix} \quad (16.11)$$

The curvatures, surface areas and volumes of ellipsoids of arbitrary aspect ratio can be calculated numerically. In order to determine the shape parameters (a distribution due to the inhomogeneity of the structure), we need estimates also of the population of chain lengths,

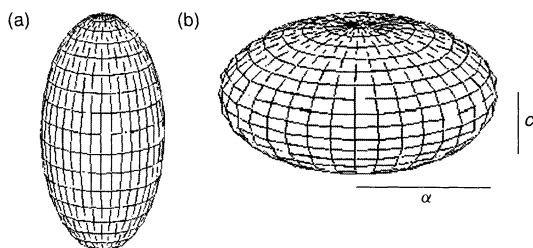


Figure 16.31. (a) Prolate (axial ratio 2), and (b) oblate (axial ratio $c/a = 0.5$) ellipsoids of revolution

$l_{u,v}$ within an ellipsoidal aggregate. (These are calculated from the *skeleton* of the structure (at intersections of parallel surfaces). The skeleton of prolate ellipsoids lies along the axis of revolution (the vertical axis in Figure 16.31; that of the oblates lies in the mirror plane normal to that axis.) We estimate an average shape parameter of the aggregate, $\langle s \rangle$, by weight-averaging local shape parameters by their surface area (i.e. weighted by the surface metric, $g_{u,v}$), as follows:

$$\begin{aligned} \langle s \rangle &\equiv \frac{\iint_{\text{ellipsoid}} s \, da}{\iint_{\text{ellipsoid}} da} \\ &= \frac{\iint_{u,v} \left(1 + H_{u,v} l_{u,v} + \frac{K_{u,v} l_{u,v}^2}{3} \right) \sqrt{g_{u,v}} \, du \, dv}{A} \end{aligned} \quad (16.12)$$

where A denotes the area of the ellipsoid (cf. equations (16.4) and (16.5)) and $g_{u,v}$ the metric.

The results are plotted in Figure 16.32. Prolate ellipsoids approach cylinders as their aspect ratio, $(c/a) \rightarrow \infty$, oblates approach discs as $a/c \rightarrow 0$, and their average shape parameters approach those of the cylinder (1/2) and plane (1), as expected.

The swelling exponents for ellipsoidal micelles can also be estimated from the volume and chain length data. These exponents are dependent on the details of the swelling mechanism. Assuming swelling occurs by parallel displacement of the polar–apolar interface (i.e. equal growth/shrinkage of the chain lengths – scaled by the average distance D between micelles – within the aggregate at all points (u, v) on the ellipsoid), the exponents are closely related to the average shape

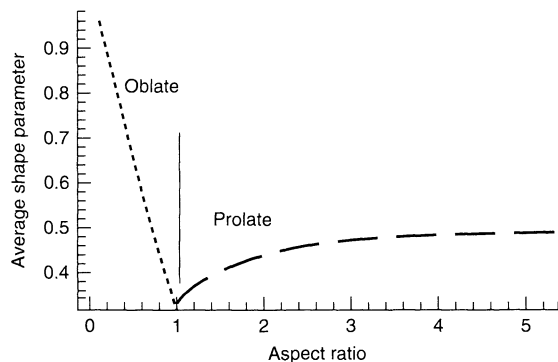


Figure 16.32. Variation of the average shape parameter of prolate and oblate ellipsoids (of revolution) as a function of the axial ratio

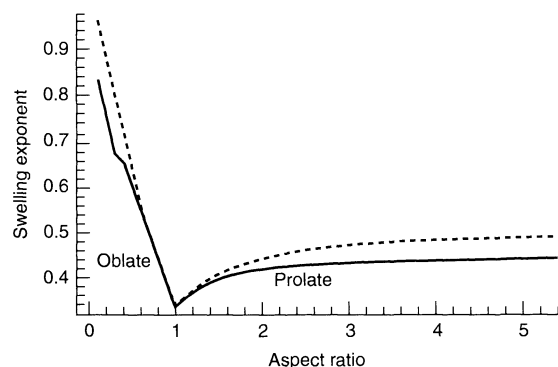


Figure 16.33. Variation of the swelling exponents of prolate and oblate ellipsoids (of revolution) as a function of the axial ratio (the dotted curves represent the average shape parameters)

parameters (as in the homogeneous cases), plotted in Figure 16.33. (Note that there is some deviation from power-law swelling, so the exponential fit is not exact, but deviations are small for moderately anisotropic micelles).

Swelling exponents between 0.33 and 0.45 (depending on the anisotropy of the micelle) are expected for prolate micelles, intermediate to the exponents for spherical and cylindrical columnar micelles. Oblate ellipsoidal micelles exhibit swelling exponents between 0.33 and 1. The upper bound – for very flat tablet-shaped micelles – overlaps with those of mesh and lamellar phases.

These data need to be approached with some caution. Note, in particular, that the exponents assume equal total (not fractional) swelling increments in all directions. Since the aggregates are themselves anisotropic, this swelling mode will deform the shape (e.g. the axial

ratio). Such a model is reasonable, although other swelling modes may operate in particular systems. (A simpler swelling model can be advanced, assuming isotropic fractional swelling, so that all lengths change by an equal fraction, thus retaining the anisotropy of the aggregate. Such a model recovers identical swelling exponents to those of the homogeneous aggregates, e.g. $1/3$ for all ellipsoidal aggregates. Such swelling behaviour is, however, less likely than that described above.)

Similar calculations can be done for ribbon mesophases. In these cases, flattening of the columnar aggregates increases the swelling exponents beyond the value for homogeneous hexagonal mesophases ($1/2$). Numerical estimates of the swelling of novel polycontinuous mesostructures – including multiple 3D networks, 3D rod and mesh packings, etc. – have not yet been made. Their geometry contains elements of sponges (saddle-shaped surfaces), columnar phases (line singularities) and discrete micellar phases (foams). Thus, it is expected that they are likely to be found in intermediate regions of the phase diagram, between discrete micellar and bicontinuous mesophases. Similarly, we expect their swelling exponents to lie in the range 0.4–0.7.

The neat distinction between morphologies and shape parameters/swelling exponents evident in Figure 16.8 is certainly obscured by the presence of inhomogeneous mesophases. In the homogeneous case, measurement of a swelling exponent is an unequivocal signature of the aggregate topology or geometry. Other data must be collected, such as viscosity and NMR data, before firm assignment of membrane topology and geometry can be made. However, we repeat that – at least until now – those lyotropic systems that are likely to form liquid crystalline mesophases are usually sufficiently homogeneous to rule out significant anisotropies or inhomogeneities in the aggregate shape.

4 MOLECULAR DIMENSIONS WITHIN LIQUID CRYSTALLINE MESOPHASES

The simplest check on the validity of a proposed mesostructure is to confirm that the various structural dimensions are commensurate with molecular values. In particular, the values of the chain length and head-group area should mirror values expected from the molecular dimensions. A number of formulae for calculating those parameters in lamellar and hexagonal mesophases can be found in the early review by Luzzati (4). Here, we will

give general formulae for globular, columnar, lamellar and bicontinuous phases.

First, the weight/weight composition of the lyotrope must be converted to polar and apolar volume fractions. To do this, we locate the interface at the polar–apolar boundary, and calculate the volume fractions of the polar and apolar moieties accordingly. This is a straightforward calculation, involving the densities of the amphiphile and solvent, and volume fraction of polar species per amphiphile molecule. This volume fraction, φ , is then used to determine the shape parameters within the mesostructure, by inverting the $\varphi(s)$ expressions given in Table 16.2 (see below). The inverse $s(\varphi)$ expressions are listed in Table 16.3 at the end of this review. Denote the volume fraction of the continuum φ_{out} , that of the interior of the aggregates φ_{in} . Thus, Type 1 mesophases have a chain volume fraction, φ_{chain} , of φ_{in} , while Type 2 phases have $\varphi_{\text{chain}} = \varphi_{\text{out}}$.

Consider first the “discrete” mesophases, containing isolated aggregates, i.e. lamellar, columnar and globular mesophases. Due to spatial frustration (which forbids dense packing of spheres or cylinders without some voids), we must include the dense packing fraction, f , for the aggregates, equal to the volume fraction of densely packed globules and columns (Figure 16.34). These parameters are listed in Table 16.2 below for the cubic and hexagonal dense packings of spheres and cylinders. Frustration requires rescaling of the continuum volume fraction, φ_{out} , to the equivalent frustration-free volume fraction.

By denoting the void volume, V_{void} , in a total volume of V and an exterior volume of V_{out} , we obtain the rescaled outer volume fraction as follows:

$$\varphi'_{\text{out}} = \frac{V - V_{\text{void}}}{V_{\text{out}} - V_{\text{void}}} = \frac{\varphi_{\text{out}} - (1 - f)}{f} \quad (16.13)$$

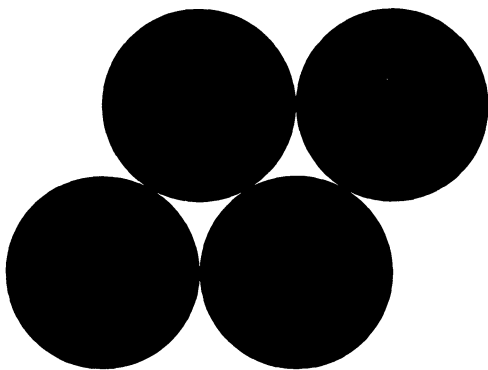


Figure 16.34. Dense packing of smoothly curved globular objects inevitably leaves voids – an example of spatial frustration

while the inner volume fraction remains unchanged, as it is frustration-free, i.e. $\varphi'_{\text{in}} = \varphi_{\text{in}}$. The shape parameters are then calculated from the inverse equations given in Table 16.3 below.

Given the shape parameters, generic equations can be drawn up for the molecular dimensions within the mesophase. We have the following:

$$s_{\text{in}} = \frac{\varphi_{\text{in}} V_{\text{cell}}}{A t_{\text{in}}}; s_{\text{out}} = \frac{\varphi'_{\text{out}} f V_{\text{cell}}}{A t'_{\text{out}}} \quad (16.14)$$

where A is the interfacial area within the total unit cell volume V_{cell} and t'_{out} is the thickness of the outer volume, excluding the voids. Equating areas gives the following relationships:

$$t_{\text{in}} = \frac{s_{\text{out}} t'_{\text{out}} \varphi_{\text{in}}}{s_{\text{in}} f \varphi'_{\text{out}}}; t_{\text{out}} = \frac{s_{\text{in}} t_{\text{in}} f \varphi'_{\text{out}}}{s_{\text{out}} \varphi_{\text{in}}} \quad (16.15)$$

Now, the combined thicknesses of the apolar and polar domains scales linearly with the lattice parameter of the mesophase, depending on the symmetry of the phase (see Table 16.4 below):

$$\kappa \equiv \frac{t_{\text{in}} + t'_{\text{out}}}{\alpha} \quad (16.16)$$

so that:

$$t_{\text{in}} = \frac{\kappa \alpha s_{\text{out}} \varphi_{\text{in}}}{s_{\text{out}} \varphi_{\text{in}} + s_{\text{in}} [\varphi_{\text{out}} - (1 - f)]};$$

$$t'_{\text{out}} = \frac{\kappa \alpha s_{\text{in}} [\varphi_{\text{out}} - (1 - f)]}{s_{\text{out}} \varphi_{\text{in}} + s_{\text{in}} [\varphi_{\text{out}} - (1 - f)]} \quad (16.17)$$

For amphiphile–water lyotropes of Type 1, these equations fix the molecular dimensions. Since the inner domain consists exclusively of amphiphile chains, t_{in} defines the average chain length in the aggregate, l . Similarly, Type 2 amphiphile–water lyotropes have an approximate chain length of t'_{out} . (Better estimates of the true unfrustrated length, t_{out} , can be achieved knowing the packing geometry, although the correction is small, except for small chain-volume fractions.) Chain lengths in more complex lyotropes, containing, for example, polar and apolar solvents, can also be determined with these equations.

Other structural parameters, including the head-group area per surfactant (a), and the aggregation number (number of amphiphiles per globular aggregate, N) can be reckoned also. The aggregation numbers within globular micelles, N , are given by the following:

$$N = \frac{\varphi_{\text{in}} V_{\text{cell}}}{n v_{\text{chains}}} \quad (\text{for Type 1 mesophases}) \quad (16.18)$$

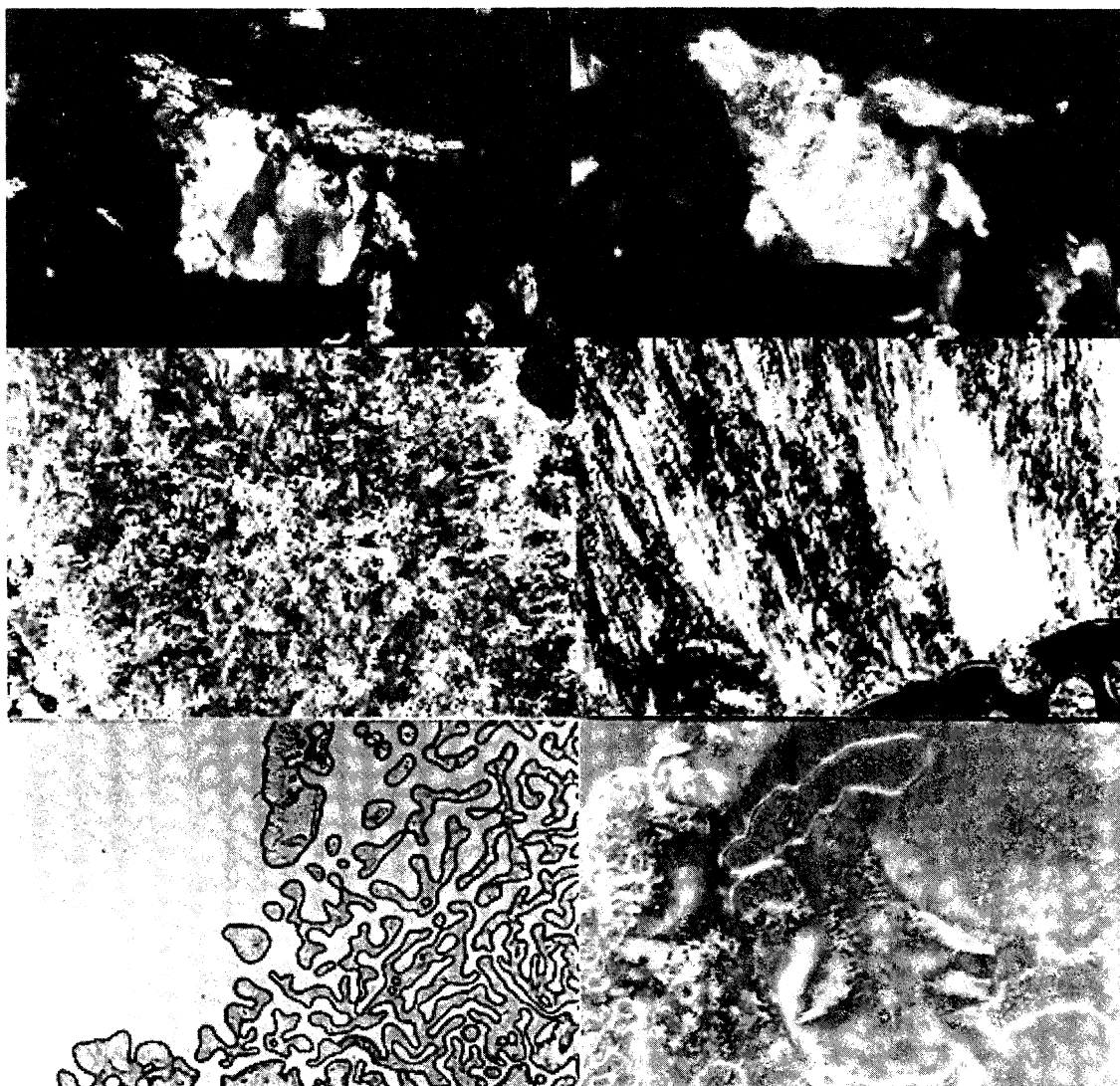


Figure 16.35 (Plate 1). All strontium myristate. Top left: 100× crossed polars – room-temperature *lamellar*. Top right: 100× crossed polars 90°C – *lamellar*. Middle left: 100× crossed polars, gypsum plate in, heated to 218°C – *rhombohedral*. Middle right: 200× crossed polars, gypsum plate in, cooled from rhombohedral–cubic phase boundary, oscillated near 210–215°C – *rhombohedral* (bright) and *cubic* (dark). Bottom left: 100× parallel polars, cooled to 210 from 218°C – *cubic* to *rhombohedral* transition. Bottom right: 200× crossed polars, gypsum plate in, cooled from 290°C and oscillated near 260°C – *hexagonal*

and:

$$N = \frac{\varphi_{\text{out}} V_{\text{cell}}}{n v_{\text{chains}}} \quad (\text{for Type 2 mesophases}) \quad (16.19)$$

The average head-group area per amphiphile are given by the expressions:

$$a = \frac{v_{\text{chains}}}{t_{\text{in}} s_{\text{in}}} \quad (\text{Type 1 mesophases}) \quad (16.20)$$

and:

$$\text{where } n \text{ denotes the number of globular micelles (aggregates) per crystallographic unit cell (see Table 16.4).} \quad a = \frac{v_{\text{chains}}}{t'_{\text{out}} s_{\text{out}}} \quad (\text{Type 2 mesophases}) \quad (16.21)$$

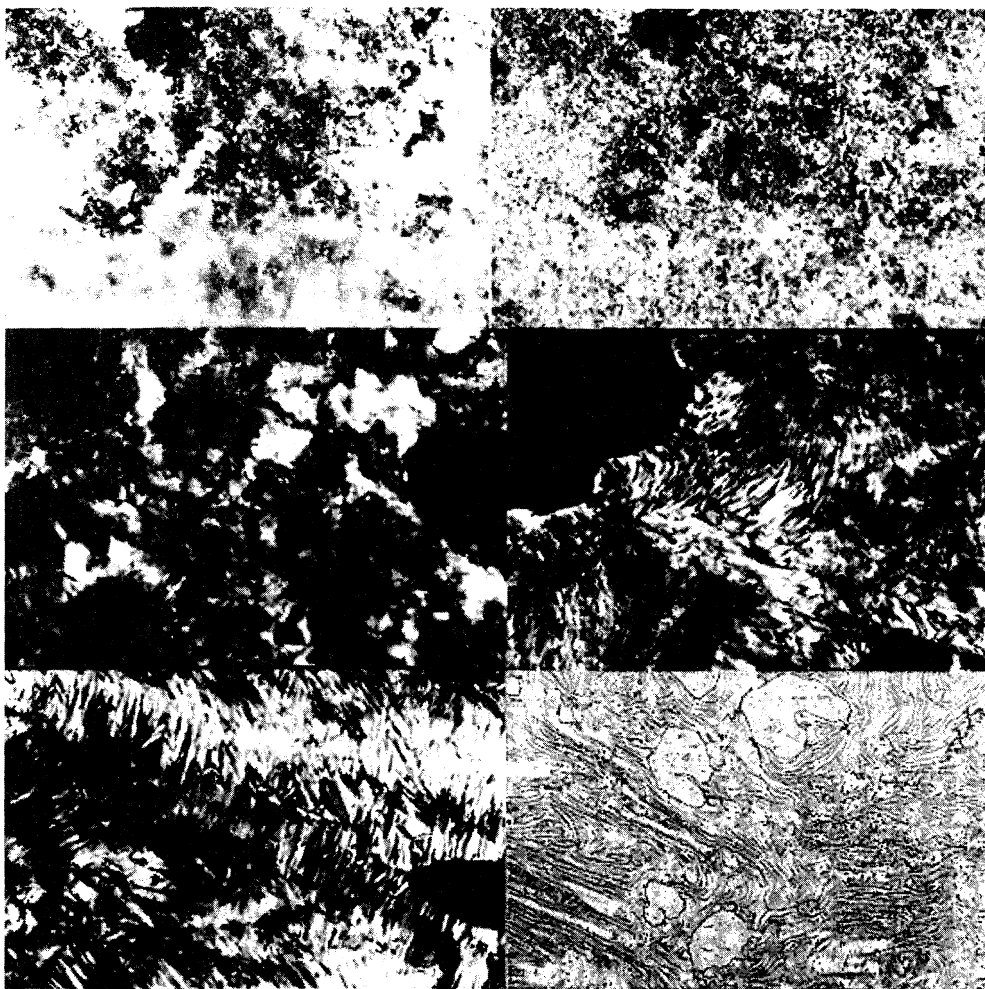


Figure 16.35 (Plate 2). All copper myristate. Top left: 100× crossed polars, 70°C – *lamellar*. Top right: 100× crossed polars, 116.3°C – *lamellar*. Middle left: 100× crossed polars, 140.0°C – *hexagonal*. Middle right: 100× crossed polars, 198°C – *hexagonal*. Bottom left: 100× parallel polars, cooled from 190.8°C to room temperature – *lamellar* with remnant *hexagonal* textures

Analogous calculations for bicontinuous mesophases can be carried out (the results are plotted in Figure 16.21). In this case, the spatial frustration is reflected in the homogeneity index (h) for the particular mesophase. The equations have been derived in detail elsewhere (11). For Type 1 bicontinuous mesophases, the chain length is equal to the inner thickness, as follows:

$$l = t_{in} = \left[\frac{h}{4\pi(g-1)} \right]^{1/3} (\gamma - 1) \quad (16.22)$$

where γ is the single physical root:

$$3\gamma - \gamma^3 = \varphi_{\text{polar}} \quad (16.23)$$

For Type 2 bicontinuous mesophases, the chain length is equal to the inner thickness, given by:

$$l = t_{out} = \alpha \left[\frac{h}{4\pi(g-1)} \right]^{1/3} \left[\sqrt{3} \sin\left(\frac{\Delta}{3}\right) - \cos\left(\frac{\Delta}{3}\right) \right] \quad (16.24)$$

where:

$$\Delta = \pi + \tan^{-1} \left(\frac{\sqrt{1 - \varphi_{\text{chains}}^2}}{-\varphi_{\text{chains}}} \right) \quad (16.25)$$

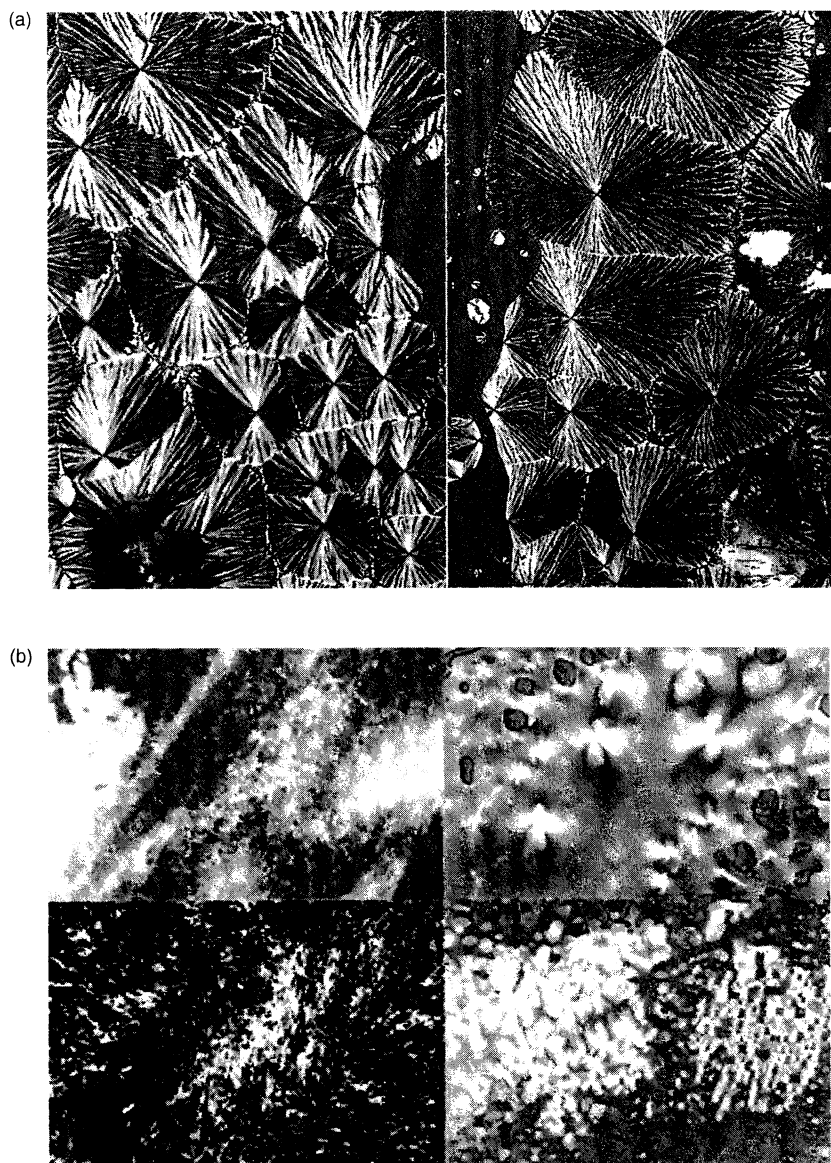


Figure 16.35 (Plate 3). (a) Zirconium myristate/myristic acid, cooled to room temperature from 119°C, gypsum plate in – *hexagonal*. Left image, 40× crossed polars; right image, 100× crossed polars. (b) All calcium myristate. Top left: 100× crossed polars, gypsum plate in, heated to 90.2°C – *lamellar*. Top right: 100× crossed polars, gypsum plate in, cooled to 90°C – *lamellar*. Bottom left: 100× crossed polars, 144.8°C – *tetragonal*. Bottom right: 100× crossed polars, gypsum plate in, cooled to 20 from 90°C – *lamellar*

5 ACKNOWLEDGEMENTS

I am particularly grateful to my colleagues, Robert Corkery, Jevon Longdell, Maura Monduzzi and Stuart Ramsden, for providing me with sample data and model structures.

6 REFERENCES

1. Seddon, J., in *Handbook of Liquid Crystals*, Vol. 1, Demus, D. (Ed.), Wiley, New York 1998, Section 8.4.

www.iran-mavad.com

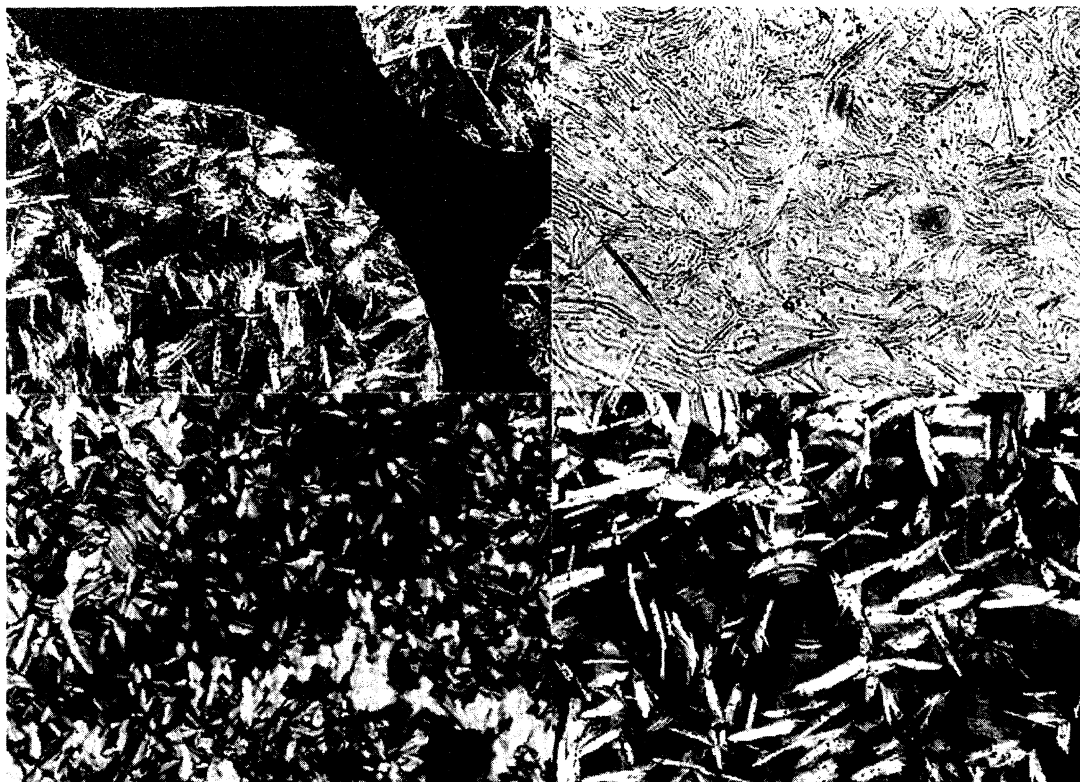


Figure 16.35 (Plate 4). All lead myristate. Top left: 100× crossed polars, gypsum plate in, cooled from melt into “bâtonnet” (crystalline phase). Top right: 100× partially crossed polars, gypsum plate in, ca. 108–110°C, cooling transition from hexagonal to bâtonnet. Bottom left: 200× crossed polars, gypsum plate in, 112°C, cooled from melt into hexagonal. Bottom right: 200× crossed polars, gypsum plate in, ca. 108–110°C, cooling transition from hexagonal to bâtonnet

- Blackmore, E. S. and Tiddy, G. J. T., Phase behaviour and lyotropic liquid crystals in cationic surfactant–water systems, *J. Chem. Soc., Faraday Trans. 2*, **84**, 1115–1127 (1988).
- Israelachvili, J. N., Mitchell, D. J. and Ninham, B. W., Theory of self-assembly of hydrocarbon amphiphiles into micelles and bilayers, *J. Chem. Soc., Faraday Trans. 2*, **72**, 1525–1568 (1976).
- Luzzati, V., X-ray diffraction studies of lipid–water systems, in *Biological Membranes*, Chapman, D. (Ed.), Academic Press, New York, 1968, pp. 71–123.
- Hyde, S. T., Andersson, S., Larsson, K., Blum, Z., Landh, T., Lidin, S. and Ninham, B. W., *The Language of Shape*, Elsevier, Amsterdam, 1997.
- McGrath, K. and Kléman, M., Spiral textures in lyotropic liquid crystals: First order transition between normal hexagonal and lamellar gel phases, *J. Phys. II (France)*, **3**, 903–926 (1993).
- Hagblätt, H., The structure of intermediate ribbon phases in surfactant systems, *Liq. Crys.*, **12**, 667–688 (1992).
- Seddon, J. and Robins, J., Inverse micellar lyotropic cubic phases, in *Foams and Emulsions*, Sadoc J. F. and Rivier, N. (Eds), Kluwer, Dordrecht, The Netherlands, 1999, pp. 423–430.
- Clerc, M., A new symmetry for the packing of amphiphilic direct micelles, *J. Phys. II (France)*, **6**, 961–968 (1996).
- Hyde, S. T., Bicontinuous structure in lyotropic liquid crystals and crystalline hyperbolic surfaces, *Curr. Opinion Solid State Mater. Sci.*, **1**, 653–662 (1996).
- Engblom, J. and Hyde, S. T., On the swelling of bicontinuous lyotropic mesophases, *J. Phys. II (France)*, **5**, 171–190 (1995).
- Anderson, D. M. and Wennerström, H., Self diffusion in bicontinuous cubic phases, L₃ phases and microemulsions, *J. Phys. Chem.*, **94**, 8683–8694 (1990).
- Eriksson, P. O. and Lindblom, G., Lipid and water diffusion in bicontinuous cubic phases measured by NMR, *Biophys. J.*, **64**, 129–136 (1992).
- Anderson, D. M., A new technique for studying microstructures: ²H bandshapes of polymerised

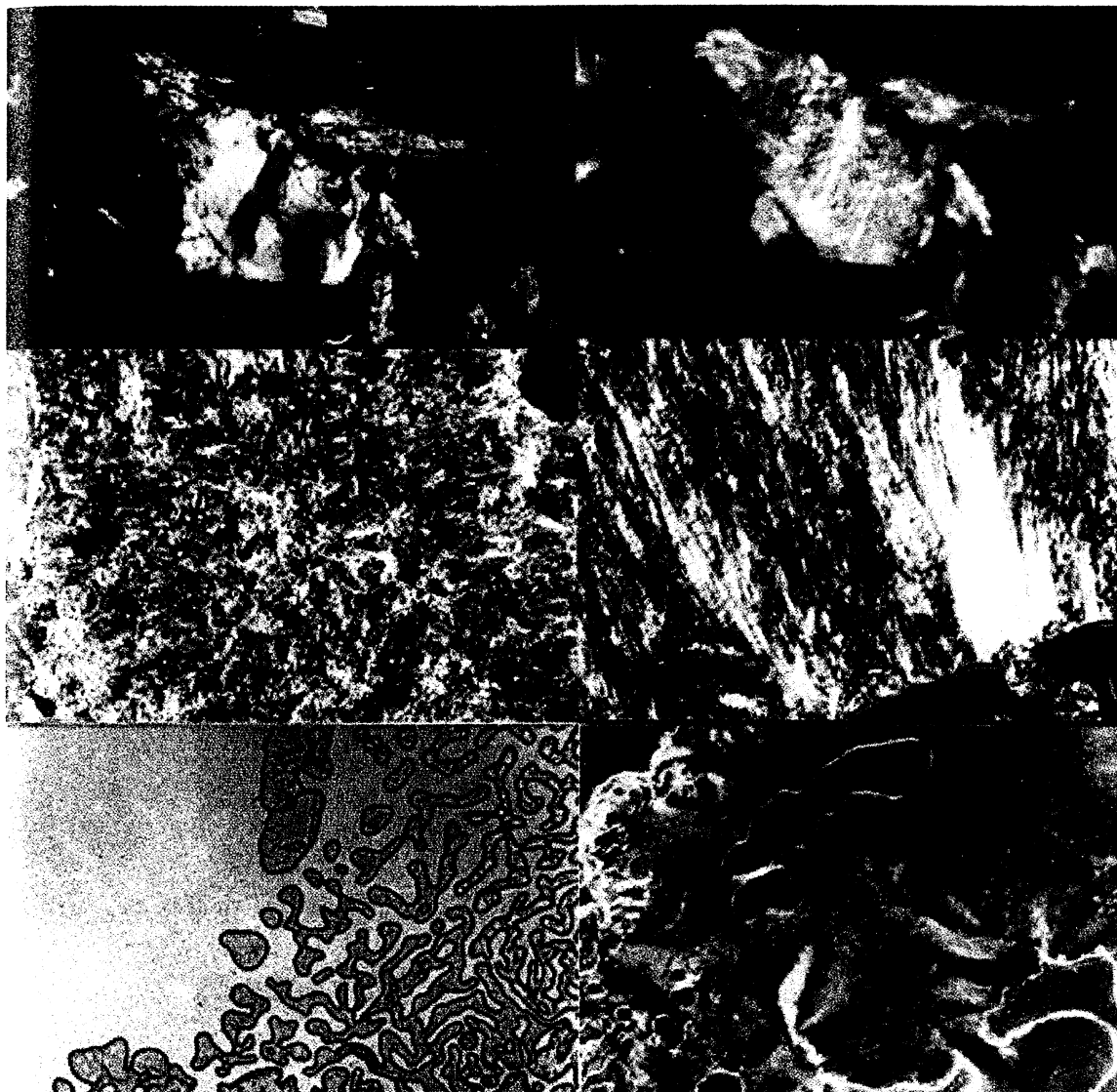


Plate 1 All strontium myristate. Top left: 100× crossed polars – room-temperature *lamellar*. Top right: 100× crossed polars 90°C – *lamellar*. Middle left: 100× crossed polars, gypsum plate in, heated to 218°C – *rhombohedral*. Middle right: 200× crossed polars, gypsum plate in, cooled from rhombohedral–cubic phase boundary, oscillated near 210–215°C – *rhombohedral* (bright) and *cubic* (dark). Bottom left: 100× parallel polars, cooled to 210 from 218°C – *cubic* to *rhombohedral* transition. Bottom right: 200× crossed polars, gypsum plate in, cooled from 290°C and oscillated near 260°C – *hexagonal* (see also **Figure 16.35**, page 325)

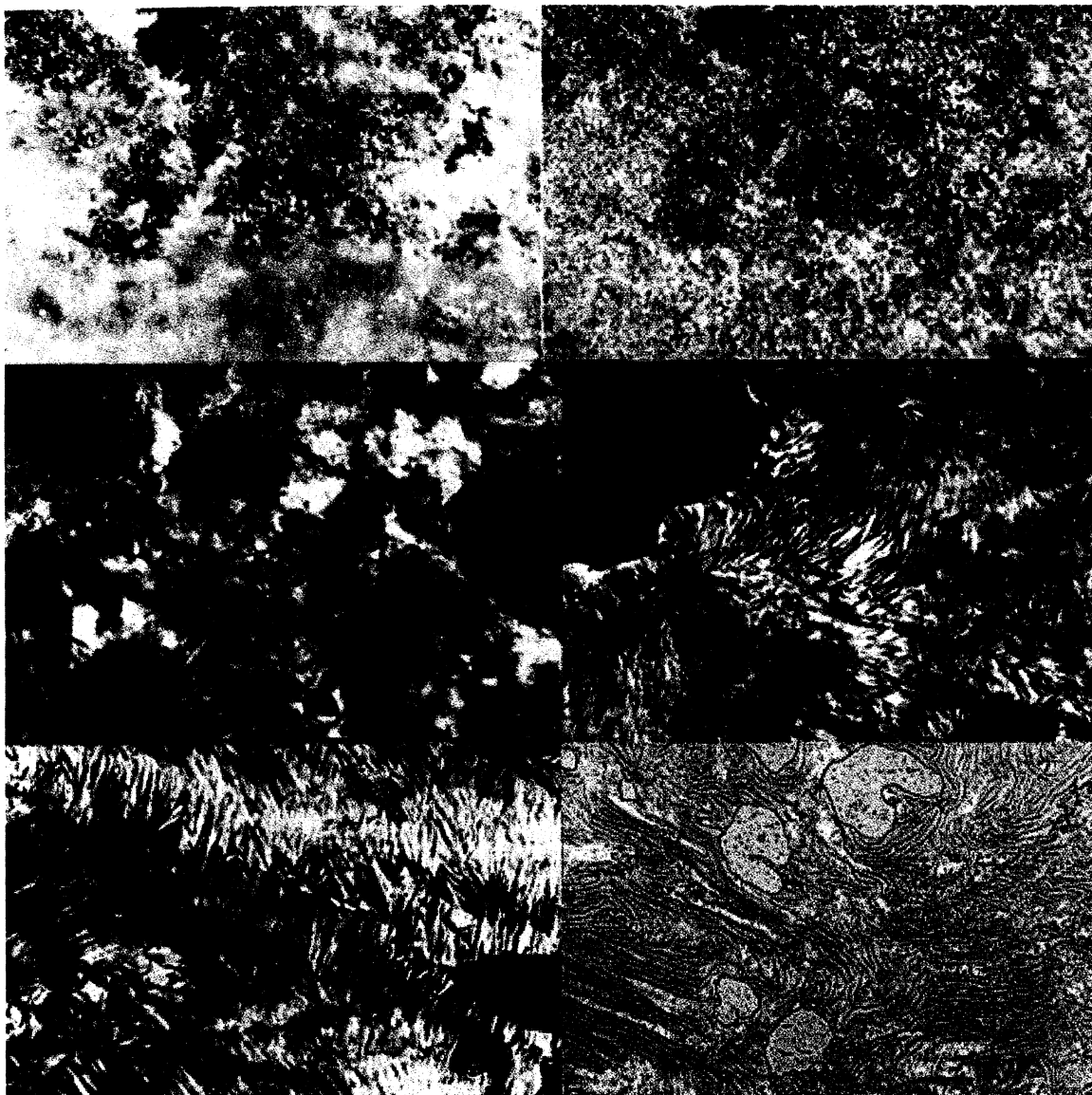
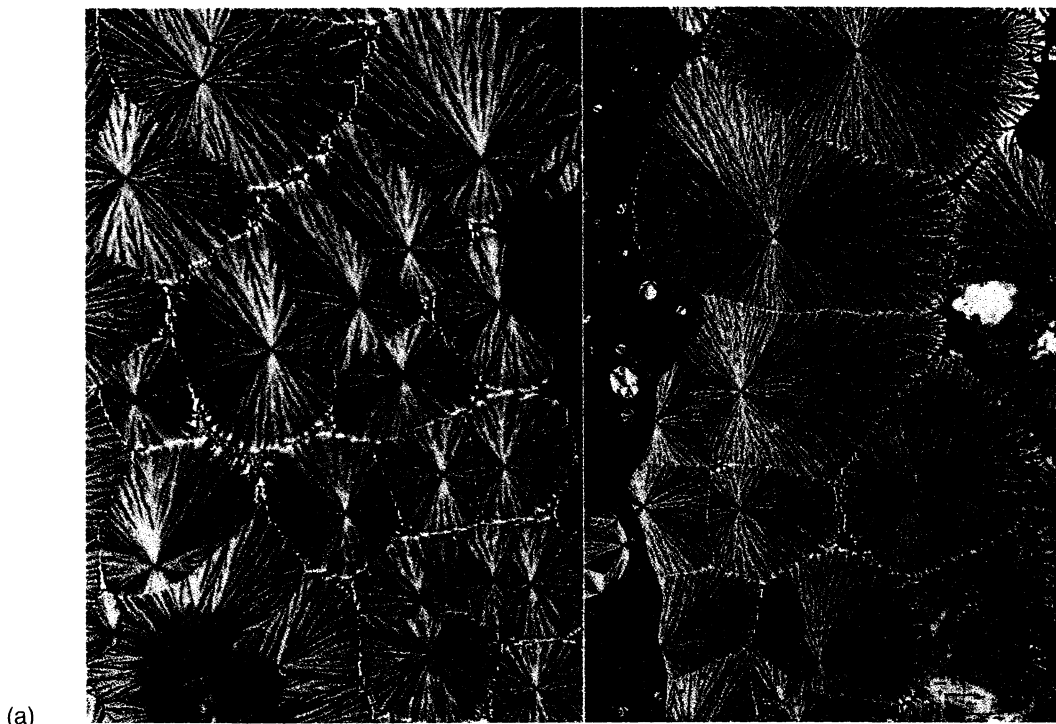
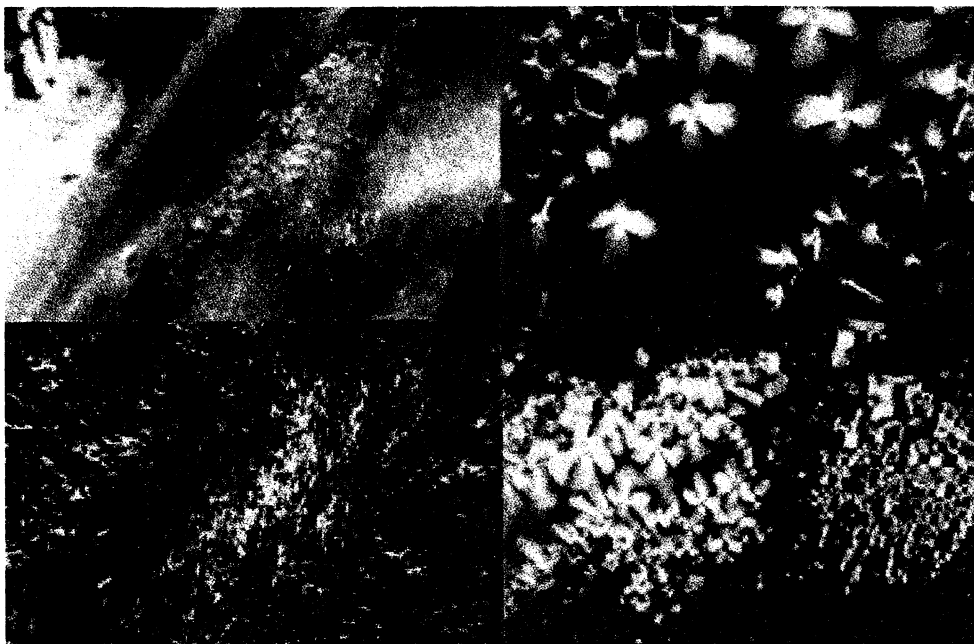


Plate 2 All copper myristate. Top left: 100× crossed polars, 70°C – *lamellar*. Top right: 100× crossed polars, 116.3°C – *lamellar*. Middle left: 100× crossed polars, 140.0°C – *hexagonal*. Bottom left: 200× crossed polars, 198°C – *hexagonal*. Bottom right: 100× parallel polars, cooled from 190.8°C to room temperature – *lamellar* with remnant *hexagonal* textures (see also **Figure 16.35**, page 326)



(a)



(b)

Plate 3 (a) Zirconium myristate/myristic acid, cooled to room temperature from 119°C, gypsum plate in – *hexagonal*. Left image, 40× crossed polars; right image, 100× crossed polars. (b) All calcium myristate. Top left: 100× crossed polars, gypsum plate in, heated to 90.2°C – *lamellar*. Top right: 100× crossed polars, gypsum plate in, cooled to 90°C – *lamellar*. Bottom left: 100× crossed polars, 144.8°C – *tetragonal*. Bottom right: 100× crossed polars, gypsum plate in, cooled to 20 from 90°C – *lamellar* (see also **Figure 16.35**, page 327)

www.iran-mavad.com

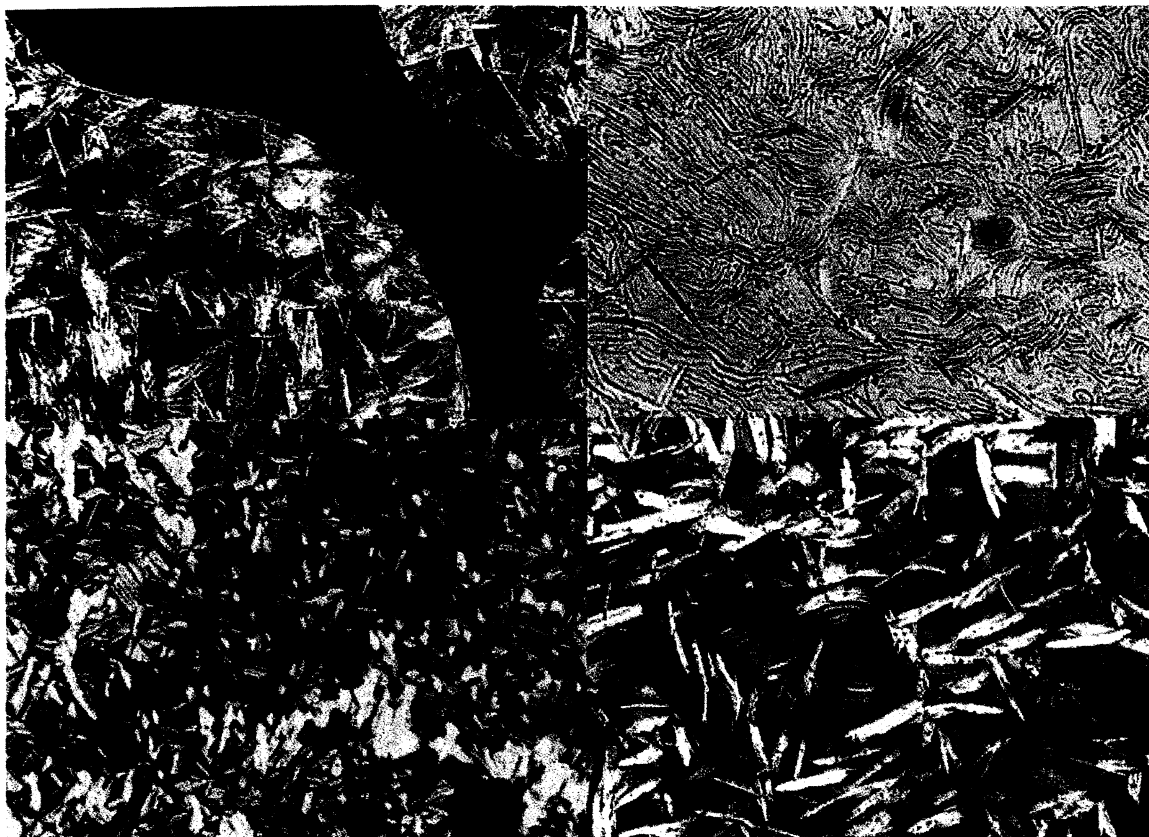


Plate 4 All lead myristate. Top left: 100× crossed polars, gypsum plate in, cooled from melt into “*bâtonnet*”(crystalline phase). Top right: 100× partially crossed polars, gypsum plate in, ca. 108–110°C, cooling transition from *hexagonal* to *bâtonnet*. Bottom left: 200× crossed polars, gypsum plate in, 112°C, cooled from melt into *hexagonal*. Bottom right: 200× crossed polars, gypsum plate in, ca. 108–110°C, cooling transition from *hexagonal* to *bâtonnet* (see also **Figure 16.35**, page 328)

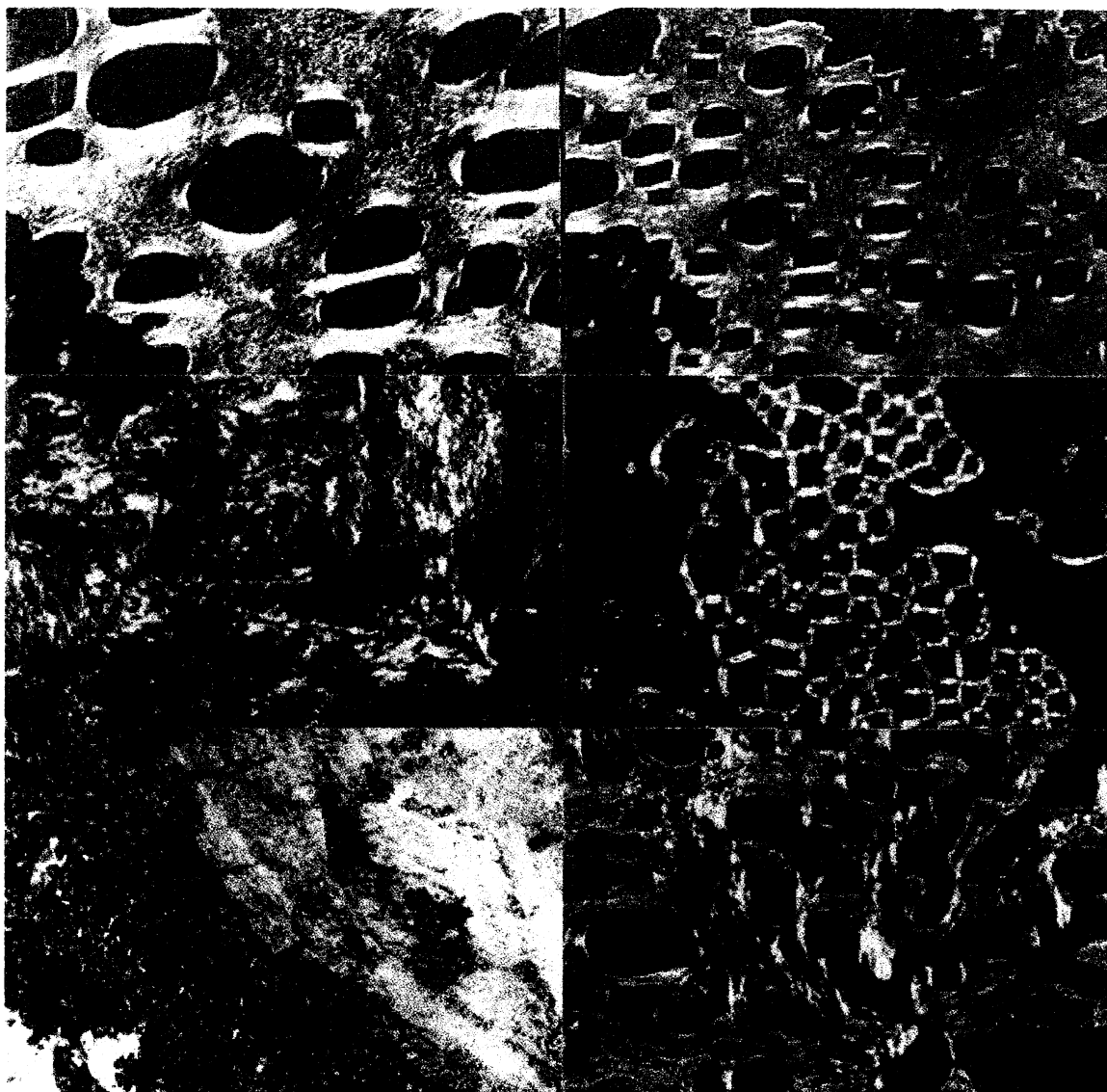


Plate 5 Top left: lanthanum myristate (Lamy), 100× crossed polars, gypsum plate in, 120.1°C – *smectic C*. Top right: Lamy, 100× crossed polars, gypsum plate in, 152.3°C – *smectic C'*. Middle left: lanthanum palmitate, 100× crossed polars, gypsum plate in, 126.3°C – *smectic C*. Middle right: Lamy, 100× crossed polars, gypsum plate in, 152.3°C – immediately post melting. Bottom left: cerium stearate (Cest), 100× crossed polars, 79.6°C – *lamellar*. Bottom right: Cest, 100× crossed polars, gypsum plate in, 124.0°C – *smectic C* (see also **Figure 16.35**, page 329)

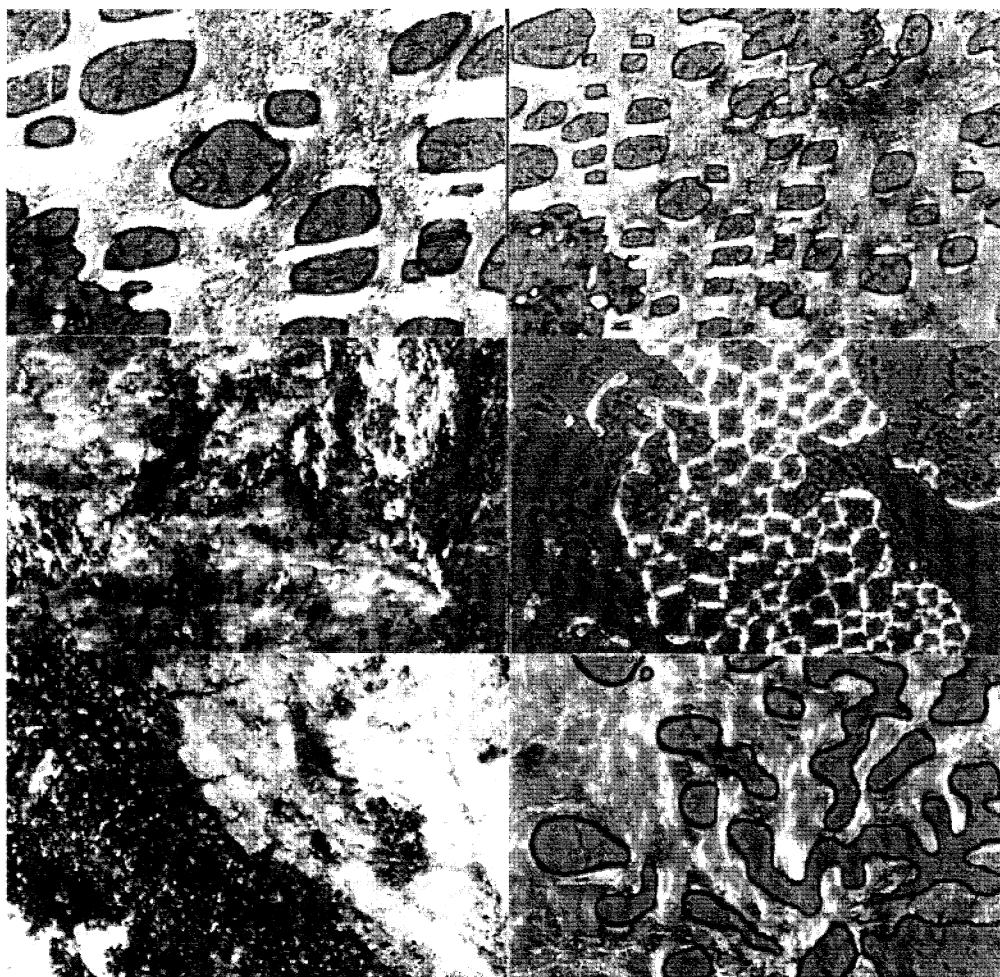


Figure 16.35 (Plate 5). Top left: lanthanum myristate (Lamy), 100× crossed polars, gypsum plate in, 120.1°C – *smectic C*. Top right: Lamy, 100× crossed polars, gypsum plate in, 152.3°C – *smectic C'*. Middle left: lanthanum palmitate, 100× crossed polars, gypsum plate in, 126.3°C – *smectic C*. Middle right: Lamy, 100× crossed polars, gypsum plate in, 152.3°C – immediately post melting. Bottom left: cerium stearate (Cest), 100× crossed polars, 79.6°C – *lamellar*. Bottom right: Cest, 100× crossed polars, gypsum plate in, 124.0°C – *smectic C*

surfactants and counterions in microstructures described by minimal surfaces, *J. Phys. (France)*, Colloque C-7, **51** (Suppl.), C7-1–C7-409 (1990).

15. Luzzati, V., Tardieu, A. and Gulik-Krzywicki, T., Polymorphism of lipids, *Nature (London)*, **217**, 1028–1030 (1968).
16. Rendall, K., Tiddy, G. J. T. and Trevethan, M. A., Optical microscopy and NMR studies of mesophases formed at compositions between hexagonal and lamellar phases in sodium *n*-alkanoate + water mixtures and related surfactant systems, *J. Chem. Soc., Faraday Trans. 1*, **79**, 637–649 (1983).

17. Fontell, K., X-ray diffraction by liquid crystals – amphiphilic systems, in *Liquid Crystals and Plastic Crystals*, Vol. 2, Gray, G. W. and Winsor, P. A. (Eds), Ellis Horwood, Chichester, 1974, pp. 80–109.
18. Fogden, A. and Hyde, S. T., Continuous transformations of cubic minimal surfaces, *Eur. J. Phys., B*, **7**, 91–104 (1999).
19. O'Keeffe, M. and Hyde, B. G., *Crystal Structures I. Patterns and Symmetry*, Mineralogical Society of America, Washington, DC, 1996.
20. Hyde, S. T., Swelling and structure, *Langmuir*, **13**, 842–851 (1997).

Table 16.1. Lyotropic liquid crystalline mesophases that are currently recognized; the ratio s of spacings between allowed (reciprocal) lattice Bragg reflections are listed

Class	Mesophase	Descriptor (homogeneity index, γ , g)	Symmetry (dimensionality)	Peak ratios (observed reciprocal spacings) or (hk) (2D), (hkl) (3D) reflections	Notes All phases have diffuse ca. 4.2 \AA^{-1} wide-angle scattering peaks, except L_β
<i>Smectic</i>	Lamellar	L_α, L_β	Smectic (1D)	1:2:3:4 ... , etc.	Gel phase, L_β , also has 2D chain (wide-angle) lattice
<i>Mesh</i>	Rhombohedral	R_1, R_2	(1D)	1:2:3:4 ... , etc.	Turbostratic (no in-plane register between sheets) Dependent on a α cell parameters ^a
	Tetragonal	T_1, T_2	$R\bar{3}m$ (3D) (1D) I422 (3D)	(003), (101), (012) ... (006) (most intense reflections only) 1:2:3:4 ... , etc. (002), (101), (110) ... (103), ... (004)	Turbostratic Dependent on α, c cell parameters. $d^{-2} = (h\alpha^*)^2 + (k\alpha^*)^2 + (lc^*)^2$
<i>Sponge</i>	Bicontinuous cubics (V_1, V_2)	P ($Q^{229}, Im\bar{3}m$) (0.716,3,3) D ($Q^{224}, Pn\bar{3}m$) (0.750,2,3) G ($Q^{230}, Ia\bar{3}d$) (0.766,5,3)	$Im\bar{3}m$ (3D) $Pn\bar{3}m$ (3D) $Ia\bar{3}d$ (3D)	$\sqrt{2}:\sqrt{4}:\sqrt{6}:\sqrt{8}:\sqrt{10} \dots$, etc. (most intense reflections only) $\sqrt{2}:\sqrt{3}:\sqrt{4}:\sqrt{6}:\sqrt{8} : \dots$, etc. $\sqrt{6}:\sqrt{8}:\sqrt{14}:\sqrt{16}:\sqrt{18}:\sqrt{20}$: etc.	Other structures have been suggested: I-WP ($Im\bar{3}m$) (0.742,4,4) F-RD ($Fm\bar{3}m$) (0.658,4,6) C(P) ($Im\bar{3}m$) (0.664,9,9)
<i>Columnar</i>	Hexagonal (H_1, H_2)	$p6m$	(2D)	$\sqrt{3}:\sqrt{4}:\sqrt{7}:\sqrt{12}$	–
	Ribbon	cmm (centred rectangular) $pmm, pgg, p2$	(2D) (2D)	(11):(20):(22):(31):(40):... , etc. –	“Intermediate” spacings depend on α, β parameters: $d^{-2} = (h\alpha^*)^2 + (k\beta^*)^2$ Primitive rectangular and oblique phases also reported
<i>Micellar</i>	Discrete cubic (I_1, I_2)	–	bcc packing $Im\bar{3}m$ (3D) fcc packing $Fm\bar{3}m$ (3D) $Pm\bar{3}n$ (3D) $Fd\bar{3}m$ (3D)	$\sqrt{2}:\sqrt{4}:\sqrt{6}:\sqrt{8}:\sqrt{10} \dots$, etc. $\sqrt{3}:\sqrt{4}:\sqrt{8}:\sqrt{11}:\sqrt{12} \dots$, etc. $\sqrt{2}:\sqrt{4}:\sqrt{5}:\sqrt{6}:\sqrt{8} : \dots$, etc. $\sqrt{3}:\sqrt{8}:\sqrt{11}:\sqrt{12}:\sqrt{16}$	Bilayer lines the faces of the Kelvin foam – Clathrate Clathrate (two distinct micelles)
	Hexagonal micellar	–	$P6_3mmc$ (3D)	$\sqrt{(4/3)}:\sqrt{(4/R^2)}:\sqrt{(4/3 + 1/R^2)}:$ $\sqrt{(4/3 + 4/R^2)}:\sqrt{4}$	One case reported to date ($R = 1.6$) ^b

^aNote: for rhombohedral lattices, angle θ , the (hkl) spacings scale as:

$$\sqrt{\frac{h^2 + k^2 + l^2 + [h^2 + (k-l)^2 - 2h(k+l)] \cos(\vartheta)}{1 + \cos(\vartheta) - 2\cos^2(\vartheta)}}$$

^bSee ref. (9).

Table 16.2. Shape parameters (equations (16.1) and (16.4)) and approximate swelling exponents (s and s' , cf. equation (16.8)) for known lyotropic mesophases. The (variable) constants “ h ” and “ f ” depend on the specific symmetry of the phase (“ h ” is the homogeneity index, ideal equal to $3/4$ (cf. Table 16.1); “ f ” is the interstitial packing fraction for dense sphere and circle packings, equal to unity for ideal homogeneous packings)

Mesophase	Shape parameter, Type 1 (\approx swelling exponents: s (Type 1), s' (Type 2)) (apolar volume fraction, $\varphi(s)$ variation)	Shape parameter, Type 2 (apolar volume fraction, $\varphi(s)$ variation)
<i>Lamellar</i>	1	1
<i>Sponge</i>	$\frac{1}{2} \leftrightarrow \frac{2}{3}$ $\varphi(s) = \frac{8}{3}h \left[\frac{s \left(s - \frac{1}{2} \right)^2}{\left(s - \frac{1}{3} \right)^3} \right], h \approx \frac{3}{4}$	$\succ \frac{2}{3}$ $\varphi(s) = \frac{4}{3}h \left[\frac{s(s-1)^{1/2}}{\left(s - \frac{1}{3} \right)^{3/2}} \right], h \approx \frac{3}{4}$
<i>Mesh</i>	$\frac{1}{2} \leftrightarrow \frac{2}{3}$ $\varphi(s) < \frac{4}{3}h \left[\frac{s \left(s - \frac{1}{2} \right)^2}{\left(s - \frac{1}{3} \right)^3} \right], h \approx \frac{3}{4}$	$\succ \frac{2}{3}$ $\varphi(s) < \frac{4}{3}h \left[\frac{s \left(s - \frac{1}{2} \right)^2}{\left(s - \frac{1}{3} \right)^3} \right], h \approx \frac{3}{4}$
<i>Columnar: Circular cylinders</i>	$\frac{1}{2}$	$\succ 1$ $\varphi(s) \approx f \left[\frac{s(s-1)}{\left(s - \frac{1}{2} \right)^2} \right] + (1-f)$ $f \approx 0.905$ (hexagonal)
<i>Globular: spherical micelles</i> (cf. Figures 16.29 and 16.33 for ellipsoidal micelles)	$\frac{1}{3}$	$\succ 1$ $\varphi(s) \approx f \left[\frac{s(3-18s+18s^2-(12s-3)^{1/2})}{18 \left(s - \frac{1}{3} \right)^3} \right] + (1-f)$ $f \approx 0.740$ (fcc, hcp), 0.710 (Fd $\bar{3}$ m), 0.680 (bcc), 0.523 (Pm $\bar{3}$ n)
<i>Bicontinuous monolayers</i>	$\frac{1}{2} \leftrightarrow \frac{2}{3}$ $\varphi(s) = \frac{4}{3}h \left[\frac{s \left(s - \frac{1}{2} \right)^2}{\left(s - \frac{1}{3} \right)^3} \right], h \approx \frac{3}{4}$	$\succ \frac{2}{3}$ $\varphi(s) = \frac{4}{3}h \left[\frac{s \left(s - \frac{1}{2} \right)^2}{\left(s - \frac{1}{3} \right)^3} \right], h \approx \frac{3}{4}$

Table 16.3. Formulae for calculations of molecular dimensions within a lyotropic mesophase (see Table 16.2 for further legends)

Mesophase	Inner shape parameter, s_{in} (surfactant parameter for Type 1 phases)	Outer shape parameter, s_{out} (surfactant parameter for Type 2 phases)
<i>Lamellar</i>	$\Delta(\varphi_{in}) = \frac{1}{3} \cos^{-1} \left(1 - \frac{4h\varphi_{out}}{3} \right)$	$\Delta(\varphi_{out}) = \frac{1}{3} \cos^{-1} \left(\frac{4h\varphi_{out}}{3} \right)$
<i>Sponge</i>	$s(\varphi_{in}) = \cos[\Delta(\varphi_{in})] - 3^{1/2} \sin[\Delta(\varphi_{in})]$	$s(\varphi_{out}) = \frac{3 - \{\cos[\Delta(\varphi_{out})] - 3^{1/2} \sin[\Delta(\varphi_{out})]\}^2}{3 - 3\{\cos[\Delta(\varphi_{out})] - 3^{1/2} \sin[\Delta(\varphi_{out})]\}^2}$
<i>Columnar: Circular cylinders</i>	$\frac{1}{2}$	$\varphi'_{out} = \frac{\varphi_{out} - (1 - f)}{f}$
		$s(\varphi'_{out}) \approx \frac{1}{2} \left[1 + \left(\frac{1}{1 - \varphi'_{out}} \right)^{1/2} \right]$
<i>Globular: Spherical micelles</i>	$\frac{1}{3}$	$\varphi'_{out} = \frac{\varphi_{out} - (1 - f)}{f}$
		$s(\varphi'_{out}) \approx \frac{1}{3} \left[1 + \left(\frac{1}{1 - \varphi'_{out}} \right)^{1/3} + \left(\frac{1}{1 - \varphi'_{out}} \right)^{2/3} \right]$

Table 16.4. Relationships between lattice parameter (α) and combined polar and apolar thicknesses

Mesophase	Lattice parameter/total aggregate thickness, $\frac{t_{in} + t_{out}}{\alpha}$	Number of aggregates per unit cell
H: hexagonal (p6mm cylinder packing)	$\frac{1}{2}$	1
I: fcc (Fm $\bar{3}$ m sphere packing)	$\frac{\sqrt{2}}{4}$	4
I: bcc (Im $\bar{3}$ m sphere packing)	$\frac{\sqrt{3}}{4}$	2
I: clathrate 1 (Pm $\bar{3}$ n sphere packing)	$\frac{\sqrt{2}}{4}, \frac{1}{4}$	6
I: clathrate 2 (Fd $\bar{3}$ m sphere packing)	$\frac{\sqrt{11}}{16}, \frac{\sqrt{3}}{8}$	24

CHAPTER 17

Characterization of Microemulsion Structure

Ulf Olsson

Lund University, Lund, Sweden

1	Introduction	333	7.1	The emulsification failure and spherical microemulsion droplets	344
2	Experimental Techniques	334	7.2	Solubilization limits from curvature energy	345
2.1	NMR self-diffusion	334	7.3	Experimental system	345
2.2	NMR spin relaxation	334	7.4	Droplet radius and volume fraction	345
2.3	Electrical conductivity	335	7.5	Proof of a discrete droplet structure from self-diffusion data	346
2.4	Small-angle scattering	335	7.6	Hydrodynamic radius	347
2.5	Light scattering	335	7.7	Concentration dependence or independence of droplet size	347
2.6	Viscosity	335	7.8	NMR relaxation	347
2.7	Electron microscopy	335	7.9	Small-angle neutron scattering	347
3	Curvature and Curvature Energy	336	7.10	Interactions	349
3.1	Surfactant film curvature	336	7.11	Static light scattering	349
3.2	The flexible surface model	336	7.12	Low shear viscosity	349
3.3	Competing microstructures and their curvatures	336	7.13	Diffusion	350
4	Useful Experimental Systems: The Oligoethylene Oxide Surfactants	337	8	The Droplet to Bicontinuous Transition	351
5	Phase Behaviour	338	9	Sponge Phases	352
5.1	General phase equilibria	338	10	References	355
6	Structural Inversion and the Spectrum of Microstructures	342			
7	Characterization of a Droplet Microemulsion	344			

1 INTRODUCTION

The fact that aqueous surfactant solutions can solubilize non-water-soluble compounds has been known for a long time. Studies of this phenomenon were mostly restricted to the relatively weak solubilization power of ionic surfactants until Schulman in 1943 demonstrated that comparable amounts of water and oil could be made

miscible by adding, in addition to an ionic surfactant, an alcohol. Fifteen years later he gave these thermodynamically stable solutions the name “microemulsions”, being convinced that their microstructures were simply miniature emulsion droplets of either kind. Today, we know that the structural polymorphism of microemulsions is much richer than this, i.e. droplets are not necessarily spherical and the structure can also be bicontinuous.

Oil and water do not mix, but one-phase systems with substantial amounts of both of these components can form in the presence of surfactant. In these phases, oil and water still do not mix on the molecular level and there are domains of water and oil of a colloidal size. These polar and apolar regions are separated by a monolayer film of surfactant molecules. The domains can be macroscopically ordered, in which case we have a liquid crystal, or they can be disordered, forming an isotropic liquid phase. At a given composition of oil, water and surfactant, the oil/water ratio determines the relative volume fraction of apolar and polar domains, while the polar/apolar interfacial area is fixed by the surfactant content. It is important to realize that space can be divided into two different types of regions in many different ways even when the area-to-volume ratio is fixed. This is the basis of the rich variation of structures found in surfactant–water–oil systems. The main thermodynamic driving force for making oil and water mix into a homogeneous phase comes from the preference for the surfactant to form a monolayer. However, given a certain polar/apolar interfacial area, other more subtle effects determine the preference for one structure relative to another. In our current understanding, the three most important free energy contributions are due to the curvature of the surfactant monolayers, entropies on the aggregate level and surface forces or aggregate interactions.

In this present chapter, we will discuss how we can characterize microemulsion structures. A number of different experimental methods will be mentioned but we will mainly focus on results obtained by nuclear magnetic resonance (NMR) self-diffusion measurements since this is a straightforward approach to distinguish between droplet and bicontinuous structures. Examples from structural studies will mainly be taken from non-ionic surfactant systems since such surfactants are capable of forming the whole spectrum of microemulsion structures without the addition of cosurfactant or salt.

2 EXPERIMENTAL TECHNIQUES

2.1 NMR self-diffusion

NMR self-diffusion experiments have been a very important experimental tool for investigating microemulsion structures. In this experiment, the molecular self-diffusion coefficients of water, oil and surfactant can be determined within the same experiment and by comparing their diffusion coefficients important information is obtained about the structure. In particular it is more or

less trivial to distinguish between droplet and bicontinuous structures. For an oil-in-water droplet structure, the surfactant and oil both diffuse as droplets and therefore have the same diffusion coefficient. From this value, a hydrodynamic radius can be estimated. The water, on the other hand, has a diffusion coefficient which is only slightly reduced when compared to pure water since water makes up the continuous solvent. In the case of water-in-oil droplets, the roles of water and oil are interchanged. In the case of a bicontinuous structure, the situation is very different. Here, the diffusion coefficients of water, oil and surfactant are all high. Water and oil diffuse freely within the continuous water and oil domains, respectively. Their diffusion coefficients are only slightly reduced compared to the neat solvents due to the obstruction imposed by the opposite domain. The molecules cannot penetrate the polar/apolar interface, but rather are reflected by it. The surfactant film is also continuous and the surfactant molecules perform a free lateral diffusion within the film. The lateral surfactant diffusion coefficient is often significantly higher than that of typical droplets and one therefore often finds a higher surfactant diffusion coefficient in bicontinuous microemulsions compared to droplet microemulsions. Being such an important experimental technique, the NMR self-diffusion approach for microemulsion studies has been extensively reviewed (see, e.g. ref. (1)).

2.2 NMR spin relaxation

With NMR spin relaxation experiments, one can measure the rate of molecular reorientation or tumbling. Since surfactants have a preferred orientation within the surfactant film, the mechanism of reorientation involves the rotational diffusion of, say a droplet, and the lateral diffusion of surfactant molecules within the curved surfactant film. Spin relaxation measurements on surfactant molecules thus can give information on droplet sizes (1). In the case of small droplets, the reorientation is fast, while it is slow for large droplets. If the lateral diffusion coefficient is known from other measurements, a quantitative analysis can also be made. Since droplet size determinations by NMR are not as direct as, for example with small-angle scattering experiments, it has not found very wide use. In addition, the fact that quantitative spin relaxation studies generally require specifically deuterium-labelled surfactants has made the approach less straightforward. It is, however, worthwhile to point out one particular advantage with the NMR relaxation technique. In contrast to translational diffusion, the rotational diffusion of colloidal

particles shows a very weak concentration dependence. Thus, for a given droplet size, the NMR relaxation rates of a surfactant nucleus are essentially the same in dilute solutions and concentrated dispersions. NMR relaxation experiments can therefore be useful to test if droplet sizes remain constant or vary with the concentration in concentrated systems. In fact, the relaxation experiment is very sensitive to droplet growth. For example, the rotational diffusion coefficient of a spherical colloidal particle depends on the inverse radius to the third power. Due to this very strong size dependence, even very small variations in droplet size can be detected by NMR spin relaxation experiments.

2.3 Electrical conductivity

Electrical conductivity measurements are simple to perform and the equipment is inexpensive. The method can be applied to distinguish between water-in-oil microemulsions, where the conductivity is low, and oil-in-water or bicontinuous microemulsions, which are conducting.

2.4 Small-angle scattering

In small-angle scattering experiments with X-rays or neutrons, the radiation wavelength (1–10 Å) is smaller than typical structural length-scales in microemulsions. Thus, it is, for example, possible to determine the size and shape of droplets from the magnitude and angular dependence of the scattered intensity (2). With neutrons, one has the advantage that normal hydrogen and deuterium have significantly different scattering lengths. The scattering contrast between heavy water and hydrocarbons is therefore very high and the technique is also sensitive in very dilute systems. By mixing, for example, heavy and normal water, the contrast can also be varied which may be important for careful testing of theoretical models. By varying the contrast and even matching the contrast between different components of a mixture, selective parts can be highlighted, as, for example, the surfactant film, in the scattering experiment. By matching the scattering length densities of water and oil, Strey *et al.* was able to demonstrate that the structure of a balanced bicontinuous microemulsion, containing equal volumes of water and oil, and that of a so-called sponge phase are essentially the same (3). The important difference is that the microemulsion consists of a monolayer separating water and oil, while the sponge phase consists of a bilayer separating two solvent domains of the same

kind (say water). With the absence of contrast between water and oil, the microemulsion became similar to the sponge phase from an optical point of view.

2.5 Light scattering

Because the wavelength of visible light is much larger than typical structural length-scales in microemulsions, this method cannot give any detailed information on microemulsion structure. With dynamic light scattering, one may, however, determine the collective diffusion coefficient of droplets from which one can determine a hydrodynamic radius if the influence of interactions are properly corrected for. With uncharged systems, the correction is usually small, while in the case of long-range electrostatic interactions the correction can be substantial. With static light scattering the interaction between droplets can be investigated. Within a two-component (solvent plus droplets) approximation, one measure the osmotic compressibility from the scattered intensity extrapolated to zero scattering angle. Here, one should mention that osmotic pressure can also be measured directly in a membrane osmometer.

2.6 Viscosity

Viscosity is, of course, not a useful technique to investigate microemulsion structure. Like diffusion, osmotic pressure and compressibility, the viscosity is sensitive to interactions and it is rather an interesting technique to study interactions in systems of known structure. It can, however, report on shape changes of microemulsion droplets since a growth of spherical droplets into larger non-spherical shapes is followed by a significant increase in the solution viscosity.

2.7 Electron microscopy

Microemulsion structure can be observed by electron microscopy (EM). Jahn and Strey (4) were the first to publish reliable electron microscopy images of microemulsions. Their systematic study involved both droplet and bicontinuous structures, using the so-called “freeze–fracture” technique where a replica of the sample is made which is then monitored by the electron microscope. Another technique, Cryo transmission electron microscopy (Cryo-TEM), is probably less suitable for microemulsions with larger oil contents. In this technique, a thin slice of the sample is directly monitored

and is therefore more sensitive to radiation damage. EM experiments, however, are not simple routine experiments and this is probably the reason why, apart from the successful results of Jahn and Strey, not many EM studies of microemulsions have been published.

3 CURVATURE AND CURVATURE ENERGY

3.1 Surfactant film curvature

Besides describing the microstructure in terms of droplet size and shape, one often also considers the curvature of the polar-apolar interface, i.e. the curvature of the surfactant film. In particular, one is doing this when interpreting structure and phase equilibria by using the concept of curvature elasticity, forming a model free energy in terms of curvature energy. The local curvature at a given point on a surface is described by at least two parameters in a curvature tensor (2×2). The two directions along the surface, corresponding to the maximum and minimum curvatures at a given point, happen to be perpendicular. They also correspond to the principal directions and thus the principal frame in which the curvature tensor is diagonalized. Here, one also has to be aware of the fact that curvature also has a sign related to the two sides of the surface. Thus, the minimum curvature may have the largest magnitude, but is negative. In microemulsions, one often uses the sign convention that curving towards oil is positive while curving towards water is negative. The curvatures in the principal directions are called the principal curvatures, for which we here use the notation c_1 and c_2 , respectively. In the case of a sphere of radius R , $c_1 = c_2 = 1/R$ (or $-1/R$), while for a cylinder of radius R_c , $c_1 = 1/R_c$ (or $-1/R_c$) and $c_2 = 0$. In discussions of curvature energy, it is convenient to describe the curvature by using combinations of c_1 and c_2 , rather than c_1 and c_2 , explicitly. The two most commonly used combinations are the so-called "mean curvature", $H = (c_1 + c_2)/2$ and the "Gaussian curvature", $K = c_1 c_2$, which are the two invariants, the trace and determinant, respectively, of the curvature tensor.

In the curvature description of surfactant films a particularly important parameter is the spontaneous (mean) curvature, H_0 . The spontaneous curvature can be defined as the inverse mean radius of curvature which the film would adopt if it was allowed to curve as a cylinder, but otherwise unconstrained (i.e. $1/2R_c$).

3.2 The flexible surface model

It has been found that the flexible surface model, using the curvature energy concept (5), is very useful in the theoretical analysis of the intriguing self-assembly structures found in nonionic surfactant systems. The basis of the model is to picture a monolayer or a bilayer as a geometrical surface and for each configuration of the surface assign a curvature (free) energy G_c obtained as a surface (Σ) integration of a local curvature free energy density g_c , as follows:

$$G_c = \int_{\Sigma} dA g_c \quad (17.1)$$

The total free energy is then obtained from the partition function containing a summation of the Boltzmann factor, $\exp(-G_c/k_B T)$, over all allowed surface configurations.

It is customary to expand the local curvature free energy density to second order in the curvatures, as follows:

$$g_c = 2\kappa(H - H_0)^2 + \bar{\kappa}K \quad (17.2)$$

where H is the mean and K the Gaussian curvature. The two expansion coefficients are called the bending rigidity, κ , and the saddle splay constant, $\bar{\kappa}$. Equation (17.2) has been used in a number of discussions of free energies, structure and phase equilibria in amphiphile-solvent systems, starting with Helfrich's work on the undulation forces (6). In each specific application, one has to introduce constraints on the allowed surface configurations. Typically, one disallows edges, holes, intersections and bifurcations. Sometimes there is also a constraint on the topology of the surfaces as, for example, in the description of lamellar phases. In any case, it is a demanding problem to achieve a proper Boltzmann-averaged summation over the possible surface configurations to obtain the partition function.

3.3 Competing microstructures and their curvatures

The surfactant films can be monolayers or bilayers, where bilayers, which consist of two oppositely oriented monolayers, can be normal or reverse, swollen with solvent or non-swollen. The films can enclose a finite volume (micelles, vesicles, etc.) or be continuous in one (cylinders) two (planar films) or three (multiply connected films) dimensions. The three-dimensional continuous structures are often referred to as bicontinuous, since the sub-volumes on either side of the dividing

surface are continuous in three dimensions. Such structures occur in bicontinuous microemulsions, bicontinuous cubic phases and L_3 phases.

The mean curvature term of the curvature energy is minimized for surfaces having a constant mean curvature H equal to the spontaneous mean curvature H_0 . In general, for constant mean curvature structures, this depends on the area per unit volume, the mean curvature and the polar/apolar volume ratio. The area of the surfactant film, having a finite thickness, depends on where in the film it is evaluated, unless the film is planar. For C_mE_n surfactants, a natural choice is to evaluate the area at the polar/apolar interface separating the hydrocarbon block from the oligo(ethylene oxide) block. Thus, the apolar volume fraction, ϕ_o , includes the surfactant hydrocarbon chains, while the polar volume fraction, ϕ_w , includes the oligo(ethylene oxide) chains, and $\phi_o + \phi_w = 1$. The interfacial area per unit volume is given by ϕ_s/l_s . Here, $l_s = v_s/a_s$ is the surfactant length, where v_s is the molecular volume and a_s is the area the surfactant occupies at the polar/apolar interface. The non-bicontinuous structures of constant mean curvature are spheres, cylinders and planes (lamellae). Counting the curvature towards oil as positive, and considering oil-droplet structures, we have the following:

$$\text{sphere} : H = \frac{1}{R} = \frac{\Phi_s}{3\Phi_o l_s} \quad (17.3a),$$

$$K = \frac{1}{R^2} = \left(\frac{\Phi_s}{3\Phi_o l_s} \right)^2 \quad (17.3b)$$

$$\text{cylinder} : H = \frac{1}{2R_{\text{cyl}}} = \frac{\Phi_s}{4\Phi_o l_s} \quad (17.4a),$$

$$K = 0 \quad (17.4b)$$

$$\text{lamellae} : H = 0 \quad (17.5a),$$

$$K = 0 \quad (17.5b)$$

Here, $l_s = v_s/a_s$ is the surfactant length, where v_s is the molecular volume and a_s is the area which the surfactant occupies at the polar–apolar interface. For reverse structures, ϕ_o in equations (17.3)–(17.5), should be replaced by $-\phi_w$.

The properties of periodic (bicontinuous) surfaces of constant mean curvature has been studied by Anderson *et al.* (7) for a number of different families of surfaces. For so-called balanced surfaces, $\phi_o = 1/2$ corresponds to a minimal surface. To first order in the departure from the balanced state, $(1/2 - \phi_o)$, the mean curvature varies with the composition as follows:

$$H = \beta \left(\frac{1}{2} - \phi_o \right) \frac{\Phi_s}{l_s} \quad (17.6)$$

Here, $\beta \approx 2$ is a numerical coefficient (7) which shows only a weak dependence on the particular family of constant mean curvature surfaces, and hence on the coordination number of the structure.

In a multiply connected (bicontinuous) bilayer structure, occurring in the sponge phase, the average mean curvature of the bilayer mid-plane vanishes by symmetry. The average monolayer mean curvature, evaluated at the polar–apolar interface, is however non-zero, and, in fact, is towards the solvent. Considering the bilayer mid-plane to be a minimal surface, the polar–apolar interface can be modelled either as a parallel surface to the minimal surface or as a constant mean curvature surface with the same family as the minimal surface. These two ways give essentially identical results. Using the constant mean curvature surface approach, the mean curvature of the polar–apolar interface can be calculated by using equation (17.6). Considering a normal, possibly oil-swollen bilayer, ϕ_o in equation (17.6) should be replaced with $(1/2 + \phi_o/2)$, which gives the following:

$$H = -\beta \frac{\phi_o \phi_s}{2l_s} \quad (17.7)$$

Similarly for the case of a reverse bilayer, we have:

$$H = \beta \frac{\phi_w \phi_s}{2l_s} \quad (17.8)$$

Given the particular microstructure, these equations can now be used to evaluate the mean curvature of the surfactant monolayer in various parts of the phase diagram.

4 USEFUL EXPERIMENTAL SYSTEMS: THE OLIGOETHYLENE OXIDE SURFACTANTS

Alkyl oligoethylene oxide surfactants, with the composition $\text{CH}_3(\text{CH}_2)_{m-1}(\text{OCH}_2\text{CH}_2)_n\text{OH}$ (below abbreviated as C_mE_n), can be considered as being short AB block copolymers. Typical sizes are $m = 10-16$ and $n = 3-8$, although other values are also used in applications. At the oil–water interface, the polar and apolar groups stick out to a similar extent into the respective solvents. At the interface, there is a lateral head–head and a lateral tail–tail interaction. By varying the n/m ratio, one can tailor the surfactant to either prefer an interface that is curved towards water (low n/m ratios) or towards oil (high n/m ratios).

Of special importance is the state when the surfactant film does not have a preference to curve either towards water or towards oil. For a given n/m ratio,

this balanced state occurs at a given temperature, T_0 , which corresponds to the “phase inversion temperature” (PIT) (8) identified in emulsion systems. The temperature T_0 depends on the nature of the oil through its ability to penetrate into the apolar part of the surfactant film.

The curvature properties of the surfactant film is for the nonionic surfactants a strong function of temperature. This is mainly due to the strong temperature dependence of water–ethylene oxide interactions. Water changes from a good to a bad solvent with increasing temperature as seen by the lower consolute boundary (“clouding”) in the water–polyethylene oxide (PEO) and the water–oligoethylene oxide surfactant phase diagrams. At lower temperatures, the ethylene oxide layer prefers to swell to high water contents, thus resulting in a preferred curvature towards oil. At higher temperatures, the ethylene oxide layer prefer a lower water content and the film thus tends to curve towards water. In addition, as the temperature increases, the number of *gauche*-conformations in the alkyl chains increases, hence enhancing the lateral repulsion on the apolar side.

We can quantitatively describe this curvature property of the films in terms of the spontaneous mean curvature, H_0 . At T_0 , or the PIT, $H_0 = 0$ by definition. By studying how solution structures vary with temperature, one can estimate the temperature dependence of H_0 . If we define curvature towards water as negative, the coefficient δ in the expansion:

$$H_0(T) = \delta(T - T_0) + \dots, \text{ etc.}$$

is negative and has a value of the order of $\delta \approx -10^{-3} \text{ \AA}^{-1}/\text{K}$.

In the binary water–surfactant system, the spontaneous curvature of the polar–apolar interface is still a useful concept, although there is no oil. However, the alkyl chains of the surfactant face another layer of surfactant alkyl chains. The spontaneous mean curvature is also in this case strongly temperature-dependent, for the same molecular reasons, although the balanced state occurs at a higher temperature than in the presence of oil. For the water– C_{12}E_5 system, $H_0 = 0$ at $t \approx 55^\circ\text{C}$, which is $\approx 20^\circ\text{C}$ above the PIT for water– C_{12}E_5 –decane.

5 PHASE BEHAVIOUR

Microemulsion structure is strongly linked to phase behaviour and therefore in this context it is useful to also consider the microemulsion phase behaviour. Oil-in-water droplet microemulsions are

typically found near the water corner of ternary surfactant–water–oil phase diagrams. Analogously, we may expect a water-in-oil droplet structure in a microemulsion phase which is located near the oil corner. Typical bicontinuous microemulsions contain similar amounts of water and oil. Associated with droplet microemulsions, there is a maximum solubility of the dispersed solvent and beyond this limit one has a co-existence between the saturated microemulsion and the excess dispersed solvent. A bicontinuous microemulsion, on the other hand, can be simultaneously saturated with both water and oil, thus giving a three-phase equilibrium with both solvents in excess.

Expressed in terms of spontaneous curvature, we expect an oil-in-water droplet microemulsion when $H_0 \gg 0$. The composition of this phase is such that it corresponds to a droplet radius $R \approx 1/H_0$. Similarly, we expect a phase of water-in-oil droplets when $H_0 \ll 0$. Microemulsion droplets do not become larger than about 300–400 Å. For spontaneous curvatures near zero, a bicontinuous structure is apparently more stable.

5.1 General phase equilibria

In order to illustrate the phase behaviour of microemulsions, it is most convenient to consider the systems with nonionic surfactants of the ethylene oxide type. These have been studied extensively by Shinoda and Kunieda and co-workers and by Kahlweit and Strey and co-workers (for more recent reviews, see, e.g. refs (9) and (10)). At low surfactant concentrations, there is a general sequence of phase equilibria, often referred to as Winsor equilibria (11). The equilibrium conditions for the microemulsion phase, L, changes from equilibrium with excess oil (Winsor I) to equilibrium with excess water (Winsor II), via a three-phase equilibrium with excess water and oil (Winsor III). For nonionics, this sequence occurs when increasing the temperature, while for quaternary or ternary systems, it can be observed with increasing salinity or cosurfactant-to-surfactant ratio.

At constant pressure, it is convenient to present the composition–temperature phase behaviour in terms of a phase prism, as illustrated in Figure 17.1. A sequence of constant temperature sections is illustrated in Figure 17.2. Applied to nonionics, phase diagram (a) would correspond to the lowest temperature ($< T_0$) and (i) to the highest temperature ($> T_0$). At lower temperatures (a), a water-rich microemulsion is stable. We note that the phase boundary corresponding to the maximum solubility limit of oil is essentially a straight

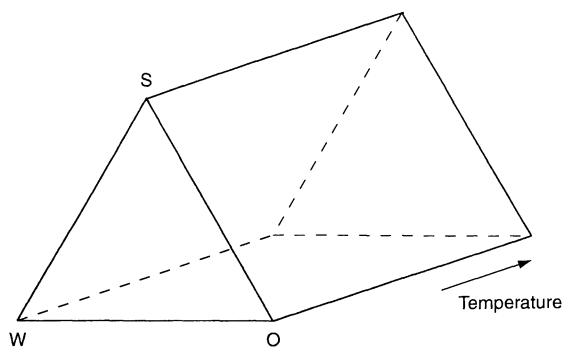


Figure 17.1. The phase prism, describing the phase behaviour of a ternary system at constant pressure

line at constant ϕ_s/ϕ_o , corresponding to a given constant droplet radius. Safran and co-workers (12) have in their theoretical work termed the incomplete solubilization

of oil (L + O) “emulsification failure” and we denote the phase boundary here as the “emulsification failure boundary” (EFB). Increasing the temperature (b), there is an increased solubility of oil and the EFB shifts to lower ϕ_s/ϕ_o , thus increasing the droplet radius. At lower oil content, there is an additional phase boundary with a critical point (or, it can be a closed loop, disconnected from the binary water–surfactant axis, with two critical points) and tie-lines roughly parallel to the water–surfactant axis. This two-phase region (essentially W + L), separating a concentrated and a dilute aqueous microemulsion, is connected to the liquid–liquid phase separation (clouding) in the binary water–surfactant system, and indicates the presence of effectively attractive interactions. With increasing the temperature, the critical point on the oil-rich side of the W + L region moves to a higher oil content. In fact, this critical point moves faster than the emulsification failure boundary, and finally touches it at a critical

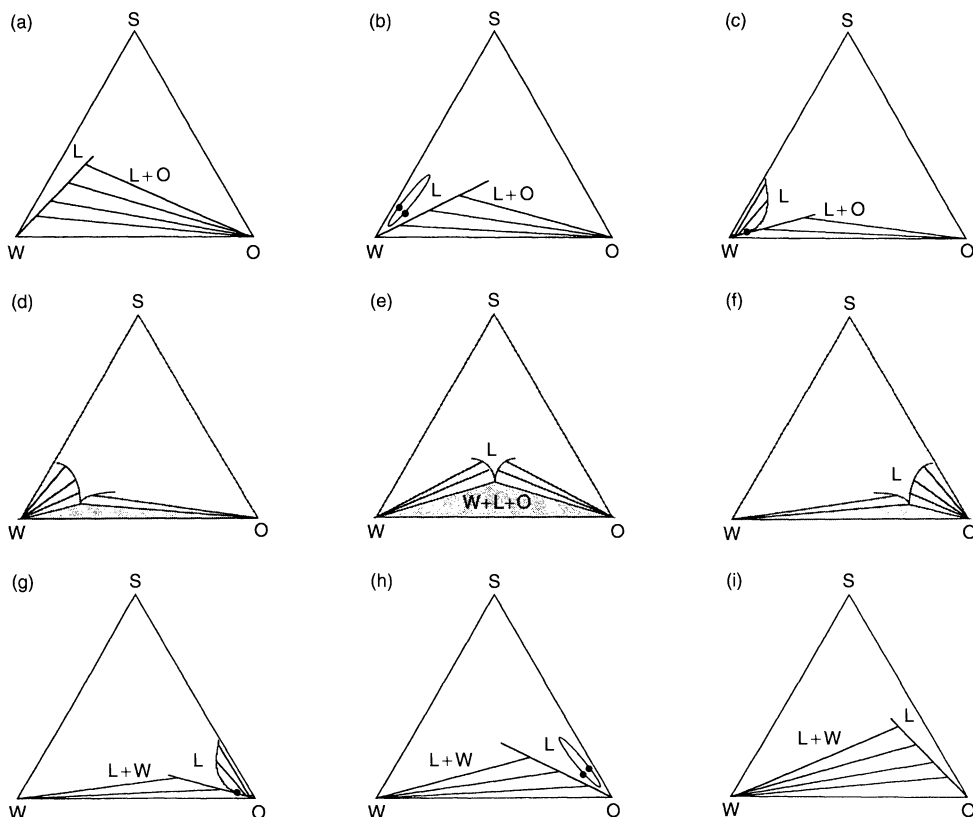


Figure 17.2. A sequence of isothermal schematic phase diagrams of a ternary system: L denotes the liquid microemulsion phase, W and O are essentially pure water and oil phases, respectively, while L + O is the Winsor I, L + W is the Winsor II and W + L + O is the Winsor III equilibrium. For nonionic surfactant–water–oil systems, the sequence from (a) to (i) is obtained with increasing temperature

www.iran-mavad.com

end-point (c). Hence, there is a line of critical points extending from the binary water–surfactant system into the ternary phase prism, which terminates at a critical end-point, at temperature T_1 , where the two binodals, involving $W + L$ and $L + O$, respectively, touch each other.

From the critical end-point, a three-phase triangle ($W + L + O$) develops when the temperature is increased above T_l (the subscript “l” here denotes the lower temperature limit of the three phase triangle) (d). The microemulsion “corner” of the three-phase triangle moves from the water to the oil side with increasing temperature ((d)–(f)). At a particular temperature, T_0 , the triangle is isosceles and the microemulsion contains equal amounts of water and oil (e). This is often referred to as a balanced microemulsion. The latter has a bicontinuous structure with a zero average mean curvature since the interface separates two geometrically identical sub volumes.

The phase equilibria at temperatures above T_0 , ((f)–(i)) are essentially mirror images of the behaviour at lower temperatures, with a critical end-point on the oil-rich side at T_u and an emulsification failure boundary, here corresponding to the maximum water solubility, which moves to higher ϕ_s/ϕ_w with increasing temperature.

To determine complete ternary phase diagrams, in particular at a number of different temperatures, is a lengthy process, and has been carried out for only for a few systems. Rather, one often reduce the number of composition degrees of freedom by one and studies a planar section through the phase prism. The section defined by $\phi_w = \phi_o$ (“fish-cut”) is shown schematically in Figure 17.3. In this section, one can determine T_l and T_u and the minimum amount of surfactant necessary to solubilize equal amounts of water and oil, which we here denote as ϕ_s^* . The lower ϕ_s^* , then the more “efficient” is the surfactant. We see also that the microemulsion at higher surfactant concentrations is in equilibrium with a lamellar phase (L_α), a typical feature of long-chain surfactants.

A section through the phase prism at constant surfactant concentration (“Shinoda-cut”) is particularly illustrative. This shows the interrelation between the temperature-dependence and the dependence on the water-to-oil ratio. By choosing the surfactant concentration to be slightly above ϕ_s^* , one obtains a phase behaviour that is illustrated schematically in Figure 17.4. This section contains a rich variety of microstructures, e.g. the microemulsion phase which has a surfactant monolayer structure and the lamellar phase and the sponge phase which both have a bilayer an-

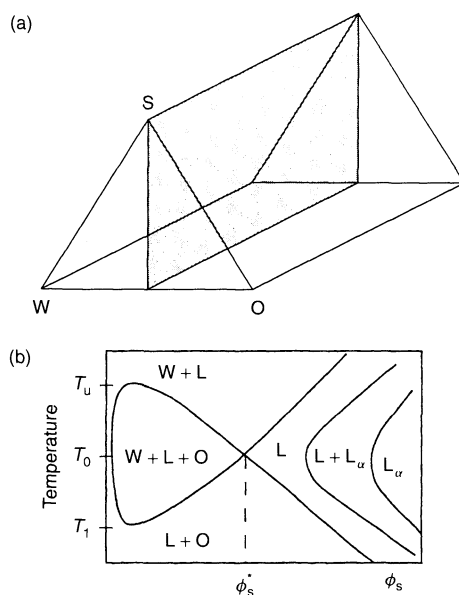


Figure 17.3. (a) Illustration of the section through the phase prism at equal volumes of water and oil. (b) A schematic phase diagram plotted as temperature versus the surfactant concentration ϕ_s : T_l and T_u are the lower and upper temperatures, respectively, of the three-phase equilibrium $W + L + O$, while T_0 is the temperature at which the three-phase triangle is isosceles, i.e. when the middle-phase microemulsion contains equal amounts of water and oil. The latter condition is also termed as “balanced”. The parameter ϕ_s^* is the surfactant concentration in the middle-phase microemulsion at balanced conditions

structure. As illustrated in Figure 17.4, the microemulsion and sponge phases join up near equal amounts of water and oil. Hence, there is in principal only one single liquid phase, L , which shapes a cross in this $T-\phi_o$ plane. The microemulsion, or monolayer channel, is wider and extends from the water to the oil side with increasing temperature. The sponge or bilayer channel is more narrow and extends from the water to the oil side with decreasing temperature, although interrupted by the balanced microemulsion. We note also that the sponge phase extends from the binary water–surfactant system.

The water-rich (lower ϕ_o) sponge phase has a normal bilayer structure separating two water sub-domains. With increasing ϕ_o (replacing water with oil), there is an increasing swelling of the bilayer with oil. The oil-rich (higher ϕ_o sponge phase, on the other hand, has a water-swollen reverse bilayer structure.

Figures 17.5 and 17.6 are experimentally determined phase diagrams at constant surfactant concentrations. Figure 17.5 shows the $C_{12}E_5$ –water–tetradecane system

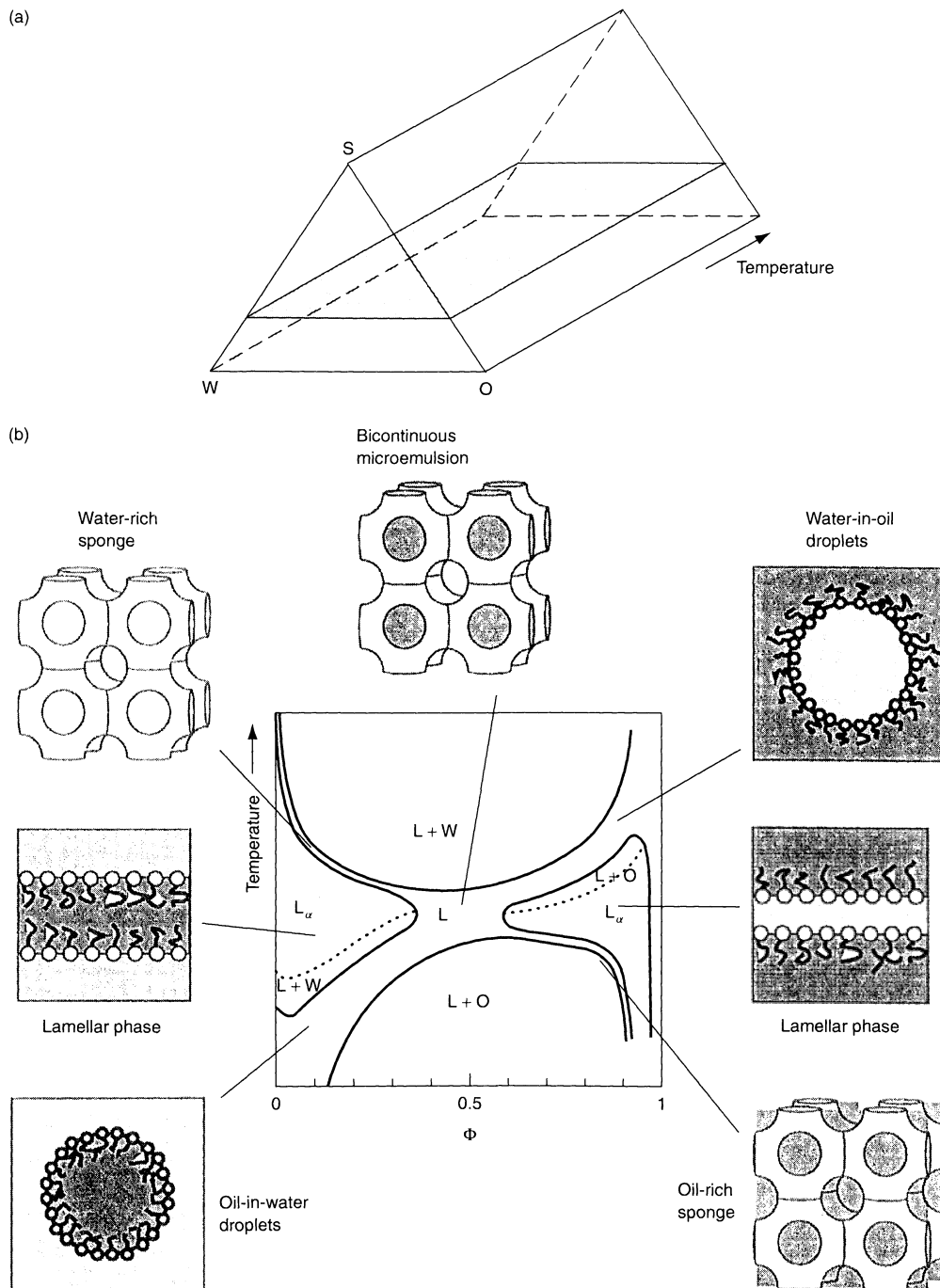


Figure 17.4. (a) Illustration of a section at constant surfactant concentration through the phase prism. (b) A schematic phase diagram, plotted as temperature versus the volume fraction of oil, ϕ , at constant surfactant concentration. Illustrated are also various microstructures found in different regions of the isotropic liquid phase, L. At higher temperatures, the liquid phase is in equilibrium with excess water ($L + W$), and at lower temperatures with excess oil ($L + O$). At intermediate temperatures, a lamellar phase is stable at higher water contents and at higher oil contents, respectively

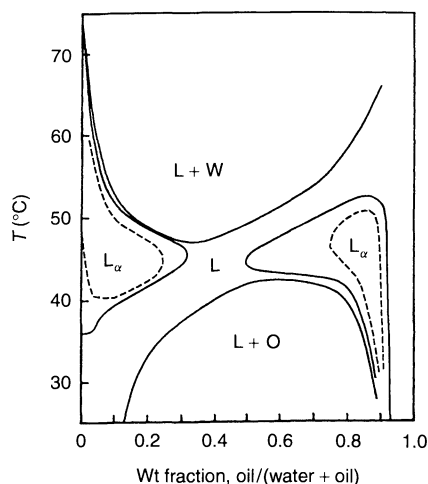


Figure 17.5. Experimental phase diagrams at a constant surfactant concentration of 16.6 wt% in the $C_{12}E_5$ - D_2O -tetradecane system (redrawn from ref. (13))

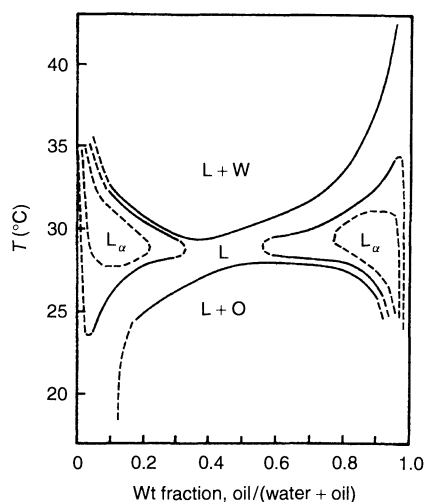


Figure 17.6. Experimental phase diagrams at a constant surfactant concentration of 7.0 wt% in the $C_{12}E_5$ - D_2O -cyclohexane/hexadecane system. The cyclohexane to hexadecane weight ratio is equal to unity (redrawn from ref. (14))

at 16.6 wt% surfactant (redrawn from ref. (13)), while Figure 17.6 shows the $C_{12}E_5$ -water-cyclohexane/hexadecane system at 7.0 wt% surfactant (redrawn from ref. (14)). The horizontal axes in these figures correspond to the weight fraction, oil/(water + oil).

A minor drawback of the nonionic surfactants in systematic studies is their high solubilities in oil. In the absence of water, the surfactant and oil form essentially

simple molecular liquid mixtures. Hence, the typical microemulsion behaviour terminates at a ϕ_o slightly below 1. This is also why the oil-rich sponge phase does not extend completely to the oil side. Typically, the oil domains of the microemulsion contains molecularly dispersed surfactant with a concentration of typically 1–2 wt%. In spite of high oil solubilities, the nonionic surfactant systems are very suitable experimental model systems for microemulsions and related phases due to their convenient temperature-dependences and the ability to form these phases with a single-component film. The oil solubility has basically no important consequences, except for quantitative considerations at very high oil contents.

6 STRUCTURAL INVERSION AND THE SPECTRUM OF MICROSTRUCTURES

The microstructure inverts from disconnected oil droplets in water to disconnected water droplets in oil, via a bicontinuous microstructure when increasing ϕ_o along the microemulsion channel (13, 14). A simple and convenient way to study the structural inversion is by monitoring the self-diffusion coefficients for the molecules on the two sides of the surfactant film, i.e. water and oil. Figures 17.7 and 17.8 show the variations of D/D_0 for water and oil with ϕ_o along the microemulsion channel for the two systems displayed in Figures 17.5 and 17.6. D/D_0 is a normalized self-diffusion coefficient, with

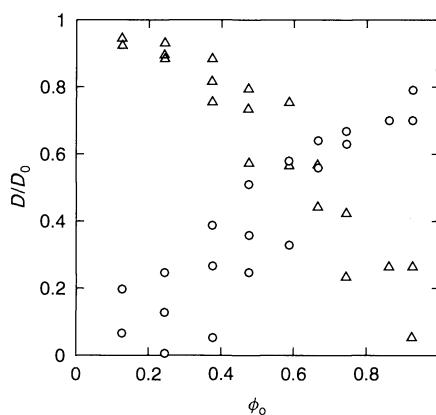


Figure 17.7. The variation of the reduced self-diffusion coefficients, D/D_0 , of water (Δ) and tetradecane (\circ) with the volume fraction of tetradecane within the microemulsion channel of the system displayed in Figure 17.5. (data taken from

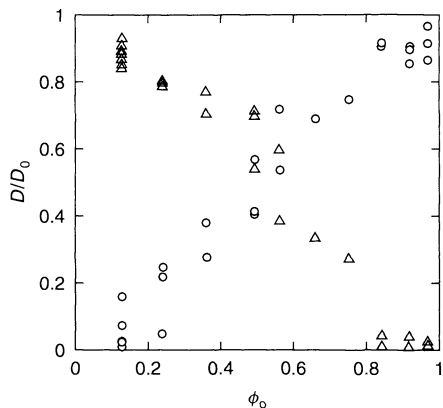


Figure 17.8. The variation of the reduced self-diffusion coefficients, D/D_0 , of water (Δ) and cyclohexane (\circ) with the total oil volume fraction within the microemulsion channel of the system displayed in Figure 17.6. (data taken from ref. (14))

D being the observed self-diffusion coefficient in the microemulsion and D_0 the self-diffusion coefficient in the neat solvent at the same temperature. D/D_0 hence corresponds to an obstruction factor, which decreases for water but increases for oil as ϕ_o increases. The two curves cross around $\phi_o = 0.5$ with $D/D_0 \approx 0.6$. This value is close the value of 0.66 ± 0.01 (15) which is numerically found for the obstruction factor for bicontinuous minimal surface structures.

Anderson and Wennerström (15) have calculated the diffusion for some different constant mean curvature surface structures, serving as model structures for cubic phases, sponge phases and bicontinuous microemulsions. The D/D_0 ratio depends on Φ_o , but there is also a significant dependence on the topology, or the coordination number of the structure, i.e. on the particular family of constant mean curvature surfaces. Near $\phi_o = 0.5$, these authors found D/D_0 to vary linearly with ϕ_o , and the relationship can be written as follows:

$$D/D_0 \approx 0.66 \pm \beta(\phi_o - 0.5) \quad (17.9)$$

where “ \pm ” should be read as “+” in the case of oil diffusion and “−” in the case of water. The numerical coefficient β depends on the particular family of surfaces, i.e. on the topology or coordination number of the structure. The bicontinuous structure can be viewed as connected arms or cylinders and the coordination number tells of the way in which the arms are connected. For example, a coordination number of three means that the arms are connected three-by-three at each junction. The value of β was solved for two structures, the D-family, having a coordination number of 4 and the P-family

having a coordination number of 6. For the D-family, they found $\beta = 0.54$ and for the P-family $\beta = 0.78$.

The value of D/D_0 in the balanced state, $\phi_o = 0.5$, is, of course, equal for the two sides of the film. The value of 0.66 can be understood as follows. Locally, the diffusion paths of the solvent molecules are obstructed in one dimension by the presence of the interface. The molecules can diffuse only in two out of three dimensions, thus reducing the diffusion coefficient for macroscopic displacements to 2/3 of its unobstructed value.

Moving away from the balanced state, D/D_0 for the less abundant solvent decreases, while D/D_0 for the more abundant solvent increases, when the coordination number increases. This dependence on the coordination number can be understood from the fact that the obstruction effect is strongly dependent on the relative “diameter” of the connected “arms” of the structure (a sort of “bottle-neck” effect). The higher the coordination number, then the more narrow are these arms for the less abundant solvent while they are wider for the abundant solvent. Thus, the slopes of D/D_0 versus ϕ_o for the two solvents become steeper with increasing coordination number.

Self-diffusion data from bicontinuous structures contain, in principal, information on the average coordination number of the microstructure. The experimental results can, however, not be compared with the theoretical results directly. There is an additional reduction of D/D_0 due to solvation of the surfactant film (a lateral friction felt by the solvent molecules in the solvent layers closest to the film) and an obstruction due to the finite film volume. These effects, which both increases with the surfactant-to-solvent ratio can however be included in the model, as will be discussed for the case of the sponge phase in one of the following sections. Extending the model to include solvation, however, introduces additional parameters which will affect the uncertainty.

The variations of D/D_0 observed at constant ϕ_o in Figures 17.7 and 17.8 are not due to experimental uncertainties (self-diffusion coefficients are measured with an accuracy of typically a few percent) but to structural variations with temperature at constant composition. This can, for example, be seen in Figure 17.9, where we have plotted D/D_0 as a function of T for a sample with $\phi_o = 0.47$ in the tetradecane system. The D/D_0 ratio for water decreases, while it increases significantly for oil, when the temperature is varied between 42 and 47°C. On the other hand, there is a striking independence of D/D_0 when varying ϕ_o at constant temperature, as can be seen in Figure 17.10. This suggests that the scattering of data points seen in Figures 17.7 and 17.8 can

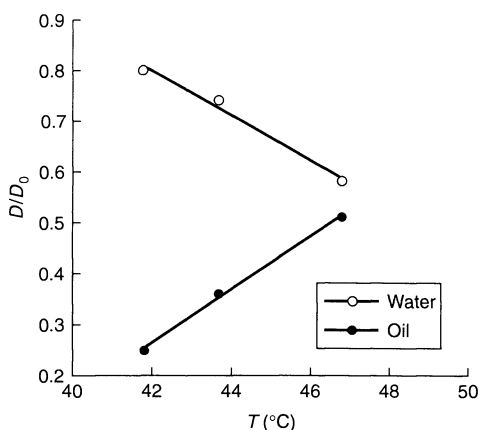


Figure 17.9. The variation of the reduced self-diffusion coefficients, D/D_0 , of water and oil with temperature for a sample with $\phi = 0.47$ in the tetradecane system (see Figure 17.5) (data taken from ref. (13))

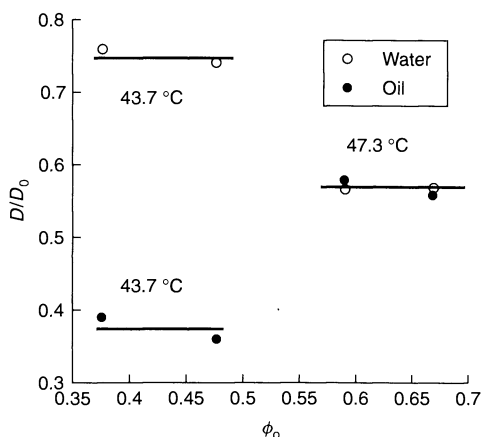


Figure 17.10. The variation of the reduced self-diffusion coefficients, D/D_0 , of water and oil with volume fraction at two different temperatures, 43.7 and 47.3°C, respectively, in the tetradecane system (see Figure 17.5) (data taken from ref. (13))

be removed when plotting the data against temperature, rather than ϕ_o .

The results from the two different systems can be compared directly by considering the temperature difference $(T - T_0)$ where T_0 is the temperature at the balanced state, where the two D/D_0 curves cross. Looking at the phase diagrams of the two systems (Figures 17.5 and 17.6), we see that the microemulsion channels have different slopes in the two systems. This slope scales approximately as ϕ_s , thus suggesting that if we want to compare the two systems on a common temperature

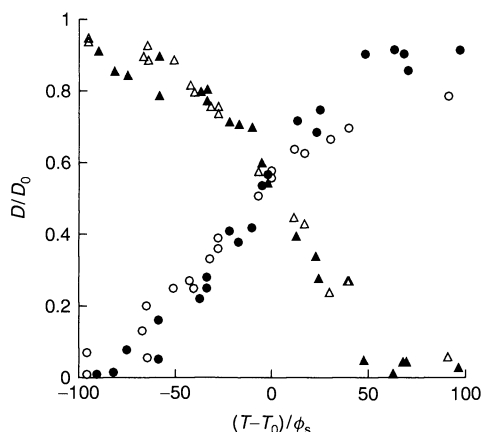


Figure 17.11. The reduced self-diffusion coefficients, D/D_0 , of water (Δ , \blacktriangle) and oil (\circ , \bullet) for the two systems, $C_{12}E_5-D_2O$ -tetradecane and $C_{12}E_5-D_2O$ -cyclohexane/hexadecane, plotted as a function of the reduced temperature $(T - T_0)/\phi_s$. Filled symbols represent the tetradecane system, while unfilled symbols represent the cyclohexane/hexadecane system

scale we should choose the re-scaled temperature $(T - T_0)/\phi_s$. Figure 17.11 shows the variations of D/D_0 for water and oil as a function of this re-scaled temperature. The data points from the two systems fall essentially on the same universal curves, thus indicating that the microstructure in the bicontinuous part of the channel is similar when comparing the two systems with the re-scaled temperature. The significance of the re-scaled temperature can be rationalized as follows. The mean curvature of a bicontinuous structure is proportional to the interfacial area per unit volume, and hence to ϕ_s . If the slope in H_0 versus T is equal in the two systems, it then follows that $(H - H_0)$ is the same in the two systems when compared at $(T - T_0)/\phi_s$ for a given ϕ_o .

7 CHARACTERIZATION OF A DROPLET MICROEMULSION

7.1 The emulsification failure and spherical microemulsion droplets

In this section, we will discuss the characterization of a droplet microemulsion in more detail and in particular we will focus on spherical droplets. It turns out that spherical droplets are present in particular regions of the phase diagram, namely near the phase boundary, or solubilization limit, where the microemulsion is in equilibrium with the dispersed solvent (i.e. oil in the case of oil-in-water droplets).

7.2 Solubilization limit from curvature energy

Based on equations (17.1) and (17.2) Safran and co-workers (12) analysed the stability requirements for various shapes, by comparing spheres, cylinders and planes. The sphere is the shape having the highest volume for a given interfacial area. Spherical oil-in-water droplets are therefore found at the phase boundary when the microemulsion is saturated with oil. Approximating the phase boundary as corresponding to the oil chemical potential $\mu_o = 0$, the radius of the spheres is given by the following:

$$r = \frac{1}{H_0} \left(1 + \frac{\bar{\kappa}}{2\kappa} \right) + \frac{k_B T}{\kappa} f(\phi) \quad (17.10)$$

where the last term corresponds to an entropy of mixing, with ϕ here being the volume fraction of the micelles.

In we want to make a quantitative comparison with theory we have to specify in more detail where in the surfactant film, which has a finite thickness, we evaluate the curvature. For the nonionic surfactant of $C_{12}E_5$, it turns out that the interface separating oil and the alkyl chain of $C_{12}E_5$ from the ethylene oxide chain and water has an essentially invariant area, a_s , per molecule, independent of the curvature. It is therefore useful to define the curvature at this particular interface.

7.3 Experimental system

The experimental system we will be focussing on is the ternary $C_{12}E_5$ /water/decane system. The partial phase diagram (data taken from ref. (16)) at constant surfactant-to-oil ratio, $\phi_s/\phi_o = 0.815$, is presented in Figure 17.12, plotted as temperature versus the volume fraction of surfactant plus oil. We note that the phase diagram is very similar to that of the binary $C_{12}E_5$ -water system. At higher water contents, we see the sequence of a liquid micellar phase (L_1) (here as oil-swollen micelles) and a lamellar phase (L_α), plus a sponge phase (in Figure 17.12, denoted as L_3) with increasing temperature. At lower temperatures, there is an incomplete solubilization of the oil and the L_1 phase is in equilibrium with excess oil.

As in the binary $C_{12}E_5$ system, the micelles in the L_1 phase grow with increasing temperature, although in the ternary system the growth is only minor due to the fact that the spherical micelle is already relatively large (for the given surfactant-to-oil ratio it contains approximately 1500 surfactant and 4000 oil molecules). When increasing the temperature further, in the polar-apolar interface that essentially is located in

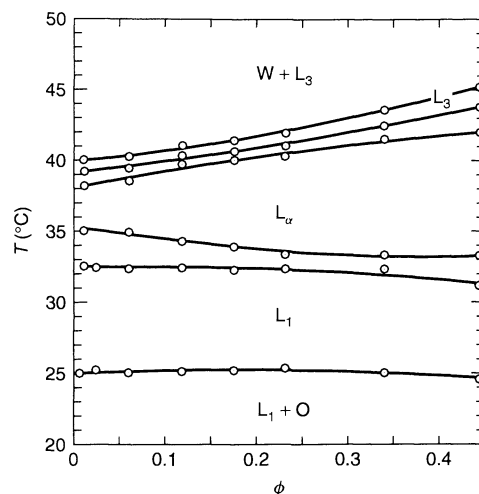


Figure 17.12. Partial phase diagram of the $C_{12}E_5$ -water (H_2O)-decane system at a constant surfactant-to-oil ratio, ϕ_s/ϕ_o : L_1 denotes the microemulsion phase, and L_α the lamellar liquid crystalline phase. In addition, there is the sponge phase (here denoted as L_3) at higher temperatures. Of particular interest here is the lower phase boundary of the microemulsion phase ($\approx 25.0^\circ\text{C}$ with H_2O and $\approx 23.5^\circ\text{C}$ with D_2O), below which the microemulsion co-exists with excess oil ($L_1 + O$) (data taken from ref. (16), reproduced by permission of The Royal Society of Chemistry)

lamellar and L_3 phases are formed where the aggregates have essentially an infinite aggregation number. This counter-intuitive behaviour, which goes against the preference of entropy, we today understand as being the result of a decreasing spontaneous curvature, H_0 , of the surfactant film with increasing temperature.

The lower phase boundary can be identified as the solubility limit, as already discussed above. The phase boundary, which is temperature-independent up to approximately $\phi = 0.5$, corresponds to a dilution line of concentration-invariant spherical oil-in-water microemulsion droplets.

7.4 Droplet radius and volume fraction

Below, we will be concerned with spherical microemulsion droplets, composed of a core of decane and covered by the surfactant $C_{12}E_5$. For this system, there exists an extensive set of accurate experimental data and we can identify three different characteristic radii for these droplets, as illustrated in Figure 17.13. We define a hydrocarbon radius, r_{hc} , which corresponds to the radius

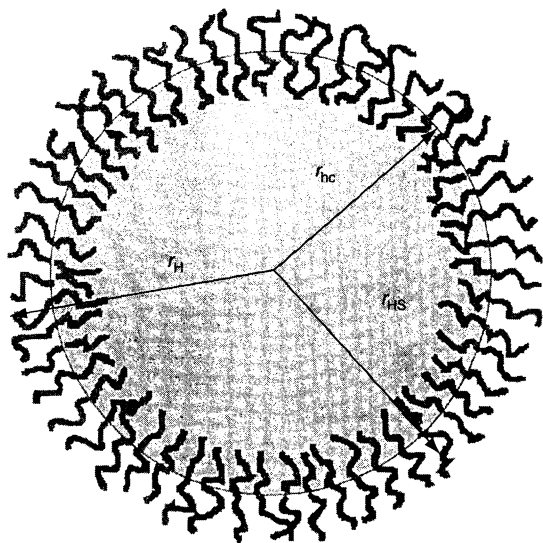


Figure 17.13. Illustration of a spherical oil-in-water droplet stabilized by the nonionic surfactant $C_{12}E_5$. The radius r_{hc} encloses the oil and the alkyl chain of the surfactant, while the droplet properties are also characterized by a hard-sphere radius (r_{HS}) and a hydrodynamic radius (r_H), with $r_{hc} < r_{HS} < r_H$.

the middle of the surfactant film. This interface encloses the oil and the alkyl chains of the surfactant. The radius depends on the surfactant-to-oil ratio and on the area, a_s , occupied per surfactant molecule at this interface, and can be written as follows:

$$r_{hc} = \frac{3(\phi_o + 0.5\phi_s)l_s}{\phi_s} \quad (17.11)$$

where $l_s (= v_s/a_s)$ is the surfactant volume-to-area ratio where $v_s \approx 700 \text{ \AA}^3$. The factor $0.5\phi_s$ results from the fact that the alkyl chain volume of $C_{12}E_5$ is approximately half of the total molecular volume. The parameter r_{hc} can be measured by small-angle neutron scattering.

In addition, the droplets have a hydrodynamic radius, r_H , which is obtained from the diffusion coefficient extrapolated to infinite dilution. As will be shown below, the droplet interactions can, to a very good approximation, be described in terms of hard spheres. A third characteristic radius, the hard-sphere radius, r_{HS} , then enters to describe the interactions. Associated with the three radii, there are three different characteristic droplet volumes, and therefore three different characteristic droplet volume fractions. If $\phi = \phi_s + \phi_o$ denotes the total volume fraction of surfactant and oil, the hard sphere volume fraction, ϕ_{HS} , can be written as follows:

$$\frac{\phi_{HS}}{\phi} = \frac{\left(\frac{4\pi}{3}r_{HS}^3\right)}{\left(\frac{4\pi}{3}r_{hc}^3\right) + Nv_{EO}} \quad (17.12)$$

where $N = 4\pi r_{hc}^2/a_s$ is the number of surfactant molecules per micelle (aggregation number) and v_{EO} is the volume of the E_5 segment. With $v_{EO} = 0.5v_s$, equation (17.12) can be recast as the following:

$$\frac{\phi_{HS}}{\phi} = \frac{\phi - \phi_s/2}{\phi} \left(\frac{r_{HS}}{r_{hc}}\right)^3 \quad (17.13)$$

An analogous expression for the hydrodynamic volume fractions, ϕ_H , is obtained by replacing r_{HS} by r_H in the above equations.

7.5 Proof of a discrete droplet structure from self-diffusion data

In Figure 17.14, we have plotted the self-diffusion coefficients of surfactant and oil as a function of the droplet volume fraction. The data were obtained at 23.5°C along the (EFB), using D_2O as the solvent (17). (With D_2O replacing H_2O , the phase boundaries are shifted downwards by $1.5\text{--}2^\circ\text{C}$, or otherwise the phase diagrams are equivalent.) The surfactant and oil diffusion coefficients are identical over the whole range of volume fractions. This shows that the surfactant and the oil diffuse together in the form of swollen micelles and proves that we have a structure of closed discrete droplets over the whole concentration range. The measured diffusion

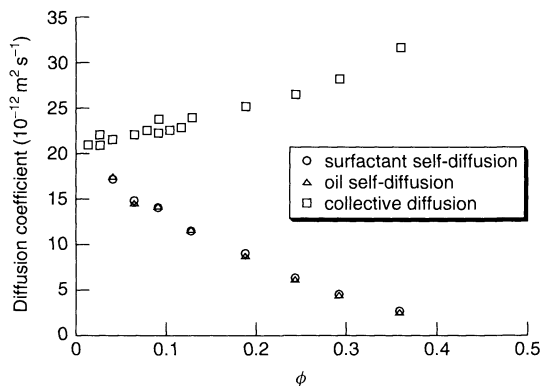


Figure 17.14. Self-diffusion coefficients of surfactant (O) and oil (Δ), and collective diffusion coefficients (□), obtained by dynamic light scattering, plotted as a function of the volume fraction of droplets, ϕ (data taken from ref. (17))

coefficients correspond to the self-diffusion coefficients of the droplets.

7.6 Hydrodynamic radius

The droplet self-diffusion coefficient extrapolated to infinite dilution corresponds to the free diffusion coefficient, D_0 , in the absence of interactions. In the present system, we obtain $D_0 = 2.0 \cdot 10^{-11} \text{ m}^2 \text{ s}^{-1}$. The free diffusion coefficient is related to the hydrodynamic radius, R_H , according to the Stokes–Einstein relationship, as follows:

$$D_0 = \frac{k_B T}{6\pi\eta R_H} \quad (17.14)$$

where η is the solvent viscosity and $k_B T$ is the thermal energy. From the value of D_0 , we obtain, via equation (17.14) $R_H = 95 \text{ \AA}$.

A hydrodynamic radius can also be obtained from collective diffusion, D_c , data measured by using dynamic light scattering (DLS). In Figure 17.14, we have also included some results obtained from DLS measurements. By extrapolating the D_c values to infinite dilution, we find the same value of D_0 as that obtained from the self-diffusion experiments.

7.7 Concentration dependence or independence of droplet size

As shown above, we can easily determine a hydrodynamic radius at high dilution where interactions are negligible. The situation, however, becomes more problematic at higher concentrations, where, for example, diffusion coefficients depend on both size and on interactions. As seen in Figure 17.14, the droplet self-diffusion coefficient decreases with increasing volume fraction. Is this decrease due to interactions only or is it also a consequence of droplet growth?

There are two different experiments that are useful for investigating the variation of droplet size with concentration, namely NMR relaxation and small-angle scattering. In NMR relaxation experiments on a surfactant, one probes the combined motion of droplet tumbling and the surfactant lateral diffusion within the curved surfactant film. These two processes are both essentially independent of droplet interactions. In small-angle scattering, the influence of interactions becomes small for scattering vectors $q \gg 2\pi/d$, where d is the average inter-droplet separation, and the scattering is dominated by single-particle properties.

7.8 NMR relaxation

Using a deuterium-labelled surfactant, $\text{CH}_3(\text{CH}_2)_{10}\text{CD}_2(\text{OCH}_2\text{CH}_2)\text{OH}$, deuterium relaxation experiments were performed in the microemulsion phase. For large droplets like these, the surfactant reorientational motion is slow and one has $R_2 \gg R_1$, where R_1 and R_2 are the longitudinal and transverse relaxation rates, respectively. The most interesting relaxation rate is R_2 , which is sensitive to the slow motion. The slower the motion, then the larger is R_2 . Thus, a droplet growth is followed by an increase in R_2 . If R_2 is concentration-independent, this is a very strong indication that the droplet size does not vary with concentration. Figure 17.15 shows plots of the relaxation rate difference, $\Delta R = R_2 - R_1$ (here, $\approx R_2$), as a function of the droplet volume fraction at different temperatures, using H_2O as solvent. At 25°C , which corresponds to near the EFB with H_2O as solvent, ΔR is concentration-independent, thus demonstrating that the droplet size does not vary with concentration. At 29°C , on the other hand, ΔR increases with increasing concentration as a result of micellar growth. For a more detailed discussion of these data and a quantitative analysis, the reader is referred to ref. (18).

7.9 Small-angle neutron scattering

With small-angle scattering, one can measure the size of the droplets. Figure 17.16 shows the small-angle

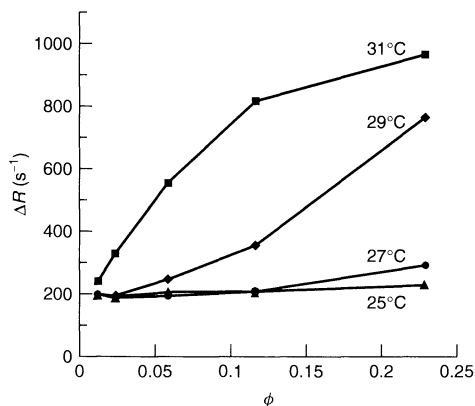


Figure 17.15. The variation of the observed relaxation rate difference, $\Delta R = R_2 - R_1 (\approx R_2)$, as a function of sample concentration at four different temperatures in the microemulsion phase. At 25°C , ΔR is independent of the droplet concentration, thus demonstrating that the droplet size is constant. At 29 and 31°C , ΔR increases significantly with the concentration, here demonstrating droplet growth (data taken from ref. (18), reproduced by permission of Springer-Verlag)

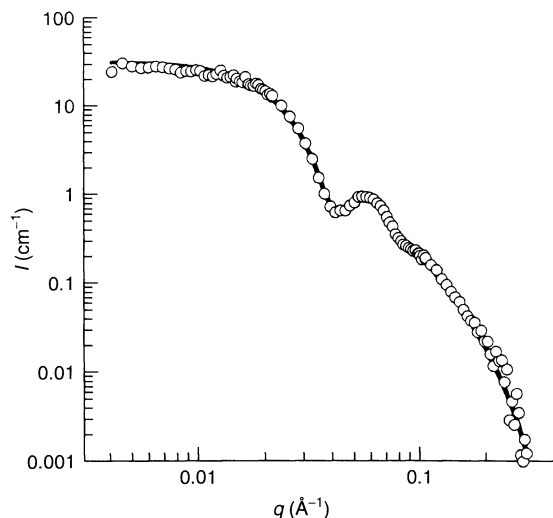


Figure 17.16. SANS spectrum from a sample of $\phi = 0.02$, where the scattering length density of the oil is matched to that of water. The continuous line is the best two-parameter fit with a form factor of a shell yielding the radius $r_{hc} = 75 \text{ \AA}$ and a Gaussian relative standard deviation $\sigma/r_{hc} = 0.16$ (data taken from ref. (19))

neutron scattering (SANS) from a dilute sample of $\phi = 0.02$ where the oil and water has been contrast-matched (using D_2O and a mixture of $C_{10}D_{22}$ and $C_{10}H_{22}$), thus resulting in coherent scattering from the surfactant film alone (19). A fit to the data, shown as a continuous line, corresponds to a spherical shell having the radius $r_{hc} = 75 \text{ \AA}$ and a relative polydispersity $\sigma/r_{hc} = 0.16$. This polydispersity contains contributions from both size (volume) and shape polydispersity. Their relative contributions are not accurately known; however, contrast-match experiments indicate that it is the shape polydispersity that dominates. The radius r_{hc} we refer to as the “hydrocarbon radius”. This is the radius of the spheres that encloses the oil and the alkyl chains of the surfactant. We, of course, expect r_{hc} to be smaller than r_H , since outside of r_{hc} we have the water-swollen layer of penta(ethylene oxide)(E_5).

For the scattering intensity from a solution of droplets, one can often consider the following relationship:

$$I(q) \sim \phi S(q) P(q) \quad (17.15)$$

where $S(q)$ is the structure factor, describing inter-droplet correlations and $P(q)$ is the form factor, corresponding to the single-particle scattering function. The factor $P(q)$ is known for many different morphologies

droplet shapes and contrast conditions. A recent review has been published by Pedersen (20). Apart from the trivial concentration-dependence due to the factor ϕ in equation (17.15), $S(q)$ also depends on the droplet concentration. In the absence of interactions, i.e. at infinite dilution, $S(q)$ equals unity for all q . This infinite dilution approximation was used in the fit shown in Figure 17.16. With increasing concentration, S decreases at low q , and may show a peak (or several damped oscillations) at intermediate q , but levels off at unity for high q . The number of oscillations depends on the degree of ordering in the structure, which is also influenced by polydispersity. For hard-sphere systems, which only have excluded volume interactions, polydispersity effects are relatively strong and $S(q)$ may contain only one peak. As $S(q)$ approaches unity at higher q , one can study the influence of concentration on droplet size by comparing scattering curves at different concentrations, which have been normalized by the volume fraction, ϕ . In Figure 17.17, we show a sequence of such normalized scattering curves. The fact that the normalized curves overlap at higher q values shows that the droplet size is indeed independent of the concentration. At lower q values, however, the curves differ due to the concentration dependence of $S(q)$ in this q range.

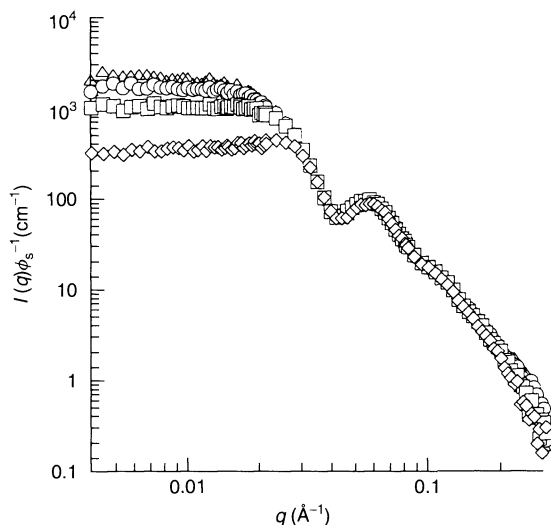


Figure 17.17. SANS intensities, normalized by the surfactant concentration, at four different droplet concentrations, $\phi := \Delta, 0.026; \circ, 0.065; \square, 0.13; \diamond, 0.25$. The overlap of the curves at higher q demonstrate that the droplet size and shape is independent of the droplet concentration (data taken from

7.10 Interactions

From self-diffusion data, we have found that the structure is composed of closed droplets. NMR data and SANS data, analysed at higher q values, have demonstrated that the droplets have a concentration-independent size. The SANS data have also given us one size of the droplets, i.e. the hydrocarbon radius (and the shape), while collective and self-diffusion data have provided us with a value for the hydrodynamic radius. Knowing that we have identified a dilution line of spherical droplets of constant size, we can now turn to investigate the interactions. The latter affect properties such as osmotic pressure, diffusion and viscosity. The osmotic pressure, π , can be measured, for example, in a membrane osmometer. A more common experiment for colloidal systems, however, is to measure the osmotic compressibility $(\partial\pi/\partial\phi)^{-1}$. For a binary system, the osmotic compressibility is proportional to the structure factor at $q = 0$, as follows:

$$S(0) = \frac{k_B T}{V_d} \left(\frac{\partial\pi}{\partial\phi} \right)^{-1} \quad (17.16)$$

where V_d is the volume of a droplet. In a small-angle scattering experiment, it is often difficult to reach sufficiently low q values to be able to estimate $S(0)$ accurately. With visible light, on the other hand, the q range is sufficiently low and $S(0)$ can be accurately determined in a static light scattering experiment. The droplets of the present system are uncharged, and below we will show, by analysing light scattering, diffusion and viscosity data, that they, to a very good approximation, behave as hard spheres.

7.11 Static light scattering

In a static light scattering experiment, the effective structure factor, $S(0)$ at zero scattering vector can be measured accurately, as obtained from extrapolating the light scattering intensity to $q = 0$. Figure 17.18 shows the variation of the excess Rayleigh ratio, i.e. the absolute scattering intensity, $\Delta R(0)$, extrapolated to zero scattering vector with the volume fraction of droplets, ϕ (17). For monodisperse hard spheres, an accurate expression for $S(0)$ exists due to the hard-sphere equation of state of Carnahan and Starling (21). The experimental data shown in Figure 17.18 were fitted with the Carnahan–Starling equation for $S(0)$ by using two adjustable parameters, namely the hard-sphere radius, r_{HS} , and the hydrocarbon radius, r_{hc} . This fit of the data

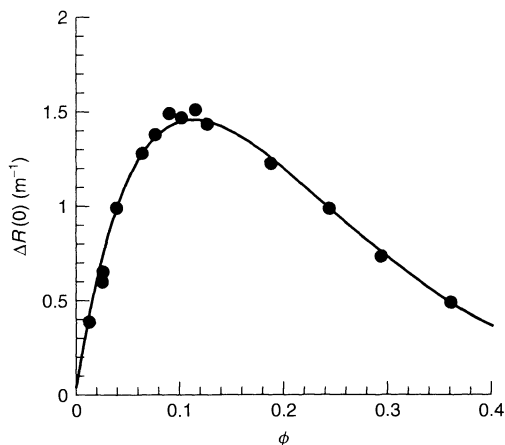


Figure 17.18. Variation of the excess Rayleigh ratio, ΔR , extrapolated to zero scattering vector, as a function of the droplet volume fraction, ϕ . The solid line is the best two-parameter fit using the Carnahan–Starling equation for the hard-sphere equation of state. The two fitted parameters were $r_{HS} = 86 \text{ \AA}$ and $r_{hc} = 76 \text{ \AA}$ (data taken from ref. (17))

shown in Figure 17.18 as a continuous line, results in an almost perfect match with the data. The parameters were found to be $r_{HS} = 86 \text{ \AA}$ and $r_{hc} = 76 \text{ \AA}$, with the latter being in excellent agreement with the SANS data. From r_{HS} , we also obtain the corresponding hard-sphere volume fraction $\phi_{HS} = 1.14\phi$. The fact that we are able to describe the system so well by assuming monodisperse spheres indicates that any polydispersity effects are minor.

7.12 Low shear viscosity

The low shear viscosity, η , has been measured by using capillary and, at higher concentrations, a cone-plate rheometer (22). The two techniques gave equivalent results in the overlapping concentration range. The variation of the normalized low shear viscosity, η/η_0 , where η_0 is the water solvent viscosity, with the hard-sphere volume fraction, ϕ_{HS} , is shown in Figure 17.19. For comparison, we have also plotted data from van der Werff and de Kruif (23) for hard-sphere silica dispersions of three different sizes. As can be seen, there is a perfect agreement between the microemulsion and silica data. The continuous line in Figure 17.19 shows the Quemada expression (24), as follows:

$$\eta/\eta_0 = (1 - \phi_{HS}/\phi_m)^{-2} \quad (17.17)$$

with $\phi_m = 0.63$, which provides an accurate description

In Figure 17.19, which mainly highlights the concentrated regime, we saw that the relevant parameter for describing the concentration was the hard-sphere volume fraction ϕ_{HS} . At high dilution, on the other hand, the viscosity is governed by the hydrodynamic volume

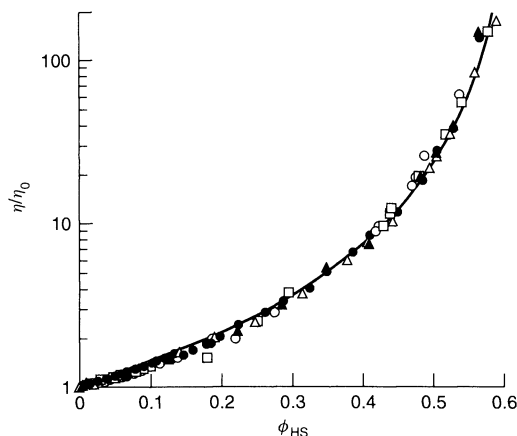


Figure 17.19. Variation of the normalized low shear viscosity, η/η_0 , with the hard-sphere volume fraction, ϕ_{HS} . Samples from the microemulsion (data taken from ref. (22)) were measured in a capillary (●) or in a cone and plate rheometer (▲). Open symbols show the data obtained for different radii of coated silica spheres in oil, taken from ref. (23), reproduced by permission of society of Rheology. The continuous line shows the prediction of equation (17.17)

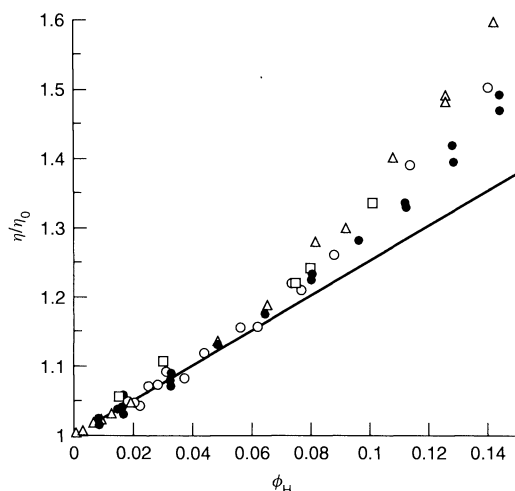


Figure 17.20. Concentration dependence of the normalized low shear viscosity in the dilute regime, plotted as a function of ϕ_H . The continuous line is plotted according to equation (17.18). The symbols are the same as those used in Figure 20.19, Vol. I

fraction ϕ_H , which in the microemulsion corresponds to 1.36ϕ . In Figure 17.20, we have plotted the concentration dependence of η/η_0 in the dilute regime, where the concentration is now represented by ϕ_H . The microemulsion and silica data are in good agreement at lower concentrations. The continuous line in Figure 17.20 follows the Einstein relationship (25), as follows:

$$\eta/\eta_0 = 1 + \frac{5}{2} \phi_H \quad (17.18)$$

As can be seen, the data agree well with the Einstein relationship below $\phi_H \approx 0.05$. At $\phi_H \approx 0.09$, the data obtained from the microemulsion system begin to deviate from the silica system. Above this concentration, direct interactions become important and ϕ_H is no longer the relevant concentration variable for the microemulsion particle. In fact, ϕ_H overestimates the effective concentration, which is now better described by ϕ_{HS} .

7.13 Diffusion

The concentration dependence of the collective (D_c) and self-diffusion (D_s) coefficients of the droplets were presented above in Figure 17.14. In Figure 17.21, we have re-plotted the data as D_c/D_0 and D_s/D_0 as functions of ϕ_{HS} . We recall that D_0 denotes the diffusion coefficient extrapolated to infinite dilution. In Figure 17.21, we also show, for comparison, D_c data on silica dispersions taken from the work of Kops-Werkhoven and Fijnaut (26) and D_s data from the work of van Megen and Underwood measured on traces of silica particles in dispersion of poly(methyl methacrylate) spheres (27). As can be seen, there is a good agreement between the different systems, both in the collective and self-diffusion data; D_c increases approximately linearly with ϕ_{HS} , and $D_c/D_0 \approx 1 + 1.3\phi_{HS}$, up to high volume fractions.

It is known from simple liquids that there is a correlation between D_s and η , where the product $D_s\eta$ is approximately constant upon variations in pressure or temperature (28). A similar correlation was also found in a colloidal hard-sphere system (29), with $D_s/D_0 = (\eta/\eta_0)$, which implies that the variation of D_s/D_0 can be described by the inverse of the relationship describing η/η_0 , as follows:

$$D_s/D_0 = (1 - \phi_{HS}/\phi_m)^2 \quad (17.19)$$

This equation is shown as a continuous line in Figure 17.21 and as can be seen, it provides a good

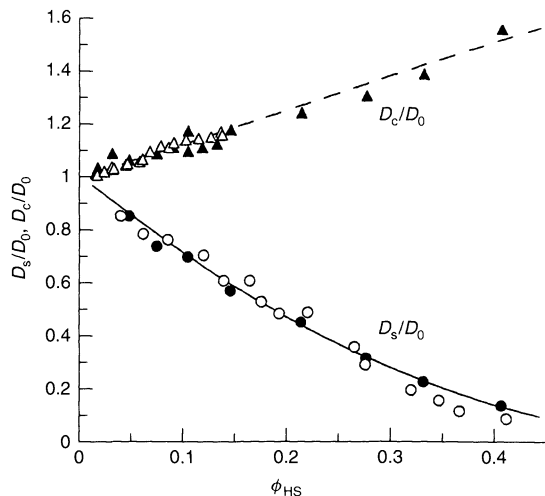


Figure 17.21. Variation of the normalized collective (D_c/D_0) (▲) and long-time self-diffusion (D_s/D_0) (●) coefficients with the hard-sphere volume fraction ϕ_{HS} . All filled symbols refer to microemulsion data (taken from ref. (17)). The D_c/D_0 data, shown as open triangles correspond to silica spheres, taken from ref. (26), while the D_s/D_0 data, shown as open circles, correspond to the self-diffusion of traces of silica spheres in a dispersion of poly(methyl methacrylate) spheres (data taken from ref. (27)). The dashed line represents the equation, $D_c/D_0 = 1 + 1.3\phi_{HS}$, while the continuous line represents the relationship, $D_s/D_0 = (1 - \phi_{HS}/0.63)^2$

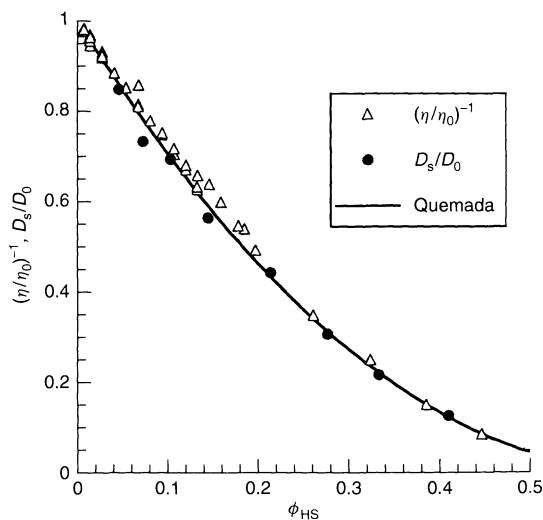


Figure 17.22. Plots of the normalized self-diffusion coefficient (D_s/D_0) and the inverse normalized low shear viscosity η/η_0 as a function of the hard-sphere volume fraction ϕ_{HS} . The open circles correspond to η/η_0 and the filled circles to $(D_s/D_0)^{-1}$, while the continuous line represents the Quemada function, i.e. $(1 - \phi_{HS}/0.63)$

description of the self-diffusion data. The correlation between the low shear viscosity and the long-time self-diffusion data becomes even clearer when diffusion and viscosity data are plotted together, as is done in Figure 17.22.

8 THE DROPLET TO BICONTINUOUS TRANSITION

The Winsor I and Winsor II equilibria (emulsification failure) results from a finite swelling of droplets, and correspond to saturated solutions in equilibrium with excess solubilize. In the Winsor III equilibrium, the (middle-phase) microemulsion has a bicontinuous structure. Similar to the Winsor I and II equilibria, the three-phase equilibrium can be considered as a finite swelling of the bicontinuous microstructure. The three-phase triangle forms from critical end-points, on the water-rich and one on the oil-rich side. The onset of three phase equilibria appears to be correlated with a micellar to bicontinuous structural transition in the microemulsion phase.

The micellar to bicontinuous transition can easily be detected by self-diffusion experiments. For example, in the case of an oil-in-water droplet structure, the surfactant and oil diffusion coefficients are essentially equal, and correspond to the self-diffusion coefficient of the micelle. On the other hand, in a bicontinuous microemulsion the two are no longer necessarily equal. Generally, one finds that the oil diffusion coefficient is higher than the surfactant diffusion coefficient (typically an order of magnitude difference). Furthermore, the self-diffusion coefficients are generally much higher in the bicontinuous structure when compared to the micellar microemulsion.

With nonionic surfactants, it is possible to generate an oil-in-water droplet to bicontinuous structural transition at constant composition by increasing the temperature. This transition can be studied in more detail by using self-diffusion experiments with mixed solvents. In a system where the oil was an equal weight mixture of cyclohexane (1) and hexadecane (2) the transition from normal oil-swollen micelles to a bicontinuous microstructure was studied by monitoring the variation of the self-diffusion coefficient ratio, $K = D_1/D_2$, as a function of the temperature (14). In the neat binary oil mixture, $K = K_0 = 1.69$. In the case of a closed droplet structure, the two oils will have the same diffusion coefficient, and $K = 1$. In a bicontinuous structure, on the other hand, the oil molecules diffuse in an oil-continuous medium and we expect $K = K_0$. In Figure 17.23, the

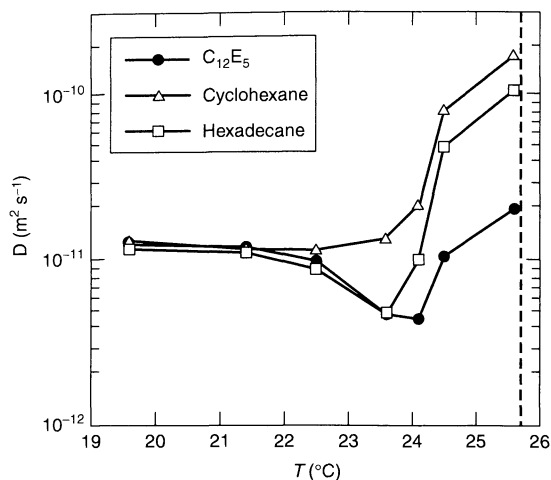


Figure 17.23. The variation of the self-diffusion coefficients of $C_{12}E_5$ (●), cyclohexane (Δ) and hexadecane (□) with temperature in the microemulsion phase. The sample composition is 7.0 wt% $C_{12}E_5$, 9.9 wt% oil (an equal weight mixture of cyclohexane and hexadecane) and 83.2 wt% D_2O (data taken from ref. (14))

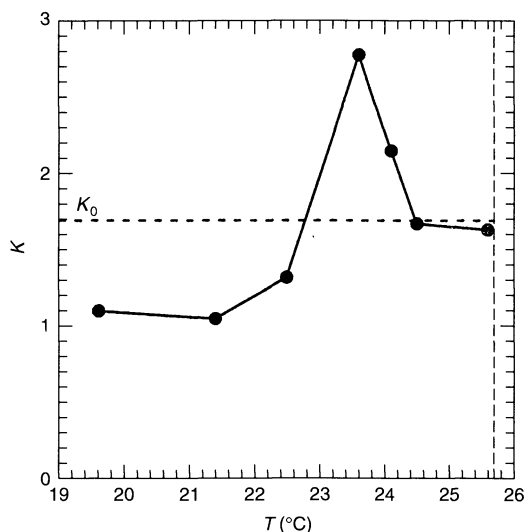


Figure 17.24. The variation of the self-diffusion coefficient ratio, $K = D_1/D_2$, with temperature; D_1 and D_2 are the self-diffusion coefficients of cyclohexane and hexadecane, respectively (data taken from ref. (14))

self-diffusion coefficients of the surfactant and the two oils are given as a function of temperature, for a sample containing 7.0 wt% $C_{12}E_5$, 9.9 wt% oil (being equal weights of cyclohexane and hexadecane) and 83.2 wt%

of D_2O . Figure 17.24 shows the temperature variation of the ratio $K = D_1/D_2$ obtained from the data of Figure 17.23. At lower temperatures, $K = 1$ and the oil and surfactant have equal self-diffusion coefficients, as expected for a closed droplet structure. At higher temperatures, close to the upper phase boundary, $K = K_0$ and the self-diffusion coefficients of the three species are all different, with $D_1 > D_2 \gg D_s$. Here, the microstructure is effectively bicontinuous. At intermediate temperatures, between the droplet and bicontinuous structures, K passes through a maximum and takes values significantly larger than K_0 . As discussed above, the droplets at lower temperatures experience essentially hard-sphere interactions. The particular variation of K in the micellar to bicontinuous transition indicates that the transition occurs via adhesive or “sticky” interactions. In micellar clusters with extensive micellar contacts, lighter and less hydrophobic oil molecules (cyclohexane) can selectively migrate, while larger oil molecules (hexadecane) remain essentially trapped. Note that in micellar clusters, the structure is effectively “ethylene oxide continuous”, while the remaining oil has a discontinuous structure. Hence, cyclohexane molecules do not necessarily migrate through water but rather through the less polar ethylene oxide double layer produced from two micelles at contact. Upon increasing the temperature, the ethylene oxide/water film between the micelles eventually breaks and the microstructure then becomes bicontinuous.

9 SPONGE PHASES

Sponge phases and balanced (bicontinuous) microemulsions are two structurally related liquid phases in that both have a disordered multiply connected film dividing two sub-volumes of equal volume fractions (30). In sponge phases, the film is a bilayer, and the two sub-volumes contain solvent of the same kind (water or oil). In a balanced microemulsion, on the other hand, there is a monolayer film, separating water from oil. The phase equilibria of the two phases is also similar. At higher surfactant concentrations, the phases are in equilibrium with a lamellar phase, and at lower surfactant concentrations with excess solvent. In the microemulsion case, the equilibrium with excess solvent results in a three-phase equilibrium, since water and oil are not miscible. Due to these similarities, and to the fact that sponge phases also occur in ternary mixtures, it is interesting to also discuss sponge phase properties within the present context.

In the case of sponge phases, the bilayer concentration can generally be varied over a large range

of concentrations. Evidence for the particular sponge-like structure comes mainly from self-diffusion (31) and small-angle scattering experiments (32), although freeze–fracture electron microscopy pictures obtained from a sponge phase have also been published (33). From self-diffusion data, one finds that the structure is both solvent- and bilayer- continuous. As for the balanced microemulsion, the solvent diffusion coefficient approaches, at high dilution, 2/3 of its value in pure solvent. In small-angle scattering, one can observe a peak in the structure factor, which reports on the structural length-scale. Except at very high concentrations, the structural length-scale varies approximately as ϕ_b^{-1} , where ϕ_b is the bilayer volume fraction. This scaling, which is the same as in the lamellar phase, is a consequence of the structure being made up of infinite films. Evidence of a bilayer structure can also be obtained from analysing the scattered intensity at higher value of q .

In contrast to the balanced microemulsions, the sponge phases in many systems undergo a transition at higher concentrations to an ordered (bicontinuous) cubic phase (there are no bicontinuous cubic phases with a monolayer structure), offering interesting opportunities to compare the properties of the two phases. One such system, which has been extensively studied, is the sodium di-2-ethylhexyl sulphosuccinate (AOT)–water–NaCl system (34). Below, we will discuss some self-diffusion data obtained from this system where we will, in particular, compare the diffusion behaviour in the sponge phase with that in the cubic phase at higher concentrations. By comparing the results from the two phases, and from a quantitative analysis of the sponge phase data, one can draw conclusions regarding the average coordination number of the sponge phase microstructure.

In the ordered cubic state, the bilayer topology, which can be quantified in terms of a coordination number of the two solvent labyrinths, can be determined from the space group. The far most common bicontinuous cubic phase structure belong to the space group Ia3d. A model for this structure involves the gyroid minimal surface which has the lowest possible coordination number, which is 3 in this case. This is also the structure of the cubic phase in the AOT–water–NaCl system. In the liquid sponge phase, on the other hand, one can only define an average coordination number since the structure in the liquid phase is disordered.

In Figures 17.25 and 17.26, water and surfactant diffusion data are presented as a function of the surfactant volume fraction, ϕ_s . The water diffusion data are presented relative to the diffusion constant in brine of the same salinity. The data contain several interesting

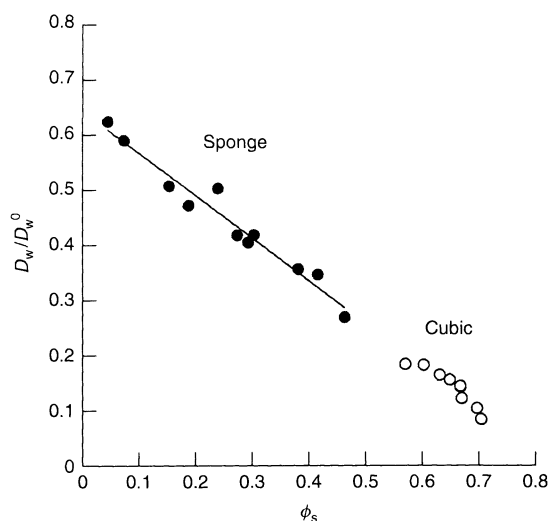


Figure 17.25. The variation of the reduced water self-diffusion coefficient with ϕ_s in the sponge (filled symbols) and the bicontinuous cubic (open symbols) phases. The continuous line corresponds to $D_w/D_w^0 = 0.66 - 0.77\phi_s$ and is a linear fit to the data from the sponge phase (data are taken from ref. (31))

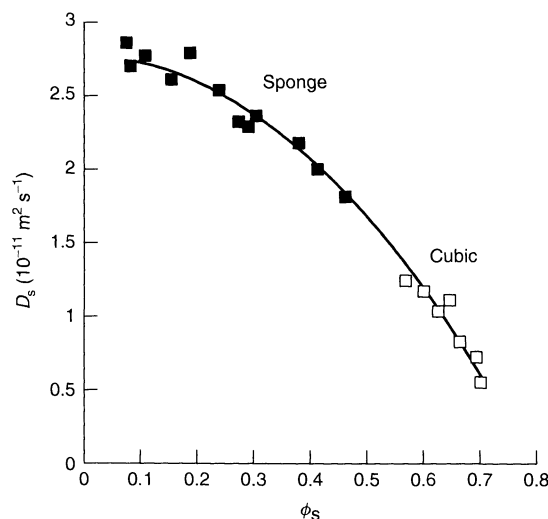


Figure 17.26. The variation of the surfactant self-diffusion coefficient with ϕ_s in the sponge (filled symbols) and the bicontinuous cubic (open symbols) phases. The continuous line corresponds to $D_s = 4.2(2/3 - (b'' + 2c/3)\phi_s^2)10^{-11} \text{ m}^2 \text{ s}^{-1}$ (see text for details) (data are taken from ref. (31))

features. First, the surfactant diffusion in the sponge phase show a very weak concentration-dependence. This is consistent with the concept that the diffusion

corresponds to a lateral diffusion within a continuous surfactant film. This is a very different behaviour when compared to that of a droplet structure (see Figure 17.14 above) in which case the surfactant diffusion coefficient decreases strongly with increasing concentration. Secondly, the relative water diffusion coefficient approach 2/3 at high dilution which is also consistent with an infinite bilayer film. Thirdly, very important result is also the smooth variation of the water and surfactant self-diffusion coefficients across the sponge-to-cubic phase transition. This result demonstrates that the microstructure of the two phases are topologically related.

Diffusion data from a sponge phase can also be analysed by using the model calculations of Anderson and Wennerström (15) (as discussed above) in connection with self-diffusion data from a balanced microemulsion. For the case of a bilayer structure, we have the following:

$$D_w/D_w^0 = 0.66 - b'\phi_b \quad (17.20)$$

and:

$$D_s/D_{sl} = 2/3 - b''\phi_b^2 \quad (17.21)$$

Here, D_w and D_s are, respectively, the water and surfactant self-diffusion coefficients in the sponge phase; D_w^0 is the diffusion coefficient of the neat solvent, which here corresponds to brine of the same salinity as in the sponge phase, and D_{sl} is the lateral diffusion coefficient of the surfactant in the surfactant film, while b' and b'' are coefficients which depend on the topology. Anderson and Wennerström have given numerical values for a few surfaces, although unfortunately not including the gyroid. For the case of the D-surface (coordination number of 4), $b' = 0.27$, although b'' was not solved for this surface. For the P-surface (coordination number of 6), $b' = 0.39$ and $b'' = 0.45$. These authors also investigated an asymmetric surface (the I-WP surface) and a general trend in the results was that b' increased with increasing topology.

Extrapolating the water diffusion data to infinite dilution, we obtain $D_w/D_w^0 = 0.66$, in agreement with a bilayer-continuous structure. In order to analyse the concentration dependence quantitatively, however, one needs to take into account hydration effects. These can be estimated from spin relaxation and quadrupolar line splittings of water ^2H and ^{17}O nuclei, suggesting that roughly 15 water molecules per AOT molecule are dynamically perturbed by the water-surfactant interface (35). Furthermore, the reorientation dynamics in the perturbed state is less than a factor of ten, and probably only a factor of three, which is slower than in the bulk (35).

A simple model that takes into account the hydration effects on the self-diffusion is a two-site discrete exchange model with a hydration and a bulk site. Here, we assume that n_h water molecules per AOT hydrate the water-surfactant interface and that these water molecules are free to diffuse laterally within the hydration layer, with a diffusion constant, D_{hw}^0 , which is slightly smaller (by a factor of 3) than D_w^0 . The remaining (bulk) water is obstructed by a bilayer volume fraction that equals ϕ_s plus the volume fraction of the hydration water. With fast exchange between the bulk and the hydration states, equation (17.20) can be recast as follow:

$$D_w/D_w^0 = a' - \left\{ b' + n_h \frac{\rho_s M_w}{\rho_w M_s} \left[a' + b' - \frac{2}{3} (D_{hw}^0/D_w^0) \right] \right\} \phi_b \quad (17.22)$$

where ρ and M refer to the density and molecular weight, respectively. By setting $n_h = 15$ and $D_{hw}^0/D_w^0 = 1/3$, in accordance with the spin relaxation data (35), the slope in Figure 17.25 corresponds to $b' = 0.27$, which is then consistent with a coordination number of four. Extrapolating to infinite dilution, we find $D_s = 2.8 \times 10^{-11} \text{ m}^2 \text{ s}^{-1}$, corresponding to $D_{sl} = 4.2 \times 10^{-11} \text{ m}^2 \text{ s}^{-1}$. This value is higher than the lateral diffusion constant of $0.27 \times 10^{-11} \text{ m}^2 \text{ s}^{-1}$, measured previously at 60 wt% AOT in the binary AOT-water L_α phase (36). This indicates that D_{sl} is concentration-dependent, which complicates a quantitative analysis. The D_s data follow roughly the functional form of equation (17.21); however, from a fit (shown as the continuous line in Figure 17.26), we obtain $b'' = 1.1$, which is significantly larger than the value of 0.3–0.4 expected for a low average coordination number. It is easy to verify that the D_s data are not consistent with a linear concentration-dependence of D_{sl} . Instead we will assume that the concentration dependence of D_{sl} follows $D_{sl} = 4.2(1 - c\phi_b^2) \times 10^{-11} \text{ m}^2 \text{ s}^{-1}$, which when inserted into equation (17.21) gives, to the lowest order, $D_s = 4.2(2/3 - (b'' + 2c/3)\phi_b^2) \times 10^{-11} \text{ m}^2 \text{ s}^{-1}$. From our two values of D_{sl} , we obtain $c = 1.2$, and with this value, the concentration dependence of D_s is consistent with $b'' = 0.3$. Hence, if our assumption regarding the concentration-dependence is correct, the D_s data from the sponge phase are quantitatively consistent with a bilayer continuous microstructure with a low (< 6) average coordination number.

The calculations above demonstrate the necessity of correcting diffusion data for hydration effects in concentrated systems and points to a way in which this can be achieved. The correction nevertheless involves

a number of uncertainties which consequently introduce relatively large uncertainties into the extracted values of b' and b'' . The strongest evidence in the present system for a low coordination number comes from the smooth variation of diffusion coefficients across the phase transition.

The sponge to cubic transition has also been studied in the ternary $C_{12}E_5$ /water/tetradecane system (36). In this system, a bicontinuous cubic phase (here the space group is also Ia3d) is formed which upon diluting with the oil is transformed into a sponge phase. In this case, the bilayer is reversed and swollen by water, while oil is the solvent. Figure 17.27 shows the self-diffusion coefficients of all three components in the cubic phase and in the sponge phase near the cubic transition. In addition, in this case there is no jump in the diffusion coefficients when going from the cubic to the isotropic sponge phase (37).

The bilayer sponge phase and the monolayer bicontinuous microemulsion are strongly related. Having similar structures, they are governed by similar thermodynamics and hence show related phase equilibria (38). As we saw in the phase diagrams of Figures 17.5 and 17.6 (and schematically in Figure 17.4), the sponge

phase can also join up with the bicontinuous microemulsion. Going from the sponge to the microemulsion structure must involve a fusion of the two monolayers of the sponge phase into a single monolayer. This is an interesting transition, which has not yet been studied in detail.

10 REFERENCES

1. Lindman, B. and Olsson, U., Structure of microemulsions studied by NMR, *Ber. Bunsenges. Phys. Chem.*, **100**, 344–363 (1996).
2. Glatter, O., Strey, R., Schubert, K.-V. and Kaler, E. W., Small angle scattering applied to microemulsions, *Ber. Bunsenges. Phys. Chem.*, **100**, 323–335 (1996).
3. Strey, R., Winkler, J. and Magid, L., Small-angle neutron scattering from diffuse interfaces: I. Mono- and bilayers in the water-octane- $C_{12}E_5$ System. *J. Phys. Chem.*, **95**, 7502–7507 (1991).
4. Jahn, W. and Strey, R., Microstructure of microemulsions by freeze fracture Electron Microscopy. *J. Phys. Chem.*, **92**, 2294–2301 (1988).
5. Safran, S. A., *Statistical Thermodynamics of Surfaces, Interfaces, and Membranes*, Addison-Wesley, Reading, MA, 1994.
6. Helfrich, W., Steric Interactions of Fluid Membranes in Multilayer Systems., *Z. Naturforsch.*, **33a**, 305–315 (1978).
7. Anderson, D. M., Davis, H. T., Scriven, L. E. and Nitsche, J. C. C., Periodic surfaces of prescribed mean curvature, *Adv. Chem. Phys.*, **77**, 337–396 (1990).
8. Shinoda, K. and Friberg, S. E., *Emulsions and Solubilization*, Wiley-Interscience, New York, 1986.
9. Schubert, K.-V. and Kaler, E. W., Nonionic microemulsions, *Ber. Bunsenges. Phys. Chem.*, **100**, 190–205 (1996).
10. Lekkerkerker, H. N. W., Kegel W. K. and Overbeek, J. Th. G., Phase behavior of ionic microemulsions, *Ber. Bunsenges. Phys. Chem.*, **100**, 206–217 (1996).
11. Winsor, P. A., *Solvent Properties of Amphiphilic Compounds*, Butterworth, London, 1954.
12. Safran, S. A., Saddle-splay modulus and the stability of spherical microemulsions, *Phys. Rev. A*, **43**, 2903–2904 (1991).
13. Olsson, U., Shinoda, K. and Lindman, B., Change of the structure of microemulsions with the hydrophile-lipophile balance of nonionic surfactant As revealed by NMR self-diffusion studies, *J. Phys. Chem.*, **90**, 4083–4088 (1986).
14. Olsson, U., Nagai, K. and Wennerström, H., Microemulsions with nonionic surfactants. I. Diffusion process of oil molecules, *J. Phys. Chem.*, **92**, 6675–6679 (1988).
15. Anderson, D. M. and Wennerström, H., Self-diffusion in bicontinuous cubic Phases, L3 phases, and microemulsions, *J. Phys. Chem.*, **94**, 8683–8694 (1990).
16. Leaver, M. S., Olsson, U., Wennerström, H., Strey, R. and Würz, U., Phase behaviour and structure in a non-ionic surfactant-oil-water mixture, *J. Chem. Soc., Faraday Trans.*, **91**, 4269–4274 (1995).

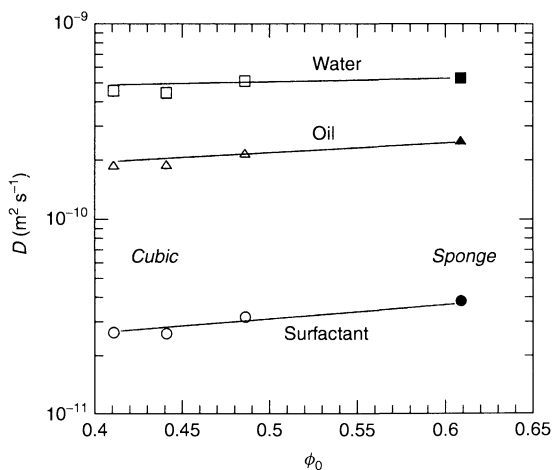


Figure 17.27. Self-diffusion coefficients of water (\square , \blacksquare), oil (\triangle , \blacktriangle) and surfactant (\circ , \bullet) in the bicontinuous cubic and oil-rich sponge phases of the $C_{12}E_5$ -water-tetradecane system. The $C_{12}E_5$ -to-water weight ratio is kept constant at 60/40, and the diffusion coefficients are plotted as a function of the oil volume fraction, ϕ_0 . Experiments were performed at the following temperatures: in the cubic phase at $\phi_0 = 0.41$ and 0.44 , $T = 20^\circ\text{C}$; in the cubic phase at $\phi_0 = 0.48$, $T = 23^\circ\text{C}$; in the sponge phase at $\phi_0 = 0.61$, $T = 25^\circ\text{C}$. The fact that the diffusion constants are essentially the same in the two phases demonstrates that the ordered (cubic) and disordered (sponge) structures are very similar (data taken from ref. (37)).

17. Olsson, U. and Schurtenberger, P., Structure, interactions and diffusion in a ternary nonionic microemulsion near emulsification failure, *Langmuir*, **9**, 3389–3394 (1993).
18. Leaver, M. S., Olsson, U., Wennerström, H. and Strey, R., Emulsification failure in a ternary system, *J. Phys. II*, **4**, 515–531 (1994).
19. Bagger-Jørgensen, H., Olsson, U. and Mortensen, K., Microstructure in a ternary microemulsion studied by small angle neutron scattering, *Langmuir*, **13**, 1413–1421 (1997).
20. Pedersen, J. S., Analysis of small-angle scattering data from colloids and polymer solutions: modeling and least-squares fitting, *Adv. Colloid Interface Sci.*, **70**, 171–210 (1997).
21. Carnahan, N. F. and Starling, K. E., Equation of state for nonattracting rigid spheres, *J. Chem. Phys.*, **51**, 635–636 (1969).
22. Leaver, M. S. and Olsson, U., Viscosity of a nonionic microemulsion near emulsification failure, *Langmuir*, **10**, 3449–3454 (1994).
23. van der Werff, J. C. and de Kruif, C. G., Hard sphere colloidal dispersions: the scaling of rheological properties with particle size, volume fraction and shear rate., *J. Rheol.*, **33**, 421–454 (1989).
24. Quemada, D., Rheology of concentrated disperse systems and minimum energy dissipation principle, *Rheol. Acta*, **16**, 82–94 (1977).
25. Einstein, A., *Investigations on the Theory of Brownian Motion*, Dover, New York, 1956.
26. Kops-Werkhoven, M. M. and Fijnaut, H. M., Dynamic light scattering and sedimentation experiments on silica dispersions at finite concentrations, *J. Chem. Phys.*, **74**, 1618–1625 (1981).
27. van Megen, W. and Underwood, S. M., Tracer diffusion in concentrated colloidal dispersions. III. Mean squared displacement and self-diffusion coefficients, *J. Chem. Phys.*, **91**, 552–559 (1989).
28. Packhurst Jr, H. J. and Jonas, J., Dense liquids. II. The effect of density and temperature on viscosity of tetramethylsilane and benzene, *J. Chem. Phys.*, **63**, 2705–2709 (1975).
29. van Bladeren, A., Peetermans, J., Maret, G. and Dhont, J. K. G., Long-time self-diffusion of spherical colloidal particles measured with fluorescence recovery after photobleaching, *J. Chem. Phys.*, **96**, 4591–4603 (1992).
30. Anderson, D., Wennerström, H., and Olsson, U., Isotropic bicontinuous solutions in surfactant–solvent systems: The L3 phase, *J. Phys. Chem.*, **93**, 4243–4253 (1989).
31. Balinov, B., Olsson, U. and Söderman, O., Structural similarities between the L3 and bicontinuous cubic phases in the AOT–brine system, *J. Phys. Chem.*, **95**, 5931–5936 (1991).
32. Gazeau, D., Bellocq A. M., Roux, D. and Zemb, T., Experimental evidence for random surface structures in dilute surfactant solutions, *Europhys. Lett.*, **9**, 447–452 (1989).
33. Strey, R., Jahn, W., Porte, G. and Bassereau, P., Freeze fracture electron microscopy of dilute lamellar and anomalous isotropic (L3) phases, *Langmuir*, **6**, 1635–1639 (1990).
34. Fontell, K., Influence of electrolyte on phase equilibria and phase structure in the binary system of di-2-ethylhexyl sulphosuccinate and water, in *Colloidal Dispersions and Micellar Behavior*, ACS Symposium Series, vol. 9, American Chemical Society, Washington, DC, 1975, pp. 270–277.
35. Carlström, G. and Halle, B., Water dynamics in microemulsion droplets. A nuclear spin relaxation study, *Langmuir*, **4**, 1346–1352 (1988).
36. Lindblom, G. and Wennerström, H., Amphiphilic diffusion in model membrane systems studied by pulsed NMR, *Biophys. Chem.*, **6**, 167–171 (1977).
37. Olsson, U., Würz U. and Strey, R., Cylinders and bilayers in a ternary nonionic surfactant system, *J. Phys. Chem.*, **97**, 4535–4539 (1993).
38. Wennerström, H. and Olsson, U., On the flexible surface model of sponge phases and microemulsions, *Langmuir*, **9**, 365–368 (1993).

CHAPTER 18

Measuring Particle Size by Light Scattering

Michal Borkovec

University of Geneva, Geneva, Switzerland

1	Introduction	357	4	Dynamic Light Scattering	365
2	Particle Size Distribution	358	4.1	Basic principles	365
2.1	A few common definitions	359	4.2	Illustrative examples	366
2.2	Averages and moments	359	5	Simultaneous and Time-Dependent	
2.3	Simple analytical expressions	360	Methods	368	
3	Static Light Scattering	360	5.1	Probing aggregation by simultaneous	
3.1	Essentials of a scattering		static and dynamic light		
experiment	360		scattering	368	
3.2	Various light scattering regimes	361	6	Conclusion	369
3.3	Illustrative examples	363	7	References	369

1 INTRODUCTION

Light scattering represents one of the most powerful particle sizing techniques. Together with the new developments in real-time data analysis, no other technique surpasses its versatility, speed and wide range of applicability. A modern goniometer set-up offers two techniques at once, namely static light scattering (SLS) and dynamic light scattering (DLS). The angular range can be substantially extended for SLS with a small-angle light scattering (SALS) set-up. These three techniques allow us to size particle over a very wide size range, they can be used to study nearly monodisperse as well as highly polydisperse samples, and can be used to differentiate between different particle shapes. The great advantage of light scattering is that the method operates entirely *in situ*, meaning that the sample remains undisturbed during the whole experiment. For this reason, light scattering can be used to probe flexible and unstable particles (e.g. polymers and micelles), it provides information about inter-particle interactions, and

can be used to monitor the kinetics of time-dependent processes, such as particle aggregation or growth of emulsion droplets. In this chapter, we shall solely focus on particles suspended in liquids, and will not discuss applications to other systems, such as aerosols or gels. All of these techniques have been reviewed in substantial detail previously (1–6).

Due to its great versatility, however, light scattering is susceptible to superficial data interpretation, and is sometimes claimed to produce erroneous results. While such claims rather reflect the lack of know-how than a weakness of the technique, one must contend that light scattering, as any other technique, has its drawbacks. The most important of these being the very strong scattering power of many types of particles in water, thus making quantitative data analysis complicated and sometimes even impossible. (On the other hand, the very same strong scattering power makes the technique highly sensitive.) To study turbid or highly concentrated samples, much progress was made in the development of diffusing wave spectroscopy (7), as

well as in the design of selective detection of singly scattered light from multiply scattering samples, such as three-dimensional cross-correlation or the two-colour set-up (8–10). Our entire discussion here will focus on situations where single scattering is dominant. The other often quoted weaknesses are the small magnitudes of the scattering vector inherent to the light scattering experiment. However, the latter shortcoming is clearly subjective; while this range is clearly sub-optimal for nanometre-sized micelles, it could not be positioned better for the study of sub-micron particles.

Many other techniques for particle sizing are available. While we shall not attempt to cover all of these methods in this present chapter in a comprehensive fashion, a few pertinent comparisons will be given. A detailed discussion of these methods can be found elsewhere (11).

Most closely related to (static) light scattering are techniques using other radiation sources, most importantly small-angle X-ray scattering (SAXS) and small-angle neutron scattering (SANS). Due to shorter wavelengths, both techniques have the advantage of a favourable range of the scattering vector for polymers, micelles and nano-sized particles (12). Neutron scattering provides the unique possibility of contrast variation by changing the isotopic substitution of the sample. While contrast variation is used most often with neutrons, such techniques can be also used for light or X-rays in specialized situations. More recently, ultra-small-angle X-ray and neutron scattering (USAXS and USANS) have become possible and cover a similar range of the scattering vector as in light scattering. The main disadvantage of all of these techniques is that the instruments are usually not accessible on an day-to-day basis, as they rely on major facilities (e.g., synchrotron, spallation sources, etc.).

Another class of very powerful techniques for particle sizing is single-particle counting [11, 13, 14]. Here, the sample suspension is pumped through a narrow capillary, where the particles are being separated and can be detected individually, typically through conductivity measurements or light scattering. With single-particle detection, the technique attains excellent resolution and one obtains good statistics at the same time. The technique works best with micron-sized particles, as sub-micrometre particles can be already difficult to detect. A further disadvantage of the technique is that it does not entirely operate *in situ*, since in the hydrodynamic focussing cell rather high shear rates are being generated. Soft particles may deform or aggregates can be disrupted.

Direct microscopy still represents the most reliable tool for a detailed size distribution analysis of solid particles. The size distribution, as well as detailed information about particle shape, can be inferred from appropriate micrographs in an extremely reliable fashion (11, 15). Besides classical electron microscopy techniques, the modern direct probe techniques (e.g. atomic force microscopy) offer additional potential for particle sizing, especially since one can routinely attain nanometre resolution in the particle height (16). However, the accuracy has its cost; even with modern image analysis tools the data analysis remains tedious even for almost monodisperse samples (and extremely laborious for highly polydisperse ones). Furthermore, precise calibration of the magnification is tiresome but necessary, and the preparation of representative samples is entirely non-trivial. In particular, the latter aspect represents the most serious drawback of this method, as eventual fractionation or shrinkage of the particles during preparation is most difficult to exclude. Cryo-transmission electron microscopy represents probably the most reliable technique in this respect.

In spite of their long history, sedimentation and centrifugation still represent very powerful sizing tools, particularly for very polydisperse samples of solid particles (11, 17). Sedimentation methods are now conveniently automated, and offer an interesting sizing tool for particles in the lower micrometre range. A centrifuge can be used to extend the lower limit well into the nanometre size range, whereby a modern analytical ultracentrifuge is particularly powerful in this respect. These techniques work best with particles of uniform composition, since there is no way to distinguish between simultaneous variations in size and density of the particles.

More recently, a number of other techniques for particle sizing have emerged. An interesting class represent the flow-field fractionation methods (18). The main advantage of such a methodology is that the applied external field can be varied (e.g. flow field, magnetic field, etc.), particles can be separated according to various properties (e.g., diffusion coefficient, magnetic moment, etc.). Another recent interesting tool are various ultrasonic techniques (19), where the size distribution is being extracted from analysis of the absorption spectra of acoustic waves. The interesting aspect of the latter techniques is that they can be well applied to very concentrated and turbid samples.

2 PARTICLE SIZE DISTRIBUTION

Different definitions of the “particle size distribution” and of the “average particle radius” are common (4, 11).

For a proper data interpretation, it is absolutely crucial to specify which of the different definitions is being used. Unfortunately, many authors are often not entirely clear on this point.

2.1 A few common definitions

The simplest way to introduce the size distribution is by counting. Suppose that we measure the size of each particle (e.g. with a microscope), sort the particles according to their size into “bins”, and then count the particle number in each bin. This process leads to the *number-weighted distribution*. Let us introduce the particle number density, $N(R)$, where $N(R) dR$ represents the number of particles per unit volume with radii between R and $R + dR$, whereby we assume spherical particles for simplicity. The total particle concentration C , being defined as the number of particles per unit volume, is given by the following:

$$C = \int_0^\infty N(R) dR \quad (18.1)$$

The normalized *number distribution* is now defined as follows:

$$p(R) = C^{-1} N(R) \quad (18.2)$$

since its integral is unity.

Another common way to introduce the distribution is by weighting. Imagine that we sort all particles according to their size into bins as discussed before, but instead of counting the individual particles, we weigh all the particles within each bin with a balance. This process leads to the *mass-weighted distribution*. This distribution is simply proportional to $R^3 N(R)$, since the volume of a particle (and thereby its mass at constant particle density) is proportional to R^3 . The quantity $R^3 N(R) dR$ is proportional to the mass fraction between R and $R + dR$. The unknown proportionality constant can be obtained through an appropriate normalization and the distribution reads as follows:

$$p_n(R) = \frac{R^n N(R)}{\int_0^\infty R^n N(R) dR} \quad (18.3)$$

For $n = 0$, we recover the *number-weighted distribution*, namely $p_0(R) = p(R)$, while for $n = 3$ the *mass-weighted distribution* is obtained. Of course, other weights can be introduced, for example, $n = 2$ corresponds to the *area-weighted distribution*, while $n = 6$ is sometimes referred to as the *intensity-weighted distribution* for reasons to be discussed later.

Cumulative particle size distributions represent another class of commonly discussed quantities, either introduced as the *undersize fraction*:

$$P_n(R) = \int_0^R p_n(R') dR' \quad (18.4)$$

or as the *oversize fraction*:

$$Q_n(R) = 1 - P_n(R) = \int_R^\infty p_n(R') dR' \quad (18.5)$$

Again, these cumulative distributions can be weighted in a different way.

2.2 Averages and moments

Other useful characteristics of any probability distribution are its moments. For the particle size distribution, we can introduce the moments with different weight, but for simplicity we shall only refer to moments defined with respect to the number-weighted distribution. The moment of order m is defined as follows:

$$\langle R^m \rangle = \int_0^\infty R^m p(R) dR \quad (18.6)$$

where $\langle \dots \rangle$ will be used as shorthand notation for averaging over the particle size distribution. The first moment, denoted as $\bar{R} = \langle R \rangle$, is the mean of the distribution, and is also referred to as the *average particle radius*. The second moment is related to the width of the distribution, which is commonly parametrized through the standard deviation σ , defined as follows:

$$\sigma^2 = \langle R^2 \rangle - \bar{R}^2 \quad (18.7)$$

or the dimensionless *polydispersity index* ε (also referred to as the *coefficient of variation*):

$$\varepsilon = \frac{\sigma}{\bar{R}} \quad (18.8)$$

Moments for the distributions with different weights have been introduced similarly, but they can be always related to the number-weighted moments introduced here. For simplicity, we shall only use the number-weighted moments in the following discussion.

The moments do not only represent useful characteristics of the size distribution, but enter various other important quantities. For example, the particle volume fraction ϕ is related to the number concentration and to the third moment of the distribution as follows:

$$\phi = \frac{4\pi}{3} C \langle R^3 \rangle \quad (18.9)$$

Another commonly used characteristics is the *specific surface area*, a , of the particles (per unit particle mass). Again this quantity can be expressed in terms of the moments, namely:

$$a = \frac{3 \langle R^2 \rangle}{\rho \langle R^3 \rangle} \quad (18.10)$$

where ρ is the particle density.

2.3 Simple analytical expressions

Particle size distributions have often been approximated by various analytical functions. Note that a physically meaningful distribution is non-zero only for non-negative radii, and for this reason the popular Gaussian distribution is not very convenient. (However, this function can still be used to approximate narrow size distributions.) An important distribution without this drawback is the generalized exponential distribution (or Schultz distribution) (6, 20), given as follows:

$$p(R) \propto R^{\nu-1} \exp(-\nu R/\bar{R}) \quad (18.11)$$

where $\nu = 1/\varepsilon^2$. For sufficiently small polydispersities ($\varepsilon \ll 1$), the distribution becomes equivalent to a Gaussian. Another advantage of this distribution is that all its moments are readily calculated. In fact, they can be expressed in terms of a simple recursion relation:

$$\langle R^{m+1} \rangle = (1 + m\varepsilon^2) \bar{R} \langle R^m \rangle \quad (18.12)$$

A similar distribution of this kind is the log-normal distribution, for which the moments also can be evaluated explicitly.

Another important particle size distribution, which is also contained in equation (18.11), is the simple power-law (17, 21):

$$p(R) \propto R^{\nu-1} \quad (18.13)$$

In order to be normalizable, this distribution can be only valid over the size range $R_{\min} \leq R \leq R_{\max}$, which is limited by the cut-off values R_{\min} and R_{\max} . Such distributions are very important in various applications, and their properties depend strongly on the value of the exponent ν . In many situations, the exponent falls into the range of $2 < \nu < 3$, and in such cases it was referred to as the *fragmentation fractal dimension*. Such size distributions have distinctive properties. When the cut-off values are sufficiently far apart (i.e. $R_{\min} \ll R_{\max}$), the moment $\langle R^3 \rangle$, which defines the volume fraction, is dictated by the upper cut-off R_{\max} , while an *aphod multiplier*

the surface area, being related to $\langle R^2 \rangle$, is related to the lower cut-off. If particles of different shape and composition are being considered, the size distribution function becomes a function of several variables. For example, for cylindrical particles the size distribution will be a function $p(r, L)$ where r is the cylinder radius and L its length. As we have discussed for one-dimensional distributions above, two-dimensional probability distributions can be similarly characterized by their moments. This procedure is described in most statistical textbooks. The mass-weighted distribution and any other associated distributions can be introduced in a similar way.

3 STATIC LIGHT SCATTERING

Static light scattering (SLS) represents an old but still an extremely useful technique. In a modern scattering setup, the sample is illuminated with a laser beam, and the intensity of the scattered light is monitored as a function of the scattering angle (see Figure 18.1).

3.1 Essentials of a scattering experiment

Here we shall only give a brief summary of the pertinent relationships, as detailed accounts are given in various classical monographs (2, 3). The sample is illuminated with an incident light beam with an intensity I_0 and a wave vector \vec{k}_i . (We shall only consider the case where the light is polarized perpendicular to the scattering plane.) The magnitude of the wave vector is given by $k_i = 2\pi n/\lambda$, where λ is the wavelength of the light in vacuum and n is the refractive index of the sample. The intensity of the scattered light I is proportional to the square of the magnitude of its electric field. If one considers two scattering elements within a particle at distance \vec{r} , the electric field of the scattered

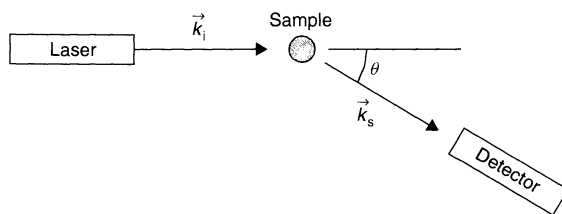


Figure 18.1. Schematic of a light scattering experiment. The sample is illuminated by an incident beam of wave vector \vec{k}_i from a laser and the scattered light with wave vector \vec{k}_s is monitored at a known scattering angle θ by a detector, usually

light with a scattering vector \vec{k}_s will be proportional to $\exp(i\Delta\phi)$ where i is the imaginary unit and the optical phase shift $\Delta\phi = \vec{r} \cdot \vec{k}_i - \vec{r} \cdot \vec{k}_s = \vec{r} \cdot \vec{q}$. Thereby, we have introduced the scattering vector, as follows:

$$\vec{q} = \vec{k}_i - \vec{k}_s \quad (18.14)$$

Given the fact that the wavelengths of the scattered and incident light are virtually identical ($k_i \simeq k_s$, elastic scattering), the magnitude of the scattering vector is therefore:

$$q = \frac{4\pi n}{\lambda} \sin(\theta/2) \quad (18.15)$$

and is given by the scattering angle θ . As the scattering angle is being varied, constructive and destructive interferences of the scattered light occur, and the angular dependence contains information about particle size and shape (see Figure 18.2). Qualitatively, the inverse magnitude of the scattering vector represents the “yardstick” which is used in the scattering experiment to probe the sample. The experiment will respond best to objects whose size is comparable to q^{-1} .

At this point let us recall the two common experimental arrangements for SLS. The classical goniometer set-up is shown in Figure 18.1, and is used in most modern instruments. The sample is illuminated with a focussed laser beam, and the scattered light is detected either with a movable arm or with a fixed array of detectors (some instruments combine both options). While this set-up is optimal for static as well as dynamic light scattering, the range of scattering vectors is limited by the accessible range of scattering angles, i.e. 20–160°. For the popular argon ion laser, with a wavelength of 514 nm and an aqueous suspension, one obtains a range of scattering vectors from about 0.005–0.033 nm⁻¹, i.e. about one order of magnitude.

This range can be extended to much smaller scattering vectors, although the classical goniometer set-up is not suitable for such a purpose due to stray light at small angles. Small-angle light scattering (SALS) measurements can be routinely carried out down to small scattering angles with a different instrumental set-up (17).

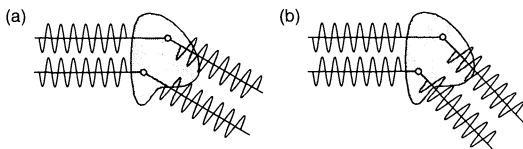


Figure 18.2. Representation of the interference patterns occurring during light scattering from a particle. As light is being scattered from two different scattering volume elements, the scattered waves will interfere. These interferences can be either (a) destructive, or (b) constructive

The most popular way to avoid these problems is to illuminate a large sample with an expanded laser beam, and to place a focussing lens behind the sample. At the focal plane, where the illuminating beam is focussed to a very small illuminated spot, one can record the scattering intensities with an array of photosensitive diodes or a charge-coupled device (CCD) camera. By choosing a sufficiently large focal length of the lens, scattering angles $< 0.01^\circ$ can be achieved. In order to scan a wide angular range at the same time, it is necessary to choose different focal lengths, as can be nowadays achieved automatically.

3.2 Various light scattering regimes

The differences in the optical path lengths are negligible for small particles. However, when the particle size is comparable to the inverse of the scattering vector magnitude, interference effects do occur and the angular variation of the scattering intensity pertains to information about the particle size and shape. For a suspension of particles the scattering intensity can be written as follows: (4, 6):

$$I(q) = K P(q) S(q) \quad (18.16)$$

where $P(q)$ is the form factor, $S(q)$ the structure factor, and K is a constant, which depends on the optical properties of the particles, their concentration and the details of the optical set-up.

The form factor $P(q)$ is related to the particle size and shape, while the structure factor $S(q)$ incorporates the effects of particle–particle interactions. For a dilute suspension ($C \rightarrow 0$) the latter factor becomes immaterial, and $S(q) \rightarrow 1$. It is precisely this dilute regime, which is of central interest for particle sizing, as the effects of particle interactions can be difficult to interpret.

For sufficiently small particles, there is no angular variation of the scattering intensity, as the particles are small compared to the “yardstick” (Rayleigh limit). In spite of this fact, the absolute scattering intensity contains information on the particle size, as the overall scattering power strongly increases with increasing particle size. For a fixed wavelength and intensity, the constant K entering equation (18.16) is proportional to:

$$K \propto C \langle \alpha^2 \rangle \quad (18.17)$$

where α is the polarizability of the particles, and C the number concentration introduced above. (The proportionality constant in equation (18.17) is usually calibrated by using a scattering standard, such as toluene.)

The polarizability, in turn, is proportional to the particle volume, $\alpha \propto R^3$, and the difference between the refractive indices of the particle and the solvent, with the latter quantity being accessible from differential refractometry measurements. For homogeneous spheres of radius R , the ratio between the scattering intensity and the particle volume fraction, I/ϕ , is proportional to R^3 , and this quantity can be used to estimate the particle size. For a polydisperse system, the signal is proportional to the following ratio of moments:

$$\frac{\langle R^6 \rangle}{\langle R^3 \rangle} \simeq \bar{R}^3 (1 + 12\varepsilon^2 + \dots) \quad (18.18)$$

and thus contains information on particle size and polydispersity. This method is standard practice for the determination of the molecular weight of polymers, but can be equally well applied for the sizing of small particles in solution. Under most circumstances, no detailed information about the particle size distribution can be obtained, except if the system allows for a contrast variation experiment. In this case, I/ϕ is a direct measure of $\langle \alpha^2 \rangle / \langle R^3 \rangle$, which does contain detailed information on particle size as well as the polydispersity. An application of this powerful technique will be discussed below.

Let us now focus on larger particles, whose size is comparable with the “yardstick” of the scattering experiment. In a dilute suspension, the angular dependence of the scattered intensity is proportional to the form factor $P(q)$. This angular dependence contains information about particle size and shape. For not too large particles and sufficiently weak contrast, the form factor can be related to the square of the phase shift within the particle (2), as follows:

$$P(q) \propto \int \exp(i\vec{r} \cdot \vec{q}) \Delta n(\vec{r}) d^3\vec{r} \quad (18.19)$$

where $\Delta n(\vec{r})$ is the difference of the refractive index between the particle and the solvent. The normalization constant is chosen such that $P(q) \rightarrow 1$ as $q \rightarrow 0$. The above expression represents the so-called Rayleigh–Debye–Gans (RDG) approximation, and its accuracy will be addressed below. For a solid sphere, equation (18.19) is readily evaluated. The result reads as follows:

$$P(q) = \frac{9}{(qR)^6} [\sin(qR) - qR \cos(qR)]^2 \quad (18.20)$$

where R is the radius of the sphere. For particles, which are small compared to the wavelength, only the regime of small q is relevant. For a polydisperse system, the

scattering intensity is given by the average over the size distribution:

$$I(q) \propto \langle \alpha^2 P(q) \rangle \propto \langle R^6 P(q) \rangle \quad (18.21)$$

where the square of the polarizability α represents the weight for each particle size. For solid and not too large particles, $\alpha \propto R^3$ and the weighting factor of the size distribution is R^6 . For this reason, the size distribution $p_6(R) \propto R^6 p(R)$ is referred to as the *intensity-weighted distribution*.

Quite generally, equation (18.19) can be expanded in a Taylor series with the following result:

$$P(q) = 1 - \frac{R_g^2}{3} q^2 + \dots, \text{ etc.} \quad (18.22)$$

which defines R_g as the radius of gyration. Equation (18.22) is commonly written as the Guinier approximation:

$$P(q) = \exp\left(-\frac{R_g^2 q^2}{3}\right) \quad (18.23)$$

A plot of the logarithm of the scattering intensity as a function of the square of the scattering vector yields a straight line, the slope of which gives the gyration radius of the particles.

For a solid sphere of radius R , its gyration radius is given by $R_g = \sqrt{3/5}R$, as can be verified by expanding equation (18.20). While equation (18.22) applies for any type of particles, the gyration radius must be interpreted accordingly. For the situation of polydisperse spheres, the gyration radius is related to the moments of the distribution, and reads:

$$R_g = \sqrt{\frac{\langle R^8 \rangle}{\langle R^6 \rangle}} \simeq \bar{R} \left(1 + \frac{15}{2} \varepsilon^2 + \dots\right) \quad (18.24)$$

In a polydisperse sample, the gyration radius will be always larger than the number-averaged radius. Gyration radii have been tabulated for various other particle shapes. For example, for a cylinder one has $R_g = \sqrt{R^2/2 + L^2/12}$, where R is the cylinder radius, and L its length.

Of course, static light scattering is most useful for particle sizing when the particle size and the length of the “yardstick”, q^{-1} , become comparable. The range of scattering vectors can be extended by two to three orders of magnitude with the SALS set-up, where particles over the entire micrometre to millimetre range can be analysed. In this regime, however, neither the Guinier nor the RDG approximation are valid. While larger particles can be analysed by using the Fraunhofer theory,

it is best to rely on the exact *Mie theory* of scattering from a sphere. While the resulting expressions for the form factor are rather complex, they can be used for data analysis in a straightforward fashion. The exact evaluation of the form factors with the Mie theory can be carried out quickly on any modern personal computer, and one can thus easily avoid any pitfalls from the use of any approximate theories. The particle size distribution can be extracted by combining direct deconvolution schemes with the Mie theory, and such algorithms have been developed by various researchers and are also available for commercial instruments (22, 23). In contrast to the RGD approximation, the refractive index of the particles enters the Mie theory in a non-trivial fashion, and thus must be known for detailed data analysis. However, numerous methods for the determination of the refractive index for scattering data are available.

It is essential to note that all of the above methods are only applicable if particle-particle interactions are negligible. In most non-aqueous solvents, as well as in water at sufficiently high salt concentration (say $> 10\text{mM}$), as a rule of thumb such interactions can be neglected when the volume fraction $< 10^{-2}$, but in many situations even higher particle concentrations may be adequate. This rule holds for systems where Coulombic interactions are unimportant, with the most notable exception being highly charged particles in deionized water. In such a system, the interactions are very long-ranged and can be important down to volume fractions of 10^{-5} . If interactions cannot be eliminated, one can study the scattering properties of the sample as a function of the particle concentration. The simplest approach is to extrapolate the scattering properties to infinite dilution. The other possibility is to estimate the effect of interactions on the structure factor $S(q)$ through an approximate theory.

3.3 Illustrative examples

Let us discuss a few applications of static light scattering for particle sizing. The first example will be the use of static light scattering to measure the size distribution of very monodisperse latex particles, while the second example will illustrate the determination of the polydispersity index of inverse micelles by contract variation. The last example will emphasize the use of small-angle light scattering to measure a very wide particle size distribution.

Static light scattering is most powerful when the particle size is comparable to the inverse magnitude of

the scattering vector. An example of such a situation is a scattering experiment on a suspension of almost monodisperse latex particles (24). The small polydispersity of such particles can be reliably determined by SLS. The scattering intensity of a dilute suspension of latex particles is shown in Figure 18.3. In this figure, the continuous line is the best fit assuming spherical particles with a size distribution following a generalized exponential distribution and using the Mie theory to calculate the optical response of the particles. The best-fit results are an average radius of $\bar{R} = 291\text{ nm}$, a polydispersity index $\varepsilon = 0.038$ and the refractive index for polystyrene of 1.596, which also follows from the fit. In order to achieve such a good fit, it is essential to introduce a reflection correction into the calculation, which originates from the fact that the light intensity seen by the detector at scattering angle θ contains a contribution from scattered light at the scattering angle $180^\circ - \theta$. The derived parameters compare favourably with transmission electron microscopy results which yield $\bar{R} = 290\text{ nm}$ and $\varepsilon = 0.047$.

While such scattering results contain a wealth of detailed information, this statement only applies for a rather narrow size distribution within a favourable size range. A precise estimate of such small polydispersities requires the presence of at least one minimum in the form factor, thus limiting the analysis to sufficiently large particles.

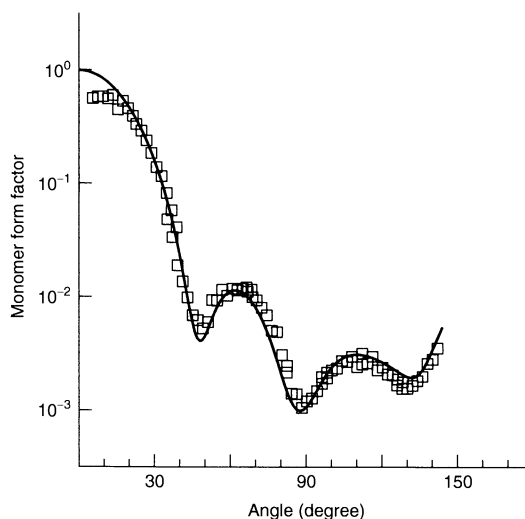


Figure 18.3. Static light scattering from latex particles. The experimental points are fitted with the exact Mie theory and a size distribution including polydispersity. The resulting average radius is $\bar{R} = 291\text{ nm}$ and the polydispersity index $\varepsilon = 0.038$ (reproduced from ref. (24)), with permission from Academic Press

For very small particles, there is no angular dependence of the scattering intensity, and not even an gyration radius can be extracted. However, the absolute scattering intensity contains information about the particle size, but in most cases only an average particle size can be extracted. However, if the system investigated allows a systematic variation of the optical contrast, one has a powerful method at hand, from which even small polydispersities can be obtained reliably. Such situations are not that uncommon – they readily occur for water-in-oil microemulsions, but are also conceivable for other types of layered nanoparticles.

As an example for this situation, consider water-in-oil microemulsion droplets. Ricka *et al.* (20) have studied such a system using the surfactant sodium bis(2-ethylhexyl) sulfosuccinate (AOT). By varying the water–surfactant ratio, one can systematically tune the droplet size. Based on elementary geometrical considerations, the average radius of the water pool droplet \bar{R} can be shown to be given by the following:

$$\bar{R} \simeq L\omega \quad (18.25)$$

where ω is the molar water–surfactant ratio. As the refractive index of the surfactant is rather high, and it is quite low for water, the average refractive index of the droplet increases with increasing droplet size. Since the droplets are dispersed in an oil (*n*-hexane), which has an intermediate refractive index, the polarizability of the droplet goes through zero at one particular droplet radius – such droplets become invisible and do no longer scatter light. Close to such an optical matching point, the scattering properties of the system are dictated by the polydispersity of the sample, and static light scattering becomes an extremely sensitive probe of the polydispersity.

Figure 18.4 shows the results obtained from such SLS experiments. The scattering intensity is plotted as $\langle \alpha^2 \rangle / \langle R^3 \rangle$ as a function of the molar water-to-surfactant ratio, ω . The experimental data are compared with a coated sphere model containing two adjustables, with one being the proportionality constant L entering equation (18.25), and the second the polydispersity index of the droplets ε . The former parameter only causes a vertical shift of the curve, while its shape is entirely determined by the polydispersity. Three different polydispersity indices were used to predict this curve, and the results turn out to be very sensitive to these values. Thus, the polydispersity index can be determined from such an experiment with good confidence, and the result yields the values $\varepsilon \simeq 0.12$ and $L \simeq 0.15$ nm.

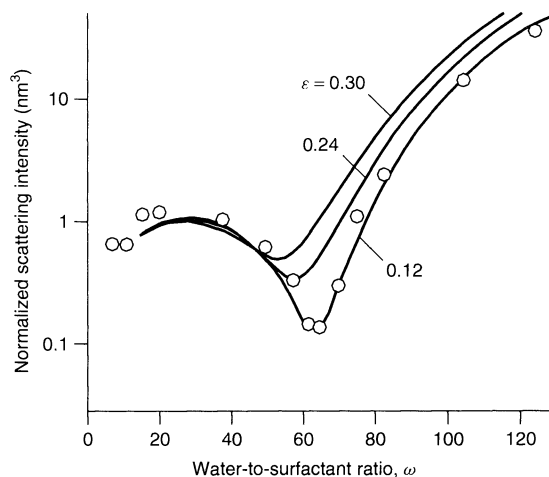


Figure 18.4. Static light scattering from water-in-oil microemulsion droplets with the surfactant sodium bis(2-ethylhexyl) sulfosuccinate (AOT). The normalized static scattering intensity $\langle \alpha^2 \rangle / \langle R^3 \rangle$ is shown as a function of the water-to-surfactant molar ratio ω . The continuous lines are calculated with a coated sphere model for different polydispersity indices (20)

The previous two examples did illustrate situations where rather narrow size distribution were analysed. The final example of this section serves the purpose of showing the excellent ability of SALS to analyse wide size distributions in the micrometre size range. While this technique covers a substantial range of particle sizes, its resolution is more limited than for classical SLS.

Figure 18.5 shows the particle size distribution of a complex mixture of mineral particles, namely a natural soil, as measured by various methods (17). This figure illustrates the importance of the power-law type size distribution (cf. equation (18.13)), which holds in this particular case over about three orders of magnitudes, covering the range of about 20 nm to 40 μ m. The functional form of the distribution is modified outside of these limits. The exponent turns out to be $\nu \simeq 2.8$.

Focus on the data in Figure 18.5 which are above a few micrometres. One set of measurements was obtained by SALS, where the scattering data were analysed via the Mie theory and regularized direct inversion. The analysis thus yielded the full size distribution over the size range of about 0.5–100 μ m. Comparison with classical sedimentation and sieving techniques, as easily applicable in this case, reveals that SALS represents an extremely reliable technique. Moreover, the light scattering experiment requires only a few minutes, while the other techniques are much more laborious and time-consuming. While the full Mie theory was used

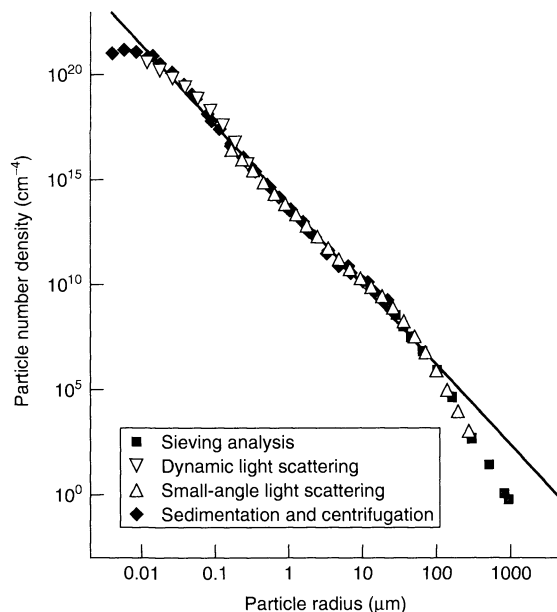


Figure 18.5. Numbered-weighted size distribution for a non-calcareous soil measured by a number of different methods (17), reproduced by permission of Soil Science Soc. of America

to analyse the data, the results are rather insensitive to assumptions concerning the refractive index of the particles. This statement particularly applies to particles larger than a few micrometres, where the Fraunhofer theory is a good approximation.

Furthermore, all of these techniques assume the particles to be spherical. This assumption is not too well satisfied for this system, as the particles are rather irregularly shaped, and often plate-like (i.e. clay minerals). Each technique thus measures a radius of an equivalent sphere, but as Figure 18.5 illustrates, the data obtained from different techniques do not differ that much and all of these methods can be used to obtain a reasonable estimate of the size distribution. More detailed measurements would require direct image analysis and consideration of particle asymmetry. While such image analysis techniques can be used in a rather straightforward fashion for monodisperse samples, they tend to become extremely difficult to use for polydisperse ones.

4 DYNAMIC LIGHT SCATTERING

Dynamic light scattering (DLS), also referred to as quasi-elastic light scattering or photon correlation

spectroscopy, represents another useful technique for the sizing of sub-micrometre particles. Since its invention about two decades ago, this technique has now matured into an excellent tool, not only for particle sizing, but for many other applications as well. Detailed reviews can be found elsewhere (4, 6).

4.1 Basic principles

The principle of the measurement is illustrated in Figure 18.6. As particles diffuse due to thermal motion, the scattered light undergoes interference effects, and the scattered intensity fluctuates randomly with time. The information about particle size is contained in the rate of decay of the fluctuations, i.e. rapid diffusion of small particles leads to fast decay, while slow fluctuations result from the motions of larger particles. With modern correlator techniques, one can easily record the intensity correlation function $\langle I(t)I(0) \rangle$ of the scattered light. This correlation function is written as follows:

$$g_2(t) = \frac{\langle I(t)I(0) \rangle}{\langle I^2 \rangle} \quad (18.26)$$

and can be related to the normalized correlation function of the electric field of the scattered light $g_1(t)$ by the Siegert relationship;

$$g_2(t) = 1 + g_1(t)^2 \quad (18.27)$$

Depending on the experimental set-up, this relationship may apply in a slightly modified form, although the correlation function $g_1(t)$ can be usually measured to good accuracy.

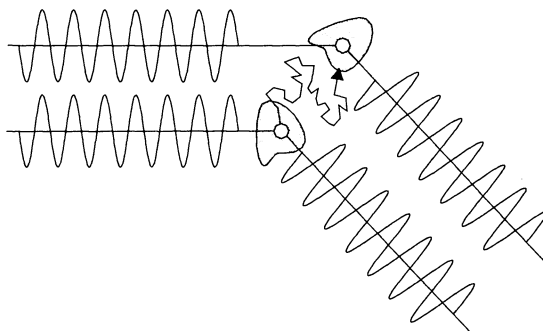


Figure 18.6. Representation of the interference patterns occurring during dynamic light scattering from a particle. As the particle undergoes Brownian motion, the scattered light interferes, and leads to temporal fluctuations of the scattered intensity

When one considers a suspension of monodispersed spherical particles, this correlation function decays exponentially according to the following:

$$g_1(t) = \exp(-\Gamma t) \quad (18.28)$$

where the decay rate constant is given by:

$$\Gamma = q^2 D \quad (18.29)$$

where q is the magnitude of the scattering vector and D is the diffusion coefficient. This relationship shows that the rate of the decay depends on the magnitude of the scattering vector, and thus the scattering angle (cf. equation (18.15)). The inverse decay rate can be thought of as the time the particle needs to diffuse past the “yardstick” of the scattering experiment, q^{-1} . Thus, with increasing scattering angle, the fluctuations decay more rapidly, since the “yardstick” gets shorter.

DLS measures the diffusion coefficient of the particles, but this quantity is closely linked to the particle size by the Stokes–Einstein relationship:

$$D = \frac{k_B T}{6\pi\eta R_h} \quad (18.30)$$

where k_B is the Boltzmann constant, T the absolute temperature, η the viscosity of the solvent, and R_h the hydrodynamic radius of the particles. For a sphere, the latter quantity coincides with the particle radius R , namely $R_h = R$. Since the decay rate of the time-correlation function can be measured very accurately, the particle size can be reliably determined.

The technique works best for monodisperse suspensions, and can be used to make size measurements with an accuracy which is better than a few percent. However, the method is not too sensitive to small polydispersities. Moderately polydisperse systems can be analysed as well, and different methods are available for this purpose. A popular approach is the so-called *cumulant analysis*; in this one expands the correlation function as follows:

$$\ln g_1(t) = -\mu_1 t + \frac{\mu_2}{2} t^2 + \dots \quad (18.31)$$

and obtains the cumulants $\mu_1 = \Gamma$, μ_2 , etc. by least-squares techniques. Depending on the number of the cumulants considered, one refers to a cumulant analysis of the first order, second order, etc. In most situations, the second-order analysis is most practical. The first cumulant yields an apparent hydrodynamic radius (cf. equations (18.29) and (18.30)), while the second cumulant represents a measure of the particle polydispersity. Another approach is to extract the actual distribution of

apparent diffusion coefficients with suitable regularized inversion methods.

In a polydisperse system, the correlation function is given by a weighted average according to the individual scattering power of the particles:

$$g_1(t) = \frac{\langle \alpha^2 P(q) e^{-q^2 D t} \rangle}{\langle \alpha^2 P(q) \rangle} \quad (18.32)$$

For sufficiently small particles, one has $P(q) = 1$ and the polarizability $\alpha \propto R^3$, which introduces a weighting of R^6 into the average. In this experiment, the *intensity-weighted size distribution* given by $p_6(R) \propto R^6 p(r)$ also enters the problem.

Evaluating the first cumulant in this approximation, we find that the apparent hydrodynamic radius is given by the following:

$$R_h = \frac{\langle R^6 \rangle}{\langle R^5 \rangle} = \bar{R}(1 + 5\varepsilon^2) \quad (18.33)$$

Since larger particles scatter much more strongly, they are thus appropriately weighted in the dynamic light scattering experiment. In a polydisperse system, the apparent hydrodynamic radius is significantly larger than the average-number-weighted radius.

4.2 Illustrative examples

Let us illustrate these principles with a few examples. Figure 18.7 shows the number-weighted size distribution of uniform iron oxide particles (hematite, α -Fe₂O₃) (15). The continuous line is obtained from DLS based on a regularized deconvolution of the correlation function. The histogram was obtained by direct counting based on a electron micrograph. One observes that both methods are in reasonable agreement. The average radius and polydispersity index obtained by DLS are $\bar{R} \simeq 51$ nm and $\varepsilon \simeq 0.23$, while from electron microscopy one has $\bar{R} \simeq 46$ nm and $\varepsilon \simeq 0.21$, respectively. The slight deviations are not surprising since the particles are no perfect spheres, but somewhat cuboidal. Clearly, the DLS approach is obviously much faster and simpler, and DLS indeed represent an extremely versatile sizing method, with the possibility of estimating the size distribution in many cases.

DLS is applicable over a very wide size range. Figure 18.8 shows the hydrodynamic radii of water-in-oil microemulsion nano-sized droplets stabilized by the surfactant sodium bis(2-ethylhexyl) sulfosuccinate (AOT) (20). One observes that the droplet size increases roughly linearly with the water-to-surfactant ratio,

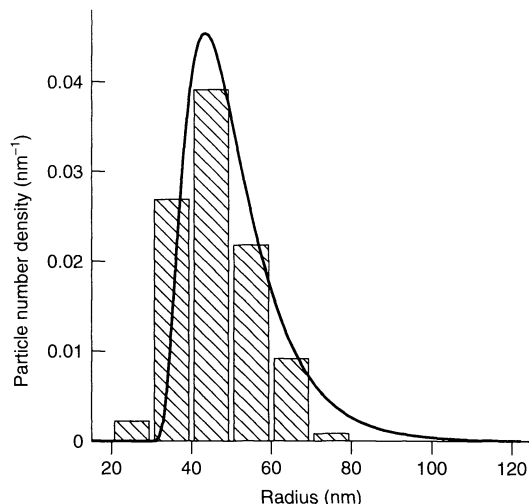


Figure 18.7. Number-weighted particle size distribution of uniform iron oxide particles. The continuous line is obtained from direct deconvolution of dynamic light scattering data, and the histogram is based on direct counting in transmission electron micrographs (reproduced from ref. (15)), with permission from Academic Press

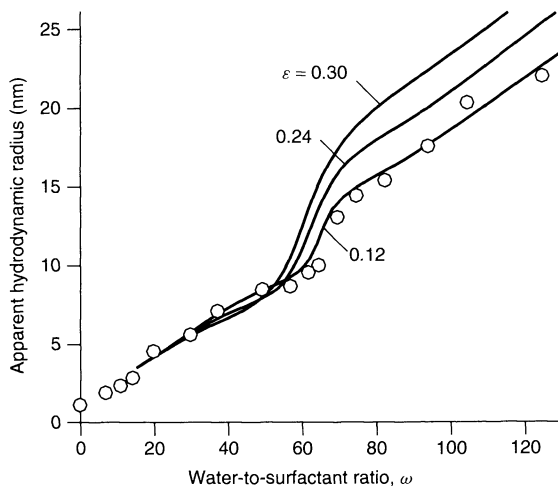


Figure 18.8. Dynamic light scattering measurements of the apparent hydrodynamic radii of water-in-oil microemulsion droplets with the surfactant sodium bis(2-ethylhexyl) sulfosuccinate (AOT) as a function of the water-to-surfactant molar ratio ω . The continuous lines are calculated with a coated sphere model for different polydispersity indices (20)

as predicted by equation (18.25), although the data show a hump at intermediate ratios. This hump is not related to a discontinuity in the increasing droplet radius, but has solely to do with the optical

properties of the polydisperse droplets. Furthermore, above we have discussed the static scattering intensity for the same system, which displays a profound minimum at the same water-to-surfactant ratio (cf. Figure 18.4). This minimum is related to the fact that the droplet polarizability goes through zero at that particular optical matching point. The same phenomenon explains the hump in the apparent hydrodynamic radii. Below the matching point, only the smaller droplets are weighted more strongly since the larger ones are invisible. Above the matching point, the larger droplets are weighted more strongly. Using a model for the droplet polarizability, the same phenomenon can be explained quantitatively. By employing the parameters extracted from the SLS data, we can predict the DLS data in a consistent fashion. While the polydispersity can be also estimated from the second cumulant in DLS, this estimate is no longer reliable in a system with a small polydispersity. Already for these microemulsion droplets, this technique does overestimate the polydispersity substantially. As a rule, second cumulants obtained from DLS cannot distinguish a perfectly monodisperse system from a system with a polydispersity index up to 10%.

While DLS can be a useful tool for investigating very polydispersed systems, it must be applied for that purpose with caution. Due to the much stronger scattering power of larger particles, the smaller particles cannot often be detected. On the other hand, with DLS one can obtain very precise information on the tail of the distribution for large particles. A useful approach is to study polydispersed samples by fractionation (e.g. by centrifugation, filtration, chromatography, etc.) and then to analyse the individual fractions by SLS or DLS (17, 25).

Figure 18.5 also illustrates such an application (17). The size distribution in the sub-micrometre size range was obtained by combining ultracentrifugation and DLS. The sample was fractionated by ultracentrifugation, and the particle sizes in the different fractions were obtained by DLS. It turns out that the results are well comparable to results obtained from the ultracentrifuge measurements. This application illustrates the usefulness of DLS even for very polydispersed samples.

The application of DLS to non-spherical particles is generally less straightforward. For asymmetrical particles, the correlation function has not only contributions from the translational diffusion of the particles but also from their rotational diffusion. In such a situation, it is essential to analyse the angular dependence of the data in detail, since the q -dependences for the translational and rotational contributions are different. Details of these methods are given elsewhere (4, 26).

5 SIMULTANEOUS AND TIME-DEPENDENT METHODS

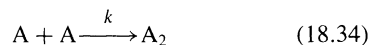
While SLS and DLS do now represent classical techniques, their possibilities keep expanding. One important development is the combination of static and dynamic light scattering. Modern goniometers do now allow for accurate simultaneous static and dynamic measurements, and the combination of these two techniques has become increasingly popular (24, 27, 28). Recently, data analysis algorithms have become available, which treat static and dynamic light scattering data recorded at different scattering angles simultaneously. Obviously, such analytical tools improve the resolution and the range of particle sizes that can be investigated. Moreover, a combination of static and dynamic light scattering data provides additional information, which would not be available otherwise. A well-known application is the consideration of the ratio of the gyration and hydrodynamic radii, which represents a sensitive probe of the particle shape. For a compact sphere, $R_g/R_h \simeq 0.77$, while this ratio is 0.95, 1.6, and 2.3 for discs, worm-like chains, and stiff rods, respectively. For example, this parameter was used to demonstrate that the mixed micelles formed out of bile salt and lecithin were rod-like in shape (29).

An additional advantage of modern light scattering set-ups is the increased speed of data accumulation. While on a classical goniometer, a full angular scan could have taken several hours, with a modern multi-angle instrument such a measurement can be performed within fractions of a second for SLS, and within a minute or less for simultaneous SLS and DLS detection. This improved time-resolution not only shortens the time needed for sample analysis, but opens up entirely new possibilities for studying the kinetics of time-dependent processes, such as particle aggregation, emulsion stability, nucleation, and micelle formation (6, 15, 21).

5.1 Probing aggregation by simultaneous static and dynamic light scattering

While there is no point in reviewing many of the interesting developments in this rapidly advancing field, it is probably helpful to discuss one example illustrating the substantial potential of these techniques. Let us focus on the recent measurements of absolute aggregation rate constants of particle aggregation (13). This example does not only illustrate the possibilities of such time-resolved techniques for the study of kinetic processes, but also demonstrates that simultaneous SLS and DLS can provide access to novel information.

Colloidal particles aggregate in concentrated electrolyte solutions by diffusion (fast aggregation regime). The onset of this process is controlled by the formation of particle dimers, as illustrated in the following scheme:



where A denotes the monomer and A_2 a particle dimer. The rate constant k of this process is of central relevance, and it is important to have methods at hand to measure this quantity accurately. SLS was already used for that purpose some time ago (30). As particles aggregate, the scattering intensity will change. In the early stages of the aggregation, where only monomers and dimers dominate, one can show that the initial rate of the relative change in the scattering intensity is given by the following:

$$\mathcal{S} = \left. \frac{1}{I} \frac{dI}{dt} \right|_{t \rightarrow 0} = kC_0 \left[\frac{I_2(q)}{2I_1(q)} - 1 \right] \quad (18.35)$$

where C_0 is the initial number concentration of monomers per unit volume and $I_1(q)$ and $I_2(q)$ the scattering intensities of the monomer and the dimer, respectively. These scattering intensities are proportional to the corresponding form factors, but include the difference in the absolute scattering intensity of the monomer and dimer. Clearly, from a measurement of this static signal \mathcal{S} , the absolute aggregation rate can be inferred, provided that the scattering intensities are known. While the scattering intensity of the monomer $I_1(q)$ is readily measured, the scattering intensity for the dimer $I_2(q)$ can only be easily calculated within the RDG approximation. However, this approximation may not be particularly accurate for larger particles, and thus the measured values of the rate constants will be as good as the available theoretical estimate of $I_2(q)$.

DLS can be used for the same purpose, and one can show that the initial rate of change in the apparent hydrodynamic radius (as obtained from the first cumulant) obeys a similar relationship:

$$\mathcal{D} = \left. \frac{1}{R_h} \frac{dR_h}{dt} \right|_{t \rightarrow 0} = C_0 k \left(1 - \frac{R_1}{R_2} \right) \frac{I_2(q)}{2I_1(q)} \quad (18.36)$$

where R_1 and R_2 are the apparent hydrodynamic radii of the monomer and dimer, respectively. Similarly, as with SLS, from the dynamic signal \mathcal{D} we can extract the rate constant, although beside the scattering functions the hydrodynamic radius of the dimer R_2 must also be known.

With the possibility of performing SLS and DLS simultaneously, the mentioned ambiguities can be eliminated. By combining equations (18.35) and (18.36), we

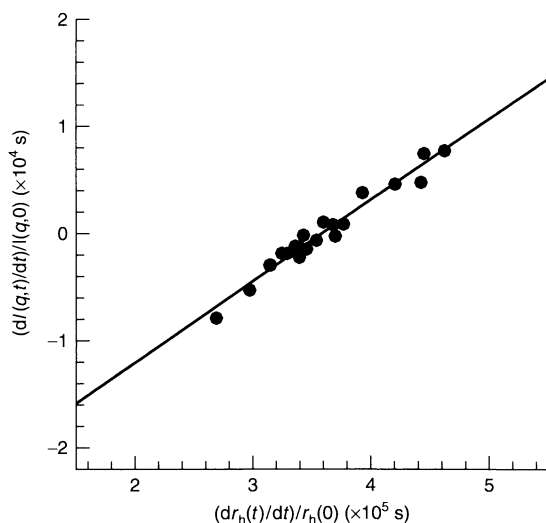


Figure 18.9. Scatter plot of the static signal S as a function of the dynamic signal D for latex particles of 580 nm diameter in 1M KCl electrolyte. The intercept of the straight line yields an absolute aggregation rate constant of $7.3 \times 10^{-18} \text{ m}^3 \text{ s}^{-1}$ (reproduced from ref. (13)), with permission from Academic Press

find that:

$$S = (1 - R_1/R_2)^{-1}D - C_0k \quad (18.37)$$

Thus, plotting the static signal S as a function of the dynamic signal D yields a straight line, and its intercept gives the absolute aggregation rate constant. This analysis is now free of any assumptions about the optical or hydrodynamic properties of the dimer. However, the prerequisite is simultaneous availability of time-resolved SLS and DLS data.

As an example of the feasibility of this technique, consider Figure 18.9. In this figure, we show the mentioned scatter plot of the dynamic signal D as a function of the static signal S for latex particles of 580 nm diameter in 1M KCl electrolyte. The technique yields an absolute rate constant of $7.3 \times 10^{-18} \text{ m}^3 \text{ s}^{-1}$, a value which is in good agreement with independent determinations with a single-particle counting technique. The latter technique yields a value of $6.9 \times 10^{-18} \text{ m}^3 \text{ s}^{-1}$.

6 CONCLUSION

In this chapter, we have discussed various light scattering methods for particle sizing. With static light scattering (SLS), one can achieve excellent resolution as

well as cover a wide range of particle sizes, although this technique can be only applied to particles in the sub-micrometre range and above. While some information on particle size can be also obtained by SLS in the nanometre size range, the more versatile technique for this size range is dynamic light scattering (DLS). The latter method is very accurate and can be often used for the determination of entire size distributions.

While SLS and DLS both represent very powerful techniques for particle sizing, they work best if combined with other methods based on different principles, such as, for example, centrifugation or direct imaging. No technique is foolproof, however, and a reliable measurement of a particle size distribution can be only achieved by integrating different techniques. However, within any effort of this kind, light scattering methods do represent an absolutely indispensable element.

7 REFERENCES

1. Russel, W. B., Saville, D. A. and Schowalter, W. R., *Colloidal Dispersions*, Cambridge University Press, Cambridge, UK, 1989.
2. Kerker, M., *The Scattering of Light and Other Electromagnetic Radiation*, Academic Press, New York, 1969.
3. Bohren, C. F. and Huffman, D. R., *Absorption and Scattering of Light by Small Particles*, John Wiley, New York, 1998.
4. Berne, B. J. and Pecora, R., *Dynamic Light Scattering*, Krieger Publishing Company, Malabar, India, 1990.
5. Burchart, W., Static and dynamic light scattering from branched polymers and biopolymers, *Adv. Polym. Sci.*, **48**, 1–124 (1983).
6. Schuretenbereg, P. and Newman, M. E., Characterization of biological and environmental particles using static and dynamic light scattering, in *Environmental Particles*, Buffle, J. and van Leeuwen, H. P. (Eds), Lewis Publishers, Ann Arbor, MI, 1993, pp. 37–115.
7. Pine, D. J., Weitz, D. A., Chaikin, P. M. and Herbolzheimer, E., Diffusing-wave spectroscopy, *Phys. Rev. Lett.*, **60**, 1134–1137 (1988).
8. Schätzel, K. J., Suppression of multiple scattering by photon cross-correlation techniques, *J. Mod. Opt.*, **38**, 1849–1865 (1991).
9. Urban, C. and Schurtenberger, P., Application of a new light scattering technique to avoid the influence of dilution in light scattering experiments with milk, *Phys. Chem. Chem. Phys.*, **1**, 3911–3915 (1999).
10. Lehner, D., Kellner, G., Schnablegger, H. and Glatter, O., Static light scattering on dense colloidal systems: new instrumentation and experimental results, *J. Colloid Interface Sci.*, **201**, 34–47 (1998).
11. Allen, T., *Particle Size Measurement*, 4th Edn, Chapman and Hall, London, 1990.

12. Brumberger, H. (Ed.), *Modern Aspects of Small-Angle Scattering*, Proceedings of the NATO Advanced Study Institute on Modern Aspects of Small-Angle Scattering, Kluwer Academic Publishers, Dordrecht, The Netherlands, 1994.
13. Holthoff, H., Schmitt, A., Fernández-Barbero, A., Borkovec, M., Cabrerizo-Vílchez, M. A., Schurtenberger, P. and Hidalgo-Álvarez, R., Measurement of absolute coagulation rate constants for colloidal particles: comparison of single and multiparticle light scattering techniques, *J. Colloid Interface Sci.*, **192**, 463–470 (1997).
14. Stoll S. and Pfefferkorn, E., Kinetics of heterocoagulation, *J. Colloid Interface Sci.*, **160**, 149–157 (1993).
15. Schudel, M., Behrens, H., Holthoff, H., Kretschmar, R. and Borkovec, M., Absolute aggregation rate constants of hematite particles in aqueous suspensions: a comparison of two different surface morphologies, *J. Colloid Interface Sci.*, **196**, 241–253 (1997).
16. Semmler, M., Mann, E. K., Ricka, J. and Borkovec, M., Diffusional deposition of charged latex particles on water–solid interfaces at low ionic strength, *Langmuir*, **14**, 5127–5132 (1998).
17. Wu, Q., Borkovec, M. and Sticher, H., On particle size distributions in soils, *Soil Sci. Soc. Am. J.*, **57**, 883–890 (1993).
18. Colfen, H. and Antonietti, M., Field-flow fractionation techniques for polymer and colloid analysis, *Adv. Polym. Sci.*, **150**, 67–187 (2000).
19. Alba, F., Crawley, G. M., Fatkin, J., Higgs, D. M. J. and Kippax, P. G., Acoustic spectroscopy as a technique for the particle sizing of high concentration colloids, emulsions and suspensions, *Coll. Surf., A*, **153**, 495–502 (1999).
20. Ricka, J., Borkovec, M. and Hofmeier, U., Coated droplet model of microemulsions: optical matching and polydispersity, *J. Chem. Phys.*, **94**, 8503–8509 (1991).
21. Lin, M. Y., Linday, H. M., Weitz, D. A., Ball, R. C., Klein, R. and Meakin, P., Universality in colloid aggregation, *Nature (London)*, **339**, 360–362 (1989).
22. Mittelbach, R. and Glatter, O., Direct structure analysis of small-angle scattering data from polydisperse colloidal particles, *J. Appl. Crystallogr.*, **31**, 600–608 (1998).
23. Bryant, G., Abeynayake, C. and Thomas, J. C., Improved particle size distribution measurements using multiangle dynamic light scattering 2. refinements and applications, *Langmuir*, **12**, 6224–6228 (1996).
24. Holthoff, H., Borkovec, M. and Schurtenberger, P., Determination of light scattering form factors of latex particle dimers with simultaneous static and dynamic light scattering in an aggregating suspension, *Phys. Rev., E*, **56**, 6945–6953 (1997).
25. Lloyd, L. L., Kennedy, J. F. and Knill, C. J., Light scattering and chromatography in combination, in *Light Scattering: Principles and Development*, Brown, W. (Ed.), Claredon Press, Oxford, UK, 1996, pp.
26. Chu, B., Xu, R. and Dinapoli, A., Light scattering studies of a colloidal suspension of iron oxide particles, *J. Colloid Interface Sci.*, **116**, 182–195 (1987).
27. Egelhaf, S. and Schurtenberger, P., A Fiber-optics-based light scattering instrument for time-resolved simultaneous static and dynamic measurements, *Rev. Sci. Instrum.*, **67**, 540–545 (1996).
28. Chu, B., Zukang, Z. and Moser, H. O., A time-resolved light-scattering photometer, *Rev. Sci. Instrum.*, **63**, 2954–2957 (1992).
29. Schurtenberger, P. and Cavaco, C., Polymer-like lecithin reverse micelles I. A light-scattering study, *Langmuir*, **10**, 100–108 (1994).
30. Lips, A. and Willis, E., Low angle light scattering technique for the study of coagulation, *J. Chem. Soc., Faraday Trans. 1*, **69**, 1226–1236 (1973).

CHAPTER 19

Measurement of Electrokinetic Phenomena in Surface Chemistry

Norman L. Burns

Amersham Pharmacia Biot, Sunnyvale, CA, USA

1	Introduction	371	3.1.2	The rectangular electrophoresis chamber	377
2	Theory of Electrokinetic Phenomena	372	3.1.3	Limitations of electrokinetic measurements	378
2.1	Origin of surface charge	372	3.2	Streaming potential	379
2.2	The electrical double-layer	373	3.3	Sedimentation potential	379
2.3	Origin of electrokinetic phenomena	374	4	Surface Characterization and Electrokinetic Phenomena	379
3	Measurement of Electrokinetic Phenomena	375	5	References	382
3.1	Electrophoresis and electroosmosis	375			
3.1.1	The cylindrical electrophoresis chamber	376			

1 INTRODUCTION

When an aqueous solution comes into contact with a solid surface, a charge generally develops at the interface due to the adsorption of charged species or due to the ionization of specific functional groups on the surface. In such cases, the properties of an interface can be dictated to a large part by the electrostatic forces operating therein. These electrostatic forces can play a direct role in the behaviour of a two-phase system, e.g. creating repulsive or attractive forces that can sway the disposition of a colloidal particle. They may also be indirect, e.g. an osmotic pressure may develop when the concentration of ions counter-in-charge to the interface are increased due to the close physical proximity of an adjacent surface. In elucidating surface physical properties and the behaviour of colloidal systems, the characterization of surface charge is important. One way in which the surface charge at an interface can be probed is through the measurement of

electrokinetic phenomena that can be induced at an interface.

Electrokinetic phenomena refers to dynamic processes that occur when viscous or electrical forces are applied to a charged interface. The most common of these phenomena are electrophoresis, electroosmosis, streaming potential and sedimentation potential.

Electrophoresis refers to the motion of suspended charged species, e.g. a solid or discontinuous phase, induced by an electric field. *Electroosmosis*, on the other hand, is the motion of the continuous phase induced by an electric field. Conversely, *streaming potential* refers to the electric field produced by motion of a continuous liquid phase over a charged solid, or discontinuous, phase. *Sedimentation potential* refers to the electric field induced by the motion of a charged species through a continuous liquid phase.

In classical terms, electrokinetic phenomena can be described by the Navier–Stokes equation for steady laminar fluid flow to which is added an electrical body

force term and the condition of continuity (1):

$$\eta \nabla^2 \mathbf{v} - \nabla p + \rho_e \mathbf{E} = 0 \quad (19.1)$$

$$\nabla \cdot \mathbf{v} = 0 \quad (19.2)$$

accounting for the viscous forces ($\eta \nabla^2 \mathbf{v}$), pressure gradients (∇p) and electrical body forces ($\rho_e \mathbf{E}$) acting on a parcel of fluid, where η is the viscosity of the fluid medium, \mathbf{v} the fluid velocity, p the pressure, ρ_e the local charge distribution, and \mathbf{E} the electric field.

Equation (19.1) describes the balance of forces when external forces are applied at a charged interface. With this equation, it can be readily understood that application of an electric field upon a fluid region possessing a net charge would result in translational fluid motion and/or a pressure gradient. If applied to a charge-bearing solid suspended in solution, the result would be translational motion of the solid (electrophoresis). The region in solution bearing charges countering that of the solid would be subject to the electric field as well, thus resulting in fluid flow about the solid (electroosmosis). Conversely, a flow forced about the solid region would result in an electric field (streaming potential) as a result of the flux of ions near the surface.

Equation (19.1) also gives insight into the type of information available from measurement of electrokinetic phenomena, namely information concerning net charge and/or fluid properties near the interface. It is upon charge distribution and surface rheological properties that electrokinetic phenomena depend.

In the following sections, the relationship between surface charge and electrokinetic phenomena is expounded in terms of classical theory. First, a few possible mechanisms and models for the development of charge at a surface in contact with an aqueous solution are described in order to form a basis for the formation of an electrical double-layer at an interface. Secondly, the electrical double-layer is discussed in terms of an equilibrium charge distribution and electrostatic potential near the interface. With an adequate description of the interface, the discussion turns to explication of electrokinetic phenomena according to the charge distribution in the electrical double-layer and the Navier–Stokes equation. A section then follows which describes common methods and experimental requirements for the measurement of electrokinetic phenomena. The discussion closes with a few examples of the use of measurement of the pH dependence of electroosmosis as an analytical characterization technique from this present author's own experience. The intention is to provide

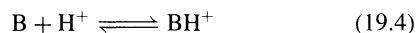
the reader with the equations to model the underlying basis of electrokinetic phenomena, insight into appropriate experimental factors for measurement, and the tools to interpret electrokinetic phenomena in terms of their source.

2 THEORY OF ELECTROKINETIC PHENOMENA

In order to extract information from the measurement of electrokinetic phenomena according to equation (19.1), it is necessary to account for the distribution of charge at the interface. Excess charge at a surface can originate from two sources, i.e. either from ionization of bound surface functional groups, or from the adsorption of charged species. In the following sections, models will be presented for the formation of surface charge and related to electrokinetic phenomena through classical electrostatic theory.

2.1 Origin of surface charge

In the absence of specific adsorption of electrolyte ions, surface charge is considered to originate from the acid–base dissociation of ionizable groups. In terms of acid groups (AH) and basic groups (B), the respective pH-dependent equilibria between surface sites and solution at the interface may be represented as follows:



The respective equilibria may be described by the following:

$$K_a = \frac{[\text{A}^-][\text{H}^+]_s}{[\text{AH}]} \quad (19.5)$$

$$K_b = \frac{[\text{BH}^+]}{[\text{B}][\text{H}^+]_s} \quad (19.6)$$

where K_a is an acid dissociation constant, K_b is the base dissociation constant, and $[\text{H}^+]_s$ is the hydronium ion concentration at the surface. The total number of respective acid and basic sites, N_a and N_b , can be represented as the sum of charged and uncharged species:

$$N_a = [\text{A}^-] + [\text{AH}] \quad (19.7)$$

$$N_b = [\text{BH}^+] + [\text{B}] \quad (19.8)$$

Given i distinct acid types and j basic types on the surface, each with its own equilibrium, the total surface

charge (σ_s) can be represented by the following:

$$\begin{aligned}\sigma_s &= e \sum_j [\text{BH}^+]_j - e \sum_i [\text{A}^-]_i \\ &= \sum_j \left[\frac{e N_b}{1 + 10^{(\text{pH}_s - \text{pK}_b^j)}} \right] - \sum_i \left[\frac{e N_a}{1 + 10^{(\text{pK}_a^i - \text{pH}_s)}} \right]\end{aligned}\quad (19.9)$$

Another way in which a surface may acquire a charge is through specific adsorption of charged species. In terms of the charged species (C) in solution and the adsorption site (S) at the surface, the equilibrium may be represented by the following:



$$K_C = \frac{[\text{CS}]}{[\text{C}][\text{S}]} \quad (19.11)$$

while the surface charge is given by the following:

$$\sigma_s = e[\text{CS}] = \left[\frac{e N_S}{1 + 10^{(\text{pC} + \text{pK}_C)}} \right] \quad (19.12)$$

for:

$$N_S = [\text{S}] + [\text{CS}] \quad (19.13)$$

In a likewise manner, surface charge can be expressed in terms of solution species and surface sites for a large number of possible means of acquiring surface charge, e.g. amphoteric functional groups or ion-pair formation (2).

2.2 The electrical double-layer

With an adequate description of surface charge it is now necessary to account for the ion distribution near the charged surface. Figure 19.1 shows the simplest schematic representation for this distribution of charge, namely the electrical double-layer according to Gouy and Chapman. The net bound charge at the surface (σ_0) is countered by diffuse charge in solution of a net value σ_d such that:

$$\sigma_0 + \sigma_d = 0 \quad (19.14)$$

The charge density in the volume adjacent to the surface (ρ_e) is the sum of the N ionic species of concentration c^i carrying respective charges $z^i e$, where e is the Coulombic charge, as follows:

$$\rho_e = -e \sum_{i=1}^N z^i c^i \quad (19.15)$$

The electric field flux within a fluid volume of charge density ρ_e in a continuous dielectric medium, such as water, can be described in terms of the permittivity ϵ of the medium and electric potential Ψ by Poisson's equation:

$$\rho_e = -\epsilon \nabla^2 \Psi \quad (19.16)$$

Assuming an equilibrium balance of electrical and diffusional forces, the charge distribution in the interfacial region can be described according to the following:

$$kT \nabla \ln c^i + z^i e \nabla \Psi = 0 \quad (19.17)$$

which in the scheme of Figure 19.1 yields the Boltzmann equation:

$$c_0^i = c_\infty^i \exp\left(\frac{-z^i e \Psi}{kT}\right) \quad (19.18)$$

This expression can be used to relate ion concentrations at the surface (c_0^i), to those in the bulk (c_∞^i); Ψ_0 is the potential at the surface ($x = 0$) relative to that in the bulk solution.

The diffuse double-layer charge over a surface of area S may be taken by integration of the charge density over the surface (defined by Ω):

$$\sigma_d S = \iint_{\Omega} \rho_e dS \quad (19.19)$$

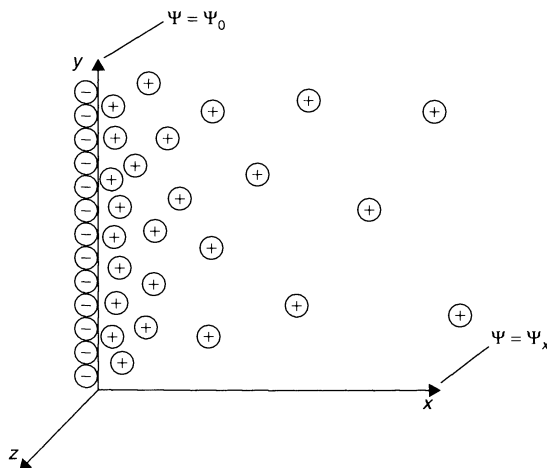


Figure 19.1. Schematic of the Gouy–Chapman electrical double-layer. The net bound charge at a solid surface ($x = 0$) is countered by diffuse charge in solution. The co-ions in the diffuse double layer are omitted for clarity

For the flat double-layer and a 1:1 electrolyte in the scheme of Figure 19.1, we have:

$$\sigma_d = \int_0^\infty \rho_e dx = -(8c\epsilon kT)^{1/2} \sinh\left(\frac{e\Psi_0}{2kT}\right) \quad (19.20)$$

Note that the potential (Ψ) decays from its surface value to a value of zero at some point in the bulk. By inserting equations (19.15) and (19.18) into Poisson's equation and applying the appropriate boundary conditions ($\Psi = \Psi_0$ at $x = 0$, and $\Psi = 0$ at $x = \infty$), the resulting equation can be integrated twice to yield the following:

$$\tanh\left(\frac{e\Psi_x}{4kT}\right) = \tanh\left(\frac{e\Psi_0}{4kT}\right) \exp\left[-\left(\frac{2ce^2x^2}{\epsilon kT}\right)^{1/2}\right] \quad (19.21)$$

This expression relates the potential at the surface to that at some distance $x(\Psi_x)$.

2.3 Origin of electrokinetic phenomena

With a model of the distribution of charges near the solid-liquid interface, it is now possible to discuss electrokinetic phenomena in terms of surface charge. Referring back to equation (19.1), the Navier-Stokes equation can be solved for electrokinetics given the appropriate boundary conditions. In the scheme of Figure 19.1, consider the application of an electric field of strength E_∞ tangential to the surface (in the z -direction). The electrical forces acting on the

diffuse counterions in solution create shear forces and a corresponding electroosmotic fluid flow.

Assuming constant viscosity and permittivity, and negligible pressure gradients as a result of the fluid flow, integration of equation (19.1) from the hydrodynamic plane of shear where the fluid velocity is zero ($v = 0$), to a point in the bulk where the potential is zero and fluid velocity is constant (v_{eo}), gives the following:

$$v_{eo} = -\frac{\epsilon E_\infty}{\eta} \zeta \quad (19.22)$$

where ζ is the potential at the plane of shear.

This equation, known as the Helmholtz-Smoluchowski equation, relates the potential at a planar bound surface region to an induced electroosmotic fluid velocity (3). Figure 19.2 shows a possible scenario for the location of the plane of shear and electrical potential ζ . If ζ can be related to the surface potential Ψ_0 at the experimental substrate by using an appropriate model of the potential profile behind the plane of shear, then the equations in the previous sections provide us with a means to relate electrokinetic phenomena to surface charge, temperature, solution concentrations of electrolyte and position of the hydrodynamic plane of shear.

As far as representing the real experimental system, the model adopted considers only a homogenous planar region of charge-bearing groups at a surface. Electrolyte species are assumed to behave as point charges in a continuous dielectric medium distributed in the mean potential created by the surface and by the ions located in their mean position. Thus, correlation

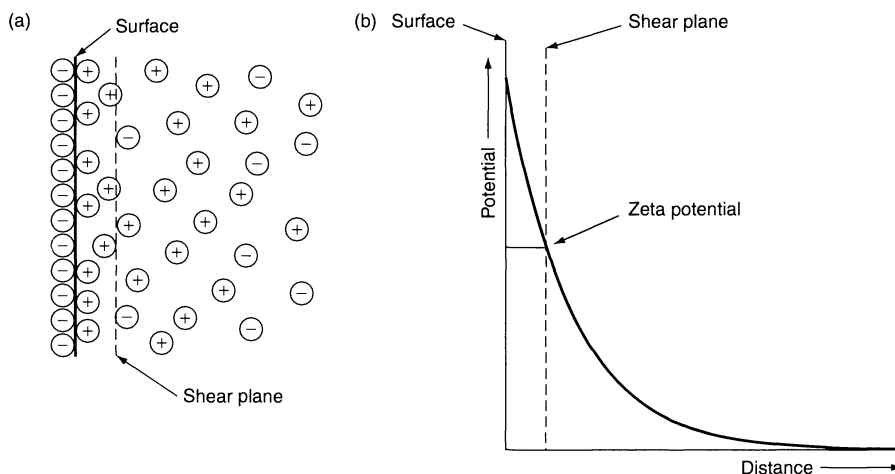


Figure 19.2. (a) Position of the hydrodynamic plane of shear in the electrical double-layer and (b) the associated concept of the zeta potential

between the instantaneous positions of the ions in solution are neglected. The charges are assumed to obey the Poisson–Boltzmann equation up to the plane of shear. Furthermore, in using the Helmholtz–Smoluchowski equation the viscosity and permittivity are assumed to be constant in the interfacial region with a well-defined plane of shear.

A number of more sophisticated models have been proposed to describe electrokinetic phenomena at surfaces (1–4). Considerations have included the distance of closest approach of counterions, a stagnant layer near the surface in the double-layer, conduction behind the hydrodynamic shear plane, variability of permittivity and viscosity in the electrical double layer, discreteness of charge on the surface, surface roughness, surface porosity and surface-bound water. Perhaps the most commonly used model has been the Gouy–Chapman–Stern–Grahame model. This model separates the counterion region into a compact, surface-bound “Stern” layer, wherein potential decays linearly, and a diffuse region which obeys the Poisson–Boltzmann relation.

Another useful model that has been employed in recent years is the soft-layer model of Ohshima and Furusawa for an ion-penetrable surface charge layer (4). In this model, the soft layer is defined as a region having fixed viscosity, frictional property and charge, with the charge distribution of mobile ions in the soft layer being considered separately in the Navier–Stokes equation. Such a model can yield layer thickness and charge density of adsorbed polyelectrolytes, or effective thicknesses of adsorbed neutral polymers.

A problem with using the “more-sophisticated” models is the concomitant increase in the number of parameters needed to describe the electrokinetic phenomena, in particular electrokinetically inaccessible parameters, e.g. viscosity. Model parameters must be assumed, or acquired from independent experimental techniques.

In light of these considerations, experimentally derived parameters from models of electrokinetic phenomena should be viewed as approximate. Absolute quantitative values are not their essence. Experimentally derived parameters have proven useful as a qualitative basis for discussion of the observed properties of specific systems. Despite the limitations of extant models in providing quantitative values of surface charge, one thing is for certain – electrokinetic phenomena are related to surface charge in such a way as to provide useful information concerning the source and magnitude of surface charge. In some systems, information about the thicknesses of viscous layers at an interface, e.g. adsorbed layers, can also be realized.

3 MEASUREMENT OF ELECTROKINETIC PHENOMENA

The classic experimental approach when measuring electrokinetic phenomena is to measure either the velocity of the respective phases, in the case of electrophoresis and electroosmosis, or the strength of the induced electric field under relative phase motion, in the case of streaming potential and sedimentation potential. A number of experimental set-ups can be used to measure electrokinetic phenomena. However, the appropriate experimental set-up for a given system is usually determined by the size, shape and state of the substrate of interest. The following provides a discussion of some common experimental regimes for measurement of electrokinetic effects.

3.1 Electrophoresis and electroosmosis

The most common method employed for particle electrophoresis is the use of closed, free-fluid electrophoresis chambers (5). In this method, particles suspended in a fluid medium are electrophoresed in an enclosed electrode chamber. Particle mobility is determined optically through the chamber wall. However, if the chamber surface is charged, electroosmosis is induced at the chamber walls due to the applied electric field. A hydrodynamic circulatory flow in the chamber thus results. This hydrodynamic flow complicates mobility determination since the flow will impose upon the particle’s mobility. This hydrodynamic flow must be taken into account. Particle mobility must either be measured in regions of the cell where there is no significant fluid flow, or the fluid velocity must be measured and subtracted from the observed particle velocity.

If the chamber or a fixed surface is of interest, however, the bulk hydrodynamic flow reflects electroosmotic fluid flow at the surface and the particle can be used as a tracer to visualize the bulk fluid flow. Thus, a chamber surface may be characterized electrokinetically, according to electroosmotic fluid flow, with an accurate description of the hydrodynamics of the fluid flow in the chamber.

The hydrodynamics of fluid flow in micro-particle electrophoresis chambers are described by solutions to the Navier–Stokes equation for steady laminar fluid flow (equation (19.1)) with boundary values defined by the chamber geometry. When considering the dimensions of an experimental chamber compared to the thickness of the double-layer (mm to nm), fluid flow at the surface would appear to move at a constant velocity. In other

words, the region of varying velocity, viscosity, charge density, potential, etc., in the electrical double-layer is not observable. Thus, viscosity is constant in the bulk hydrodynamic problem. Accordingly, the electrical force term $\rho_e \mathbf{E}$ in equation (19.1) can be ignored since the net charge density in the observable region is zero. Solutions to this equation:

$$\eta \nabla^2 \mathbf{v} - \nabla p = 0 \quad (19.23)$$

are subject to boundary conditions defined by the chamber geometry. Based on solutions to this equation, the following is a description of measurements of particle electrophoresis and electroosmosis in the two most common chamber geometries, i.e. cylindrical and rectangular.

3.1.1 The cylindrical electrophoresis chamber

In one experimental design, electrophoresis of particles can be observed in cylindrical capillaries, such as with the Rank Brothers (Cambridge, UK), apparatus, schematically illustrated in Figure 19.3 (5). In this design, the capillary (typically quartz, 2 mm internal diameter) serves as an electrophoresis chamber or as an experimental substrate. The chamber is filled with a dilute suspension of particles and fitted with electrodes (blank platinum, platinum black, palladium, or silver/silver chloride, depending upon the application) at each end of the chamber. The chamber is then immersed in a thermostated water bath and the electrophoresis of the particles is observed with a microscope at various locations across the diameter of the capillary. A DC power supply provides electric field strengths in the range 1–150 V/cm. The particle velocity is taken across an ocular graticule in the microscope assembly, while the locations of the particles are determined by two-axis distance micrometers mounted on the Rank assembly.

Defining particle mobility as the velocity per unit electric field strength, the apparent particle mobility (U_p) at a given location in the cell is calculated according to the following:

$$U_p \equiv \frac{v_p}{E_\infty} = \frac{d\kappa\pi R^2}{tI} \quad (19.24)$$

where v_p is the observed particle velocity, E_∞ the applied field strength, d the distance the particle has travelled over time t , R the radius of the capillary, κ the conductivity of the fluid medium, and I the electric current. The current is monitored with a voltmeter during electrophoresis, and the conductivity of the fluid medium is also measured.

Figure 19.4 shows typical pH-dependent particle mobility profiles across the diameter of a closed cylindrical chamber for a negatively charged particle and a chamber made of quartz. In the closed cell, fluid flow at the surface is compensated by a return flow down the centre of the cell resulting in a parabolic distribution of particle velocities. In the quartz cell, electroosmosis is greater at higher pH levels due to the dissociation of silanol groups at the surface and a corresponding increase in negative charge at the surface. The particle velocity at a given location is the sum of the intrinsic electrophoretically induced particle velocity and the electroosmotically induced fluid velocity.

Description of the hydrodynamics in the cylindrical capillary experimental design is fairly simple. Considering only electrostatic and fluid frictional forces acting on the suspended particles, the apparent particle mobility at a given location (r) across the diameter of the capillary may be represented by a solution to equation (19.23) in the scheme of a coordinate system with the origin in the centre of the capillary (as in Figure 19.5):

$$U_p = U_{eo} \left[2 \left(\frac{r}{R} \right)^2 - 1 \right] + U_{el} \quad (19.25)$$

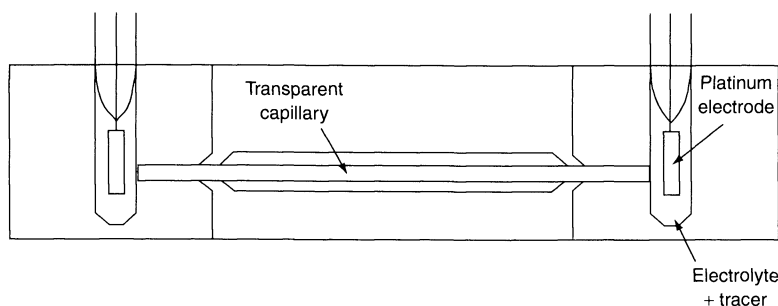


Figure 19.3. Schematic of the modified “Rank Mark II” electrophoresis chamber

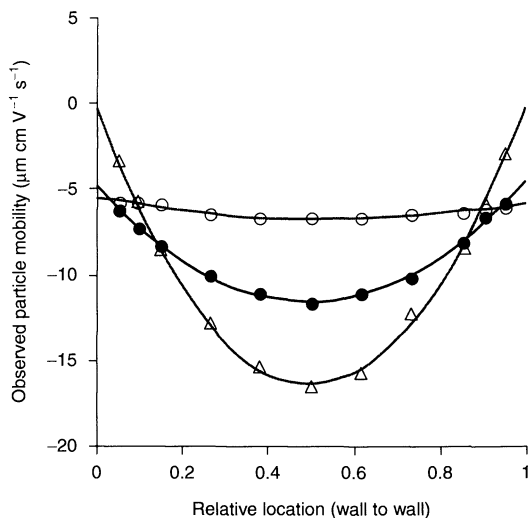


Figure 19.4. Apparent particle mobility in 7.5mM NaCl of a sulfated polystyrene latex particle across the diameter of a closed quartz cylindrical chamber. The profiles are associated with varying degrees of electroosmosis at pH 2(○), pH 6(●) and pH 11(Δ)

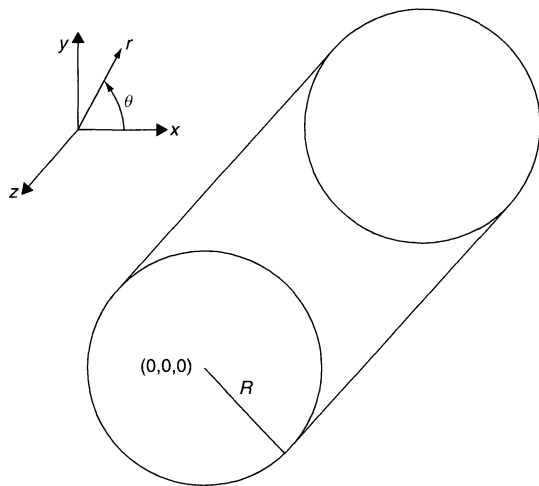


Figure 19.5. The coordinate system for describing the hydrodynamics of fluid flow in the cylindrical chamber

where U_{eo} is the wall electroosmotic fluid mobility, R is the capillary radius, and U_{el} is the intrinsic electrophoretic mobility of the particle. By using equation (19.25), the electroosmotic fluid mobility at the chamber surface and the particle electrophoretic mobility can be taken from a linear least-squares fit of the experimentally observed particle mobility

versus the relative location (r/R) data. Alternatively, if only particle mobility is of interest, the particle electrophoretic mobility can be observed directly at “stationary levels” where the net fluid flow is zero, as follows:

$$r = \frac{R}{\sqrt{2}} \quad (19.26)$$

3.1.2 The rectangular electrophoresis chamber

Consider now the general case of a rectangular electrophoresis chamber of width $2a$ and depth $2b$ as shown in Figure 19.6. In such a chamber, the upper surface, lower surface and sidewalls may possess different electrokinetic properties. Solutions to equation (19.23) describing the fluid flow in the chamber in this case are subject to the following conditions:

$$\int_0^{2b} \int_{-a}^a v(x, y) dx dy = 0 \quad (19.27)$$

$$v(a, y) = v_u \quad (19.28)$$

$$v(-a, y) = v_l \quad (19.29)$$

$$v(x, 0) = v(x, 2b) = v_s \quad (19.30)$$

where v_u , v_l and v_s are the respective electroosmotic fluid flows induced at the upper surface, the lower surface, and the sidewalls. Equation (19.27) follows from the fact that net fluid flow in a closed system must be zero, and equations (19.28)–(19.30) from the fact that fluid velocity at the chamber walls must correspond to the respective induced electroosmotic flows.

A solution to equation (19.1) fulfilling the requirements of equations (19.27)–(19.30) may take the following form (6):

$$v(x, y) = v_u f(x, y) + v_l g(x, y) + v_s h(x, y) \quad (19.31)$$

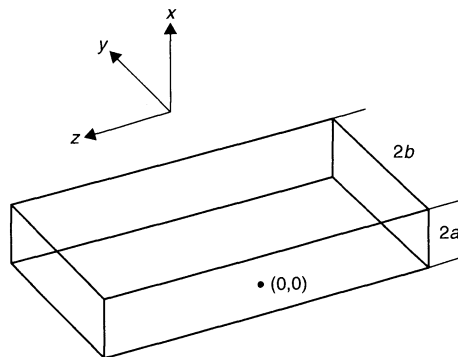


Figure 19.6. The coordinate system for describing the hydrodynamics of fluid flow in the rectangular chamber

where:

$$f(x, y) = \frac{3K_2 - 12ab}{6K_1 - 8a^3b}(x^2 - a^2 - \chi_1) + \frac{x - \chi_2}{2a} + \frac{1 - \chi_3}{2} \quad (19.32)$$

$$g(x, y) = \frac{3K_2 - 12ab}{6K_1 - 8a^3b}(x^2 - a^2 - \chi_1) - \frac{x - \chi_2}{2a} + \frac{1 - \chi_3}{2} \quad (19.33)$$

$$h(x, y) = \chi_3 + \frac{K_2}{6K_1 - 8a^3b}(x^2 - a^2 - \chi_1) \quad (19.34)$$

$$\chi_1 = \frac{32a^2}{\pi^3} \sum_{n=0}^{\infty} \frac{(-1)^{n+1}}{(2n+1)^3} \cosh \left[\frac{(2n+1)\pi}{2a}(y-b) \right] \times \cos \left[\frac{(2n+1)\pi}{2a}x \right] \operatorname{sech} \left[\frac{(2n+1)\pi}{2a}b \right] \quad (19.35)$$

$$\chi_2 = -\frac{2a}{\pi} \sum_{n=0}^{\infty} \frac{(-1)^{n+1}}{n+1} \cosh \left[\frac{(n+1)\pi}{a}(y-b) \right] \times \sin \left[\frac{(n+1)\pi}{a}x \right] \operatorname{sech} \left[\frac{(n+1)\pi}{a}b \right] \quad (19.36)$$

$$\chi_3 = -\frac{4}{\pi} \sum_{n=0}^{\infty} \frac{(-1)^{n+1}}{2n+1} \cosh \left[\frac{(2n+1)\pi}{2a}(y-b) \right] \times \cos \left[\frac{(2n+1)\pi}{2a}x \right] \operatorname{sech} \left[\frac{(2n+1)\pi}{2a}b \right] \quad (19.37)$$

$$K_1 = \int_0^{2b} \int_{-a}^a \chi_1 dx dy = \frac{512a^4}{\pi^5} \sum_{n=0}^{\infty} \frac{(-1)^{n+1}}{(2n+1)^5} \times \tanh \left[\frac{(2n+1)\pi}{2a}b \right] \quad (19.38)$$

$$K_2 = \int_0^{2b} \int_{-a}^a \chi_3 dx dy = -\frac{64a^2}{\pi^3} \sum_{n=0}^{\infty} \frac{(-1)^{n+1}}{(2n+1)^3} \times \tanh \left[\frac{(2n+1)\pi}{2a}b \right] \quad (19.39)$$

Accordingly, in terms of the electrophoretic particle mobility (U_{el}) and the electroosmotic fluid mobility, we have:

$$U_p(x, y) = \frac{v_p(x, y)}{E_z} = U_u f(x, y) + U_l g(x, y) + U_s h(x, y) + U_{el} \quad (19.40)$$

Given a large chamber width-to-depth ratio, equation (19.31) reduces to a second-order polynomial within the vertical plane of symmetry of the cell (i.e. for large values of b/a and small values for $y-b$, both $\chi_1 - \chi_3$ and $K_1 - K_2$ become negligibly small). The equation also simplifies somewhat for the case where electroosmosis is equivalent at all of the chamber surfaces, namely:

$$U_p(x, b) = U_{eo} \left[\frac{3x^2 - a^2}{2a^2} \right] + U_{el} \quad (19.41)$$

in the vertical plane of symmetry of a chamber with a large width-to-depth ratio and equivalent electroosmotic fluid flow at the chamber surfaces.

Regardless of chamber dimensions or asymmetries with respect to electroosmosis at the surfaces, both particle mobility and electroosmotic fluid mobility at the chamber surface can be determined from a linear least-squares fit of equation (19.40) to the observed particle mobilities in selected locations in the chamber. Chamber surfaces may also serve as experimental substrates, for example, removable plates that form the chamber surfaces. Particle mobility may be observed directly where stationary levels with respect to electroosmosis may be identified, i.e. where $v(x, y) = 0$. (The interested reader is left to solve these equations according to their own specifications.)

3.1.3 Limitations of electrokinetic measurements

In theory, there are no limits to the accessibility of electrokinetic data. However, there are a number of physical situations which limit the range of electrokinetic data which can be obtained in the above described experimental set-ups. The experimental techniques described above require visual determination of particle velocities and are typically limited to the range 3–100 $\mu\text{m/s}$. Additionally, according to equation (19.24), current and solution conductivity affect the particle mobility. In experimental practice, the limit for current in the cell is around 300 μA with the use of blank platinum electrodes. Under higher currents, electrolytic reactions at the electrodes result in electrode polarization, heating and subsequent formation of gas bubbles and thermal convection in the cell. Furthermore, solution conductivity measurements are not reliable below about 10 $\mu\text{S/cm}$. The above limitations restrict the typical range of solution ionic strengths at which one can work

to 0.1–100mM.

One way to increase the range of measurement is with the use of light scattering (Doppler electrophoresis) to determine particle velocities. Such methods are used in contemporary commercially available analytical particle electrophoresis apparatus, such as the "Malvern Zeta-Sizer" and the "Coulter DELSA 4440". In addition, in recent years, image analysis methods have been used to determine particle velocity in systems employing traditional optical microscopy to observe the particles (7).

Another method for the determination of electrophoretic mobility which has emerged in recent years is that of the measurement of the electrokinetic sonic amplitude (ESA) for a particle subjected to an alternating current (8). This "electroacoustic" effect is a result of the oscillation of the particles near the electrodes where a sound wave is produced that can be picked up by a pressure transducer located behind the electrode. The ESA pressure signal is simultaneously proportional to the dynamic mobility of the particle, the particle volume fraction and the density difference between particle and solvent. Thus, the electroacoustic effect is appropriate for concentrated dispersions where conventional electrophoretic methods are inappropriate. However, one disadvantage of the method is that it is not appropriate to systems having low density differences between the particles and suspending liquid.

For porous and fibrous materials, it is often most convenient to measure electroosmosis across a packed bed or plug (9). In this case, bulk electroosmotic fluid flow must be measured directly in an open circuit, or the pressure difference measured across a closed cell.

3.2 Streaming potential

As mentioned in the introduction, there exist two electrokinetic phenomena that are converse to electrophoresis and electroosmosis in that measurable electric fields are produced under the application of mechanical forces which produce relative phase motion at a charged interface. A streaming potential is produced when a liquid flows over a charged surface due to the flux of counterions in the mobile phase. In terms of the chamber geometries already presented for electrophoresis and electroosmosis, the corollary for streaming potential can be discussed. Consider the cylindrical system of Figure 19.5 where a fluid is forced through a capillary of length l having a charged surface. Assuming the conditions of the Navier–Stokes equation and the Poisson–Boltzmann relationships presented above, the electrical potential difference across the ends of the capillary can be represented by the following relationship:

$$\Delta E = \frac{\varepsilon \zeta}{\eta \lambda} \Delta P \quad (19.42)$$

where ΔE is the streaming potential, ΔP is the pressure gradient across the capillary and λ is the conductivity of the system.

Thus, a streaming potential can be measured across the capillary by placing electrodes at the inlet and outlet, and can be related to a zeta potential ζ at the hydrodynamic plane of shear, given the viscosity and permittivity of the fluid and the applied pressure (or flow rate through the capillary).

As with electroosmosis, streaming potential can also be measured in other chamber geometries, at flat plates, or in porous plugs. Limitations of the method are subject to the applied pressure, avoidance of turbulent flow and substrates of high surface conductivity (3, 9).

3.3 Sedimentation potential

Standing out on its own in the realm of electrokinetic phenomena is sedimentation potential. The electrical potential difference across a capillary chamber (or column) of sedimenting particles can be described according to the following equation:

$$\Delta E = \frac{\varepsilon \zeta}{\eta \lambda} \phi g \Delta \rho \quad (19.43)$$

where ϕ is the particle volume fraction, g is the gravitational constant and $\Delta \rho$ is the density difference between the particle and fluid medium. From this equation, it can be seen that concentrated suspensions and high particle densities are conducive to obtaining a measurable potential. This phenomena has rarely been exploited due to the very small electrical potential that develops under common rates of sedimentation of charged particles. Sedimentation potentials are commonly of the order of magnitude of 1 mV. Although this is an easily measurable quantity, electrode polarization and drift make accurate measurement difficult. However, recently Masataka Ozaki has used a rotating column method that avoids electrode polarization and drift to accurately measure sedimentation potential and to calculate zeta potentials. The results obtained compare favourably to those obtained with electrophoresis measurements (10).

4 SURFACE CHARACTERIZATION AND ELECTROKINETIC PHENOMENA

To characterize a surface electrokinetically involves the measurement of one of the above electrokinetic effects.

With disperse colloidal systems it is practical to measure the particle electrophoretic mobility (induced particle velocity per unit applied electric field strength). However, for a non-dispersed system one must measure either an induced streaming potential or an electroosmotic fluid flow about the surface.

Having accounted for the origin of electrokinetic phenomena and various means to measure such phenomena at a wide variety of surfaces, armed with the equations of the previous sections, focus will now shift to interpreting electrokinetic phenomena as a means of characterizing a surface or interface in terms of charge and fluid properties near the interface. In comparing different electrokinetic methods, the results are commonly reduced to a single parameter, i.e. the *zeta potential*. In doing so, it is easy to forget that zeta potential is not a measurable parameter but rather a conceptual entity that is identified with a hydrodynamic plane of shear, which in actuality may or may not be well-defined. While electrokinetic phenomena are experimentally derived, zeta potential is derived from a model of the electrokinetic phenomena. Thus, incorporated into the zeta potential are any inadequacies of a particular model. Particularly problematic is the case of electrophoresis where the geometry and size of particles do not allow for analytical solutions for zeta potential. In addition, incorporated into the zeta potential parameter is the effect of electrolyte concentration. Figure 19.7 shows the dependence of zeta potential on electrolyte concentration and charge. From this figure, it can be seen that the zeta potential is highly dependent upon electrolyte concentration, even where surface charge is equivalent. In incorporating the electrolyte concentration dependence, the concept of zeta potential has been extremely useful in elucidating particle–particle and surface–surface interactions under specified experimental conditions. It has also served as a unifying parameter for comparison of the equivalence among the various measurable manifestations of electrokinetic phenomena. However, zeta potential in itself is not such a useful parameter in characterizing the intrinsic charging properties of a surface. In characterizing the intrinsic properties of a surface it is much more useful to go beyond the concept of zeta potential and extract relative values of charge from an appropriate model of charge development, e.g. acid–base dissociation. Additionally, information can be obtained about adsorbed interfacial layers, e.g. effective thickness.

In the previous sections, a simple model of the interface was employed in order to relate, in the simplest way, the various electrokinetic phenomena. Although not an entirely complete account of the interface or the mechanisms behind electrokinetic phenomena, the

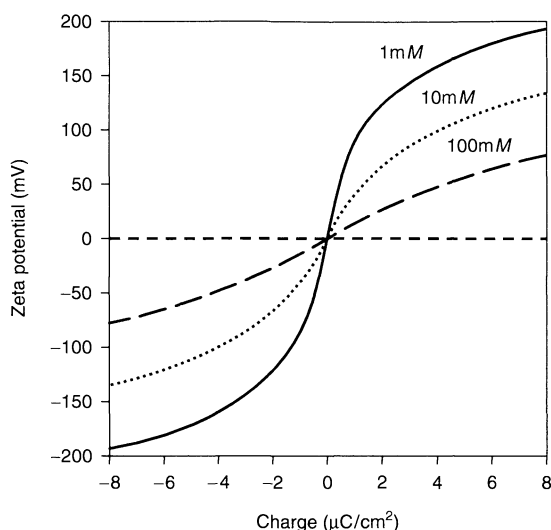


Figure 19.7. The dependence of zeta potential on charge and electrolyte concentration for a 1:1 electrolyte according to the Guoy–Chapman model of the interface (Figure 19.1) and classical electrokinetic theory

model provides a basis for discussion of charging phenomenon at an interface and a semi-quantitative account of ionizable surface groups.

An example of quantitation of ionizable surface groups comes from the pH-dependence of electroosmosis induced at surfaces upon which thin polymeric films have been deposited from a cold plasma in a radio-frequency glow discharge apparatus (6). Plasma polymerization has become an important means of modifying surfaces in materials applications. Applications receiving much attention recently have been the use of plasma polymerization to obtain biocompatible materials, and to produce functional surfaces for attachment of biologically active substances. In this respect, many studies of protein adsorption have been performed on model plasma polymer surfaces. Among these studies, relevant surface properties include wetting, charge, composition and “conformational mobility”. Thus, in characterizing these surfaces, determination of charging properties and functional group density is desired.

Figure 19.8 shows the pH-dependence of zeta potential in 1mM NaCl for three plasma polymer surfaces having different functional characteristics. The respective surfaces of this figure are plasma-polymerized acrylic acid, hexamethyldisiloxane (HMDSO) and 1,2-diaminocyclohexane (DACH). It is evident from the figure that these surfaces have very different electrokinetic surface properties. This pH-dependence clearly

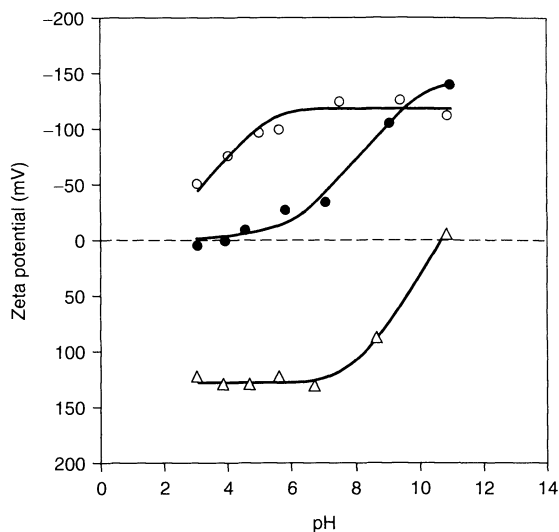


Figure 19.8. The pH dependence of zeta potential for three plasma polymer surfaces in 1mM NaCl: (O), acrylic acid; (●), HMDSO; (Δ), DACH

distinguishes the acid–base properties of the respective surfaces.

The plasma-polymerized acrylic acid surface is a hydrophilic surface containing carboxylic acid groups in the surface layer. The film deposited is commonly envisaged as a cross-linked poly(acrylic acid). By using a single-site dissociation model, the acrylic acid surface of Figure 19.8 can be described as having a single-acid ionizable surface group of pK_a 2.9 and density 8.8 nm^2 per acid group, values which are consistent with surface carboxylic groups.

Plasma-polymerized HMDSO is a hydrophobic, cross-linked polysiloxane network. The HMDSO surface of Figure 19.8 can be modelled as having two distinct acid surface groups, i.e. one of pK_a 7.3 and density 5.6 nm^2 per group, and one of pK_a 4.2 and density 200 nm^2 per group. These values are consistent with a surface containing a considerable number of silanol groups (of pK_a 7.3) and a small number of organic acid groups (of pK_a 4.2), perhaps resulting from oxidation of the surface induced by residual polymer free radicals.

The DACH surface of Figure 19.8 represents a freshly prepared surface (less than one day old). This can be modelled as having a single basic ionizable group of pK_b 10.4 and density 5.0 nm^2 per group, and an acid group of $pK_a < 2$ and density 15 nm^2 per group. The pK of the acid site in this case is somewhat ambiguous since the highly positively charged surface would bring the surface pH outside the range of the acid group (i.e.

the bulk pH of 3 would correspond to a surface pH of 5; in effect the titration begins at pH 5).

Another example of the type of information that can be extracted from electrokinetic data is the hydrodynamic thickness of ion-penetrable surface layers, e.g. surface-bound, neutral, hydrophilic polymers such as polyethers and polysaccharides (11). Surface-bound, neutral, hydrophilic polymers are known to dramatically reduce protein adsorption. The passivity of these surfaces has been attributed to steric repulsion, bound water, high polymer mobility, and excluded volume effects, all of which render adsorption unfavourable. Consequently, these polymer-modified surfaces have proven useful as biomaterials. Specific applications include artificial implants, intraocular and contact lenses, and catheters. Additionally, the inherent non-denaturing properties of these compounds has led to their use as effective tethers for affinity ligands, surface-bound biochemical assays and biosensors.

While the advantages and applications of immobilizing hydrophilic polymers on surfaces are well documented, full characterization of surface-localized polymers in terms of density and film thickness is rare. Studies have shown that adsorbed neutral, hydrophilic polymers attenuate electrokinetic effects, presumably due to displacement of the hydrodynamic plane of shear. In the examples shown in Figure 19.9, poly(ethylene glycol)s (PEGs) were grafted on to quartz capillary

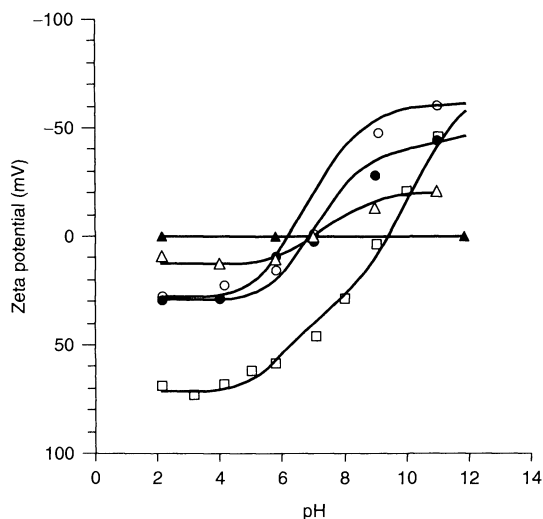


Figure 19.9. The effect of molecular weight on the pH-dependence of zeta potential for PEG grafted to an APS-modified quartz surface in 7.5mM NaCl: \square , without PEG; \circ , PEG 500; \bullet , PEG 3400; Δ , PEG 8000; \blacktriangle , PEG 35000

Table 19.1. Best-fit site-dissociation model parameters for poly(ethylene glycol)s (PEGs) of various molecular weights grafted to APS-modified quartz (cf. Figure 19.9)

Treatment	pK_a	pK_b	$N_a(\text{nm}^{-2})$	$N_b(\text{nm}^{-2})$	$d(\text{\AA})$
APS	6.9	10	0.40	0.50	13
APS/PEG 500	7.5	10	0.40	0.06	16
APS/PEG 3400	7.5	10	0.40	0.10	24
APS/PEG 8000	7.5	10	0.40	0.09	50
APS/PEG 35000	—	—	—	—	> 100

surfaces and characterized with respect to the pH-dependence of the induced electroosmotic fluid flow. PEG derivatives were tethered to quartz surfaces activated a priori with a sub-layer containing a reactive functional group, i.e. 3-aminopropyltriethoxysilane (APS).

Figure 19.9 shows the pH-dependences of the zeta potential for succinimidyl-carbonate-derivatized linear PEGs of different molecular weights grafted to APS-modified quartz. When compared to the APS control, the PEG graft resulted in a shift in the point of zero charge and a molecular-weight-dependent shift in the plateaux attained at the high and low pH values. From model fits it was possible to derive the graft density and effective hydrodynamic thickness for each of the grafts. Table 19.1 summarizes the best-fit data for a model based on a single-acid and a single-basic site with an independent parameter, d , defining the plane of shear, i.e. the hydrodynamic thickness of the polymer layer. The acid site is presumed to originate from surface silanols and the basic site from amino groups on the surface. The reaction of the PEG carbonate with an amine on the surface resulted in a urethane linkage which renders the amino group non-ionizable. Graft density can be considered as being the difference in basic site density before and after reaction. For this specific system, the graft density was independent of molecular weight, while the effective hydrodynamic thickness increased monotonically with molecular weight. An additional noteworthy feature was a shift in the acid pK associated with the silanol group, which increased by half of a pK unit. This can be explained in terms of the PEG hydrogen-bonding with the silanol.

In the preceding examples, the measurement of electrokinetic phenomena has been shown to be useful in characterizing a surface in terms of source of charge and surface interfacial properties. The literature abounds with similar examples. Other than accounting for surface charge, the zeta potential derived from electrokinetic measurements have also been useful as the sole parameter for characterizing the electrostatic contribution to

forces between surfaces, e.g. in the DLVO theory. This contribution, as mentioned previously, is paramount in understanding the stability of colloidal dispersions and the interaction of colloidal particles with macroscopic surfaces. The measurement of electrokinetic phenomena will continue to play an important role in understanding the behaviour of complex systems as scientists in the field of surface and colloid chemistry continue to engineer and characterize macroscopic systems of greater and greater complexity, while at the same time to evaluate and control more and more subtle forces operating at the microscopic level.

5 REFERENCES

1. Russel, W. B., Saville, D. A. and Schowalter, W. R., *Colloidal Dispersions*, Cambridge University Press, Cambridge, UK, 1989.
2. James, R. O. and Parks, G. A., Characterization of aqueous colloids by their electrical double-layer and intrinsic surface chemical properties, in *Surface and Colloid Science*, Vol. 12, Matijevic, E. (Ed.), Wiley, New York, 1982, pp. 119–216.
3. Hunter, R. J., *Zeta Potential in Colloid Science*, Academic Press, London, 1981.
4. Ohshima, H. and Furusawa, K., (Eds), *Electrical Phenomena at Interfaces: Fundamentals, Measurements, and Applications*, Surfactant Science Series, Vol. 76, Marcel Dekker, New York, 1998.
5. Seaman, G. V. F., Electrokinetic behaviour of red cells, *The Red Blood Cell*, 2nd Edn, Surgenor, D. M. (Ed.), Academic Press, New York, 1975, pp. 1135–1229.
6. Burns, N. L., Surface characterization through measurement of electroosmosis at flat plates, *J. Colloid Interface Sci.*, **183**, 249–259 (1996).
7. Grasselli, Y. and Bossis, G., Three-dimensional particle tracking of micronic colloidal particles, in *Surface Characterization Methods*, Milling, A. J. (Ed.), Surfactant Science Series, Vol. 87, Marcel Dekker, New York, 1999, pp. 269–284.
8. Hunter, R. J., Recent developments in the electroacoustic characterization of colloidal suspensions and emulsions, *Colloid Surf., A*, **141**, 37–65 (1998).
9. Dukhin, S. S. and Deraguin, B. V., *Electrokinetic Phenomena*, Surface and Colloid Science Series, Vol. 7, Matijevic, E. (Series Ed.), Wiley, New York, 1974.
10. Ozaki, M., Ando, T. and Mizuno, K., A new method for the measurement of sedimentation potential: rotating column method, *Colloid Surf., A*, **159**, 477–480, (1999).
11. Burns, N. L., Van Alstine, J. M. and Harris, J. M., Poly (ethylene glycol) grafted to quartz: analysis in terms of a site-dissociation model of electroosmotic fluid flow, *Langmuir*, **11**, 2768–2776 (1995).

CHAPTER 20

Measuring Interactions between Surfaces

Per M. Claesson and Mark W. Rutland

Royal Institute of Technology, and Institute for Surface Chemistry, Stockholm, Sweden

1	Introduction	383	4.1	Polar surfaces	394
2	Surface Force Techniques	384	4.2	Non-polar surfaces	396
2.1	Measurements of surface separation and spring deflection	385	5	Measurements in Aqueous Surfactant Systems	397
2.2	Measurements of the force	387	5.1	Polar surfaces	398
2.3	Surface geometry	387	5.2	Concentrated surfactant systems	399
2.4	Surface deformation effects	388	5.3	Interactions between particles and fluid surfaces	400
2.5	Measurement of dynamic surface forces	388	5.4	Measurements in aqueous polymer solutions	400
3	Measurements between Solid Surfaces in Air	389	5.5	Interactions due to adsorbed polyelectrolyte layers	402
3.1	Adhesion	389	6	Measurements in Non-Aqueous Systems	404
3.2	Capillary condensation	390	7	References	407
3.3	Frictional forces	390			
3.4	van der Waals forces	392			
4	Measurements in Aqueous Electrolyte Solutions	393			

1 INTRODUCTION

The measurement of surface forces has long been recognized as a crucial precursor to the understanding of colloidal systems and can be traced back to 1928, when Tomlinson optically measured the adhesion of glass fibres with a view to understanding dispersion forces (1) and although he was unsuccessful in shedding further light on the issue, his crossed-fibre geometry is still in use today. Tomlinson is the unsung pioneer of the field of surface interactions – having performed the first documented surface force measurements at a time when no reliable theories of the dispersion interaction existed, he went on to publish a molecular theory of friction the following year. While forgotten for many years, the gist of this theory has been resurrected from obscurity after being independently proposed in

1989 (2) as the “Cobblestone Model”, which is now widely accepted.

Glass surfaces (spheres) remained the substrates of choice for surface force measurement over the subsequent few years and the next developments in the field were the correlation of adhesive measurements with surface energy (3) and interferometric measurement of the separation (4). The latter innovation allowed both force and distance information to be simultaneously determined for the first time and thus the experimental force curve, if not born, was at least conceived during the 1930s.

The leading groups in the study of surface forces during the 1940s and 1950s were the Dutch and Russian groups (responsible for the so-called DLVO theory (5, 6)), and both of these groups developed surface force measurement techniques during the 1950s to measure

dispersion forces across a vacuum. The Russian version employed a novel pivot arm with a force feedback mechanism (7) and was thus the first “light lever” technique. The Dutch group (8) used a capacitance gauge to measure spring deflection and rather ambitiously used two parallel flat surfaces with an interferometric alignment technique. The development of surface force measurement continued into the late 1960s when Tabor and Winterton (9) developed a technique employing mica surfaces (which are molecularly smooth) glued on to polished silica discs in a crossed cylindrical geometry, coupled with white light, Fringes of Equal Chromatic Order (FECO) interferometry. This device had much better distance resolution and finer separation control than the previous instruments and is the precursor to the “modern” Surface Force Apparatus (SFA) developed during the 1970s. An admirable, and far more complete history of the development of Surface Force Measurement, has been compiled by Craig (10).

The modern SFA of Israelachvili (11, 12) revolutionized the field, and colloid science in general, since it allowed measurement of forces in liquids, and thus the verification of DLVO theory, as well as the quantification of many other types of force, in both aqueous and non-aqueous systems which are discussed more fully in the ensuing chapter. Due to the importance of surface forces in practical systems, many other analogous and complementary techniques have evolved over the last twenty five years. The technique of Derjaguin and co-workers mentioned earlier has been developed (13) and further refined (14) for crossed-fibre measurements, and since it is not dependent on interferometry has thus enabled measurements between opaque metallic surfaces for the first time. Parsegian and co-workers (15, 16) have developed the valuable Osmotic Stress technique, enabling force–distance profiles, primarily between phospholipid layers, to be determined through measurement of the mean bilayer spacing in a liquid crystalline phase under varying osmotic stresses. This has allowed energetic comparisons of force profiles between phospholipids obtained with different techniques and models of the short-range hydration or protrusion force. Total internal reflection microscopy (17) has also been used to study interactions between a colloidal particle in Brownian motion and a flat plate, and extremely sensitive measurements employing a single vesicle allow specific molecular interactions to be determined (18). The Measurement and Analysis of Surface Interactions and Forces (MASIF) (19) approach was developed during the early 1990s and permits non-interferometric measurement of force–distance profiles between glass surfaces with a similar resolution in force normalized by

radius and distance to the SFA (which is largely limited to mica surfaces, although glass surfaces have been used, as have sapphire crystals (20, 21)). Tonck, Georges, Montfort and co-workers in France have also been active in the development of novel dynamic surface force measurement apparatus (22, 23). More recently, a simple adhesion apparatus for deformable polymers has been developed, commonly dubbed the JKR apparatus (24). Numerous other techniques have been developed, some based closely on techniques already described, while others are quite novel, but space does not permit their description here. Luckham and Costello have produced an excellent review of the various modern techniques available for the measurement of inter-particle forces (25).

The most significant advance since the development of the SFA came when Ducker and co-workers (26, 27) glued a “super-colloidal” silica sphere on to an Atomic Force Microscope (AFM) cantilever and used the AFM to measure the forces between the sphere and a flat glass surface. The simplicity and reliability of the technique, coupled with its accessibility and the fact that interferometry is not required, means that it has revolutionized surface force measurement and allowed a wealth of substrates to be examined (28–43).

In this present chapter, we will describe the types of surface forces which can be expected in different types of systems (classified by conditions rather than as a description of different types of forces) and will concentrate primarily on three types of surface force measuring techniques. These are the SFA of Israelachvili (and as modified by others) (44–46), the AFM colloid probe technique (these two techniques are by far the most widely exploited), and the MASIF technique which provides high-resolution data from a purpose-built non-interferometric instrument.

2 SURFACE FORCE TECHNIQUES

When performing measurements of the interactions between surfaces at molecular separations, some precautions have to be taken. Adsorbed contaminants and particles may easily corrupt the measurements. Hence, one needs to take great care while handling the instruments, the surfaces and the solvents. Protective clothes are recommended, as well as carrying out as much work as possible in clean rooms and laminar flow cabinets. During measurements, it is important to avoid vibrations and unwanted temperature changes. Hence, the room temperature should be controlled and the use of an anti-vibration table is appropriate. Before the experiment

proper is started, it is advisable to make some simple tests to determine that the surfaces are clean. Measurements of the adhesion forces in air, and long-range double-layer forces and adhesion forces in dilute aqueous electrolyte solutions may be appropriate since there are many data in the literature describing results from such measurements.

As described in the introduction, there are several different methods available for measuring the force between two interfaces as a function of their separation. Basically, one needs to have the means for controlling and measuring the separation and the force. This can be carried out in many different ways. In order to compare experimental and theoretical results, it is also necessary to know the geometry of the interfaces with a good precision. How this information is obtained when employing three different types of surface force techniques will be described below. We will consider the interferometric surface force apparatus (SFA) of Israelachvili and Adams (47), the "bimorph" instrument (MASIF) of Parker (19), and the atomic force microscope colloidal probe technique first used by Ducker *et al.* (26). The thin film balance technique used for measuring interactions between two fluid interfaces is described by Bergeron in the following chapter in this volume.

First, we note that a force versus distance curve may be obtained in two fundamentally different ways. The force can be controlled and the resulting separation measured. This is the principle used in the thin film balance. Alternatively, the distance can be controlled and the resulting force determined, and this is the method utilized in the SFA, AFM and MASIF approaches. The methodology used in these latter techniques does, however, differ in several important respects. Perhaps the most fundamental difference is how the force and the surface separation are determined.

2.1 Measurements of surface separation and spring deflection

The SFA is shown schematically in Figure 20.1. This instrument exists in many versions (44, 47–49). The interacting surfaces are enclosed in a stainless steel measuring chamber, the volume of which varies between 400 and 10 ml, depending on which version and which attachment is used. In case there is the need to use very small volumes one may simply place a droplet ($V \approx 50 \mu\text{l}$) of the solution between the two surfaces. The latter method is preferable when working with turbid solutions, such as emulsions (50). However, a drawback with the droplet method is that the measurements

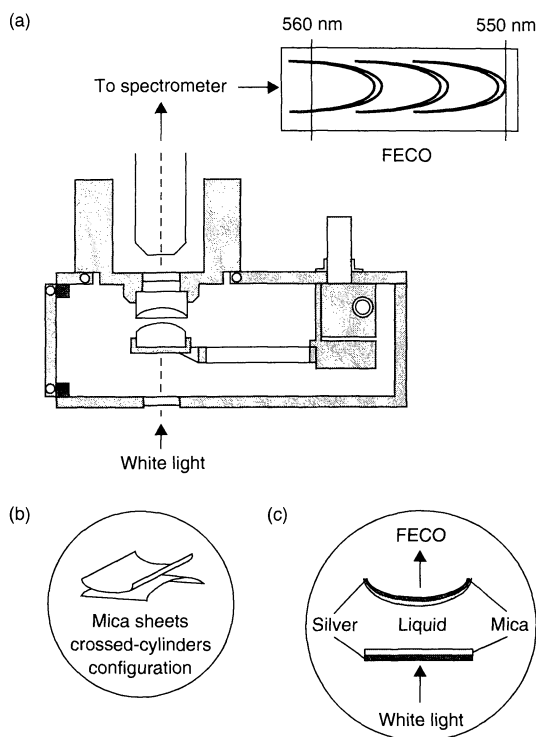


Figure 20.1. (a) A schematic of the main components of the interferometric surface force apparatus. The stainless-steel measuring chamber contains the two interacting surfaces. One mica surface is glued to a silica disc which is attached to a piezo-electric crystal (topmost part). The other surface, also glued to a silica disc, is mounted on a double-cantilever force-measuring spring. The surfaces are oriented in a crossed cylinder configuration (b). White light enters through the window in the bottom of the chamber, where it is multiply reflected between the silver layers, and a standing wave pattern, fringes of equal chromatic order (FECO), are generated (c). The standing waves exit through the top window and the wavelengths and fringe shapes are analysed in a spectrometer

often become less precise due to an increased problem caused by, e.g. temperature drifts. Care should also be taken in order to minimize evaporation; the measuring chamber should be hermetically sealed and the atmosphere inside equilibrated. Placing a small beaker with the appropriate solution within the measuring chamber achieves this.

White light interferometry is used for measuring the surface separation. The white light enters through a window in the bottom of the stainless-steel measuring chamber, and then becomes multiply reflected between the silvered backs of the interacting surfaces, normally mica glued to half-cylindrical silica discs with a radius of curvature of about 2 cm. Only light with wavelengths

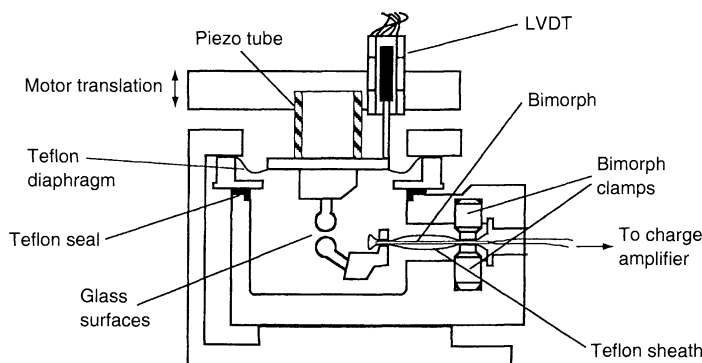


Figure 20.2. A schematic of the MASIF apparatus. One surface is mounted at the end of a bimorph force sensor and the other is mounted at the end of a piezo-electric tube actuator. The force sensor is enclosed in a Teflon sheath mounted inside the small stainless-steel measuring chamber (volume ~ 10 ml). The LVDT displacement sensor is used to directly measure the displacement of the upper surface during force measurements

that interfere constructively with each other will be able to leave the optical cavity. When the outgoing light is inspected in a spectrometer, a series of curved interference lines, i.e. fringes of equal chromatic order, is observed (see Figure 20.1). The wavelengths of the fringes depend on the optical distance between the silver layers, i.e. on the thickness and refractive index of the substrates used, their separation and the refractive index of the separating medium. The shape of the fringes reflects the curvature of the surfaces. The distance moved by one of the surfaces (ΔD_m) and the change in surface separation between the two surfaces (ΔD_s) are measured and the bending of the force measuring spring (D_{bend}) is calculated from the following:

$$D_{\text{bend}} = \Delta D_m - \Delta D_s = \alpha V - \Delta D_s \quad (20.1)$$

The movement of one of the surfaces is induced by using either a piezo-electric crystal or by means of a motor acting on a differential spring system. The motion induced by the piezo device (or motor) is calibrated by using the standing wave pattern, giving the expansion factor (α) in terms of the derivative of the displacement with respect to applied voltage (V) to the piezo-electric crystal ($\alpha = dD/dV$). This calibration must be carried out with the surfaces far apart so that no surface forces are active. In practice, one starts with the surfaces far apart and bring them closer to each other in a step-wise fashion. At large separations, the change in surface separation is proportional to the change in voltage. However, as soon as a force starts to act the surface separation is changing less (repulsive forces) or more (attractive forces) than at large separation. The difference is due to the bending of the spring. The force is then simply calculated by application of Hooke's law

In contrast, in MASIF and AFM instruments, shown schematically in Figures 20.2 and 20.3, respectively, one measures the motion of one surface and the bending of the spring. Thus, the surface separation has to be calculated. In the MASIF and AFM systems, a piezo-electric device is used for changing the position of one of the surfaces. The expansion of the piezo device can be calibrated by using interferometry or, in the case of the AFM, standard gratings. The bending of the spring is determined from the signal (S) of a bimorph force sensor (MASIF) or from a split photodiode (AFM). The sensitivities ($\beta = dD_{\text{bend}}/dS$) of these force sensors can be calculated when changing the voltage applied to the piezo actuator while having the surfaces in direct contact. In this so-called constant compliance region, the bending of the spring is equal to the change in position of the surface attached to the piezo actuator, i.e. $\beta \Delta S = \alpha \Delta V$. In the above discussion, it has been assumed that the piezo expansion is linear with applied voltage. This is a good approximation for certain piezo-electric materials and when the applied voltage is not too high. However, if more accurate measures of the piezo expansion is needed one may use position-sensitive detectors such as capacitors (51) or linear variable displacement transducer (LVDT) devices (19).

It is important to remember that in MASIF and AFM measurements the distance is measured relative to the constant compliance region. Hence, no information on the thickness of firmly adsorbed layers is obtained. In contrast, in SFA measurements the interferometric distance determination allows the use of an absolute distance scale. The zero distance is often defined as the distance between the surfaces in contact in dry air, or alternatively, in dilute electrolyte solutions. This

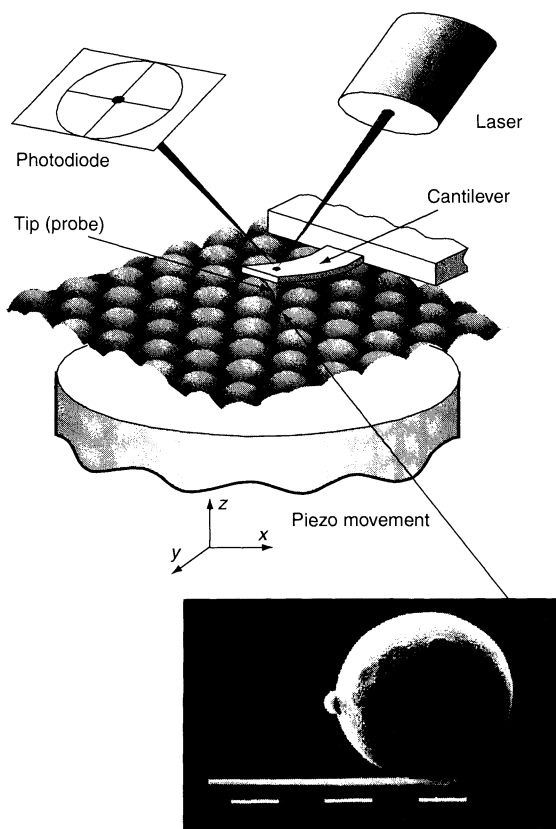


Figure 20.3. A schematic of the AFM set-up. The lower surface is attached to a xyz -piezo scanner. During force measurements, the piezo device is ramped in the z -direction. The colloidal probe (not shown) is glued to the cantilever. A laser beam is reflected from the back of the cantilever. The position of the laser beam is registered by a split photodiode, thus measuring the bending of the cantilever. The inset shows a cellulose particle glued to an AFM cantilever (98). The main figure has been drawn by Lachlan Grant, Institute for Surface Chemistry, Stockholm

allows a direct measurement of the layer thickness. The interferometric technique also allows a determination of the refractive index of the adsorbed layer.

2.2 Measurements of the force

Once the spring bending has been determined the force is seemingly simply calculated by application of Hooke's law, as follows:

$$F = k D_{\text{bend}} \quad (20.2)$$

This requires that the spring constant be known. In the SFA and the MASIF, the spring constant is determined

by adding small weights to the spring and the deflection is measured with a microscope. For MASIF users, some care should be taken since in our experience the bending of the bimorph spring, enclosed in a Teflon sheet, is slightly nonlinear with applied weight. It is recommended that as small weights as possible are used, which means that the magnification of the microscope should be as large as possible. An alternative way of determining the spring constant with the MASIF is to determine the change in resonance frequency with applied weights. This method has, however, been criticized (52), since the spring design is more complicated than the simple beam for which theory is available. Several techniques are available for determining the spring constant for the AFM and these are discussed in Ref. (53). Often, the spring constant is calculated from the dimensions of the cantilever (54, 55), or the resonance technique above may be used where super-colloidal particles are attached as weights. After attachment of a known weight, the AFM head may be inverted and the change in deflection can be used to determine k (56). Measurement of a hydrodynamic interaction (57) in a fluid of known viscosity and using particles of known radius is also a possibility (56) since the measured force is a function of the approach speed, the surface separation, the viscosity and the particle radius – all of which can be accurately determined (see equation (20.4) below).

2.3 Surface geometry

In order to be able to compare data obtained from two different experiments, the geometry of the interacting surfaces needs to be known with a great precision. In order to facilitate such a comparison, the measured force (F) is normalized by the radius (R) of the interacting surfaces. With the help of the Derjaguin approximation (58, 59) one obtains the following:

$$2\pi G_f(D) = \frac{F_c(D)}{\sqrt{R_1 R_2}} = \frac{F_{sf}}{R} = \frac{F_{ss}}{\left(\frac{R_1 R_2}{R_1 + R_2}\right)} \quad (20.3)$$

where G_f is the free energy of interaction per unit area between flat surfaces. The subscripts f , s and c stand for flat surface, sphere and crossed cylinder, respectively. The crossed cylinder geometry is normally used in SFA measurements, whereas two spheres or a sphere and a flat surface are normally used in the MASIF and the AFM system.

It is important to note that the radius that enters equation (20.3) is the local radius. In the SFA, the local radius is easily determined from the shape of

the interference fringes (53, 60). The situation is more complicated in the MASIF and the AFM. For the glass surfaces often used in the MASIF, the local radius can, to a first approximation, be set equal to the macroscopic radius. However, a better precision can be obtained by capturing a video image of the surface and analysing the curvature using standard imaging analysis programs. To determine the (global) radius of the colloidal probe, an electron micrograph picture is normally required. Another possible way to determine the radius of the surfaces is to measure the hydrodynamic force (F_h) in a liquid with known viscosity (η) and calculate the radius from the following relationship:

$$F_h = \frac{6\pi\eta v R^2}{D} \quad (20.4)$$

where v is the speed of approach, and R is the sphere radius in the flat-sphere geometry, i.e. the geometric mean radius in crossed-cylinder geometry, and the harmonic mean radius in sphere-sphere geometry, provided that the spheres are of approximately equal size.

For surfaces with more complex geometry, e.g. the standard AFM tip, it becomes very difficult to assess the correct geometry and for this reason the force measurements become more qualitative.

2.4 Surface deformation effects

In the discussions above, it has been assumed that the surfaces are non-deformable. This is, however, not correct, as significant, easily measurable, deformations occur under the action of strong repulsive and attractive forces. Such effects invalidate the Derjaguin approximation. Experimental studies (61, 62) have shown that the deformation as a function of applied load is

well described by the Johnson–Kendall–Roberts (JKR) theory (63) when the surfaces adhere to each other, while in the non-adhesive case the Hertz theory (64) is appropriate (62). For the silica–glue–mica system, it has been shown that the deformation does not occur in the mica surfaces themselves but rather in the supporting glue and/or silica (62). This means that the surface deformation does not affect the measured surface separation in an SFA experiment since the thickness of the mica sheets remains constant. For MASIF and AFM, the situation is more complex. First, surface deformation effects may mean that the assumption of a constant compliance region is not correct. This has been demonstrated to be important for studies of polymer-coated surfaces (65). Secondly, in MASIF and AFM measurements the deformation of the two interacting surfaces will be indistinguishable from a change in surface separation. This makes it difficult to accurately measure steep short-range forces with these latter techniques. The problem is more severe in the MASIF than in the AFM systems since larger surfaces are used with the former technique. Some features of the SFA, MASIF and AFM techniques are compared in Table 20.1.

2.5 Measurement of dynamic surface forces

Dynamic surface forces include hydrodynamic interactions and viscoelastic properties of adsorbed layers, as well as frictional forces. All of the techniques described above can be used for measuring hydrodynamic interactions. However, in order to study viscoelastic properties and frictional forces, some modifications to the techniques need to be introduced. This may include oscillating the surfaces in the normal (66–69) or tangential

Table 20.1. Some features of common force measuring techniques

Feature	SFA	MASIF	AFM
Surface requirements	Smooth, transparent, sheet-like (mostly mica)	Smooth, hard (mostly glass)	Smooth, well-defined geometry
Interaction geometry	Crossed cylinders	Two spheres, sphere-flat	Two spheres, sphere-flat
Typical radius	1–2 cm	1–2 mm	10–100 μm
Surface approach mode	Stepwise	Continuous, typical speed of 5–200 nm/s	Continuous, typical speed of 50–1000 nm/s
Absolute distance detection	Yes (via interferometry)	No	No
Distance resolution	1–2 \AA	1–2 \AA	1–2 \AA
Force resolution	$\times 10^{-7}$ N	$\times 10^{-8}$ N	$\times 10^{-9}$ N
Resolution in F/R	$\times 10$ $\mu\text{N/m}$	$\times 10$ $\mu\text{N/m}$	$\times 10$ $\mu\text{N/m}$

www.iran-mavad.com

directions (70, 71), or to slide the surfaces tangentially (69, 72–75). The developments in this area up to 1997 have been reviewed by Luckham and Mani-maaran (76), and this paper is highly recommended to the interested reader.

3 MEASUREMENTS BETWEEN SOLID SURFACES IN AIR

3.1 Adhesion

The simplest surface force measurement that can be made with any of the surface force techniques, or the JKR instrument, is the force required to separate two like surfaces in adhesive contact – this is usually referred to as the pull-off force, $F(0)$. From this value, it is possible to deduce the work of adhesion and thus the surface energy providing that there is no capillary condensate around the contact area. However to do this, an understanding of the contact mechanics of the two surfaces must be achieved. For a sphere on flat geometry, the deformation of the sphere under adhesive and applied load has been calculated by several authors. The simplest case (for that where there is no adhesion) is that of Hertz (64) where the contact radius a is given by the following:

$$a^3 = \frac{RF}{K} \quad (20.5)$$

where R is the radius of the sphere, F is the force and K is the elastic modulus. The Derjaguin–Muller–Toporov (DMT) theory constrains the geometry of the contact to Hertzian, while taking into account surface forces (77). The relationship between the surface energy in air, γ ,

and the pull-off force for this approach is as follows:

$$F(0) = -4\pi R\gamma \quad (20.6)$$

By far the most commonly used approach is that due to Johnson, Kendall and Roberts – the JKR theory (63). In this approach, the sphere deforms subject to an adhesive force, without accounting for surface forces. Thus, an attractive “neck” forms at zero load when the surfaces are in contact. The contact radius is given by the following:

$$a^3 = \frac{R}{K} \left[F + 3\pi RW + \sqrt{6\pi RW F + (3\pi RW)^2} \right] \quad (20.7)$$

where in this case W is the work of adhesion, equal to 2γ for like surfaces. For the JKR theory, the pull-off force is given by the following:

$$F(0) = -3\pi R\gamma \quad (20.8)$$

This theory appears to work adequately for most SFA experiments, and is the basis for the so-called JKR apparatus which measures the deformation of a rubbery polydimethylsiloxane (PDMS) hemisphere against a flat surface (see Figure 20.4, taken from ref. (78)) The difficulty with the JKR theory is the prediction of infinite stress at the contact boundary. The true situation lies somewhere between the DMT and JKR limits and rather complicated numerical models employing a Lennart–Jones potential to describe the surface forces resolve this issue (79, 80). As a general rule, the JKR theory is most appropriate for large R values and deformable materials, whereas the DMT approach is better for stiff materials and small deformations.

Adhesion hysteresis is often observed, analogously to contact angles, as the force–area curves measured

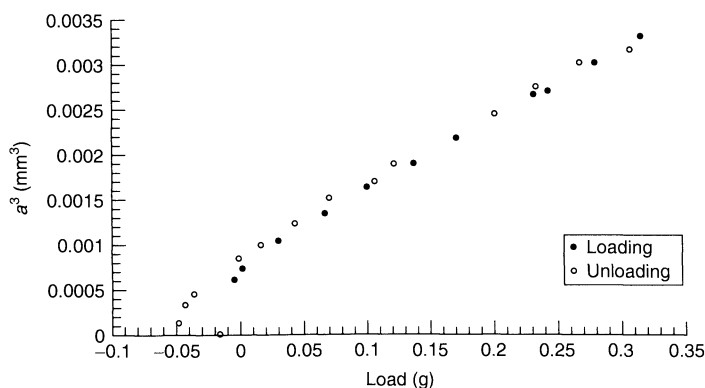


Figure 20.4. The relationship between the contact area and the applied load of a PDMS sphere in contact with a hydrophobised mica surface (78)

for loading and unloading cycles (for example, as measured in the JKR apparatus, or SFA) sometimes fall on different curves. This has been predicted by Attard and Parker (81) from a consideration of the mechanics of closing (loading) and opening (unloading) the “crack” surrounding the contact circle. In addition, (time-dependent) rearrangement of surface molecules in the contact area (for example, interpenetration of polymer chains) will lead to a larger adhesion on unloading than on loading.

3.2 Capillary condensation

Condensation of vapour in thin slits or pores occurs at high vapour pressures if the liquid wets the solid surface. The SFA is ideal for studying this phenomenon, since the slit size can be controlled (and measured) over the nm to micron range. This was first utilized by Fisher and Israelachvili (82) who confirmed the validity of the Kelvin equation down to very small radii of curvature. As a result of this, the separation at which a discontinuity in the interference fringes in contact occurs (due to a change in the refractive index going from precipitate to vapour) can be used to infer the relative vapour pressure – obviating the need for its measurement (83). The interferometric technique also allows pre-contact measurement of the thickness of the thin liquid film adsorbed from vapour to the surfaces. In many cases, the results can be explained by the action of van der Waals forces calculated from Lifshitz theory for a solid interacting with vapour across a liquid film (84). The point at which the adsorbed films fuse as the capillary condensation transition occurs can also be measured and such measurements have led Curry and Christenson to conclude that the mechanism of this transition is inconsistent with a van der Waals force film thickening except for rather thick films. Instead, they speculate that for thinner films the film thickness is actually fluctuation-enhanced (84).

We note that analogous condensation effects can take place in a liquid – for example, surface-induced phase transitions in self-assembly fluids (85, 86) – and it has also been speculated that the mechanism of the hydrophobic interaction involves a similar spinodal decomposition where vapour films on the hydrophobic surfaces grow and fuse (87).

It can be shown (59) that the presence of a capillary condensate around the contact will only alter the pull-off force compared to the dry state (see previous section), if the surface energy in the presence of vapour, γ_{SV} , is very different to the surface energy in air (or more

strictly vacuum), γ . The Laplace pressure contribution is as follows (59):

$$F = 4\pi R\gamma_L \cos \theta \quad (20.9)$$

where θ is the contact angle of the condensate on the solid surface and γ_L is the liquid surface tension. The interfacial energy is different for the surface inside the liquid condensate compared to that in air, and thus γ_{SL} replaces γ in equations (20.7) and (20.8). By combining equations (20.7) and (20.9), we obtain the total pull-off force as follows:

$$F(0) = 4\pi R(\gamma_L \cos \theta + \gamma_{SL}) = 4\pi R\gamma_{SV} \quad (20.10)$$

The last equality follows from the Young equation. It has been suggested that this equation should be modified in certain limiting cases (88).

3.3 Frictional forces

The measurement of friction requires both that the surfaces can be moved laterally to one another and that the lateral (frictional) force associated with this movement can be measured. This can currently be carried out by using the “Mark III t-SFA”, (where “t” stands for tribological) or the AFM with lateral force mode. In the former case, a motorized micrometer arrangement is fitted laterally to the upper surface with strain gauges attached, and the double-cantilever spring can be replaced by a bimorph arrangement which can also be laterally displaced for studying viscoelastic responses. In the latter system, the scanning movement of the AFM is employed for lateral movement, while the torsion applied to the cantilever is measured by a four-quadrant photodiode; obtaining the torsional spring constant is rather difficult (89) but not insurmountable – and changes in frictional force *within* an experiment can always be obtained. The term “friction” is rather a catch-all expression and in fact covers many different types of energy-dissipative mechanisms which resist the lateral movement of surfaces. Some of these mechanisms involve mechanical damage to the surfaces (“wear friction”) and these do not interest us under the mantle of surface forces. Only “wear-free” friction will be briefly considered here, which still covers rather a wide area involving interfacial friction (sliding of two surfaces in dry contact), boundary friction (where two surfaces are separated by a monolayer or bilayer) and hydrodynamic lubrication (where the two surfaces have a liquid film between them). Moreover, kinetic, static and stick–slip friction exist as different regimes, at least

within the first two of these categories. In contrast to most of the other types of forces described in this chapter, the molecular mechanisms of friction are not yet well established and so what follows is just a brief mention of a few key experiments.

The SFA technique has been successfully applied in several systems, e.g. see refs (71, 90, 91), and was used to perform the first measurement of *interfacial friction*, where the frictional force was shown to be linearly dependent on the *area of contact* rather than on the applied load (72). The contact area of two mica surfaces was measured simultaneously with frictional forces at various loads and the JKR theory was used to describe the deformation (63). (This gives a far more complicated load–friction relationship for single-asperity contacts.) In the same experiment and at high loads, surface damage occurred which led to multi-point contact and correspondingly classical *Amonton* friction behaviour where the load and friction were linearly related. It is now reasonably well understood that Amontonian friction results from multiple-point contact of surfaces and that as the load is increased the number of contacts and/or the area of each contact increases. For single contacts, the frictional force is dependent on the area of contact (which nonetheless varies with applied load for any geometry other than parallel surfaces). Correlations of frictional parameters with adhesion hysteresis have been observed (92–94), rather than with the absolute value of the adhesion which might be expected from the “cobblestone model of friction” (2, 95). Briefly, this model of friction assumes that the lattices of two surfaces in contact intercalate slightly, depending on the relevant atomic sizes, and that for sliding to occur, the surfaces need to be separated slightly against both the adhesion and applied load. As the surfaces move past each other, they “crash” into the next minimum which dissipates energy as sound and heat (see Figure 20.5). The phenomenon of stick–slip in boundary friction regimes has been investigated (73, 92, 96) and been shown to depend on phase transitions within ultra-thin layers separating the surfaces. Stick–slip also occurs due to mechanical instabilities with rougher surfaces (97).

Both the t-SFA and AFM can be used for measurements of both sliding and static friction. However, the AFM is incapable of measuring the contact area (or indeed the surface separation to distinguish between different frictional regimes). Using the colloid-probe technique does, of course, provide the versatility to examine a broad range of surfaces, for example, cellulose surfaces (98) (see Figure 20.6), although it is important that a careful load–force relationship be determined and

www.iran-mavad.com

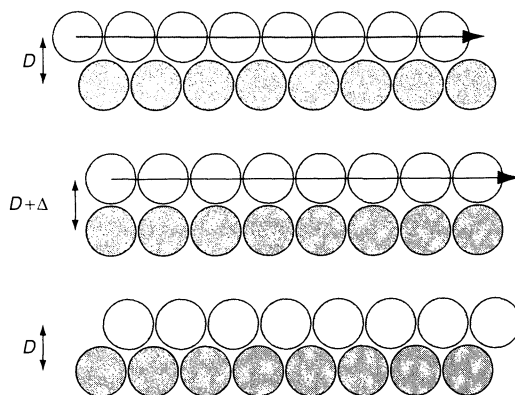


Figure 20.5. Schematic of the “cobblestone model”. Work must be done to separate the two surfaces to permit sliding. The surfaces then crash back into the next stable position, and some of this energy is lost as heat and sound

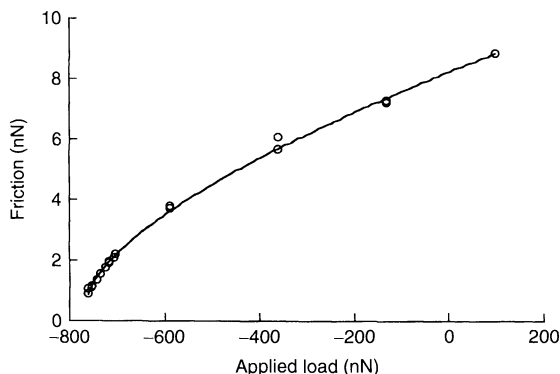


Figure 20.6. The friction–load relationship for an 18 μm sphere of cellulose in contact with a silanated, oxidized silicon wafer (98). Data from both loading and unloading is shown. The continuous line is a fit relating the frictional force linearly to the area of contact, assuming that the load–area relationship is described by the DMT theory

fitted with contact mechanical theory (see Section 3.1 above). To establish which frictional regime is relevant, and indeed which deformation model of the surfaces is most appropriate. For example, the measurements shown in Figure 20.6 could not be fitted with the JKR theory, although the DMT theory fitted the data well. Maugis and Carpick have, respectively, produced a general transition equation (79) and convenient experimental approach (99) for treating cases where the deformation falls between the limits of the JKR and DMT theories. Frictional force “measurement” provides the basis of a type of AFM mode – lateral force microscopy, where

changes in friction are used to map the surface rather than the more conventional height measurement – this is well established and is not discussed here.

3.4 Van der waals forces

The attraction between two uncharged bodies in vacuum is always attractive since the sum of all of the rather short-range intermolecular forces between the respective molecules in the two bodies is significant over relatively large separations. Similarly, two uncharged bodies of the same material interacting across a fluid will always attract each other; however, two bodies of different materials may experience repulsion depending upon their dielectric properties (100). In practice, surface force measurements in air lead to attractive van der Waals interactions, which can be well fitted by the Lifshitz theory (101, 102). This is one of the interactions which is responsible for coagulation of dispersions, and which tends to resist redispersion of a powder in a fluid (such as an aerosol or sedimented paint formulation). The strength of the van der Waals interaction is also important for the floc structure of nanoparticles, for example, in ceramics processing, which is crucial for understanding subsequent properties of the sintered material. The van der Waals interaction of two media, (1) and (2), across a third (3), is given by the following:

$$F_{\text{vdW}} = -\frac{A_{132}R}{6D^2} \quad (20.11)$$

where R is the radius of the equivalent sphere on flat (see equation (20.3)) and A_{132} is the Hamaker constant. Both the Hamaker (103) and Lifshitz theories of the van der Waals interaction have the same form, although the Lifshitz approach is preferred since the Hamaker constant is more easily calculated for this case – it employs a continuum approach, avoiding the limitation of Hamaker's theory in which "neighbour effects" are ignored. The non-retarded Hamaker constant is approximately calculated from the Lifshitz theory by the following equation (58, 59):

$$A \approx \frac{3}{4}kT \left(\frac{\epsilon_1 - \epsilon_3}{\epsilon_1 + \epsilon_3} \right) \left(\frac{\epsilon_2 - \epsilon_3}{\epsilon_2 + \epsilon_3} \right) + \frac{3h\nu_e}{8\sqrt{2}} \times \frac{(n_1^2 - n_3^2)(n_2^2 - n_3^2)}{\sqrt{(n_1^2 - n_3^2)(n_2^2 - n_3^2)} \left[\sqrt{(n_1^2 + n_3^2)} + \sqrt{(n_2^2 + n_3^2)} \right]} \quad (20.12)$$

Here ϵ_i and n_i are the dielectric constant and refractive index, respectively, of medium i and ν_e is the dominant

absorption frequency in the UV region (assumed to be the same for all media). For the symmetrical case, the equation simplifies greatly. The description of van der Waals forces given here is necessarily brief – for an excellent description and derivation, the reader is once again referred to Israelachvili's excellent text, *Intermolecular and Surface Forces* (59).

The measurement of van der Waals forces in air is complicated by the fact that the spring is unstable for steeply attractive forces, hence leading to jumps. Thus, only the longer-range part of the force can be measured and compared with theoretical predictions. Depending on the instrument, spring constant and Hamaker constant, the force in this region can be close to the resolution limits. For compressible materials, fitting of the theory is fairly arbitrary if the deformation of the surfaces cannot be directly measured (since the zero separation obtained in constant compliance will not be the same as zero separation for the undeformed surfaces). However, if the Hamaker constant is large, and reasonable data are obtained prior to the jump, a fit of the van der Waals theory might be used to obtain a measure of the deformation. An example of a van der Waals interaction is shown in Figure 20.7 where a cellulose surface prepared by Langmuir–Blodgett deposition (104) on hydrophobized mica interacts in air with a glass surface (105). The line is not a fit, but is calculated using the Hamaker constant determined from dielectric data of the materials.

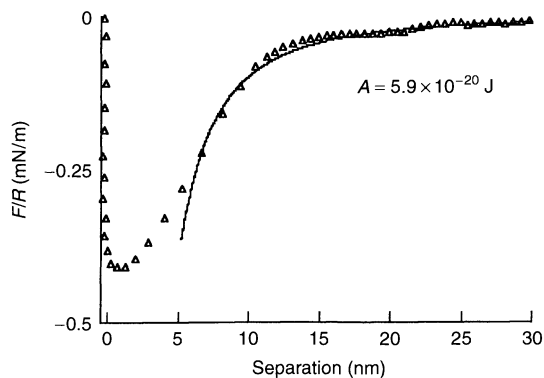


Figure 20.7. A van der Waals interaction plot measured by using the MASIF between a glass surface and a cellulose-coated glass surface. The fit is only valid at larger separations; below about 10 nm, the surfaces are in an unstable "jump" and the data no longer reflect the true interaction (105). The Hamaker constant was not a fitting parameter but was calculated by Lennart Bergström (Institute for Surface Chemistry, Stockholm) from the complete Lifshitz theory

4 MEASUREMENTS IN AQUEOUS ELECTROLYTE SOLUTIONS

Electrostatic double-layer forces act between surfaces immersed in electrolyte solutions as long as at least one of them carries a net charge. Counterions to the surface (ions that are oppositely charged to the surface) are attracted to the latter, whereas ions with like charge (co-ions) are repelled. The ion distribution outside the surface is thus different from that in the bulk solution and can be calculated from the charge of the ions and the electrostatic potential at a given point (arising from contributions from the surface and all ions). The total ion concentration in the neighbourhood of a charged surface is larger than in the bulk solution since the accumulation of counterions is larger than the depletion of co-ions. When the ion distribution is disturbed by the presence of a second surface, a force arises known as the *electrostatic double-layer force*. The most common theoretical treatment of this force is carried out in the nonlinear Poisson–Boltzmann approximation (59, 106). This approximation works best when the surface charge density is small, the ion concentration low, and when the ions present are monovalent.

For small surface charge densities the free energy of interaction per unit area, W_{dl} , between flat surfaces is given by the following (107):

$$W_{\text{dl}} = \frac{\kappa^{-1}}{\varepsilon_0 \varepsilon} \left[\frac{(\sigma_1^2 + \sigma_2^2) e^{-\kappa D} + 2\sigma_1 \sigma_2}{e^{\kappa D} - e^{-\kappa D}} \right] \quad (20.13)$$

which, when both surfaces are charged, for large surface separations reduces to the following:

$$W_{\text{dl}} = \frac{2\kappa^{-1}\sigma_1\sigma_2}{\varepsilon_0 \varepsilon} e^{-\kappa D} \quad (20.14)$$

where σ_i is the surface charge density of surface i , ε_0 is the permittivity of vacuum, ε is the static dielectric constant of the solvent, and D is the surface separation. The Debye screening length given by, κ^{-1} ,

$$\kappa^{-1} = \sqrt{\frac{\varepsilon_0 \varepsilon k T}{2000 N_A q^2 I}} \quad (20.15)$$

where k is the Boltzmann constant, T is the absolute temperature, N_A is the Avogadro number, and q is the elementary charge. The ionic strength, I , is given by the following:

$$I = \frac{\sum_i z_i^2 c_i}{2} \quad (20.16)$$

where z_i is the valency of ion i , and c_i is the concentration of ion i expressed in molar quantities.

From the above equations, we can learn several important facts. First, we note that the double-layer force decays exponentially with surface separations at large separations, with a decay length equal to the Debye screening length, provided that both surfaces are charged. Secondly, the Debye-length and the range of the double-layer force decreases with the ionic strength of the medium. Thirdly, surfaces having the same charge always repel each other. Some calculated forces curves, using equation (20.13), are shown in Figure 20.8. The surface charge density of the first surface is kept constant at 1 mC/m^2 and the double-layer interaction energy for the cases when the second surface has a charge density of

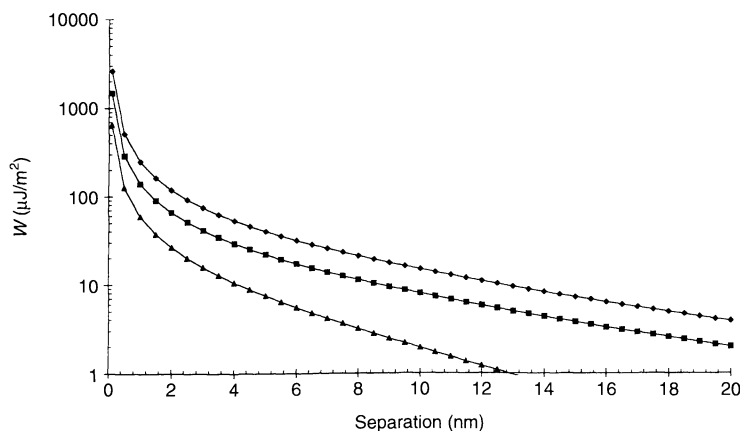


Figure 20.8. The double-layer free energy of interaction per unit area between two flat surfaces as a function of surface separation in an aqueous solution of 1 mM ionic strength. One of the surfaces has a surface charge density of 1 mC/m^2 , whereas the surface charge density of the other surface is 1 mC/m^2 (◆), 0.5 mC/m^2 (■) and zero (▲)

1 mC/m^2 , 0.5 mC/m^2 and zero are illustrated. The ionic strength is 1 mM in all cases. Clearly, the magnitude of the double-layer force decreases with decreasing charge of the second surface. The smaller decay length of the force for the case of one surface being uncharged is due to the fact that term two in equation (20.13) vanishes.

Equation (20.13) also shows that surfaces having opposite sign of their charges attract each other at large separations but repel each other at small separations (providing that the magnitude of the charges are not exactly equal, in which case the force is purely attractive). Some calculated force curves illustrating this are shown in Figure 20.9. In this figure, the lower curve corresponds to the case when the two surfaces have opposite sign but equal magnitude (1 mC/m^2) of their charge. In this case, the attraction increases monotonically with decreasing surface separation. As the magnitude of the surface charge density of one of the surfaces is reduced, the attractive double-layer force becomes weaker and changes into a repulsion at smaller separations. The distance at which the interaction changes sign moves to larger separations when the difference in magnitude of the surface charge densities increases.

The results illustrated in Figures 20.8 and 20.9 are approximate, and further calculated under the assumption that the surface charge density is independent of the surface separation. In many real situations, e.g. oxide surfaces and latexes with weak ionic groups, the surface charge density will vary with the distance between the two surfaces. This has profound effects on the double-layer interaction between unlike surfaces (108–111).

4.1 Polar surfaces

Muscovite mica is a layered aluminosilicate mineral that can easily be cleaved into large molecularly smooth sheets, which has made it the favourite substrate for force measurement studies employing the interferometric surface force apparatus. When immersed in aqueous solution, the mica surface acquires a net negative charge due to dissociation of potassium ions located on the exposed basal plane. The forces acting between two mica surfaces across a range of NaI solutions are illustrated in Figure 20.10 (112). In all cases, a repulsive double-layer force is found to dominate at large separations. This conclusion is based on the observation that the decay length of the force is identical to the Debye length as predicted by the Poisson–Boltzmann theory. In dilute electrolyte solutions, the repulsive double-layer force is at short separations, below 3–4 nm, overcome by an attractive van der Waals force. This is the behaviour predicted by the famous DLVO theory (5, 6) which takes into account additive contributions from double-layer and van der Waals forces. However, at higher salt concentrations a strong repulsive force persists also at small separations (see the force curve for 30mM NaI presented in Figure 20.10). Pashley made a thorough investigation of how this short-range interaction depends on the ionic strength and the type of ions present in solution (113, 114). He concluded that the molecular origin is dehydration of adsorbed cations on the mica surface. For this reason, the short-range repulsion has been called a *hydration force*. Short-range repulsive forces not

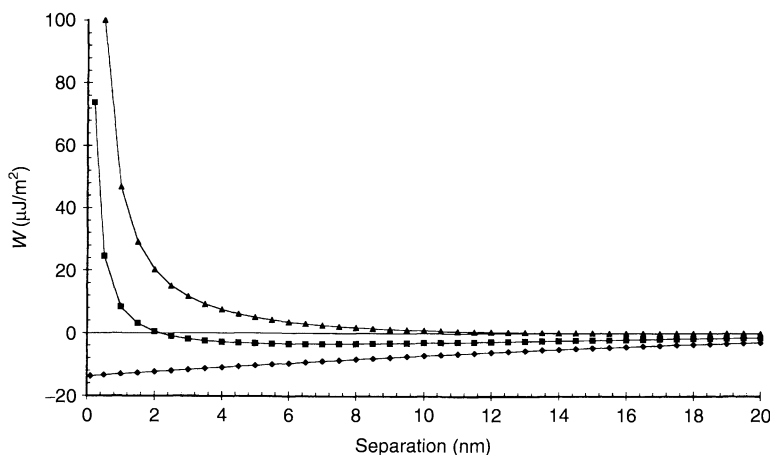


Figure 20.9. The double-layer free energy of interaction per unit area between two flat surfaces as a function of surface separation in an aqueous solution of 1 mM ionic strength. One of the surfaces has a surface charge density of 1 mC/m^2 , whereas the surface charge density of the other surface is -1 mC/m^2 (◆), -0.5 mC/m^2 (■) and -0.1 mC/m^2 (▲).

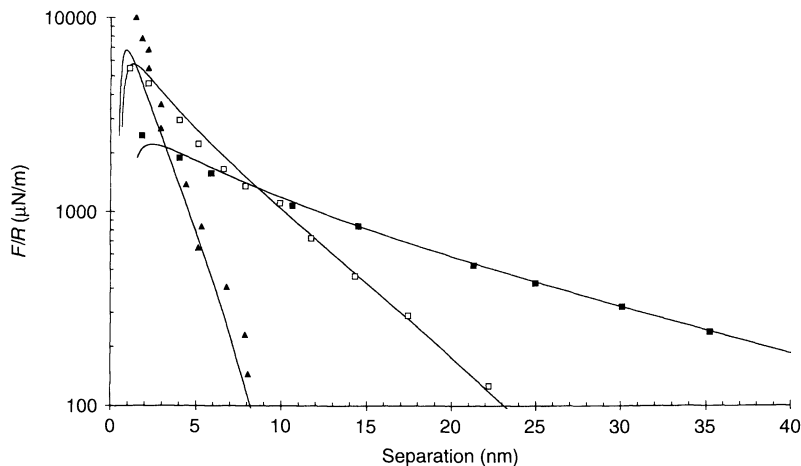


Figure 20.10. Force normalized by radius as a function of surface separation measured between mica surfaces across aqueous NaI solutions, with concentrations of 0.3mM (■), 3mM (□) and 30mM (▲). The lines are theoretically calculated DLVO forces using constant-charge boundary conditions, with Debye lengths in accordance with the electrolyte concentration and surface charge densities (surface potentials on isolated surfaces) of 4.1 mC/m² (74 mV) 15 mC/m² (81 mV) and 34 mC/m² (66 mV), respectively (112)

accounted for by the DLVO theory are also observed between glass and silica surfaces (21, 115, 116) and between bilayers of surfactants and lipids (16). They are all commonly referred to as hydration forces even though the molecular origin may be different. In the case of mica, the origin is suggested to be dehydration of adsorbed cations, while for silica and glass short polymeric chains and surface roughness may also contribute to the short-range repulsion, and for surfactant layers one has contributions from both dehydration and confinement of the molecular motion perpendicular to the surface (117).

The charging properties of cellulose surfaces has been explored by Carambassis and Rutland using the AFM colloidal probe technique (32). The force measured between two cellulose spheres, one attached to the force-measuring spring of the AFM and one residing on a flat surface, is illustrated in Figure 20.11. Again, it was found that the long-range force had a decay length in agreement with that expected for a double-layer interaction. However, in 0.1mM KBr a strong non-DLVO repulsion dominates at distances below 20 nm. This repulsion is a steric repulsion due to confinement of some cellulose chains extending out into solution. It is interesting to note that the range of the steric repulsion decreases with increasing electrolyte concentration, despite the fact that the surface charge density increases (32).

It thus may seem that the Poisson–Boltzmann (PB) theory of the double-layer force is confirmed by

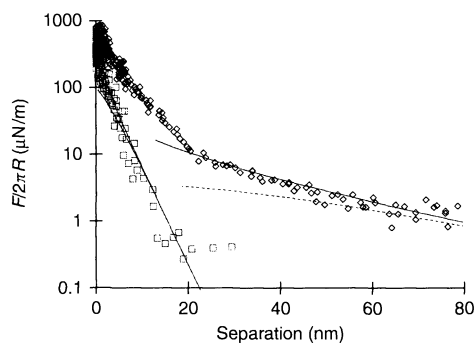


Figure 20.11. Force normalized by radius as a function of surface separation measured between cellulose spheres immersed in aqueous KBr solutions of concentrations 0.1mM (◇) and 10mM (□) (32). The lines are theoretically calculated DLVO forces using constant charge boundary conditions, with Debye lengths in accordance with the electrolyte concentration and surface charge densities (surface potentials on isolated surfaces) of 0.4 mC/m² (17 mV) and 4.9 mC/m² (21 mV), respectively

experiments. This is, in most cases, true for the decay length of the measured force. However, it has to be emphasized that the surface potential (or the surface charge density) is used as a fitting parameter when comparing experimental and theoretical results. Hence, it is not proved that the PB-theory predicts the correct magnitude of the double-layer force for a given surface charge density. In fact, there is strong theoretical evidence to the contrary (118–120). The PB-model neglects ion–ion

correlation effects and ion size effects, both of which are important for strongly charged surfaces and ions. For instance, it has been convincingly shown that ion-ion correlation effects influence the short-range interaction between mica surfaces immersed in CaCl_2 solutions (121). The large size of quaternary ammonium ions also influences the short-range interactions, which phenomenologically can be accounted for by introducing a Stern layer (122). To conclude, it is advisable to regard surface potentials and surface charges deduced from force measurements as being *apparent* values. Despite this, it is fair to say that the forces acting between smooth polar surfaces in aqueous solutions are fairly well understood. This is, however, not the case for the forces acting between non-polar surfaces in water.

4.2 Non-polar surfaces

A large number of experimental reports on the forces acting between non-polar surfaces in aqueous solutions have been described in the literature during the last 20 years or so (for a review, see ref. (123)). The results reported agree in only one respect. The adhesion between the surfaces is high, as expected from the large interfacial energy towards water. However, the range of the measured attraction differs considerably in the different investigations. This fact is illustrated by the data presented in Figure 20.12, which includes results obtained for three different non-polar surfaces. The most hydrophobic surfaces, the plasma-polymerized

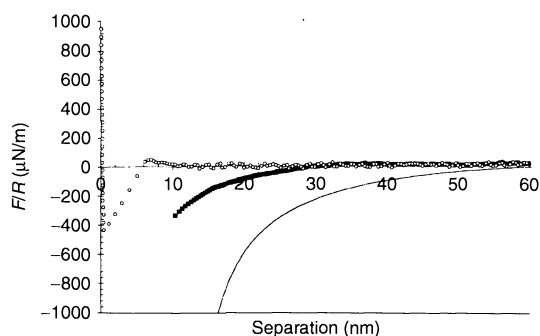


Figure 20.12. Force normalized by radius between three different kinds of hydrophobic surfaces: continuous line, DDOA-coated mica surfaces ($\Theta_A = 94^\circ$, $\Theta_R = 60^\circ$) (125); ■, glass silanated with 3,3-dimethylbutyldimethylchlorosilane ($\Theta_A = 100^\circ$, $\Theta_R = 70^\circ$); ○, glass coated with a plasma-polymer film of hexamethyldisiloxane ($\Theta_A = 109^\circ$, $\Theta_R = 98^\circ$) (124). The macroscopic contact angle of water on each surface is given within parentheses

layers of hexamethyldisiloxane, show the least long-range attraction. In fact, the range of the attraction is in this case consistent with that of a van der Waals force (124). A more long-range attraction is present between uncharged silanated glass surfaces. In this case, the range of the attraction is larger than expected for a van der Waals force and one has to conclude that another attractive force is present. Mica coated with a deposited layer of dimethyldioctadecylammonium ions (DDOA) is also uncharged. This surface is more heterogeneous than the others mentioned above, as judged from the contact angle hysteresis. It is remarkable that the most long-range attraction is present between these surfaces (125).

Still, other results clearly show that the attractive force starts with a discontinuity in the force curve (33, 126, 127). One such example, obtained with the AFM colloidal-probe technique using silica/glass surfaces reacted with fluorinated silanes, is illustrated in Figure 20.13.

Considering this variability of the experimental results it is not surprising that also a great number of theoretical approaches have been taken when trying to explain this so-called “hydrophobic” attraction. In a recent review, Christenson and Claesson (123) suggested that the experimental results could be sub-divided into the following three classes.

- (i) A short-range strongly attractive force between seemingly stable surfaces. This type of interaction is found between polymerized Langmuir-Blodgett layers, some bulk polymers and chemically modified surfaces. A typical result is provided in ref. (128). These results may represent the “true hydrophobic interaction” between macroscopic non-polar surfaces.
- (ii) An attraction of variable range and strength that starts with a discontinuity in the force curve. This type of force has been reported for some silanated surfaces and for thiol-modified gold surfaces. There is ample evidence that this force is due to bridging bubbles, and this attraction is present only when the water contact angle is larger than 90° (129).
- (iii) A very long-range attraction that decays exponentially with surface separation. This type of interaction is found between Langmuir-Blodgett layers that are rather heterogeneous as judged from the contact angle hysteresis (130). The molecular reason for this force is not clear, but the large range and the sensitivity to addition of salt indicate that it may have an electrostatic origin.

It thus seems that other properties of the surface, in addition to the wetting properties, are of importance

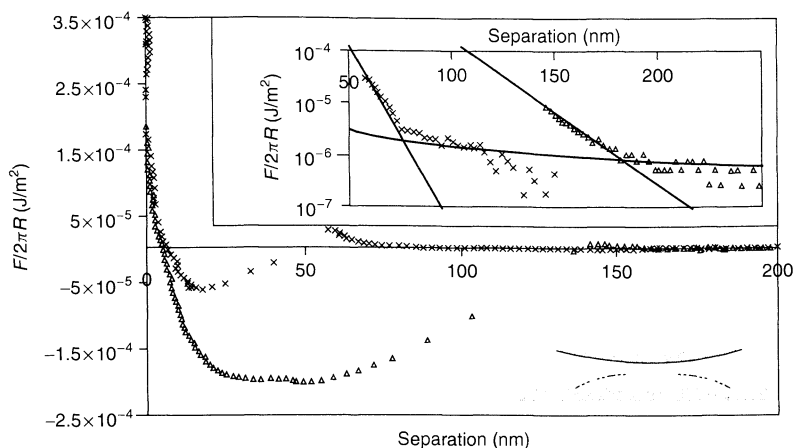


Figure 20.13. Force normalized by radius measured between a flat silicon oxide plate and a glass sphere chemically modified with a fluorinated silane. The forces were determined in 0.19M (Δ) and 9.5M NaCl (\times) solutions. The gaps in the data signify rapid jumps toward contact due to a strong attraction. Reproduced from (33), Copyright (1998) by the American Physical Society

for the range of the attractive force. It also seems that more than one molecular mechanism is operative. It is beyond the scope of this present contribution to discuss the forces between non-polar surfaces in water in any further detail. The interested reader is therefore referred to the review by Christenson and Claesson (123).

5 MEASUREMENTS IN AQUEOUS SURFACTANT SYSTEMS

For the most part the forces observed in aqueous surfactant systems have the same origins as those observed in aqueous systems with the addition of so-called *protrusion* and *steric forces* (15, 117, 131–134).

On non-polar surfaces, surfactants adsorb with their non-polar groups towards the hydrophobic surface (so-called hydrophobic adsorption) and at high enough concentrations form monolayers or “soloids” (surface colloids, or adsorbed aggregates). Atomic force microscopy (AFM) images indicate that these adsorbed films can have different structures, depending on the surfactant and the substrate structure (135–143). Thus, at low concentrations the forces reflect those observed between hydrophobic surfaces, whereas at higher coverages the forces correspond to those between hydrophilic surfaces, with properties reflecting those of the surfactant head-group.

As charged surfactants adsorb to a non-polar surface, the double-layer force increases as a result of the buildup of adsorbed charged material, and the

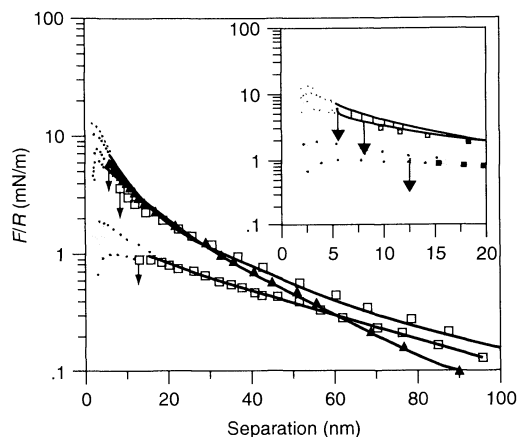


Figure 20.14. Interactions between hydrophobized mica surfaces in solutions of dodecylamine chloride. The double-layer force increases with increasing surfactant concentration as more positively charged surfactant adsorbs (144), reproduced with permission from Academic Press

“hydrophobic” interaction disappears. This is illustrated in Figure 20.14 (144). The surfaces jump into an adhesive contact at separations longer than those predicted by van der Waals theory and this has been described as being due either to a residual hydrophobic attraction (144) or to the spontaneous departure of the adsorbed surfactant (145). At high concentrations of surfactant, the adsorption is so strong that the surfaces no longer jump into adhesive contact and no adhesion is observed

on separation (144). The short-range repulsive force which prevents the non-polar surfaces achieving contact consists of a steric barrier associated with the adsorbed surfactant, plus a very short-ranged exponential repulsion (decay length of ca. 2 Å) which is variously thought to be due to hydration of the head-groups, or due to protrusion of the head-groups associated with thermal motion (15, 117, 131–134).

The surface forces measured between non-polar surfaces to which nonionic surfactants have adsorbed are generally short-ranged, thus reflecting the head-group properties. In general, a short-ranged hydration steric or protrusion force is observed (146–150). (This, together with high surface elasticity and close to zero spontaneous monolayer curvature, is an important factor in explaining the good foaming properties of many nonionic surfactants associated with formation of very “dry”, or thin, films.) Interactions between polyoxyethylene head-groups and water are very temperature-sensitive and the interactions between non-polar surfaces with adsorbed polyoxyethylene surfactant reflect this. At higher temperatures, the interaction with water is worsened and the repulsive hydration force is replaced by an attraction, which in surfactant–water mixtures causes clouding. The temperature-dependence of the interaction is illustrated in Figure 20.15, where the force between hydrophobized mica surfaces to which *n*-dodecyl penta-oxyethylene surfactant has adsorbed is shown (148).

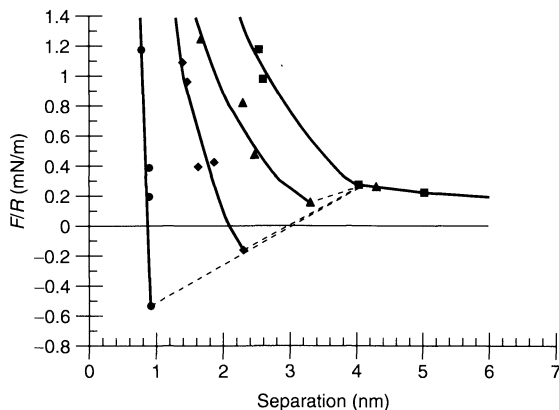


Figure 20.15. The interaction between two hydrophobized mica surfaces with adsorbed nonionic surfactant C12E5. As the temperature is increased from room temperature (■), the profile changes from purely repulsive (steric plus a small residual double-layer interaction) to strongly attractive (●) as the cloud point is surpassed and the head-group interaction becomes favourable (water becomes a poorer solvent for polyoxyethylene) (148), reproduced by permission of The Royal Society of Chemistry

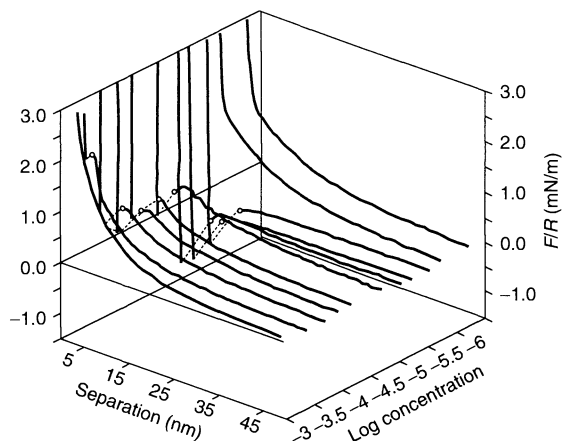


Figure 20.16. Effect of increasing cetyltrimmonium bromide (CTAB) concentration on the surface interactions of two glass surfaces. At low concentrations, there is a negative charge and double-layer interactions which decrease as the cationic CTA adsorbs. At higher concentrations, the double-layer force reappears due to a positive surface charge resulting from overcompensation by the CTA ions. Around the CMC, a barrier is observed corresponding to contact of head-groups from the two opposing surfaces (156)

5.1 Polar surfaces

A great deal of work has been performed in this area, mainly with mica and glass as the polar substrates (19, 30, 150–161). In most cases, a surfactant of opposite charge to the surface has been studied, usually an amine or trimethylammonium head-group. In the absence of adsorbed surfactant, the forces are as described in the previous section on interactions in aqueous electrolyte solutions. Figure 20.16 illustrates the effect of surfactant on the measured forces. As the surfactant concentration is increased, the surfactant begins to adsorb due to favourable electrostatic interactions, thus resulting in a reduction in the double-layer force. Simultaneously, the surface becomes more hydrophobic due to the buildup of hydrocarbon chains on the surface and this leads to an increased adhesion of the surfaces. Eventually, charge neutralization occurs and no double-layer force is observed. Sometimes, a long-ranged hydrophobic force is observed at this point, and in one case it has been successfully fitted (162) with the correlations theory of the hydrophobic interaction (163, 164). As the concentration is built up above charge neutralization, the double-layer force builds up again as charge-reversal takes place. This has been explained both in terms of overcompensation of the surface charge within the “monolayer” and by adsorption of monomers

to the hydrophobic surface (cf. previous section). Of these, the latter is the most likely, as at higher concentrations a steric, charged layer is observed which can be pushed away from the contact area. At high concentrations (above the critical micelle concentration (CMC)) the layer cannot be pushed out if the substrate is deformable (e.g. as in the SFA where the glue deforms (81)). However, on a rigid substrate it can be pushed out, and the range of the step gives a measure of the size of the second layer. If the substrate has a high charge density, the forces indicate that adsorption can be treated in terms of the formation of a hydrophobic monolayer, to which subsequent adsorption occurs just as to a non-polar surface (see previous section). However, when the surface charge is low, electrostatic interactions are insufficient to build a monolayer below the CMC, and as the concentration is increased to the CMC, the forces are consistent with small micellar type aggregates (165).

This last situation is analogous to the adsorption of nonionic surfactants to polar surfaces. The driving forces for adsorption are weaker, so bilayer structures are not in general favoured at concentrations around the CMC and below. Figure 20.17 shows the forces between two glass surfaces in a solution of pentaerythritol dodecylether (C12E5) above the CMC (31). There is a force wall associated with the adsorbate which is relatively easily pushed through. The small adhesion on separation of the

surfaces indicates that after pushing out the adsorbate, the contact is only slightly hydrophobic – this is consistent with micellar type aggregates rather than second-layer adsorption to a hydrophobic monolayer structure. Similar studies have been performed in three-component systems where the micelles in bulk are swollen with oil (166, 167), and in this case the repulsive barrier increases in range, thus indicating that the oil also swells the surface aggregates.

We note that surface force measurements between mica surfaces in dodecylammonium chloride solutions have been well correlated with flotation in the analogous system and the results of some of the parameters extractable from force measurements (layer thickness and adhesion) are plotted against contact angle and flotation in Figure 20.18.

5.2 Concentrated surfactant systems

At high surfactant concentrations, the force curves become rather complex, often displaying an oscillatory force profile (85, 86, 168–175). The measured interactions now reflect how the organization of the self-assembly structures of the surfactants changes as the gap between the surfaces is varied. The oscillatory forces may occur due to the presence of micelles or due to the systematic removal of lamellae in bilayer structured fluids. Furthermore, attractive forces associated with

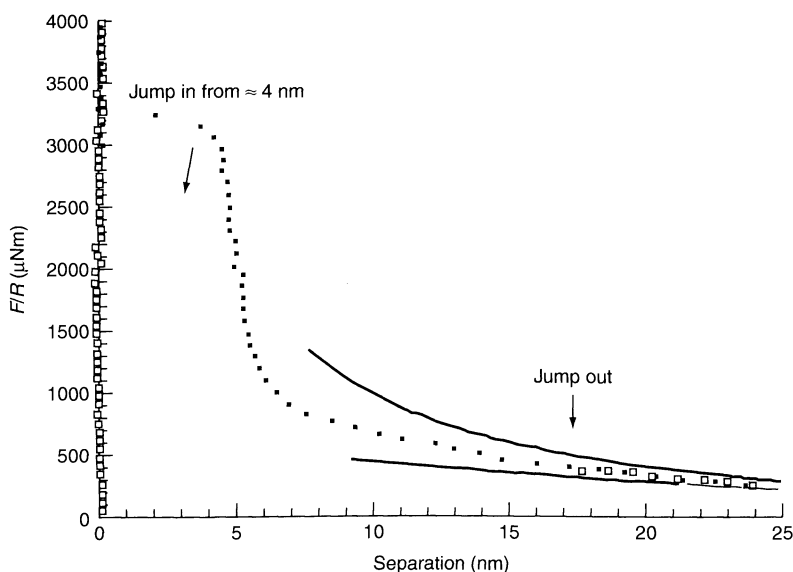


Figure 20.17. Interaction of two glass surfaces (AFM) in a solution of C12E5 above the CMC. A force wall is observed due to adsorbed aggregates which are relatively easily displaced (31)

www.iran-mavad.com

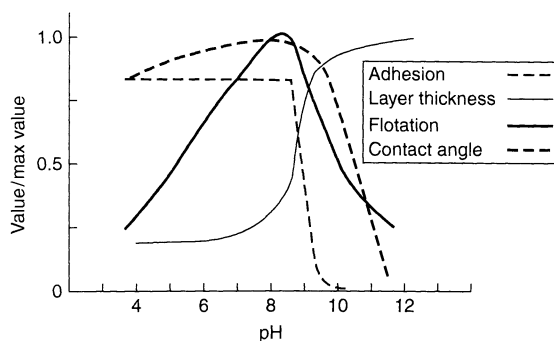


Figure 20.18. Correlations of surface force measurements with flotation measurements on the same surfactant system (157), reproduced with permission from Steinkopff Publishers

surface-induced phase changes can be observed, analogous to capillary condensation.

5.3 Interactions between particles and fluid surfaces

The first measurements between a particle and a bubble were performed independently by Ducker *et al.* (29) and Butt (176), both of whom used the AFM colloid-probe technique. Fielden *et al.* (177) subsequently also investigated the effect of particle hydrophobicity and ageing on these interactions. While agreement is not complete, the general picture is that for negatively charged hydrophilic particles a bubble interface behaves as an elastic body which deforms under repulsive double-layer forces. For hydrophobic particles, a hydrophobic type of interaction is observed, thus leading to engulfment of the hydrophobic particle into the bubble, and a correspondingly large pull-off force. If surfactant is added to the system, it adsorbs to both interfaces and the bubble then can behave elastically and loses its hydrophobic properties. Measurements between a solid surface and a deformable liquid interface have also been performed by Horn and co-workers (45, 178, 179) using a surface force apparatus incorporating a mercury interface, and by Hartley *et al.* (40) using a decane droplet and silica particle. At long-range, there was a double-layer interaction indicating that the oil–water interface was significantly negatively charged, but at smaller separations an engulfment phenomenon was observed analogous to that found with bubbles. The effect of surfactant at the interface hindered engulfment but apparently made the surfaces more deformable due to the lowered interfacial tension.

5.4 Measurements in aqueous polymer solutions

Uncharged or charged polymers are often added to aqueous dispersions in order to impose stability or to cause flocculation. Hence, it is clear that polymers present in solution and adsorbed on to surfaces may generate either repulsive or attractive interactions depending on the conditions used. Factors which determine the sign, range and magnitude of polymer induced forces are, e.g. solvent/polymer interaction (the chi-parameter, χ), polymer/surface interaction (the surface chi-parameter, χ_s), surface coverage and polymer concentration (180).

Several theoretical models describing surface interactions between irreversibly adsorbed flexible polymers have been developed. The most common approaches are based on scaling arguments (181) or on self-consistent mean field calculations (180). The irreversibility criterion implies that the polymer adsorption/desorption rate has to be slow when compared to the approach rate of the surfaces. Under such circumstances, the total amount of polymers on the surfaces is independent of the surface separation and the system is not in true equilibrium with the bulk solution. However, it is often the case that the speed of approach is sufficiently slow for the irreversibly adsorbed polymers to adopt the most favourable conformation for each surface separation. Hence, there is equilibrium within the layer. This situation is referred to as *quasi-equilibrium*, or *restricted equilibrium*.

At high surface coverage, interactions between polymers adsorbed on to different surfaces give rise to a steric force. This originates from an increase in segment density between the surfaces which reduces the number of segment–solvent contacts as well as the number of possible conformations of the adsorbed chains. Under quasi-equilibrium conditions, the second contribution always becomes increasingly repulsive as the surface separation is decreased and will always dominate at small enough separations. The contribution from changes in solvation may be either repulsive or attractive depending on the solvent quality. It is unfavourable for polymer chains to interpenetrate in good solvents ($\chi > 0.5$), whereas such a process is favourable in poor solvents ($\chi < 0.5$). The solvent quality is a measure of the strength of the interaction between individual segments compared to those between segment and solvent, and is commonly expressed by the χ -parameter. Under poor solvency conditions, the outer part of the interaction between polymer-coated surfaces is expected to be attractive. It may be noted that under full equilibrium conditions a purely attractive force should arise between surfaces coated with homopolymers. Hence, in

this case the steric stabilization is entirely due to the slow desorption of the polymer.

A polymer gives rise to an attractive bridging interaction when segments belonging to the same molecule are bound to two surfaces. This occurs most easily when the surface coverage is low. The polymer gains entropy when the surfaces come closer together and this is the molecular mechanism behind the attraction. The bridging attraction may be the dominant force at large separations. However, steric effects generate repulsive forces at smaller separations. The lengths of the polymer tails extending from the surface determine the range of the attraction.

Ethyl(hydroxyethyl)cellulose, EHEC, is a water-soluble macromolecule that has been much studied despite it not being a very well characterized polymer. It consists of a cellulose backbone with grafted ethyl and oligo(ethylene oxide) side-chains. The solution properties, particularly the cloud point temperature, can be tuned by varying the (average) graft density of the substituents. EHEC adsorbs strongly to hydrophobic surfaces due to the presence of hydrophobic side-chains. Hence, non-polar surfaces can easily be pre-coated with an EHEC layer that does not desorb during normal experimental time-scales (weeks) (182, 183). The forces acting between two hydrophobized mica surfaces pre-coated with EHEC across water is shown in Figure 20.19. A long-range steric force is detected at separations below 180 nm. This increases monotonically when the surfaces come closer together. The forces measured on separation are, at distances above 40 nm, significantly lower than those measured on approach. If the measurements had been carried out under quasi-equilibrium conditions, the same force curve would have been detected on approach and on separation. However, for the data shown in Figure 20.19 these are clearly determined under non-equilibrium conditions. This is, unfortunately, a rather common situation when the forces between polymer-coated surfaces are studied, and this invalidates comparison between theory and experiment. A hysteresis-free situation is, however, more commonly encountered when forces between surfaces coated with block copolymers are studied, and in such cases detailed comparisons between theory and experiment are possible (65).

Some proteins, particularly globular ones, are possibly the only true monodisperse water-soluble polymers that are available today. The globular proteins are however very different from synthetic polymers since they are built from many different types of segments and have a well-defined three-dimensional structure. Surface force measurements can provide a great deal of information

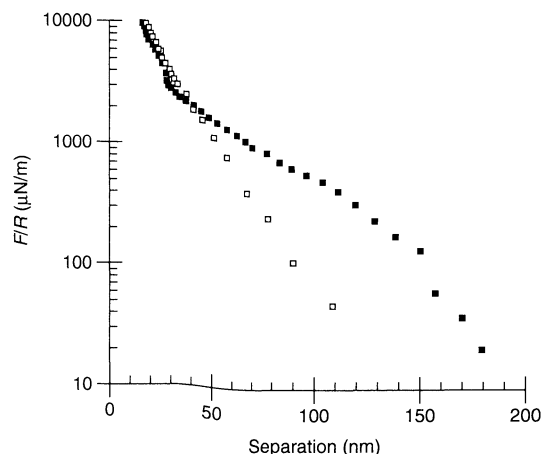


Figure 20.19. Force normalized by radius measured between two hydrophobized mica surfaces pre-coated with a layer of EHEC as a function of surface separation. The forces were measured in water. The EHEC mean molecular weight was 127,000 g/mol, the degree of substitution was 1.9 for ethyl chains and 0.9 for oligo(ethylene oxide) chains. This gave a cloud point of 34.4°C. The forces measured on approach are represented by (■) and those measured on separation by (□) (183)

on the interfacial properties of proteins (184), including orientation on surfaces (185), surface denaturation (186) and the molecular events leading to desorption by, e.g. addition of surfactants (187). The forces acting between two mica surfaces pre-coated with lysozyme are shown in Figure 20.20. At distances below 35 nm, a very weak double-layer force is observed, which is due to a slight mismatch of the charges in the adsorbed layer (from protein and small ions) and the supporting mica surface (188). A van der Waals attraction causes the surfaces to jump from a separation just below 20 nm to 12 nm. At smaller separations, a very strong repulsion due to compression and dehydration of the protein layer is experienced. By considering the adsorbed amount, the evolution of the layer thickness with increasing protein concentration and the solution dimension of the adsorbed protein it was suggested that the layer consists of a mixture of “end-on” and “side-on” adsorbed proteins, and possibly some “side-on” dimers (185). The protein layers adhere weakly to each other as can be seen on separation.

The interactions between proteins and various surfaces are of great importance in many technological processes, including prevention of fouling during membrane filtration, protein separation in chromatographic media and in biomedical processes. To this end, some studies of the interaction between EHEC-coated surfaces and

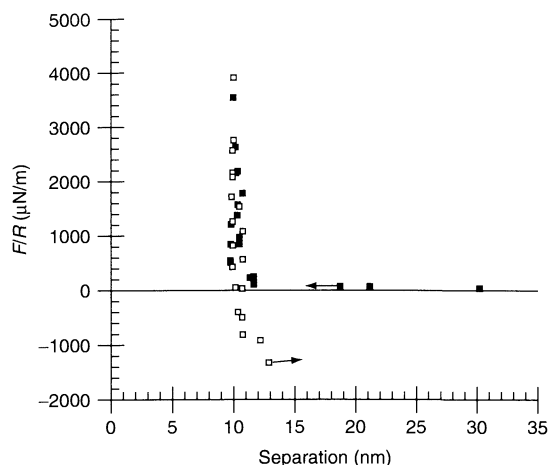


Figure 20.20. Force normalized by radius as a function of surface separation between mica surfaces pre-coated with lysozyme. The forces were measured in a 1mM NaCl solution, with the forces measured on approach (■) and on separation (□) being illustrated. The arrows indicate inward and outward jumps (188), reprinted with permission from Elsevier Science

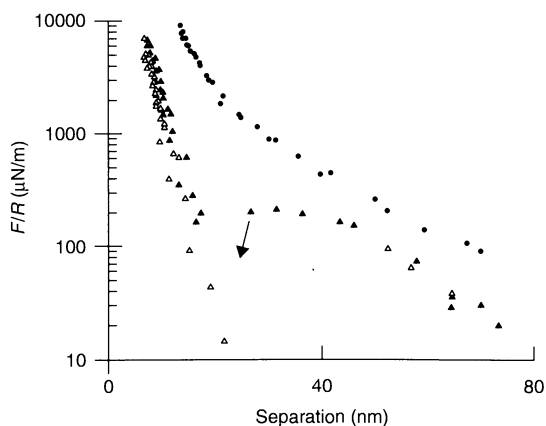


Figure 20.21. Force normalized by radius as a function of surface separation between one EHEC-coated surface and one lysozyme-coated surface. The forces were measured in 1mM NaCl at 21–23°C (●), and at 45°C on approach (▲) and separation (Δ) (189)

protein-coated surfaces as a function of temperature has been carried out (189). The data shown in Figure 20.21 show that the forces are purely repulsive at room temperature (21–23°C) and dominated by the steric repulsion arising from compression of the EHEC layer. However, as the temperature is increased to 45°C, which is well above the cloud point (CP) of this particular EHEC fraction used (CP = 34.4°C), the interaction changes significantly

dramatically. The long-range repulsion is significantly reduced, which is related to the compaction of the EHEC layer due to the worsening of the solvency (182). In addition, once the small repulsion has been overcome there is an attraction between the lysozyme layer and the EHEC layer. This result suggests that the decrease in the protein-repellent ability of PEO-containing polymers at elevated temperatures (190) is related to the decreased steric repulsion generated by these polymers. Furthermore, the van der Waals interactions between the polymer layer and the protein will increase as water is expelled from the polymer layer at higher temperatures.

5.5 Interactions due to adsorbed polyelectrolyte layers

Interactions between polyelectrolyte-coated surfaces have been extensively studied during the last few years (191–194). It is found that under low ionic strength conditions, highly charged polyelectrolytes adsorb in a very flat conformation on oppositely highly charged surfaces (195). This is due to the strong electrostatic attraction between the polyelectrolyte and the surface. As the electrostatic forces are decreased by increasing the ionic strength (196) or by reducing the charge density of the polymer (197), the adsorbed layer adopts a more extended structure, and it becomes more like that formed by nonionic polymers. The forces acting between surfaces fully coated with polyelectrolytes often have important contributions from double-layer forces and steric interactions.

The bridging mechanism is slightly different for polyelectrolyte-coated surfaces when compared to surfaces bearing adsorbed nonionic polymers. The bridging mechanism, in the case of nonionic polymers, is caused by chains attached to two surfaces. For polyelectrolytes, however, the polymers do not need to be bound to two surfaces to cause bridging. This is due to the long-range nature of electrostatic forces. Hence, a bridging attraction arises when the polyelectrolyte has some segments sufficiently close to one of the surfaces and others close to the other surface to interact with the electrostatic potential emanating from them. Thus, a part of the polyelectrolyte is attracted to one surface and another part to a second surface. As for nonionic polymers, this bridging attraction has mainly an entropic origin (195). An example of a measured bridging attraction between polyelectrolyte-coated glass surfaces is shown in Figure 20.22. The strength of the attraction is significantly larger than the expected van der Waals force,

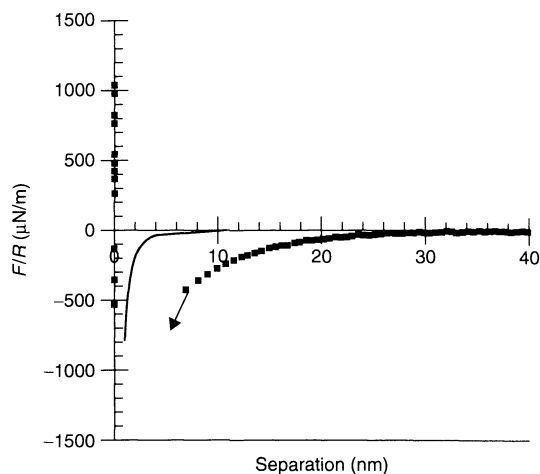


Figure 20.22. Force normalized by radius as a function of surface separation between two glass surfaces across a 0.1M NaCl solution containing 1 ppm poly(vinyl amine). The forces were measured after 30 min, i.e. before adsorption equilibrium had been established (237)

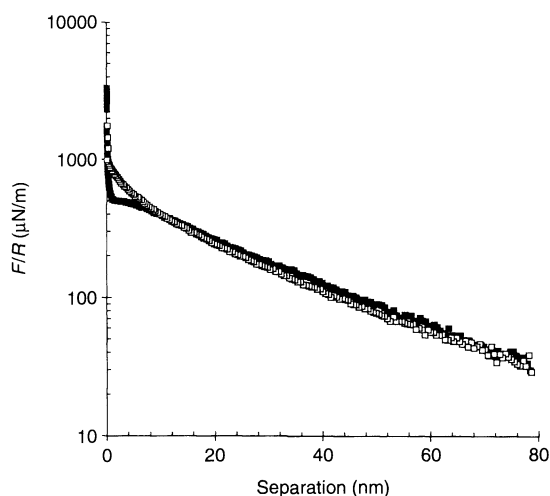


Figure 20.23. Force normalized by radius as a function of surface separation between one cellulose surface prepared by the Langmuir–Blodgett technique and one glass surface. The forces were measured after 30 min (■) and 24 h (□) immersion in 0.1M NaCl (105)

which is in agreement with other experimental and theoretical studies (195).

Polyelectrolytes are commonly used in the paper-making industry as wet- and dry-strength additives and as retention agents. This has lately inspired research on how polyelectrolytes affect interactions between two cellulose surfaces and between one cellulose surface and other materials (105, 198). In order to conduct such experiments, model cellulose surfaces have to be prepared by spin coating (199), Langmuir–Blodgett (LB) deposition techniques (104) or in the form of spherical cellulose particles (32). It is often found that the model cellulose surfaces swell when first immersed in water, particular at elevated pH-values (32). One example of this behaviour is illustrated in Figure 20.23, which contains data for the forces acting between a cellulose LB multilayer and a glass surface in 0.1M NaCl (105). The long-range interaction is due to a repulsive double-layer force caused by the negative charges present on the glass surface and the cellulose surface. This force is not significantly affected by the exposure time to the aqueous phase. However, the short-range forces change character. At short exposure times (< 1 h), an attractive force contribution is present at short separations, seen as a reduction in the slope of the total force at distances below 8 nm, and a comparatively strong adhesion (7 mN/m) is observed on separation. After prolonged adsorption times (\approx 24 h), the attractive force contribution has become negligible away from contact-faces. However,

and a stronger increase in repulsion (for $D < 8$ nm) with decreasing separation is apparent. The adhesion is also reduced significantly to less than 0.5 mN/m. These changes have been attributed to swelling of the cellulose coating (105).

Addition of a cationic polyelectrolyte, poly(vinyl amine) (PVAm), to the solution has pronounced effects on the interaction. At a PVAm concentration of 1 ppm, no long-range double layer force is present, indicating that the adsorbed polyelectrolytes have neutralized the surfaces (105). Higher polyelectrolyte concentrations result in a recharging of the surfaces, as illustrated in Figure 20.24. It is clear that the magnitude of the double-layer force increases with the PVAm concentration and that a steric force dominates the interaction at distances below 8 nm. The range and magnitude of the steric interaction are not significantly affected by the presence of the polyelectrolyte, which is in line with the flat adsorption conformation of polyelectrolytes in low-ionic-strength solutions.

In many applications, e.g. in household care and personal care, both polyelectrolytes and surfactants are present in the formulations. In cleaning applications, it is often the case that surfactants are added in order to remove charged or uncharged polymers or proteins from surfaces. Comparatively little is known about the properties of polymer–surfactant systems at inter-

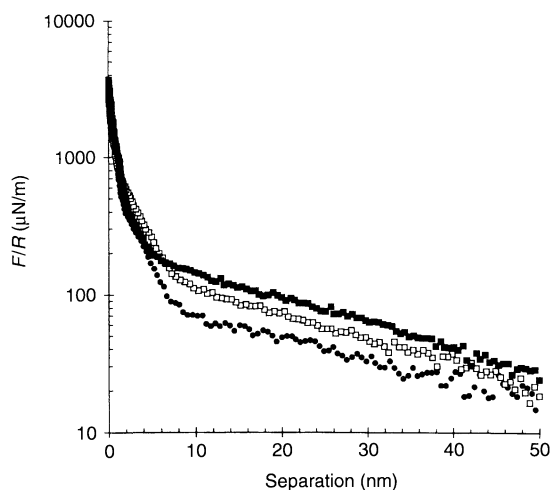


Figure 20.24. Force normalized by radius as a function of surface separation between one cellulose surface prepared by the Langmuir–Blodgett technique and one glass surface. The solution contained 0.1mM NaCl and poly(vinyl amine) at concentrations of 2 (●), 5 (□) and 10 ppm (■) (105)

properties of these rather complex systems have been advanced during the last few years due to applications of ellipsometry (200, 201), reflectometry (202, 203), surface-sensitive spectroscopic techniques (204, 205), neutron reflectivity (206) and surface force measurements (207–215). This topic has recently been reviewed (216), and here we will only mention two complications. First, it has been noted that the equilibration in polyelectrolyte–surfactant systems is very slow and the order in which the components are added affects the layer properties significantly (217). Furthermore, in many cases highly viscous adsorbed layers are formed, which renders it virtually impossible to measure equilibrium forces (215).

6 MEASUREMENTS IN NON-AQUEOUS SYSTEMS

The forces acting between surfaces across non-polar media are often dominated by structural forces that arise due to changes in the liquid density in the gap between the surfaces as they approach each other (59, 218). The appearance of a structural force is due to the geometrical constraints imposed by the confining walls and does not require any attractive or repulsive solvent–surface interaction. The structural forces are of rather short-range, below 10 molecular diameters, and vary in a periodical fashion from repulsive to

attractive as the surfaces come closer together. The amplitude of the oscillations becomes larger as the gap between the surfaces decreases. The periodicity of the oscillations is related to some characteristic size of the molecules. For spherical molecules, it is found that the periodicity corresponds well with the diameter of the molecule (219, 220), whereas for alkanes outside of mica surfaces the periodicity is close to the thickness of one alkane chain (221, 222), thus indicating that the molecules are ordered parallel to the surface. The number of oscillations in the force curve is smaller in liquids of flexible alkanes when compared to those in liquids of more spherical and rigid molecules. It is interesting that even a small degree of branching in alkane molecules prevents packing in ordered layers, and in such liquids the force law is no longer oscillatory (223). It is also well established that the structural force is significantly reduced when the surfaces are randomly rough on a molecular length-scale (224).

The structural forces between two polar mica surfaces and between two non-polar modified mica surfaces across anhydrous triolein are illustrated in Figure 20.25 (225). The polar surfaces do not interact with each other until they are less than about 6 nm apart. The fact that no long-range forces are observed shows that the surfaces are uncharged, as expected from the low dielectric constant of triolein. A very steep repulsive force is encountered when the surface separation is below 6 nm. At high enough loads, this force barrier is overcome and the surfaces move to as close as 2 nm from each other. On separation, it is observed that the surfaces adhere to each other and a rather strong attractive force has to be overcome before they detach. The measured interaction is a structural force caused by the change in the packing

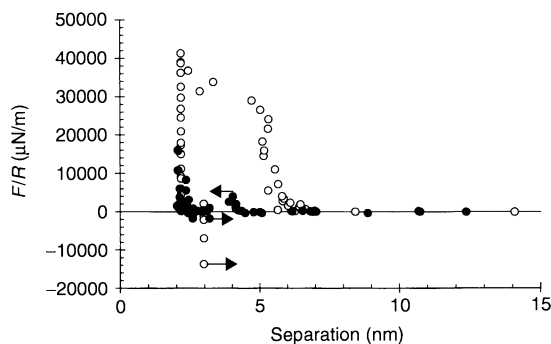


Figure 20.25. Force normalized by radius as a function of separation between two polar mica (○) surfaces and between two non-polar modified mica surfaces (●) across anhydrous triolein. The arrows indicate inward and outward jumps (225)

of the triolein molecules in the gap between the surfaces as they are brought together.

The forces between two non-polar surfaces across triolein also show two repulsive branches (226). However, many features of the interaction profile are very different. First, the force barriers appear, for the non-polar surfaces, at separation of 45–40 and 25–20 Å, respectively. In particular, the outer force barrier is located at a smaller separation than in the case of polar surfaces. This indicates that the orientation of triolein molecules outside polar and non-polar surfaces is significantly different. In order to understand this, we have to consider the structure of triolein. The triolein molecule consists of a slightly polar glyceryl unit connected to three non-polar oleic acid chains. The extended length of triolein is about 27 Å, and the length along the glyceryl unit is about 5 Å. A comparison of the positions of the force barriers in the case of polar surfaces (60–50 Å and 30–20 Å) with the dimensions of the molecule strongly indicates that one layer of triolein is bound to each mica surfaces, and that the molecules are directed with the long axis perpendicular to the surface. We suggest that dipolar interactions between the glyceryl group and the polar mica surface favour this orientation. On the other hand, there is no dramatic difference in interaction between a non-polar surface and the various parts of the triolein molecule. Hence, there is no clear preferential orientation of triolein outside of such surfaces. A consequence of this is that the layering of the molecules in the gap between the surfaces is less pronounced than for a polar surface, and therefore a much smaller force is needed in order to overcome the first repulsive barrier.

Some water absorbed from the surrounding air is, if extreme drying procedures are not employed, always present in the non-polar oil. The molar water solubility is not high in triglyceride oils. However, even when water is present in a small amount it accumulates at polar surfaces, which is expected to influence the surface forces. The forces measured between polar mica surfaces across triolein with different water activities, ranging from 0.23 to 1, are displayed in Figure 20.26. Clearly, the main effect observed when increasing the water activity is a reduction in the magnitude of the outer force barrier located at a separation of about 50 Å. This barrier is nearly gone at a water activity of 0.75. The reason is that the polar water molecules interact more favourably with the polar surface than the triolein molecules. This is also seen by the very low contact angle of water on mica in triolein, i.e. about 0°. The accumulation of the small water molecules in the interfacial region thus disturbs the packing of the larger triolein molecules and this explains the reduction in the force barrier.

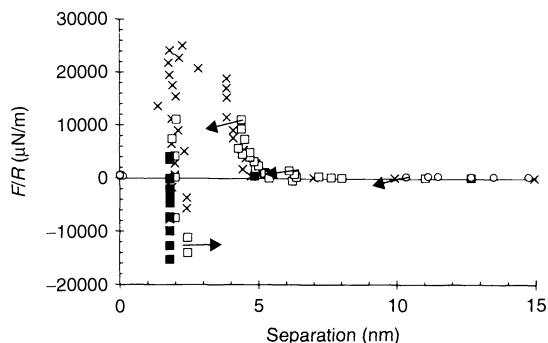


Figure 20.26. Force normalized by radius as a function of separation between two polar surfaces across triolein at a water activity of 0.23 (X), 0.47 (□), 0.75 (■), and 1 (○). The arrows indicate inward and outward jumps (226)

Close to water saturation, the interaction forces change dramatically. Both force barriers disappear, and instead a strong attraction is observed at separations below about 100 Å. The reason for this attraction, which pulls the polar surfaces into molecular contact at $D = 0$, is the formation of a water capillary condensate in the contact region. The force needed to separate the surfaces from this contact is very large, $350 \pm 50 \text{ mN/m}$, i.e. more than a factor of 20 larger than the force holding the surfaces together at the lower water activities. The results presented above demonstrate that small amounts of water in a non-polar medium have dramatic effects on the interaction between polar particles. This, of course, will affect the stability of such dispersions and thus also the rheological properties.

Finally, we note that structural forces are also observed in complex liquids. These may arise due to changes in the spatial distribution of micelles (227) or polyelectrolytes (228–230), or be due to the internal structure of polyelectrolyte–surfactant aggregates (211, 231).

The interactions of polymer-bearing surfaces in non-aqueous systems are determined by the solvent quality in the same way as in aqueous solutions (see previous section). Steric forces, bridging forces and attractive forces, due to favourable segment–segment interactions, all occur depending on the solvent quality, polymer coverage and polymer length. Clearly, a much wider range of solvent qualities can in general be achieved in non-aqueous conditions for any given polymer and this can be utilized to tune the properties of a dispersion. Particles which are sterically stabilized in non-aqueous solvents can readily be made to flocculate by a change in the solvent composition. Plunkett *et al.* (232)

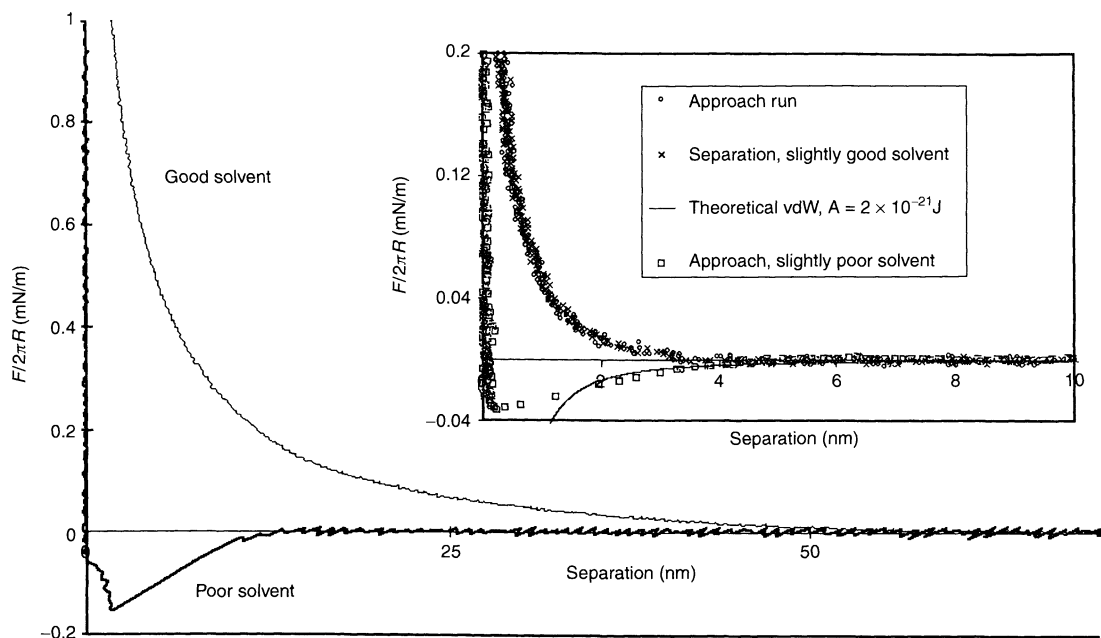


Figure 20.27. The interaction profiles between glass surfaces with grafted polyhydroxystearate layers in heptane–ethanol mixtures. The forces become increasingly repulsive as the solvent quality deteriorates (232)

has studied how the solvent quality determines the interaction profile for grafted polyhydroxystearate layers on glass. The solvent used was a mixture of heptane (good solvent) and ethanol (poor solvent); the reason for the solvent choice was that for compositions of the order of 40% ethanol, the theta temperature exists close to room temperature, and thus the solvent quality can be sensitively controlled through temperature, as well as through changes in the composition. Figure 20.27 shows the data obtained from this study. In good solvent conditions, a long-range, monotonic steric force is observed, whereas in poor solvent conditions the force is rather shorter-ranged and attractive (aside from a small repulsive barrier close to contact). The ethanol mole fraction was changed by about 5% at room temperature to effect this change. The inset in this figure shows the forces at close to theta conditions and in this case the solvent quality was tuned by temperature changes. The MASIF instrument was used for this study, which permits temperature changes from about 10 to 45°C, with a resolution of the order of 0.1°C (strictly the range is greater than this, but temperature drifts make measurement increasingly awkward away from ambient temperature). In the last case, the forces are sufficiently small that hydrodynamic forces become significant, and this component

has been subtracted from the force. The polydispersity of the polymer makes it difficult to apply theoretical fits to the data (the theories assume grafted molecules of uniform length). Hadziioannou *et al.* (233) performed a much earlier work studying the solvent effects close to the theta temperature (polystyrene adsorbed to mica in toluene) and showed that the range of the inter-segment attraction varied with the molecular weight, as expected.

One of the problems faced with polymer systems is that of equilibrium. Not only may adsorbed polymers desorb during compression, but the polymer may not be able to achieve its equilibrium configuration for a given separation over the time-scale of the experiment. Several groups have thus built modified surface force apparatuses to perform viscoelastic measurements on confined films, not only to determine relaxation rates for grafted polymers, but also to determine the effect of confinement on the physical properties of the films and to study friction and lubrication (see Section 2.5 above). Storage and loss moduli can be extracted from the response to oscillations in the frequency range of approximately 10^{-2} to 10^2 Hz. Montfort and co-workers, for example, have used normal oscillations to study the viscoelasticity of polybutadiene films on metal surfaces in hydrocarbons (234, 235). At such sufficiently small separations that the polymers could interact with one another, the

storage modulus increased significantly (approximately two orders of magnitude at low frequency, where the values plateaued due to the steric forces). The behaviour of the adsorbed molecules was determined to lie between that of molecules in rubbery and glassy melts, thus indicating restricted motion of the polymer chains. Granick and Hu have used their tangential shear SFA to study, among other things, the shear/confinement behaviour of polymer melts (236). These authors studied a polymer with a low glass transition temperature, i.e. polyphenylmethylsiloxane (PPMS), using very small (2 Å) amplitudes which thus do not disrupt any adsorbed films. They observed that the moduli scaled with the radii of gyration (R_G), and that at separations less than $5R_G$ a fluid-like to solid-like transition was observed, thus indicating that confinement significantly altered the polymer properties.

7 REFERENCES

- Tomlinson, G., Molecular cohesion, *Phil. Mag.*, **6**, 695–712 (1928).
- McClelland, G. M., *Adhesion and Friction*, Springer, Berlin, 1989.
- Bradley, R. S., The Cohesive force between solid surfaces and the surface energy of solids, *Phil. Mag.*, **13**, 853–862 (1932).
- Rayleigh, Lord A study of glass surfaces in optical contact, *Proc. R. Soc. Lond., A*, **156**, 326–349 (1936).
- Derjaguin, B. V. and Landau, L., *Acta Physicochim. USSR*, **14**, 633–662 (1941).
- Verwey, E. J. N. and Overbeek, J. T. G., *Theory of Stability of Lyophobic Colloids*, Elsevier, Amsterdam, 1948.
- Derjaguin, B., Titjvskaja, A., Abricossova, I. I. and Malkina, A., Investigations of the forces of interaction of surfaces in different media and their application to the problem of colloid stability, *Discuss. Faraday Soc.*, **18**, 24–41 (1954).
- Overbeek, J. and Sparnaay, M., Experiments on long-range attractive forces between macroscopic objects, *J. Colloid Interface Sci.*, **343**–345 (1952).
- Tabor, D. and Winterton, R. H. S., Surface forces: direct measurement of normal and retarded van der Waals forces, *Nature (London)*, **219**, 1120–1121 (1968).
- Craig, V., Application of the light lever technique to the direct measurement of colloidal forces, Ph. D. Thesis, Australian National University, 1996.
- Israelachvili, J. N., Thin film studies using multi-beam interferometry, *J. Colloid Interface Sci.*, **44**, 259–272 (1973).
- Israelachvili, J. N. and Adams, G. E., Direct measurements of long range forces between two mica surfaces in aqueous solutions, *Nature (London)*, **262**, 774–776 (1976).
- Derjaguin, B. V., Rabinovich, Y. I. and Churaev, N. V., Measurement of forces of molecular attraction of crossed fibers as a function of width of air gap, *Nature (London)*, **265**, 520–521 (1977).
- Knapshinsky, L., Katz, W., Ehmke, B. and Sonntag, H., Interaction forces between crossed quartz filaments in presence of adsorbed poly(vinyl alcohol), *Colloid Polym. Sci.*, **260**, 1153–1156 (1982).
- LeNeveu, D. M., Rand, R. P. and Parsegian, V. A., Measurements of forces between lecithin bilayers, *Nature (London)*, **259**, 601–603 (1976).
- Parsegian, V. A., Fuller, N. and Rand, R. P., Measured work of deformation and repulsion of lecithin bilayers, *Proc. Natl. Acad. Sci. USA*, **76**, 2750–2754 (1979).
- Prieve, D. C., Lou, F. and Lanni, F., Brownian-motion of a hydrosol particle in a colloidal force-field, *Faraday Discuss. Chem. Soc.*, **83**, 297–307 (1987).
- Evans, E., Berk, D. and Leung, A., Detachment of agglutinin-bonded red-blood-cells. Forces to rupture molecular-point attachments, *Biophys. J.*, **59**, 838–848 (1991).
- Parker, J. L., Surface force measurements in surfactant systems, *Prog. Surf. Sci.*, **47**, 205–271 (1994).
- Horn, R. G., Clarke, D. R. and Clarkson, M. T., Direct measurement of surface forces between sapphire crystals in aqueous solutions, *J. Mater. Res.*, **3**, 413–416 (1988).
- Horn, R. G., Smith, D. T. and Haller, W., Surface forces and viscosity of water measured between silica sheets, *Chem. Phys. Lett.*, **162**, 404–408 (1989).
- Tonck, A., Georges, J. M. and Loubet, J. L., Measurements of intermolecular forces and the rheology of dodecane between alumina surfaces, *J. Colloid Interface Sci.*, **126**, 150–163 (1988).
- Pelletier, E., Montfort, J. P., Lapique, F., Loubet, J. L., Tonck, A. and Georges, J. M., Response of thin polymer layers confined between solid-surfaces and submitted to normal oscillatory deformations, *Nuovo Cimento Soc. Ital. Fis. D*, **16**, 789–793 (1994).
- Falsafi, A., Deprez, P., Bates, F. S. and Tirrell, M., Direct measurement of adhesion between viscoelastic polymers: A contact mechanical approach, *J. Rheol.*, **41**, 1349–1364 (1997).
- Luckham, P. F. and Costello, B. A. D. L., Recent developments in the measurement of interparticle forces, *Adv. Colloid Interface Sci.*, **44**, 183–239 (1993).
- Ducker, W. A., Senden, T. J. and Pashley, R. M., Direct measurement of colloidal forces using an atomic force microscope, *Nature (London)*, **353**, 239–241 (1991).
- Ducker, W. A., Senden, T. J. and Pashley, R. M., Measurements of forces in liquids using a force microscope, *Langmuir*, **8**, 1831–1836 (1992).
- Ducker, W. A., Forces between alumina surfaces in salt solutions: Non-DLVO forces and the implications for colloidal processing, *J. Am. Ceram. Soc.*, **77**, 437–443 (1994).
- Ducker, W. A., Xu, Z. G. and Israelachvili, J. N., Measurements Of hydrophobic and DLVO forces in bubble-surface interactions in aqueous solutions, *Langmuir*, **10**, 3279–3289 (1994).

30. Ducker, W. A. and Clarke, D. R., Controlled modification of silicon nitride interactions in water via zwitterionic surfactant adsorption, *Colloid Surf., A*, **93**, 275–292 (1994).
31. Rutland, M. W. and Senden, T. J., Adsorption of the poly(oxy ethylene) nonionic surfactant C12E5 to silica: a study using atomic force microscopy, *Langmuir*, **9**, 412–418 (1993).
32. Carambassis, A. and Rutland, M. W., Interactions between cellulose surfaces; effect of electrolyte, *Langmuir*, **19**, 5584–5590 (1999).
33. Carambassis, A., Jonker, L. C., Attard, P. and Rutland, M. W., Forces measured between hydrophobic surfaces due to a submicroscopic bridging bubble, *Phys. Rev. Lett.*, **80**, 5357–5360 (1998).
34. Veeramasuneni, S., Yalamanchili, M. R. and Miller, J. D., Measurement of interaction forces between silica and alpha-alumina by atomic force microscopy, *J. Colloid Interface Sci.*, **184**, 594–600 (1996).
35. Yoon, R. and Pazhianur, R., Direct force measurement between hydrophobic glass sphere and covellite electrode in potassium ethyl xanthate solutions at pH 9.2, *Colloid Surf., A*, **144**, 59–69 (1998).
36. Nalaskowski, J., Drelich, J., Hupka, J. and Miller, J. D., Preparation of hydrophobic microspheres from low-temperature melting polymeric materials, *J. Adhes. Sci. Technol.*, **13**, 1–17 (1999).
37. Arai, T., Aoki, D., Okabe, Y. and Fujihira, M., Analysis of surface forces on oxides in aqueous solutions using AFM, *Thin Solid Films*, **273**, 322–326 (1996).
38. Toikka, G., Hayes, R. A. and Ralston, J., Evidence of charge reversal from direct force measurements involving dissimilar metal sulfides in aqueous electrolyte, *J. Chem. Soc., Faraday Trans.*, **93**, 3523–3528 (1997).
39. Hartley, P. G., Larson, I. and Scales, P. J., Electrokinetic and direct force measurements between silica and mica surfaces in dilute electrolyte solutions, *Langmuir*, **13**, 2207–2214 (1997).
40. Hartley, P. G., Grieser, F., Mulvaney, P. and Stevens, G. W., Surface forces and deformation at the oil–water interface probed using AFM force measurement, *Langmuir*, **15**, 7282–7289 (1999).
41. Hook, M. S., Hartley, P. G. and Thistlethwaite, P. J., Fabrication and characterization of spherical zirconia particles for direct force measurement using the atomic force microscope, *Langmuir*, **15**, 6220–6225 (1999).
42. Power, D., Larson, I., Hartley, P., Dunstan, D. and Boger, D. V., Atomic force microscopy studies on hydroxypropylguar gels formed under shear, *Macromolecules*, **31**, 8744–8748 (1998).
43. Considine, R. F., Hayes, R. A. and Horn, R. G., Forces measured between latex spheres in aqueous electrolyte: Non-DLVO behavior and sensitivity to dissolved gas, *Langmuir*, **15**, 1657–1659 (1999).
44. Parker, J. L., Christenson, H. K. and Ninham, B. W., Device for measuring the force and separation between two surfaces down to molecular separations, *Rev. Sci. Instrum.*, **60**, 3135–3138 (1989).
45. Connor, J., Horn, R. and Miklavic, S., Measurement of surface forces acting between deformable surfaces, *Uzbek J. Phys.*, **1**, 99–112 (1999).
46. Peachey, J., van Alsten, J. and Granick, S., Design of an apparatus to measure the shear response of ultrathin liquid-films, *Rev. Sci. Instrum.*, **62**, 463–473 (1991).
47. Israelachvili, J. N. and Adams, G. E., Measurements of forces between two mica surfaces in aqueous electrolyte solutions in the range 0–100 nm., *J. Chem. Soc., Faraday Trans. 1*, **74**, 975–1001 (1978).
48. Klein, J., Forces between mica surfaces bearing adsorbed macromolecules in liquid media, *J. Chem. Soc., Faraday Trans. 1*, **79**, 99–118 (1983).
49. Israelachvili, J. N. and McGuiggan, P. M., Adhesion and short-range forces between surfaces I: New apparatus for surface force measurements, *J. Mater. Res.*, **5**, 2223–2231 (1990).
50. Blomberg, E., Claesson, P. M. and Wårnheim, T., Surface interactions in emulsions and liposome solutions, *Colloid Surf., A*, **159**, 149–157 (1999).
51. Pelletier, E., Montfort, J. P., Loubet, J. L., Tonck, A. and Georges, J. M., Relaxation experiments of polymeric systems confined in very narrow gaps, *J. Polym. Sci., Polym. Phys. Edn.*, **34**, 93–102 (1996).
52. Attard, P., Schulz, J. C. and Rutland, M. W., dynamic surface force measurement – I – van-der-Waals collisions, *Rev. Sci. Instrum.*, **69**, 3852–3866 (1998).
53. Claesson, P. M., Ederth, T., Bergeron, V. and Rutland, M. W., Techniques for measuring surface forces, *Adv. Colloid Interface Sci.*, **67**, 119–183 (1996).
54. Sader, J. E., Larson, I., Mulvaney, P. and White, L. R., Method for the calibration of atomic-force microscope cantilevers, *Rev. Sci. Instrum.*, **66**, 3789–3798 (1995).
55. Neumeister, J. M. and Ducker, W. A., Lateral, normal, and longitudinal spring constants of atomic force microscopy cantilevers, *Rev. Sci. Instrum.*, **65**, 2527–2531 (1994).
56. Senden, T. J. and Ducker, W. A., Experimental determination of spring constants in atomic force microscopy, *Langmuir*, **10**, 1003–1004 (1994).
57. Chan, D. Y. C. and Horn, R. G., The drainage of thin liquid films between solid surfaces, *J. Chem. Phys.*, **83**, 5311–5324 (1985).
58. Derjaguin, B., Untersuchungen über die Reibung und Adhäsion, *Kolloid. Z.*, **69**, 155–164 (1934).
59. Israelachvili, J. N., *Intermolecular and Surface Forces*, Academic Press, London, 1991.
60. Tabor, D. and Winterton, R. H. S., The direct measurement of normal and retarded van der Waals forces, *Proc. R. Soc. London, A*, **312**, 435–450 (1969).
61. Maugis, D. and Gauthier-Manuel, B., JKR–DMT transition in the presence of a liquid meniscus, *J. Adhes. Sci. Technol.*, **8**, 1311–1322 (1994).
62. Horn, R. G., Israelachvili, J. N. and Pribac, F., Measurement of the deformation and adhesion of solids in contact, *J. Colloid Interface Sci.*, **115**, 480–482 (1987).

63. Johnson, K. L., Kendall, K. and Roberts, A. D., Surface energy and the contact of elastic solids, *Proc. R. Soc. London, A*, **324**, 301–313 (1971).
64. Hertz, H., Über die berührung fester elastischer Körper, *J. Reine Angew. Math.*, **92**, 156–171 (1881).
65. Schillén, K., Claesson, P. M., Malmsten, M., Linse, P. and Booth, C., Properties of poly(ethylene oxide)–poly(butylene oxide) diblock copolymers at the interface between hydrophobic surfaces and water, *J. Phys. Chem.*, **101**, 4238–4252 (1997).
66. Israelachvili, J., Measurements of the viscosity of thin fluids films between two surfaces with and without adsorbed polymers, *Colloid Polym. Sci.*, **246**, 1060–1065 (1986).
67. Klein, J., Kamiyama, Y., Yoshizawa, H., Israelachvili, J. N., Fredrickson, G. H., Pincus, P. and Fetters, L. J., Lubrication forces between surfaces bearing polymer brushes, *Macromolecules*, **26**, 5552–5560 (1993).
68. Dhinojwala, A. and Granick, S., Surface forces in the tapping mode: Solvent permeability and hydrodynamic thickness of adsorbed polymer brushes, *Macromolecules*, **30**, 1079–1085 (1997).
69. Georges, J. M., Tonck, A., Loubet, J. L., Mazuyer, D., Georges, E. and Sidoroff, F., Rheology and friction of compressed polymer layers adsorbed on solid surfaces, *J. Phys. (France) II*, **6**, 57–76 (1996).
70. Van Alsten, J. and Granick, S., Shear rheology in a confined geometry: polysiloxane melts, *Macromolecules*, **23**, 4856–4862 (1990).
71. Luengo, G., Schmitt, F., Hill, R. and Israelachvili, J. N., Thin film rheology and tribology of confined polymer melts – contrasts with bulk properties, *Macromolecules*, **30**, 2482–2494 (1997).
72. Homola, A., Israelachvili, J. N., Gee, M. L. and McGuigan, P. M., Measurement of and relation between the adhesion and friction of two surfaces separated by molecularly thin liquid films, *J. Tribol.*, **111**, 675–682 (1989).
73. Yoshizawa, H. and Israelachvili, J. N., Fundamental mechanism of interfacial friction 2. stick–slip friction of spherical and chain molecules, *J. Phys. Chem.*, **97**, 11300–11313 (1993).
74. Klein, J., Kumacheva, E., Perahia, D., Mahalu, D. and Warburg, S., Interfacial sliding of polymer-bearing surfaces, *Faraday Discuss. Chem. Soc.*, **98**, 173–188 (1994).
75. Mate, C. M., McClelland, G. M., Erlandsson, R. and Chiang, S., Atomic-scale friction of a tungsten tip on a graphite surface, *Phys. Rev. Lett.*, **59**, 1942–1945 (1987).
76. Luckham, P. F. and Manimaaran, S., Investigating adsorbed polymer layer behaviour using dynamic surface force apparatuses – a review, *Adv. Colloid Interface Sci.*, **73**, 1–46 (1997).
77. Derjaguin, B. V., Muller, V. M. and Toporov, Y. P., Effect of contact deformations on the adhesion of particles, *J. Colloid Interface Sci.*, **53**, 314–326 (1975).
78. Rundlöf, M., Wågberg, L., Poptoshev, E., Rutland, M. and Claesson, P., Application of the JKR method to the measurement of adhesion to cellulose, *J. Colloid Interface Sci.*, **230** (2), 441–447 (2000).
79. Maugis, D., Adhesion of spheres: the JKR–DMT transition using a Dugdale model, *J. Colloid Interface Sci.*, **150**, 243–269 (1992).
80. Muller, V. M., Yushenko, V. S. and Derjaguin, B. V., On the influence of molecular forces on the deformation of an elastic sphere and its sticking to a rigid plane, *J. Colloid Interface Sci.*, **77**, 91–101 (1980).
81. Attard, P. and Parker, J. L., Deformation and adhesion of elastic bodies in contact, *Phys. Rev. A*, **46**, 7959–7971 (1992).
82. Fisher, L. R. and Israelachvili, J. N., Experimental studies on the applicability of the Kelvin equation to highly curved concave menisci, *J. Colloid Interface Sci.*, **80**, 528–541 (1981).
83. Christenson, H. K. and Yaminsky, V. V., Adhesion and solvation forces between surfaces in liquids studied by vapor-phase experiments, *Langmuir*, **9**, 2448–2454 (1993).
84. Curry, J. E. and Christenson, H. K., Adsorption, wetting, and capillary condensation of nonpolar fluids in mica slits, *Langmuir*, **12**, 5729–5735 (1996).
85. Petrov, P., Olsson, U., Christenson, H. K., Miklavic, S. and Wennerström, H., Forces between macroscopic surfaces in a sponge phase, *Langmuir*, **10**, 988–990 (1994).
86. Antelmi, D. A., Kekicheff, P. and Richetti, P., Measurement of the interactions between macroscopic surfaces inducing a 1st-order phase-transition – the sponge lamellar transformation, *J. Phys. (France), II*, **5**, 103–112 (1995).
87. Attard, P., Bridging bubbles between hydrophobic surfaces, *Langmuir*, **12**, 1693–1695 (1996).
88. Fogden, A. and White, L. R., Contact elasticity in the presence of capillary condensation. The nonadhesive Hertz problem, *JCIS*, **138**, 414–430 (1990).
89. Bogdanovic, G., Meurk, A. and Rutland, M., Tip friction – artefact and torsional spring constant determination, *Colloid Surf. B*, **19**, 397–405 (2000).
90. Ruths, M., Steinberg, S. and Israelachvili, J. N., Effects of confinement and shear on the properties of thin films of thermotropic liquid crystals, *Langmuir*, **12**, 6637–6650 (1996).
91. Yamada, S. and Israelachvili, J. N., Friction and adhesion hysteresis of fluorocarbon surfactant monolayer-coated surfaces measured with the surface forces apparatus, *J. Phys. Chem., B*, **102**, 234–244 (1998).
92. Yoshizawa, H., Chen, Y. L. and Israelachvili, J., Recent advances in molecular-level understanding of adhesion, friction and lubrication, *Wear*, **168**, 161–166 (1993).
93. Israelachvili, J. and Berman, A., Irreversibility, energy-dissipation, and time effects in intermolecular and surface interactions, *Isr. J. Chem.*, **35**, 85–91 (1995).
94. Schmitt, F. J., Yoshizawa, H., Schmidt, A., Duda, G., Knoll, W., Wegner, G. and Israelachvili, J., Adhesion energy hysteresis and friction between ultrathin polyglutamate films measured with the surface forces apparatus, *Macromolecules*, **28**, 3401–3410 (1995).
95. Tomlinson, G. A., A molecular theory of friction, *Phil. Mag.*, **7**, 905–939 (1929).

96. Berman, A. D., Ducker, W. A. and Israelachvili, J. N., Origin and characterization of different stick-slip friction mechanisms, *Langmuir*, **12**, 4559–4563 (1996).
97. Israelachvili, J., in *Handbook of Micro/Nanotribology*, Bhushan, B. (Ed.), CRC Press, Boca Raton, FL (1995), 267–319.
98. Bogdanovic, G., Tiberg, F. and Rutland, M. W., Sliding friction between cellulose and silica surfaces, *Tribol. Lett.*, **Submitted** (2000).
99. Carpick, R., Ogletree, D. and Salmeron, M., A general equation for fitting contact area and friction vs. load measurements, *J. Colloid Interface Sci.*, **211**, 395–400 (1998).
100. Meurk, A., Luckham, P. and Bergström, L., Direct measurement of repulsive and attractive van der Waals forces between inorganic materials, *Langmuir*, **13**, 3896–3899 (1997).
101. Lifshitz, E. M., The theory of molecular attractive forces between solids, *J. Exper. Theor. Phys. USSR*, **29**, 94–110 (1955).
102. Lifshitz, E. M., The theory of molecular attractive forces between solids, *Sov. Phys. JETP*, **2**, 73–83 (1956).
103. Hamaker, H. C., The London–van der Waals attraction between spherical particles, *Physica*, **4**, 1058–1072 (1937).
104. Holmberg, M., Berg, J., Stemme, S., Ödberg, L., Rasmussen, J. and Claesson, P. M., Surface force studies of Langmuir–Blodgett cellulose films, *J. Colloid Interface Sci.*, **186**, 369–381 (1997).
105. Poptoshev, E., Rutland, M. and Claesson, P. M., Surface forces in aqueous poly(vinyl amine) solutions. 2. Interactions between glass and cellulose, *Langmuir*, **16**, 1987–1992 (2000).
106. Evans, D. F. and Wennerström, H. *The Colloidal Domain*, 2nd Edn, VCH, New York, 1998.
107. Parsegian, V. A. and Gingell, D., On the electrostatic interaction across a salt solution between two bodies bearing unequal charges, *Biophys. J.*, **12**, 1192–1204 (1972).
108. Derjaguin, B. V., A theory of the heterocoagulation, interaction and adhesion of dissimilar particles in solutions of electrolytes, *Discuss Faraday Soc.*, **18**, 85–98 (1954).
109. Bell, G. M. and Peterson, G. C., Calculation of the electric double-layer force between unlike spheres, *J. Colloid Interface Sci.*, **41**, 542–566 (1972).
110. Devereux, O. F. and de Bruyn, P. L., *Interaction of Plane-Parallel Double Layers*, The MIT Press, Cambridge, MA, 1963.
111. Chan, D., Healy, T. W. and White, L. R., Electrical double-layer interactions under regulation by surface ionization equilibrium – dissimilar amphoteric surfaces, *J. Chem. Soc., Faraday Trans. 1*, **72**, 2844–2865 (1976).
112. Claesson, P. M., Experimental evidence for repulsive and attractive forces not accounted for by conventional DLVO theory, *Prog. Colloid Polym. Sci.*, **74**, 48–54 (1987).
113. Pashley, R. M., DLVO and hydration forces between mica surfaces in Li⁺, Na⁺, K⁺ and Cs⁺ electrolyte solutions: A correlation of double-layer and hydration forces with surface cation exchange properties, *J. Colloid Interface Sci.*, **83**, 531–546 (1981).
114. Pashley, R. M., Hydration forces between mica surfaces in aqueous electrolyte solutions, *J. Colloid Interface Sci.*, **80**, 153–162 (1981).
115. Vigil, G., Xu, Z., Steinberg, S. and Israelachvili, J., Interactions of silica surfaces, *J. Colloid Interface Sci.*, **165**, 367–385 (1994).
116. Claesson, P. M., Parker, J. L. and Fröberg, J., New surfaces and techniques for studies of interparticle forces, *J. Disp. Sci. Technol.*, **15**, 375–397 (1994).
117. Israelachvili, J. N. and Wennerström, H., Entropic forces between amphiphilic surfaces in Liquids, *J. Phys. Chem.*, **96**, 520–531 (1992).
118. Kjellander, R., Ion–ion correlations and effective charges in electrolyte and macroion systems, *Ber. Bunsenges. Phys. Chem.*, **100**, 894–904 (1996).
119. Kjellander, R., Åkesson, T., Jönsson, B. and Marcelja, S., Double-layer interactions in mono- and divalent electrolytes: A comparison of the anisotropic hypernetted chain theory and Monte Carlo simulations, *J. Chem. Phys.*, **97**, 1424–1431 (1992).
120. Attard, P., Mitchell, J. and Ninham, B. W., Beyond Poisson-Boltzmann: images and correlations in the electric double layer. II Symmetric electrolyte, *J. Chem. Phys.*, **89**, 4358–4367 (1988).
121. Kjellander, R., Marcelja, S., Pashley, R. M. and Quirk, J. P., A theoretical and experimental study of forces between charged mica surfaces in aqueous CaCl₂ solutions, *J. Chem. Phys.*, **92**, 4399–4407 (1990).
122. Claesson, P. M., Horn, R. G. and Pashley, R. M., Measurements of surface forces between mica sheets immersed in aqueous quaternary ammonium ion solutions, *J. Colloid Interface Sci.*, **100**, 250–263 (1984).
123. Christenson, H. K. and Claesson, P. M., Direct measurements of the force between hydrophobic surfaces in water, *Adv. Colloid Interface Sci.*, **91**, 391–436 (2001).
124. Parker, J. L., Claesson, P. M., Wang, J.-H. and Yasuda, H. K., Surface forces between plasma polymer films, *Langmuir*, **10**, 2766–2773 (1994).
125. Claesson, P. M. and Christensson, H. K., Very long range attractive forces between uncharged hydrocarbon and fluorocarbon surfaces in water, *J. Phys. Chem.*, **92**, 1650–1655 (1988).
126. Parker, J. L., Claesson, P. M. and Attard, P., Bubbles, cavities, and the long-ranged attraction between hydrophobic surfaces, *J. Phys. Chem.*, **98**, 8468–8480 (1994).
127. Ederth, T., Claesson, P. and Liedberg, B., Self-assembled monolayers of alkanethiolates on thin gold films as substrates for surface force measurements. Long-range hydrophobic interactions and electrostatic double-layer interactions, *Langmuir*, **14**, 4782–4789 (1998).
128. Wood, J. and Sharma, R., How long is the long-range hydrophobic attraction?, *Langmuir*, **11**, 4797–4802 (1995).
129. Ederth, T., in *Novel surfaces for force measurements, PhD thesis* (Royal Institute of Technology, Stockholm), (1999).

130. Hato, M., Attractive forces between surfaces of controlled "hydrophobicity" across water: a possible range of "hydrophobic interactions" between macroscopic hydrophobic surfaces across water, *J. Phys. Chem.*, **100**, 18530–18538 (1996).
131. Parsegian, V. A., Rand, R. P. and Fuller, N. L., Direct osmotic stress measurements of hydration and electrostatic double-layer forces between bilayers of double-chained ammonium acetate surfactants, *J. Phys. Chem.*, **95**, 4777–4782 (1991).
132. Parsegian, V. A. and Rand, R. P., On molecular protrusion as the source of hydration forces, *Langmuir*, **7**, 1299–1301 (1991).
133. Israelachvili, J. N. and Wennerström, H., Hydration or steric forces between amphiphilic Surfaces, *Langmuir*, **6**, 873–876 (1990).
134. Israelachvili, J. and Wennerström, H., Role of hydration and water structure in biological and colloidal interactions, *Nature (London)*, **379**, 219–224 (1996).
135. Manne, S. and Gaub, H. E., Molecular organisation of surfactants at solid–liquid interfaces, *Science*, **270**, 1480–1482 (1995).
136. Wanless, E. J., Davey, T. W. and Ducker, W. A., Surface aggregate phase transition, *Langmuir*, **13**, 4223–4228 (1997).
137. Lamont, R. E. and Ducker, W. A., Surface-induced transformations for surfactant aggregates, *J. Am. Chem. Soc.*, **120**, 7602–7607 (1998).
138. Wanless, E. J. and Ducker, W. A., Organization of sodium dodecyl sulfate at the graphite–solution interface, *J. Phys. Chem.*, **100**, 3207–3214 (1996).
139. Lamont, R. and Ducker, W., Organized structure of lithium perfluorooctanesulfonate at the graphite–solution interface, *J. Colloid Interface Sci.*, **191**, 303–311 (1997).
140. Ducker, W. A. and Wanless, E. J., Surface–aggregate shape transformation, *Langmuir*, **12**, 5915–5920 (1996).
141. Patrick, H., Warr, G., Manne, S. and Aksay, I., Self assembly structures of nonionic surfactants at graphite/solution interfaces, *Langmuir*, submitted August 6th, 1997.
142. Grant, L. M. and Ducker, W. A., Effect of substrate hydrophobicity on surface–aggregate geometry – zwitterionic and nonionic surfactants, *J. Phys. Chem., B*, **101**, 5337–5345 (1997).
143. Grant, L. M., Tiberg, F. and Ducker, W. A., Nanometer-scale organization of ethylene oxide surfactants on graphite, hydrophilic silica, and hydrophobic silica, *J. Phys. Chem., B*, **102**, 4288–4294 (1998).
144. Herder, P. C., Forces between hydrophobized mica surfaces immersed in dodecylammonium chloride solution, *J. Colloid Interface Sci.*, **134**, 336–345 (1990).
145. Claesson, P. M. and Kjellin, U. R. M., Studies of interactions between interfaces across surfactant solutions employing various surface force techniques, in *Modern Characterization Methods of Surfactant Systems*, Binks, B. P. (Ed.), Surfactant Science Series, Vol. **83**, Marcel Dekker, New York (1999), 255–333.
146. Waltermo, Å., Claesson, P. M. and Johansson, I., Alkyl glucosides on hydrophobic surfaces studied by surface force and wetting measurements, *J. Colloid Interface Sci.*, **183**, 506–514 (1996).
147. Waltermo, Å. in *Surface forces between surfactant-coated interfaces*, PhD thesis (Royal Institute of Technology, Stockholm), (1996).
148. Claesson, P. M., Kjellander, R., Stenius, P. and Christenson, H. K., Direct measurements of temperature-dependent interactions between non-ionic surfactant layers, *J. Chem. Soc., Faraday Trans. 1*, **82**, 2735–2746 (1986).
149. Claesson, P. M., Eriksson, J. C., Herder, C. E., Bergensstahl, B., Pezron, E., Pezron, I. and Stenius, P., Forces between non-ionic surfactant layers, *Faraday Discuss. Chem. Soc.*, **90**, 129–142 (1990).
150. Herder, C. E., Claesson, P. M. and Herder, P. C., Interaction between amine oxide surfactant layers adsorbed on mica, *J. Chem. Soc., Faraday Trans. 1*, **85**, 1933–1943 (1989).
151. Claesson, P. M., Herder, P. C., Rutland, M. W., Waltermo, Å. and Anheide, B., Amine functionalized surfactants: pH effects on adsorption and interaction, *Prog. Colloid Polym. Sci.*, **88**, 64–73 (1992).
152. Ericsson, B., Hegg, P.-O. and Mårtensson, K., Effect of cationic amphiphiles and temperature on lysozyme conformation, *J. Disp. Sci. Technol.*, **8**, 271 (1987).
153. Herder, P. C., The Royal Institute of Technology, Stockholm, (1988).
154. Parker, J. L. and Rutland, M. W., Time-dependent adhesion between glass surfaces in dilute surfactant solutions, *Langmuir*, **9**, 1965–1967 (1993).
155. Pashley, R. M. and Israelachvili, J. N., A comparison of surface forces and interfacial properties of mica in purified surfactant solutions, *Colloid Surf.*, **2**, 169–187 (1981).
156. Rutland, M. W. and Parker, J. L., Surface forces between silica surfaces in cationic surfactant solutions: adsorption and bilayer formation at normal and high pH, *Langmuir*, **10**, 1110–1121 (1994).
157. Pugh, R. J., Rutland, M. W., Manev, E. and Claesson, P. M., A fundamental study of mica flotation in dodecylamine collector, *Prog. Colloid Polym. Sci.*, **98**, 284–287 (1995).
158. Rutland, M. W. and Senden, T. J., amin/afm, In Preparation,
159. Rutland, M. W., Surface forces in calcium soap systems, Manuscript in Preparation,
160. Rutland, M., Waltermo, Å. and Claesson, P. M., pH-dependent interactions between mica surfaces in aqueous dodecylammonium/dodecylamine solutions, *Langmuir*, **8**, 176–183 (1992).
161. Rutland, M. and Pugh, R. J., Calcium soaps in flotation deinking – fundamental studies using surface force and coagulation techniques, *Colloid Surf., A*, **125**, 33–46 (1997).
162. Kekicheff, P. and Spalla, O., Long-range electrostatic attraction between similar, charge-neutral walls, *Phys. Rev. Lett.*, **75**, 1851–1854 (1995).

163. Attard, P., Long-range attraction between hydrophobic surfaces, *J. Phys. Chem.*, **93**, 6441–6444 (1989).
164. Tsao, Y., Yang, S. X., Evans, D. F. and Wennerström, H., Interactions between hydrophobic surfaces. Dependence of temperature and alkyl chain length, *Langmuir*, **7**, 3154–3159 (1991).
165. Abraham, C., in *School of Chemistry* (University of Sydney, Sydney), 1996.
166. Tiberg, F. and Ederth, T., Interfacial Properties of non-ionic surfactants and decane microemulsions at the silica water interface. An ellipsometry and surface force study, *J. Phys. Chem. B*, **104**, 9689–9695 (2000).
167. Giasson, S., Kuhl, T. L. and Israelachvili, J. N., Adsorption and interaction forces of micellar and microemulsion solutions in ultrathin films, *Langmuir*, **14**, 891–898 (1998).
168. Antelmi, D. A., Kekicheff, P. and Richetti, P., The confinement-induced sponge to lamellar phase transition, *Langmuir*, **15**, 7774–7788 (1999).
169. Kekicheff, P., Richetti, P. and Christenson, H. K., Structure and elastic properties of lamellar mesophases from direct force measurements, *Langmuir*, **7**, 1874–1879 (1991).
170. Parker, J. L., Richetti, P., Kekicheff, P. and Sarman, S., Direct measurement of structural forces in a supermolecular fluid, *Phys. Rev. Lett.*, **68**, 1955–1958 (1992).
171. Richetti, P. and Kekicheff, P., Direct measurement of depletion and structural forces in a micellar system, *Phys. Rev. Lett.*, **68**, 1951–1954 (1992).
172. Richetti, P., Kekicheff, P. and Barois, P., Measurement of the layer compressibility modulus of a lamellar mesophase with a surface forces apparatus, *J. Phys. (France), II*, **5**, 1129–1154 (1995).
173. Richetti, P., Moreau, L., Barois, P. and Kekicheff, P., Measurement of the interactions between two ordering surfaces under symmetric and asymmetric boundary conditions, *Phys. Rev. E*, **54**, 1749–1762 (1996).
174. Petrov, P., Miklavic, S., Olsson, U. and Wennerström, H., A confined complex liquid. Oscillatory forces and lamellae formation from an L3 phase, *Langmuir*, **11**, 3928–3936 (1995).
175. Petrov, P., Olsson, U. and Wennerström, H., Surface forces in bicontinuous microemulsions: water capillary condensation and lamellae formation, *Langmuir*, **13**, 3331–3337 (1997).
176. Butt, H. J., A technique for measuring the force between a colloidal particle in water and a bubble, *J. Colloid Interface Sci.*, **166**, 109–117 (1994).
177. Fielden, M. L., Hayes, R. A. and Ralston, J., Surface and capillary forces affecting air bubble–particle interactions in aqueous electrolyte, *Langmuir*, **12**, 3721–3727 (1996).
178. Horn, R. G., Bachmann, D. J., Connor, J. N. and Miklavic, S. J., The effect of surface and hydrodynamic forces on the shape of a fluid drop approaching a solid surface, *J. Phys., Condensed Matter*, **8**, 9483–9490 (1996).
179. Miklavic, S. J., Horn, R. G. and Bachmann, D. J., Colloidal interaction between a rigid solid and a fluid drop, *J. Phys. Chem.*, **99**, 16357–16364 (1995).
180. Fleer, G. J., Cohen Stuart, M. A., Scheutjens, J. M. H. M., Cosgrove, T. and Vincent, B., *Polymers at Interfaces*, Chapman & Hall, London, 1993.
181. de Gennes, P. G., Polymers at interfaces: A simplified view, *Adv. Colloid Interface Sci.*, **27**, 189–209 (1987).
182. Malmsten, M., Claesson, P. M., Pezron, E. and Pezron, I., Temperature-dependent forces between hydrophobic surfaces coated with ethyl(hydroxyethyl)cellulose, *Langmuir*, **6**, 1572–1578 (1990).
183. Blomberg, E. and Claesson, P. M., Interactions between poly(ethylene oxide) coated surfaces and between such surfaces and proteins, *J. Disp. Sci. Technol.*, **19**, 1107–1126 (1998).
184. Claesson, P. M., Blomberg, E., Fröberg, J. C., Nylander, T. and Arnebrant, T., Protein interactions at solid surfaces, *Adv. Colloid Interface Sci.*, **57**, 161–227 (1995).
185. Blomberg, E., Claesson, P. M., Fröberg, J. C. and Tilton, R. D., Interaction between adsorbed layers of lysozyme studied with the surface force technique, *Langmuir*, **10**, 2325–2334 (1994).
186. Fröberg, J. C., Arnebrant, T., McGuire, J. and Claesson, P. M., Effects of structural stability on the characteristics of adsorbed layers of T4 lysozyme, *Langmuir*, **14**, 456–462 (1997).
187. Fröberg, J. C., Blomberg, E. and Claesson, P. M., Desorption of lysozyme layers by sodium dodecyl sulfate studied with the surface force technique, *Langmuir*, **15**, 1410–1417 (1999).
188. Blomberg, E., Claesson, P. M. and Fröberg, J. C., Surfaces coated with protein layers: a surface force and ESCA study, *Biomaterials*, **19**, 371–386 (1998).
189. Blomberg, E., (in preparation).
190. Gölander, C. G., Herron, J. N., Lim, K., Claesson, P. M., Stenius, P. and Andrade, J. D., Properties of immobilized PEG films and the interaction with protein: experiments and modeling, in *Poly(Ethylene Glycol) Chemistry: Biotechnical and Biomedical Applications*, Harris, E. J. M. (Ed.), Plenum Press, New York, (1992), 221–245.
191. Luckham, P. F. and Klein, J., Forces between mica surfaces bearing adsorbed polyelectrolyte, poly-L-lysine, in aqueous media, *J. Chem. Soc., Faraday Trans. 1*, **80**, 865–878 (1984).
192. Afshar-Rad, T., Bailey, A. I., Luckham, P. F., MacNaughtan, W. and Chapman, D., Forces between poly-L-lysine of molecular weight range 4000–75 000 adsorbed on mica surfaces, *Colloid Surf.*, **25**, 263–277 (1987).
193. Dahlgren, M. A. G. in *How polyelectrolytes behave at solid surfaces, PhD thesis*. (Royal Institute of Technology, Stockholm), (1995).
194. Hartley, P. G. and Scales, P. J., Electrostatic properties of polyelectrolyte modified surfaces studied by direct force measurements, *Langmuir*, **14**, 6948–6955 (1998).
195. Dahlgren, M. A. G., Waltermo, Å., Blomberg, E., Claesson, P. M., Sjöström, L., Åkesson, T. and Jönsson, B., Salt effects on the interaction between adsorbed cationic polyelectrolyte layers – theory and experiment, *J. Phys. Chem.*, **97**, 11769–11775 (1993).

196. Dahlgren, M. A. G., Hollenberg, H. C. M. and Claesson, P. M., The order of adding polyelectrolyte and salt affects surface forces and layer structures, *Langmuir*, **11**, 4480–4485 (1995).
197. Claesson, P. M., Dahlgren, M. A. G. and Eriksson, L., Forces between polyelectrolyte coated surfaces: relation between surface interaction and floc properties, *Colloid Surf.*, **93**, 293–303 (1994).
198. Holmberg, M., Wigren, R., Erlandsson, R. and Claesson, P. M., Interactions between cellulose and colloidal silica in the presence of polyelectrolytes, *Colloid Surf., A*, **129–130**, 175–183 (1997).
199. Neuman, R., Berg, J. and Claesson, P. M., Direct measurements of surface forces in papermaking systems, *Nordic Pulp Paper Res. J.*, **8**, 96–104 (1993).
200. Shubin, V., Petrov, P. and Lindman, B., The effects of surfactants on adsorbed layers of a cationic polyelectrolyte, *Colloid Polym. Sci.*, **272**, 1590–1601 (1994).
201. Shubin, V., Adsorption of cationic polymer onto negatively charged surfaces in the presence of anionic surfactants, *Langmuir*, **10**, 1093–1100 (1994).
202. Furst, E. M., Pagac, E. S. and Tilton, R. D., Coadsorption of polylysine and the cationic surfactant cetyltrimethylammonium bromide on silica, *Ind. Eng. Chem. Res.*, **35**, 1566–1574 (1996).
203. Pagac, E. S., Prieve, D. C. and Tilton, R. D., Kinetics and mechanism of cationic surfactant adsorption and coadsorption with cationic polyelectrolyte at the silica–water interface, *Langmuir*, **14**, 2333–2342 (1998).
204. Neivandt, D. J., Gee, M. L., Tripp, C. P. and Hair, M. L., Coadsorption of polystyrenesulfonate and cetyltrimethylammonium bromide on silica investigated by attenuated total reflection techniques, *Langmuir*, **13**, 2519–2526 (1997).
205. Neivandt, D. J. in *Co-adsorption of polyelectrolytes and surfactants at the silica–solution interface: A spectroscopic study*, PhD thesis. (The University of Melbourne, Melbourne), (1998).
206. Creeth, A., Staples, E., Thompson, L., Tucker, I. and Penfold, J., Composition of mixed surfactant–polymer layers adsorbed at the air/water interface as determined by specular neutron reflectivity, *J. Chem. Soc., Faraday Trans.*, **92**, 589–594 (1996).
207. Ananthapadmanabhan, K. P., Mao, G.-Z., Goddard, E. D. and Tirrell, M., Surface force measurements on a cationic polymer in the presence of an anionic surfactant, *Colloid Surf.*, **61**, 167–174 (1991).
208. Shubin, V. and Linse, P., Effect of electrolytes on adsorption of cationic polyacrylamide on silica: ellipsometric study and theoretical modeling, *J. Phys. Chem.*, **99**, 1285–1291 (1995).
209. Shubin, V. and Linse, P., Self-consistent-field modeling of polyelectrolyte adsorption on charge-regulating surfaces, *Macromolecules*, **30**, 5944–5952 (1997).
210. Anthony, O., Marques, C. M. and Richetti, P., Bulk and surface behaviour of cationic guar in solutions of oppositely charged surfactants, *Langmuir*, **14**, 6086–6095 (1998).
211. Claesson, P. M., Dedinaite, A., Blomberg, E. and Sergeyev, V. G., Polyelectrolyte–surfactant association at solid surfaces, *Ber. Bunsenges. Phys. Chem.*, **100**, 1008–1013 (1996).
212. Claesson, P. M., Fielden, M., Dedinaite, A., Brown, W. and Fundin, J., Interactions of a 30% charged polyelectrolyte and an anionic surfactant in bulk and at a solid–liquid interface, *J. Phys. Chem., B*, **102**, 1270–1278 (1998).
213. Kjellin, U. R. M., Claesson, P. M. and Audebert, R., Interactions between adsorbed layers of a low charge density cationic polyelectrolyte on mica in the absence and presence of anionic surfactant, *J. Colloid Interface Sci.*, **190**, 476–484 (1997).
214. Fielden, M. L., Claesson, P. M. and Schillén, K., Investigation of a 31% charged cationic polyelectrolyte interacting with sodium dodecyl sulfate in bulk solution and as a preadsorbed layer on mica. Low ionic strength, *Langmuir*, **14**, 5366–5375 (1998).
215. Dedinaite, A. and Claesson, P. M., Interfacial properties of aggregates formed by cationic polyelectrolyte and anionic surfactant, *Langmuir*, **16**, 1951–1959 (2000).
216. Claesson, P. M., Dedinaite, A. and Poptoshev, E., Polyelectrolyte–surfactant interactions at solid–liquid interfaces studied with surface force techniques, in *Physical Chemistry of Polyelectrolytes*, Radeva, T. (Ed.), Surfactant Science Series, Vol. 99, Marcel Dekker, New York, (2001), 447–507.
217. Dedinaite, A. in *Surface force studies of association phenomena at solid-liquid interfaces*, PhD Thesis. (Royal Institute of Technology, Stockholm), (1999).
218. Christenson, H. K., Non-DLVO forces between surfaces – solvation, hydration and capillary effects, *J. Disp. Sci. Technol.*, **9**, 171–206 (1988).
219. Horn, R. G. and Israelachvili, J. N., Direct measurement of structural forces between two surfaces in a nonpolar liquid, *J. Chem. Phys.*, **75**, 1400–1411 (1981).
220. Christenson, H. K. and Blom, C. E., Solvation forces and phase separation of water in a thin film of nonpolar liquid between mica surfaces, *J. Chem. Phys.*, **86**, 419–424 (1987).
221. Christenson, H. K., Horn, R. G. and Israelachvili, J. N., Measurement of forces due to structure in hydrocarbon liquids, *J. Colloid Interface Sci.*, **88**, 79–88 (1982).
222. Christenson, H. K., Gruen, D. W. R., Horn, R. G. and Israelachvili, J. N., Structuring in liquid alkanes between solid surfaces: force measurements and mean-field theory, *J. Chem. Phys.*, **87**, 1834–1841 (1987).
223. Israelachvili, J. N., Kott, S. J., Gee, M. L. and Witten, T. A., Forces between mica surfaces across hydrocarbon liquids – effects of branching and polydispersity, *Macromolecules*, **22**, 4247–4253 (1989).
224. Christenson, H. K., Interactions between hydrocarbon surfaces in a non-polar liquid. Effect of surface properties on solvation forces, *J. Phys. Chem.*, **90**, 4–6 (1986).
225. Claesson, P. M., Dedinaite, A., Bergenståhl, B., Campbell, B. and Christenson, H. K., Interactions between

- hydrophilic mica surfaces in triolein: triolein surface orientation, solvation forces, and capillary condensation, *Langmuir*, **13**, 1682–1688 (1997).
226. Dedinaite, A., Claesson, P. M., Campbell, B. and Mays, H., Interactions between modified mica surfaces in triglyceride media, *Langmuir*, **14**, 5546–5554 (1998).
 227. Kékicheff, P. and Richetti, P., Effect of electrolyte on the depletion and structural forces in a micellar system, *Prog. Colloid Polym. Sci.*, **88**, 8–17 (1992).
 228. Asnacios, A., Espert, A., Colin, A. and Langevin, D., Structural forces in thin films made from polyelectrolyte solutions, *Phys. Rev. Lett.*, **78**, 4974–4977 (1997).
 229. Milling, A. J., Depletion and structuring of sodium polystyrenesulfonate at the silica–water interface, *J. Phys. Chem.*, **100**, 8986–8993 (1996).
 230. Bergeron, V., Langevin, D. and Asnacios, A., Thin-film forces in foam films containing anionic polyelectrolyte and charged surfactants, *Langmuir*, **12**, 1550–1556 (1996).
 231. Dedinaite, A., Claesson, P. M. and Bergström, M., Polyelectrolyte–surfactant layers: adsorption of preformed aggregates versus adsorption of surfactants to preadsorbed polyelectrolyte, *Langmuir*, **16**, 5257–5266 (2000).
 232. Plunkett, M., Rödner, S., Bergström, L. and Rutland, M., Interactions of surfaces bearing grafted polyhydroxystearate layers I: Static interactions., *J. Adh. Sci.* (submitted).
 233. Hadziioannou, G., Patel, S., Granick, S. and Tirrell, M., Forces between surfaces of block copolymers adsorbed on mica, *J. Am. Chem. Soc.*, **108**, 2869–2876 (1986).
 234. Pelletier, E., Montfort, J. P., Loubet, J. L., Tonck, A. and Georges, J. M., Dynamics of compressed polymer layers adsorbed on solid surfaces, *Macromolecules*, **28**, 1990–1998 (1995).
 235. Pelletier, E., Montfort, J. P. and Lapique, F., Surface force apparatus and its application to nanorheological studies, *J. Rheol.*, **38**, 1151–1168 (1994).
 236. Granick, S. and Hu, H. W., Nanorheology of confined polymer melts. 1. Linear shear response at strongly adsorbing surfaces, *Langmuir*, **10**, 3857–3866 (1994).
 237. Poptoshev, E., Rutland, M. and Claesson, P., Surface forces in aqueous polyvinylamine solutions I: glass surfaces, *Langmuir*, **15**, 7789–7794 (1999).

CHAPTER 21

Measuring the Forces and Stability of Thin-Liquid Films

Vance Bergeron

Ecole Normale Supérieure, Paris, France

1	Introduction	415	3.1	General approach	424
2	Measurements of Forces in Thin-Liquid Films	417	3.2	Electrostatic double-layer forces	424
2.1	Disjoining pressure isotherms	417	3.3	Dispersion forces	425
2.2	Thin-film balance	417	3.4	Steric (entropic forces)	426
2.2.1	Historical background	417	3.5	Supramolecular forces	427
2.2.2	General procedure	418	3.5.1	Micellar structural forces	427
2.2.3	Film thickness measurements	419	3.5.2	Bilayer and lamellar structural forces	428
2.2.4	Optical system	420	3.5.3	Structures and forces in polymer- and polymer/surfactant-containing films	429
2.2.5	Pressure measurement	421	3.6	Hydrophobic forces	430
2.2.6	Direct pressure measurement	421	4	Common Black Film Stability	431
2.2.7	Pressure via lamellae profiles	422	4.1	General description	431
2.2.8	Pressure system	422	4.2	Spatial fluctuations	431
2.2.9	Complications	423	4.3	Surfactant density fluctuations	432
3	Disjoining Pressure Components/Interpretation	424	5	References	433

1 INTRODUCTION

Historically, the measurement of forces between solid and fluid interfaces began at approximately the same time. However, with the advent of the Surface Force Apparatus (SFA) and Atomic Force Microscope (AFM) over the last few decades, studies concerning the direct measurement of interactions between solid interfaces have received more attention than those concentrated on fluid interfaces (i.e. thin-liquid films – films which have at least one fluid–fluid interface such as foam, emulsion

or solid/fluid/fluid films) (1, 2). As a consequence, many of the interpretations used to rationalize the stability and interactions within films confined by fluid interfaces has relied on analogies based upon findings with solid interfaces. Nonetheless, the field of thin-liquid films has been far from stagnant and many excellent books and monographs dedicated exclusively to this subject are available (3–5). These works include both hydrodynamic and thermodynamic descriptions of thin-liquid films with a good overview of the measurements and theories used to understand such systems. Here, we

focus on some of the most common techniques used to measure forces and stability in thin-liquid films, together with certain recent advances made in the force–structure relationships within these films. This is accompanied by a brief description of the theoretical models currently used to account for the force–stability relationships in these systems.

The practical importance of understanding thin-fluid films is easily realized when considering the fact that the stability of a foam or an emulsion relies on the stability of the individual films that separate the discontinuous phases which make up these dispersed systems. This point is illustrated in Figure 21.1 for a foam, where the inset depicts an individual thin-liquid film with adsorbed surfactant monolayers at each surface. It is important to note that these surfaces are not rigid and the surfactant monolayers can be extremely diffuse, unlike the case for most solid surfaces. Indeed, neutron reflectivity measurements from an individual air–water interface reveal a surfactant monolayer structure as represented schematically in Figure 21.2. The combination of these detailed structural studies at individual interfaces with corresponding measurements within thin-liquid films is now providing a much clearer picture of the similarities and differences between films confined by fluid and solid interfaces; such differences are essential for a full understanding of thin-film stability.

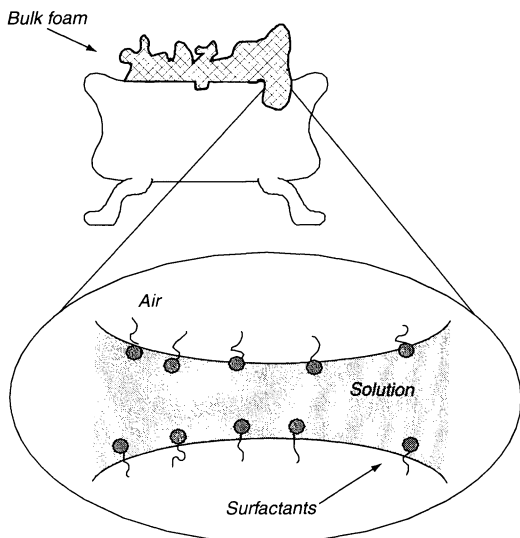


Figure 21.1. Foam is a dispersion of gas in a liquid solution which forms a collection of thin-liquid films. The stability of these films is governed by surface-active molecules (“surfactants”) which adsorb to the solution–air interface (from ref. (6)), with permission from Elsevier Science

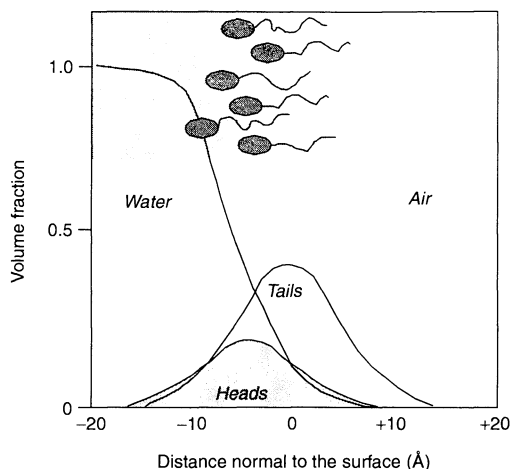


Figure 21.2. Schematic of the interfacial region for an adsorbed surfactant layer at the air/water interface

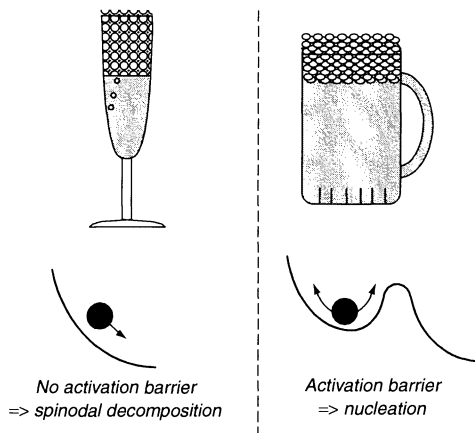


Figure 21.3. Typically, foams can be categorized as short-lived systems where film rupture is described as a spinodal decomposition (champagne foams), or long-lived systems in which energy barriers create an activation energy and film rupture is governed by a nucleation process (robust beer foams) (from ref. (7), reproduced with permission from IOP publishing limited)

It is also important to recognize that foams and emulsions are, in an absolute sense, thermodynamically unstable; however, it is often possible to classify a particular system as relatively short-lived “dynamically” stabilized (ca. minutes) or one that can remain stable for very long periods (ca. days or years). A champagne foam is a classic example of the former, while robust beer foams and cosmetic creams fall into the latter category (see Figure 21.3). As already mentioned, this remarkable difference in a dispersion’s lifetime is

a consequence of the primary mechanisms that govern the stability of the individual films separating the discontinuous phase. In rapidly coalescing dispersions, the film lifetimes are controlled by the drainage rate of the intervening continuous phase (i.e. dominated by hydrodynamic phenomena), while long-lived systems require additional time to overcome energy barriers that hold the film in a metastable thermodynamic state, thus preventing coalescence. These stabilizing barriers arise from surface-force interactions (i.e. disjoining pressures) created by having two interfaces in close proximity. In fact, for some cases overcoming these barriers can take so long that other factors such as Ostwald ripening and gas diffusion determine the ultimate lifetime of the dispersion. Hence, understanding and controlling the energy barriers that inhibit thin-film coalescence has great practical benefits for the utilization of these dispersed systems. To this end, the direct measurement of forces and structures that arise in surfactant-laden thin-liquid films is an essential element for the application of colloidal systems consisting of such films.

2 MEASUREMENT OF FORCES IN THIN-LIQUID-FILMS

2.1 Disjoining pressure isotherms

The *disjoining pressure* is a concept commonly used in the field of foams and emulsions (fluid systems) and is completely analogous to what is referred to as *surface forces* when considering interactions in thin films separated by two solid phases (e.g. solid dispersions). The primary difference is simply based on the historical origins of the different schools working on the subject and the actual parameters measured when conducting experimental investigations with these different systems. As the present work is focussed on fluid systems, we will adopt the former in order to be historically consistent.

Briefly, the interactions between two interfaces can be quantified as an excess pressure, Π , versus the separation distance (i.e. the film thickness, h), which at constant temperature is defined as a *disjoining pressure isotherm*. Note that the term “disjoining” is somewhat misleading in that attractive forces produce a *conjoining* force. Nevertheless, both repulsive and attractive forces are embodied in the disjoining-pressure concept. When formulated in terms of thermodynamic variables, the disjoining pressure becomes the work required to change the thickness of a film at constant temperature, T , overall pressure, P , area, A , and number of moles, N_i , which can be expressed by a change in the Gibbs free energy,

Table 21.1. Some of the common techniques used to measure the forces that occur between thin-liquid films. Further details for each technique can be found in ref. (6)

Technique	Type of thin-liquid film investigated
Thin-Film Balance (TFB)	Foam, emulsion and wetting
Emulsion Ferrofluid (EFF)	Emulsion
Centrifugal	Emulsion
Osmotic Stress	Emulsion
Micropipet	Emulsion
Light Scattering	Foam

G , of the film, as follows:

$$\Pi(h) = - \left(\frac{dG}{dh} \right)_{T,P,A,N_i} \quad (21.1)$$

Several techniques have been developed to quantify the disjoining pressure in thin-liquid films, and Table 21.1 provides a list of the most commonly used methods, together with the type of films that have been investigated using them. Among the methods listed in this Table 21.1, one of the biggest differences found is the range of pressures (forces) accessible with each technique. The Thin-Film Balance (TFB) and Emulsion Ferrofluid (EFF) techniques cover a pressure range that includes low to moderately high pressures (10^{-10} – 10^5 Pa), while the Centrifugal and Osmotic Stress techniques are useful in the moderate to high pressure range (10^4 – 10^8 Pa). It is also worth mentioning a version of the TFB that uses a miniaturized cell which is convenient for drainage observations of small-diameter films ($< 50 \mu\text{m}$ diameter) exposed to fairly moderate capillary pressures. Conversely, the Micropipet and Light Scattering methods are best suited for relatively low pressures (< 2000 Pa). In the pressure ranges for which these various techniques overlap, good correspondence between the different methods has been found when comparing the same or similar chemical systems.

2.2 Thin-film balance

2.2.1 Historical background

Due to the flexibility of fluid interfaces, the mechanical techniques used in the surface-force instruments cannot generally be applied. Instead, the forces in a thin-liquid film can be balanced by an applied capillary pressure, which is at the origin of the technique referred to as the “Thin-Film Balance” (TFB). The general concept was first realized by Derjaguin and Obuchov when they

trapped air bubbles underneath a glass slide which had been horizontally submerged in an aqueous solution. Buoyancy forces from the bubble created a pressure drop, which then drained the fluid from between the bubble and solid interface. Eventually, drainage stopped when the surface forces within the film balanced the forces due to buoyancy, thus leaving a thin-liquid film, which prevented the air from contacting the solid. Since these surface forces kept the air from joining the solid surface, Derjaguin coined the name “disjoining pressure”, Π .

Following Derjaguin and Obuchov's initial experiments, various types of apparatus were constructed to directly manipulate the capillary pressure imposed on an individual thin-liquid film; however, the design which emerged as the simplest was pioneered by Scheludko and Exerowa. The so-called “Scheludko cell”, illustrated in Figure 21.4(a), is simply a capillary tube (2–4 mm diameter) with a small hole drilled in the side so that liquid can be withdrawn to adjust the capillary pressure applied on the film. This cell is still widely used to measure film thinning and dynamics. However, due to the limited range of applied capillary pressures, the Scheludko cell has only been operated in a dynamic mode, to study film thinning phenomena and to deduce disjoining pressure relationships via film-drainage observations. In 1966, Mysels and Jones eliminated the low-capillary-pressure restriction of the Scheludko cell by introducing a porous porcelain disc with a circular hole, instead of a capillary tube, (Figure 21.4(b)). With this device, they measured equilibrium foam–film disjoining pressure isotherms, at pressures greater than 100 kPa. Shortly after this, Exerowa and Scheludko extended Mysels' original porous-plate design by welding a porous glass filter to the end of a capillary tube. These film holders have the advantage of not requiring glue, which can potentially contaminate the solution, and their shape can

be easily tailored to impose small capillary pressures or induce specific film profiles required for delicate low-pressure measurements. Disjoining pressure isotherms for asymmetric air/solution/oil (i.e. pseudo-emulsion) films have also been measured by using the porous-frit holders.

Conceptually, the disjoining pressure measurement between asymmetric solid/fluid/fluid interfaces is identical to that with two fluid interfaces, and can be realized by attaching a solid to the bottom or top of the holders pictured in Figure 21.4 or by simply sandwiching bubbles (drops) against a solid as they exit a capillary tube. Drop/bubble sandwiching techniques date back to the early work of Derjaguin and have been used extensively throughout the years to study the drainage of thin-liquid films against a solid substrate. Modern variations of the technique have been used to measure disjoining pressure isotherms between solids and air (or oil) separated by aqueous thin-liquid films.

At this point, we will distinguish the techniques mentioned thus far, from those used for molecularly thin films on solids. Isotherms in this regime generally fall under the classification of adsorption isotherms and the measurement techniques are quite different from those described here. For a review of these techniques, we refer the interested reader to the text by Adamson (8).

2.2.2 General procedure

To measure equilibrium disjoining pressure isotherms, single films are formed in a hole drilled through a porous glass disc, which has been fused to the end of a capillary tube and saturated with the surfactant solution under investigation. The film holder is enclosed in a hermetically sealed chamber with the free end of the capillary tube exposed to a constant reference pressure.

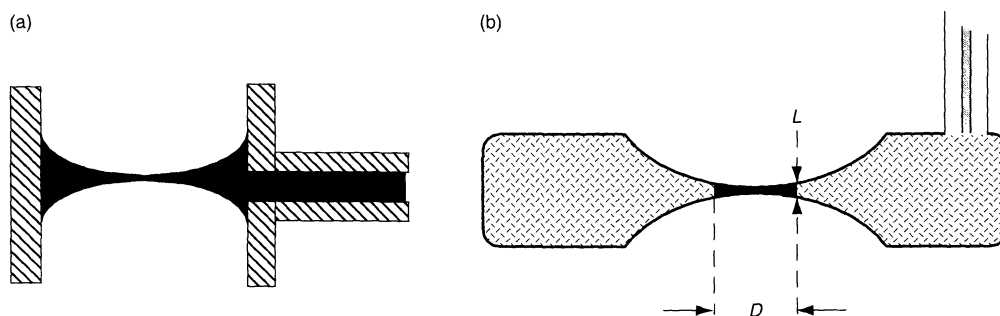


Figure 21.4. Cross-sectional view of typical film-holders used in the thin-film balance: (a) Scheludko cell; (b) porous disc holder (from ref. (11))

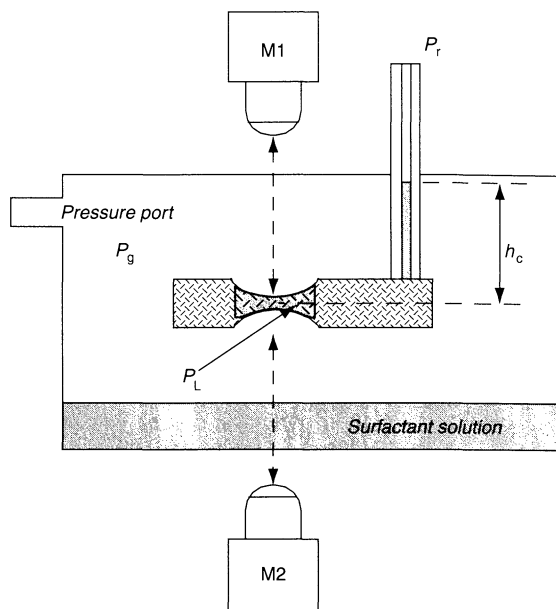


Figure 21.5. Schematic of the pressure cell and film holder for a typical thin-film balance. The film can be optically interrogated from above and/or below (from ref. (11))

Excess solution is also placed in the cell to provide an equilibrated environment. A schematic of the pressure cell and film holder used for this approach is shown in Figure 21.5. Often, the cell is thermostated and mounted on a vibration-isolation system to control temperature and minimize mechanical disturbances. Manipulation of the cell pressure alters the imposed capillary pressure, P_c ($P_c = P_g - P_L$; g , gas and L , liquid) and sets the disjoining pressure in the film (see below). The film can be optically interrogated from above or below (e.g. by reflected-light video microscopes, M1 and M2 in Figure 21.5) and film thicknesses deduced via thin-film interferometry. Standard ellipsometric methods, and X-ray (or neutron) reflectivity can also be used to determine the film thickness. Once the film thickness is determined, the pressure in the cell is changed, and the film is then given time to re-establish a local equilibrium at a new thickness. Repeating this procedure by gradually increasing and decreasing the gas pressure provides the necessary data to map out the entire repulsive part of the disjoining pressure isotherm.

2.2.3 Film thickness measurements

Most commonly, film thickness measurements are obtained using reflected-light thin-film interferometry.

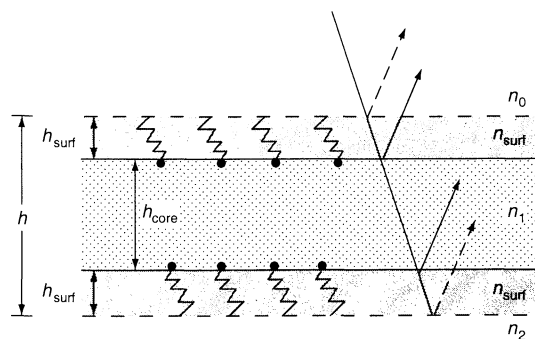


Figure 21.6. Schematic of a three-layer model of a thin-liquid surfactant-laden film (from ref. (11))

The principle underlying this measurement is schematically represented in Figure 21.6. Light waves, reflected from the top surface of the film, interfere with refracted waves that reflect off the bottom surface of the film. Optical path differences between the interfering waves generate a phase difference which can be used to extract the film thickness. This process is well understood and details can be found in various textbooks dedicated to the subject, for example, ref. (9).

For normally incident light on a homogeneous, non-absorbing film, the reflectivity is given by the following:

$$\frac{I^r}{I_0} = \frac{r_1^2 + r_2^2 + 2r_1 \cos(\alpha)}{1 + r_1^2 r_2^2 + 2r_1 r_2 \cos(\alpha)} \quad (21.2)$$

where:

$$r_1 = \frac{n_1 - n_0}{n_1 + n_0} \text{ and } r_2 = \frac{n_2 - n_1}{n_2 + n_1}$$

are the Fresnel equations for zero angle of incidence, and n_i is the refractive index of phase i with $i = (0, 1, 2)$ corresponding to the incident, film, and transmitting medium respectively; α is the phase angle, I^r is the intensity of the reflected light, and I_0 is the incident light intensity. The phase angle is given by the following:

$$\alpha = \frac{2\pi}{\lambda} 2n_1 h \cos(\gamma)$$

where h is the film thickness, λ is the wavelength of light, and γ is the angle of incidence, which is zero in most cases.

Various experimental techniques can be used to exploit equation (21.2) and determine the film thickness. However, the one most commonly implemented in thin-liquid film work, i.e. the microinterferometric technique, is due to Scheludko. In order to obtain film thicknesses with the standard interference equations, a measurement

of both the reflected and incident light intensity focused on the film are needed. The light reflected normal to the film is easily collected and measured with a sufficiently sensitive photometering device (e.g. photomultiplier, photodiode, etc.). However, we can avoid directly measuring the incident intensity by employing the ratio technique developed by Scheludko. This method scales I^r by the interference maximum, I_{\max}^r , and minimum, I_{\min}^r , values of the reflected intensity that occur at integer multiples of the film thickness, $h = \lambda/4$. In essence, the film at known thicknesses is used to calibrate the instrument. This is experimentally accomplished by successively thinning the film, via changes in the capillary pressure, and recording the I_{\max} and I_{\min} values. Application of the technique also requires expressions for the maximum and minimum reflected intensities at $h = \lambda/4$, which subsequently depend on phase changes that occur upon reflection of the light, and hence changes in refractive indices. These expressions are summarized in Table 21.2. For symmetric films, (i.e. foam and emulsion films) $r_1 = -r_2$ (i.e. $n_0 = n_2$ in Figure 21.6), and combination of the appropriate expressions in Table 21.2 with equation (21.2) yields the following:

$$h_w = \left(\frac{\lambda}{2\pi n} \right) \arcsin \left\{ \frac{\Delta}{1 + [4R/(1-R)^2]^{(1-\Delta)}} \right\}^{\frac{1}{2}}$$

where:

$$\Delta = \frac{I^r - I_{\min}}{I_{\max} - I_{\min}} \text{ and } R = \left(\frac{n_1 - n_0}{n_1 + n_0} \right)^2$$

As a first-order approximation, the film is assumed to be homogeneous with a refractive index equal to 1.33 (i.e. water), and h_w represents the equivalent water thickness. In order to account for surfactant layers adsorbed at the interface, h_w is typically corrected with the three-layer model developed by Duyvis (10), (see Figure 21.6), as follows:

$$h = h_w - 2 \left(\frac{n_{\text{surf}}^2 - n_1^2}{n_1^2 - n_0^2} \right) h_{\text{surf}}$$

where h is the total film thickness, n_{surf} is the refractive index of the hydrocarbon surfactant layer, h_{surf} is the thickness of one of the hydrocarbon surface layers, n_1 is the refractive index of the aqueous core, and n_0 is the refractive index of the incident medium. The actual aqueous core thickness is found from $h_{\text{core}} = h - 2h_{\text{surf}}$. Values for n_{surf} and h_{surf} depend on the adsorption density of the surfactant molecules at the film interface. Thus, assumptions concerning the values of n_{surf} and h_{surf} give rise to a small uncertainty in the thickness values. However, this is typically not a serious problem, particularly when working with relatively thick films (> 10 nm). One common approximation is to use the refractive index of an oil having equivalent chemical structure to the surfactant tails for a value of n_{surf} , and estimating $h_{\text{surf}} = \Gamma v$, where Γ is the surfactant adsorption density and v is the partial molar volume of the oil chosen to mimic the surfactant tails.

The working optical equation for asymmetric films (i.e. $n_0 \neq n_2$) is a generalization of equation (21.2). As an example, again for non-absorbing films, by combining the appropriate I_{\max}^r/I_0 and I_{\min}^r/I_0 expressions from Table 21.2 (i.e. $n_0 < n_1 < n_2$) with equation (21.2) we obtain the following:

$$h_w = \left(\frac{\lambda}{4\pi n} \right) \arccos \left[\frac{1}{2r_1 r_2} \Theta - (1 + r_1^2 r_2^2) \right] \quad (21.3)$$

where:

$$\Theta = \left\{ \frac{(1 - r_1^2)(1 - r_2^2)}{1 - \Delta \left[\left(\frac{r_1 + r_2}{1 + r_1 r_2} \right)^2 - \left(\frac{r_1 - r_2}{1 - r_1 r_2} \right)^2 \right] - \left(\frac{r_1 - r_2}{1 - r_1 r_2} \right)^2} \right\}$$

Equation (21.3) reduces to the optical model used for foam films by replacing Δ with $1 - \Delta$ to account for differences in optical phase shifts upon reflection, and by setting $r_1 = -r_2$. As with the symmetric case, Duyvis' optical corrections for the adsorbed surfactant layers can be applied to extract specific distances within the film.

Table 21.2. I_{\max}^r/I_0 and I_{\min}^r/I_0 expressions for various combinations of refractive indices

Ratio	(1) $n_0 < n_1 < n_2$ or (2) $n_0 > n_1 > n_2$	(3) $n_0 < n_1 > n_2$ or (4) $n_0 > n_1 < n_2$
I_{\max}^r/I_0	$\left(\frac{r_1 + r_2}{1 + r_1 r_2} \right)^2$	$\left(\frac{r_1 - r_2}{1 - r_1 r_2} \right)^2$
I_{\min}^r/I_0	$\left(\frac{r_1 - r_2}{1 - r_1 r_2} \right)^2$	$\left(\frac{r_1 + r_2}{1 + r_1 r_2} \right)^2$

2.2.4 Optical system

A typical optical system consists of a specially equipped reflected-light microscope supplied with a heat-filtered light source (e.g. 200 W Xe-Hg arc lamp). After reflection from the film at normal incidence, the light passes through a beam-splitter where it is transmitted to both a video camera and fibre-optic probes located in the microscope oculars. Video monitoring is crucial for understanding film dynamics and validating geometric

assumptions used for film-thinning, pressure measurements and optical modelling. Moreover, using a white-light source for the incident illumination provides more information, as the reflected beam can then be analysed at multiple wavelengths simultaneously (e.g. both the thickness and refractive index can be determined when monitoring multiple wavelengths). Hence, after collecting the reflected light, it is filtered for a specific wavelength and the intensity is recorded with a sensitive photometer.

2.2.5 Pressure measurement

At equilibrium and in the flat portion of a thin-liquid film, the disjoining pressure, Π , equals the capillary pressure, P_c . Therefore, measurements of the capillary pressure are used to evaluate Π . Two methods can be utilized to determine P_c , i.e. direct pressure measurements and lamella-profile measurements. In the latter case, the mean curvature of the meniscus is obtained and P_c is determined by using Laplace's equation.

2.2.6 Direct pressure measurement

With reference to the pressure-cell schematic shown in Figure 21.5, we outline the pressure balance needed to measure Π directly, given by the following:

$$\Pi = P_c = P_g - P_L$$

where P_g is the gas pressure in the cell, and P_L is the bulk liquid pressure in the plateau-border region. Substituting into this an expression for P_L which relies on the reference pressure, P_r , gives the following:

$$\Pi = P_g - P_r + \frac{2\sigma}{r_{\text{tube}}} - \Delta\rho gh_c \quad (21.4)$$

where σ is the surface tension of the solution, r_{tube} is the radius of the capillary tube, $\Delta\rho$ is the density difference between the solution and gas, h_c is the height of solution in the capillary tube above the film, and g is the gravitational constant. Each term on the right side of equation (21.4) can be measured independently. The first term, $(P_g - P_r)$, is measured with a differential pressure transducer, while the pressure jump in the capillary tube, $2\sigma/r_{\text{tube}}$, is easily found by measuring the radius of the tube and the surface tension of the surfactant solution. For low pressure work (< 100 Pa), the hydrostatic correction, $\Delta\rho gh_c$, must be carefully determined by measuring h_c . This can be accomplished with an accurate cathetometer, utilizing the microscope

objective as a reference to locate the horizontal position of the film (i.e. the measured working distance for the objective can be used to determine how far below the film is located, which gives an accurate measurement of the horizontal location of the film). When Π is large (~ 1 kPa) the last two terms in equation (21.4) are negligible, and the pressure difference, $P_g - P_r$, is sufficient to evaluate Π . In this case, P_r is referenced to the atmospheric pressure, P_A , and Π is simply the excess gas pressure in the cell.

The minimum capillary which can be imposed on the film, $P_{c_{\text{min}}}$, is determined by the meniscus curvature when the film is first generated. Larger meniscus radii correspond to smaller capillary pressures. It should also be noted that for a stable meniscus, the curvature must be concave towards the non-wetting phase (e.g. the gas phase for foam films), and therefore only positive capillary pressures can be applied to the film (i.e. it is impossible to measure negative regions of the disjoining pressure isotherm with this method). For completely wetting film holders, the meniscus curvature is set by the dimensions of the hole used to support the film. Thus, $P_{c_{\text{min}}}$ can be minimized for a given hole diameter, D , by lowering the hole aspect ratio, L/D , where L is the hole depth. We demonstrate this effect by calculating the largest inscribed circle that can be placed in the film holder, such that its horizontal tangent is located in the centre of the hole, (i.e. at $L/2$, see Figure 21.7). The radius of this circle, a , is then used in conjunction with Laplace's equation to determine $P_{c_{\text{min}}} (= 2\sigma/a)$. Simple geometry gives the following expression for a in terms of the hole dimensions:

$$a = \frac{D^2 + L^2}{4L}$$

This relationship indicates that a decreasing L/D increases a , and hence lowers $P_{c_{\text{min}}}$. Further details can be found elsewhere (11).

To prevent imbibition of the non-wetting phase, which would destroy the continuous liquid connection needed to apply equation (21.4), the maximum imposed capillary pressure must not exceed the entry pressure for the porous-disc film holder. This pressure can be estimated by $P_{c_{\text{max}}} = 2\sigma/r_{\text{pore}}$, where r_{pore} is the pore radius of the porous material used. Therefore, discs with smaller pores are required for higher capillary pressures. Standard porous discs can be found with nominal pore diameters from 50 to 1 μm . Thus, when using a porous frit with pore diameters ~ 1 μm , a typical surfactant solution ($\sigma = 30$ mN/m) gives $P_{c_{\text{max}}} \sim 120$ kPa for foam films. Due to low interfacial tensions, this value can be much lower for emulsion films. Special porous

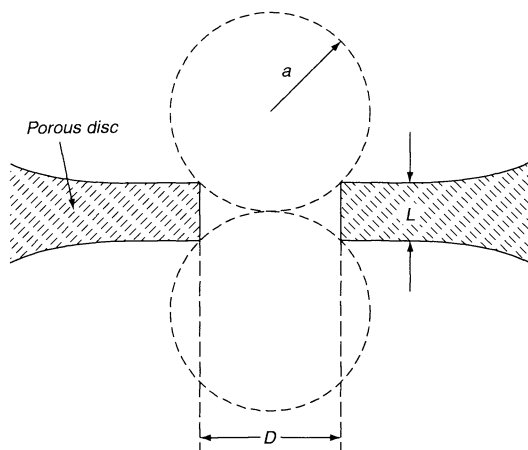


Figure 21.7. Representation of how the aspect ratio, L/D , of the film holder affects the maximum inscribed circle radius and hence the minimum capillary pressure attainable

materials can be found with smaller pores (e.g. “Vycor”) and hence higher imbibition pressures, however, the viscous resistance to the moving fluid in these materials then becomes a serious problem. Similarly, care must be taken when large-pore discs are used, because, over the course of the measurement, liquid may drain from the disc and significantly change the hydrostatic term in equation (21.4) under low-pressure conditions. In some cases, this can be circumvented by carefully melting the outer layer of the porous glass disc to seal the larger holes responsible for drainage.

2.2.7 Pressure via lamellae profiles

An alternative way to measure P_c is by direct application of Laplace’s equation. This method is schematically represented in Figure 21.8, for which Laplace’s equation

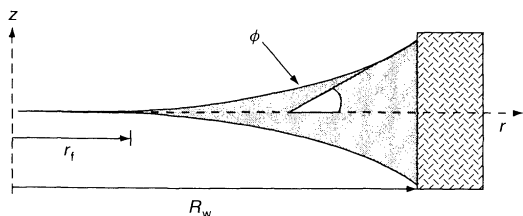


Figure 21.8. Schematic of the geometric constraints used to obtain capillary pressure measurements via the lamella profile (from ref. (11))

takes the following form:

$$P_c = \frac{1}{r} \frac{\partial}{\partial r} \left\{ \frac{r \frac{\partial z}{\partial r}}{\left[1 + \left(\frac{\partial z}{\partial r} \right)^2 \right]^{1/2}} \right\} \sigma \quad (21.5)$$

Upon integrating equation (21.5) and applying the boundary conditions that the meniscus-wall contact angle is $(90 - \phi)$ and the film-meniscus contact angle is zero, given as follows:

$$\frac{\partial z}{\partial r_{R_w}} = \tan \phi, \text{ and } \frac{\partial z}{\partial r_{r_f}} = 0$$

we obtain the following:

$$P_c = \frac{2\sigma R_w}{R_w^2 - r_f^2} \left[\frac{\tan \phi}{\sqrt{1 + (\tan \phi)^2}} \right]$$

where R_w is the radius of the hole used to form the film, and r_f is the film radius. For $\phi = \pi/2$ (i.e. completely wetting walls) this expression reduces to the following form:

$$P_c = \frac{2\sigma R_w}{R_w^2 - r_f^2} \quad (21.6)$$

Thus when applicable, equation (21.6) gives P_c from measurements of the film and holder radius. However, this equation is of limited use with film holders having $L/D < 1$. This condition demands that when the film is first formed, a finite contact angle will exist between the meniscus and the wall ($\phi \neq \pi/2$, and will change with increasing P_c). Furthermore, in all film holders, at high capillary pressures the meniscus of the film conforms to the wall and the detailed geometric features of the holder, which impose different boundary conditions for equation (21.5), and calculation of the film-meniscus profile becomes intractable. Nevertheless, for low capillary pressures, perfectly wetting walls and $L/D > 1$, equation (21.6) has been used directly, or slightly modified along with experimental calibration.

2.2.8 Pressure system

Capillary-pressure changes in the system are accomplished through changes in the cell gas pressure via a precise syringe pump. Additional volume can be placed in the gas supply line to decrease the sensitivity and allow micro-adjustments to be made to the pressure. By increasing the total volume of the measurement cell, a given syringe displacement will result in a smaller total volume change and hence a smaller relative pressure

change. In order to minimize temperature fluctuations (which can influence the pressure), insulation is needed for the syringe and any dead-volume vessels. Once these precautions are taken the syringe-pump drive can be linked to the pressure transducer used to measure P_c for automatic pressure control. High-pressure measurements (> 1 kPa) are much easier to carry out and normally do not require elaborate pressure control.

When small differential pressures are measured, special precautions must be taken in order to prevent unwanted pressure fluctuations and to ensure precise pressure control. Pressure isolation can be achieved by referencing the pressure, P_r , to a humidified steel chamber (~ 1 m³). Although the system is closed, the steel vessel is chosen large enough to prevent the overall pressure from rising significantly.

2.2.9 Complications

Many of the complications encountered with the thin-film balance (TFB) have been discussed in the previous sections (i.e. low pressure control, optical correction for surfactant layers, etc.); however, there are a few more details that are worth mentioning. The first and most obvious one concerns cleanliness. As with surface tension measurements, the high energy interfaces in aqueous-based thin-liquid films tend to concentrate surface-active contaminants. Moreover, as the porous discs used have large surface areas, the possibilities for contamination can present serious problems. New porous frits can be cleaned sufficiently by combination of acid washing in warm HCl solutions, boiling and sonication in distilled water, followed by exposure to elevated temperatures (via flame or oven) and copious rinsing with high-purity water (for rinsing, extensive flushing by drawing water through the frit via a vacuum system works well). Additional care must also be taken when performing measurements with cationic-based surface-active components (e.g. trimethylammonium bromides). These chemicals tend to extract minute quantities of multivalent borosilicate ions from the Pyrex discs, which can effect disjoining pressure measurements. The extent of the problem depends upon the quality of the Pyrex glass and the manufacturing methods used to produce the porous disc holders. In suspected systems, it is advisable to pre-soak the frits for a short time (~ 20 min) with the surfactant solution to be used, followed by another round of copious rinsing with pure water. This step serves to extract any silicates susceptible to being leached out into the solution. Although quite time-consuming, this routine works well. Used frits can be rejuvenated by the same methods but it is safer to

only use one type of surfactant per frit. Once cleaned, the frits should be thoroughly soaked in the bulk solution under study to guarantee complete saturation throughout the frit.

A common misunderstanding, which can lead to thickness calibration problems, is that the amplitude of the I_{\max} and I_{\min} values should always increase with decreasing interference order and that the last interference maximum should always be higher than all previous values. Although this is a common experimental observation, it arises from film-thinning dynamics, and is not a fundamental consequence of thin-film interferometry. For thin plane-parallel films with negligible light adsorption, the intensity of monochromatic light reflected at zero angle of incidence produces equal interference extreme values for each interference order (9). The common observation of an increasing I_{\max} results from thickness averaging over film areas that are not plane-parallel. As the film thins, it becomes more plane-parallel, with less severe averaging, accompanied by an increase in the I_{\max} values. The departure from plane-parallel thinning is well understood and is referred to as "film-dimpling". In order to garner accurate I_{\max} and I_{\min} values, the film area probed for measurement of the reflected intensity must be small enough to capture plane-parallel regions of the film at thickness intervals corresponding to the interference extrema. Moreover, the numerical aperture of the objective used to magnify the film image must be sufficiently small (~ 0.2) to ensure illumination and detection of light at zero angle of incidence. Normally, extremely small optical probe diameters are used when applying the Scheludko interference method; however, it is impossible to guarantee that each time a film thins, the area probed has remained sufficiently plane-parallel to define accurate I_{\max} and I_{\min} values. Therefore, calibration must be carried out several times on a series of different films. Simultaneous visual observations should also be made to help facilitate the interpretation of the optical signal. Finally, we note that for foam films, the I_{\min} value actually corresponds to zero reflection from the film, and hence rupturing the film is the easiest way to define their I_{\min} values.

Another complication which is involved in film thickness determination can arise if the film is not situated perpendicular to the incident illumination. This will occur when either the film is curved or the holder is misaligned. Film curvature can be induced by holder wetting problems, poorly drilled holes or when measuring asymmetric fluid systems (i.e. pseudo-emulsion films). Fortunately, direct observations and thickness scans across the film will easily reveal serious problems. For difficult systems, quantitative inspection

methods can also be employed, such as topographical interferometry; however, these methods are not typically required.

3 DISJOINING PRESSURE COMPONENTS/INTERPRETATION

3.1 General approach

Changes in the interfacial region which generate the disjoining pressure in a thin-liquid film originate from intermolecular forces. It is customary to separate the various contributions of the disjoining pressure into different components, as follows:

$$\Pi(h) = \Pi_{\text{dl}} + \Pi_{\text{van}} + \Pi_{\text{steric}} + \Pi_{\text{supra}} + \text{etc.} \quad (21.7)$$

where the subscripts in this equation indicate the following contributions: “dl”, electrostatic double-layer forces; “van”, London–van der Waals dispersion forces; “st”, steric and short range structural forces (e.g., entropic confinement forces); “supra”, forces arising from supramolecular structuring. Of course, models based on the application of equation (21.7) make the key assumption that the various contributions to the disjoining pressure are additive. However, it is not always clear that this assumption is valid, and in some cases it may lead to anomalous results.

Combination of the first two components listed in equation (21.7), i.e. Π_{dl} and Π_{van} , constitute the well-known DLVO theory. These two basic contributions are used throughout colloid science to describe particle interactions and provide the foundation for understanding colloid stability. Typically they are treated separately and additive as suggested by equation (21.7), although extended Poisson–Boltzmann theory shows that the distinction made between van der Waals and double-layer forces is somewhat of an illusion. In addition, more complex behaviour can occur due to “image forces” and ionic correlations.

In what follows, we briefly review each of the components in equation (21.7) separately for the purpose of highlighting the molecular origins of the disjoining pressure isotherm. For a comprehensive review, several texts and monographs are available (1, 2, 12).

3.2 Electrostatic double-layer forces

One of the first and most studied contributions to the disjoining pressure arises from “electrostatic” interactions.

These interactions result from overlapping of the electric double-layers that develop at charged interfaces. In the simplest case, a repulsive force between the interfaces develops due to entropic confinement of the counterions which neutralize a charged interface. When the separation distance between two charged interfaces approaches twice the characteristic length for decay of the diffuse ionic atmospheres, λ , an additional external force is required to maintain the separation distance. From classical Debye–Hückel theory, the characteristic length over which ions from a univalent electrolyte will act is given by the following:

$$\lambda = 1/\kappa = \sqrt{\frac{\epsilon kT}{8\pi n^0 e^2}} \sim C^{-1/2}$$

where λ is called the Debye length, n^0 is the number density of ions, e is the elementary charge, ϵ is the dielectric constant of the medium, T is the temperature, k is the Boltzmann constant and C is the concentration of electrolyte (mol/l). This expression provides the important result that the decay length decreases as the electrolyte concentration increases (i.e. interactions become shorter-range because of ionic screening).

The electrostatic double-layer forces are obtained by solving the Poisson–Boltzmann equation under a variety of different boundary conditions. There exists an extensive literature concerning the calculation of the electrostatic repulsion between interfaces, and therefore only two of the classic results will be given here as illustrative examples.

In most cases, only relatively simple approximations for Π_{dl} are needed to capture the essential physics of double-layer interaction forces. Such approximations are typically valid for small surface charges where linearization of the Poisson–Boltzmann equation is acceptable. Under these conditions and assuming univalent electrolytes, examples of constant surface potential and constant surface charge models for Π_{dl} are given by the following:

$$\Pi_{\text{dl}}^{\psi} = \frac{\epsilon \psi_0^2}{8\pi} [\text{sech}^2(\kappa h)]$$

Constant surface potential

$$\Pi_{\text{dl}}^{\sigma} = \frac{2\pi\sigma_0^2}{\epsilon} \left[\frac{1 + \text{sech}(\kappa h/2)}{\tanh(\kappa h/2)} \right]^2$$

Constant surface charge

where ψ_0 is the potential and σ_0 is the charge density at the interface. The constant surface potential model can be further simplified for large separation distances

and small potentials to give the following well-known form (1, 2, 12):

$$\prod_{dl}^{\psi} = 64n^0 kT \gamma^2 \exp(-\kappa h)$$

where:

$$\gamma = \left[\frac{\exp(Z/2) - 1}{\exp(Z/2) + 1} \right], \text{ and } Z = \frac{e\psi_0}{kT}$$

Under the conditions assumed, this expression is also valid for constant-charge systems since little discharge occurs if the degree of double-layer overlap is small. More elaborate models for Π_{dl} include charge regulation boundary conditions at the surface and effects due to ionic correlation and image forces.

3.3 Dispersion forces

In addition to electrostatic double-layer forces, London–van der Waals dispersion forces have long been recognized as being important in thin-liquid films. The calculation of these forces has been approached in two different ways, namely microscopically and macroscopically.

The microscopic method, credited to Hamaker, came first and is based on pair-wise summation of the individual dispersion interaction between molecules. Casimir and Polder later supplemented this approach by including the correction for electromagnetic retardation. The molecular interaction potential used is typically represented by the following expression:

$$u(r) = -\frac{3}{2} \left(\frac{\bar{h}v_1\bar{h}v_2}{\bar{h}v_1 + \bar{h}v_2} \right) \frac{\alpha_1\alpha_2}{r^6}$$

where $u(r)$ is the interaction potential between two spherically symmetric molecules, (1) and (2), \bar{h} is the Planck constant, v_i is a characteristic electronic frequency for each molecule in its unexcited state, and α_i is the polarizability of molecule i . In order to obtain the force of interaction between two macroscopic bodies, this potential is integrated over the volume of the system, which for two plane-parallel surfaces separated by a vacuum gap yields the following:

$$\prod_{van} = -\frac{A_{12}}{6\pi h^3}$$

where A_{12} is known as the Hamaker constant. At large separations, retardation effects (finite response times of the induced dipoles) can become important, and lead

to a decreased interaction which decays faster ($\Pi_{van} \sim 1/h^4$). When the interaction between two different bodies, (1) and (2), is mediated by a third phase, (3) (e.g. aqueous films “3” sandwiched between phase “1” and phase “2”), the potential energy of interaction, Ω_{132} , becomes:

$$\Omega_{132} = A_{132} \int \int \frac{dV_1 dV_2}{r^6}$$

where:

$$A_{132} = (A_{12} + A_{33} - A_{23} - A_{13})$$

and V_i corresponds to the volume of phase i , and A_{132} is the composite Hamaker constant. Like the electrostatic component, many elaborate models have been developed to handle different geometries and more complex systems (e.g. multilayered films) (2).

The fundamental shortcoming of this microscopic approach stems from the assumed pair-wise additivity of the molecular interactions. However, this problem is overcome if we adopt an alternative point of view and consider the interacting bodies as a continuous medium. This macroscopic approach was developed by Lifshitz, and the theory now bears his name. The basic idea of the theory is that the interaction between the bodies is considered to take place through a fluctuating electromagnetic field. In this approach, the fields are calculated on the basis of the exact Maxwell equations, so that the effects of retardation, caused by finite propagation velocities of the electromagnetic waves, are automatically taken into account. The Lifshitz result for a thin uniform film of phase “3” between two semi-infinite phases, “1” and “2”, is given by the following:

$$\begin{aligned} \prod_{van} = & \frac{\bar{h}}{2\pi^2 c^3} \int_0^\infty \int_1^\infty p^2 \xi^2 \varepsilon_3^{3/2} \\ & \times \left\{ \left[\frac{(s_1 + p)(s_2 + p)}{(s_1 - p)(s_2 - p)} \exp\left(\frac{2p\xi}{c} h\sqrt{\varepsilon_3}\right) - 1 \right]^{-1} \right. \\ & + \left[\frac{(s_1 + p\varepsilon_1/\varepsilon_3)(s_1 + p\varepsilon_2/\varepsilon_3)}{(s_1 - p\varepsilon_1/\varepsilon_3)(s_2 - p\varepsilon_1/\varepsilon_3)} \right. \\ & \left. \left. \exp\left(\frac{2p\xi}{c} h\sqrt{\varepsilon_3}\right) - 1 \right]^{-1} \right\} dp d\xi \quad (21.8) \end{aligned}$$

where:

$$s_1 = \sqrt{\varepsilon_1/\varepsilon_3 - 1 + p^2} \text{ and } s_2 = \sqrt{\varepsilon_2/\varepsilon_3 - 1 + p^2}$$

while c is the speed of light, and ε_1 , ε_2 , and ε_3 are functions of the imaginary frequency, $\omega (= i\xi)$. However, the quantity $\varepsilon(i\xi)$ is a real function that can

be evaluated from the following expression:

$$\varepsilon(i\xi) = 1 + \frac{2}{\pi} \int_0^\infty \frac{\omega \varepsilon''(\omega)}{\omega^2 + \xi^2} d\omega$$

In the above expression, $\varepsilon''(\omega)$ is the imaginary part of the dielectric response function and $\omega \varepsilon''(\omega)$ measures the spontaneous electric field fluctuations in a body, as well as a substance's ability to dissipate applied electrical energy (12).

Needless to say, equation (21.8) is a bit cumbersome and its original derivation is rather lengthy. However, many subsequent treatments of the macroscopic theory are now available which provide both a more readily understandable approach and many useful approximate expressions. In fact, by using the method of Parsegian and Ninham to determine the dielectric response function from absorption data and reflectance measurements, it is now quite straightforward to calculate dispersion forces from Lifshitz's theory.

Although the macroscopic approach is a great improvement over the classical Hamaker summations, it is not expected to hold when a film becomes so thin that its dielectric properties change with thickness or when molecular orientation is important. This can be an important consideration for aqueous films which undergo structuring near the interface.

3.4 Steric (entropic forces)

Entropic confinement forces are a third class of forces that occur in ultra-thin surfactant films (< 5.0 nm) and between bilayers in solution. The parameter Π_{steric} is introduced into equation (21.7) to cover contributions to the disjoining pressure that are responsible for the stability observed in so-called "Newton black soap films" (see Figures 21.9 and 21.10). In concept, this component is similar to the "adsorption component of disjoining pressure", originally introduced by Derjaguin, that arises from the steric repulsion occurring when adsorbed layers overlap. More recently, Israelachvili and Wennerström (13) have outlined the physical origin of these forces more precisely and have carefully categorized the various modes by which they operate. The general classifications given by them include the following:

- (i) *Undulation* – forces created by undulations of the interface (inversely proportional to the bending modulus, K_b , $\Pi_u \sim 1/K_b$).
- (ii) *Peristaltic* – forces generated by peristaltic fluctuations as two fluid interfaces approach (inversely

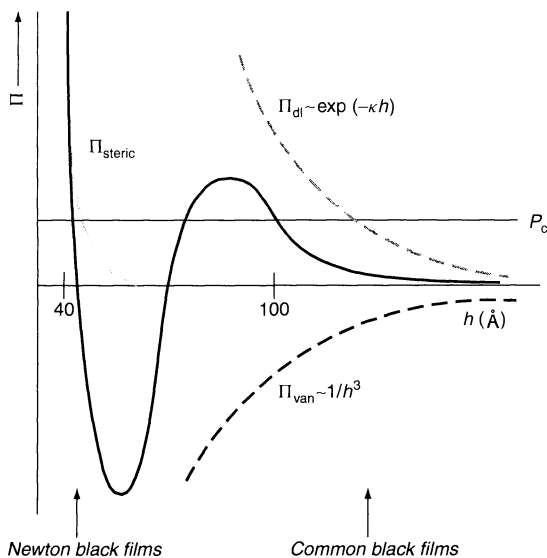


Figure 21.9. Schematic representation of a disjoining pressure isotherm that includes contributions from Π_{dl} , Π_{van} and Π_{steric}

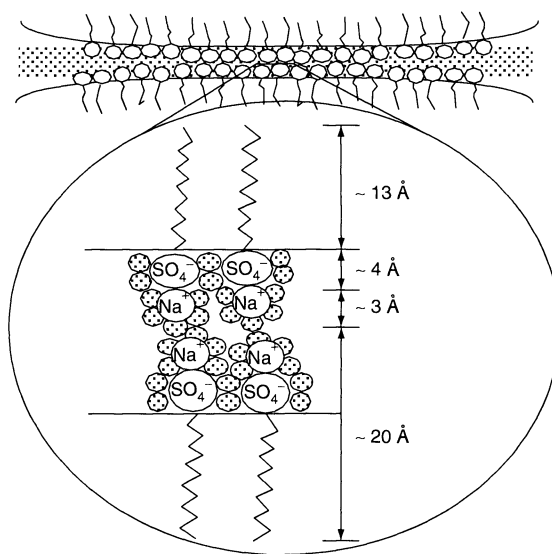


Figure 21.10. Schematic diagram showing the profile of a Newton black film of sodium dodecyl sulfate. Filled circles correspond to water in the first hydration shell, surfactant head-groups are labelled and the hydrocarbon chain is depicted by the irregular lines (from ref. (11))

proportional to the compressibility modulus, K_a , $\Pi_p \sim 1/K_a$).

- (iii) *Head-group overlap* – a steric stabilization force that becomes important in systems containing

large nonionic head-groups. These forces can be described by theories used for polymer “brushes”.

- (iv) *Protrusion* – molecular scale protrusions of surfactant molecules at the interface. The parameter Π_{pro} can be approximated from the following:

$$\Pi_{\text{pro}} = \frac{n\beta(h/\zeta) \exp(-h/\zeta)}{[1 - (1 + h/\zeta) \exp(-h/\zeta)]}$$

where $\zeta = kT/\beta$ is the protrusion decay length, n is the density of protrusion sites, and β is an interaction parameter (J/m).

A semi-quantitative treatment of these entropic confinement forces is presented by Israelachvili and Wennerström in their review.

Solvation forces are also important in extremely thin films, or when water is the solvent, hydration forces. These forces originate from molecular ordering of the solvent at the interface. When two interfaces approach, this ordering is disturbed, resulting in forces of attraction and repulsion. These short-range interactions can be very complex and depend on how the molecules structure at an individual surface, and then on how this structure is modified once a second surface is encountered. The simplest solvents display force curves that oscillate with a periodicity equal to the solvent's molecular diameter and can be roughly modelled by treating the molecules as hard-spheres between two hard walls. Water, however, has strong dipoles that can lead to hydrogen bonding and long-range dipole polarization. These effects generate repulsive “hydration” or attractive “hydrophobic” interactions, in addition to the short-range oscillatory interaction.

Figure 21.9 shows a schematic of a foam-film disjoining pressure isotherm which includes the entropic force contributions, Π_{steric} , superimposed on the classical DLVO components, Π_{dl} and Π_{van} . It is important to note that thermodynamically metastable films can exist only in negatively sloping regions of the isotherm. Hence, the portion of the curve with a positive slope separates the isotherm into two metastable regions, namely thick (~ 50 nm) common black films (CBFs) and thinner (~ 4 nm) Newton black films (NBFs). In foam, the CBF stability is normally due to the electric double-layer forces, while the NBF stability is not so well understood, but can be accounted for by the short-range entropic confinement forces outlined above.

X-ray reflectivity experiments and molecular dynamic calculations confirm the schematic representation of the NBF pictured in Figure 21.10. In this figure, the filled circles represent water molecules in the first hydration shell which surround the polar head-groups

of sodium dodecyl sulfate (SDS) surfactant molecules adsorbed to an air–water interface. The hydrocarbon chain of the surfactant (i.e. surfactant tails) are indicated by the irregular lines that extend out of the aqueous film region. Approximate thicknesses have been indicated and from the picture it is clear that very little space is left for unbound water and the interior of the NBF film resembles a solid-like structure.

3.5 Supramolecular forces

Relatively new types of forces, due to supramolecular structuring of amphiphilic molecules and polymers, within foam films have been recently measured. Moreover, several works dating from the turn of the 20th century have demonstrated film-thinning phenomena (commonly referred to as *film stratification*) which arise from supramolecular forces. The general form of the force curves obtained for these systems is summarized in Figure 21.11.

In systems studied thus far, the forces can be extremely long range (> 50 nm) and oscillatory, having a periodicity set by the *effective* size of the structures responsible for the forces. The most common occurrence of supramolecular structural forces in thin films is when relatively high concentrations of surfactant are present in a system. In such systems, a variety of structures can form depending on the nature and composition of the amphiphile in the system, ionic strength, and external conditions such as temperature. Therefore, modelling supramolecular forces typically requires assumptions about the structures that are present in the film. The two most frequently encountered structures in thin-liquid soap films are repeating units of surfactant bilayers or ordered arrays of micellar domains.

3.5.1 Micellar structural forces

Mysels was the first to suggest that micelles can contribute to the disjoining forces in foam films (14, 15). The first treatment describing this phenomena within a theoretical thermodynamic framework was by Pollard and Radke (16), who utilized density functional theory (DFT) to calculate a micellar contribution to the disjoining pressure, Π_{mic} . This method sums the force exerted on the interfaces by the micelles in the film, as follows:

$$\Pi_{\text{mic}} = -\frac{1}{2} \int_0^h \rho(x; h) \left[\frac{dU_{\text{m-1}}(x)}{dx} + \frac{dU_{\text{m-2}}(h-x)}{dx} \right] dx - P_B$$

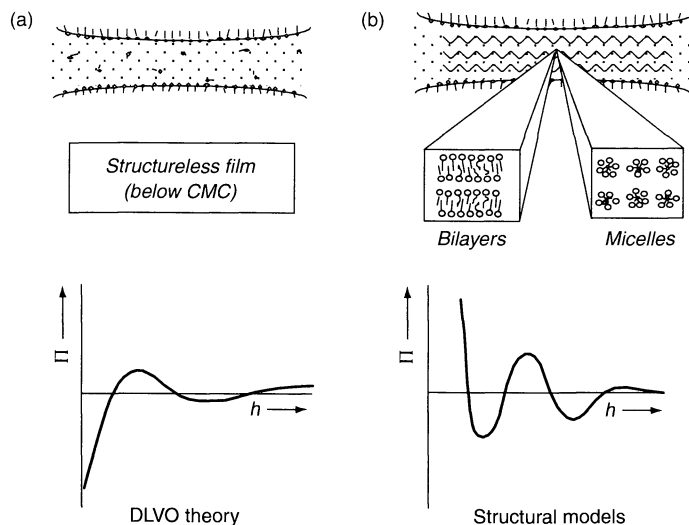


Figure 21.11. The general form of the force curves for systems (a) with and (b) without supramolecular structuring. Only two types of structures are depicted; however, many different types can occur depending on the system (from ref. (11))

where x defines the location in the film, U_{m-i} is the interaction potential between a micelle and interface i , and P_B is the reference bulk pressure of the fluid in equilibrium with the film. Here, $\rho(x; h)$ is the number-density distribution of micelles in the film, which is obtained from variational differentiation of the Helmholtz free energy, F , with respect to $\rho(x; h)$,

$$\frac{\delta F[\rho(x)]}{\delta \rho(x)} = -\mu + U^{\text{ext}}$$

where μ is the chemical potential and U^{ext} is the external potential (i.e. a typical DLVO-type potential). Calculations using this scheme show that charged micelles have energetically preferred locations within the film, which cause them to create a micellar density profile that has an oscillatory form. Thus, the density distribution of micelles in the film forms a series of peaks that define the most probable position of finding a micelle in the interior of the film (see Figure 21.11). As the film thickness decreases, micelles are “squeezed” out of the film and the number of density peaks decreases concomitantly. Since the micelle structuring generates multiple values of the film thickness that are thermodynamically unstable ($\partial \Pi / \partial h > 0$), the squeezing out process occurs in a discrete manner, changing from one metastable configuration to the next. That is, DFT allows us to interpret the oscillatory branches of the force curve as arising from micellar structuring in the film via the local thermodynamic minimum set-up at

different film thicknesses, and *not* kinetic trapping as originally postulated.

One important point concerning forces generated by micellar structuring is the difference in the magnitude of the forces found between SFA (Surface Force Apparatus) measurements and those obtained for foam films. In foam films, the magnitudes are low, of the order of 100 Pa, while SFA measurements on similar systems exceed 10^4 Pa. This difference most likely comes from physical differences between the interfaces in the two experiments. SFA measurements confine a fluid between two solid interfaces, which support more stress and have much lower levels of fluctuations when compared to fluid interfaces. Thus, solid interfaces can promote a higher degree of supramolecular order. The calculations of Pollard and Radke are consistent with this fact. Conversely, a fluid interface is flexible and can absorb energy through deformations (bending modes) which will diffuse the ordering between the interfaces. The spatial and density fluctuation effects on the measured forces and metastable states of “stratifying” foam and emulsions films are analogous to the discussion provided below concerning “Common Black Film Stability” in Section 4.

3.5.2 Bilayer and lamellar structural forces

Clearly different types of molecular structuring in addition to micellar (e.g. bilayer, liquid crystal, etc.) can

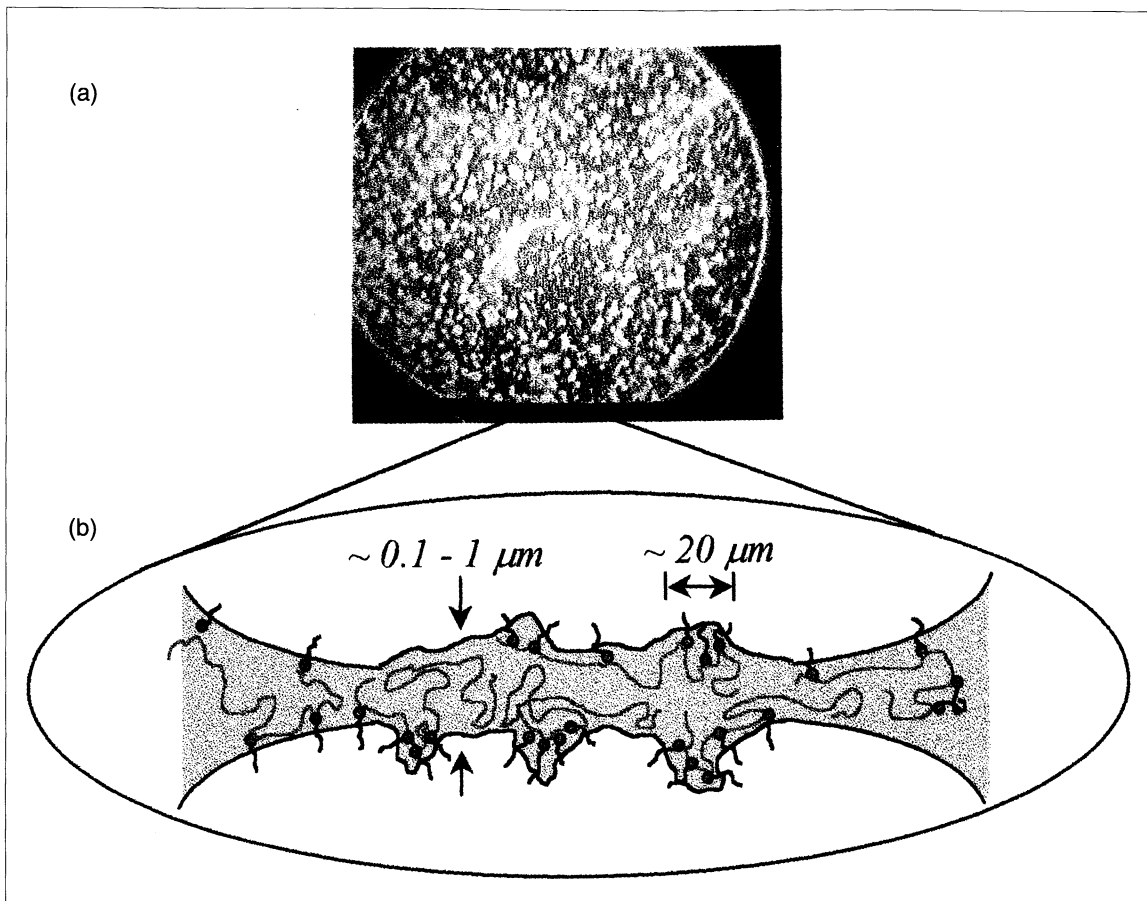


Plate 6 (a) Thin-film interference image of an individual foam film stabilized by adsorbed polymer/surfactant complexes which create a gelled network within the film, and (b) a schematic which shows a representative cross-sectional view of such a film (see also **Figure 21.13**, page 430)

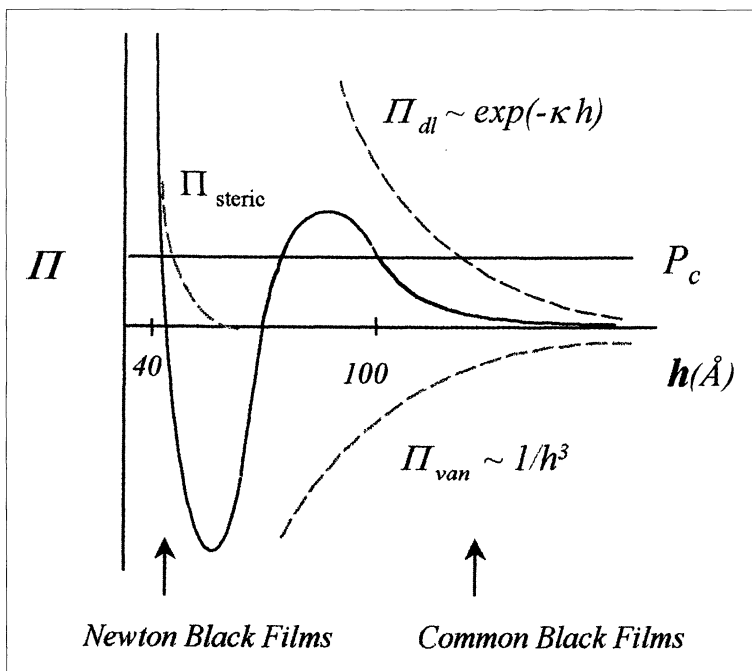


Plate 7 Schematic representation of a disjoining pressure isotherm that includes contributions from Π_{dl} , Π_{van} and Π_{steric} (see also **Figure 21.9.**, page 426)

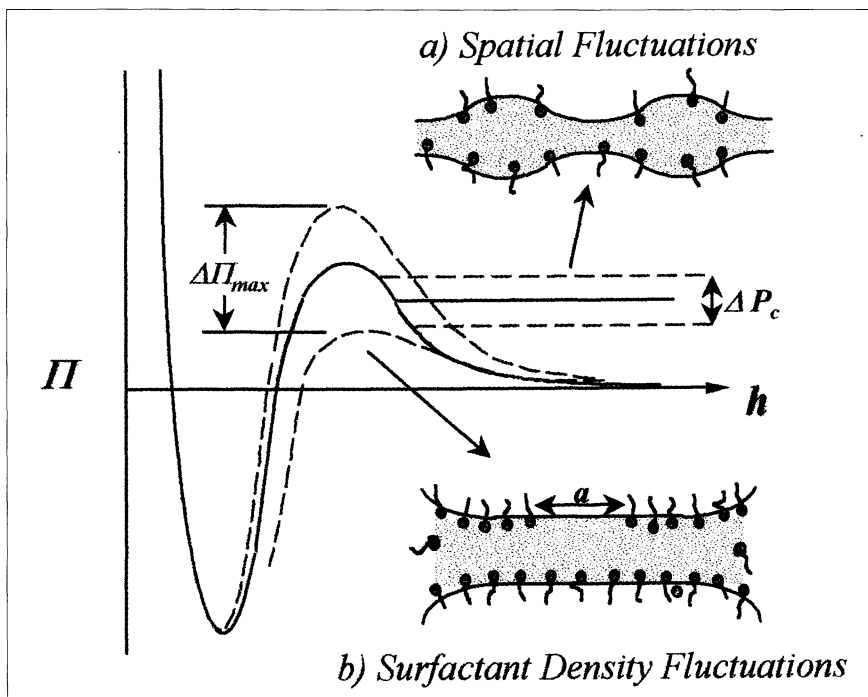


Plate 8 A schematic depicting how fluctuations in the capillary pressure, ΔP_c , and the disjoining pressure, $\Delta \Pi_{max}$, influence the local barrier height relative to the imposed capillary pressure along the film: (a) a typical spatial fluctuation; (b) a local depletion zone due to monolayer density fluctuations (see also **Figure 21.14.**, page 431)

occur and modelling these systems in foam films has received little attention. However, some theories have been developed for the structural component of the disjoining pressure in thin films of liquid crystals. Their thermodynamic premise is based on the concept of surface tension anisotropy (i.e. variation of nematic liquid crystal interfacial tension with molecular orientation at the interface). The primary contributions to the force results from a balance of two torques, as follows:

- τ_{el} – elastic torque opposing disalignment of molecules
- τ_s – surface torque opposing an increase of surface free enthalpy or surface tension

For more dilute systems (e.g. vesicular solutions), thin-film-containing highly flexible bilayers can be obtained. In this case, bilayer undulation forces (so-called “Helfrich forces”) can play a role. These forces are repulsive and originate from the entropic confinement of bilayers in a film. Although in some cases good agreement is found between theory and experiment, there still remains many unexplored problems that should prove to be both challenging and exciting problems for future research.

3.5.3 Structures and forces in polymer- and polymer/surfactant-containing films

Some of the newest force/structure relationships within thin films have been found when soluble polymers are added to a system. Whether or not low-molecular-weight surfactants are present, polymer (and protein)-containing systems reveal many different thin-film properties. As most practical systems do contain both surfactants and polymers, we have outlined in Figure 21.12 a summary of the four most commonly seen adsorption/complexation interactions that occur between various mixtures of the two. This general summary is clearly not exhaustive, but, as these situations often arise it is convenient to identify the general categories as follows: I, *synergistic adsorption*; II, *repulsion or non-interactive*; III, *surface depletion*; IV, *competitive or indifferent adsorption*. Case I, synergistic adsorption, is often encountered with oppositely charged polyelectrolyte–surfactant mixtures, while Case II can occur when the polyelectrolyte carries the same charge as an ionic surfactant in solution or when a non-interacting, non-adsorbing polymer is present. Case III often takes place for surfactants that have a strong hydrophobic interaction with the polymer and the resulting complex becomes less surface-active. Finally, Case IV is less common

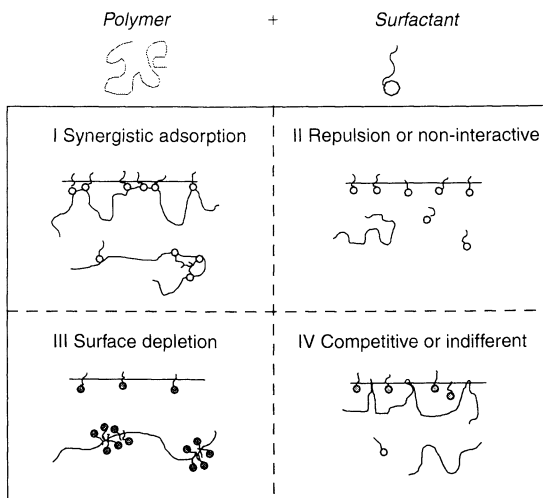


Figure 21.12. A summary of the four most commonly seen adsorption/complexation interactions that occur between various mixtures of polymers and surfactants

and requires non-interacting polymer-surfactant systems that adsorb independently to the interface. It should also be noted that the various situations dependent on the relative concentrations of the different components and one particular chemical system can change its behaviour depending on the solution composition. The interested reader is referred to the text by Goddard and Ananthapadmanabhan (17) for a detailed review of polymer/surfactant interactions and their adsorption to interfaces.

Although quantitative thin-film force measurements of polymer/surfactant-containing systems are relatively new, quite fascinating behaviour has already been found. In particular, the strongly interacting synergistic adsorption system (e.g. Case II) containing an anionic polyelectrolyte and a cationic surfactant has been extensively studied. This system has revealed both oscillatory force versus distance profiles, and interfacial gel formation within individual films.

At relatively low polymer adsorption levels, oscillatory force profiles similar to those observed for micellar solutions are also seen in polyelectrolyte-containing systems. As with micellar structuring, these oscillations originate from an inhomogeneous density distribution of polymer (or polymer/surfactant complexes) within the film. Furthermore, the characteristic length-scale of the oscillatory forces indicate that this structuring is controlled by electrostatic interactions. To date, no complete theory describing this phenomenon exists;

however, Monte Carlo simulations of confined polyelectrolytes in thin films clearly predict non-homogenous density profiles and oscillations in the force–distance isotherms. These simulations lead to the interpretation that force oscillations will arise when the chains from one density-rich region are forced close enough to sample an adjacent high-density region. At this point, the two regions merge to occupy the same “Coulombic well”, thus resulting in a discrete jump in film thickness and expulsion of any excess polymer. The process was originally expressed as “polymer bridging”, but this type of bridging should not be confused with the bridging which involves polymer adsorption – this present case is simply a *fusion of density-rich polymer regions* which is analogous to the fusion of micelle-rich regions which generate similar oscillatory force profiles in concentrated surfactant solutions.

When there is high polymer (or polymer/surfactant complex) adsorption on to a fluid interface, a thin film containing a gel-like network can be created when two such interfaces are brought into contact. An example of these gelled films can be found in Figure 21.13. The film pictured in this figure is much thicker than common soap films, as can be seen by the strong iridescent colours it produces via thin-film interference under white-light illumination. Each colour corresponds to a different film thickness and it is evident that the thickness is highly heterogeneous throughout the film. In fact, there are two types of heterogeneities, namely microscopic, of the order of 20 μm diameter, which appear

as spots scattered throughout the film, and much larger irregularly shaped macroscopic domains. A schematic diagram of a typical film cross-section is provided below the photograph in Figure 21.13. Although the general features of these gelled films are highly reproducible, it should be noted that the structures formed are not equilibrium structures and their form and properties depend on the rate of film formation. When films are formed quickly, the polymer chains extending from the surface do not have time to rearrange into an equilibrium configuration and thus they get trapped (quenched) into a complicated network of knotted overlapping adsorption layers. Furthermore, unlike solid surfaces, thin-liquid films have highly deformable interfaces that succumb to the local pressures generated by squeezing the entangled polymer network. Surface tension forces are not strong enough to prevent this deformation, and thus these films develop a very heterogeneous thickness profile. This deformation results in a distribution of energy which has not been considered in previous surface force theories, and hence standard polymer interaction theories between flat surfaces cannot be applied to these systems. It is clear that the gel-like films described here play an important role in film stabilization and various other thin-film properties, and thus the complex behaviour seen with these systems remains one of the many exciting areas for future work.

3.6 Hydrophobic forces

It is now well-established that a long-range ($> 10\text{ nm}$) attractive force operates between hydrophobic surfaces immersed in water and aqueous solutions. This force can be much stronger than those predicted on the basis of van der Waals interactions and is termed the *hydrophobic force*. So far, no generally accepted theory has been developed for such forces, although the hydrophobic force is thought to arise from overlapping solvation zones as two hydrophobic species come together. In fact, Eriksson and co-workers have used a square-gradient variational approach to show that the mean field theory of repulsive hydration forces can be modified to account for some aspects of hydrophobic attraction. Conversely, Ruckenstein and Churaev have suggested a completely different origin that attributes the attraction to the coalescence of “vacuum gaps” at the hydrophobic surfaces. The exact origins and character of the hydrophobic attraction remains an open question which is currently the subject of extensive research.

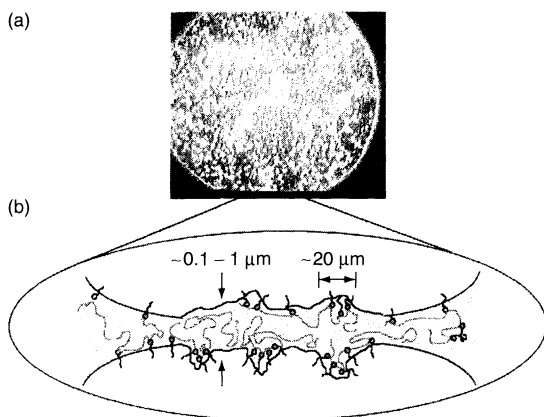


Figure 21.13. (a) Thin-film interference image of an individual foam film stabilized by adsorbed polymer/surfactant complexes which create a gelled network within the film, and (b) a schematic which shows a representative cross-sectional view of such a film

4 COMMON BLACK FILM STABILITY

4.1 General description

The disjoining pressure isotherm shown in Figure 21.9 represents the energy barrier referred to in our earlier discussions concerning the long-term stability of films (see also Figure 21.3). From these discussions, it should be evident that when an external capillary pressure in excess of the maximum disjoining pressure is applied to the film, we will breach the energy barrier holding the film in its metastable state and film rupture can then occur. However, a classical DLVO approach, which simply balances repulsive and attractive interactions across the film to gauge the magnitude of the energy barrier cannot fully explain the film stability behaviour witnessed in foam and emulsion systems.

Recently, certain limitations of applying classical DLVO concepts to foam and emulsion films have been revealed (18). Unfortunately a classical DLVO force analysis of film rupture treats the film surfaces as solid uniformly charged non-deforming walls; however, foam and emulsion films have both spatial and surfactant density (i.e. charge) fluctuations occurring at the interface. In reality, these fluctuations are superimposed on one another, but for clarity the schematics shown in Figure 21.14 depict the two cases separately. Since film rupture (and/or a thickness transition) from a metastable state is essentially a nucleated “wetting phase transition”, fluctuations can be important near the phase spinodal, as with bulk phase transitions near the critical point. By using simplified analyses, one can discover useful insights into which processes and system parameters are important for controlling the fluctuations not accounted for in DLVO theory.

The original work of Vrij (19) has spawned considerable attention concerning the effect that spatial fluctuations have on the *spinodal decomposition* of unstable film states; however, the early work of De Vries (20) seems to be one of the few that addresses *nucleated* rupture of rather thick foam films (i.e. CBFs). Likewise, understanding how surfactant density fluctuations might directly affect the DLVO forces and metastability of foam and emulsion films has received very little attention. We note that nucleated rupture of ultra-thin NBFs has been treated, but these films do not undergo thickness variations and are essentially molecular leaflets for which the repulsive disjoining forces are not as well understood. Thus, for NBFs it is not clear whether continuum concepts apply (i.e. surface tension, etc.) and the activation energy for film rupture may be governed by different physical parameters.

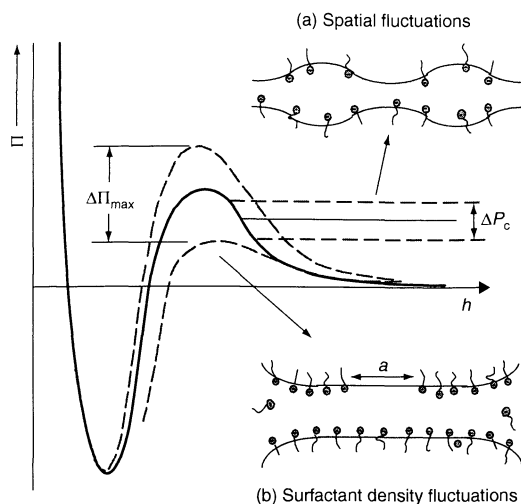


Figure 21.14. A schematic depicting how fluctuations in the capillary pressure, ΔP_c , and the disjoining pressure, $\Delta \Pi_{\max}$, influence the local barrier height relative to the imposed capillary pressure along the film: (a) a typical spatial fluctuation; (b) a local depletion zone due to monolayer density fluctuations

Consideration of the simple disjoining pressure isotherms presented in Figure 21.14 helps us to understand within the framework of familiar DLVO concepts which film properties control the fluctuations responsible for overcoming the energy barriers that hold a simple CBF in its metastable state. The continuous curve shown in this figure represents a typical DLVO profile for a system trapped in a metastable energy minimum at a particular imposed capillary pressure. The dashed lines and curves in the figure correspond to how fluctuations influence the disjoining pressure maximum, $\Delta \Pi_{\max}$, and variations in the applied capillary pressure, ΔP_c . As with the standard DLVO premise, when the applied pressure exceeds the disjoining pressure, the film has overcome the barrier trapping the film in a local thermodynamic minimum. After this point is reached, the spinodal decomposition analysis of Vrij describing the lifetime of a thermodynamically unstable film is formally applicable. The important point which needs to be made is how fluctuations can promote this unstable stage.

4.2 Spatial fluctuations

The spatial fluctuations shown in Figure 21.14(a) manifest themselves as pressure fluctuations along the film, (ΔP_c in the figure). The probability of a certain fluctuation depends on the energy expended to create it, and

is given as follows:

$$P_s \sim C_s \exp\left(-\frac{\Delta G_s}{kT}\right)$$

where P_s is the probability of the spatial fluctuation, c_s is a constant and ΔG_s is the energy expended. For a pure fluid, a simple one-dimensional energy analysis for a sinusoidal fluctuation of the type pictured was worked out by Vrij and Overbeek. When surfactant is present, Bergeron has shown that ΔG_s becomes (18):

$$\Delta G_s = (\varepsilon + \sigma) \frac{2B^2\pi^2}{\Lambda} - \Lambda B^2 \frac{d\Pi}{dh} \quad (21.9)$$

where:

$$\varepsilon = \frac{d\sigma}{d\ln a} = \varepsilon_d + i\eta_s\omega$$

where ε is the surface dilatational modulus, ε_d and η_s the elastic and shear dilatational moduli, respectively, ω the frequency of the disturbance (we note that $\varepsilon_d \sim \varepsilon_0$ when $\omega \sim \infty$), B the amplitude of the disturbance and Λ its wavelength. The second term in equation (21.9) accounts for the change in interaction energy accompanying the disturbance and is normally a small contribution to the overall energy change. The difference between equation (21.9) and Vrij's classical expression is the surface modulus term which arises from having surfactant adsorbed to the interface. Higher-order surface curvature terms can also be incorporated into the analysis but they are typically small in comparison to ε and σ . Since the surface modulus (i.e. elasticity) may in some cases exceed the surface tension, it can actually become the most influential contribution countering the disturbance. Hence, with reference to equation 21.9 we see that high surface moduli decrease the probability of the disturbance (i.e. *dampen the spatial fluctuations*). The hydrodynamic influence associated with this surface moduli effect is often qualitatively expressed as a Gibbs–Maringoni stabilization mechanism. Some time ago, Lucassen and Hansen demonstrated experimentally that surfactant monolayers do indeed have a strong dampening effect on surface fluctuations.

The film size can also have an influence on the energetics of the spatial fluctuations. This effect was originally identified by Vrij, and is also revealed in equation (21.9) by scaling the film diameter with the wavelength of the disturbances. In summary, for very small films λ will be restricted by the film diameter and consequently only short-wavelength disturbances are possible. Thus, when the film dimensions restrict the wavelength for a disturbance, a fixed-amplitude wave will expend more energy and the disturbance will be less probable in these wavelength-restricted films. That is, small metastable common black films

should be less susceptible to spatial fluctuations, and hence show an increased stability. The actual film size where this becomes important depends on the system. However, Vrij has shown that spatial fluctuations can be significantly dampened in micron-sized films.

4.3 Surfactant density fluctuations

Interfacial surfactant density fluctuations (see Figure 21.14(b)) are another phenomenon not accounted for in a classical DLVO description of thin-film forces. For ionic surfactants, these fluctuations induce charge fluctuations which in turn can influence the height of the DLVO barrier, $\Delta\Pi_{\max}$. Applying a standard statistical thermodynamic approach to the interface provides a simple method for investigating which physical properties influence surfactant density fluctuations at the air–water interface. Analogous to bulk density fluctuations, surface density fluctuations can be expressed by the following:

$$\frac{\langle(\Delta\Gamma)^2\rangle}{\langle\Gamma\rangle^2} = \frac{kT}{\Gamma^2 a} \left(\frac{d\Gamma}{d\mu}\right)_T$$

where the right-hand side of the above equation represents the mean-square relative deviation from the mean of the surfactant adsorption, μ is the chemical potential and a is the area over which the surface fluctuation is considered. In addition, surface thermodynamics provide the following relationship:

$$\left(\frac{d\Gamma}{d\mu}\right)_{T,N} = \frac{\Gamma^2}{\varepsilon_0}$$

Substitution of this expression into the previous equation reveals a direct analogy between the role played by the surface elasticity (i.e. Gibbs elasticity) and the bulk compressibility in modulating density fluctuations:

$$\text{Adsorption-density fluctuations} \quad \frac{\langle(\Delta\Gamma)^2\rangle}{\langle\Gamma\rangle^2} = \frac{kT}{\varepsilon_0 a} \quad (21.10a)$$

$$\text{Bulk-density fluctuations} \quad \frac{\langle(\Delta\rho)^2\rangle}{\langle\rho\rangle^2} = \frac{kT\kappa}{v} \quad (21.10b)$$

Here, ρ represents the bulk density, κ is the bulk compressibility factor and v is the molar volume. This analogy demonstrates the notion that compressibility is inversely related to elasticity.

Finally, we can express the probability of having a given fluctuation, P_Γ , by the following:

$$P_\Gamma \sim c_\Gamma \exp\left(-\frac{\Delta\Gamma^2}{2\langle\Delta\Gamma^2\rangle}\right)$$

and with the help of equation (21.10a) we find that the probability to expose a bare surface of the size a , as depicted in Figure 21.14(b), becomes:

$$P_{\Gamma} \sim c_{\Gamma} \exp\left(-\frac{\varepsilon_0 a}{KT}\right)$$

The charge fluctuations associated with the ionic surfactant density fluctuations described by this expression will likely become important when a is of the order of the film thickness and when the time-scale for film rupture (or transition) is close to that of the fluctuation period. It is important to note that high surface elasticities will diminish the probability of surfactant density fluctuations, and thus produce films less sensitive to these fluctuation phenomena.

Although the above discussions are somewhat qualitative and only consider thermally induced fluctuations, they do provide an important physical insight concerning film rupture, namely that the surface elasticity plays a key role in dampening both spatial and density fluctuations in foam and emulsion films. When these fluctuations are dampened, the probability of overcoming the activation barrier which holds a film in a metastable state is lower and the film will be more stable. This solidifies the intuitive notion that not only is the height of the activation barrier important, but also the system's ability to resist disturbances. In addition, these simplified analyses provide a clear picture of how the surface elasticity influences the energetics of the film-rupture process. Whether or not disturbances are thermally or mechanically induced, a cohesive surfactant monolayer with a broad-frequency, high surface elasticity will promote film stability.

5 REFERENCES

- Derjaguin, B. V., Churaev, N. V. and Miller, V. M., *Surface Forces*, Kitchener, J. A. (Ed.), Consultants Bureau, New York, 1987.
- Israelachvili, J. N., *Intermolecular and Surface Forces*, 2nd Edn, Academic Press, San Diego, CA, 1992.
- Scheludko, A., Thin liquid films, *Adv. Colloid Interface Sci.*, **1**, 391–464 (1967).
- Ivanov I. B., (Ed.), *Thin Liquid Films, Fundamentals and Applications*, Surfactant Science Series, Vol. 29, Marcel Dekker, New York, 1988.
- Exerowa, D. and Kruglyakov, P. M., *Foam and Foam Films*, Elsevier, Amsterdam 1998.
- Bergeron, V., Measurement of forces and structure between fluid interfaces, *Curr. Opinion Colloid Interface Sci.*, **4**, 249–255 (1999).
- Bergeron, V., Forces and structure in thin-liquid films, *J. Phys., Condensed Matter*, **11**, 215–238 (1999).
- Adamson, A. W., *Physical Chemistry of Surfaces*, 3rd Edn, Wiley, New York, 1976.
- Vasicek, A., *Optics of Thin Films*, North-Holland, Amsterdam, 1960.
- Duyvis, E. M., The equilibrium thickness of free liquid films, *Ph.D. Thesis*, University of Utrecht, 1962.
- Bergeron, V., Forces and structure in surfactant-laden thin-liquid films, *Ph.D. Thesis*, University of California, Berkeley, CA, 1993.
- Hunter, R. J., *Foundations of Colloid Science*, Vol. 1, Clarendon Press, Oxford, UK, 1987.
- Israelachvili, J. N. and Wennerstrom, H., Entropic forces between amphiphilic surfaces in liquids, *J. Phys. Chem.*, **96**, 520–531 (1992).
- Overbeek, J. Th. G., Black soap films, *J. Phys. Chem.*, **64**, 1181–1185 (1960).
- Lyklema, J. and Mysels, K. J., A study of double layer repulsion and van der Waals attraction in soap films, *J. Am. Chem. Soc.*, **87**, 2539–2546 (1965).
- Pollard, M. L. and Radke, C. J., Density functional theory of micelle structuring in thin micellar liquid films, *J. Chem. Phys.*, **8**, 6979–6985 (1994).
- Goddard, E. D. and Ananthapadmanabhan, K. P., *Interactions of Surfactants with Polymers and Proteins*, CRC press, Boca Raton, FL, 1993.
- Bergeron, V., Disjoining pressures and film stability of alkyltrimethylammonium bromide foam films, *Langmuir*, **13**, 3474–3482 (1997).
- Vrik, A., Possible mechanisms for the spontaneous rupture of thin, free liquid films, *Discuss. Faraday Soc.*, **42**, 23–33 (1966).
- De Vries, A. J., Foam stability, Part V. Mechanism of film rupture, *Recl. Trav. Chim. Pays-Bas*, **77**, 441–461 (1958).

CHAPTER 22

Measuring Adsorption

Bengt Kronberg

Institute for Surface Chemistry, Stockholm, Sweden

1	Introduction	435	2.7	Surface tension	438
2	Adsorption at Particle Surfaces	436	2.8	Serum replacement method	440
	2.1 Separation of particles from the bulk solution	436	2.9	Determination of adsorbed amount by chromatographic retention	442
	2.2 Determination of surfactant concentration	437	2.10	Direct measurement of surfactant adsorption on particles	443
	2.3 Refractive index	437	3	Measurement of Surfactant Adsorption at a Solid Macroscopic Surface	443
	2.4 UV/visible spectroscopy	437	4	References	444
	2.5 Electrical conductivity	438			
	2.6 Potentiometry	438			

1 INTRODUCTION

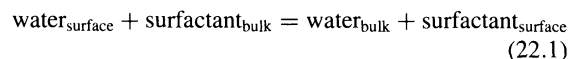
Adsorption of surfactants at solid surfaces is one of the key issues in technical surface chemistry. In, for example, one litre of a 50% solids latex suspension with a particle size of 0.2 mm there is a total particle surface exceeding 15.000 m². Thus, it is not surprising that the surface chemistry, including the adsorption, determines the properties of such suspensions.

The adsorption is most commonly characterized by the adsorption isotherm, which is obtained when the adsorbed amount of surfactant is plotted versus the surfactant solution concentration in equilibrium with the surface. The adsorption isotherm gives information on the maximum total amount of surfactant that can be adsorbed on the surface. It also gives information on the affinity of the surfactant towards the surface.

Adsorption can be viewed as a partitioning of surfactant and water between the bulk liquid phase and the surface phase. If the surfactants exhibit some affinity for the surface, albeit small, the surfactant concentration at the surface will exceed that in the bulk solution.

Since surfactants are prone to self-aggregate, there will be a larger probability of self-assembly at the surface than in the bulk solution. The driving force for this is the well-known hydrophobic effect, namely the hydrocarbon moieties of the surfactants tend to aggregate in order to avoid contact with the water molecules.

By viewing the adsorption as a partitioning, we can set up the following equilibrium for the surfactant and water in the surface phase and in the bulk liquid phase:



with the following expression for the equilibrium constant:

$$K^{\bullet} = \frac{[\text{water}]_{\text{bulk}} [\text{surfactant}]_{\text{surface}}}{[\text{water}]_{\text{surface}} [\text{surfactant}]_{\text{bulk}}} \quad (22.2)$$

The concentration of water in the bulk liquid phase can be considered constant, irrespective of the surfactant bulk concentration, due to the very low surfactant concentrations (in the order of 10⁻⁶ in units of mole fraction). If we express the surfactant concentration in terms of surface coverage, Θ , and realize that the water

concentration at the surface is $(1 - \Theta)$, we then obtain the following expression:

$$K = \frac{\Theta}{(1 - \Theta)C} \quad (22.3)$$

where C is the surfactant bulk concentration and K is a constant. The equation can be readjusted to the more familiar Langmuir-type expression, as follows:

$$\Theta = \frac{KC}{1 + KC} \quad (22.4)$$

The surface coverage is normally estimated from the following:

$$\Theta = \frac{\Gamma}{\Gamma_M} \quad (22.5)$$

where Γ_M is the maximum adsorbed amount of surfactant. By inserting this expression into the previous one, we find:

$$\frac{1}{\Gamma} = \frac{1}{\Gamma_M} + \frac{1}{\Gamma_M K} \frac{1}{C} \quad (22.6)$$

and thus the Γ_M and K values can be obtained from a plot of $1/\Gamma$ over $1/C$, where the intercept gives Γ_M and the slope ($= 1/\Gamma_M K$) yields the equilibrium constant, K . It should be noted, however, that such a procedure is very sensitive to the experimental values obtained at low concentrations at the expense of those obtained at higher concentrations. In order to compensate for this, one should also make a plot of C/Γ versus C according to the following:

$$\frac{C}{\Gamma} = \frac{1}{\Gamma_M K} + \frac{C}{\Gamma_M} \quad (22.7)$$

which is obtained from equation (22.6). From such a plot, the slope yields the Γ_M , while the intercept gives the K . This plot is more sensitive to the experimental points obtained at higher concentrations. Normally, an average of Γ_M and K , as obtained from the two plots, should be used. Finally, it is recommended to plot the calculated adsorption isotherm together with the experimental data, in order to elucidate how well the equation and parameters describe the isotherm.

From the maximum adsorbed amount of surfactant, Γ_M , one calculates the cross-sectional area per surfactant molecule in the close-packed monolayer, A_2 (expressed in $\text{\AA}^2/\text{molecule}$) through the following:

$$A_2 = \frac{M}{\Gamma_M 6.023} \quad (22.8)$$

where M is the molecular weight of the surfactant and Γ_M is expressed in mg/m^2 .

2 ADSORPTION AT PARTICLE SURFACES

The adsorption of surfactants at the surface of particles is most commonly measured. The reason for this being that particles have a large surface area which facilitates the measurements. In most cases, the adsorption is obtained through the measurement of the depletion of surfactants from solution, generally known as the *depletion* method. Here, a surfactant solution of known concentration, C_0 , and volume, V , is mixed with the particles. The system is then left to attain equilibrium, which normally takes 1–24 h. The particles are thereafter separated from the bulk solution and the surfactant concentration is determined, thus giving C_{eq} . The adsorbed amount is then obtained from $V(C_0 - C_{eq})$. This quantity is normally expressed by either the total mass or the total surface area of the particles. The latter quantity is, of course, preferred since it is a general quantity which is not specific for the particular sample of the particles being used. It requires the knowledge of the specific surface area of the particles, a_{sp} . Hence, we have the following:

$$\Gamma = \frac{(C_0 - C_{eq})V}{ma_{sp}} \quad (22.9)$$

where m is the total mass of the particles.

The specific surface area of a powder is conveniently determined through a Brunauer–Emmett–Teller (BET) analysis. Here, the adsorption of nitrogen is determined and then analysed. Since the cross-sectional surface area of a nitrogen molecule is known, the total area of a powder sample can therefore be determined. BET analysis is conveniently carried out by using commercial instruments build solely for this purpose. In some cases, the solid sample cannot be treated (dried) to give a dry powder. In such cases, the specific surface area can be determined by the adsorption of a surfactant, with a known cross-sectional surface area, that adsorbs as a monolayer at that specific surface. This method is, of course, rather uncertain since it requires the assumption of monolayer adsorption.

2.1 Separation of particles from the bulk solution

Most commonly, the particles are separated through ultracentrifugation, which generates a g force of ca. 10^5 times the normal gravitational force. Another alternative is to separate by filtration. Here, it should be noted that normal cellulose acetate filters leak some organic material and they should therefore be washed

by passing distilled water through them. Normally, an amount of 100 ml is sufficient to clean the filters. The amount leaked from the filters can easily be followed by measurements of the UV spectrum in the region 250–190 nm.

2.2 Determination of surfactant concentration

The crucial point in measuring surfactant adsorption is to determine the surfactant concentration in the bulk solution. There are various methods to determine the bulk concentration, with the most common ones being described below.

2.3 Refractive index

Since the refractive index of an organic substance, such as a surfactant, is different from that of water it should in principle be possible to determine the surfactant concentration through measurement of the refractive index of the solution. This is indeed a feasible way. However, the method suffers from the drawback that it is not specific. Thus, small amounts of organic material will contribute to the total refractive index of the solution. Since surfactant concentrations are normally very low, small amounts of impurities will cause large variations in the measured surfactant concentration. Furthermore, the adsorbed amount is obtained as the difference between two measured concentrations (equation (22.9)) and is thus very sensitive to variations in the determined concentrations. One such source of organic impurity was mentioned previously – this is the material that is leaked from cellulose acetate filters when separating the particles from the solution by filtration. Thus, the non-specificity of this approach renders it less attractive as a method to determine the adsorption through depletion of surfactants in the solution.

2.4 UV/visible spectroscopy

Some surfactants have a built-in chromophore and are hence easily characterized with respect to concentration, C , through UV/visible (vis) spectroscopy. Here, we make use of the Lambert–Beer law relating the intensity of the transmitted light, I , to the concentration of the chromophore, as follows:

$$\frac{I}{I_0} = e^{-\varepsilon cd}$$

where I_0 is the intensity of the incident light, ε is the molar absorption coefficient and d is the thickness of the cell.

Since each surfactant molecule has one chromophore group, UV/vis spectroscopy determines the number of molecules per unit volume. This is in contrast to the refractive index where the mass per unit volume is determined. This difference is unimportant as long as the surfactant is monodisperse. If the surfactant is polydisperse, however, which is the case for most technical samples, the method of concentration determination will have a large impact on the results (as will be discussed below).

Let us, for the sake of simplicity, assume that we have a bimodal nonionic surfactant sample with an octyl- or nonylphenol hydrophobe, attached to the polyoxyethylene chain, adsorbing at a hydrophobic surface. Let us give the short-EO-chain surfactant a total molecular weight which is half of that of the long-EO-chain surfactant. If a solution of the two species are brought into contact with a hydrophobic surface, the short-EO-chain surfactant species, which is more hydrophobic, will preferentially adsorb at the surface. Let us further assume that originally the two species were present in equivalent amounts (on a molar basis) and that only the short-EO-chain surfactant adsorbs (to 100%). Thus, the longer-EO-chain surfactant remains in the solution. Measuring the solution concentration using UV/vis spectroscopy, we will find that half of the surfactant molecules are adsorbed, while the other half remain in solution. On the other hand, when measuring the solution concentration by using the refractive index we find that one third of the surfactant species adsorb on the surface while two thirds remain in solution. Thus, it is indeed very important to recognize the influence on the method of surfactant analysis on the interpreted adsorption. Of course, in a monodisperse surfactant sample, where only one species is present, the analysis method is not important for the results.

Unfortunately, not all surfactants carry a chromophore. If the surfactant is charged, be it anionic or cationic, the concentration can be determined by a two-phase titration. In this technique, the aqueous surfactant solution is brought into contact with an organic phase, normally chloroform. A second surfactant, carrying a chromophore and an opposite charge to the original surfactant, is then added to the aqueous solution. The two surfactants will form a water-insoluble complex which is transferred into the organic phase. Using UV/vis spectroscopy to determine the concentration of surfactant complex in the organic phase then facilitates

the determination of the adsorbed amount of a charged surfactant not carrying a chromophore.

An elegant form of the two-phase titration method for the determination of an anionic surfactant is the following. Benzethonium chloride (Hyamin 1622, Rohm and Haas) is used as a cationic surfactant, while a mixture of diimidium bromide (cationic) and disulfon blue VN (anionic) is used as the indicator. The anionic surfactant forms a pink complex with the cationic diimidium bromide, which dissolves in the chloroform. Upon titration with Hyamin 1622, a stronger complex is formed with the anionic surfactant. Hyamin 1622 thus displaces the diimidium bromide and the organic phase is decolorized, while the aqueous phase turns red. Excess Hyamin 1622 forms a blue salt with the anionic disulfon blue VN, which then dissolves in the organic phase.

2.5 Electrical conductivity

Since ionic surfactants carry a charge with an accompanying counterion, these will contribute to the electrical conductivity of aqueous solutions. Thus, by measuring the electrical conductivity, the adsorption of ionic surfactants can then be determined.

However, conductivity measurements should be used with caution. The reason for this being that the equivalent conductance values of salts such as charged surfactants with their counterions are rather low (by a factor of 5–7) compared to that of hydrogen, or hydroxyl, ions. Thus, the pH-dependence of the conductance could overshadow the contribution from the surfactants and one therefore needs to keep a good control of the pH. This is particularly important for surfactants at low concentrations.

2.6 Potentiometry

In potentiometry, the electrical potential caused by the presence of a specific ion is measured. The most well-known example is the pH electrode, which measures the hydrogen ion activity, or concentration, in solution.

There are specific surfactant electrodes available for analysing surfactant solutions. Here, the surfactant selectively penetrates the membrane of the electrode, thus causing an electrical potential. One fundamental problem of potentiometry is that the measured potential is not linearly dependent on the concentration of the species, but rather proportional to the logarithm of its concentration, as depicted in Figure 22.1. Thus, in measuring adsorption the accuracy is low since the adsorbed amount reflects a more hydrophobic system than is used

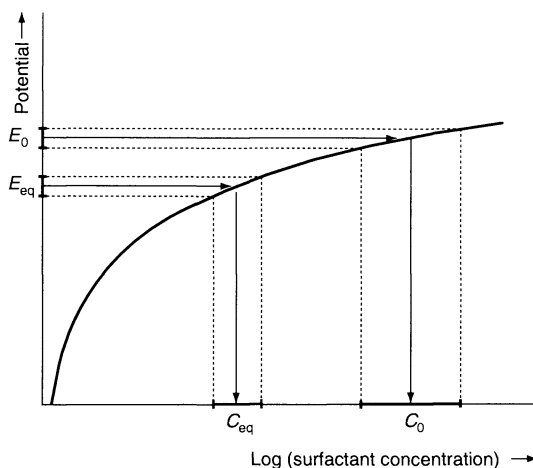


Figure 22.1. The measured electrical potential from a surfactant electrode varies logarithmically with surfactant activity, or concentration, resulting in a low accuracy in the determination of Γ (equation (22.9))

amount is obtained from the difference between two concentrations according to equation (22.9), and as illustrated in the figure.

2.7 Surface tension

The most obvious method to determine the surfactant concentration is to measure the surface tension of the solution. The surface tension gradually decreases as a function of surfactant concentration up to the CMC of the surfactant, as depicted in Figure 22.2. At surfactant concentrations above the CMC, the surface tension does not change significantly. Thus, the measurements must be performed at surfactant concentrations below the CMC.

Measuring surfactant concentration by using surface tension suffers from the same drawback as the potentiometric measurements, i.e. the change in surface tension varies with the logarithm of the surfactant concentration, rendering a low accuracy in the calculated adsorbed amount. Another drawback is due to the fact that the method is very sensitive to the most surface-active species in the measured sample. In the adsorption of a polydispersed surfactant sample on a hydrophobic surface, the most hydrophobic surfactant species will adsorb and the more hydrophilic species will remain in the solution. In the calibration, however, the original sample is used and hence the calibration

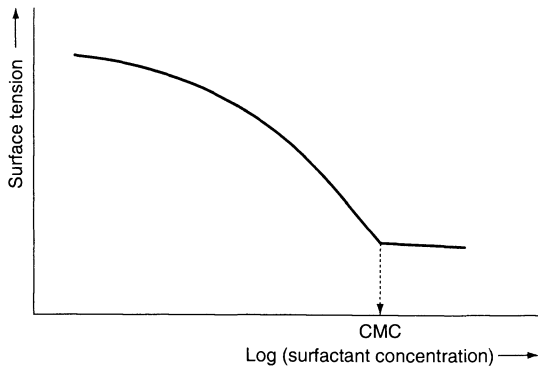


Figure 22.2. The surface tension of a surfactant decreases continuously with increasing concentration, up to the critical micelle concentration (CMC)

in the measurements. Hence, the determined surface tension of a surfactant solution which has been in contact with hydrophobic particles is higher than it should be (due to the absence of the most hydrophobic species), (see Figure 22.3). Since the original solution is used for the calibration, the measured surfactant concentration is lower than if the right calibration curve were

used (see Figure 22.3). The resulting adsorption, as calculated from equation (22.9), is hence higher according to the figure.

One way to circumvent the problem raised above is to measure the dynamic surface tension, instead of the equilibrium surface tension (described so far). The dynamic surface tension is the surface tension measured at short times after a surface has been formed and hence it is a non-equilibrium property. If an imaginary cut is made through a liquid and the molecules are not allowed to relax into an equilibrium state, the surface tension at the cut section will be the arithmetic average of the surface tensions of the present components. After equilibrium is reached, however, the most surface-active species, the one with the lowest surface tension, will be found in excess at the liquid/air surface. This relaxation of the surface tension, from an arithmetic mean to an equilibrium surface tension, is called the *dynamic surface tension*. If the surface tension is measured at short times after a surface has been formed, it reflects the surfactant bulk concentration, without the preferential adsorption of the more surface-active species which are present in small amounts. Hence, dynamic surface tension measurements are preferred for determining

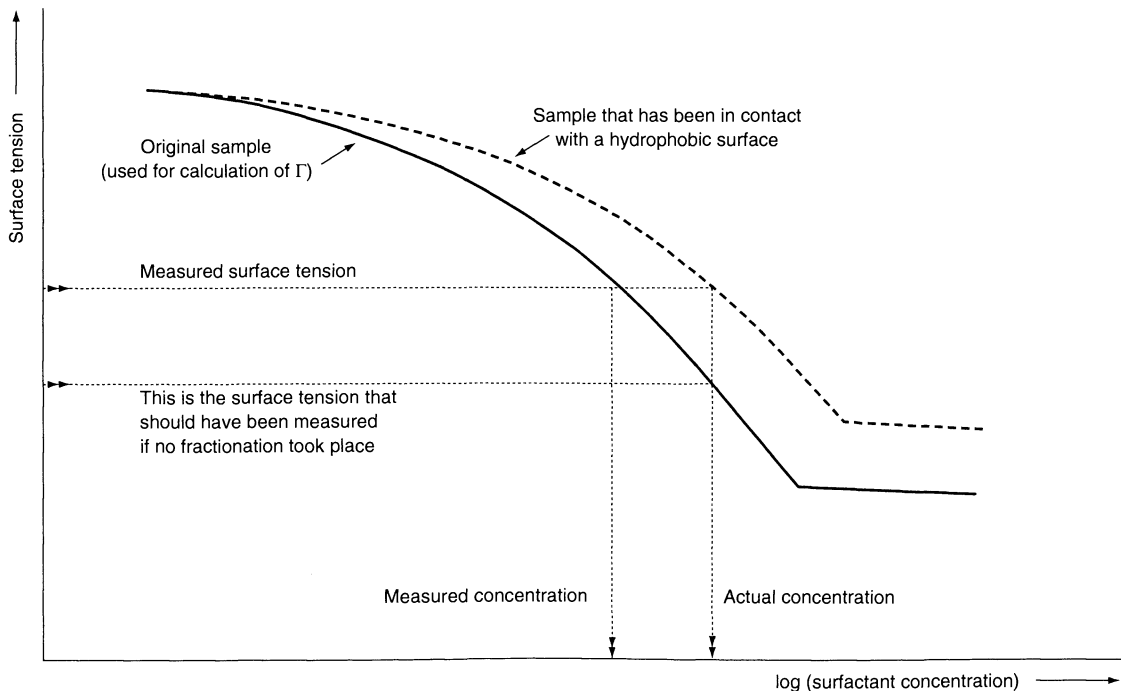


Figure 22.3. Due to the fractionation of a polydispersed surfactant sample, the measured adsorption is larger than the real adsorption if the surfactant concentration is determined by surface tension

the surfactant adsorption by measurements of surface tension. Dynamic surface tension can be determined by the maximum bubble method. Here, a capillary is immersed into the surfactant solution and a gas is then allowed to flow through it. A pressure sensor measures the pressure required to form gas bubbles and this pressure is proportional to the surface tension. This technique allows surface tensions to be determined at times down to 1 ms.

One advantage in using the surface tension, however, is that one does not need to separate the particles from the solution in order to measure the surfactant concentration. Surface tension measurements can be performed in a slurry, or emulsion, since the particles do not adhere to the liquid/air surface, i.e. they are not surface-active. If the surfactant concentration is above the CMC, however, the system needs to be diluted. In this case, the particles need to be separated from the solution since otherwise a dilution of the system will cause desorption of the adsorbed surfactants.

A special case of using surface tension for the determination of surfactant concentration is the “soap titration method” (1). Here, the particle dispersion is subjected to measurements of surface tension under the addition of surfactant solution. Knowing the total particle surface area and the surface tension as a function of the total amount of added surfactant, it is possible to directly calculate the adsorption isotherm. The soap titration rests on the assumption that equal surface tension corresponds to equal surfactant activity (concentration) in the solution, and hence equal values of surfactant adsorption on the particle surface.

For a series of different particle concentrations, titration curves are obtained by plotting the measured surface tension versus the total weight of surfactant added, as shown schematically in Figure 22.4(a). From these titration curves, we obtain values of total surfactant needed to render a certain surface coverage (as discussed below).

Consider a dispersion with a particle concentration p (in weight fraction). The total added amount of surfactant, at a certain surface tension γ , is VC_0 , where V is the added volume of surfactant solution with a concentration of C_0 . The total adsorbed amount of surfactant is then $VC_0 - V_{\text{tot}}C(\gamma)$, where $C(\gamma)$ is the equilibrium surfactant concentration corresponding to the specific surface tension, γ , and hence corresponding to the adsorption $\Gamma(\gamma)$, and V_{tot} is the total volume of the dispersion. Setting the particle specific surface area to a_{sp} we then have the following:

$$\Gamma a_{\text{sp}} p = VC_0 - V_{\text{tot}}C(\gamma) \quad (22.11)$$

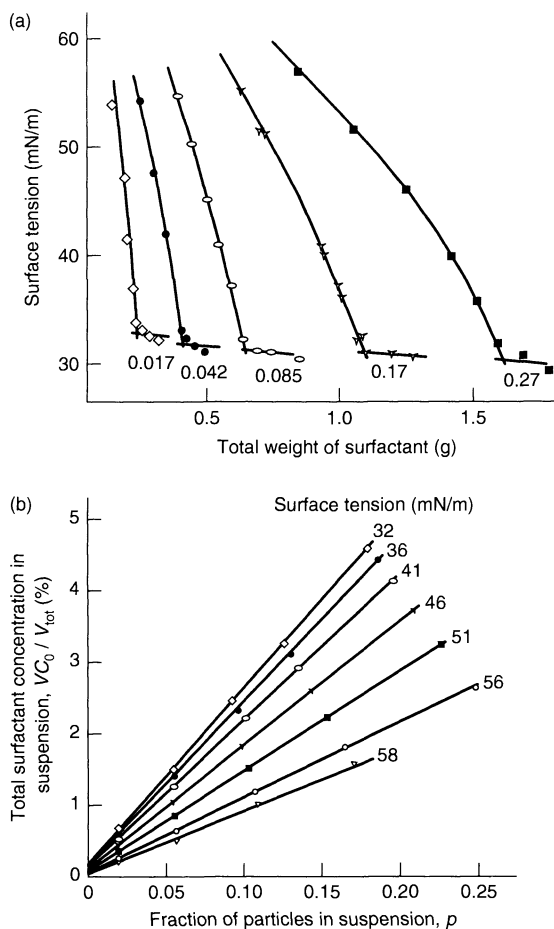


Figure 22.4. In the soap titration method, the surface tension is determined with added surfactant for various batches of dispersions, with solid contents p . (b) Plots of VC_0 / V_{tot} versus p according to the soap titration method, rendering the $\Gamma(\gamma)$ and $C(\gamma)$ from the slope and intercept, respectively, according to equation (22.11)

and hence plots of VC_0 / V_{tot} versus p for the various surface tensions give straight lines with a slope which renders $\Gamma(\gamma)$ and an intercept equal to $C(\gamma)$, which is the equilibrium surfactant concentration at this surface coverage. Figures 22.4(a) and 22.4(b) show schematically such a construction for the determination of the adsorption isotherm.

2.8 Serum replacement method

In the serum replacement technique (2, 3), the dispersion is confined in a stirred flow cell. The confinement of the

particles is achieved by a filter with a pore size less than the particles. The adsorption isotherm can be determined either by measuring the desorption from a suspension containing the surfactant or by the adsorption of the surfactant to a surface of the dispersed particles.

In the latter case, the dispersion is first cleaned by flowing pure water through the cell until the difference in conductivity between the inlet water and the effluent is less than 10 mS m^{-1} . Thereafter, a surfactant solution is allowed to flow slowly through the cell and its concentration is determined at the outlet. Typical conditions for such a set-up are as follows: cell volume, 20 ml; effluent batches, 3–5 ml; total particle surface area, 10 m^2 ; surfactant inlet concentration, 2–3 times the CMC; residence time of the surfactant solution, 1 h.

A schematic of a serum replacement cell is shown in Figure 22.5. Figures 22.6(a) and 22.6(b) show, respectively, a surfactant concentration profile obtained from a serum replacement set-up and the corresponding isotherm. Important parameters for such a set-up are the flow-through speed (too high a stirring speed will clog the filter, while too low a speed will give a low accuracy to the results) and the stirring rate (too high a stirring rate might cause coagulation, while too low a rate will cause the filter to clog). The flow-through speed should be adjusted such that the residence time of the surfactant solution in the cell is at least 1 h in order to assure that equilibrium has been attained.

If C_0 and C are the concentrations (in mass per unit volume) in the inlet and effluent, respectively, a mass balance will give the following expression for the

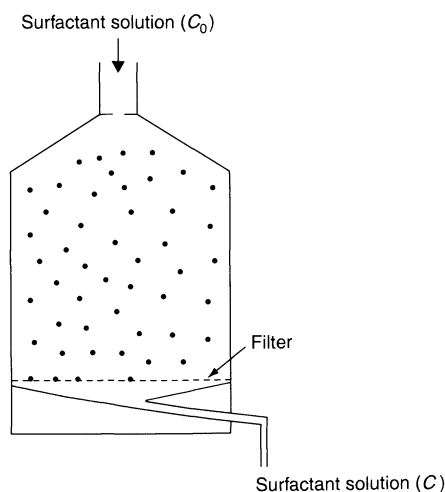


Figure 22.5. Schematic of the serum replacement cell for determination of surfactant adsorption isotherms

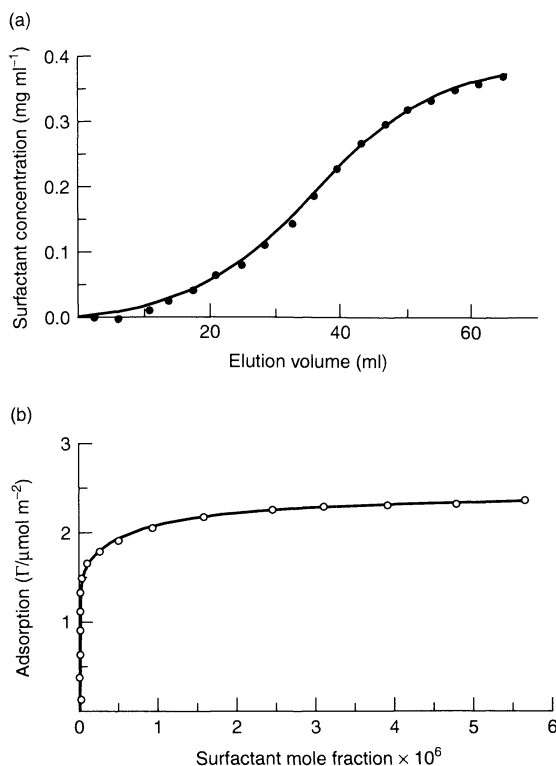


Figure 22.6. (a) Surfactant concentration profile from an experiment where a surfactant solution is flowed through a serum replacement cell containing a dispersion, and (b) the corresponding isotherm

accumulation of surfactant in the cell during the flow of a volume dV of solution through the cell, as follows:

$$(C_0 - C) dV = V_c dC + A d\Gamma \quad (22.12)$$

where dC and $d\Gamma$ are the accompanying changes in solution and surface concentrations, respectively. Here, A is the total particle surface area and V_c is the cell volume.

The adsorption isotherm is obtained from the following expression, which is obtained from an integration, or as in this case, a summation over batches, of equation (22.12):

$$\Gamma_n = \frac{1}{A} \left[\sum_{i=1}^n \Delta V_i (C_0 - C_i) - C_{n,c} V_c \right] \quad (22.13)$$

where ΔV_i is the volume of batch i of the effluent and C_i is its surfactant concentration. The concentration inside the serum replacement cell, $C_{n,c}$ is obtained graphically by plotting C_i versus the total eluted volume. Note that

$C_i \neq C_{nc}$ since C_i is the mean concentration of batch i while $C_{n,c}$ represents the concentration of the last drop in that batch, assuming a negligible dead-volume.

Alternatively, the adsorption isotherm can be determined from a desorption measurement of a surfactant provided that the surfactant is not too strongly adsorbed. The equations above also apply for this situation now with $C_0 = 0$. It should be noted that strongly adsorbed surfactants, such as nonionics on latex surfaces, do not wash out well and hence measuring by desorption is not recommended.

2.9 Determination of adsorbed amount by chromatographic retention

Chromatographic retention is due to the equilibrium distribution of a probe molecule, the surfactant, between the stationary phase, the column, and the mobile phase. The retention is expressed in terms of a capacity factor, k' , relating the retention volume to the hold-up volume in the system, as follows:

$$k' = \frac{V_R - V_{MK}}{V_{MK}} = \frac{V_N}{V_{MK}} \quad (22.14)$$

where V_N is the net retention volume, i.e. the difference between the retention volume of the surfactant, V_R , and the retention volume of a marker, V_{MK} , i.e. a probe molecule that does not interact with the column, giving the mobile phase hold-up volume. The net retention volume is related to the affinity of the stationary phase,

i.e. the column, through the following:

$$V_N = K_C V_P + K_{ads} A \quad (22.15)$$

where V_P is the total volume of the stationary phase which is accessible to the probe molecule. If the stationary phase is a solid, $V_P = 0$; A is the total surface area of the stationary phase and K_C and K_{ads} are the partition coefficients of the surfactant for the absorption and adsorption, respectively. The latter is related to the distribution coefficient in equation (22.2) and is thus related to the interaction between the surfactant and the surface. The use of equation (22.15) requires a surfactant concentration "at infinite dilution", i.e. when there are no surfactant-surfactant interactions and when the surface is not covered by surfactants.

For the determination of surfactant adsorption, higher surfactant concentrations must be used. The adsorption is calculated from the integrated version of equation (22.15) (with $V_P = 0$), as follows:

$$\Gamma_i = \frac{1}{A} \int_0^{C_i} V_N dC_i \quad (22.16)$$

where C_i is the concentration of the surfactant in the mobile phase, which in turn is proportional to the height of the chromatogram (4). Adsorption broadens the chromatographic peak by tailing, as illustrated in Figure (22.7). The adsorbed amount is calculated from this tailing through the following:

$$\Gamma_i = \frac{n_i I_1}{A I_2} \quad (22.17)$$

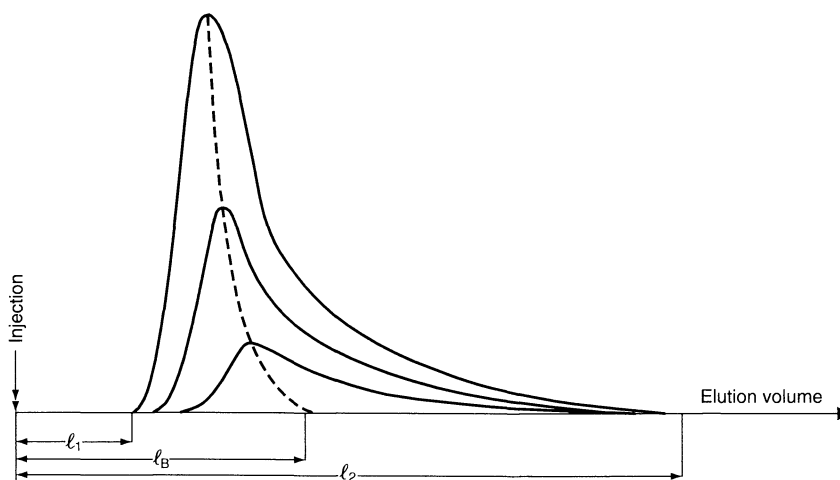


Figure 22.7. Schematic chromatograms of three surfactant sample concentrations showing the tailing of the peaks (see text for details)

where I_1 is the area under the following lines in the figure: ℓ_B , the dashed line to the top of the peak, a line drawn parallel to the X -axis from the top of the peak to the time of injection (not shown in the figure), and finally a line drawn horizontally down to the X -axis at the point of injection. The integral I_2 is the peak area, as follows:

$$I_2 = \int_{\ell_1}^{\ell_2} h d\ell \quad (22.18)$$

where ℓ_1 and ℓ_2 are the retention times (or volumes) at the beginning and at the end of the chromatographic peak. Thus, the peak shape gives the adsorption of the surfactant at the solid surface of the column material.

2.10 Direct measurement of surfactant adsorption on particles

One technique to directly determine the adsorption isotherm of surfactants on particle suspensions is by utilizing neutron scattering. The advantage of using a neutron beam for scattering experiments is the large difference in scattering cross-sections between hydrogen and deuterium. It is indeed often possible to find a mixture of H_2O and D_2O that balances the neutron scattering of a particle but not its adsorbed surfactant layer. Alternatively, the scattering from the dispersion medium can be eliminated. If the particles are sufficiently small, the volume of the surfactant layer occupies a considerable volume when compared to the particle volume, thus making it possible to determine both the adsorbed amount and the thickness of the layer. For N_p small particles, each with a volume V_p , the intensity, I , of the scattered neutrons is expressed as follows:

$$I = K(\rho_p - \rho_s)N_p V_p^2 \quad (22.19)$$

where K is a constant, and ρ_p and ρ_s are the neutron scattering length densities of the particles and solvent, respectively. Normally, the experiments are interpreted at zero scattering angle, which is obtained by extrapolation of the scattering at various angles, ϕ , in a plot where the scattering is plotted as a function of $\sin^2(\phi/2)$. The experiments are performed in a H_2O/D_2O mixture such that the scattering length density of the solvent is zero. In such systems, the scattering from the adsorbed layer is directly dependent on the number of molecules adsorbed, and hence a direct determination of the adsorption is possible (5).

3 MEASUREMENT OF SURFACTANT ADSORPTION AT A SOLID MACROSCOPIC SURFACE

The most advantageous method for determining the surfactant adsorption at macroscopic solid surfaces is *ellipsometry*. Here, elliptically polarized light is reflected at the surface, whereupon its ellipticity will change. The principle of the method is discussed below. The main advantages with this method are its accuracy (less than a monolayer can easily be determined), the fact that it measures the adsorption *in situ*, i.e. in the solution, and that due to a high time resolution it is possible to determine the kinetics of adsorption or desorption. In addition, the method is non-destructive. One prerequisite when using ellipsometry is that the surface must be able to reflect light and it cannot be birefringent. In addition, the solution through which the light is travelling must be clear.

Ellipsometry is based on the measurement of changes in the ellipticity of polarized light upon reflection at a surface. The ellipticity can be described by the ratio and phase difference of two plane-polarized light waves, one oscillating in parallel with the plane of incidence and the other perpendicular to it. When the two plane-polarized light waves have a phase shift of 90° , they are circularly polarized.

Upon reflection of light at a surface, the polarization of these light waves changes and hence the ellipticity is changed. In the technique known as *null ellipsometry*, this change is compensated by the use of a retardation plate, thus resulting in linearly polarized light reflected from the surface. The position of the optical components then provides information on the ratio and changes of the light components due to the reflection. (A retardation plate is made of a material with different refractive indexes in two perpendicular directions (fast and slow axes). A light wave parallel to the slow axis will be retarded compared to the light wave parallel to the fast axis. The retardation plate therefore induces a phase shift between the waves, which is dependent on the thickness of the plate. Thus, a retardation plate produces elliptically polarized light from linearly polarized light. (Of course, the opposite is also true, i.e. the retardation plate will produce linearly polarized light from elliptically polarized light.)

The change in the state of polarized light upon reflection is characterized by the amplitude reflection coefficient, R , of the plane parallel (p) and perpendicular (s) to the plane of incidence, as follows:

$$R_p = \frac{E_p^r}{E_p^i} \quad (22.20a)$$

and:

$$R_s = \frac{E_s^r}{E_s^i} \quad (22.20b)$$

where E is the amplitude and the indices “i” and “r” represent incident and reflected light, respectively.

In analysing the reflection from a thin film at a surface, such as that created by adsorbed surfactants, one has to take into account (i) the reflection at the film/water interface, (ii) the refraction of light into the film, and (iii) the reflection at the film/substrate interface (see Figure 22.8). Thus, the R_p and R_s coefficients will now also reflect the state of the film, i.e. the film thickness, d_1 , and its refractive index, n_1 . From the latter, it is possible to calculate the adsorbed amount at the surface, Γ .

The primary data obtained from a null ellipsometer are Φ and Δ , which are easily obtained from the position of the polarizer, compensator and analyser. These quantities are related to the R_p and R_s coefficients through the following:

$$\frac{R_p}{R_s} = \tan \Phi e^{i\Delta} \quad (22.21)$$

where Δ is a function of the phase shift, given as follows:

$$\Delta = (\delta_p^r - \delta_p^i) - (\delta_s^r - \delta_s^i) \quad (22.22)$$

and Φ is related to the change in amplitude upon reflection. If the refractive indices of the medium (mostly water) and the substrate are known, it is possible to calculate the effective refractive index, n_1 , and thickness, d_1 , of the adsorbed film. Unfortunately, it is not possible to obtain an analytical expression for these quantities and an iterative process has to be applied.

Most frequently, silica or modified silica are used in ellipsometry measurements. Normally, a silicon wafer is oxidized to SiO_2 in order to increase the sensitivity

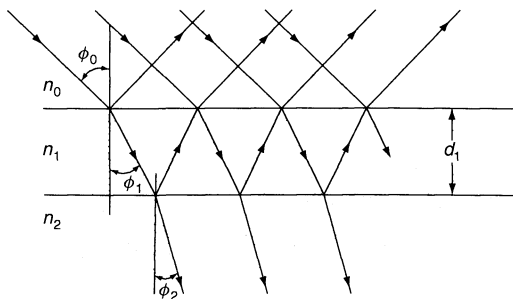


Figure 22.8. The reflection of light from a film (thickness d_1 and refractive index n_1) on top of a substrate (index “2”).

in determining the thickness of the adsorbed surfactant layer. There are then two layers, i.e. SiO_2 and surfactant layers, which affect the ellipticity of the reflected light and hence additional data are necessary in order to obtain information on the surfactant layer. This may be obtained by performing repeated measurements at different degrees of incidence of the light. Alternatively, characterization of the substrate may be performed by measurements in different surrounding media having different refractive indices to obtain the thickness and refractive index of the SiO_2 layer.

The benefits of ellipsometry when compared to other techniques used for thickness determinations are its simplicity and the fact that it is very rapid and non-destructive. This makes it possible to study the kinetics of both the adsorption and desorption of surfactants.

From the optical values obtained from ellipsometric measurements, i.e. n_1 and d_1 , it is possible to determine the adsorbed amount, Γ . This quantity is most commonly extracted from ellipsometry measurements since it is rather insensitive to the optical model used. The adsorbed amount, Γ , is evaluated from the following expression:

$$\Gamma = \frac{(n_1 - n_0)d_1}{dn/dc} \quad (22.23)$$

where dn/dc is the refractive index increment of the surfactant solution.

4 REFERENCES

1. Paxton, T. R., Adsorption of emulsifier on polystyrene and poly(methyl methacrylate) latex particles, *J. Colloid Interface Sci.*, **31**, 19–30 (1969).
2. (a) Ahmed, S. M., El-Aasser, M. S., Pauli, G. H., Poehlein, G. W. and Vanderhoff, J. W., Cleaning latexes for surface characterisation by serum replacement, *J. Colloid Interface Sci.*, **73**, 388–405 (1980); (b) Ahmed, S. M., El-Aasser, M. S., Micale, F. J., Poehlein, G. W. and Vanderhoff, J. W., Desorption of sodium lauryl sulfate from polystyrene latex particle surfaces, in *Solution Chemistry of Surfactants*, Vol. 2, Mittal, K. L. (Ed.), Plenum Press, London, 1979, pp. 853–864.
3. Kronberg, B., Käll, L. and Stenius, P., Adsorption of non-ionic surfactants on latexes, *J. Disp. Sci. Technol.*, **2**, 215–232 (1981).
4. Chuduk, N. A., Eltekov, Yu. A. and Kiselev, A. V., Study of adsorption from solutions on silica by liquid chromatography method, *J. Colloid Interface Sci.*, **84**, 149–154 (1981).
5. Harris, N. M., Ottewill, R. H. and White, J. W., Determination of adsorption of surface active agents on latex particles by small angle neutron scattering, in *Adsorption from Solution*, Ottewill, R. H. and Rochester, C. H. and Smith, A. L. (Eds), Academic Press, London, 1983, pp. 139–154.

Index – Volume 2

- absorption, molecular 243–244
- ACRPAC *see* analysis of capillary rise profile around a cylinder
- adhering bubble methods 253–254
- adhesion 125–126, 389–390
- ADSA *see* axisymmetric drop shape analysis
- adsorption
 - electrokinetics 371
 - measurement 435–444
 - thin-liquid films 416
- advancing contact angles 129–130
- Aerosol OT *see* sodium bis(2-ethylhexyl)sulfosuccinate
- aerosols 9
- AFM *see* atomic force microscopy
- ageing effects 154–155
- aggregation 15–19
 - see also* coagulation; coalescence; flocculation
- AKD *see* alkyl ketene dimer
- alcohols
 - bilayer solubilization 172
 - foaming 24
 - microemulsions 63, 64–66, 69
- alkane thiols 99–116
- alkyldimethylaminioxides (DMAOs) 196–199, 201–202, 208–210, 213
- amino acids 175–177
- Amonton friction 391
- amphiphiles
 - domain morphology 303–304, 306
 - Langmuir–Blodgett films 80–81
 - liquid crystals 300
 - microemulsions 57–58
- amphoteric surfactants
 - see also* zwitterionic surfactants
- analysis of capillary rise profile around a cylinder (ACRPAC) 268
- anionic surfactants 147
- antifoamers 143–157
- antipercolation threshold 181–182
- AOT *see* sodium bis(2-ethylhexyl) sulfosuccinate
- APGs *see* alkylpolyglycosides
- aqueous polymer solutions 400–402
- aqueous systems 143–156, 190–199
- atomic force microscopy (AFM)
 - surface forces 384–388, 390–391, 395, 397, 399–400
 - thin-liquid films 415
- attenuated total reflection (ATR) spectroscopy 101, 102
- autopoiesis 50–52
- axisymmetric drop shape analysis (ADSA) 253–254, 255–263, 264, 265–266
- azobenzene chromophore 91
- back-scatter technique 37, 39
- Berthelot's (geometric mean) combining rule 127
- BET *see* Brunauer–Emmett–Teller
- bicontinuous phases
 - characterization 352
 - domain morphology 302, 303, 306, 310–315, 316–317
 - mesophases 302, 303, 306, 310–315, 316–321
 - microemulsions 351–352
 - phase prisms 340–342
 - ringing gels 204
- Bikerman test 32–33
- bilayers 149–150, 171–173, 199–204, 211–212
 - see also* membranes, vesicles
- binary solutions 160, 162–173
- binary surfactant–water systems 166–169
- Bingham solids 190, 204
- biologically active molecules 106–109, 111–113
- birefringence 195, 206
- black films 28–29, 30, 426, 427, 431–433
- block copolymers
 - rheology 204–205
- blue laser diodes 87–89
- Boltzmann distribution law 4
- Boltzmann equation 373
- Bragg diffraction 301
- Bragg reflections 330
- brewing industry 155–156
- bridging
 - antifoaming agents 146, 149, 151
 - ceramics 430
 - measurement 402, 405
- Brownian motion 3, 13, 16, 20, 365
- Brunauer–Emmett–Teller (BET) isotherm 436
- bubble formation 418
 - see also* foams
- bubble methods
 - contact angle 253–254
 - dynamic surface tension 227–229, 232–236
 - equilibrium surface tension 217, 221–223, 235
- cadmium arachidate 82
- calcium myristate 327
- capillary phenomena
 - condensation 390
 - contact angle measurement 252, 264–266, 268, 272–274
 - penetration 120, 136–140
 - pressures 421–423, 431
 - rise 217, 218–219
- carbohydrates 17–19
- Cassie–Baxter equation 132

- cathetometers 265
- CBFs *see* common black films
- cell attachment 107, 111–113
- cell opening 41
- cell-surface interactions 17–18
- cellular foams 37
- cement foams 42
- centrifugation 358, 365, 367, 417
- chain length 245, 248
- champagne foams 416
- channel defects 319
- chemisorption 100–101
- chiral mesophases 316
- chirality 50–51
- cholesterics 299–300
- chromatographic retention 442–443
- clays 3, 8–9
- clouding
 - cloud point defoamers 148
 - curvature 338
- CMC *see* critical micelle concentration
- coagulation 15–19
- cobblestone model 383, 391
- cohesion 125–126
- cohesion energy 269–270
- collective diffusion 346–347, 350–351
- columnar mesophases 308–310
 - see also* rod-like micelles
- command surfaces 91–92
- commercial processes *see* manufacture
- commercial surfactants 63–64
- comminution 4–5
- common black films (CBFs) 427, 431–433
- competing microstructures 336–337
- competitive adsorption 429
- composite surfaces 131–132
- compressible fluids 68
- computers 89–90, 92–95
- concentration effects 287–288, 347, 380
- concrete foams 42
- condensation 4, 5–6
- condensed phases 189–190
- conductivity 213, 242, 335, 438
- contact angles
 - see also* Young equation
 - definitions 133–134
 - hysteresis 129, 130–133
 - measurement 251–280
 - particle/water interface 150
 - temperature dependence 269, 276–277
 - thin-liquid films 422
 - wetting 119–140
- contamination, films 423
- copolymers
 - rheology 204–205
- copper myristate 326
- cosurfactants 63, 64, 65–66
- Coulombic wells 430
- counterions 246
- Cox–Merz rule 211
- critical micelle concentration (CMC)
 - see also* micelles
 - foams 25–26, 28, 29
 - influencing factors 241, 245–246
 - measurement 239–249
 - micellization 190–191
 - non-aqueous media 246–248
 - self-diffusion NMR 286
 - surface forces 398–399
 - surface tension 438–439
 - surfactants 162–166
- critical surface tension 126–127
- cryo-transmission electron microscopy (Cryo-TEM) 193, 196, 198, 335, 358
- crystal growth
- cubic phases
 - domain morphology 311–314
 - rheology 204–205
 - self-diffusion 353–355
 - thermotropic behaviour 209
- cumulant analysis 366
- curvature 70–72, 160–161, 169, 301–321, 336–338, 345
- cylindrical electrophoresis chambers 376–377
- cylindrical micelles 193–194, 199
- data processing 89–90, 92–95
- DDAB *see* didodecyltrimethylammonium bromide
- de-wetting 146, 149
- Debye screening length 393–395
- Debye–Hückel equation 424
- defects 317–319
- defoamers 143, 154–155
 - see also* antifoamers; foam breaking
- deformation 388
- density fluctuations 431, 432–433
- deoxyribonucleic acid (DNA) 84, 85
- depletion method 436
- Derjaguin–Muller–Toporov (DMT) theory 389, 391
- detergency
- deuterium labelling 289–290
- diameter axisymmetric drop shape analysis (ADSA-D) *see* axisymmetric drop shape analysis
- didodecyltrimethylammonium bromide (DDAB) 181–184
- dielectric relaxation 11
- diffusion coefficient 244
- dilation 190, 206, 235, 237
- dimensional analysis 274
- 1,2-dimyristoyl-*sn*-glycero-3-phosphatidylcholine (DMPC) 50, 51–52
- Discovery space shuttle 236
- disjoining pressure 417, 424–430, 431
- Disorder–Open–Connected–Cylinder (DOC) model 181, 182–184
- dispersions
 - emulsions 55–56
 - methodology 4–5
 - monolayer-protected metal clusters 113–114
 - solid 3–20
 - solubilization 159
 - thin-liquid films 416, 425–426
- DLS *see* dynamic light scattering
- DLVO theory 13–15, 17, 29
- DMAOs *see* alkyltrimethylaminooxides
- DMPC *see* 1,2-dimyristoyl-*sn*-glycero-3-phosphatidylcholine
- DMT *see* Derjaguin–Muller–Toporov theory
- DNA *see* deoxyribonucleic acid
- DOC *see* Disorder–Open–Connected–Cylinder model

- DODAB surfactant 48, 49
 domain morphology 301–321
 double-chain surfactants 160
 double-layers 11–14
 drag reduction 210
 drop methods
 contact angle 253–254, 255–263, 264
 dynamic surface tension 230–236
 equilibrium surface tension 217, 220–223, 235
 droplet microemulsions 344–352
 droplet sedimentation 271–272
 dry wetting 122–123
 Du Noüy ring method 217, 220
 Dupré equation 125–126
 dye micellization 243
 dye solubilization 242–243, 247–248
 dynamic light scattering (DLS) 242, 247, 294–296, 357, 365–369
 dynamic surface forces 388–389
 dynamic surface tension 218, 225–238, 439–440

 eddy currents 284–285
 EFF *see* emulsion ferrofluid techniques
 EHEC *see* ethyl(hydroxyethyl)cellulose
 Einstein relationship 350
 elasticity 206
 electrical behaviour
 colloidal dispersions 9–13
 conductivity 213, 242, 335, 438
 dispersion 5
 electrical double-layer 373–374
 see also zeta potential
 electroacoustic sonic amplitude (ESA) 379
 electrokinetic potential *see* zeta potential
 electrokinetics 371–382
 see also electroosmosis; electrophoresis; sedimentation potential; streaming potential
 electrolytes
 antifoaming agents 154
 critical micelle concentration 246
 electrostatic double-layers 393–397
 electron microscopy (EM) 335–336
 electronic properties 83–84, 92–95
 electrooptics 89–90
 electroosmosis 371–372, 375–379
 electrophoresis 371–372, 375–379
 electrostatics
 colloidal dispersions 13–15
 double-layers 424–425
 solubilization 165, 185
 ellipsoids of revolution 322–323
 ellipsometry 443–444
 EM *see* electron microscopy
 emulsification
 failure 339, 344, 351–352
 emulsion ferrofluid (EFF) techniques 417
 emulsion films 30–31
 emulsions
 see also emulsification; microemulsions
 antifoaming agents 152–154
 characterization 55–56
 definition 4
 formation 74
 thin-liquid films 417
 encapsulation
 end-functionalization 105–109
 engulfment (particle behaviour) 275
 entropic interactions 426–427
 environmental issues
 EON *see* equivalent ethoxy number
 equation of state 127–128, 252–253, 270, 274
 equilibrium contact angles 129–130
 equilibrium films 28–29
 equilibrium phases 56
 equilibrium surface tension 217–224
 equivalent ethoxy number (EON) 161
 ESA *see* electroacoustic sonic amplitude
 ether oils 67
 ethoxylated alcohols 55–63, 69–70, 71–73
 ethyl(hydroxyethyl)cellulose (EHEC) 401–402
 Euclidean solids 190
 EWG *see* European Working Group
 excess solubilization 178–180

 fatty acids 49–52, 82
 ferromagnetic colloids 7
 Fick's law 16, 17
 films
 see also foams
 film pressure concept 122–123
 film-dimpling 423
 flotation 269
 stratification 427
 thin-liquid 415–433
 wetting 122–123
 fish-cuts, phase prisms 340
 flexible surface model 336
 flip-flop (transverse diffusion) 47, 50
 flocculation
 colloidal dispersions 15–16
 definition 15–16
 fluorescence quenching 281, 290–292
 foam breaking 143–157
 foams 23–43
 bubble formation 418
 characterization 415–416, 433
 film rupture mechanisms 26
 foaming agents 40–41
 industrial materials 37–43
 micellar structural forces 427–428
 preparation 24–25, 40–43
 stability 25–37
 foodstuffs
 foam breaking 155–156
 foams 24–27, 43
 force methods 217–221
 fractional amino acid transfer 176–177
 fragmentation fractal dimension 360
 free energy 121–134
 see also interfacial tension; surface tension
 freeze-fracture technique 335, 353
 frequency doubling 88–89
 frictional forces 390–392
 fringes of equal chromatic order (FECO) interferometry 384
 froth 25
 funnel-shaped test 33–34

- gas-filled polymer foams 38, 40
- gel phases
 - definition 4
 - domain morphology 307–308
 - foam stabilization 27
 - rheology 204
 - vesicle bilayers 46–47
- gel-like networks 430
- genus concept 304–306, 314
- geometric mean combining rule 127
- Gibbs elasticity 27–28, 235
- Gibbs equations
 - adsorption 242
 - solubilization 164
- Gibbs free energy 122
- Gibbs triangle 57–60
- Gibbs–Marangoni effect 27–28
- Girifalco–Good–Fowkes–Young equation 129
- globules 304, 306, 310, 316
- gold 3, 4, 6, 99–116
- goniometer–telescopes 254, 260–262, 263
- goniometry 357, 368
- Gouy–Chapman model 373–374, 375
- Gouy–Chapman–Stern–Grahame model 380
- granules 269–277
- grazing incidence X-ray diffraction 80, 82
- Guinier approximation 362

- haematite 7
- Hagen–Poiseuille equation 272
- Hamaker theory 392
- hard-sphere radius 346
- head space measurement 35
- head-group overlap 426–427
- heat of immersion 269
- Helfrich forces 429
- Helmholtz free energy 122
- Helmholtz–Smoluchowski equation 374–375
- heterogeneity 130
- hexagonal mesophases 308–309
- hexagonal phases 167, 308–309
- hexamethyldisiloxane (HMDSO) 380–381
- HLB *see* hydrophilic–lipophilic balance
- HMDSO *see* hexamethyldisiloxane
- homogeneity 314, 321–323, 330
- honeycombs 316
- Hookean solids 190, 194
- Hooke's law 387
- hydration interactions 394
- hydrocarbon radius 345–346, 348
- hydrodynamic forces 375, 380–382, 388–389, 417
- hydrodynamic radius 334, 346, 347, 368–369
- hydrolysis 6–7
- hydrophilic–lipophilic balance (HLB)
 - microemulsions 61, 63, 69
 - solubilization 161, 167
- hydrophobic effect 240
- hydrophobicity
 - foams 151–152
 - interactions 430
 - micelles 162
- hyperpolarizability 87–88
- hysteresis 268, 401

- image analysis 35, 36
- immersional wetting 126
- indifferent adsorption 429
- indifferent ions 10
- industrial materials 37–43
- infrared (IR) spectroscopy 101–102, 105–106
- inhomogeneous surfaces 129–130, 135–136
- integrated circuits 93–95
- intensity-weighted distribution 362, 366
- interfacial curvature 301–321
- interfacial tension
 - definition 121
 - measurement 218–223, 225–226, 230–232, 235, 258–260
 - microemulsions 70, 72–73
 - sedimentation volume 269–270
 - wetting thermodynamics 127–129
- interference microscopy 263–264
- interferometry 384–385
- intermediate phases 316–317
- ionic surfactants 64–66, 165–166
- ionization 371

- Johnson–Kendall–Roberts (JKR) theory 388, 389–390, 391
- Jönsson model 165–166

- kaolinite 8–9
- kinetics 55
- Krafft point 245
- Krafft temperature *see* Krafft point
- kugelschaum, foaming 24–25

- LAC *see* limiting association concentration
- lamellae lifetime measurement 37
- lamellae profiles 422
- lamellar phases
 - see also* liquid crystals
 - bilayer solubilization 171–173
 - domain morphology 307, 308, 316
 - phase prisms 340–341
 - rheology 199–204
 - rigid interface solubilization 185
 - shear behaviour 211–214
 - smectics 300, 307, 315
- lamellar structural forces 428–429
- laminar flow 18
- Langmuir–Blodgett (LB) films 79–98
 - command surfaces 91–92
 - deposition 80–83, 85
 - historic perspective 99
 - molecular electronics 92–95
 - nanoparticles 83–84
 - nonlinear optical devices 85–90
 - sensors 90–91
 - surface forces 392, 396, 403–404
- lanthanum myristate 329
- lanthanum palmitate 329
- Laplace equations 121, 252, 272, 421, 422
- laser light 86–89
- latex 8
- LB *see* Langmuir–Blodgett
- lead myristate 328

- life, origins 50
- Lifshitz theory 390, 392, 425–426
- light scattering
 - see also* goniometry; static light scattering
 - CMC determination 242, 247
 - droplet microemulsions 349
 - dynamic 242, 247, 294–296, 357, 365–369
 - micelle size/shape 281, 294–296
 - microemulsions 335
 - particle size 357–370
 - small-angle 357, 362, 364–365
 - thin-liquid films 417
- limiting association concentration (LAC) 165
- lindane 178–184
- line tension approach 123–124
- liposomes 45, 49–50
- liquid crystals
 - foam stabilization 29–30
 - Langmuir–Blodgett films 82, 91
 - lyotropic 299–338
 - nematic 82, 299–300
 - smectics 300, 307, 315
 - solids/melts 299–301
 - solubilization 166–169, 173
 - vesicle bilayers 46–47
- liquid magnets 7
- LOEC *see* lowest observed effect concentration
- low shear viscosity 349–350
- lyotropic liquid crystals 299–338

- MAC *see* maximum additive concentration
- magnetic properties
 - colloids 246
 - Langmuir–Blodgett films 84
 - liquids 7
- Maltese cross textures 308
- Marangoni flow 27–28, 146, 230
- MASIF *see* measurement and analysis of surface interactions and forces
- mass action models 163–164
- mass-weighted distributions 359
- maximum additive concentration (MAC) 163, 166, 170–171
- maximum bubble methods 217, 223, 227–229, 440
- Maxwell model 194–195
- measurement and analysis of surface interactions and forces (MASIF) 384–388, 406
- melts, liquid crystals 299–301
- membranes 46, 49–52, 171–173
- meniscus formation 136–137
- meniscus height 82–83
- meniscus radii 421
- mesh mesophases 302, 305–306, 315–316
- mesomorphism 300, 302
- mesophases
 - bicontinuous 302, 303, 306, 310–315, 316–317
 - columns 308–310
 - cubic 311–314
 - gels 307–308
 - hexagonal 308–309
 - lamellar 307, 308, 316
 - lyotropic liquid crystals 299–338
 - meshes 302, 305–306, 315–316
 - molten 318–319
 - morphology 301–321
 - polycontinuous 316–317
 - ribbons 309–310
 - ringing gels 204
 - smectics 300, 307, 315
- metals
 - clusters 113–114
 - foams 41–42
 - ion hydrolysis 6–7
 - nanoparticles 83–84, 113–114
- micelles
 - see also* critical micelle concentration; rod-like micelles
 - antifoaming agents 148
 - aqueous solutions 190–192
 - cylindrical 193–194, 199
 - foam films 427–428
 - non-aqueous media 246–248
 - reversed 169–171, 174–177, 181–184
 - self-assembly 239–241
 - self-reproduction 50
 - size/shape measurement 281–297
 - solubilization 162–169
 - stability 148
 - structure 162
 - vesicle comparison 45
- Michelson optics 264
- microcellular plastic foams 40
- microdomains 173
- microemulsions 55–77
 - see also* emulsions
 - antifoaming agents 152–153, 154
 - applications 73–74
 - bicontinuous 351–352
 - characterization 333–356, 364
 - definitions 56
 - Disorder–Open–Connected–Cylinder model 181
 - domain morphology 302, 317–319
 - droplet 344–352
 - formation 56, 68–70
 - interfacial tensions 70, 72–73
 - ionic surfactants 64–66
 - mesophases 300
 - microstructures 70–72, 342–344
 - mixed surfactants 63–64, 66–67
 - nonionic surfactants 57–64, 66–67
 - phase behaviour 57–70, 178, 338–342, 344–345
 - relaxation NMR 290
 - reversed 9
 - scattering techniques 293
 - soft surfactant systems 174–181
 - solubilization 169–171, 173, 174–185
 - stiff surfactant systems 181–185
- microinterferometry 419–420
- microparticle electrophoresis chambers 375
- micropipets 417
- microscopic study 34–35
- microstructures 342–344
- middle mesophases 308–309
- Mie theory 362–365
- mixed films 30
- MLVs *see* multi-lamellar vesicles
- mobility 375–377
- moist wetting 122–123
- molal volume 244

- molecular absorption 243–244
- molecular dimensions 323–332
- molecular electronics 92–95
- molten mesophases 318–319
- monodisperse particles 6
- monolayer-protected clusters (MPC) 113–114
- monolayers 80–82, 99–116, 146, 147
- morphology 301–321
- motorized syringe methods 258
- multi-lamellar vesicles (MLVs) 45–46

- nanoassembly computers 93–95
- nanoparticles 83–84, 113–114
- Navier–Stokes equation 371–372, 374
- NBFs *see* Newton black films
- neat mesophases (smectics) 300, 307, 315
- nematic liquid crystals 82, 299–300
- neutron scattering *see* small-angle neutron scattering
- Newton black films (NBFs) 29, 30, 426, 427
- Newtonian liquids 190, 192–194
- NLO *see* nonlinear optical
- nonaqueous media 67, 246–248
- noninteracting micelles 191–192
- noninteractive adsorption 429
- nonionic surfactants
 - microemulsions 57–64, 66–67
 - solubilization 166–169
- nonlinear optical (NLO) devices 85–90
- non-Newtonian fluids 19–20
- nonpolar solvents 67, 246–248
- nonpolar surfaces 396–398
- nonwetting surfaces 121
- nuclear magnetic resonance (NMR) spectroscopy
 - calibration 283–284
 - intermediate mesophases 316
 - micelle shape/size 281–290
 - microemulsions 334–335, 347, 349
 - pulsed gradient spin-echo 282, 284–286, 288–289
 - relaxation 281–282, 289–290, 334–335, 347
 - self-diffusion 281–289, 302, 334
- nucleation 5–6, 416, 431
- null ellipsometry 443
- number-weighted distributions 359

- o/w see* oil-in-water
- oblate ellipsoids of revolution 322–323
- oblate micelles 286–287
- oil-in-water (*o/w*) microemulsions 55–74, 177–181, 184–185
- oil-swollen lamellar phases 185
- oils 145, 147, 148–149, 151–154
- oligoethylene oxide surfactants 337–338
- open-cell structures 41
- optical fibre probes 35, 38
- optical storage devices 87
- ordered phases 307–317
- organic monolayers 79–98, 99–116
- origins of life 50
- orthokinetic coagulation 18–19
- oscillating jet method 229–230
- oscillatory force profiles 399–400

- osmometry 244, 247
- osmosis 349, 417
- oversize fraction 359

- palisade layer 162
- paper
 - foam breaking 143, 145
- parachute morphology 49
- partial molal volume 244
- partial wetting 121
- particle size 357–370
- particle suspension layer stability 271–272
- particulates 150–152, 153
- Pascalian liquids 190
- patterned self-assembling monolayers 109–113
- PB *see* Poisson–Boltzman theory
- PEGs *see* poly(ethylene glycol)s
- pendant drop method 217, 221–222, 233
- penetration
 - capillary 120, 136–140
 - surfactant aggregates 166–168
- PEO–PPO–PEO block copolymers 168, 204–205
- peptization 3
- Percus–Yevick approximation 205
- peristaltic forces 426
- Perrin black films *see* Newton black films
- PGSE NMR *see* pulsed gradient spin-echo nuclear magnetic resonance
- pH effects
 - electrokinetics 372, 376–377, 380
 - fatty acid vesicles 49
 - particle mobility 376–377
 - zeta potential 380–381
- phase behaviour
 - foam stabilization 31
 - inversion 61, 338
 - microemulsions 57–70, 178, 338–342, 344–345
 - separation 40
 - transition temperature 46–47, 50–52
- phase prisms 339–342
- phospholipid bilayers 45, 46–47, 49–52
- photochromism 91–92
- photomicroscopy 275–276
- photonic devices 85–90
- plasma polymerization 380–381
- plastics 37–38, 40–41
- plate methods 236–237
- point of zero charge (PZC) 9–10
- Poiseuille approximation 227
- Poisson–Boltzmann (PB) theory 12–13, 202–203, 373–374, 393–396, 424
- polar interactions 129
- polar layer 162
- polar surfaces 394–396, 398–399
- polarization (optical) 86, 367
- polarized attenuated total reflection infrared spectroscopy 101, 102
- polycontinuous mesophases 316–317
- polydimethylsiloxanes 145
- polydispersity 18, 199–202
- polydispersity index 359, 363–364
- polyederschäum, foaming 24–25

- polyelectrolytes 402–404, 429
 poly(ethylene glycol)s (PEGs) 106–107, 381–382
 polymerization
 plasma 380–381
 vesicles 49
 polymers
 foam stabilization 26
 latex dispersions 8
 microemulsion additives 67–68, 69
 patterned self-assembling monolayers 111
 plastic foams 37–38, 40–41, 42
 wetting 126–127
 polyurethane foam 38, 41, 42
 porosity 120, 136–140, 269–277
 porous disc holders 418
 potentiometry 438
 powders 136, 138–140, 269–277
 prebiological phases 50
 precursor films 135
 pressure drop technique 35–36
 pressure effects 62, 68, 69, 246
 pressure methods 217, 223, 227–229, 234–236
 probing aggregation 368–369
 profile axisymmetric drop shape analysis (ADSA-P) *see*
 axisymmetric drop shape analysis
 prolate ellipsoids of revolution 322–323
 prolate micelles 286–287
 proteins 106–109, 401
 protolysis 9–10
 protrusion 397, 427
 pseudo-binary phase diagrams 178–179
 pseudo-emulsions 30–31, 152–154
 pseudo-phase model 163, 173
 pulsed gradient spin-echo nuclear magnetic resonance (PGSE
 NMR) 282, 284–286, 288–289
 puncture defects 319
 PZC *see* point of zero charge

 quasi-equilibrium 400
 Quemada function 349, 351

 radius of gyration 295
 Rayleigh limit 349, 361–362
 Rayleigh–Debye–Gans (RDG) approximation 362, 363, 368
 reaction rates, vesicles 50
 receding contact angles 129–130, 150
 rectangular electrophoresis chambers 377–378
 reflected-light interferometry 419
 reflected-light video microscopy 419
 refractive index 242, 420, 437
 rejection (particle behaviour) 275
 relaxation, NMR 281–282, 289–290, 334–335, 347
 repulsion forces 429
 restricted equilibrium 400
 reversed phases
 micelles 169–171, 174–177, 181–184
 microemulsions 9
 rheology
 colloidal dispersions 19–20
 dilatational 237
 surfactants 189–214
 rheopexy 190, 206
 ribbon phases 309–310
 ring methods 236–237
 ringing gels 204
 robust beer foams 416
 rod-like micelles
 birefringence 195, 206
 domain morphology 304, 306, 308–310
 rheology 193–199
 shear behaviour 206–210
 Ross–Miles pour test 34
 rotor mixers 34, 35
 rough surfaces 129–130
 rupture, films 431
Saccharomyces cerevisiae (yeast) 112

 SALS *see* small-angle light scattering
 salts, microemulsions 62, 64–66, 69
 SAMs *see* self-assembling monolayers
 SANS *see* small-angle neutron scattering
 SAXS *see* small-angle X-ray scattering
 Scheludko cells 418
 Schulze–Hardy rule 17
 SDS *see* sodium dodecyl sulfate
 secondary black films *see* Newton black films
 sedimentation 358, 365
 sedimentation potential 371, 379
 sedimentation volume 269–271, 273
 self-assembling monolayers (SAMs) 99–116
 self-diffusion
 cubic phases 353–355
 droplet microemulsions 350–351
 microemulsions 342–344, 346–347
 NMR 281–289, 302, 334
 sponge phases 352–355
 self-reproduction 50–52
 semiconductors 83–84, 93–95
 sensors, Langmuir–Blodgett films 90–91
 serum replacement method 440–442
 sessile drop methods 217, 221–222, 253–254, 257–258
 SFA *see* surface force apparatus
 shape methods 217, 221–223, 232–234
 shape parameters, mesophases 331, 332
 shear behaviour 205–214, 349–350
 shear moduli 202–204
 shear planes 374–375
 Shinoda-cuts, phase prisms 340
 Siegert relation 295, 365
 silica, colloidal 7–8
 single-lamellar vesicles (SLVs) 45–46
 single-particle counting 358
 single-phase fluids 159
 ‘slip-stick’ patterns 260–261
 SLS *see* static light scattering
 SLVs *see* single-lamellar vesicles
 small-angle light scattering (SALS) 357, 362, 364–365
 small-angle neutron scattering (SANS)
 mesophases 301, 316
 micelles 281, 292–294
 microemulsions 71–72, 335, 347–349, 358
 rheology 205, 206, 211–212

- small-angle X-ray scattering (SAXS)
 - mesophases 301, 316
 - micelles 281, 292–294
 - microemulsions 335, 358
 - rheology 211
- 'Smart' surfaces 91–92
- smectics 300, 307, 315
- soaps 440
- sodium bis(2-ethylhexyl) sulfosuccinate (AOT) 65–67, 248, 364, 366–367
- sodium chloride 62, 64–66
- sodium dodecyl sulfate (SDS) 241, 426, 427
- soft surfactant systems 174–181
- sol, definition 4
- solid dispersions
 - aggregation processes 15–19
 - electrical properties 9–13
 - rheology 19–20
 - stability 5, 9, 13, 15
 - synthesis 4–9
- solidification fronts 274–277
- 'solloids' 397
- solubilization
 - antifoaming agents 147–148
 - binary solutions 160, 162–173
 - definition 159
 - Jönsson model 165–166
 - limit 345
 - micelles 162–165
 - organic compounds 246
 - soft surfactant systems 174–181
 - steric effects 166–169
 - stiff surfactant systems 181–184
 - ternary systems 173–184
 - water-in-oil microemulsions 169–171, 174–177, 181–184
- solutions, spreading behaviour 136
- solvents
 - diffusion 288
 - exchange model 172
 - surface forces 404–407
- space partitioners 316–317
- Sparge tube technique 32–33
- spatial fluctuations 431–432
- specific surface area 360
- spinning drop method 217, 222–223
- spinodal decomposition 416, 431
- sponge phases
 - characterization 352–355
 - domain morphology 302, 305–306, 316, 317–319
 - liquid crystals 300
 - phase prisms 340–342
- spontaneous curvature 70–72, 160–161, 169
- SPR *see* surface plasmon resonance
- spreading 124–126, 134–136, 146, 149–150
- spring deflection 385–387
- SSFQ *see* steady-state fluorescence quenching
- stabilization
 - common black films 431–433
 - foams 25–37
 - micelles 148
 - thin-liquid films 416–417, 426, 430
- stalagmometers 230–231
- static light scattering (SLS)
 - CMC determination 242, 247
 - micelle shape/size 294–296
 - microemulsions 349
 - particle size 357, 360–365, 368–369
- steady-state fluorescence quenching (SSFQ) 281, 290–292
- steric effects
 - forces 397, 405, 424, 426–427
 - solubilization 166–169
- 'sticky' contacts 208, 210
- stiff surfactant systems 181–185
- Stokes–Einstein equation 230–231, 347, 366
- stratification 29, 30
- streaming potential 371–372, 379
- stretching (antifoaming agents) 146, 149
- strontium myristate 325
- structural inversion 342–344
- structural viscous liquids 190
 - see also* shear behaviour
- sugars 171–172
- supercritical fluids 68
- superlattices 83
- superspreaders 149–150
- suprafluid liquids 190
- supramolecular forces 427–430
- supramolecular structuring 424
- surface charge
 - electrokinetics 371–382
- surface force apparatus (SFA) 384–385, 390–391, 415, 428
- surface plasmon resonance (SPR) 102, 103
- surface tension
 - CMC determination 241–242
 - component approach 128–129
 - contaminant detection 163
 - definition 121
 - dynamic 225–238
 - equilibrium 217–224
 - film flotation 269
 - gradients 150
 - measurement 217–224, 225–238, 438–442
 - sedimentation volume 273
 - solidification fronts 274–277
 - wetting 126–127
- surfaces
 - see also* surface charge; surface tension
 - conduction 11–13
 - depletion 429
 - genus concept 304–306, 314
 - geometry 387–388
 - separation measurement 385–387
 - surface–surface interactions 383–414
 - viscosity 27, 147
- surfactant films 336, 354
- surfactant monolayer model 173
- surfactants
 - see also* zwitterionic surfactants
 - adsorption 436–444
 - anionic 147
 - antifoaming agents 147, 149
 - aqueous solutions 190–191
 - commercial 63–64

- concentration measurement 436–444
- cosurfactants 63, 64, 65–66
- emulsions 55
- ionic 64–66
- microemulsions 55–74
- nonionic 57–64, 66–67, 166–169
- rheology 189–214
- shear behaviour 205–214
- solubilization 159–186
- structure 245
- surface forces 397–404
- thin-liquid films 415–417
- vesicles 45, 48
- suspension layer stability 271–272
- suspensions
 - definition 4
- swelling
 - domain morphology 319–321, 323
 - exponents 331
 - surfactant aggregates 166–168
- syneresis 3
- synergistic effects 151–152, 429

- Tanford's formulae 303
- Tanner's law 134
- temperature effects
 - contact angle 269, 276–277
 - critical micelle concentration 246
 - liquid crystals 300
 - microemulsions 60–70, 71–72
 - nuclear magnetic resonance 284
 - vesicle phase transition 46–47, 50–52
- tensiometry 217–224, 225–238
- ternary systems 160–161, 173–185
- TFB *see* thin-film balance
- thermodynamics
 - microemulsions 56
 - vesicles 48–49
 - wetting 120, 121–134
- thermoplastic foams 40
- thermotropic liquid crystals 300
- thin-film balance (TFB) method 36, 39, 417–424
- thin-liquid films 415–430, 431–433
- thixotropy 190
- three-phase contact lines 259–260, 265–266
- time-resolved fluorescence quenching (TRFQ) 281, 290–292
- titration, soaps 440
- topology 301, 314, 316–321
- transition (particle behaviour) 275–276
- transverse diffusion (flip-flop) 47, 50
- TRFQ *see* time-resolved fluorescence quenching
- Triton X-*n* solutions 228
- turbulent flow 18–19

- ultracentrifugation 367
- ultrasound 155–156, 244
- ultraviolet (UV) spectroscopy 437–438
- undersize fractions 359
- undulation forces 426

- unilamellar vesicles *see* single-lamellar vesicles

- van der Waals interactions
 - colloidal dispersions 13–15, 16–17
 - measurement 392
 - sedimentation 269, 272
 - thin-liquid films 424
 - wetting thermodynamics 127, 128
- vapour phase methods 9
- vapour pressure osmometry 244, 247
- vesicles
 - antifoaming agents 149–150
 - autopoiesis 50–52
 - bilayer solubilization 171–173
 - fatty acids 49–50
 - formation 47–49
 - phase structure/transition 46–47
 - polymerization 49
 - rheology 200–204, 211–213
- viscoelasticity
 - measurement 388–389
 - rheology 190, 193–198
- viscosity
 - antifoaming agents 147
 - CMC determination 244
 - colloidal dispersions 19–20
 - dilational 235
 - foam stabilization 26, 27
 - microemulsions 335
 - rheology 192–199
 - shear behaviour 206–207, 211
- visible spectroscopy 437–438
- volatility of liquids 122–123
- volume fraction 345–346, 349–350

- w/o *see* water-in-oil
- Washburn equation 138–139, 272
- water
 - see also* aqueous systems
 - solubilization 169–171
- water-in-oil (w/o) microemulsions 169–171, 174–177, 181–184
- waveguide format 88, 89
- Weaver–Bertucci equation 143–144
- wedge model 180–181
- wetting 119–142
 - capillary penetration 136–140
 - imperfect solid surfaces 129–134
 - Langmuir–Blodgett films 82–83, 91–92
 - porous surfaces 138–140
 - solid surfaces 126–129
 - spreading 124–126, 134–136
 - tension 126
 - thermodynamics 120, 121–134
 - thin-liquid films 431
- wicking 120, 132
- Wilhelmy plate method 217–218, 219–220, 267–269
- Winsor equilibria, emulsification failure 161, 178, 351–352

- X-ray photoelectron spectroscopy (XPS) 105–106

- X-ray reflectivity 427
X-ray scattering *see* small-angle X-ray scattering
XPS *see* X-ray photoelectron spectroscopy
- yeast (*Saccharomyces cerevisiae*) 112
- Young equation
background 120, 133–134, 252
modification 122–131
porous solids 74, 138–139
- Young–Laplace equation 219, 222–223
- zeta potential
electrokinetics 374, 380–381
- Zimm plots 295
- zirconium myristate 327
- zwitterionic surfactants
critical micelle concentration 245
rheology 196–199, 201–202, 208–210, 213

Index – Volume 1

- α -crystalline phase 477
- α -olefinesulfonates 276–277
- α -sulfo fatty acid methylesters 277–278
- ab initio* polymerizations 194–195
- absorbency 138–139, 154–158, 159–162
- acetals 391–393
- acid fracturing 263
- acid–base interactions 233
- additives, phase behaviour 497–502
- adhesion 157–158, 334–336
- adjuvants 341–342
- adsorbable organic halogen (AOX)-containing substances 284
- adsorption
 - adsorbed films 252, 253
 - adsorber dyes 101–103
 - adsorption isotherms 167–168, 379–380
 - competitive 105–107
 - detergency 58–61
 - experimental techniques 237, 381
 - paper manufacture 132–136
 - polymeric surfactants 377–384
 - sensitizing dyes 98
 - surfactants 232–238, 240–241
- AEEA *see* aminoethylethanolamine
- aerobic batch tests 516–517
- aerosols 15
- AFM *see* atomic force microscopy
- agglomeration 79, 114, 206–208, 239
- aggregate, roads 334
- aggregation 79, 186, 188, 445–447
 - see also* coagulation; coalescence; flocculation
- agriculture 73–83, 341–342
- agrochemicals 80–83
- AKD *see* alkyl ketene dimer
- alcohol ethoxylates 301–302
- alcohols
 - nonionic hydrophobes 294–296
- algicides 318–321
- alkane sulfonates 282–285
- alkanolamides 306–307
- alkenyl succinic anhydride (ASA) 141, 143–144
- alkyd emulsions 113, 402–403
- alkyl chain length 484–488
- alkyl ketene dimer (AKD) 141, 142–144, 158
- alkyl *N*-methylglucamides 305
- alkyl quaternary ammonium salts 311–312, 314, 315–316, 318, 329–330
- alkylamines 328
- alkylbenzene sulfonates 278–282
- alkylene oxides 296
- alkylether carboxylates 275–276
- alkylether sulfates 275, 524–525
- alkylglucosides 392–393
- alkylphenol ethoxylates (APEOs) 302–303, 528–529
- alkylphenols 296
- alkylpolyglucosides 409
- alkylpolyglycosides (APGs) 304, 529
- alkylsulfates 273–275, 524–525
- AMBER force field 539–540, 541, 545
- amidopropylamines 327
- amine ethoxylates 307
- amine oxides 305–306, 324, 325–327
- amines 297
- aminoethylethanolamine (AEEA) 356–359
- amorphous dispersions 91
- amphipathic structure 232–233, 376
- amphiphiles
 - see also* hydrophobes; surfactants
 - drugs 4, 7
- amphitropic mesophases 496
- amphoacetates 349–350, 356–359
- amphoteric surfactants 294, 323, 349–350, 351, 355–372, 532–534
 - see also* zwitterionic surfactants
- anaerobic testing 515, 517
- anchoring 140, 205, 374, 377–378, 383
- anion-active sequestrents 291
- anionic surfactants 271–292, 520–525
- antifoamers 71, 263
- antisetling agents 79–80
- antistat layers 86–87
- antithixotropy 209
- AOX *see* adsorbable organic halogen-containing substances
- APEOs *see* alkylphenol ethoxylates
- APGs *see* alkylpolyglycosides
- aquatic toxicity 518–519, 524–525, 529, 531–532, 534
- aqueous dispersions 39
- aqueous injection moulding 216
- ASA *see* alkenyl succinic anhydride
- asphalt *see* bitumen
- asphaltic emulsions 265
- assessment criteria 514–520
- associative phase separation 453, 456–458
- associative thickeners 105–107, 449
- atomic force microscopy (AFM)
 - dispersions 242
 - latices 109–110
 - paper 127, 149, 165, 166
 - surfactant migration 398
- autophobicity 142
- autoxidation 398–399

- bactericides 318–321
- barrier coatings 152–154
- batch polymerizations 194–195
- batch tests 516–517
- Bendtsen test 165
- BET *see* Brunauer–Emmett–Teller
- betaines 349–355, 363–364, 396–397, 533
- BiAS *see* Bismuth active substances
- bicontinuous phases
 - aggregates 473, 475, 477–478
 - liquid crystals 473, 475, 477–478, 482
 - microemulsions 460–462, 482
 - ringing gels 353
- bilayers
- binder burnout 216–217
- binder–emulsion preparation 107–110
- binders 111–113, 116, 149
- Bingham solids 208–209
- bio-surfactants 521
- bioaccumulation 515, 520
- bioadhesion 14
- bioavailability 8–9
- biocides 318–321, 333–334, 360
- biodegradability
 - amphoteric surfactants 532–534
 - anionic surfactants 279, 521–524
 - cationic surfactants 531
 - cleavable surfactants 391, 394, 395
 - drug delivery systems 26–30
 - legislation 512–513
 - nonionic surfactants 527–529
 - surfactants 509–510, 515–517
- biomagnification 515, 520
- biostatic activity 319–320
- bis-surfactants *see* Gemini surfactants
- bismuth active substances (BiAS) 513, 527
- bitumen 265, 334–337
- bleaching 125
- block copolymers
 - adsorption 374, 377–384
 - drug delivery 8, 11, 13, 15–16, 21–25
 - nonionic surfactants 303–304, 491–493
- blood substitute formulations 9
- blooming 116
- boundary conditions 227, 540
- Bragg–William approximations 378
- Brewster-angle microscopy 538
- bridging
 - flocculation 136–137, 205
- brightening 125
- Bristow wheel 160
- Brønsted acidity 231–232
- Brunauer–Emmett–Teller (BET) isotherm 167–168
- bubble formation 255, 274
 - see also* foams
- builders 54, 61, 65, 288
 - condensation 161–162
 - dynamics 159–160
- carbohydrates 300–301
- carboxybetaines 350–354
- carrier effect 64
- casting 203, 212–213, 215–216
- cationic surfactants 309–348, 460, 529–532
- centrifugal casting 212
- ceramics 201–218
- chain length 297, 302
- chain lubricants *see* conveyor lubricants
- chain scission 217
- chain–chain interactions 236
- charge regulated surfaces 227–228
- charge-stabilized particles 136–137
- CHARMM force fields 545
- chelating agents 332
- chemical flooding 259–262
- chemical interactions 236
- chemical pulping 125
- chemically heterogeneous dispersions 40–42
- chemically homogeneous dispersions 40
- chemisorption 248
- clathrate hydrates 468
- clean-up, oil spills 264
- cleansing *see* detergency
- cleavable surfactants 291, 390–397
- clouding
 - detergency 69
 - hydrotropes 321–322, 414, 415
 - liquid crystals 480–481
 - nonionic surfactants 485–488
 - oxyethylene surfactants 442
 - surfactant–polymer systems 454–456, 463
- CMC *see* critical micelle concentration
- coalescence 106
- coatings 29–30, 146–154
- cobinders 148–149
- cobuilders 64–65
- cold isostatic pressing 214
- collectors, flotation 246–249
- colloidal processing 203
- colloidal silver 91, 92
- columnar mesophases
 - see also* rod-like micelles
- commercial processes *see* manufacture
- commercial surfactants 484, 492
- comminution 180–184, 190–191, 193
- compaction of DNA 460
- competitive adsorption 105–107, 109
- complexation 61–65, 96
- compression rheology 211–212
- computer simulation 537–550
- concentration effects 435–437
- concentration profiles 542, 544
- condensation 184–185, 190–191
- conditioning 327–328
- conductivity 87
- conformation 377–381, 543, 545
- consolidation 41, 124–125, 212–216, 239, 240
- constant charge surfaces 227
- constant potential surfaces 227
- consulate point 488
- contact angles

- see also* Young equation
 crude oil 254, 255
 conveyor lubricants 332–334
 cooperative binding 447, 451–452
 copolymers
 adhesion 86
 adsorption 374, 377–384
 drug delivery 8, 11, 13, 15–16, 21–25
 nonionic surfactants 303–304, 491–493
 pigment dispersion 119
 corrosion inhibition 263–264, 288, 307, 340
 cosmetics 327–328, 368–369, 511
 cosolutes 425–427, 435, 438, 442, 448
 cosurfactants 497–498
 Couette flow technique 183
 Coulombic forces 540
 counterions 274, 431, 468–469
 coupled units tests 527–528
 coupler dispersions 99–101
 coupling agents 409, 412–414
 CPP *see* critical packing parameter
 cracking process 265–266
 cratering, paints 121
 creaming, emulsions 186
 critical association concentration (CAC) 446–447, 452, 456
 critical micelle concentration (CMC)
 see also micelles
 amphoterics 362–363
 competitive adsorption 106–107
 detergency 55–56
 Gemini surfactants 388–389, 390
 micellization 253, 467–472
 surfactant–polymer systems 446–447
 surfactants 237, 388–390, 422–427
 critical packing parameter (CPP) 45, 422, 432–433
 critical solution temperature 189–190
 critical surface tension 120–121
 Cross equation 209
 ‘cross-talk’ 87, 92
 crude oil 252, 254, 255, 265–266
 cryoporometry 169–170
 crystal growth 79
 see also Ostwald ripening
 crystallization 416–417
 cubic phases
 drug delivery 12, 20
 multicomponent systems 492, 494, 498–499
 phase behaviour 481
 structure 472, 473–475
 curtain coating 88
 cyclic acetals 391–392
 cyclodextrin solutions 16–17

 Darcy’s law 152
 deagglomeration 206–208
 Debye–Hückel equation 131
 DEEDMAC *see* diethylester dimethylammonium chloride
 defects 202
 defoamers 263
 see also antifoamers; foam breaking
 deformation 146
 degradation products 515
 denaturation temperature 46

 deoxyribonucleic acid (DNA) 12–13, 460
 DEQs *see* diesterquaternaries
 destabilization 40–42
 detergency 53–72
 alkyl sulfates 274
 amphoterics 365, 366–367
 anionic surfactants 279–282
 betaines 350
 cationic surfactants 310, 314–318, 321–327
 cleavable surfactants 395
 environmental issues 511, 513, 521
 fabric softeners 314–318
 hydrotropes 415–416
 mesophases 503
 nonionic surfactants 302, 303, 305
 sulfosuccinates 289
 developer scavengers 87–88
 dewatering 152
 di-tallow dimethylammonium chloride (DTDMAC) 530–532
 di-tallow imidazolinester (DTIE) 530–532
 dialkyldimethyl quaternary ammonium salts 311–312, 314, 315, 318
 diesterquaternaries (DEQs) 530–532
 diethylene triamine quaternary ammonium salts 315–316
 diethylester dimethylammonium chloride (DEEDMAC) 530–532
 differential scanning calorimetry (DSC) 170
 dimeric surfactants *see* Gemini surfactants
 direct casting 215–216
 direct coagulation casting 215
 direct flotation 345
 disc-nematic phases 489
 disinfection 318–319, 368
 dispersants 116–119, 147–148, 288, 291
 dispersions
 absorber dyes 101–102
 agriculture 79
 aqueous 39
 ceramics 206–208
 chemically heterogeneous 40–42
 chemically homogeneous 40
 coupler 99–101
 drug delivery 8–15
 emulsions 99–100
 mixed micellization 100
 nanocrystalline 100–101
 natural systems 175–176
 oil-continuous 39
 paint pigments 113–119
 particle processing 238–243
 photography 91–92
 stabilization 381–384
 disproportionation 41
 dissipative particle dynamics (DPD) simulation method 537, 546–547, 548
 dissociation 221
 distillation 416
 disulfine blue active substances (DSBAS) 513
 DLVO theory 130–132
 DNA *see* deoxyribonucleic acid
 dodecyl-1,3-propylenebis(ammonium chloride) (DoPDAC) 495
 dodecyl-1,3-propylenebis(ammonium chloride) (DoPDAC) *see* dodecyl-1,3-propylenebis(ammonium chloride) 495

- double-chain surfactants
 - see also* lipids
- DPD *see* dissipative particle dynamics
- drained casting 212–213
- drilling mud 259
- droplet size
 - agrochemical sprays 80–83
 - comminution 181–183
 - monomer emulsions 191
 - Ostwald ripening 186–187
 - polymerization techniques 195–198
 - surfactant role 111–113
- drugs (pharmaceutical) 3–6, 8–23
- dry pressing 214
- dry strength, paper 145
- drying, ceramics 216–217
- DSBAS *see* disulfine blue active substances
- DSC *see* differential scanning calorimetry
- DTDMAC *see* di-tallow dimethylammonium chloride
- DTIE *see* di-tallow imidazolinester
- dynamic swelling 185, 191

- EC₅₀ tests 518–519, 524–525, 530, 532
- edge penetration 161
- EDTA *see* ethylenediaminetetraacetic acid
- EEC *see* European Economic Community Directives
- elastic interaction 382–383
- electrical behaviour
 - conductivity 233–236
- electrical double-layer 222–223
 - see also* zeta potential
- electroacoustic sonic amplitude (ESA) 102–103
- electrokinetic potential *see* zeta potential
- electrokinetics 102–103
 - see also* electroosmosis; electrophoresis; sedimentation potential; streaming potential
- electrolytes
 - detergency 59, 60, 72
 - foaming 72
 - micellization 425–427
 - phase behaviour 500–501
 - surface charge 221–222
 - surfactant–polymer systems 454–460
- electron spectroscopy for chemical analysis (ESCA) 51, 109, 111–113, 162–163, 397
- electronic properties 87
- electroosmosis 225
- electrophoresis 97, 102–103, 224, 336
- electrophoretic deposition (EPD) 213–214
- electrostatics
 - air 50
 - double-layers 204–205
 - liquids 42
 - patch aggregation 136, 137
 - responsive systems 25–26
 - stabilization 108
 - surface charge 226–229
 - surfactant–polymer systems 448
- electrosteric stabilization 206
- elongational rheology 153
- emulsifiable concentrates 73, 74–76
- emulsification
 - comminution 179, 180–184
 - condensation 179, 184–185
 - emulsifiers 179–180
 - foodstuffs 42, 45, 47
 - paints 105, 107–110
 - photography 91, 99–100
 - photolability 397
 - spontaneous 185
- emulsion concentrates 76–78
- emulsion polymerization 107–110, 175–200, 288, 290–291, 400–402
- emulsions
 - see also* emulsification; microemulsions
 - alkyd 113
 - bitumen 335–336
 - drug delivery 8–9
 - foodstuffs 40–41
 - miniemulsions 176, 177, 195–196
 - monomer 191–196
 - multiple 73
 - nanoemulsions 77
 - petroleum industry 256–259, 262, 263
 - photography 85–86, 87–89
 - radical polymerization 196–198
 - separation 265–266
 - spontaneous 74–76
 - stability 186–190
 - suspoemulsions 73
- encapsulation 28, 418
 - see also* microencapsulation
- enhanced oil recovery (EOR) 259, 262–263
- entropic interactions 382–383
- environmental issues
 - see also* biodegradability
 - amphoteric surfactants 364, 365, 532–534
 - analytical techniques 513–514
 - anionic surfactants 279–280, 284, 520–525
 - aquatic toxicity 524–525, 529, 531–532, 534
 - assessment criteria 514–520
 - cationic surfactants 321, 332, 340, 529–532
 - ethoxylated surfactants 107, 117
 - eutrophication 61, 116
 - industry 510–512
 - legislation 512–513
 - nonionic surfactants 303, 305, 525–529
 - oil industry 264–265, 340
 - risk assessment 534–535
 - softening agents 332
 - zwitterionic surfactants 364, 365
- EOR *see* enhanced oil recovery
- EPD *see* electrophoretic deposition
- equivalence points 96–97
- ESA *see* electroacoustic sonic amplitude
- ESCA *see* electron spectroscopy for chemical analysis
- ester quaternary ammonium salts 316–317, 329–330, 395–397
- ethoxylated amines 327, 328–329
- ethoxylated quaternary ammonium salts 329–330
- ethoxylated surfactants 107
- ethoxymer distribution 299–300, 302
- ethylene oxide 298–300, 303–304
- ethylenediaminetetraacetic acid (EDTA) 332
- European Economic Community (EEC) Directives 512–513
- European Working Group (EWG) 512–513
- eutrophication 61, 116

- EWG *see* European Working Group
- extenders 114
- extraction 416
- extrusion coating 88
- extrusion molding 214
- fabric softeners 314–318
- fatty acids 277–278, 352–353
- fatty alcohols 273, 275
- fatty amines 318
- fatty nitriles 311
- Feldspar, flotation 346
- fibre collapse point 129
- fibre lignin content 125–127
- fibre properties, paper 125–128, 129
- fillers, paper 129
- films
 see also foams
 morphology 109–110
- filter dyes 101–103
- first-effect concentrations 526
- fixation, emulsions 196–198
- flexibility 438
- floculation
 ceramics 205, 209–211, 213
 emulsion concentrates 76, 77
 foodstuffs 43, 44
 nanoparticles 135
 paper 129–130, 135–138, 141–142, 151
 pigment dispersion 114
 polymeric surfactants 381–382, 383
 selective 243–245
- Flory–Huggins theory 229–230, 374–375
- Flory–Krigbaum theory 382
- flotation 246–249, 289, 344–347
- fluidization 265
- fluorosurfactants 122, 291
- foams
 see also films
 amphoterics 365, 366–367
 anionic surfactants 274, 275, 280
 bubble formation 255, 274
 cationic surfactants 325
 detergency 71–72
 foodstuffs 41–42
 petroleum industry 254–256, 262–263
 stabilizers 306
- foodstuffs 39–52
 cationic surfactants 332–334
 environmental issues 512
 nonionic surfactants 297, 307–308
- force fields 539–541
- fracturing fluids 340
- free energy
 see also interfacial tension; surface tension
- free rosin distributions 140
- free volume theory 230
- functionality tests 46
- fungicides 318–321
- GC *see* gas chromatography
- gel phases
 betaines 353
 ceramics 215
 drug delivery 21–23, 29
 structure 476–477
 surfactant–polymer systems 455–456, 462–463
- gelatin 86, 97
- gemini surfactants 314, 354, 385–390, 469, 496–497
- gene therapy 11–12
- Geography-Referenced Exposure Assessment Tool for European Rivers (GREAT-ER) 535
- Gibbs equations
 adsorption 75, 76–77, 252, 389
 phase rule 466, 467
- Gibbs–Helmholtz equation 177
- Gibbs–Marangoni effect 255
- Gibbs–Thompson equation 169–170
- glucamides 327
- Gouy–Chapman model 222–223
- graft copolymers 374, 377–384
- granules 214
- GREAT-ER *see* Geography-Referenced Exposure Assessment Tool for European Rivers
- Griffith equation 201
- grinding, dispersion 114
- hair care 327–328, 354, 368
- hard surface cleaning 321–326, 367–368
- heat treatment 245
- heat-developable materials 90
- heavy metal ions 288–289
- Helmholtz model 222
- hemimicelles 236, 237, 238
- heterogeneity 40–42, 155–156, 202–203
- heteronuclear Overhauser effect 546
- heterophase polymerizations 181, 184, 185, 190
- hexagonal phases 473, 479, 481, 492
- high performance liquid chromatography (HPLC) 362, 513–514
- HLB *see* hydrophilic–lipophilic balance
- homogeneity 540
- homopolymers 373–374
- HPLC *see* high performance liquid chromatography
- hydrate inhibitors 340
- hydration interactions 42–43
- hydrogen bonding 230, 244, 489
- hydrolysis 100, 143–144, 391–397
- hydrophiles 298–301
- hydrophilic–lipophilic balance (HLB)
 anionic surfactants 275
 cationic surfactants 310
 emulsions 180, 257–258
 lipids 44–45, 48
 paint pigments 117
 spontaneous emulsification 74
- hydrophobic effect 467–469
- hydrophobicity
 interactions 233, 428–429, 449, 452
 lipids 12–13
 micelles 294–297
 modification 447–452, 461
- gas adsorption 167–168
- gas chromatography (GC) 362

hydrophobizing *see* sizing
 hydrotropes 321–323, 407–420, 500

IEP *see* isoelectronic point
 image analysis 164–166
 immunization 28
in situ particle size measurement 239
in situ-forming carrier systems 20
 inclusion complexes 17
 industrial syntheses *see* manufacture
 infrared (IR) spectroscopy 163
 inisurfs 401–402
 initiators 194, 400
 injection molding 214
 inner salts 350
 insulin adsorption 5
 interfacial polymerization 73
 interfacial tension
 oil recovery 261
 polymers 178
 spontaneous emulsification 74–76
 intermediate phases 477–479
 internal sizing 138–145
 International Organization for Standardization (ISO) 516, 517
 interpenetration 241–242
 inverse micellar solutions 411
 inverse phases 499
 inverse polymerization 180
 ion adsorption 220
 ion dissolution 220–221
 ion exchange 61–65, 233
 ion pairing 233
 ionic strength 226, 240
 ionic surfactants 493–497
 ionization 221
 IR *see* infrared spectroscopy
 isoelectronic point (IEP) 46, 96–97, 224, 225–226, 246–248
 isomorphous substitutions 221

kaolin 147
 Kelvin equation 161, 168
 ketals 393–394
 kinetics 433–434
 Kleven equation 362
 Kolmogorov length 181
 Kozeny-Carman relationship 152
 Krafft point 45, 427–428, 468, 489
 Krafft temperature *see* Krafft point
 Krieger–Dougherty equation 151, 210

lamellar phases
 see also liquid crystals
 hydrotropes 411, 412–414
 micelle self-assembly 253
 phase behaviour 481
 structure 471, 472–473
 vesicles 418
 Langmuir equation 58
 Langmuir–Blodgett (LB) films
 computer simulation 538

Laplace equations 168
 laser-focusing techniques 165
 LASs *see* linear alkylbenzene sulfonates
 lateral interactions 236
 lateral structure 543
 latex 105–122
 lattices 221, 401–402
 LB *see* Langmuir–Blodgett
 LC₄₅₀ tests 518–519, 524–525, 530, 532
 legislation 512–513
 Lial process 295
 lidocaine 7, 8
 ligand complexation 96
 light scattering
 paper 129
 light sensitivity 101
 lignin content 125–127
 ligninsulfonates 292
 limited coalescence 103–104
 linear alkylbenzene sulfonates (LASs) 511, 513, 521, 523–526
 linearized Poisson–Boltzmann distribution 228
 lipids 12–13, 44–46
 liposomes 9–12
 liquid bridges 44, 50
 liquid crystals
 agrochemical sprays 83
 chemical structure 465–508
 concentration effects 436
 drug delivery 12, 20–21
 foodstuffs 45
 formation 256
 hydrotropes 408–409, 411, 412–414, 415
 lamellar 411, 412–414, 418, 471, 472–473, 481
 lyotropic 466–467
 nematic 475–476, 483–484, 489
 phase behaviour 466, 472–502
 surfactants 66–67, 70
 vesicles 418
 liquid soaps 273
 liquid transport 162
 liquid/liquid interface 65–67
 LOEC *see* lowest observed effect concentration
 loops 231, 377–379
 lowest observed effect concentration (LOEC) 519, 527
 lyotropic liquid crystals 466–467
 lyotropic nematic phases 475

macroemulsions 176, 177
 macromolecules 15
 Maltese cross textures 473
 manufacturing processes
 amphoterics 356–360
 anionic surfactants 273–279, 282–284, 286–288, 290
 betaines 352–353, 355
 block copolymers 303
 cationic surfactants 311–314
 Gemini surfactants 386
 Lial process 295
 nonionic surfactants 294–297, 298–300, 302–308
 OXO process 274, 295
 Shell Higher Olefin Process 295

- Williamson synthesis 275, 276
 Ziegler process 279, 294–295
 mass action models 429
 matte beads 87, 103–104
 MBAS *see* methylene blue active substances
 MD *see* molecular dynamics
 mean field approximations 378
 mechanical pulping 125
 membrane emulsification 183
 mercerization 337, 338, 339
 mercury porosimetry 168–170
 mesh mesophases 477–478, 494
 mesogenic properties 490
 mesophases
 additives 497–502
 hydrogen bonding 489
 liquid crystals 465–508
 lyotropic liquid crystals 466–467
 meshes 477–478
 ringing gels 353
 metabolites 515, 519
 metals
 processing 512
 methyl ester ethoxylates 307–308
 methylene blue active substances (MBAS) 512, 513
 MHC *see* minimal hydrotropic concentration
 micelles
 see also critical micelle concentration; rod-like micelles
 agrochemical sprays 83
 amphoterics 362–363
 cationic surfactants 324
 computer simulation 544–546
 concentration effects 435–437
 coupler dispersions 100
 detergency 55–56, 59
 drug delivery 15–16
 Gemini surfactants 388–390
 hemimicelles 236, 237, 238
 inverse solutions 411
 kinetics 433–434
 liquid crystals 465–466, 467–472
 mixed 100, 442, 451–452
 molecular dynamics 544–546
 nonionic 440–442
 phase behaviour 481
 polymeric surfactants 376
 self-assembly 252–254
 solvent effects 434
 sponge phase 439–440
 structure 421–423, 431–432, 437–441, 467–472
 surfactant adsorption 236–237
 temperature effects 440–442
 thermodynamic models 428–430
 Michael addition reactions 359–360
 microemulsions
 see also emulsions
 agriculture 73
 bicontinuous 460–462, 482
 condensation 184–185
 detergency 68–70
 drugs 7, 17
 emulsion polymerization 176
 formation 253, 258–259
 hydrotropes 412, 414
 surfactant–polymer systems 460–462
 microencapsulation 73–74
 microorganisms 319–320
 migration, films 397
 mineral flotation 246–249, 344–347
 miniemulsions 176, 177, 195–196
 minimal hydrotropic concentration (MHC) 409, 412
 mining 344–347, 512
 mixed micelles 100, 442, 451–452
 mixed surfactants 498–499
 mobility 543
 modelling, Langmuir–Blodgett films 537–550
 molecular dynamics (MD) 537–550
 molecular recognition 244
 monolayers 541–544
 monomer emulsions 191–196
 multiple emulsions 73
 multiple equilibrium model 429–430
 nanocrystalline dispersions 91, 100–101
 nanoemulsions 77
 nanoparticles 135
 nanoparticulate semiconductors 87
 NaPA *see* sodium polyacrylate
 necking, ceramics 207
 nematic liquid crystals 475–476, 483–484, 489
 neutralization flocculation 137
 nitrogen-containing polymers 327
 NMR *see* nuclear magnetic resonance spectroscopy
 no observed effect concentration (NOEC) 284, 519, 526–527, 530, 532
 nonionic hydrophiles 298–301
 nonionic hydrophobes 294–297
 nonionic micelles 440–442
 nonionic surfactants 293–308
 block copolymers 491–493
 environmental issues 525–529
 phase behaviour 480–491
 nonpolar solvents 434
 nuclear magnetic resonance (NMR) spectroscopy
 amphoterics 361–362
 hydrotropes 412
 micellization 430–431
 porosity 170
 nucleation 95
 OECD *see* Organization for Economic Co-operation and Development
 oil ganglia 259, 261
 oil industry *see* petroleum industry
 oil-continuous dispersions 39
 oils 499–500
 oily streaks 473
 oligopeptides 4–5
 optical density 409–410
 optical textures 472–473, 474
 oral care 369
 oral drug administration 8–9, 13, 18, 28
 Organization for Economic Co-operation and Development (OECD) tests 513, 518, 520, 523, 527–528, 533–534
 organoclays 343–344

- ortho esters 394–395
- osmosis 211–212
- Ostwald ripening
 - dynamic swelling 191
 - emulsion concentrates 77–78, 79
 - emulsions 185–188, 191
 - foams 41
 - photography 95–96
- overcoating 87
- OXO process 274, 295
- oxyethylene surfactants 440–442

- π -stacking 467
- packing density 211
- paints 105–122, 397, 403–404
- paper 123–173
 - absorbency 154–158, 159–162
 - cationic surfactants 331–332
 - environmental issues 512
 - formation 128–138
 - internal sizing 138–145
 - polymer adsorption 132–136
 - porosity 167–171
 - surface properties 155–156, 158–159, 162–166
 - surface treatment 146–154
 - wettability 154–159
- paraphenylenediamines 89, 90, 93
- parenteral drug administration 9–10, 19–20
- Parker–Print–Surf (PPS) test 165
- particle size 239
- particulates 48–51, 91–92, 94–99
- patch flocculation 136, 137
- PB *see* Poisson–Boltzman theory
- PCS *see* photon correlation spectroscopy
- pearl-necklace model 447–448
- PEC *see* predicted environmental concentrations
- PEGs *see* poly(ethylene glycol)s
- penetration
 - capillary 160–162
 - drug delivery 11
 - molecular dynamics 544, 545
- PEO *see* poly(ethylene oxide)
- PEO–PPO–PEO block copolymers 11, 13, 15–16, 21–25
- peptization 334, 336–337
- perfluorocarbon fluids 179
- personal care 327–330, 344, 354, 364–369
- petrol sulfonates 278
- petroleum industry 251–267, 295–296, 337–341, 343–344, 512
- Peyer's patches 28
- PGSE NMR *see* pulsed gradient spin-echo nuclear magnetic resonance
- pH effects
 - amphoterics 350
 - betaine esters 396
 - ceramics 204–205, 215
 - dispersions 240
 - drug delivery 25–26
 - effects on sizing 141–142
 - selective flocculation 245
 - surface charge 221–222
 - thickener stability 323–324
 - zeta potential 225–226, 248–249
 - zwitterions 350, 352–353
- pharmacy 3–38, 369, 418–419, 511
- phase behaviour
 - amphiphilic drugs 7, 8
 - computer simulations 547–550
 - hydrotropes 412–414, 500
 - in situ*-forming carrier systems 20
 - inversion 44, 186, 189–190, 258
 - ionic surfactants 493–497
 - liquid crystals 466, 472–502
 - micelles 481
 - nonionic surfactants 480–491
 - separation 43, 186, 429
 - surfactant–polymer systems 452–463
 - surfactants 67–71, 480–497
 - zwitterions 493
- phase rule 466, 467
- phosphated alcohols 285–287
- phosphobetaines 354–355
- phosphoric acid esters 285–289
- photography 85–104, 176, 192–193
- photolability 397
- photon correlation spectroscopy (PCS) 381
- physico-chemical processes 421–443, 515, 517–518
- Pickering stabilizers 192–193
- picture framing 121
- pigments 108–109, 113–119, 147
- plasticity 208
- plastics 91, 512
- PNEC *see* predicted no-effect concentrations
- Poisson–Boltzmann (PB) theory 205, 226–228
- polar solvents 434
- polarizing microscopy 75, 472
- polyamines 333
- polycarboxylates 64–65
- polydispersity index 19
- polyelectrolytes 116–119, 132–136, 147–148
- poly(ethylene oxide) (PEO) 5–6
- polyglucoside surfactants 489–491
- polyhydroxy surfactants 489
- polyhydroxybenzenes 412
- polymerization
 - binder-emulsion preparation 107–110
 - emulsions 107–110, 175–200, 288, 290–291, 400–402
 - inverse 180
 - radical 176, 196–198
 - surfactants 107–110, 397–405
 - suspensions 103–104, 176, 192–193
- polymers
 - adsorption 132–136, 229–232, 241
 - bridging mechanism 136–137
 - drug delivery 13–14, 23, 27–29
 - electronically conducting 87
 - nitrogen-containing 327
 - particle interactions 43, 205–206
 - surfactant–polymer systems 445–463
 - surfactants 373–384
- polyoxyethylene surfactants 287–288, 486–487, 502
- polyphosphated alcohols 285–287
- polysaccharides 44, 46–48
- porosimetry, mercury 168–170
- porosity 167–171
- post-emulsified binders 111–113

- potash, flotation 347
 powders 50–51, 202–203
 PPS *see* Parker–Print–Surf test
 predicted environmental concentrations (PEC) 512–513, 535
 predicted no-effect concentrations (PNEC) 513, 519, 535
 pressure filtration 203
 proline 417
 propionates 359–360
 propylene oxide 300, 303–304
 protein crystals 467
 proteins 5, 46
 pulping 125
 pyrolysis 217
- quasi-lattice model 378
 quaternary ammonium salts
 agricultural adjuvants 341–342
 biocides 318–321
 cleavable surfactants 395–397
 cosmetics 316–317, 329–330
 detergency 314–318, 327
 environmental issues 530–532
 manufacture 311–314
 mineral flotation 345, 347
 oilfields 338–340
 organoclay 343–344
 paper 331
 thickeners 323
 quinonediimines 89, 93–94
- radical polymerization 176, 196–198
 Raman spectroscopy 163
 rayon 337, 338, 339
 refractive index 114
 RES *see* reticuloendothelial system
 responsive drug delivery 24–26
 retention, paper 129–130, 141–142
 reticuloendothelial system (RES) 9
 reverse flotation 345
 reversed phases
 liquid crystals 472–473, 480, 499
 Rhebinder effect 79
 rheology
 associative thickeners 449
 ceramics 208–212
 dispersions 239–240
 elongational 153
 foams 254
 foodstuffs 41
 liquid crystals 466
 mesophases 503
 modifiers 148–149, 343
 paper coatings 149–152
 surfactants 338–340, 389–390
 rheopexy 209
 rhombohedral mesh phases 477–478, 494
 ribbon phases 477–478, 495
 ringing gels 353
 rinse-added softeners 317
 risk assessment 534–535
 road construction 334–337
 rod-like micelles
 cationic surfactants 324
 concentration 437
 flexibility 438
 rolling-up mechanism 59, 65–67
 rosins 140–142
 rotator phase 477
- salting-in 407, 409–410, 500
 scanning electron microscopy (SEM) 127, 170–171
schlieren nematic texture 475
 SDS *see* sodium dodecyl sulfate
 secondary ion mass spectrometry (SIMS) 163
 secondary surfactants 365, 367
 sedimentation 186
 sedimentation potential 225
 seed particles 194
 segregative phase separation 453, 456–458
 selective flocculation 243–245
 self-emulsifiable oils 73
 SEM *see* scanning electron microscopy
 sensitization (paper) 97–98, 137
 separation 59, 416–417
 sequestration 288–289, 291
 sewage treatment *see* waste-water treatment
 SFA *see* surface force apparatus
 SFF *see* solid freeform fabrication
 shear behaviour 149–152, 208–210
 Shell Higher Olefin Process (SHOP) 295
 SHOP *see* Shell Higher Olefin Process
 short-chain sulfonates 291
 short-oil alkyds 113
 silicates, flotation 345
 silicone surfactants 122, 291–292
 silver halides 87–88, 90–92, 94–99
 SIMS *see* secondary ion mass spectrometry
 sizing 125, 138–145, 152–153
 skin care
 amphoterics 364–365, 366–367, 368
 betaines 354
 cationic surfactants 327–328, 344
 organoclay 344
 slide hopper coating 88
 slip casting, ceramics 203, 212
 SLNs *see* solid lipid nanoparticles
 slurries 176
 smectites, organoclay 343–344
 soaps 272–273, 280
 sodium dodecyl sulfate (SDS) 494
 sodium polyacrylate (NaPA) 147–149
 solid formulations, agriculture 73–74
 solid freeform fabrication (SFF) 216
 solid lipid nanoparticles (SLNs) 12–13
 solid loading, ceramics 210–211
 solid/liquid interfaces 58–61
 solubility 46, 178, 375–376
 solubilization
 capacity 69
 hydrotropes 409–412, 415, 418–419
 micelles 431, 432
 surfactant–polymer systems 447
 solvation shells 545
 solvents
 foodstuffs 43

- micellization 434
- multicomponent systems 501–502
- paints 119
- speciality surfactants 121–122, 385–405
- spin finishing 337, 338, 339
- sponge phases
 - block copolymers 492–493
 - liquid crystals 482
 - micelles 439–440
- spontaneous emulsification 74–76, 185
- sprays, agriculture 80–83
- stabilization
 - aggregation 188
 - coupler dispersions 99–100
 - dispersions 381–384
 - electrostatic 108
 - foams 306
 - foodstuffs 40–42
 - microemulsions 412, 414
 - Ostwald ripening 186–187
 - paper manufacture 130
 - steric 9, 205, 377, 381–384
 - suspension polymerization 192–193
 - suspensions 209–210, 212, 213
- starches, co-binders 149
- static cling 317
- steady shear 149–152
- stereolithography 216
- steric effects
 - stabilization 9, 205, 377, 381–384
- Stern plane 224–225, 235
- Stern–Graham model 223
- stiff gels, ceramics 215
- Stokes–Einstein equation 377
- streaming potential 224–225
- stress-craze inhibitors 333–334
- structural viscous liquids
 - see also* shear behaviour
- stylus contact method 165
- subbing layers 85
- sulfobetaines 354–355
- sulfochlorination 282–284
- sulfosuccinates 289–291, 524–525
- sulfoxidation 284
- supersaturation 184
- support base, photography 85
- surface charge
 - aqueous media 220–229
 - flotation 246–249
 - molecular dynamics 545
 - selective flocculation 243–244
- surface tension
 - agrochemical sprays 80–83
 - betaines 363–364
 - detergency 54–58
 - Gemini surfactants 388
 - paints 120–121
 - perfluorocarbon fluids 179
 - polymers 178
 - surfactant–polymer systems 445–446
- surfaces
 - see also* surface charge; surface tension
 - activity 4–6, 44–48, 73, 105
 - modification 403–404
 - morphology 125
 - reactions 247–249
 - roughness 155–156, 158–159, 163–166
 - treatment 125, 138–145, 146–154, 245
- surfactant affinity difference 258
- surfactant number *see* critical packing parameter
- surfactant systems, drug effects 6–8
- surfactant–polymer flooding 259–262
- surfactant–polymer systems 445–463
- surfactants
 - see also* zwitterionic surfactants
 - adsorption 232–238, 240–241
 - agriculture 73
 - amphipathic structure 232–233, 376
 - amphoteric 294, 323, 349–350, 351, 355–372, 532–534
 - anionic 271–292, 520–525
 - antifoaming agents 71–72
 - cationic 309–348, 529–532
 - cleavable 291, 390–397
 - commercial 484, 492
 - computer simulation 537–550
 - corrosion inhibition 263–264
 - cosurfactants 497–498
 - detergency 54–55, 58–61, 65–71
 - dispersions 240–241
 - droplet size 111–113
 - environmental issues 509–536
 - ethoxylated 107
 - experimental techniques 237
 - foams 254–256
 - Gemini 314, 354, 385–390, 469, 496–497
 - hydrophilic–lipophilic balance 180, 275, 310
 - hydrotropes 500
 - ionic 493–497
 - liquid crystals 465–508
 - mixed 498–499
 - molecular dynamics 537–550
 - nonionic 293–308, 480–493, 525–529
 - oil spill clean-up 264–265
 - paints 105–110
 - petroleum industry 252–256, 259–265
 - phase behaviour 67–71, 480–493
 - physico-chemical properties 421–443
 - polymeric 373–384
 - polymerizable 107–110, 397–405
 - secondary 365, 367
 - self-assembly 252–254
 - speciality 121–122, 385–405
 - surfactant–polymer systems 445–463
 - swelling 190
 - usage trends 510–511
 - UV-curable 403–404
- surfmers (polymerizable surfactants) 107–110, 397–405
- suspension polymerization 103–104, 176, 192–193
- suspensions
 - agriculture 78–80
 - ceramics 203, 205, 208–212
 - consolidation 212–216
 - foodstuffs 41
- suspoemulsions 73
- swelling
 - agents 184
 - drug delivery systems 25
 - emulsions 190–191

- heterophase polymerizations 190
- radical polymerization 197
- surfactant–polymer systems 462–463
- syntheses *see* manufacturing processes
- synthetic sizing agents 140
- tails 231, 377–379
- targeted drug administration 10–11
- temperature effects
 - drug delivery 24–25
 - micelles 425–428, 437, 440–442
 - oxyethylene surfactants 440–442
- tetrapropylenebenzene sulfonate (TPS) 279
- textiles 511–512
- thermodynamics
 - drug delivery 15–23
 - emulsions 176–179
 - micellization 428–430
 - polymer adsorption 229–230
 - polymeric surfactants 374–375
- thermoporosimetry 169–170
- thermotropic liquid crystals 466
- thickening 148–149, 323–325
- thixotropy 209, 210
- threshold effect 64, 288
- tilt angles 538, 542
- titania (titanium dioxide) 114
- toothpastes 369
- topical drug administration 11, 18–19
- topography, paper 163–166
- toxicology
 - amphoterics 364–365
 - aquatic 518–519, 524–525, 529, 531–532, 534
 - surfactants 515
- TPS *see* tetrapropylenebenzene sulfonate
- train formation 231, 377–379
- transport of liquids 162
- transurfs 401
- triglycerides 41, 296, 297
- twin surfactants *see* Gemini surfactants
- Ultra Turrax system 183
- ultrasound 182–183
- ultraviolet (UV) curable surfactants 403–404
- vaccination, oral 28
- van der Waals interactions
 - ceramics 203–204, 205, 207
 - DLVO theory 131–132
 - emulsion concentrates 76
 - liquids 42–43
 - molecular dynamics 539–540
 - pigment dispersion 115
 - powder systems 50
- vapour transport 161
- vesicles
 - hydrotropes 418
- viscoelasticity
 - ceramics 210
 - paper coatings 151–152
 - thickeners 325
- viscose 337, 338, 339
- viscosity
 - see also* thickening
 - amphoteric surfactants 365, 366–368
 - ceramics 209–211
 - dispersions 240
 - Gemini surfactants 390
 - micelle concentration 436
 - surfactant–polymer systems 449, 452
 - volume restriction interaction 382–383
- Washburn equation 159–161
- washing *see* detergency
- waste-water treatment 510, 515, 517, 520, 529
- water
 - see also* aqueous systems
 - bridges 50
 - flooding 261
 - hardness 61–65, 272–273, 288, 314
 - water-borne paints 116–119
 - water-continuous phases 479–480
- Wenzel's equation 155
- wet strength, paper 145–146
- wetting
 - agriculture 73, 78–79, 81–83
 - amphoterics 365
 - anionic surfactants 285, 288
 - cationic surfactants 325–326
 - counterions 274
 - crude oil 254, 255
 - detergency 54–58
 - foodstuffs 48–49
 - paints 119–121
 - paper 127–128, 142, 144, 154–159
 - pigment dispersion 114
 - sulfosuccinates 289, 290
- wicking 161
- Williamson synthesis 275, 276
- Winsor's *R* ratio 258
- wood preservatives 318, 320–321
- X-ray photoelectron spectroscopy (XPS) 144–145, 162–163
- xanthogenation 337, 338, 339
- XPS *see* X-ray photoelectron spectroscopy
- Young equation
 - agriculture 78–79
 - detergents 56
 - petroleum 254
- zeolites 61–65
- zeta potential
 - experimental techniques 237–238
 - flotation 248–249
 - manipulation 225–226
 - measurement 224–225
 - surfactant adsorption 235, 237–238
- Ziegler process 279, 294–295
- Zisman plots 120–121
- zwitterionic surfactants
 - characterization 361–372
 - chemistry 349–355
 - emulsions 257
 - paints 118
 - phase behaviour 493

Cumulative Index

- α -crystalline phase V1 477
- α -olefinesulfonates V1 276–277
- α -sulfo fatty acid methylesters V1 277–278
- ab initio* polymerizations V1 194–195
- absorbency V1 138–139, V1 154–158, V1 159–162
- absorption, molecular V2 243–244
- acetals V1 391–393
- acid fracturing V1 263
- acid–base interactions V1 233
- ACRPAC *see* analysis of capillary rise profile around a cylinder
- additives, phase behaviour V1 497–502
- adhering bubble methods V2 253–254
- adhesion V1 157–158, V1 334–336, V2 125–126, V2 389–390
- adjuvants V1 341–342
- ADSA *see* axisymmetric drop shape analysis
- adsorbable organic halogen (AOX)-containing substances V1 284
- adsorption
 - adsorbed films V1 252, V1 253
 - adsorber dyes V1 101–103
 - adsorption isotherms V1 167–168, V1 379–380
 - competitive V1 105–107
 - detergency V1 58–61
 - electrokinetics V2 371
 - experimental techniques V1 237, V1 381
 - measurement V2 435–444
 - paper manufacture V1 132–136
 - polymeric surfactants V1 377–384
 - sensitizing dyes V1 98
 - surfactants V1 232–238, V1 240–241
 - thin-liquid films V2 416
- advancing contact angles V2 129–130
- AEEA *see* aminoethylethanolamine
- aerobic batch tests V1 516–517
- Aerosol OT *see* sodium bis(2-ethylhexyl)sulfosuccinate
- aerosols V1 15, V2 9
- AFM *see* atomic force microscopy
- ageing effects V2 154–155
- agglomeration V1 79, V1 114, V1 206–208, V1 239
- aggregate, roads V1 334
- aggregation V1 79, V1 186, V1 188, V1 445–447, V2 15–19
 - see also* coagulation; coalescence; flocculation
- agriculture V1 73–83, V1 341–342
- agrochemicals V1 80–83
- AKD *see* alkyl ketene dimer
- alcohol ethoxylates V1 301–302
- alcohols
 - bilayer solubilization V2 172
 - foaming V2 24
 - microemulsions V2 63, V2 64–66, V2 69
 - nonionic hydrophobes V1 294–296
- algicides V1 318–321
- alkane sulfonates V1 282–285
- alkane thiols V2 99–116
- alkanolamides V1 306–307
- alkenyl succinic anhydride (ASA) V1 141, V1 143–144
- alkyd emulsions V1 113, V1 402–403
- alkyl chain length V1 484–488
- alkyl ketene dimer (AKD) V1 141, V1 142–144, V1 158
- alkyl *N*-methylglucamides V1 305
- alkyl quaternary ammonium salts V1 311–312, V1 314, V1 315–316, V1 318, V1 329–330
- alkylamines V1 328
- alkylbenzene sulfonates V1 278–282
- alkyldimethylaminioxides (DMAOs) V2 196–199, V2 201–202, V2 208–210, V2 213
- alkylene oxides V1 296
- alkylether carboxylates V1 275–276
- alkylether sulfates V1 275, V1 524–525
- alkylglucosides V1 392–393
- alkylphenol ethoxylates (APEOs) V1 302–303, V1 528–529
- alkylphenols V1 296
- alkylpolyglucosides V1 409
- alkylpolyglycosides (APGs) V1 304, V1 529
- alkylsulfates V1 273–275, V1 524–525
- AMBER force field V1 539–540, V1 541, V1 545
- amidopropylamines V1 327
- amine ethoxylates V1 307
- amine oxides V1 305–306, V1 324, V1 325–327
- amines V1 297
- amino acids V2 175–177
- aminoethylethanolamine (AEEA) V1 356–359
- Amonton friction V2 391
- amorphous dispersions V1 91
- amphipathic structure V1 232–233, V1 376
- amphiphiles
 - see also* hydrophobes; surfactants
 - domain morphology V2 303–304, V2 306
 - drugs V1 4, V1 7
 - Langmuir–Blodgett films V2 80–81
 - liquid crystals V2 300
 - microemulsions V2 57–58
- amphitropic mesophases V1 496
- amphoacetates V1 349–350, V1 356–359
- amphoteric surfactants V1 294, V1 323, V1 349–350, V1 351, V1 355–372, V1 532–534
 - see also* zwitterionic surfactants
- anadrobe testing V1 515, V1 517

- analysis of capillary rise profile around a cylinder (ACRPAC) V2 268
- anchoring V1 140, V1 205, V1 374, V1 377–378, V1 383
- anion-active sequestrents V1 291
- anionic surfactants V1 271–292, V1 520–525, V2 147
- antifoamers V1 71, V1 263, V2 143–157
- antipercolation threshold V2 181–182
- antisetling agents V1 79–80
- antistat layers V1 86–87
- antithixotropy V1 209
- AOT *see* sodium bis(2-ethylhexyl) sulfosuccinate
- AOX *see* adsorbable organic halogen-containing substances
- APEOs *see* alkylphenol ethoxylates
- APGs *see* alkylpolyglycosides
- aquatic toxicity V1 518–519, V1 524–525, V1 529, V1 531–532, V1 534
- aqueous dispersions V1 39
- aqueous injection moulding V1 216
- aqueous polymer solutions V2 400–402
- aqueous systems V2 143–156, V2 190–199
- ASA *see* alkenyl succinic anhydride
- asphalt *see* bitumen
- asphaltic emulsions V1 265
- assessment criteria V1 514–520
- associative phase separation V1 453, V1 456–458
- associative thickeners V1 105–107, V1 449
- atomic force microscopy (AFM)
- dispersions V1 242
 - latices V1 109–110
 - paper V1 127, V1 149, V1 165, V1 166
 - surface forces V2 384–388, V2 390–391, V2 395, V2 397, V2 399–400
 - surfactant migration V1 398
 - thin-liquid films V2 415
- attenuated total reflection (ATR) spectroscopy V2 101, V2 102
- autophobicity V1 142
- autopoiesis V2 50–52
- autoxidation V1 398–399
- axisymmetric drop shape analysis (ADSA) V2 253–254, V2 255–263, V2 264, V2 265–266
- azobenzene chromophore V2 91
- back-scatter technique V2 37, V2 39
- bactericides V1 318–321
- barrier coatings V1 152–154
- batch polymerizations V1 194–195
- batch tests V1 516–517
- Bendtsen test V1 165
- Berthelot's (geometric mean) combining rule V2 127
- BET *see* Brunauer–Emmett–Teller
- betaines V1 349–355, V1 363–364, V1 396–397, V1 533
- BiAS *see* Bismuth active substances
- bicontinuous phases
- aggregates V1 473, V1 475, V1 477–478
 - characterization V2 352
 - domain morphology V2 302, V2 303, V2 306, V2 310–315, V2 316–317
 - liquid crystals V1 473, V1 475, V1 477–478, V1 482
 - mesophases V2 302, V2 303, V2 306, V2 310–315, V2 316–321
 - microemulsions V1 460–462, V1 482, V2 351–352
 - phase prisms V2 340–342
- ringing gels V1 353, V2 204
- Bikerman test V2 32–33
- bilayers V2 149–150, V2 171–173, V2 199–204, V2 211–212
- see also* membranes, vesicles
- binary solutions V2 160, V2 162–173
- binary surfactant–water systems V2 166–169
- binder burnout V1 216–217
- binder–emulsion preparation V1 107–110
- binders V1 111–113, V1 116, V1 149
- Bingham solids V1 208–209, V2 190, V2 204
- bio-surfactants V1 521
- bioaccumulation V1 515, V1 520
- bioadhesion V1 14
- bioavailability V1 8–9
- biocides V1 318–321, V1 333–334, V1 360
- biodegradability
- amphoteric surfactants V1 532–534
 - anionic surfactants V1 279, V1 521–524
 - cationic surfactants V1 531
 - cleavable surfactants V1 391, V1 394, V1 395
 - drug delivery systems V1 26–30
 - legislation V1 512–513
 - nonionic surfactants V1 527–529
 - surfactants V1 509–510, V1 515–517
- biologically active molecules V2 106–109, V2 111–113
- biomagnification V1 515, V1 520
- biostatic activity V1 319–320
- birefringence V2 195, V2 206
- bis-surfactants *see* Gemini surfactants
- bismuth active substances (BiAS) V1 513, V1 527
- bitumen V1 265, V1 334–337
- black films V2 28–29, V2 30, V2 426, V2 427, V2 431–433
- bleaching V1 125
- block copolymers
- adsorption V1 374, V1 377–384
 - drug delivery V1 8, V1 11, V1 13, V1 15–16, V1 21–25
 - nonionic surfactants V1 303–304, V1 491–493
 - rheology V2 204–205
- blood substitute formulations V1 9
- blooming V1 116
- blue laser diodes V2 87–89
- Boltzmann distribution law V2 4
- Boltzmann equation V2 373
- boundary conditions V1 227, V1 540
- Bragg diffraction V2 301
- Bragg reflections V2 330
- Bragg–William approximations V1 378
- brewing industry V2 155–156
- Brewster-angle microscopy V1 538
- bridging
- antifoaming agents V2 146, V2 149, V2 151
 - ceramics V2 430
 - flocculation V1 136–137, V1 205
 - measurement V2 402, V2 405
- brightening V1 125
- Bristow wheel V1 160
- Brønsted acidity V1 231–232
- Brownian motion V2 3, V2 13, V2 16, V2 20, V2 365
- Brunauer–Emmett–Teller (BET) isotherm V1 167–168, V2 436
- bubble formation V1 255, V1 274, V2 418
- foams

- bubble methods
 - contact angle V2 253–254
 - dynamic surface tension V2 227–229, V2 232–236
 - equilibrium surface tension V2 217, V2 221–223, V2 235
- builders V1 54, V1 61, V1 65, V1 288
- CAC *see* critical association concentration
- cadmium arachidate V2 82
- calcium, detergency V1 61–65
- calcium carbonate V1 147
- calcium myristate V2 327
- cancer therapy V1 9–10
- capillary phenomena
 - condensation V1 161–162, V2 390
 - contact angle measurement V2 252, V2 264–266, V2 268, V2 272–274
 - dynamics V1 159–160
 - penetration V2 120, V2 136–140
 - pressures V2 421–423, V2 431
 - rise V2 217, V2 218–219
- carbohydrates V1 300–301, V2 17–19
- carboxybetaines V1 350–354
- carrier effect V1 64
- Cassie–Baxter equation V2 132
- casting V1 203, V1 212–213, V1 215–216
- cathetometers V2 265
- cationic surfactants V1 309–348, V1 460, V1 529–532
- CBFs *see* common black films
- cell attachment V2 107, V2 111–113
- cell opening V2 41
- cell-surface interactions V2 17–18
- cellular foams V2 37
- cement foams V2 42
- centrifugal casting V1 212
- centrifugation V2 358, V2 365, V2 367, V2 417
- ceramics V1 201–218
- chain length V1 297, V1 302, V2 245, V2 248
- chain lubricants *see* conveyor lubricants
- chain scission V1 217
- chain–chain interactions V1 236
- champagne foams V2 416
- channel defects V2 319
- charge regulated surfaces V1 227–228
- charge-stabilized particles V1 136–137
- CHARMM force fields V1 545
- chelating agents V1 332
- chemical flooding V1 259–262
- chemical interactions V1 236
- chemical pulping V1 125
- chemically heterogeneous dispersions V1 40–42
- chemically homogeneous dispersions V1 40
- chemisorption V1 248, V2 100–101
- chiral mesophases V2 316
- chirality V2 50–51
- cholesterics V2 299–300
- chromatographic retention V2 442–443
- clathrate hydrates V1 468
- clays V2 3, V2 8–9
- clean-up, oil spills V1 264
- cleansing *see* detergency
- cleavable surfactants V1 291, V1 390–397
- clouding
 - cloud point defoamers V2 148
 - curvature V2 338
 - detergency V1 69
 - hydrotropes V1 321–322, V1 414, V1 415
 - liquid crystals V1 480–481
 - nonionic surfactants V1 485–488
 - oxyethylene surfactants V1 442
 - surfactant–polymer systems V1 454–456, V1 463
- CMC *see* critical micelle concentration
- coagulation V2 15–19
- coalescence V1 106
- coatings V1 29–30, V1 146–154
- cobblestone model V2 383, V2 391
- cobinders V1 148–149
- cobuilders V1 64–65
- cohesion V2 125–126
- cohesion energy V2 269–270
- cold isostatic pressing V1 214
- collective diffusion V2 346–347, V2 350–351
- collectors, flotation V1 246–249
- colloidal processing V1 203
- colloidal silver V1 91, V1 92
- columnar mesophases V2 308–310
 - see also* rod-like micelles
- command surfaces V2 91–92
- commercial processes *see* manufacture
- commercial surfactants V1 484, V1 492, V2 63–64
- comminution V1 180–184, V1 190–191, V1 193, V2 4–5
- common black films (CBFs) V2 427, V2 431–433
- compaction of DNA V1 460
- competing microstructures V2 336–337
- competitive adsorption V1 105–107, V1 109, V2 429
- complexation V1 61–65, V1 96
- composite surfaces V2 131–132
- compressible fluids V2 68
- compression rheology V1 211–212
- computer simulation V1 537–550
- computers V2 89–90, V2 92–95
- concentration effects V1 435–437, V2 287–288, V2 347, V2 380
- concentration profiles V1 542, V1 544
- concrete foams V2 42
- condensation V1 184–185, V1 190–191, V2 4, V2 5–6
- condensed phases V2 189–190
- conditioning V1 327–328
- conductivity V1 87, V2 213, V2 242, V2 335, V2 438
- conformation V1 377–381, V1 543, V1 545
- consolidation V1 41, V1 124–125, V1 212–216, V1 239, V1 240
- constant charge surfaces V1 227
- constant potential surfaces V1 227
- consulate point V1 488
- contact angles
 - see also* Young equation
 - crude oil V1 254, V1 255
 - definitions V2 133–134
 - hysteresis V2 129, V2 130–133
 - measurement V2 251–280
 - particle/water interface V2 150
 - temperature dependence V2 269, V2 276–277
 - thin-liquid films V2 422
 - wetting V2 119–140
- contamination, films V2 423
- conveyor lubricants V1 332–334
- cooperative binding V1 447, V1 451–452

- copolymers
 adhesion **V1 86**
 adsorption **V1 374, V1 377–384**
 drug delivery **V1 8, V1 11, V1 13, V1 15–16, V1 21–25**
 nonionic surfactants **V1 303–304, V1 491–493**
 pigment dispersion **V1 119**
 rheology **V2 204–205**
 copper myristate **V2 326**
 corrosion inhibition **V1 263–264, V1 288, V1 307, V1 340**
 cosmetics **V1 327–328, V1 368–369, V1 511**
 cosolutes **V1 425–427, V1 435, V1 438, V1 442, V1 448**
 cosurfactants **V1 497–498, V2 63, V2 64, V2 65–66**
 Couette flow technique **V1 183**
 Coulombic forces **V1 540**
 Coulombic wells **V2 430**
 counterions **V1 274, V1 431, V1 468–469, V2 246**
 coupled units tests **V1 527–528**
 coupler dispersions **V1 99–101**
 coupling agents **V1 409, V1 412–414**
 Cox–Merz rule **V2 211**
 CPP *see* critical packing parameter
 cracking process **V1 265–266**
 cratering, paints **V1 121**
 creaming, emulsions **V1 186**
 critical association concentration (CAC) **V1 446–447, V1 452, V1 456**
 critical micelle concentration (CMC)
 see also micelles
 amphoterics **V1 362–363**
 competitive adsorption **V1 106–107**
 detergency **V1 55–56**
 foams **V2 25–26, V2 28, V2 29**
 Gemini surfactants **V1 388–389, V1 390**
 influencing factors **V2 241, V2 245–246**
 measurement **V2 239–249**
 micellization **V1 253, V1 467–472, V2 190–191**
 non-aqueous media **V2 246–248**
 self-diffusion NMR **V2 286**
 surface forces **V2 398–399**
 surface tension **V2 438–439**
 surfactant–polymer systems **V1 446–447**
 surfactants **V1 237, V1 388–390, V1 422–427, V2 162–166**
 critical packing parameter (CPP) **V1 45, V1 422, V1 432–433**
 critical solution temperature **V1 189–190**
 critical surface tension **V1 120–121, V2 126–127**
 Cross equation **V1 209**
 ‘cross-talk’ **V1 87, V1 92**
 crude oil **V1 252, V1 254, V1 255, V1 265–266**
 cryo-transmission electron microscopy (Cryo-TEM) **V2 193, V2 196, V2 198, V2 335, V2 358**
 cryoporometry **V1 169–170**
 crystal growth **V1 79**
 see also Ostwald ripening
 crystallization **V1 416–417**
 cubic phases
 domain morphology **V2 311–314**
 drug delivery **V1 12, V1 20**
 multicomponent systems **V1 492, V1 494, V1 498–499**
 phase behaviour **V1 481**
 rheology **V2 204–205**
 self-diffusion **V2 353–355**
 structure **V1 472, V1 473–475**
 thermotropic behaviour **V2 209**
 cumulant analysis **V2 366**
 curtain coating **V1 88**
 curvature **V2 70–72, V2 160–161, V2 169, V2 301–321, V2 336–338, V2 345**
 cyclic acetals **V1 391–392**
 cyclodextrin solutions **V1 16–17**
 cylindrical electrophoresis chambers **V2 376–377**
 cylindrical micelles **V2 193–194, V2 199**

 Darcy’s law **V1 152**
 data processing **V2 89–90, V2 92–95**
 DDAB *see* didodecyldimethylammonium bromide
 de-wetting **V2 146, V2 149**
 deagglomeration **V1 206–208**
 Debye screening length **V2 393–395**
 Debye–Hückel equation **V1 131, V2 424**
 DEEDMAC *see* diethylester dimethylammonium chloride
 defects **V1 202, V2 317–319**
 defoamers **V1 263, V2 143, V2 154–155**
 see also antifoamers; foam breaking
 deformation **V1 146, V2 388**
 degradation products **V1 515**
 denaturation temperature **V1 46**
 density fluctuations **V2 431, V2 432–433**
 deoxyribonucleic acid (DNA) **V1 12–13, V1 460, V2 84, V2 85**
 depletion method **V2 436**
 DEQs *see* diesterquaternaries
 Derjaguin–Muller–Toporov (DMT) theory **V2 389, V2 391**
 destabilization **V1 40–42**
 detergency **V1 53–72**
 alkyl sulfates **V1 274**
 amphoterics **V1 365, V1 366–367**
 anionic surfactants **V1 279–282**
 betaines **V1 350**
 cationic surfactants **V1 310, V1 314–318, V1 321–327**
 cleavable surfactants **V1 395**
 environmental issues **V1 511, V1 513, V1 521**
 fabric softeners **V1 314–318**
 hydrotropes **V1 415–416**
 mesophases **V1 503**
 nonionic surfactants **V1 302, V1 303, V1 305**
 sulfosuccinates **V1 289**
 deuterium labelling **V2 289–290**
 developer scavengers **V1 87–88**
 dewatering **V1 152**
 di-tallow dimethylammonium chloride (DTDMAC) **V1 530–532**
 di-tallow imidazolinester (DTIE) **V1 530–532**
 dialkyldimethyl quaternary ammonium salts **V1 311–312, V1 314, V1 315, V1 318**
 diameter axisymmetric drop shape analysis (ADSA-D) *see* axisymmetric drop shape analysis
 didodecyldimethylammonium bromide (DDAB) **V2 181–184**
 dielectric relaxation **V2 11**
 diesterquaternaries (DEQs) **V1 530–532**
 diethylene triamine quaternary ammonium salts **V1 315–316**
 diethylester dimethylammonium chloride (DEEDMAC) **V1 530–532**
 differential scanning calorimetry (DSC) **V1 170**

- diffusion coefficient **V2 244**
dilation **V2 190, V2 206, V2 235, V2 237**
dimensional analysis **V2 274**
dimeric surfactants *see* Gemini surfactants
1,2-dimyristoyl-*sn*-glycero-3-phosphatidylcholine (DMPC) **V2 50, V2 51–52**
direct casting **V1 215–216**
direct coagulation casting **V1 215**
direct flotation **V1 345**
disc-nematic phases **V1 489**
Discovery space shuttle **V2 236**
disinfection **V1 318–319, V1 368**
disjoining pressure **V2 417, V2 424–430, V2 431**
Disorder–Open–Connected–Cylinder (DOC) model **V2 181, V2 182–184**
dispersants **V1 116–119, V1 147–148, V1 288, V1 291**
dispersions
absorber dyes **V1 101–102**
agriculture **V1 79**
aqueous **V1 39**
ceramics **V1 206–208**
chemically heterogeneous **V1 40–42**
chemically homogeneous **V1 40**
coupler **V1 99–101**
drug delivery **V1 8–15**
emulsions **V1 99–100, V2 55–56**
methodology **V2 4–5**
mixed micellization **V1 100**
monolayer-protected metal clusters **V2 113–114**
nanocrystalline **V1 100–101**
natural systems **V1 175–176**
oil-continuous **V1 39**
paint pigments **V1 113–119**
particle processing **V1 238–243**
photography **V1 91–92**
solid **V2 3–20**
solubilization **V2 159**
stabilization **V1 381–384**
thin-liquid films **V2 416, V2 425–426**
disproportionation **V1 41**
dissipative particle dynamics (DPD) simulation method **V1 537, V1 546–547, V1 548**
dissociation **V1 221**
distillation **V1 416**
disulfine blue active substances (DSBAS) **V1 513**
DLS *see* dynamic light scattering
DLVO theory **V1 130–132, V2 13–15, V2 17, V2 29**
DMAOs *see* alkyltrimethylammonium oxides
DMPC *see* 1,2-dimyristoyl-*sn*-glycero-3-phosphatidylcholine
DMT *see* Derjaguin–Muller–Toporov theory
DNA *see* deoxyribonucleic acid
DOC *see* Disorder–Open–Connected–Cylinder model
DODAB surfactant **V2 48, V2 49**
dodecyl-1,3-propylenebis(ammonium chloride) (DoPDAC) **V1 495**
domain morphology **V2 301–321**
DoPDAC *see* dodecyl-1,3-propylenebis(ammonium chloride)
double-chain surfactants **V2 160**
see also lipids
double-layers **V2 11–14**
DPD *see* dissipative particle dynamics
drag reduction **V2 210**
drained casting **V1 212–213**
drilling mud **V1 259**
drop methods
contact angle **V2 253–254, V2 255–263, V2 264**
dynamic surface tension **V2 230–236**
equilibrium surface tension **V2 217, V2 220–223, V2 235**
droplet microemulsions **V2 344–352**
droplet sedimentation **V2 271–272**
droplet size
agrochemical sprays **V1 80–83**
comminution **V1 181–183**
monomer emulsions **V1 191**
Ostwald ripening **V1 186–187**
polymerization techniques **V1 195–198**
surfactant role **V1 111–113**
drugs (pharmaceutical) **V1 3–6, V1 8–23**
dry pressing **V1 214**
dry strength, paper **V1 145**
dry wetting **V2 122–123**
drying, ceramics **V1 216–217**
DSBAS *see* disulfine blue active substances
DSC *see* differential scanning calorimetry
DTDMAC *see* di-tallow dimethylammonium chloride
DTIE *see* di-tallow imidazolinester
Du Noüy ring method **V2 217, V2 220**
Dupré equation **V2 125–126**
dye micellization **V2 243**
dye solubilization **V2 242–243, V2 247–248**
dynamic light scattering (DLS) **V2 242, V2 247, V2 294–296, V2 357, V2 365–369**
dynamic surface forces **V2 388–389**
dynamic surface tension **V2 218, V2 225–238, V2 439–440**
dynamic swelling **V1 185, V1 191**
EC₅₀ tests **V1 518–519, V1 524–525, V1 530, V1 532**
eddy currents **V2 284–285**
edge penetration **V1 161**
EDTA *see* ethylenediaminetetraacetic acid
EEC *see* European Economic Community Directives
EFF *see* emulsion ferrofluid techniques
EHEC *see* ethyl(hydroxyethyl)cellulose
Einstein relationship **V2 350**
elastic interaction **V1 382–383**
elasticity **V2 206**
electrical behaviour
colloidal dispersions **V2 9–13**
conductivity **V1 233–236, V2 213, V2 242, V2 335, V2 438**
dispersion **V2 5**
electrical double-layer **V1 222–223, V2 373–374**
see also zeta potential
electroacoustic sonic amplitude (ESA) **V1 102–103, V2 379**
electrokinetic potential *see* zeta potential
electrokinetics **V1 102–103, V2 371–382**
see also electroosmosis; electrophoresis; sedimentation potential; streaming potential
electrolytes
antifoaming agents **V2 154**
critical micelle concentration **V2 246**
detergency **V1 59, V1 60, V1 72**
electrostatic double-layers **V2 393–397**
foaming **V1 72**
micellization **V1 425–427**
phase behaviour **V1 500–501**

- electrolytes (*Continued*)
 surface charge V1 221–222
 surfactant–polymer systems V1 454–460
 electron microscopy (EM) V2 335–336
 electron spectroscopy for chemical analysis (ESCA) V1 51,
 V1 109, V1 111–113, V1 162–163, V1 397
 electronic properties V1 87, V2 83–84, V2 92–95
 electrooptics V2 89–90
 electroosmosis V1 225, V2 371–372, V2 375–379
 electrophoresis V1 97, V1 102–103, V1 224, V1 336, V2
 371–372, V2 375–379
 electrophoretic deposition (EPD) V1 213–214
 electrostatics
 air V1 50
 colloidal dispersions V2 13–15
 double-layers V1 204–205, V2 424–425
 liquids V1 42
 patch aggregation V1 136, V1 137
 responsive systems V1 25–26
 solubilization V2 165, V2 185
 stabilization V1 108
 surface charge V1 226–229
 surfactant–polymer systems V1 448
 electrosteric stabilization V1 206
 ellipsoids of revolution V2 322–323
 ellipsometry V2 443–444
 elongational rheology V1 153
 EM *see* electron microscopy
 emulsifiable concentrates V1 73, V1 74–76
 emulsification
 comminution V1 179, V1 180–184
 condensation V1 179, V1 184–185
 emulsifiers V1 179–180
 failure V2 339, V2 344, V2 351–352
 foodstuffs V1 42, V1 45, V1 47
 paints V1 105, V1 107–110
 photography V1 91, V1 99–100
 photolability V1 397
 spontaneous V1 185
 emulsion concentrates V1 76–78
 emulsion ferrofluid (EFF) techniques V2 417
 emulsion films V2 30–31
 emulsion polymerization V1 107–110, V1 175–200, V1
 288, V1 290–291, V1 400–402
 emulsions
see also emulsification; microemulsions
 alkyd V1 113
 antifoaming agents V2 152–154
 bitumen V1 335–336
 characterization V2 55–56
 definition V2 4
 drug delivery V1 8–9
 foodstuffs V1 40–41
 formation V2 74
 miniemulsions V1 176, V1 177, V1 195–196
 monomer V1 191–196
 multiple V1 73
 nanoemulsions V1 77
 petroleum industry V1 256–259, V1 262, V1 263
 photography V1 85–86, V1 87–89
 radical polymerization V1 196–198
 separation V1 265–266
 spontaneous V1 74–76
 stability V1 186–190
 suspoemulsions V1 73
 thin-liquid films V2 417
 encapsulation V1 28, V1 418
see also microencapsulation
 end-functionalization V2 105–109
 engulfment (particle behaviour) V2 275
 enhanced oil recovery (EOR) V1 259, V1 262–263
 entropic interactions V1 382–383, V2 426–427
 environmental issues
see also biodegradability
 amphoteric surfactants V1 364, V1 365, V1 532–534
 analytical techniques V1 513–514
 anionic surfactants V1 279–280, V1 284, V1 520–525
 aquatic toxicity V1 524–525, V1 529, V1 531–532, V1
 534
 assessment criteria V1 514–520
 cationic surfactants V1 321, V1 332, V1 340, V1
 529–532
 ethoxylated surfactants V1 107, V1 117
 eutrophication V1 61, V1 116
 industry V1 510–512
 legislation V1 512–513
 nonionic surfactants V1 303, V1 305, V1 525–529
 oil industry V1 264–265, V1 340
 risk assessment V1 534–535
 softening agents V1 332
 zwitterionic surfactants V1 364, V1 365
 EON *see* equivalent ethoxy number
 EOR *see* enhanced oil recovery
 EPD *see* electrophoretic deposition
 equation of state V2 127–128, V2 252–253, V2 270, V2
 274
 equilibrium contact angles V2 129–130
 equilibrium films V2 28–29
 equilibrium phases V2 56
 equilibrium surface tension V2 217–224
 equivalence points V1 96–97
 equivalent ethoxy number (EON) V2 161
 ESA *see* electroacoustic sonic amplitude
 ESCA *see* electron spectroscopy for chemical analysis
 ester quaternary ammonium salts V1 316–317, V1
 329–330, V1 395–397
 ether oils V2 67
 ethoxylated alcohols V2 55–63, V2 69–70, V2 71–73
 ethoxylated amines V1 327, V1 328–329
 ethoxylated quaternary ammonium salts V1 329–330
 ethoxylated surfactants V1 107
 ethoximer distribution V1 299–300, V1 302
 ethylene oxide V1 298–300, V1 303–304
 ethylenediaminetetraacetic acid (EDTA) V1 332
 ethyl(hydroxyethyl)cellulose (EHEC) V2 401–402
 Euclidean solids V2 190
 European Economic Community (EEC) Directives V1
 512–513
 European Working Group (EWG) V1 512–513
 eutrophication V1 61, V1 116
 EWG *see* European Working Group
 excess solubilization V2 178–180
 extenders V1 114
 extraction V1 416
 extrusion coating V1 88
 extrusion molding V1 214

- fabric softeners V1 314–318
- fatty acids V1 277–278, V1 352–353, V2 49–52, V2 82
- fatty alcohols V1 273, V1 275
- fatty amines V1 318
- fatty nitriles V1 311
- Feldspar, flotation V1 346
- ferromagnetic colloids V2 7
- fibre collapse point V1 129
- fibre lignin content V1 125–127
- fibre properties, paper V1 125–128, V1 129
- Fick's law V2 16, V2 17
- fillers, paper V1 129
- films
 - see also* foams
 - film pressure concept V2 122–123
 - film-dimpling V2 423
 - flotation V2 269
 - morphology V1 109–110
 - stratification V2 427
 - thin-liquid V2 415–433
 - wetting V2 122–123
- filter dyes V1 101–103
- first-effect concentrations V1 526
- fish-cuts, phase prisms V2 340
- fixation, emulsions V1 196–198
- flexibility V1 438
- flexible surface model V2 336
- flip-flop (transverse diffusion) V2 47, V2 50
- flocculation
 - ceramics V1 205, V1 209–211, V1 213
 - colloidal dispersions V2 15–16
 - definition V2 15–16
 - emulsion concentrates V1 76, V1 77
 - foodstuffs V1 43, V1 44
 - nanoparticles V1 135
 - paper V1 129–130, V1 135–138, V1 141–142, V1 151
 - pigment dispersion V1 114
 - polymeric surfactants V1 381–382, V1 383
 - selective V1 243–245
- Flory–Huggins theory V1 229–230, V1 374–375
- Flory–Krigbaum theory V1 382
- flotation V1 246–249, V1 289, V1 344–347
- fluidization V1 265
- fluorescence quenching V2 281, V2 290–292
- fluorosurfactants V1 122, V1 291
- foam breaking V2 143–157
- foams V2 23–43
 - see also* films
 - amphoterics V1 365, V1 366–367
 - anionic surfactants V1 274, V1 275, V1 280
 - bubble formation V1 255, V1 274, V2 418
 - cationic surfactants V1 325
 - characterization V2 415–416, V2 433
 - detergency V1 71–72
 - film rupture mechanisms V2 26
 - foaming agents V2 40–41
 - foodstuffs V1 41–42
 - industrial materials V2 37–43
 - micellar structural forces V2 427–428
 - petroleum industry V1 254–256, V1 262–263
 - preparation V2 24–25, V2 40–43
 - stability V2 25–37
 - stabilizers V1 306
- foodstuffs V1 39–52
 - cationic surfactants V1 332–334
 - environmental issues V1 512
 - foam breaking V2 155–156
 - foams V2 24–27, V2 43
 - nonionic surfactants V1 297, V1 307–308
 - force fields V1 539–541
 - force methods V2 217–221
 - fractional amino acid transfer V2 176–177
 - fracturing fluids V1 340
 - fragmentation fractal dimension V2 360
 - free energy V2 121–134
 - see also* interfacial tension; surface tension
 - free rosin distributions V1 140
 - free volume theory V1 230
 - freeze-fracture technique V2 335, V2 353
 - frequency doubling V2 88–89
 - frictional forces V2 390–392
 - fringes of equal chromatic order (FECO) interferometry V2 384
 - froth V2 25
 - functionality tests V1 46
 - fungicides V1 318–321
 - funnel-shaped test V2 33–34
- gas adsorption V1 167–168
- gas chromatography (GC) V1 362
- gas-filled polymer foams V2 38, V2 40
- GC *see* gas chromatography
- gel phases
 - betaines V1 353
 - ceramics V1 215
 - definition V2 4
 - domain morphology V2 307–308
 - drug delivery V1 21–23, V1 29
 - foam stabilization V2 27
 - rheology V2 204
 - structure V1 476–477
 - surfactant–polymer systems V1 455–456, V1 462–463
 - vesicle bilayers V2 46–47
- gel-like networks V2 430
- gelatin V1 86, V1 97
- gemin surfactants V1 314, V1 354, V1 385–390, V1 469, V1 496–497
- gene therapy V1 11–12
- genus concept V2 304–306, V2 314
- Geography-Referenced Exposure Assessment Tool for European Rivers (GREAT-ER) V1 535
- geometric mean combining rule V2 127
- Gibbs elasticity V2 27–28, V2 235
- Gibbs equations
 - adsorption V1 75, V1 76–77, V1 252, V1 389, V2 242
 - phase rule V1 466, V1 467
 - solubilization V2 164
- Gibbs free energy V2 122
- Gibbs triangle V2 57–60
- Gibbs–Helmholtz equation V1 177
- Gibbs–Marangoni effect V1 255, V2 27–28
- Gibbs–Thompson equation V1 169–170
- Girifalco–Good–Fowkes–Young equation V2 129
- globules V2 304, V2 306, V2 310, V2 316
- glucamides V1 327
- gold V2 3, V2 4, V2 6, V2 99–116
- goniometer–telescopes V2 254, V2 260–262, V2 263

- goniometry **V2** 357, **V2** 368
 Gouy–Chapman model **V1** 222–223, **V2** 373–374, **V2** 375
 Gouy–Chapman–Stern–Grahame model **V2** 380
 graft copolymers **V1** 374, **V1** 377–384
 granules **V1** 214, **V2** 269–277
 grazing incidence X-ray diffraction **V2** 80, **V2** 82
 GREAT-ER *see* Geography-Referenced Exposure Assessment
 Tool for European Rivers
 Griffith equation **V1** 201
 grinding, dispersion **V1** 114
 Guinier approximation **V2** 362
- haematite **V2** 7
 Hagen–Poiseuille equation **V2** 272
 hair care **V1** 327–328, **V1** 354, **V1** 368
 Hamaker theory **V2** 392
 hard surface cleaning **V1** 321–326, **V1** 367–368
 hard-sphere radius **V2** 346
 head space measurement **V2** 35
 head-group overlap **V2** 426–427
 heat of immersion **V2** 269
 heat treatment **V1** 245
 heat-developable materials **V1** 90
 heavy metal ions **V1** 288–289
 Helfrich forces **V2** 429
 Helmholtz free energy **V2** 122
 Helmholtz model **V1** 222
 Helmholtz–Smoluchowski equation **V2** 374–375
 hemimicelles **V1** 236, **V1** 237, **V1** 238
 heterogeneity **V1** 40–42, **V1** 155–156, **V1** 202–203, **V2** 130
 heteronuclear Overhauser effect **V1** 546
 heterophase polymerizations **V1** 181, **V1** 184, **V1** 185, **V1** 190
 hexagonal mesophases **V2** 308–309
 hexagonal phases **V1** 473, **V1** 479, **V1** 481, **V1** 492, **V2** 167, **V2** 308–309
 hexamethyldisiloxane (HMDSO) **V2** 380–381
 high performance liquid chromatography (HPLC) **V1** 362, **V1** 513–514
 HLB *see* hydrophilic–lipophilic balance
 HMDSO *see* hexamethyldisiloxane
 homogeneity **V1** 540, **V2** 314, **V2** 321–323, **V2** 330
 homopolymers **V1** 373–374
 honeycombs **V2** 316
 Hookean solids **V2** 190, **V2** 194
 Hooke's law **V2** 387
 HPLC *see* high performance liquid chromatography
 hydrate inhibitors **V1** 340
 hydration interactions **V1** 42–43, **V2** 394
 hydrocarbon radius **V2** 345–346, **V2** 348
 hydrodynamic forces **V2** 375, **V2** 380–382, **V2** 388–389, **V2** 417
 hydrodynamic radius **V2** 334, **V2** 346, **V2** 347, **V2** 368–369
 hydrogen bonding **V1** 230, **V1** 244, **V1** 489
 hydrolysis **V1** 100, **V1** 143–144, **V1** 391–397, **V2** 6–7
 hydrophiles **V1** 298–301
 hydrophilic–lipophilic balance (HLB)
 anionic surfactants **V1** 275
 cationic surfactants **V1** 310
 emulsions **V1** 180, **V1** 257–258
 lipids **V1** 44–45, **V1** 48
 microemulsions **V2** 61, **V2** 63, **V2** 69
- paint pigments **V1** 117
 solubilization **V2** 161, **V2** 167
 spontaneous emulsification **V1** 74
 hydrophobic effect **V1** 467–469, **V2** 240
 hydrophobicity
 foams **V2** 151–152
 interactions **V1** 233, **V1** 428–429, **V1** 449, **V1** 452, **V2** 430
 lipids **V1** 12–13
 micelles **V1** 294–297, **V2** 162
 modification **V1** 447–452, **V1** 461
 hydrophobizing *see* sizing
 hydrotropes **V1** 321–323, **V1** 407–420, **V1** 500
 hyperpolarizability **V2** 87–88
 hysteresis **V2** 268, **V2** 401
- IEP *see* isoelectronic point
 image analysis **V1** 164–166, **V2** 35, **V2** 36
 immersional wetting **V2** 126
 immunization **V1** 28
in situ particle size measurement **V1** 239
in situ-forming carrier systems **V1** 20
 inclusion complexes **V1** 17
 indifferent adsorption **V2** 429
 indifferent ions **V2** 10
 industrial materials **V2** 37–43
 industrial syntheses *see* manufacture
 infrared (IR) spectroscopy **V1** 163, **V2** 101–102, **V2** 105–106
 inhomogeneous surfaces **V2** 129–130, **V2** 135–136
 inisurfs **V1** 401–402
 initiators **V1** 194, **V1** 400
 injection molding **V1** 214
 inner salts **V1** 350
 insulin adsorption **V1** 5
 integrated circuits **V2** 93–95
 intensity-weighted distribution **V2** 362, **V2** 366
 interfacial curvature **V2** 301–321
 interfacial polymerization **V1** 73
 interfacial tension
 definition **V2** 121
 measurement **V2** 218–223, **V2** 225–226, **V2** 230–232, **V2** 235, **V2** 258–260
 microemulsions **V2** 70, **V2** 72–73
 oil recovery **V1** 261
 polymers **V1** 178
 sedimentation volume **V2** 269–270
 spontaneous emulsification **V1** 74–76
 wetting thermodynamics **V2** 127–129
 interference microscopy **V2** 263–264
 interferometry **V2** 384–385
 intermediate phases **V1** 477–479, **V2** 316–317
 internal sizing **V1** 138–145
 International Organization for Standardization (ISO) **V1** 516, **V1** 517
 interpenetration **V1** 241–242
 inverse micellar solutions **V1** 411
 inverse phases **V1** 499
 inverse polymerization **V1** 180
 ion adsorption **V1** 220
 ion dissolution **V1** 220–221
 ion exchange **V1** 61–65, **V1** 233
 ion pairing **V1** 233

- ionic strength **V1** 226, **V1** 240
 ionic surfactants **V1** 493–497, **V2** 64–66, **V2** 165–166
 ionization **V1** 221, **V2** 371
 IR *see* infrared spectroscopy
 isoelectronic point (IEP) **V1** 46, **V1** 96–97, **V1** 224, **V1** 225–226, **V1** 246–248
 isomorphous substitutions **V1** 221
- Johnson–Kendall–Roberts (JKR) theory **V2** 388, **V2** 389–390, **V2** 391
 Jönsson model **V2** 165–166
- kaolin **V1** 147
 kaolinite **V2** 8–9
 Kelvin equation **V1** 161, **V1** 168
 ketals **V1** 393–394
 kinetics **V1** 433–434, **V2** 55
 Klevens equation **V1** 362
 Kolmogorov length **V1** 181
 Kozeny–Carman relationship **V1** 152
 Krafft point **V1** 45, **V1** 427–428, **V1** 468, **V1** 489, **V2** 245
 Krafft temperature *see* Krafft point
 Krieger–Dougherty equation **V1** 151, **V1** 210
 kugelschaum, foaming **V2** 24–25
- LAC *see* limiting association concentration
 lamellae lifetime measurement **V2** 37
 lamellae profiles **V2** 422
 lamellar phases
 see also liquid crystals
 bilayer solubilization **V2** 171–173
 domain morphology **V2** 307, **V2** 308, **V2** 316
 hydrotropes **V1** 411, **V1** 412–414
 micelle self-assembly **V1** 253
 phase behaviour **V1** 481
 phase prisms **V2** 340–341
 rheology **V2** 199–204
 rigid interface solubilization **V2** 185
 shear behaviour **V2** 211–214
 smectics **V2** 300, **V2** 307, **V2** 315
 structure **V1** 471, **V1** 472–473
 vesicles **V1** 418
 lamellar structural forces **V2** 428–429
 laminar flow **V2** 18
 Langmuir equation **V1** 58
 Langmuir–Blodgett (LB) films **V2** 79–98
 command surfaces **V2** 91–92
 computer simulation **V1** 538
 deposition **V2** 80–83, **V2** 85
 historic perspective **V2** 99
 molecular electronics **V2** 92–95
 nanoparticles **V2** 83–84
 nonlinear optical devices **V2** 85–90
 sensors **V2** 90–91
 surface forces **V2** 392, **V2** 396, **V2** 403–404
 lanthanum myristate **V2** 329
 lanthanum palmitate **V2** 329
 Laplace equations **V1** 168, **V2** 121, **V2** 252, **V2** 272, **V2** 421, **V2** 422
 laser light **V2** 86–89
 laser-focusing techniques **V1** 165
- LASs *see* linear alkylbenzene sulfonates
 lateral interactions **V1** 236
 lateral structure **V1** 543
 latex **V1** 105–122, **V2** 8
 lattices **V1** 221, **V1** 401–402
 LB *see* Langmuir–Blodgett
 LC₄₅₀ tests **V1** 518–519, **V1** 524–525, **V1** 530, **V1** 532
 lead myristate **V2** 328
 legislation **V1** 512–513
 Lial process **V1** 295
 lidocaine **V1** 7, **V1** 8
 life, origins **V2** 50
 Lifshitz theory **V2** 390, **V2** 392, **V2** 425–426
 ligand complexation **V1** 96
 light scattering
 see also goniometry; static light scattering
 CMC determination **V2** 242, **V2** 247
 droplet microemulsions **V2** 349
 dynamic **V2** 242, **V2** 247, **V2** 294–296, **V2** 357, **V2** 365–369
 micelle size/shape **V2** 281, **V2** 294–296
 microemulsions **V2** 335
 paper **V1** 129
 particle size **V2** 357–370
 small-angle **V2** 357, **V2** 362, **V2** 364–365
 thin-liquid films **V2** 417
 light sensitivity **V1** 101
 lignin content **V1** 125–127
 ligninsulfonates **V1** 292
 limited coalescence **V1** 103–104
 limiting association concentration (LAC) **V2** 165
 lindane **V2** 178–184
 line tension approach **V2** 123–124
 linear alkylbenzene sulfonates (LASs) **V1** 511, **V1** 513, **V1** 521, **V1** 523–526
 linearized Poisson–Boltzmann distribution **V1** 228
 lipids **V1** 12–13, **V1** 44–46
 liposomes **V1** 9–12, **V2** 45, **V2** 49–50
 liquid bridges **V1** 44, **V1** 50
 liquid crystals
 agrochemical sprays **V1** 83
 chemical structure **V1** 465–508
 concentration effects **V1** 436
 drug delivery **V1** 12, **V1** 20–21
 foam stabilization **V2** 29–30
 foodstuffs **V1** 45
 formation **V1** 256
 hydrotropes **V1** 408–409, **V1** 411, **V1** 412–414, **V1** 415
 lamellar **V1** 411, **V1** 412–414, **V1** 418, **V1** 471, **V1** 472–473, **V1** 481
 Langmuir–Blodgett films **V2** 82, **V2** 91
 lyotropic **V1** 466–467, **V2** 299–338
 nematic **V1** 475–476, **V1** 483–484, **V1** 489, **V2** 82, **V2** 299–300
 phase behaviour **V1** 466, **V1** 472–502
 smectics **V2** 300, **V2** 307, **V2** 315
 solids/melts **V2** 299–301
 solubilization **V2** 166–169, **V2** 173
 surfactants **V1** 66–67, **V1** 70
 vesicle bilayers **V2** 46–47
 vesicles **V1** 418
 liquid magnets **V2** 7
 liquid soaps **V1** 273
 liquid transport **V1** 162

- liquid/liquid interface V1 65–67
 LOEC *see* lowest observed effect concentration
 loops V1 231, V1 377–379
 low shear viscosity V2 349–350
 lowest observed effect concentration (LOEC) V1 519, V1 527
 lyotropic liquid crystals V1 466–467, V2 299–338
 lyotropic nematic phases V1 475
- MAC *see* maximum additive concentration
 macroemulsions V1 176, V1 177
 macromolecules V1 15
 magnetic properties
 colloids V2 246
 Langmuir–Blodgett films V2 84
 liquids V2 7
 Maltese cross textures V1 473, V2 308
 manufacturing processes
 amphoterics V1 356–360
 anionic surfactants V1 273–279, V1 282–284, V1 286–288, V1 290
 betaines V1 352–353, V1 355
 block copolymers V1 303
 cationic surfactants V1 311–314
 Gemini surfactants V1 386
 Lial process V1 295
 nonionic surfactants V1 294–297, V1 298–300, V1 302–308
 OXO process V1 274, V1 295
 Shell Higher Olefin Process V1 295
 Williamson synthesis V1 275, V1 276
 Ziegler process V1 279, V1 294–295
 Marangoni flow V2 27–28, V2 146, V2 230
 MASIF *see* measurement and analysis of surface interactions and forces
 mass action models V1 429, V2 163–164
 mass-weighted distributions V2 359
 matte beads V1 87, V1 103–104
 maximum additive concentration (MAC) V2 163, V2 166, V2 170–171
 maximum bubble methods V2 217, V2 223, V2 227–229, V2 440
 Maxwell model V2 194–195
 MBAS *see* methylene blue active substances
 MD *see* molecular dynamics
 mean field approximations V1 378
 measurement and analysis of surface interactions and forces (MASIF) V2 384–388, V2 406
 mechanical pulping V1 125
 melts, liquid crystals V2 299–301
 membrane emulsification V1 183
 membranes V2 46, V2 49–52, V2 171–173
 meniscus formation V2 136–137
 meniscus height V2 82–83
 meniscus radii V2 421
 mercerization V1 337, V1 338, V1 339
 mercury porosimetry V1 168–170
 mesh mesophases V1 477–478, V1 494, V2 302, V2 305–306, V2 315–316
 mesogenic properties V1 490
 mesomorphism V2 300, V2 302
 mesophases
 additives V1 497–502
 bicontinuous V2 302, V2 303, V2 306, V2 310–315, V2 316–317
 columns V2 308–310
 cubic V2 311–314
 gels V2 307–308
 hexagonal V2 308–309
 hydrogen bonding V1 489
 lamellar V2 307, V2 308, V2 316
 liquid crystals V1 465–508
 lyotropic liquid crystals V1 466–467, V2 299–338
 meshes V1 477–478, V2 302, V2 305–306, V2 315–316
 molten V2 318–319
 morphology V2 301–321
 polycontinuous V2 316–317
 ribbons V2 309–310
 ringing gels V1 353, V2 204
 smectics V2 300, V2 307, V2 315
 metabolites V1 515, V1 519
 metals
 clusters V2 113–114
 foams V2 41–42
 ion hydrolysis V2 6–7
 nanoparticles V2 83–84, V2 113–114
 processing V1 512
 methyl ester ethoxylates V1 307–308
 methylene blue active substances (MBAS) V1 512, V1 513
 MHC *see* minimal hydrotropic concentration
 micelles
 see also critical micelle concentration; rod-like micelles
 agrochemical sprays V1 83
 amphoterics V1 362–363
 antifoaming agents V2 148
 aqueous solutions V2 190–192
 cationic surfactants V1 324
 computer simulation V1 544–546
 concentration effects V1 435–437
 coupler dispersions V1 100
 cylindrical V2 193–194, V2 199
 detergency V1 55–56, V1 59
 drug delivery V1 15–16
 foam films V2 427–428
 Gemini surfactants V1 388–390
 hemimicelles V1 236, V1 237, V1 238
 inverse solutions V1 411
 kinetics V1 433–434
 liquid crystals V1 465–466, V1 467–472
 mixed V1 100, V1 442, V1 451–452
 molecular dynamics V1 544–546
 non-aqueous media V2 246–248
 nonionic V1 440–442
 phase behaviour V1 481
 polymeric surfactants V1 376
 reversed V2 169–171, V2 174–177, V2 181–184
 self-assembly V1 252–254, V2 239–241
 self-reproduction V2 50
 size/shape measurement V2 281–297
 solubilization V2 162–169
 solvent effects V1 434
 sponge phase V1 439–440
 stability V2 148
 structure V1 421–423, V1 431–432, V1 437–441, V1 467–472, V2 162
 surfactant adsorption V1 236–237
 temperature effects V1 440–442

- thermodynamic models V1 428–430
vesicle comparison V2 45
- Michael addition reactions V1 359–360
- Michelson optics V2 264
- microcellular plastic foams V2 40
- microdomains V2 173
- microemulsions V2 55–77
see also emulsions
agriculture V1 73
antifoaming agents V2 152–153, V2 154
applications V2 73–74
bicontinuous V1 460–462, V1 482, V2 351–352
characterization V2 333–356, V2 364
condensation V1 184–185
definitions V2 56
detergency V1 68–70
Disorder–Open–Connected–Cylinder model V2 181
domain morphology V2 302, V2 317–319
droplet V2 344–352
drugs V1 7, V1 17
emulsion polymerization V1 176
formation V1 253, V1 258–259, V2 56, V2 68–70
hydrotropes V1 412, V1 414
interfacial tensions V2 70, V2 72–73
ionic surfactants V2 64–66
mesophases V2 300
microstructures V2 70–72, V2 342–344
mixed surfactants V2 63–64, V2 66–67
nonionic surfactants V2 57–64, V2 66–67
phase behaviour V2 57–70, V2 178, V2 338–342, V2 344–345
relaxation NMR V2 290
reversed V2 9
scattering techniques V2 293
soft surfactant systems V2 174–181
solubilization V2 169–171, V2 173, V2 174–185
stiff surfactant systems V2 181–185
surfactant–polymer systems V1 460–462
- microencapsulation V1 73–74
- microinterferometry V2 419–420
- microorganisms V1 319–320
- microparticle electrophoresis chambers V2 375
- micropipets V2 417
- microscopic study V2 34–35
- microstructures V2 342–344
- middle mesophases V2 308–309
- Mie theory V2 362–365
- migration, films V1 397
- mineral flotation V1 246–249, V1 344–347
- miniemulsions V1 176, V1 177, V1 195–196
- minimal hydrotropic concentration (MHC) V1 409, V1 412
- mining V1 344–347, V1 512
- mixed films V2 30
- mixed micelles V1 100, V1 442, V1 451–452
- mixed surfactants V1 498–499
- MLVs *see* multi-lamellar vesicles
- mobility V1 543, V2 375–377
- modelling, Langmuir–Blodgett films V1 537–550
- moist wetting V2 122–123
- molal volume V2 244
- molecular absorption V2 243–244
- molecular dimensions V2 323–332
- molecular dynamics (MD) V1 537–550
- molecular electronics V2 92–95
- molecular recognition V1 244
- molten mesophases V2 318–319
- monodisperse particles V2 6
- monolayer-protected clusters (MPC) V2 113–114
- monolayers V1 541–544, V2 80–82, V2 99–116, V2 146, V2 147
- monomer emulsions V1 191–196
- morphology V2 301–321
- motorized syringe methods V2 258
- multi-lamellar vesicles (MLVs) V2 45–46
- multiple emulsions V1 73
- multiple equilibrium model V1 429–430
- nanoassembly computers V2 93–95
- nanocrystalline dispersions V1 91, V1 100–101
- nanoemulsions V1 77
- nanoparticles V1 135, V2 83–84, V2 113–114
- nanoparticulate semiconductors V1 87
- NaPA *see* sodium polyacrylate
- Navier–Stokes equation V2 371–372, V2 374
- NBFs *see* Newton black films
- neat mesophases (smectics) V2 300, V2 307, V2 315
- necking, ceramics V1 207
- nematic liquid crystals V1 475–476, V1 483–484, V1 489, V2 82, V2 299–300
- neutralization flocculation V1 137
- neutron scattering *see* small-angle neutron scattering
- Newton black films (NBFs) V2 29, V2 30, V2 426, V2 427
- Newtonian liquids V2 190, V2 192–194
- nitrogen-containing polymers V1 327
- NLO *see* nonlinear optical
- NMR *see* nuclear magnetic resonance spectroscopy
- no observed effect concentration (NOEC) V1 284, V1 519, V1 526–527, V1 530, V1 532
- nonaqueous media V2 67, V2 246–248
- noninteracting micelles V2 191–192
- noninteractive adsorption V2 429
- nonionic hydrophiles V1 298–301
- nonionic hydrophobes V1 294–297
- nonionic micelles V1 440–442
- nonionic surfactants V1 293–308
block copolymers V1 491–493
environmental issues V1 525–529
microemulsions V2 57–64, V2 66–67
phase behaviour V1 480–491
solubilization V2 166–169
- nonlinear optical (NLO) devices V2 85–90
- non-Newtonian fluids V2 19–20
- nonpolar solvents V1 434, V2 67, V2 246–248
- nonpolar surfaces V2 396–398
- nonwetting surfaces V2 121
- nuclear magnetic resonance (NMR) spectroscopy
amphoterics V1 361–362
calibration V2 283–284
hydrotropes V1 412
intermediate mesophases V2 316
micelle shape/size V2 281–290
micellization V1 430–431
microemulsions V2 334–335, V2 347, V2 349
porosity V1 170
pulsed gradient spin-echo V2 282, V2 284–286, V2 288–289

- nuclear magnetic resonance (NMR) spectroscopy (*Continued*)
 relaxation V2 281–282, V2 289–290, V2 334–335, V2 347
 self-diffusion V2 281–289, V2 302, V2 334
 nucleation V1 95, V2 5–6, V2 416, V2 431
 null ellipsometry V2 443
 number-weighted distributions V2 359
- o/w *see* oil-in-water
- oblate ellipsoids of revolution V2 322–323
 oblate micelles V2 286–287
- OECD *see* Organization for Economic Co-operation and Development
- oil ganglia V1 259, V1 261
 oil industry *see* petroleum industry
 oil-continuous dispersions V1 39
 oil-in-water (o/w) microemulsions V2 55–74, V2 177–181, V2 184–185
 oil-swollen lamellar phases V2 185
 oils V1 499–500, V2 145, V2 147, V2 148–149, V2 151–154
 oily streaks V1 473
 oligoethylene oxide surfactants V2 337–338
 oligopeptides V1 4–5
 open-cell structures V2 41
 optical density V1 409–410
 optical fibre probes V2 35, V2 38
 optical storage devices V2 87
 optical textures V1 472–473, V1 474
 oral care V1 369
 oral drug administration V1 8–9, V1 13, V1 18, V1 28
 ordered phases V2 307–317
 organic monolayers V2 79–98, V2 99–116
 Organization for Economic Co-operation and Development (OECD) tests V1 513, V1 518, V1 520, V1 523, V1 527–528, V1 533–534
 organoclays V1 343–344
 origins of life V2 50
 ortho esters V1 394–395
 orthokinetic coagulation V2 18–19
 oscillating jet method V2 229–230
 oscillatory force profiles V2 399–400
 osmometry V2 244, V2 247
 osmosis V1 211–212, V2 349, V2 417
 Ostwald ripening
 dynamic swelling V1 191
 emulsion concentrates V1 77–78, V1 79
 emulsions V1 185–188, V1 191
 foams V1 41
 photography V1 95–96
 overcoating V1 87
 oversize fraction V2 359
 OXO process V1 274, V1 295
 oxyethylene surfactants V1 440–442
- π -stacking V1 467
 packing density V1 211
 paints V1 105–122, V1 397, V1 403–404
 palisade layer V2 162
 paper V1 123–173
 absorbency V1 154–158, V1 159–162
 cationic surfactants V1 331–332
- environmental issues V1 512
 foam breaking V2 143, V2 145
 formation V1 128–138
 internal sizing V1 138–145
 polymer adsorption V1 132–136
 porosity V1 167–171
 surface properties V1 155–156, V1 158–159, V1 162–166
 surface treatment V1 146–154
 wettability V1 154–159
- parachute morphology V2 49
 paraphenylenediamines V1 89, V1 90, V1 93
 parenteral drug administration V1 9–10, V1 19–20
 Parker–Print–Surf (PPS) test V1 165
 partial molal volume V2 244
 partial wetting V2 121
 particle size V1 239, V2 357–370
 particle suspension layer stability V2 271–272
 particulates V1 48–51, V1 91–92, V1 94–99, V2 150–152, V2 153
 Pascalian liquids V2 190
 patch flocculation V1 136, V1 137
 patterned self-assembling monolayers V2 109–113
 PB *see* Poisson–Boltzman theory
 PCS *see* photon correlation spectroscopy
 pearl-necklace model V1 447–448
 PEC *see* predicted environmental concentrations
 PEGs *see* poly(ethylene glycol)s
 pendant drop method V2 217, V2 221–222, V2 233
 penetration
 capillary V1 160–162, V2 120, V2 136–140
 drug delivery V1 11
 molecular dynamics V1 544, V1 545
 surfactant aggregates V2 166–168
 PEO *see* poly(ethylene oxide)
 PEO–PPO–PEO block copolymers V1 11, V1 13, V1 15–16, V1 21–25, V2 168, V2 204–205
 peptization V1 334, V1 336–337, V2 3
 Percus–Yevick approximation V2 205
 perfluorocarbon fluids V1 179
 peristaltic forces V2 426
 Perrin black films *see* Newton black films
 personal care V1 327–330, V1 344, V1 354, V1 364–369
 petrol sulfonates V1 278
 petroleum industry V1 251–267, V1 295–296, V1 337–341, V1 343–344, V1 512
 Peyer's patches V1 28
 PGSE NMR *see* pulsed gradient spin-echo nuclear magnetic resonance
- pH effects
 amphoterics V1 350
 betaine esters V1 396
 ceramics V1 204–205, V1 215
 dispersions V1 240
 drug delivery V1 25–26
 effects on sizing V1 141–142
 electrokinetics V2 372, V2 376–377, V2 380
 fatty acid vesicles V2 49
 particle mobility V2 376–377
 selective flocculation V1 245
 surface charge V1 221–222
 thickener stability V1 323–324
 zeta potential V1 225–226, V1 248–249, V2 380–381
 zwitterions V1 350, V1 352–353

- pharmacy V1 3–38, V1 369, V1 418–419, V1 511
- phase behaviour
- amphiphilic drugs V1 7, V1 8
 - computer simulations V1 547–550
 - foam stabilization V2 31
 - hydrotropes V1 412–414, V1 500
 - in situ*-forming carrier systems V1 20
 - inversion V1 44, V1 186, V1 189–190, V1 258, V2 61, V2 338
 - ionic surfactants V1 493–497
 - liquid crystals V1 466, V1 472–502
 - micelles V1 481
 - microemulsions V2 57–70, V2 178, V2 338–342, V2 344–345
 - nonionic surfactants V1 480–491
 - separation V1 43, V1 186, V1 429, V2 40
 - surfactant–polymer systems V1 452–463
 - surfactants V1 67–71, V1 480–497
 - transition temperature V2 46–47, V2 50–52
 - zwitterions V1 493
- phase prisms V2 339–342
- phase rule V1 466, V1 467
- phosphated alcohols V1 285–287
- phosphobetaines V1 354–355
- phospholipid bilayers V2 45, V2 46–47, V2 49–52
- phosphoric acid esters V1 285–289
- photochromism V2 91–92
- photography V1 85–104, V1 176, V1 192–193
- photolability V1 397
- photomicroscopy V2 275–276
- photon correlation spectroscopy (PCS) V1 381
- photonic devices V2 85–90
- physico-chemical processes V1 421–443, V1 515, V1 517–518
- Pickering stabilizers V1 192–193
- picture framing V1 121
- pigments V1 108–109, V1 113–119, V1 147
- plasma polymerization V2 380–381
- plasticity V1 208
- plastics V1 91, V1 512, V2 37–38, V2 40–41
- plate methods V2 236–237
- PNEC *see* predicted no-effect concentrations
- point of zero charge (PZC) V2 9–10
- Poiseuille approximation V2 227
- Poisson–Boltzmann (PB) theory V1 205, V1 226–228, V2 12–13, V2 202–203, V2 373–374, V2 393–396, V2 424
- polar interactions V2 129
- polar layer V2 162
- polar solvents V1 434
- polar surfaces V2 394–396, V2 398–399
- polarization (optical) V2 86, V2 367
- polarized attenuated total reflection infrared spectroscopy V2 101, V2 102
- polarizing microscopy V1 75, V1 472
- polyamines V1 333
- polycarboxylates V1 64–65
- polycontinuous mesophases V2 316–317
- polydimethylsiloxanes V2 145
- polydispersity V2 18, V2 199–202
- polydispersity index V1 19, V2 359, V2 363–364
- polyederschaum, foaming V2 24–25
- polyelectrolytes V1 116–119, V1 132–136, V1 147–148, V2 402–404, V2 429
- poly(ethylene glycol)s (PEGs) V2 106–107, V2 381–382
- poly(ethylene oxide) (PEO) V1 5–6
- polyglucoside surfactants V1 489–491
- polyhydroxy surfactants V1 489
- polyhydroxybenzenes V1 412
- polymerization
- binder-emulsion preparation V1 107–110
 - emulsions V1 107–110, V1 175–200, V1 288, V1 290–291, V1 400–402
 - inverse V1 180
 - plasma V2 380–381
 - radical V1 176, V1 196–198
 - surfactants V1 107–110, V1 397–405
 - suspensions V1 103–104, V1 176, V1 192–193
 - vesicles V2 49
- polymers
- adsorption V1 132–136, V1 229–232, V1 241
 - bridging mechanism V1 136–137
 - drug delivery V1 13–14, V1 23, V1 27–29
 - electronically conducting V1 87
 - foam stabilization V2 26
 - latex dispersions V2 8
 - microemulsion additives V2 67–68, V2 69
 - nitrogen-containing V1 327
 - particle interactions V1 43, V1 205–206
 - patterned self-assembling monolayers V2 111
 - plastic foams V2 37–38, V2 40–41, V2 42
 - surfactant–polymer systems V1 445–463
 - surfactants V1 373–384
 - wetting V2 126–127
- polyoxyethylene surfactants V1 287–288, V1 486–487, V1 502
- polyphosphated alcohols V1 285–287
- polysaccharides V1 44, V1 46–48
- polyurethane foam V2 38, V2 41, V2 42
- porosimetry, mercury V1 168–170
- porosity V1 167–171, V2 120, V2 136–140, V2 269–277
- porous disc holders V2 418
- post-emulsified binders V1 111–113
- potash, flotation V1 347
- potentiometry V2 438
- powders V1 50–51, V1 202–203, V2 136, V2 138–140, V2 269–277
- PPS *see* Parker–Print–Surf test
- prebiological phases V2 50
- precursor films V2 135
- predicted environmental concentrations (PEC) V1 512–513, V1 535
- predicted no-effect concentrations (PNEC) V1 513, V1 519, V1 535
- pressure drop technique V2 35–36
- pressure effects V2 62, V2 68, V2 69, V2 246
- pressure filtration V1 203
- pressure methods V2 217, V2 223, V2 227–229, V2 234–236
- probing aggregation V2 368–369
- profile axisymmetric drop shape analysis (ADSA-P) *see* axisymmetric drop shape analysis
- prolate ellipsoids of revolution V2 322–323
- prolate micelles V2 286–287
- proline V1 417
- propionates V1 359–360
- propylene oxide V1 300, V1 303–304
- protein crystals V1 467

- proteins **V1** 5, **V1** 46, **V2** 106–109, **V2** 401
 protolysis **V2** 9–10
 protrusion **V2** 397, **V2** 427
 pseudo-binary phase diagrams **V2** 178–179
 pseudo-emulsions **V2** 30–31, **V2** 152–154
 pseudo-phase model **V2** 163, **V2** 173
 pulping **V1** 125
 pulsed gradient spin-echo nuclear magnetic resonance (PGSE NMR) **V2** 282, **V2** 284–286, **V2** 288–289
 puncture defects **V2** 319
 pyrolysis **V1** 217
 PZC *see* point of zero charge
- quasi-equilibrium **V2** 400
 quasi-lattice model **V1** 378
 quaternary ammonium salts
 agricultural adjuvants **V1** 341–342
 biocides **V1** 318–321
 cleavable surfactants **V1** 395–397
 cosmetics **V1** 316–317, **V1** 329–330
 detergency **V1** 314–318, **V1** 327
 environmental issues **V1** 530–532
 manufacture **V1** 311–314
 mineral flotation **V1** 345, **V1** 347
 oilfields **V1** 338–340
 organoclays **V1** 343–344
 paper **V1** 331
 thickeners **V1** 323
 Quemada function **V2** 349, **V2** 351
 quinoxalinediimines **V1** 89, **V1** 93–94
- radical polymerization **V1** 176, **V1** 196–198
 radius of gyration **V2** 295
 Raman spectroscopy **V1** 163
 Rayleigh limit **V2** 349, **V2** 361–362
 Rayleigh–Debye–Gans (RDG) approximation **V2** 362, **V2** 363, **V2** 368
 rayon **V1** 337, **V1** 338, **V1** 339
 reaction rates, vesicles **V2** 50
 receding contact angles **V2** 129–130, **V2** 150
 rectangular electrophoresis chambers **V2** 377–378
 reflected-light interferometry **V2** 419
 reflected-light video microscopy **V2** 419
 refractive index **V1** 114, **V2** 242, **V2** 420, **V2** 437
 rejection (particle behaviour) **V2** 275
 relaxation, NMR **V2** 281–282, **V2** 289–290, **V2** 334–335, **V2** 347
 repulsion forces **V2** 429
 RES *see* reticuloendothelial system
 responsive drug delivery **V1** 24–26
 restricted equilibrium **V2** 400
 retention, paper **V1** 129–130, **V1** 141–142
 reticuloendothelial system (RES) **V1** 9
 reverse flotation **V1** 345
 reversed phases
 liquid crystals **V1** 472–473, **V1** 480, **V1** 499
 micelles **V2** 169–171, **V2** 174–177, **V2** 181–184
 microemulsions **V2** 9
 Rhebinder effect **V1** 79
 rheology
 associative thickeners **V1** 449
 ceramics **V1** 208–212
 colloidal dispersions **V2** 19–20
 dilatational **V2** 237
 dispersions **V1** 239–240
 elongational **V1** 153
 foams **V1** 254
 foodstuffs **V1** 41
 liquid crystals **V1** 466
 mesophases **V1** 503
 modifiers **V1** 148–149, **V1** 343
 paper coatings **V1** 149–152
 surfactants **V1** 338–340, **V1** 389–390, **V2** 189–214
 rheopexy **V1** 209, **V2** 190, **V2** 206
 rhombohedral mesh phases **V1** 477–478, **V1** 494
 ribbon phases **V1** 477–478, **V1** 495, **V2** 309–310
 ring methods **V2** 236–237
 ringing gels **V1** 353, **V2** 204
 rinse-added softeners **V1** 317
 risk assessment **V1** 534–535
 road construction **V1** 334–337
 robust beer foams **V2** 416
 rod-like micelles
 birefringence **V2** 195, **V2** 206
 cationic surfactants **V1** 324
 concentration **V1** 437
 domain morphology **V2** 304, **V2** 306, **V2** 308–310
 flexibility **V1** 438
 rheology **V2** 193–199
 shear behaviour **V2** 206–210
 rolling-up mechanism **V1** 59, **V1** 65–67
 rosins **V1** 140–142
 Ross–Miles pour test **V2** 34
 rotator phase **V1** 477
 rotor mixers **V2** 34, **V2** 35
 rough surfaces **V2** 129–130
 rupture, films **V2** 431
- Saccharomyces cerevisiae* (yeast) **V2** 112
 SALS *see* small-angle light scattering
 salting-in **V1** 407, **V1** 409–410, **V1** 500
 salts, microemulsions **V2** 62, **V2** 64–66, **V2** 69
 SAMs *see* self-assembling monolayers
 SANS *see* small-angle neutron scattering
 SAXS *see* small-angle X-ray scattering
 scanning electron microscopy (SEM) **V1** 127, **V1** 170–171
 Scheludko cells **V2** 418
schlieren nematic texture **V1** 475
 Schulze–Hardy rule **V2** 17
 SDS *see* sodium dodecyl sulfate
 secondary black films *see* Newton black films
 secondary ion mass spectrometry (SIMS) **V1** 163
 secondary surfactants **V1** 365, **V1** 367
 sedimentation **V1** 186, **V2** 358, **V2** 365
 sedimentation potential **V1** 225, **V2** 371, **V2** 379
 sedimentation volume **V2** 269–271, **V2** 273
 seed particles **V1** 194
 segregative phase separation **V1** 453, **V1** 456–458
 selective flocculation **V1** 243–245
 self-assembling monolayers (SAMs) **V2** 99–116
 self-diffusion
 cubic phases **V2** 353–355
 droplet microemulsions **V2** 350–351
 microemulsions **V2** 342–344, **V2** 346–347

- NMR V2 281–289, V2 302, V2 334
 sponge phases V2 352–355
 self-emulsifiable oils V1 73
 self-reproduction V2 50–52
 SEM *see* scanning electron microscopy
 semiconductors V2 83–84, V2 93–95
 sensitization (paper) V1 97–98, V1 137
 sensors, Langmuir–Blodgett films V2 90–91
 separation V1 59, V1 416–417
 sequestration V1 288–289, V1 291
 serum replacement method V2 440–442
 sessile drop methods V2 217, V2 221–222, V2 253–254, V2 257–258
 sewage treatment *see* waste-water treatment
 SFA *see* surface force apparatus
 SFF *see* solid freeform fabrication
 shape methods V2 217, V2 221–223, V2 232–234
 shape parameters, mesophases V2 331, V2 332
 shear behaviour V1 149–152, V1 208–210, V2 205–214, V2 349–350
 shear moduli V2 202–204
 shear planes V2 374–375
 Shell Higher Olefin Process (SHOP) V1 295
 Shinoda-cuts, phase prisms V2 340
 SHOP *see* Shell Higher Olefin Process
 short-chain sulfonates V1 291
 short-oil alkyds V1 113
 Siegert relation V2 295, V2 365
 silica, colloidal V2 7–8
 silicates, flotation V1 345
 silicone surfactants V1 122, V1 291–292
 silver halides V1 87–88, V1 90–92, V1 94–99
 SIMS *see* secondary ion mass spectrometry
 single-lamellar vesicles (SLVs) V2 45–46
 single-particle counting V2 358
 single-phase fluids V2 159
 sizing V1 125, V1 138–145, V1 152–153
 skin care
 amphoterics V1 364–365, V1 366–367, V1 368
 betaines V1 354
 cationic surfactants V1 327–328, V1 344
 organoclay V1 344
 slide hopper coating V1 88
 slip casting, ceramics V1 203, V1 212
 ‘slip-stick’ patterns V2 260–261
 SLNs *see* solid lipid nanoparticles
 SLS *see* static light scattering
 slurries V1 176
 SLVs *see* single-lamellar vesicles
 small-angle light scattering (SALS) V2 357, V2 362, V2 364–365
 small-angle neutron scattering (SANS)
 mesophases V2 301, V2 316
 micelles V2 281, V2 292–294
 microemulsions V2 71–72, V2 335, V2 347–349, V2 358
 rheology V2 205, V2 206, V2 211–212
 small-angle X-ray scattering (SAXS)
 mesophases V2 301, V2 316
 micelles V2 281, V2 292–294
 microemulsions V2 335, V2 358
 rheology V2 211
 ‘Smart’ surfaces V2 91–92
 smectics V2 300, V2 307, V2 315
 smectites, organoclay V1 343–344
 soaps V1 272–273, V1 280, V2 440
 sodium bis(2-ethylhexyl) sulfosuccinate (AOT) V2 65–67, V2 248, V2 364, V2 366–367
 sodium chloride V2 62, V2 64–66
 sodium dodecyl sulfate (SDS) V1 494, V2 241, V2 426, V2 427
 sodium polyacrylate (NaPA) V1 147–149
 soft surfactant systems V2 174–181
 sol, definition V2 4
 solid dispersions
 aggregation processes V2 15–19
 electrical properties V2 9–13
 rheology V2 19–20
 stability V2 5, V2 9, V2 13, V2 15
 synthesis V2 4–9
 solid formulations, agriculture V1 73–74
 solid freeform fabrication (SFF) V1 216
 solid lipid nanoparticles (SLNs) V1 12–13
 solid loading, ceramics V1 210–211
 solid/liquid interfaces V1 58–61
 solidification fronts V2 274–277
 ‘soloids’ V2 397
 solubility V1 46, V1 178, V1 375–376
 solubilization
 antifoaming agents V2 147–148
 binary solutions V2 160, V2 162–173
 capacity V1 69
 definition V2 159
 hydrotropes V1 409–412, V1 415, V1 418–419
 Jönsson model V2 165–166
 limit V2 345
 micelles V1 431, V1 432, V2 162–165
 organic compounds V2 246
 soft surfactant systems V2 174–181
 steric effects V2 166–169
 stiff surfactant systems V2 181–184
 surfactant–polymer systems V1 447
 ternary systems V2 173–184
 water-in-oil microemulsions V2 169–171, V2 174–177, V2 181–184
 solutions, spreading behaviour V2 136
 solvation shells V1 545
 solvents
 diffusion V2 288
 exchange model V2 172
 foodstuffs V1 43
 micellization V1 434
 multicomponent systems V1 501–502
 paints V1 119
 surface forces V2 404–407
 space partitioners V2 316–317
 Sparge tube technique V2 32–33
 spatial fluctuations V2 431–432
 speciality surfactants V1 121–122, V1 385–405
 specific surface area V2 360
 spin finishing V1 337, V1 338, V1 339
 spinning drop method V2 217, V2 222–223
 spinodal decomposition V2 416, V2 431
 sponge phases
 block copolymers V1 492–493
 characterization V2 352–355
 domain morphology V2 302, V2 305–306, V2 316, V2 317–319
 liquid crystals V1 482, V2 300

- sponge phases (*Continued*)
 micelles **V1** 439–440
 phase prisms **V2** 340–342
 spontaneous curvature **V2** 70–72, **V2** 160–161, **V2** 169
 spontaneous emulsification **V1** 74–76, **V1** 185
 SPR *see* surface plasmon resonance
 sprays, agriculture **V1** 80–83
 spreading **V2** 124–126, **V2** 134–136, **V2** 146, **V2** 149–150
 spring deflection **V2** 385–387
 SSFQ *see* steady-state fluorescence quenching
 stabilization
 aggregation **V1** 188
 common black films **V2** 431–433
 coupler dispersions **V1** 99–100
 dispersions **V1** 381–384
 electrostatic **V1** 108
 foams **V1** 306, **V2** 25–37
 foodstuffs **V1** 40–42
 micelles **V2** 148
 microemulsions **V1** 412, **V1** 414
 Ostwald ripening **V1** 186–187
 paper manufacture **V1** 130
 steric **V1** 9, **V1** 205, **V1** 377, **V1** 381–384
 suspension polymerization **V1** 192–193
 suspensions **V1** 209–210, **V1** 212, **V1** 213
 thin-liquid films **V2** 416–417, **V2** 426, **V2** 430
 stalagmometers **V2** 230–231
 starches, co-binders **V1** 149
 static cling **V1** 317
 static light scattering (SLS)
 CMC determination **V2** 242, **V2** 247
 micelle shape/size **V2** 294–296
 microemulsions **V2** 349
 particle size **V2** 357, **V2** 360–365, **V2** 368–369
 steady shear **V1** 149–152
 steady-state fluorescence quenching (SSFQ) **V2** 281, **V2** 290–292
 stereolithography **V1** 216
 steric effects
 forces **V2** 397, **V2** 405, **V2** 424, **V2** 426–427
 solubilization **V2** 166–169
 stabilization **V1** 9, **V1** 205, **V1** 377, **V1** 381–384
 Stern plane **V1** 224–225, **V1** 235
 Stern–Graham model **V1** 223
 ‘sticky’ contacts **V2** 208, **V2** 210
 stiff gels, ceramics **V1** 215
 stiff surfactant systems **V2** 181–185
 Stokes–Einstein equation **V1** 377, **V2** 230–231, **V2** 347, **V2** 366
 stratification **V2** 29, **V2** 30
 streaming potential **V1** 224–225, **V2** 371–372, **V2** 379
 stress-craze inhibitors **V1** 333–334
 stretching (antifoaming agents) **V2** 146, **V2** 149
 strontium myristate **V2** 325
 structural inversion **V2** 342–344
 structural viscous liquids **V2** 190
see also shear behaviour
 stylus contact method **V1** 165
 subbing layers **V1** 85
 sugars **V2** 171–172
 sulfobetaines **V1** 354–355
 sulfochlorination **V1** 282–284
 sulfosuccinates **V1** 289–291, **V1** 524–525
 sulfoxidation **V1** 284
 supercritical fluids **V2** 68
 superlattices **V2** 83
 supersaturation **V1** 184
 superspreaders **V2** 149–150
 support base, photography **V1** 85
 suprafluid liquids **V2** 190
 supramolecular forces **V2** 427–430
 supramolecular structuring **V2** 424
 surface charge
 aqueous media **V1** 220–229
 electrokinetics **V2** 371–382
 flotation **V1** 246–249
 molecular dynamics **V1** 545
 selective flocculation **V1** 243–244
 surface force apparatus (SFA) **V2** 384–385, **V2** 390–391, **V2** 415, **V2** 428
 surface plasmon resonance (SPR) **V2** 102, **V2** 103
 surface tension
 agrochemical sprays **V1** 80–83
 betaines **V1** 363–364
 CMC determination **V2** 241–242
 component approach **V2** 128–129
 contaminant detection **V2** 163
 definition **V2** 121
 detergency **V1** 54–58
 dynamic **V2** 225–238
 equilibrium **V2** 217–224
 film flotation **V2** 269
 Gemini surfactants **V1** 388
 gradients **V2** 150
 measurement **V2** 217–224, **V2** 225–238, **V2** 438–442
 paints **V1** 120–121
 perfluorocarbon fluids **V1** 179
 polymers **V1** 178
 sedimentation volume **V2** 273
 solidification fronts **V2** 274–277
 surfactant–polymer systems **V1** 445–446
 wetting **V2** 126–127
 surfaces
see also surface charge; surface tension
 activity **V1** 4–6, **V1** 44–48, **V1** 73, **V1** 105
 conduction **V2** 11–13
 depletion **V2** 429
 genus concept **V2** 304–306, **V2** 314
 geometry **V2** 387–388
 modification **V1** 403–404
 morphology **V1** 125
 reactions **V1** 247–249
 roughness **V1** 155–156, **V1** 158–159, **V1** 163–166
 separation measurement **V2** 385–387
 surface–surface interactions **V2** 383–414
 treatment **V1** 125, **V1** 138–145, **V1** 146–154, **V1** 245
 viscosity **V2** 27, **V2** 147
 surfactant affinity difference **V1** 258
 surfactant films **V2** 336, **V2** 354
 surfactant monolayer model **V2** 173
 surfactant number *see* critical packing parameter
 surfactant systems, drug effects **V1** 6–8
 surfactant–polymer flooding **V1** 259–262
 surfactant–polymer systems **V1** 445–463
 surfactants
see also zwitterionic surfactants
 adsorption **V1** 232–238, **V1** 240–241, **V2** 436–444
 agriculture **V1** 73

- amphipathic structure V1 232–233, V1 376
- amphoteric V1 294, V1 323, V1 349–350, V1 351, V1 355–372, V1 532–534
- anionic V1 271–292, V1 520–525, V2 147
- antifoaming agents V1 71–72, V2 147, V2 149
- aqueous solutions V2 190–191
- cationic V1 309–348, V1 529–532
- cleavable V1 291, V1 390–397
- commercial V1 484, V1 492, V2 63–64
- computer simulation V1 537–550
- concentration measurement V2 436–444
- corrosion inhibition V1 263–264
- cosurfactants V1 497–498, V2 63, V2 64, V2 65–66
- detergency V1 54–55, V1 58–61, V1 65–71
- dispersions V1 240–241
- droplet size V1 111–113
- emulsions V2 55
- environmental issues V1 509–536
- ethoxylated V1 107
- experimental techniques V1 237
- foams V1 254–256
- Gemini V1 314, V1 354, V1 385–390, V1 469, V1 496–497
- hydrophilic–lipophilic balance V1 180, V1 275, V1 310
- hydrotropes V1 500
- ionic V1 493–497, V2 64–66
- liquid crystals V1 465–508
- microemulsions V2 55–74
- mixed V1 498–499
- molecular dynamics V1 537–550
- nonionic V1 293–308, V1 480–493, V1 525–529, V2 57–64, V2 66–67, V2 166–169
- oil spill clean-up V1 264–265
- paints V1 105–110
- petroleum industry V1 252–256, V1 259–265
- phase behaviour V1 67–71, V1 480–493
- physico-chemical properties V1 421–443
- polymeric V1 373–384
- polymerizable V1 107–110, V1 397–405
- rheology V2 189–214
- secondary V1 365, V1 367
- self-assembly V1 252–254
- shear behaviour V2 205–214
- solubilization V2 159–186
- speciality V1 121–122, V1 385–405
- structure V2 245
- surface forces V2 397–404
- surfactant–polymer systems V1 445–463
- swelling V1 190
- thin-liquid films V2 415–417
- usage trends V1 510–511
- UV-curable V1 403–404
- vesicles V2 45, V2 48
- surfmers (polymerizable surfactants) V1 107–110, V1 397–405
- suspension layer stability V2 271–272
- suspension polymerization V1 103–104, V1 176, V1 192–193
- suspensions
 - agriculture V1 78–80
 - ceramics V1 203, V1 205, V1 208–212
 - consolidation V1 212–216
 - definition V2 4
 - foodstuffs V1 41
- suspoemulsions V1 73
- swelling
 - agents V1 184
 - domain morphology V2 319–321, V2 323
 - drug delivery systems V1 25
 - emulsions V1 190–191
 - exponents V2 331
 - heterophase polymerizations V1 190
 - radical polymerization V1 197
 - surfactant aggregates V2 166–168
 - surfactant–polymer systems V1 462–463
- syneresis V2 3
- synergistic effects V2 151–152, V2 429
- syntheses *see* manufacturing processes
- synthetic sizing agents V1 140
- tails V1 231, V1 377–379
- Tanford's formulae V2 303
- Tanner's law V2 134
- targeted drug administration V1 10–11
- temperature effects
 - contact angle V2 269, V2 276–277
 - critical micelle concentration V2 246
 - drug delivery V1 24–25
 - liquid crystals V2 300
 - micelles V1 425–428, V1 437, V1 440–442
 - microemulsions V2 60–70, V2 71–72
 - nuclear magnetic resonance V2 284
 - oxyethylene surfactants V1 440–442
 - vesicle phase transition V2 46–47, V2 50–52
- tensiometry V2 217–224, V2 225–238
- ternary systems V2 160–161, V2 173–185
- tetrapropylenebenzene sulfonate (TPS) V1 279
- textiles V1 511–512
- TFB *see* thin-film balance
- thermodynamics
 - drug delivery V1 15–23
 - emulsions V1 176–179
 - micellization V1 428–430
 - microemulsions V2 56
 - polymer adsorption V1 229–230
 - polymeric surfactants V1 374–375
 - vesicles V2 48–49
 - wetting V2 120, V2 121–134
- thermoplastic foams V2 40
- thermoporosimetry V1 169–170
- thermotropic liquid crystals V1 466, V2 300
- thickening V1 148–149, V1 323–325
- thin-film balance (TFB) method V2 36, V2 39, V2 417–424
- thin-liquid films V2 415–430, V2 431–433
- thixotropy V1 209, V1 210, V2 190
- three-phase contact lines V2 259–260, V2 265–266
- threshold effect V1 64, V1 288
- tilt angles V1 538, V1 542
- time-resolved fluorescence quenching (TRFQ) V2 281, V2 290–292
- titania (titanium dioxide) V1 114
- titration, soaps V2 440
- toothpastes V1 369
- topical drug administration V1 11, V1 18–19
- topography, paper V1 163–166
- topology V2 301, V2 314, V2 316–321

- toxicology
 amphoteric V1 364–365
 aquatic V1 518–519, V1 524–525, V1 529, V1 531–532, V1 534
 surfactants V1 515
 TPS *see* tetrapropylenebenzene sulfonate
 train formation V1 231, V1 377–379
 transition (particle behaviour) V2 275–276
 transport of liquids V1 162
 transurfs V1 401
 transverse diffusion (flip-flop) V2 47, V2 50
 TRFQ *see* time-resolved fluorescence quenching
 triglycerides V1 41, V1 296, V1 297
 Triton X-*n* solutions V2 228
 turbulent flow V2 18–19
 twin surfactants *see* Gemini surfactants
- Ultra Turrax system V1 183
 ultracentrifugation V2 367
 ultrasound V1 182–183, V2 155–156, V2 244
 ultraviolet (UV) curable surfactants V1 403–404
 ultraviolet (UV) spectroscopy V2 437–438
 undersize fractions V2 359
 undulation forces V2 426
 unilamellar vesicles *see* single-lamellar vesicles
- vaccination, oral V1 28
 van der Waals interactions
 ceramics V1 203–204, V1 205, V1 207
 colloidal dispersions V2 13–15, V2 16–17
 DLVO theory V1 131–132
 emulsion concentrates V1 76
 liquids V1 42–43
 measurement V2 392
 molecular dynamics V1 539–540
 pigment dispersion V1 115
 powder systems V1 50
 sedimentation V2 269, V2 272
 thin-liquid films V2 424
 wetting thermodynamics V2 127, V2 128
 vapour phase methods V2 9
 vapour pressure osmometry V2 244, V2 247
 vapour transport V1 161
 vesicles
 antifoaming agents V2 149–150
 autopoiesis V2 50–52
 bilayer solubilization V2 171–173
 fatty acids V2 49–50
 formation V2 47–49
 hydrotropes V1 418
 phase structure/transition V2 46–47
 polymerization V2 49
 rheology V2 200–204, V2 211–213
 viscoelasticity
 ceramics V1 210
 measurement V2 388–389
 paper coatings V1 151–152
 rheology V2 190, V2 193–198
 thickeners V1 325
 viscose V1 337, V1 338, V1 339
 viscosity
see also thickening
- amphoteric surfactants V1 365, V1 366–368
 antifoaming agents V2 147
 ceramics V1 209–211
 CMC determination V2 244
 colloidal dispersions V2 19–20
 dilational V2 235
 dispersions V1 240
 foam stabilization V2 26, V2 27
 Gemini surfactants V1 390
 micelle concentration V1 436
 microemulsions V2 335
 rheology V2 192–199
 shear behaviour V2 206–207, V2 211
 surfactant–polymer systems V1 449, V1 452
 visible spectroscopy V2 437–438
 volatility of liquids V2 122–123
 volume fraction V2 345–346, V2 349–350
 volume restriction interaction V1 382–383
- w/o see* water-in-oil
 Washburn equation V1 159–161, V2 138–139, V2 272
 washing *see* detergency
 waste-water treatment V1 510, V1 515, V1 517, V1 520, V1 529
 water
see also aqueous systems
 bridges V1 50
 flooding V1 261
 hardness V1 61–65, V1 272–273, V1 288, V1 314
 solubilization V2 169–171
 water-borne paints V1 116–119
 water-continuous phases V1 479–480
 water-in-oil (w/o) microemulsions V2 169–171, V2 174–177, V2 181–184
 waveguide format V2 88, V2 89
 Weaver–Bertucci equation V2 143–144
 wedge model V2 180–181
 Wenzel's equation V1 155
 wet strength, paper V1 145–146
 wetting V2 119–142
 agriculture V1 73, V1 78–79, V1 81–83
 amphoteric V1 365
 anionic surfactants V1 285, V1 288
 capillary penetration V2 136–140
 cationic surfactants V1 325–326
 counterions V1 274
 crude oil V1 254, V1 255
 detergency V1 54–58
 foodstuffs V1 48–49
 imperfect solid surfaces V2 129–134
 Langmuir–Blodgett films V2 82–83, V2 91–92
 paints V1 119–121
 paper V1 127–128, V1 142, V1 144, V1 154–159
 pigment dispersion V1 114
 porous surfaces V2 138–140
 solid surfaces V2 126–129
 spreading V2 124–126, V2 134–136
 sulfosuccinates V1 289, V1 290
 tension V2 126
 thermodynamics V2 120, V2 121–134
 thin-liquid films V2 431
 wicking V1 161, V2 120, V2 132

- Wilhelmy plate method **V2** 217–218, **V2** 219–220, **V2** 267–269
 Williamson synthesis **V1** 275, **V1** 276
 Winsor equilibria, emulsification failure **V2** 161, **V2** 178, **V2** 351–352
 Winsor's *R* ratio **V1** 258
 wood preservatives **V1** 318, **V1** 320–321
- X-ray photoelectron spectroscopy (XPS) **V1** 144–145, **V1** 162–163, **V2** 105–106
 X-ray reflectivity **V2** 427
 X-ray scattering *see* small-angle X-ray scattering
 xanthogenation **V1** 337, **V1** 338, **V1** 339
 XPS *see* X-ray photoelectron spectroscopy
- yeast (*Saccharomyces cerevisiae*) **V2** 112
 Young equation
 agriculture **V1** 78–79
 background **V2** 120, **V2** 133–134, **V2** 252
 detergents **V1** 56
 modification **V2** 122–131
 petroleum **V1** 254
 porous solids **V2** 74, **V2** 138–139
- Young–Laplace equation **V2** 219, **V2** 222–223
- zeolites **V1** 61–65
 zeta potential
 electrokinetics **V2** 374, **V2** 380–381
 experimental techniques **V1** 237–238
 flotation **V1** 248–249
 manipulation **V1** 225–226
 measurement **V1** 224–225
 surfactant adsorption **V1** 235, **V1** 237–238
 Ziegler process **V1** 279, **V1** 294–295
 Zimm plots **V2** 295
 zirconium myristate **V2** 327
 Zisman plots **V1** 120–121
 zwitterionic surfactants
 characterization **V1** 361–372
 chemistry **V1** 349–355
 critical micelle concentration **V2** 245
 emulsions **V1** 257
 paints **V1** 118
 phase behaviour **V1** 493
 rheology **V2** 196–199, **V2** 201–202, **V2** 208–210, **V2** 213